NATURE
ENVIRONMENT
& POLLUTION
TECHNOLOGY

A Multidisciplinary, International Journal
on Diverse Aspects of Environment

Technoscience Publications
website: www.neptjournal.com

Nature Environment and Pollution Technology

(An International Quarterly Scientific Research Journal)

INSTRUCTIONS TO AUTHORS

Scope of the Journal

The Journal publishes original research/review papers covering almost all aspects of environment like monitoring, control and management of air, water, soil and noise pollution; solid waste management; industrial hygiene and occupational health hazards; biomedical aspects of pollution; conservation and management of resources; environmental laws and legal aspects of pollution; toxicology; radiation and recycling, etc.

Format of Manuscript

- The manuscript (mss) should be typed in double space leaving wide margins on both the sides.
- First page of mss should contain only the title of the paper, name(s) of author(s) and name and address of Organization(s) where the work has been carried out along with the affiliation of the authors.

Nature Environment and Pollution Technology
Vol. 24, No. (S1), Special Issue, 2025
CONTENTS

The Journal is Currently **Abstracted and Indexed** in:

CNKI Scholar (China National Knowledge Infrastructure)

Scopus Cite Score (2023) 1.2

Scopus®, SJR (2023) 0.204

Index Copernicus (2022) = 132.21

Indian Science Abstracts, New Delhi, India

Chemical Abstracts, U.S.A.

Pollution Abstracts, U.S.A.

Elsevier Bibliographic Databases

Paryavaran Abstract, New Delhi, India

Zoological Records

CAB Abstracts, U.K.

Electronic Social and Science Citation Index (ESSCI)

Indian Citation Index (ICI)

CrossRef (DOI)

EBSCO: Environment Index™

ProQuest, U.K.

Google Scholar

DOAJ

Zetoc

J-Gate

Environment Abstract, U.S.A.

Centre for Research Libraries

Elektronische Zeitschriftenbibliothek (EZB)

CSA: Environmental Sciences and Pollution Management

Access to Global Online Research in Agriculture (AGORA)

Present in UGC-CARE List (Group II)

WorldCat (OCLC)

British Library

Connect Journals (India)

Indian Science

JournalSeek

Research Bible (Japan)

SHERPA/RoMEO

Directory of Science

AGRIS (UN-FAO)

Ulrich's (Refereed) database

NAAS Rating 2024 = 5.33

UDL-EDGE (Malaysia) Products like i-Journals, i-Focus and i-Future

www.neptjournal.com

Nature Environment and Pollution Technology

Design and Impact Analysis of a Grid-Connected Solar Photovoltaic System in Ibri, Oman

Arshad Mehmood† and Waleed Saif Abdullah Habib Al Kalbani

Department of Mechanical Engineering, College of Engineering, University of Buraimi, Al Buraimi 512, Oman
†Corresponding author: Arshad Mehmood; arshad.m@uob.edu.om

ABSTRACT

This study investigates the feasibility of establishing a grid-connected power system in Ibri, Oman. The primary goal is to address the rising energy demands and contribute to fighting climate change. By leveraging Ibri's resources, the research highlights the feasibility of such a system, focusing on its economic, technological, and environmental benefits. Using PVsyst software for planning and evaluation, the study assesses climate conditions, component choices, and performance predictions to ensure optimal system performance. The proposed 10.81 kWp solar power system estimates an energy production of 16,981 kWh, achieving a system efficiency of 67.2% based on the performance ratio (PR). The financial analysis estimates a payback period of 7.5 to 8.3 years, with an internal rate of return (IRR) of 11.15% and a net present value (NPV) of $32,024.28, confirming the project's viability. The system is expected to reduce carbon emissions by 379.939 tons over its lifetime, highlighting the significant ecological benefits of adopting solar energy (SE). The research demonstrates that incorporating PV systems in regions like Ibri is technically viable, economically beneficial, and environmentally advantageous. This study is a valuable resource for energy initiatives, promoting sustainable power production methods and encouraging the broader adoption of renewable technologies for a sustainable future.

INTRODUCTION

Solar energy (SE) is a sustainable option with the capacity to address the energy requirements of developing nations. Emphasizing its eco-friendly attributes, solar power has been identified as a critical avenue for achieving the IEA goal of net-zero emissions by 2050(Mukhopadhyay 2022). SE is seen as a vital contributor to enhancing energy efficiency and meeting growing energy demands (Bagwari et al. 2022). Despite its potential to mitigate greenhouse gas emissions, broader adoption is necessary to maximize its impact (Maran et al. 2022). SE's pivotal role extends beyond energy production to fostering development, job creation, and environmental preservation (Sheikholeslami 2023). There are two primary SE systems: PV and solar thermal. Solar PV systems convert light into electricity using cells and are considered a leading energy conversion method (Qingyang et al. 2021), while solar thermal captures heat for electricity generation and other uses (Shekhar 2018). Recent technological advances in solar cells and power electronics aim to boost the efficiency of solar PV generation (Nayak et al. 2022, Xu et al. 2023). The deployment of various solar configurations, including grid-tied, off-grid, large-scale, and building-integrated systems, demonstrates solar technology

versatility and its contribution to reducing emissions and utilizing space effectively (Nayak et al. 2022). Solar PV systems have a notable lifespan, maintaining operational viability for up to 30 years, and are lauded for their ease of access as a renewable source (Peters & Sinha 2021, Rahman et al. 2023). The reduction in carbon dioxide emissions by using PV modules is significant, with ongoing research to improve the reliability of PV technology through mechanical enhancements and the application of efficiency-boosting coatings (Alimi et al. 2022, Yamaguchi et al. 2022).

Oman is actively pursuing SE, with investments in solar farms and an aim to increase wind production(Charabi 2023, Emerald Insight 2022, Ninzo et al. 2023). The country's solar radiation varies seasonally, reaching its zenith in June and ebbing in December (Zurigat et al. 2007), with year-round potential for solar power generation (Gastli & Charabi 2010, Tabook & Khan 2021). Innovative site selection for PV systems employs a variety of methodologies, including fuzzy analytical processes and integrated approaches that consider environmental and economic factors, supported by tools like GIS and BIM (Guo et al. 2021, Lee et al. 2015, Yousefi et al. 2018). Oman's commitment to sustainability is evident in its ambition to source 30% of electricity from

renewables by 2030 and the national oil company's strategy to shift a significant portion of its power usage to renewable sources (Al-Badi et al. 2009, Coyle 2017). This study assesses the deployment of a 10.8 kWp grid-connected solar PV system in Ibri, Oman, harnessing the area's high solar irradiance. Utilizing PVsyst software, the research aims to optimize the plant design and performance, factoring in local environmental conditions for enhanced efficiency. Covering a literature review, case study analysis, and system design optimization, the study evaluates both technical and economic feasibility, including environmental impact. The findings suggest Ibri's potential for advancing energy self-sufficiency and sustainable development, offering strategies for efficient solar PV usage that can inform renewable energy practices and aid Oman's renewable energy goals.

MATERIALS AND METHODS

Site Information

The design of a 10.81 KWp grid-connected solar PV system for a residential building in Ad Dubayshi, Ibri, Oman (23.1186°N, 56.4872°E). Using PVsyst software for optimization, the system, covering a roof area of 127 m² out of the available 1485 m², provides a stable and cost-effective energy solution as shown in Fig. 1. The configuration allows for surplus energy to be fed back to the grid, enhancing

sustainability and offering financial incentives without the need for battery storage, suitable for both urban and remote applications.

Theoretical Background

PV systems transform sunlight into electricity by utilizing solar cells composed of semiconductor materials. These cells consist of layers of p-type and n-type semiconductors that possess different electrical properties; the p-type is abundant in positively charged holes, whereas the n-type is rich in electrons. At the junction of these layers, a depletion layer forms where charge carriers are sparse, creating an electric field as present in Fig. 2. This field is crucial for directing the movement of electrons to the n-type layer and holes to the p-type layer. When sunlight is absorbed by the semiconductor, photons energize the electrons, freeing them to move. This motion of electrons and holes under the influence of the electric field generates a flow of electricity and establishes a voltage across the cell. Connecting the solar cell to an external circuit allows this electricity to power devices, effectively converting SE into usable electric power.

System Overview and Components

The SPV system comprises elements such, as PV panels, batteries, inverters, charge controllers, cables the utility grid,

Fig. 1: Satellite view of the targeted location at coordinates 23.1186°N, 56.4872°E.
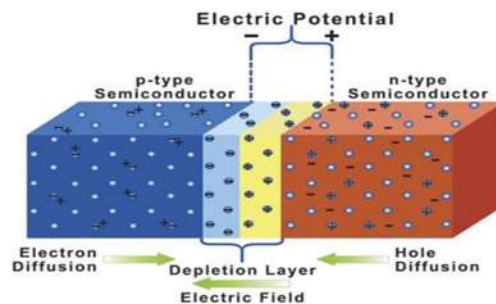
Fig. 2: Simplified version of solar cell.
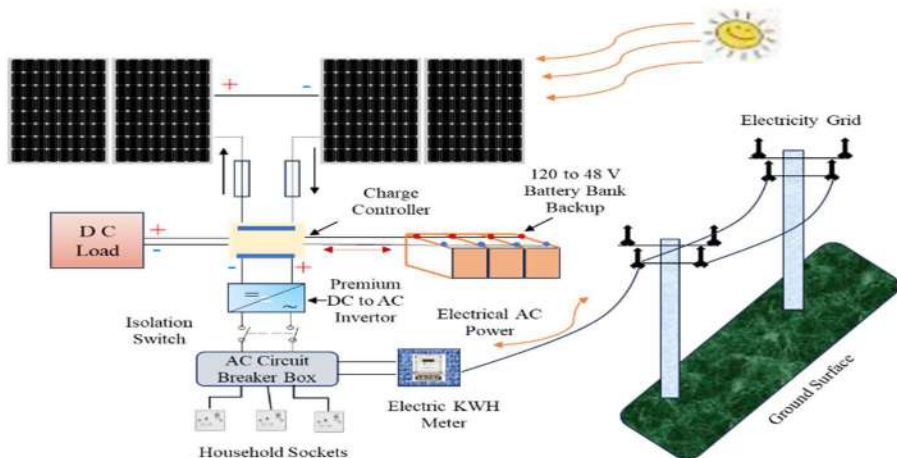
Fig. 3: A schematic representation of a solar power system connecting to the electricity grid and household sockets.

net metering, and loads as illustrated in Fig. 3. The direct current power produced by PV modules.

PV Arrays Selection

To achieve results, in this research we have tested monocrystalline solar panel models to select the most suitable PV array for different requirements, from the 'Trinca Solar' brand. Maximizing the efficiency of grid-connected PV systems involves critical components like PV arrays and inverters, analyzed using PVsyst software. This simulation, illustrated in a current-voltage (I-V) curve, demonstrates how a PV module's current and voltage respond to varying solar irradiance levels, from 200 W/m^2 to 1000 W/m^2 as depicted in Fig. 4. The curve highlights the MPP, where current and voltage multiply to yield the highest power output, decreasing as irradiance diminishes. Notably, the typical operating temperature for PV cells is 45°C, affecting performance as temperature rises. The study examines different Si-Mono PV modules under maximal solar radiation of 1000 W/m^2, showing varying power outputs:

- TSM-DD05H-08-(II)-295 generates 273.5 W with a current of 9.12 A and a voltage of 32.4 V.

- TSM-DD05H-08-(II)-305 produces 283.3 W, with a current of 9.25 A and a voltage of 33.1 V.

- TSM-DD05H-08-(II)-315 offers 292 W, with a current of 9.43 A and a voltage of 33.4 V.

- TSM-325DD14A(II) yields 299.9 W, with a current of 8.69 A and a voltage of 37.4 V.

- TSM-325DD14A(II) at 335 Wp outputs 308.9 W, with a current of 8.87 A and a voltage of 37.8 V.

This analysis underscores the influence of solar irradiance and temperature on the performance of PV modules, guiding optimal system configuration for enhanced SE utilization.

Solar Inverter

The K-solar KSY-11K on-grid solar inverter is selected for its high efficiency and performance, with a maximum efficiency of 98.20% and a EURO efficiency of 97.50%. It offers a nominal AC power output of 10.5 kW and supports a maximum DC input voltage of 1000 V, with dual MPPT inputs for optimal solar power generation from various PV array orientations as shown in Fig 5 (a, b). This transformerless inverter is lightweight and efficient, capable of delivering its full-rated power up to an ambient temperature of 45°C, with output power derating at higher temperatures. Designed for compatibility with 400 V grid systems and configurable for 50 Hz or 60 Hz, it is ideal for international applications. Featuring power factor correction to minimize reactive power charges, the inverter operates with zero power consumption at night. Suited for commercial installations, it offers robustness and versatility across different on-grid PV system configurations.

Solar Orientation Analysis

The solar orientation analysis, including tilt and azimuth angles, plays a vital role in optimizing solar panel placement for maximum energy absorption. The angle (α), ideally set to match the location's latitude, is determined to be 25° for this installation, closely aligning with the geographic latitude of 23°. The azimuth angle, crucial for directing the panels towards the sun, is measured in degrees from north (0°), with optimal solar exposure achieved when panels face true south (180°) in the Northern Hemisphere. This orientation ensures the panels capture the maximum sunlight, as direct north orientation would significantly reduce sunlight capture. Additionally, albedo, which reflects the earth's surface's ability to reflect sunlight, varies by location and surface texture. For this specific site, an albedo value of 0.2 is used,

(a)

(b)

(c)

(d)

(d)
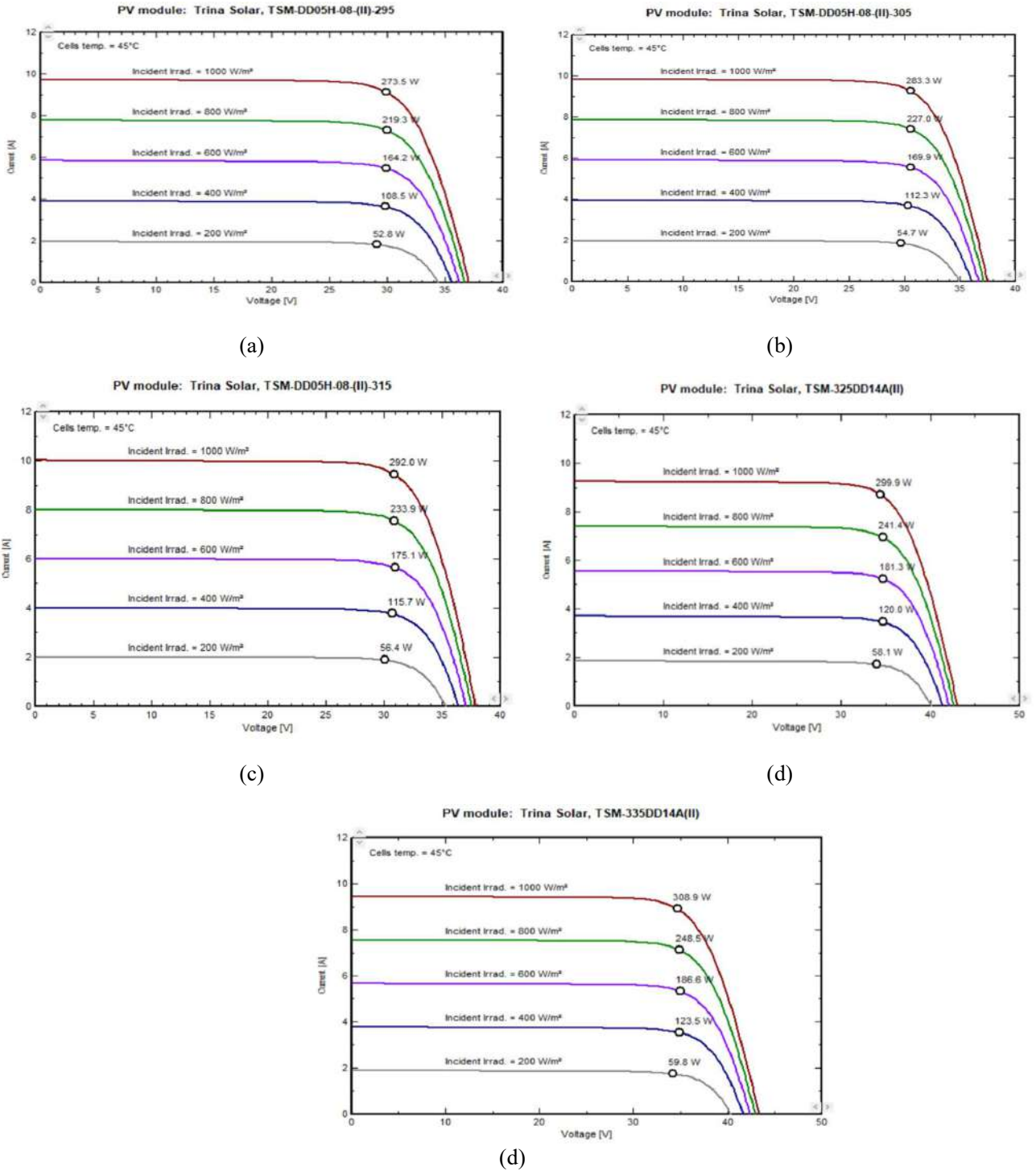
Fig. 4: The characteristics of irradiation effect by PV Si-Mono, (a) 295 Wp, 27 V; (b) 305 Wp, 27 V; (c) 315 Wp, 28 V; (d) 325 Wp, 32 V; and (e) 335 Wp, 32 V.
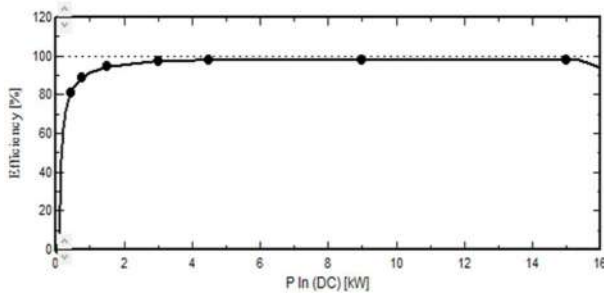
Fig. 5 (a): Efficiency vs input power curve of inverter.
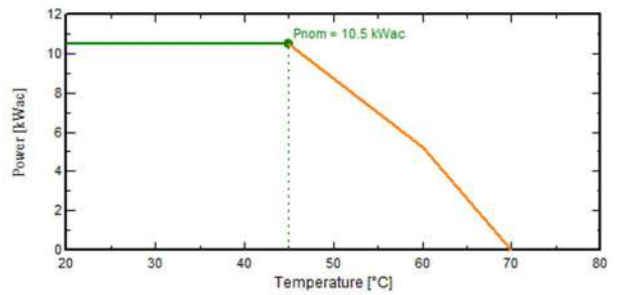
Fig. 5 (b): Power output vs temperature curve of inverter.

indicating moderate reflectivity. Adjusting both tilt and azimuth angles according to these principles is essential for enhancing the solar power system's efficiency and output.

Climatic and Geographic Resource

Fig. 6 is a sun path diagram for a specific location at Ad Dubayshi, with a latitude of 23.1886° N and a longitude of 56.4872° E, at an elevation of 333 meters. A sun path diagram is used to show the trajectory of the sun across the sky at different times of the day throughout the year. This particular diagram is set to local legal time. The curved lines represent the sun's path on given dates, marked by the numbered annotations (1 to 7), with the corresponding dates listed in the legend. These dates typically represent different times of the year, such as solstices and equinoxes, as well as points mid-way between them. For example, "1" marks the path on June 22nd, which is around the time of the summer solstice when the sun is highest in the sky. The concentric circles indicate the sun's altitude above the horizon in degrees, and the radial lines show the azimuth in degrees, where 0° is true north, 90° is east, 180° is south, and 270° is west. The shaded area signifies the periods during which the sun is above the horizon, that is, daytime. As the sun's elevation changes

throughout the day, its position moves along a particular path corresponding to the date. The time of day is indicated by the curved lines that intersect the sun paths, labeled with hour markers (from 6 am to 6 pm in this case).

Our region utilizes Meteonorm to analyze the climatic conditions. PVSyst provides weather data, including wind speed, temperature, global horizontal irradiation, and diffuse horizontal irradiation. Table 1 elaborates, on the outcomes derived from Meteonorms weather assessments.

Numerical Simulation using PVSyst

PVsyst software is a sophisticated, user-friendly tool for designing and simulating PV systems, ideal for professionals and researchers. It features an intuitive interface, and a comprehensive meteorological database, and allows for manual data input for tailored analysis. Detailed reports with graphs and tables analyze various performance metrics, optimizing PV system performance.

Site Assessment for PV

The site assessment for a PV system in Ibri, Oman, based on data from 2021 to 2023 includes three key factors: solar
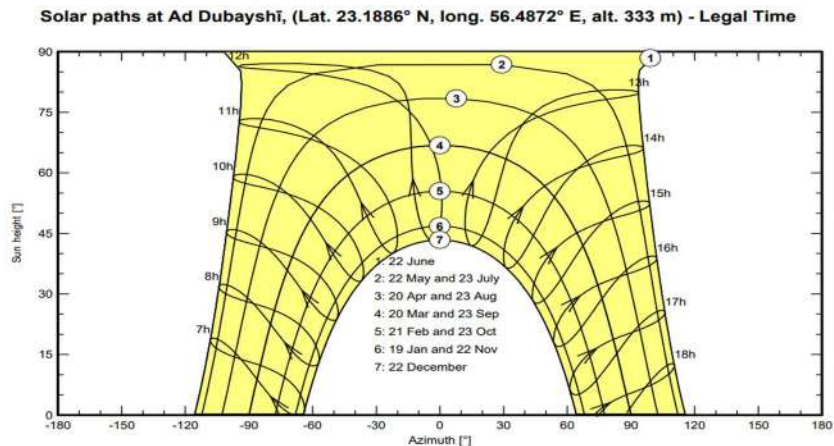
Fig. 6: Sun path diagram.

Table 1: Monthly weather from Meteonorm.

	Global horizontal irradiation	Horizontal diffuse irradiation	Temperature	Wind velocity	Linke turbidity	Relative humidity
	kWh/m^2/mth	kWh/m^2/mth	°C	m/s	[-]	%
January	140.6	35.4	18.0	2.90	4.061	58.1
February	146.4	47.5	20.3	3.30	5.036	48.0
March	178.5	74.4	24.4	3.49	6.338	37.1
April	203.7	76.4	29.0	3.40	7.000	29.2
May	216.1	91.0	34.1	3.31	7.000	23.1
June	206.3	100.0	35.7	3.40	7.000	27.1
July	199.6	104.5	37.3	3.60	7.000	29.5
August	188.4	103.6	37.0	3.49	7.000	29.9
September	181.9	77.0	34.0	3.29	7.000	32.4
October	170.2	57.4	30.5	3.00	5.261	34.1
November	147.2	34.7	24.4	2.80	4.199	48.7
December	133.1	36.1	20.0	2.70	3.951	57.1
Year	2112.0	838.0	28.7	3.2	5.904	37.9

Global horizontal irradiation year to year variability 6.1%

radiation, clearness index, and temperature. Despite high solar radiation peaking in May and June, the clearness index dips during these months due to atmospheric conditions like dust, impacting the effectiveness of radiation reaching the ground. Higher temperatures in these months could also reduce PV module efficiency. Overall, while high radiation suggests good electricity generation potential, variable clearness and high temperatures could affect overall system performance as presented in Fig. 7 (a, b). Decision-making for PV installation must consider these environmental factors along with economic and physical aspects.

Case Study

The plant has been designed by analyzing the daily electricity usage of a residential building located in Ibri Oman. To ensure a continuous supply put the loads data collection and load calculation are compulsory. The daily power demand can be calculated as follows from eq. 1 to eq. 4:

$$P_T = n \times P_R \qquad …(1)$$

$$E_T = h \times P_T \qquad …(2)$$

$$P_D = \sum E_T \qquad …(3)$$

$$E_g = 1.2 \times P_D \qquad …(4)$$

where, P_R is rated power, P_T is total power, E_T is total energy, P_D is power demand, E_g is gross energy, h is number of hours, and n is number of applications. The different appliances connected in residential buildings are given in Table 2 with their power ratings then the calculation is done for the total power and total energy based on h and n.

Performance Analysis

The analysis of the grid-connected PV system is conducted using specific parameters as recommended by the IEA. These parameters include: (Munshi 2023).
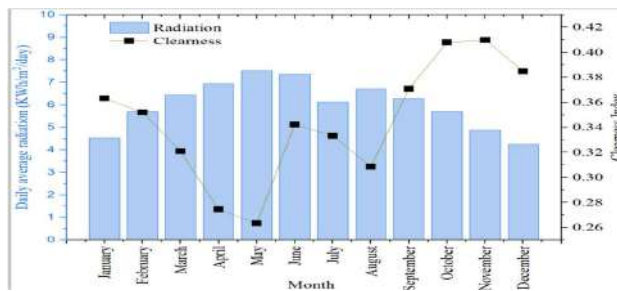
Fig. 7 (a): Global solar radiation and clearness.
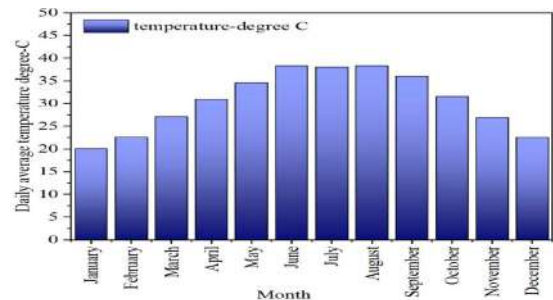
Fig. 7 (b): Average temperature yearly basis.

Table 2: Appliances used in a typical residential building.

Reference mark	Purpose	Rated power (KW)	n	Total power (KW)	Hour used h	Total energy (KWh / day)	Hours distribution
Room Air Conditioners	bedrooms and living areas	2	2	4	8	32	12 pm to 4 pm and 12 am to 4 am
Ventilation	maintaining air quality	0.1	1	0.1	24	2.4	All day
Dish and cloth washer	cleaning dishes and laundering clothes	1	1	1	2	2	12 pm to 2 pm
Refrigerator / Deep freezer	large unit	0.8	2	1.6/day	24	1.6	All day
Electric Stove /oven/Microwave	for cooking	3	1	3	6	18	9 am to 3 pm
Lighting	LED lighting	0.01	20	0.2	8	1.6	6 pm to 2 am
TV/PC/Mobile	entertainment	0.15	2	0.3	5	1.5	6 PM to 11PM
Stand by consumers	other useful household items	0.01	--	0.01	24	2.4	All day
Total Power				10.81		61.5	

Array Yield (Y_a): This represents the direct current (DC) energy generated by the solar photovoltaic (SPV) panel over a defined period (daily, monthly, or yearly) relative to its nominal power (rated capacity) at STC. It is quantified as:

$$Y_a = \frac{DC\ Energy\ Generated\ (DC\ voltage \times DC\ current \times time)}{Nominal\ Power\ at\ STC}$$
$$...(5)$$

where DC energy is expressed in kWh and nominal power in kWp.

Reference Yield (Y_r): This metric assesses the efficiency of solar irradiation capture by comparing total horizontal solar irradiance to the global irradiance at STC, yielding an equivalent number of hours at global irradiance:

$$Y_r = \frac{Total\ Horizontal\ Irradiance}{Global\ Irradiance} \quad ...(6)$$

with total horizontal irradiance in kWh/m² and global irradiance in W/m².

Final System Yield (Y_f): This ratio indicates the total AC energy output from the inverter as a proportion of the rated SPV array power:

$$Y_f = \frac{AC\ Energy\ Output}{Peak\ Power} \quad ...(7)$$

Performance Ratio (PR): An essential measure of a PV system's operational efficiency, the PR compares the actual system output to its theoretical potential by dividing the final system yield by the reference yield:

$$PR = \frac{Final\ System\ Yield}{Reference\ Yield} \quad ...(8)$$

This ratio highlights system losses during DC to AC conversion, accounting for factors such as irradiation levels, panel temperature, and grid availability.

Capacity Utilization Factor: This evaluates the actual output of a PV plant against its maximum possible output:

$$Capacity\ Utilization\ Factor =$$
$$\frac{Energy\ measured\ in\ KWh}{365 \times 24 \times Installed\ capacity\ of\ PV\ plant} \quad ...(9)$$

Inverter Efficiency: Defined as the ratio of AC output power to DC output power, reflecting the conversion efficiency of the inverter:

$$Inverter\ Efficiency = \frac{AC\ output\ power}{DC\ power} \quad ...(10)$$

System Efficiency: This is calculated by multiplying the PV module efficiency by the inverter efficiency.

Energy Output: The energy directed to the utility grid is monitored at the inverter's AC output terminals, both daily and monthly (Kim et al. 2023) .

Energy Losses: The overall efficiency and performance of a PV system are impacted by two primary types of losses:

System Losses (L_s): Resulting from inverter inefficiencies.

Array Capture Losses (L_c): Due to factors like shading, module mismatch, and soiling that affect the PV array's ability to capture and convert SE efficiently.

$$L_s = Y_a - Y_f \quad ...(11)$$
$$L_c = Y_r - Y_a \quad ...(12)$$

These comprehensive analyses provide critical insights into the performance and optimization potential of PV installations.

System Orientation

To get the right and optimal selection of Solar PV devices, simulations are performed with different solar PV device
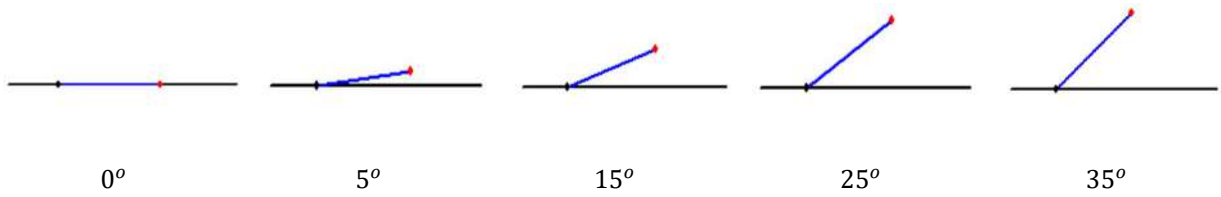
Fig. 8: Various tilt angles (α) used in simulation results for PV orientation at 0°, 5°, 15°, 25°, and 35°.

Table 3: Constant and variable in PVsyst simulation.

Selection	Parameter selection	Desired values
Constant	Longitude	E
	latitude	E
	Albedo	0.2
	Azimuth	0
	Invertor	10.5 KW
	System losses	Described in Table 3
Variable	Tilt Angle (annual basis) ⬚	, , 1, 2, 3
	PV system capacity	295, 305, 315, 325, 335

Table 4: Simulation results with PV module variants.

Simulation	PV orientation	PV					Invertor			
		Model	Capacity	No. of modules	Pnom total	Module Area	Capacity	No,	E_{array}	E_{grid}
1	Tilt 0	S- Mono (TSM-DEG5-II-295	295,27 V	38	11.21	61	10.5 Kw ac	1	16266	15887
2	Tilt5								16802	16417
3	Tilt 15								17549	17155
4	Tilt 25								17852	17453
5	Tilt 35								17705	17308
6	Tilt 0	S- Mono TSM-DD05H-08-(II)-305	305, 28V	36	10.98	58	10.5 Kw ac	1	16844	16458
7	Tilt5								17400	17007
8	Tilt 15								18175	17772
9	Tilt 25								18489	18082
10	Tilt 35								18337	17931
11	Tilt 0	S- Mono TSM-DD05H-08-(II)-315	315, 28V	38	11.97	57	10.5 Kw ac	1	17372	16979
12	Tilt5								17945	17545
13	Tilt 15								18745	18333
14	Tilt 25								19069	18653
15	Tilt 35								18912	18498
16	Tilt 0	Si-Mono TSM-325 DD14A (II)-325	325WP, 32V	34	11.05	64	10.5 Kw ac	1	16036	15660
17	Tilt5								16554	16172
18	Tilt 15								17272	16882
19	Tilt 25								17556	17161
20	Tilt 35								17408	17015
21	Tilt 0	Si-Mono TSM-325DD14A(II)-335	335WP, 32 V	32	10.72	62	10.5 Kw ac	1	16536	16154
22	Tilt5								17069	16680
23	Tilt 15								17809	17411
24	Tilt 25								18101	17699
25	Tilt 35								17949	17549

Table 5: Description of losses.

Loss Fraction	Measurement Unit	
Module Quality loss: The difference between PV module performance as specified by the manufacturer and actual performance	Loss Fraction 1.1 %	
Light-Induced Degradation Loss: decrease in efficiency that some solar panels experience when they are first exposed to sunlight.	Loss Fraction 2 %	
Soiling Losses: loss due to dust particles which gets accumulated on solar panels over time	Loss Fraction 3 %	
Series Diode Loss: Occurs due to the voltage drop across diodes which are used in solar panels to prevent reverse current flow.	Voltage drops 0.7 V	Loss Fraction 0.1% at STC
Module Mismatch Loss: occurs when there is a variation in the performance of individual solar modules in an array, which can lead to less-than-optimal energy production.	Loss Fraction 2% at MPP	
Thermal Loss according to irradiance: Occurs due to the increase in cell temperature, which typically causes a decrease in PV module efficiency.	U_c (constant) U_n (wind)	29.0 W/K 0.0 W/K/m/s
String Mismatch Loss: occurs when there is a discrepancy in output between different strings of solar panels due to variations in shading, orientation, or panel degradation.	Loss Fraction 0.1 %	
DC Wiring Losses: due to the resistance in the DC cabling that connects the solar panels to the inverter, which can cause energy to be lost as heat.	Global array res. 103 mW	Loss Fraction 1.5% of STC
Module average degradation: The annual percentage decrease in module performance over time is missing. Solar panels slowly degrade each year, reducing their output.	Years 10	Loss Factor 0.4%/year
Mismatch due to degradation: Over time, modules degrade at different rates, which can increase mismatch losses.	Imp RMS Dispersion 0.4%/year	Vmp RMS Dispersion 0.4%/year
IMA Loss Factor: possibly associated with installation and maintenance adjustments or inaccuracies in modeling versus actual performance.	ASHRAE Param: IMA Bo Param	1-bo(1/cosi-1) 0.05

models so that the results can be seen with different PV orientation variants 0°, 5°, 15°, *25°* and 35° shown in Fig. 8. These parameters are detailed in Table 3, which outlines the constant and variable parameters used in the PVsyst simulation. The results of these simulations, showcasing the performance of PV modules at varying orientations and capacities, are presented in Table 4**.**

System Losses

The proposed methodology is ensured for a 30-year lifespan for the selected site. During this period, many losses take place inside the system and become the main reasons for the malfunctioning of the mechanism. In this section various losses are described, to understand the quality of the system performance. These are explained below in Table 5.

RESULTS AND DISCUSSION

Summary of the PV System

The PV system simulation at Ad Dubayshi, using PVSyst 7.3 software without considering shading, utilized TSM-DD05H

(II)-315 modules and a KSY-11K inverter oriented at 25 degrees. The annual energy output was 16,981 kWh with a specific yield of 1,419 kWh/kWp as shown in Fig. 9 (a). The PR was 0.672, factoring in losses detailed in the system and array efficiencies. Fig. 9 (b) illustrates a positive correlation between daily energy output (kWh/day) and global solar irradiance (kWh/m²/day), demonstrating typical variability in production influenced by meteorological conditions and solar angles over the year.

Balances and Main Results

The PVsyst software analysis presents detailed performance metrics for a PV system, including global horizontal irradiation at 2112.0 kWh/m²/year and incident irradiation on the collector plane at 2111.2 kWh/m²/year. Diffuse irradiation is measured at 837.8 kWh/m² with an average ambient temperature of 28.76°C. The PV array produces a total annual energy yield of 17,375 kWh, with 16,981 kWh delivered to the grid. The system's PR averages 67.2% annually, with grid injection ranging from 1,098 kWh in December to 1,710 kWh in May.

(a)

(b)

Fig. 9: Summary of the PV system (a) Annual performance data of a grid-connected PV system; (b) Daily PV energy output relative to solar irradiance.

Normalized Performance Coefficient and PR

The International Electrotechnical Commission (IEC) has set standardized metrics such as the normalized production coefficient and PR to benchmark PV system performance.

Fig. 10 (a) in the report delineates the monthly normalized production, which is detailed in Table 6. Fig 10 (b) showcases the monthly PR. The reported normalized array losses, termed collection loss and denoted as Lc, are 1.81 kWh/kWp/day. Additionally, the normalized system losses, including

Table 6: Balances and main results.

Month	GlobHor kWh/m^2	DiffHor kWh/m^2	T_Amb °C	GlobInc kWh/m^2	GlobEff kWh/m^2	EArray kWh	E_Grid kWh	PR ratio
January	140.6	35.4	17.98	140.6	10.4	1206	1176	0.699
February	146.4	47.5	20.33	146.4	136.6	1247	1219	0.696
March	178.5	74.4	24.41	178.3	167.9	1502	1469	0.688
April	203.7	76.4	28.99	203.6	192.8	1682	1646	0.676
May	216.1	91.0	34.05	216.1	204.7	1749	1710	0.661
June	206.3	100.0	35.68	206.3	195.6	1660	1622	0.657
July	199.6	104.5	37.31	199.5	189.0	1596	1559	0.653
August	188.4	103.6	36.97	188.3	178.1	1509	1474	0.654
September	181.9	77.0	34.00	181.9	171.7	1475	1442	0.662
October	170.2	57.4	30.46	170.2	160.0	1398	1364	0.669
November	147.2	34.7	23.35	147.0	136.2	1227	1200	0.682
December	133.1	36.1	20.00	133.0	122.1	1124	1098	0.690
Year	2112.0	837.8	28.76	2111.2	1985.1	17375	16981	0.672
Legends								
GlobHor	Global horizontal irradiation							
DiffHor	Horizontal diffuse irradiation			EArray	Effective energy at the output of the array			
T_Amb	Ambient Temperature			E_Grid	Energy injected into the grid			
GlobInc	Global incident in coll. plane			PR	Performance Ratio			
GlobEff	Effective Global, corr. For IAM and shadings							
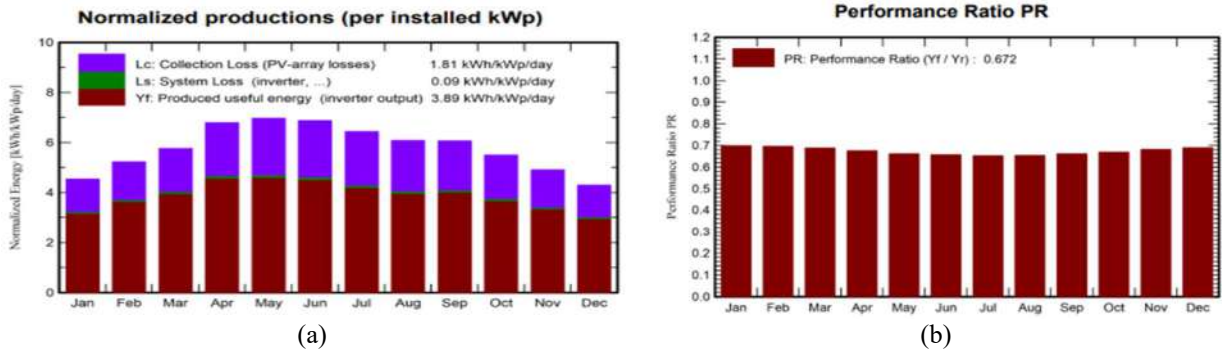
Fig. 10: (a) Monthly normalized energy production and losses; (b) Monthly PR of the PV system.

inverter losses labeled as Ls, stand at 0.09 kWh/kWp/day. The PV system's useful energy output is noted as 3.89 kWh/kWp/day. The graphical representation indicates monthly fluctuations in electricity production, with the highest in May and the lowest in December. Based on simulation results, the system's annual PR is calculated at 67.20%, as depicted in Fig 10.

PV Array Efficiency

Fig. 11 (a-e) displays the performance characteristics of the Trina Solar TSM-DD05H(II)-315 PV module under varying environmental conditions. These graphs include; Power-Voltage (P-V) Curves at Different Irradiances: Illustrates power output in watts across different voltage levels at various irradiances, with cell temperature held constant at 45°C. For example, at 1000 W/m² irradiance, maximum power output (Pmax) reaches 292.0 W, while at 200 W/m², it drops to 56.4 W. Current-Voltage (I-V) Curves at Different Temperatures: Depicts current output in amperes across voltage ranges at a constant 1000 W/m² irradiance, showing how output varies with temperature. Pmax values include 332.2 W at 10°C and 261.6 W at 70°C. Power-Voltage (P-V) Curves at Different Temperatures: Plots power output against voltage at 1000 W/m² irradiance across temperatures, showing a decrease in Pmax from 332.2 W at 10°C to 261.6 W at 70°C. Efficiency Curve Relative to STC: Details the module's efficiency relative to a standard irradiance of 1000 W/m², with an STC efficiency of 18.97%. Efficiency variations are tracked at lower irradiances, such as a 0.2% increase at 800 W/m² and a 3.0% decrease at 200 W/m². Efficiency Curve Relative to STC (Temperature Impact): Demonstrates efficiency declines as cell temperature increases, with efficiency starting around 18-20% at 25°C and decreasing to about 15-17% at 60°C under 1000 W/m² irradiance. These detailed analyses are critical for optimizing solar installations to maintain high efficiency under varying environmental conditions, allowing for system designs that adapt to temperature and irradiance changes effectively.

Solar PV System Performance and Irradiance Analysis

Fig. 12 (a), titled "System Output Power Distribution," illustrates the frequency distribution of power injected into the grid over a year. The X-axis, ranging from 0 to 8 kW, segments power into bins, with the Y-axis measuring occurrence frequency up to 600 classes (0.1 MWh each). The histogram peaks between 4 and 5 kW, marking the most common output range, with less frequent extremes on either end. Fig. 12 (b) details the distribution of solar irradiation, with the X-axis showing "Global incident in coll. plane [W/m²]" from 0 to 1200 W/m², and the Y-axis in classes of 0.01 MWh/m² up to 100 classes. Most solar power is received around 600 W/m². Fig. 12 (c) presents a "Daily System Output Energy" time series for a year, with daily values fluctuating up to 60 MWh, indicating a variable and dynamic system influenced by factors that cause significant day-to-day output variations.

Diagram of Energy Flow and Losses

Fig. 13, illustrates the energy flow and loss diagram for the PV system over the year. The global horizontal irradiation received on the collector plane is 2112 kWh/m², which is subject to a 3.07% IAM factor loss and a 3% soiling loss factor, resulting in an effective irradiation of 1985 kWh/m² on the collectors. The solar panels, with an efficiency of 18.97% at STC, convert this into a nominal energy output of 23782 kWh. The energy at the MPP is further reduced to 17375 kWh due to various losses, including a 9.79% module degradation over 25 years, losses due to irradiance and temperature, quality, and light-induced degradation (LID). Ohmic wiring loss contributes to a further 0.83% reduction. After accounting for the energy conversion efficiency of the inverter, the available energy at the inverter output totals 16981 kWh, which is the same amount of energy injected into the grid.

Comparative Analysis

The comparative analysis highlights the techno-economic viability of solar PV systems in Oman, focusing on
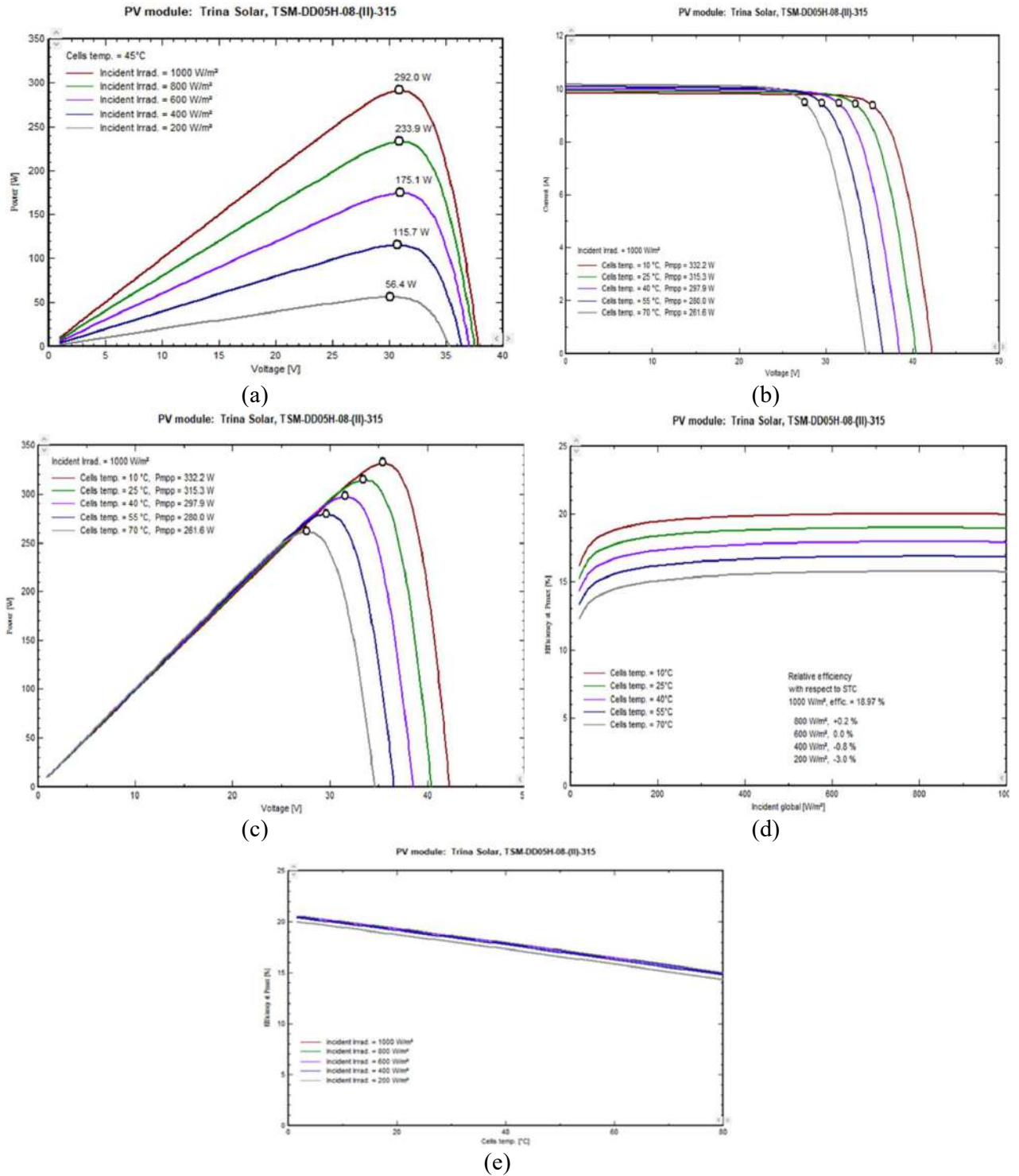
Fig. 11: (a) I-V characteristics of the PV module at various irradiance levels; (b) I-V curves of the PV module at different cell temperatures; (c) P-V curves at multiple irradiance levels for the PV module; (d) Efficiency variation of the PV module with changing irradiance; and (e) Derivative of I-V curve showing MPP tracking.

(a)   (b)   (c)
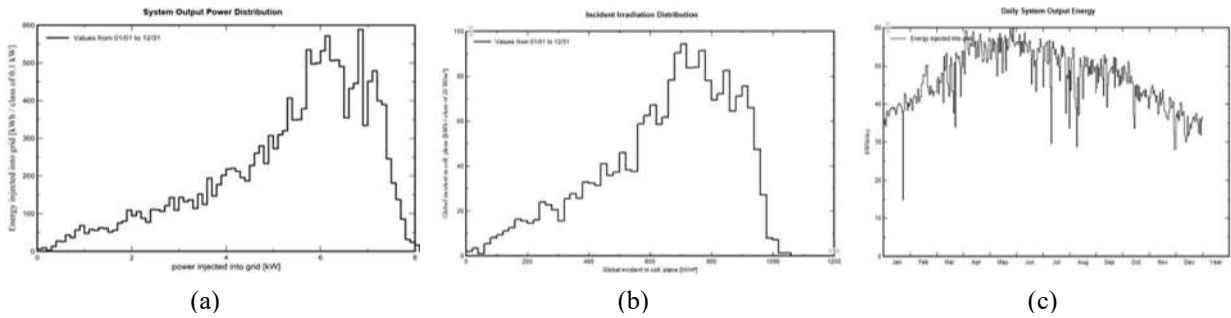
Fig. 12: (a) P_{max} – incident global production curve; (b) Incident irradiation distribution; (c) Daily energy injected into the grid.
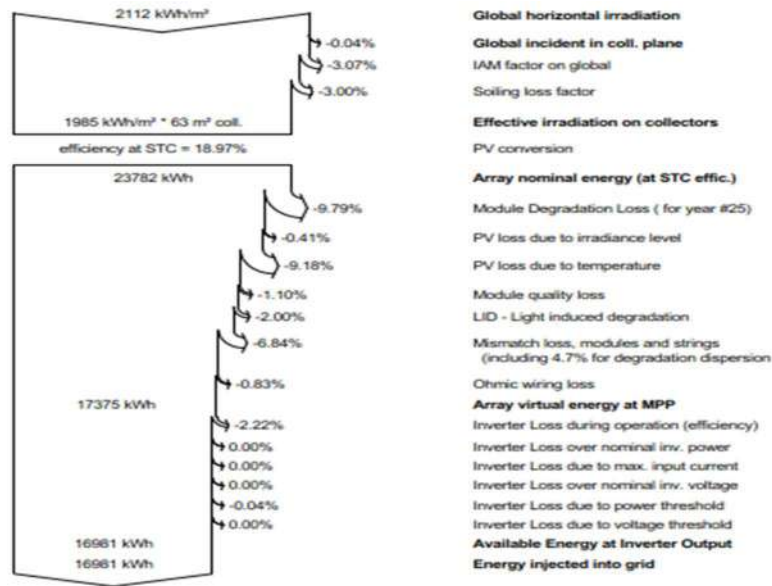
Fig. 13: Loss diagram.

feasibility, design, and economic dispatch. Key findings emphasize system efficiency, annual energy production, and payback periods, while limitations include a lack of detailed environmental analysis and focus on specific configurations, as given in Table 7.

Economic Analysis

An economic study was conducted to assess the initial capital cost and payback period for a PV installation, focusing on component costs. Costs were identified for Trinca solar modules at $195 each and Krylosar inverters at $1500 each

Table 7: Comparative analysis of solar PV system.

	Focus	Key findings	Limitations	Ref.
Techno-economic feasibility analysis of 1 MW photovoltaic grid-connected system in Oman	Feasibility analysis of 1 MW photovoltaic	Highlights the economic and technical viability of a 1 MW grid-connected system in Oman.	The study focuses on economic and technical aspects without detailed environmental analysis.	(Albadi et al. 2019)
Economic Dispatch of Oman's Main Interconnected System	Economic dispatch of the power system with a 500MW solar PV plant	Investigates economic dispatch strategies incorporating a large-scale solar PV plant.	Primarily focuses on economic dispatch without in-depth environmental impact.	(Kazem et al. 2017)
Feasibility, design, and impact analysis of a grid-connected solar PV system	Feasibility, design, and impact analysis of a grid-connected solar PV system	10.81 kWp system design, 16981 kWh annual energy production, 67.2% system efficiency, 7.5-8.3 years payback period, significant CO_2 reduction.	The study is limited to a specific location and system configuration.	Present study

Table 8: Initial investment costs and annual operating expenses for PV system.

Investment and charges					Operating cost (yearly)		
Description	**Quantity**	**Unit price**	**Total**		**Description**	**Yearly cost**	
⊟ PV modules			9,120.00	USD	⊟ Maintenance	1,040.00	USD
TSM-DD05H-08-(II)-315	38.00	195.00	7,410.00	USD	Provision for inverter re...	210.00	USD
Supports for modules	38.00	45.00	1,710.00	USD	Salaries	470.00	USD
⊟ Inverters			1,500.00	USD	Repairs	260.00	USD
KSY-11K	1.00	1,500.00	1,500.00	USD	Cleaning	100.00	USD
⊟ Other components			1,600.00	USD	Security fund	0.00	USD
Accessories, fasteners	1.00	450.00	450.00	USD	Land rent	0.00	USD
Wiring	1.00	920.00	920.00	USD	⊞ Insurance	0.00	USD
Combiner box	1.00	230.00	230.00	USD	Bank charges	0.00	USD
⊞ Studies and analysis			0.00	USD	Administrative, accounti...	0.00	USD
⊟ Installation			3,800.00	USD	⊞ Taxes	0.00	USD
Global installation cost per ...	38.00	100.00	3,800.00	USD	Subsidies -	0.00	USD
⊞ Insurance			0.00	USD			
⊞ Land costs			0.00	USD			
Loan bank charges	0.00	0.00	0.00	USD			
⊞ Taxes			0.00	USD			
	Total installation cost		16,020.00	USD	**Operating costs (OPEX)**	1,040.00	USD/year
	Depreciable asset		11,070.00	USD			

[solar panel, solar inverter], as outlined in Table 8. Costs for studies, analysis, insurance, land, loans, and taxes were excluded from this assessment, with maintenance costs estimated from other studies.

Financial parameter: Fig. 14 appears to be a financial model for this project with a 25-year lifespan starting in 2025. It assumes no inflation or production variation over time, no income tax, and includes a tax depreciation section for assets like PV modules and inverters. Financing is set at $16,020, all from own funds as depicted by the pie chart, indicating no loans or subsidies are involved. The total redeemable amount is $11,070.

Electricity sale on availability and demand: Fig. 15 shows settings for an energy pricing model with a variable tariff structure. It includes an hourly peak/off-peak tariff, feed-in tariffs for energy supplied to the grid ($0.1700/kWh for peak {equivalent to 65 Baiza} and $0.0310/kWh for off-peak {equivalent to 12 Baiza}) according to a report published on *12th June, 2017, in Times of OMAN* electric subsidy in Oman and also acknowledges daylight saving time changes, starting in March for summer and October for winter. The accompanying doughnut chart illustrates the peak (07:00-20:00) and off-peak (20:00-07:00) hours for the tariff application.

Fig. 14: Financial model overview for a 25-year project, fully self-funded.
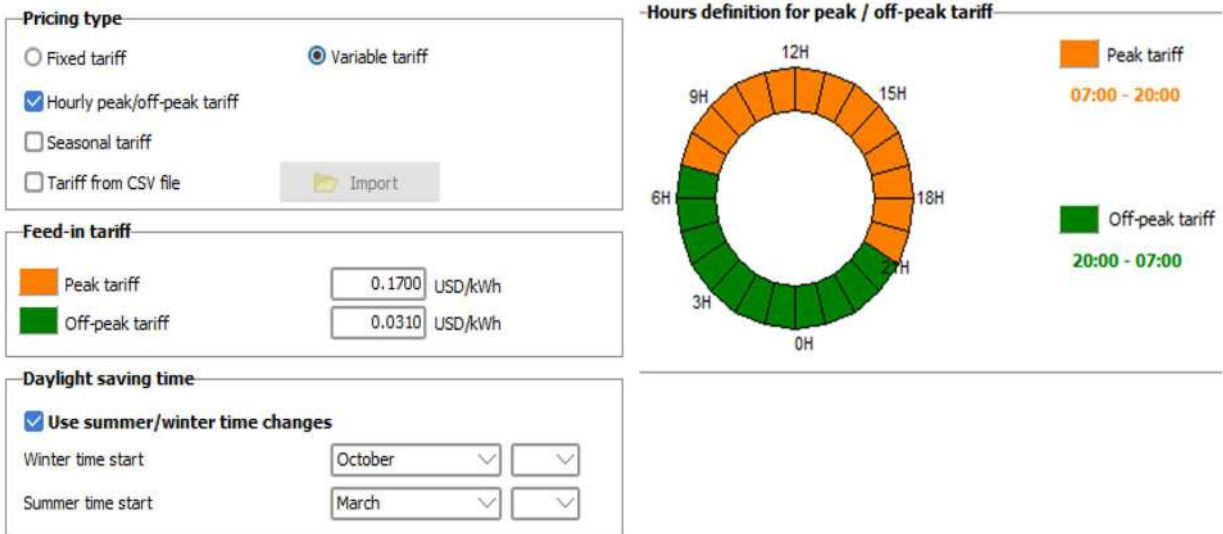
Fig. 15: Variable energy pricing model with peak and off-peak hours.

Financial result: The total installation cost for the PV system is $ 16,020.00, which is fully funded by the owner without subsidies or loans. The system has a depreciable asset value of $11,070.00 and yearly operating costs of $1,040.00 to $1,250.00. Financially, the system's NPV is $32,024.28 with an 11.15% Internal Rate of Return (IRR), and the payback period is 7.5 to 8.3 years. The Levelized Cost of Energy (LCOE) is $0.1013/kWh, and the Return on Investment (ROI) is 232.7%. PV modules constitute roughly 57.07% of the capital costs, and other components total $1,600.00. O&M practices like biweekly cleaning of PV modules are crucial for system upkeep. Financial metrics indicate that the investment

would be recoverable in about 7.5 years, assuming stable performance and savings as shown in Fig. 16.

Solar project financial forecast: Fig. 17 (a) illustrates the annual cash flow for a solar project in USD, starting with a significant initial investment depicted by a large red bar exceeding $16,000, followed by annual net incomes shown as green bars. Each subsequent year reflects profitable operations with these green bars, indicating consistent yearly earnings in the thousands. Fig. 17 (b) portrays the cumulative cash flow, beginning with the initial outlay and tracing the transition to profitability. This chart gradually transforms from red to green as the project moves toward and surpass-

Fig. 16: Project financial summary: costs, funding, returns, and profit distribution.
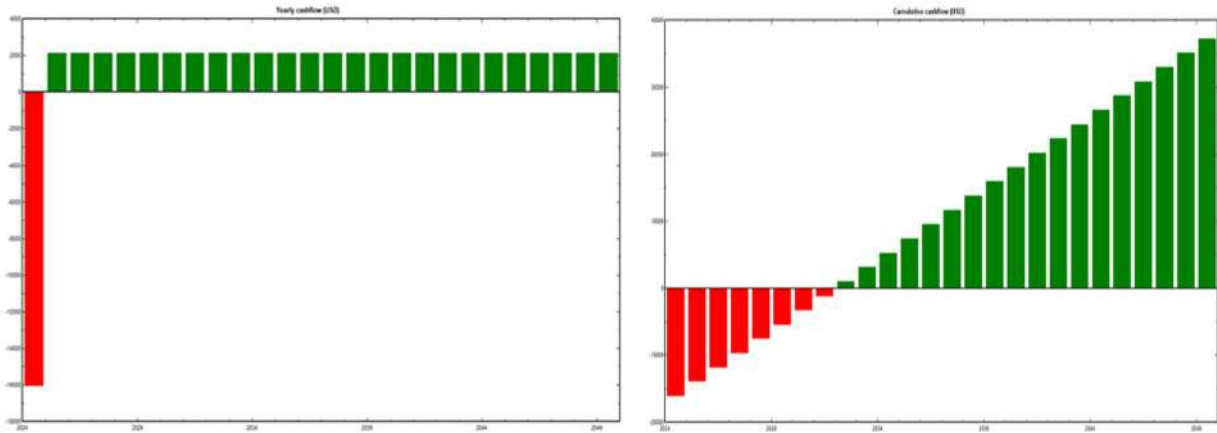
Fig. 17: (a) Yearly net loss and profit; (b) Economic feasibility.
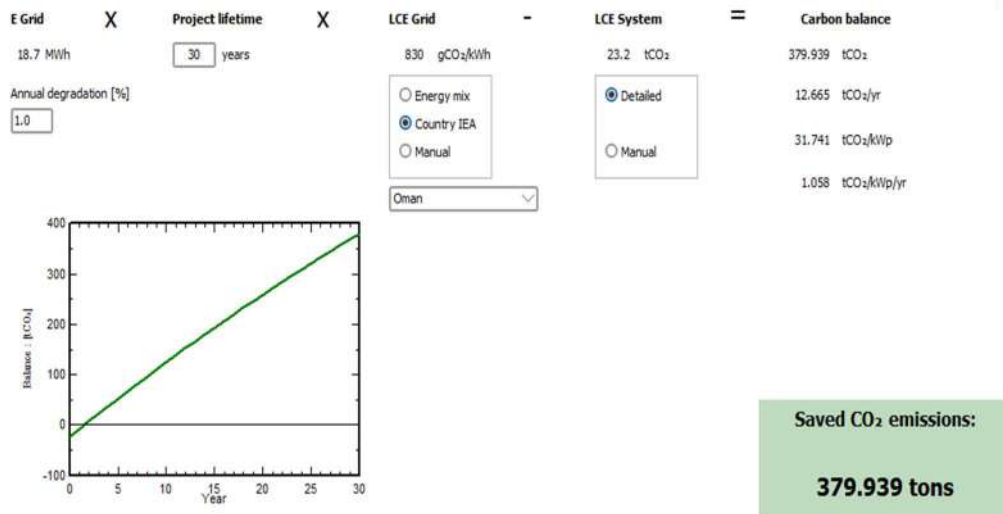
Fig. 18:Environmental impact of a 30-year solar project.

es the break-even point. Numerically, the cumulative cash flow, starting with the initial investment, reaches a positive territory exceeding $30,000 after several years, effectively visualizing the payback period and subsequent profitability for stakeholders. These visual aids are crucial for illustrating the timeline for the investment's return and ongoing financial benefits.

CO$_2$ Emission Balance

Fig. 18, presents data related to the environmental impact over the project's lifetime, set at 30 years. The grid electricity (E Grid) produced by the system is 18.7 MWh, and the system experiences a 1% annual degradation in performance. The carbon emissions factor for grid electricity (LCE Grid) in Oman is 830 gCO$_2$/kWh, whereas the system's emissions factor (LCE System) is significantly lower at 23.2 tCO$_2$. It

is likely to illustrate the cumulative carbon savings over the project's lifetime, indicating a linear increase in carbon savings as the project continues to operate. The "Carbon balance" section quantifies the total CO$_2$ savings at 379.939 tons over the project's lifetime. This breaks down to 12.665 tCO$_2$/year, and when normalized to the system production, it is 31.741 tCO$_2$/kWp or 1.058 tCO$_2$/kWp/year. The highlight of this analysis is the "Saved CO$_2$ emissions," which stands at 379.939 tons, showcasing the project's substantial environmental benefits by reducing carbon emissions compared to conventional grid energy sources.

CONCLUSION

This study examined the feasibility, methods, and key findings of a grid-connected PV system designed for a building in Ibri, Oman. The system, proposed to be 10.81

kWp, focused on cost efficiency, surplus energy utilization, and minimizing the carbon footprint. The system components included PV panels, inverters, and charge controllers, with a detailed comparison of panel types based on material composition, efficiency, costs, and applications. The PVsyst software was employed for design and simulation, considering local climate conditions and solar orientation to maximize efficiency. Key performance metrics such as the performance ratio (PR), capacity utilization factor, and system efficiency were evaluated to determine the system's effectiveness. The study emphasized the importance of these parameters in optimizing the design and performance.

The findings indicated that the PV system generated 16,981 kWh annually, with a yield of 1,419 kWh/kWp and a PR of 0.672, demonstrating efficient sunlight conversion. The in-depth evaluations of energy generation and efficiency measures highlighted the need to minimize losses. Financial analysis demonstrated a payback period of 7.5 to 8.3 years, with an IRR of 11.15% and an NPV of $32,024.28, proving economic viability. The project also predicted a reduction of 379.939 tons of CO_2 over its lifespan, showcasing significant environmental benefits. The comprehensive examination of design, simulation, installation, and performance confirmed that the system was technically feasible, financially viable, and environmentally beneficial. This study offers a valuable understanding of similar geographic and climatic conditions, guiding future projects toward achieving positive outcomes.

NOMENCLATURE

Latin Symbols		BIM	Building information model
V	Voltage	IPPs	Independent power projects
KWh	Kilowatt-hour	STC	Standard test conditions
tCO_2	Metric tons of CO2	PR	Performance ratio
KWp	Kilowatt peak	CO_2	Carbon dioxide
$	US Dollar	GIS	Geographic information system
P_T	Rated power	LCE	Life cycle emission
P_D	Total power	AC	Alternating current
E_T	Total energy	DC	Direct current
E_g	Gross energy	I-V	Current (I) versus Voltage (V)

Greek Symbols		DOD	MPP
a	Tilt angle	NPV	Net present value
b	Azimuth angle	IAM	Incidence angle modifier

Abbreviation

PV	Photovoltaic
SE	Solar energy
IEA	International energy agency
PVsyst	Photovoltaic system (software)

REFERENCES

Al-Badi, A., Malik, A., Al-Areimi, K. and Al-Mamari, A., 2009. Power sector of Oman-Today and tomorrow. *Renewable and Sustainable Energy Reviews*, 13(8), pp.2192–96. doi:10.1016/j.rser.2009.03.010.

Albadi, M.H., Al-Hinai, A.S., Al Maharbi, M.J., Al Hosni, A.M. and Al Hajri, M.A., 2019. Economic dispatch of Oman's main interconnected system in presence of 500MW solar PV plant in Ibri. *2019 IEEE Jordan International Joint Conference on Electrical Engineering and Information Technology (JEEIT 2019) Proceedings*, pp.204–08. doi:10.1109/JEEIT.2019.8717418.

Alimi, O.A., Meyer, E.L. and Olayiwola, O.I., 2022. Solar photovoltaic modules' performance reliability and degradation analysis-A review. *Energies*, 15(16), 5964. doi:10.3390/en15165964.

Bagwari, A., Samarah, A., Gangwar, R.P.S., Anandaram, H., Elkady, G., Al Ansari, M.S., Arya, G. and Uniyal, J., 2022. Solar energy technology: Step towards a bright future of the world. *International Journal of Mathematical, Engineering and Management Sciences*, 7(6), pp.982–1004. doi:10.33889/IJMEMS.2022.7.6.061.

Charabi, Y., 2023. Status and future prospects of wind energy in Oman. *Springer*. doi:10.1007/698_2022_959.

Coyle, E., 2017. A case study of the Omani electricity network and readiness for solar energy integration. *SDAR Journal of Sustainable Design & Applied Research*, 5(1), pp.1-10.

Emerald Insight, 2022. Oman's green hydrogen sector will grow over the decade. *Emerald*. Available at: https://www.emerald.com/insight/content/doi/10.1108/OXAN-DB273230/full/html

Gastli, A. and Charabi, Y., 2010. Solar electricity prospects in Oman using GIS-based solar radiation maps. *Renewable and Sustainable Energy Reviews*, 14(2), pp.790–97. doi:10.1016/j.rser.2009.08.018.

Guo, F., Gao, J., Men, H., Fan, Y. and Liu, H., 2021. Large-scale group decision-making framework for the site selection of integrated floating photovoltaic-pumped storage power system. *Journal of Energy Storage*, 43, 103125. doi:10.1016/j.est.2021.103125.

Kazem, H.A., Albadi, M.H., Al-Waeli, A.H.A., Al-Busaidi, A.H. and Chaichan, M.T., 2017. Techno-economic feasibility analysis of 1MW photovoltaic grid-connected system in Oman. *Case Studies in Thermal Engineering*, 10, pp.131–41. doi:10.1016/j.csite.2017.05.008.

Kim, G.G., Hyun, J.H., Choi, J.H., Ahn, S.H., Bhang, B.G. and Ahn, H.K., 2023. Quality analysis of photovoltaic system using descriptive statistics of power performance index. *IEEE Access*, 11, pp.28427–38. doi:10.1109/ACCESS.2023.3257373.

Lee, A.H.I., Kang, H.Y., Lin, C.Y. and Shen, K.C., 2015. An integrated decision-making model for the location of a PV solar plant. *Sustainability*, 7(10), pp.13522–41. doi:10.3390/su71013522.

Maran, K., Senthilnathan, C.R., Usha, S. and Venkatesh, P., 2022. Impact of solar energy on mitigating climate changes for a sustainable

development in India. *Proceedings of the 3rd International Conference on Power, Energy, Control and Transmission Systems (ICPECTS 2022)*. doi:10.1109/ICPECTS56089.2022.10046744.

Mukhopadhyay, S., 2022. Solar energy and gasification of MSW: Two promising green energy options. *Green Energy Systems: Design, Modelling, Synthesis and Applications*, pp.93–125. doi:10.1016/B978-0-323-95108-1.00003-3.

Munshi, A.A., 2023. Evaluation of grid-connected photovoltaic plants based on clustering methods. *Computer Systems Science and Engineering*, 45(3), pp.2837–52. doi:10.32604/csse.2023.033168.

Nayak, M.R., Srikanth, Y., Padmavathi, M. and Khasim, S.R., 2022. Enhancement of solar PV cell efficiency using instantaneous light reflection technique. *Proceedings of the International Conference on Computational Intelligence and Sustainable Engineering Solutions (CISES 2022)*, pp.202–8. doi:10.1109/CISES54857.2022.9844402.

Ninzo, T., Mohammed, J.M. and Venkateswara, R.C., 2023. Enactment of NZEB by state of art techniques in Sultanate of Oman. *i-manager's Journal on Future Engineering and Technology*, 18(3), pp.1-9. doi:10.26634/jfet.18.3.19163.

Peters, I.M. and Sinha, P., 2021. Value of stability in photovoltaic life cycles. *Conference Record of the IEEE Photovoltaic Specialists Conference*, pp.416–19. doi:10.1109/PVSC43889.2021.9518480.

Qingyang, J., Jichun, Y., Yanying, Z. and Huide, F., 2021. Energy and exergy analyses of PV, solar thermal and photovoltaic/thermal systems: A comparison study. *International Journal of Low-Carbon Technologies*, 16(2), pp.604–11. doi:10.1093/ijlct/ctaa092.

Rahman, T., Al Mansur, A., Hossain Lipu, M.S., Rahman, M.S., Ashique, R.H., Abou Houran, M., Elavarasan, R.M. and Hossain, E., 2023. Investigation of degradation of solar photovoltaics: A review of aging factors, impacts, and future directions toward sustainable energy management. *Energies*, 16(9), 3706. doi:10.3390/en16093706.

Sheikholeslami, M., 2023. Nanotechnology applications for solar energy systems. *Nanotechnology Applications for Solar Energy Systems*, pp.1-430. doi:10.1002/9781119791232.

Shekhar, R., 2018. Innovative uses of solar thermal technology. In: *Renewable Energy and Green Technology*. pp.3–9. doi:10.1007/978-981-10-4576-9_1.

Tabook, M. and Khan, S.A., 2021. The future of the renewable energy in Oman: Case study of Salalah City. *International Journal of Energy Economics and Policy*, 11(6), pp.517–22. doi:10.32479/ijeep.11855.

Xu, X., Wu, W. and Wang, Q., 2023. Efficiency improvement of industrial silicon solar cells by the POCl3 diffusion process. *Materials*, 16(5), 1824. doi:10.3390/ma16051824.

Yamaguchi, M., Masuda, T., Nakado, T., Yamada, K., Okumura, K., Satou, A., Ota, Y., Araki, K. and Nishioka, N., 2022. Analysis for solar coverage and CO_2 emission reduction of photovoltaic-powered vehicles. *IEEE Photovoltaic Specialists Conference*, pp.58–58. doi:10.1109/pvsc48317.2022.9938513.

Yousefi, H., Hafeznia, H. and Yousefi-Sahzabi, A., 2018. Spatial site selection for solar power plants using a GIS-based Boolean-fuzzy logic model: A case study of Markazi Province, Iran. *Energies*, 11(7), 1648. doi:10.3390/en11071648.

Zurigat, Y.H., Sawaqed, N.M., Al-Hinai, H. and Jubran, B.A., 2007. Analysis of typical meteorological year for Seeb/Muscat, Oman. *International Journal of Low Carbon Technologies*, 2(4), pp.323–38. doi:10.1093/ijlct/ctm027.

ORCID DETAILS OF THE AUTHORS

Arshad Mehmood: https://orcid.org/0009-0004-0750-3150

Original Research Paper

https://doi.org/10.46488/NEPT.2025.v24iS1.002

Open Access Journal

Exploring the Nexus Between Urban Land Use/Land Cover (LULC) Changes and Urban Growth Analysis Using Geoinformatics in Tumkur City, India

A. Kishor Kumar, Govindaraju†[ID], C. J. Rakesh and S. Lokanath

Department of Applied Geology, Kuvempu University, Shankaraghatta-577 451, Karnataka, India
†Corresponding author: Govindaraju; drgov@yahoo.com

ABSTRACT

For the past several decades, Tumkur has been one of the fastest-developing cities in Karnataka. Hence, an assessment concerning the identification of LULC mutations and their intensity and urban sprawl in Tumkur City has been employed using cutting-edge Geospatial techniques. In this study, multi-temporal satellite imagery such as Landsat 5 (2000), Resourcesat-1 (2005, 2009 & 2012), and Sentinel-2A (2015 & 2020) were utilized to monitor historical LULC changes, land transformation, direction of urban growth and sprawl. The outcome of the change detection demonstrates that between 2000 and 2020, the built-up area expanded significantly, from 24.94 km^2 to 60.59 km^2. Consequently, the land transformation matrix analysis shows that substantial modifications in LULC have occurred over the period, with a rise in built-up areas and plantations and a decline in agricultural land, water bodies, and scrubland. Further, urban expansion analysis using UEII (Urban Expansion Intensity Index) revealed that most of the area is in the fast-paced stage of urban expansion. Moreover, two well-known indices; the Annual Urban Spatial Expansion Index (AUSEI) and the Annual Built-up Change Index (ABCI), show a significant positive correlation between them ($R^2 = 0.69$) justifying the increased urban growth in the study area. Whereas, built-up density and the Annual Urban Spatial Expansion Index (AUSEI) show a negative correlation ($R^2 = 0.55$) indicating the presence of compactness of the core of the city. Apart from the above analysis, urban sprawl was effectively interpreted using zones formed using Shannon entropy; NNE, ESE, and SSW have high urban sprawl due to National Highways, growth of Industries, and infrastructure activities developed by the government. Further, the present study's findings will contribute to understanding land use dynamics, urban sprawl, urban growth analysis, and future projections, as well as provide crucial information for decision-making and urban planning processes, to the urban planner to support acceptable land use management and guiding plan for appropriate growth of urban areas.

INTRODUCTION

Globally, 3500 million people live in towns; by 2030, this number will rise to 6000 million (Bunyangha et al. 2021, Sustainable Development Goal 2021). As per the World Urbanization Prospects (2018) study In the future, 95% of the urban population will settle in developing countries. During this metamorphosis, the natural environment changes dramatically as human activities alter and adapt to enable urbanization (Brown et al. 2000, Montgomery et al. 2013). Several factors, including the progress of population explosion, economic progression, industrialization, and infrastructure blossoming, facilitate the expansion of urban areas (Marcotullio & Lee 2003, Dahly & Adair 2007, Rauws & de Roo 2011, Padhi & Mishra 2022). The above factors have often been described as the direct consequence of urban expansion; these factors directly lead to an increased need for land resources resulting in the alteration of land use and land

cover in a specific region. In addition, urban areas exhibit distinctive characteristics that are unique to them from rural and natural environments (Lambin et al. 2001, Maktav & Erbek 2005, Yakub & Tiffin 2017, Yin et al. 2023, Burgalassi et al. 2015). The most crucial factor behind global ecosystem modifications is transforming indigenous land cover types into artificial land use types (Dutta et al. 2020, Antipova et al. 2022). As a result, the investigation of LULC trends can serve as a basis for managing and planning natural resources at various spatial and time scales (Turner et al. 1994, Khan & Jhariya 2018).

The rate of urbanization in India slowed at first but began rising steadily in the 1920s (Mohan & Dasgupta 2004, Dadras et al. 2015). Due to industrial evolution and the increase in population growth, most people's forces commute daily to the suburbs, resulting in LULC changes (Kasraian et al. 2017, Haque & Basa 2017). Infer that conversion of

agricultural and other natural land cover types into urban areas, the urban areas have begun to expand outward (Dutta et al. 2020, Antipova et al. 2022). As a result of the analysis of LULC alterations, a plausible explanation is given for the relationship between man and the environment in the past and coming years (Lu et al. 2019, Dijoo 2021). Thus, LULC studies have the potential to help solve pressing environmental problems such as urban heat islands, pollution, global warming, loss of biodiversity climate change, and disasters, etc (Mathews & Nghiem 2021, Mohamed & Worku 2019, Yan et al. 2019, Herold et al. 2003).

The changes in LULC directly impact the urban ecosystem which imposes the establishment of sustainable urban areas (Ning et al. 2022). Nevertheless, the objective of eco-friendly urban development is to establish cities and communities that are ecologically, financially, and socially viable (Grekousis et al. 2013, Liu et al. 2019). In addition, landscape ecology and metrics can also be used to describe spatiotemporal variations and dynamics associated with the enlargement of urban centers and changes in land use caused by human activities (Yang et al. 2003, Masila 2016). It has been shown that land use and land cover can be classified, and growth in urban areas can be analyzed using a variety of techniques like Remote Sensing (RS) and Geographical Information Systems (GIS) (Jaad & Abdelghany 2021). Various methods, including unsupervised and supervised classification (Kim 2016, Didier et al. 2012), applying different indices, principal component analysis (Deng et al. 2008, Ji et al. 2006), hybrid methods (Mas et al. 2017, Grodach et al. 2022), and object-based detection methods were utilized to quantify, assess, map, and monitor urban growth.

In the present study, we utilized the geospatial method to evaluate land use and land cover changes and urban growth analysis in the study area. Scholars have utilized a few important indices to monitor and analyze urban expansion in a given area. These are Shannon's entropy, Urban Expansion Intensity Index, Built-up Density, Annual Urban Spatial Expansion Index, and Annual Built-up Change Index.

An emerging urban entity in Karnataka named Tumkur City, located near Bangalore City, is experiencing significant progress and improvement of infrastructure. As a result of notable changes in some sectors, including administration, economy, culture, and education, the city has experienced significant transformations. Few research works were carried out on urban-related matters however, no single study was carried out on urban land transition using geospatial technology. Despite this, the study area has undergone prodigious development of the urban over the past few generations. In this context, our study seeks to fill this research gap by integrating the LULC dynamics of the study area using remote sensing and geographic information systems. The specific objectives of the study are as follows: (a) to scrutinize the spatiotemporal changes of LULC in the study area between 2000 and 2020, (b) to interrogate the sprawling rate of the Tumkur City area, and (c) to schematize the pattern of urban growth using three relevant indicators, such as the AUSEI, BUDI, and ABCI. Using these scientific conclusions of the study area's past and present land-cover scenarios, planners/decision-makers can devise sustainable urban development strategies, and ecological sustainability plans will remain vital for future generations.

STUDY AREA

In Karnataka, Tumkur is one of the foremost important industrial hubs. It lies between the latitudes 13°19'00 and 13°21'19" and the longitudes 77°05'26" and 77°07'12. The Indian government picked one of seven smart cities in Karnataka as part of the Smart City Mission. In 1961, the area of Tumkur City was 12.95 km^2, in 2011, it was 64.27 km^2 (Fig. 1). According to the master plan map for 2021, it was 331.6 km^2. It is roughly 65 kilometers from the capital of Karnataka, Bangalore. Because of its nearness to the capital, the scarcity of affordable land in Bangalore, and the accessibility of resources within the study area, it is a prime site for growth in industry. It is an ideal location for setting up industries along National highways (NH 48 and NH 73). As a result of the study area, several small, medium, and large industries have been established. Four industrial areas and seven industrial estates are located in the study region. In total, four industrial areas are located in Hirehalli, Satyamagala, Arthasanahalli Phase 1, and Arthasanahalli Phase 2. A rapidly expanding population (Table 1 and Fig. 2), new infrastructure development, and the opening of new advanced industries have substantially altered Tumkur City's land use and cover classes.

MATERIALS AND METHODS

Materials

Landsat 5, Resourcesat-1, and Sentinel-2A imagery were used to perform a LULC change study. The topographic maps of India were used in the research region and utilized as ground validation. ERDAS IMAGINE & Arc GIS software was used to create land use maps to fully understand the dynamics of urban growth patterns and examine LULC changes. LULC maps have been verified by Google Earth Pro samples as well as ground truth surveys. The satellite imagery employed for this research is presented in Table 2.
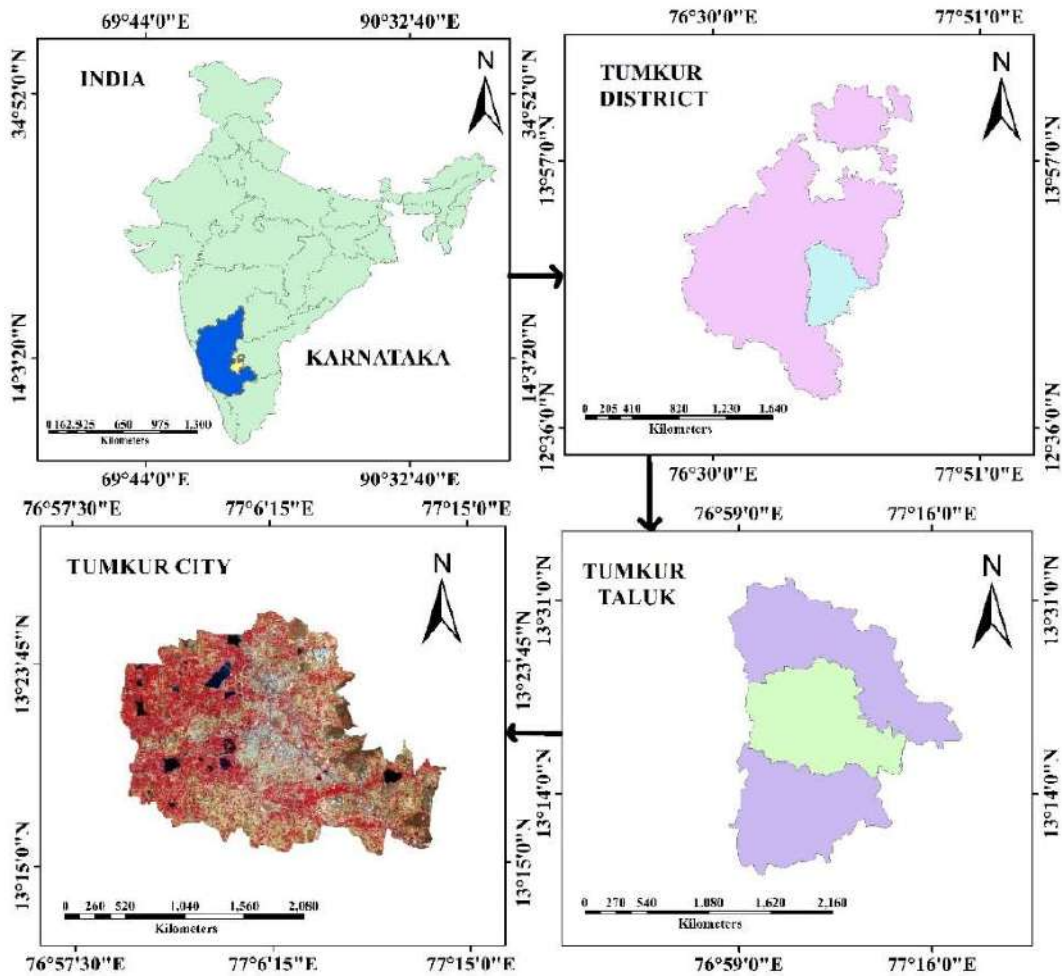
Fig. 1: The location map of the study area.

Table 1: Population-level and growth rate for the Tumkur, from 2000 to 2020.

Year	Population Data	Growth Rate
2020	361,000	1.69%
2019	355,000	2.01%
2018	348,000	1.75%
2017	342,000	2.09%
2016	335,000	1.82%
2015	329,000	2.17%
2014	322,000	1.90%
2013	316,000	1.94%
2012	310,000	1.97%
2011	302143	2.01%
2010	298,000	1.71%
2009	293,000	2.09%
2008	287,000	2.14%
2007	281,000	1.81%
2006	276,000	1.85%
2005	271,000	1.88%
2004	266,000	2.31%
2003	260,000	1.96%
2002	255,000	1.59%
2001	248929	2.87%
2000	244,000	3.39%

(Source: United Nations population projections and Census of India 2011)

Modeling Framework

The study uses remote sensing and geographic information systems to measure land use, land cover changes, and transformation matrics in Tumkur City during the last two decades. As a result, these metrics can shed insight into the extent and nature of land transformations and assist in

Tumkur City Population Data from 2000 to 2020
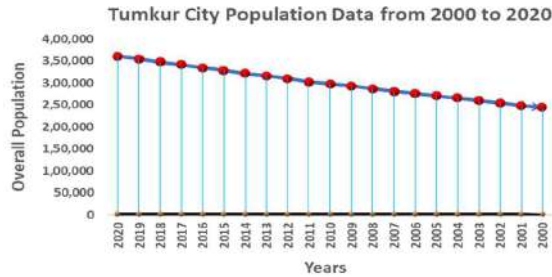
Fig. 2: Column graph of the population growth rate of Tumkur City (2000-2020).

Table 2: Various satellite images were incorporated into the study.

Sl No	Satellite Images	Resolution (in meters)	Path/Row	Observation Date	Source
1	Landsat 5	30	144/51	16/03/2000	USGS Earth Explorer
2	Resourcesat-1	23.5	93/56	06/08/2005	Bhuvan Geo Platform of ISRO
				31/03/2009	
				08/02/2012	
3	Sentinel – 2A	10	-	10/22/2015	Copernicus open-access hub
				02/03/2020	

understanding the dynamics of urban landscapes. As part of the study, five important indices are also used to measure specific aspects of urbanization. As part of the study, five important indices are also used to measure the impacts of town growth. The study area's Urban Area Expansion Intensity Index is used to determine the city's speed and rate of urbanization. In addition, the Shannon entropy measures the degree to which urban sprawl has been compacted or dispersed. A built-up density index can be used to estimate the urban area per unit of the total landscapes. The AUSEI (Annual Urban Spatial Expansion Index) measures the annual rate of urban growth in urban areas as well as the annual expansion of urban space (Dutta et al. 2019, Zhang et al. 2022). The Annual Built-Up Change Index (ABUCI) helps to provide some insight into the spatiotemporal variation in land conversion, a primary factor driving urban growth (Xie et al. 2005). BI, AUSEI, and ABUCI were intercorrelated analyses of urban growth in the form of a graph between 2000 and 2020.

Image Pre-Processing and Land Use Land Cover Analysis

Pre-processing satellite pictures facilitates recognizing atmospheric noise, such as haze created by water vapor, smog, and atmospheric components. It is necessary for obtaining meaningful and reliable findings in remote sensing. It offers a variety of methods for analyzing the standard results of images to determine the accuracy of surface features. Arc Map 10.4 and ERDAS Imagine Software (2014) was employed to find the atmospheric correction present in the satellite images and to generate apparent

reflectance. Apart from that geometric correction, Edge enhancement, and Image Filtering techniques were done to analyze the error in rectification, coordinates problem, and altitudes error. These methods are useful to improve the quality of satellite images for classification. However, land use and land cover classification is essential for analyzing the information through satellite images and knowing the arrangement of different LULC classes within the study area. Using the supervised classification method like the Gaussian Maximum Likelihood Classifier Algorithm (GMLCA) used to create land use and land cover maps of satellite images from 2000, 2005, 2009, 2012, 2015 and 2020.

Based on the NRSC level III classification scheme, eleven land use and land cover classes were classified: Scrub Forest, Forest Plantation, Water Bodies, Built-up, Double Crop, Scrubland, Land without Scrub, Fallow Land, Stony Waste, Kharif Crop, and Plantations. The LULC maps have been verified on the ground using Google Earth Pro samples. Finally, multi-temporal rasters were prepared for 2000, 2005, 2009, 2012, 2015, and 2020, and their corresponding statistics were compared to determine the transition in landscape patterns.

Land Use/Land Cover Change Dynamic Index

LU/LC change Dynamic Index is also called as Land change Dynamic Index. It used to evaluate the degree of dynamism of each class, the dynamic LULC change index examines the provided LULC classes. The following formula (1) explains how to calculate the change dynamic index (Zhang Hong et al. 2011).

$$K = \sum \frac{1}{T} * \frac{U_b - U_a}{U_a} \times 100 \qquad \text{...(1)}$$

Where K is the LULC Change Dynamic Index, U_a is an area of a certain LULC type at the initial year, U_b is an area of a certain LULC type in the final year, and T is the length of time.

Accuracy Assessment

A LULC classification's accuracy and correctness are evaluated through accuracy assessment (Ma & Redmond 1995, Sun et al. 2020). As a result, it is possible to assess the quality and reliability of classified maps, ensuring that they meet their intended purpose. The Kappa coefficient was used to assess the accuracy of land use and land cover classification at 120 randomly selected sites throughout the research region. The analysis was conducted using Ground Control Points (GCP) obtained from Google Earth Pro and a field survey.

$$KC = \frac{\sum_{i=1}^{k} n_{ii} - \sum_{i=1}^{k} n_{ii}(GiCi)}{n2 - \sum_{i=1}^{k} n_{ii}(GiCi)} \qquad \text{...(2)}$$

Estimation of Land Transformation Matrix

Evaluating a land transformation matrix is a useful way to find out how land cover and usage have changed in a specified time (Munsi et al. 2010, Roy & Roy 2010, Kindu et al. 2013, Mishra & Rai 2016a,b, Younes et al. 2023). The matrix tabulation provides necessary information regarding how the area of land classes encroached on others and shows the gains and losses related to a particular class (Naikoo et al. 2020). For measuring the extent of land transformation, we created five maps (2000–2005, 2005–2009, 2009–2012, 2012–2015, and 2015–2020) and analyzed the attributes table in ArcGIS to determine the area of different land classes. Preparation of land transformation matrix based on Equation. 3:

$$A \cdot B \times C = A \times B \cdot C =$$

$$\begin{pmatrix} S_{11} & S_{12} & \text{....} & S_{1n} \\ S_{11} & S_{22} & \text{....} & S_{2n} \\ \vdots & \vdots & & \\ S_{n1} & S_{n2} & \text{...} & S_{nn} \end{pmatrix} S \sum_{J=1}^{N} Sij$$

$$\text{...(3)}$$

Measuring Urban Area Expansion Intensity Index

The Urban Expansion Intensity Index, or UEII, is an effective tool for assessable estimation of urban spatial expansion variations (Yan et al. 2019). It calculates the level of urbanization and the rate at which urban landscapes are expanding or contracting (Zhong et al. 2020). It is an indicator that takes into account both the length of expansion and the proportional growth in the size of urban areas. To calculate the UAEII, the equation (4) has been used:

$$UAEII = \frac{UA^{t2}{}_b - UA^{t1}{}_b}{TA_b * \Delta t} \times 100 \qquad \text{...(4)}$$

[Where, UA = Urban area; b = spatial unit; t1 = initiatory year; t2 =finale year; $\Delta t = t2 - t1$; TA = Total landscapes of the appraisal field.

There are five categories in the UEII standard: leisurely - rapidity elaboration (0 to 0.28), low- rapidity elaboration (0.28 to 0.59), medium- rapidity development (0.59 to 1.05), high- rapidity development (1.05 to 1.92), and extremely high- rapidity elaboration >1.92. (Zhong et al. 2020).

Urban Sprawl Analysis Using Entropy Model

Shannon's entropy: The Shannon entropy index is the only method of evaluating urban sprawl that is widely used and widely accepted (Bhatta et al. 2010b). Shannon's entropy (Hn), is used to detect and approximately estimate urban sprawl (Bhatta et al. 2010).

Shannon's entropy is given by:

$$H_n = -\sum piloge(pi) \qquad \text{...(5)}$$

Where n is the total number of zones in the region, and Pi is the portion of the variable in the ith zone. In this study, eight subregions are identified (NNW, NNE, WNW, ENE, WSW, SSW, ESE, SSE) by vertical and horizontal grid lines that intersect at the city center (CBD), from which urbanization has spread along trunk corridor roads to the peripheral areas (Felix Ndidi Nkeki 2016). Shannon's entropy value ranges from 0 to loge (n), and values close to 0 and log (n) indicate a scattered distribution and compactness within urban areas. When entropy values (larger) close to loge (n) indicate a dispersion of urban areas or urban patches, urban sprawl is considered to be occurring (Felix Ndidi Nkeki 2016).

Graphical Analysis of Urban Growth Monitoring Using Indices

Built-up density index (BUDI): Built-up density is a major indicator for measuring the connection between the total built-up area and the total area of a geographical unit. Using this index, a region can determine its level of urbanization ratio has changed as a result of the rapid spread of the urban field, which has increased the density of the built-up area. In addition to indicating new construction locations, this index also indicates the pattern and course of urban expansion. The built-up density is calibrated using Equation 6 (Dutta et al. 2019).

$$BD = \frac{UA}{ZA} \qquad \text{...(6)}$$

BD is the built-up density, UA is the total Built-up area of the zone, and ZA is the total area of the zone.

Annual Urban Spatial Expansion Index (AUSEI): It is possible to calculate the amount of land transformed into built-up land using satellite data based on essential change detection. Tumkur City has developed a yearly urban spatial expansion index to measure the spatiotemporal changes in urban growth (Wang et al. 2023). It is employed for assessing the temporal change in urban regions. The annual Urban Spatial Expansion Index can be calculated using equation (7):

$$\text{AUSEI} = \frac{B_a - B_{ao}}{B_a(a - a_0)} \times 100 \qquad \ldots(7)$$

where $Ba - Ba_o$ is the total town area in square kilometers

at the time a (finale year) and time a_0 (initiatory year) (Dutta et al. 2019).

Annual Built-up Change Index (ABUCI): More impermeable surfaces have been created since rural areas have been converted to urban areas. The rapidity of land-use change must be quantified and to assess the conversion process relating to the development and growth of urban areas it is very essential. Expansion of urban areas occurs when the current land use and land cover are altered. Consequently, changes in built-up areas are linked to urban development. Observing spatiotemporal variation in the land conversion process, one of the primary motors of urban growth is possible by examining the annual change in built-up areas (Dutta et al. 2019). Annual Builtup Change Index calculated using equation (8).
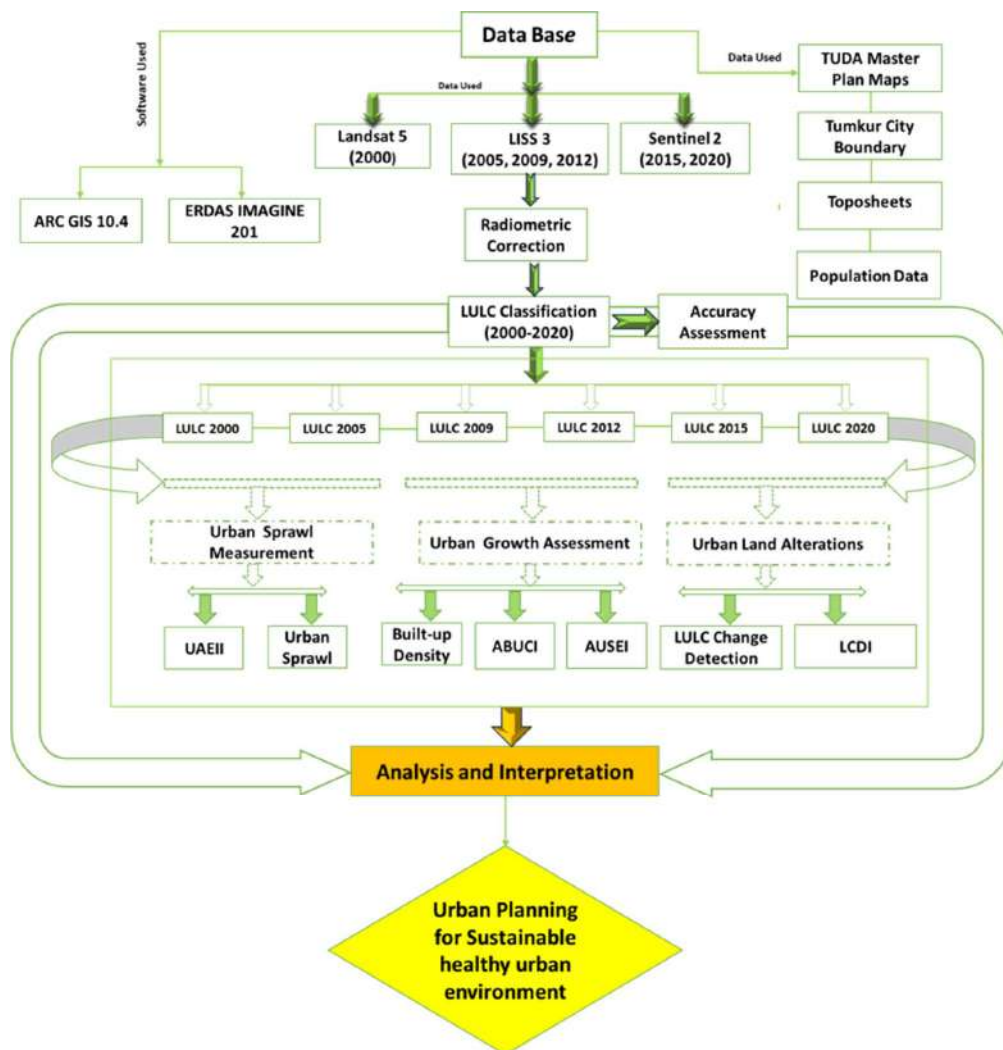
Fig. 3: Schematic representation of the methodology.

$$ABUCI = \frac{U_t - U_{to}}{t - t_0} \times 100 \qquad \ldots(8)$$

where $U_t - U_{to}$ is the total urban area in square kilometers at time t (final year) and time t_o (initial year) (Dutta et al. 2019). Fig. 3 shows the schematic representation of the methodology.

RESULTS AND DISCUSSION

Spatio-Temporal Changes of Land Use and Land Cover Pattern

A maximum likelihood classifier was used to create a land use and land cover map of the study area for the years 2000 (Landsat), 2005, 2009, 2012, (Resourcesat-1), 2015 2020 (Sentinel-2) using various satellite images (Fig. 4). The accuracy assessment result shows that the overall accuracy values are 87%, 88%, 86%, 92%, and 94% in the years 2000, 2005, 2009, 2012, 2015 and 2020, respectively, and also corresponding kappa co-efficient are 0.80, 0.82, 0.84, 0.91, 0.92 and 0.94, respectively. The land use and land cover statistics from 2000 to 2020 are shown in Table 3.

Land use and land cover pattern of 2000: The most dominant land use in the study area is kharif, covering an area of 154.46 km^2, accounting for 48% of the study area. The Hemavati River has supplied water to lakes of the Tumkur City since 1990. The availability of water in tanks has led to a gain in the area of plantations in the study region. Tumkur has a high concentration of agricultural fields due to its diverse cropping patterns, fertile soil, irrigation infrastructure, and government policies that promote agriculture. The plantations and water bodies is land use covered the area of 61.57 km^2 and 24 km^2, respectively. Different types of LULC classes were observed, such as scrub land covering 11.30 km^2, built-up covering 24.94 km^2, forest covering 7.60 km^2, stony waste covering 19.14 km^2, forest plantations covering 1.25 sq km^2, fallow land covering 1.25 km^2, double-crop covering 7.15 km^2, and land without scrub covering 0.45 km^2 respectively.

Land use and land cover pattern of 2005: The kharif was the most major land use in the study area it covers an area of 142.82 km^2. The other two dominant land use classes were plantations and waterbodies. plantations covered an area of 65.21 km^2, waterbodies covered an area of 22.59 km^2. The scrubland is one of the dominant types of land cover in the study area, covering 8.94 km^2. Built-up land covers 31.10 km^2. In addition, scrub forests covered 7.60 km^2, Stony waste covered 19.68 km^2, and forest plantations covered 1.25 km^2 of the study area, while fallow land covered 9.62 km^2, double crops covered 9.94 km^2, and land without scrub covered 1.56 km^2.

Land use and land cover pattern of 2009: In 2009, kharif was the dominant land use class, covering an area of 137.26 km^2. Plantations cover a total area of 67.82 km^2, while water bodies cover 22.08 km^2. The scrubland covered an area of 8.45 km^2 of the study region. In the total area, approximately 36.47 km^2 area land is covered by built-up land. In addition, scrub forests covered 7.60 km^2, Stony waste covered 20.02 km^2, and forest plantations covered 1.25 km^2 of the study area, while fallow land covered 9.73 km^2, double crops covered 0.45 km^2, and land without scrub covered 1.35 km^2.

Land use and land cover pattern of 2012: The kharif crop is considered the most major land use type and it covered 130.24 km^2 in the study area. The scrub forest covers an area of 7.60 km^2. Moreover, the study area comprising 39.08 km^2 of built-up areas is the most common land-use category. The water bodies with an area of 21.94 km^2, and scrubland 8.40 km^2. The plantations covered 70.46 km^2 of the study area in 2012, becoming the second major land use category and a total area of 10.49 km^2 of fallow land is covered.

Land use and land cover pattern of 2015: The study revealed that built-up areas covered 39.08 km^2 in 2015, ranking third among the various land use categories. In addition, the scrub forest contributed an area of 7.60 km^2. The kharif covered 130.24 km^2 of the study area, making it the most prevalent type of land use. Although there were 5.28 km^2 of scrubland, it remained the most common land-use category. The water bodies covered a total area of 21.21 km^2, double crop covered an area of 5.46 km^2. Additionally, plantations consisted of 73.06 km^2 in the total area.

Land use and land cover pattern of 2020: In the year 2020, the most prevalent type of land use was the kharif crop, which covered 113.19 km^2 of the study area. The built-up area covered in total area of 60.59 km^2. Water bodies covered an area of 20.44 km^2, scrubland covered the was 4.15 km^2, and plantations covered an area of 79.22 km^2. However, the study area has an area of 8.91 km^2 of fallow land, which varies yearly due to irregular rainfall patterns, water shortages, and climate change. Further, the study area has 35 km^2 of double-crop land, which has been reduced due to inadequate water facilities. The stony waste is currently 20.44 km^2, and 1.06 km^2 of land without scrub was found. Nevertheless, the scrub forest is covered with an area of 7.60 km^2.

The Magnitude of Land Use and Land Cover Changes in the Tumkur City

From 2000 to 2020, the magnitude of change and annual change rate for different land use and land cover categories are shown in Table 4. In this study, agricultural land, scrubland, and water bodies have consistently decreased; on the other hand, built-up areas, and plantations, grow

Table 3: Land Use and Land Cover Change Statistics of Tumkur City from 2000 to 2020.

Class	Area in km^2 (2000)	Area in %	Area in km^2 (2005)	Area in %	Area in km^2 (2009)	Area in %	Area in km^2 (2012)	Area in %	Area in km^2 (2015)	Area in %	Area in km^2 (2020)	Area in %
Built-up Land	24.94	7.75	32.10	9.97	36.47	11.34	39.08	12.15	55.85	17.3	60.59	18.83
Double Crop	9.85	3.06	9.94	3.09	9.73	3.02	9.77	3.04	5.46	1.70	5.35	1.66
Fallow Land	7.15	2.22	9.62	2.99	9.70	2.94	10.77	3.34	8.41	2.61	8.91	2.77
Forest Plantation	1.25	0.41	1.25	0.39	1.25	0.39	1.25	0.39	1.25	0.39	1.25	0.39
Kharif Crop	154.46	48	143.23	44.52	137.26	42.67	130.72	40.63	122.51	38.07	113.19	35.18
Land Without Scrub	0.45	0.14	1.56	0.48	1.35	0.41	1.54	0.47	1.10	0.34	1.06	0.31
Plantation	61.57	19.14	65.21	20.27	67.82	21.08	70.54	21.92	73.06	22.7	79.22	24.62
Scrub Forest	7.60	2.36	7.60	2.36	7.60	2.36	7.60	2.36	7.60	2.36	7.60	2.37
Scrub Land	11.30	3.51	8.94	2.78	8.45	2.63	8.40	2.61	5.28	1.63	4.15	1.28
Stony Waste	19.14	5.95	19.68	6.11	20.02	6.22	20.09	6.25	20.06	6.23	20.00	6.23
Water Bodies	24.00	7.46	22.59	7.02	22.08	6.86	21.94	6.82	21.21	6.59	20.44	6.35
Total Area	321.66	100	321.66	100	321.66	100	321.66	100	321.66	100	321.66	100
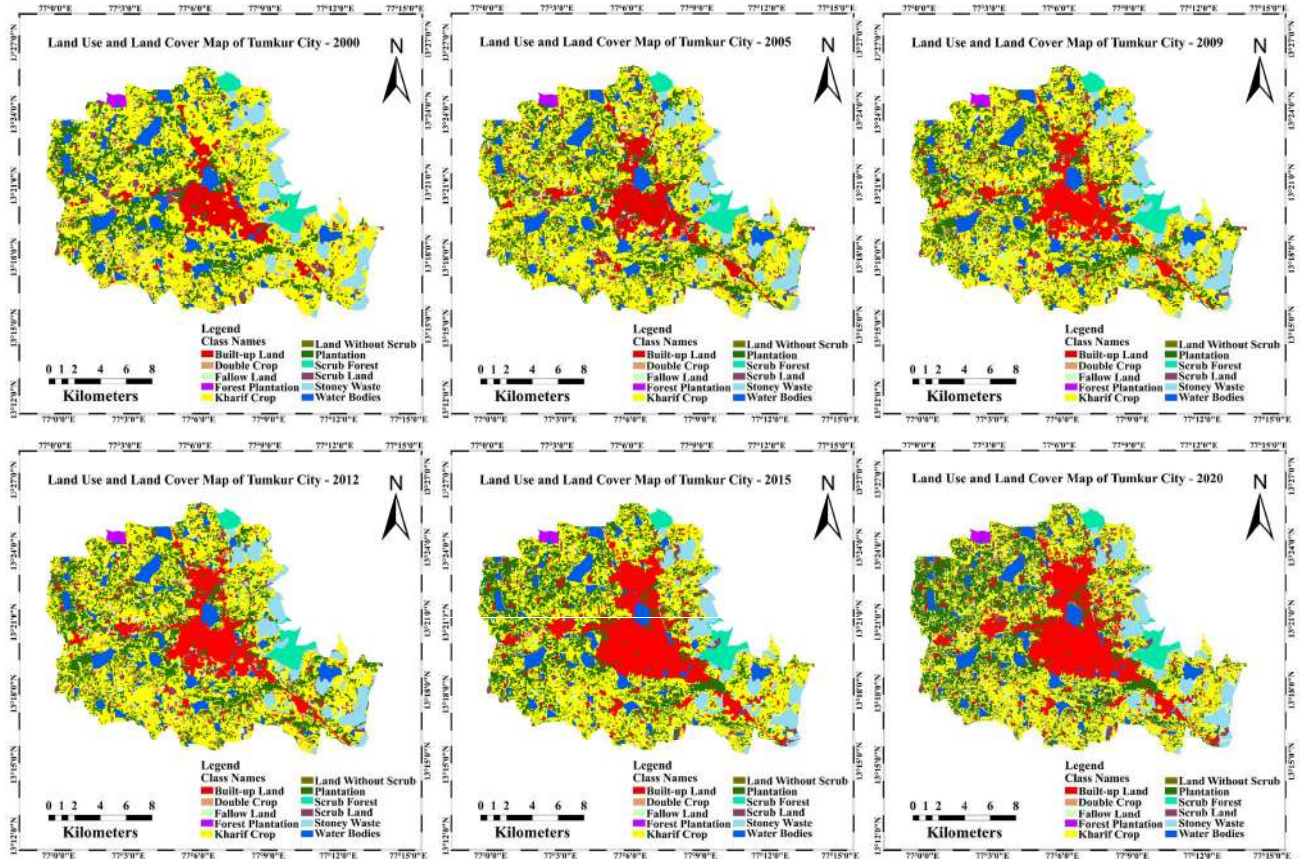
Fig. 4: Land use and land cover scenarios of Tumkur City in a) 2000, b) 2005, c) 2009, d) 2012, e) 2015, and f) 2020.

Table 4: Magnitude of change, percentage, and Annual Change Rate (ACR) of LULC in Tumkur city from 2000 to 2020.

Class Names	(2000-2005)			(2005-2009)			(2009-2012)			(2012-2015)			(2015-2020)		
	Area (km²)	%	AC Rate (%)	Area (km²)	%	AC Rate (%)	Area (km²)	%	AC Rate (%)	Area (km²)	%	AC Rate (%)	Area (km²)	%	AC Rate (%)
Built-up Land	7.16	2.2	0.22	4.37	1.35	0.13	2.61	0.81	0.08	16.5	5.21	0.52	4.74	1.47	0.14
Double Crop	0.09	0.03	0.003	0.21	0.06	0.006	0.04	0.01	0.001	4.31	1.33	0.13	0.11	0.03	0.003
Fellow Land	2.47	0.7	0.076	0.08	0.02	0.002	1.07	0.33	0.03	2.36	0.73	0.07	0.53	0.15	0.01
Forest Plantation	0.01	0.05	0.005	0.02	0.006	0.0006	0.02	0.006	0.0006	0.02	0.006	0.00	0.03	0.009	0.0009
Kharif Crop	-11.2	3.4	0.349	-5.97	1.85	0.18	-6.52	2.02	0.20	-8.21	2.55	0.25	-9.32	2.89	0.28
Land Without Scrub	1.11	0.3	0.034	0.21	0.06	0.006	0.19	0.059	0.005	0.44	0.13	0.01	0.04	0.01	0.001
Plantation	3.64	1.1	0.113	2.61	0.81	0.081	2.72	0.84	0.08	2.52	0.78	0.07	6.16	1.91	0.191
Scrub Forest	0.02	0.04	0.004	0.03	0.009	0.0009	0.01	0.003	0.0003	0.02	0.006	0.0006	0.02	0.006	0.0006
Scrub Land	-2.36	0.7	0.073	0.498	0.15	0.015	0.05	0.015	0.001	3.12	0.96	0.09	1.13	0.35	0.03
Stony Waste	0.54	0.1	0.016	0.342	0.10	0.010	0.07	0.02	0.002	0.03	0.009	0.0009	0.05	0.01	0.001
Water Bodies	-1.41	0.4	0.043	-0.51	0.15	0.015	-0.14	0.043	0.004	-0.73	0.22	0.02	-0.77	0.23	0.02

continuously, and due to rock exposure stony waste has grown a little bit. It was found that the most considerable magnitude changes between 2000 and 2005 occurred in Kharif cropland (about 11.23 km²) and built-up areas (7.16 km²). It has also been observed that significant magnitude changes between 2005 and 2009 occurred in the build-up area (1.35%) and plantation (2.61%); however, the Kharif crop decreased during this period. Furthermore, there has been vivid transmutation between 2009 and 2012, with build-up area (0.811%) followed by Kharif crops (2.026 %) and plantations (0.845%).

Furthermore, the annual changes in land area between the periods of 2012 and 2015 indicate a decrease in agricultural land (8.21 km²) followed by water bodies (0.73 km²) and double crop (4.31 km²). In contrast, built-up areas (16.57 km²), plantations (2.52 km²), and fallow lands (2.36 km²) have experienced annual increases. The magnitude results indicate that agricultural lands, scrublands, and waterbodies have consistently declined between 2015 and 2020. However, built-up areas, plantations, and fallow lands have continued to grow.

Land Use/Land Cover Degree Dynamic Index (LUCDDI) Analysis from 2000 to 2020

Land Use/Cover Degree Dynamic Index (LUCDDI) or Land Degree Dynamic Index (LDDI) values calculate the degree of land use dynamics, as shown in Table 5 and Fig. 5. The few land classes have low LDDI values that indicate a decline in the land area and few have positive values that imply gaining the area of land classes.

From 2000 to 2020, significant land changes have been witnessed, indicating that agricultural land, scrubland, and water bodies continually reduced; on the other hand, built-up areas, plantations, and stony waste experienced continuous growth. Additionally, LDDI indicates a high dynamic index value for the built-up area between 2000 and 2020, indicating that the built-up area expanded rapidly during the analysis period, while other types of land use, including agricultural areas, water bodies, and scrubland, remained with low LDDI values due to the rapid conversion of built-up. In contrast, built-up areas, plantations, and fallow land have continuously grown.

The Estimation of Land Transformation Matrix

Applying the different period land transformation matrix of LULC maps study to show the gains and losses in specific land use land cover class (Tables 6, 7, 8, 9, 10) Over the period between 2000 and 2020, large areas of agricultural land (154.2 km²) will be converted into non-agriculture classes such as built-up land, plantations, and other classes

(113.33 km^2) due to the increase in the growth of major road networks like NH 48, NH 73, moreover, increase in the population growth, development activities carried out by government leads to boom the real estate of areas, growth of industrial areas in study area and quarrying activities. During the study period, the area of fallow land has extend due to proper water facilities. and economic stability and double crop have decreased consecutively due to inadequate water facilities, economic instability, and infertility of soil.

The built-up areas have increased and been encroached on by agricultural land, scrubland, and water bodies. This has influenced the expansion of urban areas due to an increase in better road networks like NH 48, NH 73, and state highways, development of industrial areas, and further, infrastructure activities developed by the Government like the development of roads, schools, colleges, and other commercial buildings. Urban regions have grown due to the population boom and the demand for housing, infrastructure, and commercial space. The scrubland is diminishing as it is converted into agricultural land, plantation, and built-up areas in a relatively short period; this is due to the development of industries, population growth, and economic stability. Moreover, due to the proper water facilities in areas and economic stability from 2000 to 2020, areas of plantation have increased and encroached by areas of water bodies, agricultural land, and scrubland. The few areas of water bodies are converted into agricultural land, plantations, and built-up areas like parks and residential areas due to the development of infrastructure development and the boom of real estate.

Quantification of Urban Sprawl using Shannon's Entropy

The Shannon entropy is often used to calibrate urban growth patterns' dispersion or compactness. Typically, Shannon's entropy ranges from 0 to log (n), with n representing the number of land use classes or categories. The entropy values higher than the log (n) value indicate the dispersion of urban areas in particular zones. Similarly, the entropy value is lower than log (n) which shows the compactness of urban areas in the particular zones. The Radar chart shows that between 2000 and 2020, the amount of entropy has increased irregularly (Fig. 6). The entropy values obtained are 0.999 in 2000, 0.998 in 2005, 0.980 in 2009, 0.997 in 2012, 1.010 in 2015 and 0.990 in 2020. Shannon's entropy for the year 2000 is 0.999, and the log n value of this is 0.9030, which means that the development of urban built-up is more towards the dispersion. Nevertheless, it was quite high for the year 2015, and the value of entropy is 1.010 and the log n value is 0.9030. New residential areas, a few infrastructure activities implemented by the smart city mission, and new industries development added during this period are the main reasons

Table 5: Land Use Cover Dynamic Index of all classes (2000 to 2020).

Class	2000-2005	2005-2009	2009-2012	2012-2015	2015-2020
Built-up Land	5.74	3.40	2.38	14.30	2.82
Double Crop	0.18	-0.52	0.13	-14.70	-0.40
Fallow Land	6.90	0.20	3.67	-7.30	1.18
Forest Plantation	-0.03	-0.03	-0.02	0.053	-0.07
Kharif Crop	-2.42	-1.04	-1.58	-2.09	-1.52
Land Without Scrub	4.95	-3.36	4.69	-9.52	-0.72
Plantation	1.18	1.05	1.33	1.19	1.68
Scrub Forest	-0.02	0.02	0.02	0.02	-0.02
Scrub Land	-4.17	-3.70	-0.19	-12.30	-4.28
Stony Waste	0.56	0.43	0.11	-0.04	0.06
Water Bodies	-1.17	-0.56	-0.21	-1.10	-1.09

for the increase in dispersion between 2009 and 2020. Shannon's entropy values are calculated year-wise (Table 11) and each zone for all the two decades is presented in Table 12.

Interestingly the entropy values of all eight zones are close to log (n) values, indicating a high degree of dispersion. A residential area, an industrial area such as Hirehally, and national highways such as NH 48 and NH 73 in the East South East zone have a lower entropy value (1.020) than the West South East zone. From 2000, the index value increased gradually and reached 1.180 log (n) in 2014 compared to 1.0792 in 2000, indicating an increase in sprawl. The Values of entropy for the North and North East zone are 0.998, 0.99, 0.99, 1.035, 1.01, and 1.15 in 2000, 2005, 2009, 2012, 2015 and 2020, respectively. As a result, the present of three industrial areas has increased. According to TUDA Report from 2000 to 2020, TUDA Developed 80 Layouts in villages present in North North East zones. ENE zone records the least sprawl extent and intensity when compared with other zones due to the presence of hill areas and quarrying activities. The values of entropy for the West and North West zone are 0.98, 1.05, 1.07, 0.9915, 1.01, and 1.020 in 2000, 2005, 2009, 2012, 2015, and 2020 respectively. As a result, urban edge sprawl has spread further away from the urban cluster, although at a maximal rate, along such an axis. On the other hand, the SSE zone is undergoing maximum contemporary urban growth and haphazard sprawl patterns influenced by industry, while on the other hand, there are high concentrations of residential areas. The entropy value was 0.9923 in 2000, showing a gradual increase throughout, and reached an index value of 1.02 against 0.9030 log (n) in the year 2020. This is due to the impact of increasing residential areas and newly established developmental activities conducted by the smart city mission. From 2000 to 2020, the West South West zone has remained consistent over
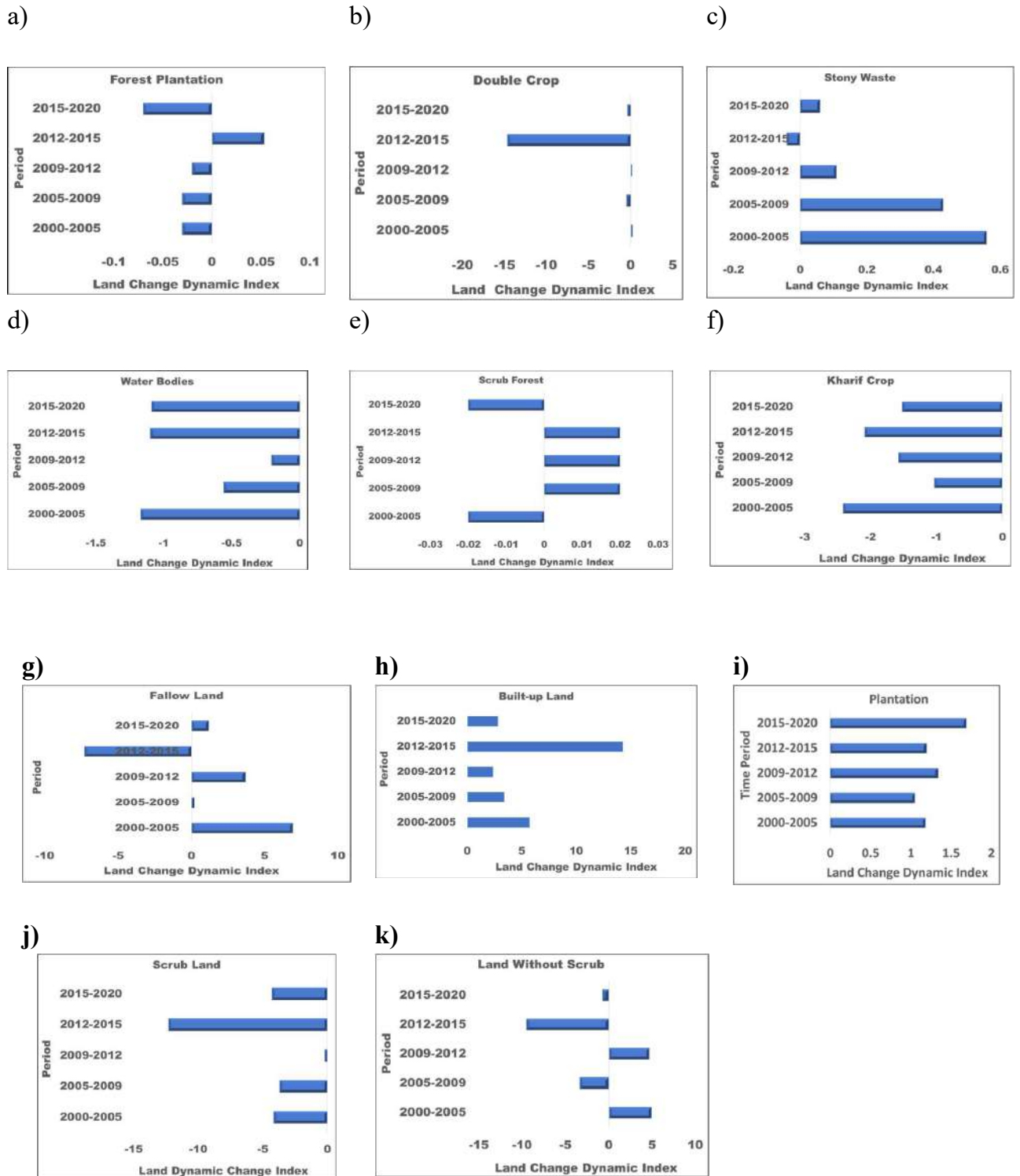
Fig. 5: Bar Graph showing the LDDI values of different land use and land cover classes from 2000 to 2020.

Table 6: Land Transformation Matrix of LULC of Tumkur City during 2000-2005.

LU/LC CLASSES	2000 in km²												
	Builtup Land	Double Crop	Fallow Land	Forest Plantation	Kharif Crop	Land Without Scrub	Plantation	Scrub Forest	Scrub Land	Stony Waste	Water Bodies	Total	Gain(+)
2005 in km²													
Builtup Land	16.6	0.4	0.2	0.0	10.4	0.0	1.7	0.0	0.4	0.1	0.2	32.1	13.4
Double Crop	0.2	0.3	0.3	0.0	5.5	0.0	2.2	0.0	0.6	0.2	0.1	9.9	9.6
Fallow Land	0.2	0.3	0.3	0.0	5.7	0.1	1.2	0.0	1.0	0.2	0.1	9.6	9.3
Forest Plantation	0.0	0.0	0.0	1.2	0.0	0.0	0.0	0.0	0.0	0.0	0.0	1.3	0.1
Kharif Crop	2.4	5.8	5.9	0.0	102.2	0.2	12.2	0.1	5.4	2.1	2.3	143.1	44.4
Land Without Scrub	0.1	0.0	0.0	0.0	1.1	0.1	0.1	0.0	0.0	0.2	0.0	1.6	1.5
Plantation	1.8	2.7	1.8	0.1	22.8	0.0	32.5	0.0	2.0	0.3	1.0	65.2	32.5
Scrub Forest	0.0	0.0	0.0	0.0	0.0	0.0	0.0	7.5	0.0	0.0	0.0	7.6	0.1
Scrub Land	0.5	0.2	0.3	0.0	4.9	0.1	0.9	0.0	1.5	0.5	0.1	8.9	7.5
Stony Waste	0.0	0.0	0.1	0.0	3.6	0.0	0.1	0.0	0.3	15.3	0.0	19.6	4.1
Water Bodies	0.2	0.1	0.1	0.0	1.5	0.0	0.5	0.0	0.1	0.2	20.0	22.6	2.6
Total	25.0	9.8	7.1	1.3	154.2	0.5	61.5	7.6	11.3	19.1	24.0	**321.51**	
Loss(–)	-6.9	-9.5	-6.7	-0.1	-55.9	-0.4	-28.9	-0.1	-9.8	-3.8	-3.8		

Table 7: Land Transformation Matrix of LULC of Tumkur City during 2005-2009.

LU/LC CLASS	2005 in km²												
	Built-up Land	Double Crop	Fallow Land	Forest Plantation	Kharif Crop	Land Without Scrub	Plantation	Scrub Forest	Scrub Land	Stony Waste	Water Bodies	Total	Gain (+)
2009 in km²													
Builtup Land	30.54	0.43	0.56	0.00	3.73	0.04	0.98	0.00	0.02	0.00	0.15	36.47	5.91
Double Crop	0.00	7.10	0.07	0.00	2.47	0.00	0.09	0.00	0.00	0.00	0.00	9.73	2.47
Fellow Land	0.17	0.01	2.85	0.00	6.43	0.01	0.19	0.00	0.03	0.00	0.02	9.71	6.86
Forest Plantation	0.00	0.00	0.00	1.26	0.00	0.00	0.01	0.00	0.00	0.00	0.00	1.27	0.01
Kharif Crop	1.23	1.46	5.26	0.01	122.94	0.26	5.03	0.00	0.29	0.11	0.66	137.26	14.31
Land Without Scrub	0.05	0.00	0.00	0.00	0.11	1.18	0.00	0.00	0.00	0.00	0.00	1.35	0.16
Plantation	0.07	0.94	0.88	0.01	6.80	0.00	58.76	0.00	0.27	0.00	0.03	67.76	9.01
Scrub Forest	0.00	0.00	0.00	0.00	0.00	0.00	0.00	7.60	0.00	0.00	0.00	7.60	0.01
Scrub Land	0.00	0.00	0.00	0.00	0.07	0.00	0.00	0.00	8.32	0.00	0.06	8.45	0.13
Stony Waste	0.00	0.00	0.00	0.00	0.37	0.07	0.01	0.00	0.00	19.56	0.00	20.02	0.08
Water Bodies	0.04	0.01	0.00	0.0	0.24	0.00	0.13	0.00	0.00	0.00	21.66	22.08	0.42
Total	32.11	9.95	9.62	1.28	143.16	1.57	65.21	7.61	8.93	19.68	22.59	**321.69**	
Loss(–)	-1.56	-2.85	-6.77	-0.02	-20.22	-0.39	-6.44	-0.01	-0.29	-0.11	-0.92		

Table 8: Land Transformation Matrix of LULC of Tumkur City during 2009-2012.

LU/LC CLASS	2009 in km²												
2012 in km²	Built-up Land	Double Crop	Fallow Land	Forest Plantation	Kharif Crop	Land Without Scrub	Plantation	Scrub Forest	Scrub Land	Stony Waste	Water Bodies	Total	Gain(+)
Builtup Land	36.33	0.13	0.03	0.00	2.09	0.00	0.43	0.00	0.00	0.00	0.07	39.08	2.75
Double Crop	0.00	6.14	0.11	0.00	3.49	0.00	0.03	0.00	0.01	0.00	0.00	9.77	3.64
Fallow Land	0.00	0.07	3.78	0.00	6.42	0.01	0.45	0.00	0.00	0.03	0.01	10.77	6.99
Forest Plantation	0.00	0.00	0.00	1.24	0.01	0.01	0.00	0.00	0.00	0.00	0.00	1.26	0.01
Kharif Crop	0.01	3.21	5.48	0.01	120.64	0.05	0.11	0.01	0.38	0.00	0.83	130.74	10.09
Land Without Scrub	0.00	0.00	0.03	0.00	0.26	1.26	0.00	0.00	0.00	0.00	0.00	1.55	0.29
Plantation	0.01	0.13	0.25	0.00	3.21	0.02	66.65	0.00	0.11	0.01	0.08	70.48	3.22
Scrub Forest	0.00	0.00	0.00	0.00	0.00	0.00	0.00	7.60	0.00	0.01	0.00	7.61	0.01
Scrub Land	0.00	0.00	0.00	0.00	0.48	0.00	0.00	0.00	7.93	0.00	0.00	8.40	0.48
Stony Waste	0.00	0.04	0.03	0.00	0.04	0.00	0.00	0.00	0.00	19.97	0.01	20.09	0.12
Water Bodies	0.12	0.01	0.01	0.00	0.63	0.00	0.08	0.00	0.02	0.00	21.06	21.94	0.87
Total	36.48	9.73	9.71	1.25	137.26	1.36	67.76	7.61	8.45	20.03	22.07	**321.69**	
Loss (−)	-0.13	-3.59	-5.94	-0.01	-16.63	-0.08	-1.10	-0.01	-0.52	-0.05	-1.01		

Table 9: Land Transformation Matrix of LULC of Tumkur City during 2012-2015.

LU/LC CLASS	2012 in km²												
2015 in km²	Builtup Land	Double Crop	Fallow Land	Forest Plantation	Kharif Crop	Land Without Scrub	Plantation	Scrub Forest	Scrub Land	Stony Waste	Water Bodies	Total	Gain (+)
Builtup Land	34.47	1.60	1.65	0.00	9.58	0.25	6.19	0.00	1.37	0.27	0.48	55.86	21.39
Double Crop	0.17	0.19	0.30	0.00	3.31	0.02	1.27	0.00	0.13	0.01	0.05	5.45	5.26
Fallow Land	0.25	0.52	0.47	0.02	4.73	0.13	1.67	0.00	0.29	0.23	0.08	8.39	7.92
Forest Plantation	0.00	0.00	0.00	1.20	0.05	0.00	0.01	0.00	0.00	0.00	0.00	1.26	0.06
Kharif Crop	2.08	4.23	5.01	0.01	82.71	0.67	21.80	0.01	3.00	2.16	1.65	123.35	40.62
Land Without Scrub	0.01	0.01	0.08	0.00	0.50	0.12	0.07	0.00	0.05	0.25	0.00	1.10	2.07
Plantation	1.80	2.81	2.59	0.00	26.01	0.11	37.85	0.05	1.17	0.21	0.50	73.12	35.25
Scrub Forest	0.00	0.00	0.00	0.00	0.01	0.00	0.00	7.55	0.00	0.04	0.00	7.61	-.05
Scrub Land	0.09	0.09	0.33	0.00	1.50	0.01	0.43	0.01	1.96	0.76	0.09	5.28	3.31
Stony Waste	0.10	0.24	0.30	0.00	2.07	0.22	0.54	0.03	0.34	16.11	0.06	20.02	3.90
Water Bodies	0.09	0.07	0.12	0.02	1.12	0.01	0.62	0.00	0.09	0.03	19.02	21.18	2.15
Total	39.08	9.76	10.86	1.25	131.60	1.54	70.46	7.66	8.42	20.07	21.93	**321.69**	
Loss (−)	-4.59	-9.57	-10.30	-0.03	-48.88	-1.42	-32.60	-0.07	-6.45	-3.96	-2.91		

Table 10: Land Transformation Matrix of LULC of Tumkur City during 2015-2020.

LU/LC CLASS		2015 in km2											
		Builtup Land	Double Crop	Fallow Land	Forest Plantation	Kharif Crop	Land Without Scrub	Plantation	Scrub Forest	Scrub Land	Stony Waste	Water Bodies	Total	Gain (+)
2020 in km^2	Builtup Land	54.97	0.23	0.25	0.00	4.02	0.06	0.549	0.000	0.182	0.047	0.258	60.58	5.61
	Double Crop	0.030	3.57	0.60	0.00	0.58	0.00	0.417	0.000	0.105	0.000	0.027	5.354	1.77
	Fellow Land	0.000	0.794	6.20	0.000	0.894	0.00	0.535	0.000	0.429	0.035	0.018	8.908	2.70
	Forest Plantation	0.000	0.000	0.009	1.195	0.010	0.00	0.003	0.000	0.000	0.000	0.043	1.259	0.04
	Kharif Crop	0.262	0.260	0.38	0.034	107.83	0.00	2.669	0.000	0.681	0.344	0.742	113.21	5.37
	Land Wit hout Scrub	0.012	0.000	0.00	0.00	0.00	0.99	0.00	0.00	0.00	0.00	0.00	1.012	0.01
	Plantation	0.502	0.490	0.605	0.030	8.38	0.00	68.706	0.000	0.259	0.015	0.235	79.22	10.51
	Scrub Forest	0.000	0.000	0.000	0.000	0.08	0.00	0.000	7.54	0.00	0.00	0.00	7.63	0.089
	Scrub Land	0.00	0.100	0.294	0.000	0.01	0.037	0.126	0.000	3.918	0.002	0.016	4.51	0.59
	Stony Waste	0.00	0.00	0.038	0.00	0.27	0.00	0.00	0.033	0.070	19.61	0.020	20.05	0.43
	Water Bodies	0.070	0.004	0.019	0.000	0.39	0.000	0.056	0.000	0.041	0.000	19.851	20.43	0.58
	Total	55.851	5.458	8.415	1.260	122.5	1.105	73.06	7.581	5.68	20.06	21.20	321.69	
	Loss (-)	-0.876	-1.88	-2.21	-0.03	-14.6	-1.21	-4.35	-0.03	-1.74	-0.443	-1.35		

the temporal period, with minimal fluctuations. Compared to other zones, the WSW zone recorded the least amount and severity of sprawl. From 2000 to 2020 few areas like Hegere and Malasadra villages have of new residential areas developed. But future WSW developed very rigorously due to the National Highway projects proposal going on and some developmental activities implemented by Smart city mission by the central government. The NNW zone is facing the maximum expansion of built-up areas and a haphazard sprawl pattern greatly influenced by industries, and new residential areas present on the adjacent sides of highways and villages. The study discloses that built-up area growth and land use patterns have shifted, and a complex pattern of urban sprawl has developed in various directions. Figs. 7 and 8 show the Urban expansion Map and integrated map of Tumkur City.

Monitoring Urban Expansion Intensity Index (UEII)

A UEII describes the nature of the urban expansion of Tumkur City; the zone-wise statistics are presented in Table 13. Between 2000 and 2020, there was an urban expansion intensity index of 0.11 at the lowest point and 2.60 at the highest point, which is considered a high rate of urban expansion. Between 2000 and 2005, the overall study area had an expansion intensity index of 0.53, which is considered moderate for urban expansion. Furthermore, between 2009 and 2012, the UEII increased dramatically from 0.23 to 1.77 from 2012-2015; this rapid increase in UEII indicates an increased likelihood of urban sprawl occurring as a result of various infrastructure projects initiated by the government, an increase in industries, and an increase in population. In the period (2000 to 2020), the highest UEIIs have been observed in zones with built-up fringe areas and high sprawled urban expansion rates. In the period 2005-2009, urban land in Tumkur City began dispersing to the east, north, west, and south-south west, but in the period 2012-2020, urban land began to disperse almost in all directions (i.e. south, southeast, west, and southwest). Fig. 9 shows that the UEII values in different zones have increased in different directions from 2000 to 2020. It is evident from the significant increase in UEII that urban sprawl is becoming more prevalent. It implies that there was notable urban sprawl during this time, reflecting the spread of urban regions into previously undeveloped or rural areas.

Monitoring of Urban Growth using Regression Analysis

Spatio-temporal pattern of built-up density: It was determined the built-up density in each spatial unit of Tumkur city to identify the density of urbanized areas and their spatio-temporal variation. To identify the density of

Table 11: Shannon's entropy index of Tumkur city (zone-wise).

Year	Built-up Area (sq. km)	Entropy Value	Log (n)
2000	24.94	0.999	0.9030
2005	32.10	0.998	0.9030
2009	36.47	0.980	0.9030
2012	39.08	0.997	0.9030
2015	55.85	1.010	0.9030
2020	60.59	0.990	0.9030
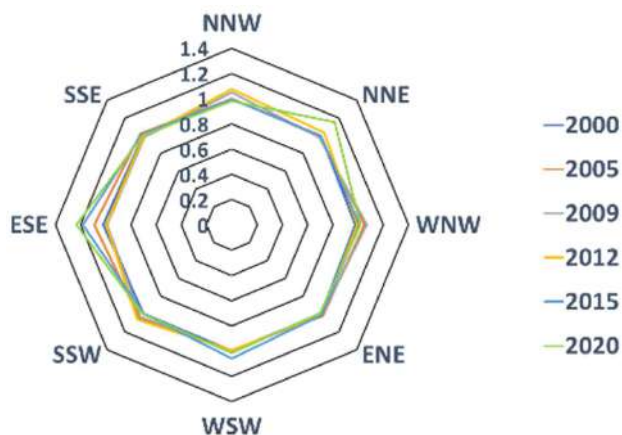
Fig. 6: Radar map depicting zone-specific urban sprawl patterns throughout time.

urbanized areas and their spatiotemporal variation, it was determined the built-up density within each spatial unit of Tumkur City. Built-up density in all zones of Tumkur city areas was very low in 2000 and continued to increase in 2020 has been observed. It is estimated that the built-up density in zones like the NNE, ESE, and SSW will be higher in 2020 than in 2000 (Tables 14 and 15). The TUDA is constructing large residential and industrial developments in these areas, such as Hirehalli, Satyamagala, Antharasanahally Phase 1 and Antharasanahally Phase 2. Some industrial estates have been developed by KIADB along NH 4 in the northern part of the city since 2009. These include Sathyamagala, Lingapura, and Antharasanahally. According to SSE statistics, built-up density has increased from 0.0694 to 0.2009 between 2000 and 2020, indicating that the development of urban built-up is moving toward dispersion. In the WNW zone, which is essentially an NH 73, a new residential area and lesser built-up density value (0.7754) in 0.0845, the index value progressively increased to reach 0.1602 in 2020, indicating an increase in sprawl. During 2000-2020, the built-up density in the WSW zone increased considerably, but compared with other zones, it is still relatively low. As for the ENE zone, the built-up density value is higher, primarily due to the highways, such as NH 48, connecting major cities within the country. The NNW zone is experiencing rapid urban

Table 12: Shannon Entropy values of different zones from 2000 to 2020.

Year	Zones							
	NNW	NNE	WNW	ENE	WSW	SSW	ESE	SSE
2000	0.999	0.998	0.98	0.995	0.998	0.9923	1.020	0.996
2005	1	0.99	1.05	0.990	0.9915	1.04	1.09	1.025
2009	1.05	0.98	1.07	0.991	0.98	1.03	0.99	0.98
2012	1.075	1.035	0.9915	0.992	0.992	1.058	0.995	0.991
2015	0.9955	0.998	1.01	0.998	0.997	1.098	1.180	1.015
2020	0.98	1.15	1.020	0.99	0.998	1	1.23	1
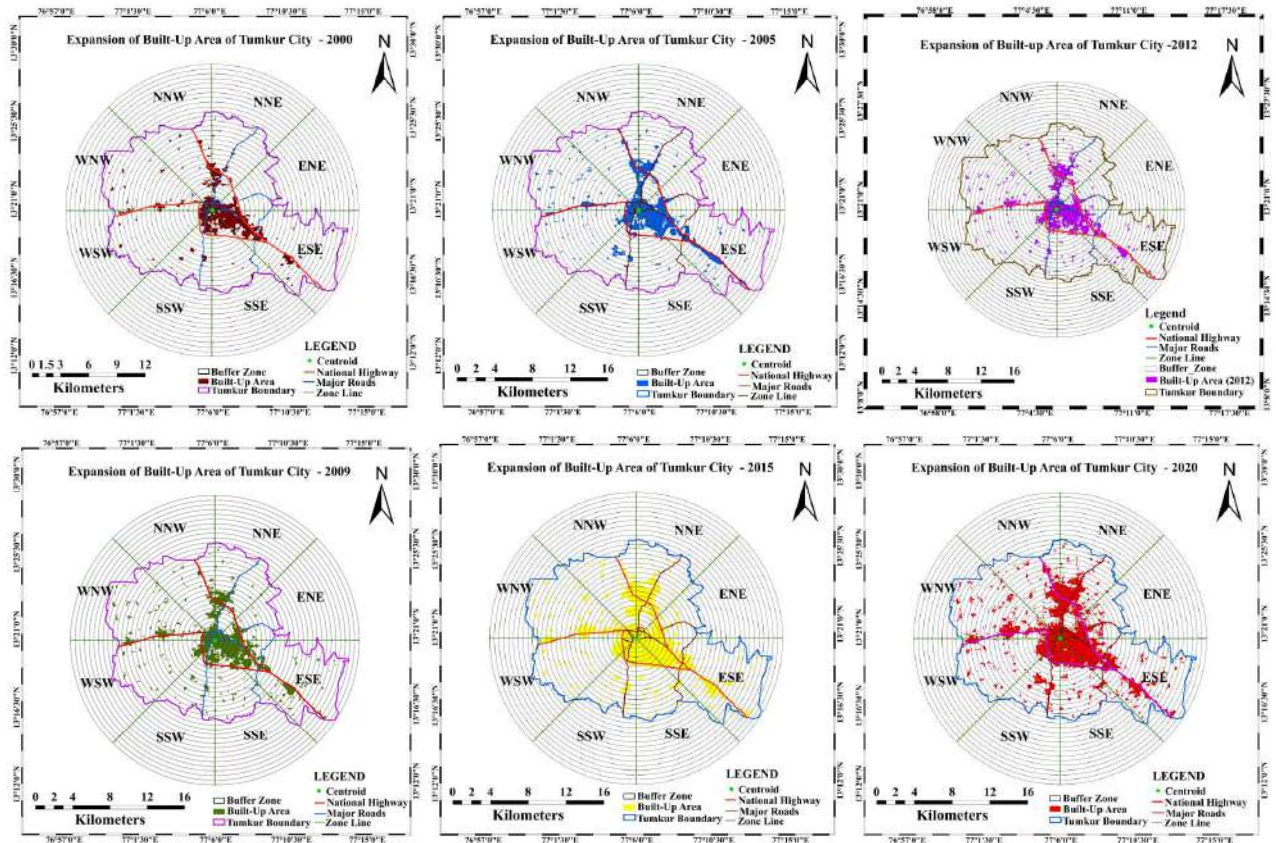
Fig. 7: Urban expansion Map of Tumkur City in (a) 2000, (b) 2005, (c) 2009 (d) 2012, (e) 2015, (f) 2020.

growth and a haphazard sprawl pattern greatly influenced by National Highway 48. From 2000 to 2020, TUDA has developed a wide range of residential areas.

Annual Urban Spatial Expansion Index (AUSEI)

The higher values of AUSEI show the development of built-up areas increased and lower values are an indication of a decrease in the growth of built-up areas during the period. The AUSEI index is useful for determining the geographical pattern of urban growth at a given period. From 2000-2012, the urban expansion index of all zones showed a slight variation in growth, whereas from 2012-2015, the value of the urban expansion index increased (Table 16). In the period 2012 to 2015, the highest rate of urban expansion was recorded in areas and the presence of new residential areas in the core of the city and outside of the city. As a consequence of the sudden increase in urban values during 2012, heavily influenced by National Highway 48 on the one hand and the numerous residential areas developed by TUDA from 2000 to 2020 on the other, the urban expansion values of the WNW zone declined from 2000 to 2012. Heggere is located near the National Highway 76. Some wards, such as Bheemasadra
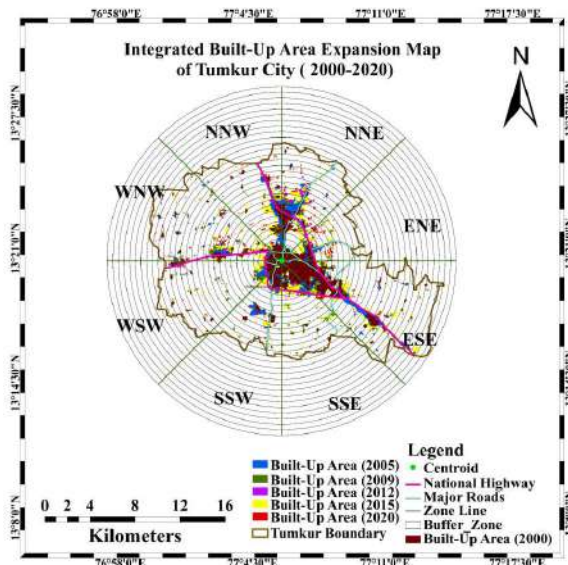
Fig. 8: Integrated Urban Expansion Map of the Tumkur City from 2000 to 2020.
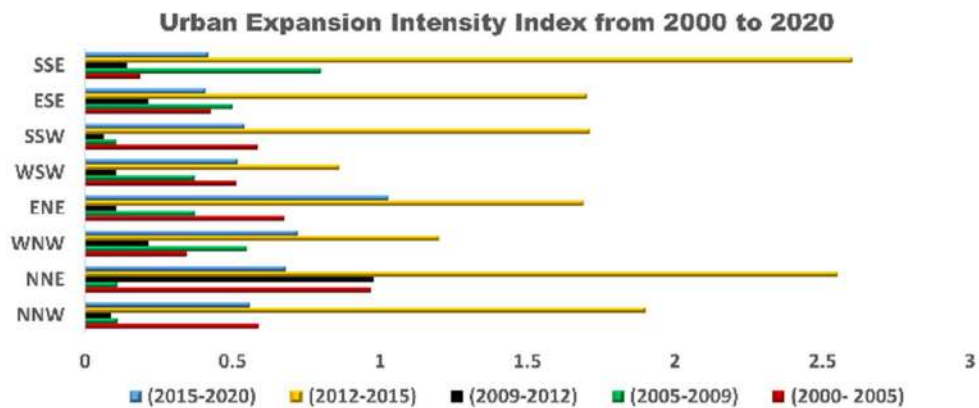
Fig. 9: Bar chart of UEII from 2000 to 2020.

Table 13: Urban Expansion Intensity Index of all zones (2000 to 2020).

Zones	Year				
	2000-2005	2005-2009	2009-2012	2012-2015	2015-2020
NNW	0.588	0.11	0.0875	1.90	0.56
NNE	0.97	0.1098	0.9796	2.55	0.68
WNW	0.348	0.5492	0.2160	1.20	0.723
ENE	0.676	0.373	0.107	1.69	1.030
WSW	0.5147	0.3712	0.1049	0.863	0.5164
SSW	0.585	0.108	0.064	1.71	0.54
ESE	0.4272	0.50130	0.2131	1.70	0.4097
SSE	0.1869	0.80	0.14468	2.60	0.4178
Total	0.5367	0.3653	0.2395	1.77	0.912

and KHB Colony, were influenced by the expansion of the urban area. From 2000 to 2012, urban expansion values in zones such as ESE, SSW, and NNE were very low. Since 2012, urban expansion values have increased as an output of the progression of industrial areas and several infrastructure projects developed by Smart City Mission. Some wards such as Bheemasadra and KHB Colony, were influenced by the expansion of the urban area. From 2000 to 2012, urban expansion values in zones such as ESE, SSW, and NNE were very low. Since 2012, urban expansion values have increased due to the development of industrial areas and some infrastructure projects developed by Smart City Mission. During the period 2000 to 2020, the development of better road networks by the government and economic progress has led to a rise in settlements in rural villages in the ESE,

Table 14: The Built-up areas of different zones in Tumkur City.

Zones	Total Area	2000	2005	2009	2012	2015	2020
NNW	38.08	2.505	3.626	3.56	3.89	6.08	7.158
NNE	37.77	3.195	5.034	5.18	6.31	9.20	10.44
WNW	54	2.352	3.29	4.39	4.74	6.70	8.654
ENE	21.74	1.972	2.75	3.03	3.10	4.208	5.328
WSW	44.46	1.338	2.460	3.12	3.26	4.412	5.56
SSW	25.92	2.35	3.113	2.98	3.05	4.433	5.13
ESE	68.82	9.19	10.66	12.04	11.95	15.125	16.53
SSE	29.95	2.08	2.36	3.32	3.45	5.848	6.019

Table 15: Built-up Density of different zones in Tumkur City areas.

Zones	2000	2005	2009	2012	2015	2020
NNW	0.0658	0.0952	0.0991	0.1021	0.1596	0.1879
NNE	0.0845	0.1332	0.1378	0.1670	0.2435	0.2764
WNW	0.0435	0.0609	0.0814	0.0877	0.1240	0.1602
ENE	0.0907	0.1244	0.1392	0.1425	0.1935	0.2450
WSW	0.0300	0.0553	0.0701	0.0733	0.0992	0.1250
SSW	0.0906	0.1206	0.1114	0.1176	0.1710	0.1981
ESE	0.1335	0.1548	0.1724	0.1656	0.2197	0.2401
SSE	0.0694	0.0787	0.1108	0.1151	0.1952	0.2009

SSW, and NNE zones such as Machenahalli, Basavapatna, Maraluru, Singanahalli, Arakere, Yallapura, etc. Between 2000 and 2012, the Urban Expansion Index value varied in the SSW zone, but between 2012 and 2020, it increased. This indicated a rise in the growth of urban areas due to the few residential layouts developed by TUDA and the few infrastructure projects developed by Smart City Mission's Central Government.

As a result of urban expansion values varying from 2000 to 2012 in the few zones like WNW, NNW, SSE, and WSW, large residential areas are present, built-up areas are developed along national and state highways, and industrial areas and industrial estates are developed by the Karnataka Industrial Area Development Board (KIADB). Expansion values have increased between 2012 and 2015 but have slowed down since 2015. This indicated that the expansion of built-up areas is slow compared to 2000 to 2015, but the built-up area is expanded.

Annual built-up change index (ABUCI): The yearly rate of change in built-up areas was established by calculating the total built-up area in high-density and low-density classes each year and detecting the change over successive years (Table 17). The pattern of the annual change rate in Tumkur city is that, as a whole, the built-up areas of the rural have not experienced a significant rate of annual built-up change during the period from 2000 to 2012. In

contrast, after 2012, the zones, especially ESE, SSW, and NNE experienced annual change at a faster rate. The study reveals the presence of industrial areas such as Hirehalli, Antharasanahally Phase 1 and Antharasanahally Phase 2, Satyamagala, and the presence of new residential areas both within and outside the city. Between 2012 and 2015, the real estate market experienced a boom, which affected the rate of change annually. The rate of annual built-up change in the WNW zone was only 18.8 % in 2000–2005, which increased about three times (65.38 %) in the later period, 2012–2015. This zone experienced the highest rate of change in built-up areas, followed by SSE and NNWUrbanization is caused by the conversion of agricultural land, scrubland, and other land-use and land-cover types. The study shows that outside of the center region, there is lots of prospective space for future development of urban growth.

In contrast, core regions are often packed, with little or no possibility for additional expansion, resulting in a spatial pattern of built-up change over time. In 2000, the rate of change in the NNW zone was estimated to be 22 %. However, the rate of change is three times greater (72.6 %) between 2012 and 2015. This shows that urban areas are expanded and influenced by the boom of real estate in those areas. Compared to other zones such as NNW, NNE, and ESE, the rate of change of built-up in ENE, SSE, and WSW is low. This indicated that the built-up is expanding in city

areas and a few villages like Hettenahalli, Kaidala, etc. In rural areas, settlements increased as a result of better road connectivity between cities and rural areas, and because of the presence of highways, real estate booms occurred between 2010 and 2020.

Assessing Interrelationship among BD, AUSEI and ABUCI: The correlation coefficients of the Built-up Density index (BD), Annual Urban Spatial Expansion Index (AUSEI), and Annual Built-up Change Index (ABUCI) were estimated by regression analysis to identify the interrelationships among them. It is evident from the correlation between the urban expansion index and the annual rate of change in the built-up area that they are well correlated and have a significant positive relationship. There is a strong correlation between the ABUCI and AUSEI since areas with a high AUSEI are also experiencing high rates of annual change in built-up areas, and vice versa. In 2012–2015, there was a very strong correlation between the two variables. The correlation between built-up density and urban expansion index shows a very strong negative correlation with a significant correlation coefficient (Fig. 10). According to the results, R^2 was 0.5258, 0.5027, 0.5516, 0.5225, and 0.622 for the various periods. The data indicate that areas with a high density of built-up areas have not expanded as much. In contrast, urban expansion has occurred primarily in areas with a low density of built-up areas. AUSEI has been comparatively higher in these areas since they have

not yet been fully developed and still have sufficient lands for potential growth. In comparing the relationship between built-up density and the annual rate of change in a built-up area, it was discovered that there was a high negative correlation between the two variables. For 2000, 2005, 2009, 2012, 2015, and 2020, with an R^2 value of 0.560, 0.5439, 0.6223, 0.5368 and 0.5267, respectively. In high-density regions, there were no notable changes; conversely, in low-density areas, there were significant alterations. On the other hand, the abundance of vacant land made low-density built-up regions ideal for conversion. Land-use land-cover dynamics in core and peri-urban areas are important for the development of smart cities, particularly in the planning of sustainable land use. For the implementation of smart city missions, it is necessary to consider information regarding spatio-temporal variations in urban growth. Interrelationship results revealed that rapid urban growth experienced in the study area leads increase in some consequences.

CONCLUSION

From 2000 to 2020, geospatial techniques were used to analyze Tumkur City's urban land use and land cover changes and, according to the change magnitudes, the Land Use/Cover Degree Dynamic Index and LULC transformation matrix revealed that increased large areas of built-up land were contributed by kharif crop, scrubland and waterbodies, and increased plantations contributed by kharif crop and

Table 16: The AUSEI values of different zones in Tumkur City (2000-2020).

Zones	Year				
	2000- 2005	2005-2009	2009-2012	2012-2015	2015-2020
NNW	6.1787	0.2457	1.4685	12.01	6.1787
NNE	7.305	0.70	5.96	10.47	2.37
WNW	5.7142	6.26	2.4613	9.75	4.5158
ENE	5.39	2.68	0.7526	9.912	4.120
WSW	9.12	5.2884	1.431	9.761	4.129
SSW	4.90	-0.9416	0.546	10.399	2.73
ESE	2.748	2.86	0.1377	17.107	2.830

Table 17: The ABUCI values of different zones in Tumkur City (2000-2020).

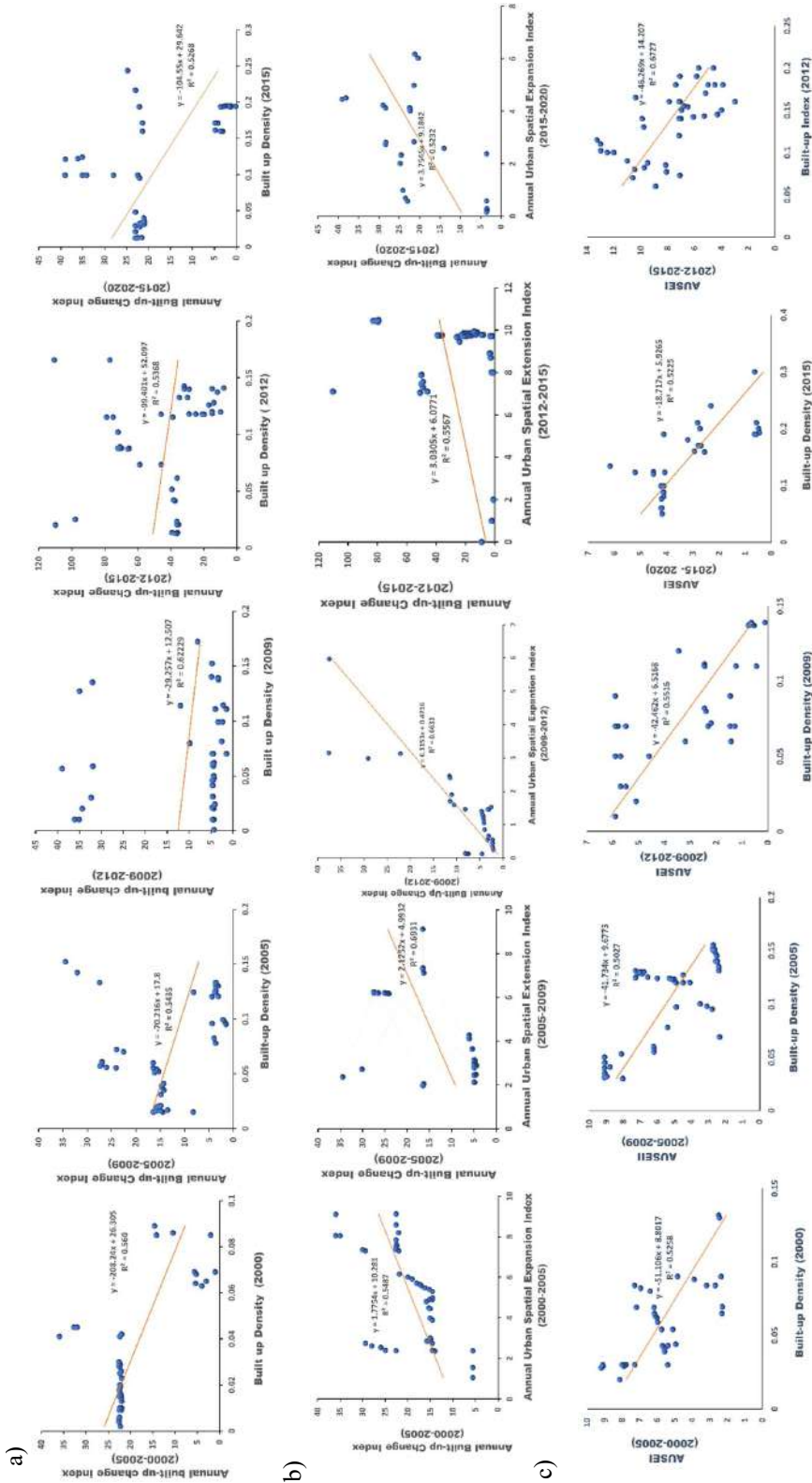| Zones	Year				
	2000- 2005	2005-2009	2009-2012	2012-2015	2015-2020
NNW	22	4.35	3.33	72.6	21.4
NNE	36	3.65	37.66	96.33	24.8
WNW	18.8	27.5	11.66	65.38	39.1
ENE	14.6	8.25	3.33	35.93	22.4
WSW	22.6	16.5	4.66	39	23
SSW	15.2	3.15	2.33	46	14
ESE	5.6	24.13	4.33	79.66	3.58

Fig. 10: Interrelationships Scatter plot among Built-up Density and ABUCI (**a**), ABUCI and AUSEI (**b**), Built-up Density and ABUCI (**c**)

scrubland. Further, the study focused on determining the built-up land patterns using urban sprawl and urban growth analysis by deriving various indices. The derived entropy values greater than the Log (n) values in Shannon Entropy indicate large built-up areas are expanding in the zones such as WNW, NNE, ENE, and ESE due to the development of the road network system, population growth, and industrial growth, which shows an increase in the urban sprawl. Further, the urban growth analysis carried out by the UEII statistics shows a high level of urban expansion after 2009, and the correlation between built-up density, ABUCI, and ASEI results indicated the expansion of urban areas, mainly in the center and industrial regions of the city. The study's overall findings have demonstrated how beneficial it is to utilize geospatial technology to investigate the degree and stress of urbanization on land and water resources. The conversion of kharif into plantations built-up land indicated increased food insecurity due to the growth of real estate. Further, the present study's findings will provide to understanding of land use dynamics, urban sprawl, urban growth analysis, and future projections, as well as provide crucial information for decision-making and urban planning processes to the urban planners, supporting the improvement of policy implications on supportable land use management and guiding strategies for appropriate urban development.

REFERENCES

Antipova, A., Momeni, E. and Banai, R., 2022. Analysis of Urban Sprawl and Blight Using Shannon Entropy Index: A Case Study of Memphis, Tennessee. In *Advances in Urbanism, Smart Cities, and Sustainability* (pp. 322-299). CRC Press. http://dx.doi.org/21-9781003126195/10.1201.

Bhatta, B., Saraswati, S. and Bandyopadhyay, D., 2010. Quantifying the degree-of-freedom, degree-of-sprawl, and degree-of-goodness of urban growth from remote sensing data. *Applied Geography*, 30(1), pp. 96-111. https://doi.org/10.1016/j.apgeog.2009.08.001.

Brown, D.G., Pijanowski, B.C. and Duh, J.D., 2000. Modeling the relationships between land use and land cover on private lands in the Upper Midwest, USA. *Journal of Environmental Management*, 59(4), pp. 247-263. https://10.12691/aees-1-6-5.

Bunyangha, J., Majaliwa, M.J., Muthumbi, A.W., Gichuki, N.N. and Egeru, A., 2021. Past and future land use/land cover changes from multi-temporal Landsat imagery in Mpologoma catchment, eastern Uganda. *The Egyptian Journal of Remote Sensing and Space Science*, 24(3), pp. 675-685. http://dx.doi.org/10.1016/j.ejrs.2021.02.003.

Burgalassi, D. and Luzzati, T., 2015. Urban spatial structure and environmental emissions: A survey of the literature and some empirical evidence for Italian NUTS 3 regions. *Cities*, 49, pp. 134-148. https://doi.org/10.1016/j.cities.2015.07.008.

Dadras, M., Shafri, H.Z., Ahmad, N., Pradhan, B. and Safarpour, S., 2015. Spatio-temporal analysis of urban growth from remote sensing data in Bandar Abbas city, Iran. *The Egyptian Journal of Remote Sensing and Space Science*, 18(1), pp. 35-52. http://dx.doi.org/10.1016/j.ejrs.2015.03.005.

Dahly, D.L. and Adair, L.S., 2007. Quantifying the urban environment: a scale measure of urbanicity outperforms the urban–rural dichotomy. *Social Science & Medicine*, 64(7), pp. 1407-1419. https://psycnet.apa.org/doi/10.1016/j.socscimed.2006.11.019.

Deng, J.S., Wang, K., Deng, Y.H. and Qi, G.J., 2008. PCA-based land-use change detection and analysis using multitemporal and multisensor satellite data. *International Journal of Remote Sensing*, 29(16), pp. 4823-4838. http://dx.doi.org/10.1080/01431160801950162.

Didier, S., Peyroux, E. and Morange, M., 2012. The spreading of the city improvement district model in Johannesburg and Cape Town: urban regeneration and the neoliberal agenda in South Africa. *International Journal of Urban and Regional Research*, 36(5), pp. 915-935. DOI:10.1111/j.1468-2427.2012.01136.

Dijoo, Z.K., 2021. Urban heat island effect concept and its assessment using satellite-based remote sensing data. *Geographic Information Science for Land Resource Management*, pp. 81-98. https://doi.org/10.1002/9781119786375.ch5.

Dutta, D., Rahman, A., Paul, S.K. and Kundu, A., 2019. Changing pattern of urban landscape and its effect on land surface temperature in and around Delhi. *Environmental monitoring and assessment*, 191, pp.1-15.

Dutta, D., Rahman, A., Paul, S.K. and Kundu, A., 2020. Estimating urban growth in peri-urban areas and its interrelationships with built-up density using earth observation datasets. *The Annals of Regional Science*, 65, pp. 67-82. https://link.springer.com/article/10.1007/s00168-020-00974-8.

Grekousis, G., Manetos, P. and Photis, Y.N., 2013. Modeling urban evolution using neural networks, fuzzy logic and GIS: The case of the Athens metropolitan area. *Cities*, 30, pp. 193-203. https://doi.org/10.1016/j.cities.2012.03.006.

Grodach, C. and Guerra-Tao, N., 2022. Industrial lands, equity, and economic diversity: a comparative study of planned employment areas in Melbourne, Australia. *Urban Research & Practice*, pp. 1-17. https://doi.org/10.1080/17535069.2022.2080583.

Haque, M.I. and Basak, R., 2017. Land cover change detection using GIS and remote sensing techniques: A spatio-temporal study on Tanguar Haor, Sunamganj, Bangladesh. *The Egyptian Journal of Remote Sensing and Space Science*, 20(2), pp. 251-263. http://dx.doi.org/10.1016/j.ejrs.2016.12.003

Herold, M., Couclelis, H. and Clarke, K.C., 2005. The role of spatial metrics in the analysis and modeling of urban land use change. *Computers, Environment and Urban Systems*, 29(4), pp.369-399. http://dx.doi.org/10.1016/j.compenvurbsys.2003.12.001.

Hong, Z., Hailin, L. and Zhen, C., 2011. Analysis of land use dynamic change and its impact on the water environment in Yunnan plateau lake area—A case study of the Dianchi lake drainage area. *Procedia Environmental Sciences*, 10, pp.2709-2717.

Jaad, A. and Abdelghany, K., 2021. The story of five MENA cities: Urban growth prediction modeling using remote sensing and video analytics. *Cities*, 118, p.103393.

Ji, W., Ma, J., Twibell, R.W. and Underhill, K., 2006. Characterizing urban sprawl using multi-stage remote sensing images and landscape metrics. *Computers, Environment and Urban Systems*, 30(6), pp.861-879. https://doi.org/10.1016/j.compenvurbsys.2005.09.002.

Kasraian, D., Maat, K. and van Wee, B., 2019. The impact of urban proximity, transport accessibility and policy on urban growth: A longitudinal analysis over five decades. *Environment and Planning B: Urban Analytics and City Science*, 46(6), pp.1000-1017. http://dx.doi.org/10.1177/2399808317740355.

Khan, R. and Jhariya, D.C., 2018. Assessment of land-use and land-cover change and its impact on groundwater quality using remote sensing and GIS techniques in Raipur City, Chhattisgarh, India. *Journal of the Geological Society of India*, 92, pp.59-66. https://doi.org/10.1007/s12594-018-0953-3.

Kim, C., 2016. Land use classification and land use change analysis using satellite images in Lombok Island, Indonesia. *Forest Science and Technology*, 12(4), pp.183-191. https://doi.org/10.1080/21580103.2016.1147498.

Kindu, M., Schneider, T., Teketay, D. and Knoke, T., 2013. Land use/land cover change analysis using object-based classification approach in Munessa-Shashemene landscape of the Ethiopian highlands. *Remote Sensing*, 5(5), pp.2411-2435. http://dx.doi.org/10.3390/rs5052411.

Lambin, E.F., Turner, B.L., Geist, H.J., Agbola, S.B., Angelsen, A., Bruce, J.W., Xu, J., 2001. The causes of land-use and land-cover change: moving beyond the myths. *Global Environmental Change*, 11(4), pp.261-269. https://doi.org/10.1016/S0959-3780(01)00007-3.

Liu, Y., Song, W. and Deng, X., 2019. Understanding the spatiotemporal variation of urban land expansion in oasis cities by integrating remote sensing and multi-dimensional DPSIR-based indicators. *Ecological Indicators*, 96, pp.23-37. http://dx.doi.org/10.1016/j.ecolind.2018.01.029.

Lu, Y., Wu, P., Ma, X. and Li, X., 2019. Detection and prediction of land use/land cover change using spatiotemporal data fusion and the Cellular Automata–Markov model. *Environmental Monitoring and Assessment*, 191, pp.1-19. https://link.springer.com/article/10.1007%2Fs10661-019-7200-2.

Maktav, D. and Erbek, F.S., 2005. Analysis of urban growth using multi-temporal satellite data in Istanbul, Turkey. *International Journal of Remote Sensing*, 26(4), pp.797-810. http://dx.doi.org/10.1080/01431160512331316784.

Marcotullio, P.J. and Lee, Y.S.F., 2003. Urban environmental transitions and urban transportation systems: A comparison of the North American and Asian experiences. *International Development Planning Review*, 25(4), pp.325-354. http://dx.doi.org/10.3828/idpr.25.4.2.

Mas, J.F., Lemoine-Rodríguez, R., González-López, R., López-Sánchez, J., Piña-Garduño, A. and Herrera-Flores, E., 2017. Land use/land cover change detection combining automatic processing and visual interpretation. *European Journal of Remote Sensing*, 50(1), pp.626-635.

Masila, S.M., 2016. Effects of land degradation on agricultural land use: a case study of smallholder farmers indigenous knowledge on land use planning and management in Kalama division, Machakos county (Doctoral dissertation). http://dx.doi.org/10.9734/cjast/2019/v34i330134.

Mathews, A.J. and Nghiem, S.V., 2021. Examining Urban Built-up Volume: Three-Dimensional Analyses with Lidar and Radar Data. In: *Urban Remote Sensing: Monitoring, Synthesis, and Modeling in the Urban Environment*, pp.17-45. https://doi.org/10.1002/9781119625865.ch2.

Mohamed, A. and Worku, H., 2019. Quantification of the land use/land cover dynamics and the degree of urban growth goodness for sustainable urban land use planning in Addis Ababa and the surrounding Oromia special zone. *Journal of Urban Management*, 8(1), pp.145-158. https://doi.org/10.1016/j.jum.2018.11.002.

Mohan, R. and Dasgupta, S., 2004, June. Urban development in India in the twenty first century: policies for accelerating urban growth. In: *Fifth Annual Conference on Indian Economic Policy Reform*, Stanford Centre for International Development. Retrieved from http://scid.stanford.edu/sites/default/files/publications/231wp.pdf.

Montgomery, M.R., Stren, R., Cohen, B. and Reed, H.E., 2013. *Cities transformed: demographic change and its implications in the developing world*. Routledge. http://dx.doi.org/10.4324/9781315065700.

Munsi, M., Malaviya, S., Oinam, G. and Joshi, P.K., 2010. A landscape approach for quantifying land-use and land-cover change (1976–2006)

in middle Himalaya. *Regional Environmental Change*, 10, pp.145-155. http://dx.doi.org/10.1007/s10113-009-0101-0.

Naikoo, M.W., Rihan, M. and Ishtiaque, M., 2020. Analyses of land use land cover (LULC) change and built-up expansion in the suburb of a metropolitan city: Spatio-temporal analysis of Delhi NCR using landsat datasets. *Journal of Urban Management*, 9(3), pp.347-359. https://doi.org/10.1016/j.jum.2020.05.004.

Ning, Y., Liu, S., Zhao, S., Liu, M., Gao, H. and Gong, P., 2022. Urban growth rates, trajectories, and multi-dimensional disparities in China. *Cities*, 126, p.103717. https://doi.org/10.1016/j.cities.2022.103717.

Nkeki, F.N., 2016. Spatio-temporal analysis of land use transition and urban growth characterization in Benin metropolitan region, Nigeria. *Remote Sensing Applications: Society and Environment*, 4, pp.119-137. http://dx.doi.org/10.1016/j.rsase.2016.08.002.

Padhi, B. and Mishra, U.S., 2022. Assessment of living condition of urban slum dwellers in India in the New Millennium. *Urban Research & Practice*, 15(4), pp.604-626.

Rauws, W.S. and de Roo, G., 2011. Exploring transitions in the peri-urban area. *Planning Theory & Practice*, 12(2), pp.269-284. http://dx.doi.org/10.1080/14649357.2011.581025.

Turner, B., Meyer, W.B. and Skole, D.L., 1994. Global land-use/land-cover change: towards an integrated study. *Ambio*, 23(1), pp.91-95. Available at: http://www.jstor.org/stable/4314168?origin=JSTOR-pdf.

Xie, Y., Mei, Y., Guangjin, T. and Xuerong, X., 2005. Socio-economic driving forces of arable land conversion: A case study of Wuxian City, China. *Global Environmental Change*, 15(3), pp.238-252. http://dx.doi.org/10.1016/j.gloenvcha.2005.03.002.

Yakub, M. and Tiffin, P., 2017. Living in the city: urban environments shape the evolution of a native annual plant. *Global Change Biology*, 23(5), pp.2082-2089. https://doi.org/10.1111/gcb.13528.

Yang, L., Xian, G., Klaver, J.M. and Deal, B., 2003. Urban land-cover change detection through sub-pixel imperviousness mapping using remotely sensed data. *Photogrammetric Engineering & Remote Sensing*, 69(9), pp.1003-1010. https://doi.org/10.14358/PERS.69.9.1003.

Yin, P., Li, X., Mao, J., Johnson, B.A., Wang, B. and Huang, J., 2023. A comprehensive analysis of the crop effect on the urban-rural differences in land surface phenology. *Science of The Total Environment*, 861, p.160604. https://doi.org/10.1016/j.scitotenv.2022.160604.

Younes, A., Ahmad, A., Hanjagi, A.D. and Nair, A.M., 2023. Understanding Dynamics of Land Use & Land Cover Change Using GIS & Change Detection Techniques in Tartous, Syria. *European Journal of Geography*, 14(3), pp.20-41. https://doi.org/10.48088/ejg.a.you.14.3.020.041.

Zhang, B., Li, W. and Zhang, C., 2022. Analyzing land use and land cover change patterns and population dynamics of fast-growing US cities: Evidence from Collin County, Texas. *Remote Sensing Applications: Society and Environment*, 27, p.100804. https://doi.org/10.1016/j.rsase.2022.100804.

Zhong, Y., Lin, A., He, L., Zhou, Z. and Yuan, M., 2020. Spatiotemporal dynamics and driving forces of urban land-use expansion: A case study of the Yangtze River economic belt, China. *Remote Sensing*, 12(2), p.287. https://doi.org/10.3390/rs12020287.

ORCID DETAILS OF THE AUTHORS

Govindaraju: https://orcid.org/0000-0002-0119-4826

Environmental Impact Assessment of Air Quality Issues Caused by the Granite Quarrying and Stone Processing Industry in Ramanagara District, Karnataka State, India

V. Nagaraja† , **C. J. Rakesh, H. N. Sindhu and N. Harishnaika**

Department of PG Studies and Research in Applied Geology, Kuvempu University, Jnanasahyadri, Shankaraghatta-577451, Shivamogga District, Karnataka State, India

†Corresponding author: V. Nagaraja; nagarajavlr02@gmail.com

ABSTRACT

The environmental impacts of mining, quarrying, and the stone processing industry are significant, affecting air quality, health, and the socioeconomic status of communities worldwide. Key contributors to air pollution include the waste of raw materials from quarrying, non-compliance with scientific protocols, and the extraction of natural mineral resources. The rapid increase in pollution sources, such as dust, water, and noise, has led to the release of various pollutants into the atmosphere, degrading local air quality. This study conducted sampling at twelve sites, adhering to the Central Pollution Control Board's (CPCB) monitoring guidelines. Twelve metrics, including PM_{10}, $PM_{2.5}$, SO_2, NOx, CO, O_3, Pb, NH_3, C_6H_6, C_2OH_{12}, As, and Ni, were measured twice a week over a three-month period (January 2024 to March 2024) by the National Ambient Air Quality Standards (NAAQS) in the research area. The results indicated that while SO_2 and NOx levels were within permissible limits at all monitored locations, Suspended Particulate Matter (SPM) levels were high at every station. The average baseline levels of PM_{10} (37.17 µg/m³ to 70.52 µg/m³), $PM_{2.5}$ (16.98 µg/m³ to 39.85 µg/m³), SO_2 (5.29 µg/m³ to 13.91 µg/m³), NOx (9.8 µg/m³ to 29.71 µg/m³), CO (0.15 mg/m³ to 0.32 mg/m³), O_3 (6.9 µg/m³ to 15.37 µg/m³), and NH_3, Pb, Ni, As, C_2OH_{12}, and C_6H_6 were below the detection levels (BDL) and limits of quantification (LOQ), all within the National Ambient Air Quality Standards for commercial, industrial, and residential areas during the study period. This research highlights the urgent need for effective pollution control measures to mitigate the adverse environmental and health impacts of these industries.

INTRODUCTION

Quarrying is the process of extracting minerals from the upper crust of the earth. The natural resources of the world, including land, soil, air, dust, noise, water, the biosphere, human health, society, and the socioeconomic status of the populace, are severely being harmed by the quarrying and stone processing industries (Gbeve 2013, Emmanuel 2018, Umar et al. 2023). This is because there are no scientific techniques for managing granite reserves and resources, and they are overexploited by humans (Vallack et al. 1998, Ukpong 2012, Sreekala et al. 2023). In addition to air, noise, dust, and water pollution, land degradation, biodiversity loss, topographical relief, flooding, extremely cold temperatures, forest fires, changes in the climate and seasonal pattern variation, greenhouse effects, and health risks from drilling, blasting, and ground vibration, we are currently dealing with serious environmental issues (Singh et al. 2010, Jahed Armaghani et al. 2015, Kittipongvises 2017).

For four or five centuries, natural resources have been overexploited without regard for the consequences to the ecosystem, which has led to these problems (Sheikh et al. 2011, Melodi 2017). The most damaging human activities are those that harm the ecosystem both immediately and over time (Mwangi 2014, Ming'ate et al. 2016). The environment is seriously threatened by overexploitation and negligent practices in the mining and stone processing industries (Odewumi et al. 2015, Okafor et al. 2023).

The primary environmental effects of granite quarries were the creation of artificial ponds, isolated artificial reliefs, regular-shaped depressions, erosion and instability of quarry scarps, partial or total destruction of fluvial terraces, piezometric surface depression, altered groundwater flow direction, formation of periodically flooded areas, permanent removal of areas from agricultural use, changes to farming practices, and pedological changes in soil (Oyinloye et al. 2015, Kofi-Boye 2017, Leon-Kabamba et al. 2020,

Rathore 2020, Roja 2022). To ensure that these regions can eventually be exploited again, people should work toward degraded environment regeneration at every stage of quarrying activities (Saha et al. 2011, Santizo 2022).

The surrounding landscapes of quarrying places are severely impacted by the difficulties in disposing of waste rock (Singh et al. 2010, Sayara 2016). A significant global concern, aside from the granite industry, is human-caused air pollution (Singhal 2018, Salem 2021, Sreekala et al. 2023). Understanding the ways that metropolitan areas impact the chemistry, composition, and life cycles of the atmosphere in several hundred-kilometer downwind regimes can be achieved by considering them as concentrated sources of massive anthropogenic emissions of pollutants (Yeh et al. 1980, Ajibade et al. 2022). Additionally, research on the global epidemiological impacts of air pollution has demonstrated that particulate matter and gaseous pollutants can seriously impair human health, leading to respiratory disorders, heart disease, and cardiopulmonary death (Abdul-Wahab et al. 2015 & 2022, Zimwara et al. 2021).

Fossil fuels and their derivatives are being used more frequently as a result of emerging countries' increasing industry, urbanization, technological innovation, and modernization (Ajah et al. 2018, Zimwara et al. 2021). Thus, the primary challenge facing emerging nations is reducing air pollution, particularly in quickly expanding megacities (Daspan et al. 2018). Estimates from the World Health Organization indicate that air pollution causes nearly two million premature deaths annually, including lung infections, heart attacks, respiratory diseases, and even cancer (Haseeb 2018, Werner et al. 2019). The use of fossil fuels with poor environmental performance, improper land use patterns, industrialization, fast population growth, an increase in vehicles, inadequate transportation infrastructure, improper land use patterns, and-most importantly-ineffective environmental regulations are some of the factors contributing to India's rising air pollution levels (Chattopadhyay et al. 2010, Henry et al. 2017).

The World Health Organization's (WHO) recommended health thresholds for air pollution are exceeded in the majority of Indian cities with populations greater than two million people (Halwenge 2015, Martins et al. 2017). With the aid of remote sensing and GIS software, monitoring the concentrations of various ambient air quality indicators not only prevents detrimental health effects but also provides policymakers with a foundation for successful environmental regulations (Moeletsi 2018, Werner et al. 2019). SPM (suspended particulate matter), SO_2 (sulfur dioxide), and NOx (nitrogen oxide), together with other chemicals generated by numerous businesses, particularly the granite industry, are the main pollutants causing environmental destruction in the area. Reduced plant photosynthesis, noise and dust pollution, structural flaws, biodiversity loss, and nuisance dust are only a few of the problems that quarrying is frequently linked to (Nandan et al. 2017, Omeiza et al. 2022).

People's property and health are being significantly impacted by industrial site noise, ground vibrations, drainage, and particulate matter (Sunyer 2001, Stieb et al. 2005). Potential effects of these include decreased agricultural productivity, significant harm to the region's road network, and environmental issues such as soil erosion, vegetation loss, building fissures, biodiversity loss, and topographical changes (Sun et al. 2016, Sayara et al. 2016). Because it generates a variety of contaminants, the granite quarrying and processing industry is dangerous (Tsiouri et al. 2015).

Today, those who live near quarries have extremely terrible lives as a result of pollution. Health problems can affect anyone at any moment; respiratory and skin conditions are two examples (Zanobetti et al. 2009, Yakovleva 2017). The term "AQI" (air quality index) is used because it is challenging to provide high-quality data regarding the concentration of several environmental indicators (Wright 2009, Trivedi et al. 2009 & 2010). The common spaces and woodlands of the communities are covered in waste material, often known as by-products (Yasobant et al. 2017, Abeya 2023).

A significant amount of inert dust is discharged into the sky during the quarrying process, and depending on the wind direction, this dust can travel up to 4 or even 5 kilometers (Chowdhury 2004, Aarthy et al. 2018). This causes cloudbursts, which in turn cause downpours and flash floods by preventing the formation of rain clouds (Ekpa et al. 2022 & 2023). Because it entails the direct exploitation of resources, quarrying is distinct. It supplies the building sector with raw materials. The construction sector needs a lot of stone for its projects. The increasing need for building materials, including aggregate, sand, gravel, and rocks, as well as industrial manufacturing, is driving the market for quarry commodities. This leads to the mismanagement of natural resources, which is detrimental to the ecology and economy.

The objective of the current study is to assess how the granite quarrying, stone-cutting, crushing, and stone-processing activities that are conducted in the study region affect the local environment. The state of Karnataka is home to most of the rich mineral and ore resources, such as bauxite, iron, manganese, gold, copper, and some significant rocks like gneiss, granite, granodiorites, and doleritic dykes.

The Ramanagara region of Karnataka State's granite quarries are the subject of this study's environmental effects. To develop mitigation and control techniques, the research
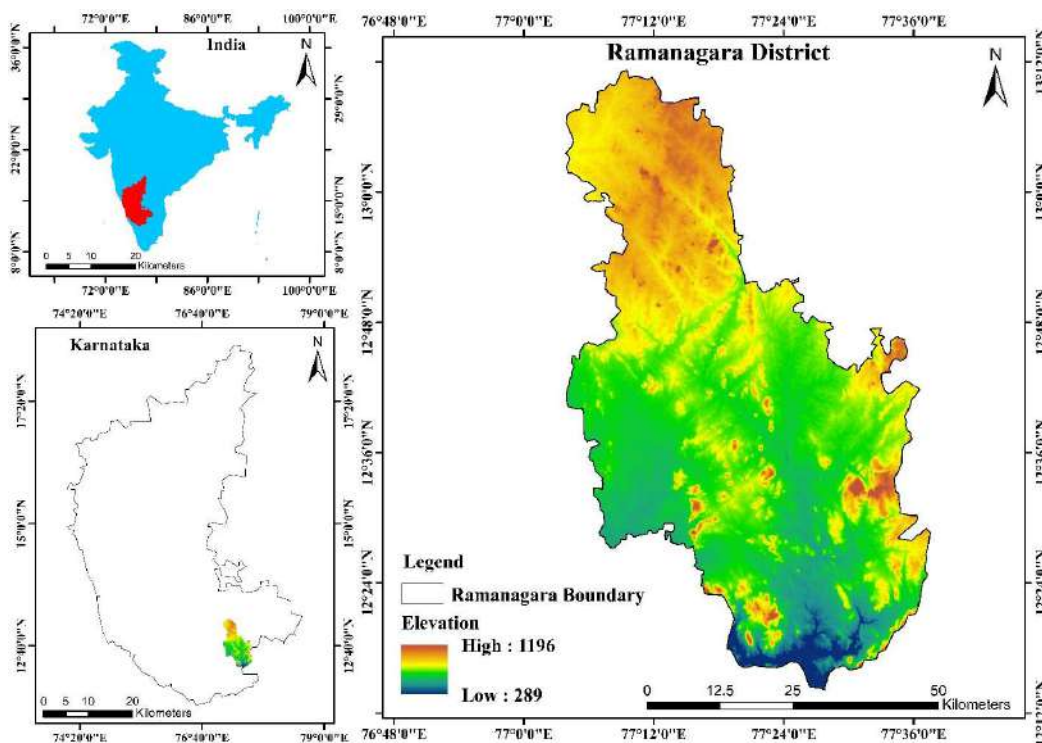
Fig. 1: Study region with data on elevation.

will gather and analyze air samples, calculate their impact on air quality in residential, industrial, and quarry contexts, and use the results. This research will help future researchers and add to the body of information about the quarrying business. In this district, the local inhabitants and the environment are being negatively impacted by the stone processing and quarrying businesses.

STUDY AREA

On August 23, 2007, the former Bengaluru Rural District-which included the taluks of Ramanagara, Channapatna, Kanakapura, and Magadi-was divided into the Ramanagara district. According to Bhat et al. 1991 & 1994, and Swamy 1998, its largest lengths are 102.25 kilometers in the north-south direction and 62.08 kilometers in the east-west direction. The district is composed of 823 settlements spread over a 3516 km^2 physical area, of which 699.46 km^2-or around 17.21% of the district's total area-are forest. The district's headquarters are in the town of Ramanagara, which is situated roughly 50 miles southwest of Bengaluru, the state capital.

The district of Ramanagara is located between latitudes 12.72°N and 77.27°E. Fig. 1 shows the contour lines that delineate the district's most notable high and low elevation zones, which are located at elevations of 1196 and 289 meters above mean sea level, respectively. There are 742.50 meters above sea level on average. The district borders Mandya on the west, Bangalore Urban on the northeast, and Tumakuru, Bangalore Rural, and Bangalore Urban on the north.

MATERIALS AND METHODS

Materials

The toposheet was used in this study to derive the morphological area. Toposheet numbers are compiled by the Indian government's Survey of India (SOI). D43R4_57G4, D43R8_57G8, D43X1_57H1, D43X2_57H2, D43X3_57H3, D43X5_57H5, D43X6_57H6, D43X7_57H7, D43X8_57H8, D43X9_57H9, D43X10_57H10, and D43X11_57H11 are some instances of toposheet numbers.

Elevation and land cover data are obtained from DEM Cartosat-1 and LISS satellite photos on the ISRO Bhuvan website. The meteorological and air quality data sets come from a field investigation, a few official technical publications, and the Open Government Data (OGD) platform in India. Several government bodies, such as the Department of Mines and Geology (DMG) and the Ramanagara district mineral survey report, have provided reports and information about quarrying. Table 1 indicates these data sets.

Table 1: Datasets utilized in the field investigation

Data name	Resolution	website
DEM	10m	Indian Geo platform (Bhuvan)
LISS 3	30m	Indian Geo platform (Bhuvan)
Landsat 8	30m	USGS
Toposheets	1:50000	SOI(survey of India)
Rainfall and temperature	0.5*0.5 km	IMD(India meteorological department)
Quarry and rocks	-	DMG(department of Mines and Geology
Air quality	-	open governmental data (OGD) platform, India

Methodology

Compiling information from many sources: Primary and secondary sources served as the foundation for this investigation. Field and market surveys, maps, questionnaires, interviews, and laboratory tests are examples of primary sources. Books, journals, published and unpublished reports, and official government documents are examples of secondary sources. The effects of air pollution on the local ecology, people, flora and wildlife, crops, and surroundings were evaluated using field surveys and general observations. The Ramanagara district of the Indian state of Karnataka, which is renowned for its rich granite deposits, diversity, and amount of forest cover, is the only area covered by the study. Using a systematic and random selection process, a sample of the homes at the randomly selected quarry sites was created, resulting in the sample households.

The sample consisted of only one or two hundred adjacent towns or residences that are both directly and indirectly affected by the quarrying activity. Field research and a standardized questionnaire were used to collect data from the families. A research study report was prepared for the analysis in the Ramanagara district locations using baseline data collected at many sites throughout a single season (January 2024 to March 2024). The data are shown in Table 2. These figures were used to assess the possible harm caused by the stone-processing and quarrying industries. They provided guidance on the best course of action for the quarry site and industry, as well as resources for management, government organizations, and mitigation strategies. For this research project, the findings of the analysis report and study summary were carefully considered.

Choosing study sites for the sampling process: Table 3 shows the location, with sampling locations labeled in different environmental settings. Climate data, topography and terrain, human settlements, health status, accessibility to the monitoring site, resource availability, representativeness of the region for establishing baseline status, and representativeness about likely impact areas were taken into account when choosing the locations for ambient air quality monitoring.

Guidelines for collecting ambient air quality samples: For three months, ambient air quality was monitored twice a week in each region. The following parameters were used to create baseline data for the air environment: lead (Pb), arsenic (As), nickel (Ni), free silica, benzene (C_6H_6), Benzo (a) pyrene C_2OH_{12}, ammonia (NH_3), ozone (O_3), nitrogen dioxide (NO_X), sulfur dioxide (SO_2), carbon monoxide (C_O); particulate matter ($PM_{2.5}$), and (PM_{10}) size less than 10 μm. A comparison has been conducted between the national ambient air quality guidelines and the measured concentrations of pollutant parameters.

Equipment for gathering samples: Particulate matter (PM_{10} and $PM_{2.5}$) was detected using Envirotech 271; combo PM_{10} and $PM_{2.5}$ samplers; breathable dust samplers (Envirotech APM 460 BL); and fine particulate samplers (APM 550). Gaseous pollutants, such as SO_2, NO_X, O_3, and NH_3, were sampled using Ecotech's AAS 109, Envirotech's APM 411, and Ecotech's APM 460 gaseous pollution samplers. Electrochemical sensor technology was used for carbon monoxide monitoring. Every year, the monitoring instruments need repairs and calibrations.

Techniques for analysis and sampling: Table 4 enumerates the sampling and analytical methods utilized to track ambient

Table 2: Parameter derived from multiple sources

Sl. No.	Attribute	Parameter	Source of Data
1.	Climatology and Meteorology	Wind speed, Wind direction, Dry bulb temperature, Wet bulb temperature, Relative humidity, Rainfall, Solar radiation, Cloud cover and Environmental Lapse.	Field research, collecting data from a variety of locations, including industrial, residential, and quarry sites.
2.	Geology, rock and Soil	Geological history	Field research, Primary and secondary sources, satellite photos, topographical maps, etc.
3.	Ambient Air Quality	PM_{10}, $PM_{2.5}$, SO_2, NOx, Pb, CO, O_3, C_6H_6, As, Ni, NH_3, C_2OH_{12}, Free Silica etc.	Monitored Data (12 locations)

Table 3: Location and the gathering of samples in various environments

Location Code	Sample code	Locations	Latitude	Longitude	Distance (km) from Ramanagara town	Azimuth Directions	Environmental setting
QL 1	AAQ1	Doddamudawadi quarry site	12°37'38.08" N	77°22'47.27" E	15.74	SE	Commercial
QL 2	AAQ2	Yadamaranahalli quarry site	12°24'54.09"N	77°22'56.53"E	35.54	S	Commercial
QL 3	AAQ3	Hanakadaburu, kodi-halli hobali quarry site	12°24'17.24"N	77°32'50.28"E	45.4	SE	Commercial
QL 4	AAQ4	Hanakadaburu, kodi-halli hobali quarry site	12°23'49.59"N	77°32'39.51"E	46.58	SE	Commercial
QL 5	AAQ5	Achalu quarry site	12°27'55.43"N	77°21'18.06"E	30.37	S	Commercial
QLV 6	AAQ6	Hanakadaburu village	12°24'1.12"N	77°32'51.18"E	46.5	SE	Residential
QLV 7	AAQ7	Kodahalli village	12°25'9.41"N	77°18'34.70"E	33.66	SW	Residential
QLV 8	AAQ8	Achalu village	12°28'30.11"N	77°21'47.08" E	28.55	S	Residential
QLV 9	AAQ9	Harohalli village	12°40'53.59"N	77°28'26.33"E	21.3	SE	Residential
QLV 10	AAQ10	Bidadi village	12°47'56.48"N	77°23'9.77"E	15.67	NE	Residential
QLIN 11	AAQ1I	Harohalli Industrial area	12°41'0.05"N	77°26'43.60"E	18.27	SE	Industrial
QLIN 12	AAQ12	Bidadi industrial area	12°47'54.84"N	77°23'0.33"E	14.51	NE	Industrial

Table 4: Techniques for data analysis for ambient air quality parameter Assessment (NAAQS).

Sl. No.	Parameters	Analytical method	NAAQ standards: 2009	
1.	Sulphur Dioxide (SO_2), μg/m^3	IS: 11255 (Part 2)/USEPA Method 6	50 (Annual)	80 (24 Hours)
2.	Nitrogen Dioxide (NO_2), μg/m^3	IS: 5182 (Part - guidelines Volume1 6): 2006 /CPCB	40 (Annual)	80 (24 Hours)
3.	Particulate Matter ($PM_{2.5}$), μg/m^3	In house method (Gravimetric method) based on CPCB guidelines Volume1	40(Annual)	60 (24hours)
4.	Particulate Matter (PM_{10}), μg/m^3	IS:5182 (Part–guidelines Volume1 23): 2006/CPCB	60 (Annual)	100 (24 hours)
5.	CO, mg/m^3	IS:5182(Part–10):1999(Reaff:2006) CPCB guidelines Volume1	2 (8 hours)	4 (1hour)
6.	Pb, μg/m^3	IS:5182(Part–22):2004(Reaff:2006) CPCB guidelines Volume1	0.5 (Annual)	1 (24 hours)
7.	O_3, μg/m^3	In house method (Spectrophotometric method) based on CPCB guidelines Volume1	100 (8hours)	180 (1hour)
8.	NH_3, μg/m^3	In house method (Spectrophotometric method) based on CPCB guidelines Volume1	100 (Annual)	400 (24 hours)
9.	Benzene, μg/m^3	GC FID/ GC MS based on IS 5182 (Part:12) / CPCB guidelines Volume1	5 (Annual)	5 (Annual)
10.	Benzo (a) pyrene, ng/m^3	In House Validated Method By HPCL, UV and GC MS Based on IS:5182(Part– 12) CPCB guidelines Volume1	1 (Annual)	1 (Annual)
11.	Arsenic, ng/m^3	In house method (AAS method) Based on CPCB guidelines Volume 1	6 (Annual)	6 (Annual)
12.	Nickel, ng/m^3	In house method (AAS method) Based on CPCB guidelines Volume 1	20 (Annual)	20 (Annual)

air quality. The closest power sources, which included homes at each AAQ station or governmental entities including Panchayat offices, schools, and temples, were used to power the AAQ equipment.

Table 5 displays the frequency and techniques of monitoring. The analysis report and summary of the air quality survey results were carefully considered for this study project.

Table 5: The frequency and monitoring techniques.

Attributes	Sampling		Measurement Method	Remarks
	Network	Frequency		
Meteorology				
Wind speed, Wind direction, Dry bulbtemperature, Wet bulb temperature, Relativehumidity, Rainfall, Solar radiation, Cloud cover and Environmental Laps	Selected locations	Continuous for 3 Months	Weather monitorswith the database	As per Meteorological department standard. Primary or secondary data
Air Environment				
Particulate Matter (PM_{10})	Selected locations	24 hourly-Twice a week for 3months in non-Monsoon season	Gravimetric (High-Volume with Cyclone)	As per CPCB standards under 18th November 2009 Notification for NationalAmbient Air Quality Standards (NAAQS). Field survey, Primary or secondary data
Particulate Matter ($PM_{2.5}$)			Gravimetric (High-Volume with Cyclone)	
Oxides of Sulphur (SO_2)			EPA Modified West and Gaeke method	
Oxides of Nitrogen (NOx)			Arsenite Modified Jacob and Hochheiser	
Carbon Monoxide (CO)			Gas Analyzer (NDIR)	
Ozone (O_3)			UV photometric	
Ammonia (NH_3)			Indophenol Blue Method	
Lead (Pb)			Atmospheric Absorption Spectrometer	
Arsenic (As)				
Nickel (Ni)				
Benzene			GC-MS/MS	
Benzo Alpha Pyrene			GC-MS/MS	

RESULTS AND DISCUSSION

The Geological Setting of the Granite Quarry in the Study Area

The Ramanagara district's geology: According to Bhat et al. (1994), Syed Abrar et al. (2000 & 2005), Swamy (1998), the rocks in the district come from the Sargur group, the Peninsular Gneissic Complex (PGC), the Charnockite group, the Closepet granite, and the basic and more recent intrusive. The Charnockite group's representative is Charnockite. Lenses found in gneisses, migmatite, amphibolite, and banded magnetite quartzite, which appears as tiny bands— are all part of the Sargur group. Granites, gneisses, and migmatite make up the PGC, which is situated east and west of the Closepet granite (Bhat et al. 1991 & 1994, Simha et al. 2015, Venkatesha et al. 2015). Within the gneisses, the intrusive bodies containing the Closepet granite stretch 50 km in length and 15-20 km in width, with a near-N-S trend. There are reported to be enclaves of migmatite, gneisses, quartzite, and amphibolites among the various compositions found in the Closepet granite. The common intrusives are dolerite, gabbro, pyroxenite, and rarely norite. Dolerite is the most common of the fundamental dikes (Paranthaman

et al. 1995, Swamy 1998, Syed Abrar et al. 2000 & 2005). Three main lineaments in the district go to NNW-SSE. These lineaments range in length from 45 to 70 kilometers. According to the interpretation of this data, a deep-seated fault that is trending NNW-SSE crosses the Closepet granites (Suresh Babu 1995).

The main land uses in the areas covered by quarry leases are plan land, hills, vegetation, various rock formations, and soil cover or overburden. Pebbles are most common in low-lying, loose soils, and most of the leased areas have thin patches of dirt covering them that are between 0.5 and 10 meters thick. Both on higher ground and in deposits at the surface, there are rock outcrops. Reddish-brown soil capping covers the majority of the hill's northern, western, and eastern sections at the lower elevation of the quarry lease area.

The field investigation's findings indicate that the geological setting of the granite quarry area is influenced by several variables, such as the quarry's topography, size, potential deposit formation type, material quality, mineral structure and texture, color, and chemical makeup, as well as the availability of resources, the company's financial standing, the intended output, market, price, supply and demand, and so forth.

Table 6: Lithostratigraphy and rock types in Ramanagara District

Soil Clover	
I. **Younger intrusive** (More recent invasion)	Extremely potassic rocks; dolerite/gabber/diorite/norite dykes; felsite/felsite porphyry dykes; coarse-grained pink/grey porphyritic granite.
II. **Closepet granite (2400–2100 Million years)**	Pink/grey porphyritic granite with coarse grain; pink granites (less mafic); grey granites; pink hornblende granite; pink equigranular/porphyrite migmatites.
III. **Peninsular Gneissic Complex (3000 Million years)**	Grey migmatites, biotite gneiss, leucogneiss and homophonous gneiss, charnockite and migmatite.
IV. **Sargur group (> 3000 Million years)**	Garnet-sillimanite gneiss, quartzite (fuchsite and BMQ), meta-ultramafites, amphibolites (both massive and schistose), and banded magnetite quartzite.
Not visible is the base	

With an average thickness of fewer than 0.5 meters, the dirt in the middle of the ridge is only present in the spaces between the stones. The established stratigraphic succession of the research region is displayed here, based on fieldwork and observations. The rock types and lithostratigraphy of the Ramanagara District are depicted in Table 6.

The study area is situated in Seismic Zone III, which is characterized as having a very high potential for earthquake shocks of 5 or 6 on the Richter scale, and Seismic Zone IV, commonly known as the high damage risk zone.

In this district, sand mining and defined and non-specified minor mineral leases in Kanakapura, Ramanagara, Channapatna, and Magadi Taluk were conducted in parallel with taluk-wise quarrying operations for dimension stone, construction stone, brick earth, crushers, and stone cutting facilities. Moreover, the area has more crushing factories
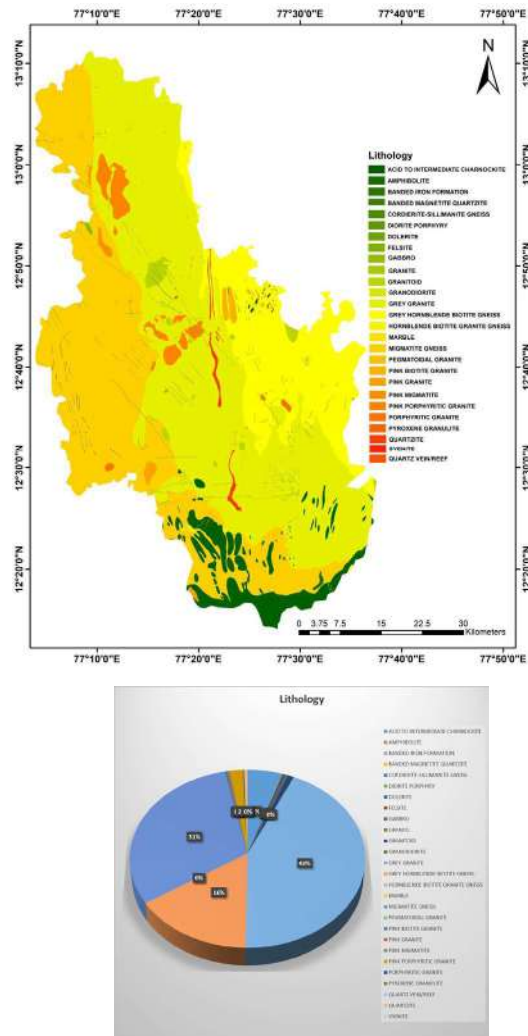
Fig. 2: Lithology and its percentage of Ramanagara district.

per square mile than other districts, and four to five decades ago; it was home to several granite quarries and crushing businesses.

The environment is contaminated by the stone-cutting and quarrying processes' noise, dust, water, and other factors. The associated radioactivity varies depending on the surrounding environment due to dust emissions from quarrying and crushing processes. Fig. 2 displays the lithology and area of the Ramanagara district.

Within the research region of the Ramanagara district, which spans a total geographical area of 3516.21 sq.

km, various types of rocks are dispersed as follows: The region encompassed 173.6 sq. km of acid to intermediate charnockite; 3.12 sq. km of amphibolite; 4.24 sq. km of banded iron formation; 1.2 sq. km of banded magnetite quartzite; 0.3 sq. km of cordierite-sillimanite gneiss; 0.96 sq. km of diorite porphyry; 12.4 sq. km of dolerite; 3.26 sq. km of felsite; 12.82 sq. km of gabbro; 0.54 sq. km of granite; 29.36 sq. km of granitoid; 3.23 sq. km of granodiorite; 1522.9 sq. km of grey Granite; 545.83 sq. km of grey hornblende biotite gneiss; 0.69 sq. km of hornblende biotite granite gneiss; 0.59 sq. km of marble; 1080.64 sq. km of migmatite
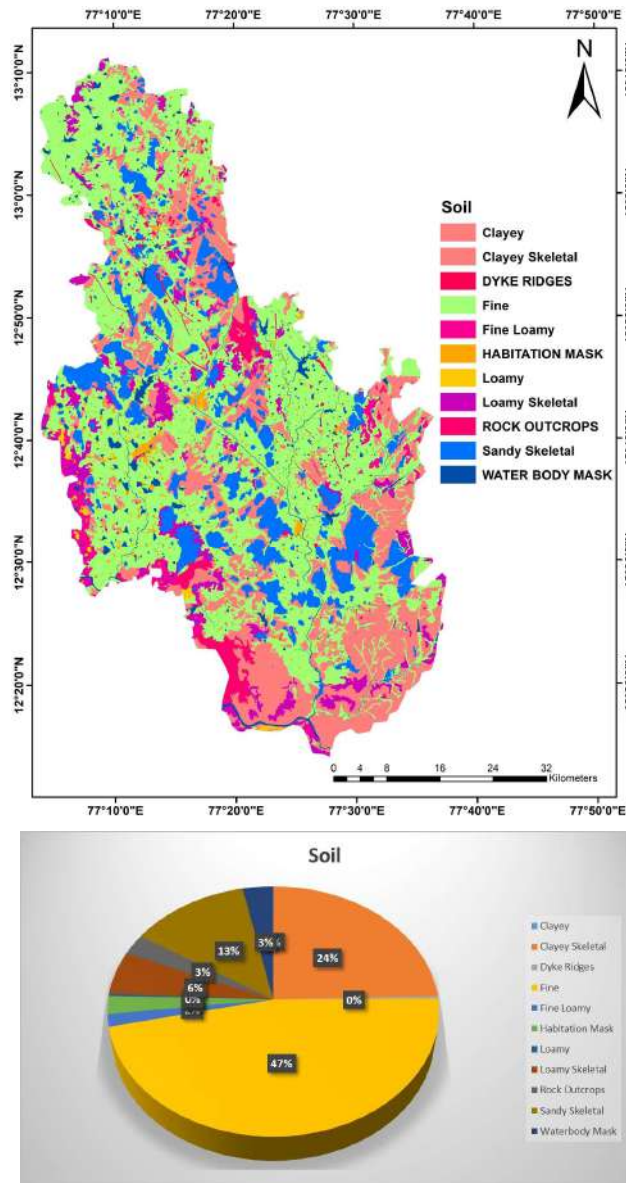
Fig. 3: Conditions of the soil and its percentage in the study area.

gneiss; 3.37 sq. km of pegmatoidal granite; 12.03 sq. km of pink biotite granite; 8.07 sq. km of pink granite; 6.92 sq. km of pink migmatite; 66.46 sq. km of pink porphyritic granite; 4.66 sq. km of porphyritic granite; 2 sq. km of pyroxene granulite; 0.23 sq. km of quartz vein/reef; 16.19 sq. km of quartzite; and 0.57 sq. km of syenite. The Ramanagara district is entirely covered in rocks. Gray granite and migmatite gneiss are the two main lithologies in this area. The region is roughly 1552 km^2 and 1080 km^2.

The Ramanagara District's Soil Type and Proportion Covered

Although dirt is essential to air pollution, it usually serves no purpose in the quarrying process or other associated operations. About 60% of the Ramanagara district is covered with red, sandy soil (Hema et al. 2012). The remaining soil is loamy and reddish-brown. Geology and soil are closely related in a pedogenic system because of the combined effects of parent material, climate, biosphere, terrain, relief, stage, age, maturity, and time of rock weathering conversion, rainfall, solar radiation, and management (enhancement and degradation/erosion). The main regions with red sandy soil include the taluks of Channapatna, Kanakapura, Magadi, and Ramanagara due to their varied topographies (Caruthers 1984, Hema et al. 2013, Ganesha et al. 2017). Fig. 3 list every type of soil.

With a total land area of 3516.21 sq. km, the Ramanagara district contains a variety of soil types that are scattered throughout the research region, including the following: 8.59.7 sq.km of skeletal clayey; 17.09 sq.km of dyke ridges; 1634.47 sq.km of fine; 54.79 sq.km of fine loamy; 81.91 sq.km of habitation mask; 12.23 sq.km of loamy; 192.06 sq.km of skeletal loamy; 98.34 sq.km of rock outcrops; 445.7 sq.km of sandy skeletal; 117.54 sq.km of water body mask of habitation.

The Methods Used in the Ramanagara District for Granite Quarrying Operations

In the Ramanagara district region, the majority of stone quarrying activities employ opencast extraction techniques. In open-cast quarrying, significant overburdens such as organic plant cover and topsoil must be removed to reach the

Table 7: Quarrying activities in the Ramanagara district areas leased by the government as of 2022-23.

Sl. No	Taluk	Building stone	Ornamental or dimension stone	Brick earth	Crusher Units	M-sand units
1	Ramanagara	38	02	-	29	08
2	Kanakapura	25	52	-	03	02
3	Magadi	19	04	O2	10	02
4	Channapatna	-	02	-	-	-
	Total	82	60	02	42	12
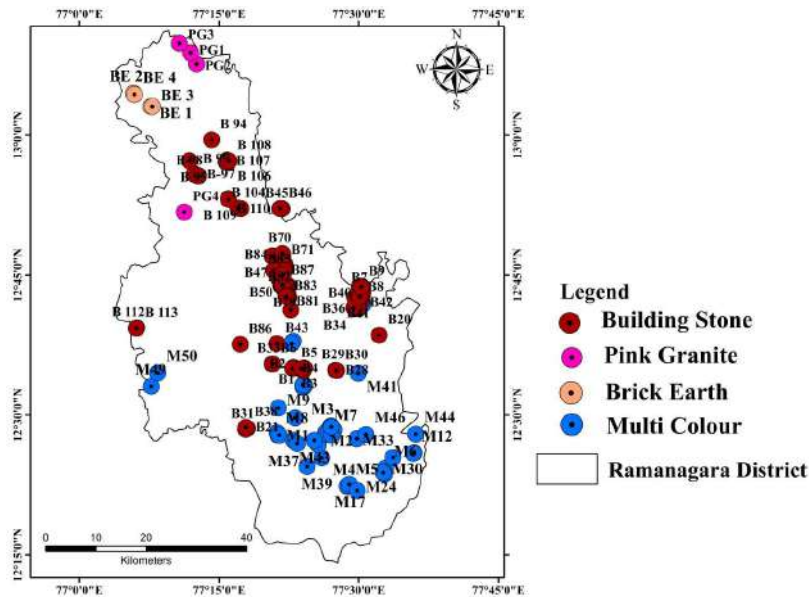
Fig. 4: Quarrying areas spreading in the Ramanagara district.

mineral reserves. The following procedures are involved in extracting granite through open-cast quarrying for dimension or ornamental stone: clearing the area, loading waste or well-dressed materials, transportation, processing raw materials, quality control, shifting, management of stockyards, and recycling waste materials as khandas or brick materials (Rajan Babu et al. 2000 & 2002 & 2003, Drew et al. 2002, Gbeve 2013, Eshiwani 2014,). Stone quarrying, stone crusher buildings, and sand mining are subject to additional operational limitations. There is evidence that these actions have a detrimental effect on the ecosystem.

There are various phases of quarrying operations, and each one has a unique impact on the environment. These phases typically entail deposit exploration and prospecting, the development and preparation of quarries, the use of materials from the quarries, and the processing of the minerals collected at the various installations to create products that may be marketed (Chalekode 1978, Kuzu et al. 2005, Ibrahim et al. 2018, Chaanda et al. 2019). However, there are numerous other environmental risks associated with open-cast quarrying practices. As of 2022–23, Table 7 indicates that the following Ramanagara district lands have been leased by the government (department of mines and geology) for quarrying purposes. Fig. 4 shows the quarrying areas spreading in the Ramanagara district.

Quarry Rock has the third and fourth positions in the world's non-fuel mineral commodities value and volume rankings. However, the quarry's operations deteriorate the land's condition and raise air pollution levels, which negatively impacts the neighborhood's residents and workers (Bada et al. 2013, Bassey et al. 2021).

According to Amankwah et al. (2019) and Bakamwesiga et al. (2021), and the outcome shows that the dust produced during the operation is carried by the atmosphere and travels significant distances from the crusher and quarrying sites to the nearby communities. Table 8 shows that the list of equipment needed to operate a quarry varies according to production capacity.

The amount of air pollution depends on the local microclimate, the size, composition, and volume of dust in the surrounding air, and one of the main causes of air pollution is noise from quarry sites. For example, the mining and processing of granite produce silica dust (Loveson et al. 1997, Esguerra 2008, Doley et al. 2010, Eshiwani 2014, Amankwah et al. 2019).

Dust not only tends to accumulate on surfaces, making it unsightly, but it can also be harmful, especially to people who have respiratory problems. Dust can physically injure plants nearby by obstructing their internal organs and abrading their

Table 8: The minimum machinery and equipment required for quarrying operation (minimum production of 100 cubic meter) and impact on natural environment

Sl. No.	Type	Nos.	Size/ capacity	Make	Motive Power	Impact on natural environment
1.	Compressor	2	440 cfm	Atlas Copco	Diesel/ Electricity/DG	Air, noise, emission pollution
2.	Jack hammer	10	33mm dia.	Atlas Copco	-	Air, noise, dust pollution
3.	Hydraulic rock breaker/Excavator	2	1.2 cu. M or 380 HP	Sany – SY210C-9 or Tata Hitachi	Diesel	Air, noise, dust, emission pollution, ground vibration
4.	Tipper	2	20 tons	Tata	Diesel	Air, noise, dust, emission pollution, ground vibration
5.	Water tanker	1	5000 liter	Mahindra	Diesel	Air, noise, dust, emission pollution
6.	Tractor	1	04 tons	Mahindra	Diesel	Air, noise, dust, emission pollution
7.	JCB	1	----	JCB	Diesel	Air, noise, dust, emission pollution
8.	Diamond wire saw machine	2	40 and 60 hp.	---	Electricity	Air, water, dust pollution
9.	Quarry core drilling machine	1	---	---	Diesel/ Electricity/DG	Air, dust, noise, water pollution
10.	Diesel generator	2	320 KVA and 26 KVA	Cummins	Diesel/Electricity	Air, emission, noise pollution
11.	Accessories	---	All size drilling rods and other machine spare parts	----	---	---

leaves and cuticles. Dust may also have chemical effects that jeopardize the plants' long-term survival (Tiba 2017, Ogbonna et al. 2018, Timofeeva et al. 2022, Abdul-Wahab et al. 2022).

Quarry dust is linked to a multitude of leaf diseases, including abscission (early leaf fall), epinasty (bending of the leaf downward due to a faster rate of growth on the upper surface), necrosis (death of a portion of the leaf), and chlorosis (yellowing of the leaf due to loss or decrease of chlorophyll). Quarry dust is also a major source of air pollution (Sanjay Vediya 2014, Sayara et al. 2016, Sairanen et al. 2018 & 2019, Ekpa et al. 2022 & 2023, Opondo et al. 2023). According to Abayomi et al. 2014, Hamzart-Giwa et al. 2023, the quantity and quality of resource discovery, extraction, stonecutting procedures, and transportation to the final destination determine the impact on the air environment. According to Busuyi (2008), Olusegun et al. (2009), Akanwa et al. (2016 & 2017), Abhishek Pandey (2018) the rate of production and transportation also affects the intensity of these processes.

In the regions where stone crushing, quarrying, and stone processing are conducted, some of the sources of emissions or dust creation are as follows: dust from drill bits and blasting; dust from stone bodies and objects dug out and extracted. Transporting waste and dressing materials or processing materials from quarries to stockyards and disposal sites; loading, unloading, and moving finished items; and movement of vehicles on haul highways (Thompson et al. 1984, Iqbal et al. 2001, Moibi 2007, Ojeaga et al. 2023). A region's wind direction and speed have a direct bearing on the probability of dust pollution spreading in the study area.

The research area's major wind direction is west, and during the AAQ monitoring period, data on wind speed and direction were concurrently gathered. The ambient air quality of the research region has been evaluated using a network of twelve ambient air quality stations. The study region's meteorological characteristics were taken into consideration when building these stations, along with several other elements such as a densely populated area, industrial and residential development, and environmental sensitivity. It was noted that there are no ecosystems surrounding the intended exploratory well placements, and all of the wells are situated inside open spaces.

The principal inhabited the region and the predominant wind directions were considered when choosing the AAQ sites. Baseline ambient air quality evaluations provide information about the site's surroundings and are an essential component of research on environmental impact assessments. In addition to the impact of the surrounding topography, notable variations in the predominant winds and weather patterns are seen in the winter, summer, and post-monsoon seasons. A methodical program of air quality surveillance is used to evaluate the baseline air quality in the research region.

The quarrying site reported temperatures as high as 33°C and as low as 19°C during the research period. It was found that the quarry zone had an average temperature of 26°C. Throughout the trial, the average relative humidity ranged from 34% to 63%. In the Ramanagara District, there was some rainfall during the study period. There were five days of rain on average. The most rain that fell in March was 12 mm, while the least was 8 mm. The district receives roughly 931.58 mm of rain annually on average. During the winter monsoon, the majority of winds are north-easterly, whereas during the summer monsoon, they are south-westerly. During the three-month investigation, monthly wind speeds in the quarry zones ranged from 4.9 m/s to 5.6 m/s.

The AERMET data includes daily records for temperature, relative humidity, air pressure, solar radiation, precipitation, wind speed, and wind direction. AERMET reformats meteorological data to make it suitable for use as input in the AERMOD model (Neshuku 2012). The stone quarrying and stone-processing sectors won't alter the climate. When evaluating and keeping track of ambient air quality, soil and geological features are crucial.

Air Quality Index (AQI) Quantification

Monitoring sites have been reporting the ambient air pollution they have observed within a specific time frame (e.g., daily) by utilizing a grading system based on the AQI universal standard. The AQI is used to compare current pollution levels to ensure that impact reduction requirements are being followed and to increase public awareness of the risks associated with regular exposure to pollution. Even though the AQI is just a number that represents some aspects of air quality, to make its meaning clear to the general public, it is combined with various messaging, color schemes, graphics, and labels for the different categories of air quality (such as "good," "moderate," or "hazardous" as per CPCB (200) guidelines.

Based on a set of standards, the Air Quality Index (AQI) is an environmental indicator that provides information on the general condition and trend of the ambient air in a given area. This tool uses the weighted values of different air pollution parameters to create a single or multiple-number representation. The AQI is a useful tool for assessing and measuring the overall ambient air quality of a particular area since it accounts for the combined impact of all contaminants. The AQI can also be used to control equipment that, for example, raises the concentrations of some pollutants while reducing

Table 9: Air Quality Index grading system

AQI Value	Remarks	Health Concern
00 – 25	Clean air (CA)	None/minimal health effect
26 – 50	Light air pollution (LAP)	Possible respiratory or cardiac effect for most sensitive group, skin allergies, cough etc.
51 – 75	Moderate Air Pollution (MAP)	Increasing symptoms of respiratory and cardiovascular illness, skin allergies, cough, asthma, etc.
76 – 100	Heavy Air Pollution (HAP)	Aggravation of heart and lung diseases, asthma, eye irritation, skin diseases, etc.
> 100	Severe Air Pollution (SAP)	Serious aggravation of heart and lung Diseases, risk of death in children, asthma, cough, eye diseases, mental disorder etc.

others, or to create alternate strategies for preventing air pollution.

The AQI can be calculated using a variety of formulas and methods. Nonetheless, the following calculation has been used in this instance to determine the AQI value:

$$AQI = \frac{1}{4} \times (ISPM/SSPM + ISO_2/SSO_2 + INOx/SNOx) \times 100$$

Individual measurements obtained during sampling that correlate to ISPM, IRSPM, ISO_2, and INOx are respirable particulate matter, suspended particulate matter, sulfur dioxide, and oxides of nitrogen, respectively. For ambient air quality, the Central Pollution Control Board of India (CPCB) has set SSPM, SRSPM, SSO_2, and SNOx criteria. Higher air pollution levels and associated health risks are correlated with higher AQI numbers. Table 9 lists the five categories that comprise the AQI scale. It outlines the range of air quality as well as any possible health hazards.

Examination of the Surrounding Air Quality in the Study Area

Sampling was done after GPS and remote sensing pinpointed the precise locations. Samples and measurements of the chemical components of atmospheric pollutants were taken at twelve different locations using an air particle counter and a fuel gas analyzer. Every location had an air particle counter accessible to measure SPM. The SPM concentration was printed and recorded by the instrument. A fuel gas analyzer was used to determine the extra air pollutants (NOx,
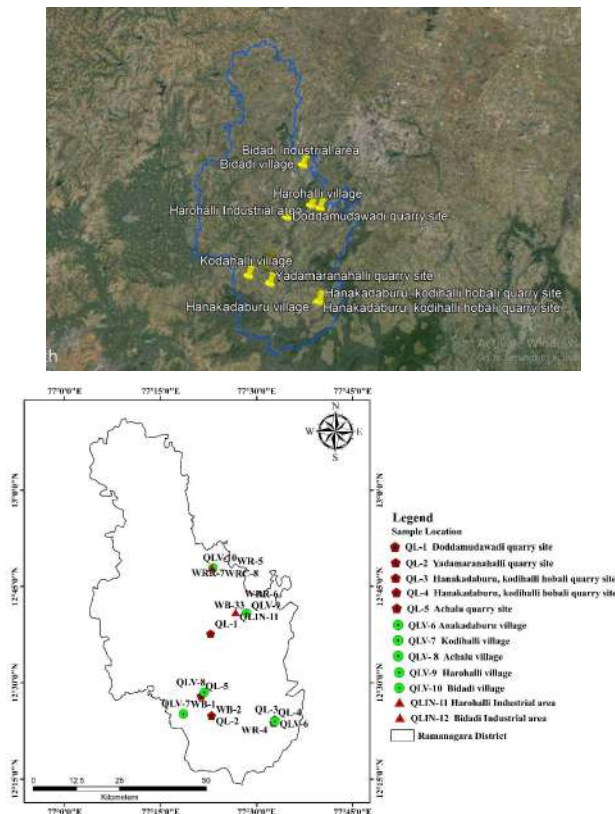
Fig. 5: Sites of ambient air quality monitoring.

Table 10: A summary of the results for ambient air quality.

Summary of Ambient Air Quality Results

Sample code number	PM10 µg/m3			PM2.5 µg/m3			SO2 µg/m3			NOX µg/m3			O3 µg/m3			CO mg/m3			NH3 µg/m3	Pb µg/m3	C6H6 µg/m3	C2OH12 ng/m3	As ng/m3	Ni ng/m3
	Min	Max	Avg	Min	Max	Avg	Min	Max	Avg	Min	Max	Avg	Min	Max	Avg	Min	Max	Avg	Max	Max	Max	Max	Max	Max
AAQ1	43.1	67.34	55.22	23.42	33.54	28.48	6.1	7.82	6.96	11.31	18.46	14.88	8.2	11.1	9.65	0.11	0.15	0.13	<5	<0.1	<0.1	<0.01	<1	<1
AAQ2	42.16	60.08	51.12	22.34	31.36	26.85	5.29	7.54	6.415	10.97	15.64	13.30	6.9	10.1	8.5	0.13	0.19	0.16	<5	<0.1	<0.1	<0.01	<1	<1
AAQ3	38.72	57.21	47.96	24.63	33.86	29.24	7.21	9.53	8.37	12.21	14.56	13.38	11.6	13.6	12.6	0.15	0.29	0.22	<5	<0.1	<0.1	<0.01	<1	<1
AAQ4	42.87	61.09	51.98	23.25	33.13	28.19	5.98	8.52	7.25	12.79	18.23	15.51	12.3	14.8	13.55	0.12	0.19	0.15	<5	<0.1	<0.1	<0.01	<1	<1
AAQ5	48.25	67.32	57.78	18.64	22.67	20.65	8.67	11.78	10.22	13.21	17.61	15.41	9.4	11.37	10.38	0.16	0.27	0.21	<5	<0.1	<0.1	<0.01	<1	<1
AAQ6	46.87	64.83	55.85	19.45	29.48	24.46	6.84	8.63	7.73	13.89	18.73	16.31	7.6	13.1	10.35	0.14	0.23	0.18	<5	<0.1	<0.1	<0.01	<1	<1
AAQ7	48.25	63.64	55.94	23.78	31.63	27.70	6.6	8.5	7.55	13.6	18.26	15.93	12.1	14.6	13.35	0.15	0.29	0.22	<5	<0.1	0.01	0.01	0.02	0.1
AAQ8	37.17	49.28	43.22	16.98	23.83	20.40	7.21	10.28	8.74	9.8	13.9	11.85	8.7	12.4	10.55	0.13	0.19	0.16	<5	<0.1	0.01	0.01	0.02	0.1
AAQ9	49.48	70.52	60	27.96	39.85	33.90	10.5	14.97	12.73	20.85	29.71	25.28	8.9	13.62	11.26	0.16	0.27	0.21	<5	0.05	0.01	0.01	0.02	0.1
AAQ10	45.48	64.82	55.15	24.52	34.95	29.73	6.95	9.9	8.42	14.1	20.1	17.1	10.4	12.79	11.59	0.15	0.31	0.23	<5	0.05	0.01	0.01	0.02	0.1
AAQ11	46.65	66.49	56.57	26.09	37.19	31.64	8.4	11.97	10.18	17.99	25.63	21.81	12.2	14.6	13.4	0.18	0.29	0.23	<5	0.05	0.01	0.01	0.02	0.1
AAQ12	47.84	68.18	58.01	26.26	37.34	31.8	9.76	13.91	11.83	20.17	28.75	24.46	12.8	15.37	14.08	0.17	0.32	0.24	<5	0.05	0.01	0.01	0.02	0.1
NAAQ standard - Industrial/ Residential/ Rural and Other Area	100 (24 Hours)			60 (24 Hours)			80 (24 Hours)			80 (24 Hours)			180 (1hour)			4 (1hour)			400 (24 hours)	1 (24 hour)	5 (Annual)	1 (Annual)	6 (Annual)	20 (Annual)

Note: BDL (Below detectable limit), DL (Detectable limit), BLQ (Below Detectable Limit), LOQ (Limit of Quantification) - Ammonia (µg/m3) – BDL (<5); Lead,(µg/m3) - BDL (<0.1). and BLQ (LOQ 0.05); Benzene, µg/m3 - BDL(<0.1) and BLQ(LOQ 1); Benzo[a] pyrene ng/m3 - BDL(<0.01) and BLQ(LOQ 1); Arsenic ng/m3 - BDL,(<0.01) and BLQ(LOQ 1); Nickel ng/m3 - BDL(<1) and BLQ(LOQ 2); Nickel ng/m3 - BDL(<1) and BLQ(LOQ 10).

SOx, H2S, and CxHx). The equipment was calibrated and constructed correctly, and additional equipment was utilized to print the read-off of the atmospheric concentration of each gas on a screen.

The direction and speed of the wind were measured using an electrically powered digital anemometer. The selection criteria for monitoring locations include the following: topography and terrain; meteorological circumstances (both upwind and downwind locations); residential and sensitive areas within the study area; regional baseline air quality and pollution levels; and representation of possibly impacted areas.

Throughout one (1) season or three months (January 2024 to March 2024), the ambient air quality in the research region was measured twice a week by the NAAQS for twelve parameters (PM_{10}, $PM_{2.5}$, SO_2, NOx, CO, O_3, Pb, NH_3, C_6H_6, C_2OH_{12}, As, and Ni). The Central Pollution Control Board's (CPCB) monitoring criteria were followed when sampling was done at each location. PM_{10}, $PM_{2.5}$, SO_2, NO_x, CO, Pb, O_3, NH_3, C_6H_6, C_2OH_{12}, As, and Ni, maximum values at all study locations are well under the National Ambient Air Quality Standards for residential, commercial, and industrial areas (Tiwari et al. 2012).

Throughout the study, the average baseline levels of PM_{10} (37.17 to 70.52 $\mu g/m^3$), $PM_{2.5}$ (16.98 to 39.85 $\mu g/m^3$), SO_2 (5.29 to 13.91 $\mu g/m^3$), NOx (9.8 to 29.71 $\mu g/m^3$), CO (0.15–0.32 mg/m^3), O_3 (6.9 to 15.37 $\mu g/m^3$), and some BDL and LOQ were found to be well within the National Ambient Air Quality Standards for both commercial, residential and industrial areas. Places to monitor ambient air quality are depicted in Fig. 5. The observed data for each location was used to calculate several measures, including the maximum, minimum, and average.

Findings from the Analysis of Ambient Air Quality

The quarrying and stone processing industries are known to produce air pollution issues due to many reasons, such as truck traffic, blasting, and drilling. Small-scale quarrying is unlikely to significantly impact the current air quality in the core zone. Using environmental controls in a way that reduces the likelihood of contamination is necessary to reduce air pollution. The test results that are enclosed concern the surrounding area and ambient air quality at the quarry. Using the observed data for each location, several metrics were computed, including the maximum, minimum, and average. The overall summary of the ambient air quality test findings is shown in Table 10. Fig. 6 shows that the graphical representation of air quality monitoring results.

Observations in the Sampling Areas

PM_{10} concentrations were measured to be at a maximum of 70.52 $\mu g/m^3$ and a minimum of 37.17 $\mu g/m^3$ respectively. The village of Harohalli had the highest concentration, while the village of Achalu recorded the lowest. The range of average values was 43.225 $\mu g/m^3$ to 60.00 $\mu g/m^3$. The $PM_{2.5}$ values were measured to be 39.85 $\mu g/m^3$ at the maximum and 16.98 $\mu g/m^3$ at the minimum. The village of Harohalli had the highest concentration, while the village of Achalu recorded the lowest. The measured average values fell between 20.655 $\mu g/m^3$ to 33.905 $\mu g/m^3$. The measurements of SO_2 concentrations at the maximum and minimum were 13.91 $\mu g/m^3$ and 5.29 $\mu g/m^3$ respectively. The
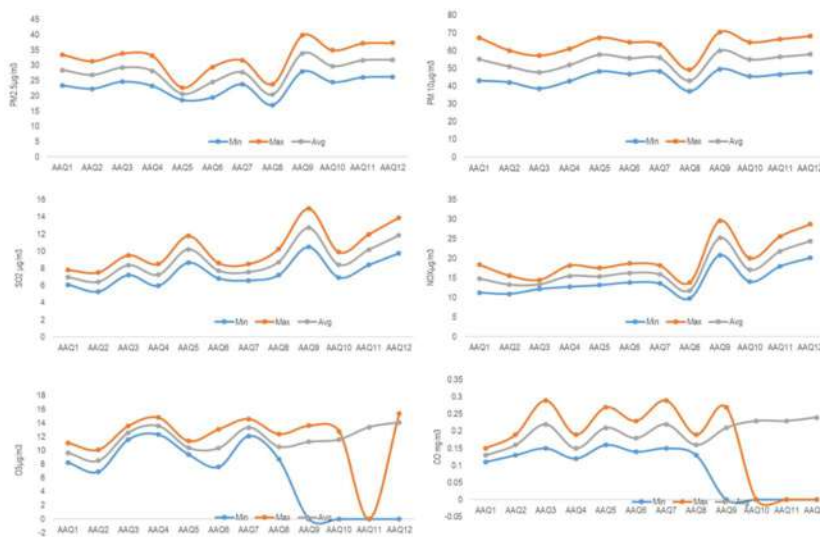

Fig. 6: Graphical representation of air quality monitoring results.

Bidadi industrial sector recorded the highest concentration, while the Yadamaranahalli quarry site recorded the lowest. The measured average values fell between the ranges of 6.415 µg/m^3 to 12.735 µg/m^3. There was a maximum of 29.71 µg/m^3 and a low of 9.8 µg/m^3 for the concentration of NOx. The settlement of Achalu village recorded the lowest concentration, while the village of Harohalli recorded the largest concentration. From 11.85 µg/m^3 to 25.28 µg/m^3, the average levels were found to be present.

The observed CO values were 0.32 mg/m^3 at the maximum and 0.15 mg/m^3 at the minimum. The Doddamudawadi quarry site had the lowest concentration, whereas the Bidadi industrial area had the highest concentration. It was noted that the average values fell between 0.13 mg/m^3 and 0.245 mg/m^3. The reported values for O_3 concentrations were 15.37 µg/m^3 for the maximum and 6.9 µg/m^3 for the minimum. The Bidadi industrial sector had the highest concentration, while the Yadamaranahalli quarry site recorded the lowest concentration. The observed average values fell between 8.5 µg/m^3 and 14.08 µg /m^3. The Central Pollution Control Board's (CPCB) guidelines for industrial, rural, residential, commercial, and other areas are well under the limits in the research sites, while the concentrations of NH_3, Pb, Ni, As, C_6H_6 and C_2OH_{12} were all below detectable levels at all locations.

Numerous factors and parameters, such as the climate, topography, extent and method of quarry operation, use of equipment and machinery, population density, density of highly polluted industrial areas, density of road vehicles, density of forest fires, density of vegetation, and so on, affect the distribution of the aforementioned chemical elements in different quarry locations, local areas, residential areas, and industrial areas. Air pollution levels are higher throughout the entire area as a result of the previously described factors. The observation detailed the areas where the lower and higher levels of air pollution were spreading at the sampling locations.

Air Pollution Effects on Human Health

Quarrying is viewed as essential to human survival on a global scale. This is because it has contributed to the growth and development of every country, region, and sub-region. As a result, it is easier to build concrete structures, and the state's road and bridge infrastructure is developed, both of which have a significant positive economic impact on the nation (William et al. 2006, Sahu et al. 2018, William 2020). Furthermore, it produced jobs that were both direct and indirect, which made it easier for individuals to find work and support themselves (Peter et al. 2018, Samba et al. 2022). The study found that because it gave individuals economic

power and maintained their well-being, quarrying was an especially sustainable industry (Ako et al. 2015, Ugbogu et al. 2009). This implies that, in addition to agriculture, quarrying provides a sizeable portion of the local population's income (Fugiel et al. 2017, Yasobant et al. 2017).

The local people, the environment, wildlife, workers, the population's socioeconomic situation, health, and society are all impacted by the various barriers, problems, and challenges that come with stone quarrying (Nartey et al. 2012, Turyahabwe et al. 2021). These problems include changes in topography, degradation, and abandonment of land, loss of ecosystems and biodiversity, emissions, noise and dust pollution, air pollution, and water pollution, including the release of ionizing radiation into the atmosphere (Sanjay Vediya 2014, Pal et al. 2019). These results indicate that places that were productive in the past have become unproductive, which is upsetting the ecosystem as a whole.

Deforestation and land degradation therefore affect biodiversity (Rani et al. 2017). Due to their role as mosquito habitats and rain-retaining materials, open quarries and deforestation have been associated with an increase in non-communicable diseases, including malaria. This also affects the cost of buying and selling real estate (Owolabi et al. 2020).

The results of the study show how much dust is produced throughout several stages of the quarrying process, including drilling, stone blasting and crushing, loading, and transporting the finished products. The larger dust particles settle close to one another, while the thinner ones spread out widely, depending on the direction and speed of the wind. Different levels of particulate matter (PM) are produced based on its size, which also affects how long and how far it travels when suspended in the air (Romo-Kroger et al. 1989, Pradhananga et al. 2020).

Based on their aerodynamic diameter, the sizes are divided into $PM_{2.5}$ (equal to or less than 2.5 micrometers) and PM_{10} (equivalent to or fewer than 10 micrometers) particles. The average diameter of human hair is between 50 and 70 µm; therefore, these sizes are less than that (Ogbonna et al. 2020, Chamdimba et al. 2023). Dispersed particulate matter can cause several issues, depending on its size. According to William (2020) and Ekpa et al. (2022 & 2023), for example, it can lead to poor visibility near quarry and crusher units, reduced agricultural yields because dust cover on plant surfaces blocks light needed for photosynthesis, ophthalmic disease because particulates carry pathogens, and respiratory disorders in humans and animals.

It is common knowledge that employees in quarries disobey health and safety; laws. People often forget to wear safety gear, like dust masks, helmets, and appropriately

Fig. 7: The safety and health conditions of the workers at the quarry sites and field visit images from several quarries and crusher unit.

protected clothing (Sanjay Vediya 2014, Sayara et al. 2016, Hassan 2023). As a result, they come into contact with small dust particles. Their health is consequently adversely affected (Vandana et al. 2020, William et al. 2006). Numerous health problems, including lung infections, skin and eye infections, respiratory and pulmonary disorders, and lung collapse, can be brought on by dust exposure (Ndinwa et al. 2014, Mbandi 2017, Nemer et al. 2020).

The Ramanagara district quarry workers found that their lack of protective gear and the dust from the quarries had caused respiratory difficulties. In addition to dyspnea, these symptoms before and after the quarry operation include coughing, wheezing, asthma, headaches, eye issues, chest discomfort, heart problems, mental stress, throat infections, allergies, and skin disorders (Sinha et al. 2000, Singhal et al. 2022, Abeya 2023). Based on the previously indicated facts-that dust is irksome, that dust has an impact on health, and

Table 11: The summary of air pollution impacts on human health

Pollutants	Environmental impacts on human health
Ozone (O_3)	Ozone is linked to brief effects on the respiratory system in humans especially asthma, including reductions in pulmonary function in those engaging in mild to moderate exertion., various diseases and early mortality. Ozone depletion damages vegetation and reduces visibility, among other negative effects.
Particulate matters ($PM_{2.5}$ & PM_{10})	Particulate matter has varying effects on health, and as particle size drops, so does the likelihood that the particle will have an impact on human health. Particles smaller than 1 μm entered the lower parts of the lungs, while larger particles lodged in the throat and nose, measuring more than 10 μm. Death, both acute and chronic bronchitis.
Sulphate (SO_4)	Chest troubles, respiratory disorders, mild RADs, days missed from work, and moderate to severe asthma symptoms are all examples of lower and upper respiratory illnesses.
Carbon monoxide (CO)	As a result of its interaction with hemoglobin in human blood, it lowers the blood's transport of oxygen. When CO levels are high, those who have cardiovascular illness or chronic heart disease may feel pain in their chest. Reduced delay to angina onset, hospital admissions, mortality, and congestive heart failure. CO can cause unconsciousness and death, damage manual dexterity and vision.
Nitrogen oxides (NO_2)	Short- and long-term impacts of nitrogen dioxide on human health are evident; children's respiratory disorders are more common in the former case, while the latter reduces immunity to respiratory infections. In addition to lowering auxiliary beat frequency and increasing permeability of cell membranes, NO_2 exposure also makes asthmatics more sensitive to respiratory infections and inhaled allergens.
Sulphur dioxide (SO_2)	Another gas that negatively affects human health is sulfur dioxide, since it can have a severe effect on the respiratory system. Asthma sufferers' lung function is altered by the emission, which is directly correlated with fuel's sulfur content. Sensitive people's respiratory symptoms are made worse. Respiratory symptoms, alterations in pulmonary function, and morbidity among asthmatics who exercise.
Lead (Pb)	Deaths, high blood pressure, non-fatal heart attacks, non-fatal strokes, and declines in IQ.

that rain-covered roofs are unclean-the impact of quarrying on human health is examined. The safety and health conditions of the workers at the quarry sites are depicted in the Fig. 7, which also include field visit images from several quarries and crusher unit.

The results demonstrated that all respondents (100%) considered noise and dust to be health hazards and a major source of annoyance. Dust almost always contaminates rain that falls from roofs. Additionally, every respondent mentioned that noise, dust, water, and floodwaters could be connected to their on-going health issues. Numerous illnesses and health problems are signs of the detrimental impacts of stone processing and quarrying, particularly for the villages close to crushers. There is also a connection between acid rain and quarrying (Maduka et al. 2014, Boutemedjet et al. 2019).

According to the study, acid rain is known to damage plants, worsen air pollution, and sicken people and animals brought on by quarrying. There are several quarrying-related health risks. An analysis showed a connection between the vibrations caused by quarrying and fractures. This could lead to building collapses, which would cause fatalities and injuries. When asked how they felt about the quality of the air right now, respondents said that 24% thought it was poor and 76% said the stone-cutting and quarrying sectors should be held accountable. Since the quarry owner is providing benefits, the majority of respondents chose not to react. Thus, it seems logical that stone-cutting and quarrying have an impact on air quality. Table 11 provides a summary of how typical air contaminants affect human health.

TECHNIQUES FOR MITIGATION AND CONTROL MEASURES

The following mitigation and control techniques, corrective measures, and remedies have been suggested for the granite quarrying and stone processing industries: a sizable buffer zone, or "green belt," ought to be created surrounding the industrial area. Providing dust masks for laborers. Allowing the staff to don the appropriate personal protective equipment. Avoid overcharging blast holes by using controlled blasting techniques. It is advisable to regularly monitor the quality of the surrounding water, air, and noise. It is also suggested that you use effective, quiet equipment. Hazardous places should be avoided, and signboards displaying instructions should be posted.

Dust pollution will be managed with the use of electrostatic precipitators. By using silica in water quarrying and groundwater dust control systems, silica-related problems can be minimized. At sensitive locations, such as haul roads, crusher and screening plants, mineral handling facilities, quarrying facilities, and stone processing plants, dust suppression is enforced using heavy dust sprinklers and road watering trucks. Mineral handling, HEMM, crushing, and screening equipment must be provided in dust extraction facilities. Hoods, water sprays, and dust collectors are helpful pieces of equipment for controlling drilling dust. Moreover, suitable chute design, vulcanizing conveyor belt joints, under-belt cleaning equipment, hoods, transfer points, and dust suppression and/or extraction systems for conveyors are frequently employed as dust pollution management techniques. Enclosures used in mineral handling plants must be well secured.

All vehicles, including trucks, dumpers, and transport vehicles, must be leak-proof. Use the proper components when spraying to stop dust from flying. Highways and other roads should be adequately coated with chemical additives to successfully limit dust emissions. Haul roads and service roads should be graded regularly. Haul roads should also have any loose dirt and collected dust removed. Appropriate maintenance, such as checking exhaust emissions and establishing speed limitations on the cars and earthmoving equipment. When transporting stone products, make sure tippers and dumpers are not overloaded, and cover heavy tippers with tarpaulins.

Utilizing vegetation to stabilize significant regions that generate dust and waste yards. Reduce the number of open regions and seal off the area used for stone quarrying and processing to reduce the amount of dust produced. Ideal enclosed areas for equipment and supply storage for building projects. Utilizing and maintaining machinery and equipment efficiently to lower air emissions, noise pollution, and energy use. The exhaust vent of the DG set will have enough stack height to ensure that gaseous emissions diffuse rapidly. Vehicles must receive routine maintenance and oversight to guarantee that their fuel usage and emissions are within permitted limits. Inspecting construction sites, stone processing plants, and quarry activities regularly to ensure that waste debris is promptly removed and disposed of in landfills, recycled, or used in other ways. Grading transport and service roads and removing accumulated dusty material regularly.

CONCLUSIONS AND RECOMMENDATIONS

Conclusions

We start with an analysis of the field work, laboratory and desk work data in order to track the quality of the air in the Ramanagara district. Twelve metrics, including $PM_{2.5}$, PM_{10}, SO_2, NOx, CO, O_3, Pb, NH_3, C_6H_6, C_2OH_{12}, As, and Ni, were monitored twice a week for three months (January

2024 to March 2024) by the National Ambient Air Quality Standards (NAAQS) in the study area. This indicates the greater distance that the air quality covers. According to the Central Pollution Control Board (CPCB) monitoring recommendations, sampling was carried out at each location. The NAAQS in the research area measured twelve metrics twice a week for one (01) season, or three months (January 2024 to March 2024), including PM_{10}, $PM_{2.5}$, SO_2, NOx, CO, O_3, Pb, NH_3, C_6H_6, C_2OH_{12}, As, and Ni. The findings showed that SPM is high in every station, even if SO_2 and NOx levels are within allowable bounds in all measured locations. The study found that the average baseline levels of PM_{10} (37.17 µg/m^3 to 70.52 µg/m^3), $PM_{2.5}$ (16.98 µg/m^3 to 39.85 µg/m^3), SO_2 (5.29 µg/m^3 to 13.91 µg/m^3), NOx (9.8 µg/m^3 to 29.71 µg/m^3), CO (0.15 mg/m^3 to 0.32 mg/m^3), O_3 (6.9 µg/m^3 to 15.37 µg/m^3), and NH_3, Pb, Ni, As, C_6H_6 and C_2OH_{12} were below detectable limit (BDL) and limit of quantification (LOQ) are all well within the National Ambient Air Quality Standards for commercial, industrial, and residential areas at all monitoring locations for the duration of the study. Apart from the environment, they can also have a major detrimental impact on infrastructure, transportation, agriculture, population density, mining, quarrying, human health, etc. The research areas' stone-processing and granite-quarrying businesses don't significantly harm the air quality. The distribution of air quality source potential in Ramanagara district was evaluated in this research work.

Recommendations

1. Environmental preservation is of utmost importance to the stone quarrying and processing industry. The business will abide by all environmental regulations. A well-manicured greenbelt will be preserved by the quarry operation. Furthermore, all environmental statute standards shall be continuously implemented and upheld.

2. By introducing both natural and artificial techniques to stop the spread of dust in the neighborhood, air pollution caused by billowing dust can be avoided. One way to lessen the harm that the dust from the quarries causes to the environment is to plant densely packed, quickly growing trees around the quarries and on any reserved area they own. The same quickly growing trees with dense foliage should also be added to the proposed buffer zone to increase its density. Rather than using corrugated sheets attached to the side of crushing plants in certain quarries, man-made and natural solutions can be implemented to reduce the amount of dust that blows into the area, thereby mitigating the problem of air pollution caused by billowing dust.

3. In order to improve the green canopy, prevent the spread of dust and other airborne pollutants, stop soil erosion, stop land degradation, and address other issues, reforestation is mandated by the quarrying and stone processing industry plan.

4. There should be frequent environmental audits carried out on all the quarries within the research area. In order to evaluate the effectiveness of the quarries' conservation or anti-pollution program, a methodical analysis of their interactions with the environment is conducted.

5. Regular health awareness efforts should also be conducted to inform the public about the possible dangers of unhygienic surroundings. To help enhance the health status of its residents, the local government should mandate frequent health assessment studies.

6. Local government agencies should be held to a higher standard of accountability and should take an active role in resolving public complaints regarding the detrimental effects of the granite business. Steer clear of quarrying in environmentally vulnerable areas.

REFERENCES

Aarthy, A., Sudarsan, J.S., Wilfett, J. and Rajan, R.J., 2018. Study on impact of air quality due to quarrying activity in and around Rathinamangalam area of Kancheepuram district, Tamil Nadu, India. *Journal of Mines, Metals, and Fuels*, 66(1).

Abayomi, D. and Kehinde, I., 2014. Environmental effects of quarrying activities in Oba-Ile, Akure, Ondo State, and South-West Nigeria. *International Journal of Engineering Research & Technology*, 3(1), pp.1103-1113.

Abdul-Wahab, S., Osman, I. and Al-Shukaili, N., 2022. Air quality assessment for Kunooz Gabbro quarry in Oman: assessment of PM10. *International Journal of Pioneering Technology and Engineering*, 1(02), pp.61-72.

Abdul-Wahab, S.A., Fgaier, H., Elkamel, A. and Chan, K., 2015. Air quality assessment for the proposed Miller Braeside quarry expansion in Canada: TSP. *Air Quality, Atmosphere & Health*, 8, pp.573-589.

Abeya, C., 2023. Impacts of stone quarrying on the environment and socio-economy of the local community: the case of Aira District, West Wollega Zone. *Journal of Science, Technology, and Arts Research*, 12(1), pp.90-108.

Ajah, J.N. and Chukwu, E.N., 2018. Investigative effect of stone crushing dust on the health of workers of quarry industry at Umuoghara community of Ezza-North local government in Ebonyi State. *IOSR Journal of Nursing and Health Science (IOSR-JNHS)*, 7(6), pp.80-91.

Ajibade, O.M., Olisa, O.G., Oladipupo, S.D., Adegoke, C.B. and Adebayo, O.H., 2022. Health impact assessment of quarrying in some parts of southwestern Nigeria. *Arabian Journal of Geosciences*, 15(8), p.777.

Akanwa, A., Onwuemesi, F. and Chukwurah, G., 2016. Effects of open-cast quarrying techniques on vegetation cover and the environment in south-eastern Nigeria. *American Scientific Research Journal for Engineering, Technology, and Sciences (ASRJETS)*, 21(1), pp.227-240.

Akanwa, A.O., Okeke, F.I., Nnodu, V.C. and Iortyom, E.T., 2017. Quarrying and its effect on vegetation cover for a sustainable development using high-resolution satellite images and GIS. *Environmental Earth Sciences*, 76(14), p.505.

Ako, T.A., Onoduku, U.S., Waziri, S.H., Adegbe, M., Chukwu, J.N. and Kajena, C.M., 2015. Assessment of the environmental impacts of marble quarrying on surface water at Kwakuti, Niger State, North Central Nigeria. *International Journal of Engineering and Advanced Research Technology*, 1(1), pp.64-70.

Amankwah, E.O., Owusu-Boateng, G. and Maxwell, A.B., 2019. Trend analysis on air quality and lung function—a case of Consar Stone Quarry Limited, Barekese. *American Journal of Environmental Resource Economics*, 4, pp.44-53.

Bada, B.S., Olatunde, K.A. and Akande, O.A., 2013. Air quality assessment in the vicinity of the quarry site. *Environment and Natural Resources Research*, 3(2), p.111.

Bakamwesiga, H., Mugisha, W., Kisira, Y. and Muwanga, A., 2021. An assessment of air and water pollution accrued from stone quarrying in Mukono District, Central Uganda.

Bassey, P.E. and Okon, N.P., 2021. Perspectives and experiences of the effects of quarrying on the environment and agricultural activities of the quarry communities in Akamkpa Local Government Area of Cross River State, Nigeria. *International Journal of Science and Academic Research*, 2(07), pp.1767-1773.

Bhat, P.G.K. and Subramani, N., 1990-91. Report on the Second Generation Geological Mapping in Parts of Satnuru—Kadihalli Area, Kanakapura Taluk, Bangalore District, Karnataka. (Unpublished Progress Report for 1990-91).

Bhat, S.K. and Suresh Babu, V., 1994. Survey for ornamental stones with special reference to pink granite in parts of Kanakapura taluk, Bangalore district. Department of Mines and Geology, Karnataka. (DMG Reports).

Boutemedjet, A., Bounouala, M., Idres, A. and Benselhoub, A., 2019. Assessment of dust pollution related to granite quarry operations in Kef Bouacida, Annaba (Algeria). *Scientific Bulletin of the National Mining University*, (1).

Busuyi, A.T., 2008. Assessment of the socio-economic impacts of quarrying and processing of limestone at Obajana, Nigeria. *European Journal for Social Sciences*.

Caruthers, R.M., 1984. Reviews of geophysical techniques for groundwater exploration in crystalline basement Terrain. British Geological Survey Report No. RGRG85/3. Assessment of physico-chemical parameters of groundwater quality in Ramanagaram taluk, Karnataka. (DMG Reports).

Chaanda, M.S., Onwuteaka, D. and Garba, M.A., 2019. Environmental Impact of Granite Mining in Tattara Area, North Central Nigeria. *IOSR Journal of Applied Geology and GeophysicsI*, 7(6), pp. 14-24.

Chalekode, P.K., 1978. Emissions from the Crushed Granite Industry: State of the Art. (Govt Reports).

Chamdimba, G., Vunain, E. and Maoni, M., 2023. Assessment of particulate matter exposure to ambient air and its impact on workers at two granite quarry mines at Njuli, Southern Malawi. *Environmental Monitoring and Assessment*, 195(9), p.1069.

Chattopadhyay, S., Gupta, S. and Saha, R.N., 2010. Spatial and temporal variation of urban air quality: a GIS approach. *Journal of Environmental Protection*, 1(03), pp.264.

Chowdhury, M.Z., 2004. Characterization of fine particle air pollution in the Indian subcontinent. Georgia Institute of Technology.

Daspan, R.I., Obadiah, E.G., Lekmang, I.C., Dibal, H.U., Chup, A.S., Daku, S. and Azi, B., 2018. Preliminary Assessment of the Trace Element Composition of Dust from Two Granite Quarries on the Jos Plateau and Their Possible Health Implications.

Doley, D. and Rossato, L., 2010. Mineral particulates and vegetation: Modelled effects of dust on photosynthesis in plant canopies. *Air Quality and Climate Change*, 44(2), pp.22-27.

Drew, L.J., Langer, W.H. and Sachs, J.S., 2002. Environmentalism and natural aggregate mining. *Natural Resources Research*, 11, pp.19-28.

Ekpa, I.D., Laniyan, D.G., Agbor, C.N., Ben, U.C. and Okon, J.E., 2022. Effect of air pollution from quarry activities on agriculture and plant biodiversity in south-eastern Nigeria (Preprint). https://doi.org/10.21203/rs.3.rs-1819483/v1

Ekpa, I.D., Laniyan, D.G., Agbor, C.N., Ben, U.C. and Okon, J.E., 2023. Effect of particulate matter from quarry activities on crops and plant biodiversity in south-eastern Nigeria. *Environmental Monitoring and Assessment*, 195(7), p.837.

Emmanuel, D.A., 2018. Environmental impact of quarry activities in Supare-Akoko, Ondo State, Nigeria. *Geography Planning Science*, 3(1), pp.101-111.

Esguerra, N.A., Amistad, F.T. and Rabena, A.R., 2008. Characterizing the environmental effects of the quarrying industry: The case of strategic quarry sites in the Ilocos Region. *The Vector: International Journal of Emerging Science, Technology, and Management (IJESTM)*, 17(1).

Eshiwani, F., 2014. Effects of quarrying activities on the environment in Nairobi County: A Case Study of Embakasi District. (Doctoral Dissertation, University of Nairobi).

Fugiel, A., Burchart-Korol, D., Czaplicka-Kolarz, K. and Smolinski, A., 2017. Environmental Impact and Damage Categories Caused by Air Pollution Emissions from the Mining and Quarrying Sectors of European Countries. *Journal of Cleaner Production*, 143(2), pp.159-168.

Ganesha, A.V., Krishnaiah, C., Krishnegowda and Suresh, S., 2017. Assessment of physico-chemical parameters of groundwater quality in Ramanagaram taluk, Karnataka. *Special Publication Journal of Engineering Geology, EGCON*, pp.255-263.

Gbeve, B., 2013. Environmental Impacts of Construction Aggregate Mining in the Greater Accra Region (A Case Study of Amasaman in the Ga West Municipality). (Doctoral Dissertation).

Halwenge, J.A., 2015. Dust pollution and its health risks among rock quarry workers in Kajiado County, Kenya. Available at: https://pdfs.semanticscholar.org/ee32/fb69d83d6d678c07ebdccffc590e426a4646.pdf [Accessed 1 Mar. 2019].

Hamzart-Giwa, O.G., Odiyi, B.O. and Afolabi, O.J., 2023. Environmental Effects of Quarrying Activities in Akure, Ondo State, Nigeria. *World News of Natural Sciences*, 49, pp.122-136.

Haseeb, Z., 2018. Monitoring of the environment, health, and socio-economic impacts of limestone quarrying near Chakwal, Pakistan. *Pakistan Journal of Science*, 70(4).

Hassan, I.A 2023. Socio-economics and health impact of quarry sites on the surrounding localities in Ogun State, Nigeria. Nig. J. Pure & Appl. Sci., 36(2), pp. 4638-4655. : https://doi.org/10.48198/NJPAS/23.A04

Hema, H.C. and Govindaiah, S., 2012. Morphometric analysis using remote sensing and GIS techniques in the sub-watersheds of Kanakapura watershed, Arkavathi river basin, Ramanagara district, Karnataka, India. *Environmental Geochemistry*, 15(2), pp.47-56.

Hema, H.C., Govindaiah, S., Jayaramaiah, R. and Shahinfar, H., 2013. Remote sensing and GIS application for land use and land cover mapping in the Kanakapura watershed of Ramanagara district, Karnataka, India. *The Indian Mineralogist Spl*, 47(1 & 2), pp.41-57.

Henry, A.E., Getrude, A.O., Chibuisi, O.F., Shu, E.N., Ignatius, C., Stella, I.A.I., and Halilu, T.B., 2017. Occupational health hazards associated with continuous exposure to quarry activities among quarry workers in Ebonyi State, South East Geopolitical Zone, Nigeria. *Journal of Environmental Science, Toxicology and Food Technology*, 11, pp.10-19.

Ibrahim, W.H.W., Marinie, E., Yunus, J., Asra, N. and Sukor, K.M., 2018. Air quality assessment on human well-being in the vicinity of the quarry site. In: *IOP Conference Series: Earth and Environmental Science*, 117(1), p.012010.

Iqbal, M.Z. and Shafiq, M., 2001. Periodic effect of cement dust pollution on the growth of some plant species. *Turkish Journal of Botany*, 25(1), pp.19-24.

Jahed Armaghani, D., Hajihassani, M., Monjezi, M., Mohamad, E.T., Marto, A. and Moghaddam, M.R., 2015. Application of two intelligent systems in predicting the environmental impacts of quarry blasting. *Arabian Journal of Geosciences*, 8, pp.9647-9665.

Kittipongvises, S., 2017. Assessment of the environmental impacts of limestone quarrying operations in Thailand. *Environmental and Climate Technologies*, 20(1), pp.67-83.

Kofi-Boye, R., 2017. Health Effects of Limestone Quarrying in Yilo Krobo and Lower Manya Krobo Municipalities. (Doctoral Dissertation, Ensign Global College).

Kuzu, C. and Ergin, H., 2005. An assessment of the environmental impacts of quarry-blasting operations: a case study in Istanbul, Turkey. *Environmental Geology*, 48, pp.211-217.

Leon-Kabamba, N., Ngatu, N.R., Muzembo, B.A., Kakoma, S., Michel-Kabamba, N., Danuser, B. and Hirao, T., 2020. Air quality in the working environment and the respiratory health of female Congolese stone quarry workers. *Tropical Medicine and Infectious Disease*, 5(4), p.171.

Loveson, V.J., Singh, T.N. and Singh, P.K., 1997. Impact of Noise Pollution on Workers' Health at Cement Plants. *Indian Mining & Engineering Journal*, 36(11), pp.31-34.

Maduka, S.O., Osim, E.E. and Dimkpa, U., 2014. Respiratory symptoms and blood eosinophil level in workers exposed to quarry dust in south-eastern Nigeria. *Journal of Environmental and Occupational Science*, 3, pp.175-179.

Martins, I.O., Osu Charles, I. and Iwuoha, G.N., 2017. Impact of stone quarrying on the health of residents in Nigeria. *Life Science Journal*, 14(10).

Mbandi, I.J., 2017. Assessment of the Environmental Effects of Quarrying in Kitengela Subcounty of Kajiado in Kenya. (Doctoral dissertation, University of Nairobi).

Melodi, M.M., 2017. Assessment of the environmental impacts of quarry operations in Ogun State, Nigeria. *FUOYE Journal of Engineering and Technology*, 2(2), p.2579-0625.

Ming'ate, F.L.M. and Mohamed, M.Y., 2016. Impact of stone quarrying on the environment and the livelihood of communities in Mandera County, Kenya. *Journal of Scientific Research and Reports*, 10(5), pp.1-9.

Moeletsi, R.S., 2018. Remote sensing of land cover change within granite quarries. (Master's thesis, University of Johannesburg (South Africa)).

Moibi, N.M., 2007. Effects of quarrying on the environment: a case study of Tala, Machakos District, Kenya. (Research dissertation)

Mwangi, S.N., 2014. An assessment of the environmental impacts of quarrying activities in Ndarugo Area, Kiambu County. Bachelor Degree Project, Kenyatta University, Kenya.

Nandan, A., Tauseef, S.M. and Siddiqui, N.A., 2017. Assessment of ambient air quality parameters in various industries in Uttarakhand, India. In: *Materials, Energy, and Environment Engineering: Select Proceedings of ICACE 2015*. Springer Singapore, pp.279-290.

Nartey, V.K., Nanor, J.N. and Klake, R.K., 2012. Effects of quarry activities on some selected communities in the lower Manya Krobo District of the Eastern Region of Ghana.

Ndinwa, G.C.C. and Ohwona, C.O., 2014. Environmental and health impact of solid mineral exploration and exploitation in south-northern Nigeria: a case study of IGARRA in EDO STATE. *Review of Environmental and Earth Sciences*, 1, pp.24-36.

Nemer, M., Giacaman, R. and Husseini, A., 2020. Lung function and respiratory health of populations living close to quarry sites in Palestine: A cross-sectional study. *International Journal of Environmental Research and Public Health*, 17(17), p.6068.

Neshuku, M.N., 2012. Comparison of the performance of two atmospheric dispersion models (AERMOD and ADMS) for open pit mining sources of air pollution. University of Pretoria (South Africa).

Odewumi, S.C., Aminu, A.A., Momoh, A. and Bulus, J.A., 2015. Environmental Impact of Mining and Pedogeochemistry in the Agunjin Area, Southwestern Nigeria.

Ogbonna, P.C., Kalu, E.N. and Nwankwo, O.U., 2018. Determination of heavy metals in sawdust particles, distribution in soil, and accumulation in plants at Ahiaeke timber market in Umuahia, Nigeria. *Nigerian Journal of Environmental Sciences and Technology*, 2(2), p.160.

Ogbonna, P.C., Ukpai, N.P. and Ubuoh, E.A., 2020. Assessment of particulate matter (PM2.5, PM10) in the air, elemental composition of granite, and weather parameters at a quarry site in Ngwogwo, Ebonyi State, Nigeria. *Nigerian Journal of Environmental Science and Technology*, 4(1), pp.182-196.

Ojeaga, K. and Atufe, A., 2023. Assessment of PM2.5 Around Rock Quarrying Sites and Residential Communities of Iyuku and Ikpeshi, Estako West, Akoko Edo, and Edo State. *Journal of Science and Technology Research*, 5(2).

Okafor, O.C., Njoku, C. and Akwuebu, A.N., 2023. Environmental impact of quarrying on air quality in Ebonyi State, Nigeria. *Environmental Sciences Europe*, 35(1), p.98.

Olusegun, O., Adeniyi, A. and Adeola, G.T., 2009. Impact of granite quarrying on the health of workers and nearby residents in Abeokuta, Ogun State, Nigeria. *Ethiopian Journal of Environmental Studies and Management*, 2(1).

Omeiza, L., Sangari, D. and Ogah, A., 2022. Effects of quarry on the air quality in Mpape, Bwari Area Council, FCT Abuja, Nigeria.

Oniyide, G.O., Idowu, K.A. and Anikoh, G.A. Investigations of the Environmental Effects of Granite Rock Quarrying (A Case Study of Ebenezer Quarry, Akure, Nigeria).

Opondo, E.O., Ajayi, D.D. and Makindi, S.M., 2023. Impacts of quarrying activities on the environment and livelihood of people in Border II sub-location, Nyando sub-county, Kisumu County, Kenya. *Environmental Quality Management*, 32(3), pp.147-160.

Owolabi, A. and Adesida, P., 2020. The Environmental and Health Implications of Quarrying Activities in the Host Community of Oba-Ile in Akure, Nigeria. *Journal of Human Environment and Health Promotion*, 6(1), pp.6-10.

Oyinloye, M.A. and Ajayi, E.A., 2015. Environmental impact assessment of quarry activities in Oba-Ile, Ondo State, Nigeria. *The Journal of MacroTrends in Energy and Sustainable*, 3(1), pp.32-45.

Pal, S. and Mandal, I., 2019. Impact of aggregate quarrying and crushing on socio-ecological components of the Chottanagpur plateau fringe area of India. *Environmental Earth Sciences*, 78(23), p.661.

Pandey, A., 2018. Environmental impact and damage categories caused by air pollution emissions from mining and quarrying sectors of European countries. *Journal of Cleaner Production*, 97, pp.1008-1020.

Paranthaman, S. and Ahmad, Md., 1994-1995. Resource Survey Of Ornamental Granite And Dike Rocks For Polishing And Dimensional Stone Industry In Parts Of Kanakapura Taluk, Bangalore Rural District, Karnataka. (GSI Reports).

Peter, M.C., Alozie, C.E. and Azubuine, C.I., 2018. Stone quarrying impacts air and soil water in Ebonyi State, Nigeria. *Journal of Pollution Effects & Control*, 6(2). DOI: 10.4172/2375-4397.1000225.

Pradhananga, P. and Elzomor, M., 2020. Environmental implications of quarry rock dust: a sustainable alternative material to sand in concrete. In: *Construction Research Congress 2020*, pp.916-924. Reston, VA: American Society of Civil Engineers.

Rajan Babu, A., Behera, P.K. and Gupta, R.N., 2003. Eco-friendly stone quarrying-some Issues. In: *Seminar on safe & Environmental friendly quarrying, Mining Engineers Association of India, Bangalore*. (National Seminar).

Rajan Babu, A., Behera, P.K., Subrahmanyam, D.S. and Gupta, R.N., 2002. Development of guidelines for improving recovery in granite mining operation. (Final report 2002. NIRM).

Rajan Babu, A., Subrahmanyam, D.S. and Gupta, R.N., 2000. Performance improvement in dimensional stone quarrying through affordable scientific approach-A Case Study. In: *Internal conference on Technology Management for Mining, Processing, & Environment at IIT, Kharagpur*, pp.108-115. (Internal conference).

Rani, H.B., Swamy, S., Bharath, A.L., Dinakar, R.P.H. and Raghu, A.V., 2017. Impact of quarrying and crushing on soil quality: a case study

in Tumkur district, Karnataka. *International Journal of Research—Granthaalaya*, 5.

Rathore, K.K., 2020. Environmental impacts of mining and processing of minerals: A review. *SGVU Journal of Climate Change and Water*, 7, pp.85-93.

Roja, K., 2022. Environmental Impact Assessment of Mining and Quarrying in Madurai District.

Romo-Kroger, C.M., Morales, R., Llonad, F., Auriold, P. and Wolleter, G.E., 1989. Risks of airborne particulate exposure in a copper mine in Chile. *Industrial Health*, 27(2), pp.95-99.

Saha, D.C. and Padhy, P.K., 2011. Effects of the stone crushing industry on Shorea robusta and Madhuca indica foliage in Lalpahari forest. *Atmospheric Pollution Research*, 2(4), pp.463-476.

Sahu, S.P., Yadav, M., Rani, N. and Das, A.J., 2018. Assessment of occupational health exposure to particulate matter around opencast coal mines in India: a case study. *Arabian Journal of Geosciences*, 11, pp.1-11.

Sairanen, M. and Rinne, M., 2019. Dust emissions from the crushing of hard rock aggregates. *Atmospheric Pollution Research*, 10(2), pp.656-664.

Sairanen, M., Rinne, M. and Selonen, O., 2018. A review of dust emission dispersions in rock aggregate and natural stone quarries. *International Journal of Mining, Reclamation, and Environment*, 32(3), pp.196-220.

Salem, H.S., 2021. Evaluation of the Stone and Marble Industry in Palestine: environmental, geological, health, socioeconomic, cultural, and legal perspectives, in view of sustainable development. *Environmental Science and Pollution Research*, 28(22), pp.28058-28080.

Samba, G., Fokeng, R.M., Nfor, J.T., Ngwaimbi, R.C. and Youogo, C.M.K., 2022. Effects of quarrying activities on environmental sustainability in Makenene, Centre Region, Cameroon. *Journal of Environmental Earth Science*, 12(1), pp.12-19.

Sanjay Vediya, S.V., 2014. Dust pollution monitoring by higher groups of plants near the stone quarrying industry—a case study in Vadagam, Arravali District, Gujarat. *Lifesciences Leaflets*, 53, pp.57-60.

Santizo, I.P., 2022. Impacts of Granite Quarrying: The Case of Subsistence Farmers in the São Pedro River Valley. (Doctoral dissertation, University of the Incarnate Word).

Sayara, T., 2016. Environmental impact assessment of quarries and stone-cutting industries in Palestine: a case study of Jammain. *Journal of Environment Protection and Sustainable Development*, 2(4), pp.32-38.

Sayara, T., Hamdan, Y. and Basheer-Salimia, R., 2016. Impact of air pollution from quarrying and stone-cutting industries on agriculture and plant biodiversity. *Resources and Environment*, 6(6), pp.122-126

Sheikh, A., Rana, S.V.S. and Pal, A., 2011. Environmental health assessment of stone crushers in and around Jhansi, UP, India. *Journal of Ecophysiology and Occupational Health*, pp.107-115.

Simha, L. and Babu, M., 2015. Evaluation of Water Quality in and around Byramangala Reservoir, Ramanagaram District, Karnataka, India. *Evaluation*, 8(02), pp.215-221.

Singh, G., Pal, A., Niranjan, R.K. and Kumar, M., 2010. Assessment of environmental impacts by mining activities: A case study from the Jhansi open-cast mining site in Uttar Pradesh, India. *Journal of Experimental Sciences*, 1(1).

Singhal, A. and Goel, S., 2022. Impact of Sandstone Quarrying on the Health of Quarry Workers and Local Residents: A Case Study of Keru, Jodhpur, India. In: *Treatment and disposal of solid and hazardous wastes*. Cham: Springer International Publishing, pp.97-118.

Singhal, A., 2018. Environmental Impacts of Sandstone Quarrying at Keru, Jodhpur, Rajasthan. Indian Institute of Technology, Kharagpur.

Sinha, R.K., Pandey, D.K. and Sinha, A.K., 2000. Mining and the environment: a case study from the Bijolia quarrying site in Rajasthan, India. *Environmentalist*, 20, pp.195-203.

Sreekala, S., Geena, P. and Jyothi, S.N., 2023. Environmental impact assessment of a quarry in a taluk in southern Kerala, India. In: *AIP Conference Proceedings*, 2764(1). AIP Publishing.

Stieb, D.M., Doiron, M.S., Blagden, P. and Burnett, R.T., 2005. Estimating the public health burden attributable to air pollution: an illustration using the development of an alternative air quality index. *Journal of Toxicology and Environmental Health, Part A*, 68(13-14), pp.1275-1288.

Sun, L., Wei, J., Duan, D.H., Guo, Y.M., Yang, D.X., Jia, C. and Mi, X.T., 2016. Impact of land use and land cover change on urban air quality in representative cities in China. *Journal of Atmospheric and Solar-Terrestrial Physics*, 142, pp.43-54.

Sunyer, J.J.E.R.J., 2001. Urban air pollution and chronic obstructive pulmonary disease: a review. *European Respiratory Journal*, 17(5), pp.1024-1033.

Suresh Babu, 1995. Survey and assessment of ornamental granite in parts of Magadi taluk, Bangalore district. Department of Mines and Geology, Karnataka. (DMG Reports).

Swamy, M.M., 1998. A report on regional assessment and inventory of the resources of dimensional stones, commercial granites, and ornamental stones of closepet granites in parts of Kanakapura, Ramanagaram, and Magadi taluks, Bangalore rural districts, Karnataka. GSI, Southern Region (field season 1994-95), Bangalore. (GSI Unpublished Report).

Syed Abrar, Mulgundmuth, S.F. and Badami, R.B., 2000. Assessment of Ornamental Stones in Ramanagaram Taluk, Bangalore District. Department of Mines and Geology, Bangalore (Field Season 1992-93). (DMG Reports).

Syed Abrar, Smeulla, 2005. Ornamental Stone Resources of Channapatna Taluk, Bangalore. DMG, Karnataka. (DMG Reports).

Thompson, J.R., Mueller, P.W., Flückiger, W. and Rutter, A.J., 1984. The effect of dust on photosynthesis and its significance for roadside plants. *Environmental Pollution Series A, Ecological and Biological*, 34(2), pp.171-190.

Tiba, M.N., 2017. The environmental impact and risk generated by the extraction of construction rocks in quarries: a case study of Turcoaia Quarry. *Research Journal of Agricultural Science*, 49(4).

Timofeeva, S.S. and Murzin, M.A., 2020. Assessing the environmental risk of mining enterprises by the integral indicator of dust emissions. In: *IOP Conference Series: Earth and Environmental Science*, 408(1), p.012067. IOP Publishing.

Tiwari, S., Chate, D.M., Srivastava, M.K., Safai, P.D., Srivastava, A.K., Bisht, D.S. and Padmanabhamurty, B., 2012. Statistical evaluation of PM10 and distribution of PM1, PM2.5, and PM10 in ambient air due to extreme fireworks episodes (Deepawali festivals) in megacity Delhi. *Natural Hazards*, 61, pp.521-531.

Trivedi, R., Chakraborty, M.K. and Tewary, B.K., 2009. Dust dispersion modeling using a fugitive dust model at an opencast coal project of Western Coalfields Limited, India. *Journal of Scientific and Industrial Research*, 8, pp. 71-78.

Trivedi, R., Mondal, A., Chakraborty, M.K. and Tewary, B.K., 2010. A statistical analysis of ambient air quality around opencast coal projects in Wardha Valley coalfields, Western Coal Fields Limited, India. *Indian Journal of Environmental Protection*, 30(12), pp.969-977.

Tsiouri, V., Kakosimos, K.E. and Kumar, P., 2015. Concentrations, sources, and exposure risks associated with particulate matter in the Middle East Area—a review. *Air Quality, Atmosphere, and Health*, 8(1), pp.67-80.

Turyahabwe, R., Asaba, J., Mulabbi, A. and Osuna, C., 2021. Environmental and Socio-economic Impact Assessment of Stone Quarrying in Tororo District, Eastern Uganda. *East African Journal of Environment and Natural Resources*, 4(1), pp.1-14.

Ugbogu, O.C., Ohakwe, J. and Foltescu, V., 2009. Occurrence of respiratory and skin problems among manual stone-quarrying workers. *African Journal of Respiratory Medicine*, 2009, pp.23-26.

Ukpong, E.C., 2012. Environmental impact of aggregate mining in the crush rock industry in Akamkpa local government area of Cross River State. *Nigerian Journal of Technology*, 31(2), pp.128-138.

Umar, J. and Oriri, O., 2023. Environmental Effects of the Quarry Site on the Adjoining Neighborhood in Oluyole Local Government, Oyo State, Nigeria. *Ghana Journal of Geography*, 15(3), pp.223-257.

Vallack, H.W. and Shillito, D.E., 1998. Suggested guidelines for deposited ambient dust. *Atmospheric Environment*, 32(16), pp.2737-2744.

Vandana, M., John, S.E., Maya, K. and Padmalal, D., 2020. Environmental impact of quarrying of building stones and laterite blocks: a comparative study of two river basins in the Southern Western Ghats, India. *Environmental Earth Sciences*, 79, pp.1-15.

Venkatesha, G., Kumar, C. and Gowda, P.R., 2015. Assessment and spatial distribution of groundwater quality in Bidadi industrial area, Ramanagara district, Karnataka, using water quality index (WQI) and GIS.

Werner, T.T., Bebbington, A. and Gregory, G., 2019. Assessing the impacts of mining: Recent contributions from GIS and remote sensing. *The Extractive Industries and Society*, 6(3), pp.993-1012.

William, B. and Hugh, D., 2006. Reducing the Environmental Effect of Aggregate Quarrying: Dust, Noise, and Vibration. Edited by Abbie Drew, MIRO.

William, L., 2020. Assessment of the Effects of Quarrying Activities on the Environment: A Case Study of Lengijave Village, Arusha District. (Doctoral dissertation, The Open University of Tanzania).

Wright, C., 2009. Air pollution monitoring and evaluation framework for South Africa: prioritizing vulnerable communities. *WIT Transactions on Biomedicine and Health*, 14, pp.55-64.

Yakovleva, N., 2017. *Corporate Social Responsibility in The Mining Industry*. Routledge. (Edited Book)

Yasobant, S. and Boondesh, N., 2017. Occupational and Environmental Impacts of Granite Quarry Activities in Chittoor District of Andhra Pradesh, India. India (August 8, 2017).

Yeh, H.C. and Schum, G.M., 1980. Models of human lung airways and their application to inhaled particle deposition. *Bulletin of Mathematical Biology*, 42(3), pp.461-480.

Zanobetti, A. and Schwartz, J., 2009. The effect of fine and coarse particulate air pollution on mortality: a national analysis. *Environmental Health Perspectives*, 117(6), pp.898-903.

Zimwara, D., Maphosa, E., Goriwondo, W.M. and Nyadongo, S.T., 2021. Modelling the environmental impacts of noise and dust from quarry stone mining in Harare—a case study of Pomona Quarry. *Zimbabwe Journal of Science and Technology*, 16(1), pp.25-35.

ORCID DETAILS OF THE AUTHORS

V. Nagaraja: https://orcid.org/0009-0000-2895-9166

Impact of COVID-19 on the Yearly Concentration Reduction of Three Criteria Air Pollutants and Meteorological Parameters' Effects on Aerosol Dispersion

R. M. Kharabsheh[1] and A. N. Bdour[2]†

[1]R&I Centre for the Conservation of Biodiversity and Sustainable Development (CBDS), Faculty of Forestry and Natural Environment Engineering, Universidad Politécnica de Madrid, Spain

[2]Department of Civil Engineering, Faculty of Engineering, The Hashemite University, P.O. Box 330127, Zarqa 13133, Jordan

†Corresponding author: A. N. Bdour; bdour@hu.edu.jo

ABSTRACT

The primary objective of this study is to evaluate the reduction percentage in the yearly concentrations of sulfur dioxide (SO_2), nitrogen dioxide (NO_2), and CO before and after COVID-19 in Amman, the capital city of Jordan, which has the highest population and traffic densities, and Zarqa, an industrial area with 55% of different types of industries. Additionally, this study examines the effect of metrological parameters such as temperature, humidity, and wind speed on air pollutant dispersion, particularly particulate matter 10 (PM_{10}), which is considered uncontrollable. Furthermore, this study highlights the critical environmental and health effects of air pollution. The Ministry of Environment measured the yearly concentration of air pollutants (SO_2, NO_2, CO, and PM_{10}) in three areas (Amman, Zarqa, and Irbid) in 12 stations in nearby industrial, urban, and traffic areas using the nitric oxide (NO) NO_2 chemiluminescence analyzer Model 42i, hydrogen sulfide (H_2S) and SO_2 analyzer model 450iQ, and PM_{10} Peta Attenuation analyzer. The few air pollution studies in Jordan have primarily focused on average yearly concentrations of SO_2, NO_2, CO, and PM_{10} without considering the monthly or daily variations that greatly concern health and the environment. The results of the present study reveal that during the COVID-19 pandemic, there was a significant decrease in the annual concentrations of H_2S, SO_2, and NO_2 as the reduction percentage in Amman 70, 58, 87% respectively, and in Zarqa 36, 62, 72% respectively. However, there is a slight reduction in CO and PM_{10} with 39 and 18% at Amman and 19% and 40% at Zarqa. This decrease is attributed to the reduction of primary sources of air pollutants, which are linked to the reductions in traffic volume and industrial activities during the lockdown. Furthermore, the results show that the Jordanian government has implemented regulations to address air pollution in residential areas. These regulations aim to prevent the burning of trees and smoking. The government is also adopting new transportation technologies to reduce the impact of CO_2 and other pollutants produced by diesel and gasoline vehicles. The use of green fuels like synthetic natural gas, green methanol, or ammonia, as well as the increasing use of electric cars, are being encouraged. Implementing the bus rapid transit system, which started in 2021 and includes linked lines in the east and west areas of Jordan, has reduced the number of cars used and solved the main issues in crowded regions. Overall, the country has taken significant steps to address and control air pollution.

INTRODUCTION

Geo-Climatic Situation in Jordan

Jordan is divided into three main geographic and climatic areas: the Jordan Valley, where Amman is located, the Mountain Heights Plateau, and the eastern desert or Badia region. The main desert areas are 200-300 km from Amman. These areas include Safawi, which is filled with dunes and hills (Abu-Sharar et al. 2012), and the Al-Azraq and Rewashed regions in the eastern part of Jordan, which

constitute 40% of Jordan's deserts (Khatatbeh et al. 2020). Fig. 1 shows the locations of desert areas in Jordan.

Fifteen percent of the desert area in Amman is located in Qasr Al-Qastal, Al-Muaqar, and Al-Mushatta, which are around 22, 26, and 25 km to the east of Amman. Meanwhile, 10% is located in Al-Halabat (around 25 km from Zarqa to the northeast), and 5% is in Qasr Al-Kharranah and Quseir Amra. Although Jordan's climate can vary from Mediterranean to desert, the country's landscape is typically relatively dry. The desert regions' wintertime temperatures
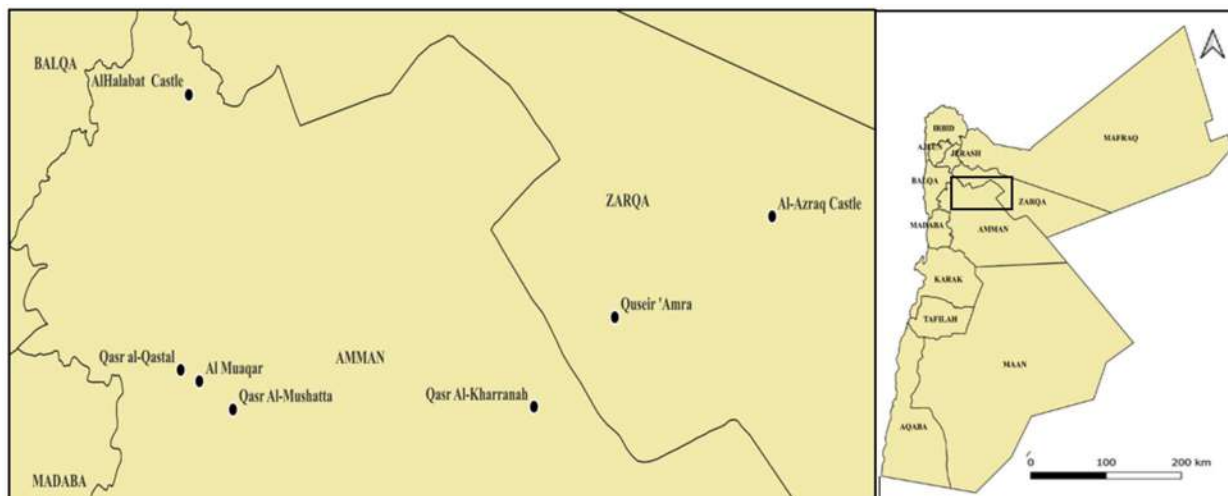
Fig. 1: Locations of desert areas in Jordan.

range from 19 to 22°C, while temperatures in the highlands in the south and north range from 9 to 13°C. Almost 75% of all precipitation occurs in the winter. The dry Sirocco (Khamsin) winds, which impact Jordan's climate and can cause spikes in temperature of up to 15°C, can cause significant temperature anomalies. High daytime temperatures result from the Shamal winds, which blow from the north and northeast (Abdulla 2020).

Current Air Pollution Situation in Jordan

Air pollution in Jordan has a significant impact on public health as (Bdour et al. 2008) identified that health outcomes, including respiratory issues, skin conditions, and malignancies, are consistent with the known health effects of exposure to air pollutants such as PM_{10} and SO_2. For example, 33.7% of people in this region suffer from chronic diseases, 25.6% have aches or infections, and 19.8% have a family history of cancer, PM_{10} causes respiratory disorders like bronchitis or asthma damages the immune system (Endale et al. 2024, Rajagopalan et al. 2020, Rozita et al. 2022), CO causes asphyxia at high concentrations (WHO, chronic diseases from air pollution report 2013). NO_2 has an impact on Asthma symptoms and respiratory infections (Muhaidat et al. 2019). SO_2 has an impact on throat and nose irritability and bronchitis.

The sources of air pollutants can be classified into two categories. The first is natural sources, such as dust storms from desert areas that produce a particle known as particulate matter 10 (PM_{10}). Researchers have found that the average number of dust storms in Jordan was 17.22, with a coefficient of variation of 46% (Ghanem 2020). The duration of storms ranged from one to four days, and the majority (54.1%) of them occurred in the spring, particularly in

April (22.2%). The yearly numbers of storms in different regions in Jordan are as follows: 13 in Irbid in the north, 182 in Al-Jafar in the south, and 102 in Safawi in the east. The dust storm intensified in the south and east (Bdour et al. 2008).

The second category of air pollutant sources is artificial sources, such as urban and construction pollutants. These pollutants are produced by human activities. The population in Jordan increased from 933,102 in 1960 to 10,302,651 in 2022, which translates to a population growth rate of 1.03%. As a result, the demand for constructing buildings has increased significantly (Department of Statistics Jordan, n.d.). Moreover, transportation significantly decreases the concentration of CO, CO_2 and PM_{10} in the atmosphere, and the number of diesel and gasoline vehicles in three active zones in Jordan (Amman, Zarqa, Irbid) reached 655,323, 30,044, and 56,106, respectively, according to a Ministry of Transportation statistical report (Department of Transportation, 2023). Another important source of air pollution is the industrial sector. For example, a petroleum refinery produced sulfur dioxide (SO_2), CO, and CO_2, an Asmara waste water purification plant produced hydrogen sulfide (H_2S), SO_2, and nitrogen dioxide (NO_2), and the Ramallah iron and steel industry produced SO_2, CO, and CO_2. A petroleum refinery in Zarqa to the north of Amman produced a sulfur concentration of 300 ppb, which decreased to 50 ppb (reflecting a 95% removal efficiency rate) after a sulfur recovery unit was installed (Khatatbeh et al. 2020). A Lafarge concrete factory produced CO and CO_2, and a pottery factory produced different heavy metals, as seen in Fig. 2 below.

The three main air pollution sources in Jordan can also classified as residential, transportation, and industry
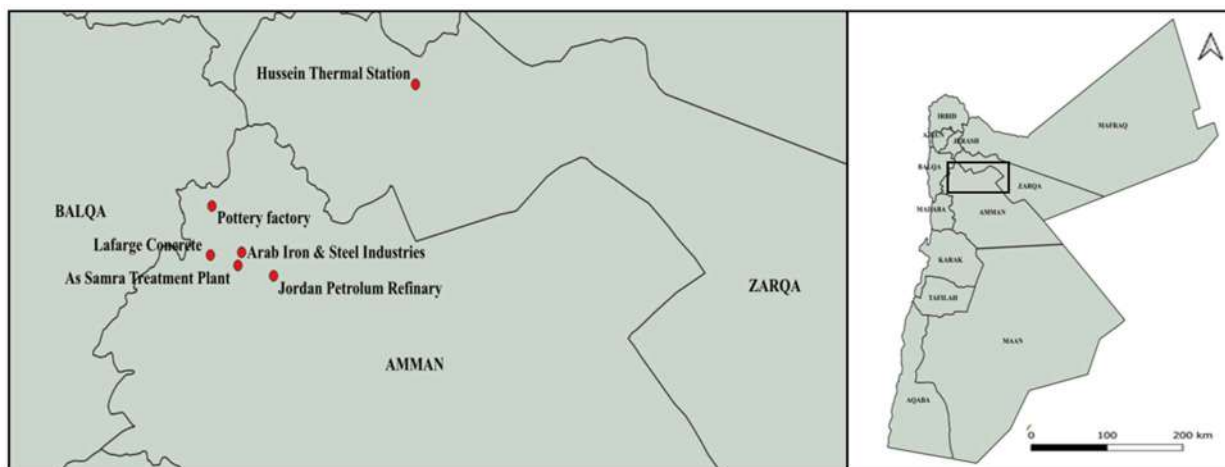
Fig. 2: Locations of industrial areas in Jordan.

Table 1: Sources of major air pollutants in Jordan.

	Sources	Pollutant's Produced	Area/city/ Neighbor	References
Residential	Heating, Burning, Smoking	CO, CO_2	Jerash	(AL-Kurdi & Al Hadidi 2015)
	Construction materials and equipment	NMHC, CO, HAPs, VOCs, PAHs	Amman	(Sa'adeh et al. 2019)
	On-site construction	PM_{10}	Amman	(Rajagopalan et al. 2020)
	Pesticides in plants	NO_X	Amman	(Hamed et al. 2010)
Transportation	Diesel and gasoline vehicles	CO, CO_2, SO_2, NO_2, PM_{10}	Amman, Zarqa, Irbid	(Hamdi et al. 2008)
	Unleaded petrol (90 and 95 octane)	CO, CO_2	Amman, Zarqa	(Alnawaiseh et al. 2015)
	Traffic lights	CO_2, SO_2, NO_2	Amman	(Ministry of Environment Jordan 2019)
	Heating, burning, and smoking	CO, CO_2	Amman, Zarqa	(Saleh 1995)
Industry	Pharmaceuticals factories	Microorganisms and bio-aerosols	Amman	(Zemouri et al. 2017)
	Lime quarries	CO_2, CO, NOx, SOx, $PM_{2.5}$, PM_{10}, CH_4, NMVOCs, NH_3	Abu-Alanda	(US Department of Economic and Social Affairs 2016)
	The burning of lubricating oils	Polycyclic aromatic hydrocarbons (PAH)	Bayader	(WHO, 2019)
	Bakeries	PM_{10}	Amman	(Abu-Allaban & Abu-Qdais, 2011)
	Pottery factories	PM_{10}, NO_X, SO_2, CO, NH_3	Amman	(Khatatbeh et al. 2020)
	Cement industry	SO_2	Zarqa	(Odat 2009)
	Jordan petroleum refinery	CO_2, CO, NOx, SOx, H_2S	Zarqa	(Al-Mashaqbeh et al. 2015)

pollutants. Table 1 displays the pollutants produced in different cities in Jordan according to previous research.

Jordan Current Legislations and Standards Regarding Air Pollution

Several studies and information regarding the sources of air pollution have been produced in Jordan, particularly in the last 10 years (Ghanem 2020). The natural desert and the growth of industrial sectors directly affect human health and the environment. The petroleum industry produces harmful emissions like SO_2, the cement industry produces NH_3 SO_2, CO, and CO_2, and the pharmaceutical industry produces microorganisms and bioaerosols. Some air pollutants are now under control with the use of filters and air scrubbers,

while other pollutants are difficult to control, especially when they come from natural sources such as PM_{10}, parallel to the changing of weather and sandstorms. According to the air quality index (AQI), the air pollution situation depends on the human activities and pollutants produced. For instance, the AQI of SO_2, NO_2, and ozone are within the recommended Jordanian limits 1140/2006 for ambient air quality standards and 1189/2006 for the maximum permissible limits of air pollutants emitted from stationary sources. However, the AQI of PM_{10} is always high, especially in Madaba and Tafileh to the south of Jordan, which is an arid area. Table 2 shows the Jordanian limits of the main air pollutants (Ministry of Environment Jordan 2019).

Limited studies investigated the annual and daily concentration of air pollutants and compared the values with Jordanian standards, for instance, Odat (2009) studied the yearly average concentration of these pollutants in various regions in Jordan, revealing that the results met Jordanian standards limits (1140/2006). The exception was PM_{10}, which was 105.2 μg/L in 2014, exceeding the Jordanian standard limit of 70 μg/L (Odat 2009). Another study included the yearly concentration values of SO_2, NO_2, CO, and CO_2 in three regions (Amman, Irbid, and Zarqa) from 2016 to 2019 and after 2020, demonstrating sharp (30-50%) reductions in their concentrations, as was expected after COVID-19. However, this study only focused on the yearly average concentrations of these pollutants and did not consider daily or monthly average concentrations (Dabbour et al. 2021). Moreover, a study on the daily PM_{10} concentration in Amman and Zarqa cities from March 6 to May 28, 2014, revealed high values (up to 150 μg) exceeding the Jordanian standard limit for PM_{10}, which is 120 μg/L. This study aims not only to evaluate the yearly concentrations of pollutants in Jordan but also to highlight the sharp decrease in their monthly concentrations during COVID-19 (i.e., from March 2020 to August 2020) because of the lake use of transportation methods and the industrial sector.

MATERIALS AND METHODS

Study Sites

Amman is the capital of Jordan with coordinates (31.9544° N, 35.9106° E), Fifteen percent of the desert area in Amman is located in Qasr Al-Qastal, Al-Muaqar, and Al-Mushatta, which are around 22, 26, and 25 km to the east of Amman. Meanwhile, 10% is located in Al-Halabat around 25 km from Zarqa to the northeast of Amman with coordinates (32.0608° N, 36.0942° E), and 5% is in Qasr Al-Kharranah and Quseir Amra. These areas are considered to be the main natural source of PM_{10} as seen in Fig. 1.

The main artificial source of air pollution in Amman is the industry as the Ramallah iron and steel industry produces SO_2, CO, and CO_2, A Lafarge concrete factory produces CO and CO_2, and a pottery factory produces different heavy metals, the Ramallah iron and steel industry produced SO_2, CO, and CO_2. For example, a petroleum refinery produced sulfur dioxide (SO_2), CO, and CO_2, an Asmara waste water purification plant produced hydrogen sulfide (H_2S), SO_2, and nitrogen dioxide (NO_2), and A petroleum refinery in Zarqa to the north of Amman produced a sulfur concentration of 300 ppb, which decreased to 50 ppb (reflecting a 95% removal efficiency rate) after a sulfur recovery unit was installed (Khatatbeh et al. 2020). As seen in Fig. 2.

Table 2: Jordanian ambient air quality limits (1140/2006).

Air pollutants	Sampling time	Maximum allowable limit	Number of limit breaches
Sulfur Dioxide (SO_2)	1 hour	0.3 ppm	Three times during any of the 12 months in a year
	24 hours	0.14 ppm	Once a year
	1 year	0.04 ppm	---------------------
Nitrogen Dioxide (NO_2)	1 hour	26 ppm	Three times during any of the 12 months in a year
	8 hours	9 ppm	Three times during any of the 12 months in a year
Carbon monoxide (CO)	1 hour	0.21 ppm	Three times during any of the 12 months in a year
	24 hours	0.08 ppm	Three times during any of the 12 months in a year
	1 year	0.05 ppm	-
Hydrogen sulfide (H_2S)	1 hour	0.03 ppm	Three times during any of the 12 months in a year
	24 hours	0.01 ppm	Three times during any of the 12 months in a year
	1 year	8 μg/L	-
	1 year	70 μg/L	-
Particulate matter (PM_{10})	24 hours	120 μg/m^3	Three times during any of the 12 months in a year
	1 year	70 μg/m^3	-

Data Collection and Instruments

This study analyzes the daily, monthly, and annual records of air pollutant concentrations in Amman and Zarqa using Excel and maps drawn using QGIS. The considered air pollution data was obtained from the Ministry of Environment. The records include measurements of H_2S, SO_2, NO_2, CO, and PM_{10}. Nitric oxide (NO) and NO_2 concentrations were measured using a chemiluminescence analyzer (Model 42i), while SO_2 and H_2S concentrations were determined using an SO_2 analyzer (Model 450i Q). Particulate matter (PM_{10}) was measured using a Beta Attenuation Analyzer. The meteorological parameters were measured at the same period as wind speed, the direction of the wind, as well as the temperature and humidity levels measured by retractable telescopic mast 8-10 meters and ultrasonic metrological sensors. Seven monitoring stations in Amman and three stations in Zarqa were considered as shown in Table 3. Although these monitoring stations provide valuable data, they may not fully represent the air quality across the country. Some areas with high air pollution levels might not have monitoring stations due to a lack of coverage. Fig. 3 shows the distribution of these monitoring stations in Amman, Zarqa, and Irbid. Furthermore, ensuring the completeness and accuracy of the recorded data is crucial, as any gaps or errors can impact the analysis and decision-making processes.

This study also explores the influences of meteorological parameters, such as temperature, humidity, and wind speed, on the dispersion of air pollutants, particularly PM_{10}. Additionally, this research emphasizes the critical environmental and health issues associated with air pollution.

This investigation analyzes the daily, monthly, and yearly records of air pollutant concentrations in Amman and Zarqa,

Table 3: Air pollution stations in Jordan.

Station Name	Station Name	Location	Type of Station	Pollutants
KHG	King Hussein Gardens	Amman	Industrial	NO_2, SO_2, O_3, PM_{10}, MET
GAM	Greater Amman Municipality	Amman	Urban	NO_2, SO_2, O_3, PM_{10}, CO
TAB	Bus Station Tabarbour	Amman	Urban	CO, PM_{10}, NO_2
MAH	Marka/Mahata	Amman	Traffic	NO_2, SO_2, PM_{10}
UNI	University Street/Swelieh	Amman	Traffic	NO_2, PM_{10}
KAC	King Abdullah City	Irbid	Industrial	NO_2, SO_2, PM_{10}
YAR	Yarmouk	Amman	Urban	NO_2, SO_2, PM_{10}
HAJ	Wadi Hajjar Health Center	Zarqa	Traffic	NO_2, SO_2, CO, PM_{10}, MET
MAS	Massane	Zarqa	Industrial	NO_2, SO_2, PM_{10}
HH	Hashemite Hall	Zarqa	Urban	NO_2, SO_2, PM_{10}
HSC	Al Hassan Sport City	Irbid	Traffic	NO_2, CO, PM_{10}
BAR	Al Barah Street	Irbid	Background	NO_2, SO_2, O_3, PM_{10}, MET
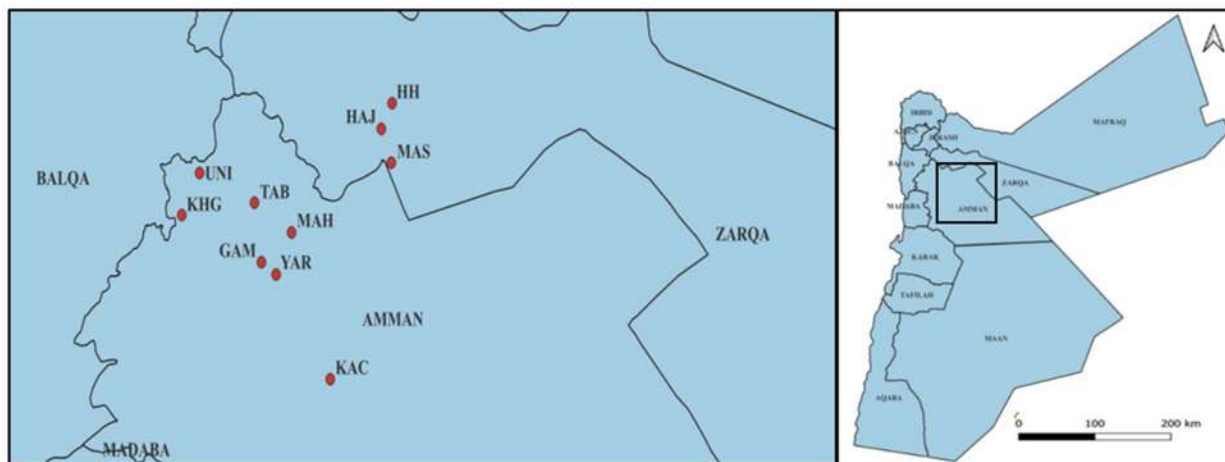
Fig. 3: Distribution of the selected monitoring stations in Amman, Zarqa, and Irbid.

a city with a significant industrial sector representing 55% of the country's industrial facilities. The considered air pollution data was obtained from the Ministry of Environment. The records include measurements of SO_2, NO_2, CO, and PM_{10}. Six monitoring stations in Amman and three stations in Zarqa were considered. Additionally, three stations in Irbid, an area hosting Syrian refugees, were considered.

RESULTS AND DISCUSSION

COVID-19 Impacts and Pollutants' Reduction Trends

COVID-19 has significantly reduced certain pollutants, as many factories, companies, and transportation methods came to a halt between March 2020 and August 2020. Figs. 4 to 13 illustrate the yearly and monthly pollutant concentration trends during this period.

The average yearly concentrations of air pollutants were evaluated before and after COVID-19, as shown in Fig. 4. The concentration of H_2S decreased sharply in 2020 in

Amman to 70% due to the reduction in the water consumption rate by factories and companies during the pandemic and the subsequent increase in 2021 (though it remained below the expected value due to improvements in some facilities like filter installation). Regarding Zarqa, upgrading the largest wastewater treatment plant-As Samara-located northeast of Zarqa, and improving some oxidizers and biological filters reduced the amount of H_2S after 2018. The concentration reduction of 36% in Zarqa in 2020 was noticeable but less than in Amman since 55% of different types of industries are there. The average daily standard Jordanian limit for H_2S concentration is 10 ppb (the yearly standard limit was unavailable). Fig. 5 shows the monthly concentration of H_2S during COVID-19 (March 2020 to August 2020).

The reduction of H_2S concentration in treatment plants has led to a gradual decrease in SO_2 levels in Amman and Zarqa during the COVID-19 period to 58% at Amman and 62% at Zarqa, as shown in Figs. 6 and 7. The high concentration of SO_2 in 2015 was due to the high sulfur

Fig. 4: Average yearly air concentration of H_2S (ppb) from 2015–2021 in Amman and Zarqa.

Fig. 5: Monthly air concentration of H_2S (ppb) in Amman and Zarqa.

Fig. 6: Average yearly air concentration of SO_2 (ppb) from 2015–2021 in Amman and Zarqa.

Fig. 7: Monthly air concentration of SO_2 (ppb) in Amman and Zarqa.

production in petroleum refinery plants operating without desulfurization units. Shatnawi & Abu-Qdais (2021) showed that the concentrations of air pollutants during the pandemic decreased compared to before the pandemic period (Shatnawi & Abu-Qdais 2021). Their results were based on an analysis using the ANN model of the expected air pollutants based on Scenario II before and after the pandemic. Decreases in NO_2, SO_2, and PM_{10} concentrations were 72%, 52%, and 29%, respectively. Notably, the Jordanian yearly standard limit for SO_2 is 40 ppb.

Figs. 8 and 9 show that Amman had significantly higher concentrations of NO_2 resulting from fertilizer, agriculture, and green land activities, which decreased sharply after the pandemic to 87% in Amman and 72% in Zarqa. The main reason that the public facility and garden directorates developed an integrated green infrastructure strategy and increased the number of parks and gardens by over 143, according to the Amman Green City Action Plan, which was

enacted from 2019 to 2021. In Zarqa, which is considered an industrial region, the level of NO_2 emissions is lower than in Amman; nevertheless, the concentration of NO_2 decreased during COVID-19. Dabbour et al. (2021) estimated a 25.5% reduction in NO_2 concentrations in Amman by 2020. The average daily Jordanian limit for NO_2 concentration is 80 ppb, while the yearly standard limit is currently unavailable (Dabbour et al. 2021).

CO emissions in Jordan are caused by various sources, including transportation, industry, and wastewater treatment plants. The pandemic resulted in a significant decrease in CO concentrations from March 2020 30% in Amman and 19% in Zarqa, as shown in Figs. 10 and 11. However, the concentration of CO was higher in Amman than in Zarqa, which has a high population growth rate due to the use of different transportation methods, which are the main source of CO. The high concentration of CO in Zarqa in 2021 was due to recitation and construction works on Army
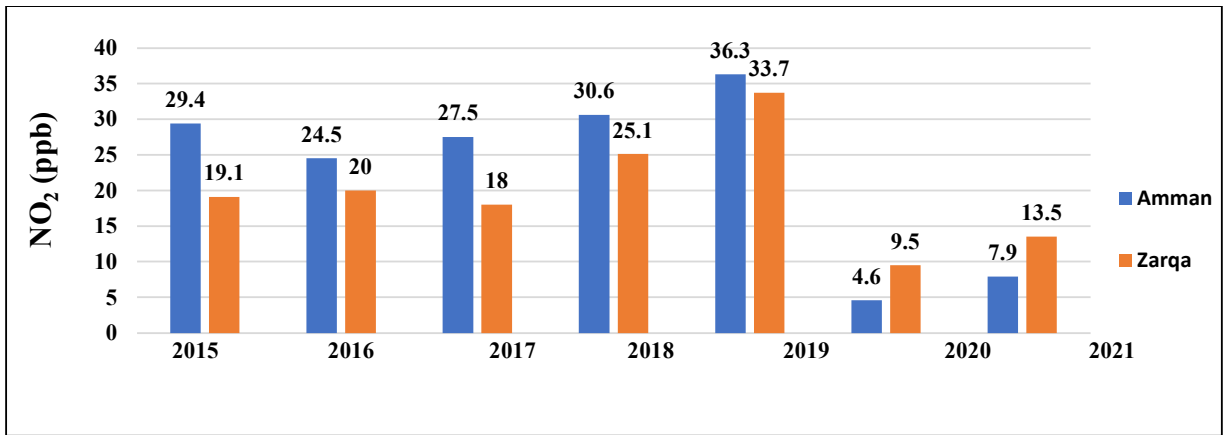
Fig. 8: Average yearly air concentration of NO$_2$ (ppb) from 2015-2021 in Amman and Zarqa.
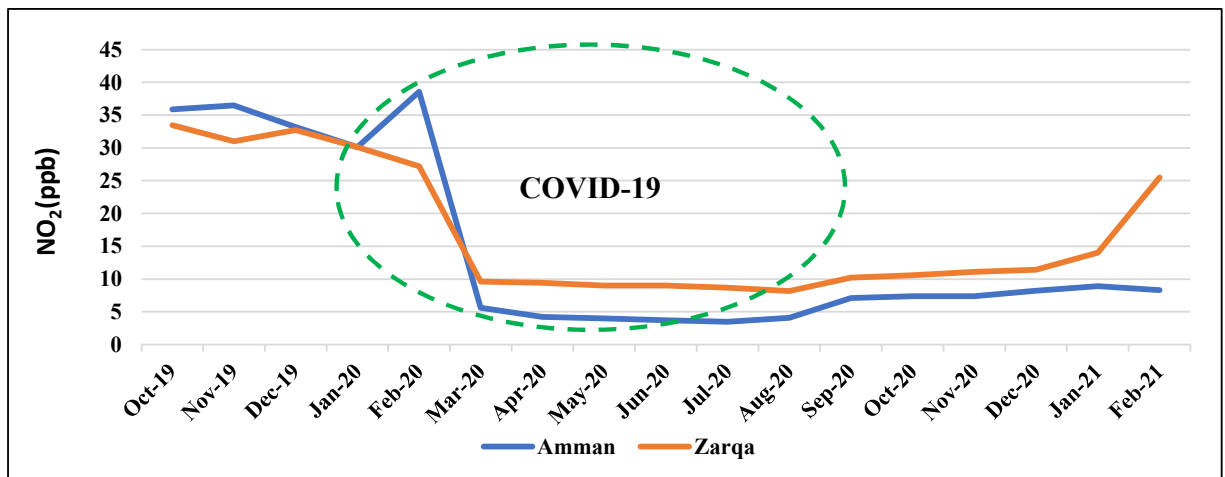
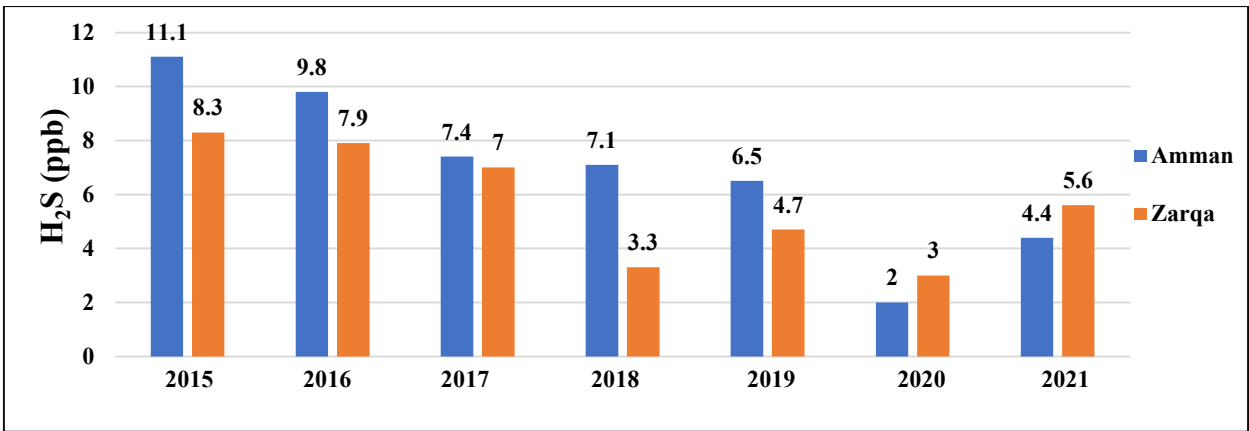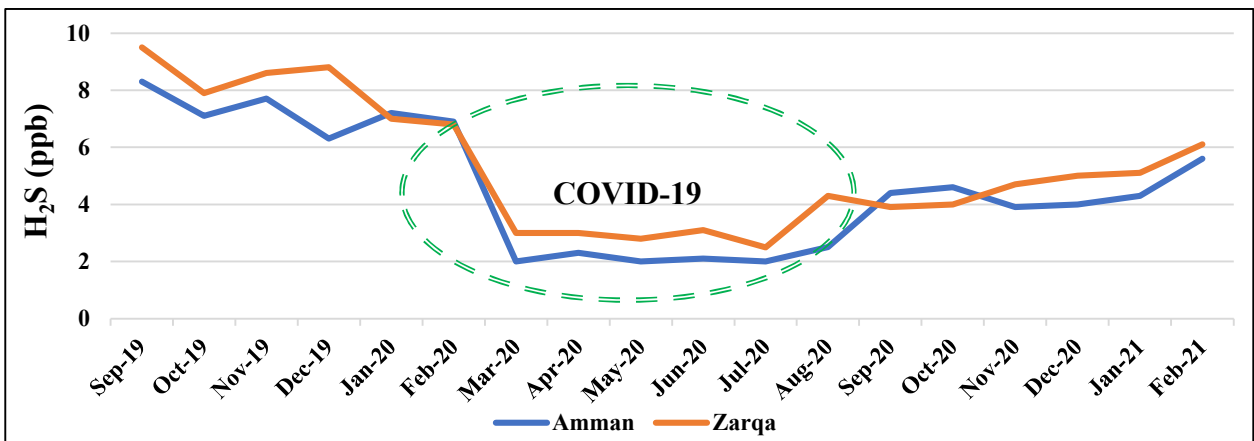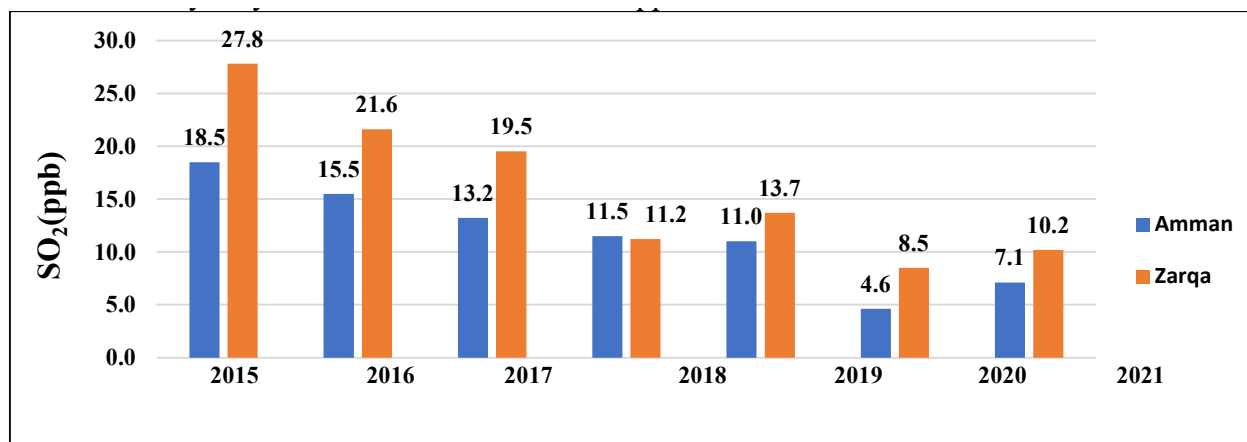Fig. 9: Monthly air concentration of NO$_2$ (ppb) in Amman and Zarqa.
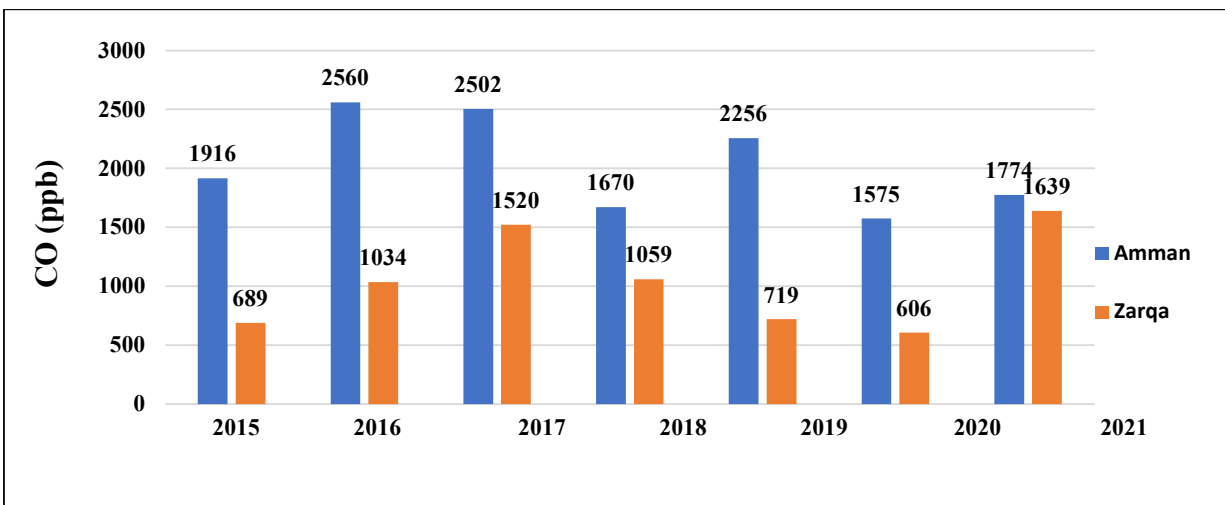
Fig. 10: Average yearly air concentration of CO (ppb) from 2015–2021 in Amman and Zarqa.
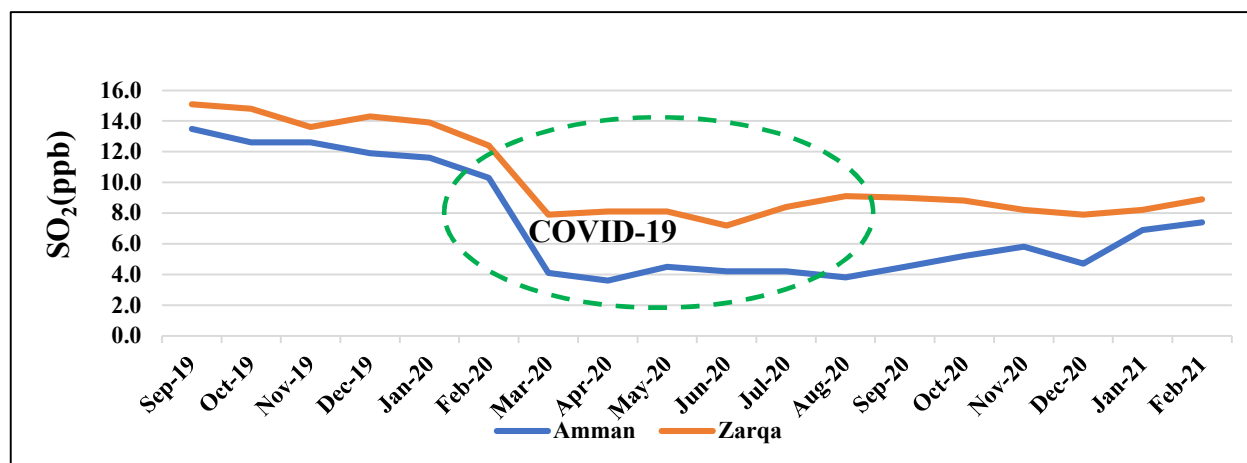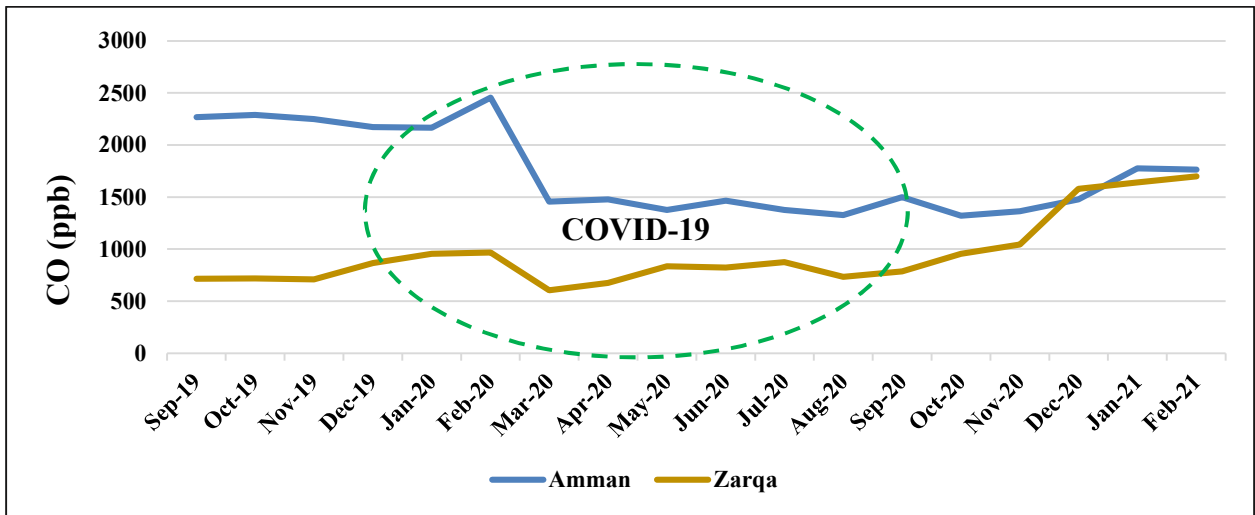
Fig. 11: Monthly air concentration of CO (ppb) in Amman and Zarqa.

Street in Zarqa, 16.8 km from Amman. Shotar et al. (2021) found a 70.4% increase in the death rate associated with CO concentrations in Jordan from 2015 to 2018, followed by a sharp decrease to 20.1% in 2020 (Shotar et al. 2021). Currently, there are no Jordanian standard limits for the yearly concentration of CO.

PM_{10} is a pollutant that is difficult to control and is produced from both natural sources, such as dust, and human activities, such as transportation and industrial activity. In 2015, a sandstorm in April produced a high concentration of PM_{10} (reaching up to 1000 ppb). In 2016, a second sandstorm occurred in the southern desert of Jordan; as a result, PM_{10} concentrations in Jordan remained above the national yearly standard limit of 70 µg/L, as shown in Figs. 12 and 13. The reduction of PM_{10} during COVID-19 was 18% in Amman and 49% in Zarqa. According to the Ministry of Environment, the percentage of PM_{10} reached 40% in the Zarqa region in 2021 due to increased quarrying and construction activities, which may have contributed to further increases in PM_{10} concentrations. According to Shatnawi & Abu-Qdais (2021), as mentioned earlier, PM_{10} levels dropped during 2020. Specifically, a decrease of 29% in Amman and 32% in the Zarqa region were observed. PM_{10} experienced a slightly greater decline than other pollutants during COVID-19.

Meteorological Effects Display on Air Pollution in Amman and Zarqa

Recent research has established a clear and direct link
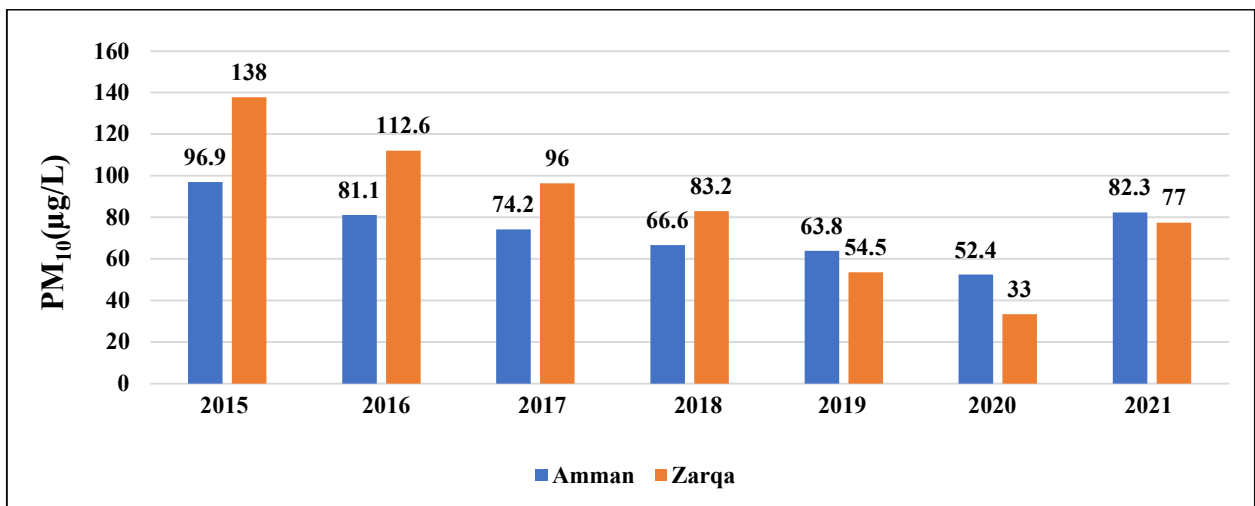
Fig. 12: Average yearly air concentration of PM_{10} (µg/L) from 2015-2021 in Amman and Zarqa.
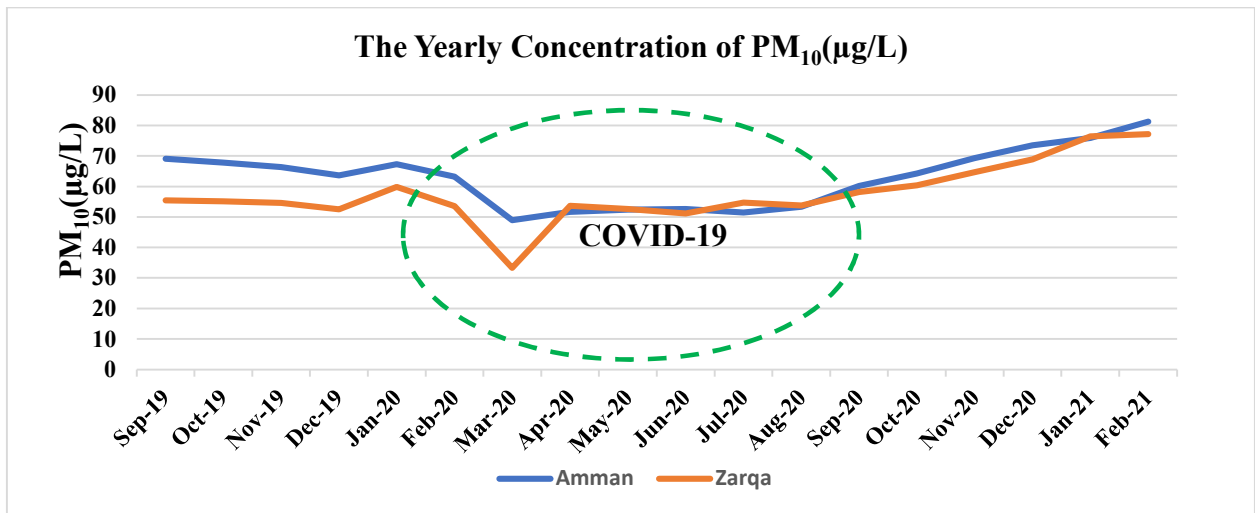
Fig. 13: Monthly air concentration of PM_{10} (μg/L) in Amman and Zarqa.

between climate change-including changes in precipitation, temperature, wind speed, and humidity, and increased air pollution in Jordan. The combination of reduced rainfall, elevated temperatures, high humidity, and strong wind speeds have contributed to heightened levels of air pollution (Al-Smairan & Al-Nhoud 2019). In March 2019, the average yearly maximum temperature and humidity, as depicted in Table 4, was within the typical ranges in both Amman and Zarqa. However, during the COVID-19 pandemic, wind speed was the dominant parameter responsible for reducing the concentration of pollutants, such as CO, SO_2, and NO_2, to about 30% of their usual levels.

Dabbour et al. (2021) examined the impact of meteorological parameters on air pollution dispersion in three zones (Amman, Zarqa, and Irbid). The collected data on annual concentrations of pollutants (CO, SO_2, NO_2, and PM_{10}) and conducted a Sobol sensitivity test. The results showed that in Amman, SO_2 increased significantly with humidity, wind speed, and pressure, while the NO_2 level was directly proportional to temperature. There was no relationship found between meteorological conditions and PM_{10}. Industrial sources of pollution in Amman included the largest cement manufacturer (Lavarge), which produced CO, SO_2, and NO_2, as well as the steel industry (Arab Iron and Steel Industry), which also produced PM_{10} and $PM_{2.5}$.

A pottery factory to the north of Amman, near Irbid, also contributed to air pollution, as shown in Table 3.

In Zarqa, the concentrations of CO, SO_2, and NO_2 were directly proportional to the rise in humidity. NO_2 levels also increased with wind speed, while pressure played a significant role in increasing CO concentrations. However, no correlation was observed between PM_{10} concentrations and meteorological conditions. In Irbid, known as the "city of refugees," temperature had the greatest influence on NO_2 levels, high humidity had the most significant impact on SO_2 concentrations, and pressure had the strongest influence on PM_{10} concentrations (Matouq et al. 2013a).

Another important source of air pollution is the industrial sector (e.g., the petroleum refinery, Asmara wastewater purification plant, and Ramallah iron and steel industry). The petroleum refinery in Zarqa produced a sulfur concentration of 300 ppb, which decreased to 50 ppb (which reflects a 95% removal efficiency rate) after a sulfur recovery unit was installed. Wastewater treatment plants significantly impact air pollution; since the 1980s, wastewater has either been discharged into valleys or mixed with fresh water before being reused. The largest wastewater treatment facility in Jordan is located in Asmara, 60 km from Amman, which was established in 2007. It had a maximum capacity of 15,000-20,000 m^3/day, which increased to 267,000 m^3/day in 2008

Table 4: Metrological parameters (temperature, humidity, and wind speed) in Amman and Zarqa during COVID-19.

Year	Region	T (°C)	Humidity (%)	Wind Speed (km/h)	SO_2	NO_2	CO	PM_{10}
2019	Amman	17	64.5	7.5	11	36.3225.6	2,256	63.8
	Zarqa	25	50.1	9.6	13.7	33.762.7	719	54.5
2020	Amman	16	66.3	8.9	4.6	4.6201.8	1,575	52.4
	Zarqa	27	56.2	10	8.5	9.562.9	606	33

and 367,000 m³/day in 2015 (Bdour & Nidal Hadadin 2005). The amount of H_2S and SO_2 in the final sludge in Asmara was reduced by an upgraded desulfurization facility.

The land area of Jordan experiences an annual rainfall of less than 200 mm, resulting in poor structural stability of soils and a high susceptibility to erosion during shallow rainstorm events (Hammad et al., 2018). According to predictions by Ghanem (2020), droughts and smoke clouds are expected to increase, especially during the summer, while rainfall is anticipated to decrease by 30%. Additionally, temperature has been increasing at a rate of approximately 0.04°C per year (Abdulla 2020, Tabieh et al. 2014). Over the past decade, maximum wind speeds have also increased, reaching 25 km/h. Furthermore, humidity levels have risen to 68% over the past two years, as reported in a 2021 Amman climate weather report.

Several studies in Zarqa have indicated that warming influences rainfall volume reduction. For instance, if the temperature increases annually by 4 °C and rainfall decreases by 10%, it can lead to a 12.4% reduction in cultivated areas (Al Saodi et al. 2023, Tabieh et al. 2014). Meanwhile, in the mid, south, and southeastern regions of Amman; the Zarqa Basin; and Jordan overall, rainfall has decreased by 10-15% over the past two decades. Desert stations have reported even greater reductions in rainfall. Previous studies have confirmed that the evaporation factor for the Zarqa River basin is 90%. However, evaporation has increased due to the shifting of rainfall storms toward the summer season. Consequently, this study suggests that the potential evaporation value has increased from 90% to 91% (Matouq et al. 2013b).

Air Pollution's Impacts on Public Health and the Environment

Effect of air pollution on human health: Khatatbeh et al. (2020) conducted a study in Al-Hashmiya (Zarqa region) and highlighted the negative impact of air pollution on public health, particularly in areas near industrial sources of pollution. They identified that health outcomes, including respiratory issues, skin conditions, and malignancies, are consistent with the known health effects of exposure to air pollutants such as PM_{10} and SO_2. For example, 33.7% of people in this region suffer from chronic diseases, 25.6% have aches or infections, and 19.8% have a family history of cancer (Bdour et al. 2008). The high percentages of chronic diseases, aches and infections, and family histories of cancer among the population living near the oil refinery indicate an urgent need for effective measures to reduce air pollution levels in these areas.

This study was conducted in a specific location and may not represent the entire country. Further studies are necessary to identify areas with the highest levels of air pollution and their impact on public health to inform the development of effective policies and interventions to mitigate these

Table 5: Health effects and sources of air pollutants in Jordan.

Pollutants	Health Effects	Locations	Reference
PM_{10}	Respiratory disorders like bronchitis or asthma damage the immune system. Affects the body's ability to fight infection. High blood pressure, strokes, and lung cancer.	Aljafer Ma'an Karak	(Endale et al. 2024, Rajagopalan et al. 2020, Rozita et al. 2022)
CO, CO_2	Causes asphyxia at high concentrations. Reduces the blood's ability to carry oxygen to cells and organs.	Amman	(WHO, chronic diseases from air pollution report, 2013).
NOx	Asthma symptoms and respiratory infections. Chronic lung disease at high concentrations.	Zarqa	(Muhaidat et al. 2019)
SO_2	Throat and nose irritability. Bronchitis.	Zarqa	(Hadadin & Tarawneh 2007)
O_3	Damages live cells when it reacts with biological membranes. Asthma and reduced lung function.	Amman	(Dabbour 2021)
VOC exposure	Poor coordination and nausea. Irritation of the eyes, nose, and throat. Headaches and neck pain. Damage the kidneys, liver, and nervous system at high concentrations.	Zarqa	(WHO, chronic diseases from air pollution report, 2013 (Rozita et al. 2022))
Nonmethane hydro-carbons (NMHCs)	Chronic obstructive pulmonary disease. Damage to the central nervous system. High cardiorespiratory.	Amman Zarqa	(Herndon et al., 2020; Bhosale et al. 2023)
HAPs (benzene, trichloroethylene, mercury, chromium, and dioxin)	Asthma and lung cancer. Birth defects, reproductive effects, and neurodevelopmental effects.	Zarqa	(International Agency for Research on Cancer, report 2013)

Table 6: Environmental effects associated with air pollutants in Jordan.

Pollutants	Environmental Effects	Locations	Reference
PM_{10}	Affects water's clarity and quality (increased turbidity). Deposition and subsequent uptake by plants. Significantly affects growth and reproduction in some plants. Damage in leaves in some plants.	Irbid	(Shatnawi & Abu-Qdais 2021)
CO, CO_2 (Construction or vehicles)	Global warming. Destroys the Earth's ozone layer.	Amman	(AL-Kurdi & Al Hadidi 2015)
NOx	Damages leaves, slows growth, and lowers agricultural production.		AL-Kurdi & Al Hadidi 2015)
SO_2	Sulfuric acid, which causes acid rain, leads to deforestation. Acidifies waterways to the detriment of aquatic life.	Amman Zarqa Azraq Aljafer	(WHO 2019)
O_3	Decreases the growth and survival of tree seedlings. Decreases agricultural crop and commercial forest yields.	Aqaba	(Gertler et al. 2011)
Volatile organic compound (VOC) exposure	Increases plant diseases, delays seed formation and hinders fertilization. Increases production of low-level ozone as a result of photochemical processes with high temperatures and heat waves.	Amman	(Al Jaber 2016)
Nonmethane-hydrocarbons (NMHC)	Considerably increases the amount of propane and ethane in the air around highways, causing ground-based ozone pollution.	Amman	(Salameh et al. 2015)

effects. Table 5 lists air pollutants' sources and health effects.

Effects of air pollution on the environment: Naber's (2010) environmental analysis related to achieving sustainable development in Jordan indicated that air pollution is the primary cause of environmental degradation in Jordan, with air pollution responsible for the highest annual cost of environmental degradation in terms of gross domestic product, followed by water (0.81%), waste (0.23%), and soil (0.11%). Meanwhile, over the past 10 years, the impact of air pollution on ecosystems has grown significantly, leading to global warming, the loss of vegetation, and stratospheric ozone. Table 6 shows the links between various Jordan air pollutants and their environmental impacts.

CONCLUSIONS

The air pollution in Jordan is a critical problem that has increased over time. This study explains that there was a significant decrease in the annual concentrations of H_2S, SO_2, and NO_2 during the COVID-19 lockdown, with reductions of 70%, 58%, and 87%, respectively in Amman, and 36%, 62%, and 72%, respectively in Zarqa. However, there was only a slight reduction in CO and PM_{10}, with decreases of 39% and 18% in Amman and 19% and 40% in Zarqa, from March 20 to August 20, 2020. This decrease is attributed to the reduction of primary sources of air pollutants, linked to reduced traffic volume and industrial activities during the lockdown. It is also concluded that wind speed was the dominant parameter

responsible for reducing the concentration of pollutants like CO, SO_2, and NO_2 to about 30% of their usual levels.

The issue of sandstorms in 75% of Jordan poses a significant challenge in decreasing the levels of PM10 in the atmosphere. As a result, PM_{10} is a significant concern in Jordan and the Middle East because the natural sources of PM_{10}, especially sandstorms in the southern region, are difficult to control and cause health and environmental effects. The Ministry of Environment plans to install advanced instruments in southern areas to better monitor pollution. However, many industries still lack environmental awareness and a sense of responsibility. The Jordan Environmental Monitoring Directorate, established in 2003, oversees air quality through the national ambient air quality monitoring network. However, from 2015 to 2018, air pollutant concentrations (NO_2, CO, SO_2, and O_3) in Amman and Zarqa exceeded the Jordanian standard limit of 1140/2006.

During the COVID-19 pandemic, annual concentrations of air pollutants significantly decreased due to reduced traffic and industrial activities. Sandstorms, affecting 75% of Jordan, present a major challenge in reducing PM10 levels, with significant health and environmental impacts. The Ministry of Environment plans to install advanced monitoring instruments in southern regions, although many industries lack environmental awareness and responsibility. The industrial sector employs filter technologies to reduce emissions, such as bag filters in cement and steel factories,

ceramic filters in medical waste incinerators, and particulate matter and chemical filters for manganese production. The high cost of implementing these technologies poses a challenge for the private sector.

The Jordanian government has implemented regulations to address air pollution in residential areas, focusing on preventing tree burning and smoking. New transportation technologies are being adopted to reduce CO_2 and other pollutants from diesel and gasoline vehicles. Green fuels like synthetic natural gas, green methanol, or ammonia, along with increased use of electric cars, are being promoted. The bus rapid transit system, implemented in 2021, has reduced car usage and alleviated congestion in urban areas.

RECOMMENDATIONS

- Encourage and promote the use of public transportation, such as bus rapid transit, as well as environmentally friendly transportation methods like bicycles or walking, to reduce the number of cars on the road and reduce air pollution.

- Enforce regular technical inspections of automobiles to ensure they meet safety and emission standards, either through on-the-spot inspections or regular checks at specialized traffic centers.

- Promote the use of peripheral parking areas near train and bus stations for those who spend extended periods at work or school to reduce traffic in the city center and alleviate pressure on short-term parking areas.

- Improve the efficiency of heating systems by using mechanical means, such as outdoor air intakes connected to the HVAC system, as well as natural ventilation methods, such as openings, joints, and cracks in walls, floors, ceilings, and areas around windows and doors.

- Adopt advanced technologies to measure and monitor air pollutants in the environment, such as high-tech laser particle sensors, beta attenuation, chemiluminescence, and UV fluorescence.

- Implement improved processes for treating waste, such as condensate run-off from autoclaves for medical waste, molten salt oxidation for energy production from solid waste, and composting organic waste for use as fertilizer.

- Encourage a circular economy with a focus on reducing waste and lowering greenhouse gas emissions by eliminating waste and pollution and promoting sustainable practices.

REFERENCES

Abdulla, F., 2020. 21st Century Climate Change Projections of Precipitation and Temperature in Jordan. *Procedia Manufacturing*, 44, pp. 197–204. https://doi.org/10.1016/j.promfg.2020.02.222

Abu-Allaban, M. and Abu-Qdais, H., 2011. Impact assessment of ambient air quality by cement industry: A case study in Jordan. *Aerosol and Air Quality Research*, 11(7), pp. 802–810. https://doi.org/10.4209/aaqr.2011.07.0090

Abu-Sharar, T.M., Al-Karablieh, E.K. and Haddadin, M.J., 2012. Role of Virtual Water in Optimizing Water Resources Management in Jordan. *Water Resources Management*, 26(13), pp. 3977–3993. https://doi.org/10.1007/s11269-012-0116-z

Al Jaber, H.I., 2016. Salvia ceratophylla from Jordan: Volatile Organic Compounds, Essential oil composition and antioxidant activity. *Jordan Journal of Chemistry*.

Al Saodi, R., Al Kuisi, M. and Al Salaymeh, A., 2023. Assessing the vulnerability of flash floods to climate change in arid zones: Amman–Zarqa Basin, Jordan. *Journal of Water and Climate Change*, 14(9), pp. 4376–4403. https://doi.org/10.2166/wcc.2023.237

Al-Kurdi, H. and Al Hadidi, D., 2015. High Health Council General Secretariat National Human Resources for Health Observatory Annual Report, 2014 Supervised By.

Al-Mashaqbeh, A., Abu-Allaban, M. and Al-Malabah, A., 2015. Air Quality Impact of the Upgraded Al-Samra Waste Water Treatment Plant. *Jordan Journal of Earth and Environmental Sciences*, 7(1).

Alnawaiseh, N.A., Hashim, J.H. and Md Isa, Z., 2015. Relationship between Vehicle Count and Particulate Air Pollution in Amman, Jordan. *Asia Pacific Journal of Public Health*, 27(7), pp. NP1742–NP1751. https://doi.org/10.1177/1010539512455046

Al-Smairan, M. and Al-Nhoud, O., 2019. Feasibility Study to Install Wind Farm in Bab Al-Hawa, Irbid, Northwest of Jordan. *Modern Mechanical Engineering*, 9(1), pp. 30–48. https://doi.org/10.4236/mme.2019.91004

Bdour, A.N., Hamdi, M.R., Shawaqfeh, M.S. and Al-Hussinat, M.M., 2008. Enhancing public participation in local air pollution assessment: A citizen participation prototype from Zarqa governorate, Jordan. *Environmental Engineering Science*, 25(7). https://doi.org/10.1089/ees.2007.0066

Bdour, A.N. and Hadadin, N., 2005. Potentials and Limitations of Wastewater Reuse in Rural Areas in Jordan: The Reuse Options in the Jordan Valley. *Journal of Agronomy*, 4(5), pp. 315–322. https://doi.org/10.3923/ja.2005.315.322

Bhosale, C.S., Mane, P.R., Salunkhe, J.S., Mothgare, V.M., Sutar, S.S., Manglekar, S.B., Jadhav, A.S. and Raut, P.D., 2023. Ambient Air Quality Monitoring with Reference to Particulate Matter (PM10) in Kolhapur City. *Nature Environment and Pollution Technology*, 22(4), pp. 2029–2037. https://doi.org/10.46488/NEPT.2023.v22i04.028

Dabbour, L., Abdelhafez, E. and Hamdan, M., 2021. Effect of climatology parameters on air pollution during COVID-19 pandemic in Jordan. *Environmental Research*, 202, p. 111742. https://doi.org/10.1016/j.envres.2021.111742

Department of Statistics Jordan, n.d. Department of Statistics report 2019.

Department of Transportation, U., 2023. *Transportation Statistics Annual Report 2023*.

Endale, T.A., Raba, G.A., Beketie, K.T. and Feyisa, G.L., 2024. Exploring the trend of aerosol optical depth and its implication on urban air quality using multi-spectral satellite data during the period from 2009 to 2020 over Dire Dawa, Ethiopia. *Nature Environment and Pollution Technology*, 23(1), pp. 1–15. https://doi.org/10.46488/NEPT.2024.v23i01.001

Gertler, A., Darko Koracin, A., Walker, M., Miller, G., Solieman, A., Abu-Allaban, M., Luria, M., Read, M.H. and Dean, A., 2011. Ozone levels in the north and south of Jordan: Effects of transboundary air pollution. *Doctor of Philosophy*.

Ghanem, A.A., 2020. Climatic characteristics of dust storms in Jordan. *American Journal of Climate Change*, 9(2), pp. 136–146. https://doi.org/10.4236/ajcc.2020.92010

Hamdi, M.R., Bdour, A. and Tarawneh, Z., 2008. Diesel quality in Jordan: Impacts of vehicular and industrial emissions on urban air quality. *Environmental Engineering Science*, 25(9). https://doi.org/10.1089/ees.2007.0234

Hamed, A., Hilal, A., Mohammad, M. and Alhaija, A., 2010. Nutrients in water and sediments of King Talal Dam-Jordan. *Jordan Journal of Biological Sciences*, 3(3), pp.87-100.

Hammad, B., Al–Abed, M., Al–Ghandoor, A., Al–Sardeah, A. and Al–Bashir, A., 2018. Modeling and analysis of dust and temperature effects on photovoltaic systems' performance and optimal cleaning frequency: Jordan case study. *Renewable and Sustainable Energy Reviews*, 82, pp. 2218–2234. https://doi.org/10.1016/j.rser.2017.08.070

Khatatbeh, M., Alzoubi, K., Khabour, O. and Al-Delaimy, W., 2020. Adverse health impacts of living near an oil refinery in Jordan. *Environmental Health Insights*, 14, p. 117863022098579. https://doi.org/10.1177/1178630220985794

Matouq, M., El-Hasan, T., Al-Bilbisi, H., Abdelhadi, M., Hindiyeh, M., Eslamian, S. and Duheisat, S., 2013a. The climate change implication on Jordan: A case study using GIS and Artificial Neural Networks for weather forecasting. *Journal of Taibah University for Science*, 7(1), pp. 44–55. https://doi.org/10.1016/j.jtusci.2013.04.001

Matouq, M., El-Hasan, T., Al-Bilbisi, H., Abdelhadi, M., Hindiyeh, M., Eslamian, S. and Duheisat, S., 2013b. The climate change implication on Jordan: A case study using GIS and Artificial Neural Networks for weather forecasting. *Journal of Taibah University for Science*, 7(1), pp. 44–55. https://doi.org/10.1016/j.jtusci.2013.04.001

Ministry of Environment Jordan, 2019. Ambient Air Quality Monitoring Report 2019. Amman, Jordan.

Muhaidat, R., Al-Qudah, K., Al-Taani, A.A. and AlJammal, S., 2019. Assessment of nitrate and nitrite levels in treated wastewater, soil, and vegetable crops at the upper reach of Zarqa River in Jordan. *Environmental monitoring and assessment*, 191, pp.1-11.

Odat, S., 2009. Diurnal and seasonal variation of air pollution. *Jordan Journal of Earth and Environmental Sciences*.

Rajagopalan, S., Brauer, M., Bhatnagar, A., Bhatt, D.L., Brook, J.R., Huang, W., Münzel, T., Newby, D., Siegel, J. and Brook, R.D., 2020. Personal-level protective actions against particulate matter air pollution exposure: a scientific statement from the American Heart Association. *Circulation*, 142(2). https://doi.org/10.1161/CIR.0000000000000931

Rozita, W.M.W., Zamtira, S., Mohd, F.I., Mohd, T.L., Nurul, I.A., Muhammad, I.M., Mohamad, A.R., Nor, I.A.H. and Shamila, M.H., 2021. Analysis of air quality in Malaysia during movement control order (MCO) Due to COVID-19 Pandemic. *Nature Environment and Pollution Technology*, 20(1), pp. 1–10. https://doi.org/10.46488/NEPT.2021.v20i01.001

Sa'adeh, H., Aburugia, S. and Chiari, M., 2019. An assessment of the impact of construction work on fine particulate matter in the University of Jordan: A PIXE study. *X-Ray Spectrometry*, 48, pp. 569–578. https://doi.org/10.1002/xrs.3105

Salameh, T., Sauvage, S., Afif, C., Borbon, A., Léonardis, T., Brioude, J., Waked, A. and Locoge, N., 2015. Exploring the seasonal NMHC distribution in an urban area of the Middle East during ECOCEM campaigns: very high loadings dominated by local emissions and dynamics. *Environmental Chemistry*, 12, p. 316. https://doi.org/10.1071/EN14154

Saleh, H.A.K., 1995. Magnitude of industrialization in Jordan. *GeoJournal*, 37, pp. 125–132. https://doi.org/10.1007/BF00814893

Shatnawi, N. and Abu-Qdais, H., 2021. Assessing and predicting air quality in northern Jordan during the lockdown due to the COVID-19 virus pandemic using artificial neural network. *Air Quality, Atmosphere & Health*, 14, pp. 643–652. https://doi.org/10.1007/s11869-020-00968-7

Shotar, A., Shatnawi, R., Halalsheh, M., Rub, H., Hussein, N., Shoter, S., Obeidat, M. and Asal, O., 2021. Epidemiological study of carbon monoxide deaths in North Jordan 2009-2018. *Materia Socio Medica*, 33, p. 184. https://doi.org/10.5455/msm.2021.33.184-187

Tabieh, M., Al-Karablieh, E., Salman, A., Al-Rimawi, A. and Al-Qudah, H., 2014. An assessment of climate change impacts on the socioeconomics of Zarqa River Basin. *Jokull Journal*.

US Department of Economic and Social Affairs, 2016. *International Trade Statistics Yearbook 2015: Trade by Country*. United Nations Publication.

World Health Organization (WHO), 2021. *WHO Global Air Quality Guidelines: Particulate Matter (PM2.5 and PM10), Ozone, Nitrogen Dioxide, Sulfur Dioxide and Carbon Monoxide*.

Zemouri, C., de Soet, H., Crielaard, W. and Laheij, A., 2017. A scoping review on bio-aerosols in healthcare and the dental environment. *PLoS One*, 12, e0178007. https://doi.org/10.1371/journal.pone.0178007

ORCID DETAILS OF THE AUTHORS

R.M. Kharabsheh: https://orcid.org/0000-0001-7151-4939
A.N. Bdour: https://orcid.org/0000-0001-6244-9530

Appraising the Degrees of Sprawl, Freedom and Goodness of Urban Growth Detection Using Geoinformatics Approach - A Study of Tumkur City in Karnataka State, India

A. Kishor Kumar, Govindaraju[iD]**, C. J. Rakesh and S. Lokanath**

Department of Applied Geology, Kuvempu University, Shankaraghatta-577451, Karnataka, India
†Corresponding author: Govindaraju; drgov@yahoo.com

ABSTRACT

The urban expansion analysis plays a significant role in the physical, social, and environmental dimensions of the cities. The research was conducted to monitor the urban growth and urban sprawl analysis of Tumkur city from 2000 to 2020 using multispectral satellite data (Landsat-5, Landsat-7, Resourcesat-1, Landsat-8, Sentinel-2A). Various methods like urban-related indices (AUER, UEII, and NDBI), and statistical methods (Degree of Freedom, Shannon Entropy, and Degree of Goodness) were used in the present research work. The AUER (Annual Urban Expansion Rate) and UEII (Urban Expansion Intensity Index) study of urban indices reveal that the urban area has expanded from 24.94 km^2 to 60.59 km^2 due to the development of commercial buildings, single-use zones, and low-density areas. The analysis of NDBI (Normalised Difference Built-up Index) indicates that the expansion of urban infrastructure, industrial growth, and population increase cause significant damage to vegetation in the city center compared to other areas. The study of the Degree of Freedom and Shannon entropy indicates that high compactness appeared in the core, whereas other regions are experiencing significant expansion. The method of freedom of goodness (2000 = - 0.093 to 2020 = - 0.159) demonstrates that the currently unfavorable conditions of urban growth have appeared in Tumkur city and it leads to numerous adverse effects on present and future generations. This study will help urban planners and decision-makers maintain the proper land use planning to reduce urban sprawl and its associated consequences, allowing for sustainable urban development.

INTRODUCTION

Urban areas constitute less than 1 percent of the Earth's surface area. However, they contribute to 90 percent of the global economy, with 50 percent of the world's population residing in cities. Additionally, cities consume 65 percent of the planet's resources and are responsible for 70 percent of the greenhouse gases emitted into the atmosphere (Martinuzzi et al. 2007, Almeida et al. 2005). By the World Urbanization Prospects-2018, 95% of the population will be settled in towns in developing countries in the coming years. Urbanization is a societal and spatial process that affects human societies in many ways. This process leads to changes in human practices that impact urban communities negatively. Urbanization and urban growth are two main urban development phases that must be clearly outlined (Bhatta et al. 2010, Dadras et al. 2015). Urbanization refers to the increasing proportion of a population residing in urban areas, while urban growth pertains to the actual increase in population within urban areas. Urban growth is

a key indicator of the development of urban areas and it is a comprehensive approach that involves various ideas.

Urban growth is influenced by a multitude of factors, including natural population growth, improvements in transportation and communication, the availability of facilities for education and recreation, urban planning policies, topographical factors, uneven spatial development, changes in living habits brought about by modernization and transformation, mining and investment, migration, commercialization, and industrialization, etc (Manna et al. 2024, Alam & Banerjee 2023).

The expansion of cities has many detrimental effects, such as the significant loss of biodiversity brought about by habitat destruction and fragmentation, pollution of air and water, soil contamination from waste disposal, heat island effect, improper waste management, higher rates of crime and violence due to socioeconomic inequities, and an increased risk of disease due to poor health practices and overpopulation (Nkeki 2016). Significant dangers from

man-made and natural catastrophes can arise from unplanned and mismanaged urban expansion in cities. When properly planned and managed, urban growth can reduce poverty and inequality by improving employment opportunities and quality of life, including through better education and health. But when poorly planned, urbanization can lead to so many consequences like traffic congestion, higher crime rates, pollution, increased levels of inequality, economic inequality, and social exclusion. Urban expansion influences the increased demand for land and changes in a region's land use and cover areas (Yakub & Tiffin 2017). Proper analysis of urban development is crucial to examine its past records, as well as natural, geographical, societal, and financial influences.

Urbanization in India

India's urbanization rate initially decreased but then grew gradually in the 1920s (Mohan & Dasgupta 2004, Dadras et al. 2015). After a few decades, urbanization has become more significant in India, which accounts for just 2.5 percent of the world's total land area yet produces about 16 percent of its people. (UNEP 2001). Compared to a gain of 2.1% between 1991 and 2001, it has climbed from 27.7% to 31.1% between 2001 and 2011, a growth of 3.3% (Bhagat 2011). According to this analysis, India's urban population is expected to almost triple, to 600 million people, by 2031 (Raftery 2012). The nation's fast urbanization has drastically changed the urban environment, changing land use and cover and placing a great deal of strain on the nation's natural resources. Given the extent of urbanization, it shows that one must study those topics to maintain unfavorable living circumstances and local environmental issues that would plague Indian towns (Mohan et al. 2011, Saxena et al. 1997).

Proper land-use planning and comprehending the dynamics of growth and the effects of driving variables to manage urban development effectively is essential. Urban growth monitoring involves remotely observing an object or phenomenon at different times to study changes resulting from human modification of the environment (Hegazy & Kaloop 2015, Li et al. 2018). The urban growth analysis is helpful for local planning authorities to manage growth and development under the region's environmental or ecological carrying capacity and maintain sustainable urban development in cities (Das & Das 2019, Haregeweyn et al. 2012).

There are already many methods like the Geospatial method, Machine Learning Method, Statistical methods, Land use Prediction Models, and other different models used to monitor the urban land transition, urban studies, and urban growth in different study areas (Ramachandra et al. 2013, Mishra & Rai 2016, Rahman et al. 2017, Chen et al. 2020).

Present Study

The present study employed geospatial methods and statistical models to examine the urban area expansion of the study region over two decades. The use of GIS and RS methodologies has enabled the creation of various statistical scales and parameters to quantify urban sprawl and monitor urban growth (Bhatta et al. 2010). These technologies provide cost-effective and efficient ways to study the physical expressions and patterns of urban sprawl (Barnes et al. 2001). In recent years, remote sensing data and geographical information systems (GIS) techniques have been increasingly used to understand urban patterns and processes and simulate urban growth, urban land transition, and urban sprawl development (Patra et al. 2018, Wang & Munkhnasan et al. 2021, Fertner 2018, Ngolo et al. 2023, Mohan et al. 2020). Remote sensing provides reliable scientific tools for calculating the built-up area, using intertemporal satellite images, and studying the multispectral space. The GIS may use multi-agent data evaluation methods to analyze the data gathered by remote sensing with the embedded decision-making support features (Basu et al. 2023, Mohan et al. 2020, Mohan & Kandya 2015, Verma & Garg 2022). Various methods, including unsupervised and supervised classification (Kim 2016, Mohan & Kandya 2015, Ji et al. 2006), hybrid methods (Mas et al. 2017), and object-based detection methods were utilized to quantify, assess, mapping, and monitor urban growth in cities. Scholars have utilized a few important indices to monitor and analyze urban expansion in a given area. These indices include the Annual Urban Expansion Rate Index (AUERI), which measures the rate of urban expansion, and the Urban Expansion Intensity Index (UEII), which assesses the intensity of urban areas. Additionally, they use the Normalised Difference Built-up Index to analyze the built-up area. The scholar used statistical analysis like the person" 's Chi-square and 'Shannon's entropy' to analyze the disparity of urban growth in the study area (Dewa et al. 2022). The new "degree-of-goodness" method is applied to statistically monitor urban growth in the present study (Akshaya 2021).

Tumkur City, also known as Tumakuru City, is a growing urban entity in Karnataka, undergoing substantial expansion and development. The city has witnessed significant developments in many areas, including the economy, governance, culture, and education. Opportunities for infrastructure development, employment creation, and bettering the standard of living for locals are presented by this urbanization process. Tumkur city, on the other hand, has undergone a considerable rural-to-urban shift during the last few decades. Apart from that, most of Karnataka's studies on urban expansion have concentrated on the Bangalore

metropolitan region rather than on Tumkur City which is very close to Bangalore (Ramachandra et al. 2019, Govind & Ramesh 2019, Raj et al. 2021, Shukla 2020, Kannan et al. 2021, Kanga 2022). Urban surface water quality, urban groundwater quality, sewage waste management, and urban solid waste management are the few research works conducted in the study area (Bhaskar & Nagendrappa 2008, Kumara & Belagali 2010, Manjunath et al. 2020). Furthermore, as far as we know, studies have yet to use the most recent spatial data and statistical methods to investigate the spatiotemporal assessment, urban land transition, urban sprawl, and urban growth monitoring in Tumkur City. From this point of view, this study attempts to close this gap by employing geographic and statistical methods to monitor the expansion of the study region. The study's objectives are (1) The examination of urban sprawl by using the Shannon entropy technique and the chi-square test. (2) to assess and analyze the behavior of urban expansion in the research region using a new methodology called "Degree of Goodness." Using these scientific findings, planners, decision-makers, and urban designers in the study area will contend that implementing ecological sustainability plans and employing sustainable urban development strategies will enhance the quality of life for present and future generations residing in cities.

STUDY AREA

Tumkur City is located southeast of Bangalore (Fig. 1). It is located between the latitudes 13°19'00" and 13°21'19" and longitudes 77°05'26" and 77°07'12". Tumkur city is located at an altitude of 835 m (2739.5 ft) above the mean sea level. The major city of Tumkur Distinct is the eleventh populated city in Karnataka. It is one of the seven smart cities in Karnataka, selected by the Indian government as part of the Smart City Mission. In 1961, the area of Tumkur city was 12.95 km^2; in 2011, it was increased to 64.27 km^2. According to the master plan map for 2021, it was 331.6 km^2. Tumkur is an ideal location for setting up industries along National highways (NH 48 and NH 73). It contains many industrial areas and industrial estates. According to the United Nations Population Projections and Census of India 2011 report the population of Tumkur city was 302000 in 2011, and, it is expected to rise to 506000 in 2030. According to Karnataka Municipal Reforms, cell reports declared that 37 slum areas are present in Tumkur City. Monitoring urban growth is crucial for local planning authorities to manage urban growth and development within the region's ecological or environmental carrying capacity since the growing population and the expansion of urban areas have led to several difficulties. For the benefit
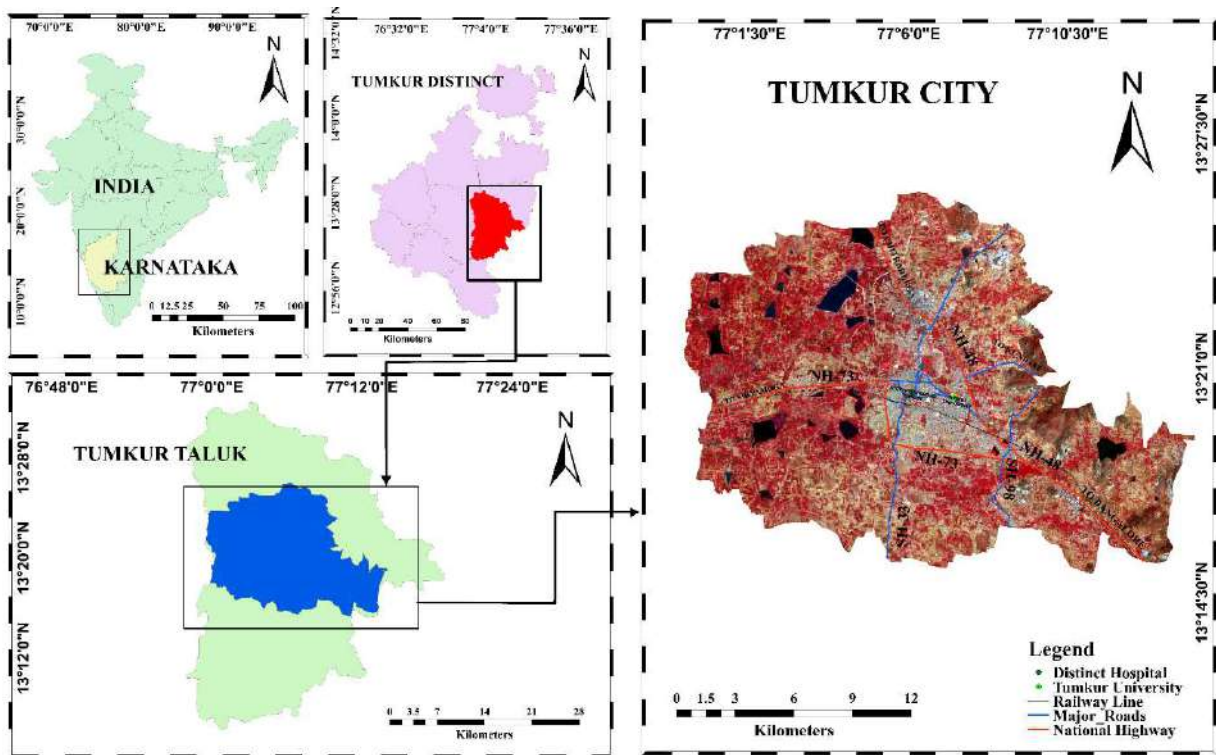

Fig. 1: Location map of study area.

of sustainability, urban authorities need to understand the nature of the urban growth in Tumkur city. With the rapid urbanization process, the demand for urban land is growing continuously, and urban growth has put tremendous pressure on protecting regional ecological environments and conserving incredible ruins.

DATA SOURCES AND METHODOLOGY

Materials

A LULC map and Urban growth change analysis were carried out using Landsat, LISS III, and Sentinel satellite images. LULC maps have been verified by Google Earth Pro samples as well as ground truth surveys. (Table 1) The city's population statistics from the United Nations Population Projections and the Census of India.

Modeling Framework

Image pre-processing and urban growth analysis: For meaningful and reliable results to be obtained, pre-processing of satellite images is crucial. To get appropriate outcomes initially, detecting atmospheric noise, such as haze formed by water vapor, smog, and atmospheric elements, is very necessary. It offers a variety of methods for analyzing the standard results of images to determine the accuracy of surface features.

A maximum likelihood classifier was used to create land use and land cover maps of the study area using satellite images 2000 (Landsat 5), 2005, 2009, 2012, (Resourcesat-1), 2015, 2020 (Sentinel-2A). Eleven land use and land cover categories have been chosen for LULC classification. These are Built-up areas, Fallow land, Double Crop, Scrub Land, Water Bodies, Scrub Land, Stoney Waste, Plantation, Kharif Crop, Scrub Forest, and Forest Plantation.

For the analysis, the zone-wise extracted built-up areas were used for monitoring the urban growth of the study area. The total area is partitioned into 8 equal sectors forming 8 different directions (North North West (NNW), North North East (NNE), West North West (WNW), East North East (ENE), West South West (WSW), South South West (SSW), East South East (ESE), South South East (SSE). This has been divided into multiple zones to extract the built-up area in different directions so that they can statistically be compared. It is worth mentioning that the radius of the circle should be large enough so that it includes the entire urban extent or the metropolitan area within it. Urban extent is a dynamic phenomenon; it changes over time, however, it is largest in the latest temporal instant. Therefore, the circle should be drawn in consideration of the latest image of the study. This has resulted in a matrix (Table 2) that shows built-up areas for each zone and each temporal instant. Fig. 2 briefly the flowchart of the entire methodology. The drawn circles are concentric and include the entire scope of the study from the center of the city. Hence, the circles have been drawn in a way that they include the regions constructed based on a radius of 500 m from each other and in different geographic directions. This division has been made such that the process of changes in construction in different parts and directions could be statistically compared. Essentially, the structure of urban boundaries is a dynamic process and greatly changes in different directions with time.

NDBI Index: The NDBI Index, assesses the expansion of urban areas, particularly ones built up or with artificial structures. NDBI is a built-up index image proposal by Zha (2003) using Landsat Thematic Mapper (TM) images

Table 1: Lists of satellite images used in LULC and NDBI investigations.

Data type and materials	Data source	(Row/Path)	Purposes
Topographical sheet	Naivik (Survey of India)	-	LULC
Landsat 5 (16/03/2000)	USGS Earth Explorer	(Row/Path Number = 144/51)	LULC
LISS III (06/08/2005)	Bhuvan (ISRO)	(Row/Path Number = 93/56)	
LISS III (31/03/2009)			
LISS III (08/02/2012)			
Sentinel (22/10/2015)	USGS Earth Explorer	-	
Sentinel (13/02/2020)		-	
Landsat 5 (18/02/2005)		(Row/Path Number = 144/51)	NDBI
Landsat 5 (18/04/2009)			
Landsat 5 (17/04/2012)			
City and Ward Boundary	Tumkur Urban Development Authority	-	LULC
The ground survey field attributes /Training data	Field measurement and observation	-	LULC

(Bramhe et al. 2018). NDBI maps are primarily based on two bands: Short Wave Infrared and Infrared Bands (Zheng et al. 2021, Vadakkuveettil & Grover 2023) Additionally, it ranges from -1 to +1, just like NDVI and other indices. The following formula was used to determine NDBI:

$$NDBI = \frac{Shortwave\ Infrared\ wavelength - Near\ infrared\ Wavelength}{Shortwave\ Infrared\ wavelength + Near\ infrared\ Wavelength}$$

...(1)

Measuring Urban Area Expansion Intensity Index: The Urban Expansion Intensity Index, (UEII), could be a valuable tool for quantitatively assessing the urban spatial expansion difference (Yan et al. 2019). It calculates the level of urbanization and the rate at which town landscapes are expanding or contracting (Zhong et al. 2020). It is an indicator that takes into account both the length of expansion (Dong et al. 2007, Qiao et al. 2014, Al-Sherif et al. 2014, Yan et al. 2019, Xian et al. 2019) and the proportional growth in the size of urban areas is used. To calculate the UAEII, the following equation has been used :

$$UAEII = \frac{UA^{t2}_b - UA^{t1}_b}{TA_b * \Delta t} * 100$$

...(2)

Where, UA = Urban area; b = spatial unit; t1 = base year; t2 = ending year; Δt = t2 - t1, the difference of urban land at the base year and ending year of spatial unit i; TA = Total landscapes of the study region.

There are five categories in the UEII standard: slow-speed development (0 to 0.28), low-speed development (0.28 to 0.59), medium-speed development (0.59 to 1.05), high-speed development (1.05 to 1.92), and extremely high-speed development >1.92. (Zhong et al. 2020).

Annual Urban Expansion Rate (AUERI): The AUER calculates the mean annual expansion rate of built-up land expansion for the entire study area between the base year and the final year. The index yields an estimate depicting the quantum rate at which built-up land of a given region is changing (Alam et al. 2023, Acheampong et al. 2017).

The annual Urban Expansion Rate was calculated by using the formula.

$$A = \left[(ULAt^{t2} | ULAt^{t1})^{\frac{1}{t2-t1}} - 1 \right] * 100$$

...(3)

Where, UA = Urban area; b = spatial unit; t1 = base year; t2 = ending year; Δt = t2 - t1, the difference of urban land at the base year and ending year of spatial unit i; TA = Total landscapes of the study region.

Urban Sprawl Analysis Using Entropy Model

Shannon's Entropy: The Shannon Entropy Index (H)

analyzed the urban spatial dispersion pattern (Dewa et al. 2022). The information theory, developed by Shannon (1948), gives entropy a statistical character. Richness and evenness, the two primary components of the Shannon Entropy Index, are used to calculate the degree of spatial concentration of built-up area. While evenness refers to the proportion of each object in a class, richness encompasses the number of classes or objects analyzed (Masisi et al. 2008, Al Sharif et al. 2014, Dewa et al. 2022).

Shannon's entropy is given by

$$Hn = \sum_{i=1}^{n} piloge(pi)$$

...(4)

Where Pi is the portion of the variable in the ith zone (in this example, the proportion of built-up area or urban patches in each zone. Greater entropy values show an uninterrupted dispersion of built land, which reflects urban sprawl, whereas lower entropy values show cluttering or less fragmentation of developed areas, which suggests a reduced chance of sprawl. (Antipova et al. 2022).

Pearson's Chi-square Test: Pearson's chi-square statistics considers the checking of freedom amongst pairs of variables chosen to explain the same category of land-cover change. Therefore, the chi-square test was performed with Pearson's chi-square expression: (observed _ expected)^2 /expected to determine the degree of freedom. It reveals the freedom or degree of deviation for the observed urban growth over the expected (Mohamed & Worku 2019, Al-Sherif 2014).

$$x_i^2 = \sum_{j=1}^{m} \frac{(M_J - M_J^E)^2}{M_J^E}$$

...(5)

Where, xi^2 is degree of freedom, Mj is observed built-up area in j-th column for a specific row, Mj^E is expected built-up area in j-th column for a specific row. The expected built-up growth for each variable was calculated by the products of marginal totals, divided by the grand total. Therefore, the expected growth MEij for the i-th row and j-th column is

$$M_{IJ}^E = \frac{M_I^S \times M_J^S}{M_g}$$

...(6)

Where,

MiS = Row Total

MJS = Column Total

Mg = Grand Total

Degree-of-Goodness: Since the chi-square (degree of freedom) and entropy (degree of sprawl) are different measures, one may sometimes contradict the other. Due to that, the 'degree of goodness' method necessitates urban growth analysis (Bhatta et al. 2010, Dadras et al. 2015). The

degree of goodness is a direct measurement method. For this measurement, positive values are indicative of goodness, while negative ones are indicative of badness (Bhatta et al. 2010, Dadras et al. 2015).

$$G_i = log_e \left[\frac{1}{x_i{}^2 \left(\frac{H_i}{log_e(m)} \right)} \right] \qquad ...(7)$$

RESULTS AND DISCUSSION

The accuracy assessment result shows that the overall accuracy values are 87%, 88%, 86%, 92%, and 94% in the years 2000, 2005, 2009, 2012, 2015, and 2020 respectively,

and also corresponding kappa co-efficient in corresponding years are 0.80, 0.82, 0.84, 0.91, 0.92 and 0.94 respectively.

Urban Extent

To extract the built-up and non-built-up areas in a particular period after creating land use and land cover maps using temporal satellite images. Examining these classified images, even cursorily, one can see that the expansion of the city in the specified zones of the study area, some zones are very compact while in others more open space between built-up areas. In 2000, the built-up area was very low, but in 2020, the built-up area expanded compared to 2000 (Fig.
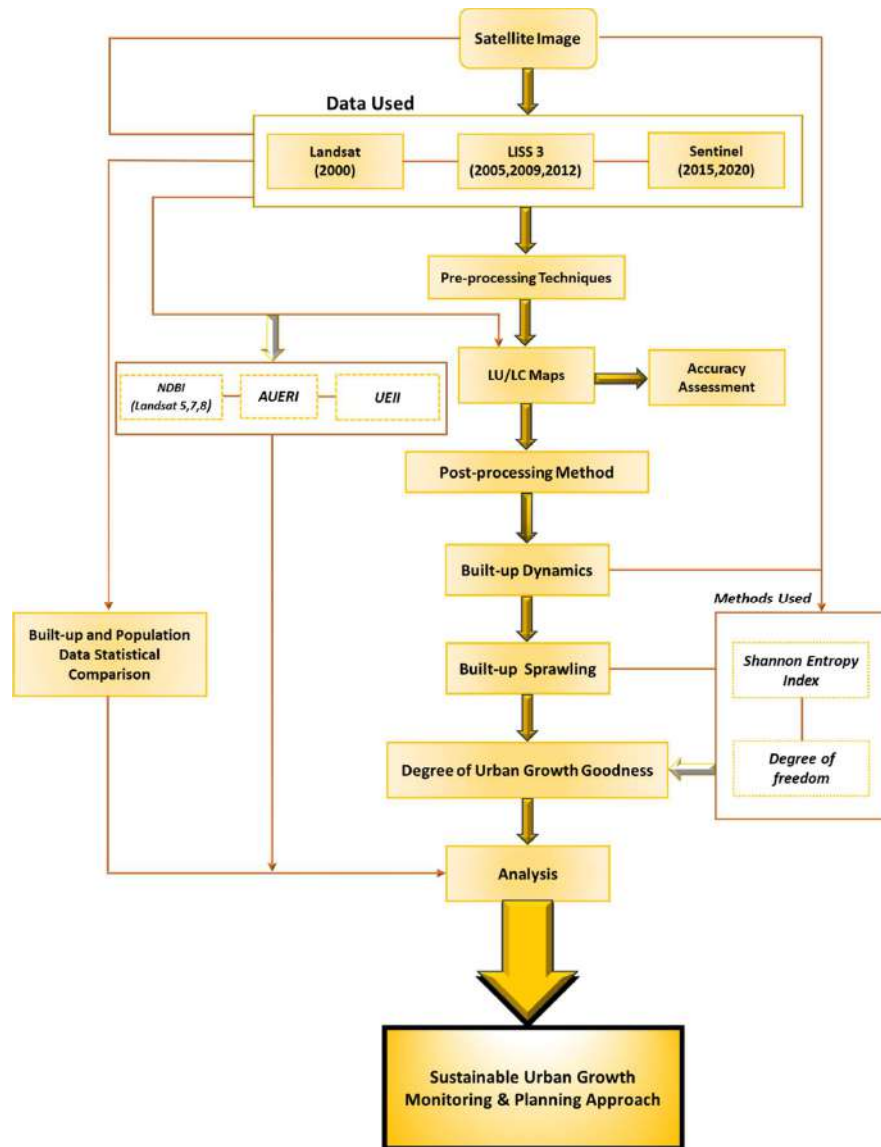
Fig. 2: Methodological flowchart used for the present study.
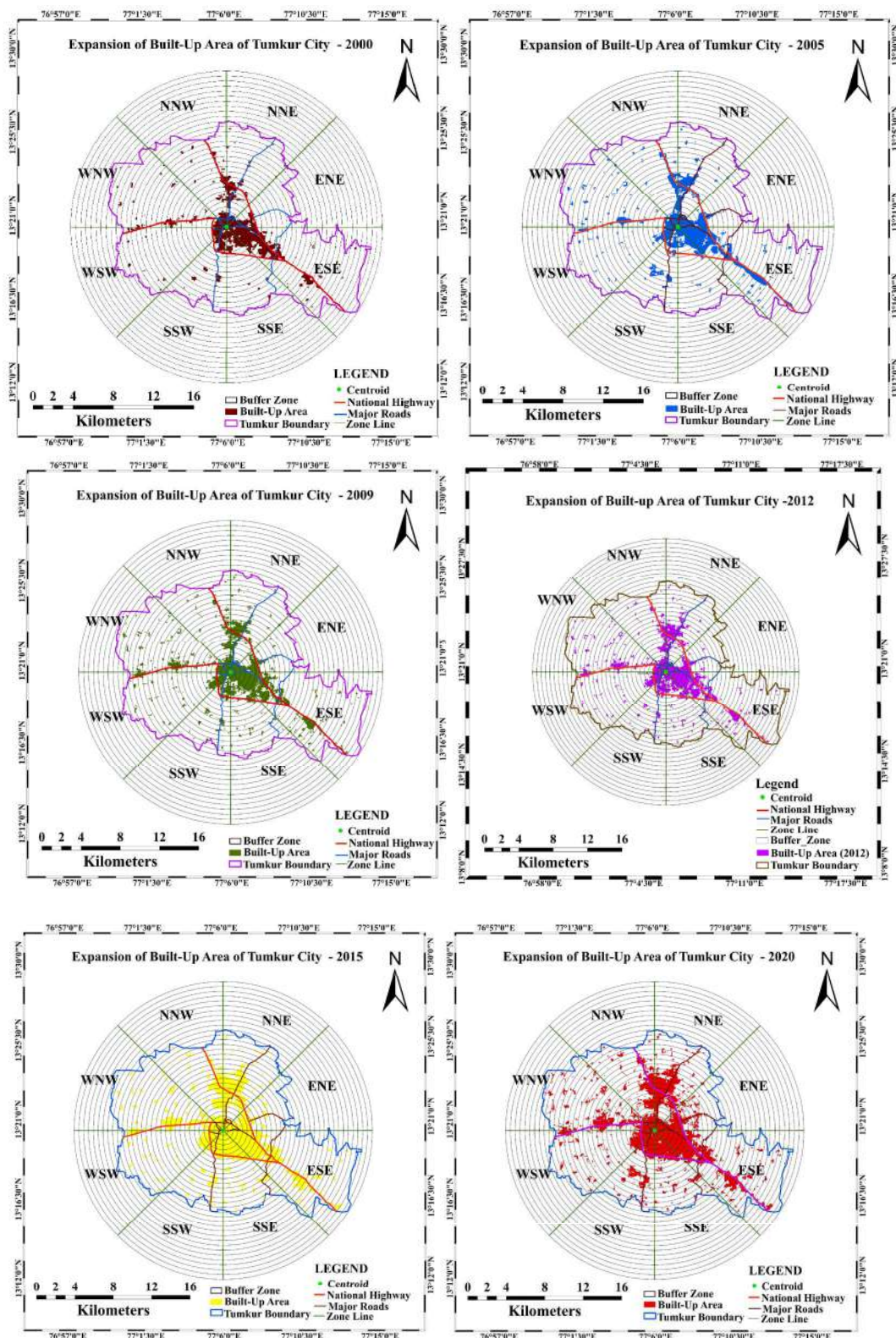
Fig. 3: Urban Sprawl Map of Tumkur City in 2000, 2005, 2009, 2012, 2015 and 2020.

Table 2: The Built-up areas of different zones in Tumkur City from 2000 to 2020.

Zones	Total Area (Sq. km)	2000	2005	2009	2012	2015	2020
NNW	38.08	2.505	3.626	3.56	3.89	6.08	7.158
NNE	37.77	3.195	5.034	5.18	6.31	9.20	10.44
WNW	54	2.352	3.29	4.39	4.74	6.70	8.654
ENE	21.74	1.972	2.75	3.03	3.10	4.208	5.328
WSW	44.46	1.338	2.460	3.12	3.26	4.412	5.56
SSW	25.92	2.35	3.113	2.98	3.05	4.433	5.13
ESE	68.82	9.19	10.66	12.04	11.95	15.125	16.53
SSE	29.95	2.08	2.36	3.32	3.45	5.848	6.019

Table 3: Annual Urban Expansion Rate values from 2000 to 2020.

Zones	2000 - 2005	2005 - 2009	2009 - 2012	2012 - 2015	2015 -2020
NNW	7.66	0.49	1.30	15.80	3.29
NNE	9.66	0.81	6.59	13.25	2.56
WNW	6.96	7.47	2.56	10.74	5.24
ENE	6.51	2.87	0.75	9.60	4.83
WSW	12.95	6.12	1.32	9.50	4.73
SSW	5.78	0.69	0.46	8.98	2.98
ESE	3.01	3.09	1.13	5.88	1.79
SSE	2.55	8.90	1.15	17.15	0.56
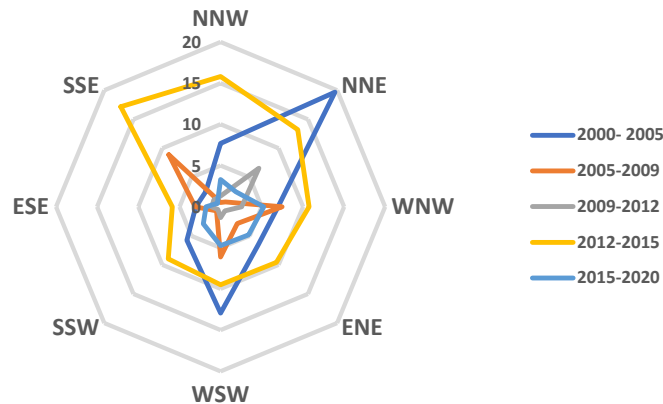
Fig. 4: Radar chart of Annual Urban Expansion Rate (AUER) of different zones.

3). The built-up areas of different zones are mentioned in Table 2.

Annual Urban Expansion Rate (AUER)

The urban expansion rate of zones from 2000 to 2005 could be faster compared to the AUER value of 2005 to 2009. Due to population growth, development of industries, and other reasons, the zone's speed of urban area expansion is high, and few areas of the zone are very low due to improper infrastructure facilities, etc. However, in the case of the 2009 to 2015 period, the AUER rate is very high. This is an indication of the development of built-up areas. According to the AUER, the scores are given in Table 3.

Zone-wise Annual Urban Expansion Rate (AUER) result for the region is presented in Fig. 4. This is designed to indicate the directional distribution of sprawl among the 8 quadrats. From 2000 to 2020 the AUER values were very high in zones like NNE, ENE, ESE, and WNW compared to other zones which indicated the growth of built-up in the form of commercial buildings, residential areas, infrastructure facilities, etc. in the area. From 2000 to 2020, in a few zones like NNW, WNW, WSW, and SSW,

Table 4: Urban Expansion Intensity Index of all zones (2000 to 2020).

Zones	Year				
	2000-2005	2005-2009	2009-2012	2012-2015	2015-2020
NNW	0.588	0.11	0.0875	1.90	0.56
NNE	0.97	0.1098	0.9796	2.55	0.68
WNW	0.348	0.5492	0.2160	1.20	0.723
ENE	0.676	0.373	0.107	1.69	1.030
WSW	0.5147	0.3712	0.1049	0.863	0.5164
SSW	0.585	0.108	0.064	1.71	0.54
ESE	0.4272	0.50130	0.2131	1.70	0.4097
SSE	0.1869	0.80	0.14468	2.60	0.4178
Total	0.5367	0.3653	0.2395	1.77	0.912

the settlement area increased due to population growth, the development of infrastructure facilities, and the growth of the transport network. After 2009, the rise of real estate, high industrial development, better resource availability, and the

development of the transport system led to an increase in the development of settlements.

From 2000 to 2005, a few small-scale industries improved in a few villages like Nandhihalli, Chikkahalli, Chokkenahalli, Manchakalkuppe villages, and a few wards in Tumkur city limits. The development of settlements in the urban core region especially wards like Someshwarapura, Batawadi, M.G Road, Sapthgiri Extension, Ashokanagar, Upparhalli, Shanthinagara, Gandhi Nagara, Banashankari, Sadhashivanagara, Hegade Colony, K.H.B. Colony, Chikkepete, Sriranganagar, Kuvempunagara, Vinayakanagara, Vidyanagara is very high compared to periphery region of study area. The improvement of national highways and major roads in the study area led to the development of a few layouts in Shettyhalli, Kaytasandra, Badihallli, Sanapalya, Hirehalli, Kotkahalli, Habbathanahalli, Heggere, Hirehalli, Manchakalukuppe villages (Figs. 7, 8 and 9).
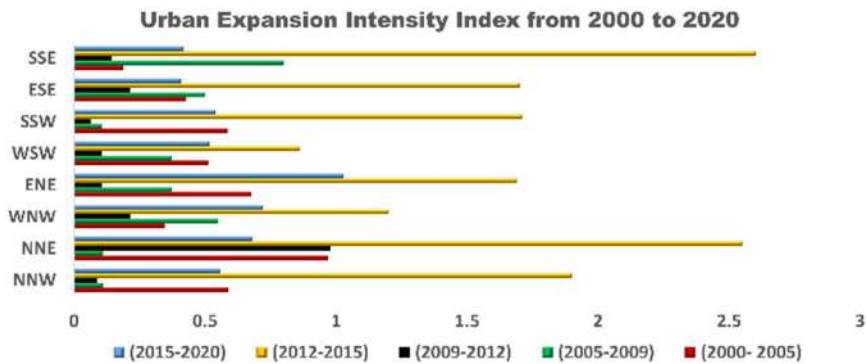
Fig. 5: Bar chart of UEII from 2000 to 2020.

Table 5: Observed growth in built-up area (in km^2).

Year	NNW	NNE	WNW	ENE	WSW	SSW	ESE	SSE	TOTAL
(2000-2005)	1.121	1.839	0.938	0.778	1.121	0.763	1.47	0.28	8.311
(2005-2009)	0.066	0.146	1.1	0.28	0.66	0.133	1.38	0.96	4.825
(2009-2012)	0.33	1.13	0.35	0.07	0.14	0.072	0.09	0.13	2.31
(2012-2015)	2.19	2.89	1.96	1.108	1.152	1.383	3.175	2.390	16.248
(2015-2020)	1.078	2.042	1.954	1.12	1.48	0.697	1.405	0.172	9.615
Total	4.785	8.047	6.332	3.356	4.222	2.78	7.52	3.93	41.209

Table 6: Expected growth in built-up area (in km^2).

Year	NNW	NNE	WNW	ENE	WSW	SSW	ESE	SSE
(2000-2005)	0.9650	0.9420	1.277	0.6768	0.8514	0.5606	1.5165	0.7925
(2005-2009)	2.6800	0.9421	0.7413	0.3929	0.4943	0.3254	1.5166	0.4601
(2009-2012)	0.2682	0.4510	0.3549	0.1881	0.2366	0.1558	0.4215	0.2202
(2012-2015)	1.886	3.1729	2.4965	0.6768	0.8514	1.0961	2.9650	1.5495
(2015-2020)	1.116	1.877	1.4774	0.7830	0.9850	0.6486	1.7545	0.9169

Table 7: Degree of freedom for urban growth in each zone.

Year	NNW	NNE	WNW	ENE	WSW	SSW	ESE	SSE
(2000-2005)	0.0248	0.028	0.089	0.015	0.085	0.073	0.00139	0.330
(2005-2009)	0.4359	0.672	0.172	0.032	0.054	0.113	0.283	0.074
(2009-2012)	0.0141	0.037	0.000045	0.074	0.143	0.031	0.260	0.036
(2012-2015)	0.3460	0.402	0.117	0.031	0.020	0.145	0.014	0.455
(2015-2020)	0.0013	0.014	0.154	0.144	0.248	0.0036	0.069	0.605

From 2005 to 2009, the settlements expanded in rural areas like Kanehalli, Kotkahalli, Palasadra, J.I Thimmlapura, Kupparu, Chokkenahalli, Hirehalli, Pandithanahalli, Kundhuru in the area. The agricultural land has been converted into single-zone development of built-up areas in the form of residential, commercial, and educational institutions developed in Kunkamanahalli, Maranaipalya, Ballapura, Banavara, Gondapura, Hodhekallu, Byatha, Shinganahalli, Muthsandra, Vaddarahalli, etc. The new layouts were developed in industrial and surrounding areas like Maranaikanapaliya Rangapura, Birennakallu, Seegepalya, and Annenahalli villages.

From 2009 to 2012, the growth of large industries led to the conversion of agricultural land and scrubland into commercial and layouts for residential purposes. From 2012 to 2015 period, the central government's Smart City Mission implemented in Tumkur City influenced the development of infrastructure facilities like the improvement of the bypass, development of new schools and colleges, and construction of the corridor. During this period the large conversion of agricultural land in Hosahalli, Haronahalli, and Kuppur areas, and scrubland transformed into settlements in the form of layouts, in the Peripery of Haronahalli, Goolaharuve, Maraluru Amanikere, Kallahalli areas.

From 2015 to 2020 the central government implemented the Bharat Mala Project (development of NH4 and NH 73 highways), the Smart City Mission project, and many other projects that led to the development of more settlements in the form of residential infrastructure, and roads for connecting newly developed built-up areas in core and periphery regions, and the large compactness that appeared in core areas indication of urban agglomeration. During this period residential, educational, and commercial

Table 8: Degree-of-freedom for urban growth in each temporal span.

Year	Degree of Freedom
(2000-2005)	0.64969
(2005-2009)	1.43602
(2009-2012)	0.5976
(2012-2015)	1.5343
(2015-2020)	1.2420

areas in highways and major roads connected areas like Kannenahalli, Bugadanahalli, Agalakunte, Asalipura, Ballapura, Banavara, Gowdihalli, Keggere, Doddasarangi, Kotkahalli, Mudigere, Palasandra, Hethenahalli, Gangasadra, Hosahalli, Adhalapura, Halanuru areas are developed.

Analysis of Urban Expansion Intensity Index

Between 2000 and 2020, an urban expansion intensity index of 0.11 at the lowest point and 2.60 at the highest point is considered a high urban expansion rate. UEII describes the nature of the urban expansion of Tumkur City; the zone-wise statistics are presented in Table 4. Between 2000 and 2005, the overall study area had an expansion intensity index of 0.53, considered moderate for urban expansion. During the initial stage of the growth of industries, the government's small infrastructure projects, improper transport facilities, and other different causes are the main reasons for the slow expansion of urban growth.

From 2005 to 2009, urban land in Tumkur City began dispersing to the east, north, west, and south-southwest, but in 2012-2020, urban land began to disperse almost in all directions. (i.e., South South East, West South West).

Furthermore, between 2009 and 2012, the UEII increased dramatically from 0.23 to 1.77 from 2012-2015; this rapid increase in UEII indicates an increased likelihood of urban sprawl occurring as a result of various infrastructure projects initiated by the government, an increase in industries, and increase in population. Fig. 5 notices that the UEII values in different zones have increased in different directions from 2000 to 2020. It is evident from the significant increase in UEII that urban sprawl is becoming more prevalent. It suggests that there was noticeable urban sprawl during this period, indicating the expansion of urban areas into previously undeveloped or rural areas. The large agricultural land, scrubland, and Plantations were converted into urban settlements.

Pearson's Chi-Square Statistics and Urban Growth

To determine the 'degree of freedom', a Chi-square test was performed with Pearson's chi-square expression: (observed_expected)^2/expected. It reveals the freedom or

Table 9: Shannon's entropy index of Tumkur City (zone-wise).

Year	Built-up Area (sq. km^2)	Entropy Value	Log (n)
2000	24.94	0.999	0.9030
2005	32.10	0.998	0.9030
2009	36.47	0.980	0.9030
2012	39.08	0.997	0.9030
2015	55.85	1.010	0.9030
2020	60.59	0.990	0.9030

degree of deviation for the observed urban growth over the expected. The observed urban growth and expected urban growth are presented in Table 5 and Table 6.

Overall freedom indicates a lack of equal weightage and lack of consistency in planning with the entire city. The higher degree of freedom for a zone is an indication of unstable development within the zone with the change of time.

The degree of freedom in each zone varies from one zone to another. The highest degree of freedom value is 0.672, recorded in the NNE zone, and the lowest is 0.000045, recorded in WNW. Table 7 shows that the freedom is high

for NNW, NNE, ESE, and SSE. It indicates that those zones have harmful urban growth due to a lack of consistency in urban planning in the city. The very low degree of freedom of zones ENE, WSW, SSW, and WNW have low urban growth in the city. However; it is worth mentioning that a higher degree of freedom is not only considered as sprawl, instead it should be regarded as the disparity in growth as a process and/or pattern.

On the other hand, poor urban planning can bring opposite harmful effects like heavy traffic congestion, insufficient infrastructure, improper waste management, sanitation, and other issues in the city. The higher degree of freedom in different periods refers to the need for consistency in planning, managing, and controlling urban growth (Table 8). From 2012 to 2015 high degree of freedom indicated highly tremendous urban growth due to sizeable agricultural land transformed into built-up areas, both sides of highways and minor roads, etc.

Quantification of Urban Sprawl Using Shannon's Entropy

The Radar chart shows that between 2000 and 2020, the
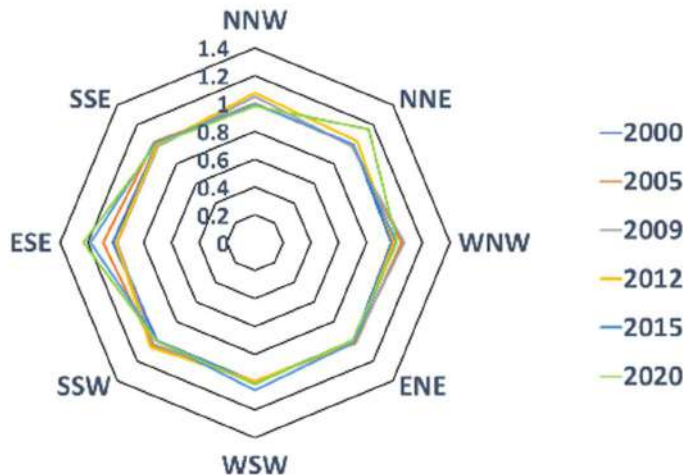
Fig. 6: Radar chart characterizing zone-wise urban sprawl pattern by temporal period.

Table 10: Shannon Entropy values of different zones from 2000 to 2020.

Year	Zones							
	NNW	NNE	WNW	ENE	WSW	SSW	ESE	SSE
2000	0.999	0.998	0.98	0.991	0.990	0.99	1.02	0.99
2005	1	0.99	1.05	0.995	0.998	1.04	1.09	1.02
2009	1.05	0.98	1.07	0.996	0.987	1.03	0.99	0.98
2012	1.075	1.035	0.991	0.997	0.995	1.05	0.99	0.99
2015	0.99	0.99	1.01	0.99	0.99	1.09	1.18	1.01
2020	0.98	1.15	1.02	0.99	0.99	1	1.23	1

Table 11: Shannon Entropy in different periods.

Years	Shannon Entropy
(2000-2005)	1.1208
(2005-2009)	1.01
(2009-2012)	1.09
(2012-2015)	1.20
(2015-2020)	1.05

amount of entropy has increased irregularly. The entropy values obtained are 0.999 in 2000, 0.998 in 2005, 0.980 in 2009, 0.997 in 2012, 1.010 in 2015 and 0.990 in 2020. Shannon's entropy for the year 2000 is 0.999, and the log n value of this is 0.9030, which means that the development of urban built-up is more towards the dispersion (Table 9). Nevertheless, it was pretty high after 2015, and the entropy value is 1.010, and the log n value is 0.9030. New residential

(Source: Google Earth Map)

Fig. 7: Urban area development on both the sides of National Highway and agricultural land into Built-up land in the Heggere area.

(Source Google Earth Map).

Fig. 8: Low-density development, Single-used developments, Commercial development in Tumkur city.

(Source: Google Earth Map)

Fig. 9: The Growth of built-up areas in Satyamangala Industrial areas.

Table 12: Degree of goodness for urban growth.

Year	Zones							
	NNW	NNE	WNW	ENE	WSW	SSW	ESE	SSE
(2000-2005)	-1.56	-1.51	1.010	-1.78	1.030	-1.079	-2.79	0.426
(2005-2009)	0.316	-0.123	0.690	1.02	1.201	-0.881	-0.497	-1.071
(2009-2012)	-1.765	-1.366	1.16	-1.090	0.762	1.19	-0.487	1.08
(2012-2015)	0.344	-0.33	0.85	1.07	1.65	-0.777	-1.77	-0.275
(2015-2020)	1.10	-1.79	0.772	-0.797	0.564	2.36	-1.097	0.78

Table 13: The Overall Degree of Goodness for Urban Growth.

Years	Degree of Goodness	Behavior
(2000-2005)	- 0.093	Badness
(2005-2009)	-0.205	Badness
(2009-2012)	-0.1418	Badness
(2012-2015)	-0.079	Badness
(2015-2020)	-0.159	Badness

Table 14: Correlation of area statistics of Built-up land.

Year	Supervised	NDBI
2000	24.94	25.77
2005	32.10	33.51
2009	36.47	37.58
2012	39.08	40.78
2015	55.85	56.67
2020	60.59	61.53

areas, a few infrastructures implemented by smart city missions, and the development of new industries added during this period are the main reasons for the increase in dispersion between 2009 and 2020. Shannon's entropy values are calculated year-wise (Table 10), and each zone for all two decades is presented in Table 11.

Interestingly, the entropy values of all eight zones are close to log (n) values, indicating a high degree of dispersion. The index value increased gradually and reached 1.180 log (n) in 2014 indicating an increase in sprawl. KIADB has developed industrial estates at Sathyamanagar, Lingapura, and Antharasanahally along NH 4 in the northern part of the city and also in Hirehalli towards Bangalore. According to TUDA Report from 2000 to 2020, TUDA Developed 80 Layouts in North North East zones. ENE zone records the least sprawl extent and intensity when compared with other zones due to the presence of hill and quarrying activities. The urban edge sprawl has spread further away from the urban cluster, although at a maximal rate, along such an axis. On the other hand, the SSE zone is undergoing maximum contemporary urban growth and haphazard sprawl patterns influenced by industry. The core areas of all zones were more compact compared peripheral region. This shows severe development of built-up areas appeared in the study area.

The entropy value was 0.9923 in 2000 which is a gradual increase throughout and reached an index value of 1.02. This is due to the impact of increasing residential areas and newly established developmental activities conducted by the smart city mission. From the year 2000 to 2020, the WSW zone has remained consistent over the temporal period, with minimal fluctuations. WSW zone records the least sprawl extent and intensity compared to other zones. The NNW zone faces

maximum expansion of built-up areas and haphazard sprawl patterns greatly influenced by industries (Fig. 6).

The development of industries leads to, the conversion of agricultural land into urban use (Fig. 7). The low-density development took place in small mining areas in villages like Maidala, Ajjappanahalli, Thippanahalli, Machanahalli, Hosahalli, Amalapura, Devaraypattna, H Byarsandra (Fig. 8 & 9).

Combination of Chi-square Test and Shannon Entropy Models

The Chi-square model for calculating the degree of freedom and the Shannon entropy model for computing the degree of sprawl have different measurements, which may contradict each other in some cases (as evident in the current study). Thus, it is also vital to determine the degree of goodness for urban growth. The degree of goodness is a direct measurement method. For this measurement, positive values are indicative of goodness, while negative ones are indicative of badness (Tables 12 and 13).

The development of industries and the growth of Population have created so many problems like no proper road facilities, lack of sewage, improper drainage facilities, unhygienic and sub-standard living conditions, lack of sanitation, lack of water supply and other amenities. In this study, however, the demonstrated approach of determining the goodness had a significant limitation: it needed to consider any policy variables of the past. It is worth mentioning that although industrialized countries may have proper planning policies for their cities, the cities in developing countries lack such policies in most cases, and they grow with all

2000   2005
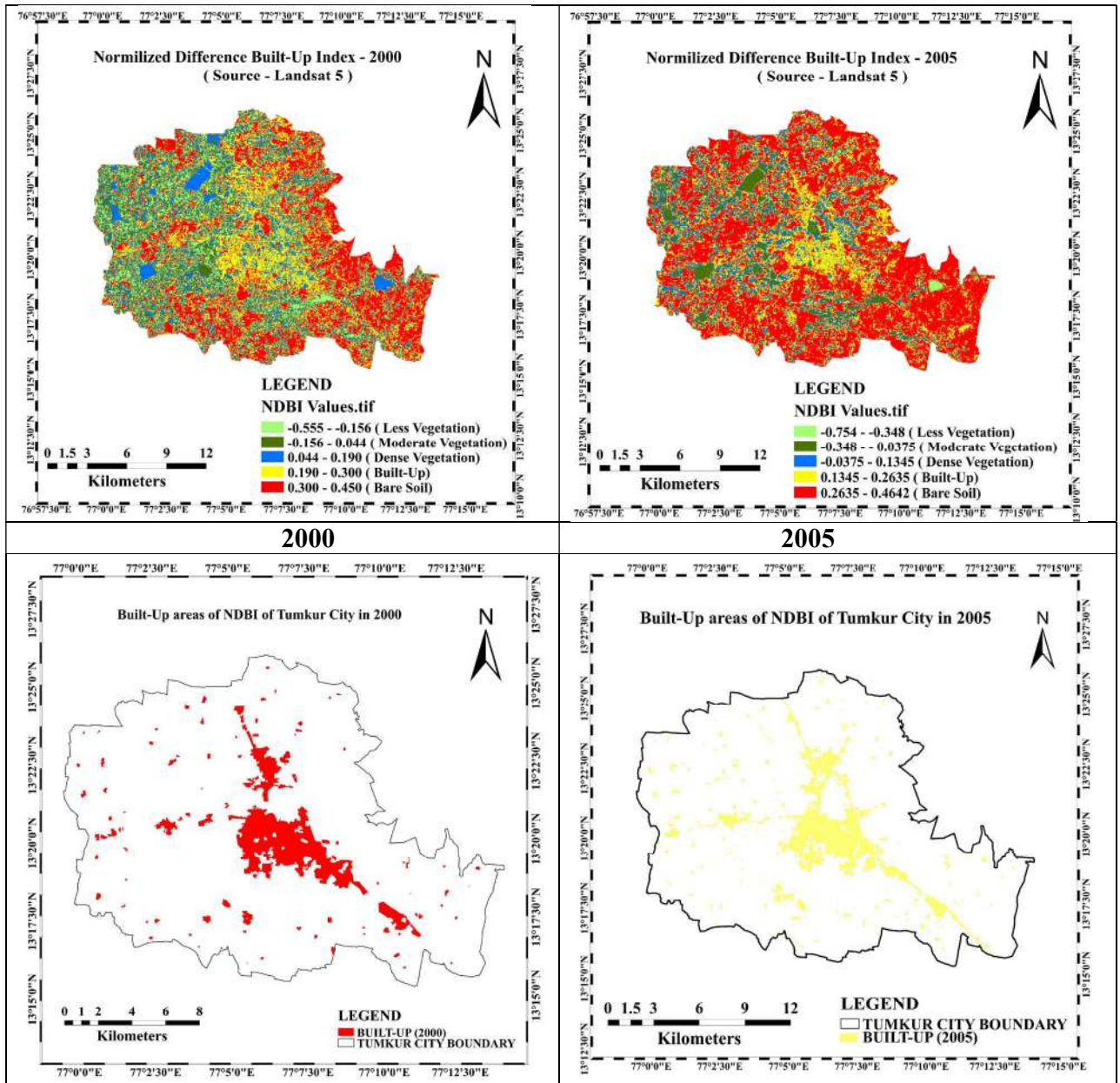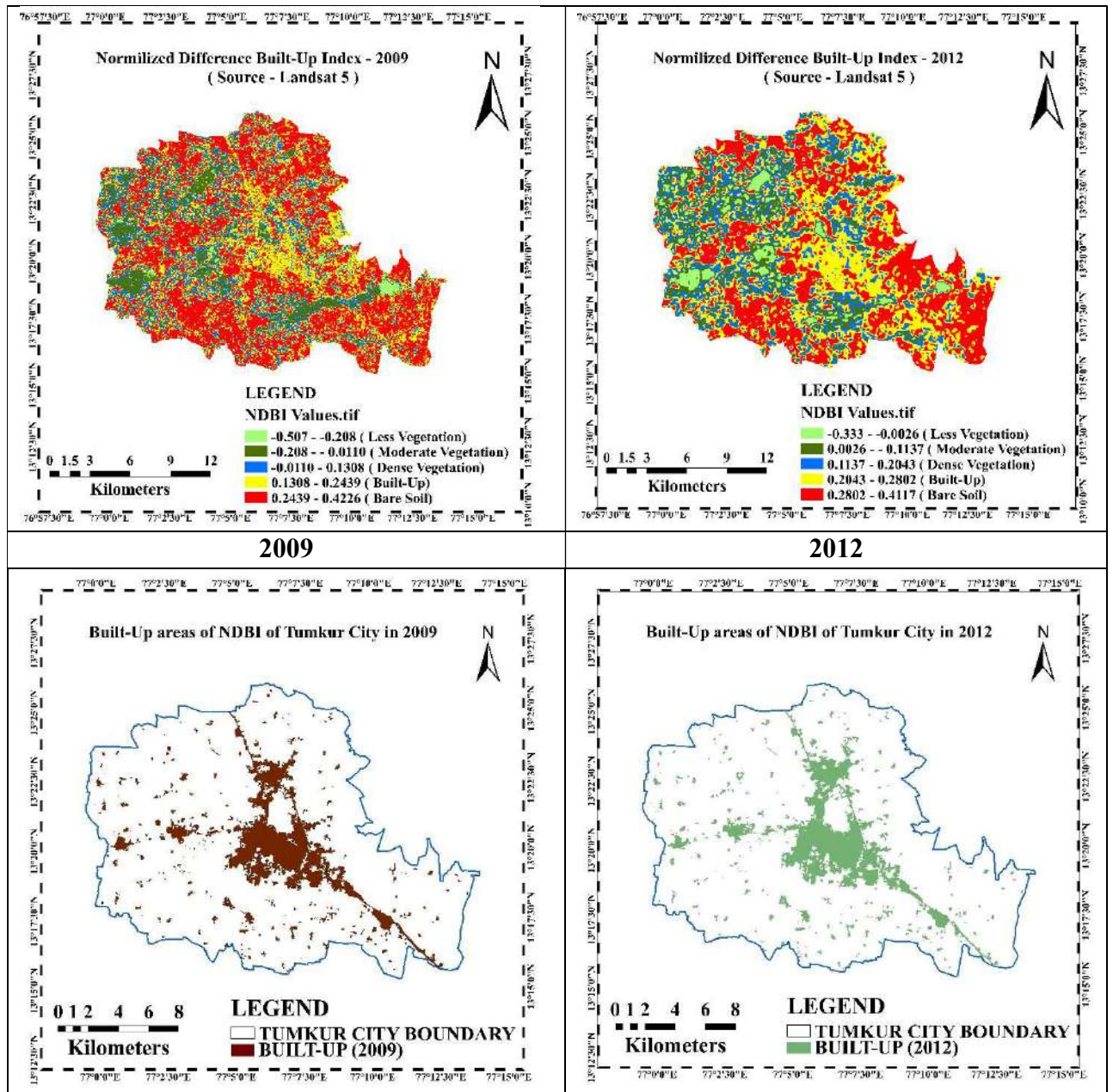
Figure Cont....

Figure Cont....
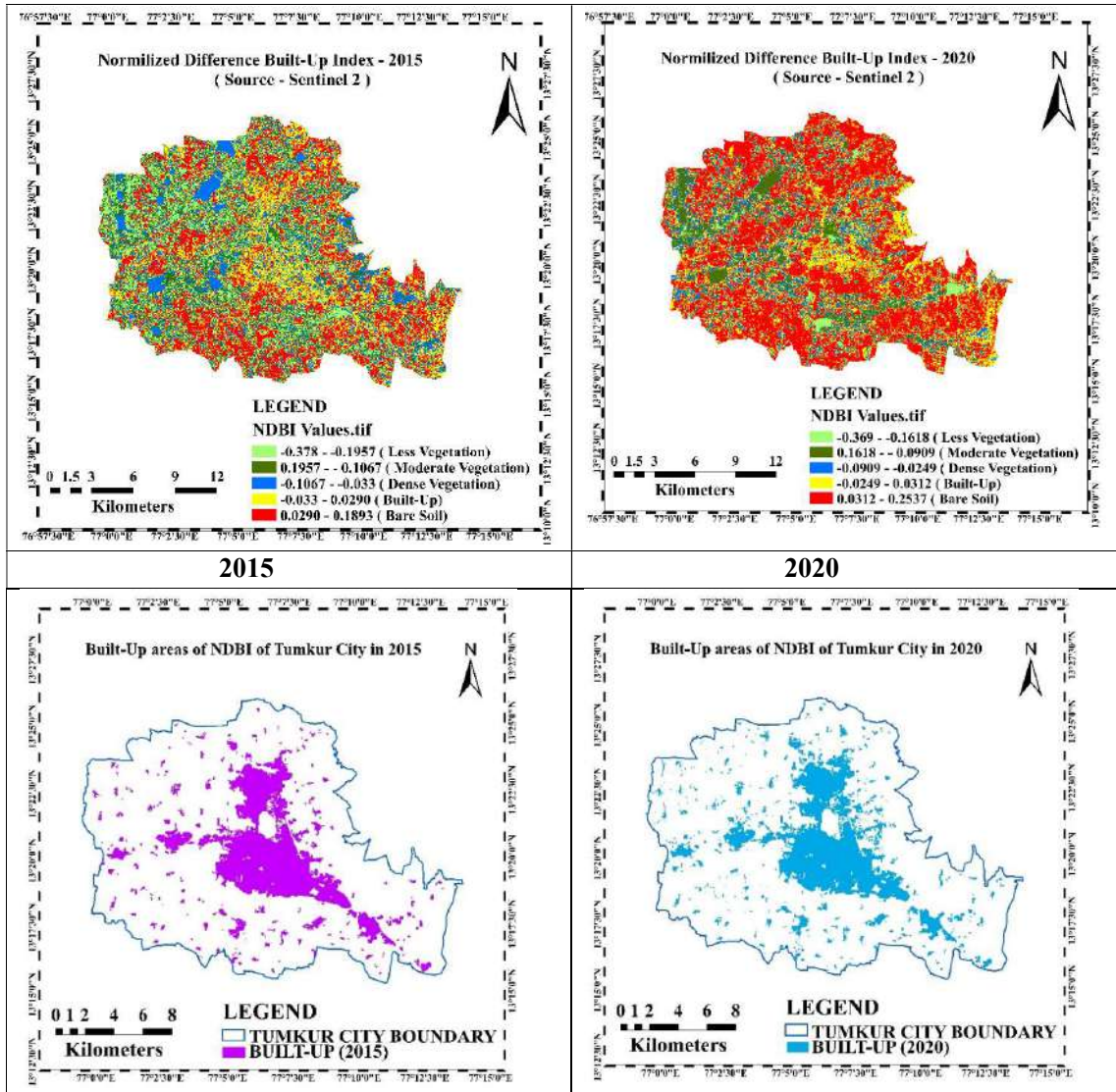
Fig. 10: NDBI and Built-up area map of NDBI in the Tumkur city area in (a) 2000, (b) 2005, (c) 2009 (d) 2012, (e) 2015, (f) 2020.
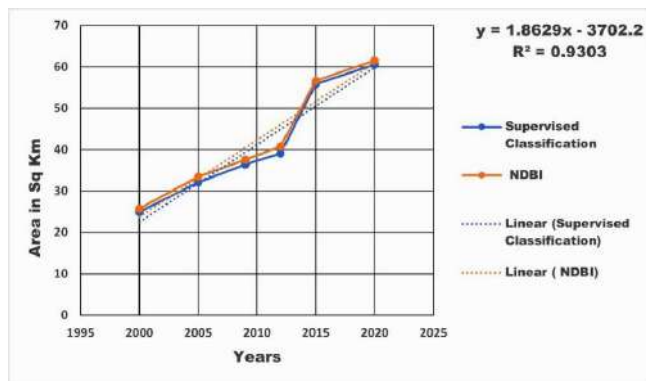
Fig. 11: Correlation Graph of Built-up areas of Supervised Classification and Built-up areas of NDBI.

Table 15: Population-level and growth rate for the Tumkur, from 2000 to 2020.

Year	Population Data	Growth Rate
2020	361,000	1.69%
2019	355,000	2.01%
2018	348,000	1.75%
2017	342,000	2.09%
2016	335,000	1.82%
2015	329,000	2.17%
2014	322,000	1.90%
2013	316,000	1.94%
2012	310,000	1.97%
2011	302143	2.01%
2010	298,000	1.71%
2009	293,000	2.09%
2008	287,000	2.14%
2007	281,000	1.81%
2006	276,000	1.85%
2005	271,000	1.88%
2004	266,000	2.31%
2003	260,000	1.96%
2002	255,000	1.59%
2001	248929	2.87%
2000	244,000	3.39%

(Source: United Nations population projections and Census of India 2011)

Fig. 12: Column graph of the Population growth rate of Tumkur City (2000-2020).
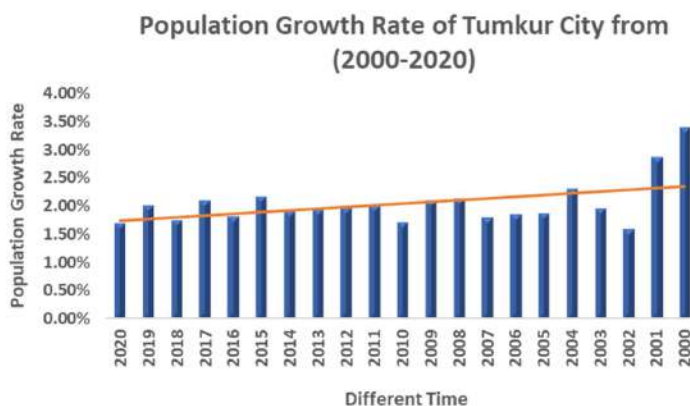
Fig. 13: Line graph of Tumkur City population data from (2000 to 2020).

Table 16: Population data and Built-up area of Tumkur City.

Year	Area (sq km^2)	Population Data
2000	24.94	244000
2005	32.10	271000
2009	36.47	293000
2012	39.08	310000
2015	55.85	329000
2020	60.59	361000

freedoms. Therefore, the demonstrated approach will benefit the cities in developing countries. According to the latest data collected by the Karnataka State Pollution Control Board (2018), Tumkur city is the first place in high air pollution cities in Karnataka. Tumakuru recorded a PM 10 level of 146 micrograms per cubic meter. The vehicular emissions and industrial emissions are the main reasons for the high pollution rate in Tumkur city.

Temporal Analysis of NDBI

An analysis of NDBI values in Tumkur between 2000 and 2020 is presented in Fig. 10. According to the NDBI indexes, the percentage of urban areas has increased significantly between these periods. Built-up areas of the core region have increased from 7.75 percent to 18.85 percent of the area. During 2000 the rural areas, where agricultural lands and vegetation are predominant, the NDBI index values were the lowest. Table 14 indicates that in the comparison between the two methods the built-up areas are almost the same and Fig. 11 shows a positive correlation between the two methods built-up areas. During the 2009 period, the expansion rate of urban areas in peripheral regions and industrial areas increases. During 2012 the agricultural land converted into built-up areas. A scattered settlemen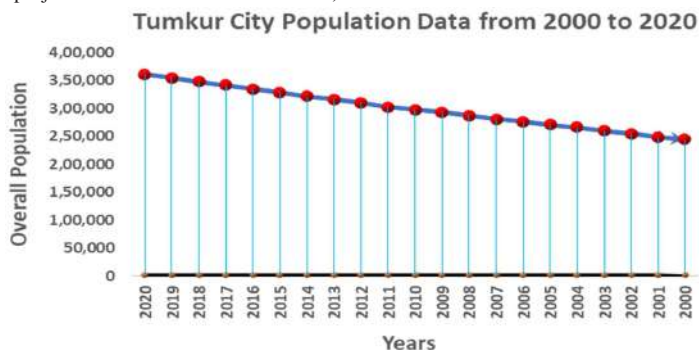t was converted into dense settlements during this period. From 2015 to 2020 NDBI values were very high in bare soil, and vegetation cover which indicated the conversion of water bodies, agricultural land, and vegetation into built-up areas in the form of large new layouts.

The statistics show a positive correlation between Built-up areas of NDBI and Supervised classification.

Population Data Analysis of Tumkur City (2000-2020)

According to Fig. 12 and Fig. 13, the population of Tumkur City in 2000 was 244,000, but in 2020 the population increased to 361,000. From 2000 to 2020, on average, every year, 5000 people were added to the list of population growth. Table 15 statistical analysis revealed that due to population growth, increased tremendously. The migration of people plays a major role in population growth apart from that, the growth of built-up areas in rural areas increased yearly.

Table 16 statistics analysis revealed that population increases lead to causes of urban area growth.

CONCLUSION

The current study aims to investigate the urban growth of the Tumkur city using the retrieved spatial satellite data spanning two decades (2000-2020) using urban-related indices, and new statistical methods. The AUEII study revealed that the values of different years, like 2000, 2005, 2009, and 2012 are moderate, indicating the slow urban development activities present in Tumkur city. Year to year, the variation of built-up land occupancy due to sizeable agricultural land and vegetation cover converted into built-up areas. The UEII statistics show the expansion rate from 2000 to 2009 was a little slow later the growth of industries, implementation of various government infrastructure projects, and increasing population growth leads the expansion of built-up areas. The expansion of built-up land in rural areas gradually increases and leads to the destruction of vegetation like plantations and scrubland. During the expansion period large water bodies areas converted into built-up areas and agricultural land. The Normalised Built-up Index depicted that from 2000 to 2009 the peripheral region and rural areas had NDBI values low compared to the core of the city. After 2009 increasing built-up areas leads to increases in those areas. Pearson's Chi-square test and Shannon Entropy analysis revealed most urban sprawl appeared in the area. The degree of goodness is very which shows compactness in a few areas and expansion in a few regions. Finally, urban growth is the expansion of built-up due to population growth, destruction of agricultural land, and few water bodies. The degree of goodness model can be regarded as a sustainable development index and constitutes a vital tool for future researchers. Using these scientific conclusions of the study area's planners/ decision makers, and urban designers will maintain that sustainable urban development strategies for controlling the presence of an environmental imbalance in cities and to implement ecological sustainability plans will improve the living conditions of future generations in cities.

REFERENCES

Acheampong, R.A., Agyemang, F.S. and Abdul-Fatawu, M., 2017. Quantifying the spatio-temporal patterns of settlement growth in a metropolitan region of Ghana. *GeoJournal*, 82, pp.823-840. Available at: https://link.springer.com/article/10.1007/s10708-016-9719-x [Accessed 9 October 2024].

Akshaya, D.K., 2021. Urban Spatial Growth Analysis of Tiruchirappalli Local Planning Area. Available at: https://www.researchgate.net/publication/349053941_Urban_Spatial_Growth_Analysis_of_Tiruchirappalli_Local_Planning_Area [Accessed 9 October 2024].

Alam, I., Nahar, K. and Morshed, M.M., 2023. Measuring urban expansion pattern using spatial matrices in Khulna City, Bangladesh. *Heliyon*, 9(2).

Available at: https://doi.org/10.1016/j.heliyon.2023.e13193 [Accessed 9 October 2024].

Almeida, C., Monteiro, A.M.V., Câmara, G., Soares-Filho, B.S., Cerqueira, G.C., Pennachin, C.L. and Batty, M., 2005. GIS and remote sensing as tools for the simulation of urban land-use change. *International Journal of Remote Sensing*, 26(4), pp.759-774. Available at: http://dx.doi.org/10.1080/01431160512331316865 [Accessed 9 October 2024].

Al-Sharif, A.A., Pradhan, B., Shafri, H.Z.M. and Mansor, S., 2014. Quantitative analysis of urban sprawl in Tripoli using Pearson's Chi-Square statistics and urban expansion intensity index. In: *IOP Conference Series: Earth and Environmental Science*, 20(1), p.012006. Available at: http://dx.doi.org/10.1088/1755-1315/20/1/012006 [Accessed 9 October 2024].

Antipova, A., Momeni, E. and Banai, R., 2022. Analysis of urban sprawl and blight using Shannon entropy index: a case study of Memphis, Tennessee. In *Advances in Urbanism, Smart Cities, and Sustainability* (pp. 322-299). CRC Press.

Barnes, K.B., Morgan III, J.M., Roberge, M.C. and Lowe, S., 2001. Sprawl development: its patterns, consequences, and measurement. Towson University, Towson, 1, p.24. Available at: http://chesapeake.towson.edu/landscape/urbansprawl/download/Sprawl_white_paper.pdf [Accessed 9 October 2024].

Basu, T., Das, A. and Pereira, P., 2023. Exploring the drivers of urban expansion in a medium-class urban agglomeration in India using the remote sensing techniques and geographically weighted models. *Geography and Sustainability*, 4(2), pp.150-160. Available at: https://doi.org/10.1016/j.geosus.2023.03.002 [Accessed 9 October 2024].

Batty, M. and Howes, D., 2001. Predicting temporal patterns in urban development from remote imagery. Available at: http://refhub.elsevier.com/S1110-9823(15)00008-3/h0040 [Accessed 9 October 2024].

Bhagat, R.B., 2011. Internal migration in India: Are the underprivileged migrating more?. *Asia-Pacific Population Journal*, 25(1), pp.27-45.

Bhaskar, C.V. and Nagendrappa, G., 2008. A comparative study of ground water quality and water quality index of certain selected areas situated around Tumkur city, Karnataka. *Current World Environment*, 3(1), p.75. Available at: http://dx.doi.org/10.12944/CWE.3.1.10 [Accessed 9 October 2024].

Bramhe, V.S., Ghosh, S.K. and Garg, P.K., 2020. Extraction of built-up areas from Landsat-8 OLI data based on spectral-textural information and feature selection using support vector machine method. *Geocarto International*, 35(10), pp.1067-1087.

Deka, J., Tripathi, O.P. and Khan, M.L., 2011. Urban growth trend analysis using Shannon Entropy approach-A case study in North-East India. *International Journal of Geomatics and Geosciences*, 2(4), pp.1062-1068.

Dewa, D.D., Buchori, I., Sejati, A.W. and Liu, Y., 2022. Shannon Entropy-based urban spatial fragmentation to ensure sustainable development of the urban coastal city: A case study of Semarang, Indonesia. *Remote Sensing Applications: Society and Environment*, 28, p.100839. Available at: https://doi.org/10.1016/j.rsase.2022.100839 [Accessed 9 October 2024].

Dong, W., Zhang, X., Wang, B. and Duan, Z., 2007. Expansion of Ürümqi urban area and its spatial differentiation. *Science in China Series D: Earth Sciences*, 50, pp.159-168. Available at: https://doi.org/10.1007/s11430-007-5016-3 [Accessed 9 October 2024].

Fertner, C., Jørgensen, G., Nielsen, T.A.S. and Nilsson, K.S.B., 2016. Urban sprawl and growth management–drivers, impacts and responses in selected European and US cities. *Future Cities and Environment*, 2, pp.1-13. Available at: https://doi.org/10.1186/s40984-016-0022-2 [Accessed 9 October 2024].

Haregeweyn, N., Fikadu, G., Tsunekawa, A., Tsubo, M. and Meshesha, D.T., 2012. The dynamics of urban expansion and its impacts on land use/land cover change and small-scale farmers living near the urban fringe: A case study of Bahir Dar, Ethiopia. *Landscape and urban planning*, 106(2), pp.149-157.

Hegazy, I.R. and Kaloop, M.R., 2015. Monitoring urban growth and land use change detection with GIS and remote sensing techniques in Daqahlia governorate Egypt. *International Journal of Sustainable Built Environment*, 4(1), pp.117-124. Available at: https://doi.org/10.1016/j.ijsbe.2015.02.005 [Accessed 9 October 2024].

Kanga, S., Meraj, G., Johnson, B.A., Singh, S.K., PV, M.N., Farooq, M. and Sahu, N., 2022. Understanding the linkage between urban growth and land surface temperature—A case study of Bangalore City, India. *Remote Sensing*, 14(17), p.4241. Available at: http://dx.doi.org/10.3390/rs14174241 [Accessed 9 October 2024].

Kumar, A. and Pandey, A.C., 2013. Spatio-temporal assessment of urban environmental conditions in Ranchi Township, India using remote sensing and geographical information system techniques. *International Journal of Urban Sciences*, 17(1), pp.117-141. Available at: https://doi.org/10.1080/12265934.2013.766501 [Accessed 9 October 2024].

Kumara, K.S. and Belagali, S.L., 2010. A study on the coliform bacterial density and heavy metal concentration of Tumkur city sewage. *Nature, Environment and Pollution Technology*, 9(2), pp.235-240.

Manjunath, K.V., Singh, B.C. and Harshitha, S., 2020. Study and analysis of waste management in Tumakuru city. *Journal of Advanced Research in Industrial Engineering*, 2(2).

Manna, H., Sarkar, S., Hossain, M. and Dolui, M., 2024. Modeling and predicting spatio-temporal land use land cover changes and urban sprawling in Kalaburagi City Corporation, Karnataka, India: a geospatial analysis. *Modeling Earth Systems and Environment*, 10(1), pp.809-832.

Martinuzzi, S., Gould, W.A. and González, O.M.R., 2007. Land development, land use, and urban sprawl in Puerto Rico integrating remote sensing and population census data. *Landscape and Urban Planning*, 79(3-4), pp.288-297. Available at: https://doi.org/10.1016/j.landurbplan.2006.02.014 [Accessed 9 October 2024].

Mas, J.F., Lemoine-Rodríguez, R., González-López, R., López-Sánchez, J., Piña-Garduño, A. and Herrera-Flores, E., 2017. Land use/land cover change detection combining automatic processing and visual interpretation. *European Journal of Remote Sensing*, 50(1), pp.626-635.

Masisi, L., Nelwamondo, V. and Marwala, T., 2008, November. The use of entropy to measure structural diversity. In *2008 IEEE International Conference on Computational Cybernetics* (pp. 45-41). IEEE.

Mohamed, A. and Worku, H., 2019. Quantification of the land use/land cover dynamics and the degree of urban growth goodness for sustainable urban land use planning in Addis Ababa and the surrounding Oromia special zone. *Journal of Urban Management*, 8(1), pp.145-158. Available at: https://doi.org/10.1016/j.jum.2018.11.002 [Accessed 9 October 2024].

Mohan, M. and Kandya, A., 2015. Impact of urbanization and land-use/land-cover change on diurnal temperature range: A case study of tropical urban airshed of India using remote sensing data. *Science of the Total Environment*, 506, pp.453-465. Available at: https://doi.org/10.1016/j.scitotenv.2014.11.006 [Accessed 9 October 2024].

Ngolo, A.M.E. and Watanabe, T., 2023. Integrating geographical information systems, remote sensing, and machine learning techniques to monitor urban expansion: an application to Luanda, Angola. *Geospatial Information Science*, 26(3), pp.446-464. Available at: https://doi.org/10.1080/10095020.2022.2066574 [Accessed 9 October 2024].

Nkeki, F.N., 2016. Spatio-temporal analysis of land use transition and urban growth characterization in Benin metropolitan region, Nigeria. *Remote Sensing Applications: Society and Environment*, 4, pp.119-137. Available at: https://doi.org/10.1016/j.rsase.2016.08.002 [Accessed 9 October 2024].

Patra, S., Sahoo, S., Mishra, P. and Mahapatra, S.C., 2018. Impacts of urbanization on land use/cover changes and its probable implications on local climate and groundwater level. *Journal of Urban*

Management, 7(2), pp.70-84. Available at: https://doi.org/10.1016/j.jum.2018.04.006 [Accessed 9 October 2024].

Qiao, Z., Tian, G., Zhang, L. and Xu, X., 2014. Influences of urban expansion on urban heat island in Beijing during 1989–2010. *Advances in Meteorology*, 2014. Available at: https://doi.org/10.1155/2014/187169 [Accessed 9 October 2024].

Raftery, A.E., Li, N., Ševčíková, H., Gerland, P. and Heilig, G.K., 2012. Bayesian probabilistic population projections for all countries. *Proceedings of the National Academy of Sciences*, 109(35), pp.13915-13921.

Saxena, A., Jat, M.K. and Choudhary, M., 1997. Analysis of urban growth using geospatial techniques. *Image*, 1000(4), pp.28-50.

Tian, G., Jiang, J., Yang, Z. and Zhang, Y., 2011. The urban growth, size distribution and spatio-temporal dynamic pattern of the Yangtze River Delta megalopolitan region, China. *Ecological Modelling*, 222(3), pp.865-878. Available at: https://doi.org/10.1016/j.ecolmodel.2010.09.036 [Accessed 9 October 2024].

United Nations, 2018. World Urbanization Prospects. Available at: https://population.un.org/wup/ [Accessed 9 October 2024].

Vadakkuveettil, A. and Grover, A., 2023. Bi-temporal characterization of terrestrial temperature in relation to urban land use land cover dynamics and policies in Kozhikode Urban Area, India. *Land Use Policy*, 132, p.106782. Available at: https://doi.org/10.1016/j.landusepol.2023.106782 [Accessed 9 October 2024].

Verma, R. and Garg, P.K., 2022. Multi-temporal urban growth analysis with expansion indicators in Lucknow constituency by open-source data, India. *Journal of Urban Management*, 11(4), pp.412-423. Available at: https://doi.org/10.1016/j.jum.2022.07.001 [Accessed 9 October 2024].

Xian, S., Li, L. and Qi, Z., 2019. Toward a sustainable urban expansion: A case study of Zhuhai, China. *Journal of Cleaner Production*, 230, pp.276-285. Available at: https://doi.org/10.1016/j.jclepro.2019.05.087 [Accessed 9 October 2024].

Yakub, M. and Tiffin, P., 2017. Living in the city: urban environments shape the evolution of a native annual plant. *Global Change Biology*, 23(5), pp.2082-2089.

Yan, Y., Ju, H., Zhang, S. and Jiang, W., 2019. Spatiotemporal patterns and driving forces of urban expansion in coastal areas: A study on urban agglomeration in the Pearl River Delta, China. *Sustainability*, 12(1), p.191. Available at: https://doi.org/10.3390/su12010191 [Accessed 9 October 2024].

Yu, S., Du, W., Zhang, X., Hong, Y., Liu, Y., Hong, M. and Chen, S., 2023. Spatiotemporal changes in NDVI and its driving factors in the Kherlen River Basin. *Chinese Geographical Science*, 33(2), pp.377-392. Available at: https://doi.org/10.1007/s11769-023-1337-1 [Accessed 9 October 2024].

Zha, Y., Gao, J. and Ni, S., 2003. Use of normalized difference built-up index in automatically mapping urban areas from TM imagery. *International journal of remote sensing*, 24(3), pp.583-594.

Zheng, Y., Tang, L. and Wang, H., 2021. An improved approach for monitoring urban built-up areas by combining NPP-VIIRS nighttime light, NDVI, NDWI, and NDBI. *Journal of Cleaner Production*, 328, p.129488. Available at: https://doi.org/10.1016/j.jclepro.2021.129488 [Accessed 9 October 2024].

Zhu, Z., Woodcock, C.E., Rogan, J. and Kellndorfer, J., 2012. Assessment of spectral, polarimetric, temporal, and spatial dimensions for urban and peri-urban land cover classification using Landsat and SAR data. *Remote Sensing of Environment*, 117, pp.72-82. Available at: https://doi.org/10.1016/j.rse.2011.07.020 [Accessed 9 October 2024].

ORCID DETAILS OF THE AUTHORS

Govindaraju: https://orcid.org/0000-0002-0119-4826

Evaluation of the Photodegradation of Atrazine in the Presence of β-cyclodextrin Polymer: Experimental Design and Kinetic Study

O. S. Ayanda[1]† , S. O. Adewuyi[1], S. M. Yahaya[2] , O. Adeyi[3] , S. M. Nelana[4] and M. J. Klink[4]

[1]Nanoscience Research Unit, Department of Industrial Chemistry, Federal University Oye Ekiti, P.M.B 373, Oye Ekiti, Ekiti State, Nigeria

[2]Department of Soil Science, Faculty of Agriculture/Institute for Agricultural Research, Ahmadu Bello University, P.M.B. 1044, Zaria, Nigeria

[3]Department of Chemical Engineering, Michael Okpara University of Agriculture, P.M.B 7267, Umudike, Abia State, Nigeria

[4]Department of Chemistry, Vaal University of Technology, South Africa

†Corresponding author: O. S. Ayanda; osayanda@gmail.com

ABSTRACT

The degradation of atrazine (ATZ) was studied in the presence of β-cyclodextrin (β-CD) under ultraviolet light irradiation. The β-CD was characterized by modern analytical techniques and the different operating parameters of photodegradation were investigated. Experimental results revealed irregular shapes in the structure of β-CD, and the functional groups of β-CD were present in the glucose units. The BET surface area of β-CD was 285.02 m^2/g with a pore volume of 0.172 cc/g and a pore diameter of 2.138 nm, whereas, the x-ray diffraction analysis revealed the polycrystalline nature of β-CD. The z-average diameter of the particle size distribution was determined as 63.21 nm, thermogravimetric analysis data demonstrated weight loss events while the differential thermal analysis data revealed associated energy changes during phase transitions. The photodegradation of ATZ in the presence of β-CD resulted in 80.80% and 59.40% degradation, respectively, for 6.25 mg/L and 100 mg/L of ATZ after 60 min of irradiation time. The treatment method could be described by the Langmuir-Hinshelwood kinetic model, with k_c equals 0.1462 $mgL^{-1}min^{-1}$ and K_{LH} equals 10.45 × 10^{-2} Lmg^{-1}. Thus, photodegradation with β-CD as a catalyst could be effectively used for the remediation of pesticide-contaminated wastewater.

INTRODUCTION

β-cyclodextrin (β-CD) is an amphiphilic molecule with a hydrophobic inner cavity rich in electrons (Kasprzak & Poplawska 2018). It serves as a host molecule for the supramolecular inclusion of a variety of guest molecules which results in host-guest inclusion complexes (Duan et al. 2020, Morin-Crini et al. 2018). Thus, the application of β-CD for the selective eradication of organic pollutants is a possibility. The capability of β-CD has been noticed to promote the degradation of organic pollutants. In recent years, numerous studies have investigated the application of ⬛-CD in photocatalysis, revealing its prospect as an effective and versatile material for environmental remediation. One significant study was conducted by Liu et al. (2020), this comprehensive review highlights cyclodextrin-based adsorbents as assuring materials for wastewater treatment due to their outstanding physicochemical properties. This

material shows excellent performance in removing heavy metals, dyes, endocrine-disrupting chemicals, and mixed pollutants from water. The photocatalytic decoloration of organic dyes (Velusamy et al. 2014), and organophosphorus pesticides (Kamiya et al. 2001) by β-CD has been reported. Liu et al. (2011) also reported the photocatalytic degradation of pesticides with sulfonated β-CD and in a work by Zhou et al. (2019), the adsorptive removal of carbamazepine, chloroxylenol, and bisphenol A from water through β-CD polymer has been investigated. Another significant contribution comes from the work of Zhang et al. (2021), the authors explored polyacrylonitrile/β-cyclodextrin composite nanofibrous membranes with TiO_2 and graphene oxide (GO) which were prepared via electrospinning. The results showed the highest photocatalytic efficiency under sunlight, degrading methyl blue (MB) (93.52 ± 1.83%) and methyl orange (MO) (90.92 ± 1.52%). This eco-friendly and reusable PAN/β-cyclodextrin/TiO_2/GO nanofibrous membrane holds

significant potential for the effective removal of dyes from industrial wastewaters.

A recent study by Yadav et al. (2022) delved into the various cyclodextrin-based materials such as composites, nanocomposites, polymers, hydrogels, membranes, and immobilized supports for diverse environmental applications. Cyclodextrin's eco-friendly nature promotes green processes, and the reversible equilibrium of the inclusion phenomenon allows for innovative pollutant removal techniques, including supramolecular chemistry, biodegradation, and advanced oxidation, enabling complete pollutant removal and cyclodextrin recycling. In a recent experimental study conducted by Jia et al. (2024), a novel nano-adsorbent, CD/CA-g-CS, was synthesized by chemically binding β-CD with chitosan (CS) and citric acid (CA) for efficient dye removal from wastewater. The material exhibited outstanding adsorption capacities for cationic and anionic dyes, surpassing previous adsorbents. CD/CA-g-CS demonstrated effective removal of mixed dyes in simulated sewage and real industrial wastewater, with an additional antibacterial activity of over 99.99% against E. coli, making it a promising solution for high-efficiency dyeing wastewater remediation. Conclusively, the collective results from these studies show the rising importance of β-CD in enhancing photocatalysis for environmental applications. The studies mentioned above provide important visions into the mechanisms over which β-CD improves photocatalytic efficiency and provide a foundation for further research in modifying β-CD based materials for particular environmental remediation challenges. As scientists continue to investigate the potential of β-CD in photocatalysis, these studies pave the technique for the development of novel and effective strategies for tackling environmental pollutants.

The herbicide atrazine (ATZ) is often used to manage weeds and has been found in surface and groundwater in many places throughout the world. ATZ is an endocrine disruptor that is frequently present in soil ecosystems where it accumulates because of its low volatility, delayed hydrolysis, high chemical stability, and poor biodegradability (Altendji & Hamoudi 2023). Therefore, addressing the deterioration of ATZ in water through appropriate methods is crucial. Therefore, the study aims to investigate the photocatalysis of ATZ using β-CD polymer as a photocatalyst. The objectives are (i) the characterization of β-CD polymer (ii) the investigation of the effect of operating conditions on the reaction advancement and (iii) the investigation of the kinetics and mechanism of photodegradation of ATZ by β-CD polymer. An innovative way to combat water pollution is by photocatalytic reaction, in which the catalyst and light source photon work in concert to break down the target pollutant.

MATERIALS AND METHODS

Chemical Reagents

β-CD polymer produced by Wacker CH was obtained from Sigma Aldrich. ATZ standard, (2-Chloro-4-ethylamino-6-isopropylamino-1,3,5-triazine) was also obtained from Sigma Aldrich. Other chemical and reagents include ethanol, sodium hydroxide and hydrochloric acid. Distilled water was used for all analytical preparations.

Instrumentations

Fourier transform infrared spectroscopy (FTIR) was used to determine the functional group present in β-CD polymer. The scanning electron microscope - energy dispersive X-ray spectroscopy (SEM-EDS) Phenon Prox model, manufactured by Phenom-World Eindhoven, Netherlands was used to carry out the morphology analysis. Other characterizations include x-ray diffraction (XRD) (Empyrean Malvern Panalytical Diffractometer), thermogravimetric analysis - differential thermal analysis (TGA-DTA) (PerkinElmer TGA 4000), Brunauer, Emmett, and Teller (BET) and particle size analysis.

Photocatalysis of Atrazine

The aqueous ATZ was photodegraded at ambient temperature in a photocatalytic reactor operating under ultraviolet (UV) light at a wavelength of 254 nm (Altendji & Hamoudi 2023). A mixture of 25 mL of ATZ solution and catalyst was vigorously stirred under UV light irradiation for 5 - 60 min in the dark. The aliquots were sampled and filtered to remove the solid phase. Detection of the concentration of ATZ was done by Shimadzu UV-1650 PC at a maximum wavelength of 220 nm (Assaker & Rima 2012). The degradation efficiency (%) was obtained using Equation 1 (Aremu et al. 2022).

$$\%Degradation = \frac{ATZ_0 - ATZ_t}{ATZ_0} \times 100 \qquad ...(1)$$

where ATZ_0 and ATZ_t are the initial and final concentrations of ATZ, respectively.

RESULTS AND DISCUSSION

EDS and SEM Analysis of β-Cyclodextrin

The SEM image presented in Fig. 1a showcases the morphology of β-CD polymer. Notably, the image reveals irregular shapes in the structure of β-CD. This suggests that the β-CD polymer is not uniform in its structure. This variability can impact its properties and performance and it is indicative of the agglomeration or aggregation of β-CD particles. This observation aligns
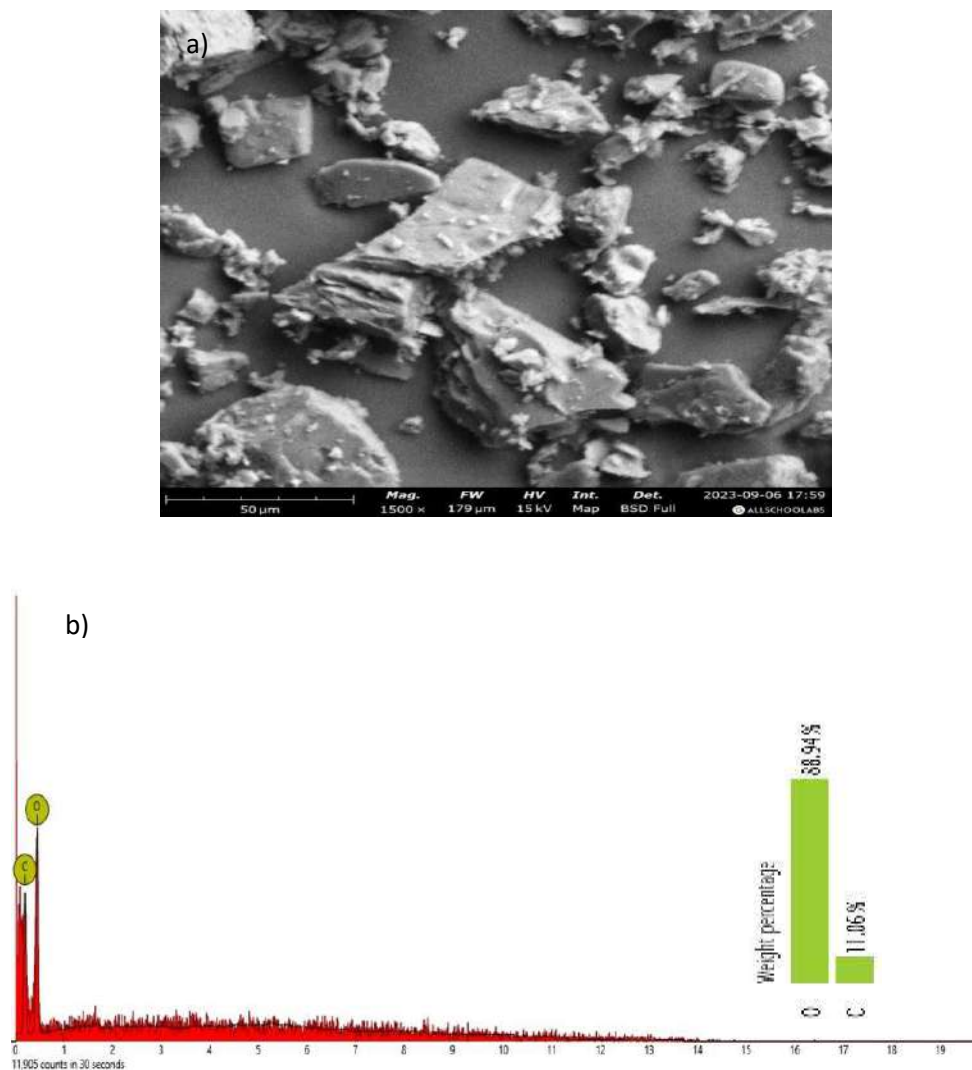
Fig. 1: SEM micrograph and EDS spectrum of β-cyclodextrin.

closely with the research findings reported by Rachmawati et al. (2013), which focused on the synthesis of molecular inclusion complexes involving curcumin and β-CD nanoparticles.

Fig. 1b illustrates the EDS spectrum obtained from the analysis of β-CD polymer. Within the figure, the spectrum qualitatively reveals the relative abundance of elements found in the β-CD sample. From this spectral data, two distinct elements emerge as being present in the β-CD, namely oxygen (O) and carbon (C). Notably, Fig. 1b underscores that oxygen (O) is the predominant element within the analyzed β-CD polymer. The analysis demonstrates that oxygen constitutes the majority of the composition at 88.94%, with carbon accounting for the remaining 11.06%.

TGA-DTA of β-Cyclodextrin Polymer

The TGA-DTA curves obtained for β-CD polymer provide valuable insights into the material's thermal behavior, with the DTA data offering a complementary perspective on the energy changes during phase transitions. Fig. 2 displays the TGA-DTA curve for β-CD polymer. Notably, a weight loss event is observed between 90.14°C and 90.32°C, resulting in a substantial reduction in weight from 99.997% to 96.356%. The TGA curve indicates a significant weight loss, typically associated with thermal decomposition or degradation. In the context of β-CD, this suggests that the sample undergoes decomposition, leading to the release of volatile components and a corresponding weight loss. The DTA data offer further insights into these observations. At around 32°C in the DTA curve, an endothermic peak is evident, indicating the
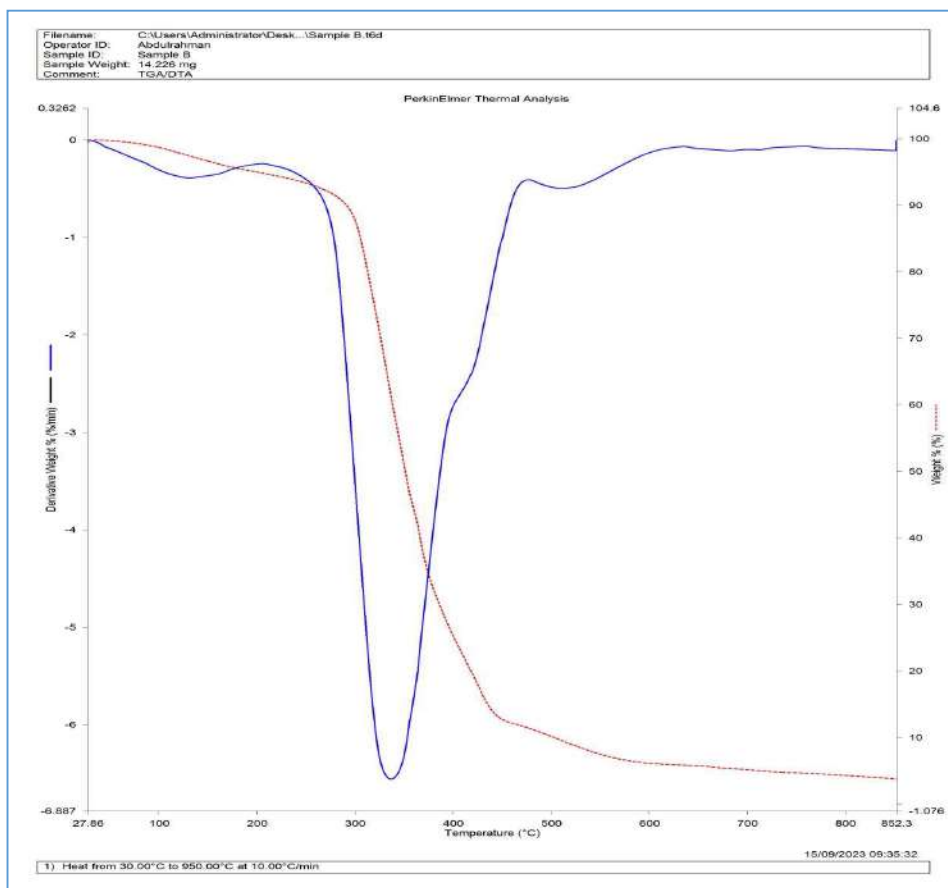
Fig. 2: TGA-DTA curves for β-cyclodextrin polymer.

absorption of heat during this phase transition such as melting or dehydration (Rajamohan et al. 2022). The endothermic nature of this peak confirms that energy is absorbed during the transition, consistent with the decomposition process indicated by the TGA data.

Subsequently, at approximately 38°C in the DTA curve, an exothermic peak is observed, signifying the release of heat. This corresponds to an exothermic phase transition, which in the context of β-CD, could be linked to crystallization or another exothermic process. The release of heat during this transition aligns with the weight loss and decomposition noted in the TGA data, further supporting the idea that significant changes are occurring within the materials. As we move to higher temperatures, the TGA data indicate two more weight loss events, one between approximately 290°C and 240°C and another between 417°C and 435°C. These events likely signify pronounced changes or decomposition in the β-CD sample. The DTA data continue to corroborate the TGA findings. Notably, an endothermic peak at 505°C is observed, indicating another energy-absorbing phase transition or

process at this elevated temperature. This endothermic peak aligns with the weight loss events observed in the TGA data and further supports the idea of structural or phase transformations in the β-CD samples under extreme thermal conditions.

Fourier Transform Infra-Red Spectroscopy of β-Cyclodextrin

The FTIR spectrum of β-CD polymer (Fig. 3) shows peaks that correspond to the functional groups present in the glucose units of β-CD, such as C-H, C-O, and O-H bonds. These peaks are important for identifying β-CD. Fifteen (15) absorption bands were observed in the FTIR spectrum of β-CD and included bands observed at wavenumbers of 704.46 cm^{-1}, 752.92 cm^{-1}, 857.28 cm^{-1}, 939.28 cm^{-1}, 1021.29 cm^{-1}, 1077.20 cm^{-1}, 1151.74 cm^{-1}, 1252.38 cm^{-1}, 1334.38 cm^{-1}, 1367.93 cm^{-1}, 1416.38 cm^{-1}, 1640.02 cm^{-1}, 2102.21 cm^{-1}, 2929.68 cm^{-1} and 3265.14 cm^{-1}. The peaks obtained from the FTIR data of β-CD polymer are consistent with those reported in
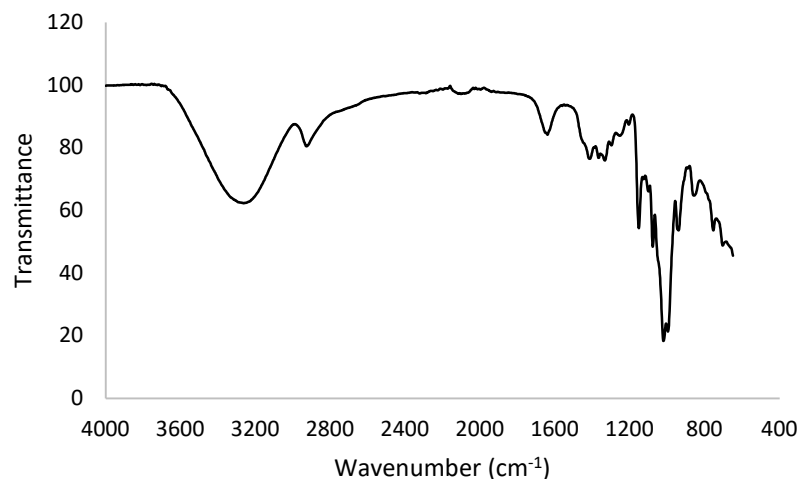
Fig. 3: FTIR spectrum of β-cyclodextrin.

the literature (Bratu et al. 2004, Sambasevam et al. 2013).

The FTIR data of the β-CD polymer were analyzed to assign the appropriate functional group to the various peaks. The peak at 704.46 cm^{-1} was attributed to the out-of-plane bending of C-H bonds in the glucose units of β-CD, while the peak at 752.92 cm^{-1} was assigned to the rocking vibration of C-H bonds in the glucose units of β-CD. The peaks at 857.28 cm^{-1}, 939.28 cm^{-1}, 1021.29 cm[-1,] 1077.20 cm^{-1}, 1151.74 cm^{-1}, and 1252.38 cm^{-1} were attributed to the stretching vibration of C-O bonds in the glucose units of β-CD. The peaks at 1334.38 cm^{-1}, 1367.93 cm^{-1}, and 1416.38 cm^{-1} were assigned to the stretching and bending vibrations of C-H bonds in the glucose units of β-CD. The peak at 1640.02 cm^{-1} was assigned to the stretching vibration of O-H bonds in the glucose units of β-CD. The peak at 2102.21 cm^{-1} was attributed to the stretching vibration of C≡C bonds typically found in alkynes. The peaks at 2929.68 cm^{-1} and 3265.14 cm^{-1} were assigned to the stretching vibration of C-H and O-H bonds in the glucose units of β-CD, respectively (Rachmawati et al. 2013). The identification of functional groups in the FTIR data of β-CD polymer is important for understanding its molecular structure and properties.

BET Analysis and Particle Size Distribution of β-Cyclodextrin

Fig. 4 shows the BJH cumulative pore distribution of β-CD. β-CD exhibited a surface area of 285.02 m^2/g. The pore size was determined by the Barrette-Joyner-Halenda (BJH) method. The pore volume of β-cyclodextrin was 0.172 cc/g, it exhibits a slightly larger pore diameter of 2.138 nm.

Fig. 5 illustrates the particle size distribution of β-CD, revealing a broad spectrum of particle sizes ranging from as small as 0.4 nm to as large as 10,000 nm (or 10 μm). This distribution is characterized by two key parameters: particle size, expressed in nanometers, representing the physical dimensions of β-CD particles, and intensity, denoted in percentage, which signifies the relative abundance of particles within specific size intervals. As depicted in the figure, there is a noticeable trend in the intensity values as particle size increases, signifying variations in the relative abundance of particles across different size ranges. The z-average diameter of this distribution is determined to be 63.21 nm, indicating that the mean size of β-CD particles within the sample falls within this size range. The obtained value of 63.21 nm is far lower than the 173.212 μm reported for hydroxypropyl-β-cyclodextrin (Li et al. 2018). Crucially, the distribution curve unveils the presence of three distinct peaks, a characteristic feature of a multimodal distribution. These peaks represent separate populations of β-CD particles, each characterized by unique sizes and relative abundances.

The first and most prominent peak, centered at approximately 102.8 nm, exhibits a high intensity of 83.5%, signifying a substantial concentration of β-CD particles within this size range. Notably, this peak displays a relatively wide standard deviation of 130.5 nm, indicating notable variability in the sizes of β-CD particles within this particular range. Conversely, the second peak, located around 2.319 nm, displays a lower intensity of 8.5%. This peak represents a population of considerably smaller β-CD particles. Remarkably, the standard deviation for this peak is remarkably low at 1.606 nm, suggesting a high degree of uniformity in particle size, with particles tightly clustered

around the mean. Lastly, the third peak, characterized by a z-average diameter of 3528 nm and an intensity of 5.1%, corresponds to larger β-CD particles. Analogous to the first peak, this segment also exhibits a relatively large standard deviation of 1280 nm, indicating considerable variation and heterogeneity in particle sizes within this range. In summary, the particle size distribution data of β-CD underscores the diverse nature of particle sizes within the sample. The presence of multiple peaks signifies the coexistence of

distinct populations of β-CD particles with varying sizes and relative abundances. This data is pivotal for tailoring β-CD for specific applications where particle size plays a crucial role, such as drug delivery systems, encapsulation, and other innovative uses in pharmaceuticals and materials science.

XRD Pattern of β-Cyclodextrin

XRD analysis was harnessed to delve into the intricate realm of phase composition and crystallite structure within the
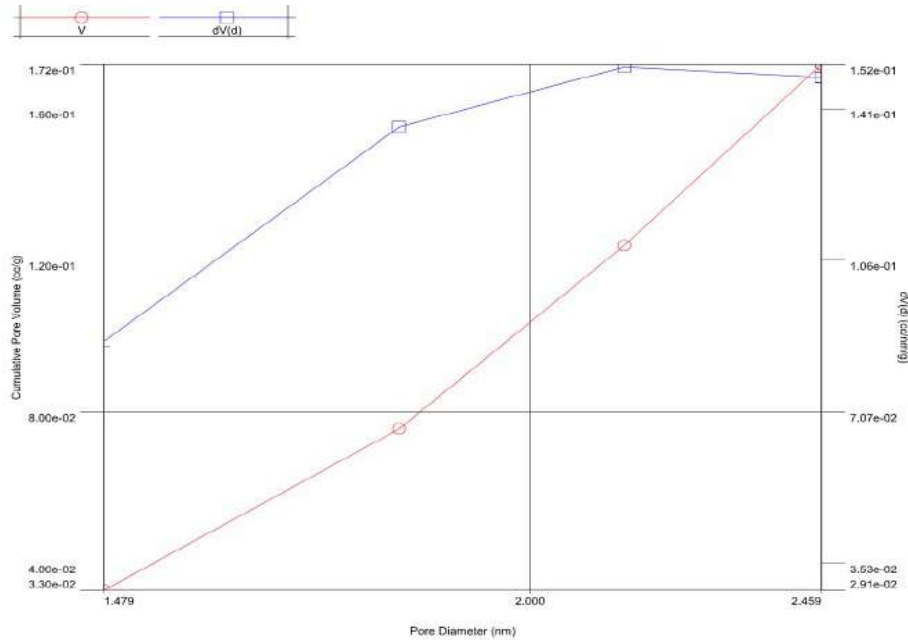
Fig. 4: BJH pore size distribution of β-cyclodextrin.
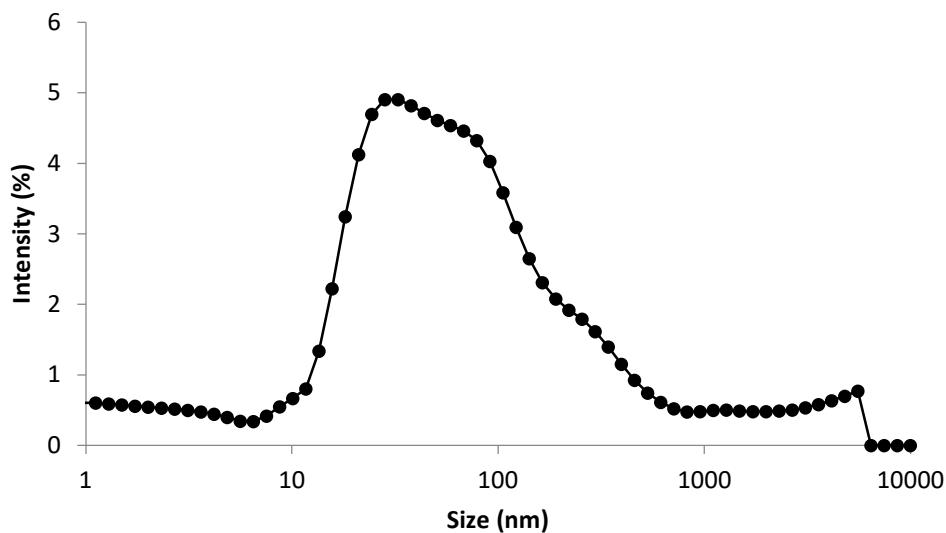
Fig. 5: Particle size distribution of β-cyclodextrin.
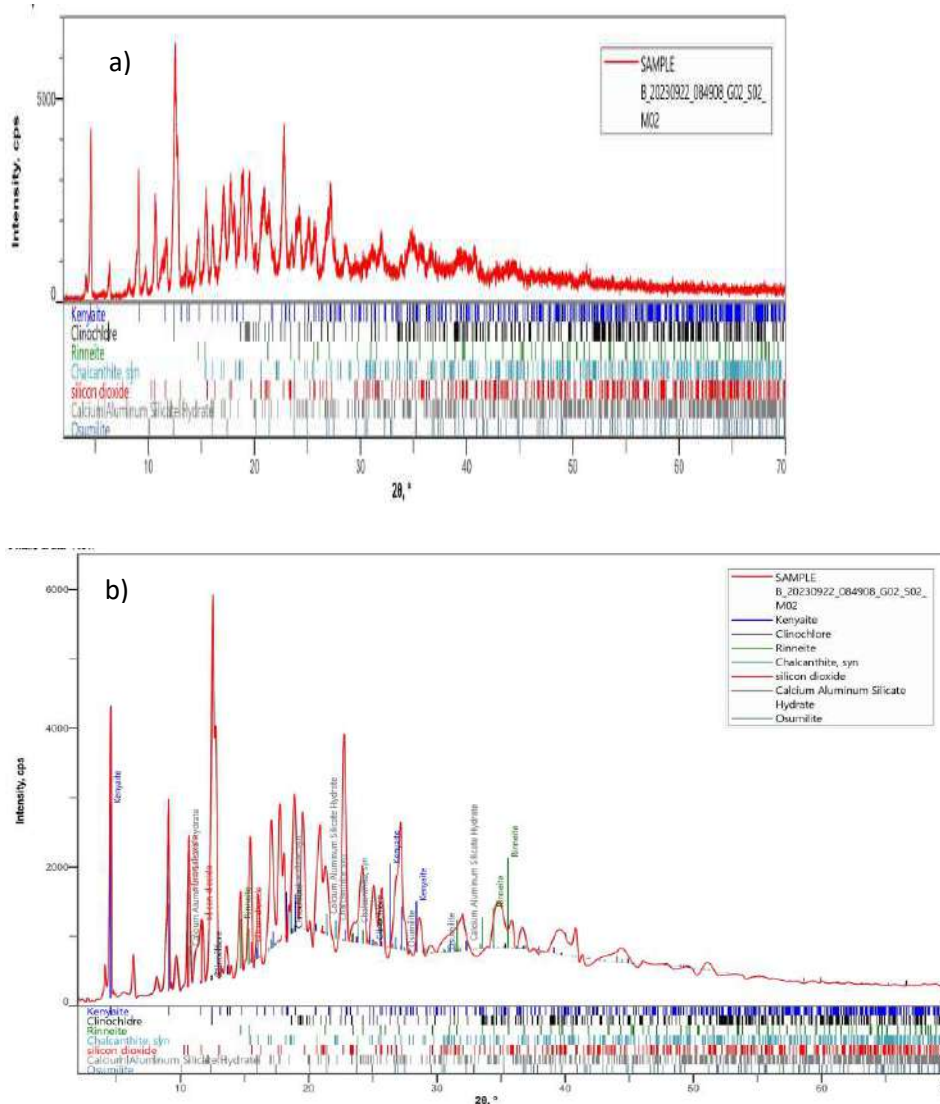
Fig. 6: XRD pattern of β-cyclodextrin (a), and β-cyclodextrin matched with standard (JCPDS card file).

XRD pattern of β-CD polymer. The findings, prominently featured in Fig. 6a unveiled a vivid portrayal of the XRD pattern of β-CD, covering a 2θ range from 0° to 70°. This XRD analysis astutely revealed the polycrystalline nature of β-CD, as evidenced by the presence of multiple peaks at various 2θ angles. This observation aligns harmoniously with previous research, as supported by the work of Musuc et al. (2020). In the XRD patterns of β-CD, a total of thirty-three (33) distinguishable peaks graced the spectrum. However, seven of these peaks stood out as particularly prominent. Positioned at 2θ angles of 4.600°, 9.0620°, 12.53°, 12.767°, 17.78°, 22.783°, and 27.08°, these peaks were accompanied by integrated intensities of 50, 447, 626, 923, 511, 675, and 597 counts per second (cps) respectively. Notably, the 2θ

values corresponding to these peaks closely mirrored the findings presented by Musuc et al. (2020).

Fig. 6b presents a comprehensive XRD analysis of β-CD polymer, thoughtfully compared with established standards, specifically the JCPDS card 00-054-1476. This analytical approach sought to unravel the phase composition and crystallite structure of the material, providing critical insights into its underlying characteristics. The findings depicted in Fig. 6b offer a compelling depiction of the XRD pattern of β-CD, extending over a 2θ range. What becomes apparent from this examination is the striking resemblance between the analyzed sample's XRD pattern and the reference standard for β-CD decahydrate ($C_{42}H_{70}O_{35}$-$C_7H_7NO_2 \cdot 10H_2O$) as

represented by the JCPDS card 00-054-1476. The XRD analysis indicates that all the diffraction peaks present in the sample's pattern are consistent with the monoclinic structure of β-CD decahydrate, further confirming its identity. This alignment between the sample's XRD pattern and the standard is significant, as it unequivocally establishes that the material under analysis is indeed β-CD decahydrate. The distinct peaks, their positions, and the overall pattern concur with the established reference, reinforcing the identity of the material.

Photocatalysis of Atrazine by β-Cyclodextrin

Effect of the irradiation time and β-cyclodextrin dosage: In the photocatalytic degradation of the ATZ using β-CD, the results demonstrate a dosage-dependent impact on the photocatalytic degradation over the specified time intervals

(Fig. 7). The lowest dosage of 0.1g β-CD at 5 minutes exhibited the lowest degradation efficiency of 6.2%, while the highest dosage of 0.5 g exhibited a higher degradation of 17.6%. This trend continued through the subsequent time of the study, with the 0.5 g dosage consistently outperforming the 0.1 g dosages. Remarkably, at 60 minutes, the 0.1 g dosage caused 47.4% degradation, while the 0.5g dosage attained a moderately higher degradation efficiency of 59.4%.

Kinetics of Degradation

By assuming pseudo-first-order reaction kinetics, Equation 2 was used to deduce the photocatalytic rate constants (Ayanda et al. 2021).

$$-\frac{dATZ}{dt} = kATZ \Leftrightarrow \ln\left(\frac{ATZ_0}{ATZ_t}\right) = kt \qquad \ldots(2)$$
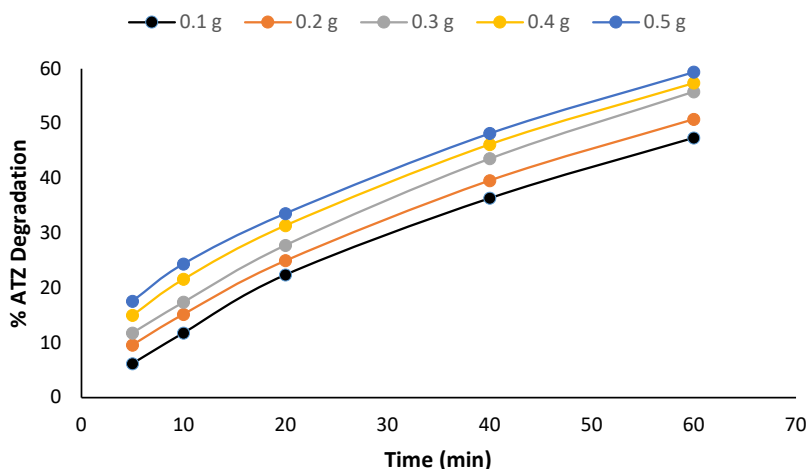
Fig. 7: Effect of the irradiation time and β-cyclodextrin dosage on the photocatalytic degradation of atrazine. *Experimental Condition:* Atrazine concentration = 50 mg/L, Volume of solution = 25 mL, Time = 5-60min, Nanomaterials dosage = 0.1-0.5g.
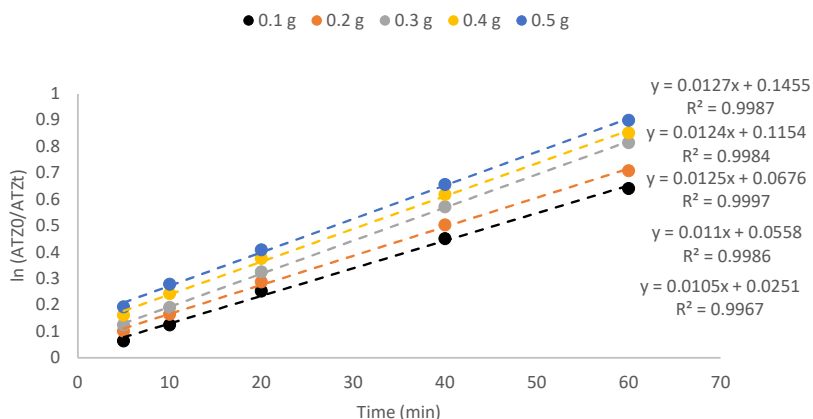
Fig. 8: Kinetics of atrazine photocatalytic degradation.

The kinetic plot is shown in Fig. 8. The removal of ATZ with variation in β-**CD** dosage (0.1-0.5 g) best fits pseudo-first-order kinetics with rate constants k and R^2 values of 0.0105 min^{-1}, 0.011 min^{-1}, 0.0125 min^{-1}, 0.0124 min^{-1} and 0.0127 min^{-1}. The R^2 values are 0.9967, 0.9986, 0.9997, 0.9984 and 0.9987, respectively.

Effect of Initial Concentration of Atrazine

For β-CD degradation of ATZ considering the initial concentration of ATZ, the results also reveal a concentration-dependent trend, showcasing that, higher initial concentrations of ATZ result in decreased degradation efficiencies (Fig. 9). For instance, at the lowest concentration of 6.25 mg/L, degradation rates were 28.0% at 5 minutes to 80.8% at 60 minutes. As the initial concentration increases to 100 mg/L, the resultant degradation rates decrease, ranging from 15.0% at 5 minutes to 59.4% at 60 minutes. This outcome aligns with common observations in photocatalysis, where higher initial concentrations can lead to increased competition for active sites on the catalyst surface, potentially affecting the overall efficiency of the photocatalytic process (Bagheri et al. 2017, Østergaard et al. 2024, Rehan et al. 2024).

Mechanism of degradation: The degradation of ATR by UV light catalyzed by β-CD followed the pseudo-first-order kinetics and depended on the concentration of ATR in the bulk solution (Equation 3). The integration of Equation 3 leads to Equation 4. Fig. 10 represents a plot of
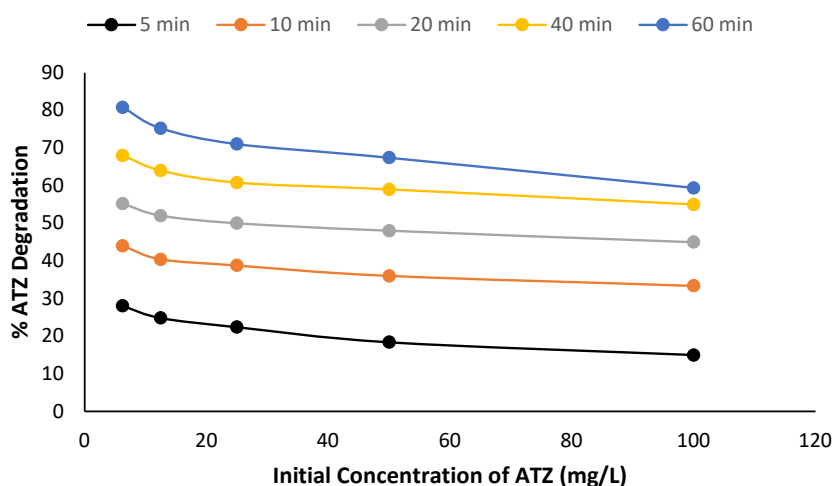
Fig. 9: Effect of initial concentration of atrazine. *Experimental Condition:* Atrazine concentration = 6.25-100 mg/L, Volume of solution = 25 mL, Time = 5-60min, Nanomaterials dosage = 0.5g.
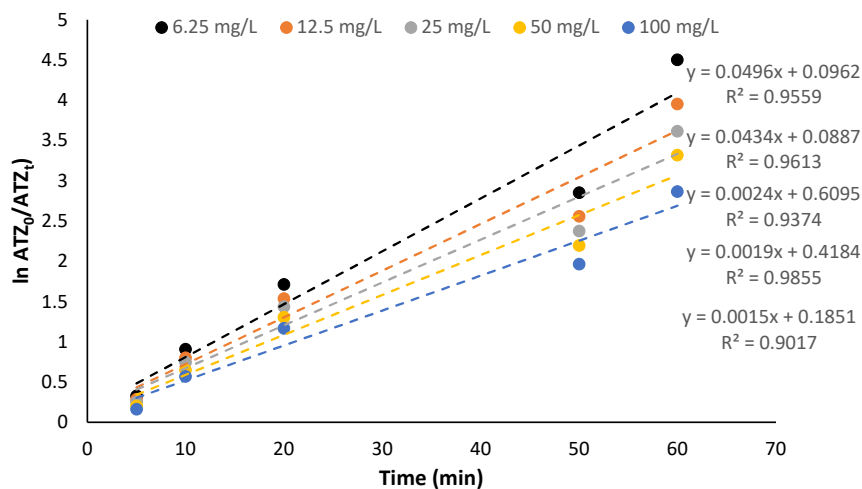
Fig. 10: Plot of $\ln\left(\dfrac{ATZ_o}{ATZ_t}\right)$ vs Time.
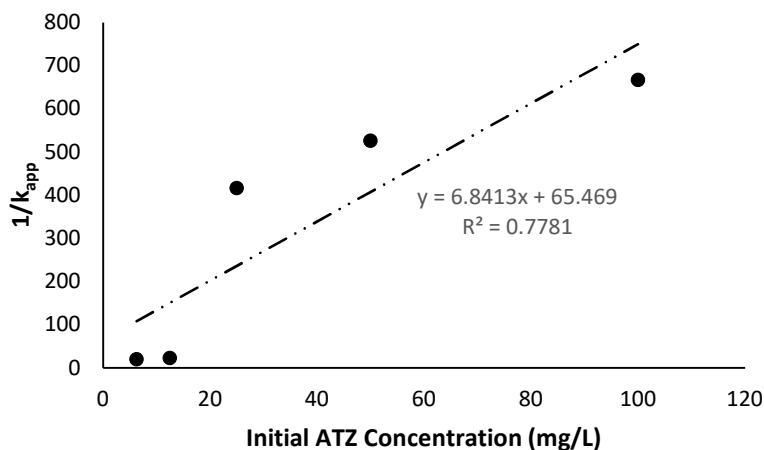
Fig. 11: Langmuir-Hinshelwood kinetic plot.

$$\ln\left(\frac{ATZ_o}{ATZ_t}\right) \text{ vs } t.$$

$$r = -\frac{dATZ}{dt} = k_{app}t \qquad \ldots(3)$$

$$\ln\left(\frac{ATZ_o}{ATZ_t}\right) = k_{app}t \qquad \ldots(4)$$

The apparent pseudo-first-order rate constants obtained from the Langmuir–Hinshelwood model for UV light-catalyzed degradation of ATZ using β-CD, signified by k_c 0.1462 mgL^{-1}min^{-1} and K_{LH} 10.45×10^{-2} Lmg^{-1} (Table 1), gave important understandings into the mechanism of the reaction. The relatively higher K_{LH} and lower k_c values imply a substantial adsorption affinity and a moderate degradation rate, implying that the degradation efficiency is influenced by the adsorption of the reactant onto the β-CD surface (Jerjes et al. 2020). This result underlines the potential of β-CD as a catalyst in UV light-induced degradation reactions.

To determine the mechanism of action of the UV light catalyzed by β-CD, a heterogeneous kinetic model

Table 1: The apparent pseudo-first-order rate constants (*kapp*), R^2, and Langmuir–Hinshelwood model constants.

Atrazine (mg/L)	Rate Equations	K_{app} (min^{-1})	R^2	k_c (mg/L/min)	K_{LH} (L/mg)
6.25	0.0496x + 0.0962	0.0496	0.9559	0.1462	10.45×10^{-2}
12.5	0.0434x + 0.0887	0.0434	0.9613		
25	0.0024x + 0.6095	0.0024	0.934		
50	0.0019x + 0.4184	0.0019	0.9855		
100	0.0015x + 0.1851	0.0015	0.9017		
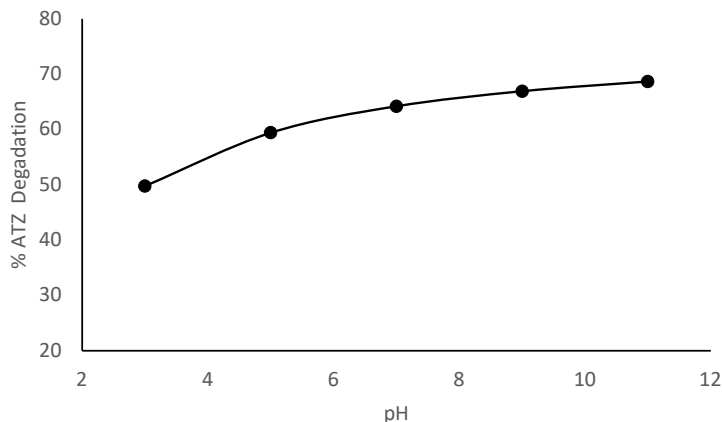
Fig. 12: Effect of pH on the photocatalytic degradation of atrazine. *Experimental Condition:* Atrazine concentration = 50 mg/L, Volume of solution = 25 mL, Time = 60min, Nanomaterials dosage = 0.5g.

(Equation 5) based on a Langmuir-Hinshelwood (L-H) model was applied (Ayanda et al. 2022), as presented in Fig. 11.

$$\frac{1}{k_{app}} = \frac{1}{k_c K_{LH}} + \frac{ATZ_o}{k_c} \qquad \dots(5)$$

The apparent pseudo-first-order rate constants (k_{app}), R^2 values, and the Langmuir-Hinshelwood model constants are presented in Table 1.

Effect of pH: Examining the influence of pH on the photocatalytic degradation of ATZ using β-CD also revealed an interesting result (Fig. 12). The results show that at pH 3, the lowest degradation of 49.76% was observed, signifying that the acidic conditions may have disturbed the photocatalytic activity of β-CD. As the pH increases, there is a steady increase in degradation efficiency, with pH 5 resulting in 59.4%, pH 7-64.2%, pH 9-66.9%, and the highest degradation observed at pH 11 with 68.7%.

This pH-dependent pattern supports the general understanding of photocatalytic reactions, where the surface charge of the catalyst and the nature of reactive species can be influenced by the pH of the solution (Li et al. 2019).

CONCLUSIONS

Cyclodextrins are cyclic oligosaccharides that have a high capacity for molecular inclusion. Within the discipline of environmental chemistry, cyclodextrins have been observed for their capacity to facilitate the breakdown of contaminants in aqueous solutions. Therefore, this study involved the detailed characterization of β-CD polymer, followed by the photocatalytic degradation of ATZ using β-CD polymer as a catalyst. The EDS analysis revealed oxygen (O) and carbon (C) as the main constituents of the β-CD. The identification of functional groups by FTIR helped to understand the molecular structure and properties of β-CD. The surface area of β-CD was 285.02 m²/g with the z-average diameter determined as 63.21 nm. The XRD analysis indicated that all the diffraction peaks present in the sample's pattern are consistent with the monoclinic structure of β-CD decahydrate. The TGA data demonstrate weight loss events, suggesting decomposition or significant changes in β-CD, while the DTA data reveal associated energy changes during phase transitions. The endothermic and exothermic peaks in the DTA curve align with the weight loss events observed in the TGA data, providing a comprehensive and coherent understanding of β-CD's thermal behavior.

The remediation studies demonstrated a dosage-dependent impact on the photocatalytic degradation over the specified time intervals, and considering the initial concentration of ATZ, the results revealed a concentration-dependent trend,

showcasing that, higher initial concentrations of ATZ result in decreased degradation efficiencies. The photodegradation of ATZ in the presence of β-CD is pH-dependent i.e., a higher percentage degradation was observed at higher pH when compared to a lower pH of ATZ solution. The highest degradation efficiency of 80.80% was achieved when 25mL of 6.25 mg/L of ATZ was subjected to UV irradiation in the presence of 0.5 g of β-CD for 60 min. This study has shown that ATZ can be effectively treated with UV light and β-CD polymer as a photocatalyst.

REFERENCES

Altendji, K. and Hamoudi, S., 2023. Efficient photocatalytic degradation of aqueous atrazine over graphene-promoted g-C₃N₄ nanosheets. *Catalysts*, 13(9), p.1265.

Aremu, O.H., Akintayo, C.O., Nelana, S.M., Klink, M.J. and Ayanda, O.S., 2022. Optimization of influential parameters for the degradation of metronidazole contained in aquaculture effluent via sonocatalytic process: kinetics and mechanism. *Nature Environment and Pollution Technology*, 21(4), pp.1875-1885.

Assaker, K. and Rima, J., 2012. Improvement of spectrophotometric method for the determination of atrazine in contaminated water by inducing of Mannich reaction. *Journal of Food Research*, 1(4), p.17.

Ayanda, O.S., Aremu, O.H., Akintayo, C.O., Sodeinde, K.O., Igboama, W.N., Oseghe, E.O. and Nelana, S.M., 2021. Sonocatalytic degradation of amoxicillin from aquaculture effluent by zinc oxide nanoparticles. *Environmental Nanotechnology, Monitoring & Management*, 16, p.100513.

Ayanda, O.S., Oforkansi, C.C., Aremu, O.H., Ogunjemiluyi, O.E., Olowoyeye, O.L. and Akintayo, C.O., 2022. Degradation of amido black dye using ultra-violet light catalyzed by iron oxide nanoparticles: kinetics and mechanism of degradation. *Catalysis Research*, 2(3), pp.1-11.

Bagheri, S., TermehYousefi, A. and Do, T.O., 2017. Photocatalytic pathway toward degradation of environmental pharmaceutical pollutants: structure, kinetics and mechanism approach. *Catalysis Science & Technology*, 7(20), pp.4548-4569.

Bratu, I., Veiga, F., Fernandes, C., Hernanz, A. and Gavira, J.M., 2004. Infrared spectroscopic study of triacetyl-β-cyclodextrin and its inclusion complex with nicardipine. *Spectroscopy*, 18(3), pp.459-467.

Duan, Z., Zhang, M., Bian, H., Wang, Y., Zhu, L., Xiang, Y. and Xia, D., 2020. Copper (II)-β-cyclodextrin and CuO functionalized graphene oxide composite for fast removal of thiophenic sulfides with high efficiency. *Carbohydrate Polymers*, 228, p.115385.

Jerjes, W., Theodossiou, T.A., Hirschberg, H., Høgset, A., Weyergang, A., Selbo, P.K., Hamdoon, Z., Hopper, C. and Berg, K., 2020. Photochemical internalization for intracellular drug delivery. From basic mechanisms to clinical research. *Journal of Clinical Medicine*, 9(2), p.528.

Jia, J., Wu, D., Yu, J., Gao, T., Guo, L. and Li, F., 2024. Upgraded β-cyclodextrin-based broad-spectrum adsorbents with enhanced antibacterial property for high-efficient dyeing wastewater remediation. *Journal of Hazardous Materials*, 461, p.132610.

Kamiya, M., Kameyama, K. and Ishiwata, S., 2001. Effects of cyclodextrins on photodegradation of organophosphorus pesticides in humic water. *Chemosphere*, 42(3), pp.251-255.

Kasprzak, A. and Poplawska, M., 2018. Recent developments in the synthesis and applications of graphene-family materials functionalized with cyclodextrins. *Chemical Communications*, 54(62), pp.8547-8562.

Li, C., Huang, Y., Dong, X., Sun, Z., Duan, X., Ren, B., Zheng,

S. and Dionysiou, D.D., 2019. Highly efficient activation of peroxymonosulfate by natural negatively-charged kaolinite with abundant hydroxyl groups for the degradation of atrazine. *Applied Catalysis B: Environmental*, 247, pp.10-23.

Li, Y., He, Z.D., Zheng, Q.E., Hu, C. and Lai, W.F., 2018. Hydroxypropyl-β-cyclodextrin for delivery of baicalin via inclusion complexation by supercritical fluid encapsulation. *Molecules*, 23(5), p.1169.

Liu, Q., Zhou, Y., Lu, J. and Zhou, Y., 2020. Novel cyclodextrin-based adsorbents for removing pollutants from wastewater: A critical review. *Chemosphere*, 241, p.125043.

Liu, Z.B., Yang, C. and Zhao, S.C., 2011. Research of photocatalytic degradation of pesticide with sulfonated β-cyclodextrin. *Advanced Materials Research*, 183, pp.1442-1445.

Morin-Crini, N., Fourmentin, M., Fourmentin, S., Torri, G. and Crini, G., 2018. Silica materials containing cyclodextrin for pollutant removal. *Cyclodextrin Applications in Medicine, Food, Environment and Liquid Crystals*, pp.149-182.

Musuc, A.M., Anuta, V., Atkinson, I., Popa, V.T., Sarbu, I., Mircioiu, C., Abdalrb, G.A., Mitu, M.A. and Ozon, E.A., 2020. Development and characterization of orally disintegrating tablets containing a captopril-cyclodextrin complex. *Pharmaceutics*, 12(8), p.744.

Østergaard, M.B., Egea-Corbacho, A., Wang, D., Deganello, F., Boffa, V. and Jørgensen, M.K., 2024. A self-cleaning thermocatalytic membrane for bisphenol A abatement and fouling removal. *Journal of Membrane Science*, 693, p.122336.

Rachmawati, H., Edityaningrum, C.A. and Mauludin, R., 2013. Molecular inclusion complex of curcumin–β-cyclodextrin nanoparticle to enhance curcumin skin permeability from hydrophilic matrix gel. *AAPS PharmSciTech*, 14, pp.1303-1312.

Rajamohan, R., Raorane, C.J., Kim, S.C. and Lee, Y.R., 2022. One pot synthesis of copper oxide nanoparticles for efficient antibacterial activity. *Materials*, 16(1), p.217.

Rehan, M., Montaser, A.S., El-Shahat, M. and Abdelhameed, R.M., 2024. Decoration of viscose fibers with silver nanoparticle-based titanium-organic framework for use in environmental applications. *Environmental Science and Pollution Research*, pp.1-22.

Sambasevam, K.P., Mohamad, S., Sarih, N.M. and Ismail, N.A., 2013. Synthesis and characterization of the inclusion complex of β-cyclodextrin and azomethine. *International Journal of Molecular Sciences*, 14(2), pp.3671-3682.

Velusamy, P., Pitchaimuthu, S., Rajalakshmi, S. and Kannan, N., 2014. Modification of the photocatalytic activity of TiO_2 by β-Cyclodextrin in decoloration of ethyl violet dye. *Journal of Advanced Research*, 5(1), pp.19-25.

Yadav, M., Thakore, S. and Jadeja, R., 2022. A review on remediation technologies using functionalized cyclodextrin. *Environmental Science and Pollution Research*, 29(1), pp.236-250.

Zhang, R., Ma, Y., Lan, W., Sameen, D.E., Ahmed, S., Dai, J., Qin, W., Li, S. and Liu, Y., 2021. Enhanced photocatalytic degradation of organic dyes by ultrasonic-assisted electrospray TiO_2/graphene oxide on polyacrylonitrile/β-cyclodextrin nanofibrous membranes. *Ultrasonics Sonochemistry*, 70, p.105343.

ORCID DETAILS OF THE AUTHORS

O. S. Ayanda: https://orcid.org/0000-0001-8022-8010

S. M. Yahaya: https://orcid.org/0000-0002-0159-8740

O. Adeyi: https://orcid.org/0000-0003-3479-5318

M. J. Klink: https://orcid.org/0000-0002-9131-6312

Eco Trauma: Unveiling the Anthropocentric Destruction, the Pathway to Apocalypse

Gajalakshmi G. and Meenakshi S.†

Department of English, School of Social Sciences and Languages, Vellore Institute of Technology, Vellore-632014, India

†Corresponding author: Meenakshi S.; meenakshi.s@vit.ac.in

ABSTRACT

Humans have evolved to the point where we are the most sophisticated animals in the world. The point of evolution is for creatures to become more suited to their natural habitat. A new degree of evolutionary adaption has been attained through humans. Massive technological advancements, new governments, and metropolises have all taken place. Every one of these societal advancements has one overarching goal: to ensure that our species continues to exist. As a species, we've figured out how to divide ourselves up into nations defined by shared values, religion, geography, and history. Divergences in geography, culture, and history have always been a source of contention among human beings. These disparities have, in the worst-case scenarios, led to war. Many various things, including religion and wealth, have sparked wars throughout history. War, though, never ends well; destruction is an inevitable byproduct. After a conflict, everyone is talking about how many lives were lost, how much property was destroyed, and how much money was spent. But the ecosystem is a quiet casualty of war. Seldom given a second thought are the deaths and devastation that befall Earth's ecosystems, natural resources, and population. One can not help but question the impact of modern warfare on the environment and the consequences for humanity as a whole. The moral and social consequences of modern warfare's assault on the environment can be seen by looking at the historical record of environmental degradation caused by this conflict. It is possible to learn about past and future efforts to safeguard the environment from human aggression by considering the problem from philosophical, scientific, and religious vantage points. If the Earth is to be further devastated by contemporary weaponry and combat, the loss endured by the environment will make the death toll of any contemporary battle appear negligible. The preservation of the natural world is crucial to the continuation of the human race.

INTRODUCTION

The Anthropocene Epoch is an informal designation within the field of geology, employed to delineate the latest epoch in the chronology of Earth's history, during which the influence of human activity on the planet's climate and ecosystems became notably substantial. The term "Anthropocene" originates from the Greek terms "anthropo," meaning "man," and "cene," meaning "new." It was introduced and gained prominence in the year 2000 by biologist Eugene Stormer and chemist Paul Crutzen. The inquiry around the commencement of the Anthropocene, a purported novel geological epoch, has generated much scholarly discourse among scientists. One widely accepted hypothesis posits that the phenomenon under consideration originated around the onset of the Industrial Revolution in the 19th century. This pivotal period witnessed a substantial alteration in human activities, resulting in a significant perturbation of

carbon and methane levels within the Earth's atmosphere. There are differing perspectives regarding the proposed commencement of the Anthropocene epoch, with some advocating for its initiation to be traced back to the year 1945. During this period, human beings conducted the initial testing of the atomic bomb, subsequently deploying atomic bombs on the cities of Hiroshima and Nagasaki in Japan. The radioactive particles that ensued were identified in soil samples on a global scale. The experimental detonation of the bomb and the subsequent formation of a mushroom cloud gave rise to a potent and emblematic representation of the immense capacity for destruction inherent in the human race. The devastation caused due to war is less, but the aftereffects are tremendous.

Looking at the past is the first step in morally assessing the impact of war on the environment. One can start to discern a pattern of ecological devastation by looking closely at the

recent history of conflict. "The first fireball flung at the first enemy, in prehistory, probably began it all" (Davis 1998) although environmental degradation has been going on for far longer than that. The destruction of farms and fields, the damming of rivers, and the poisoning of water supplies have all been done by armies throughout history in the name of war. Even in biblical accounts, such as "the story of Samson and Philistines...tells of...direct environmental destruction," we witness examples of such devastation. "Samson set fire to the Philistines' fields, orchards, and olive trees" (Ghorani-Azam et al. 2016). According to Judges 9:45, while scouring the ancient city of Schechem, Abimelech had his warriors pour salt on the land, rendering it sterile. By destroying the city's water supply, Genghis Khan conquered Mediaeval Baghdad—one of the most advanced civilizations of its time (Clark 1993). The devastation of crops and other natural resources was just the beginning of ancient conflict. Evidence of chemical warfare dates back to the Peloponnesian War (674–2000 B.C.), the Battle of Constantinople in 674, and India circa 2000 B.C. (Graham 1993). Biological warfare was employed during the 1300s Mongol siege of Kaffa. Plague victims' corpses were hurled over city walls by the Mongols (Graham 1993). Not only did these chemical and biological weapons wipe out human populations, but they also damaged ecosystems and altered water cycles in the process. There would be an end to life on Earth as chemicals and biological agents seeped into the ecosystem. These earliest examples of ecological devastation due to human conflict show how far a man can push the environment, even with very basic tools and strategies.

The environmental damage has now reached a new degree of catastrophe. Environmental harm has escalated to unprecedented levels due to the development of chemical, nuclear, and biological weapons of mass destruction. This extraordinary degree of ecological devastation was first observed in World War I, the first big war. During this brutal conflict, new weaponry was introduced, each one capable of causing horrific damage. The French landscape and agriculture were levelled by the trenches. Because of how bad the destruction was in certain places; people are still feeling the effects today. Over 250,000 acres of arable land were declared unusable due to the extensive damage they sustained in the Somme conflict. Fighting also cut down 494,000 acres of forest in France. Allied war efforts required the harvesting of more than 20 billion board feet (Clark 1993). As with human populations, animal populations in Europe were decimated by the conflict. The wisent, or European buffalo, population was nearly wiped out due to the extensive clearing of forests across Europe (Graham 1993). The environmental devastation caused by World War I was not limited to Europe. The unexpected effects of the war on

American environmental health were substantial. The war effort necessitated farmers to produce more food than they could reasonably consume. This led to the widespread belief that the soil in many Great Plains areas was nutrient deficient and hence unproductive. Many North American species had their habitats destroyed when farmland expanded across the plains and into woodlands and wetlands.

PAST STUDIES OF RELEVANCE

The research paper investigates the impact of warfare on the environment using large-N statistical models. The authors theorize on the potential effects of warfare on CO_2 emissions per capita, NOx emissions per capita, forest change, and overall environmental stress reduction. They find that warfare significantly affects the environment, with impacts varying based on the environmental attribute examined, the location of the fighting (at home or abroad), and the level of economic development of the country. The study finds that warfare reduces CO_2 emissions, with weaker effects in less developed countries (LDCs) compared to developed countries (DCs). Contrary to conventional wisdom, warfare at home increases deforestation while promoting forest growth when fought abroad, especially in LDCs. Warfare at home reduces NOx emissions for the LDCs but increases them for the DCs, while warfare abroad increases NOx emissions for both. Additionally, warfare increases aggregated environmental stress, particularly for the LDCs when fought at home and for the DCs when fought abroad. The study also provides insights into the implications of the findings for policymakers and suggests the need for further research on this topic. The research paper offers an empirical examination of the impact of warfare on the environment, providing valuable insights into the potentially substantial effects of warfare on various environmental indicators. The research paper, authored by Rafael Reuveny, Andreea S. Mihalache O'Keef, and Quan Li, delves into the effects of armed conflict on the environment, focusing on its impact on CO_2 emissions, forest change, NOx emissions, and environmental stress reduction. The authors acknowledge the assistance received from Nils Petter Gleditsch, three anonymous referees, and Melanie Arnold. Overall, the research paper aims to provide a comprehensive analysis of the impact of armed conflict on the environment, utilizing statistical data and analyses to explore the relationship between warfare and environmental variables. The paper's findings contribute to the understanding of the environmental consequences of armed conflict and provide valuable insights for policymakers and researchers.

The paper "*Impact of War on the Environment: A Critical Study of Afghanistan*" discusses the challenges in accurately documenting war fatalities, including those of

combatants and civilians, as well as quantifying the physical and environmental impacts of the conflict in Afghanistan. It highlights the environmental degradation caused by armed conflict, including the devastation of physical property, environmental pollution, and climate change, leading to mass migration and threats to human health. The paper emphasizes the need for environmental protection during armed conflict, citing international humanitarian law and protocols. It also discusses the adverse impacts of the US war in Afghanistan on the environment, natural resources, and the health of US service members and civilians. The paper provides a comprehensive analysis of the environmental consequences of war and the need for effective environmental protection measures during armed conflict.

The research paper delves into the complexities surrounding the principles, approaches, and methods for achieving full reparation for armed conflict-related environmental damage in the law of State responsibility. The paper examines the legal definition of the environment as an object of protection under international law and discusses practical challenges in international compensation for wartime environmental damage. It also delves into the valuation of environmental losses, particularly in the context of armed conflict, and the challenges in quantifying ecological services that are not traded in the market. The paper emphasizes the dynamic nature of the environment and the interactivity between human and natural systems. It provides insights into the practical challenges in assessing wartime environmental damage, including the temporal scale for reparation, limited baseline information, and establishment of the causal nexus. It also discusses the difficulties in quantifying environmental damage and valuing ecosystem services in monetary terms. Moreover, the paper addresses the impact of environmental damage on public health and emphasizes the relationship between reparation for the environment and the well-being of humankind. It also highlights the need to consider the relationship between environmental damage and public health as integral components of the reparation process. The paper highlights the difficulties in establishing causality and the need for specific criteria for environmental damage resulting from armed conflict. It also addresses the challenges of valuing environmental damage and suggests the establishment of a permanent UN body to evaluate and compensate for environmental damage during armed conflicts. The paper emphasizes the evolving nature of environmental protection in relation to armed conflict and the importance of protecting the environment in times of peace and conflict.

The paper discusses the impact of human evolution on the development of societies, governments, and conflicts, leading to the organization of humans into different countries based on various factors. It explores how disagreements and conflicts have arisen as a result of differences in borders, values, and heritage, leading to wars fought for reasons such as religion and money. The paper provides a historical analysis of the environmental destruction caused by modern warfare, including examples from World War I, World War II, the Vietnam War, and the Gulf War. It highlights the catastrophic environmental effects of warfare, such as the destruction of farmland, forests, wildlife, and ecosystems, as well as the release of chemicals and oil spills. The paper also addresses the ethical, moral, and social ramifications of the environmental toll of war and discusses the responsibility of humans to protect the environment. It mentions international treaties and laws aimed at protecting the environment during warfare and the efforts made within the U.S. military to become more environmentally conscious (Ellis-Petersen 2019). Ultimately, the paper concludes that war has significantly reduced the overall environmental health of the Earth and suggests that the only way to truly protect the environment from war is to end war itself.

MATERIALS AND METHODS

This study employed qualitative research methods. The qualitative study findings were gathered from a variety of secondary sources, including media articles, academic journal articles, and past theses. A discourse analysis method was used throughout this study, and several case studies were gathered from news articles and journals to provide a brief overview of the impacts of the climate crisis. For this research, various approaches were taken to bring forward the major issues of the study. Through the research and statistics available, the relationship between the environment and humans is clear. War has various impacts on the environment, but the main cause is human intervention.

War and Consequences

Throughout history, conflicts and military engagements have persisted, leading to a continuous series of wars up until the present day. The planet Earth has a rich historical record of warfare, which has undergone significant transformations for millennia. Historically, it was customary for a warrior to go from his place of residence in the early hours of the day to engage in combat. The individual possessed the understanding that, unless subjected to fatal harm or rendered unable to function, he would be reunited with his community later that evening. However, over time, this phenomenon transformed, as certain conflicts extended over prolonged periods, spanning several decades. The tools employed in warfare undergo continuous evolution and growth, although the fundamental context of conflicts remains largely unaltered. In ancient times, the warrior relied on the forest

as a crucial resource for its influence on the air quality of the area. However, the introduction of fire as a weapon likely had an impact on the contemporary environment. Without a doubt, the ramifications of fire resulting from natural occurrences, such as lightning discharges and volcanic outbursts, would have been considerably more severe during that period. In contemporary times, warfare has seen significant transformations. The weaponry exhibits a diverse range of capabilities and adaptability, resulting in multifaceted impacts on the environment and air quality that humans inhale. These consequences manifest before, during, and after each occurrence, in addition to the primary objective of eliminating adversaries. Currently, it is feasible to observe unfolding events in real time. However, there is a notable absence of discourse regarding the anticipated consequences for individuals directly involved in these operations, the noncombatant populace, and future generations burdened by air pollution.

While wars are primarily driven by political, economic, social, and ideological factors, environmental considerations can play a role in the dynamics and armed conflicts. War solely doesn't happen for environmental reasons, but the factors initiating war have environmental factors often intertwined. What is immediately striking is that today's regional conflicts take place against a background of widespread poverty and misery in particularly stressed countries. Sometimes, in highly militarized but weak, poorly performing states and fragmented societies with endemic competition between ethnic or religious groups. The scarcity of natural resources and environmental degradation may also be the reason for interring group violence and anti-regime struggles. Conflicts happen over scarce natural resources like water, minerals, land, etc. Nations engage in conflict to gain strategic resources such as oil or valuable minerals. Environmental factors need not be the prime reason for a conflict to arise, but indirectly, in all aspect's environment becomes a point where either conflict arises or it is being affected due to the conflict. For instance, from Table 1 the causes and consequences can be seen.

From Table 2, it is known that conflicts are a widespread phenomenon. Throughout history, with the arrival of the Industrial Revolution and following developments in armament, warfare has become a powerful and threatening phenomenon. The battles that occurred in ancient times under the governance of monarchs did have environmental repercussions, although they did not have a long-lasting impact. Wood was utilized as the major material in the production of weapons. Wars have resulted in various adverse effects, including the depletion of forests, disruption of agricultural practices, and devastation of urban areas.

Nevertheless, these disputes involved humans rather than automatons. The wars did not result in substantial

Table 1: War and its causes.

WARS	CAUSES
IRAQ WAR (2003-2011)	Control of oil resources
CONGO WARS (1996-2003)	Control of minerals such as Colton, which is used in electronic devices.
1st LIBERIAN CIVIL WAR (1989-1997)	Over resources such as rubber, iron, and timber.
DARFUR CONFLICT (2003-PRESENT)	Over scarce resources like water and land.
NIGER DELTA CONFLICT (2004- present)	Control of oil resources.
SOUTH CHINA SEA DISPUTES (ongoing)	Claim overfishing rights, oil, natural gas reserves, and control over shipping lanes.
ANGOLAN CIVIL WAR (1975-2002)	Control over oil wealth.

Table 2: War and consequences. Wars that caused heavy environmental damage.

Wars	Consequences
Vietnam War (1955-1975)	Destroyed jungle foliage, land-water contamination, long long-lasting ecological damage.
Gulf War (1990-1991)	The Gulf oil spill caused damage to the marine ecosystem.
Iraq War (2003-2011)	The burning of oil wells and targeting of industrial facilities led to air and soil pollution.
Yugoslav War (1991-2001)	Destruction of oil sites and bombing of infrastructure contributed to pollution.
Syrian Civil War (2011- Present)	Destruction of chemical plants and oil spills led to pollution of water and soil.
Kuwait War (1990-1991)	Release of oil into Persian Gulf, burning of oil fields and oil wells.
Cambodian Civil War (1967-1975)	The bombing by the US caused environmental damage.
Lebanese Civil War (1975-1990)	The destruction of infrastructure and the release of pollutants contributed to long-term environmental challenges.

enduring repercussions. The widespread dissemination of nuclear weapons in modern times has greatly contributed to the incidence of armed conflict, mostly fuelled by scientific progress. This development has had significant and harmful repercussions on both present and future generations. As an illustration, the United States rapidly utilized nuclear weapons in Hiroshima and Nagasaki, leading to long-lasting hereditary abnormalities throughout the impacted populace, encompassing children and future generations.

Political Ecology

The study conducted in anthropology, geography, and allied fields is very significant for its examination of how structural forces, such as capitalist economic processes and power dynamics, contribute to environmental change in our increasingly linked world. The approach was characterized by a famous political scientist named Richard A Matthew. He has made a significant contribution to the study of environmental dimensions of armed conflict. He put forth the political ecology theory to understand the environmental consequences of armed conflict. Armed conflict can lead to environmental degradation, impacting communities' access to essential resources and exacerbating vulnerabilities. He also explores how military activities contribute to environmental harm. These include the use of weapons and tactics that can lead to deforestation, soil contamination, and habitat destruction.

Air Pollution

Aristotle regarded air as one of the five important elements of life on the planet. Pollution of the air must concern everyone. In the declaration of the 1972 Stockholm Conference, there was no mention of the relevance of war in the pollution of the environment, although, in Principle 6, there is a reference to '…. the release of heat to such quantities or concentrations to exceed the capacity of the environment……'. The environmental consequences of war, specifically in relation to air pollution, are initiated by the research, experimentation, and evaluation of various components associated with military weaponry, equipment, and ammunition, as well as the essential training required for their deployment (Protopsaltis 2012).

Beginning in 1945 and continuing until 2009, several governments were actively working towards the creation of nuclear weapons. According to the findings of the study, which included more than two thousand tests carried out over sixty-four years, there is no space for doubt regarding the major impact on air quality, as stated in Fig. 1. It was largely believed that this influence was caused by the emission of chemicals into the atmosphere, in addition to the subsequent addition of heat to the system of the Earth (Protopsaltis 2012). The patterns of natural air currents over land and sea were influenced by these elements, which in turn affected the flora, wildlife, and human population of the globe. Wars have been around for a very long time on Earth and have "evolved" in a significant way throughout history. Historically, to engage in combat, warriors would leave their homes during the early morning hours to make their way to the battlefield. The individual was aware of the fact that they would be reunited with their community later that evening, provided that they were not exposed to any harm that might result in death or physical impairment. On the other hand, this phenomenon went through substantial changes over time, as many confrontations lasted for several decades. Even though the underlying framework of battles is mostly unchanged, the technologies that are used in warfare are always evolving and growing. When it came to the acquisition of wood, which was used in the manufacturing of bows and arrows, historical warriors relied heavily on the forest as a vital resource available to them. However, the conflict had a relatively minor impact on the air quality of the environment even though the forest was
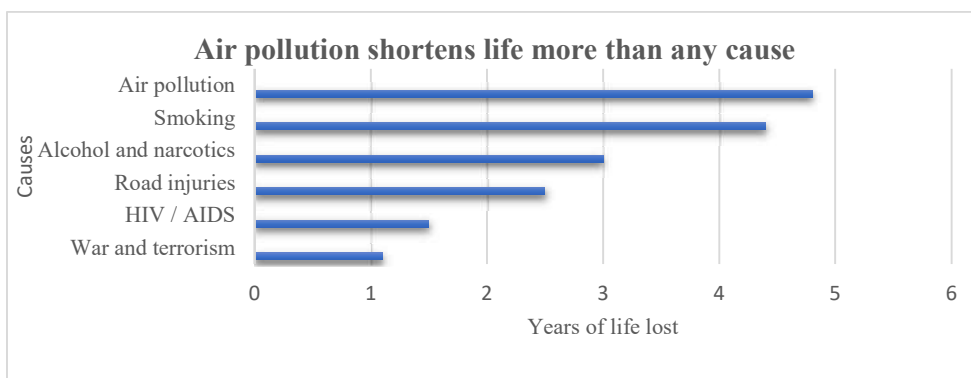

Fig. 1: Causes of Air Pollution.

significantly affected by its consequences. The use of fire as a weapon, on the other hand, very likely had some impact on the environment that we live in today. Without a shadow of a doubt, the repercussions of fires that were caused by natural phenomena, such as lightning strikes and volcanic eruptions, would have been significantly more catastrophic during that period.

Throughout modern history, there have been substantial shifts in the character of warfare. The weapons demonstrate a wide range of capabilities and adaptability, which results in a variety of effects, particularly on the environment that is surrounding it and the air quality that people breathe in. In addition to the fundamental purpose of eradicating the presence of the opponent, these repercussions reveal themselves before, during, and after each instance of weapon deployment (Protopsaltis 2012). The ability to witness events in real-time is currently available, although there is little to no discussion about the potential implications that may be incurred by persons who are involved in the operations, civilians who are not involved in the conflict, and future generations who will be impacted by the air pollution that is caused by these activities. Fire has always been a significant component in battle, and it appears that it reached a respectable degree of proficiency during World War II. This is something that has been the case throughout the years. In the course of carpet-bombing air operations, incendiary bombs were developed and later utilized on a massive scale. Guernica was the target of continuous bombing by the Spanish Air Force and its allies for forty-eight hours during the Spanish Civil War in 1937. The bombing lasted for the whole duration of the conflict. Consequently, this bombardment led to the formation of a firestorm, which was distinguished by the development and maintenance of its wind system because of the increased intensity of the fire. A state that is comparable to that which is seen in an industrial incinerator may be observed in the scenario that was presented earlier, in addition to the fact that human lives were lost in the situation. Nevertheless, within the walls of an industrial incinerator, all materials are exposed to controlled combustion processes following regulatory standards, with the primary goal of reducing the amount of pollution that is released into the atmosphere. In the context of the Guernica tragedy, all of the things that were preventing the advancement of the fire were destroyed, and there was no sort of protection against air contamination. Certain types of pollution may be still present in the present day. It is dependent on the meteorological conditions that are now in place whether or not there is a possibility of getting airborne and engaging in continuous migration.

During World War II, many cities in Germany, Poland, and Japan were affected by the production of firestorms

that were similar to the phenomenon. Both in the places that were immediately affected by the war and in regions that were placed along the predominant air currents, the potential environmental implications that could have resulted from the actions of the war were not fully examined or acknowledged, both at the time of the conflict and in future years. Given the highly intense and concentrated character of firestorms, it is of the utmost importance to conduct an assessment of the volume of the heat that is produced during these events (Nilson & Burke 2002). Thermal energy is distributed throughout the surrounding air, with the majority of it being contained within the atmosphere of the Earth, and as a result, it contributes to the overall thermal load. World War I was one of the most significant wars that took place in the early part of the twentieth century with a significant impact. During the conflict, which lasted for more than four years, both sides deployed a significant amount of military force, with the majority of their operations taking place within the European continent. The event represented the beginning of the widespread use of chemical weaponry as well as the deployment of munitions that were becoming increasingly powerful. The majority of the thermal energy that was produced during this conflict was unable to escape from the system of the planet when it was released. Over time, it went through the process of dispersion and became mixed in with the air in the atmosphere, which affected the thermal conditions that were already present inside the air. The fight in Ethiopia and the battle in the Spanish Civil War were both subsequent events that occurred within the period immediately following World War II. In the beginning, the majority of the conflict took place in Europe; however, it eventually was extended to include both Asia and the Pacific. The struggle covered numerous forms of warfare, including ground conflicts, naval engagements, the targeting and destruction of cargo vessels, aerial fighting and bombings, the deployment of flying bombs and ballistic missiles, and finally, the usage of atomic armament. Between the years 1939 and 1945, a substantial period of intense conflict took place in many different regions, including Japan, Europe, the Middle East, North Africa, and the Pacific islands. Around twenty-five cities in Europe and fifty-five cities in Japan were affected by destruction that ranged from forty percent to eighty percent.

The Keelings curve in Fig. 2, generated by the Intergovernmental Panel on Climate Change (IPCC), is presented here. This passage was subsequently cited in an Inconvenient Truth by AI Gore. The graph displays the temporal variation of the "temperature average." Additionally, it displays the coordinates of the recorded temperature. The IPCC graph illustrates a steady rise in temperature from 1900 to 1950, reaching its highest

The Keeling Curve: current global average

Atmospheric CO_2, parts per million
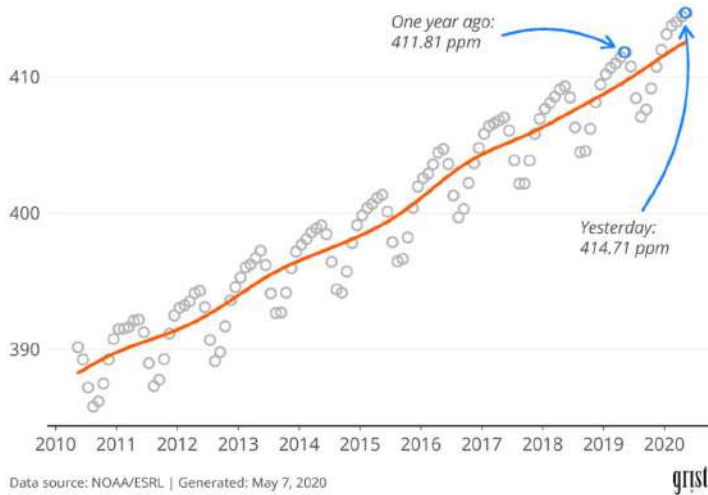
Fig. 2: The Keelings curve.

How many people die from air pollution each year?

Estimates of the global death toll from air pollution published in major recent studies

'All sources' includes both anthropogenic and natural sources:
• The largest source of natural air pollution is airborne dust in the world's deserts. Other natural sources are fires, sea spray, pollen, and volcanoes.
• Anthropogenic sources include electricity production; the burning of solid fuels for cooking and heating in poor households; agriculture; industry; and road transport.

Data on annual death tolls from other causes is the latest data from the World Health Organization, UCDP, and Global Terrorism Database as of November 2021.
OurWorldinData.org – Research and data to make progress against the world's largest problems.
Licensed under CC-BY by the author Max Roser

Fig. 3: Death rate due to air pollution.

point during World War II. There are two notable surges towards the conclusion of World War II, which align with escalated warfare, including the devastation of numerous cities and the release of thermal energy from atomic weaponry.

There is a noticeable increase in temperature fluctuations noted from the time of the Spanish Civil War to the beginning of World War II. The temperature experienced a gradual decrease until 1975, followed by a significant increase until 2005. The increase in numbers corresponds

to the enduring state of war that continued until 2005. Since 1970, there has been a clear association between the increase in the height of the ordinates and the incidence of key events such as the Gulf War, the Iran-Iraq War, war activities in Southern Europe, the war in Afghanistan, and the World Trade Center tragedy. These events likely had a significant impact on the rise in temperature within the Earth's atmosphere. The Gaia hypothesis suggests that the biotic and physical components of the Earth are closely linked, forming an intricate network of interactions that maintain the climatic and biochemical conditions of our planet in a stable state of balance. Undoubtedly, based on the evidence, one may argue that the planet's design, probably implemented during its construction, does not allow for trivial actions.

Effects of Air Pollution

The World Health Organisation (WHO) presents empirical evidence establishing associations between exposure to air pollution and the occurrence of type 2 diabetes, obesity, systemic inflammation, Alzheimer's disease, and dementia. The International Agency for Research on Cancer (IARC) has officially designated air pollution, specifically PM2.5, as a prominent contributor to the development of cancer (Greentumble 2018). According to a recent comprehensive global analysis, prolonged exposure to certain factors has the potential to impact many bodily organs, hence potentially worsening and intensifying pre-existing health issues. Children and teenagers are considered to be particularly susceptible to many health risks due to the ongoing development of their bodies, organs, and immune systems.
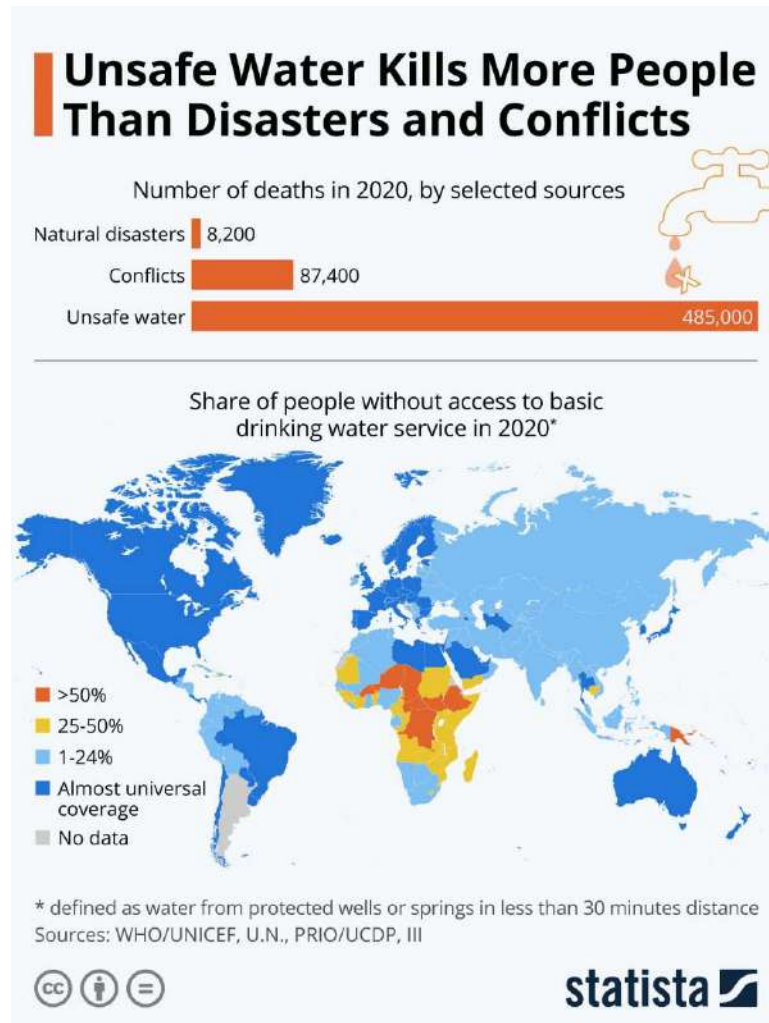
Fig. 4: Death due to water pollution (Buchholz 2022).

Childhood exposure to air pollution has detrimental effects on health and is associated with an elevated susceptibility to diseases in adulthood, as shown in Fig. 3. However, children possess limited agency in safeguarding their well-being or exerting influence over air quality policies (Roser 2023).

Water Pollution

Thomas Homer-Dixon contends that it is difficult to locate distinct historical or modern instances of significant conflicts driven primarily by shortages of renewable resources like crops, woods, fish, and freshwater, despite worries that future conflicts may be fought over water. In August 1995, Ismail Serageldin, the Vice-President for environment sustainable development at the World Bank, presented a fresh report on global water challenges during a meeting in Stockholm. The research and its accompanying speech delineated an incipient water crisis in the Middle East, North Africa, and several nations, encompassing India and China. Mr. Serageldin stated that soon, the primary limitation for agricultural productivity in many regions will be the availability of water rather than land. Water resources are essential for promoting sustainable development and have a pivotal role in attaining Sustainable Development Goals (Clark 1993). Armed conflicts have the potential to disrupt water systems in various ways, leading to adverse effects that range from the supply of essential water services to development initiatives. Water, often hailed as the essence of life, is also recognized as a major transmitter of diseases. Consequently, the world is rapidly heading towards an impending catastrophe (Haseena et al. 2017).

According to a study undertaken by the World Health Organisation (WHO), water serves as a vector for several diseases (Lin et al. 2022). Female individuals who ingest this contaminated water are prone to transmitting the consequences to subsequent generations. Recent research has discovered the presence of microplastics in breast milk. The researchers assert that although the inference may be imprecise, it is highly likely that the pathogen entered the body via consumption of contaminated food and drink. Significant quantities of plastic debris are indiscriminately disposed of in the environment, while microplastics pervade the entire world, spanning from the peak of Mount Everest to the depths of the oceans. Individuals ingest the minuscule particles by ingestion of food and water, as well as inhalation, and these particles have been detected in the excrement of both infants and adults (Schillinger et al. 2020). Fig. 4 shows how dangerous water pollution is than other causes.

Chemical defoliants were used on an estimated ten percent of the land in South Vietnam between the years 1961 and 1975 to boost the effectiveness of bombing operations during the Vietnam conflict. This was done to boost the effectiveness of bombing operations (Rathi 2016). The usage of chemical agents has a significant influence on the water resources that are available in the region (region). The repercussions included a variety of factors, including the contamination of water sources, the increase in runoff and sedimentation, and the increase in the number of malarial illnesses that occurred as a result of bodies of water that remained stagnant. The coastal areas that have been cleared of vegetation have also witnessed an increase in their vulnerability to the harm that is produced by storms. Approximately one-quarter of the world's population is currently dealing with a severe lack of water, and they are facing acute water shortages for at least one month out of every year. According to Kitty van der Heijden, a specialist in hydro politics and the chief of international cooperation at the foreign ministry of the Netherlands, the absence of water would encourage individuals to commence migration(Schillinger et al. 2020). According to estimates provided by the United Nations and the World Bank, approximately forty percent of the world's population is affected by water scarcity. There is a possibility that over 700 million people could be put at risk by drought conditions by the year 2030, which could result in the prospect of people being forced to relocate. Many people, including van der Heijden, have expressed their concern about the potential outcomes that could be brought about by this circumstance. "If there is no water, politicians are going to try and get their hands on it, and they might start to fight over it," adds the politician (Milne 2021).

Over the 20th century, the rate of water consumption on a global scale increased at a rate that was greater than twice as fast as the rate of population growth. In the present moment, the presence of this incongruity is forcing a great number of urban places, ranging from Rome to Cape Town, Chennai to Lima, to impose water rationing measures. Since 2012, water crises have been routinely ranked among the top five of the Global Risks by Impact list, which is compiled by the World Economic Forum (Lin et al. 2022). This has been the case for almost a decade, beginning in 2012. The year 2017 was marked by the occurrence of severe droughts, which played a key role in compounding the most catastrophic humanitarian catastrophe that has occurred since the Second World War. Approximately twenty million people were forced to flee their homes across Africa and the Middle East as a direct consequence of this crisis. This was mostly due to the simultaneous shortages of food and the subsequent wars that arose when these shortages occurred. For the past three decades, Peter Gleick, who is the chairman of the Pacific Institute in Oakland, has been spending his time researching the connection between water scarcity, war, and migration (Rothschild & Haase 2023). As a result of his belief that water disputes are on the rise, he made the following statement:

"With very rare exceptions, no one dies of literal thirst; however, more and more people are dying from contaminated water or conflicts over access to water."

Water Pollution and Maternal Health

Pollution can have detrimental effects on human reproductive processes through various mechanisms, such as decreasing sperm count, motility, and morphology, disrupting hormonal balance, increasing the risk of miscarriage, and impairing the functionality of reproductive organs (Haseena et al. 2017). The implications have the potential to cause infertility and reduce the chances of obtaining successful conception and pregnancy. Hepatitis E virus (HEV) is a pathogen that is transmitted via the contamination of water systems with fecal matter (Bartram 2008). Furthermore, it is linked to the occurrence of disease outbreaks in both children and pregnant women. SARS is a highly contagious viral illness that affects the respiratory system. The number 12. SARS infection during pregnancy is linked to occurrences of spontaneous miscarriage, premature birth, and intrauterine growth restriction. Research examining pregnant women with SARS found that three deaths occurred among twelve patients, and four women experienced spontaneous miscarriages during their first trimester (Wong et al. 2004). Walker et al. (2011) conducted a study to examine the impact of copper poisoning on pregnant women. Elevated copper levels are associated with intrauterine growth restriction (IUGR), preeclampsia, and neurological disorders. The investigations additionally indicate that the build-up of this substance in the body's tissues might lead to heart failure, liver cirrhosis, pancreatic malfunction, and neurological abnormalities (Roberts et al. 2003). The main effects of water pollution are PCOS, the menstrual cycle is affected, poor puberty and breast development, endometriosis, delay in pregnancy and steroidogenesis, and steroid hormone levels, causing an imbalance in the human body.

It is well established that the consumption of water with high levels of radioactive toxicants by pregnant women exposes them to an increased risk of spontaneous abortion, as seen in Fig. 5. Pollutants found in water not only specifically affect women. It affects both genders, in which women are more vulnerable to the changes. Infection in women is like a disease to the entire generation. Children are born malnutritional. That is underdeveloped and dies at an early age. From the perspective of water resources, arsenic, nitrate, chromium, etc., are highly associated with cancer. Ingestion of arsenic from drinking water can cause skin cancer and also kidney and bladder cancer (Marmot 2007). The potential cancer risk posed by arsenic in the water supply of the United States population is potentially like the risks associated with tobacco smoke and radon exposure inside residential environments (Smith et al. 1992). Nevertheless, there is variability in the individual susceptibility to the carcinogenic effects of arsenic. A controlled study conducted in northern Chile between 1994 and 1996 revealed a strong correlation between the presence of arsenic in drinking water and the incidence of lung cancer (Ferreccio et al. 2000) The study involved individuals who had been diagnosed with lung cancer and were admitted to a hospital, with their frequency being matched accordingly. Research has also demonstrated a synergistic relationship between smoking and the consumption of arsenic-contaminated drinking water in the development of lung cancer. The association between exposure to elevated levels of arsenic in drinking water and the occurrence of liver cancer was seen, although this relationship did not reach statistical significance
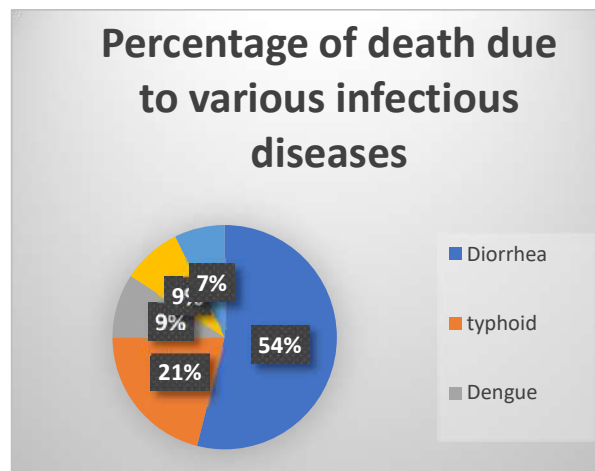

Fig. 5: Death due to pollution.

Table 3: Consequences of lead.

Parts of the Body	Consequences of Lead
Brain	Any exposure is linked to lowered IQ, ADHD, hearing loss, and damaged nerves. Acute exposure can cause convulsions, loss of body movement, coma, stupor hyperirritability, and death.
Heart	They have a significant increase in high blood pressure after the age of 50
Hormones	It disrupts Vitamin D levels, which impairs cell growth, maturation, and tooth and bone development.
Blood	Lead inhibits the body's ability to make hemoglobin, which leads to anemia. This reduces oxygen flow to organs, causing fatigue, rapid heartbeat, dizziness, light-headedness, and shortness of breath.
Kidneys	Chronic inflammation resulting from this might potentially lead to kidney failure, hematuria, pyrexia, emesis, dermatitis, cognitive impairment, somnolence, unconsciousness, increased body mass, and alterations in urinary patterns.
Reproductive System	Moderate exposure not only lowers sperm count but also damages them. Chronic exposure can diminish the concentration, total count, and motility of sperm.

for exposure levels below 0.64 mg.L^{-1} (Lin et al. 2022). From Table 3, the consequences of lead consumption can be seen.

Soil Pollution

Land pollution is defined as the degradation or even destruction of the earth's surface and soil as a result of human activities. Sources of soil pollution can be direct, for example, from dumping toxic chemicals directly onto a site, or indirect, for example, where toxic chemicals leach through the soil from particulates that have settled from air pollution from a nearby lead smelter (Heiderscheidt 2018). It can also be degraded by transforming the land by clearing it so that beneficial organisms can no longer provide services supporting growth and protect it from further erosion.

The causes of Land pollution are 1) Deforestation and soil erosion. 2) Agricultural chemicals 3) Industrialization 4) Mining 5) Landfills 6) Human Sewage 7) Industrialization 8) Construction activities 9) Nuclear waste

These pollutants in the land have an adverse effect on the environment. Due to the chemicals disposed in the land, the groundwater gets poisoned, making it unfit for drinking and other purpose. Due to a wide range of negative consequences, there is mass displacement of people from one place to another. Migration increases pressure on the lands, as they must meet the requirements of the entire population. `

The global population growth and escalating food demand are leading to the conversion of forests and grasslands into agricultural land(Roser 2023) The natural vegetation possesses extensive root systems that effectively anchor the soil in its original position. Several of the substitute crops, such as cotton, coffee, wheat, and soybeans, lack extensive root systems, which contribute to soil erosion. Consequently, the inability of the soil to absorb surplus rainfall exacerbates flooding. Additionally, it facilitates the efficient drainage of fertilizers and other substances that have been applied (Heiderscheidt 2018). Farmers regularly administer potent fertilizers, pesticides, fungicides, herbicides, and insecticides directly onto the crops and soil. Substances that are not sprayed or carried by wind over the land can infiltrate the soil either by being absorbed through the roots of plants or by means of the remains of the targeted insects, creatures, and dead (Alengebawy & Abdelkhalek 2021). The pollution eradicates the thriving organisms that are accountable for producing fresh vegetative growth. In 2016, the Food and Agriculture Organisation of the United Nations disclosed that a staggering 75 billion tonnes of soil are annually depleted worldwide, leading to the forfeiture of hundreds of billions of dollars in agricultural output. Furthermore, it is worth noting that a significant proportion of food, specifically 95 percent, is cultivated on soil worldwide. This highlights contamination as a significant issue in terms of land pollution.

An exemplary instance of soil contamination is the Vietnam War (1955-1975), during which the extensive utilization of herbicides, notably Agent Orange, had profound and enduring impacts on soil and the environment. The substance in question was dioxin, a very poisonous molecule that had significant adverse effects on the environment. Dioxin exposure has been associated with a broad spectrum of health problems, such as cancer and congenital abnormalities. Global land contamination is a significant issue caused by the unrestricted dumping of industrial solid and hazardous waste. The output of industrial solid and hazardous waste has significantly increased due to growing industrialization, resulting in a severe environmental impact. India experienced severe crop failure in the late 1980s. As a result, farmers are compelled to seek artificial fertilizers and pesticides to enhance the productivity of their crops. A factory was established in Bhopal (Heinzerling et al. 2016) in response to the increased demand. Methyl isocyanate (MIC), a very toxic chemical, poses significant risks to human health. Inhabitants of Bhopal residing near the pesticide facility started experiencing irritation caused by the methyl isocyanate (MIC) and subsequently commenced evacuating the city. Pregnant women at the time of the incident experienced an increased likelihood of giving birth to children with elevated cancer risk and who

were born prematurely (Carrington 2022). The individuals who survived the Bhopal Gas Tragedy have encountered a variety of health issues throughout the years. The concerns encompass respiratory, neurological, musculoskeletal, ophthalmic (pertaining to the eyes), and endocrine conditions. Furthermore, women who have been exposed to hazardous gas have seen a notable rise in miscarriages, stillbirths, neonatal death, monthly irregularities, and premature onset of menopause (Lin et al. 2022).

The production of carbide needed more attention. Without proper knowledge and maintenance to cover the entire population's needs, the consequences are the greatest Bhopal Gas tragedy. The poisonous gas killed over 2000 people and still has its aftereffects on the soil. Mans's greed and lack of knowledge led to such a great disaster. The consequences affect not only a single person but a whole generation to come.

Plant-Animal Ecosystem

Human actions, including the use of fossil fuels, ocean acidification, pollution, deforestation, and forced migrations, pose a substantial danger to diverse types of life. It is anticipated that over 33% of coral species, freshwater mollusks, sharks, and rays, 25% of all mammal species, 20% of all reptile species, and 16% of all bird species will become extinct (Arif 2020) A study undertaken by the Worldwide Fund for Nature (WWF) found that by 2100, a marine area over 2.5 times the size of Greenland might reach ecologically

dangerous levels of microplastics. According to the WWF, plastic pollution is widespread in the water, and it is anticipated that almost every marine animal has encountered it (Schillinger et al. 2020). The WWF has documented 2,141 species that have been detected coming into contact with plastic waste in their native environments. The research states that numerous marine ecosystems, including highly contaminated regions such as the Mediterranean, the East China and Yellow Seas, and the Arctic Sea ice, have already been beyond the threshold for acceptable levels of plastic pollution.

The anthropocentric pollution is not only harming humankind but also bringing great destruction to the ecosystem (Nguyen 2021). Animals and birds are vulnerable to the toxins present in the air and water. In the Bhopal Gas Tragedy, when there was an outbreak of emission of harmful gas people managed to survive by some measures. But there was a total loss to the livestock present there. During the crisis, animals and birds are unaware of the harmful consequences, and they lose their lives (Fahad 2022). Due to this, many species are on the verge of being extinct. Species die due to fight, hunger, or old age. But now they become extinct, as they are not able to tolerate the harsh environment. Birds who migrate change their ways and get distracted due to improper seasons. The onset of migration gets delayed. People are in a future where the rainy season becomes summer, and summers are prolonged too much. The world has recorded the hottest summer ever in history. To quench
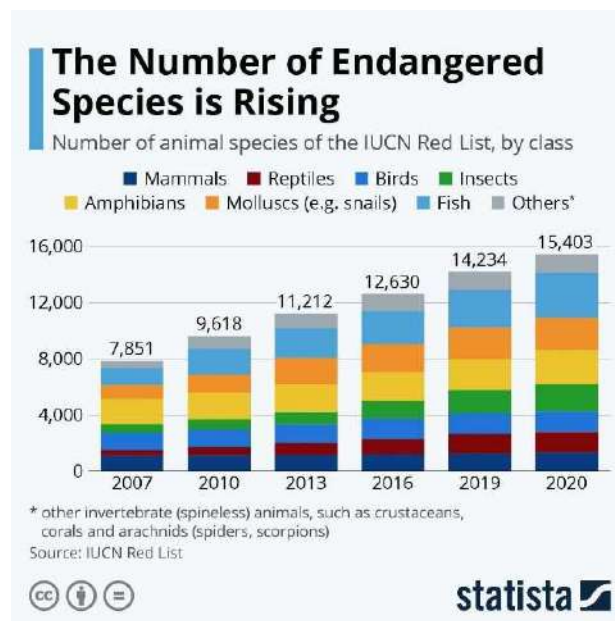

Fig. 6: Endangered species list (Nguyen 2021).

the thirst, animals, and birds drink polluted water, and there are all the consequences, as seen in Fig. 6.

Global apprehension revolves around the impact of environmental degradation on human beings. It is sometimes overlooked that these contaminants also have an impact on animals and birds. When people possess knowledge of preventive procedures for all possible events, their five sensory organs are rendered incapable of responding. Air pollution has the potential to harm wildlife by interfering with their endocrine function, causing damage to their organs, making them more susceptible to stress and diseases, reducing their reproductive success, and potentially leading to death (Fahad 2022). Several instances of historical data, such as the occurrence of cattle deaths during livestock events in the 1890s, the air pollution scenario in the Meuse Valley in the 1930s, and the cattle death episode in Belgium in 1911, indicate a potential connection. The discharge of arsenic in the United States in 1908 resulted in the widespread illness and death of certain livestock and horses. In addition, the release of industrial smoke in England in 1914 resulted in respiratory ailments among cattle, leading to a decline in wool production in sheep. Wildlife is highly vulnerable to the detrimental effects of industrial pollutants. Moreover, there is compelling historical data that precisely supports this claim. In 1963, the release of asbestos in South Africa resulted in lung damage in baboons and rats. In addition, the release of fluoride in Canada in 1967 resulted in the occurrence of Fluorosis among whitetail deer. In addition, other historical instances of pollutant emissions have demonstrated the consequences of population reduction, bioaccumulation, hypocalcemia, hypoproteinaemia, blindness, genetic alterations, reduced corneal protein in hares, diminished antler quality in Roe deer, and eventual mortality. These are the consequences of various chemical emissions, such as Arsenic, hydrogen sulfate, fly ash, cadmium, oxidants, lead, mercury, sulfur dioxide, ozone, and so on. Anthropogenic pollution poses a significant risk to the preservation of wildlife habitats. Humans have traditionally viewed the air, water, and soil as places to dispose of trash without adequately considering the ecological repercussions of pollution. Wildlife populations are consistently exposed to a vast range of toxins that are discharged into the environment.

DISCUSSION

The universe's problems originate within everyone. Humanity established empires to fulfill its desires and avarice yet remains oblivious to the repercussions they are encountering. To combat sloth, he devises machines that ultimately supplant humans and defy the laws of nature. According to Elon Musk, we are currently in an era where artificial intelligence is poised to dominate the planet. "AI is more powerful than nukes," as stated by Elon Musk. During a recent discussion among school pupils, it was observed that while youngsters are conscious of the evolving environment, they fail to recognize their role as contributors to its degradation. The melting of glaciers is mostly attributed to excessive heat resulting from the usage of fossil fuels, as well as the detrimental effects of air and water pollution. These factors contribute to global warming, which subsequently leads to ozone depletion and ultimately causes the glaciers to melt. The younger generation must comprehend that every activity they engage in is detrimental to the environment. From the act of discarding plastic waste to leaving the refrigerator door ajar, every action adds to the deterioration of the environment. Individuals sometimes fail to comprehend the gravity of the matter unless they undergo it themselves. The younger generation should promptly assume their obligations towards nature. Lessons about the environment and its various impacts should be incorporated into their everyday curriculum. They should possess knowledge of the saying, "As you sow, so shall you reap."

War has negative impacts on the environment. War is caused due to political greed. People are always concerned about how to outlive others, whereas they are least bothered by how it affects others. Countries show off their power through war. They are unaware of how many devastations these wars bring. In the olden days, the war brought destruction to the environment when compared to the modern bio war. Bio war has an impact on a generation ahead. The study of how structural forces, like capitalist economic processes and power dynamics, contribute to environmental change in our increasingly interconnected world is a major contribution of anthropology, geography, and related sciences. Richard A. Matthew, a well-known political scientist, typified the methodology. He has significantly advanced the field of research on the environmental aspects of armed conflict. To comprehend the effects of armed conflict on the environment, he proposed the political ecology hypothesis. Environmental deterioration can result from armed conflict, which can affect populations' access to vital resources and exacerbate vulnerabilities. He also looks at the connection between military operations and environmental damage. These include the employment of tools and strategies that have the potential to cause habitat damage, soil contamination, and deforestation.

There is an innate drive in every human being to ensure their survival, procreate, and pass their genes on to the next generation. Consequently, people gravitate towards others who share their values, ethics, and worldviews because we

are social beings. Wars have broken out over these divergent ideologies throughout human history. Looking at how conflict has affected the environment throughout history reveals that current human fighting has drastically worsened the planet's environmental health. Applying notions from religion, philosophy, and science also makes it obvious that protecting the environment is essential to human survival and that people, being intelligent animals, have a responsibility to do it. A lot of work remains, but we have made progress in preventing further environmental degradation. If we look at the situation closely enough, we can see that stopping war is the only option to save the ecosystem from destruction. "Wherever there are military maneuvers, there will be some [environmental] damage" (Graham 1993), regardless of how ecologically conscious future forces may be. The scene of any battlefield will be one of devastation; war is a horrible thing. The environment is indirectly targeted by contemporary weapons such as bombs, tanks, and other military vehicles, which devastate ecosystems; battleships pollute the seas; and chemical and biological warfare might wipe out all life on Earth. So, ending war is the only way to safeguard the environment from its destructive effects. Unfortunately, we aren't yet technologically sophisticated enough to disseminate the lovely concept of world peace. The only way to safeguard the environment from human conflict, therefore, is for there to be peace. Despite our many differences, many people believe that people will eventually learn to live in peace with one another. But worst-case scenario: human war wipes out Earth, its people, and its resources to the point that there is no longer any habitable planet.

CONCLUSION

The age of the Earth is approximately 4.5 billion years. The age of humanity is around 140,000 years. Humanity's tenure on Earth has been relatively brief, yet the consequences of its actions endure indefinitely. The individual has chosen to identify as Homo sapiens, a term that translates to "wise man." However, the question arises as to whether this individual truly possesses the level of intelligence implied by this designation. There are numerous locations where mankind has demonstrated wisdom. He has successfully divided the atom and constructed equipment capable of interstellar navigation. He embarks on a quest to discover new habitats in another universe. The process of splitting atoms resulted in the emergence of nuclear warfare as he pursued his ambition to explore the galaxy, disregarding and neglecting his current planet. This lacks wisdom. Wisdom exhibits distinct characteristics. Intelligence is vocal, while wisdom is attentive. The man shielded his ears from the cries of Mother Nature and turned a blind eye to all her pleas

for assistance. Wisdom recognizes that every action elicits an equal and opposite reaction. Therefore, if we possessed wisdom, we would not be surprised by the occurrence of more intense storms, prolonged periods of drought, hurricanes, and wildfires. There is a significantly higher level of pollution compared to previous times. Increased carbon emissions result in a higher number of trees being deforested. Human activities have accelerated the rate of animal extinction by a factor of 1000 compared to the natural rate. In the next years, it is expected that every animal depicted in books will become extinct. Species that have outlasted humans will become extinct due to our actions. The genuine crisis does not lie in global warming or environmental deterioration. It is the human-centered perspective. Problems are manifestations of humanity and consequences of human activity.

REFERENCES

Alengebawy, A. and Abdelkhalek, S.T., 2021. Heavy metals and pesticides toxicity in agricultural soil and plants: ecological risks and human health implications. Available at: https://www.mdpi.com/2305-6304/9/3/42 [Accessed 26 September 2024].

Arif, A., 2020. Water pollution and industries. *Pure and Applied Biology*, 9. Available at: https://doi.org/10.19045/bspab.2020.90237.

Bartram, J., 2008. Flowing away: water and health opportunities. Available at: https://www.ncbi.nlm.nih.gov/pmc/articles/PMC2647355/ [Accessed 26 September 2024].

Buchholz, K., 2022. Unsafe water kills more people than disasters and conflicts. Available at: https://www.statista.com/chart/17445/global-access-to-safe-drinking-water/ [Accessed 22 November 2023].

Carrington, D., 2022. Microplastics found in human breast milk for the first time. *The Guardian*. Available at: https://www.theguardian.com/environment/2022/oct/07/microplastics-human-breast-milk-first-time [Accessed 7 October 2022].

Clark, M., 1993. Review of *The Ecology of War: Environmental Impacts of Weaponry and Warfare*. *Human Ecology Review*, 1, pp.195–198.

Davis, L., 1998. Birds suffer from air pollution, just like we do. *Audubon California*. Available at: https://ca.audubon.org/news/birds-suffer-air-pollution-just-we-do [Accessed 28 November 2023].

Ellis-Petersen, H., 2019. "Bhopal's tragedy has not stopped": the urban disaster still claiming lives 35 years on. *The Guardian*.

Fahad, 2022. How does air pollution affect the animals? *Earth Remind*. Available at: https://www.earthreminder.com/how-does-air-pollution-affect-the-animals/ [Accessed 28 November 2023].

Ferreccio, C., González, C., Milosavjlevic, V., Marshall, G., Sancha, A.M. and Smith, A.H., 2000. Lung cancer and arsenic concentrations in drinking water in Chile. *Epidemiology*, 11, pp.673–679. Available at: https://doi.org/10.1097/00001648-200011000-00010.

Ghorani-Azam, A., Riahi-Zanjani, B. and Balali-Mood, M., 2016. Effects of air pollution on human health and practical measures for prevention in Iran. *Journal of Research in Medical Sciences*, 21, p.65. Available at: https://doi.org/10.4103/1735-1995.189646.

Graham, L.D.S., 1993. *The Ecology of War: Environmental Impacts of Weaponry and Warfare*. Available at: https://search.worldcat.org/title/ecology-of-war-environmental-impacts-of-weaponry-and-warfare/oclc/1148941797 [Accessed 26 September 2024].

Greentumble, 2018. The main causes of land pollution. Available at: https://greentumble.com/the-main-causes-of-land-pollution [Accessed 28 November 2023].

Haseena, M., Malik, M., Javed, A., Arshad, S., Asif, N., Zulfiqar, S. and Hanif, J., 2017. Water pollution and human health. *Environmental Risk Assessment and Remediation*, 1. Available at: https://doi.org/10.4066/2529-8046.100020.

Heiderscheidt, D., 2018. The impact of World War One on the forests and soils of Europe, 7.

Heinzerling, A., Hsu, J. and Yip, F., 2016. Respiratory health effects of ultrafine particles in children: a literature review. *Water, Air, and Soil Pollution*, 227, p.32. Available at: https://doi.org/10.1007/s11270-015-2726-6.

Lin, L., Yang, H. and Xu, X., 2022. Effects of water pollution on human health and disease heterogeneity: a review. *Frontiers in Environmental Science*, 10.

Marmot, M., 2007. Achieving health equity: from root causes to fair outcomes. *The Lancet*, 370, pp.1153–1163. Available at: https://doi.org/10.1016/S0140-6736(07)61385-3.

Milne, S., 2021. How water shortages are brewing wars. Available at: https://www.bbc.com/future/article/20210816-how-water-shortages-are-brewing-wars [Accessed 20 November 2023].

Nguyen, L., 2021. What animals will be extinct by 2100? *Earth.Org*. Available at: https://earth.org/what-animals-will-be-extinct-by-2100/ [Accessed 28 November 2023].

Nilson, C. and Burke, T., 2002. Environmental extremists and the eco-terrorism movement. *University of Nebraska–Lincoln*. Available at: https://www.unl.edu/eskridge/ecoterrorism.html [Accessed 16 November 2023].

Protopsaltis, C., 2012. Air pollution caused by war activity. Presented at the Air Pollution 2012, A. Coruna, Spain, pp.93–98. Available at: https://doi.org/10.2495/AIR120091.

Rathi, A., 2022. Psychological Impact of Victims of War and Conflict, 2010. APA.

Roberts, E.A. and Schilsky, M.L., Division of Gastroenterology and Nutrition, Hospital for Sick Children, Toronto, Ontario, Canada, 2003. A practice guideline on Wilson disease. Hepatology, 37, pp.1475–1492. Available at: https://doi.org/10.1053/jhep.2003.50252.

Roser, M., 2023. Data review: how many people die from air pollution? Our World in Data.

Rothschild, J. and Haase, E., 2023. The mental health of women and climate change: direct neuropsychiatric impacts and associated psychological concerns. International Journal of Gynaecology and Obstetrics, 160, pp.405–413. Available at: https://doi.org/10.1002/ijgo.14479.

Schillinger, J., Özerol, G., Güven-Griemert, Ş. and Heldeweg, M., 2020. Water in war: understanding the impacts of armed conflict on water resources and their management. WIREs Water, 7, e1480. Available at: https://doi.org/10.1002/wat2.1480.

Smith, A.H., Hopenhayn-Rich, C., Bates, M.N., Goeden, H.M., Hertz-Picciotto, I., Duggan, H.M., Wood, R., Kosnett, M.J. and Smith, M.T., 1992. Cancer risks from arsenic in drinking water. Environmental Health Perspectives, 97, pp.259–267. Available at: https://doi.org/10.1289/ehp.9297259.

Walker, L.R., Rattigan, M. and Canterino, J., 2011. A case of isolated elevated copper levels during pregnancy. Journal of Pregnancy, 2011, 385767. Available at: https://doi.org/10.1155/2011/385767.

Wong, S.F., Chow, K.M., Leung, T.N., Ng, W.F., Ng, T.K., Shek, C.C., Ng, P.C., Lam, P.W.Y., Ho, L.C., To, W.W.K., Lai, S.T., Yan, W.W. and Tan, P.Y.H., 2004. Pregnancy and perinatal outcomes of women with severe acute respiratory syndrome. American Journal of Obstetrics and Gynecology, 191, pp.292–297. Available at: https://doi.org/10.1016/j.ajog.2003.11.019.

ORCID DETAILS OF THE AUTHORS

Gajalakshmi G.: https://orcid.org/0009-0000-3572-3215

Estimation of Hydraulic Conductivity Using Geoelectrical and Infiltrometer Observations

Novia Anggita[1†], Dwinanti Rika Marthanty[2] and Abdul Halim Hamdany[2]

[1]Department of Civil Engineering, Faculty of Engineering, University of Indonesia, Depok 16424, Indonesia
[2]Faculty of Engineering, University of Indonesia, Depok 16424, Indonesia
†Corresponding author: Novia Anggita; 12.novianggita@gmail.com

ABSTRACT

Hydraulic conductivity (K) as a parameter in surface and subsurface water interaction is an important study to research. Field observations using geoelectrics with the Schlumberger configuration and using infiltrometers with double ring were chosen as methods to estimate the (K) which aims to recognize the characteristics of the relationship between (K) obtained from different observation results. The estimated (K) obtained from infiltrometer observations are quite significant compared to geoelectric observations which range from 2.715×10^{-7} m/s to 6.132×10^{-7} m/s, while geoelectrical values range from 1.965×10^{-8} m/s to 3.896×10^{-9} m/s. In this study, the soil conditions in geoelectric observations were carried out in an unsaturated state and infiltrometer observations were in a saturated state. This soil condition is used as one of the reasons for interpreting the research results in this study, that the hydraulic conductivity in unsaturated soil conditions decreases compared to saturated soil.

INTRODUCTION

The hydrological cycle, as the primary focus in hydrology, is presented as a system with various processes occurring within it. Infiltration, as one of the processes in the hydrological cycle, becomes a crucial phenomenon in the interaction between surface water and groundwater. The infiltration process is influenced by the land cover above it and the conditions of the land. When considering the physical properties of the soil, these influencing factors comprise soil porosity, grain size, and hydraulic conductivity, interpreted as the soil's capacity to facilitate fluid flow. The flow entering the hydrological system in the form of precipitation can flow into rivers either on the surface as overland flow (surface runoff) or as subsurface flow after infiltrating into the ground (Cherry et al. 1979). According to Guymon (1994), the unsaturated zone in the hydrological cycle plays a role in channeling water that falls or pools on the surface into the ground or temporarily storing it near the surface for plant use. Cherry et al. (1979) describe unsaturated flow as a multiphase flow through porous media, involving both air and water phases. The flow through these porous media is regulated by hydraulic conductivity and soil permeability coefficients. Numerous studies have been conducted to investigate the interaction between surface

water and groundwater in various case studies, employing diverse methods. In an integrated study, utilizing electrical resistivity tomography and infiltration methods to delineate the characteristics and potential of the unsaturated zone in crystalline rocks (Warsi et al. 2019), they asserted that water falling on the surface traverses the unsaturated zone, recognized as an active region controlling the flux of water between the surface and groundwater. The geoelectric method was applied to a lithologically complex porous aquifer in the Anthemountas Basin, Northern Greece, by Kazakis et al. (2016) to estimate the hydraulic properties of the aquifer using Archie's Law and Kozeny's equation. A similar approach was also employed by Niwas et al. (2012) in the Ruhtral aquifer in Germany, utilizing the cementation factor (m) and alpha factor (m) parameters to calculated porosity in estimating the hydraulic parameters of an aquifer. The application of geoelectric methods can also be utilized to estimate groundwater infiltration, as demonstrated by (Hossain et al. 2021). They computed hydraulic conductivity values using Archie's equation, as employed by (Niwas et al. 2012). However, the commonly used electrical resistivity equations do not apply to silty and clayey soils. Therefore, to calculate porosity, cementation factors were computed based on research conducted by (Choo et al. 2016). The estimated hydraulic conductivity values were used as

parameters to calculate infiltration rates using the Green-Ampt model. In his book, Briaud (2013) describes the sealed double-ring infiltrometer test method developed by Trautwein & Danil in 1994 to measure hydraulic conductivity at shallow depths in soils above the groundwater table. The movement of surface water and atmospheric moisture to the groundwater system is significantly controlled by the hydraulic characteristics of the vadose zone above it. The movement of soil moisture through the unsaturated zone plays a crucial role in hydrological processes. According to (Zou et al. 2023), hydraulic conductivity is a dominant hydraulic parameter that governs the flow characteristics in the unsaturated zone, making its determination fundamental for groundwater dynamics characterization and prediction.

Based on a comprehensive review of various literature, this study is designed to identify the relationship between hydraulic conductivity values from different observations, including geoelectric and infiltrometer measurements. Geoelectric observations yield resistivity values used to estimate hydraulic conductivity, considering hydraulic parameters such as porosity, grain size diameter, and material formation factors comprising cementation and alpha factors. Double-ring infiltrometer observations provide infiltration rates and capacities using the Horton model to quantify them into hydraulic conductivity values.

STUDY AREA

The research area is located within the Faculty of Engineering University of Indonesia, in the city of Depok, West Java (Fig. 1). The study region falls within the Jakarta groundwater basin, as defined by the Ministry of Energy and Mineral

Resources Regulation number 2/2017 regarding Indonesian Groundwater Basins. According to the Medium-Term Investment Program Plan (RPIJM) for the city of Depok from 2015 to 2019, the research area is predominantly characterized by the Alluvial Fan Rock Unit, consisting of deposits such as clay, sand and gravel, and conglomerate (Fig. 2). The average rainfall over the last ten years from the FT UI Rainfall Station is recorded at 121.12 mm. Based on Fig. 1 of the observation area, there is an orange line representing the observation span for the geoelectrical survey along 80 meters. The length of this span does not indicate any special explanation but is merely due to the limitation of the land at the observation site. The green point represents the midpoint of the geoelectrical observation span, and the two blue points, each located 10 meters from the midpoint, are taken as representative points for the infiltrometer observation. Several observation points have been made within the area delineated by the red line; however, only the points and locations indicated in the figure are explained and selected for analysis in this study.

In all discussions, the flow rate through porous media is regulated by hydraulic conductivity and soil permeability coefficients. Fitts (2013) explains that the physical properties of water and the distribution of pore space determine the amount of water stored in a specific volume and how easily water can move through the material. The physical properties of water consist of the mass density of water (ρ_w) valued at 1000 kg/m^3, and viscosity (μ) of 0.0014 kg/(s.m). Physical properties of porous media, such as porosity (φ) and grain size (d) are determining factors for hydraulic conductivity. Soil test in the laboratory was conducted to obtain soil index
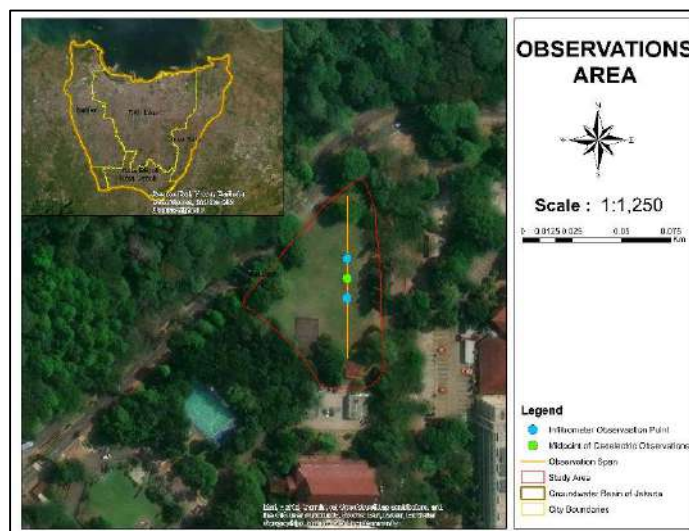
Fig. 1: Observation area.
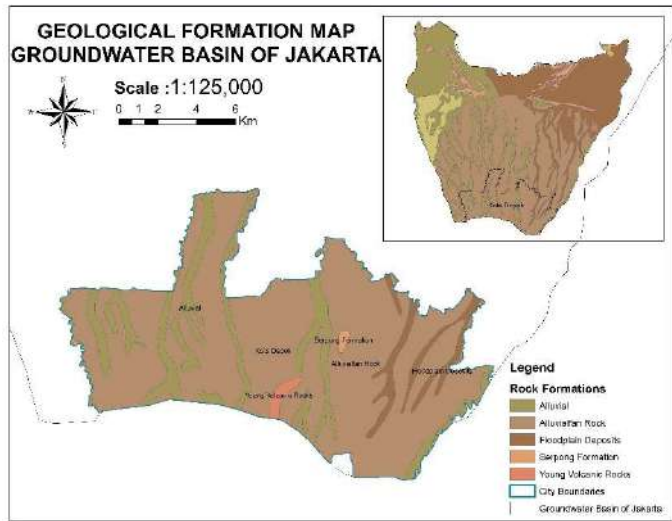
Fig. 2: Geological formation of the study area.
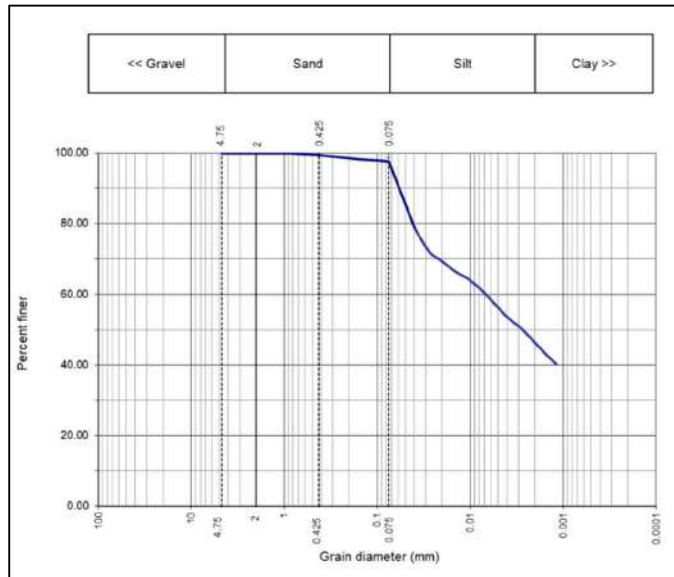
Fig. 3: Grain size distribution curve.

property data, which consists of water content at 46.19%, as well as the results of hydrometer testing analysis indicating 2.5% sand, 52.5% silt, and 46% clay, with grain size distribution depicted in Fig. 3. The visual description of the soil is silty with high plasticity (MH).

MATERIALS AND METHODS

The estimation of hydraulic conductivity is obtained by analyzing field observations, which include geoelectric measurements and infiltrometer measurements. Fetter (1994) explains in his book that the hydraulic conductivity value of soil material can be measured in the laboratory using a permeameter, commonly known as permeability testing. Therefore, in this study laboratory permeability testing is conducted as a control value to estimate the hydraulic conductivity from geoelectrical and infiltrometer observations. The procedure for laboratory permeability testing starts with collecting samples from the observation site, specifically at the midpoint of the observation span indicated by the green point in Fig. 1. Samples are taken using the hand boring method at depths of 0.3-0.5 meters and 1.7-2.0 meters to obtain undisturbed soil. Once the soil samples are collected and ready for permeability testing, a series of

permeameter testing equipment is prepared and checked to ensure they are operational. Remove the soil sample from the sampling tube and place it into the permeability test tube. Measure the height of the soil sample for testing. The falling head method will be used for this test, and the calculations to determine the hydraulic conductivity value will be based on the provided explanations by Briaud (2013) and Fetter (1994). In this stage of the permeability test, the soil is saturated for approximately 5 hours. Then an initial reading is taken to determine the initial water level, followed by another reading approximately 16 hours later to measure the final water level. Permeability testing for soil samples at depths of 0.3 to 0.5 meters yielded a hydraulic conductivity value of 8.33×10^{-8} m/s, whereas at depths of 1.5 to 2 meters, it was 2.67×10^{-10} m/s. The hydraulic conductivity values derived from laboratory permeability testing are also utilized to aid in interpreting the hydraulic conductivity characteristics observed through geoelectrical and infiltrometer methods.

Geoelectric Observations

Geoelectric observations were conducted in the open green field within the Faculty of Engineering, Universitas Indonesia, with a span length of 80 meters using the Schlumberger configuration. This aimed to acquire a series of vertical electrical sounding (VES) data, consisting of potential difference and electrical current values, which would be used as parameters for calculating electrical resistivity. Measurements were carried out using the IRES T300F 1D instrument with a reading precision of 0.001 mV. Measurements are carried out in relatively flat regions, spanning from 0° N to 180° S. Electrodes must be installed directly in contact with the ground and positioned in a linear alignment. The electrode arrangement resembling the Schlumberger configuration is depicted in the accompanying diagram (Fig. 4). Electrodes M and N function as potential electrodes, while electrodes A and B serve as current electrodes.

The vertical electrical sounding (VES) data obtained from observations, consisting of potential difference (ΔV) and

electrical current (I) values, were analyzed to obtain resistivity values (ρ_a). This involved the preliminary calculation of the geometric factor ($K_{schlumberger}$) for the Schlumberger configuration, expressed as follows (Kirsch, 2009):

$$K_{Schlumberger} = \pi \cdot \frac{(AB/2)^2 - (MN/2)^2}{MN} \qquad ...(1)$$

$$\rho_a = K_{schlumberger} \frac{\Delta V}{I} \qquad ...(2)$$

Three sets of VES data were obtained from three separate geoelectric observations conducted at different times. These sets of VES data were then interpreted using Progress v.3.0 software, following the data processing guidelines for 1D resistivity interpretation with Progress software as outlined by Setiadi (2015).

Analysis of Resistivity Values and Hydraulic Parameters

The resistivity values used in estimating hydraulic conductivity are obtained from the interpretation results of the VES data. Kirsch (2009) in his book states, that the electrical resistivity of most minerals is high (except for: clay, metal ores, and graphite), and electrical current primarily flows through pore water. According to the famous Archie's law, the resistivity of a water-saturated clay-free material is defined as follows:

$$\rho_{Aquifer} = \rho_{water} \cdot F \qquad ...(3)$$

Where $\rho_{aquifer}$ represents the specific resistivity of saturated sand, ρ_{water} is defined as the resistivity of pore water, and F is a formation factor that combines all material properties affecting the flow of electrical current, such as porosity, pore shape, and cementation factor, expressed as follows:

$$F = a \, \varphi^{-m} \qquad ...(4)$$

The constant represents the influence of mineral grains on electrical current. If the mineral grains are perfect insulators, then a equals 1. The value of a will decrease
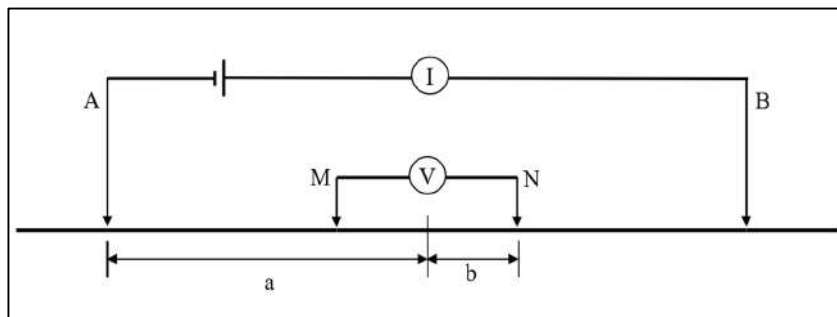

Fig. 4: Schlumberger configuration schematic.

if mineral grains contribute to electrical conductivity to a certain degree. Typical values for *a* and *m* according to Schön (1996), as provided by Worthington (1993), for sand are 1 and 1.3, and for sandstone are 0.7 and 1.9. Choo et al. (2016) researched to modify the cementation factor values applicable to clay and silt soil types, expressed by the following equation:

$$m = m_{sand} . (1 - VF_c) + m_{clay} . VF_c \qquad ...(5)$$

Where m_{sand} and m_{clay} are the cementation factors for pure sand and clay respectively and VF_c is the fraction of clay. The values for pure sand and pure clay are 1.55 and 2.11, and the tortuosity parameter (*a*) is assumed to be 1 because it is related to the length of the current flow path, which is nearly the same for unconsolidated sediments as explained by (Niwas et al. 2012). Thus, the porosity value can be calculated using the modified mathematical formula as follows:

$$\varphi = \sqrt[m]{\frac{\rho_w . a}{\rho}} \qquad ...(6)$$

Thus, the obtained porosity values can be utilized to calculate the coefficient of permeability, as stated by (Kazakis 2016), as follows:

$$k = \frac{d^2}{180} \frac{\varphi^3}{(1 - \varphi)^2} \qquad ...(7)$$

Freeze et al. (1979) defined hydraulic conductivity as the proportionality constant in Darcy's law, which is a function of porous media and fluid. Hydraulic conductivity (*K*) is influenced by the permeability coefficient (*k*), gravitational acceleration (*g*), fluid density (ρ), and viscosity (*m*) of fluid expressed as follows:

$$K = \frac{k \, \rho g}{\mu} \qquad ...(8)$$

Two models for estimating hydraulic conductivity using Archie's Law are explained in this study. The first model, represented by equation …(3), where the value of *F* is obtained from the graph depicting the relationship between the formation factor F and grain size by (TNO 1976), expressed in the following equation by Kirsch (2009) in his book:

$$F = 1,26 \, y^{-1,20} \qquad ...(9)$$

$$y = 0,149 \log M + 0.331 \qquad ...(10)$$

With M representing the grain size in micrometers, the grain size diameter ranges from 0.001 mm to 0.039 mm as obtained from laboratory soil test.

Infiltrometer Observations and Horton Model Infiltration Rate Analysis

Infiltration observations to determine the surface water

infiltration into the soil were conducted at the same location and span as the geoelectric observations. Infiltrometer observations were carried out to obtain data on water table decline (D*h*) over time intervals (D*t*). The infiltrometer used was a double-ring infiltrometer with a ring height of 20 cm, inner diameter of 15 cm, and outer diameter of 30 cm. The observation procedure for the infiltrometer is based on SNI 7752:2012 regarding the method for measuring soil infiltration rates using a double-ring infiltrometer, which refers to ASTM D 3385-88, Standard Test Method for Infiltration Rate of Soils in Field Using Double-Ring Infiltrometer. The infiltrometer observation points can be seen in Fig. 1, the process begins by preparing the ground for placing a double-ring infiltrometer. The rings are then uniformly inserted into the soil to a depth of 2 to 3 cm using a rubber mallet. Before this, a measuring tool with a vertical ruler is fixed to both parts of the ring to facilitate water height readings. Water is introduced into the ring initially at a height of 15 cm. Subsequently, readings and recording of water level reductions are conducted at intervals of 1 minute for the first 10 minutes, 2 minutes up to 30 minutes, and then at 5, 10, to 15-minute intervals. Measurements cease once the water level reduction stabilizes over time. The observation data, represented by the decline in the water table (*h*), is quantified into the volume (*V*) of water that infiltrates into the soil by multiplying the water table height (*h*) with the inner ring area (*A*). Subsequently, it is presented in the form of a graph illustrating cumulative infiltration, which depicts the relationship between the infiltration volume (*F*) and the accumulated time (*t*). Infiltrometer measurements serve as a reference for estimating the infiltration rate using the Horton model. To quantify the infiltration rate with the Horton model, several Horton parameters such as initial infiltration rate (f_0), final infiltration rate (f_c) and recession contant (*k*) are required. These three Horton parameters will be calculated using the Solver program in Microsoft Excel, allowing the Horton model infiltration rate (*f*) to be calculated based on the following equation (Wanielista et al. 1990):

$$f(t) = f_c + (f_0 - f_c) . \, e^{-k.t} \qquad ...(11)$$

The total volume of infiltrate using Horton's equation is determined by integrating the area under the curve, or:

$$F = \int_0^t f(t) \, dt = f_c \, t + \frac{(f_0 - f_c)}{K} (1 - e^{-K.t}) \qquad ...(12)$$

As explained by (Briaud 2013) based on Darcy's law, which describes the flow through soil, hydraulic conductivity is defined as follows:

$$K = \frac{\frac{V_f}{A}}{\frac{\Delta h_t}{\Delta_z}} \qquad ...(13)$$

Where, V_f represents the volume of water infiltrating into the soil at time t, A is the area of the infiltrometer ring, Dh_t is the vertical distance from the bottom layer to the water level at the outer ring, and D$_z$ is the thickness of the layer. The values of h_t and z are assumed to be the same, based on the water height entering the soil, resulting in the quotient Dh_t and D$_z$ being equal to 1. The relationship between the volume of infiltrated water and the area of the infiltrometer ring is then translated into the value of the Horton infiltration rate in meters per hour, which has been calculated previously.

RESULTS

Geoelectrical Observation Result and Data Interpretation

Geoelectrical observations using the Schlumberger configuration yield varying results at each electrode spacing, as do the obtained resistivity values. For VES 1 data, the smallest resistivity value is 0.094 ohm.m at an electrode spacing of up to 5 m from the 80 m span, and the highest resistivity value is 182.126 ohm.m at a distance of 16 m from the span. The smallest resistivity value for VES 2 data is 1.056 ohm.m at a 5 m electrode spacing from the span, and 161.541 ohm.m at

30 m from the span, while for VES 3 data, resistivity values of 3.606 ohm.m at 60 m electrode spacing from the span, and 347.199 ohm.m at 40 m from the span were obtained. The calculation results of resistivity values vary significantly based on field observation data, which consist of potential difference and electric current data at each electrode spacing arranged according to the configuration used. Three sets of VES data from observations are summarized in Table 1.

Theoretically, soil and rock layers have resistivity values that are highly influenced by the composition of minerals contained within them. The magnitude of resistivity can be influenced by the porosity, and permeability of the material, and detached sedimentary rocks typically have lower resistivity compared to consolidated sedimentary rocks. Resistivity values typically depict and define the type of soil and rock. Electrical resistivity observations can provide insights into the depth of soil layers and rock formations across the span of measurements, through the interpretation of VES (Vertical Electrical Sounding) data. Interpretation is carried out using Progress v.3.0 software by constructing a parameter model comprising layer depths and their corresponding resistivity values, utilizing iterative trial-and-error methods to achieve a close fit between observed and

Table 1: VES data interpretation result.

VES 1		VES 2		VES 3	
Depth (m)	ρA (ohm.m)	Depth (m)	ρA (ohm.m)	Depth (m)	ρA (ohm.m)
0	1.49	0	0.83	0	2.95
0.36	0.05	0.35	1.93	0.35	7.48
1.75	166.56	0.59	1.58	0.55	110.05
5.79	2.61	1.76	2.52	1.7	172.59
10.78	10.01	3.5	35.67	3.41	169.01
25.76	130.05	6.8	3.71	7.4	402.62
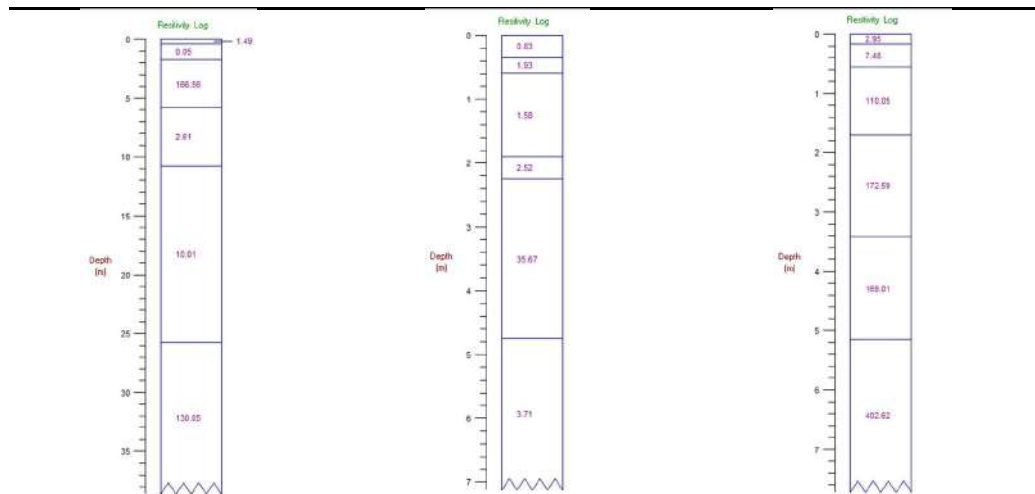
Fig. 5: Interpretation data with layer thickness and resistivity values.

interpreted values (Setiadi 2015). Interpretation results from three sets of VES data collected at the same observation point with an 80-meter span are presented in Table 1 and Fig. 5.

There are a total of 6 soil/rock layers with different thicknesses and resistivity values from the three VES data sets. The interpretation results of VES data 1 can estimate up to a depth of 35 meters with a resistivity value of 130.05 ohm.m. 7 meters with a resistivity value of 3.71 ohm.m for VES data 2, and 7 meters with 402.62 ohm.m for VES data 3. There are two layers with relatively similar depths but different resistivity values. For a layer depth of 0.3 m, the resistivity values obtained from VES data 1, 2, and 3 respectively are 0.05 ohm.m; 1.93 ohm.m; and 7.48 ohm.m. Meanwhile, at a depth of 1.7 m the resistivity values are 166.56 ohm.m; 1.52 ohm.m; and 172.59 ohm.m.

Estimation of Hydraulic Conductivity Values Based on Resistivity Values

According to equation …(3), an important hydraulic parameter to determine first, which is the formation factor (F) combining all material properties affecting electric current flow, such as the values of alpha (a), porosity ($\square$), and cementation factor (m), formulated in equation …(4).

Since the Archie equation …(3), is intended for clayey soil materials, it is necessary to reconsider the modified value of mmm based on equation …(5) by Choo et al. (2016). With m_{sand} and m_{clay} values of 1.55 and 2.11 respectively, and VF_c at 46% from laboratory soil sample testing, the value of is calculated as 1.808. Meanwhile, the alpha parameter is assumed to be 1. Two models will be explained in this study to determine the necessary hydraulic parameters. For Model 1, as described by Kirsch (2009) in his book, some formation values are related to the grain size of a material. Therefore, the value of F is obtained from a graph of the formation factor versus grain size from The Netherlands Organisation (TNO) using equations …(9) and …(10). For Model 2, in the research by Hossain et al. 2022 and based on previous studies, the range of pore water resistivity ($\square_w$) values is summarized based on the aquifer resistivity ($\square_a$). The ($\square_a$) value is obtained from observations in this study, and then interpolation of the existing data is done to determine the ($\square_w$) value.

In this study, porosity (φ) emerges as a highly influential parameter for estimating hydraulic conductivity. The interpretation outcomes are based on consistent relative depths employed in this analysis, specifically at 0 m, 0.3

Table 2: The results of hydraulic conductivity estimation model 1.

	Depth (m)	ρA (ohm.m)	d (m)	F	φ	ρw (ohm.m)	k (cm^2)	K (m/s)
VES 1	0	1.49	0.000001	4.749	0.422	0.314	1.2558E-15	8.7997E-09
	0.36	0.05	0.000001	4.749	0.422	0.011	1.2558E-15	8.7997E-09
	1.75	166.56	0.000001	4.749	0.422	35.075	1.2558E-15	8.7997E-09
VES 2	0	0.83	0.000001	4.749	0.422	0.175	1.2558E-15	8.7997E-09
	0.35	1.93	0.000001	4.749	0.422	0.406	1.2558E-15	8.7997E-09
	1.76	2.52	0.000001	4.749	0.422	0.531	1.2558E-15	8.7997E-09
VES 3	0	2.95	0.000001	4.749	0.422	0.621	1.2558E-15	8.7997E-09
	0.35	7.48	0.000001	4.749	0.422	1.575	1.2558E-15	8.7997E-09
	1.7	172.59	0.000001	4.749	0.422	36.344	1.2558E-15	8.7997E-09

Table 3: The results of hydraulic conductivity estimation model 2.

	Depth (m)	ρA (ohm.m)	m	a	ρw (ohm.m)	φ	F	d (m)	k (cm^2)	K (m/s)
VES 1	0	1.49	1.808	1	0.162	0.293	9.184	0.000001	2.805E-16	1.965E-09
	0.36	0.05	1.808	1	0.005	0.293	9.184	0.000001	2.805E-16	1.965E-09
	1.75	166.56	1.808	1	24.817	0.349	6.711	0.000001	5.560E-16	3.896E-09
VES 2	0	0.83	1.808	1	0.090	0.293	9.184	0.000001	5.560E-16	3.896E-09
	0.35	1.93	1.808	1	0.210	0.293	9.184	0.000001	2.805E-16	1.965E-09
	1.76	2.52	1.808	1	0.274	0.349	6.711	0.000001	2.805E-16	1.965E-09
VES 3	0	2.95	1.808	1	0.321	0.293	9.184	0.000001	2.805E-16	1.965E-09
	0.35	7.48	1.808	1	2.144	0.501	3.488	0.000001	2.805E-16	1.965E-09
	1.7	172.59	1.808	1	25.716	0.349	6.711	0.000001	5.560E-16	3.896E-09
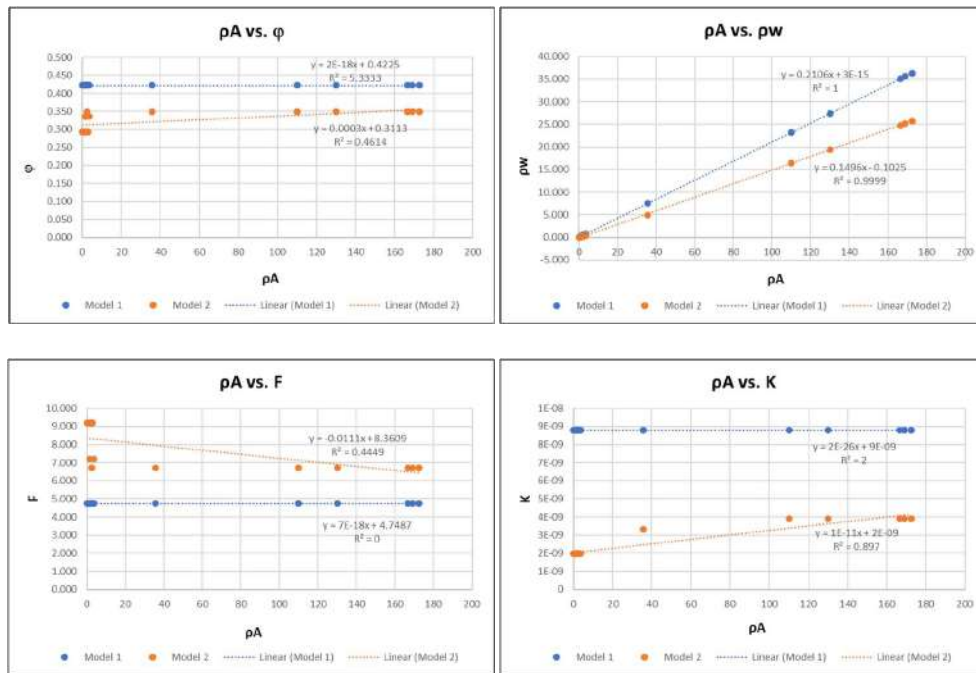
Fig. 6: The data plot of resistivity value with hydraulic parameters.

m, and 1.7 m with a grain size of 0.001 mm. The results of hydraulic conductivity estimation for both models are presented in Tables 2 and 3.

In the first model, the porosity (φ) remains constant because the estimation of the formation factor (F) is based on the same grain size diameter, with the value of (F) varying depending on changes in the grain size of the material (d). In contrast, in the second model, the porosity varies significantly even for the same grain size. From the estimation results, it is essential to understand the relationship between the hydraulic parameters and the hydraulic conductivity values. This relationship can be visualized through the data distribution and graphical plots presented in Fig. 6. Based on the analysis using two modeling approaches to estimate hydraulic conductivity values from resistivity measurements obtained from geoelectrical field observations, the formation factor significantly impacts the determination of (K) values.

Tables 4 and 5 summarize the estimated hydraulic conductivity values for different grain sizes.

The selection of the model parameters can be observed from the data plots of resistivity values against various hydraulic parameters, such as porosity (□), pore water resistivity (□$_w$) formation factor (F), and hydraulic conductivity (K). Based on the obtained R² values, Model 2 is preferred, as it has a better R² value compared to Model 1 and aligns with Fitts (2013) theory on the properties of porous media, where porosity represents a small portion of

pore space within the volume of soil material components. Porosity is defined as the ratio of the volume of voids, consisting of air and water volumes, to the total volume of soil material. The total volume comprises the volumes of air, water, and solid material. In this study, it is assumed that there are no changes to the total volume. Changes in soil conditions occur across dry, unsaturated, and saturated conditions based on the three phases composing the soil material. Soil is considered unsaturated when the pore volume is partially filled with water and partially with air, while saturated soil indicates air voids being fully occupied by water. At a saturation degree of 100%, the volume of void equals the volume of water, whereas a saturation degree of 0% implies the volume of void equals the volume of air. These conditions do not alter the volume of the void hence, the porosity value remains constant.

Estimation of Hydraulic Conductivity Values Through Soil Infiltration

The infiltrometer observation started at $t = 0$ hr and continued until $t = 1,667$ hr, with intervals of 1 minute for the first 10 minutes, 2 minutes for the subsequent minutes up to 30 minutes, 5 minutes for the following minutes up to 60 minutes, and 10 minutes for the next minutes up to 100 minutes (SNI 7752:2012). The results of the infiltrometer observation include the actual volume of water infiltrated into the soil in the field and the infiltration volume analyzed

Table 4: The results of hydraulic conductivity estimation model 1 based on grain size.

	Depth (m)	ρA (obs) (ohm.m)	Grain size (mm)				
			0.001	0.005	0.011	0.020	0.039
VES 1	0	1.49	8.7997E-09	5.1962E-07	3.6925E-06	1.6176E-05	8.3711E-05
K (m/s)	0.36	0.05	8.7997E-09	5.1962E-07	3.6925E-06	1.6176E-05	8.3711E-05
	1.75	166.56	8.7997E-09	5.1962E-07	3.6925E-06	1.6176E-05	8.3711E-05
VES 2	0	0.83	8.7997E-09	5.1962E-07	3.6925E-06	1.6176E-05	8.3711E-05
K (m/s)	0.35	1.93	8.7997E-09	5.1962E-07	3.6925E-06	1.6176E-05	8.3711E-05
	1.76	2.52	8.7997E-09	5.1962E-07	3.6925E-06	1.6176E-05	8.3711E-05
VES 3	0	2.95	8.7997E-09	5.1962E-07	3.6925E-06	1.6176E-05	8.3711E-05
K (m/s)	0.35	7.48	8.7997E-09	5.1962E-07	3.6925E-06	1.6176E-05	8.3711E-05
	1.70	172.59	8.7997E-09	5.1962E-07	3.6925E-06	1.6176E-05	8.3711E-05

Table 5: The results of hydraulic conductivity estimation model 2 based on grain size.

	Depth (m)	ρA (obs) (ohm.m)	Grain size (mm)				
			0.001	0.005	0.011	0.020	0.039
VES 1	0	1.49	1.9654E-09	4.9136E-08	2.3782E-07	7.8618E-07	2.9894E-06
K (m/s)	0.36	0.05	1.9654E-09	4.9136E-08	2.3782E-07	7.8618E-07	2.9894E-06
	1.75	166.56	3.8961E-09	4.9134E-07	2.3781E-06	7.8615E-06	2.9893E-05
VES 2	0	0.83	1.9654E-09	4.9136E-08	2.3782E-07	7.8618E-07	2.9894E-06
K (m/s)	0.35	1.93	1.9654E-09	4.9136E-08	2.3782E-07	7.8618E-07	2.9894E-06
	1.76	2.52	8.3059E-08	4.0201E-07	1.3290E-06	5.0533E-06
VES 3	0	2.95	1.9654E-09	4.9136E-08	2.3782E-07	7.8618E-07	2.9894E-06
K (m/s)	0.35	7.48	1.9654E-08	4.9136E-08	2.3782E-07	7.8618E-07	2.9894E-06
	1.70	172.59	3.8961E-09	8.3059E-08	4.0201E-07	1.3290E-06	5.0533E-06

using the empirical Horton model, presented in Table 6 and Fig. 7.

The total volume of infiltrate obtained using the Horton model is considered satisfactory because the Sum of Squared Errors (SSE) from the observation and modeling results is very small and approaches zero. Additionally, the agreement between the observation and modeling results can be observed from the graph, indicating a close match. The calculation steps outlined above are used to analyze the infiltration rate, which is then utilized to estimate the hydraulic conductivity, presented in Table 7.

DISCUSSION

The estimated values of hydraulic conductivity from geoelectrical observations, infiltrometer measurements, and laboratory permeability tests are summarized in

The estimated hydraulic conductivity values obtained are quite significant compared to geoelectrical observations and permeability tests. This is also due to soil density and soil unsaturation, resulting in higher hydraulic conductivity values in infiltrometer observations, indicating a greater ability to rapidly transmit fluids. All observations were

Table 6: The actual infiltrometer observation result and Horton's Model.

		t (hr)	Δh (m)	F (Obs) (m³)	F (Horton) (m³)	SSE
Measurement 1	Point 1	1.667	0.190	0.0034	0.0039	0.0000002991
	Point 2	1.667	0.257	0.0045	0.0058	0.0000014630
Measurement 2	Point 1	1.667	0.305	0.0054	0.0053	0.0000000017
	Point 2	1.667	0.156	0.0028	0.0029	0.0000000125
Measurement 3	Point 1	1.667	0.524	0.0093	0.0093	0.0000000001
	Point 2	1.667	0.295	0.0052	0.0053	0.0000000116

Fig. 7: Scatter plot of actual infiltration and Horton's Model.

Table 7: Infiltration rate Horton's model and hydraulic conductivity.

		t (hr)	Δh (m)	f (m/jam)	K (m/s)
Measurement 1	Point 1	1.667	0.190	0.00114	3.1724E-07
	Point 2	1.667	0.257	0.00327	9.0910E-07
Measurement 2	Point 1	1.667	0.305	0.00093	2.5759E-07
	Point 2	1.667	0.156	0.00103	2.8546E-07
Measurement 3	Point 1	1.667	0.524	0.00206	5.7187E-07
	Point 2	1.667	0.295	0.00153	4.2434E-07

Table 8: The hydraulic conductivity values from three observations.

	Geolistrik		Infiltrometer		Permeability Lab	
	Depth (m)	K (m/s)	Depth (m)	K (m/s)	Depth (m)	K (m/s)
Obs 1	0.35	1.965E-09	0.1	6.132E-07	0.3	8.330E-08
	1.76	1.965E-09			1.7	2.669E-10
Obs 2	0.36	1.965E-09	0.1	2.715E-07		
	1.75	3.896E-09				
Obs 3	0.35	1.965E-08	0.1	4.981E-07		
	1.7	3.896E-09				

recorded with timestamps as seen in the figure, along with weather conditions at the time of observation. For geoelectrical observation on December 4th, rainfall was recorded on the previous days totaling 29.8 mm. For infiltrometer observations, the weather tends to be hot with rainfall occurring before the second infiltrometer observation, amounting to 38.8 mm, precisely on October 25th. And the distribution of this data can be seen from the

image in Fig. 8. The estimation of hydraulic conductivity values based on geoelectrical observations was conducted at depths of 0.3 m and 1.7 m, as well as permeability testing in the laboratory. In the infiltrometer observation, it is assumed that water seeps vertically into the soil, so the depth of the layer used is assumed to be 0.1 m.

The estimated hydraulic conductivity values obtained are quite significant compared to geoelectrical observations

Table 8: The hydraulic conductivity values from three observations.

	Geolistrik		Infiltrometer		Permeability Lab	
	Depth (m)	K (m/s)	Depth (m)	K (m/s)	Depth (m)	K (m/s)
Obs 1	0.35	1.965E-09	0.1	6.132E-07	0.3	8.330E-08
	1.76	1.965E-09			1.7	2.669E-10
Obs 2	0.36	1.965E-09	0.1	2.715E-07		
	1.75	3.896E-09				
Obs 3	0.35	1.965E-08	0.1	4.981E-07		
	1.7	3.896E-09				

Fig. 8: Plot data of estimated hydraulic conductivity values from different observations.

and permeability tests. This is also due to soil density and soil unsaturation, resulting in higher hydraulic conductivity values in infiltrometer observations, indicating a greater ability to rapidl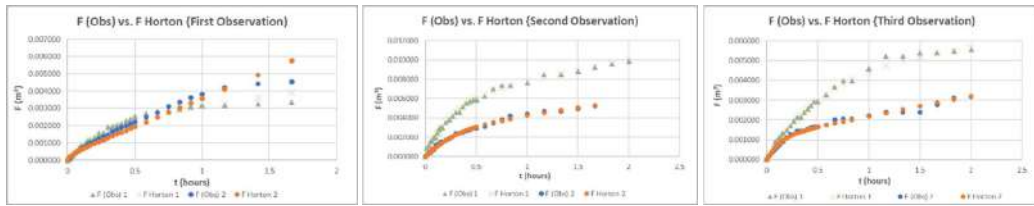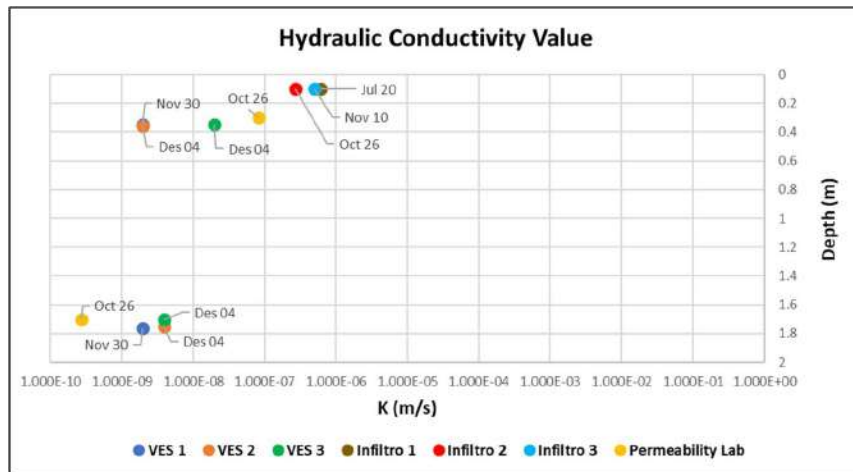y transmit fluids. All observations were recorded with timestamps as seen in the figure, along with weather conditions at the time of observation. For geoelectrical observation on December 4th, rainfall was recorded on the previous days totaling 29.8 mm. For infiltrometer observations, the weather tends to be hot with rainfall occurring before the second infiltrometer observation, amounting to 38.8 mm, precisely on October 25th.

Based on the observations, the hydraulic conductivity values from laboratory permeability tests, which are used as control values for estimates in this study, are the most accurate: 8.330×10^{-8} m/s at a depth of 0.3 meters and 2.669×10^{-10} m/s at a depth of 1.7 meters. The hydraulic conductivity values estimated from infiltrometer observations are significantly different from those obtained from geoelectrical observations and permeability tests. Geoelectrical observations yielded values in the range of 10^{-8} to 10^{-9}, while the average results from infiltrometer observations were in the range of 10^{-7}. It can be logically concluded that at a depth of 1.7 meters, the soil is more saturated compared to a depth of 0.3 meters. This difference could be because surface soil is more frequently affected by climatic and weather changes, such as exposure to sunlight, wind, and rain, which influence soil moisture and water content. Thus, it can be inferred that unsaturated soil, or soil with less water content, has a higher ability to quickly transmit fluids (water), resulting in higher surface conductivity values. However, other factors must also be considered. Specifically, the soil conditions during the observations were different: the geoelectrical observations were conducted on unsaturated soil, while the infiltrometer and laboratory permeability tests were done on saturated

soil. This supports the estimation results, based on the theory explained by Briaud (2013), regarding hydraulic conductivity values for saturated and unsaturated soils.

Briaud (2013) explains that one fundamental observation about water flow in unsaturated soil is that hydraulic conductivity decreases compared to saturated soil. When the soil becomes drier, there is more space for water to flow. However, in reality, this is not the case because air occupies those voids and cannot easily escape, so water can only flow through the remaining water in the soil. The degree of saturation significantly affects hydraulic conductivity values. When the degree of saturation decreases, water content also decreases, and water tension in the soil increases. This is the basic theory of the soil-water retention curve (SWRC). Furthermore, previous research shows the relationship between hydraulic conductivity and water tension. Hydraulic conductivity values depend on water tension; when water tension increases, the amount of water in the soil decreases, making it more difficult for water to infiltrate the soil. Therefore, hydraulic conductivity is lower in unsaturated soil.

CONCLUSION

In this study, both geoelectrical and infiltrometer observations were conducted to estimate hydraulic conductivity values. Based on the estimation results, the geoelectrical observations provided values that closely approximated the laboratory permeability test results. This is attributed to several determining parameters analyzed through assumptions and deductions based on theory and field conditions, such as the formation factor (F) consisting of porosity ($\square$), cementation (m), alpha factor (a), and pore water value. Although geoelectrical observations are generally more cost-effective and faster than drilling and

can infer depth and soil layer thickness, upon comparing the results of all three observations as described and depicted, the estimation of hydraulic conductivity values using the infiltrometer observation method was deemed more effective. This is because the values obtained from the infiltrometer observation method aligned well with the theoretical framework and field conditions. However, it is important to note that infiltrometer observation estimation is limited to surface measurements only and lacks depth information.

REFERENCES

American Standard Testing and Material, n.d. Standard test method for infiltration rate of soils in field using double-ring infiltrometer.

Briaud, J.L., 2013. *Geotechnical engineering: Unsaturated and saturated soils*. New Jersey: John Wiley and Sons, Inc.

BSN, 2012. Tata cara pengukuran laju infiltrasi tanah menggunakan infiltrometer cincin ganda. Jakarta: BSN.

Choo, H., Song, J., Lee, W. and Lee, C., 2016. Effects of clay fraction and pore water conductivity on electrical conductivity of sand-kaolinite mixed soils. *Journal of Petroleum Science and Engineering*, *147*, pp.735-745.

Fetter, C.W., 1994. *Applied hydrogeology*. New Jersey: Prentice-Hall.

Fitts, C.R., 2013. *Groundwater science*. New York: Academic Press.

Freeze, R.A. and Cherry, J.A., 1979. *Groundwater*. United States of America: Prentice-Hall, Inc.

Guymon, G.L., 1994. *Unsaturated zone hydrology*. New Jersey: Prentice-Hall, Inc.

Hossain, K., Anees, M.T., Baker, A.F.B.A., Khan, M.M.A., Khalil, A.E., Ishola, K.S., Abdullah, K., Nawawi, M. and AK, M.O., 2022. Application of geo-electrical methods for estimating water infiltration in soils. *Nature Environment and Pollution Technology*, *21*(3), pp.1279-1288.

Kazakis, N., Vargemezis, G. and Voudouris, K.S., 2016. Estimation of hydraulic parameters in a complex porous aquifer system using geoelectrical methods. *Science of the Total Environment*, *550*, pp.742-750.

Kirsch, R. ed., 2006. *Groundwater geophysics: a tool for hydrogeology*. Berlin, Heidelberg: Springer Berlin Heidelberg.

Niwas, S. and Celik, M., 2012. Equation estimation of porosity and hydraulic conductivity of Ruhrtal aquifer in Germany using near surface geophysics. *Journal of Applied Geophysics*, 84, pp.77-85.

Schön, J.C., 1996. Studying the energy hypersurface of multi-minima systems—the threshold and the lid algorithm. *Berichte der Bunsengesellschaft für physikalische Chemie*, 100(9), pp.1388-1391.

Setiadi, A., 2015. Pengolahan data resistivitas 1D dengan software Progress v.3.0.

Wanielista, M., Kersten, R. and Eaglin, R., 1990. *Hydrology: Water quantity and quality control*. New York: John Wiley and Sons, Inc.

Warsi, T., Kumar, V.S., Dhakate, R., Manikyamba, C., Rao, T.V. and Rangarajan, R., 2019. An integrated study of electrical resistivity tomography and infiltration method in deciphering the characteristics and potentiality of unsaturated zone in crystalline rock. *HydroResearch*, *2*, pp.109-118.

Worthington, P.F., 1993. The uses and abuses of the Archie equations, 1: The formation factor-porosity relationship. *Journal of Applied Geophysics*, *30*(3), pp.215-228.

Zou, C., Zhang, S., Jiang, X. and Chen, F., 2023. Monitoring and characterization of water infiltration in soil unsaturated zone through an integrated geophysical approach. *Catena*, 230, p.107243.

Organic Farming: Emerging Practices, Effect on Environment and Nutrition

P. Kashyap† and **M. Jain**

Food Science and Nutrition Division, Banasthali Vidyapith, Rajasthan-304022, India

†Corresponding author: P. Kashyap; poojakashyap14899@gmail.com

ABSTRACT

The global population surge has escalated the demand for food production. While conventional farming meets consumer demands, it often compromises food quality and safety. This method of agriculture has significant adverse effects on health and the environment, relying heavily on chemical fertilizers, costly seeds, and machinery. Conventional farming contributes to environmental degradation, food-borne illnesses, and soil infertility. In response to these issues, organic agriculture has gained prominence worldwide. The rising demand for organic products is driven by their nutritional and environmental benefits. Numerous studies have explored the advantages and disadvantages of various farming methods, comparing organic and conventional practices. This paper reviews the emerging impacts of organic farming on the environment and climate change and examines the nutritional differences and consumer preferences for vegetables produced by these two farming methods.

INTRODUCTION

The world population crossed over 8 billion on 15 November 2022 as per the Worldometer calculations and it is anticipated to peak in the 2080s at about 10.4 billion people (Gerland et al. 2022). Feeding the population is the primary concern of society. The demand for agricultural goods is anticipated to increase by 25-70% by 2050, putting additional pressure on the environment, especially on natural resources like water, soil, etc. (Hunter et al. 2017). However, the emergence of the green revolution in 1960-1970 solved the food shortage by increasing food production gradually to fulfill consumers' demand, but it also included the use of various chemicals and fertilizers to achieve its objectives. This use of artificial chemicals and fertilizers increased steadily in conventional agriculture (Azam & Shaheen 2019), which resulted in environmental degradation such as soil infertility, air pollution, excessive use of water, and the most affected is the quality of food crops.

Therefore, it became necessary to improve environmental sustainability and food quality through new innovative agricultural methods. In response to these challenges, scientists and agricultural experts started innovating new farming methods that make almost no use of chemicals, leading to an ancient form of farming, i.e., organic farming. Organic farming is the holistic approach and among the most effective chemical-restricted agricultural methods being

used to increase crop production and sustain environmental resources (Heinrichs et al. 2021). Organic farming forbids the use of fertilizers, chemicals, and genetically modified organisms (GMOs) to protect the environment, maintain soil fertility, and maintain biodiversity (Tscharntke et al. 2021). Organic farming methods have gained popularity over the years.

Despite the growing popularity of organic farming, a comprehensive understanding of its relative advantages and disadvantages compared to conventional methods remains elusive. Numerous research studies have attempted to compare the two farming methods, but there are still significant gaps. Thus, there arises a need for collective information that synthesizes and summarizes the findings from research conducted on the developments in organic farming and its comparison with conventional farming practices from the early 1920s to 2023. This paper aims to provide a comprehensive overview of conventional farming, the impact of the green revolution on farming practices in India, historical developments in organic farming, as well as an in-depth analysis of the differences and impacts of both farming practices on various aspects such as the environment, soil quality, climate change, nutritional values, and consumer perspectives. The information for this review paper was collected from different authentic databases including PubMed, Google Scholar, and reports from various organizations such as IFOAM, APEDA, USDA, etc. By

synthesizing findings from a wide range of sources, we seek to explain the potential of organic farming to address contemporary agricultural challenges while promoting environmental sustainability and nutritional quality.

CONVENTIONAL FARMING

Historically, the term 'conventional' has been used to describe the process of cultivating crops on land using fresh water for irrigation, in an open area and excessive use of fertilizers (AlShrouf 2017). This is the most common agricultural method used for growing crops. Conventional agriculture is the most prevalent farming method which is being used for crop production in industrialized nations, therefore, it is also known as industrial agriculture. This approach was designed to cultivate higher amount of food crops with a lower cost of food production, but it accomplishes this at a massive environmental cost, as a substantial quantity of energy and chemicals are needed in conventional agriculture to obtain the required amount of crop productivity (Breza-Boruta et al. 2022).

Whereas growing crops through this method benefits the economy and food security it hinders nutritional security. Environmental protection and biodiversity are typically not sustained in conventional farming as they focus only on increasing crop yield but not on sustaining environmental resources. Conventional farming methods affect the environment adversely in various ways including the excessive use of soil for cultivation, fresh water for irrigation, and high concentration of chemical fertilizers (Alshrouf 2017) and adverse effects on humans, including a decline in human health, particularly in the reproductive and neurological systems (Azam & Shaheen 2019). This farming practice produces minimal returns even while using huge amounts of resources. Many chemical formulations are being introduced in conventional farming, to improve crop production and satisfy food demand which is threatening human health and natural resources.

Green Revolution in India and its Impact

After independence, the most chronic issue India faced was food scarcity. After the subcontinent was divided into India and Pakistan in 1947, the food crisis worsened, posing numerous difficulties for India's agricultural industry. Despite a significant increase in grain output following independence, it wasn't enough to fulfill the demands of a growing population. This necessity resulted in a revolutionary movement of food production known as the 'green revolution' (Rena 2004). Since the middle of the 1960s, the green revolution has allowed many emerging nations to see significant rates of increase in their domestic food grain production. In India, for instance, the

average amount of cereal produce increased by 47% during the years 1952/53-1964/65 and 1967/1968-1977/1978. At the same time, there was a noticeable shift in the coefficient of variation surrounding the trend of total cereal output which rose from 4.7% to 5.9% (Hazell 1984, Pinstrup-Andersen & Hazell 1985). Conventional agriculture is frequently seen to be a logical progression from the green revolution which was started by Norman Borlaug in India. Durham & Mizik (2021) described this method as massive, heavily automated, and reliant on the use of various chemicals and fertilizers. The revolutionary movement of crop production or the green revolution was highly effective which reduced the food shortage progressively and increased food production, but with time, the enormous agricultural operation began to shrivel, and the quality of soil and food started deteriorating due to the continuous use of synthetic fertilizers and strong chemicals (Harish 2020).

ORGANIC FARMING

The ancient and most promising agricultural method to address the emerging concerns of the environment including farming, food quality, and safety and welfare for animals is organic farming (Dhiman 2020). Organic agriculture is the holistic approach used in sustaining environmental resources and improving the quality of products grown. This is considered to be a safer cultivation method without the use of any chemicals or pesticides. Scientific studies conducted on organic foods have reported that organic farming surpasses conventional farming in several aspects, focusing on sustainable practices that promote soil health and biodiversity including nutritional benefits, crop yield, soil quality, pesticides, and so on.

The word "organic" is derived from a living substance which is also known as natural. Thus organic refers to a substance produced naturally or by using living organisms. The International Federation for Organic Agriculture Movement (IFOAM) defined "organic agriculture as a cultivation system that promotes the sustainability of environment, soil, and humans. It relies on biological processes, bio-diversity, and processes that are suitable to natural circumstances despite using elements that have harmful effects.

Organic agriculture integrates science, creativity, and tradition to protect the environment, foster equitable relationships, and advance a better quality of life for all involved. In other words, organic farming employs a range of natural approaches including the use of organic remedies, bio-fertilizers, bio pest management, and crop rotation methods while avoiding chemicals, pesticides, and fertilizers, to improve the food quality and advance sustainability (Kontopoulou et al. 2015). Compared to conventional

farming, organic farming reduces the total quantity of nitrate that enters both ground and surface water, employs compost as fertilizer, recycles animal waste, and reduces soil loss.

Origin and History

Indian organic farming has been more significant nowadays due to its high-quality output, environmental safety, and lucrative living. Though the concept of "organic agriculture" has gained prominence recently, the pieces of evidence can be found in history. The Vedas of the "Later Vedic Period," which spanned from 1000 BC to 600 BC, are believed to have developed the first "scientific" method of organic farming (Randhawa 1986). The secret is to align with nature rather than destroy it. The three main texts in this context are "Vrikshayurveda" (the study of longevity and the health of plants), "Krishisastra" (the study of agriculture), and "Mrugayurveda" (the study of animals) (Mahale & Soree 1999).

Vedic scriptures make mention of knowledge of agriculture, plant biodiversity, etc. Panchagavya, the earliest and original organic bio-fertilizer, was used in Vedic farming. The term "Panchagavya" in Sanskrit refers to a mixture of different five products derived by cow, viz., milk, ghee, yogurt, dung, and urine. When these components are combined with water, this results in a product known as "Amrit-pani," a nourishing nectar used to irrigate the plantings and produce an abundance of healthy crops (Dhama et al. 2005, Ram & Garg 2020).

Various religious literatures such as Ramayana, Mahabharata, Rig Veda, Holy Quran, etc., have mentioned organic agriculture. Organic farming has its origins in the ancient agricultural methods that have been used for millennia in many rural settlements and villages. The historical texts of organic farming mention that it was practiced in the 'Neolithic age' by ancient civilizations around 10000 years back. The celestial cow Kamadhenu and its impact on the fertility of the soil and human existence are mentioned in Mahabharata, Kautilya Arthashastra mentioned several types of manures such as animal dung, etc. Brihad-Sanhita mentioned the techniques of manuring and how to select manures for various crops. Organic manure is also mentioned in Rig Veda and Atharva Veda II (Lichtfouse 2011).

Organic farming has been done since earlier times in the form of traditional farming and is far better than modern farming methods in the current global scenario. The father of modern organic agriculture is considered to be the British botanist Sir Albert Howard who mentioned that the ancient Indian agricultural system is superior to the present conventional farming system (Pandey & Singh 2012). The significance of decaying and dead matter for soil fertility and

sustaining life is also discussed in the old Indian scriptures. In various portions of these publications, the significance of bio-composts and reusing post-harvest leftovers have additionally been covered. The movement of organic farming has strong roots that are presently implanted in worldwide culture (Barton 2017). The benefits of organic farming for environmental protection, food and nutrition security, and the battle against climate change are well known. Convictions rooted in philosophy, religion, and ideology have also led to the commercial use of organic farming with a business perspective of caring for the environment and producing high-quality goods (Behera et al. 2012).

Major Developments in Organic Farming

Organic agricultural methods have become popular in the past few years. The major developments in organic farming are summarised in Table 1.

Global Scenario

Organic farming has grown steadily in the global marketplace over the last few decades. From the 2000s, the market for organically grown products has rapidly increased. Fig. 1 represents annual statistics on the area of organic farmland from the year 2000 to 2022. Organic farmland increased from 11 million hectares to 43.7 million hectares from the year 1999 to 2014. The worldwide market of organic products was $15.2 billion in 1999 and expanded to $80 billion in 2014 and organic producers increased to 2.3 million in the year 2014 (IFOAM 2015). The organic market continued to grow worldwide and was more than $1000 billion in 2018 and there were about 2.8 million organic producers globally, the maximum being in India (IFOAM 2019). The annual data from the year 2000 to 2022 for Indian farmland for organic products along with its percentage of the total farmland is shown in Fig. 2. The latest FiBL survey report on global organic farming shows that organic farmland continued to grow and reached more than 74.9 million hectares by the year 2020. In organic farms, there has been a 4.1% (3.0 million hectare) rise seen in 2020 (IFOAM 2020). As of March 31, 2023, 10.17 million hectares (2022–2023) of land were registered under the National Programme for Organic Production (NPOP) that are subjected to the organic certification legal procedure. This comprises a cultivable area of 5391792.97 ha and a wild harvest gathering area of 4780130.56 ha of organic farming (APEDA 2023). Numerous nations reported a noticeable increase.

IMPACT OF THE ORGANIC FARMING ON ENVIRONMENT AND BIODIVERSITY

Organic farming has a substantial positive environmental

Table 1: Major developments in organic farming.

| Major Developments	Year	Reference
Organic movement started by botanists Albert Howard and Gabrielle Howard	1921	Barton (2017)
Emergence of organic farming in Germany	1924	Paull (2011)
Rudolf Steiner's agricultural course on "Social scientific basis of agricultural development"	1924	Paull (2011)
Hans Mueler encouraged organic agriculture in Switzerland	1930	Tomaš-Simin & Glavaš Trbić (2016)
Mokichi Okada started Organic agricultural approach in Japan	1935	Okubo (1993)
Publication of "An Agricultural Testament" by Albert Howard	1940	Heckman (2006)
The book "Look to the Land" by Walter James aka Lord Northbourne and his focus on "farm as an organism"	1940	Paull (2006)
Organic Gardening magazine in the USA published by Rodale J.I. to avoid the use of chemicals in farming	1942	Klonsky & Tourte (1998)
Worldwide expansion of organic farming	1960s	Joachim (2006)
Rachel Carson's book "Silent Spring" underlined the effects of DDT and other pesticides on wildlife and the environment	1962	Santos (2017)
Principles of "Ecological Agriculture" propounded by William Albrecht	1970	Joachim (2006)
Establishment of IFOAM	1972	Geier (2007)
Foundation of Research Institute of Organic Agriculture (FiBL) in Switzerland was established	1973	Willer & Yussefi (2000)
Legislation of Organic Farming by the State of Oregon, USA	1974	Morgera et al. (2012)
Creation of the National Federation of Organic Farming in France	1978	Paull (2010)
Legislation on Organic Farming by State of California	1979	Morgera et al., (2012)
Basic standards and regulations by IFOAM for organic agriculture certifications	1980	Paull (2010)
"Report and Recommendations on Organic Farming" released by USDA	1980	USDA (1980)
Symposium on Organic Farming by American Society of Agronomy	1981	Elliott et al. (1984)
The US trade embargo in Cuba made it difficult to import chemical fertilizers which led them toward organic farming	1989	Warwick (1999)
BioFach Fair, the first fair on organic products organized by Germany	1990	Simin & Glavaš-Trbić (2016)
US Congress passed the Organic Foods Production Act (OFPA)	1990	Johnson (2008)
European Commission adopted EU regulations	1991	Morgera et al. (2012), Rundgren (2008)
EU member countries adopted EU regulations	1994	Morgera et al. (2012), Rundgren (2008)
First National Organic Program released by USDA	1997	Heckman (2006)
Introduction of Codex Alimentarius organic guidelines for animal husbandry	2001	Willer & Lernoud (2019)
Implementation of OFPA regulations	2002	Carter et al. (2015)
The first action plan on organic food and farming adopted by the European Commission	2004	Schmid et al. (2008)
Launch of National Organic Program by USDA	2006	NOP (2006)
IFOAM's new Organic Guarantee System was launched	2010	Willer & Lernoud (2019)
Marketing support to organic farmers by NABARD	2012	NABARD (2012)
Mission Organic Value Chain Development for Eastern Region (MOVCDNER)	2015	NCOF (2015)
Food Safety and Standards (Organic Food) Regulations were formed	2017	FSSAI (2017)
National Programme for Organic Production launched by APEDA in India	2018	APEDA (2018)
Launch of United Nations Decade of Family Farming 2019-2028	2019	FAO & IFAD (2019)
Implementation of organic regulations fully by 72 countries	2020	Willer et al. (2021)
Organic market reached more than 100 billion euros worldwide	2021	Willer et al. (2021)
IFOAM launched a new global map of Participatory Guarantee System Initiatives	2022	Willer et al. (2023)
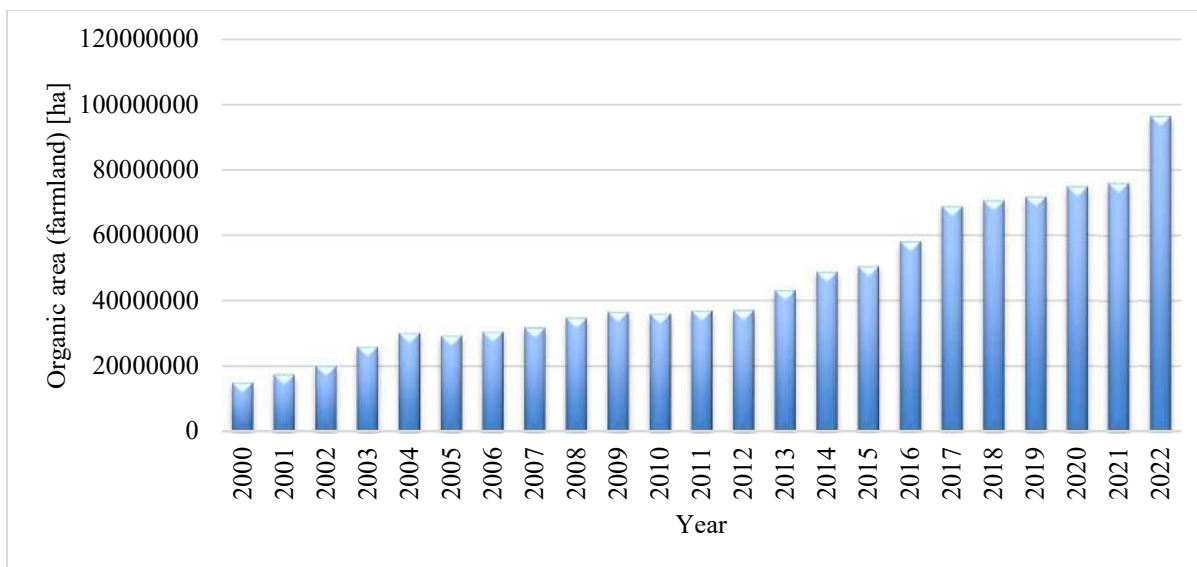
(Source: FiBL Statistics)

Fig. 1: Annual global farmland for organic products.
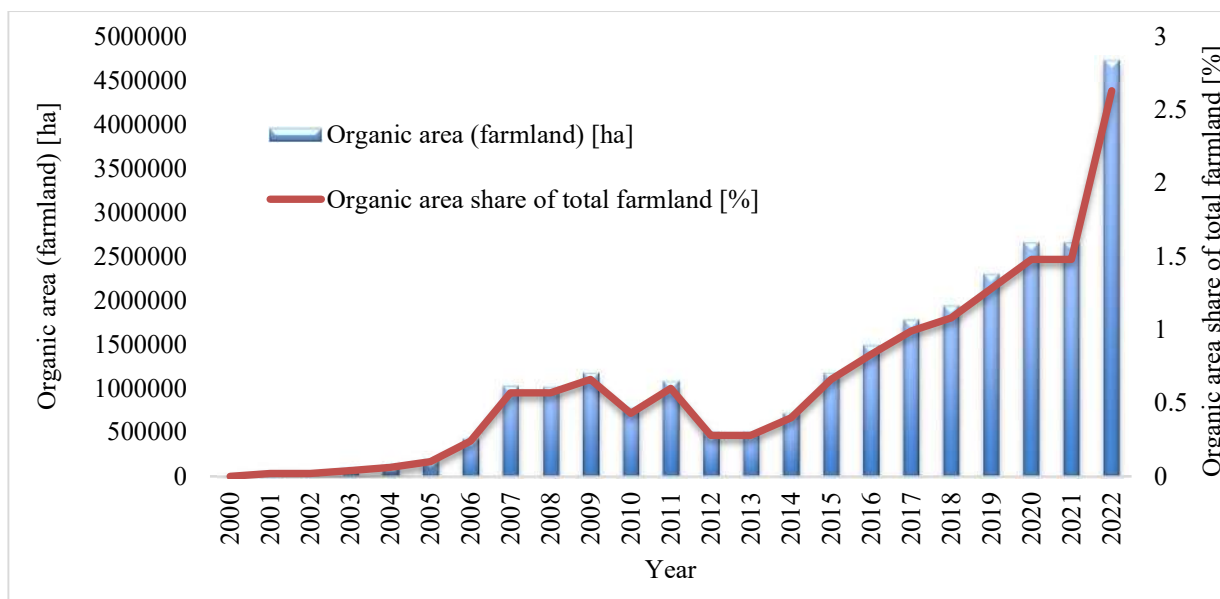
(Source: FiBL Statistics)

Fig. 2: Annual Indian farmland for organic products with a percentage share of total farmland.

impact as it encourages sustainability and lessens the harmful consequences of conventional agricultural methods. It not only emphasizes using natural fertilizers, reducing the use of artificial chemical fertilizers, and improving soil health but also contributes to preserving ecological balance (Tripathi et al. 2023, Tong et al. 2022). Organic farming methods lower agricultural production costs while also improving soil quality as they focus more on the health of the soil instead of feeding the individual plant or crop. Thus, it lessens the chances of health hazards associated with residues which helps the environment and promotes ecological balance and sustainability. In comparison with conventional and low-input approaches, organic farming in greenhouses boosts soil fertility but poses higher ecological concerns due to the rise in heavy metals and antibiotic residues. Long-term organic farming, yet carries ecological dangers since it

may raise heavy metal levels and pesticide and antibiotic residues in the soil (Moreau et al. 2022). In comparison to traditional farming practices, organic farming promotes agro-environmental sustainability by recycling nutrients, using renewable resources, controlling pests organically, decreasing pollution, and safeguarding soils and ecosystems. Research indicates that organic agricultural practices enhance the diversity and quantity of beneficial creatures, such as predators, which improves pest control. By successfully controlling herbivore populations, organic agriculture supports the preservation of the biodiversity of natural enemies. Moreover, it increases soil microbial diversity, which supports more sustainable farming methods and better crop microbiomes. Since it increases species variety and ecosystem function, organic farming has a favorable influence on biodiversity.

Soil Quality

Agricultural practices are constantly using land areas in large quantities. These agricultural land usage results in severe hazards for soil degradation that exist globally and further agricultural intensification. The physical characteristics, microbe populations, nutrients present in the soil, and quality of soil are all influenced by agricultural treatments, and these changes could potentially have detrimental effects on human society (Setälä et al. 2014). Based on several factors, organic and conventional farming techniques have different soil quality. Improved soil physical characteristics, such as increased porosity and decreased bulk density, are typically observed in organic farming (Kim et al. 2023). Furthermore, compared to conventional systems, organic systems often have improved biological soil quality, with greater levels of soil organic carbon and more earthworm abundance (Krause et al. 2022, Maucieri et al. 2022). When it comes to the health of soil, long-term studies reported that organic farming can result in stable or increased levels of soil organic carbon (Aulakh et al. 2022, Maniraho et al. 2022). In organic agricultural methods, the use of natural waste and diversified cropping enhances the soil quality, whereas conventional farming relies more on agrochemical inputs, which may lead to imbalanced soil quality.

Climate Change

A contributing factor to global warming is the greenhouse gas (GHG) emissions from agriculture. In agriculture, carbon dioxide (CO_2), methane (CH_4), and nitrous oxide (N_2O) are the primary greenhouse gases (GHGs) (Devi et al. 2023). These gases are released through a variety of agricultural practices and have a substantial impact on climate change. The primary causes of N_2O emissions in agriculture are the use of chemical fertilizers, inadequate irrigation, and the deposition of animal excrement. N_2O emissions are mostly caused due to conventional farming using continuously synthetic fertilizers. Direct processes, such as nitrification and denitrification, as well as indirect ones, like nitrate leaching and runoff, both are responsible for these emissions. Whereas using organic fertilizers in agriculture has the potential to lower N_2O emissions as it uses only organic manure, and no artificial chemicals or fertilizers are used (Mousavi et al. 2023). Research indicates that substituting a segment of synthetic nitrogen fertilizers with organic manure can reduce greenhouse gas emissions and simultaneously enhance agricultural yields and soil fertility. Furthermore, owing to improved soil conditions, replacing synthetic fertilizers with organic manure over time may both reduce and increase N_2O emissions (Xie et al. 2022, Zhao et al. 2022). Thus, switching to organic farming and using less synthetic fertilizer may be essential to lowering N_2O emissions and advancing sustainable farming methods.

CO_2 emissions from organic farming are typically higher because compared to conventional farming, soil microbial activity is higher in organic agricultural systems (Santoni et al. 2022). Additionally, hydrothermal conditions have a greater impact on CO_2 emissions in conventional and organic farming. While there is enough enzymatic activity in both systems, invertase activity is higher in organic farming. Organic food production has a reduced carbon footprint per unit area and per unit of product, which helps to reduce overall greenhouse gas emissions (Chiriacò 2022). Conversely, conventional farming is associated with greater CO_2 emissions due to variables such as higher energy inputs, such as the transportation of imported feed and the manufacturing of energy-intensive concentrates. Despite these variances, soil microbial biomass, nutrient management strategies, and crop varieties planted in the system all affect the overall impact of organic agricultural practices on CO_2 emissions.

Many researches have indicated that organic agricultural practices can mitigate the release of greenhouse gases, such as CH_4. The application of organic fertilizers, such as native organic fertilizers, has been shown to reduce CH_4 emissions in paddy fields (Ravikumar et al. 2023). The organic fertilizers exhibit lower CH_4 emissions than chemical fertilizers. Furthermore, organic farming can to reduce total GHG emissions as evidenced by the comparison of conventional and organic arable farming systems, which showed that organic farming had zero CH_4 emissions and even functioned as a greenhouse gas sink in some situations (Biernat et al. 2020). When compared to conventional farming practices, these studies demonstrate the environmental benefits of organic farming in terms of reduced CH_4 emissions. The kind of fertilizer used had an impact on CH_4 emissions; industrial chemical synthesis

Table 2: Studies conducted on nutritional differences in conventional and organic vegetables.

Fruit/Vegetable	Parameters	Inferences	Reference
Fruits and vegetables	Vitamin C, Iron, Magnesium, Phosphorus, Nitrate	Organic foods have higher concentrations of vitamin C, iron, magnesium, and phosphorus and lower levels of nitrates in organic foods.	Worthington (2001)
Marionberries, Corn, Strawberry	Total Phenolic Content (TPC)	Levels of TPC were significantly higher in organically grown	Asami et al. (2003)
Leafy vegetables	Sugars, Vitamin C, Nitrate	Sugars and vitamin C were found consistently higher in organic vegetables with lower nitrate levels.	Xu et al. (2003)
Plums	Ascorbic acid, Alpha and Gamma Tocopherols and Beta-carotene	Greater levels of ascorbic acid, alpha, and gamma tocopherols, and beta-carotene in organic plums	Lombardi-Boccia et al. (2004)
Potatoes	Chlorogenic acid, Glycoalkaloids, Vitamin C	Higher chlorogenic acid content and vitamin C content with increased concentrations of glycoalkaloids in organically produced potatoes	Hajšlová et al. (2005)
Tomatoes	Titrable Acidity, Soluble Solids, Consistency	Higher amounts of titrable acidity, soluble solids, and consistency in organically grown tomatoes	Barrett et al. (2007)
Onions	Flavonoids, Vitamin C, Anthocyanins	Higher flavonoid, vitamin C, and anthocyanin content in organically produced onions	Hallman & Rembialkowska (2007)
Green vegetables	Heavy metals	Lower content of heavy metals in organic vegetables. Conventionally grown leafy greens, green pepper and spinach, and organically grown lettuce and green pepper exceeded the Cadmium limit recommended by FAO/WHO.	Dotse (2010)
Carrot, Celery, Red beet juices	Minerals and Heavy metals	Organic juices typically contain higher concentrations of minerals and heavy metal accumulation was higher in conventional juices.	Domagała-Świątkiewicz & Gąstoł (2012)
Red beetroot plants	Ascorbic acid, Antioxidant activity, Mineral components	Higher ascorbic acid, antioxidant activity, Sodium, copper, iron, manganese, nitrogen, and lower amounts of phosphorus, potassium, and magnesium in organic product	Straus et al. (2012)
Brassica vegetables	Glucosinolates and Antioxidant profile	Glucosinolates were twice as high in organically produced vegetables and antioxidant activity was higher in organic foods.	Vicas et al. (2013)
Lettuce, Pepper, Tomato	Dietary fiber	High total dietary fiber in organic vegetables	de Souza Araújo et al. (2014)
Onion	Flavonoids and Phenols	Similar flavonoid and phenol content in both	Lee et al. (2015)
Lettuce	Microelements	Compared to lettuce produced organically, commercial lettuce had higher levels of calcium, magnesium, manganese, iron, and copper.	Kapoulas et al. (2017)
Green leafy vegetables and other vegetables	Minerals, Vitamin C, Heavy metals	Mineral and vitamin C content is higher in organic samples. Organic vegetables were free from heavy metals.	Xavier et al. (2020)
Vegetables	Antioxidant compounds	Organic vegetables showed lower nitrate content, higher phenolics, antioxidant capacity, and soluble solids whereas only a few had higher ascorbic acid.	Roumeliotis et al. (2021)
Vegetables	Carotenoids	The only raw vegetable with a greater concentration of carotenoids in organic agriculture was carrot, although conventionally cultivated zucchini and broccoli had higher amounts.	de Castro et al. (2021)
Lemon	Amino acid, fatty acid, antioxidant activity, polyphenols	Conventionally grown lemons had higher amino acid and fatty acid content whereas no differences were found in antioxidant activity and polyphenol content among conventional and organic grown	Sánchez-Bravo et al. (2023)

fertilizers markedly increased CH_4 fluxes in comparison to organic resources such as organic manures (Sosa-Rodrigues & Garcia-Vivas 2019).

NUTRITIONAL COMPARISON

The nutritional content of fruits and vegetables is influenced by several factors, including factors from production to packaging such as genetic, ecological, and agricultural factors (Roumeliotis et al. 2021). Recently, agricultural systems have received a lot of attention among the aspects that have been studied. The majority of studies have compared various qualities of organic and conventionally grown vegetables, but recent reviews have found inconsistent differences in nutritional compounds. However, most research and review articles only focused on different parameters, and when it comes to the overall nutritional composition, insufficient information is available on the nutritional differences between conventional and organic vegetables and published findings are inconsistent. The collected review on nutritional differences between conventional and organic-grown fruits and vegetables is summarised in Table 2.

CONSUMER AWARENESS AND PURCHASING BEHAVIOR

During the COVID-19 epidemic, the Food Safety and Standards Authority of India's (FSSAI) 'Eat Right India' campaign enlightened the people about the value of eating the right foods and raised awareness about the need for wholesome food. This effort improved awareness amongst consumers about the advantages of choosing organic food. Consumers are concerned about safe food, nutrition, bioactive chemicals, and the dangers of pesticides (Rahman et al. 2021). The market for organic products is rising because more customers believe these items to be better for immunity, higher quality, and more readily available through online/e-commerce platforms (IFOAM 2019). Considerations for organic food products include freshness and sustainability of consumption, extrinsic qualities, health, nutritional benefits, sensory appeal, and socio-economic status. Additionally, depending on the product category, consumer motives, preferences, and attitudes can change. A positive attitude was found among consumers regarding organic vegetables and they also believe that organic agriculture promises environmental conservation, wildlife conservation, and the conservation of environmental resources (Melović et al. 2020). Organic vegetables have their own importance and surplus value which influences the purchasing behavior of consumers. Consumers choose organic products because of their nutritional value and fewer effects on the environment (Suciu et al. 2019).

A study conducted to assess the various factors that influence the purchasing behavior of consumers in India towards organic products revealed that consumer attitude towards organic food was affected by four factors: health consciousness, knowledge of organic foods, subjective norms, and perceived price. However, purchase intention was also affected by the four factors and another factor, i.e., availability. Results also showed that income was also one of the influencing factors as high-earners were more likely to purchase organic products. The findings also suggested that highly educated consumers are more inclined to purchase organic foods than consumers who are less educated (Singh & Verma 2017). A study conducted to observe the impact of the National Organic Program in the US in 2002 reported that consumers were prepared to pay higher rates for organically produced goods, including those that include less than 100% organic components. Consumers with children were more likely to spend more for cereals with organic content levels of 70–95% and 95–99% than were those without children. Compared to men, women were more likely to pay more for all features, especially those with larger percentages of organic, pesticide- and GM-free components (Batte et al. 2007). Modern consumer trends are heavily influenced by the increasing cases of lifestyle diseases including heart disease and depression. Rana & Paul (2017) also revealed in the review paper that consumers who are health conscious are continuously choosing organic products over conventionally produced food. Additionally, the purchase intentions of many consumers are based on their commitment to health, which is positively connected with their attitude and behavior toward purchasing. Organic products are considered safer and healthier, while organic methods are considered more ecologically friendly (Paul & Rana 2012). Therefore, more and more consumers are opting for organic produce from certified organic farms as a result of society's continually expanding ecological and nutritional consciousness. In addition to serving a nutritious purpose, such food may help people stay healthy and is crucial for preventing health problems in society (Breza-Boruta et al. 2022).

COMPARISON BETWEEN ORGANIC AND CONVENTIONAL FARMING

The majority of the population is dependent on conventional products. Various studies have compared conventional and organic agriculture based on various aspects such as nutritional parameters, soil health, crop yield, pesticide residues, and many more. As per Hans & Rao (2018), conventional agriculture is large-scale whereas organic farming is a small-scale production process. Conventional farming uses pesticides and fertilizers for crop production

that not only cause environmental damage but also contaminate food crops which can cause severe health problems in human beings while organic farming uses bio-fertilizers that do not cause any harm to the ecosystem and also release nutrients using micro-organisms (Al-Khafaji et al. 2018). In terms of biodiversity, organic farming is seen to be a better ecological substitute for conventional farming, which is connected to the loss of biodiversity worldwide and supports a higher diversity of fauna. GHG emissions from organic farming are lower than those from conventional agricultural methods. This paper discusses the differences between organic and conventional food products. The studies evaluated included information on environmental impact and benefits, soil quality, impact on climate change, nutritional quality, consumer perception and preferences, and the significant developments of organic farming. Most of the variations between conventional and organic products are substantially correlated with variations in GHG emissions, heavy metals, macro- and micronutrients, and consumer preferences. According to the literature reviewed, consumer preferences for organic products are found higher as compared to conventional produce. Despite some challenges, organic agricultural practices are acknowledged for their ability to minimize pollution, minimize environmental impact, maximize biological productivity, and support a healthy ecosystem.

CONCLUSIONS

Although conventional farming can feed the rising population, excessive pesticides, and fertilizers are harmful to human health and responsible for several diseases and illnesses. In this circumstance, organic farming has shown to be a more nutrient-dense, healthful, and sustainable agricultural method. The demand for organic food is always increasing. The desire for high-quality foods, the spread of ecologically friendly manufacturing techniques, and consumers' increased interest in leading healthy lifestyles are the main causes of organic product demands. India is the largest producer of organic goods globally. India is where organic farming first emerged, and it is predicted that organic farming practices will continue to be encouraged and implemented. India will soon become a country with a balanced diet, economy, environment, and health. Organic farming is practiced worldwide due to its advantages and eco-friendly attributes. Furthermore, there is a need for organic items on the global market, and the organic produce industry has lately had the quickest growth globally. There is still a requirement for further research about yielding more food products with fewer resources while preserving the environment and human health with more nutritional, ecological, and economic benefits.

REFERENCES

Al-Khafaji, H.H., Talib, M.S. and Hadi, K.F., 2018. Effect of organic manure and plant population on growth and yield of *Vicia faba* L. *Research on Crops*, 19(3), pp.405-408. https://doi.org/10.31830/2348-7542.2018.0001.7

AlShrouf, A., 2017. Hydroponics, aeroponic and aquaponic as compared with conventional farming. *American Scientific Research Journal for Engineering, Technology, and Sciences*, 27(1), pp.247-255.

APEDA, 2018. National Programme for Organic Production. Ministry of Commerce and Industry, Government of India, New Delhi, India. Retrieved December 15, 2023, from: https://apeda.gov.in/apedawebsite/Announcements/NPOP_Training_Manual_English_E_Book.pdf

APEDA, 2023. National Programme for Organic Production. Ministry of Commerce and Industry, Government of India, New Delhi, India. Retrieved March 3, 2024, from: https://www.apeda.gov.in/apedawebsite/organic/Organic_Products.htm

APEDA. National Programme for Organic Production, Ministry of Commerce and Industry, Government of India, New Delhi, India. Retrieved February 5, 2024 from: https://www.apeda.gov.in/apedawebsite/organic/Organic_Products.htm

Asami, D.K., Hong, Y.J., Barrett, D.M. and Mitchell, A.E., 2003. Comparison of the total phenolic and ascorbic acid content of freeze-dried and air-dried marionberry, strawberry, and corn grown using conventional, organic, and sustainable agricultural practices. *Journal of Agricultural and Food Chemistry*, 51(5), pp.1237–1241. https://doi.org/10.1021/jf020635c

Aulakh, C.S., Sharma, S., Thakur, M. and Kaur, P., 2022. A review of the influences of organic farming on soil quality, crop productivity and produce quality. *Journal of Plant Nutrition*, 45(12), pp.1884–1905. https://doi.org/10.1080/01904167.2022.2027976

Azam, M.S. and Shaheen, M., 2019. Decisional factors driving farmers to adopt organic farming in India: a cross-sectional study. *International Journal of Science Economics*, 46(4), pp.562-580. https://doi.org/10.1108/IJSE-05-2018-0282

Barrett, D.M., Weakley, C., Diaz, J.V. and Watnik, M., 2007. Qualitative and nutritional differences in processing tomatoes grown under commercial organic and conventional production systems. *Journal of Food Science*, 72(9), pp.C441-C451. https://doi.org/10.1111/j.1750-3841.2007.00500.x

Barton, G.A., 2017. The myth of the peasant in the global organic farming movement. *Itinerario*, 41(1), pp.75–91. https://doi.org/10.1017/S0165115317000080

Batte, M.T., Hooker, N.H., Haab, T.C. and Beaverson, J., 2007. Putting their money where their mouths are: Consumer willingness to pay for multi-ingredient, processed organic food products. *Food Policy*, 32(2), pp.145–159. https://doi.org/10.1016/j.foodpol.2006.05.003

Behera, K.K., Alam, A., Vats, S., Sharma, H.P. and Sharma, V., 2012. Organic farming history and techniques. *Agroecology and strategies for climate change*, pp.287–328. https://doi.org/10.1007/978-94-007-1905-7

Biernat, L., Taube, F., Loges, R., Kluß, C. and Reinsch, T., 2020. Nitrous oxide emissions and methane uptake from organic and conventionally managed arable crop rotations on farms in Northwest Germany. *Sustainability*, 12(8), p.3240. https://doi.org/10.3390/SU12083240

Breza-Boruta, B., Ligocka, A. and Bauza-Kaszewska, J., 2022. Natural bioactive compounds in organic and conventional fermented food. *Molecules*, 27(13), p.4084. https://doi.org/10.3390/molecules27134084

Carter, D.P., Weible, C.M., Siddiki, S.N., Brett, J. and Chonaiew, S.M., 2015. Assessing policy divergence: How to investigate the differences between a law and a corresponding regulation. *Public Administration*, 93(1), pp.159-76. https://doi.org/10.1111/padm.12120

Chiriacò, M.V., 2022. Organic versus conventional food emissions under different carbon footprint metrics. *EGU General Assembly 2022*, Vienna, Austria, 23-27 May 2022, EGU22-2713. https://doi.org/10.5194/egusphere-egu22-2713

de Castro, N.T., de Alencar, E.R., Zandonadi, R.P., Han, H., Raposo, A., Ariza-Montes, A., Araya-Castillo, L. and Botelho, R.B.A., 2021. Influence of cooking method on the nutritional quality of organic and conventional Brazilian vegetables: A study on sodium, potassium, and carotenoids. *Foods*, 10(8), p.1782. https://doi.org/10.3390/foods10081782

de Souza Araújo, D.F., da Silva, A.M., de Andrade Lima, L.L., da Silva Vasconcelos, M.A., Andrade, S.A. and Sarubbo, L.A., 2014. The concentration of minerals and physicochemical contaminants in conventional and organic vegetables. *Food Control*, 44, pp.242-248. https://doi.org/10.1016/j.foodcont.2014.04.005

Devi, O.R., Laishram, B., Singh, S., Paul, A., Sarma, H.H., Bora, S.S. and Devi, S.B., 2023. A review on mitigation of greenhouse gases by agronomic practices towards sustainable agriculture. *International Journal of Environment and Climate Change*, 13(8), pp.278-287. https://doi.org/10.9734/ijecc/2023/v13i81952

Dhama, K., Rathore, R., Chauhan, R.S. and Tomar, S., 2005. Panchgavya (Cowpathy): an overview. *International Journal of Cow Science*, 1(1), pp.1-5.

Dhiman, V., 2020. Organic farming for sustainable environment: Review of existed policies and suggestions for improvement. *International Journal of Research and Review*, 7(2), pp.22-31.

Domagała-Świątkiewicz, I. and Gąstoł, M., 2012. Comparative study on mineral content of organic and conventional carrot, celery and red beet juices. *Acta Scientiarum Polonorum. Hortorum Cultus*, 11(2), pp.173-183.

Dotse, C.K., 2010. Assessing commercial organic and conventionally grown vegetables by monitoring selected heavy metals found in them. *Electronic Theses and Dissertations*, Department of Chemistry, East Tennessee State University, United States.

Durham, T.C. and Mizik, T., 2021. Comparative economics of conventional, organic, and alternative agricultural production systems. *Economies*, 9(2), pp.1-22. https://doi.org/10.3390/economies9020064

Elliott, L.F., Papendick, R.I. and Parr, J.F., 1984. Summary of the organic farming symposium. *Organic farming: Current technology and its role in a sustainable agriculture*, 46, pp.187-192.

Geier, B., 2007. IFOAM and the history of the International Organic Movement. In: Lockerets, W. (Ed.), *Organic Farming: an international history*. Wallingford, UK, pp.175-186. https://doi.org/10.1079/9780851998336.0175

Gerland, P., Hertog, S., Wheldon, M., Kantorova, V., Gu, D., Gonnella, G., et al., 2022. World Population Prospects 2022: Summary of Results; United Nations Department of Economic and Social Affairs: New York, NY, USA.

Hajšlová, J., Schulzová, V., Slanina, P., Janne, K., Hellenäs, K.E. and Andersson, C.H., 2005. Quality of organically and conventionally grown potatoes: Four-year study of micronutrients, metals, secondary metabolites, enzymic browning and organoleptic properties. *Food additives and contaminants*, 22(6), pp.514-534. https://doi.org/10.1080/02652030500137827

Hallman, E. and Rembialkowska, E., 2007. Selected nutrient content in red onions from organic and conventional production. *Food Science Technology Quality*, 2(51), pp.105–111.

Hans, V.B. and Rao, R., 2018. organic farming for sustainable development in India. *Acta Scientific Agriculture*, 2(12), pp.96-102.

Harish, N., 2020. Organic farming in India: Status, constraints and challenges. *International Journal of Economics*, 8(3), pp.11–15. https://doi.org/10.34293/economics.v8i3.2294.

Hazell, P.B., 1984. Sources of increased instability in Indian and US cereal production. *American Journal of Agricultural Economics*, 66(3), pp.302-311. https://doi.org/10.2307/1240797.

Heckman, J., 2006. A history of organic farming: Transitions from Sir Albert Howard's war in the soil to USDA National Organic Program. *Renewable Agriculture Food Systems*, 21(3), pp.143–150. https://doi.org/10.1079/raf2005126.

Heinrichs, J., Kuhn, T., Pahmeyer, C. and Britz, W., 2021. Economic effects of plot sizes and farm-plot distances in organic and conventional farming systems: A farm-level analysis for Germany. *Agricultural Systems*, 187, p.102992. https://doi.org/10.1016/j.agsy.2020.102992.

Hunter, M.C., Smith, R.G., Schipanski, M.E., Atwood, L.W. and Mortensen, D.A., 2017. Agriculture in 2050: Recalibrating targets for sustainable intensification. *BioScience*, 67(4), pp.386–391. https://doi.org/10.1093/biosci/bix010.

IFOAM, 2015. Into the future: Annual Report 2015. Consolidated annual report of IFOAM - Organics International. IFOAM Organic International. Retrieved February 5, 2024, from: https://www.ifoam.bio/sites/default/files/2020-03/annual_report_2015_0.pdf.

IFOAM, 2019. #We unite: Annual Report 2019. Consolidated annual report of IFOAM - Organics International & its action group. IFOAM Organic International. Retrieved February 5, 2024, from: https://www.ifoam.bio/sites/default/files/2020-12/AnnualReport2019.pdf.

IFOAM, 2020. Reflect, Reunite, Revitalize: Annual Report 2020. Consolidated annual report of IFOAM - Organics International & its action group. IFOAM Organic International. Retrieved February 5, 2024, from: https://www.ifoam.bio/sites/default/files/2021-06/Annual%20Report%202020.pdf.

Johnson, R., 2008. Organic agriculture in the United States: Program and policy issues. *Congressional Research Service, the Library of Congress*.

Kapoulas, N., Koukounaras, A. and Ilić, Z.S., 2017. Nutritional quality of lettuce and onion as companion plants from organic and conventional production in north Greece. *Scientia Horticulturae*, 219, pp.310–318. https://doi.org/10.1016/j.scienta.2017.03.027.

Kim, J.W., Hong, Y.K., Lee, C.R. and Kim, S.C., 2023. Comparison of physicochemical and biological soil properties in organic and conventional upland fields. *Korean Journal of Soil Science and Fertilizer*, 561, pp.77–89. https://doi.org/10.7745/KJSSF.2023.56.1.077.

Klonsky, K. and Tourte, L., 1998. Organic agricultural production in the United States: Debates and directions. *American Journal of Agricultural Economics*, 80(5), pp.1119–1124. https://doi.org/10.2307/1244215.

Kontopoulou, C.K., Bilalis, D., Pappa, V.A., Rees, R.M. and Savvas, D., 2015. Effects of organic farming practices and salinity on yield and greenhouse gas emissions from a common bean crop. *Scientia Horticulturae*, 183, pp.48-57. https://doi.org/10.1016/j.scienta.2014.12.012.

Krause, H.M., Stehle, B., Mayer, J., Mayer, M., Steffens, M., Mäder, P. and Fliessbach, A., 2022. Biological soil quality and soil organic carbon change in biodynamic, organic, and conventional farming systems after 42 years. *Agronomy for Sustainable Development*, 426, p.117. https://doi.org/10.1007/s13593-022-00843-y.

Lichtfouse, E., 2011. Agroecology and strategies for climate change, vol. 8. Springer Science & Business Media, New York. https://doi.org/10.1007/978-94-007-1905-7.

Lombardi-Boccia, G., Lucarini, M., Lanzi, S., Aguzzi, A. and Cappelloni, M., 2004. Nutrients and antioxidant molecules in yellow plums (*Prunus Domestica* L.) from conventional and organic productions: a

comparative study. *Journal of Agricultural and Food Chemistry*, 52, pp.90-94. https://doi.org/10.1021/jf0344690.

Mahale, P. and Soree, H., 1999. Ancient visions and new experiments of rural people. In: *Food for Thought*. India Books for Change, Bangalore.

Maniraho, E., Nkezabera, J.A., Mupenzi, C. and Nishimwe, G., 2022. Soil quality indicators under conventional and organic coffee farming systems in Rwanda. *International Journal of Plant and Soil Science*, pp.305–311. https://doi.org/10.9734/ijpss/2022/v34i1931117.

Maucieri, C., Tolomio, M., Raimondi, G., Toffanin, A., Morari, F., Berti, A. and Borin, M., 2022. Organic versus conventional farming: Medium-term evaluation of soil chemical properties. *Italian Journal of Agronomy*, 173. https://doi.org/10.4081/ija.2022.2114.

Melović, B., Dabić, M., Rogić, S., Đurišić, V. and Prorok, V., 2020. Food for thought: Identifying the influential factors that affect consumption of organic produce in today's youth. *British Food Journal*, 122(4), pp.1130–1155. https://doi.org/10.1108/BFJ-10-2019-0761.

Moreau, J., Monceau, K., Gonnet, G., Pfister, M. and Bretagnolle, V., 2022. Organic farming positively affects the vitality of passerine birds in agricultural landscapes. *Agriculture, Ecosystems and Environment*, 336, p.108034. https://doi.org/10.1016/j.agee.2022.108034.

Morgera, E., Caro, C.B. and Durán, G.M., 2012. *FAO Legislative Study 107*. Food and Agriculture Organization of the United Nations, Rome.

Mousavi, H., Cottis, T. and Solberg, S.Ø., 2023. Nitrogen enriched organic fertilizer NEO elevates nitrification rates shortly after application but has no lasting effect on nitrification in agricultural soils. *Agricultural and Food Science*, 32(4), pp.179–194. https://doi.org/10.23986/afsci.131722.

NABARD, 2012. Low input, low carbon organic agriculture – Marketing support to organic farmers to promote traditional millets and organic vegetables. Mumbai, India. Retrieved January 21, 2024, from: https://www.nabard.org/demo/auth/writereaddata/File/10_Low%20Input_Low_Carbon_Organic_Agriculture.pdf.

NCOF, 2015. National Centre for Organic and Natural Farming. Department of Agriculture & Farmers Welfare, Government of India.

NOP, 2006. National organic program. Regulations (standards) and guidelines. US Department of Agriculture. Retrieved January 27, 2024, from: http://www.ams.usda.gov/NOP/indexIE.htm.

Okubo, H., 1993. Kyusei nature farming: Historical perspective, present status, and prospects for future development with EM technology. In: *Third International Conference Kyusei Nature Farming*, Santa Bárbara, Califórnia.

Pandey, J. and Singh, A., 2012. Opportunities and constraints in organic farming: an Indian perspective. *Journal of Scientific Research*, 56, pp.47-72.

Paul, J. and Rana, J., 2012. Consumer behavior and purchase intention for organic food. *Journal of Consumer Marketing*, 29(6), pp.412-422. https://doi.org/10.1108/07363761211259223.

Paull, J., 2006. The farm as organism: The foundational idea of organic agriculture. *Elementals: Journal of Bio-Dynamics Tasmania*, 83, pp.14-18.

Paull, J., 2010. From France to the world: The international federation of organic agriculture movements (IFOAM). *Journal of Social Research & Policy*, 1(2), pp.93-102.

Paull, J., 2011. Attending the first organic agriculture course: Rudolf Steiner's agriculture course at Koberwitz, 1924. *European Journal of Social Sciences*, 21(1), pp.64-70.

Pinstrup-Andersen, P. and Hazell, P.B.R., 1985. The impact of the Green Revolution and prospects for the future. *Food Reviews International*, 1(1), pp.1-25. https://doi.org/10.1080/87559128509540765.

Rahman, S.M.E., Mele, M.A., Lee, Y.T. and Islam, M.Z., 2021. Consumer preference, quality, and safety of organic and conventional fresh fruits, vegetables, and cereals. *Foods*, 10(1), p.105. https://doi.org/10.3390/foods10010105.

Ram, R.A. and Garg, N., 2020. Antimicrobial property of amritpani, cow pat pit, jeevamrita and panchagavya on some pathogens. *Journal of Eco-friendly Agriculture*, 15(1), pp.7-9.

Rana, J. and Paul, J., 2017. Consumer behavior and purchase intention for organic food: A review and research agenda. *Journal of Retailing and Consumer Services*, 38, pp.157-165. https://doi.org/10.1016/j.jretconser.2017.06.004.

Randhawa, M.S., 1986. *A history of agriculture in India 1980-1986, vol. I-IV*. Indian Council of Agricultural Research, New Delhi.

Ravikumar, C., Senthilvalavan, P. and Manivannan, R., 2023. INM-A Potential Way of Farming in Reduction of CH4 and CO2 Emission in Rice-sunflower Sequential Cropping System. *International Journal of Environment and Climate Change*, 13(7), pp.427-435. https://doi.org/10.9734/ijecc/2023/v13i71895.

Rena, R., 2004. Green revolution: Indian agricultural experience-a paradigm for Eritrea. *Eritrean Studies Review*, 4(1), pp.103-130.

Roumeliotis, C., Siomos, A.S. and Gerasopoulos, D., 2021. Comparative nutritional and antioxidant compounds of organic and conventional vegetables during the main market availability period. *Nitrogen*, 2(1), pp.18–29. https://doi.org/10.3390/nitrogen2010002.

Rundgren, G., 2008. Best practices for organic policy. What developing country governments can do to promote the organic agriculture sector. In: *CBTF, UNEP-UNCTAD Capacity Building Task Force on Trade, Environment and Development*, New York and Geneva, United Nations.

Sánchez-Bravo, P., Martínez-Tomé, J., Hernández, F., Sendra, E. and Noguera-Artiaga, L., 2023. Conventional vs. organic: Evaluation of nutritional, functional and sensory quality of citrus limon. *Foods*, 12(23), p.4304. https://doi.org/10.3390/foods12234304.

Santoni, M., Verdi, L., Imran Pathan, S., Napoli, M., Dalla Marta, A., Dani, F.R., Pacini, G.C. and Ceccherini, M.T., 2023. Soil microbiome biomass, activity, composition and CO2 emissions in a long-term organic and conventional farming systems. *Soil Use and Management*, 39(1), pp.588-605. https://doi.org/10.1111/sum.12836.

Santos, J.L., 2017. Rachel Carson's Silent Spring: A legacy for sustainable development. In: *Environment*, pp.77-92.

Schmid, O., Dabbert, S., Eichert, C., Gonzálvez, V., Lampkin, N., Michelsen, J., Slabe, A., Stokkers, R., Stolze, M., Stopes, C. and Wollmuthová, P., 2008. Organic Action Plans. Development, implementation and evaluation. A resource manual for the organic food and farming sector. Research Institute of Organic Agriculture (FiBL); CH-Frick and European Union Group of the International Federation of Organic Agriculture Movements (IFOAM), Brussels.

Setälä, H., Bardgett, R.D., Birkhofer, K., Brady, M., Byrne, L., De Ruiter, P.C., De Vries, F.T., Gardi, C., Hedlund, K., Hemerik, L. and Hotes, S., 2014. Urban and agricultural soils: conflicts and trade-offs in the optimization of ecosystem services. Urban Ecosystems, 17, pp.239-253. doi: 10.1007/s11252-013-0311-6.

Joachim, S., 2006. Review of history and recent development of organic farming worldwide. Agricultural sciences in China, 5(3), pp.169-178.. doi: 10.1016/S1671-2927(06)60035-7.

Simin, M.T. and Glavaš-Trbić, D., 2016. Historical development of organic production. Economics of Agriculture, 63(3), pp.1083-1099. https://doi.org/10.5937/ekopolj1603083t

Singh, A. and Verma, P., 2017. Factors influencing Indian consumers' actual buying behavior towards organic food products. Journal of Cleaner Production, 167, pp.473-483. https://doi.org/10.1016/j.jclepro.2017.08.106

Sosa-Rodrigues, B.A. and García-Vivas, Y.S., 2019. Emission of greenhouse gases in the soil under the green manure effect. Agronomía Mesoamericana, 30(3), pp.767-787. https://doi.org/10.15517/AM.V30I3.36103

Straus, S., Baven, F., Turinek, M., Slatnar, A., Rozman, C. and Bavec, M., Nutritional value and economic feasibility of red beetroot (Beta vulgaris L. ssp. vulgaris Rote Kugel) from different production systems.

African Journal of Agricultural Research, 7(42), pp.5653-5660. https://doi.org/10.5897/AJAR12.1519

Suciu, N.A., Ferrari, F. and Trevisan, M., 2019. Organic and conventional food: Comparison and future research. Trends in Food Science & Technology, 84, pp.49-51. https://doi.org/10.1016/j.tifs.2018.12.008

Tomaš-Simin, M. and Glavaš Trbić, D., 2016. Historical development of organic production. Economics of Agriculture, 63(3), pp.1083-1099. https://doi.org/10.5937/ekopolj1603083t

Tong, L., Li, J., Zhu, L., Zhang, S., Zhou, H., Lv, Y. and Zhu, K., 2022. Effects of organic cultivation on soil fertility and soil environment quality in greenhouses. Frontiers in Soil Science, 2. https://doi.org/10.3389/fsoil.2022.1096735

Tripathi, K.M., Kumar, D., Mishra, S.K., Singh, S. and Shukla, S., 2023. An overview of organic farming in India and its role in sustainable agriculture. emerging issues in agricultural sciences, 5, pp.94-106. https://doi.org/10.9734/bpi/eias/v5/10607F

Tscharntke, T., Grass, I., Wanger, T.C., Westphal, C. and Batáry, P., 2021. Beyond organic farming–harnessing biodiversity-friendly landscapes. Trends in Ecology & Evolution, 36(10), pp.919-930. https://doi.org/10.1016/j.tree.2021.06.010

USDA, 1980. USDA report and recommendations on organic farming. United States Department of Agriculture.

Vicas, S.I., Teusdea, A.C., Carbunar, M., Socaci, S.A. and Socaciu, C., 2013. Glucosinolates profile and antioxidant capacity of Romanian Brassica vegetables obtained by organic and conventional agricultural practices. Plant Foods for Human Nutrition, 68(3), pp.313-321. https://doi.org/10.1007/s11130-013-0367-8

Warwick, H., 1999. Cuba's organic revolution. Ecologist, 29(8), pp.457-460.

Willer, H. and Lernoud, J., 2019. The world of organic agriculture 2019-Statistics and emerging trends. FiBL & IFOAM – Organics International. Available at: https://orgprints.org/id/eprint/37018/1/willer-lernoud-2019-world-of-organic-low.pdf (Accessed: 23 January 2024)Willer, H. and Yussefi, M., 2000. Organic agriculture worldwide: Statistics and perspectives.

Willer, H., Schlatter, B. and Trávníček, J., 2023. The world of organic agriculture: Statistics and emerging trends 2023. FiBL & IFOAM – Organics International. Retrieved January 11, 2024, from: https://www.fibl.org/fileadmin/documents/shop/1254-organic-world-2023.pdf.

Willer, H., Trávníček, J., Meier, C. and Schlatter, B., 2021. The world of organic agriculture 2021: Statistics and emerging trends. FiBL & IFOAM – Organics International. Retrieved January 23, 2024, from: https://www.fibl.org/fileadmin/documents/shop/1150-organic-world-2021.pdf.

Worthington, V., 2001. Nutritional quality of organic versus conventional fruits, vegetables, and grains. *The Journal of Alternative and Complimentary Medicine*, 7(2), pp.161-173. https://doi.org/10.1089/107555301750164244.

Xavier, J., Mythri, V., Nagaraj, R., Ramakrishna, V., Patki, P. and Semwal, A., 2020. Organic versus conventional – A comparative study on quality and nutritive value of selected vegetable crops of southern India. *SAARC Journal of Agriculture*, 18(1), pp.99-116. https://doi.org/10.3329/sja.v18i1.48385.

Xie, L., Li, L., Xie, J., Wang, J., Anwar, S., Du, C. and Zhou, Y., 2022. Substituting inorganic fertilizers with organic amendment reduced nitrous oxide emissions by affecting nitrifiers' microbial community. *Land*, 11(10), p.1702. https://doi.org/10.3390/land11101702.

Xu, H.L., Wang, R., Xu, R.Y., Mridha, M.A.U. and Goyal, S., 2003. Yield and quality of leafy vegetables grown with organic fertilizations. *Acta Horticulturae*, 627, pp.25–33. https://doi.org/10.17660/ActaHortic.2003.627.2.

Zhao, P., Bai, H., Tian, Z., Wu, Y., Yang, X., Wu, X. and Gu, J., 2022. A three-year measurement reveals that partial conversion from synthetic fertilizer to dairy manure increases cumulative nitric oxide emissions from a long-term experimental cropland. *Soil and Tillage Research*, 221, p.105419. https://doi.org/10.1016/j.still.2022.105419.

ORCID DETAILS OF THE AUTHORS

P. Kashyap: https://orcid.org/0000-0003-3028-1037
M. Jain: https://orcid.org/0000-0002-4262-2700

Optimization and Validation of the Preconcentration Technique with SBSE Coupled HPLC-UV/DAD for the Identification of Atrazine and Two of its Metabolites, 2-Hydroxyatrazine (2-HA) and Desethylatrazine (DEA) in Aqueous Samples

L. A. García-Villanueva[1†] ⓘ **, J. R. Martínez-Castro[1], G. Fernandez-Villagomez[1]** ⓘ **, G. L. Andraca-Ayala[2]** ⓘ **, J. M. Yáñez-Campuzano[3] and O. Zamora Martínez[4]**

[1]Faculty of Engineering, Geomatic and Civil Engineering Division, Sanitary and Environmental Engineering Department, National Autonomous University of Mexico. Av. Universidad 3000, Ciudad Universitaria, Coyoacán, Mexico City, Mexico

[2]Institute of Atmospheric Sciences and Climate Change, National Autonomous University of Mexico. Av. Universidad 3000, Ciudad Universitaria, Coyoacán, Mexico City, Mexico

[3]Faculty of Chemistry, National Autonomous University of Mexico. Av. Universidad 3000, Ciudad Universitaria, Coyoacán, Mexico City, Mexico

[4]Institute of Geology, Department of Environmental Sciences and Soil, National Autonomous University of Mexico. Av. Universidad 3000, Ciudad Universitaria, Coyoacán, Mexico City, Mexico

†Corresponding author: L. A. García-Villanueva; lagvillanueva@unam.mx

ABSTRACT

The purpose of this work is to address an environmental problem in Mexico, which uses significant amounts of water for agricultural activities, where atrazine is frequently used as a pesticide for weed control. Currently, there is no law prohibiting its use, even though it is considered an endocrine disruptor in some mammals and harmful to health. Due to the difficulty in the direct quantification of several herbicides, which present a low concentration in water, the present work aims to develop the optimization and validation of the preconcentration with magnetic stir bars (SBSE) in aqueous samples for the quantification of atrazine and two of its metabolites: 2-hydroxyatrazine (2-HA) and desethylatrazine (DEA), coupled to High-Performance Liquid Chromatography (HPLC-UV/DAD). For the optimization of the preconcentration technique, the nature and quantity of the solvents used in each step, contact time for retention and quantitative extraction of the analyte, as well as the effect of the concentration of the analyte on its retention on the bar were considered. Finally, it was determined that the presence of the metabolites 2-HA and DEA does not affect the sorption of atrazine on the sorption bar used. The analytical methodology can be considered as an efficient method of atrazine preconcentration for subsequent quantification via HPLC-UV/DAD in the range of 0.03 to 0.25 mg/L and in the absence of matrix interferences; its limits of detection and quantification are respectively 0.0014 mg/L and 0.0016 mg/L.

INTRODUCTION

Agriculture is the science of cultivating the land to obtain raw materials. The main reasons that have led to agricultural production have been to solve the problem of world hunger through the extensive use of agricultural practices (Carmona 2004).

Mexico uses 76% of its renewable water for agriculture, which mainly produces sugarcane, corn and sorghum. During its cultivation, atrazine is used as a pesticide for weed control. Studies worldwide consider atrazine as an endocrine disruptor, even low doses of pesticides can alter the biochemical profile, resulting in oxidative stress within

the population's brains causing hormonal imbalance, and is classified as a carcinogenic substance, it also poses various risks to the aquatic environment and its propagation in it, so it has been banned in some countries (CICOPLAFEST 2005, IARC 2014, Sharma et al. 2023).

There are studies where residual pesticides are detected in soil, water, food, biological fluids, and tissue samples. In food, different pesticides have been found in cereal grains, cacti, shrimp, vegetable oils, tomatoes, and grapes, among others (Ahmed et al. 2009, Aldana et al. 2008, Alsayeda et al. 2008). Hence the interest in studying the persistence of pesticides in the environment.

Atrazine is one of the most widely used pesticides in the world and Mexico is the second country where it is used in the greatest quantity, and where there is no law prohibiting or regulating its use. It should be noted that some Mexican standards provide maximum permissible limits in a preventive manner, mainly those referring to drinking water, wastewater discharges, and food (Bello 2016, FAO 2016, González-Márquez & Hansen 2009).

In the practice of chemical analysis, there are countless reasons to perform tests, measurements, and examinations in laboratories worldwide, for example, to control the quality of drinking and irrigation water, food, medical analysis, high value-added products among many others, which require high reliability since important decisions depend on the results that these measurements produce (Eurolab 2016). That is why it is considered necessary that the methods of analysis, as well as the analytical results, are subjected to some acceptance criterion that allows them to document their quality and verify that the experimental procedures meet the quality criteria requested by the customer and are suitable for the specific use for which they were developed. This procedure is known as method validation and is applied by countless laboratories around the world (CDER 1994).

MATERIALS AND METHODS

Equipment

- Liquid chromatographic system consisting of two model 1525 high-pressure binary pumps, a model 717 plus autosampler, and a model 2998 UV-DAD diode array detector, all from Waters, controlled by Empower 2 data acquisition software (Build 2154), also from Waters Co.
- Analytical balance with a capacity of 210.0 g and a precision of 1.0 mg, Ohaus, model Explorer.
- Ministart® syringe filters, 25 mm diameter, and 0.45 pm, Nylon (PA), 4.8 cm^2, 0.15 mL, Sartorius.
- Four-position magnetic stirring grill, without heating, model MS-01 from ELMI Ltd.
- Magnetic stirring grid model Speedsafe™ from HANNA Instruments.
- Milli-Q® plus water purifier and deionizer, model 185 from Merck-Millipore.

Materials

- Glass Twister® magnetic stirring rods with dimensions of 10 mm length x 3.2 mm diameter and a thickness of 0.5 mm of GERSTEL polydimethylsiloxane (PDMS) non-polar film coating.

- C18 Spherisorb ODS2 column, 80 A, (4.0 mm x 250 mm, i.d.), 5 pm particle size, from Waters Co.
- Cellulose nitrate membrane filters, 47 mm diameter, 0.45 pm pore size, Sartorius brand.
- Chromatographic amber glass vials, certified, Waters brand, dimensions 8 × 40 mm, 1 mL volume.
- Headspace® amber glass vials, round bottom, spiral cap, 20 mL.

Reagents and solvents

- Acetonitrile, HPLC grade (> 99.93%), Honeywell.
- Atrazine, analytical standard (99%), 100 mg ampoule, Sigma-Aldrich.
- Atrazine-2-hydroxy, analytical standard (99%), PESTANAL ®, Sigma-Aldrich.
- Atrazine-desethyl, analytical standard (99%), PESTANAL ®, Sigma-Aldrich.
- Ultra pure water, resistivity 18.2 Mfl-cm, at 25°C.
- Phosphate buffer pH = 7.2, grade R.A. (98.9%), Sigma-Aldrich. (98.9%), Sigma-Aldrich.
- Methanol, HPLC grade (> 99.9%), Honeywell.

Preparation of Solutions

Standard solutions and standards: To carry out the development of the preconcentration methodology, all solutions were prepared with chromatographic grade solvents, analytical grade reagents, and deionized water. For the analyte of interest, as well as for its potentially interfering metabolites, standard (stock) solutions of ~500 mg/L in methanol were prepared and each was transferred to an amber glass bottle to avoid photochemical degradation and stored under refrigeration. All the standards used for the development of the method were prepared by diluting the different standard solutions with deionized water.

Chromatographic analysis: All working samples were analyzed by HPLC-UV/DAD as reported by Cortes (2016). A Waters® C18 Spherisorb ODS2, 80 A, (4.0 mm x 250 mm, i.d.), 5 pm particle size column was used as stationary phase. A mixture containing acetonitrile (AcCN) and phosphate buffer of concentration equivalent to 0.005 M pH = 7.2, in a 40:60 (v/v) ratio, maintaining a flow rate of 1 mL/min in isocratic mode, was used as mobile phase. Analyte monitoring was performed at 220 nm, using an injection volume of 10 pL.

Methodology validation: Once the previously optimized working conditions were selected, we proceeded to obtain the typical parameters of an analytical validation, which are:

linear and working range, precision, limits of detection and quantification, as well as the evaluation of the effect of the study matrix.

Linear and working range: To select the working range, dilutions of atrazine concentration standards ranging from 0.005 to 5.0 mg/L were prepared from a stock solution of ~ 500 mg/L by diluting it in deionized water. Linearity was observed starting at a concentration of 0.03 mg/L and ending at 0.25 mg/L. Each calibration curve was prepared in triplicate and at least seven concentration levels were required for proper evaluation.

Precision and accuracy: Seven concentration levels (0.03 and 0.25 mg/L) were selected for the evaluation of these parameters. Each concentration level was prepared independently in triplicate. Data analysis was performed according to Miller & Miller (2002) by calculating the percentage coefficient of variability (% CV):

$$\% \, CV = \left| \frac{s}{\bar{x}} * 100 \right| \qquad \ldots(1)$$

where $\bar{x}$ is the mean or average of the measurements and is the standard deviation of the measurements.

The standard deviation, in turn, is calculated by the following equation:

$$s = \sqrt{\frac{1}{n-1} \sum_{i=1}^{n} (x_i - \bar{x})^2} \qquad \ldots(2)$$

Where x_i is the value of the i-th measurement and n is the number of measurements taken.

Limits of detection (LOD) and quantification (LOQ): For this stage, the quantification of seven dilutions of a very low concentration of the analyte (0.005 mg/L) was performed. With the values determined, in absorbance units, the mean (x) and its standard deviation (s) were calculated.

The detection limit was reported according to the equation:

$$LOD = \bar{x} + 3s \qquad \ldots(3)$$

The limit of quantification is reported as:

$$LOQ = \bar{x} + 10s \qquad \ldots(4)$$

Where $\bar{x}$ is the average of the measurements and s is the standard deviation of the measurements.

Both the limit of detection and the limit of quantification were reported according to Miller & Miller (2002). Once calculated (Eqs. 3 and 4), with the regression equation of the calibration curve, they were transformed into concentration units.

Study matrix: The evaluation of the matrix effect was carried out with five surface water samples from the Montebello Lagoons, Chiapas, which were sampled in August 2014. These samples came from the lagoons: Balamtetic, Bosque Azul, San Lorenzo, Vuelta el Agua and Yalmus.

For each sample, two liters of surface water were taken at a depth of one meter. The samples were subjected to experimental measurements in the field, such as pH and electrical conductivity with a multiparameter meter, model 9812 from HANNA Instruments. The samples were transported in a cooler and then kept under refrigeration at 4 °C, stored in polypropylene jars with lids. Before working with them, the samples were treated using a filtration system, using nitrocellulose membranes of 0.45 pm pore size.

For the evaluation of possible interferents, the standard additions method was applied to these water samples.

Fortification of samples: The five water samples from the Montebello Lagoons were fortified in duplicate with atrazine at five concentration levels between 0.03 and 0.30 pg/mL. The fortifications were carried out starting from the previously prepared ATZ standards and diluting the five samples with water for each corresponding level.

Recovery or Recoveries: This parameter was determined by direct analysis of five water samples from the Montebello Lagoons, which were subsequently fortified with atrazine at five concentration levels, ranging from 0.03 to 0.25 mg/mL. The percentage of recovery (% R) is determined by the following equation:

$$\% \, R = \left[\frac{c_F - c_U}{c_A} \right] \cdot 100 \qquad \ldots(5)$$

Where C_F is the concentration of analyte measured in the fortified sample, C_U is the concentration of analyte measured in the unfortified sample, C_A is the concentration of analyte added to the fortified sample.

With the area values determined during the analysis and the regression parameters calculated from the respective external calibration curves, the concentrations corresponding to the fortification processes were determined. The fortification processes were carried out in duplicate.

RESULTS AND DISCUSSION

Optimization of the SBSE stages

Conditioning: Since the sorption rods used for SBSE are coated with a polydimethylsiloxane (PDMS) film, which acts as a non-polar adsorbent, it was decided to use a volume of 5.0 mL of methanol, which was sufficient to cover the entire working rod. The selection of the appropriate solvent was made based on the elution power and the affinity of the solvent for atrazine to ensure efficient extraction. In addition, the use of methanol is recommended by the manufacturer, since it guarantees that the film covering the rod will have exposed the sites that interact with the molecules of the analyte to be retained, and therefore, carry out satisfactorily its sorption.

The agitation speed was selected based on the recommendations provided by the manufacturer (GERSTEL 2014, Baltussen et al. 2015), in addition to that mentioned by the developers of the SBSE methodology (Baltussen et al. 1999) and in works by other authors (Leon et al. 2003, Neng et al. 2007, Popp et al. 2001, Prieto et al. 2010). These speeds range from 500 to 1200 rpm, so it was decided to work at an average value of 750 rpm (both for the loading and desorption stages), to avoid degradation of the working rod, and given the specifications and limitations of the equipment used for this purpose.

For the contact time, it was decided to use 15 minutes and although, according to the manufacturer's description, the activation of the film takes a few minutes, this time was selected to guarantee the complete disposition of the sorption sites and, therefore, the highest retention of atrazine once the bar was in contact with the solution containing the working analyte. Finally, the sorption rods were washed with deionized water.

Evaluation of atrazine sorption

Affinity of atrazine for sorption bar: It was necessary to know if the atrazine could be retained on the working sorption bar, so in this stage, we first worked with an aqueous solution of atrazine of very low concentration, which could be quantified by HPLC, we chose to use a volume of 5.0 mL of a solution containing approximately 0.5 mg/L of atrazine. This experiment was performed in quintuplicate, and both the atrazine solution without having been in contact with the bar, identified as initial [ATZ], and that resulting from contact with the bar, indicated as [ATZ] after sorption, were analyzed using HPLC-UV/DAD, to determine their numerical values using an external calibration curve. Table 1 summarizes the conditions and values determined.

The results indicate that a certain amount of the atrazine molecules present in the initial solution were retained on the polymer film of the sorption rod, since the concentration values before and after the experiment were not equal, the concentration of atrazine determined in the solution that was in contact with the PDMS rod being lower. The ratio of the concentration after sorption to the initial concentration of atrazine was 0.73, which is equivalent to 73% of atrazine that was not retained, which, in turn, indicates that the remaining 27% corresponds to the amount of atrazine retained on the bar under these working conditions.

Evaluation of the presence of 2-hydroxyatrazine and desethylatrazine on atrazine retention: Because once atrazine (ATZ) is applied in the crop fields, it can undergo both chemical and microbiological degradation, being its main decomposition metabolites 2-hydroxyatrazine (2-HA) and desethylatrazine (DEA), it was decided to evaluate the presence of known concentrations of these two compounds, on the retention of ATZ on the sorption bar. As in the previous case, the concentration values of the three analytes were determined with the use of external calibration curves. The working conditions and numerical results are summarized in Table 2.

The results obtained indicate that the presence of 2-HA and DEA did not affect the sorption of ATZ when the sorption experiment was carried out, since the same amount of atrazine molecules were retained in the solution after sorption as those determined in the sorption experiments carried out in the absence of the two metabolites, again obtaining a percentage of atrazine retained of 27%, with a non-retained amount of 73%. Under these working conditions, the retention of 2- HA and DEA on the rod was not observed, since their concentrations were the same before and after sorption, so the ratio of concentrations of both species was practically unity. The non-retention of DEA and 2-HA can be attributed to the fact that these substances have a more polar character than atrazine, so they exhibit a greater affinity for the water used as a solvent, thus inhibiting their sorption on the working rod.

Effect of contact time on atrazine retention on the surface

Table 1: Atrazine concentration values determined, before and after sorption for a contact time of 60 min (n=5).

Contact time (min)	Volume dissolution of ATZ (mL)	[ATZ]$_{initial}$ (mg/L)	[ATZ]$_{then\ sorption}$ (mg/L)	$\dfrac{[ATZ]_{then\ sorption}}{[ATZ]_{initial}}$
60	5.0	0.56	0.41	0.73

Table 2: Evaluation of ATZ sorption on the presence of its two main metabolites (n=5).

Analyte	Contact time (min)	Volume dissolution of ATZ (mL)	[ATZ]$_{initial}$ (mg/L)	[ATZ]$_{then\ sorption}$ (mg/L)	$\dfrac{[ATZ]_{then\ sorption}}{[ATZ]_{initial}}$
2-HA	60	5.0	0.44	0.45	1.02
DEA	60	5.0	0.45	0.45	1.00
ATZ	60	5.0	0.48	0.35	0.73

Table 3: Effect of contact time on ATZ sorption. The initial concentration of atrazine is 0.46 mg/L, which is equivalent to 2.28 pg ATZ (n=5).

Volume dissolution (mL)	Time of ATZ contact (min)	[ATZ] $_{after\ sorption}$ (mg/L)	Mass in solution after sorption (pg)	ATZ mass retained (pg)
5.0	15	0.44	2.19	0.09
5.0	30	0.43	2.15	0.13
5.0	60	0.40	2.01	0.27
5.0	120	0.41	2.03	0.25

of the sorption rod: Since the contact time drastically influences the retention of analytes in sorption experiments, it was mandatory to determine the minimum contact time necessary to reach equilibrium on the atrazine retention process. For this purpose, a volume of 5.0 mL of atrazine solution of a concentration of approximately 0.5 mg/L was used, varying the working contact times. Table 3 shows the results obtained for the concentration of atrazine remaining in solution after the sorption experiment was carried out for each of the contact times, as well as the respective amount of atrazine retained on the polydimethylsiloxane rod.

Table 3 shows that, as the contact time increases, the amount of ATZ in the solution decreases, which indicates that a greater amount of this compound has been deposited on the surface of the sorption bar (more efficient sorption), it is possible to verify that after 60 minutes, the sorption remains constant, i.e. reaches equilibrium, so this contact time was selected for the following experiments.

Effect of contact time for quantitative desorption of atrazine: Considering the nature of atrazine, a solvent for which this compound presented a good affinity was sought. Initially, methanol was selected since atrazine is highly soluble in this solvent, in addition to the fact that this solvent acts as a strong eluent when working with reverse-type phases, such as the one used as the coating of the working sorption bar. For this stage, 1.0 mL of methanol was used as the extractant solvent and because desorption depends on the contact time, the minimum time necessary was sought to achieve the greatest extraction of the ATZ retained on the bar. The results obtained are presented in Table 4. As can be observed, in the contact times evaluated, there was practically no greater amount of ATZ in the solution as the contact time between the methanol and the stir bar increased, so, to increase the productivity of the methodology, it was decided to use the shortest contact time of the study (10 minutes) to carry out the desorption of the analyte.

Influence of the amount of extraction solvent: To verify if the volume of the extractant, in this case, methanol, influences the desorption process of atrazine, it was decided to evaluate five different volumes of this solvent, with n=3; the results obtained are presented in Table 5.

Although the concentration of desorbed atrazine decreases as the volume of methanol used for desorption increases, the parameter that directly indicates the effect of this variable on ATZ extraction is not the concentration determined, but the amount of atrazine in solution after desorption, since this involves the dilution effect that the analyte undergoes when exposed to different volumes of extractant.

The results indicate that the amount of atrazine extracted is practically the same for all methanol study volumes, so it was decided to perform the ATZ extraction from the bar with the smallest volume of MeOH (1.0 mL), which guarantees the least dilution effect on the concentration of atrazine once it is in solution, for its adequate quantification via HPLC-UV/DAD. The resulting preconcentration factor (5.0 mL loading/1.0 mL elution) is 5, indicating that the methodology allows the sample to be concentrated five times.

Effect of analyte concentration present on its retention on the sorption bar: Because the concentration in a sample is usually totally uncertain, it was necessary to evaluate the retention behavior of atrazine as a function of its initial concentration in solution. The concentrations used were selected based on the limit of quantification of the HPLC-UV/

Table 4: Effect of extractant (MeOH) contact time on ATZ desorption (n=3).

Volume MeOH (mL)	Contact time (min)	Mass of ATZ in solution after desorption (pg)
1.0	15	0.23
1.0	30	0.25
1.0	60	0.25
1.0	120	0.25

Table 5: Effect of MeOH volume on ATZ desorption (n = 3).

Volume (mL)	MeOH Contact time (min)	Concentration (pg/mL)	Of desorption ATZ mass in dissolution after desorption (gg)
0.5	10	0.66	0.33
0.8	10	0.34	0.28
1.0	10	0.33	0.33
1.5	10	0.18	0.27
2.0	10	0.13	0.25

Table 6: Effect of analyte concentration on its retention on the sorption bar (n = 3).

ATZ load concentration (gg/mL)	Adsorbed mass			%CV
	1	2	3	
0.03	0.028	0.025	0.022	12.54
0.05	0.035	0.040	0.035	7.80
0.08	0.054	0.054	0.059	4.90
0.10	0.068	0.066	0.068	1.70
0.15	0.098	0.094	0.101	3.65
0.20	0.125	0.132	0.128	2.82
0.25	0.154	0.154	0.157	1.00

DAD methodology (lowest initial concentration that could be quantified) and the highest initial ATZ concentration that was fully retained on the sorption bar. Table 6 summarizes the results of this experiment.

Each experiment was performed in triplicate, so Table 6 also shows the percentage values of the coefficient of variation (% CV), which indicate the degree of repeatability for each of the working concentration levels. As can be seen, in all cases acceptable CV values are presented, following the criteria for the validation of physicochemical methods (< 20%), established in document CCAyAC-P-058 (COFEPRIS 2011). Thus, the accuracy of the developed methodology is evaluated in terms of repeatability.

The graph presented in Fig. 1 shows the correlation between the initial concentration of atrazine present in the solution and the amount of analyte that was retained on the sorption rod used. This graph exhibits a clear linear dependence of the amount of atrazine retained by the bar as a function of the initial concentration of the dissolved analyte

($R^2 = 0.9968$, r = 0.9984), which is confirmed by the study of the nonparametric test of streaks, whose results indicate that the residuals of the data pairs were random and therefore these fit a straight line.

The knowledge of this behavior is of vital importance in the use of the sorption bar for the preparation of real samples, since the sorption of atrazine is conditioned by the concentration present in the solution and it is necessary to know the values of the parameters slope and ordinate to the origin, to determine the concentration of atrazine in the original sample.

Limits of detection and quantification: The determination of the detection and quantification limit values was carried out by measuring seven atrazine solutions of known concentration (0.005 mg/L) independently. Likewise, this concentration was selected based on the minimum differentiable signal/noise ratio of the chromatographic analysis system. Table 7 shows the values of the limit of detection (LOD) and limit of quantification (LOQ), which were calculated according to Miller & Miller (2002) and, employing the regression parameters of the external calibration curve, were obtained in units of concentration.

Finally, these parameters were significantly reduced compared to the direct analysis method, where values of LOD = 0.050 mg/L and LOQ = 0.070 mg/L are reported and whose methodology does not employ a sample preparation technique.

Evaluation of the effect of the study matrix: To evaluate the presence of interferents from the study matrix, five water samples from the Montebello Lagoons were fortified in
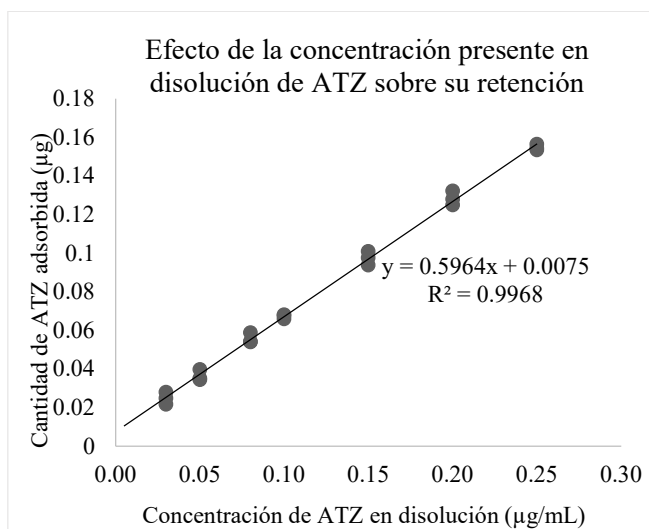

Fig. 1: Dependence of the amount of ATZ adsorbed as a function of the initial concentration present in solution (n=3).

Table 7: Detection and quantification limits of the developed methodology.

Parameter	Value (mg/L)
LOD	0.0014
LOQ	0.0016

duplicate with atrazine at five concentration levels ranging from 0.03 to 0.30 pg/mL. In all the chromatograms obtained by directly analyzing the water samples from the Montebello Lagoons, as a blank (background), the null presence of ATZ (whose retention time is 7.8) was observed; this occurred in all cases. Consequently, the slope values obtained for the five lake samples were as expected, being very similar to each other, compared to that observed for the deionized water. Since the slope values are practically the same (m ~ 0.6), it is clear that there are no interferences affecting the quantification of atrazine. For the ordinate to the origin (b), for all cases values very close to zero were obtained, while the correlation coefficients indicate the existence of a linear behavior of the adsorbed amount of atrazine as a function of its initial concentration in solution.

On the other hand, to confirm the similarity between the values of the slopes of the study samples and the value obtained for the calibration curve with deionized water, five hypothesis tests were carried out, where the value of the slope of the respective sample was compared with that of the external calibration curve, using Student's t distribution statistic, at 95% reliability (a = 0.05).

Alternatively, the matrix effect was evaluated qualitatively by graphical analysis of the amount of analyte adsorbed for each lake sample against the amount adsorbed in deionized water, as described by Thompson & Ellison (2004); for all cases, the slope obtained was practically equal to unity.

Recoveries: When observing the values of the recovery percentages for each concentration level, both for the deionized water matrix (Table 8) and for each of the fortified samples (Table 9), it can be concluded that these meet the acceptance criteria for the recovery parameter established in the manual of the Ministry of Health (COFEPRIS 2011).

Table 8: Recovery percentages as a function of analyte concentration for the water matrix deionized.

ATZ load concentration (pg/mL)	Recoveries (%) Deionized water	Acceptance criteria (%)	Result
0.03	90.00	70 - 120	Complies
0.05	102.27	70 - 120	Complies
0.08	94.39	70 - 120	Complies
0.10	105.14	70 - 120	Complies
0.15	116.82	70 - 120	Complies
0.20	115.58	70 - 120	Complies
0.25	108.25	70 - 120	Complies

Additionally, the recovery percentages can be evaluated by comparing the slopes of the external calibration curves of each of the fortified samples from five water samples from the Montebello Lagoon System with that of the deionized water matrix (Table 10).

When analyzing the values of these slopes, it can be determined that they are practically the same; therefore, there is no significant difference between the working matrices.

Finally, it can be affirmed, based on the above, that the instrumental method developed in the present methodology, once validated, is robust for the matrix.

Reproducibility: The retention times for the analyte atrazine, obtained in the present methodology, are very similar to those obtained by the direct analysis technique developed by Cortes (2016), i.e.: t_R ATZ ≈ 7.8; that is why it can be stated that the instrumental method of HPLC-UV/DAD analysis is reproducible for that substance.

CONCLUSIONS

For the preconcentration of atrazine in aqueous samples, a methodology was developed based on stir bar sorption extraction (SBSE), the following optimal conditions were found: Extraction volume (loading): 5.0 mL, Stirring speed: 750 rpm, for all cases (loading and elution), Contact time: 60 minutes, Desorption solvent or eluent: methanol

Table 9: Recovery percentages as a function of analyte concentration for each of the analyte concentrations for each of the five samples from the Montebello Lagoon Park.

Concentration Charge ATZ (pg/mL)	Recoveries (%)					Criteria Acceptance (%)	Result
	Lake 1	Lake 2	Lake 3	Lake 4	Lake 5		
0.03	76.66	102.74	88.78	93.11	107.82	70 - 120	Complies
0.05	73.66	87.91	119.87	119.16	95.19	70 - 120	Complies
0.08	119.80	91.23	112.99	88.78	83.35	70 - 120	Complies
0.20	84.86	72.76	120.80	114.80	105.69	70 - 120	Complies
0.25	86.22	84.12	113.88	81.18	118.82	70 - 120	Complies

Table 10: Percentage of recovery evaluated by comparing the slopes of the recovery curves external calibration of each of the fortified samples (from the Montebello Lagoon System) with the one from the deionized water matrix.

Matrix	Slope (m)	Recoveries (%)
Deionized water	0.5964	100.00
Lake 1	0.5905	99.01
Lake 2	0.6034	101.17
Lake 3	0.5958	99.90
Lake 4	0.5733	96.18
Lake 5	0.5826	97.69

(HPLC grade), with this the quantitative desorption of ATZ is achieved, Eluent volume: 1.0 mL, thus guaranteeing the least dilution effect and finally, Desorption or elution time: 10 minutes.

The analytical methodology developed met the parameters of linearity, precision, and accuracy, so it can be considered an efficient method of atrazine preconcentration, for its subsequent quantification in the absence of matrix interferences, by high-performance liquid chromatography, using a photodiode array detector (HPLC-UV/DAD), in the range of 0.03 to 0.25 mg/L.

The limits of detection and quantification for atrazine in this methodology are 0.0014 mg/L and 0.0016 mg/L, respectively. On the other hand, these parameters were significantly reduced compared to the direct analysis method (Cortes 2016), where values of LOD = 0.050 mg/L and LOQ = 0.070 mg/L were reported and whose methodology does not employ a preconcentration or sample preparation technique.

REFERENCES

Ahmed, A.R., Tarek, M.M., Rady, A.R. and Mohamed, Y.H., 2009. Dissipation of profenofos, imidacloprid and penconazole in tomato fruits and products. *Bulletin of Environmental Contamination and Toxicology*, 83, pp.812-817. https://doi.org/10.1007/s00128-009-9852-z.

Aldana, M.L., Valdez, S., Vargas, N.D., Salazar, N.J., Silveira, M.I., Loarca, F.G., Rodriguez, G., Wong, F.J., Borboa, J. and Burgos, A., 2008. Insecticide residues in stored grains in Sonora, Mexico: quantification and toxicity testing. *Bulletin of Environmental Contamination and Toxicology*, 80, pp.93-96. https://doi.org/10.1007/s00128-007-9302-8.

Alsayeda, H., Pascal-Lorber, S., Nallanthigal, C., Debrauwer, L. and Laurent, F., 2008. Transfer of the insecticide [14C] imidacloprid from soil to tomato plants. *Environmental Chemistry Letters*, 6, pp.229-234. https://doi.org/10.1007/s10311-007-0121-2.

Baltussen, E., Sandra, P., David, F. and Cramers, C., 1999. Stir bar sorptive extraction (SBSE), a novel extraction technique for aqueous samples: Theory and principles. *Journal of Microcolumn Separations*, 11(10), pp.737-747. https://doi.org/10.1002/(SICI)1520-667X(1999)11:10<737::AID-MCS7>3.0.CO;2-4.

Bello, K., 2016. Determinación del plaguicida paraquat en muestras tomadas de las lagunas de Montebello, Chiapas. *Tesis de licenciatura*, Facultad de Estudios Superiores Zaragoza, Universidad Nacional Autónoma México, Ciudad de México, México, 81pp.

Carmona, B., 2004. Las patentes de transgénicos como mecanismo de dominación de los países desarrollados. Análisis de la situación en México y Estados Unidos. *Tesis de licenciatura*, Licenciatura en Relaciones Internacionales, Universidad de las Américas, Puebla, México, 120pp.

CDER, 1994. Reviewer guidance. Validation of Chromatographic Methods. *Center for Drug Evaluation and Research*, US Food and Drug Administration. Manual, United States, 30 pp.

CICOPLAFEST, 2005. Acuerdo que establece la clasificación y codificación de mercancías cuya importación está sujeta a regulación por parte de las dependencias que integran la comisión intersecretarial para el control del proceso y uso de plaguicidas, fertilizantes y sustancias tóxicas. *Comisión Intersecretarial para el Control del Proceso y Uso de Plaguicidas y Sustancias Tóxicas*, Diario Oficial de la Federación, México, DOF: 12/04/2013.

COFEPRIS, 2011. CCAyAC-P-058: Criterios para la validación de métodos fisicoquímicos. *Comisión de Control Analítico y Ampliación de Cobertura*, Comisión Federal para la Protección contra Riesgos Sanitarios, Informe, Secretaria de Salud, México, 133pp.

Cortes, V., 2016. Determinación simultanea de hidroxiatrazina, desetilatrazina y atrazina por medio de CLAR-UV-DAD en muestras de agua de las lagunas de Montebello. *Boletín de la Sociedad Geológica Mexicana*, 70, pp.95-119. https://doi.org/10.18268/BSGM2018v70n1a6.

Eurolab, 2016. Guía Eurachem: La adecuación al uso de los métodos analíticos - Una Guía de laboratorio para la validación de métodos y temas relacionados. Segunda edición, P.P. Morillas y co., España, 66pp.

FAO, 2016. Pesticides as water pollutants. *Food and Agriculture Organization of the United Nations*. Available at: http://www.fao.org/docrep/W2598S/w2598s06.htm.

GERSTEL, 2014. Twister /Stir Bar Sorptive Extraction SBSE. Available from: http://www.gerstel.com/en/twister-stir-bar-sorptive-extraction.htm.

González-Márquez, L. and Hansen, A., 2009. Adsorción y mineralización de atrazina y relación con parámetros de suelos del DR 063 Guasave, Sinaloa. *Revista Mexicana de Ciencias Geológicas*, 26, pp.587-599.

IARC, 2014. IARC Monographs on the Evaluation of Carcinogenic Risks to Humans. International report 14/002. *International Agency for Research on Cancer*, 38, pp.1249-1250, Lyon, France. https://doi.org/10.1093/carcin/bgw025.

Leon, V.M., Alvarez, B., Cobollo, M.A., Munoz, S. and Valor, I., 2003. Analysis of 35 priority semivolatile compounds in water by stir bar sorptive extraction-thermal desorption-gas chromatography-mass spectrometry: I. Method optimisation. *Journal of Chromatography A*, 1-2, pp.91-101, Alicante, Spain. https://doi.org/10.1016/j.aca.2005.10.080.

Miller, J.N. and Miller, J.C., 2002. *Estadística y Quimiometría para Química Analítica*, 4th ed. Madrid, Spain, 296pp.

Neng, N.R., Pinto, M.L., Pires, J., Marcos, P.M. and Nogueira, J.M.F., 2007. Development, Optimisation and Application of Polyurethane Foams as New Polymeric Phases for Stir Bar Sorptive Extraction. *Journal of Chromatography A*, 1-2, pp.8-14. https://doi.org/10.1016/j.talanta.2011.12.010.

Popp, P., Bauer, C. and Wennrich, L., 2001. Application of stir bar sorptive extraction in combination with column liquid chromatography for the determination of polycyclic aromatic hydrocarbons in water samples. *Analytica Chimica Acta*, 436(1), pp.1-9. https://doi.org/10.1016/S0003-2670(01)00895-9.

Prieto, A., Basauri, O., Usobiaga, A., Rodil, R., Fernandez, L.A., Etxebarria, N. and Zuloaga, O., 2010. Stir-bar sorptive extraction: A view on method optimisation, novel applications, limitations and potential solutions. *Journal of Chromatography A*, 1217(16), pp.2642-2666. https://doi.org/10.1016/j.chroma.2009.12.051.

Sandra, P., Baltussen, E., David, F. and Hoffman, A., 2015. App. Note

2/2000: Stir Bar Sorptive Extraction (SBSE) applied to Environmental Aqueous Samples. *GERSTEL GmbH and Co. KG*, pp.1-6.

Sharma, A., Gupta, S. and Kaur, M., 2023. Postnatal Exposure to A Low Dose of Imidacloprid: Oxidative Stress in Brain Without Affecting Learning and Behavior in Swiss Albino Mice. *Nature Environment and Pollution Technology*, 22(3). https://doi.org/10.46488/NEPT.2023.v22i03.043.

Thompson, M. and Ellison, S.L., 2004. A review of interference effects and their correction in chemical analysis with special reference to uncertainty. *Accreditation and Quality Assurance*, 3, pp.82-97. https://doi.org/10.1007/s00769-004-0871-5.

ORCID DETAILS OF THE AUTHORS

L. A. García: https://orcid.org/0000-0003-3080-1282

G. Fernández: https://orcid.org/0000-0002-9748-4157

G. L. Andraca: https://orcid.org/0000-0002-7945-7294

Delineation of Groundwater Potential Zones Using GIS and Analytic Hierarchy Process in Parts of Varanasi and Chandauli Districts

Pooja Tripathi[1][†]**, Birendra Pratap**[1]**, Sanjay Kumar Tiwari**[2]**, Rajnish Kumar**[3]**, Sandeep Maddheshiya**[4]**, Purnendu Shekhar Shukla**[5] **and Mohammad Ashraf**[5]

[1]Department of Geophysics, Institute of Science (BHU), Varanasi, U.P., India

[2]Department of Geology, Institute of Science (BHU), Varanasi, U.P., India

[3]Geological Survey of India, India

[4]Department of Civil Engineering, Indian Institute of Technology (BHU), Varanasi, U.P., India

[5]Department of Data Science, Indian Institute of Technology, Madras, India

[†]Corresponding author: Pooja Tripathi; poojajha@bhu.ac.in

ABSTRACT

This study employs Remote Sensing (RS) and Geographic Information Systems (GIS) to delineate groundwater potential zones. Various thematic layers, including geomorphology, land use and land cover, geology, rainfall, slope, soil composition, drainage density, and the Topographic Wetness Index (TWI), were integrated using a weighted linear combination in the GIS platform's spatial analyst tool. The Analytic Hierarchy Process (AHP) was used to assign different ranks to these layers and their sublayers. Groundwater potential zones were categorized as poor (16.54%, 96.25 km²), moderate (67.20%, 391.13 km²), and good (16.26%, 94.62 km²). Validation involved observing water levels in various wells within the study area, with the results' reliability assessed using a Receiver Operating Characteristic (ROC) curve, demonstrating an accuracy of 88%. The study area faces rapid urbanization and industrialization, stressing the aquifer's groundwater availability. Identifying groundwater potential zones is thus crucial for effective groundwater development and management.

INTRODUCTION

Groundwater, serving as a fundamental water resource for potable consumption and agricultural irrigation in numerous regions within the country, is crucial for environmental sustainability and serves as a vital freshwater source for human civilization (Arkoprovo et al. 2012, Gleeson et al. 2012, Zhu & Abdelkareem, 2021). Rapid urbanization and industrialization have increased the water demand, leading to a decline in groundwater levels in certain regions, and thus, identifying potential groundwater zones is an optimal solution (Ajay Kumar et al. 2020, Melese & Belay 2021, Saravanan et al. 2021, Tamiru & Wagari 2021, Zhu & Abdelkareem 2021). Remote sensing (RS) data has been identified as a cost-effective alternative to conventional approaches, such as hydrogeological surveys (Chowdhury et al. 2009, Jha et al. 2010, Kumari & Singh 2021). Over the past few decades, the application of geospatial methods has risen as a pivotal tool in groundwater mapping (Murthy 2000). Assessing groundwater potential requires a thorough review of all factors impacting its movement, whether directly or indirectly (Gaur et al. 2011, Sternberg & Paillou

2015, Nanda et al. 2017). The integration of various satellite data sources has facilitated the comprehensive and efficient analysis of different groundwater potential zones (Shekhar & Pandey 2014). Several research studies have highlighted that identifying areas with groundwater potential is shaped by a variety of landscape, climatic, and environmental factors. These factors comprise land use and land cover (LULC), geology, geomorphology, rainfall, slope, drainage density, soil, lineament structure, topography, and river distance, among others (Jaiswal et al. 2003, Gou et al. 2015, Thapa et al. 2017, Parameswari & Padmini 2018, Das & Pal 2020, Pande et al. 2020, Doke et al. 2021). The hydrological and groundwater dynamics within a specific geographical area are determined by the underlying principles of geomorphology and geology (Shaban et al. 2006, Doke et al. 2018, Doke et al. 2021). Water percolation rates depend upon an area's geological attributes, particularly its lithological composition, thereby impacting the mechanism of groundwater replenishment (Dar et al. 2020). Groundwater replenishment relies significantly on drainage systems and analyzing basin structures to estimate recharge zones. Low drainage density areas often see higher groundwater
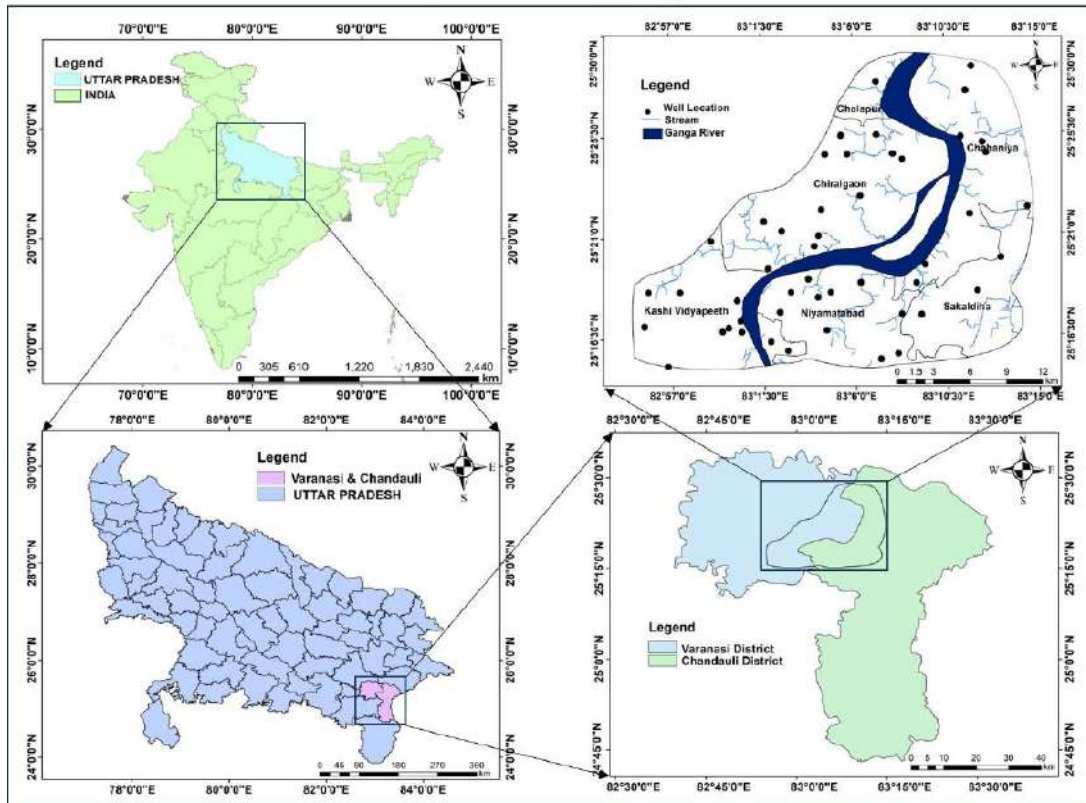
Research Area Map

Fig. 1: Map of the research area.

recharge. Topography, like steep slopes, hampers rainwater infiltration, reducing recharge. Land use changes affect water retention, impacting evapotranspiration, runoff, and recharge. Understanding this link is crucial due to landscapes' vulnerability to human activities. Efficient land use greatly influences groundwater recharge and demand dynamics (Lerner & Harris 2009, Fan 2015). The Topographic Wetness Index focuses on the moisture levels and soil attributes within a particular area (Beven & Kirkby 1979, Radula et al. 2018). In the research area, rapid development and urbanization result in limited availability of land for groundwater recharge and over-extraction of groundwater. The research focuses on identifying groundwater potential areas in parts of Varanasi and Chandauli districts in Uttar Pradesh, utilizing Geographic Information System (GIS) and Analytical Hierarchy Process (AHP) techniques. The goal of this study is to enhance the management and planning of groundwater resources.

RESEARCH AREA

The research area is situated within the Survey of India toposheets numbered 63 O/3 and 63 K/15, spanning from latitude 25°15'0" N to 25°29'0" N and longitude 82°55'0" E to 83°15'0" E in the eastern region of Uttar Pradesh, India as shown in Fig. 1. The research area is situated in part of the Indo-Gangetic plain, encompassing an area of 582 square kilometers that is predominantly characterized by alluvial plains. The research area experiences a tropical climate, significantly influenced by the monsoon. About 80% of the annual precipitation in the region is 1,020 mm and occurs during the southwest monsoon. The research area is located at an average elevation of 76 meters above mean sea level (MSL). Geologically, the area is primarily characterized by Pleistocene to recent Quaternary alluvial sediments (Raju et al. 2011). The occurrence of regular flood events leads to the sedimentation of fresh silt, clay, and loam in the more recent alluvial deposits found near drainage channels. These deposits contribute to the formation of an aquifer system distinguished by alternate sand and clay layers (Nandimandalam 2012). The research area comprises shallow as well as deeper aquifers. The shallow aquifer is situated close to the surface and is distinguished by the presence of sandy sediments. It occurs at the water table condition and is unconfined. In contrast to the alluvial

aquifer near the surface, the deeper aquifers in the research area exhibit semi-confined to confined conditions. These aquifers are situated at greater depths and are typically composed of various geological formations with lower permeability than shallow aquifers (Central Ground Water Board 2021). The decline in groundwater levels in the research area is attributed to extensive groundwater pumping, a consequence of population growth and urbanization.

MATERIAL AND METHODS

Data Source and Process of Preparing Thematic Layers

Numerous elements, such as land use and land cover (LULC), geology, geomorphology, rainfall, soil composition, slope, drainage density, and topographic wetness index (TWI) are used to categorize diverse groundwater potential zones (Yeh et al. 2016, Maity & Mandal 2019, Doke et al. 2021). The thematic maps of LULC, geomorphology, geology, rainfall,

Table 1: Data source and processing used for preparation of different thematic layers.

| Thematic Layers	Data Source	Processing
LULC	Bhuvan	The imagery downloaded from Bhuvan and the research area has been extracted.
Geomorphology	Bhukosh	The shapefile was downloaded from Bhukosh and extracted the geomorphology map of the research area.
Geology	USGS	Downloaded world geological map and intersected the geology of the research area using GIS.
Rainfall (mm/yr.)	Indian Meteorological Department (IMD), Pune	Interpolation of Rainfall values from rain gauge points using the IDW method
Slope	SRTM- Digital Elevation Model (DEM) 30 × 30 M resolution	DEM is used to extract slope (in degrees)
Soil	FAO Soil portal	Downloaded digital soil map of world shapefile and exported data of research area using GIS.
Drainage Density	SRTM- Digital Elevation Model (DEM) 30 × 30 M resolution	Created in GIS using the Line Density from Spatial Analyst
TWI	SRTM- Digital Elevation Model (DEM) 30 × 30 M resolution	Created using hydrology from the Spatial Analyst tool in GIS.
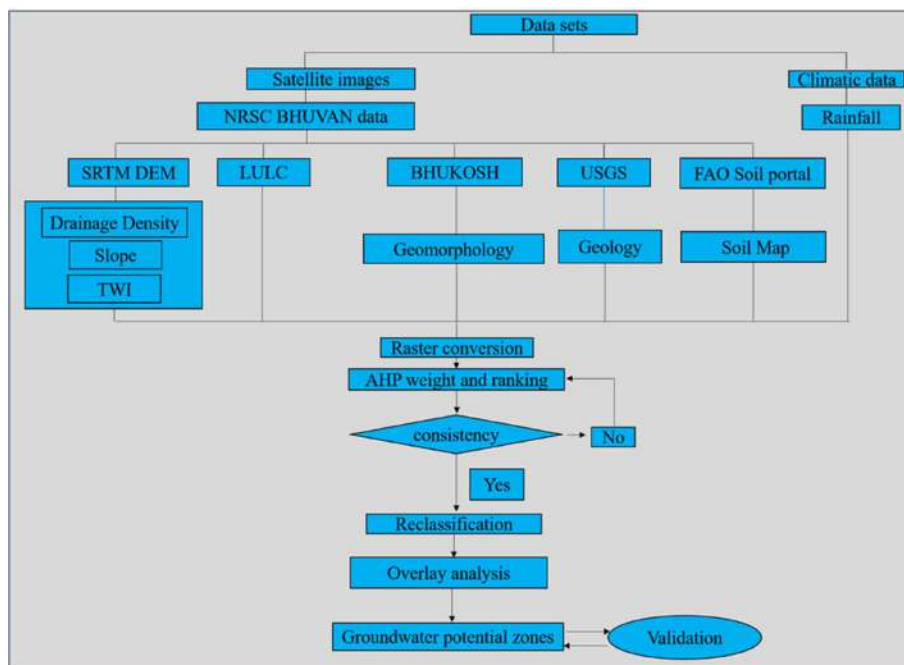
Fig. 2: The flowchart methodology of the research area.

Table 2: Pairwise comparison matrix of eight layers chosen for the present study.

Layer	LULC	GM	GG	RF	SLOPE	SOIL	DD	TWI
LULC	1	2	3	4	5	5	6	7
GM	0.5	1	2	3	4	4	5	6
GG	0.33	0.5	1	2	3	3	4	5
RF	0.25	0.33	0.5	1	2	2	3	4
SLOPE	0.2	0.25	0.33	0.5	1	1	2	3
SOIL	0.2	0.25	0.33	0.5	1	1	2	3
DD	0.167	0.2	0.25	0.33	0.5	0.5	1	2
TWI	0.14	0.167	0.2	0.25	0.33	0.33	0.5	1

LULC landuse/landcover, GM geomorphology, GG geology, RF rainfall, DD drainage density, TWI topographic wetness index.

soil, slope, drainage density, and topographic wetness index (TWI) were prepared using GSI. Table 1 provides a complete overview of the thematic layers, including their data sources and processing methods, while Fig. 2 illustrates the step-by-step methodology in the form of a flowchart.

Assigning Weights and Normalizing through the Analytical Hierarchy Process

Analytical Hierarchy Process (AHP) systematically integrates various criteria and expert opinions into groundwater potential mapping, refining map accuracy and boosting decision-making transparency and reliability (Machiwal et al. 2011, Saravanan et al. 2021). In 1980, Thomas L. Saaty introduced the Analytic Hierarchy Process (AHP), which has become a prominent GIS-based technique extensively used in demarcating zones of groundwater potential (Arulbalaji et al. 2019). AHP employs a pairwise comparison matrix (PCM) to determine the weight of individual layers in the decision-making process which is given in Table 2. Saaty's scale of relative importance and influence is utilized to assign a numerical rank ranging from 1 to 9 to each criterion. Table 3 represents the scales for pair comparison with AHP. Weightage has been assigned to various layers following their significance in identifying the potential groundwater

Table 3: Description of scales for pair comparison with AHP (source: Saaty 1980, 1990).

Strength of importance	Explanation
1	Equal importance
3	Medium importance
5	Strong importance
7	Very strong importance
9	Maximum importance
2,4,6,8	Interim number between two adjacent number

zone (Bera et al. 2020). As a result, the matrix is normalized by calculating the weight of different layers based on subjective evaluation. A normalized pairwise comparison matrix is generated by dividing each value in the matrix by the sum of its respective columns (Bordoloi et al. 2023). To get the criteria weight, the mean of each row is calculated. The sum of criteria weights is one, so it is normalized. The weight assigned to each layer in NPCM is between 0 and 1, as shown in Table 4.

The Calculation of Consistency Ratio

The Consistency Index is calculated by using the formula

Table 4: Normalized pairwise comparison matrix and criteria weights.

Layer	LULC	GM	GG	RF	SLOPE	SOIL	DD	TWI	CW
LULC	0.36	0.4	0.4	0.34	0.3	0.3	0.25	0.22	0.325
GM	0.18	0.2	0.26	0.26	0.24	0.24	0.21	0.19	0.225
GG	0.12	0.11	0.13	0.17	0.18	0.18	0.17	0.16	0.153
RF	0.09	0.07	0.066	0.086	0.12	0.12	0.13	0.13	0.10
SLOPE	0.07	0.05	0.044	0.043	0.06	0.06	0.085	0.097	0.064
SOIL	0.07	0.05	0.044	0.043	0.06	0.06	0.085	0.097	0.064
DD	0.06	0.04	0.033	0.029	0.03	0.03	0.042	0.064	0.041
TWI	0.05	0.03	0.026	0.021	0.02	0.02	0.021	0.032	0.028

LULC landuse/landcover, GM geomorphology, GG geology, RF rainfall, DD drainage density, TWI topographic wetness index.

given in Equation 1.

$$\text{Consistency index (CI)} = \frac{(\lambda\_max - 1)}{(n-1)} \qquad \ldots(1)$$

Where, λ_{max} = Principal Eigenvalue; it is the average of the weighted sum value as calculated in Table 5.

n= number of layers selected for study

The consistency ratio is determined by the ratio between the consistency index (CI) and the random consistency index (RCI), computed using Equation 2.

$$\text{Consistency ratio (CR)} = \frac{CI}{RCI} \qquad \ldots(2)$$

Eight thematic layers were chosen for the study, and according to Saaty (1980; 1990), the random consistency index (RCI) value is 1.41 which is given in Table 5. A consistency ratio (CR) equal to or less than 0.10 allows analysis to proceed; however, exceeding this value prompts a review for inconsistencies. In this research, the calculated consistency ratio (CR) falls below the threshold, indicating the analysis can proceed without issues which is calculated in Table 6.

The Calculation of Groundwater Potential Zones

Thematic layers are combined in the weighted overlay analysis method in GIS software using Equation 3.

$$\text{GWPZ} = \sum_{i}^{n}(W_{th} \times W_{sb}) \qquad \ldots(3)$$

Where GWPZ is Groundwater Potential Zone, W_{th} is Weight assigned to different layers, and W_{sb} is Weight assigned to sub-layers. Sub-layers have been given different rankings, ranging from 1 to 5, depending upon water holding capacity. Sub-layers responsible for good groundwater potential have been assigned 5 rank, and layers responsible for poor groundwater potential have been assigned 1 rank as represented in Table 7.

RESULTS AND DISCUSSION

Land Use Land Cover (LULC)

In the research area, distinct zone has different and specialized land use and land cover which is represented by Fig. 3. The ability of groundwater percolation can be affected by the properties of various types of land cover. Built-up areas, comprising urban and residential developments, commonly exhibit substantial impervious surfaces, such as roads, buildings, and pavements, covering an area of 256.27 km^2. These surfaces impede the infiltration of water into the subsurface, resulting in a decrease in the percolation of groundwater. Nevertheless, precipitation runoff tends to rapidly flow into nearby aquatic systems, resulting in a reduction in the recharge of groundwater. Agricultural lands, comprising an area of 270.37 km^2, frequently exhibit enhanced soil permeability and porosity due to the presence of crops and vegetation cover. The presence of vegetation cover decelerates the velocity of water, facilitating its percolation into the subsurface. Barren land, comprising an area of 29.08 km^2, typically exhibits a scarcity of vegetation cover and a paucity of organic material within the soil. This condition is commonly observed in rocky terrain or regions characterized by sparse vegetation. Consequently, the soil exhibits a deficiency in both structural integrity and organic matter, thereby impeding the facilitation of water infiltration. Barren land typically exhibits a reduced capacity for groundwater percolation. Water bodies, such as rivers, lakes, ponds, and reservoirs, have the potential to enhance

Table 5: The consistency indices of randomly generated reciprocal matrices (source: Saaty 1980, 1990).

Matrix size	1	2	3	4	5	6	7	8
RCI Value	0.00	0.00	0.58	0.90	1,12	1.24	1.13	1.41

Table 6: Calculation of Consistency.

Layer	LULC	GM	GG	RF	SLOPE	SOIL	DD	TWI	Weighted Sum
LULC	0.32	0.45	0.46	0.4	0.32	0.32	0.25	0.2	2.72
GM	0.16	0.22	0.3	0.3	0.26	0.26	0.2	0.17	1.88
GG	0.11	0.11	0.15	0.2	0.19	0.19	0.16	0.14	1.26
RF	0.08	0.075	0.07	0.1	0.13	0.13	0.12	0.11	0.826
SLOPE	0.06	0.056	0.05	0.05	0.06	0.06	0.08	0.08	0.52
SOIL	0.06	0.056	0.05	0.05	0.06	0.06	0.08	0.08	0.52
DD	0.05	0.045	0.04	0.03	0.03	0.03	0.04	0.057	0.33
TWI	0.046	0.037	0.03	0.025	0.02	0.02	0.02	0.028	0.23

Principal Eigenvalues (λ_{max}) =8.2076, n=8, CI=0.0296, RI=1.41, CR=0.0210

Table 7: Different ranks assigned to different subcategories.

Factor	Sub-layers	1	2	3	4	5	CR	Weight
LULC	Water Bodies	1	2	4	5		0.049364	0.483352
	Agricultural Land	0.5	1	3	4			0.302338
	Barren Land	0.25	0.5	1	2			0.136463
	Builtup Area	0.2	0.25	0.5	1			0.077847
Geomorphology	Water Bodies	1	2	4	5		0.049364	0.483352
	Active Flood Plain	0.5	1	3	4			0.302338
	Older flood plain	0.25	0.5	1	2			0.136463
	Older Alluvial Plain	0.2	0.25	0.5	1			0.077847
Geology	Alluvium	1					0	1
Rainfall	1,110-1,044	1	2	3	4	5	0.015763	0.416463
	1,110-957	0.5	1	2	3	4		0.261921
	957-854	0.33	0.5	1	2	3		0.160835
	854-762	0.25	0.33	0.5	1	2		0.098462
	762-681	0.2	0.25	0.33	0.5	1		0.062319
Slope (in degree)	0-1	1	2	3	4	5	0.015763	0.416463
	1-2	0.5	1	2	3	4		0.261921
	2-3	0.33	0.5	1	2	3		0.160835
	3-7	0.25	0.33	0.5	1	2		0.098462
	7-23	0.2	0.25	0.33	0.5	1		0.062319
Soil	Orthic Luvisols	1					0	1
Drainage Density	0-2	1	2	3	4	5	0.015763	0.416463
	2-6	0.5	1	2	3	4		0.261921
	6-11	0.33	0.5	1	2	3		0.160835
	11-16	0.25	0.33	0.5	1	2		0.098462
	16-25	0.2	0.25	0.33	0.5	1		0.062319
TWI	15.44-23.49	1	2	3	4	5	0.015763	0.416463
	12.66-15.44	0.5	1	2	3	4		0.261921
	10.32-12.66	0.33	0.5	1	2	3		0.160835
	7.99-10.32	0.25	0.33	0.5	1	2		0.098462
	4.31-7.99	0.2	0.25	0.33	0.5	1		0.062319

the process of groundwater percolation and recharge the underlying aquifer, covering an area of 26.28 km^2.

Geomorphology

The Research area exhibits distinct features, including an active floodplain, an older floodplain, and an older alluvial plain. The geomorphological map of the research area is shown in Fig. 4 which represents the essential features, for delineating groundwater potential areas. The Research area with a water body has been assigned the highest ranking. An active floodplain is an area situated adjacent to the Ganga River that experiences recurrent inundation events as a consequence of periodic flood events. An active floodplain has been given a higher ranking than an older floodplain. The older floodplain is distinguished by a different river or stream course or a landscape configuration that differs from its current state. Finally, the older alluvial plain is given the lowest ranking as it is formed by the deposition of sediments over a long period through different rivers coming from the highlands.

Geology

The entire research area is mainly alluvium of quaternary age as shown in Fig. 5. The lithological composition of the
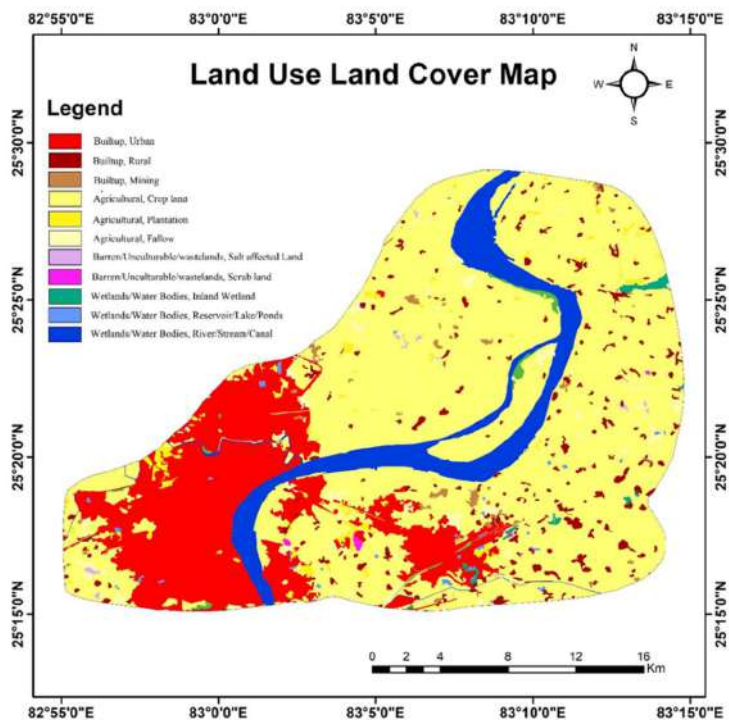
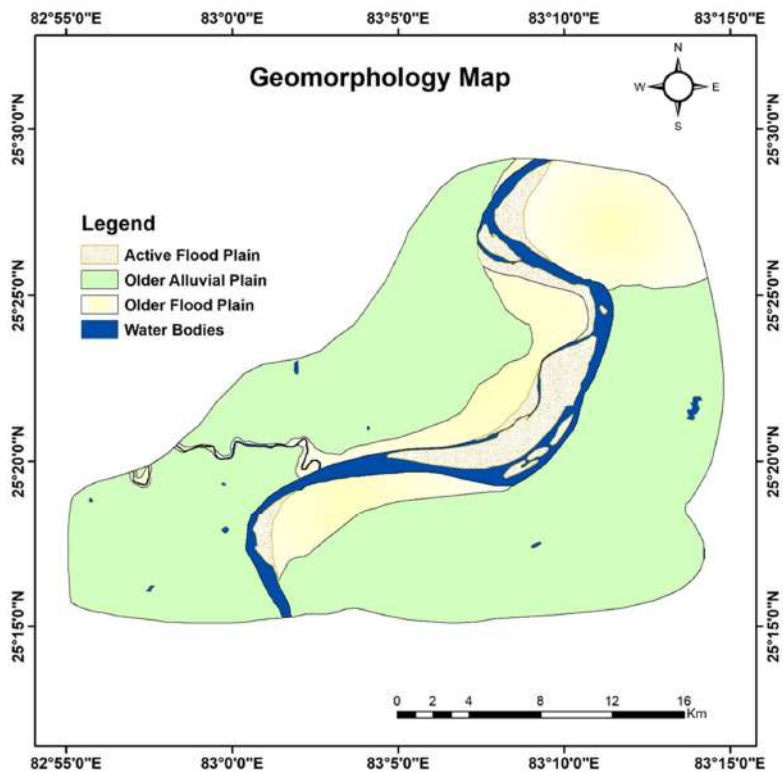Fig. 3: Land use and land cover map of research area.

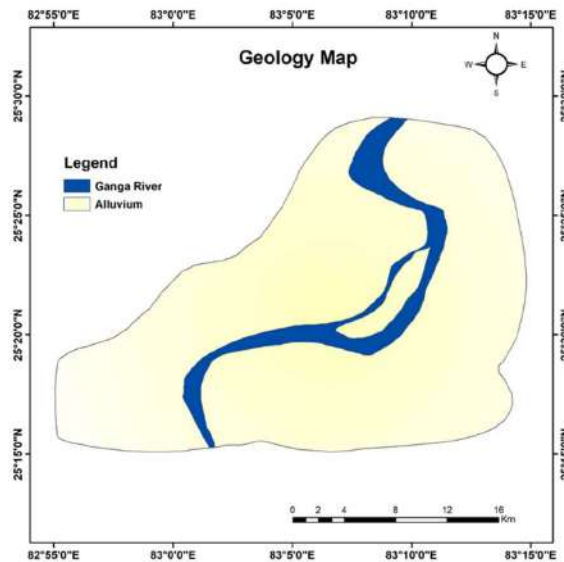Fig. 4: Geomorphology map of research area.

Fig. 5: Geology map of research area.

strata of a region has crucial significance in the assessment of its groundwater potential (Moges et al. 2019). The storage, movement, and availability of groundwater are influenced by the composition and characteristics of the sediments or rocks found in the subsurface. The research area encompasses alluvial sediments that are anticipated to consist of various components, including sands, silts, clays, and gravel. In general, these sediments exhibit good levels of porosity and permeability when compared to lithified rock formations. The sediments in the research area exhibit good

permeability, facilitating the movement of water through them and consequently enhancing their capacity to retain groundwater.

Rainfall

The research area has a tropical climate, and the monsoons have a strong effect on it. The southwest monsoon brings about 80% of the area's total annual rainfall of 1,020 mm during June and August. 10-year rainfall data has been taken from IMD, for creating a rainfall distribution map in the
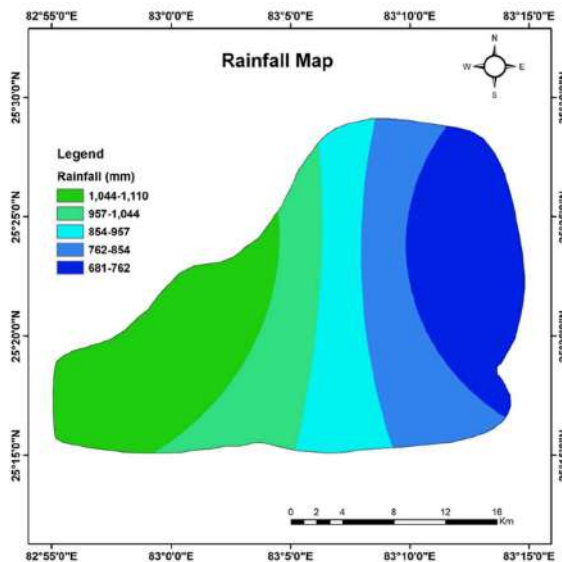

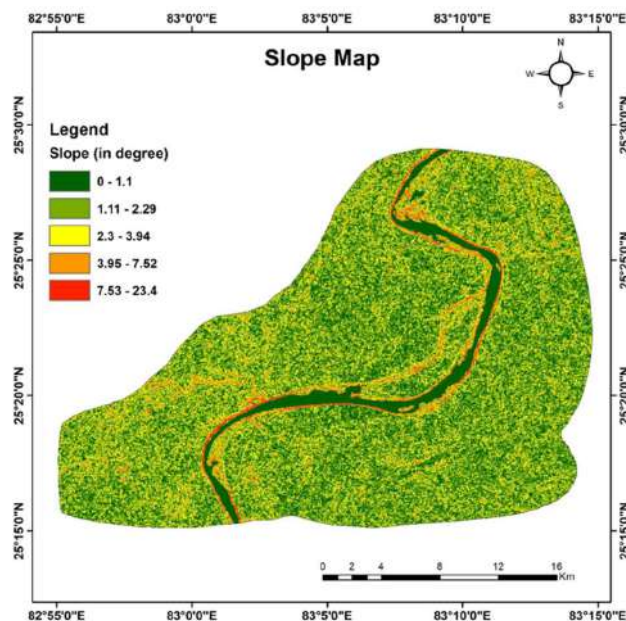Fig. 6: Rainfall map of research area.

Fig. 7: Slope map of the research area.

research area. The average annual rainfall in the research area is classified into five categories: very low (681-762), low (762-854), moderate (854-957), high (957-1044), and very high (1044-1110), as shown by Fig. 6. The eastern region of the research area exhibits a high intensity of rainfall, which gradually decreases towards the western direction of the research area. The research area with high rainfall has good groundwater potential. As a result, areas with high-intensity rainfall have been assigned a high rank, while areas with low-intensity rainfall have been assigned a low rank.

Slope

The slope is an important feature in the determination of the groundwater potential zone. The gradient of a terrain relates to the change in elevation, and it governs the impact of gravitational force on the flow of water (Kom et al. 2022). It affects the amount of water infiltration. A lower value denotes a gentle slope, while a higher value signifies a steeper slope. In areas with gentle slopes, groundwater recharge takes longer due to ample time for rainwater to seep down. Conversely, steep slopes facilitate rapid rainwater flow, minimizing percolation time. Thus, gentle slopes receive higher rankings while steep ones are ranked lower due to these differences in recharge dynamics. The slope map of the research area is represented in Fig. 7.

Soil

Soil characteristics contribute to shaping the assessment of groundwater potential. The relationship between the porosity

and permeability of soil is directly correlated to the rates of infiltration and surface runoff (Senapati & Das 2022). The predominant soil type identified in the research area is orthic luvisols. Fig. 8 shows the soil map of the research area. The diverse mineral composition and elevated nutrient levels found in these soils render them highly suitable for a broad spectrum of agricultural activities. The Luvisols are characterized by a loamy texture, consisting of a substantial amount of silt and an average clay content ranging from 30 to 45 percent (Walmsley et al. 2020). The uniformity of the soil in the research area suggests a consistent influence on its surroundings.

Drainage Density

Drainage density, the mean length of stream channels per unit area, is a measure of how frequently streams occur on the land surface (Avtar et al. 2011).

$$\text{Drainage density} = L/A \qquad \ldots(4)$$

Where, L= length of stream channels

A = Area

The assessment of drainage density in a given region is crucial for comprehending its hydrological attributes, including phenomena such as surface runoff, infiltration, and groundwater recharge. Additionally, it has the potential to offer valuable insights into the fundamental lithological composition and geomorphological mechanisms that contribute to the formation and evolution of the landscape (Murmu et al. 2019).
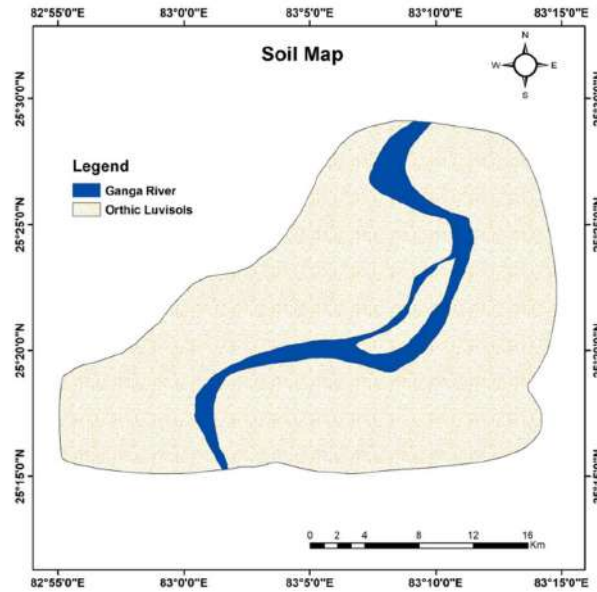
Fig. 8: Soil map of the research area.
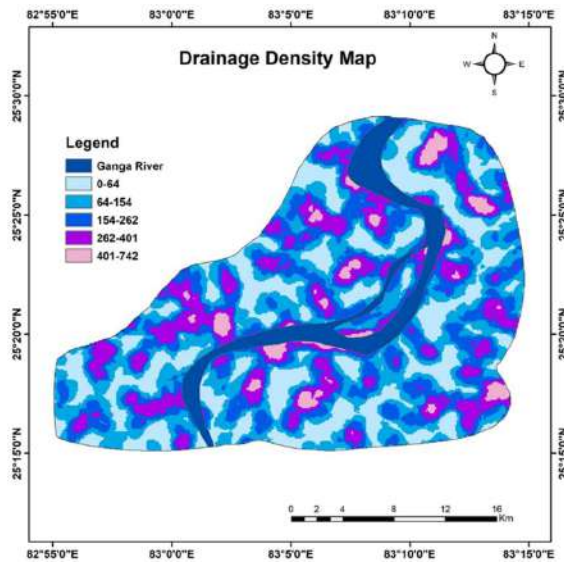
Fig. 9: Drainage density map of research area.

The rate at which groundwater is recharged depends upon the drainage density of the research area. Regions characterized by lower drainage density typically exhibit greater potential for groundwater resources as a result of increased groundwater replenishment. Areas with high drainage density typically exhibit a reduced ability for groundwater recharge as a result of the high rate of surface runoff (Ghosh et al. 2023, Prasad et al. 2008). Therefore, lower drainage density areas have been assigned a high value, and high drainage density areas have been assigned

a lower value. The drainage density of the research area is categorized into five distinct categories, namely 0-64, 64-154, 154-262, 262-401, and 401-742 as represented by Fig. 9. A higher numerical value is indicative of a region with a higher drainage density, while a lower numerical value suggests a region with a lower drainage density.

Topographic Wetness Index

It refers to the spatial distribution of water in the soil that is influenced by the topographical features of

Fig. 10: Topographic wetness index map of the research area.

the land. The determination of the index is as follows:

$$TWI = \ln (a/\tan \beta) \qquad …(5)$$

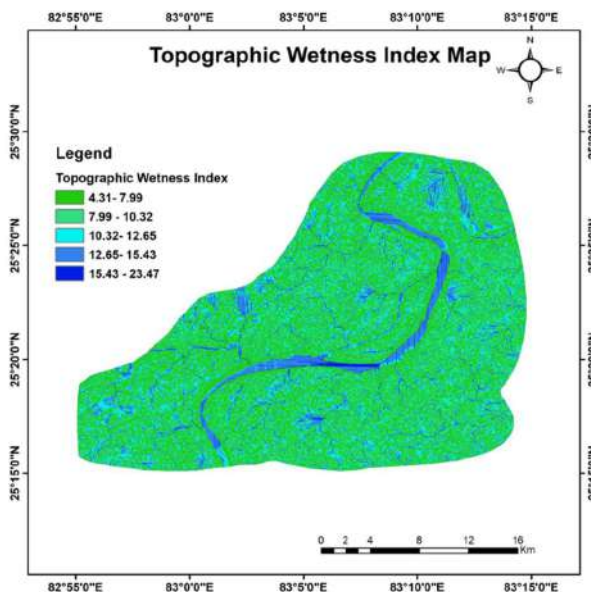The variable "a" represents the specific catchment area (SCA), which is an upslope area draining through a particular point per unit contour length. This area is equivalent to a specific grid cell width. On the other hand, "β" denotes the local slope. SCA can be evaluated in multiple ways (Beven & Kirkby.1979, Sörensen et al. 2006, Zhou et al. 2011). The topographic index is reclassified into five categories, such as 4.31–7.99, 7.99–10.32, 10.32–12.65, 12.65–15.43, and 15.43–23.47 which is shown in Fig. 10. A higher numerical value indicates a higher TWI, while a lower numerical value indicates a lower TWI.

GROUNDWATER POTENTIAL MAPPING AND VALIDATION

Various thematic layers, including LULC, geomorphology, geology, rainfall, soil, slope, drainage density, and TWI, have been generated through the spatial analyst tool within a GIS platform to find potential groundwater resources. Saaty's method for multi-criteria evaluation calculates the weights of different features and thematic layers, ranking them based on their individual importance in assessing groundwater potential. The resulting map categorizes groundwater potential areas into good, moderate, and poor classes which is demonstrated in Fig. 11.

An expanse displaying good groundwater potential spans 94.62 square kilometers, making up roughly 16.26%

of the entire research area. The primary segment of this good potential zone is located alongside the Ganga River, featuring agricultural fields, abundant vegetation, and flood plains. The moderate groundwater potential zone, the most extensive section, covers 391.13 square kilometers, accounting for about 67.20% of the total research area. In contrast, the low groundwater potential zone encompasses 96.25 square kilometers, constituting approximately 16.54% of the research area. This zone is predominantly composed of urban areas characterized by alluvial plains, limited agricultural activity, and sparse vegetation, which is given in Table 8. During the fieldwork carried out in the pre and
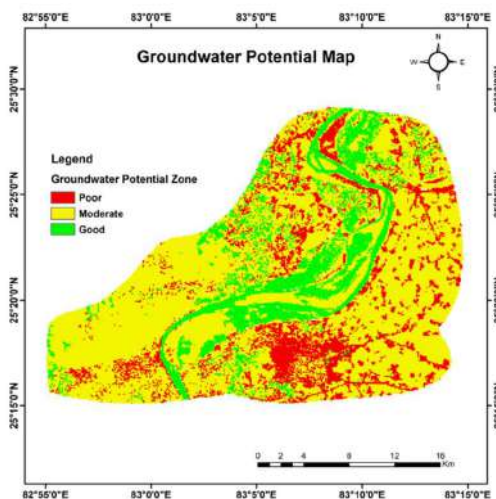

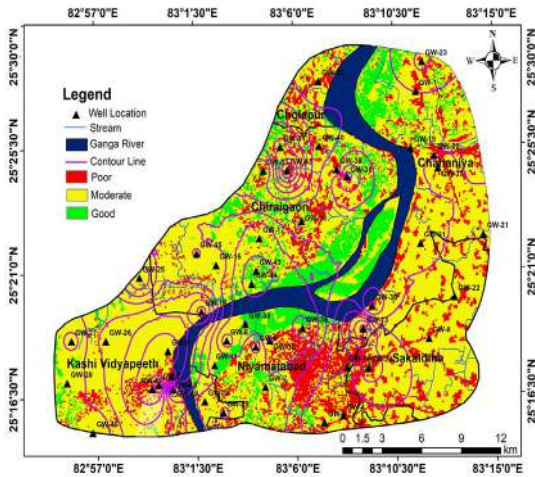Fig. 11: Groundwater potential zone of the research area.

Fig. 12: Validation of the groundwater potential map with field data

Table 8: Groundwater potential zones.

GPZ	Area (km^2)	Area (In percentage)
Poor	96.25	16.54
moderate	391.13	67.20
Good	94.62	16.26

post-monsoon periods of 2022 and 2023, various water wells were observed to collect water level data. This water level data is used to validate the groundwater potential zones. The calculation of water level fluctuations involves assessing the variance between water levels before and after the monsoon season. Areas with low water level fluctuations show good groundwater potential, whereas areas with high water level fluctuations show low groundwater potential (Bera et al. 2020, Verma & Patel 2021, Kom et al. 2022). Using the Inverse Distance Weighting Method, contours with a 0.5-meter interval are superimposed on the GPZ

map. Areas with dense contour lines show high water level fluctuations, and these are mostly urban and industrial areas. Consequentially, over-extraction of groundwater results in poor groundwater potential, whereas areas with low contour density represent low water level fluctuation, and this area is dominated by vegetation and agricultural fields, which results in good groundwater potential. The groundwater potential map of research area has been validated with field data as shown in Fig. 12.

The reliability of the findings was evaluated using the ROC curve. The ROC curve in Fig. 13 indicates a score of 0.88 (88%), which implies that the model achieves an average true positive rate (TPR) of 0.88 across all false positive rates (FPR). In simpler terms, the model correctly identifies 88% of the positive cases on average, even when accounting for false positives. This 0.88 value suggests that the model's performance in delineating the groundwater potential zones of the research area is excellent.

CONCLUSIONS

The research area comprises Varanasi and Chandauli districts, which are part of the Indo-Gangetic Plain. The rainfall pattern affects the groundwater potential zones in the research area. Areas experiencing high rainfall intensity tend to have higher groundwater potential zones, but this is influenced by various factors such as geology, geomorphology, land use and land cover (LULC), soil composition, slope, drainage density, and topographic wetness index (TWI). Geologically, the research area exhibits different lithologies including sand, silt, and clay. The aquifers exist in a multi-tier system in the research area. Sand possesses high porosity and permeability compared to silt, while clay is highly porous but lacks permeability. Therefore, sandstone forms a good aquifer, while clay forms a perched aquifer in some parts of the research area. Geomorphologically, the research
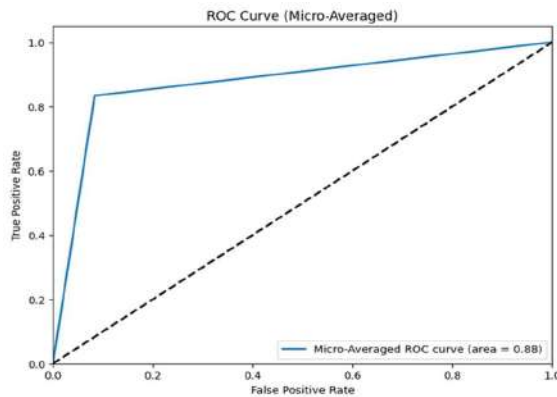

Fig. 13: The ROC curve.

area comprises water bodies (rivers, lakes, and ponds), floodplains, and alluvial plains. The areas occupied by water bodies exhibit good groundwater potential, followed by the floodplain and alluvial plain. The land use and land cover of the research area also influence groundwater potential. Areas characterized by impervious surfaces such as built-up areas, roads, and pavements have negligible percolation rates, resulting in low groundwater potential. Conversely, agricultural and forested areas exhibit high percolation rates, leading to good groundwater potential. Slope also plays an important role in groundwater potential mapping. Gentle slopes favor good groundwater potential, whereas steep slopes result in poor groundwater potential. The research area contains soil classified as orthic luvisols. All areas in the study exhibit similar soil types, resulting in consistent effects on water percolation rates. High drainage density leads to low groundwater potential, while areas with low drainage density represent groundwater potential zones. The topographic wetness index shows an opposite relationship to drainage density. All the factors have been combined using remote sensing and GIS. Different rankings have been assigned to various layers and sub-layers using the AHP method. Finally, a groundwater potential map has been generated, dividing the area into zones of good, moderate, and poor groundwater potential. As the research area is a rapidly growing city, the demand for water for various uses is increasing. Therefore, it is essential to map the different potentials of groundwater for sustainable development and management.

ACKNOWLEDGEMENTS

REFERENCES

Ajay Kumar, V., Mondal, N. C. and Ahmed, S., 2020. Identification of groundwater potential zones using RS, GIS and AHP techniques: a case study in a part of Deccan volcanic province (DVP), Maharashtra, India. *Journal of the Indian Society of Remote Sensing*, 48, pp. 497-511. https://doi.org/10.1007/s12524-019-01086-3

Arkoprovo, B., Adarsa, J. and Prakash, S. S., 2012. Delineation of groundwater potential zones using satellite remote sensing and geographic information system techniques: a case study from Ganjam district, Orissa, India. *Research Journal of Recent Sciences*, 1(9), pp. 59-66.

Arulbalaji, P., Padmalal, D. and Sreelash, K., 2019. GIS and AHP techniques based delineation of groundwater potential zones: a case study from southern Western Ghats, India. *Scientific Reports*, 9(1), p. 2082. https://doi.org/10.1038/s41598-019-38567-x

Avtar, R., Singh, C. K., Singh, G., Verma, R. L., Mukherjee, S. and Sawada, H., 2011. Landslide susceptibility zonation study using remote sensing and GIS technology in the Ken-Betwa River Link area, India. *Bulletin of Engineering Geology and the Environment*, 70, pp. 595-606. https://doi.org/10.1007/s10064-011-0368-5

Bera, A., Mukhopadhyay, B. P. and Barua, S., 2020. Delineation of groundwater potential zones in Karha river basin, Maharashtra, India, using AHP and geospatial techniques. *Arabian Journal of Geosciences*, 13, pp. 1-21. https://doi.org/10.1007/s12517-020-05702-2

Beven, K. J. and Kirkby, M. J., 1979. A physically based, variable contributing area model of basin hydrology. *Hydrological Sciences Journal*, 24(1), pp. 43-69. http://dx.doi.org/10.1080/02626667909491834

Bordoloi, A., Singh, K. K. and Gaichunglu, G., 2023. Application of analytical hierarchy process and GIS techniques to delineate the groundwater potential zones in and around Jorhat and Majuli areas of eastern Assam, India. *Modeling Earth Systems and Environment*, 9(2), pp. 1589-1612. https://doi.org/10.1007/s40808-022-01583-4

Central Ground Water Board (CGWB), 2021. Aquifer mapping and groundwater management plan, Varanasi district, Uttar Pradesh. Department of Water Resources, River Development and Ganga Rejuvenation, Ministry of Jal Shakti, Government of India. Available at: https://cgwb.gov.in/AQM/NAQUIM_REPORT/UP/VARANASI%20FINAL.pdf

Chowdhury, A., Jha, M. K., Chowdary, V. M. and Mal, B. C., 2009. Integrated remote sensing and GIS-based approach for assessing groundwater potential in West Medinipur district, West Bengal, India. *International Journal of Remote Sensing*, 30(1), pp. 231-250. https://doi.org/10.1080/01431160802270131

Dar, T., Rai, N. and Bhat, A., 2020. Delineation of potential groundwater recharge zones using analytical hierarchy process (AHP). *Geological Ecology and Landscapes*, 5(4), pp. 292-307. https://doi.org/10.1080/24749508.2020.1726562

Das, B. and Pal, S. C., 2020. Assessment of groundwater recharge and its potential zone identification in groundwater-stressed Goghat-I block of Hugli District, West Bengal, India. *Environmental Development and Sustainability*, 22(6), pp. 5905-5923. https://doi.org/10.1007/s10668-019-00457-7

Doke, A. B., Zolekar, R. B., Patel, H. and Das, S., 2021. Geospatial mapping of groundwater potential zones using multi-criteria decision-making AHP approach in a hardrock basaltic terrain in India. *Ecological Indicators*, 127, p. 107685. https://doi.org/10.1016/j.ecolind.2021.107685

Doke, A., Pardeshi, S. D., Pardeshi, S. S. and Das, S., 2018. Identification of morphogenetic regions and respective geomorphic processes: a GIS approach. *Arabian Journal of Geosciences*, 11, pp. 1-13. https://doi.org/10.1007/s12517-017-3358-5

Fan, Y., 2015. Groundwater in the Earth's critical zone: Relevance to large-scale patterns and processes. *Water Resources*, 51(5), pp. 3052-3069. https://doi.org/10.1002/2015WR017037

Gaur, S., Chahar, B. R. and Graillot, D., 2011. Combined use of groundwater modeling and potential zone analysis for management of groundwater. *International Journal of Applied Earth Observation and Geoinformation*, 13(1), pp. 127-139. https://doi.org/10.1016/j.jag.2010.09.001

Ghosh, S., Das, D., Gayen, S. K. and Bhardwaj, P., 2023. Delineation of groundwater potential zones using the AHP technique: a case study of Alipurduar district, West Bengal. *Modeling Earth Systems and Environment*, pp. 1-31. https://doi.org/10.1007/s40808-023-01733-2

Gleeson, T., Wada, Y., Bierkens, M. F. and Van Beek, L. P., 2012. Water balance of global aquifers revealed by groundwater footprint. *Nature*, 488(7410), pp. 197-200. https://doi.org/10.1038/nature11295

Gou, S., Gonzales, S. and Miller, G. R., 2015. Mapping potential groundwater-dependent ecosystems for sustainable management. *Groundwater*, 53(1), pp. 99-110.

Jaiswal, R. K., Mukherjee, S., Krishnamurthy, J. and Saxena, R., 2003.

Role of remote sensing and GIS techniques for generation of groundwater prospect zones towards rural development—an approach. *International Journal of Remote Sensing*, 24(5), pp. 993-1008. https://doi.org/10.1080/01431160210144543

Janardhana Raju, N., Shukla, U. K. and Ram, P., 2011. Hydrogeochemistry for the assessment of groundwater quality in Varanasi: a fast-urbanizing center in Uttar Pradesh, India. *Environmental Monitoring and Assessment*, 173, pp. 279-300. https://doi.org/10.1007/s10661-010-1387-6

Jha, M. K., Chowdary, V. M. and Chowdhury, A., 2010. Groundwater assessment in Salboni Block, West Bengal (India) using remote sensing, geographical information system and multi-criteria decision analysis techniques. *Hydrogeology Journal*, 18(7), pp. 1713-1728. https://doi.org/10.1007/s10040-010-0631-z

Kom, K. P., Gurugnanam, B. and Sunitha, V., 2022. Delineation of groundwater potential zones using GIS and AHP techniques in Coimbatore district, South India. *International Journal of Energy and Water Resources*, pp. 1-25. https://doi.org/10.1007/s42108-022-00188-y

Kumari, A. and Singh, A., 2021. Delineation of groundwater potential zone using analytical hierarchy process. *Journal of the Geological Society of India*, 97, pp. 935-942. https://doi.org/10.1007/s12594-021-1794-z

Lerner, D. N. and Harris, B., 2009. The relationship between land use and groundwater resources and quality. *Land Use Policy*, 26, pp. S265-S273. https://doi.org/10.1016/j.landusepol.2009.09.005

Machiwal, D., Jha, M. K. and Mal, B. C., 2011. Assessment of groundwater potential in a semi-arid region of India using remote sensing, GIS and MCDM techniques. *Water Resources Management*, 25, pp. 1359-1386. https://doi.org/10.1007/s11269-010-9749-y

Maity, D. K. and Mandal, S., 2019. Identification of groundwater potential zones of the Kumari River basin, India: an RS & GIS based semi-quantitative approach. *Environmental Development and Sustainability*, 21, pp. 1013-1034. https://doi.org/10.1007/s10668-017-0072-0

Melese, T. and Belay, T., 2021. Groundwater potential zone mapping using analytical hierarchy process and GIS in Muga Watershed, Abay Basin, Ethiopia. *Global Challenges*, 6(1), p. 2100068. https://doi.org/10.1002/gch2.202100068

Moges, D. M., Bhat, H. G. and Thrivikramji, K. P., 2019. Investigation of groundwater resources in highland Ethiopia using geospatial technology. *Modeling Earth Systems and Environment*, 5, pp. 1333-1345. https://doi.org/10.1007/s40808-019-00603-0

Murmu, P., Kumar, M., Lal, D., Sonker, I. and Singh, S. K., 2019. Delineation of groundwater potential zones using geospatial techniques and analytical hierarchy process in Dumka district, Jharkhand, India. *Groundwater for Sustainable Development*, 9, p. 100239. https://doi.org/10.1016/j.gsd.2019.100239

Murthy, K. S. R., 2000. Ground water potential in a semi-arid region of Andhra Pradesh - a geographical information system approach. *International Journal of Remote Sensing*, 21(9), pp. 1867-1884. https://doi.org/10.1080/014311600209788

Nanda, S., Annadurai, R. and Barik, K. K., 2017. Geospatial decipherment of groundwater potential of Kattankolathur block of Tamil Nadu using MCDM techniques. *Remote Sensing Applications: Society and Environment*, 8, pp. 240-250. https://doi.org/10.1016/j.rsase.2017.10.002

Nandimandalam, J. R., 2012. Evaluation of hydrogeochemical processes in the Pleistocene aquifers of middle Ganga Plain, Uttar Pradesh, India. *Environmental Earth Sciences*, 65, pp. 1291-1308. https://doi.org/10.1007/s12665-011-1377-1

Pande, C. B., Moharir, K. N., Singh, S. K. and Varade, A. M., 2020. An integrated approach to delineate the groundwater potential zones in Devdari watershed area of Akola district, Maharashtra, Central India. *Environmental Development and Sustainability*, 22, pp. 4867-4887. https://doi.org/10.1007/s10668-019-00409-1

Parameswari, K. and Padmini, T. K., 2018. Assessment of groundwater potential in Tirukalukundram block of southern Chennai Metropolitan Area. *Environmental Development and Sustainability*, 20, pp. 1535-1552. https://doi.org/10.1007/s10668-017-9952-6

Prasad, R. K., Mondal, N. C., Banerjee, P., Nandakumar, M. V. and Singh, V. S., 2008. Deciphering potential groundwater zone in hard rock through the application of GIS. *Environmental Geology*, 55, pp. 467-475. https://doi.org/10.1007/s00254-007-0992-3

Raduła, M. W., Szymura, T. H. and Szymura, M., 2018. Topographic wetness index explains soil moisture better than bioindication with Ellenberg's indicator values. *Ecological Indicators*, 85, pp. 172-179. https://doi.org/10.1016/j.ecolind.2017.10.011

Saaty, T. L., 1980. *The analytical hierarchy process: Planning, priority, resource allocation*. RWS Publications, USA.

Saaty, T. L., 1990. How to make a decision: The analytic hierarchy process. *European Journal of Operational Research*, 48(1), pp. 9-26. https://doi.org/10.1016/0377-2217(90)90057-I

Saravanan, S., Saranya, T., Abijith, D., Jacinth, J. J. and Singh, L., 2021. Delineation of groundwater potential zones for Arkavathi sub-watershed, Karnataka, India using remote sensing and GIS. *Environmental Challenges*, 5, p. 100380. https://doi.org/10.1016/j.envc.2021.100380

Senapati, U. and Das, T. K., 2022. GIS-based comparative assessment of groundwater potential zone using MIF and AHP techniques in Cooch Behar district, West Bengal. *Applied Water Science*, 12(3), p. 43. https://doi.org/10.1007/s13201-021-01509-y

Shaban, A., Khawlie, M. and Abdallah, C., 2006. Use of remote sensing and GIS to determine recharge potential zones: the case of Occidental Lebanon. *Hydrogeology Journal*, 14, pp. 433-443. https://doi.org/10.1007/s10040-005-0437-6

Shekhar, S. and Pandey, A. C., 2014. Delineation of groundwater potential zone in hard rock terrain of India using remote sensing, geographical information system (GIS) and analytic hierarchy process (AHP) techniques. *Geocarto International*, 30(4), pp. 402-421. https://doi.org/10.1080/10106049.2014.894584

Sörensen, R., Zinko, U. and Seibert, J., 2006. On the calculation of the topographic wetness index: evaluation of different methods based on field observations. *Hydrology and Earth System Sciences*, 10(1), pp. 101-112. https://doi.org/10.5194/hess-10-101-2006

Sternberg, T. and Paillou, P., 2015. Mapping potential shallow groundwater in the Gobi Desert using remote sensing: Lake Ulaan Nuur. *Journal of Arid Environments*, 118, pp. 21-27. https://doi.org/10.1016/j.jaridenv.2015.02.020

Tamiru, H. and Wagari, M., 2021. Evaluation of data-driven model and GIS technique performance for identification of groundwater potential zones: A case of Fincha Catchment, Abay Basin, Ethiopia. *Journal of Hydrology: Regional Studies*, 37, p. 100902. https://doi.org/10.1016/j.ejrh.2021.100902

Thapa, R., Gupta, S., Guin, S. and Kaur, H., 2017. Assessment of groundwater potential zones using multi-influencing factor (MIF) and GIS: a case study from Birbhum district, West Bengal. *Applied Water Science*, 7, pp. 4117-4131. https://doi.org/10.1007/s13201-017-0571-z

Verma, N. and Patel, R. K., 2021. Delineation of groundwater potential zones in lower Rihand River Basin, India using geospatial techniques and AHP. *Egyptian Journal of Remote Sensing and Space Sciences*, 24(3), pp. 559-570. https://doi.org/10.1016/j.ejrs.2021.03.005

Walmsley, A., Azadi, H., Tomeckova, K. and Sklenicka, P., 2020. Contrasting effects of land tenure on degradation of Cambisols and Luvisols: The case of Central Bohemia Region in the Czech Republic. *Land Use Policy*, 99, p. 104956. https://doi.org/10.1016/j.landusepol.2020.104956

Yeh, H. F., Cheng, Y. S., Lin, H. I. and Lee, C. H., 2016. Mapping groundwater recharge potential zone using a GIS approach in Hualian

River, Taiwan. *Sustainable Environment Research*, 26(1), pp. 33-43. https://doi.org/10.1016/j.serj.2015.09.005

Zhou, G., Wei, X., Wu, Y., Liu, S., Huang, Y., Yan, J. and Liu, X., 2011. Quantifying the hydrological responses to climate change in an intact forested small watershed in Southern China. *Global Change Biology*, 17(12), pp. 3736-3746. https://doi.org/10.1111/j.1365-2486.2011.02499.x

Zhu, Q. and Abdelkareem, M., 2021. Mapping groundwater potential zones using a knowledge-driven approach and GIS analysis. *Water*, 13(5), p. 579. https://doi.org/10.3390/w13050579

Assessing the Climate Change Impacts in the Jhelum Basin of North-Western Himalayas

R. Ahmed[1] , S. Saleem[1], T. Shamim[1†], S. Javaid[1], I. H. Malik[2], A. F. Rather[1], G. F. Wani[1], A. Bhat[3] and T. A. Wani[1]

[1]Department of Geography and Disaster Management, School of Earth and Environmental Sciences, University of Kashmir, Srinagar-190006, India

[2]School of Geography, University of Leeds, Leeds, LS2 9JT, United Kingdom

[3]State Key Laboratory of Marine Geology, Tongji University, 1239 Siping Road, Shanghai, 200092, China

†Corresponding author: T. Shamim; tahashamim11@gmail.com

ABSTRACT

Climate change, a critical global environmental crisis, profoundly impacts ecosystems, particularly in regions with delicate environmental balances. This study focuses on the Jhelum basin in the north-western Himalayas, examining the extensive effects of climate change on glaciers, snow cover, land use and land cover (LULC), land surface temperature (LST), water resources, and natural hazards. Rising temperatures have accelerated glacier melting and altered precipitation patterns, with significant implications for local water supplies and agriculture. The study analyses climate data from the Indian Meteorological Department (1990 to 2020), revealing increasing trends in both maximum and minimum temperatures, alongside variable precipitation trends across different locations. The retreat of glaciers and the expansion of glacial lakes have been observed, with lower-elevation glaciers showing the most significant reduction. LULC changes indicate a shift from agricultural land to settlements and horticulture, while LST has risen, particularly in urbanized areas, reflecting the impact of urbanization and climate change. Furthermore, the increased frequency of extreme weather events, such as floods and landslides, exacerbates the region's vulnerability, threatening infrastructure, biodiversity, and local communities. The findings highlight the necessity of comprehensive, integrated approaches to address climate change and ensure the resilience of the Jhelum basin. This research contributes valuable insights into the region's changing environmental dynamics, essential for informed decision-making and effective adaptation strategies in response to the ongoing climate crisis.

INTRODUCTION

Climate change is today's most serious environmental crisis, with far-reaching consequences for the planet's delicate ecosystems. The rate at which weather and climate patterns are changing emphasizes the importance of solving this global crisis. Studies have consistently demonstrated the far-reaching implications of climate change, encompassing a spectrum of phenomena including escalating global temperature extremes (Lindsey & Dahlman 2020, Bellard et al. 2012, Morak et al. 2013, Fischer et al. 2013), heightened frequency and severity of cyclones and floods (Holland & Bruyère 2014, Moon et al. 2019, Walsh et al. 2016, Kundzewicz et al. 2014), dwindling snow cover (Wang et al. 2014, Mir et al. 2015, 2017). In addition, there has been a noticeable increase in wildfires, desert expansion (Huang et al. 2020), and shifts in agricultural practices. Regions with development limits, as

well as those with fragile ecosystems, such as coastal, mountainous, and island locations, are especially sensitive to these effects (IPCC 6th Assessment Report 2022). Temperature and precipitation appear to be the most important markers of climate change (Fischer et al. 2013). Changes in these parameters serve as important indicators of climatic behaviour (Easterling et al. 2000, Zhang et al. 2011, Rana et al. 2017). Studies on climate change in India have revealed a consistent upward trend in temperatures throughout the twentieth century (Srivastava et al. 2001, Dash et al. 2007, Kumar et al. 1994, Soora et al. 2013, Sahai 1998, De & Mukhopadhyay 1998, Singh & Sontakke 2002). Furthermore, rainfall patterns vary by location, with some places experiencing increasing trends and others experiencing decreases of varied degrees (Kripalani et al. 1997, 2003, Singh & Sontakke 2002, Kumar et al. 1992, Misra et al. 2018, Guhathakurta et al. 2011). Projections for India imply that these trends will continue,

with temperatures rising and rainfall patterns changing by the end of the twenty-first century (Kumar et al. 2013, 2016).

Numerous studies have focused on the Himalayan region, which plays a critical role in shaping the hydrometeorological environment and is vulnerable to disasters such as floods and landslides (Shrestha et al. 2009, Xu et al. 2009, Dimri & Dash 2012, Vedwan & Rhoades 2001, Bhutiyani et al. 2010, Sabin 2020). Mountainous locations around the world, such as the Alps, Rockies, Andes, and the Himalayas, have been recognized as particularly vulnerable to climate change due to dramatic height changes over short distances, which result in accelerated warming trends (Shrestha et al. 2012, 2019, Negi et al. 2021). Observations show that the Himalayas are warming faster than the global average, with serious consequences for ecosystems and the socioeconomic well-being of the region's inhabitants, as well as those in the Indo-Gangetic and Brahmaputra plains, which rely directly or indirectly on Himalayan resources (Rautela & Karki 2015, Bhutiyani et al. 2007). Furthermore, the region has seen glaciers decrease and retreat at varied rates due to climate change (Immerzeel et al. 2010, Bolch et al. 2012, Schickhoff et al. 2016, Kääb et al. 2012). To effectively reduce and adapt to the effects of climate change, it is necessary to measure variations in key climatic variables, allowing for informed decision-making and strategic actions.

Climate change is causing a wide range of significant changes in Alpine regions like Kashmir Himalaya. Rising temperatures have sped up glacier melting and reduced snowpack, affecting hydrological regimes and jeopardizing freshwater supplies downstream. These changes heighten the risk of natural disasters such as floods and landslides, endangering infrastructure, populations, and ecosystems. Changes in precipitation patterns present issues for water resource management and agriculture, while the spread of exotic species and diseases threatens biodiversity and ecological stability. The Alpine tourism business, which relies on winter sports, is facing uncertainty as snow seasons shorten and landscapes change, affecting local economies and livelihoods. Urgent adaptation strategies and joint efforts are required to counteract these complex effects and ensure the resilience of Alpine habitats and communities in the face of ongoing climate change.

In the present study, we conducted a comprehensive evaluation of the existing scholarly literature to assess the effects of climate change in the Jhelum basin of the north-western Himalayas. Our study covers a variety of topics, including climate change in the basin and its effects on glaciers, lakes, snow cover, land use and land cover (LULC), land surface temperature (LST), water resources, and natural hazards in the region. By combining information from many sources, we hope to provide a comprehensive picture of the shifting environmental dynamics in the Jhelum basin caused by climatic shifts. Through our analysis, we hope to add to the information base required for effective decision-making and adaptation strategies in the face of climate change issues in the northern Himalayas.

STUDY AREA DESCRIPTION

The Jhelum basin, known as the valley of Kashmir, spans 15,948 square kilometers between 32° 20′-34° 50′ N and 73°
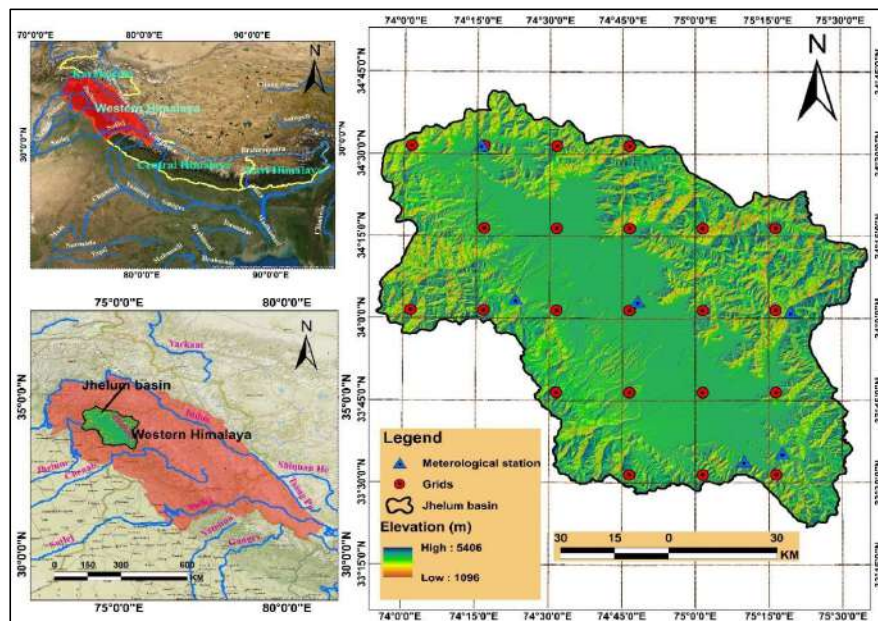

Fig. 1: Location map of the study area.

55′-75° 35′ E. Surrounded by the Great Himalayan and Pir Panjal ranges, the valley has a moderate climate with cold, moist winters and mild summers. It receives an average annual precipitation of 710 mm, predominantly from winter western disturbances and, to a lesser extent, the Indian Summer Monsoon (Fig. 1). Climate change poses significant threats to this region, particularly impacting its hydrology. Rising temperatures are likely to alter precipitation patterns, reducing snowfall and increasing rainfall in winter, which affects the timing and volume of river discharge. Accelerated glacial and snow melt will lead to higher spring flows and potential summer water shortages. These changes could result in more frequent and severe flooding, exacerbated erosion, and unpredictable water availability, challenging water resource management and the valley's ecological balance.

DATASETS AND METHODOLOGY

This study uses a comprehensive methodological framework that includes satellite data, climatic data, and a thorough literature analysis to analyze the effects of climate change on land use and land cover (LULC), land surface temperature (LST), water resources, and natural hazards in the Jhelum basin.

Data Collection

Satellite imagery from Landsat, MODIS, and Sentinel-2 was used to analyze variations in LULC and LST from 1990 to 2020. The images were processed and analyzed using remote sensing techniques to extract useful information.

Climate Data

Historical climate data, including temperature and precipitation records, were gathered from several meteorological stations in the Jhelum Basin. The dataset covers the years 1990 to 2020, offering a long-term view of regional climate patterns.

Literature Review

To contextualize and corroborate our findings, we undertook a thorough review of the current literature on climate change effects in the Jhelum basin. This review contributed to the identification of essential metrics and methodology employed in earlier studies.

Data Analysis

LULC Change Analysis.

Preprocessing: Satellite imagery was preprocessed to correct for atmospheric conditions, geometric distortions, and sensor errors.

Classification: Supervised classification approaches, such as maximum likelihood classification, were used to divide the images into distinct LULC classes.

Change Detection: Post-classification comparison methods were used to detect changes in LULC during the study period. The findings were confirmed with ground truth data and high-resolution images.

LST Change Analysis: Land surface temperatures were retrieved from thermal infrared bands from satellite images. Temporal changes in LST were examined using statistical approaches to find significant trends and spatial patterns. Urban and rural areas were compared to determine the impact of urbanization on LST.

Climate Data Analysis: Temperature and Precipitation Trends: Time series analysis of gathered climatic data was employed to identify trends in maximum and minimum temperatures, as well as precipitation patterns. Statistical approaches such as the Mann-Kendall trend test and Sen's slope estimator were used to determine the significance and rate of change.

Correlation Analysis: The relationships between climate variables and observed environmental changes (e.g., glacier retreat, and glacial lake expansion) were investigated to determine the underlying causes of these changes.

Synthesis and Integration

The findings from satellite data analysis, climate data analysis, and literature review were integrated to provide a holistic understanding of climate change impacts in the Jhelum basin. This integrated approach ensures that the results are robust and comprehensive, highlighting the interconnected nature of environmental changes in the region.

RESULTS

Climate Change in Jhelum Basin

There are many studies such as those by Kumar et al. (2010), Bhat (2010), Shafiq et al. (2018), Ahsan et al. (2021), in the Jhelum basin which reflect the changing state of temperature and precipitation variables. Due to unprecedented greenhouse gas emissions especially 1980s onwards world over, the temperature rates increased, which have also been observed in the Jhelum basin as well (Jaswal et al. 2010, Ahsan et al. 2022). This section focuses on changing precipitation and temperature during the 1990 to 2020 period. For at least 30 years climate data is required to study climate change and find effective trends (Livezey et al. 2007). Hence, 31 years data period (1990 to 2020) was selected for this study.

The average annual precipitation ranges between 74 cm (Srinagar) to 145 cm (Gulmarg) in the Jhelum basin. The average annual Tmax ranges from 20.53°C (Kupwara) to 11.93°C (Gulmarg); while the average annual Tmin ranges from 7.66°C (Srinagar) to 2.71°C (Gulmarg) in the Jhelum basin (Fig. 2). This study reveals that the precipitation is changing in the Jhelum basin, with half of the stations showing annual linear change rate ranging between -0.66 mm per year in Srinagar to -27.5 mm per year in Gulmarg; while another half of the stations show increasing linear trend varying from 1.71 mm per year in Pahalgam to 9.62 mm per year in Kupwara. Both the maximum (Tmax) and minimum (Tmin) temperatures are increasing across all the stations in the Jhelum basin except for a minute decrease in Gulmarg station. The Tmax linear change rate ranges between -0.0007°C/year in Gulmarg to 0.04°C/year in Kukernag. The T min linear change rate varies from -0.028°C/year in Gulmarg to 0.028 in Pahalgam (Fig. 3). These change rates are in line with recent studies in the basin such as Ahmad et al. 2022, Mir et al. 2023. It is important to note that the linear trend rates depend on the length and quality of the time series. Hence, these trend rates may vary depending on the time of consideration.
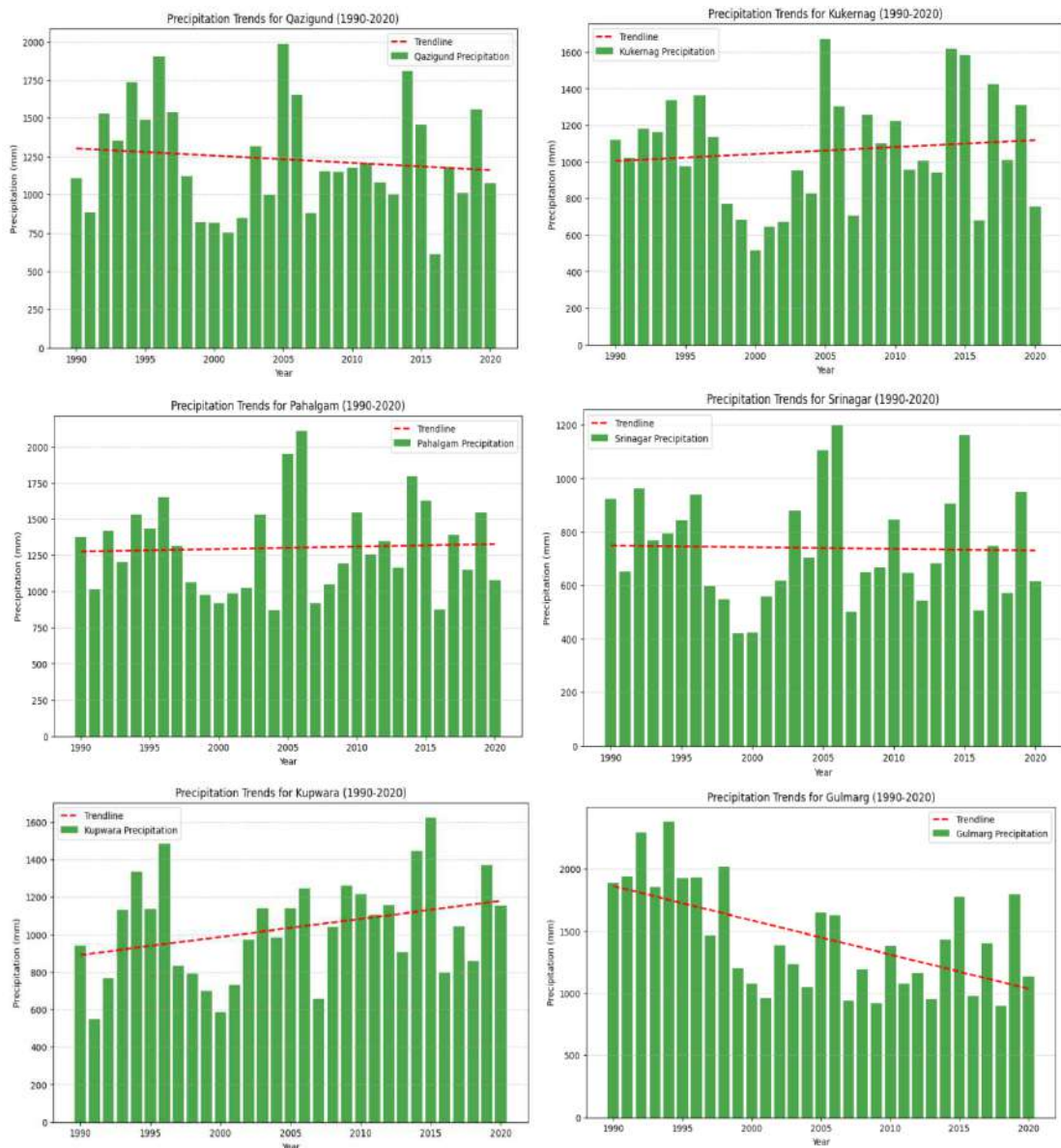
Fig. 2: Precipitation time series of different stations of Jhelum basin.
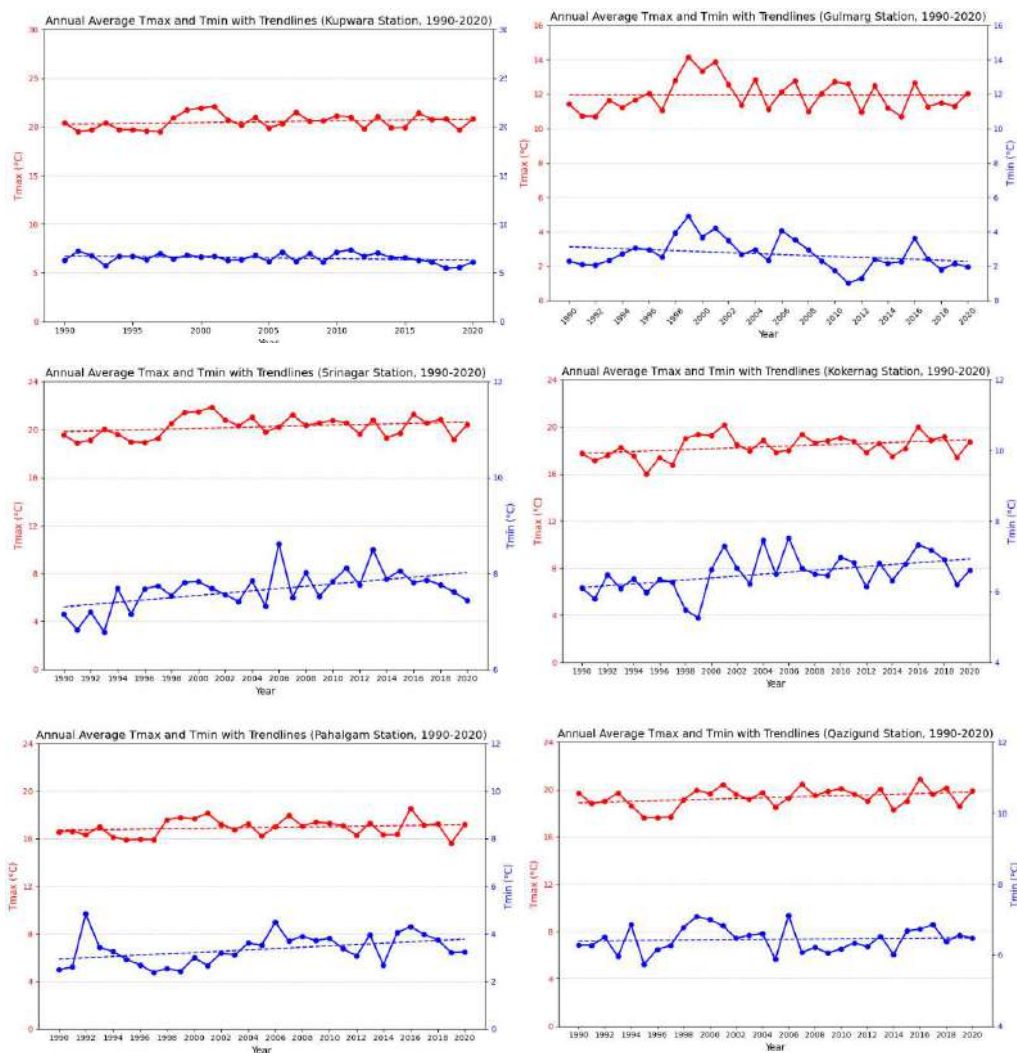
Fig. 3: T*max* and T*min* time series of different stations of Jhelum basin.

Climate Change Impacts in the North-Western Himalayas

Climate change is a global phenomenon that impacts the Earth and its systems in various ways. Primarily caused by human-induced factors such as the use of fossil fuels and deforestation, climate change has resulted in a significant shift in the global climate system. This transformative process is evident in the visible rise in global average surface temperatures, as well as an increase in extreme weather events like heatwaves, storms, floods, and wildfires (IPCC 2023, Abbass et al. 2022). The implications of this climate shift can be observed in polar regions, where melting ice caps and glaciers contribute to rising sea levels, posing a threat to coastal regions and island nations through erosion and increased vulnerability to storm surges (IPCC 2023). Climate change also exacerbates ocean acidification, which affects marine life, while weather changes disrupt habitats, impacting biodiversity (Tang 2020). Agriculture faces challenges as climate change puts stress on ecosystems, and water scarcity worsens, affecting both drinking water quality and quantity, as well as industrial needs (Du Plessis & du Plessis 2019, Cai et al. 2015). Climate change exacerbates social and political imbalances and leads to displacement (Thomas et al. 2015). Addressing this issue requires global cooperation to reduce emissions and ensure a sustainable future.

The Jhelum basin, located in the North-western Himalayan region, is experiencing significant climate

impacts that have far-reaching consequences for its ecology, people, and economy. Rising temperatures in this region have caused glaciers to retreat and altered precipitation patterns. Climate change has also affected land use and land cover (LULC), land surface temperature (LST), and stream flow while intensifying the occurrence of extreme weather events such as cloudbursts and flash floods. These changes have profound implications for water supplies, agriculture, biodiversity, and the overall well-being of the local community.

Impact on glaciers and glacial lakes: The Jhelum basin is home to approximately 307 glaciers and 393 glacial lakes, covering an area of 102.1 km^2 and 22.13 km^2, respectively. These glaciers are melting and losing mass at an alarming rate. The overall glacier area has decreased by 20%, from 85.25 km^2 to 68.17 km^2, with an annual reduction rate of 0.56 km^2. Glaciers located at lower elevations, between 3800 and 4200 meters above sea level, have experienced a 35% decrease in area, with an annual decline rate of 0.22 km^2. The number of glacial lakes has increased by 71, covering an additional area of 3.29 km^2 (Fig. 4). The recession of glaciers and expansion of glacial lakes in the region have been extensively studied and documented by Mir et al. (2018), Romshoo et al. (2020), Ahmed et al. (2021), Dar et al. (2021), Sen et al. (2023), Majeed et al. (2023) and Ahmad et al. (2021). This rapid loss of glacier mass and the growth of glacial lakes can be attributed to rising temperatures and decreasing precipitation in the region, consistent with previous research conducted by Shafiq et al. (2021), Dad et al. (2021), Bashir et al. (2023), Romshoo et al. (2020), Mir

et al. (2021), Ahsan et al. (2021), Gujree et al. (2022) and Bhat et al. (2023).

Impact on LULC and LST: Over the last two decades, the study area has witnessed a considerable change in land use and land cover (LULC), with notable changes observed in various classes. The widespread expansion of new settlements has resulted in a decrease in agricultural areas, while bare terrain, exposed rock, and horticulture have increased significantly. The conversion of agricultural land into residential buildings is visible, as seen by the increase in built-up areas. Agricultural land is widely being converted into horticulture due to climate change, economic returns, and population growth (Fig. 5). The same phenomena have also been reported in various parts of the Kashmir valley (Rasool et al. 2021, Ahmed et al. 2021, Fayaz et al. 2021). Furthermore, surface temperature has risen in the Jhelum basin from 2000 to 2020. According to the study, there was a 2-degree Celsius increase in temperature over this period, with urbanized areas, particularly around Srinagar, witnessing a noticeable spike in land surface temperature (Fig. 5). The extension of built-up regions, as well as the replacement of water bodies and vegetation with urban infrastructure, all contribute to the rise in temperature, demonstrating the impact of urbanization on local climate conditions.

Climate change in the Kashmir valley is apparent not only in LULC changes but also in land surface temperature (LST) patterns. The analysis of LST maps from 2000 to 2020 shows a steady rise in surface temperature, with a large
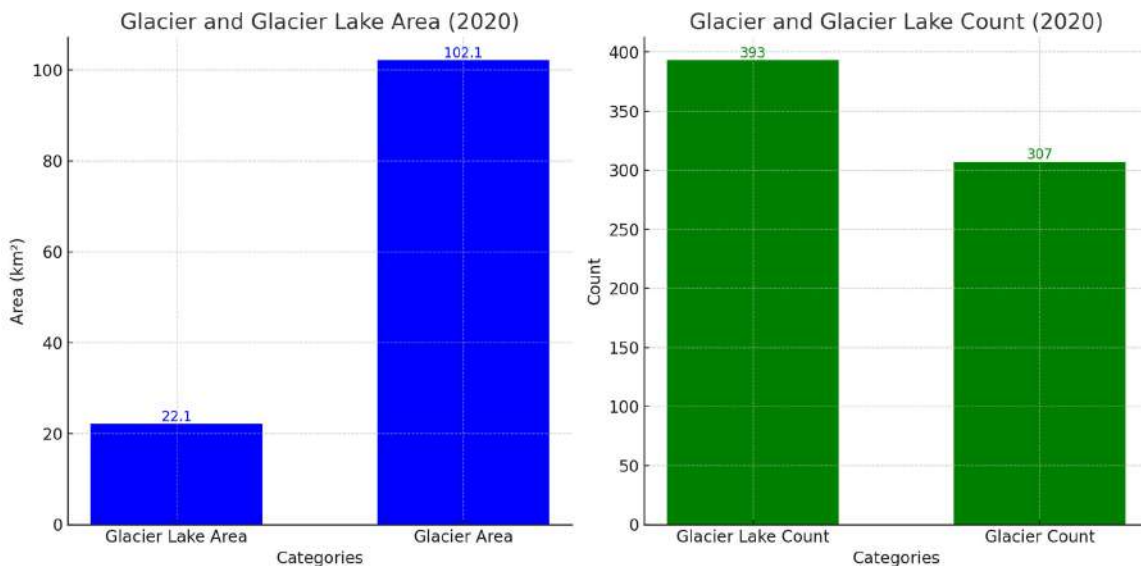

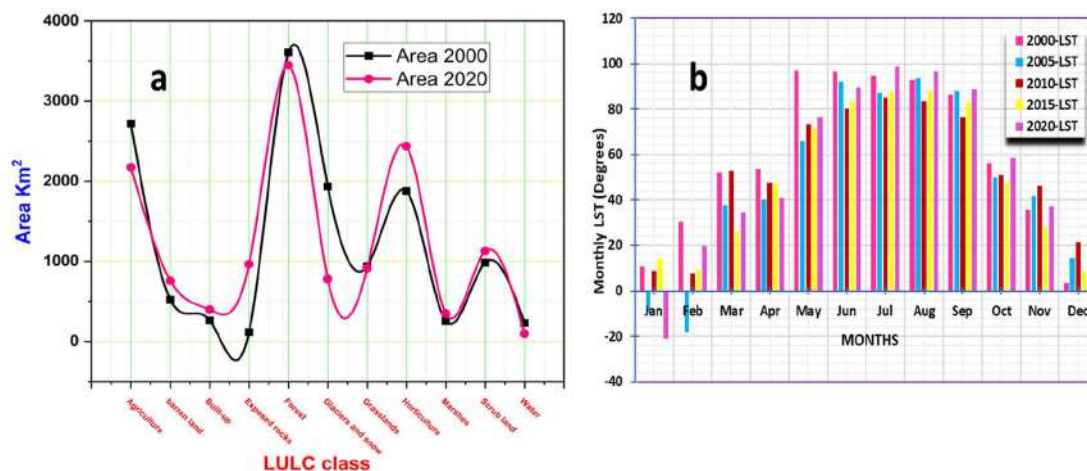Fig. 4: Glacier and Glacial Lake area and count in the Jhelum basin.

Fig. 5: LULC and LST changes in the Jhelum basin from 2000 to 2020.

increase in places experiencing extreme heat exceeding 22 degrees Celsius. Due to greater radiation release, urbanized areas, such as Srinagar, have higher LST values. The seasonal temperature differences, with summers being warmer, correspond to the valley's northern hemisphere position. The monthly and annual LST trends show a complex relationship with fluctuating temperatures, with more fluctuation in recent years (2010, 2015, and 2020). This suggests a dynamic reaction to climate change, which could be influenced by factors such as increasing urbanization, changes in land cover, and global climatic patterns. Overall, the combined study of LULC and LST highlights the varied influence of climate change on the environmental dynamics of the Jhelum basin.

Impact on water resources: The North-Western Himalayas region, crucial for water supply due to its vast glaciers and monsoon-fed rivers, is experiencing significant impacts from climate change, particularly on its water resources. Rising temperatures are causing accelerated glacial melting, leading to the formation of glacial lakes and an increased risk of outburst floods (Prakash & Nagarajan 2018). It has experienced a 21% reduction in glacier area due to climate change, impacting the main water source and increasing the risk of glacial lake outburst floods (GLOFs), threatening the socioeconomic stability of the region (Lone & Jeelani 2024). This poses an immediate danger to downstream communities and threatens long-term water scarcity as glaciers shrink. Changing precipitation patterns contribute to reduced rainfall and alter stream discharge patterns, affecting agriculture, drinking water availability, and the region's hydrological stability (Sharma & Choudhury 2021, Panwar 2020). These changes disrupt biodiversity and local livelihoods and have far-reaching consequences for major rivers that support millions in the Indian subcontinent (Negi et al. 2022,

Anjum et al. 2023). Adaptive water management practices and comprehensive strategies are necessary to address these impacts. Changes in precipitation patterns impact water resource management and groundwater reserves and result in flash floods and soil erosion (Mir et al. 2021). The quality of water resources is at risk due to increased sedimentation, higher turbidity levels, and the leaching of pollutants. These issues can cause water contamination problems and jeopardize human and aquatic ecosystem health (Lone et al. 2021). Changes in water availability affect alpine ecosystems, leading to habitat loss, shifts in species composition, and impacts on biodiversity (Roy & Rathore 2019).

As the North-Western Himalayan water sources feed major rivers that support millions in Asia, the impacts of these changes in stream discharge extend far beyond the Himalayan region. This underlines the critical need for adaptive water management practices and comprehensive strategies to address climate change impacts on stream discharge in the North-Western Himalayas. Proactive measures, such as improved water storage capacity, the construction of smaller-scale reservoirs, and enhanced water-use efficiency in agriculture, are crucial for mitigating the impacts of climate change on water resources in the North-Western Himalayas.

Impact on natural hazards: Climate change is a global, intricate, and evolving challenge that significantly influences natural hazards, particularly hydro-meteorological and climatic hazards. This rapid ongoing transformation in climate, as evidenced by changes in temperature, precipitation, and atmospheric conditions, is mainly attributed to anthropogenic factors (Hansen & Stone 2016). Consequently, it leads to a cascade of effects on various

natural hazards, especially within mountain ecosystems and neighboring landscapes. The influence is characterized by an increasing intensity and frequency of extreme weather and climatic events, encompassing cloudbursts, floods, droughts, melting glaciers, glacial lake outburst floods, snow avalanches, heatwaves, and cold waves (Srivastava & Srivastava 2020, Ramya et al. 2023). The forecasts indicate a constant upward trajectory, underscoring persistent problems and challenges confronted by communities inhabiting highly exposed mountainous and vulnerable regions (Kohler & Maselli 2009, Masson-Delmotte et al. 2021). The role of climate change in exacerbating risks related to natural hazards is particularly evident in areas where existing disaster risk management mechanisms are ill-equipped to manage new, emerging, or cascading risks. The poorest and most vulnerable people, living in the less developed regions of the world, are at the greatest risk (Wani et al. 2022). The Vale of Kashmir in the north-western part of the Indian Himalayan Region is one such example. This multi-hazard-prone region has a long history of hydro-meteorological and climatic disasters, including cloudbursts, floods, snow storms, droughts, and cold waves (Wani et al. 2022). Heavy precipitation, particularly from July to September, has resulted in unprecedented floods in the past (Ballesteros-Cánovas et al. 2020), great magnitude, defying the existing prediction mechanisms and human logic, as seen in September 2014. Climate change has led to an increase in the incidence of rainfall-induced landslides (Shah et al. 2023). Episodes of hailstorms and erratic snowfall, especially during harvest time, have become serious concerns for fruit growers who suffer heavy losses annually (Rashid et al. 2020, Bhat et al. 2023). Erratic snowfall and windstorm events have consistently challenged walnut production in the region (Mir & Kottaiveeran 2018). Farmers, heavily reliant on rainfall for crop production, are compelled to shift from one crop type to another, such as rice to maize, due to altered rainfall patterns and temperature fluctuations. The pastoralist community has suffered material and human losses due to increased occurrences of lightning, thunderstorms, and cloudbursts. While there is limited research available to ascertain the influence of climate change on natural hazards at the local level, the consequences are visible to the affected communities, examined, and documented to a certain level. The local experts unanimously agree with the global community's perspective that there is a need to address climate change in alignment with disaster risk reduction strategies and not in isolation. This holistic approach will help mitigate the impacts of disasters on human life, natural ecosystems, and biodiversity and minimize human contributions to climate change.

DISCUSSION

This study thoroughly examines the effects of climate change in the Jhelum basin, with an emphasis on evolving climatic patterns and their substantial implications for the environment, hydrology, and human activities. This study analyses 31 years of climate data from 1990 to 2020 to identify important temperature and precipitation trends, offering light on the basin's major climatic shifts. The findings of this study show a general increase in both maximum and minimum temperatures over the Jhelum basin, except for a slight decrease at Gulmarg. This trend is consistent with global patterns of rising temperatures due to increased greenhouse gas emissions. The heterogeneity in precipitation trends, with some stations experiencing drops and others experiencing increases, highlights the complexities of climate change, which is influenced by a variety of factors such as altitude, elevation, and localized weather patterns. This diversity emphasizes the significance of doing localized studies to fully assess climate change implications, as global models may not adequately capture regional specificities.

One of the most significant issues raised in this study is the effect of climate change on the hydrology of the Jhelum basin. Rising temperatures are causing glaciers and snowpacks to melt more quickly, altering stream flow patterns. According to the research, there is an increased chance of floods in the spring and early summer, followed by potential water shortages in late summer and autumn. This seasonal variation in water availability presents considerable issues to water resource management, agriculture, and local people who rely largely on continuous water supply. The formation of new glacial lakes and the growth of existing ones raises the possibility of glacial lake outburst floods (GLOFs), which can inflict massive devastation downstream. The retreat of glaciers, combined with the expansion of glacial lakes, represents not only a loss of essential water reserves but also increased disaster risks that necessitate immediate attention and mitigating measures.

This study also investigates changes in land use and cover (LULC) in the Jhelum basin. The conversion of agricultural land to residential and horticultural areas indicates socioeconomic changes caused by population expansion and shifting economic incentives. Climate change, on the other hand, influences these changes by making some types of land use more viable or required when temperatures rise and precipitation patterns shift. The growth in built-up areas, as well as the resulting rise in land surface temperatures (LST), indicate the effects of urbanization and the urban heat island effect, which exacerbates local climate change.

Extreme weather events, such as cloudbursts and flash floods, have become more frequent and intense, highlighting the region's increasing climate volatility. These incidents not only disrupt daily life but also result in huge economic losses and endanger human safety. This study emphasizes the need for better prediction systems and disaster preparedness to lessen the negative effects of such disasters.

The conclusions of this study have far-reaching consequences for the North-Western Himalayas and other similar places. Climate change's cascading effects on hydrology, land use, and extreme weather events need a comprehensive approach to climate adaptation and mitigation. Adaptive water management methods, such as increasing water storage capacity and improving water-use efficiency, are critical for dealing with fluctuating water supplies. Furthermore, including climate change considerations in land use planning and catastrophe risk reduction measures is critical for establishing resilient communities.

CONCLUSION

In conclusion, studies in the Jhelum basin indicate significant changes in temperature and precipitation patterns over the past decades. Rising greenhouse gas emissions since the 1980s have contributed to global and regional temperature increases. From 1990 to 2020, precipitation trends in the Jhelum basin show variability, with some stations experiencing decreases and others increasing. Temperature trends reveal a general increase in both maximum and minimum temperatures, except for a slight decrease at Gulmarg. These findings are consistent with recent research and underscore the importance of long-term, high-quality climate data for accurate trend analysis. The Jhelum basin in the North-western Himalayas is significantly impacted by climate change, which has caused rising temperatures, retreating glaciers, and altered precipitation patterns. These changes have affected land use, land surface temperatures, and stream flow while increasing extreme weather events like cloudbursts and flash floods. The region's glaciers are rapidly melting, leading to more glacial lakes and heightened risks of outburst floods, threatening water resources, agriculture, and local communities. Additionally, shifts in land use and rising land surface temperatures highlight the impact of urbanization and climate change on the local environment. These findings underscore the urgent need for adaptive water management practices and comprehensive strategies to mitigate the adverse effects of climate change on the Jhelum basin and beyond.

ACKNOWLEDGEMENT

REFERENCES

Abbass, K., Qasim, M.Z., Song, H., Murshed, M., Mahmood, H. and Younis, I., 2022. A review of the global climate change impacts, adaptation, and sustainable mitigation measures. *Environmental Science and Pollution Research*, 29(28), pp.42539-42559.

Ahmad, S.T., Ahmed, R., Wani, G.F., Sharma, P. and Ahmed, P., 2022. Glacier changes in Sind basin (1990–2018) of North-western Himalayas using earth observation data. *Modeling Earth Systems and Environment*, 8(2), pp.2567-2579.

Ahmed, R., Wani, G.F., Ahmad, S.T., Sahana, M., Singh, H. and Ahmed, P., 2021. A review of glacial lake expansion and associated glacial lake outburst floods in the Himalayan region. *Earth Systems and Environment*, 5(3), pp.695-705.

Ahsan, S., Bhat, M.S., Alam, A., Ahmed, N., Farooq, H. and Ahmad, B., 2021. Assessment of trends in climatic extremes from observational data in the Kashmir basin, NW Himalaya. *Environmental Monitoring and Assessment*, 193, pp.1-18.

Ahsan, S., Bhat, M.S., Alam, A., Farooq, H. and Shiekh, H.A., 2022. Evaluating the impact of climate change on extreme temperature and precipitation events over the Kashmir Himalaya. *Climate Dynamics*, pp.1-19.

Anjum, N., Ridwan, Q., Sharma, M., Hanief, M., Pant, S., Wani, Z.A. and Bhat, J.A., 2023. Changing climatic scenarios: impacts, vulnerabilities, and perception with special reference to the Indian Himalayan region. In: *Climate Change in the Himalayas,* Academic Press, pp.201-215.

Ballesteros-Cánovas, J.A., Koul, T., Bashir, A., Del Pozo, J.M.B., Allen, S., Guillet, S., ... and Stoffel, M., 2020. Recent flood hazards in Kashmir put into context with millennium-long historical and tree-ring records. *Science of The Total Environment*, 722, p.137875.

Bashir, J. and Romshoo, S.A., 2023. Bias-corrected climate change projections over the Upper Indus Basin using a multi-model ensemble. *Environmental Science and Pollution Research*, 30(23), pp.64517-64535.

Bellard, C., Bertelsmeier, C., Leadley, P., Thuiller, W. and Courchamp, F., 2012. Impacts of climate change on the future of biodiversity. *Ecology Letters*, 15(4), pp.365-377.

Bhat, M.S., 2010. Impact of Climate Change on the Water Resources of North-Western Himalayas Region and Adjoining Punjab Plains.

Bhat, M.S., Mir, S., Parrey, H.A., Thoker, I.A. and Shah, S.A., 2024. Climate change, hailstorm incidence, and livelihood security: a perspective from Kashmir valley India. *Natural Hazards,* 120(3), pp.2803-2827.

Bhutiyani, M.R., Kale, V.S. and Pawar, N.J., 2007. Long-term trends in maximum, minimum and mean annual air temperatures across the Northwestern Himalaya during the twentieth century. *Climatic Change*, 85(1), pp.159-177.

Bhutiyani, M.R., Kale, V.S. and Pawar, N.J., 2010. Climate change and the precipitation variations in the northwestern Himalaya: 1866-2006. *International Journal of Climatology,* 30(4), p.535.

Bolch, T., Kulkarni, A., Kääb, A., Huggel, C., Paul, F., Cogley, J.G. and Stoffel, M., 2012. The state and fate of Himalayan glaciers. *Science*, 336(6079), pp.310-314.

Cai, X., Zhang, X., Noël, P.H. and Shafiee-Jood, M., 2015. Impacts of climate change on agricultural water management: a review. *Wiley Interdisciplinary Reviews: Water,* 2(5), pp.439-455.

Dad, J.M., Muslim, M., Rashid, I. and Reshi, Z.A., 2021. Time series analysis of climate variability and trends in Kashmir Himalaya. *Ecological Indicators,* 126, p.107690.

Dar, R.A., Paul, O.J., Murtaza, K.O. and Romshoo, S.A., 2021. Late Quaternary glacial geomorphology of Kashmir Valley, NW Himalayas: a case study of the Sind basin. In: *Water, Cryosphere, and Climate*

Change in the Himalayas: A Geospatial Approach. Cham: Springer International Publishing, pp.145-157.

Dash, S.K., Jenamani, R.K., Kalsi, S.R. and Panda, S.K., 2007. Some evidence of climate change in twentieth-century India. *Climatic Change,* 85(3), pp.299-321.

De, U.S. and Mukhopadhyay, R.K., 1998. Severe heat wave over the Indian subcontinent in 1998, in perspective of global climate. *Current Science,* 75(12), pp.1308-1311.

Dimri, A.P. and Dash, S.K., 2012. Wintertime climatic trends in the western Himalayas. *Climatic Change,* 111, pp.775-800.

du Plessis, A. and du Plessis, A., 2019. Climate change: Current drivers, observations and impacts on the Globe's natural and human systems. *Water as an Inescapable Risk: Current Global Water Availability, Quality and Risks with a Specific Focus on South Africa,* pp.27-53.

Easterling, D.R., Evans, J.L., Groisman, P.Y., Karl, T.R., Kunkel, K.E. and Ambenje, P., 2000. Observed variability and trends in extreme climate events: a brief review. *Bulletin of the American Meteorological Society,* 81(3), pp.417-426.

Fischer, E.M. and Knutti, R., 2013. Robust projections of combined humidity and temperature extremes. *Nature Climate Change,* 3(2), pp.126-130.

Guhathakurta, P., Sreejith, O.P. and Menon, P.A., 2011. Impact of climate change on extreme rainfall events and flood risk in India. *Journal of Earth System Science,* 120, pp.359-373.

Gujree, I., Ahmad, I., Zhang, F. and Arshad, A., 2022. Innovative trend analysis of high-altitude climatology of Kashmir valley, North-West Himalaya. *Atmosphere,* 13(5), p.764.

Hansen, G. and Stone, D., 2016. Assessing the observed impact of anthropogenic climate change. *Nature Climate Change,* 6(5), pp.532-537.

Holland, G. and Bruyère, C.L., 2014. Recent intense hurricane response to global climate change. *Climate Dynamics,* 42, pp.617-627.

Immerzeel, W.W., Van Beek, L.P. and Bierkens, M.F., 2010. Climate change will affect the Asian water towers. *Science,* 328(5984), pp.1382-1385.

Jaswal, A.K. and Rao, G.P., 2010. Recent trends in meteorological parameters over Jammu and Kashmir. *Mausam,* 61(3), pp.369-382.

Kääb, A., Berthier, E., Nuth, C., Gardelle, J. and Arnaud, Y., 2012. Contrasting patterns of early twenty-first-century glacier mass change in the Himalayas. *Nature,* 488(7412), pp.495-498.

Kohler, T. and Maselli, D., 2009. Mountains and climate change. From understanding to action. *Geographica Bernensia.*

Kripalani, R.H. and Kulkarni, A., 1997. Climatic impact of El Nino/La Nina on the Indian monsoon: A new perspective. *Weather,* 52(2), pp.39-46.

Kripalani, R.H., Kulkarni, A., Sabade, S.S. and Khandekar, M.L., 2003. Indian monsoon variability in a global warming scenario. *Natural Hazards,* 29, pp.189-206.

Kumar, K.R., Kumar, K.K. and Pant, G.B., 1994. Diurnal asymmetry of surface temperature trends over India. *Geophysical Research Letters,* 21(8), pp.677-680.

Kumar, P., Wiltshire, A., Mathison, C., Asharaf, S., Ahrens, B., Lucas-Picher, P. and Jacob, D., 2013. Downscaled climate change projections with uncertainty assessment over India using a high resolution multi-model approach. *Science of the Total Environment,* 468, pp.S18-S30.

Kumar, V. and Jain, S.K., 2010. Trends in seasonal and annual rainfall and rainy days in Kashmir Valley in the last century. *Quaternary International,* 212(1), pp.64-69.

Kundzewicz, Z.W., Kanae, S., Seneviratne, S.I., Handmer, J., Nicholls, N., Peduzzi, P. and Sherstyukov, B., 2014. Flood risk and climate change: global and regional perspectives. *Hydrological Sciences Journal,* 59(1), pp.1-28.

Lindsey, R. and Dahlman, L., 2020. Climate change: Global temperature. *Climate.gov,* 16.

Livezey, R.E., Vinnikov, K.Y., Timofeyeva, M.M., Tinker, R. and van den Dool, H.M., 2007. Estimation and extrapolation of climate normals

and climatic trends. *Journal of Applied Meteorology and Climatology,* 46(11), pp.1759-1776.

Lone, S.A. and Jeelani, G., 2024. Evaluating the Potential Impact of Climate Change on Glacier Dynamics in Western Himalayas, India. In: *Climate Crisis: Adaptive Approaches and Sustainability.* Cham: Springer Nature Switzerland, pp.499-510.

Lone, S.A., Bhat, S.U., Hamid, A., Bhat, F.A. and Kumar, A., 2021. Quality assessment of springs for drinking water in the Himalaya of South Kashmir, India. *Environmental Science and Pollution Research,* 28, pp.2279-2300.

Masson-Delmotte, V., Zhai, P., Pirani, A., Connors, S.L., Péan, C., Berger, S. and Zhou, B., 2021. Climate change 2021: the physical science basis. Contribution of working group I to the sixth assessment report of the intergovernmental panel on climate change. *Journal of Earth System Science,* 2(1), p.2391.

Mir, B.H., Lone, M.A., Kumar, R. and Khoshouei, S.R., 2021. A review on the implications of changing climate on the water productivity of Himalayan glaciers. *Water Productivity Journal,* 1(3), pp.25-36.

Mir, R.A., Jain, S.K., Lohani, A.K. and Saraf, A.K., 2018. Glacier recession and glacial lake outburst flood studies in Zanskar basin, western Himalaya. *Journal of Hydrology,* 564, pp.376-396.

Mir, R.A., Jain, S.K., Saraf, A.K. and Goswami, A., 2015. Decline in snowfall in response to temperature in Satluj basin, western Himalaya. *Journal of Earth System Science,* 124, pp.365-382.

Mir, R.A., Jain, S.K., Thayyen, R.J. and Saraf, A.K., 2017. Assessment of recent glacier changes and its controlling factors from 1976 to 2011 in Baspa basin, western Himalaya. *Arctic, Antarctic, and Alpine Research,* 49(4), pp.621-647.

Mir, R.A., Majeed, Z., Ahmed, R., Jain, S.K., Ahmed, S.T., Mukhtar, M.A. and Wani, G.F., 2023. Heterogeneity in glacier area loss in response to climate change in selected basins of western Himalaya. In: *Climate Change and Environmental Impacts: Past, Present and Future Perspective.* Cham: Springer International Publishing, pp.137-174.

Mir, Z.A. and Kottaiveeran, K., 2018. Impact of climate changes with special reference to walnut production in Jammu and Kashmir. *International Journal of Social Science and Economic Research,* 3(2), pp.608-617.

Moon, I.J., Kim, S.H. and Chan, J.C., 2019. Climate change and tropical cyclone trend. *Nature,* 570(7759), pp.E3-E5.

Morak, S., Hegerl, G.C. and Christidis, N., 2013. Detectable changes in the frequency of temperature extremes. *Journal of Climate,* 26(5), pp.1561-1574.

Negi, H.S., Kumar, A., Kanda, N., Thakur, N.K. and Singh, K.K., 2021. Status of glaciers and climate change of East Karakoram in early twenty-first century. *Science of the Total Environment,* 753, p.141914.

Negi, V.S., Tiwari, D.C., Singh, L., Thakur, S. and Bhatt, I.D., 2022. Review and synthesis of climate change studies in the Himalayan region. *Environment, Development and Sustainability,* 24(9), pp.10471-10502.

Panwar, S., 2020. Vulnerability of Himalayan springs to climate change and anthropogenic impact: a review. *Journal of Mountain Science,* 17(1), pp.117-132.

Prakash, C. and Nagarajan, R., 2018. Glacial lake changes and outburst flood hazard in Chandra basin, North-Western Indian Himalaya. *Geomatics, Natural Hazards and Risk,* 9(1), pp.337-355.

Ramya, A., Poornima, R., Karthikeyan, G., Priyatharshini, S., Thanuja, K.G. and Dhevagi, P., 2023. Climate-Induced and Geophysical Disasters and Risk Reduction Management in Mountains Regions. In: *Climate Change Adaptation, Risk Management and Sustainable Practices in the Himalaya.* Cham: Springer International Publishing, pp.361-405.

Rana, A., Moradkhani, H. and Qin, Y., 2017. Understanding the joint behavior of temperature and precipitation for climate change impact studies. *Theoretical and Applied Climatology,* 129, pp.321-339.

Rashid, I., Majeed, U., Aneaus, S., Cánovas, J.A.B., Stoffel, M., Najar, N.A. and Lotus, S., 2020. Impacts of erratic snowfall on apple orchards in Kashmir Valley, India. *Sustainability,* 12(21), p.9206.

Rasool, R., Fayaz, A., ul Shafiq, M., Singh, H. and Ahmed, P., 2021. Land use land cover change in Kashmir Himalaya: Linking remote sensing with an indicator based DPSIR approach. *Ecological Indicators,* 125, p.107447.

Rautela, P. and Karki, B., 2015. Impact of climate change on life and livelihood of indigenous people of higher Himalaya in Uttarakhand, India. *American Journal of Environmental Protection,* 3(4), pp.112-124.

Romshoo, S.A., Bashir, J. and Rashid, I., 2020. Twenty-first century-end climate scenario of Jammu and Kashmir Himalaya, India, using ensemble climate models. *Climatic Change,* 162(3), pp.1473-1491.

Romshoo, S.A., Fayaz, M., Meraj, G. and Bahuguna, I.M., 2020. Satellite-observed glacier recession in the Kashmir Himalaya, India, from 1980 to 2018. *Environmental Monitoring and Assessment,* 192, pp.1-17.

Roy, A. and Rathore, P., 2019. Western Himalayan forests in climate change scenario. *Remote Sensing of Northwest Himalayan Ecosystems,* pp.265-283.

Sahai, A.K., 1998. Climate change: A case study over India. *Theoretical and Applied Climatology,* 61, pp.9-18.

Schickhoff, U., Bobrowski, M., Böhner, J., Bürzle, B., Chaudhary, R.P., Gerlitz, L. and Schwab, N., 2016. Climate change and treeline dynamics in the Himalaya. In: *Climate Change, Glacier Response, and Vegetation Dynamics in the Himalaya: Contributions Toward Future Earth Initiatives,* pp.271-306.

Shafiq, M.U., Rasool, R., Ahmed, P. and Dimri, A.P., 2019. Temperature and precipitation trends in Kashmir Valley, north western Himalayas. *Theoretical and Applied Climatology,* 135, pp.293-304.

Shah, B., Alam, A., Bhat, M.S., Ahsan, S., Ali, N. and Sheikh, H.A., 2023. Extreme precipitation events and landslide activity in the Kashmir Himalaya. *Bulletin of Engineering Geology and the Environment,* 82(8), p.328.

Sharma, A. and Choudhury, M., 2021. Changing climate and depleting water resources in the mountains with a case study from the Himalayas. In: *Water Conservation in the Era of Global Climate Change.* Elsevier, pp.411-436.

Shrestha, U.B., Gautam, S. and Bawa, K.S., 2012. Widespread climate change in the Himalayas and associated changes in local ecosystems. *PloS One,* 7(5), p.e36741.

Shrestha, U.B., Shrestha, A.M., Aryal, S., Shrestha, S., Gautam, M.S. and Ojha, H., 2019. Climate change in Nepal: a comprehensive analysis of instrumental data and people's perceptions. *Climatic Change,* 154, pp.315-334.

Singh, N. and Sontakke, N.A., 2002. On climatic fluctuations and environmental changes of the Indo-Gangetic plains, India. *Climatic Change,* 52, pp.287-313.

Soora, N.K., Aggarwal, P.K., Saxena, R., Rani, S., Jain, S. and Chauhan, N., 2013. An assessment of regional vulnerability of rice to climate change in India. *Climatic Change,* 118, pp.683-699.

Srivastava, P., 2001. Paleoclimatic implications of pedogenic carbonates in Holocene soils of the Gangetic Plains, India. *Palaeogeography, Palaeoclimatology, Palaeoecology,* 172(3-4), pp.207-222.

Srivastava, R.K. and Srivastava, R.K., 2020. Urbanization-led neo risks and vulnerabilities: a new challenge. In: *Managing Urbanization, Climate Change and Disasters in South Asia,* pp.251-296.

Tang, K.H.D., 2020. Implications of climate change on marine biodiversity. *Global Journal of Agriculture and Soil Science,* 1(1), pp.1-6.

Vedwan, N. and Rhoades, R.E., 2001. Climate change in the Western Himalayas of India: a study of local perception and response. *Climate Research,* 19(2), pp.109-117.

Walsh, K.J., McBride, J.L., Klotzbach, P.J., Balachandran, S., Camargo, S.J., Holland, G. and Sugi, M., 2016. Tropical cyclones and climate change. *Wiley Interdisciplinary Reviews: Climate Change,* 7(1), pp.65-89.

Wang, W., Huang, X., Deng, J., Xie, H. and Liang, T., 2014. Spatio-temporal change of snow cover and its response to climate over the Tibetan Plateau based on an improved daily cloud-free snow cover product. *Remote Sensing,* 7(1), pp.169-194.

Wani, G.F., Ahmed, R., Ahmad, S.T., Singh, A., Walia, A., Ahmed, P. and Mir, R.A., 2022. Local perspectives and motivations of people living in flood-prone areas of Srinagar city, India. *International Journal of Disaster Risk Reduction,* 82, p.103354.

Xu, J., Grumbine, R.E., Shrestha, A., Eriksson, M., Yang, X., Wang, Y.U.N. and Wilkes, A., 2009. The melting Himalayas: cascading effects of climate change on water, biodiversity, and livelihoods. *Conservation Biology,* 23(3), pp.520-530.

Yang, F., He, Q., Huang, J., Mamtimin, A., Yang, X., Huo, W. and Zheng, W., 2020. Desert environment and climate observation network over the Taklimakan Desert. *Bulletin of the American Meteorological Society,* 102(6), pp.E1172-E1191.

Zhang, D.D., Lee, H.F., Wang, C., Li, B., Pei, Q., Zhang, J. and An, Y., 2011. The causality analysis of climate change and large-scale human crisis. *Proceedings of the National Academy of Sciences,* 108(42), pp.17296-17301.

ORCID DETAILS OF THE AUTHORS

Rayees Ahmed: https://orcid.org/0000-0003-3192-7258

Geospatial Assessment of Soil Erosion Using Revised Universal Soil Loss Equation in Hirshabelle State of Somalia

Abdiaziz Hassan Nur[1]† , **Md. Faruq Hasan**[1] , **Susmita Sarmin**[1] , **Atia Shahin**[1] , **Abdinasir Abdullahi Mohamed**[2] **and Ali Hussein Ahmed**[2]

[1]Department of Agricultural Extension, Hajee Mohammed Danesh Science and Technology University, Dinajpur-5200, Bangladesh
[2]Faculty of Agriculture, Zamzam University of Science and Technology, Mogadishu, Somalia
†Corresponding author: Abdiaziz Hassan Nur; gaslseaziz@gmail.com

ABSTRACT

The objective of this study is to provide a thorough assessment of soil erosion in the Hirshabelle state from 2020 to 2023, utilizing the Revised Universal Soil Loss Equation (RUSLE) and advanced geospatial technologies, particularly Google Earth Engine, to guide sustainable land management strategies. The study integrates multiple datasets, including CHIRPS for rainfall measurement, MODIS for land use analysis, and a digital elevation model for slope calculation, to offer a comprehensive understanding of the factors contributing to soil erosion. The rainfall erosivity (R) factor is calculated using CHIRPS data, while the soil erodibility (K-factor) is derived from the soil dataset. The topographic condition (LS-factor) is computed using the digital elevation model, and the cover-management (C) and support practice (P) factors are determined from the NDVI and land use data, respectively. The findings reveal considerable spatial variation in soil erosion across the Hirshabelle state. The results are categorized into five levels based on the severity of soil loss: very low (<5), low (5-10), moderate (10-20), high (20-40), and very high (≥40). While areas classified under "very low" soil loss are dominant, indicating relatively stable soils, regions under "very high" soil loss signal potential land degradation and the need for immediate intervention. Furthermore, the study revealed the intricate interplay of slope, vegetation, and land use in influencing soil erosion. Areas with steeper slopes and less vegetation were more susceptible to soil loss, emphasizing the need for targeted soil conservation measures in these regions. The land use factor played a crucial role, with certain land uses contributing more to soil erosion than others.

INTRODUCTION

Soil erosion in Somalia is one of the most concerning issues, and it affects the environment, society, and economy (Oshunsanya & Nwosu 2017). A lack of vegetation in Somalia triggers another kind of degradation of the land, which was shown through the sources (Omuto et al. 2011). Soil erosion is the dominant cause of land degradation in today's sub-Saharan Africa, affecting agricultural productivity on a large scale (Karamage et al. 2016). Soil erosion is very common and causes significant damage, according to several studies and research conducted in several areas of the world (Bou-imajjane & Belfoul 2020). It has become a serious and sustained crisis in Somalia. Further, the issue has some devastating implications for the natural environment and agriculture (Yan et al. 2022). The loss of vegetation is one of the reasons for the loss of soil in Somalia (Omuto et al. 2011). Thus, the study is meant to understand the extent and impact of soil erosion in Somalia.

The researchers look forward to figuring out the causes and impacts of the same. A suitable approach to achieve the target is to characterize the dynamics of the vegetation cover. Then, the researchers seeded up to get the complete details and the value of the rate of land degradation due to soil erosion in Somalia. Soil erosion in Somalia is driven by the removal of vegetation cover, unsuitable land use practices, and urbanization, significantly exacerbating land degradation across the country (Nur et al. 2024). Such issues are often analyzed through advanced models and remote sensing tools, as demonstrated by the application of RUSLE to measure erosion and sedimentation (Alexiou et al. 2023). In East Africa, the impacts of climate change on soil erosion have been highlighted using convection-permitting climate models, emphasizing the region's vulnerability to increased erosion rates due to shifting rainfall patterns (Chapman et al. 2021). Remote sensing and geographic information systems (GIS) are critical for evaluating soil loss, sediment yield, and watershed prioritization, even in data-poor regions

(Dhaloiya et al. 2021; Patil et al. 2021). High-resolution satellite missions like Sentinel-2 offer valuable data for assessing vegetation and soil conditions, facilitating erosion monitoring and management strategies (Drusch et al. 2012). Additionally, indices like the Normalized Difference Vegetation Index (NDVI) can estimate sediment production and contribute to understanding vegetation's protective role against erosion (Lense et al. 2020).

The integration of these methodologies underscores the importance of modern tools and models in managing erosion, with specific emphasis on adapting practices to mitigate nutrient losses and ensure sustainable land management in vulnerable regions like Somalia (Chen et al. 2017; Yebra et al. 2008).

Erosion of soil is a vital environmental issue that affects multiple sites across the world (Bou-imajjane & Belfoul 2020). Soil erosion means the removal of soil in excessive quantity by various agents of erosion. Soil degradation can assume the following forms: water erosion, wind erosion, mass motion, salt excess, physical degradation, biological degradation, and chemical degradation (Abidin et al. 2021). Soil erosion can lead to a decrease in the health and productivity of agricultural lands. It is also considered to be a major threat to the natural environment (Ailincăi et al. 2011). When soil erosion is not wisely controlled and prevented, It results in significant damage to agriculture and ecosystems. The decline in soil fertility is attributed to soil erosion. Erosion causes a decline in productivity as erosion leads to physical, chemical, and biological degradation (Gaonkar et al. 2024). Soil erosion acts as the causative factor and the outcomes of land degradation (Afriyie et al. 2020). It is important to remember that soil erosion can happen in plenty of different ways. Splash erosion, sheet erosion, rill erosion, and gully erosion all take part in soil erosion (Vrieling et al. 2005). These processes are mostly caused by deforestation, urbanization, and the intensification of agriculture. Also, the worthiest land degradation problem in the whole world is water-induced soil erosion (Vrieling et al. 2005). This is a severe concern that needs watershed management interventions to avoid further stint and protect ecosystem health (Tegegne et al. 2022).

As stated in various study findings, soil erosion directly impacts its fertility. Erosion in agriculture production, infrastructure, and water quality has various negative ecological effects. The outcome of the process of water erosion causes a severe reduction in the fertility of the soil by physical, chemical, and biological degradation (Ailincăi et al. 2011). To produce valuable insights and improve our understanding of the critical factors that govern erosion and sediment transport to different places, either stronger or weaker than ever

(Tegegne et al. 2022). Soil erosion is a major environmental issue with crop-specific afflicts and land degradation (Ailincăi et al. 2011). Concentrating on suitable land management practices and constant monitoring of susceptible areas is important to prevent and control erosion (Puente et al. 2019). Implementing appropriate management strategies is critical, with severe soil erosion and its outcomes. To make this happen, efforts to preserve the soil must be undertaken once the severity of the issue is well comprehended (Tamene et al. 2006). Wischmeier & Smith's (1978) Universal Soil Loss Equation (USLE) was developed back in 1978 (Wischmeier & Smith 1978). It is one empirical model of soil erosion. It is used by most technicians to predict soil loss due to water erosion (Vezina et al. 2006, Trinh 2015, Nguyen 2011, Mc Cool et al. 1987). Remote sensing and GIS simulation are utilized to estimate and map the annual water erosion rate spatial pattern utilizing the Revised Universal Soil Loss Equation (RUSLE) (Renard et al. 1997). Earlier research into soil erosion forces had primarily focused on empirical models, physical properties-based models, nuclear tracing, and then spatial distributed multivariate models (Wang et al. 2016). The RUSLE model is a very easy-to-understand formula, needs only a few parameters, and is very accurate compared to other models (Wang & Zhao 2020). As viewed from the literature, this model is widely used and provides excellent results in predicting soil erosion (Stathopoulos et al. 2017, Rocha & Sparovek 2021, Wang & Zhao 2020). Previous studies have shown the application and widespread use to estimate cropland soil erosion at the watershed, regional, and global scales (Cui et al. 2022). It can also find the clear-cut cost and feasibility of controlling soil erosion (Orchard 2021). The accuracy with which the RUSLE model could predict the rate and spatial distribution of soil erosion using remote sensing data had been estimated in a study in China (Hua et al. 2019). Making the remote sensing data included in the RUSLE model to determine the rate of erosion of soil is user-friendly for studying the spatial distribution of erosion of soil (Orchard 2021). The above-mentioned studies, including the GIS and remote sensing techniques, have provided elaborate data about the surface and thereby had higher accuracy along with the spatial resolution for the estimation of soil erosion. These are the studies that state that GIS and remote sensing give an upper hand in getting a detailed estimation of soil erosion in a specific land area (Chala 2019). By integrating the RUSLE model with Remote sensing and GIS mapping, researchers developed a way to estimate soil loss and plan appropriate soil conservation strategies. Thus, keeping in mind the aforementioned discussion, this study aims to measure the amount of soil loss from the Hirshabelle area using the RUSLE model with the integration of GIS and remote sensing techniques.

MATERIALS AND METHODS

Study Area

Hirshabelle, officially known as Hirshabelle State of Somalia (Latitude: 3.8793° N, Longitude: 45.9040° E), is a Federal Member State in south-central Somalia (Fig. 1). It has a border with the Galmudug State in the north, the Southwest State of Somalia and Banadir region to the south, Ethiopia to the west, and the Indian Ocean to the east (Wikipedia 2018). The state is encompassed by two regions: Hiraan and Middle Shebelle (European Union Agency for Asylum 2011). Furthermore, the region confronts adverse environmental challenges, including flash flooding and short-lived, seasonal flooding. The most likely flash flood areas are Beledweyne, Jalalaqsi, Bulo Burde, Mahaday, and Jowhar. These floods are intense but brief and occur seasonally (United Nations Environment Programme 2022).

RUSLE Model

Using a combination of remote sensing and GIS, the RUSLE model was utilized to map and identify soil erosion risk regions in Hirshabelle and calculate the mean annual soil loss rate (t/ha/year) on a cell-by-cell basis. The following was constructed and discussed after raster maps of each RUSLE parameter obtained from several data sources. This model works on all continents where soil erosion due to water erosion is an issue (Laflen et al. 2003). The model can be expressed as:

$$A = R \times K \times LS \times C \times P$$

Where, A=average soil loss per unit of area (t/ha/year); R=rainfall erosivity factor (MJ mm ha^{-1} h^{-1} y^{-1}); K=is the soil erodibility factor (t h MJ^{-1} mm^{-1}); LS=topographic factor (dimensionless) including slope length (L) and steepness (S) factors; C=cover management (dimensionless); and P=support (or conservation) practice factor (dimensionless). The schematic representation of the RUSLE model is presented in Fig. 2.

Rainfall Erosivity (R-factor)

The Rainfall Erosivity (R-factor) is a key parameter in the RUSLE (Revised Universal Soil Loss Equation) model, representing the impact of rainfall intensity on soil erosion (Wagari & Tamiru 2021). It is calculated by multiplying the total kinetic energy of a rainfall event by its maximum 30-minute intensity. This factor serves as an index for assessing the potential erosive power of rainfall, enabling predictions of soil erosion risks (Mikhailova et al. 1997). Accurate computation of the R-factor helps to estimate and manage soil erosion in areas where there is a lack of time-series precipitation data. In such cases, monthly satellite precipitation data can be used to determine average annual erosivity (Pandey & Gautam 2015). Thus, estimating precipitation erosivity is crucial in data-scarce regions and can be achieved using various methods, leveraging precipitation erosivity data and satellite-based precipitation.
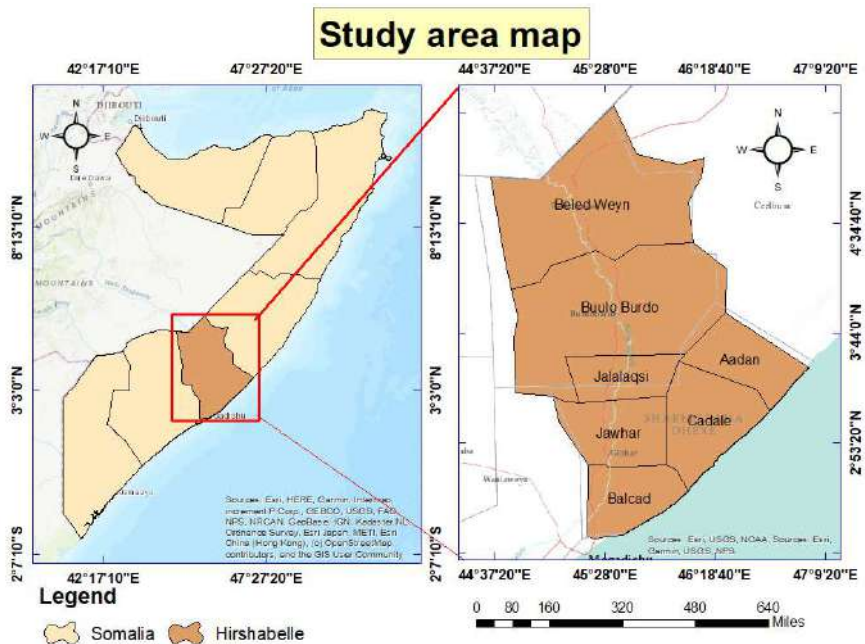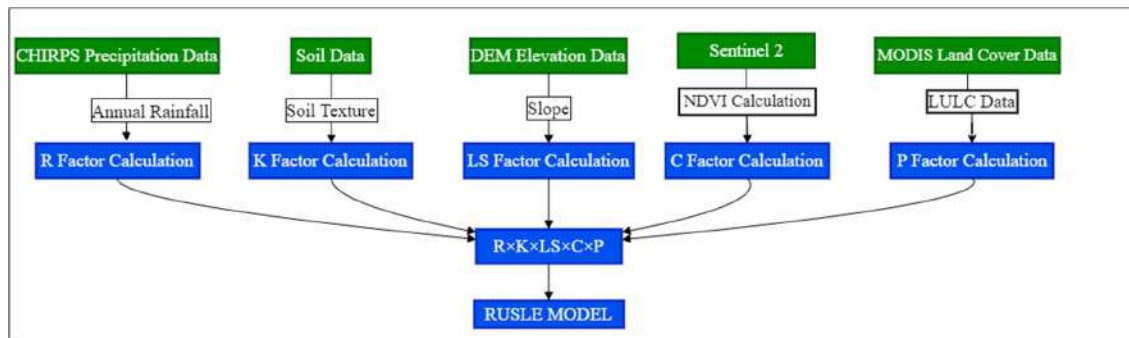

Fig. 1: Map of the study area.

Fig. 2: Flow diagram of the methodology.

Soil Erodibility (K-factor)

The K-factor is critical in calculating sediment detachment and distribution on a region's surface (Veith et al. 2017). It represents the resistance of soil to erosion when impacted by raindrop impact and concentrated flow, as defined by the RUSLE model (Bayramin et al. 2007). This factor reflects soil erodibility and helps quantify how changes in ecosystems or land management practices can reduce erosion susceptibility. In the RUSLE model, the K-factor estimates soil erosion potential based on various soil parameters, including soil texture, organic matter, and water content. Several modified algorithms exist to calculate the soil erodibility factor for different soils at specific sites (Rodrigo-Comino et al. 2020).

Slope Length and Steepness Factors (LS)

Slope length and steepness are the main topographical factors affecting soil erosion. According to Ozsoy & Aksoy (2015), erosion rates-whether water or soil erosion-are directly dependent on flow velocity. Erosion occurs at a higher rate on longer slopes (Dudiak et al. 2019). Steeper slopes gain less energy from water flowing down, leading to more significant soil displacement. In the RUSLE model, the LS factor is a dimensionless parameter that identifies variations in soil erosion intensity proportional to slope length and steepness. This factor effectively predicts and controls erosion threats by considering the slope's impact (Gashaw et al. 2017). Studies, for example, Prasannakumar et al. (2012), highlight the importance of the LS factor in understanding soil erosion risk based on slope characteristics.

Land Cover Management Factor (C-factor)

The C-factor in the RUSLE model is an important parameter that measures soil loss based on land cover, crops, and treatment practices (Gashaw et al. 2017). It is a dimensionless quantity indicating the reduction in soil loss per unit area due to specific land use practices. Monitoring or estimating soil loss due to plant cover and residual matter and evaluating efficiency levels in relation to farmland management are necessary for determining potential mitigation methods and durations (Saha 2018, Zhao et al. 2012). Different types of vegetation, structural canopies, and management strategies significantly influence soil loss and erosion rates, as defined by the C-factor.

Support Practice Factor (P-factor)

The P-factor in the RUSLE model represents the effectiveness of soil conservation practices in reducing erosion. It is calculated by dividing soil loss from a particular support practice by the soil loss from up-and-down slope cultivation (Renard et al. 1997).

Data for Estimation of Soil Erosion by RUSLE Model

Rainfall and Runoff Erosivity factor (R-factor), Soil Erodibility factor (K-factor), Topographic factor (LS-factor), Crop management factor (C-factor), and Support practice factor (P-factor) were the factors for the estimation of soil erosion by RUSLE model. The R-factor was calculated using the total precipitation data derived from CHIRPS for the particular study period. The output finally obtained was first widely multiplied by 0.363, and then 79 was added to convert the total rainfall amount given into an erosive factor. Similarly, the K-factor was calculated from the regional soil dataset. The LS factor was calculated using the DEM data. The slope percent was calculated, and the LS factor was then calculated. The C-factor was calculated using the NDVI (Normalized Difference Vegetation Index) derived from the Sentinel-2 data. Lastly, the P-factor was estimated using the MODIS land-use and land-cover dataset, and the slope percent was calculated.

RESULTS

Rainfall Erosivity (R-factor)

The CHIRPS (Climate Hazards Group InfraRed Precipitation

with Station) dataset was used for the measurement of the R-factor. The CHIRPS dataset was filtered for the 'precipitation' band for the particular period of 2020 to 2023. The next step was clipping the data to the boundaries of the Hirshabelle state. The R-factor will ascertain the erosive force of rain and is calculated as follows:

$$R = \text{Precipitation} \times 79 + 0.363$$

This R-factor has been applied to the RUSLE model mentioned by Panagos et al. (2017). The R-factor map of Hirshabelle state is depicted in Fig. 3. For the state the R-factor ranged from 181.535 to 484.344. Hence, these values showed the potential rate of soil loss to rainfall-driven erosion in the Hirshabelle state. The higher the R-factor value, the higher the susceptibility of the area to soil erosion by rainfall.

Soil Erodibility (K-factor)

The K-factor aims to determine the susceptibility of the soil particles to detachment and transport by the action of rainfall and runoff. Several soil values to assess the K-Factor were considered. The special formula and the values used seem to be region-specific, and these values seem to be based on the local soil properties. The values of the K-factor were determined by Wischmeier's procedure (1976). The estimated K factor value ranged from 0 to 0.05. We obtained specific values of 0, 0.02, 0.034, 0.042 and 0.05. These values of the K-factor provide a measure of how susceptible the soil is to erosion, and the higher the value, the more erodible the soil; in other words, higher K-values indicate places where the soil is more susceptible to erosion. Therefore, these areas are anticipated to require soil conservation procedures to stop considerable loss of soil from erosion. In contrast, for areas of lower K-values, less erosion control methods can be used. The K-factor map of the Hirshabelle state is given in Fig. 4.

Slope Length and Steepness Factors (LS-factor)

The slope was calculated from the "elevation" attribute of the digital elevation model (DEM). Then, the slope was converted from degrees to percent using the following formula:

Slope (%) = tan (slope in degrees) × 100.

Then, the LS factor was calculated using the following formula (Desmet & Govers 1996):

$$LS = (\text{Slope } 0.53 + \text{Slope}^2\ 0.076 + 0.76) \times \sqrt{(500/100)}$$

This equation is used to find the potential soil erosion with the combined impact of slope steepness and the influence of slope length. In the LS equation, (Slope × 0.53 + Slope^2 × 0.076 + 0.76) refers to the effect of slope on erosion, including both linear and quadratic effects of slope, whereas
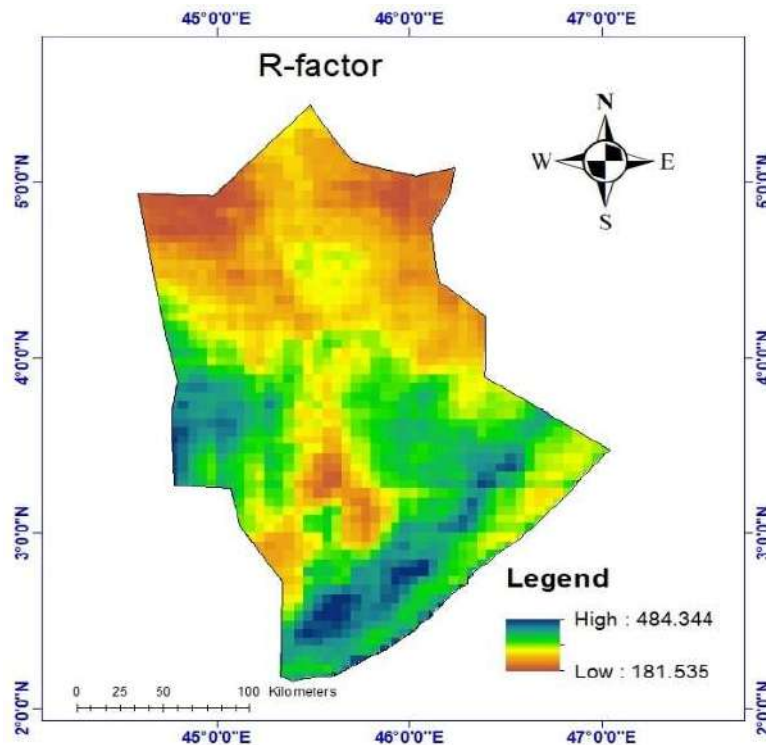
Fig. 3: Rainfall erosivity (R-factor) map of Hirshabelle state.
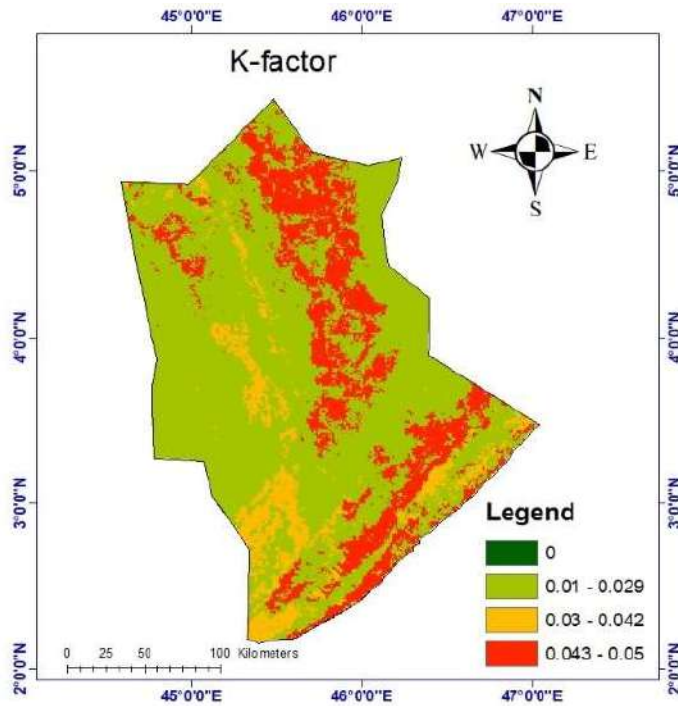
Fig. 4: Soil erodibility (K-factor) map of Hirshabelle state.

$\sqrt{(500/100)}$ represents the interference of the slope length. The square root in this function also represents a nonlinear relationship. Fig. 5 shows the steepness of the landscape slopes of the different parts of the study area, which varies from 0 (flat area) to 9.4642 (extremely steep area).

The LS factor map suggests that soil is likely to erode due to both steepness and slope length. The values of the LS factor ranged from 1.69941 (low erosion potential) to 28.1295 (high erosion potential). The map of the LS factor of Hirshabelle state is given in Fig. 6.
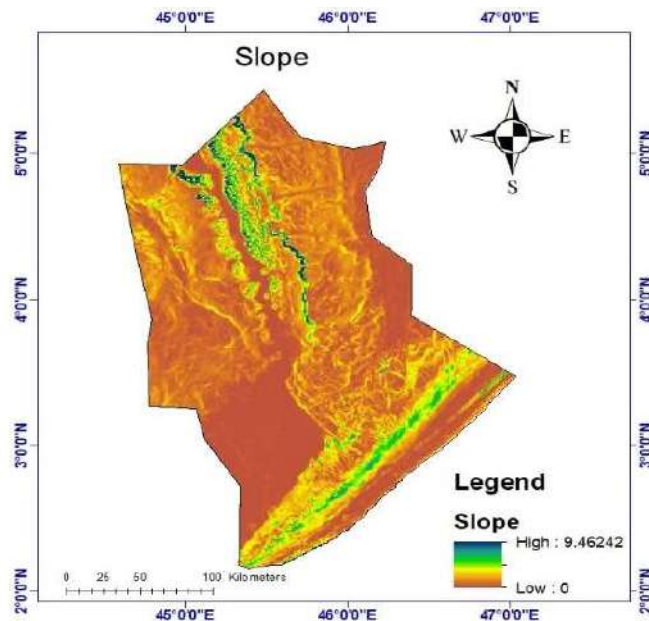
Fig. 5: Slope map of Hirshabelle state.

Normalized Difference Vegetation Index (NDVI)

The current study focuses on the Normalized Difference Vegetation Index (NDVI) and the C-factor in erosion smoothing facts. These two indispensable metrics are analyzed for the environmental and agricultural study. The Normalized Difference Vegetation Index (NDVI) is the most important vegetation index that is capable of assisting the studying scientists in estimating the vegetation health, biomass, and canopy of the land site (Li et al. 2020). It is also a straightforward graphical indicator of the measurement that consists of the metrics from the distant remote sensors. This index can provide the measurement of whether the categories that are considered for studies have resulted in any live green that is essential (Pahlevan et al. 2022). The calculation of NDVI is computed utilizing the following formula (Sarmin et al. 2023):

$$NDVI = (NIR - RED) / (NIR + RED)$$

The NDVI or Normalized Difference Vegetation Index is calculated using Band 8 (NIR) and Band 4 (RED) of the Sentinel-2 satellite (Sarmin et al. 2023). The ratio of these bands is the formula to get the NDVI and helps in understanding the health and coverage of vegetation (Reiche et al. 2018). Through the understanding of environmental landscapes provided by NDVI, soil conservation, and sustainable agriculture can be planned more accurately (Zhang et al. 2016). Hence, two crucial tools in environmental and agricultural studies are NDVI and the C-factor. The

outcome of the NDVI image after the clipping for Hirshabelle state was used to find the median value, and the values of NDVI ranged from -0.2 to 0.3. The negative value of NDVI corresponds to water, i.e., values closer to -1. Whereas close to zero (i.e., (-0.1 to 0.1)) relates to barren or open areas of rock, sand, or snow, and the higher value of NDVI (0.3 to 0.8) has temperate or tropical rainforests or areas with dense vegetation growth. The map of NDVI of Hirshabelle state is given in Fig. 7.

Vegetation Cover Management (C-factor)

C-factor represents the effect of cropping and management practices on erosion rates. The code is to calculate the C factor using NDVI derived from Sentinel-2 data. The presence of green vegetation is represented by the NDVI, as derived from the Sentinel-2 data. The specific formula seems to be derived from the transformation of the NDVI values, which is a commonly applied technique of the remote sensing study based on the C-factor Model. Fig. 8 represents the C-factor map of the study area. The values of the C-factor ranged from 0 to 1. The C-factor is the ratio between the erosion magnitude of a certain area with specific vegetation cover and crop management to the erosion magnitude of identical soil without vegetation. Hence, the understanding of NDVI and C-factor analysis can give more insight into the health of vegetation and the risk of soil erosion. The NDVI value shows substantial vegetation cover, and the C-factor model suggests that the erosion rate is significant because of this vegetation.
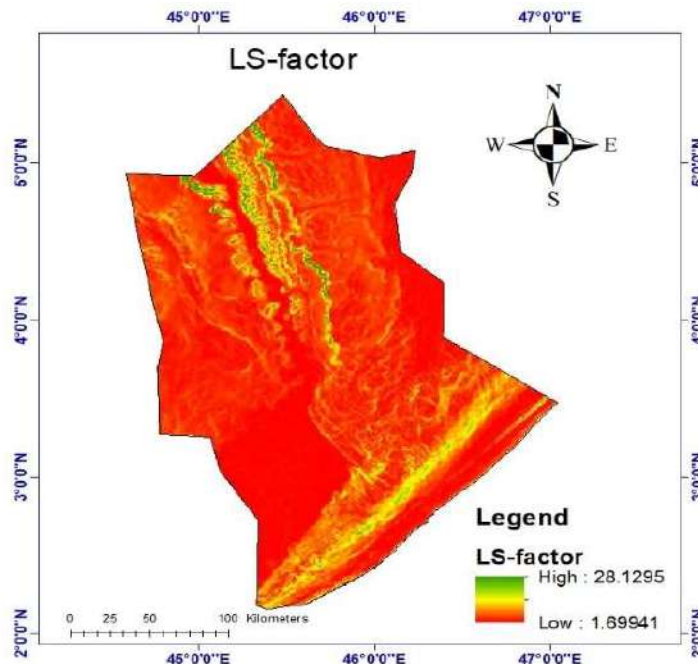
Fig. 6: LS factor map of Hirshabelle state.
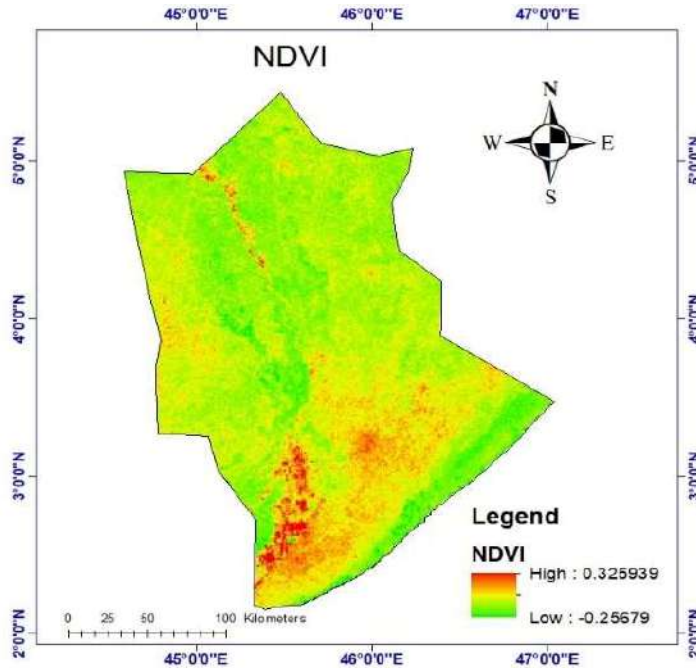
Fig. 7: NDVI map of Hirshabelle state.

Support Practice (P-factor)

The major goal of the P-factor is to account for the effect of erosion-control practices on soil loss. Based on the type of land cover from MODIS data, the slope determines the P-factor. The specific rules that are followed are expected to be region-specific and may be based on local land management practices (Dabney et al. 2012). The P-factor is the ratio of soil loss for a specific support practice to soil loss for up-and-down slope cultivation on the same type of land cover. It quantifies
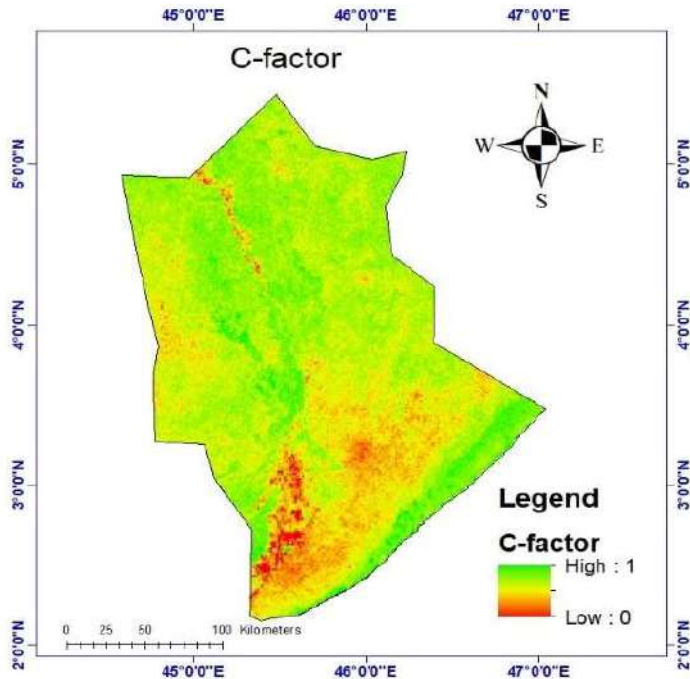
Fig. 8: C-factor map of Hirshabelle state.

the effectiveness of the various conservation practices like contour plowing or terracing. The P-factor analysis of the study area provides valuable information about the effectiveness of soil conservation practices in the area. The P-factor values of the study area (Fig. 9) range from 0.6 to 1. The lower P-factor values nearer to 0.5 indicate that the conservation practices are highly effective in preventing soil erosion. While higher P-factor values, approximately up to 1, indicate less effective practices in place or no erosion control measures are in place in the area.

Soil Loss

Soil loss was estimated using the Revised Universal Soil Loss Equation (RUSLE). The final soil loss was calculated by multiplying R, K, LS, C, and P factors. The mean values of the factors of the RUSLE model are presented in Table 1.

The soil loss analysis offers a comprehensive view of areas at risk of erosion within the defined area. The soil loss map illustrates the varying degrees of soil loss, with areas falling into one of five categories: "very low," "low," "moderate," "high," and "very high," following Housseyn et al. (2021). The distribution of areas according to soil loss classes is presented in Table 2 and depicted in Fig. 10.

DISCUSSION

The estimation of the R-factor, starting from 181.535 to a high of 484.344 (Fig. 3), suggests the variability of the potentiality of soil loss because of rainfall-triggered erosion. The better R-factor values point in the direction of areas that are greater at risk of soil erosion due to rainfall, suggesting the need for focused interventions in those regions to mitigate erosion (Fenta et al. 2020). Similarly, the computed K-factor values, starting from 0 to 0.05 (Fig. 4), offer insights into the soil's susceptibility to erosion. The higher K-values endorse areas with extra erodible soils, indicating the need for particular soil conservation measures to save excessive soil loss (Angima et al. 2003). Conversely, regions with lower K-values, signifying less erodible soils, may additionally require less extensive conservation practices. The LS-factor map (Fig. 5 and Fig. 6) highlights the capacity for soil erosion because of the combined impact of slope period and steepness. This issue is of unique importance, as regions with a high LS factor represent regions with a higher chance of soil erosion, underlining the need for tailored erosion management techniques in such regions

Table 1: Mean Values of the RUSLE Model.

Parameters	Mean Values
Mean R Factor	338.3558311
Mean K Factor	0.032564672
Mean LS Factor	2.456259309
Mean C Factor	0.370976513
Mean P Factor	0.801867416
Mean Soil Loss	8.202920923
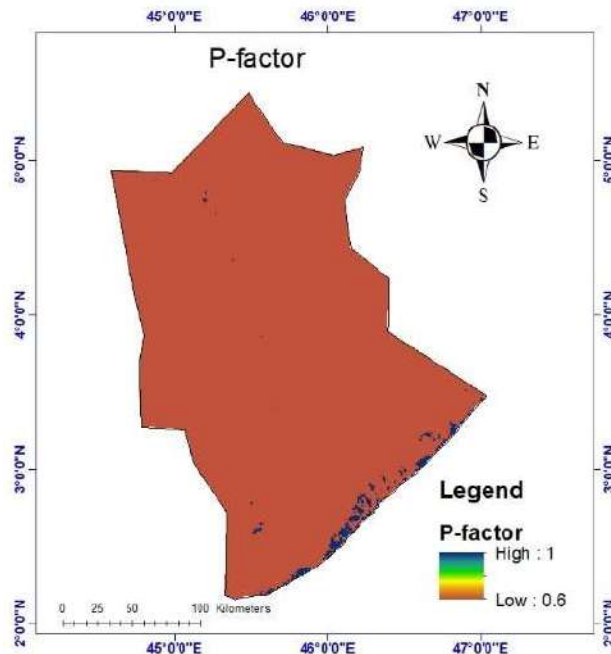
Fig. 9: P-factor map of Hirshabelle state.

Table 2: Distribution of soil loss classes along with their respective areas.

Categories	Area in hectare	Proportion of the total area (%)
Very low (Soil loss < 5)	1,005,247.882	19.11%
Low (Soil loss 5-10)	3,001,216.756	57.04%
Moderate (Soil loss 10-20)	1,089,858.46	20.71%
High (Soil loss 20-40)	150,108.38	2.85%
Very high (Soil loss $\geq$ 40)	14,884.63	0.28%

(Moses 2017). The NDVI evaluation (Fig. 7) and derived C-factor (Fig. 8) provide valuable insights into the country of plant life and its position in soil erosion in the high NDVI and C-factor derived from NDVI, presenting massive protection in opposition to soil erosion (Kogo et al. 2020). The P-factor values, ranging from 0.6 to 1 (Fig. 9), offer an indication of the efficacy of conservation practices within the vicinity. Lower P-factor values advocate that modern conservation practices are powerful at stopping soil erosion, while better values represent areas in which more efficient erosion management measures may also need to be carried out (Amsalu & Mengaw 2014). The final soil loss estimation derived from the product of R, K, LS, C, and P factors offers a comprehensive representation of the areas at risk of erosion within the Hirshabelle state (Fig. 10). The categorization of soil loss into "very low," "low," "moderate," "high," and "very high" provides a clear understanding of the severity of soil erosion in different areas (Yesuph et al. 2021). The study assessed soil erosion risks in northwest Somalia,

revealing that most of the area faces moderate erosion risk. The northern region, including Bossaso and other weather stations, demonstrates low erosivity risk due to lower annual precipitation. In contrast, southern regions, despite their steep slopes, experience higher erosion risk. These findings highlight the critical influence of precipitation and topography on soil erosion in the Hirshabelle state (Nur et al. 2024).

CONCLUSIONS

An extensive study on soil erosion in the Hirshabelle state offers vital insights into the various reasons that trigger soil loss. The primary factors that stimulate soil loss in a region are, namely, erosivity of rainfall, erodibility of soil, length, and steepness of slopes, the cover of vegetation, and support practices. Soil loss risk for the Hirshabelle area is estimated using a Revised Universal Soil Loss Equation (RUSLE). CHIRPS, MODIS, Sentinel-2, and a local soil dataset are used to predict soil loss risk and erosion for the area. Results from the NDVI and C-factor study show the importance of the presence of vegetation in the prevention of soil erosion. The study also brings out the significance of increasing and keeping vegetation safe to protect soil. The P-factor study shows that the soil conservation practices carried out in the area are quite efficient. This study also helps improve these practices further. The satellite data combined with the soil runoff models indicate that it offers a valuable and solid foundation for policymakers to make crucial choices about
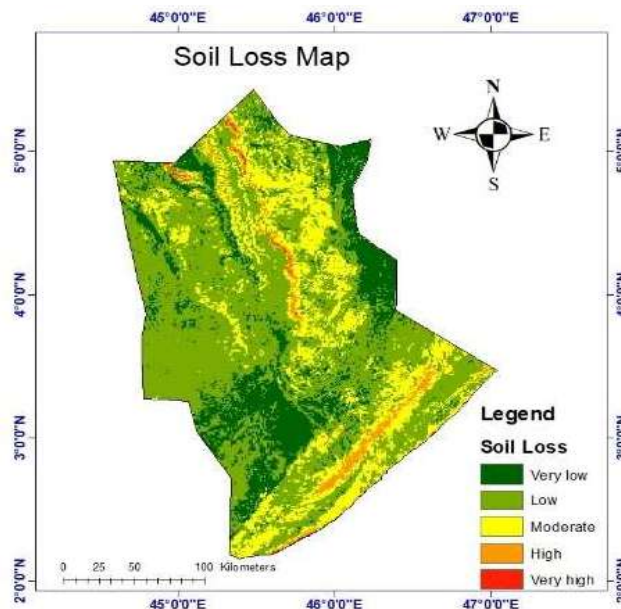
Fig. 10: Soil loss map of Hirshabelle state.

land. The changes associated with soil loss/readiness help to understand and study the areas that are prone to erosion. Since soil is the most important resource and supporting factor, conservation practices will keep the land productive and healthy. Thus, taking measures to prevent soil loss will encourage sustainable land use.

REFERENCES

Abidin, R.Z., Mahamud, M.A., Yusof, M.F., Zakaria, N.A. and Arumugam, M.A.R.M.A., 2021. Determination of cover management and soil loss risk mapping by sub-districts and river catchments of Cameron Highlands Malaysia. *Land,* 10(11), pp.1181. DOI: https://doi.org/10.3390/land10111181

Afriyie, E., Verdoodt, A. and Mouazen, A.M., 2020. Estimation of aggregate stability of some soils in the loam belt of Belgium using mid-infrared spectroscopy. *Science of The Total Environment*, 744, pp.140727. DOI: https://doi.org/10.1016/j.scitotenv.2020.140727

Ailincăi, C., Jitareanu, G., Bucur, D. and Mercuş, A., 2011. Evolution of some chemical properties of soil under influence of soil erosion and different cropping systems. *Cercetari Agronomic in Moldova,* 44(4). DOI: 10.2478/v10298-012-0044-3

Alexiou, S., Efthimiou, N., Karamesouti, M., Papanikolaou, I., Psomiadis, E. and Charizopoulos, N., 2023. Measuring annual sedimentation through high accuracy UAV-Photogrammetry data and comparison with RUSLE and PESERA Erosion Models. *Remote Sensing,* 15(5), pp.1339. DOI: https://doi.org/10.3390/rs15051339

Amsalu, T. and Mengaw, A., 2014. GIS based soil loss estimation using RUSLE model: The case of Jabi Tehinan Woreda, ANRS, Ethiopia. *Natural Resources,* 5(16), pp.616-626.

Angima, SD., Stott, D.E., O'Neill, M.K., Ong, C.K. and Weesies, G.A., 2003. Soil erosion prediction using RUSLE for central Kenyan highland conditions. *Agriculture, Ecosystems & Environment,* 97(1-3), pp.295-308.

Bayramin, İ., Basaran, M., Erpul, G. and Canga, M.R., 2007. Assessing the Effects of Land Use Changes on Soil Sensitivity to Erosion in a Highland Ecosystem of Semi-Arid Turkey. https://scite.ai/reports/10.1007/s10661-007-9864-2

Bou-imajjane, L. and Belfoul, M.A., 2020. Soil loss assessment in Western High Atlas of Morocco: Beni mohand watershed study case. *Applied and Environmental Soil Science,* 143, pp.1-15. DOI: https://doi.org/10.1155/2020/6384176

Chala, H.M., 2019. A geographic information system-based soil erosion assessment for conservation planning at West Hararghe, Eastern Ethiopia. *Civil Engineering and Environmental Systems,* 11(2), pp.19. DOI: https://doi.org/10.7176/cer/11-2-02

Chapman, S., Birch, C.E., Galdos, M.V. and Bellerby, T.J., 2021. Assessing the impact of climate change on soil erosion in East Africa using a convection-permitting climate model. *Environmental Research Letters,* 16(9), pp.094036.

Chen, X., Liu, X., Peng, W., Dong, F., Huang, Z. and Wang, R., 2017. Non-Point Source Nitrogen and Phosphorus Assessment and Management Plan with an Improved Method in Data-Poor Regions. *Water,* 10(1), pp.17. DOI: https://doi.org/10.3390/w10010017

Cui, H., Wang, Z., Yan, H., Li, C., Jiang, X., Liu, G., Hu, Y., Yu, S. and Shi, Z., 2022. Production-based and consumption-based accounting of global cropland soil erosion. *Environmental Science & Technology,* 56(14), pp.10465-10473. DOI: https://doi.org/10.1021/acs.est.2c01855

Dabney, S.M., Yoder, D.C., Vieira, D.A. and Bingner, R.L., 2012. Enhancing RUSLE to include runoff-driven phenomena. *Hydrological Processes,* 26(6), pp.910-922.

Desmet, P.J. and Govers, G., 1996. A GIS procedure for automatically calculating the USLE LS factor on topographically complex landscape units. *Journal of Soil and Water Conservation,* 51(5), pp.427-433.

Dhaloiya, A., Nain, A.S., Sharma, M.P. and Singh, A., 2021. Prioritization of watershed using Remote Sensing and Geographic Information System. *Sustainability,* 13(16), pp.9456. DOI: https://doi.org/10.3390/su13169456

Drusch, M., Del Bello, U., Carlier, S., Colin, O., Fernandez, V., Gascon, F., Hoersch, B., Isola, C., Laberinti, P., Martimort, P., Meygret, A., Spoto, F., Sy, O., Marchese, F. and Bargellini, P., 2012. Sentinel-2: ESA's optical high-resolution mission for GMES operational services. *Remote Sensing of Environment,* 120, pp.25–36. DOI: https://doi.org/10.1016/j.rse.2011.11.026

Dudiak, N.V., Pichura, V.I., Potravka, L. and Stratichuk, N.V., 2019. Geomodelling of Destruction of Soils of Ukrainian Steppe Due to Water Erosion. https://scite.ai/reports/10.12911/22998993/110789

European Union Agency for Asylum, 2011. Country of Origin Information Report Somalia: Central and Southern Somalia.

Fenta, A.A., Tsunekawa, A., Haregeweyn, N., Tsubo, M., Yasuda, H., Ebabu, K. and Kawai, T., 2020. Land susceptibility to water and wind erosion risks in the East Africa region. *Science of the Total Environment,* 703, pp.134807.

Gaonkar, V.G., Nadaf, F.M. and Kapale, V., 2024. Mapping and Quantifying Integrated Land Degradation Status of Goa Using Geostatistical Approach and Remote Sensing Data. *Nature Environment & Pollution Technology,* 23(1). DOI: https://doi.org/10.46488/NEPT.2024.v23i01.025

Gashaw, T., Tulu, T. and Argaw, M., 2017. Erosion Risk Assessment for Prioritization of Conservation Measures in Geleda Watershed, Blue Nile Basin, Ethiopia. https://scite.ai/reports/10.1186/s40068-016-0078-x

Housseyn, B., Nekkache, G.A., Kamel, K., Hamza, B. and Saleh-Eddine, T., 2021. Estimation of soil losses using RUSLE model and GIS tools: Case study of the Mellah catchment, Northeast of Algeria. *Romanian Journal of Civil Engineering,* 12 (3), pp.266-289. DOI: https://doi.org/10.37789/rjce.2021.12.3.2

Hua, T., Zhao, W., Liu, Y. and Liu, Y., 2019. Influencing factors and their interactions of water erosion based on yearly and monthly scale analysis: A case study in the Yellow River basin of China. *Natural Hazards and Earth System Sciences Discussions.* DOI: https://doi.org/10.5194/nhess-2019-122

Karamage, F., Zhang, C., Ndayisaba, F., Shao, H., Kayiranga, A., Fang, X., Nahayo, L., Nyesheja, E.M. and Tian, G., 2016. Extent of cropland and related soil erosion risk in Rwanda. *Sustainability,* 8(7), pp.609. DOI: https://doi.org/10.3390/su8070609

Kogo, B.K., Kumar, L. and Koech, R., 2020. Impact of land use/cover changes on soil erosion in western Kenya. *Sustainability,* 12(22), pp.9740.

Laflen, J.M. and Moldenhauer, W.C., 2003. Pioneering soil erosion prediction: The USLE story. *International Soil and Water Conservation Research,* 34(2). DOI: 10.1016/S2095-6339(15)30034-4

Lense, G.H.E., Moreira, R.S., Bócoli, F.A., Avanzi, J.C., Teodoro, A.E.D.M. and Mincato, R.L., 2020. Estimation of sediments produced in a subbasin using the Normalized Difference Vegetation Index. *Ciência e Agrotecnologia,* 44(4). DOI: https://doi.org/10.1590/1413-7054202044031419

Li, Z., Guo, R., Li, M., Chen, Y. and Zhang, Y., 2020. Characterizing spatiotemporal vegetation dynamics in the Greater Mekong Subregion with NDVI and EVI time series. *Journal of Forestry Research,* 31, pp.1347–1362.

Mc Cool, D.K., Brown L.C., Foster G.R., Mutchler C.K. and Meyer, L.D., 1987. Revised slope steepness factor for universal soil loss equation Transactions of American Society of Agricultural Engineers. *Transactions of the ASAE,* 30(5), pp.1387-1396. DOI: https://doi.org/10.13031/2013.30576

Mikhailova, E.A., Bryant, R.B., Schwager, S.J. and Smith, S.D., 1997. Predicting rainfall erosivity in Honduras. *Soil Science Society of American Journal*, 61(1), pp.273-279. DOI: https://doi.org/10.2136/sssaj1997.03615995006100010039x

Moses, A.N., 2017. GIS-RUSLE interphase modelling of soil erosion hazard and estimation of sediment yield for River Nzoia Basin in Kenya. *Journal of Remote Sensing and GIS*, 6(4).

Nguyen, M.H., 2011. Application USLE and GIS Tool to Predict Soil Erosion Potential and Proposal Land Cover Solutions to Reduce Soil Loss in Tay Nguyen.

Nur, A.H., Ahmed, A.H., Mohamed, A.A., Hasan, M.F. and Sarmin, S., 2024. Geospatial assessment of Aridity and Erosivity Indices in Northwest Somalia using the CORINE Model. *Journal of Environmental and Science Education*, 4(1), pp.1-11

Nur, A. H., Mohamed, A. A., and Ahmed, A. H. 2024. Spatial Assessment of Soil Erosion and Aridity in Somalia Using the CORINE Model.

Omuto, C., Balint, Z. and Alim, M., 2011. A framework for national assessment of land degradation in the drylands: A case study of Somalia. *Land Degradation and Development*, 25(2). DOI: https://doi.org/10.1002/ldr.1151

Orchard, P.J., 2021. Enabling Multi-Site Stormwater Environmental Compliance Approvals in Ontario, Canada.

Oshunsanya, S.O. and Nwosu, N.J., 2017. Suitability of universal soil loss erodibility, inter-rill and rill erodibility models for selected tropical soils. *Agricultura Tropica Et Subtropica, 50(4), pp*. 191-198. DOI: https://doi.org/10.1515/ats-2017-0020

Ozsoy, G. and Aksoy, E., 2015. Estimation of soil erosion risk within an important agricultural sub-watershed in Bursa, Turkey, in relation to rapid urbanization. *Environmental Monitoring and Assessment*, 187(6), Article 4653. DOI: https://doi.org/10.1007/s10661-015-4653-9.

Pahlevan, N., Sarkar, S., Franz, B.A., Balasubramanian, S.V. and He, J., 2022. Cross-calibration of S-NPP VIIRS and Sentinel-2A/2B MSI for improved terrestrial monitoring. Remote Sensing, 14(4), pp.681.

Panagos, P., Borrelli, P. and Meusburger, K., 2017. Estimating the RUSLE Equation Rainfall Factor in the Calculations of Global Soil Erosion. Geophysical Research Abstracts, 19.

Pandey, A. and Gautam, A.K., 2015. Soil erosion modeling using satellite rainfall estimates. *Journal of Water Resource and Hydraulic Engineering*, 4(4), pp.318-325. https://doi.org/10.5963/JWRHE0404002

Patil, M., Patel, R. and Saha, A., 2021. Sediment yield and soil loss estimation using GIS based Soil Erosion Model: A case study in the MAN Catchment, Madhya Pradesh, India. *Environmental Sciences Proceedings*, 8(1), pp.26. DOI: https://doi.org/10.3390/ecas2021-10348

Prasannakumar, V., Vijith, H., Abinod, S. and Geetha, N., 2012. Estimation of soil erosion risk within a small mountainous sub-watershed in Kerala, India, using Revised Universal Soil Loss Equation (RUSLE) and geo-information technology. *Geoscience Frontiers*, 3(2), pp.209–215. DOI: https://doi.org/10.1016/j.gsf.2011.11.003

Puente, C., Olague, G., Trabucchi, M., Arjona-Villicaña, P.D. and Soubervielle-Montalvo, C., 2019. Synthesis of Vegetation Indices using genetic programming for soil erosion estimation. *Remote Sensing*, 11(2), pp.156. DOI: https://doi.org/10.3390/rs11020156

Reiche, J., Hamunyela, E., Verbesselt, J., Hoekman, D. and Herold, M., 2018. Improving near-real time deforestation monitoring in tropical dry forests by combining dense Sentinel-1-time series with Landsat and ALOS-2 PALSAR-2. *Remote Sensing of Environment*, 204, pp.147–161.

Renard, K.G., Foster, G.R., Weesies, G.A., McCool, D.K. and Yoder, D.C., 1996. Predicting soil erosion by water: A guide to conservation planning with the Revised Universal Soil Loss Equation (RUSLE). *Environmental Science*. https://api.semanticscholar.org/CorpusID:128575343

Rocha, G.C.D. and Sparovek, G., 2021. Scientific and Technical Knowledge of Sugarcane Cover-Management USLE/RUSLE Factor.

Rodrigo-Comino, J., Senciales-González, J.M. and Ruiz-Sinoga, J.D., 2020.

The effect of hydrology on soil erosion. *Water,* 12(3), pp.839. DOI: https://doi.org/10.3390/w12030839

Saha, A., 2018. GIS Based Soil Erosion Estimation Using Rusle Model: A Case Study of Upper Kangsabati Watershed, West Bengal, India. https://scite.ai/reports/10.19080/ijesnr.2018.13.555871

Sarmin, S., Hasan, M.F., Hanif, M.A., Nur, A.H. and Shahin, A., 2023. *From Pixels to Policies: Remote Sensing for Compliance with Agriculture 4.0*. In: GRISS An Edited Book (Volume-3), Edited by S.P. Singh. Astha Foundation, Meerut, India.

Stathopoulos, N., Lykoudi, E., Vasileiou, E., Rozos, D. and Dimitrakopoulos, D., 2017. Erosion uulnerability assessment of Sperchios river basin, in East Central Greece - A GIS based analysis. *Journal of Geology,* 7(05), 621-6467. DOI: https://doi.org/10.4236/ojg.2017.75043

Tamene, L., S., Park, R., Dikau, and Vlek, P.L.G., 2006. Analysis of factors determining sediment yield variability in the highlands of Ethiopia. *Geomorphology,* 76(1), pp.76-91. DOI: https://doi.org/10.1016/j.geomorph.2005.10.007

Tegegne, M.A., Zewudu, Y. and Fentahun, T., 2022. Erosion Source Area Identification Using Rusle and Multi-Criteria Decision Analysis, Acase of Andassa Watershed, Upper Blue Nile Basin. DOI: https://doi.org/10.21203/rs.3.rs-1718698/v1

Trinh, C.T., 2015. *Soil Erosion in Vietnam (The Case of Buon Yong catchment) Universal Soil Loss Equation (RUSLE)*. Scholars Press.

United Nations Environment Programme. 2022. Flash Floods in Hirshabelle State of Somalia. DOI: https://www.unep.org/news-and-stories/story/flash-floods-hirshabelle-state-somalia

Veith, T.L., Goslee, S.C., Beegle, D.B., Weld, J. and Kleinman, P.J.A., 2017. Analyzing Within-County Hydrogeomorphological Characteristics as a Precursor to Phosphorus Index Modifications. https://scite.ai/reports/10.2134/jeq2016.10.0416

Vezina, K., Bonn F. and Pham V.C., 2006. Agricultural land-use patterns and soil erosion vulnerability of watershed units in Vietnam's northern highlands. *Landscape Ecology,* 21(8), pp.1311-1325. DOI: https://doi.org/10.1007/s10980-006-0023-x

Vrieling, A., Rodrigues, S.C. and Sterk, G., 2005. Evaluating erosion from space : A case study near Uberlândia. Sociedade & natureza, *In Sociedade & Natureza,* Special issue : International Symposium on Land Degradation and Desertification, pp. 683-696.

Wagari, M. and Tamiru, H., 2021. RUSLE model based annual soil Loss Quantification for Soil Erosion Protection: A Case of Fincha Catchment, Ethiopia. https://scite.ai/reports/10.1177/11786221211046234

Wang, H. and Zhao, H., 2020. Dynamic Changes of Soil Erosion in the Taohe River Basin Using the RUSLE Model and Google Earth Engine. *Water,* 12(5), pp.1293. DOI: https://doi.org/10.3390/w12051293

Wang, R., Zhang, S., Yang, J., Pu, L., Yang, C., Yu, L., Chang, L. and Bu, K., 2016. Integrated use of GCM, RS, and GIS for the assessment of hillslope and gully erosion in the Mushi river Sub-Catchment, Northeast China. *Sustainability,* 8, pp.317.

Wikipedia, 2018. Hirshabelle State. https://en.wikipedia.org/wiki/Hirshabelle_State

Wischmeier, W.H. and Smith, D.D., 1978. Predicting rainfall erosion losses: A guide to Conservation Planning World Association of Soil and Water Conservation, Beijing, China, p. 54

Wischmeier, W.H. and Smith, D.D., 1978. *Predicting Rainfall Erosion Losses*. *A Guide to Conservation Planning*. The USDA Agricultural Handbook No. 537, Maryland.

Wischmeier, W.H., 1976. Use and misuse of the universal soil loss equation. *Journal of Soil and Water Conservation,* 31(1), 5-9.

Yan, X., Wu, L., Xie, J., Wang, Y., Wang, C. and Ling, B., 2022. Dynamic Changes and Precision Governance of Soil Erosion in Chengde City Using the GIS Techniques and RUSLE Model. *Nature Environment & Pollution Technology*, 21(3). DOI: https://doi.org/10.46488/NEPT.2022.v21i03.009

Yebra, M., Chuvieco, E. and Riaño, D., 2008. Estimation of live fuel

moisture content from MODIS images for fire risk assessment. *Agricultural and Forest Meteorology,* 148(4), pp.523-536.

Yesuph, Y.S., Endalamaw, N.T., Sinshaw, B.G. and Ayana, E.K., 2021. Modeling soil erosion using RUSLE and GIS at watershed level in the upper Beles, Ethiopia. *Environmental Challenges,* 3, pp.100039.

Zhang, J., Xiao, X., Wu, X. and Zhou, S., 2016. A global moderate resolution dataset of gross primary production of vegetation for 2000–2016. *Scientific Data,* 5, pp.180165.

Zhao, W., Fu, B. and Chen, L.D., 2012. A Comparison Between Soil Loss Evaluation Index and the C-factor of RUSLE: A Case Study in the Loess Plateau of China. https://scite.ai/reports/10.5194/hess-16-2739-2012

Zhou, Q., Yang, S., Zhao, C., Cai, M. and Luo, Y., 2014. A soil erosion assessment of the upper Mekong river in Yunnan Province, China. *Mountain Research and Development,* 34(1), pp.36-47. DOI: https://doi.org/10.1659/MRD-JOURNAL-D-13-00027.1

ORCID DETAILS OF THE AUTHORS

Abdiaziz Hassan Nur: https://orcid.org/0009-0007-5335-7715

Md. Faruq Hasan: https://orcid.org/0000-0002-9303-5848

Susmita Sarmin: https://orcid.org/0000-0002-0094-3880

Atia Shahin: https://orcid.org/0009-0009-7530-6948

Abdinasir Abdullahi Mohamed: https://orcid.org/0000-0001-9183-5369

Ali Hussein Ahmed: https://orcid.org/0009-0003-6176-6042

Understanding the Patch Dynamics of a few Homogenous and Heterogenous Vegetational Patches

Rekha G. Dhammar, Kunal N. Odedra† and B. A. Jadeja

Department of Botany, M. D. Science College, Porbandar, Gujarat, India

†Corresponding author: Kunal N. Odedra; kunal.n.odedra1@gmail.com

ABSTRACT

Variations in size and shape distinguish vegetation patches across different ecosystems. Nonetheless, recent research highlights notable parallels in the dynamics of these patches and the mechanisms governing their formation and persistence. Two primary types, banded and spotted vegetation, characterized by their patch shapes, stem from shared mechanisms, albeit each type is predominantly influenced by a distinct driver. Banded vegetation emerges when water primarily facilitates the redistribution of materials and propagules, whereas spotted vegetation arises when wind serves as the primary redistributing force. Overall, the analysis underscores how patchy vegetation structures bolster primary production. According to Patch Dynamics theory, vegetation can be categorized into homogeneous and heterogeneous patches, with seasonal conditions playing a pivotal role in the coexistence of various vegetation types. Understanding mechanisms of coexistence necessitates a thorough grasp of the ecophysiological responses of dominant species to different patch types. Consequently, this study aimed to discern the ecophysiological reactions of species to two distinct patch categories. Throughout the examination of Patch Dynamics, both patch species exhibited the highest photosynthetic capacity within their respective patches. Parameters such as Leaf Area Index (LAI), the number of individuals (N), biomass, height (h), weight, and others manifested changes across patch types. Notably, species within the banded patch exhibited heightened sensitivity and more substantial fluctuations in their values compared to those in the spotted patch. These differential responses to distinct patches offer insights into potential mechanisms facilitating species coexistence.

INTRODUCTION

In contemporary ecology, recognizing spatial heterogeneity as a core aspect of natural systems is essential. Ecologists and wildlife biologists have primarily focused on broader scale patterns such as elevational gradients and climatic zones (Wiens 1989). Patch dynamics, investigating spatial configurations and processes within landscapes, explores how patches evolve over time (Pickett & White 1985). These patches, differing from adjacent areas, can be found in various ecosystems like forests, where stands of trees form patches (Turner et al. 2001). Understanding patch dynamics is crucial for grasping the interplay among pattern, process, and scale in ecology, forming the basis of landscape ecology, disturbance ecology, and population ecology's spatial components (Forman & Godron 1986). Despite the dynamic nature of patch dynamics, it contributes to the concept of the shifting mosaic steady state (Levin & Paine 1974). Integrating patch dynamics with hierarchy theory addresses disparities across spatial scales, crucial for biodiversity conservation and resource management. Patch dynamics intersects with key ecological concepts like island biogeography theory (MacArthur & Wilson

1967), Metapopulation Theory (Hanski 1999), succession, and disturbance ecology, providing a vital framework for understanding and preserving complex natural systems.

Foundation Work

The history of patch dynamics can be divided into two main phases. Initially, from the 1930s to the late 1970s, researchers explored spatial change and patchiness, particularly in ecosystems like rocky shores and forests. The concept expanded with seminal works like Watt's 1947 paper, hinting at its relevance in various ecosystems (Watt 1947). The 1980s witnessed the maturation of patch dynamics, coinciding with the rise of landscape ecology and spatial ecology. This period saw an expanded application of patch dynamics across diverse ecosystems (Forman 1995). Patch dynamics highlights the importance of diverse habitat patches, shaped by natural disturbances, for maintaining ecological diversity. A patch refers to a discrete area utilized by species for breeding or resources, while mosaics encompass landscape patterns like forest stands or highways. This perspective views ecological systems as mosaics of patches, varying in size, shape,

composition, and history. Patch dynamics originated in the study of vegetation structure and dynamics in the 1940s, later evolving into a predominant theme in ecology from the late 1970s to the 1990s. This framework emphasizes the dynamic interplay between heterogeneity and homogeneity within ecosystems. Patches transition between potential, active, and degraded states, influenced by colonization, abandonment, and recovery processes. Human activities like logging and farming can alter patch shape and composition, impacting nutrient cycling and species migration. Despite spatial separation, patches remain interconnected, sustaining populations and facilitating species spread (Corrado et al. 2014). Understanding patch dynamics is crucial for effective conservation. Conservation efforts involve managing patch dynamics, predicting responses to external forces, and monitoring biodiversity changes. Analysis of patch dynamics aids in predicting biodiversity fluctuations, with alterations in external conditions serving as early indicators of biodiversity collapse (Saravia & Momo 2017). The research aims to identify and monitor patches within a university campus, analyzing vegetation cover spatially and temporally. Utilizing remote sensing and field surveys, the study will assess changes in species numbers and vegetation cover, providing insights into campus ecosystem dynamics for effective conservation and management strategies.

MATERIALS AND METHODS

Study Area

The study is conducted within the campus of The Maharaja Sayajirao University of Baroda, situated in the Sayajigunj ward of Vadodara city of Gujarat (Fig. 1). The campus features a variety of vegetational patches comprising both herbs and trees. Additionally, a small river traverses the campus, hosting diverse patches of trees and annual herbs. These patches are significantly influenced by a multitude of biotic and abiotic factors, which exert considerable impact on their growth and development.

Two types of vegetation patches were identified for the study

1. **Homogeneous patch:** Characterized by uniform structure with minimal variation within the population.

2. **Heterogeneous patch:** Comprising a diverse population where individuals exhibit dissimilar characteristics.

Twenty patches, including 10 homogeneous and 10 heterogeneous, were randomly selected, encompassing various vegetation types such as herbs and trees. Special attention was paid to ensure that the patches chosen for the study were naturally grown. Monthly observations were conducted to analyze the changes occurring in different patches in response to environmental conditions and anthropogenic activities. Field visits were conducted three times during December, January, and February. The minimum patch size considered was 1×1 m^2, while the maximum patch size was 10×10 m^2. Various parameters, including the number of individuals, mean patch area, height, biomass, leaf area index (LAI), diameter at breast height (DBH), and moisture content, were measured for each patch. The detailed methodology for measuring these parameters is elaborated in the following sections. Fig. 2 shows the experimental design of the study.

Number of Patches (NP): The total number of patches for both communities was computed using GIS for the three time periods.
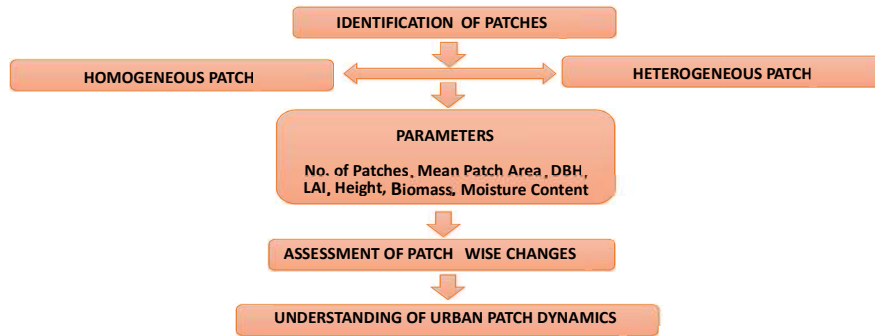

Fig. 1: The study area.

Fig. 2: Flowchart showing the experimental design of the study.

Mean Patch Area (MPA): The area of each patch within a landscape mosaic is a crucial piece of information. It is calculated as the sum of the areas (in square meters) of all patches divided by the number of patches of the same type per unit area.

Biomass: Biomass refers to the total mass of living material measured over a specific area. Since living organisms contain water, biomass is typically calculated as dry mass. To compute the Quadratic Stand Density (QSD), the basal area of the diameter class is divided by the number of trees in the class to determine the basal area of the average tree. The Harvest method is commonly used for measuring biomass: the biomass is harvested, dried in an oven to remove moisture, and then weighed to obtain the dry weight, which provides a more stable measure of biomass compared to fresh weight.

Diameter at Breast Height (DBH): Diameter at Breast Height (DBH) is a standard measure used to express the diameter of a tree trunk or bole. It is one of the most common dendrometry measurements. Electronic calipers are often utilized to measure DBH, with the measured data transmitted online via Bluetooth to a field computer. DBH is typically measured at 1.3 meters above ground level, although previous conventions varied. Some suggest using Dx instead of DBH to denote the exact height above the floor at which the diameter is measured. Instruments such as girthing tapes and calipers are commonly used to measure DBH, with girthing tapes calibrated in divisions of π centimeters. In many countries, the diameter has been measured usually at 1.3 meters above ground (Brack 2009). Previously 4.5 ft (1.37 m) was used. (Paul 2017) The height can make a substantial difference to the measured diameter (Russell & Barbara 1990). Ornamental trees are usually measured at 1.5 meters above ground. However, some authors (Brokaw & Thompson 2000) maintain that the term DBH should be abolished precisely because the heights at which the diameter is measured are so variable and because it may strongly

influence forestry calculations such as biomass. Instead, Dx was proposed whereby the x denotes the exact height above the floor (and along the stem) at which the diameter is measured.

Leaf Area Index (LAI): Leaf Area Index (LAI) is a dimensionless quantity used to characterize plant canopies. It represents the one-sided green leaf area per unit ground surface area (LAI = leaf area/ground area) in broadleaf canopies (Krebs 1999).

RESULTS AND DISCUSSION

The concept of patch dynamics stems from recognizing ecosystems as spatially heterogeneous, containing diverse mixtures of organisms and resources distributed unevenly across time and space. Ecological disturbances like floods, fires, and disease outbreaks drive much of this spatial heterogeneity by disrupting biological communities, creating patches of varying sizes, shapes, compositions, and histories. University campus studies revealed influences of environmental factors on both homogeneous and heterogeneous herb patches, with significant changes observed across all measured parameters. These studies identified 10 homogeneous patches hosting 10 herb species (Table 2, Fig. 3) and 10 heterogeneous patches hosting 55 herb species. (Table 1, Fig. 4) Population size correlated significantly with patch area, indicating that larger patches had a higher probability of supporting sustainable plant populations compared to smaller patches (Jacquemin 2002).

In Homogenous herb patches, high quantities of *Alternanthera ficoidea*, *Acalypha indica*, and *Synedrella nodiflora* were observed (79, 40, and 42 individuals, respectively). The patch occupancy of *Alternanthera ficoidea* and *Acalypha indica* was influenced by habitat and patch characteristics, with moisture content and number of individuals decreasing as patch area decreased, while height and leaf area increased (Honnay et al. 1999). *Sida acuta* occurred in the largest patch (15.2 m), experiencing a rapid

Table 1: Heterogeneous Patches.

Patch No.	Patch species	Family
1.	*Alternanthera ficoidea* (L.) P.Beauv.	Amaranthaceae
	Acalypha indica L.	Euphorbiaceae
	Elephantopus tomentosus L.	Asteraceae
2.	*Sida acuta* Burm.f.	Malvaceae
	Alternanthera ficoidea (L.) P.Beauv.	Amaranthaceae
	Cyanthillium cinereum (L.) H.Rob.	Asteraceae
	Acalypha indica L.	Euphorbiaceae
3.	*Alternanthera ficoidea* (L.) P.Beauv.	Amaranthaceae
	Cyanthillium cinereum (L.) H.Rob.	Asteraceae
	Echinochloa colona (L.) Link	Poaceae
	Tridax procumbens L.	Asteraceae
	Ziziphus mauritiana Lam.	Rhamnaceae
4.	*Sida acuta* Burm.f.	*Malvaceae*
	Alternanthera ficoidea (L.) P.Beauv.	Amaranthaceae
	Achyranthes aspera L.	Amaranthaceae
	Antigonon leptopus Hook. & Arn.	Polygonaceae
	Zinnia elegans Jacq.	Asteraceae
	Trifolium repens L.	Fabaceae
	Tephrosia purpurea (L.) Pers.	Fabaceae
5.	*Alternanthera ficoidea* (L.) P.Beauv.	Amaranthaceae
	Acalypha indica L.	Euphorbiaceae
	Eragrostis gangetica (Roxb.) Steud.	Poaceae
	Phyllanthus amarus Schumach. & Thonn.	Phyllanthaceae
	Amaranthus viridis L.	Amaranthaceae
	Cyanthillium cinereum (L.) H.Rob.	Asteraceae
	Launaea intybacea (Jacq.) Beauverd	Asteraceae
	Actinidia chinensis Planch.	Actinidiaceae
6.	*Alternanthera ficoidea* (L.) P.Beauv.	Amaranthaceae
	Parthenium hysterophorus L.	Asteraceae
	Trifolium repens L.	Fabaceae
	Sida acuta Burm.f.	*Malvaceae*
	Senna tora (L.) Roxb.	Fabaceae
7.	*Lantana camara* L.	Verbenaceae
	Acalypha indica L.	Euphorbiaceae
	Alternanthera ficoidea (L.) P.Beauv.	Amaranthaceae
	Tephrosia purpurea (L.) Pers.	Fabaceae
8.	*Synedrella nodiflora* Gaertn.	Asteraceae
	Acalypha indica L.	Euphorbiaceae
	Alternanthera ficoidea (L.) P.Beauv.	Amaranthaceae
	Phyllanthus niruri L.	Phyllanthaceae
	Sida acuta Burm.f.	*Malvaceae*
	Cyanthillium cinereum (L.) H.Rob.	Asteraceae
9.	*Phyllanthus niruri* L.	Phyllanthaceae
	Tephrosia purpurea (L.) Pers.	Fabaceae
	Synedrella nodiflora Gaertn.	Asteraceae
	Alternanthera ficoidea (L.) P.Beauv.	Amaranthaceae
	Acalypha indica L.	Euphorbiaceae
	Achyranthes aspera L.	Amaranthaceae
	Dicliptera paniculata (Forssk.) I.Darbysh.	Acanthaceae
10.	*Ocimum tenuiflorum* L.	Laminaceae
	Tephrosia purpurea (L.) Pers.	Fabaceae
	Ligustrum lucidum W.T.Aiton	Oleaceae
	Alternanthera ficoidea (L.) P.Beauv.	Amaranthaceae
	Acalypha indica L.	Euphorbiaceae
	Heliotropium indicum L.	Boraginaceae

Fig. 3: Homogeneous Patches.

Table 2: Homogeneous Patches.

Patch No.	Patch species	Family
1.	*Acalypha indica* L.	Euphorbiaceae
2.	*Sida acuta* Burm.f.	Malvaceae
3.	*Achyranthes aspera* L.	Amaranthaceae
4.	*Phyllanthus reticulatus* Poir.	Phyllanthaceae
5.	*Tephrosia purpurea* (L.) Pers.	Fabaceae
6.	*Alternanthera ficoidea* (L.) P.Beauv.	Amaranthaceae
7.	*Indigofera tinctoria* L.	Fabaceae
8.	*Synedrella nodiflora* Gaertn.	Asteraceae
9.	*Ficus hispida* L.f.	Moraceae
10.	*Barleria prionitis* L.	Acanthaceae

Fig. 4: Heterogeneous Patches.

reduction in patch area (4.99 m) and a decrease in species number from 28 to 13. *Phyllanthus reticulatus* occurred in the smallest patch (1.96 m), with a decrease in species number from 29 to 15 (Table 3).

In Heterogeneous herb patches, species like *Alternanthera ficoidea*, *Acalypha indica*, *Synedrella nodiflora*, and *Sida acuta* were commonly found across patches. Moisture content and number of individuals varied across patches with changes in patch area, while some herb species showed

an increase in height and leaf area as patch area decreased (Honnay et al. 1999). Patch No. 8 and 9 exhibited the largest patch sizes (9.3 m and 14.9 m, respectively) with rapid reductions in patch area (6.69 m and 10.74 m, respectively), resulting in both increased and decreased species numbers. Patch No. 3 had the smallest patch area (1.45 m) with similar fluctuations in species numbers across patches (Table 4). The findings from the heterogeneous patches underscored the significant role of the patch area, affirming its importance in

Table 3: Homogeneous Patches.

Patch No.	Patch Species	No. of Individuals (n)			LAI			Moisture Content (%)			Area Covered by Patch (sq. m)			Height (m)		
		DEC	JAN	FEB	DEC	JAN	FEB	DEC	JAN	FEB	DEC	JAN	FEB	DEC	JAN	FEB
1	*Acalypha indica* L.	40	35	30	0.62	0.70	1.48	2.2	7.07	7.32	8.97	5.76	3.14	0.4	0.8	1
2	*Sida acuta* Burm.f.	28	20	13	0.15	0.16	0.27	12.8	4.05	2.96	10.8	7.88	3.8	1	1.4	1.6
3	*Achyranthes aspera* L.	25	12	10	0.42	0.53	0.88	47.1	38.7	19.18	15.2	10.28	4.99	1.2	1.6	1.8
4	*Phyllanthus reticulatus* Poir.	29	18	15	0.71	0.78	1.2	36.3	10.7	5.92	1.96	1.67	1	1.5	1.7	1.8
5	*Tephrosia purpurea* (L.) Pers.	38	30	25	0.27	0.32	0.80	22.8	22.4	19.72	4.15	2.95	1.09	0.8	1	1.2
6	*Alternanthera ficoidea* (L.) P.Beauv.	79	74	69	0.48	0.57	0.72	13.1	10.4	10.14	4.15	3.45	2.54	0.45	0.6	0.8
7	*Indigofera tinctoria* L.	32	20	14	0.27	0.62	1.36	28.5	16.2	15.48	4.91	2.39	1.21	1.8	2	2.4
8	*Synedrella nodiflora* Gaertn.	42	34	28	0.48	0.81	1.19	12.4	6.78	1.44	5.55	3.15	2.11	0.5	0.8	1
9	*Ficus hispida* L.f.	25	12	10	19.6	20.7	25.1	24.3	9.22	6.95	2.54	2.1	1.5	0.4	0.5	0.6
10	*Barleria prionitis* L.	33	25	19	2.64	3.41	4.04	4.64	4.7	3.88	3.14	2.11	1.56	2	2.2	2.4

explaining the formation of plant patches and patch dynamics. Heterogeneous herb species exhibited greater sensitivity to decreases in patch area compared to homogeneous herb species, which showed lower sensitivity. Interestingly, tree species appeared to be less affected or unaffected by changes in patch area. In both homogeneous and heterogeneous tree patches, tree species were consistently present across all observed patches, with minimal changes detected. There was a slight increase observed in the number of tree species, as well as an increase in height and diameter at breast height (DBH) with an increase in height.

Species Area Curves: Species-area curves are employed to estimate the rate of decrease in species number, illustrating the positive relationship between the area of a region and the number of biological species found within it. These curves have been extensively discussed in conservation biology, particularly concerning their utility in designing optimal nature reserves and predicting the loss of species richness in regions experiencing area reduction (Higgs 1981). By utilizing species-area curves, patch sizes corresponding to approximately 90%, 75%, 50%, and 25% of the total species were interpolated to evaluate the potential impact of patch size reduction on species richness. It is crucial to delineate the chosen slope for calculation. Several parameters must be considered: firstly, the relationship between species and area can follow either a linear or power function. Secondly, the slope of the species-area curve should remain constant across spatial scales encompassing the area reduction over which species loss is estimated. Lastly, it must be determined whether the reduced area better represents an isolated entity (a true island) or merely a subsample of the original area (Connor & McCoy 2001). In homogeneous patches, the mean patch area exhibited a more pronounced decrease compared to heterogeneous patches (Fig. 5).

Eco-physiological Responses of Patches

Ecophysiology is a biological discipline that studies the adaptation of an organism's physiology to environmental conditions. It is closely related to Comparative Physiology and Evolutionary Physiology (Schulte et al. 2011). Light plays a pivotal role in the survival, growth, and development of higher plants, as highlighted by various studies (Valladares 2003, Walters & Reich 2000, Durand & Goldstein 2001, Hitsuma 2012). During patch dynamics, the light environment undergoes diurnal variations and differs by patch type. Consequently, individual plants fine-tune their physiological traits to optimize carbon gain under varying environmental conditions. Leaves serve as a prime example of a plant's ability to respond to changes in light and the environment (Poorter & Bongers 2006). Plants belonging to

Table 4: Heterogenous patches.

Patch No.	Patch species	No. of Individuals			LAI			Moisture Content (%)			Area covered by patch (sq. m)			Height (m)		
		DEC	JAN	FEB	DEC	JAN	FEB	DEC	JAN	FEB	DEC	JAN	FEB	DEC	JAN	FEB
1	Alternanthera ficoidea (L.) P.Beauv.	28	20	15	0.86	1.09	1.34	3.52	4.88	5.02	2.07	1.32	0.97	0.2	0.4	0.6
	Acalypha indica L.	6	5	3	5.92	6.06	6.48	2.62	3.02	3.31				1	1.2	1.6
	Elephantopus tomentosus L.	3	4	5	11.15	10.9	9.02	4.76	5.98	6.74				0.2	0.3	0.5
2	Sida acuta Burm.f.	8	5	4	0.55	0.54	0.53	25.4	18.4	12.2	5.6	4.3	3.79	1	1.3	1.5
	Alternanthera ficoidea (L.) P.Beauv.	32	25	12	0.74	0.69	0.55	5.8	4.1	3.6				0.1	0.2	0.4
	Cyanthillium cinereum (L.) H.Rob.	5	3	2	0.68	0.83	1.00	10.9	7.1	3.88				0.4	0.5	0.8
3	Acalypha indica L.	4	5	7	1.25	1.93	2.09	5.86	5.71	5.62	1.45	0.72	0.56	0.1	0.2	0.6
	Alternanthera ficoidea (L.) P.Beauv.	16	10	8	3.14	2.79	2.32	2.06	2.53	3.26				0.3	0.5	0.6
	Cyanthillium cinereum (L.) H.Rob.	2	3	4	7.52	8.05	9.55	7.35	7.67	7.94				0.3	0.4	0.7
	Echinochloa colona (L.) Link	26	21	10	1.98	2.22	4.73	0.18	0.29	0.51				0.2	0.4	0.5
	Tridax procumbens L.	5	6	7	4.36	3.95	3.35	6.05	4.19	2.15				0.1	0.2	0.4
	Ziziphus mauritiana Lam.	8	4	3	9.53	9.72	9.85	6	6.13	6.39				1.8	2	2.2
4	Sida acuta Burm.f.	36	30	23	0.28	0.25	0.21	35.4	15.6	6.59	8.2	6.3	4.74	1.3	1.5	1.6
	Alternanthera ficoidea (L.) P.Beauv.	64	58	19	0.34	0.31	0.29	3.39	3.34	3.27				0.06	0.1	0.3
	Achyranthes aspera L.	7	5	5	1.42	1.11	0.98	43.1	21.2	10.0				0.5	0.6	0.8
	Antigonon leptopus Hook. & Arn.	29	23	16	0.26	0.95	1.36	3.1	2.65	2.51				4.9	5.2	5.6
	Zinnia elegans Jacq.	3	2	1	0.43	0.45	0.46	12.8	9.09	7.6				1	0.6	0.4
	Trifolium repens L.	42	45	48	0.38	0.31	0.25	1.15	1.21	1.54				6.1	6.3	6.6
	Tephrosia purpurea (L.) Pers.	2	1	1	0.4	0.31	0.21	21.8	18.4	17.6				0.4	0.5	0.7
5	Alternanthera ficoidea (L.) P.Beauv.	18	12	10	0.37	0.79	1.27	2.2	2.13	1.83	4.8	2.54	1.41	0.2	0.3	0.5
	Acalypha indica L.	6	8	9	1.69	2.75	4.39	9.35	7.72	5.99				0.8	1	1.3
	Eragrostis gangetica (Roxb.) Steud.	9	3	0	0.10	0.20	0	0.01	0.17	0				0.08	0.1	0
	Phyllanthus amarus Schumach. & Thonn.	9	5	2	0.12	0.39	1.20	4.64	3.96	3.62				0.3	0.4	0.6
	Amaranthus viridis L.	4	6	8	1.79	2.5	4.23	68.6	36.0	24.8				1	1.2	1.4
	Cyanthillium cinereum (L.) H.Rob.	2	2	3	2.01	3.93	6.80	1.98	2.12	3.24				0.8	0.7	0.5
	Launaea intybacea (Jacq.) Beauverd	4	5	6	5.46	8.58	15.2	40.0	14.4	5.52				1.2	1.4	1.6
	Actinidia chinensis Planch.	1	1	2	1.63	2.87	4.48	0.58	0.74	0.84				0.1	0.2	0.4

Table Cont....

Patch No.	Patch species	No. of Individuals			LAI			Moisture Content (%)			Area covered by patch (sq. m)			Height (m)		
		DEC	JAN	FEB	DEC	JAN	FEB	DEC	JAN	FEB	DEC	JAN	FEB	DEC.	JAN.	FEB.
6	Alternanthera ficoidea (L.) P.Beauv.	36	28	21	0.61	0.46	0.43	7.1	4.12	2.72	5.2	4.52	3.2	0.8	0.6	0.4
	Parthenium hysterophorus L.	3	3	4	2.94	3.28	3.83	14.5	15.1	16.7				0.4	0.5	0.8
	Trifolium repens L.	84	76	38	0.52	0.68	0.75	2.4	1.93	1.32				0.1	0.2	0.4
	Sida acuta Burm.f.	6	5	4	0.48	0.34	0.13	7.25	7.11	7.01				1.2	1.3	1.5
	Senna tora (L.) Roxb.	2	1	1	0.48	0.45	0.44	9.4	7.28	5.7				0.6	0.5	0.3
7	Lantana camara L.	12	7	0	8.54	6.34	0	57.6	49.3	0	3	2.26	1.32	0.8	0.4	0
	Acalypha indica L.	10	8	7	1.36	2.45	3.47	4.76	3.55	3.54				0.4	0.6	0.8
	Alternanthera ficoidea (L.) P.Beauv.	37	34	28	1.27	1.32	1.47	5.82	4.13	2.31				0.8	1	1.2
8	Tephrosia purpurea (L.) Pers.	40	38	6	0.18	0.52	0.93	6.06	3.62	2.58	9.3	8.48	6.69	0.4	0.6	0.7
	Synedrella nodiflora Gaertn.	18	15	4	1.29	0.70	0.68	33.2	24.3	16.5				1	1.2	1.4
	Acalypha indica L.	14	10	7	0.82	0.94	1.23	22.4	14.0	8.29				0.8	1	1.2
	Alternanthera ficoidea (L.) P.Beauv.	26	23	9	0.35	0.33	0.32	4.9	4.67	3.37				0.9	0.7	0.4
	Phyllanthus niruri L.	3	3	4	0.13	0.26	0.33	3.4	4.24	6.5				0.8	0.6	0.7
	Sida acuta Burm.f.	8	6	11	0.22	0.18	0.13	22.8	19.4	15.2				0.6	0.8	1
	Cyanthillium cinereum (L.) H.Rob.	1	2	2	0.52	0.54	0.55	6.9	5.38	4.27				0.4	0.5	0.7
9	Phyllanthus niruri L.	1	1	2	0.17	0.12	0.07	29.5	18.3	9.47	14.9	11.2	10.74	0.2	0.3	0.4
	Tephrosia purpurea (L.) Pers.	1	2	0	0.20	0.13	0	27.2	19.4	0				0.7	0.5	0
	Synedrella nodiflora Gaertn.	1	3	2	0.58	0.53	0.41	1.03	2.32	6.33				0.4	0.5	0.8
	Alternanthera ficoidea (L.) P.Beauv.	56	44	32	0.21	0.18	0.15	18.2	8.73	4.48				1.3	1.2	1
	Acalypha indica L.	48	20	6	0.54	0.48	0.39	10.7	9.02	8.19				0.5	0.6	0.7
	Achyranthes aspera L.	26	6	3	0.58	0.56	0.55	13.2	10.6	9.79				1.6	1.8	2
	Dicliptera paniculata (Forssk.) I.Darbysh.	4	5	8	2.22	1.94	1.74	1.93	1.6	1.05				0.3	0.4	0.6
10	Ocimum tenuiflorum L.	6	2	3	0.80	2.7	4.36	14.6	9.13	5.8	1.65	0.5	0.41	0.9	1	1.2
	Tephrosia purpurea (L.) Pers.	12	5	0	1.57	3.3	0	13.4	16.6	0				0.3	0.4	0
	Ligustrum lucidum W.T.Aiton	2	1	1	18.69	19.7	20.1	42.2	25.4	7.54				0.7	1	1.3
	Alternanthera ficoidea (L.) P.Beauv.	20	16	12	4.78	5.1	6.21	12.4	8.83	5.54				1.2	0.8	0.6
	Acalypha indica L.	3	4	8	10.9	12.5	15	10.1	11.7	11.6				0.4	0.6	0.8
	Heliotropium indicum L.	1	4	6	30.46	26	22.6	11.1	18.7	42.5				0.2	0.4	0.6

different functional types develop acclimation mechanisms to optimize light utilization under low light conditions, as evidenced by studies (Miller 2004, Yoshimura 2010, Hitsuma 2012, Wyka 2012). Natural growth and regeneration in low light conditions are associated with photosynthetic capacity coupled with morphological and physiological adaptations (Gommers 2013). Changes induced by light competition reflect a plant's ability for shade avoidance or tolerance (Gommers 2013). In the present study, the evergreen *Alternanthera ficoidea*, showed increased ratios, in the homogenous patch as a result of the increase in LAI and height, which indicates that the species performs well under survival conditions also. *Eragrostis gangetica*, *Tephrosia purpurea,* and *Lantana camara* had poor shade acclimation, indicating a trade-off between high light (in the Heterogenous patch). We observed that the mortality of *Alternanthera ficoidea* was approximately two times higher than that of other species in both of the patches. The different mortality is a good indicator of their interspecific differences in high and low light tolerance. During the patch dynamics, *Alternanthera ficoidea*, *Eragrostis gangetica*, *Lantana camara,* and *Tephrosia purpurea* exhibited a higher degree of change, which was in accordance with its shorter leaf life span and higher potential photosynthetic rates. The greater changes within the patch dynamics were inherently associated with the higher flexibility in utilizing available resources in different patches. Accepting these species, other species of the Heterogeneous patches exhibited small changes with slow growth and little variation in eco-physiological traits during the patch dynamics, for evergreen species have a stable physiological performance (Böhnke & Bruelheide 2013). The various interspecific responses to the four different types of patches provide new insights into the extinction and coexistence mechanism.

Generally, an increase in the number of individuals in an area can lead to a higher leaf area index. This is because more plants contribute to the total leaf area, resulting in a denser canopy and a higher LAI. Moisture content can also affect LAI. In areas with adequate moisture, plants tend to have more leaves and a denser canopy, leading to a higher LAI. However, in drought or water-stressed conditions, plants may have fewer leaves or smaller leaf sizes, resulting in a lower LAI. (Jin et al. 2017) So, the relationship between LAI, number of individuals, and moisture content is not straightforward. It depends on various factors such as plant species, environmental conditions and management practices. The findings underscore the significance of temporal and spatial variations across different patches during patch dynamics, highlighting the fluctuating partitioning of eco-physiological traits as crucial factors for stable coexistence and avoidance of extinction (Table 5).

CONCLUSION

Based on the findings and discussions presented above, it has been demonstrated that heterogeneous patches of herbs exhibit more favorable growth conditions compared to homogeneous patches. The competition for similar resources accelerates the degradation of homogeneous patches in contrast to heterogeneous ones. The higher plant diversity observed in heterogeneous patches contributes to their increased survival rate. Therefore, the dynamic analysis of these patches holds significant importance in predicting and conserving biodiversity within urban areas. In heavily disturbed urban environments, such patches may play a vital role in plant conservation efforts, as they offer greater resilience against disturbances and invasions by other species and human activities.
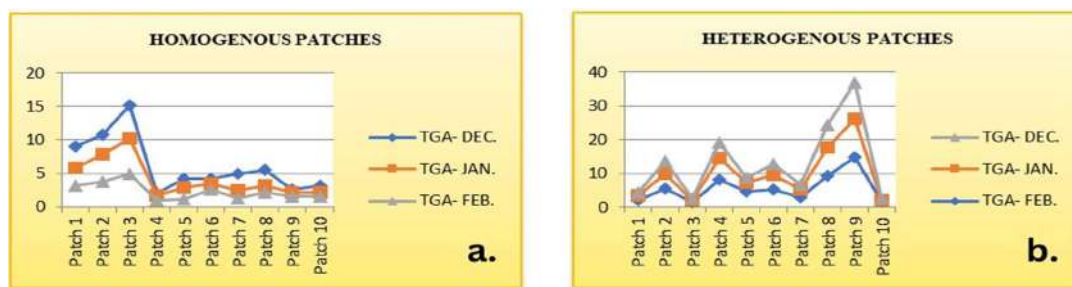
Fig. 5: Reduction in Mean Patch Area over time a. Homogenous Patches b. Heterogenous Patches.

Table 5: Rate of change in patch characteristics in patch dynamics.

No.	Rate of Change	Heterogeneous patches	Homogeneous patches
1.	Number of Individuals	7.23	15.18
2.	Moisture content	6.90	12.27
3.	LAI	0.42	-1.25
4.	Mean Patch Area	2.23	4.23
5.	Height	0.23	-0.45

REFERENCES

Böhnke, M. and Bruelheide, H., 2013. Species responses in heterogeneous patches: Small changes, slow growth and stable ecophysiological traits for evergreen species during patch dynamics. *Journal of Ecology*, 101(3), pp.550-562. http://doi.org/10.1111/1365-2745.12061.

Brack, C., 2009. Methods for measuring tree diameter at breast height. *Journal of Forestry Research*, 24(2), pp.425-430.

Brokaw, N. and Thompson, J., 2000. The h for DBH. *Forest Ecology and Management*, 129, pp.89-91.

Connor, E.F. and McCoy, E.D., 2001. The statistics and biology of the species-area relationship. *The University of Chicago Press*. https://doi.org/10.1086/283438.

Corrado, R., Cherubini, A.M. and Pennetta, C., 2014. Early warning signals of desertification transitions in semiarid ecosystems. *Physical Review E*, 90(6), p.062705. https://doi.org/10.1103/PhysRevE.90.062705.

Durand, J.L. and Goldstein, G., 2001. Light-dependent variation in stomatal control of photosynthesis in two tropical tree species. *Functional Plant Biology*, 28(2), pp.141-149. http://doi.org/10.1071/PP99115.

Forman, R.T.T. and Godron, M., 1986. *Landscape ecology*. Wiley.

Forman, R.T.T., 1995. *Land mosaics: The ecology of landscapes and regions*. Cambridge University Press, Cambridge, UK. http://doi.org/10.1017/CBO9780511525564.

Gommers, C.M., 2013. Physiological responses to light and salinity stress in the halophyte species Suaeda maritima. *Plant Biology*, 15(1), pp.122-133. http://doi.org/10.1111/j.1438-8677.2012.00667.x.

Hanski, I., 1999. *Metapopulation ecology*. Oxford University Press.

Higgs, M.D., 1981. The effect of spatial scale on the interpretability of complex ecosystems. *Conservation Biology*, 5(3), pp.371-378. http://doi.org/10.1111/j.1523-1739.1981.tb01388.x.

Hitsuma, G., 2012. Light acclimation in two co-occurring tree species of different successional status: Photosynthesis, gas exchange, photoprotection, and photoinhibition. *Trees*, 26(6), pp.1837-1846. http://doi.org/10.1007/s00468-012-0759-5.

Honnay, O., Endels, P., Vereecken, H. and Hermy, M., 1999. The role of patch area and habitat diversity in explaining native plant species richness in disturbed suburban forest patches in northern Belgium. *Diversity and Distributions*, 5, pp.129-141. http://doi.org/10.1046/j.1472-4642.1999.00065.x.

Jacquemin, B., Roche, P. and Wiegand, T., 2002. Population size and patch area for plants in dynamic landscapes: Evidence from a multispecies approach. *Ecology*, 83(5), pp.1304-1318. http://doi.org/10.1890/0012-9658

Jin, Y., Li, X., Yao, Y. and Zhang, M., 2017. Effects of individual size, density and moisture content on the leaf area index and growth of *Sorghum bicolor*. *Field Crops Research*, 206, pp.67-73. http://doi.org/10.1016/j.fcr.2017.01.011.

Krebs, C.J., 1999. *Ecological methodology*. Addison-Wesley Educational Publishing, Inc., Menlo Park.

Levin, S.A. and Paine, R.T., 1974. Disturbance, patch formation and community structure. *Proceedings of the National Academy of Sciences*, 71(7), pp.2744-2747. http://doi.org/10.1073/pnas.71.7.2744.

MacArthur, R.H. and Wilson, E.O., 1967. *The theory of island biogeography*. Princeton University Press.

Miller, C.R., 2004. Light environments influence belowground growth and morphology of seedlings in three shade-tolerant tree species. *Canadian Journal of Forest Research*, 34(12), pp.2403-2411. http://doi.org/10.1139/x04-140.

Paul, K.I., 2017. Measurements of stem diameter: Implications for individual- and stand-level errors. *Environmental Monitoring and Assessment*, 189(8), p.416. https://doi.org/10.1007/s10661-017-6109-x.

Pickett, S.T.A. and White, T.A., 1985. *The ecology of natural disturbance and patch dynamics*. Academic Press.

Poorter, H. and Bongers, F., 2006. Leaf traits are good predictors of plant performance across 53 rain forest species. *Ecology*, 87(7), pp.1733-1743. http://dx.doi.org/10.1890/0012-9658(2006).

Russell, B.M. and Honkala, B.H., 1990. *Silvics of North America: Vol-2. Hardwoods*. United States Department of Agriculture (USDA), Forest Service, Agriculture Handbook, 654.

Saravia, L.A. and Momo, F.R., 2017. Biodiversity collapse and early warning indicators in a spatial phase transition between neutral and niche communities. *OIKOS*, https://doi.org/10.1111/oik.04256.

Schulte, P.M., Healy, T.M. and Fangue, N.A., 2011. *Ecophysiology: From individuals to ecosystems*. Academic Press. http://doi.org/10.1016/B978-0-12-384715-0.X0001-3.

Turner, M.G., Gardner, R.H. and O'Neill, R.V., 2001. *Landscape ecology in theory and practice: Pattern and process*. Springer.

Valladares, F., 2003. Light heterogeneity and plants: From ecophysiology to species coexistence and biodiversity. *Progress in Botany*, 64, pp.439-471. http://doi.org/10.1007/978-3-642-55851-6_19.

Walters, M. and Reich, P.B., 2000. Are shade tolerance, survival, and growth linked? Low light and nitrogen effects on hardwood seedlings. *Ecology*, 81(3), pp.658-670. http://dx.doi.org/10.2307/2265505.

Watt, A.S., 1947. Pattern and process in the plant community. *The Journal of Ecology*, 35(2), pp.1-22. http://doi.org/10.2307/2256497.

Wiens, J.A., 1989. Spatial scaling in ecology. *Functional Ecology*, 3(4), pp.385-397. http://doi.org/10.2307/2389612.

Wyka, T.P., 2012. Light requirements for survival and growth of temperate broad leaved tree seedlings: A systematic review and meta-analysis. *Forest Ecology and Management*, 315, pp.80-94. http://doi.org/10.1016/j.foreco.2013.11.012.

Yoshimura, K., 2010. Effects of irradiance on leaf dynamics and photosynthesis in an understory palm, *Licuala cordata* (Arecaceae), in a subtropical forest. *American Journal of Botany*, 97(2), pp.249-258. http://doi.org/10.3732/ajb.0900279.

Assessing Tourists' Willingness to Pay for Sustainable Tourism in Petra, a Contingent Valuation Study

I. N. Abuamoud [ID]

School of Archaeology and Tourism, Department of Tourism Management, University of Jordan, Amman, Jordan
†Corresponding author: I.N. Abuamoud; i.abuamoud@ju.edu.jo

ABSTRACT

Tourism is a vital economic sector globally, but its growth has raised concerns about its environmental impact. The study utilized the Contingent Valuation Method and Willingness to Pay to estimate additional costs tourists would pay for sustainable tourism in Petra. A survey of 446 international tourists examined their willingness to pay higher fees for improved services, providing insights into sustainable tourism management and pricing policies. Results reveal a positive inclination towards sustainable practices, with a majority expressing willingness to pay additional fees for entry, accommodation in eco-lodges, and electric transportation services within Petra. Cultural preservation also emerged as a priority, with tourists willing to pay for cultural events and donate towards site maintenance. However, interest in culinary experiences and professional photography services was comparatively lower. Regression analyses indicate age and marital status as significant predictors of WTP, emphasizing the importance of tailored marketing strategies. Recommendations include diversifying revenue streams, integrating cultural experiences, and fostering collaborations between stakeholders to promote sustainable tourism practices. This study contributes to understanding tourists' preferences and behaviors regarding sustainable tourism, offering insights for the management and marketing of heritage sites like Petra while balancing economic growth with environmental conservation.

INTRODUCTION

Tourism is globally acknowledged as one of the world's fastest-growing economic sectors, with strong interconnections to all other industries both locally and internationally, influencing its core functioning. According to the World Tourism Organization, the numbers indicate that the tourism sector employs approximately 310 million people and generates an income exceeding $1.8 trillion. Furthermore, more than 1.3 billion tourists traveled the world in 2019 (WTTC 2023).

The impact of the COVID-19 pandemic cannot be considered as a measure of the tourism sector's effect. However, there has been a noticeable recovery in the tourism sector after the pandemic, and it is expected that the demand for tourism will continue to grow in the coming years. The significant increase in global tourism demand, fueled by the desire for adventure, entertainment, and various other reasons, has resulted in a corresponding rise in the consumption of goods and services both before, during, and after travel. However, this surge in tourism has also raised concerns among environmentalists regarding the escalating negative environmental impact.

Currently, tourism contributes to approximately 8% of all global greenhouse emissions (Bahja & Hancer 2012, Dolnicar 2012). In response to this issue, there is a growing awareness among stakeholders about the urgent need to take action to mitigate the environmental consequences associated with tourism. The focus is now on achieving sustainable tourism development through the promotion of accessible tourism, eco-tourism, and green tourism practices.

Sustainable tourism aims to minimize the negative environmental impacts of tourism while enhancing visitor experiences. The willingness to pay (WTP) method is a valuable tool for assessing tourists' readiness to incur additional costs for sustainable practices. This approach provides insights into consumer behavior and supports the development of effective pricing policies for sustainable tourism initiatives.

Mitigating the negative environmental effects of tourism typically necessitates the implementation of actions that may not align with the preferences of some tourists, potentially resulting in reduced service quality or higher investment costs (Bahja & Hancer 2021). To ensure informed and effective decision-making is essential to seek the perspectives

of various stakeholders, with particular emphasis on the input of tourists. Such engagement can prove invaluable to policymakers, enabling them to make informed choices by evaluating the tourists' willingness to pay additional costs in the pursuit of sustainable and responsible tourism practices (Ma et al. 2022).

Some governments and international organizations have implemented a range of practices, policies, and incentives to motivate tourism establishments to adopt and implement various practices, such as the use of recycled raw materials, the adoption of alternative energy sources, and other environmentally friendly actions. Furthermore, certain organizations offer awards or certifications to incentivize tourism firms to actively participate in sustainable development, accessible tourism, and the adoption of eco-friendly practices (Awang et al. 2018, Doran & Hanss 2022).

This topic has attracted numerous researchers who have studied it using various methodologies to assess the customers' willingness to pay additional costs for achieving sustainable tourism development. One of these methodologies is the willingness to pay or the contingent valuation method, which is among the most useful approaches and highly adaptable in such cases. There has been an increasing focus on utilizing the Contingent Valuation Method (CVM) to estimate the value of introducing new services or improving the quality of existing services or products. This can be attributed to improvements in valuation techniques and a growing demand for new or existing goods or services.

Tourism in Jordan has a rich history, spanning many years, with rich heritage, archaeological sites, and diverse environmental and religious attractions. Among the numerous tourism components in Jordan, are the traditional attractions of sea, sand, and sun. One standout destination in Jordan is Petra, considered the most significant historical site worldwide. The demand for tourism in Petra has been steadily increasing year after year. In 2019, the number of tourists surpassed one million, and by the end of June 2023, it had already exceeded 700,000 tourists visited Petra. Projections indicate that the number of tourists to Petra in 2023 will surpass one and a half million tourists.

However, this flow in tourism places pressure on the infrastructure and services in Petra, leading to potential environmental damage to the site and its surroundings. This study aims to address the problem of balancing the growing tourism demand in Petra with the need for sustainable tourism development and minimizing the negative environmental impact on the site and its surroundings. Hence, the purpose of this study is to address the following question: To what extent are tourists visiting Petra willing to pay additional costs to foster sustainable tourism?

In this study, the willingness to pay (WTP) approach will be adopted to examine the following hypothesis:

- Tourists visiting Petra will not demonstrate a significant willingness to pay additional costs to support sustainable tourism practices.
- The level of tourists' willingness to pay for sustainable tourism in Petra will not influenced by demographic factors such as income, education, and age.
- Tourists who perceive the environmental impact of tourism in Petra as significant will not exhibit a higher willingness to pay for sustainable tourism practices compared to those who perceive it as less significant.

PAST STUDIES

Tourism plays a vital role in achieving economic development for countries, especially developing ones. It does so by creating employment and income opportunities for individuals and governments (Goffi et al. 2019, Yanes et al. 2019). One of the challenges faced by developing countries is achieving a balance between the requirements of economic development in nations facing high unemployment rates, poverty, inadequate infrastructure, and population growth that surpasses economic growth, resulting in governments' inability to address sustainable development issues and environmental preservation (Cui 2022). Jordan is not far from these challenges, as it is the third poorest country in the world in terms of water resources (Taamneh et al. 2020), (Saad Shbaita & Gücel 2022), and has an unemployment rate of over 23%. Additionally, it faces limited natural resources, which leads to many unemployed youths. Jordan also suffers from a high public debt-to-GDP ratio, exceeding 96% (Al-Tarawneh et al. 2022), (Alharbi 2020). However, in 2019 Jordan received about 5.3 million tourists, contributing to approximately 13% of the GDP and employing over 60,000 workers in the tourism sector (MoT 2021).

Jordan seeks to attract higher numbers of tourists through promotion and marketing programs, as well as incentivizing tourism companies to do so. All of this requires the adoption of policies that maximize the importance of sustainable tourism in preserving the heritage resources, which are the backbone of tourism in Jordan, with Petra being one of the UNESCO World Heritage sites and one of the New Seven Wonders of the World.

In recent years, there has been a significant increase in the demand for environmentally friendly destinations, which has emerged as a prominent force in the global tourism industry. This trend is often referred to by various names such as alternative tourism, sustainable tourism, green tourism, and others (Eckert & Pechlaner 2019), (Khan et al. 2021).

This raises several important questions: Are sustainable practices considered as pull factors that attract visitors to specific sites? And do people perceive these practices as part of their heritage (Tu 2020)? Several studies have explored these questions and shed light on the demographic factors that impact willingness to pay (Murphy et al. 2018). This suggests that destinations promoting sustainability practices are particularly appealing to educated individuals who have a deeper understanding of environmental issues and appreciate the value of sustainable practices.

The greatest concern regarding the development of cultural heritage tourism is that increasing numbers of arrivals lead to problems with maintaining the environment. There is a strong connection between tourism and the environment since tourism depends on a healthy environment more than any other business (Revfine 2021). However, negative environmental impacts could occur if tourism is not well managed. Overcrowding, misuse of natural resources, the construction of buildings and infrastructure, and other activities associated with tourism produce impacts on the environment (Drašković & Perović 2022). Because of its nature, (Plog 1974) notes that 'tourism contains the seeds of its own destruction, tourism can kill tourism, destroying the tourism attractions which visitors come to a location to experience'. However, some of the impacts may be controlled, regulated, or directed (Sudipa et al. 2020). If properly managed, tourism has the potential for maintaining or even enhancing the cultural and natural resource base. If mismanaged, or allowed to expand with short-term goals and objectives, it has the capability of destroying the resources upon which it is built (Blanco-Cerradelo et al. 2022).

Furthermore (Abuamoud et al. 2014) found that education level and income are associated with people who choose to travel to environmentally friendly destinations. This implies that individuals with higher education and income levels are more inclined to prioritize sustainability in their travel choices. This aligns with the notion that educated individuals often have a greater awareness of environmental concerns and are more willing to support destinations that align with their values.

According to a recent report by the World Travel and Tourism Council (WTTC), an impressive 69 percent of travelers are actively in search of sustainable travel options for the year 2023 (WTTC 2023). This suggests that a significant proportion of travelers are actively seeking out destinations that offer sustainable practices and unique experiences beyond traditional mass tourism. An increasing interest in sustainable development among decision-makers, academicians, and individuals especially those who support the preservation of heritage and the environment (Fatima & Elbanna 2020, Baba et al. 2021). Also, it has become an

added value for archaeological or environmental sites that adopt sustainable policies. Several studies have addressed this topic and examined it using the willingness to pay (WTP) model and contingent valuation method by adopting several hypotheses that link tourists' willingness to pay additional costs for sustainability. These hypotheses include demographic factors such as age, income, and educational level, as well as factors related to price, service level, site nature, and importance.

In their study on determining the extent of tourists' willingness to pay for the use of environmentally friendly packaging (paper instead of plastic), tourists expressed their readiness to do so to adopt more sustainable practices. This indicates an increase in positive awareness of the environment and a sense of responsibility in embracing more sustainable policies (Herrmann et al. 2022). Other studies have addressed the identification of factors influencing individuals' willingness to pay additional costs or sacrifice personal preferences to apply environmental practices (Ali & Ali 2020). These factors revolve around income, educational level, as well as personal tastes and preferences. Certainly, higher educational attainment and income levels have a positive impact on fostering a sense of responsibility toward the environment and increasing awareness of the importance of sustainable tourism (Abuamoud et al. 2014).

In one early study by Jabarin & Damhoureyeh in 2006, both the Contingent Valuation Method and the Travel Cost Method were employed to assess the demand function and examine recreational patterns within Dibeen National Park (DNP) located in Jerash, Jordan. The Travel Cost Model was utilized, employing Poisson regression analysis for estimation purposes. The results indicated that the average monetary value assigned to recreation in Dibeen National Park amounts to $100 per individual, per day of recreation. Furthermore, the study found that the average willingness to pay for the conservation and enhancement of services was determined to be $7.8 (Jabarin & Damhoureyeh 2006).

In a separate investigation led by Shamsudin in 2009, the Contingent Valuation Method was utilized to evaluate the pricing strategy for Taman Negara National Park (TNNP) in Malaysia. The study involved surveying 180 participants, encompassing both local and international visitors, to ascertain the highest amount they were prepared to pay for non-market goods within TNNP. The results demonstrated that visitors exhibited a greater willingness to pay when it came to entrance fees (Matthew et al. 2011).

In a study conducted in Indonesia to determine tourists' willingness to pay additional costs for the conservation of sharks, the Contingent Valuation Method and willingness to pay were employed. This method helps explain tourists'

behavior and their awareness of the importance of marine tourism through their willingness to pay. The study revealed tourists' readiness to pay additional costs for the preservation and protection of the marine environment in the study area (Booth et al. 2022).

The willingness-to-pay method not only aims to measure how much individuals are willing to pay a higher price for sustainability, but it also helps us assess consumer behavior and individuals' sense of responsibility towards the environment. This is based on several factors, including awareness of the relationship between humans and the environment and the understanding that any harmful practices or irresponsible behavior pose a threat to sustainability. Additionally, factors influenced by social psychology theories, Environmental Beliefs, and income, all impact behavior toward sustainability (de Araújo et al. 2022).

Furthermore, the willingness-to-pay model also helps in studying individuals' willingness to pay an additional price for addressing the environmental damages resulting from natural disasters (Soejarwo et al. 2021). The willingness-to-pay model can be widely used, as it helps determine an acceptable addition to the original price tourists are willing to pay, compared to the original price as a baseline price (Rommel & Sagebiel 2021).

Several studies have applied psychosocial theory to explain pro-environmental behavior, to understand how individuals interact with the environment and their willingness to pay for sustainability. To gain a better understanding of people's behavior toward the environment, some studies have examined various factors, including age, income, and level of education.

Additionally, researchers have incorporated theories such as the Planned Behavior Theory and the Value-Belief-Norm Theory to further analyze this behavior (López-Mosquera & Sánchez 2012). Natural and cultural resources are considered important economic resources for the countries' economy, as they help attract tourists and contribute to economic returns. However, they are not market goods, making their economic evaluation challenging. Economists have agreed on the viability of using contingent valuation methods to assess non-market goods through using the willingness-to-pay approach (Lawton et al. 2022).

The objective of this study is to investigate how willing tourists are to pay for sustainable tourism practices. By building on prior research, the study aims to deepen our understanding of the extent to which visitors to Petra are open to incurring extra expenses to support the implementation of sustainable measures for the preservation of Petra's cultural heritage.

Tourism in Jordan

Tourism plays a pivotal role in Jordan's economy, serving as a vital source of income for thousands of people. The sector encompasses various industries such as airlines, hotels, restaurants, ground transportation, and local communities, all of which benefit from tourism activities. Over the past two decades, Jordan's tourism sector has experienced rapid development, establishing itself as one of the most attractive countries for tourism in the Middle East (Alzriqat et al. 2022). Jordan has a rich historical heritage spanning 8,000 years and its diverse natural landscapes. Additionally, Jordan stands out as a peaceful haven amidst a troubled region, boasting a stable government. During the years from 2020 to 2022, tourism worldwide faced significant challenges due to the COVID-19 pandemic, resulting in a sharp decline in tourist numbers in Jordan and globally, reaching levels exceeding 85% (Abuamoud et al. 2022). This decline led to substantial losses. However, by the end of 2022 and the beginning of 2023, the world witnessed a recovery in tourism activity reaching more than 60% worldwide and more than 83% in the Middle East, including Jordan ("UNWTO World Tourism Barometer and Statistical Annex, January 2023," 2023). In Jordan, the tourist income in the first quarter of 2023 witnessed an increase of 88.4% compared to the same period in 2022, reaching a value of $1,671.1 million, during the first quarter of 2023, the tourist income achieved an increase of 88.4%, totaling JD 1,184.8 million ($1,671.1 million), driven by the increase in the number of tourists, which reached 1,476.5 thousand tourists (Table 1), this was due to the rise in the number of overnight tourists, reaching 1.5 million tourists (CB 2023).

The significance of tourism for Jordan becomes evident when considering the country's limited natural resources. The sector accounts for more than 13% of the country's GDP and serves as a crucial source of foreign exchange. Recognizing the potential of tourism, the Ministry of Tourism projects the construction of more than 20 new hotels in Petra and the Dead Sea within the next five years. These investments are expected to create a direct impact by generating 15,000 jobs and an additional 36,000 indirect employment opportunities. Jordan's National Tourism Strategy 2021-2025 aims to

Table 1: Number of Tourists in Jordan (in thousands).

2017	2018	2019	2020	2021	2022
4,833.20	5,329.20	5,697.90	1,012.10	1,260.80	2,369.40

collaborate with the private sector to create additional new jobs, as outlined by the Ministry of Tourism (MoT 2021).

The number of workers in different tourism activities reached 54,764 employees in 2022, with a growth rate of 11.3% compared to 2021, these workers are distributed among several activities, including hotels, travel and tourism agencies, tourist restaurants, car rental offices, oriental souvenir shops, tour guides, desert safari facilitators, tourism transportation companies, diving centers, water sports, and tourist camps (MoT, Tourism sector in Jordan 2023).

Tourism Trends in Petra

Petra is located in the southern part of Jordan around 230 km from Amman. The region covers an area of (441 km^2) of which (262 km^2) is dedicated to the Petra Archaeological Park (PAP). It also includes six urban communities with a population of around 35 thousand; Petra is a UNESCO World Heritage Site since 1985 and a World Wonder since 2007. Fig. 1 shows the map of the administrative region of the Petra Development and Tourism.

In 2019, the number of visitors to Petra exceeded 1,000,000 tourists Fig. 2, rapidly approaching the maximum capacity of Petra's hotels, estimated at 2,500 rooms per night. On average, tourists stayed in Petra for about 1.3 nights per person, but plans were in motion to extend this duration to 2 nights per tourist. Consequently, the expected surge in room demand amounted to 0.54, equivalent to 1,325

additional rooms. Notably, there is a significant and growing population of young people with a preference for adventurous destinations, flavorful cuisine, unique experiences, and engaging activities.

Petra has experienced a notable upswing in tourism in 2023, signifying the recovery of tourism in Petra from the adverse impacts of the COVID-19 pandemic. This recovery is evident through the influx of foreign and local visitors. During this period, hotels have witnessed a substantial increase in occupancy rates, which had plummeted to zero percent during the peak of the pandemic. After the number of tourists to Petra exceeded one million and 100 thousand in 2023, there was optimism in the tourism sector for a promising tourist season for the years 2024 and beyond. However, political developments and the war on Gaza led to a decline in the number of tourists after October 7, reaching less than 500 tourists per day during December 2023. The number continued to rise until mid-February 2024, reaching only about a thousand tourists per day from February to April. This constitutes only about 16% of the daily number of tourists to Petra in 2023. PDTRA is introducing new tourism programs and products in Petra in 2023, including cultural and heritage festivals, as well as safari trips organized in collaboration with tourism companies. The launch of several projects in Petra, such as the Heritage Village project in the Al-Bayda area, the completion of the tourism street project, the establishment of the Al-Bayda Visitor Center, adventure
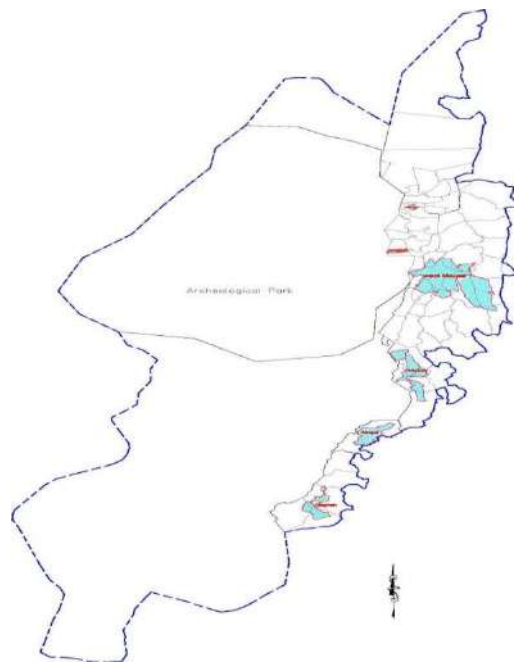
Source: PDTRA

Fig. 1: Map of the administrative region of the Petra Development and Tourism Region Authority.

vehicles, and a cable car. According to statistics released by the PDTRA, the total number of approved hotel rooms exceeds 900, with 350 rooms already operational, while efforts are underway to rehabilitate and equip an additional 550 new hotel rooms in preparation for the upcoming tourist season. Petra is currently attracting investment interest in the hotel sector, driven by the recovery of the tourism season and the investment incentives provided to stakeholders in the hotel accommodation industry. Several investors have proposed the construction of at least 500 new hotel rooms, with these proposals currently undergoing evaluation and study procedures to obtain the necessary construction approvals.

The cultural heritage component of the site is constantly at risk of damage due to weather conditions and human factors, whether from visitors or residents. This necessitates continuous monitoring, restoration, and preservation of the site. Additionally, the waste generated by tourist activities

requires proper management. Due to the geographical and topographical features of Petra, which include slopes, valleys, and the flow of rainwater and occasional floods, it poses a continuous threat to the archaeological site. Consequently, there is a need to establish infrastructure capable of accommodating floods and protecting properties and tourists.

Furthermore, the increasing investments in Petra resulting from the growing demand for tourism necessitate the development of infrastructure to provide services for both tourists and citizens. Moreover, the rising demand for tourism may create social and economic imbalances within the community. Therefore, the Petra Development and Tourism Region Authority is required to implement community protection programs that have economic and social dimensions. All of this requires budget allocation and additional costs for the local government. Thus, this study
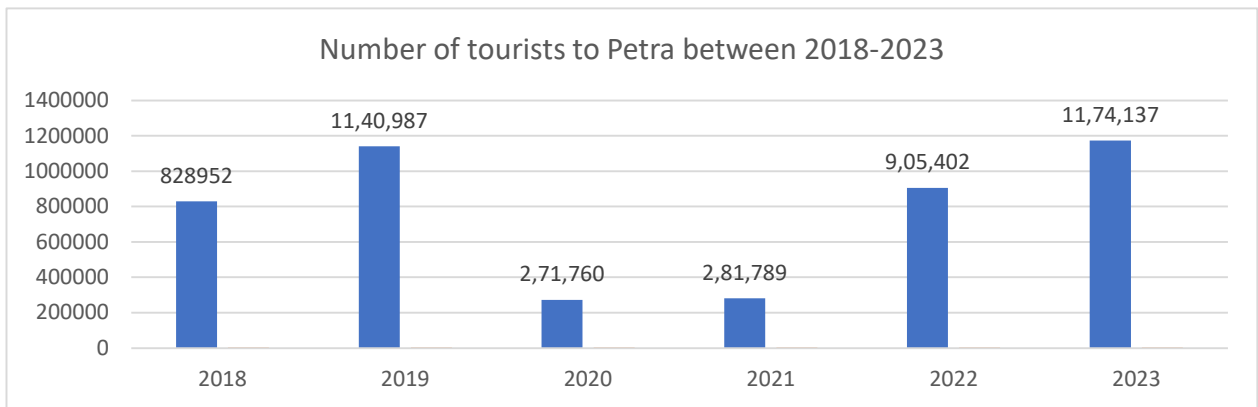
Source: PDTRA.

Fig. 2: Number of tourists to Petra between 2018-2023.

Fig. 3: Principles of sustainable tourism in Petra (created by the author).

aims to explore the extent to which tourists are willing to pay to cover these additional costs, which aim to achieve sustainable tourism in its comprehensive environmental, heritage,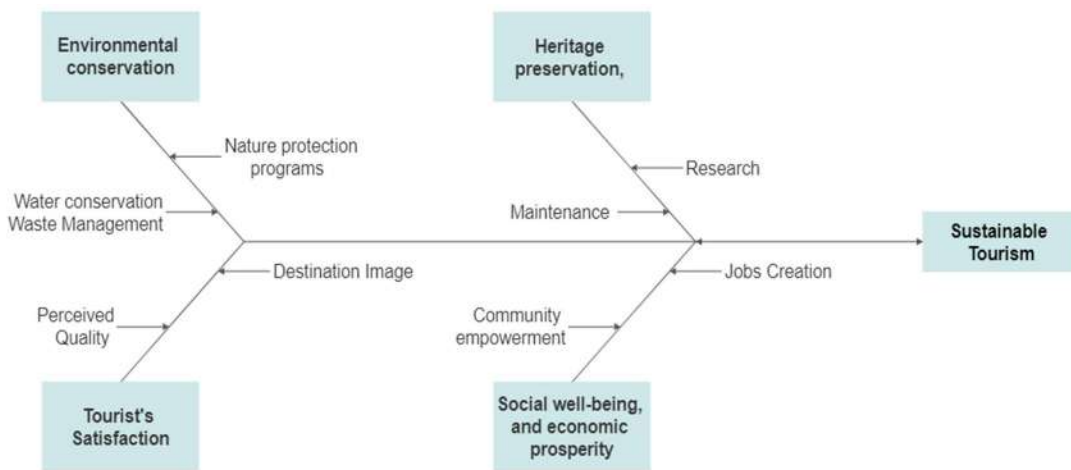 social, and economic aspects (Fig. 3). Because all these four aspects are interconnected and should be considered holistically in sustainable tourism development. By balancing environmental conservation, heritage preservation, social well-being, and economic prosperity, destinations can achieve a more sustainable and inclusive tourism model.

MATERIALS AND METHODS

In this study, the Contingent Valuation Method CVM and Willingness to Pay (WP) were applied to estimate the additional cost that tourists are willing to pay to apply sustainable tourism in the study area. The WP method is a behavioral method that assumes values from what people do, or it measures the value of people's actions. Contingent valuation measures the values of what people say, it is an attitudinal approach, in other ward measures what they say not what they do, The main theories relevant to the Willingness to Pay (WTP) model include:

Planned Behavior Theory proposes that behavior is shaped by intentions influenced by attitudes, subjective norms, and perceived control. In WTP, individuals' readiness to pay for environmental goods hinges on their sustainability attitudes, social norms, and perceived affordability. The Value-Belief-Norm Theory suggests that pro-environmental behavior stems from environmental values, beliefs, and social norms. In WTP, individuals valuing conservation and endorsing sustainable practices are inclined to pay for sustainability initiatives. While the Psychosocial Theory delves into psychological and social influences on behavior, including attitudes, beliefs, and social norms. Within WTP, it elucidates how individuals' perceptions and social influences impact their readiness to pay for sustainable practices.

(Del Saz-Salazar et al. 2015). A survey conducted on foreign tourists examined the hypothetical factors that impact respondents' willingness to pay and to estimate how much value could be captured by applying new prices for a list of services in Petra. Also, it will help to estimate the demand for the tourists' services. For the reason of this survey, respondents know the study area because they survived during their visit to Petra. They also provided a brief explanation about the reason for planning for sustainable tourism in Petra.

The CVM method assumes that the value of the site or its recreational services is reflected in how much people are willing to pay to visit the site. It is referred to as a "revealed preference" method because it uses actual behavior and choices to infer values (Thoma 2021), peoples' preferences are discovered by their choices. The CVM method is applied by collecting information about the number of visits/visitors to the site from different areas. This information allows calculate the number of visits purchased at suggested prices.

Contingent Valuation is a method of estimating the value of public goods, or non-market goods which is not subject to the laws of the market in terms of pricing. This method can help economists, and decision-makers, to estimate the impact of economic decisions and activities and estimate the monetary value of all economic benefits that a society derives from public goods like cultural heritage resources (R & Shamsudin 2009). The public good must have two characteristics. First, are non-excludible. That means we can't keep it away from people to enjoy the good. The second characteristic is non-rival in consumption. That means more than one person can enjoy the good without reducing each other enjoyment (Abuamoud et al. 2014). Cultural heritage goods typically possess public goods characteristics, and they are agreeable to the use of non-market valuation techniques. Improving environmental conditions in a particular location is considered a recreational activity to the site, and need to find out if people are willing to pay for the improvement to the site. The willingness-to-pay method helps to reach a proper pricing policy to provide visitors with quality services at fair prices and reach sustainable management of tourism sites (de Araújo et al. 2022).

The method asks individuals about their willingness to pay (WTP) for some public goods or services, to estimate the public's willingness to pay for improvements in environmental quality (Grankvist et al. 2019). Despite that the contingent valuation method has some difficulties, it is still one of the most useful and successful methods used to give decision-makers the best picture of the value of recreation on a site. Especially with public goods that are not traded in the market (Durán-Román et al. 2021). The willingness-to-pay method helps to reach an appropriate pricing policy, not only to provide quality services and products at fair prices to visitors but also to achieve successful and sustainable management of tourism sites (Bamwesigye et al. 2020). Several key determinants were determined by previous literature on the valuation of recreational services using the willingness-to-pay method. These include the education, age, and income of consumers, and characteristics and price levels and goods and services.

Data Collection

To achieve the study objectives, a questionnaire was designed to collect data from 446 international tourists who visited Petra. The questionnaire consisted of 30 questions

covering various areas, including tourists' willingness to pay additional costs for sustainability programs in Petra. The questions aim to assess the tourists' willingness to pay a higher entrance fee, accommodation, restaurants, transportation, and city tax to allow the PDTRA to apply a sustainable tourism plan.

The data was collected with help from PDTRA staff and two other students from the University of Jordan after proper training for them. The questionnaire consists of 30 questions, designed and digitally converted using a QR code. The code was distributed to 1,530 international tourists in Petra after they completed their visit to Petra, either during their return journey from the site, at the hotel, or on the bus back to Amman. The QR code opened a webpage containing information about the study's objectives and Petra's need for sustainable tourism. The form was designed in multiple languages, including English, Spanish, French, and German. The response rate was (29%) out of the total number of QR codes distributed. The data collection period took place during June, July, and August of 2023. The answers were received electronically and stored in an Excel sheet. The data was reviewed, and incomplete responses (missing information) were excluded, accounting for (missing information) percent.

Logistic models in the form below were employed to estimate the results, the LM is widely favored in recreation studies due to its ability to determine the marginal effect of each explanatory variable, Xi, on the overall probability value (Borucka 2020). The logistic formula, expressed in equation (1) below, demonstrates its general form:

$$P_i = \frac{1}{(1+\exp(-(Z)))} \qquad \ldots(1)$$

Pi represents the probability of individual i responding "Yes" to a question regarding their willingness to pay additional costs for sustainable tourism in Petar

$Z = b1 + b2X2i + b3X3i + \ldots.+ bnXni + ui,$

where the subscript i denotes the ith respondent. Xs represent predictor variables like income, education, and age, which determine pi, while b represents the coefficient vector of the descriptive variables. Zi can be calculated alongside Pi for everyone, considering their socio-economic characteristics (income, age, education, etc.). Using equation (1) ensures that the value of Pi falls between 0 and 1. The logit model can be employed to compute the marginal effect of Xs, as shown in equation (2):

$$\frac{dp}{dx} = B * (P_i) * (1 - P_i) \qquad \ldots(2)$$

This equation measures how the probability Pi changes with a one-unit change in a specific X, denoted as dp/dx.

Including the variables in the model, the following equation is obtained:

Ln 1/(1-pi) = b1 + b2x(gender) + b3x(income) + b4x(education) + b5x(age) + b6x(nationality) + b7x(occupation) …..

The dependent variable, WTP (Willingness To Pay), represents the probability of being willing to pay an additional cost for sustainable tourism in Petra. The response data has a value of 1 if the answer is "Yes" and 0 if it is "No". The predicted response value from the model indicates the probability of tourists being willing to pay which falls between 0 and 1. This limitation of values is advantageous when using the Logistic model, unlike a linear regression model with no restrictions on values.

RESULTS AND DISCUSSION

Logistic models were employed to analyze predictors of willingness to pay, revealing age and marital status as significant factors. The data reveals several key insights into respondents' willingness to incur additional costs across different services in Petra Table 2. In terms of paying an additional entry fee, the majority of respondents (55.3%) express a willingness to pay additional fees. This finding suggests that there is a market for supplementary fees, which could potentially be leveraged by businesses or organizations to enhance revenue streams. When examining the amount respondents are willing to pay for the entry fee, a significant proportion (76.1%) are prepared to pay $80 and more, indicating a threshold at which many respondents find the cost acceptable. However, it is noteworthy that a notable portion of respondents (23.9%) are unwilling to pay any additional fee, emphasizing the importance of carefully balancing pricing strategies to accommodate varying consumer preferences and financial capacities. Regarding accommodation preferences, there is a notable divergence in respondents' willingness to pay for stays in different types of lodging. While a majority express a willingness to pay for a stay in an eco-lodge (73.6%), fewer are inclined to pay for a night in a 5-star hotel (41.0%). This suggests a potential preference among respondents for more environmentally sustainable or unique lodging options, possibly reflecting broader trends towards eco-sensible consumerism. In the same direction, in terms of transportation services, a significant majority (77.2%) of respondents are willing to pay for electric transportation within Petra, indicating a demand for convenient and sustainable travel options. However, there is variation in the amount respondents are willing to pay, with a majority (61.5%) willing to pay less than $20, underscoring the importance of affordability in pricing electric transportation services.

The data provides insights into the willingness of respondents to incur additional costs for various sustainable practices and experiences within the Petra historical site. A significant majority (71.9%) express a readiness to pay extra for a meal at a restaurant within Petra that applies sustainable practices, indicating a strong interest in supporting environmentally responsible initiatives. This suggests a positive reception towards eco-friendly dining options among respondents. In addition, the majority (66.3%) are willing to pay for a 3-hour private eco-tourism guided tour in Petra, reflecting a desire for personalized and sustainable exploration experiences within the site. The data highlights the perceived value of eco-tourism initiatives in enhancing visitors' experiences.

Regarding entertainment activities in Petra, (67.7%) are willing to pay for a musical performance or cultural event inside Petra to support sustainable tourism, indicating an appreciation for cultural preservation efforts and the integration of sustainability into tourism activities. This highlights the potential for sustainable cultural events to contribute to the conservation and promotion of Petra's heritage. Among respondents, about (62.1%) of the respondents are willing to donate towards the preservation and maintenance of the historical site of Petra, demonstrating a recognition of the importance of conservation efforts and a willingness to contribute financially to safeguard Petra's cultural and natural heritage.

About (57.6%) of respondents expressed reluctance to spend on a cooking class or culinary workshop during their trip, suggesting a limited interest in culinary experiences as part of their visit to Petra. This indicates that culinary activities may not be a significant draw for visitors to the site, among respondents willing to pay for a cooking class or culinary workshop, there is a diversity in the amount they are willing to spend. The majority (39.9%) are willing to spend nothing, while others are distributed across different price ranges, with a sizable portion (27.0%) willing to spend $10. This variation suggests differing perceptions of value and affordability among respondents interested in culinary experiences.

Regarding photography within the site, a substantial majority (66.3%) are unwilling to pay for taking photos, indicating a preference for capturing their own images rather than purchasing professional photos. This may reflect a desire for personalization and authenticity in documenting their experiences at Petra. Also, there is a significant interest in adventure tours such as hiking or zip-lining, with a majority (67.7%) willing to pay for such experiences. This highlights a demand for active and adventurous experiences within Petra, potentially appealing to adrenaline-seeking tourists,

among respondents willing to pay for adventure tours, there is a diversity in the amount they are willing to spend per hour. The majority (27.2%) are willing to spend nothing, while others are distributed across different price ranges. This variation emphasizes differing perceptions of value and affordability among respondents interested in adventure tours. Visitors predominantly rated their Petra experience highly, with a significant proportion giving ratings of 9 (29.2%) or 10 (28.7%) on a scale of one to ten.

The demographic data provides valuable insights into the characteristics and preferences of visitors to Petra. Understanding the visitor profile and their preferences is essential for developing targeted marketing strategies, enhancing visitor experiences, and ensuring the sustainable management of Petra as a cultural heritage site. The data revealed several key findings. In terms of age distribution, the majority of visitors were in the 21-30 age range (44.1%), followed by 31-40 (25.3%). Gender distribution showed a relatively balanced representation, with 46.3% male and 50.8% female visitors, while the rest preferred not to say. Regarding nationality, a diverse mix of visitors was observed, with a significant proportion being Europeans, particularly Italy (20.2%) and Portugal (7.9%). The majority identified as White (53.4%) or Caucasian (14.9%). In terms of education, visitors exhibited a high level of educational attainment, with a substantial proportion holding bachelor's degrees (22.2%) or master's degrees (10.1%). Regarding income level, the majority fell into the bracket of less than $25,000 (33.4%) or $25,000-$50,000 (26.7%).

The high level of educational attainment among visitors suggests an interest in history, archaeology, and cultural heritage, aligning with Petra's significance as an archaeological marvel. The majority of visitors' income levels indicate a middle-income bracket, suggesting that Petra remains accessible to a broad range of people around the world. The positive ratings of visitors regarding their Petra experience highlight the site's appeal and the overall satisfaction of visitors. This high level of satisfaction promises well for Petra's reputation and continued success as a tourist destination. Also, the data reveals a positive attitude towards sustainable practices and experiences within Petra, suggesting a receptive audience for initiatives aimed at promoting environmental conservation and responsible tourism within the site.

Regression Analyses

The regression analyses aimed to identify predictors of tourists' willingness to pay for sustainable tourism experiences at Petra. Several independent variables were considered, including annual income, gender, education

Table 2: Preferences and ratings for sustainable tourism activities at Petra: mean and standard deviation analysis.

Question	Mean	Std. Deviation
Are you willing to pay an additional entry fees	.55	.49
Are you willing to pay an additional cost to stay one night in a 5-star hotel?	.41	.49
Are willing to pay to stay one night in an Eco Lodge?	.74	.44
Are you willing to pay for electric transportation services within Petra, including transportation to and from the historical site per day?	.78	.42
Are you willing to pay an additional cost for a meal at a restaurant within Petra, that applies sustainable practices?	.72	.45
Would you be willing to pay for a 3-hour private eco-tourism guided tour in Petra?	.67	.48
Would you be willing to pay for a musical performance/cultural event inside the site in Petra to support sustainable tourism?	.68	.46
Would you be willing to donate towards the preservation and maintenance of the historical site of Petra?	.62	.48
Would consider paying for a spa treatment or massage in Petra?	.47	.49
Would you be willing to spend on a cooking class or culinary work-shop during your trip?	.42	.49
Would be willing to pay for taking photos inside the site?	.34	.47
Would you be willing to pay for an adventure tour, such as hiking or zip-lining?	.68	.46
Would you be willing to pay for a 2 hour tour by ATV riding around Petra?	.42	.49
On a scale of one to ten, how would you rate your experience visiting Petra	8.2191	2.31
Valid N (listwise)		

level, marital status, age, and ethnicity. Overall, the models demonstrated statistically significant associations with moderate to modest effect sizes (R = 0.469, R Square = 0.220, Adjusted R Square = 0.178, p < 0.001; R = 0.377, R Square = 0.142, Adjusted R Square = 0.096, p = 0.008). Among the predictors, age consistently emerged as a significant contributor, with older individuals exhibiting less willingness to pay (β = -0.435, p < 0.001; β = -0.350, p < 0.001). Additionally, marital status was significant, indicating a higher inclination among those married or in committed relationships (β = 0.271, p = 0.004). However, gender, ethnicity, education, and annual income did not significantly influence willingness to pay (p > 0.05). The findings emphasize the pivotal roles of demographic factors such as age and marital status in shaping tourism-related decisions, highlighting the need for tailored marketing strategies. Furthermore, similar analyses for other tourism-related variables, including eco-accommodation preferences and transportation services, revealed significant associations with varying predictor significance, underscoring the complexity of decision-making processes in sustainable tourism initiatives. These results carry implications for tourism management and marketing strategies, emphasizing the importance of considering demographic factors in targeting and designing sustainable tourism experiences.

The findings of this study shed light on tourists' willingness to pay (WTP) for sustainable tourism practices in Petra. The results indicate a generally positive reception towards sustainable initiatives, with a significant proportion of respondents expressing readiness to incur additional costs for various eco-friendly services and experiences.

One notable insight is the willingness of tourists to pay additional entry fees, suggesting a potential avenue for generating revenue to support sustainability efforts within Petra. Moreover, the strong interest in eco-lodges and electric transportation services underscores the demand for environmentally responsible accommodation and travel options among visitors. This aligns with global trends towards eco-conscious consumerism and reflects a growing awareness of the environmental impact of travel.

The study also highlights the importance of cultural preservation and heritage conservation in tourists' decision-making processes. Respondents expressed willingness to support sustainable tourism through activities such as attending cultural events and donating towards the preservation of historical sites. This underscores the significance of integrating cultural experiences into sustainable tourism initiatives and underscores the potential for cultural tourism to contribute to heritage conservation efforts.

However, the findings also reveal areas where tourists may be less inclined to spend, such as culinary workshops and professional photography services. Understanding these preferences is crucial for developing targeted offerings that align with visitors' interests and maximize revenue potential while promoting sustainability.

Regression analyses further elucidate the influence of demographic factors on tourists' willingness to pay for sustainable tourism experiences. Age and marital status emerged as significant predictors, highlighting the importance of tailoring marketing strategies to different demographic segments. These insights can inform strategic decision-making and help tourism stakeholders design more effective marketing campaigns and sustainable tourism initiatives that resonate with target audiences.

The study recommends diversifying revenue streams: Explore opportunities to leverage tourists' willingness to pay for sustainable practices, such as introducing supplementary fees for entry to fund conservation efforts or offering eco-friendly accommodation and transportation options. Also to integrate cultural experiences into tourism offerings, such as organizing cultural events and heritage tours, to promote cultural preservation and enhance visitor experiences.

The study also recommends fostering collaborations between public and private sector stakeholders, as well as local communities, to jointly develop and implement sustainable tourism initiatives and share resources for conservation efforts.

CONCLUSIONS

This study illuminates tourists' positive reception towards sustainable tourism practices in Petra, Jordan, revealing a willingness to pay for eco-friendly services and experiences. Key insights include the potential for generating revenue through additional entry fees and the demand for environmentally responsible accommodation and transportation options. Moreover, the study underscores the importance of cultural preservation and heritage conservation in tourists' decision-making processes, alongside demographic factors such as age and marital status influencing willingness to pay. Recommendations include diversifying revenue streams, integrating cultural experiences, and fostering collaborations between stakeholders to promote sustainable tourism while balancing economic growth with environmental conservation. These findings offer valuable guidance for the management and marketing of heritage sites like Petra, ensuring a harmonious blend of tourism development and environmental stewardship.

REFERENCES

Abuamoud, I., Ibrahim, A. and Al-Tabini, R., 2022. Economic impact of the COVID-19 pandemic on the tourism industry. *Corporate and Business Strategy Review*, 3(2 special issue). Available at: https://doi.org/10.22495/cbsrv3i2siart13.

Abuamoud, I.N., Libbin, J., Green, J. and Rousan, R.A.L., 2014. Factors affecting the willingness of tourists to visit cultural heritage sites in Jordan. *Journal of Heritage Tourism*, 9(2). Available at: https://doi.org/10.1080/1743873X.2013.874429.

Alharbi, M.M.H., 2020. Entrepreneurship and job creation in Jordan: Challenges and prospects for start-ups. *Journal La Bisecoman*, 1(3). Available at: https://doi.org/10.37899/journallabisecoman.v1i3.114.

Ali, T. and Ali, J., 2020. Factors affecting the consumers' willingness to pay for health and wellness food products. *Journal of Agriculture and Food Research*, 2. Available at: https://doi.org/10.1016/j.jafr.2020.100076.

Al-Tarawneh, A., Obeidat, M., Khataybeh, M., Omet, G. and Haddad, F., 2022. The unemployment challenge in Jordan: The issue of employment elasticity of growth. *Corporate Governance and Organizational Behavior Review*, 6(2). Available at: https://doi.org/10.22495/cgobrv6i2p14.

Alzriqat, L., Odat, S. and Abuamoud, I., 2022. Main characteristics of trails on Yarmouk Forest Reserve, a quantitative approach to trails assessment. *Nature Environment and Pollution Technology*, 21(3). Available at: https://doi.org/10.46488/NEPT.2022.v21i03.031.

Awang, Z., Yusnita, Y. and Afthanorhan, A., 2018. Sustainable tourism: The moderating effect of tourists' educational background in the relationship between green practices and customer satisfaction. *International Journal of Engineering & Technology*, 7(4.34). Available at: https://doi.org/10.14419/ijet.v7i4.34.23574.

Baba, S., Mohammad, S. and Young, C., 2021. Managing project sustainability in the extractive industries: Towards a reciprocity framework for community engagement. *International Journal of Project Management*, 39(8). Available at: https://doi.org/10.1016/j.ijproman.2021.09.002.

Bamwesigye, D., Hlavackova, P., Sujova, A., Fialova, J. and Kupec, P., 2020. Willingness to pay for forest existence value and sustainability. *Sustainability (Switzerland)*, 12(3). Available at: https://doi.org/10.3390/su12030891.

Blanco-Cerradelo, L., Diéguez-Castrillón, M.I., Fraiz-Brea, J.A. and Gueimonde-Canto, A., 2022. Protected areas and tourism resources: Toward sustainable management. *Land*, 11(11). Available at: https://doi.org/10.3390/land11112059.

Booth, H., Mourato, S. and Milner-Gulland, E.J., 2022. Investigating acceptance of marine tourism levies to cover the opportunity costs of conservation for coastal communities. *Ecological Economics*, 201. Available at: https://doi.org/10.1016/j.ecolecon.2022.107578.

Borucka, A., 2020. Logistic regression in modeling and assessment of transport services. *Open Engineering*, 10(1). Available at: https://doi.org/10.1515/eng-2020-0029.

Cui, Y., 2022. Economic benefit evaluation model of urban street reconstruction based on parallel multigrid computing. *Scientific Programming*, 2022. Available at: https://doi.org/10.1155/2022/7848475.

de Araújo, A.F., Marques, M.I.A., Candeias, M.T.R. and Vieira, A.L., 2022. Willingness to pay for sustainable destinations: A structural approach. *Sustainability (Switzerland)*, 14(5). Available at: https://doi.org/10.3390/su14052548.

Del Saz-Salazar, S., González-Gómez, F. and Guardiola, J., 2015. Willingness to pay to improve urban water supply: The case of Sucre, Bolivia. *Water Policy*, 17(1). Available at: https://doi.org/10.2166/wp.2014.195.

Doran, R. and Hanss, D., 2022. Expectation of others' cooperation, efficacy beliefs, and willingness to sacrifice personal interests for the environment. *Scandinavian Journal of Psychology*, 63(4). Available at: https://doi.org/10.1111/sjop.12812.

Drašković, B. and Perović, O., 2022. Analysis of scientific and legal treatment of protected natural areas with reference to the most significant elements of the impact of tourism on the environment. *Ekonomika Poljoprivrede*, 69(1). Available at: https://doi.org/10.5937/ekopolj2201281d.

Durán-Román, J.L., Cárdenas-García, P.J. and Pulido-Fernández, J.I., 2021. Tourists' willingness to pay to improve sustainability and experience at destination. *Journal of Destination Marketing and Management*, 19. https://doi.org/10.1016/j.jdmm.2020.100540

Eckert, C. and Pechlaner, H., 2019. Alternative product development as strategy towards sustainability in tourism: The case of Lanzarote. *Sustainability (Switzerland)*, 11(13). https://doi.org/10.3390/su11133588

Fatima, T. and Elbanna, S., 2020. Balanced scorecard in the hospitality and tourism industry: Past, present and future. *International Journal of Hospitality Management*, 91. https://doi.org/10.1016/j.ijhm.2020.102656

Goffi, G., Cucculelli, M. and Masiero, L., 2019. Fostering tourism destination competitiveness in developing countries: The role of sustainability. *Journal of Cleaner Production*, 209. https://doi.org/10.1016/j.jclepro.2018.10.208

Grankvist, G., Johnsen, S. Å. K., and Hanss, D., 2019. Values and willingness-to-pay for sustainability-certified mobile phones. *International Journal of Sustainable Development and World Ecology*, 26(7). https://doi.org/10.1080/13504509.2019.1652212

Herrmann, C., Rhein, S. and Sträter, K.F., 2022. Consumers' sustainability-related perception of and willingness-to-pay for food packaging alternatives. *Resources, Conservation and Recycling*, 181. https://doi.org/10.1016/j.resconrec.2022.106219

Jabarin, A.S. and Damhoureyeh, S.A., 2006. Estimating the recreational benefits of Dibeen National Park in Jordan using contingent valuation and travel cost methods. *Pakistan Journal of Biological Sciences*, 9(12). https://doi.org/10.3923/pjbs.2006.2198.2206

Khan, N., Nguyen Thuy Van, A., Imran, A., Raza, H. and Sikandar, H., 2021. Ecotourism is the future of alternative tourism for environmental sustainability and natural areas protection. *Systematic Literature Review and Meta-Analysis Journal*, 1(2). https://doi.org/10.54480/slrm.v1i2.8

Lawton, R.N., Fujiwara, D. and Hotopp, U., 2022. The value of digital archive film history: willingness to pay for film online heritage archival access. *Journal of Cultural Economics*, 46(1). https://doi.org/10.1007/s10824-021-09414-7

López-Mosquera, N. and Sánchez, M., 2012. Theory of Planned Behavior and the Value-Belief-Norm Theory explaining willingness to pay for a suburban park. *Journal of Environmental Management*, 113. https://doi.org/10.1016/j.jenvman.2012.08.029

Ma, X., Talluri, S., Ferguson, M. and Tiwari, S., 2022. Strategic production and responsible sourcing decisions under an emissions trading scheme. *European Journal of Operational Research*, 303(3). https://doi.org/10.1016/j.ejor.2022.04.003

Matthew, N.K., Shuib, A., Ramachandran, S., Herman, S. and Nair, V., 2011. Exploring economic valuation and impact of rural tourism. *TEAM Journal of Hospitality and Tourism*, 8(1).

Murphy, S.E., Campbell, I. and Drew, J.A., 2018. Examination of tourists' willingness to pay under different conservation scenarios; Evidence from reef manta ray snorkeling in Fiji. *PLoS ONE*, 13(8). https://doi.org/10.1371/journal.pone.0198279

Plog, S. C. 1974. Why destination areas rise and fall in popularity. *Cornell Hotel and Restaurant Administration*, 14(4), pp. 55-58.

Revfine, 2021. Benefits of Sustainable Tourism Development. *www.Revfine.Com*.

Rommel, K. and Sagebiel, J., 2021. Are consumer preferences for attributes of alternative vehicles sufficiently accounted for in current policies? *Transportation Research Interdisciplinary Perspectives*, 10. https://doi.org/10.1016/j.trip.2021.100385

Saad Shbaita, A. and Gücel, S., 2022. Evaluation of Environmental Challenges of Jordan. *NEU Journal of Faculty of Architecture*, 4(1). https://doi.org/10.32955/neujfa202241492

Soejarwo, P.A., Rusdi, R., Kodiran, T. and Muawanah, U., 2021. Estimation of communities and tourists willingness to pay for tsunami disaster mitigation of marine tourism in the Kalianda Coastal Area, South Lampung Regency. *Jurnal Ilmu Lingkungan*, 19(1). https://doi.org/10.14710/jil.19.1.1-9

Sudipa, N., Mahendra, M.S., Adnyana, W.S. and Pujaastawa, I.B., 2020. Tourism impact on the environment in Nusa Penida tourism area. *Journal of Environmental Management and Tourism*, 11(1). https://doi.org/10.14505/jemt.11.1(41).13

Taamneh, M.M., Almaaitah, M.F. and Alqdha, H.M., 2020. Challenges facing local government in Jordan and strategies to address them. *Problems and Perspectives in Management*, 18(3). https://doi.org/10.21511/ppm.18(3).2020.33

Thoma, J., 2021. In defence of revealed preference theory. *Economics and Philosophy*, 37(2). https://doi.org/10.1017/S0266267120000073

Tu, H.M., 2020. Sustainable heritage management: Exploring dimensions of pull and push factors. *Sustainability (Switzerland)*, 12(19). https://doi.org/10.3390/su12198219

UNWTO World Tourism Barometer and Statistical Annex, January 2023. 2023. *UNWTO World Tourism Barometer*, 21(1). https://doi.org/10.18111/wtobarometereng.2023.21.1.1

Yanes, A., Zielinski, S., Cano, M.D. and Kim, S.Il., 2019. Community-based tourism in developing countries: A framework for policy evaluation. *Sustainability (Switzerland)*, 11(9). https://doi.org/10.3390/su11092506

ORCID DETAILS OF THE AUTHORS

I. N. Abuamoud: https://orcid.org/0000-0002-6029-7817

Evaluating the Tolerance and Dust Capturing Capacity of Tree Species Affected by Coal Dust Polluted Area

Kamesh[1], Brijendra Pratap Singh[1†], Shailly Misra[2] and Ramesh[1]

[1]Department of Forestry, Wildlife and Environmental Sciences, Guru Ghasidas Vishwavidyalaya (A Central University), Bilaspur, Chhattisgarh, 495009, India

[2]Department of Botany, University of Lucknow, Lucknow, Uttar Pradesh, 226026, India

†Corresponding author: Brijendra Pratap Singh; p.brijendra@gmail.com

ABSTRACT

The air pollution tolerance index (APTI) of any plant shows the tolerance capacity of plant against the air pollution. The present study exhibited the APTI and API of twenty-two trees present on the roadside coal dust-affected air pollution area of Chhal, Raigarh. APTI consists of the analysis of leaf extract pH, relative water content, total chlorophyll content, and ascorbic acid of leaves while the API consists of the APTI values of trees, morphological characteristics, and socio-economic attributes of trees. The leaf extract pH was observed to range from 6.61 ± 0.11 - 3.28 ± 0.11, relative water content from 95.4±0.4 - 83±0.89 %, total chlorophyll content from 1.16±0.06 - 0.385±0.04 mg g^{-1} and ascorbic acid from 30.54±0.67 - 10.61±0.84 mg g^{-1}. The highest APTI was 30.88±0.75 for *Tectona grandis* while the lowest was observed 15.58±0.54 for *Alstonia scholaris*. The highest API value 93.75% for *Shorea robusta* and *Ficus religiosa* was observed. The maximum dust held by a tree on the leaf surface by *Shorea robusta* (3.18 ± 0.09 mg cm^{-2}) was recorded. *Shorea robusta, Mangifera indica, Schleichera oleosa, Terminalia ballerica, Ficus benghalensis, Anthocephalus cadamba, Ficus religiosa, Peltophorum pterocarpum, Madhuca indica,* and *Terminalia tomentosa* are best performers among the selected tree species and suitable for the plantation of trees surrounding of air polluted zones.

INTRODUCTION

Urban air pollution is an ongoing problem that affects the country that is developing as well as developed, exerting a negative impact on the ecosystem (Rai et al. 2013). The concentration of gaseous and particle pollution appears to have increased over the last several decades due to continued growth in the human population, vehicle traffic, and industry (Krishnaveni & Lavanya 2014). Transportation plays the monster in air pollution (Sharma et al. 2017). India ranks third in the world for having worse air quality. Worldwide, it emits almost 305.3 $MtCO_2$, which is 0.64 percent of total GHG emissions. Only 5% of heavy-duty vehicles in India still account for 71% of the nation's CO_2 emissions and 74% of its particulate matter (https://www.ceew.in/cef/quick-reads/explains/vehicular-emissions-in-india). There is plenty of research on the initial impact of industrialized and urbanized emissions on human health (Singh et al. 2018). No mechanical or chemical technique exists that can completely obstruct pollutants that are emitted at the source. The discharge of contaminants into the atmosphere and the degradation of air quality around roadsides have an impact

on the morphology and biochemical parameters of the plants (Kaur & Nagpal 2017). As plants are the main pollution receptors, they are often employed for analysis (Rai et al. 2013). Plants are essential for enhancing air quality because they absorb gases and particulates (Kaur & Nagpal 2017). Additionally, plants scavenge a variety of airborne particles in the environment (Sharma et al. 2019).

The inherent quality of plants to tolerate air pollution is called the air pollution tolerance index (APTI) and may assist in choosing the kinds of trees to be planted near or around polluted zones.

Plant species with greater APTI values that are tolerant seem to be buffers, whereas species with a smaller value might be useful for biomonitoring (Sahu et al. 2020). Uka et al. (2019) classified plants into different categories based on their APTI value i.e., tolerant (>17), intermediate (12-16), and sensitive (<12). This statistic might be used to grow trees in various polluted locations so they are capable of encountering air pollution (Kumari & Deswal 2017). While assessing plant responses against air pollution for green belt development may not be appropriate with a single physiological parameter

estimate, the complex combination of APTI and API may have substantial implications (Ogunkunle et al. 2015). An API value can provide a reasonable answer for expanding the green belt, planting trees, and restoration because it consists of the ecological and socioeconomic characteristics of the tree species as well as APTI values (Sahu & Sahu 2015, Bora & Josi 2014). Yadav & Pandey (2020) examined the APTI and API values of several trees to choose tolerant plants that would be good for the growth of greenery in Bhatinda city's regions impacted by air pollution from traffic and industry. To suggest tolerant plants for landscaping, Sharma et al. (2019) looked at the APTI of a selection of tree species that were found alongside the National Highway-5 Solan. Trees perform as a significant pollution absorber; they are the most effective at capturing and absorbing a wide range of particulates. Plant height, density, size, age, leaf area, canopy structure, leaf inclination, exterior characteristics, and climatic conditions all affect a plant's ability to accumulate dust (Roy et al. 2020).

Raigarh is famous for several coal mines and thermal power plants and the extraction of coal from mine expansion increasing day by day. The coal used by many industries such as iron melting and thermal power plants and trucks and railways are the main transportation sources used to transport coal from mines to industries. Transportation of coal through heavy trucks produces coal dust air pollution on the roadside and the surrounding environment. Wide ranges of tree species are present on the roadside either planted or naturally. They provide a barrier to the expansion of air pollution by trapping air pollutants on the leaf surface. This study examined the tolerance capacity of trees against coal dust air pollutants around the roadside of SH-18 near Chhal, Raigarh. Chhal is famous for its open-cast coal mine project. The forests of the area are tropical, moist, and dry deciduous types of forests. Many tree species are highly beneficial for rural livelihood; they include mahua flowers, mahua seeds, kusum seeds, tendu leaves, sal seeds, char seeds, and amchur which are collected from the surrounding forest.

MATERIALS AND METHODS

The study was conducted along the roadside of State Highway-18, Chhal (India), situated at latitude 22.1105858° N and longitude 83.1222833° E (Fig. 1). The climate of the study area in the summer is much warmer (45°C–50°C), and in the winter is much colder (11°C–20°C), with 1225 mm of rainfall over a year.

Twenty-two tree species were selected, which frequently occurred along the roadway (Table 1). Tree species were selected based on abundance in the area, socioeconomic significance to the local populace, and ease of sample collection. The morphology of the tree (tree height, diameter, age) was also observed. The sampling was done from July to October 2022. Freshly, green mature leaves of trees
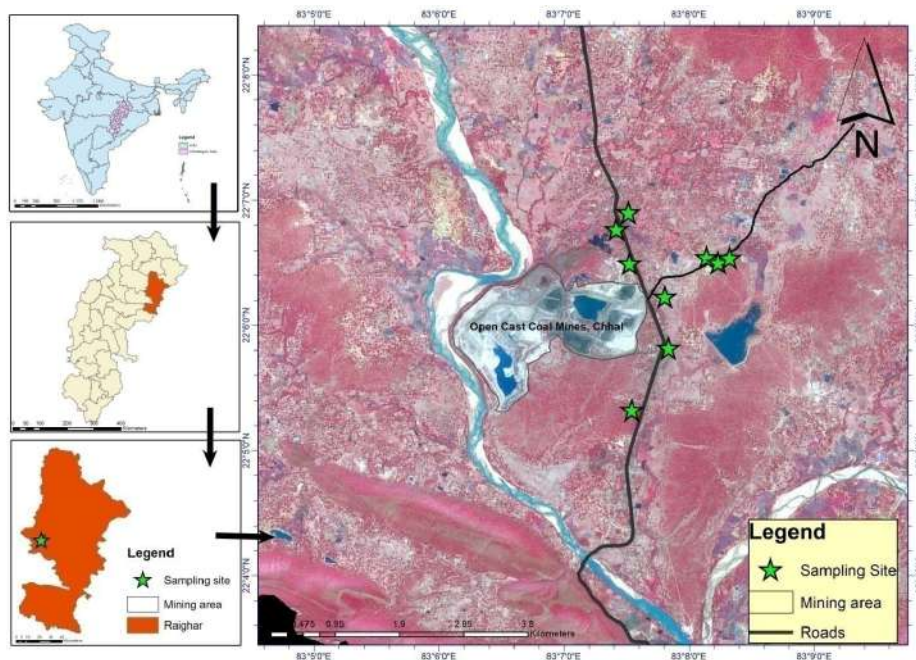

Fig. 1: Map of the study area.

Table 1: Description of tree species.

Sn	Tree species	Family	Description of tree
1	*Shorea robusta*	Depterocarpaceae	*Sal* is a semi-deciduous woody tree
2	*Bombax ceiba*	Malavaceae	*Semul* extremely large, tropical deciduous tree.
3	*Mangifera indica*	Anacardiaceae	*Mango* is a large, erect-bunch nature, evergreen fruit tree.
4	*Alstonia scholaris*	Apocynaceae	*Satparni* is an evergreen glabrous tree.
5	*Millettia pinnata*	Fabaceae	*Karanj* is a medium-sized semi-evergreen glabrous tree.
6	*Schleichera oleosa*	Sapindaceae	*Kusum* occurs in dry and mixed deciduous forests.
7	*Cassia seamia*	Fabaceae	*Kassod* is a medium-sized evergreen tree.
8	*Zyzyphus mauritiana*	Rhamnaceae	*Ber* is a medium-sized, evergreen, prickly tree.
9	*Butea monosperma*	Fabaceae	*Palash* is a medium-sized deciduous tree.
10	*Ailanthus excelsa*	Simaroubaceae	*Maharukh* is a huge deciduous tree.
11	*Sysygium cuminii*	Myrtaceae	*Jamun* evergreen - tropical tree.
12	*Buchanania lanzan*	Anacardiaceae	*Chironji* is a sub-deciduous tree.
13	*Terminalia bellirica*	Combrataceae	*Harra* is a deciduous tree.
14	*Ficus benghalensis*	Moraceae	*Bargad* is a huge-spread evergreen tree.
15	*Azadirachta indica*	Meliaceae	*Neem* is a medium height-evergreen tree, termite-resistant wood.
16	*Anthocephalus cadamba*	Rubiaceae	*Kadamba* is a mid-huge deciduous tree.
17	*Ficus religiosa*	Moraceae	*Peepal* is a large, semi-evergreen tree.
18	*Tectona grandis*	Lamiaceae	*Sagon* is a tall and gorgeous tree.
19	*Peltophorum pterocarpum*	Fabaceae	*Yellow gulmohar* is a semi-evergreen tree.
20	*Madhuca indica*	Sapotaceae	*Mahua* is a mid-sized to large tropical deciduous tree.
21	*Albizia procera*	Fabaceae	*Safed siris* is an exposed crown semi-deciduous tree.
22	*Terminalia tomentosa*	Combrataceae	*Saja* is a large deciduous tree.

were collected from the roadside in the early morning at the lower branches (at a height of 2-4 m). Leaves samples were collected and bagged in polythene, quickly transferred to the laboratory, and kept in refrigerator (3-5°C) for analysis.

Ascorbic Acid Analysis (AA)

The AA was analyzed by using the 2, 6 dichlorophenol Indephenol dye titration methods (Roy et al. 2020). 1gm of leaf sample was crushed with a 4% oxalic acid addition and centrifuged for 10 minutes at 3000 rpm. The centrifuged sample was filtered, and the made-up volume was 25 mL with 4% oxalic acid added. 5 mL of leaf sample was pipette out with 10 mL of oxalic acid (4%) and titrated against the dye. Titration was stopped when a pink color appeared.

$$AA \text{ (mg g}^{-1}) = \frac{0.5 * V2 * 25 \text{ mL} * 100}{V1 * 5\text{mL} * \text{Weight of sample (g)}}$$

Here, V1 is the volume of dye titrated against the ascorbic acid working standard.

V2 is the volume of dye titrated against the sample.

Relative Water Content (RWC)

The RWC was formulated by taking the fresh weight (FW), turgid weight (TW), and dry weight (DW) of a leaf sample (Kaur & Nagpal 2017).

$$\text{RWC (\%)} = \frac{\text{FW} - \text{DW}}{\text{TW} - \text{DW}} \times 100$$

Leaf Extracts pH

A digital pH meter was used to analyze the pH of the leaf extract. 0.5 g of leaf sample was crushed using a mortal pestle, and pH was analyzed (Singare & More 2020).

Total Chlorophyll Content (TCC)

The TCC was analyzed using the 80% acetone method using a spectrophotometer (Roy et al. 2020). 0.5 g of leaf sample was crushed with 80% acetone and centrifuged with the extract (at 3000 rpm for 10 min.) and makeup sample for 25 mL. The absorbance of the supernatant was analyzed at 663nm and 645nm through a spectrophotometer.

$$TCC \text{ (mg g}^{-1}) = \frac{(20.2 * A\ 645 + 8.02 * A\ 663) * V}{1000 * \text{Weight of sample (g)}}$$

Here, A 645 is the absorbance at 645 nm, A 663 is the absorbance at 663 nm, and V is the volume of the sample.

Air Pollution Tolerance Index (APTI)

The APTI was demonstrated by the following equation (Sharma et al. 2019).

$$APTI = \frac{AA\,(TCC+pH)+RWC}{10}$$

Here, AA= Ascorbic acid (mg g^{-1})

TCC= Total chlorophyll content (mg g^{-1})

pH= pH of leaf extract

RWC= Relative water content (percentage)

Anticipated Performance Index

API was determined by encompassing the biological features of the tree, such as tree habit, tree type, structure of the canopy, and structure of the lamina, along with the air pollution tolerance index of each tree (Table 2). The highest plus that can be received for any tree species is 16 (Yadav & Pandey 2020). The score percentage can be categorized as:

$$Score\ \% = \frac{Total\ (+)\ recieved\ by\ tree\ species}{16} \times 100$$

Dust Capturing Capacity

Dust deposition on the surface of the leaf was determined (Rai & Panda 2014, Noor et al. 2015). The amount of dust was calculated for twenty-two tree species by taking the initial and final weight of the beaker in which the leaf samples were washed. It is expressed in milligrams per square centimeter (mg cm^{-2}) and calculated by using the formula as follows:

Dust capturing capacity =

$$\frac{Weight\ of\ leaf\ with\ dust\ (milligrams) - Weight\ of\ leaf\ without\ dust(milligrams)}{Total\ area\ of\ leaf\ (centimeter\ square)}$$

Statistical Analysis

A one-way ANOVA at a 5% level of significance was used (SPSS software IBM version 16.0). For all variables, the mean with a standard error of five replicated values was used

Table 2: Gradation of tree species based on the anticipated performance index values (Sharma et al. 2019, Uka et al. 2019).

SN	Grading characters		Pattern of Assessment	Grading allotted
1	Tolerance	APTI	< 5	+
			5.1 -10	++
			10.1 – 15	+++
			15.1 -20	++++
			>20	+++++
2	Biological and socioeconomic	Tree Height	Small	-
			Medium	+
			Large	++
		Canopy structure	Sparse/irregular/globular	-
			Spreading crown/open/semi-dense	+
			Spreading dense	++
		Type of tree	Deciduous	-
			Evergreen	+
3	Lamina structure	Size	Small	-
			Medium	+
			Large	++
		Texture	Smooth	-
			Cariaceous	+
		Hardness	Delineate	-
			Hardy	+
4	Socio-economic importance	Economic value	<3 uses	-
			3 – 4	+
			>5 uses	++

to indicate all of the results. The degree of interaction among the variables was calculated using the linear regression analysis.

RESULTS AND DISCUSSION

Green plants release huge quantities of oxygen into their environment, which enhances the quality of the air in a particular area through adsorption, absorption, accumulation, and purification of pollutants. They function as living filters that mitigate air pollution with no adverse effects (Kaur & Nagpal 2017).

Tree Growth Characteristics

Table 3 shows the growth characteristics of selected trees. The highest girth (m) was recorded for *Schlecharia oleosa* (4.32±0.21), and the lowest was reported for *Zyzyphus mauritiana* (0.69±0.01). The highest tree diameter (cm) was observed for Shorea robusta (90.94±3.18) and the lowest for *Zyzyphus mauritiana* (21.89±0.48). The maximum tree height (m) received was Shorea robusta (26.38±0.23), and the minimum was *Alstonia scholaris* (8.12±0.12). The maximum tree age (year) received by Madhuca indica was about

110.2±2.4, and the minimum was 11.6±0.51 for *Alstonia scholaris*. The maximum leaf area (cm^2) was recorded for *Tectona grandis* (293.6±0.87), and the minimum was *Albizia procera* (5.2±0.37). In the present study, tree growth parameters such as girth, diameters, height, age, and leaf area differed because all tree species have their phenological characteristics, like some trees being very tall and others having a slow growth rate (Nayak et al. 2015). The leaf area of *Tectona grandis* is relatively higher than that of the other tree species because it's larger in leaf size.

Relative Water Content

In the results of the current study, RWC fluctuated significantly ($P<0.05$) for all types of trees. The highest percentage of RWC was recorded for *Ficus religiosa* (95.4±0.4) and the lowest was recorded for *Azadirachta indica* (83±0.89) as shown in Table 4. Amulya et al. (2015) revealed that plant leaves provide the most RWC in areas affected by air pollution. Under exposure to air pollution, the increases in transpiration rates therefore plants get higher water content to maintain their physiological process (Rai et al. 2013, Kumar et al. 2018). At the very low relative

Table 3: Growth parameters of selected trees.

Tree Species	Girth (meter)	Diameter (centimeter)	Height (meter)	Age (Year)	Leaf Area (cm^{-2})
Shorea robusta	2.86±0.1	90.94±3.18	26.38±0.23	84.2±1.16	112±0.71
Bombax ceiba	1.27±0.02	40.35±0.63	13.05±0.23	14.4±0.51	95.2±0.58
Mangifera indica	2.21±0.03	70.32±1.06	15.96±0.39	41.6±0.81	80±0.71
Alstonia scholaris	0.84±0.02	26.73±0.61	8.12±0.12	11.6±0.51	64.2±0.37
Millettia pinnata	1.44±0.03	45.82±1.01	10.09±0.24	28.6±0.51	99±0.84
Schlecharia oleosa	4.32±0.21	137.58±6.78	17.41±0.18	66.4±0.75	213.2±0.97
Cassia seamia	0.79±0.02	25.26±0.69	12.47±0.28	21.4±0.75	9.4±0.51
Zyzyphus mauritiana	0.69±0.01	21.89±0.48	8.32±0.19	18.4±0.51	5.2±0.58
Butea monosperma	1.39±0.06	44.36±1.83	11.37±0.23	21.2±0.58	194.8±0.58
Ailanthus excelsa	1.91±0.05	60.77±1.7	17.99±0.19	15.8±0.37	156.4±0.93
Sysygium cuminii	1.55±0.11	49.26±3.42	15.6±0.31	27.4±1.03	86.2±0.86
Buchanaia lanzan	0.82±0.05	25.96±1.5	14.2±1.57	15.2±0.58	112.2±0.86
Terminalia bellirica	1.41±0.02	44.8±0.58	13.05±0.19	74.8±1.32	90.4±0.93
Ficus benghalensis	2.71±0.05	86.36±1.44	12.18±0.33	62.2±1.16	156±0.71
Azadirachta indica	1.49±0.06	47.28±1.86	12.89±0.31	32.6±0.98	19±0.71
Anthocephalus cadamba	1.02±0.08	32.52±2.69	15.34±0.19	15.2±0.66	77.6±0.93
Ficus religiosa	1.65±0.05	52.5±1.5	10.69±0.23	74.8±0.97	111±0.71
Tectona grandis	0.74±0.03	23.55±0.97	12.4±0.35	24.8±0.66	293.6±0.87
Peltophorum pterocarpum	1.29±0.07	41.05±2.29	12.61±0.3	14.6±0.24	48±0.71
Madhuca indica	2.65±0.06	84.45±1.99	15.4±0.18	110.2±2.4	105±0.71
Albizia procera	0.73±0.05	23.1±1.71	10.5±0.24	14±0.45	5.2±0.37
Terminalia tomentosa	1.68±0.04	53.58±1.17	21.32±0.44	33.8±0.58	77.2±0.97

water content, the net CO_2 exchange, CO_2 assimilation, and photosynthetic rate ultimately obtain low. A greater RWC enhances the capacity of a plant to tolerate air pollution (Nayak et al. 2015). Many investigations conducted by researchers show that the relative water content of trees increases in response to pollution, and the RWC varies at different pollution levels. The accumulation of dust on roadside tree leaves is exacerbated by heavy traffic. A similar investigation was reported by Govindaraju et al. (2012) relative water content (%) 95.14 ± 2.81 for *Ficus religiosa* and 79.85 ± 1.49 for *Azadirachta indica*. The higher relative water content showed maximum drought tolerance capacity.

Leaf Extracts pH

The study exhibited variations in leaf extract pH significantly (P<0.05) for different tree species. The highest leaf extract pH was observed at 6.61±0.11 for *Albizia procera* and the lowest was 3.28±0.11 for *Cassia seamia* while most of the tree species showed an acidic nature of leaf pH (Table 4). The lowest pH value indicates that the tree has better tolerance than other trees. The regulation of plant potential for pollution is significantly influenced by pH level. The diffusion of gaseous air pollutants like NO_2, CO_2, and SO_2 in the cell sap and their subsequent conversion into acid and electrons may be due to the acidic pH. Gaseous SO_2 diffuses through cellular pores (stomata) and dissolves in water to create sulfites, bisulfate, and their ionic species. This process generates protons, which, in turn, affect the pH of cells (Sharma et al. 2019, Noor et al. 2015). High pH increases ascorbic acid synthesis in plants and increases their resistance to air pollution, while low pH inhibits the breakdown of the hexose sugar into ascorbic acid. Ogunrotimi et al. (2017) showed a similar result for *Cassia seamia* (4.62) in polluted sites of Lle Lfe City, Southeast Nigeria. A result was reported on pH 3.96 for *Cassia seamia* in the industrial polluted site in Ludhiana, India (Verma et al. 2023). The pH of leaf extracts is crucial in controlling plants' sulfur dioxide conductivity (Maawali & Sulaiman 2017). A result of acidic pollutants like SO_2 and NO_x in the surrounding air, this influences the pH of the leaf (Swami & Chauhan 2015). Low leaf pH extract exhibited a strong association with air pollution due to its reactivity and also

Table 4: Biochemical response of selected tree species.

Tree Species	pH	Relative Water Content (%)	Total Chlorophyll content (mg.g^{-1})	Ascorbic acid (mg.g^{-1})	APTI
Shorea robusta	5.5±0.05	92.8±0.86	1.16±0.06	15.1±0.84	19.34±0.58
Bombax ceiba	5.45±0.09	90.8±0.58	0.85±0.02	15.76±0.91	19.01±0.48
Mangifera indica	5.18±0.07	91.4±0.51	0.534±0.02	16.38±0.87	18.49±0.44
Alstonia scholaris	5.85±0.1	87.8±0.58	0.56±0.09	10.61±0.84	15.58±0.54
Millettia pinnata	6.29±0.07	91.2±0.58	0.718±0.04	11.01±0.77	16.85±0.59
Schlecharia oleosa	6.25±0.09	87.2±0.58	0.385±0.04	11.81±0.78	16.56±0.53
Cassia seamia	3.28±0.11	92.2±0.58	0.465±0.02	18.95±0.94	16.28±0.3
Zyzyphus mauritiana	6.5±0.12	90±0.55	0.937±0.02	12.9±0.68	18.62±0.62
Butea monosperma	6.58±0.11	85.2±0.58	0.552±0.02	10.71±0.74	16.16±0.59
Ailanthus excelsa	6.19±0.07	89.2±0.86	0.908±0.03	18.38±0.91	21.95±0.59
Sysygium cuminii	4.61±0.09	91.8±0.73	0.402±0.02	14.7±0.84	16.54±0.41
Buchanaia lanzan	4.82±0.05	91.8±0.58	0.749±0.07	17.86±0.68	19.12±0.37
Terminalia bellirica	4.79±0.12	84.6±0.51	0.603±0.05	19.18±0.59	18.77±0.68
Ficus benghalensis	6.38±0.06	91±0.71	0.777±0.03	20.75±0.72	23.94±0.48
Azadirachta indica	6.6±0.04	83±0.89	0.644±0.03	28.46±0.63	28.91±0.42
Anthocephalus cadamba	4.56±0.12	94.6±0.51	0.578±0.06	24.52±0.81	22.06±0.6
Ficus religiosa	6.56±0.06	95.4±0.4	0.732±0.01	17.98±0.54	22.65±0.4
Tectona grandis	6.53±0.13	91.2±0.86	0.755±0.04	30.36±0.9	30.88±0.75
Peltophorum pterocarpum	6.48±0.08	92±0.71	0.845±0.05	24.52±0.77	27.16±0.57
Madhuca indica	6.58±0.06	84.2±0.86	0.828±0.02	23.81±0.69	26.08±0.7
Albizia procera	6.61±0.11	92±0.89	0.813±0.02	25.79±0.34	28.34±0.06
Terminalia tomentosa	5.48±0.08	88.4±0.87	0.475±0.04	30.54±0.67	26.95±0.32

reduced photosynthesis by modifying the stomatal activity (Sharma et al. 2019, Rai & Panda 2014). Chauhan et al. (2012) showed that the plants at the mining site had lower pH within leaf sap, which may have been caused by the SO_2 and NO_x levels in the surrounding atmosphere. It also affects the chlorophyll content in the leaves; reducing in lower leaf extract pH (Kamesh et al. 2023, Shah et al. 2020).

Total Chlorophyll Content

Table 4 shows the total chlorophyll content of leaves (mg g^{-1}) for selected tree species and showed significant (P<0.05) differences for each tree species. The maximum chlorophyll content was received at 1.16±0.06 mg g^{-1} for *Shorea robusta* and the lowest was 0.385±0.04 mg g^{-1} for *Schleichera oleosa*. While the maximum tree species showed relatively lower total chlorophyll content in the study area. Dust content on the surface of leaves is the main barrier to the reaching of sunlight for chlorophyll pigments present in the leaves. One of the most harmful effects of abiotic stress is the reduction of photosynthesis. The principal effect of stress on plants is damage to chloroplasts, a sign of the breakdown of pigments in the leaves (Shah et al. 2020). The chlorophyll pigment converts solar energy into chemical energy that plant cells can utilize as a source of food. An air pollutant that includes SO_2, NO_2, CO_2, and suspended particulate matter might enter organs from stomata and partly disintegrate chloroplasts, which can reduce the chlorophyll concentration (Shrestha et al. 2021). Plant production and, consequently, their ability to withstand air pollution both decline when chlorophyll concentration falls. Less chlorophyll implies that plants are far more sensitive to polluted air. Bhattacharya et al. (2013) recorded that the chlorophyll content of leaves decreases in polluted sites, and found that the photosynthesis of plant systems has begun to deteriorate as pollution levels reach every year (Kumari & Deswal 2017).

Ascorbic Acid

The ascorbic acid of leaves (mg g^{-1}) for selected tree species observed differs significantly (P<0.05) level of significance. The maximum ascorbic acid content of was observed for *Terminalia tomentosa* (30.54±0.67 mg g^{-1}) and the minimum was *Alstonia scholaris* (10.61±0.84 mg g^{-1}) as shown in Table 4. Living cells need ascorbic acid for survival. Therefore, it has been shown that plants with low ascorbic acid concentrations are less tolerant of stress (Shah et al. 2020). Although it participates in various physiological processes, and highly significant organic antioxidant for plants to function properly. It has a powerful reductant, and electron donor, removes imbalanced oxidative stress, and decreases the toxicity of SO_2. When a plant suffers from stress condition, the plant produces more ascorbic

acid to combat the stress condition (Bhattacharya et al. 2013). Under stressful conditions, ascorbic acid, an effective antioxidant, protects plant cell division and cell membrane stability by absorbing harmful free radicals and reactive oxygen released when protoxidized from SO_2 to SO_3. In the present study tree species such as *Ficus benghalensis*, *Azadirachta indica*, *Anthocephalus cadamba*, *Tectona grandis*, *Peltophorum pterocarpum*, *Madhuca indica*, *Albizia procera*, and *Terminalia tomentosa* showed >20 mgg^{-1} ascorbic acid which was relatively higher than other trees. The results of this investigation accord closely with the findings (Ogunkunle et al. 2015, Bora & Josi 2014, Pandey et al. 2015). Plants become more tolerant of a contaminated environment as the ascorbic content in their leaves rises. Air pollution tolerance is significantly influenced by ascorbic acid's capacity to shield plant tissues from the damaging effects of air pollutants (Shrestha et al. 2021).

Air Pollution Tolerance Index

The air pollution tolerance index significantly differed (P<0.05) with tree species. The highest APTI was 30.88±0.75 for *Tectona grandis* followed by *Azadirachta indica*> *Albizia procera*> *Peltophorum pterocarpum*> *Terminalia tomentosa*> *Madhuca indica*> *Ficus benghalensis*> *Ficus religiosa*> *Anthocephalus cadamba*> *Ailanthus excelsa*> *Shorea robusta*> *Buchanaia lanzan*> *Bombax ceiba*> *Terminalia bellirica*> *Zyzyphus mauritiana*> *Mangifera indica*> *Millettia pinnata*> *Schlecharia oleosa*> *Sysygium cuminii*> *Cassia seamia*> *Butea monosperma* while lowest was 15.58±0.54 for *Alstonia scholaris* as shown in Table 4. Results were reported by Das et al. (2010) for the industrial area of Rourkela with a 10.77 APTI value for *Alstonia scholaris*, while the unlike findings for *Tectona grandis* 8.86 APTI value. Take & Kadke (2017) reported an APTI value of 14.6 for *Tectona grandis* and 13.09 for *Alstonia scholaris*. These findings could be accounted for by the potential that plants differentiate geographically and climatically from one place to another. It also fluctuates due to variations in humidity, temperature, air quality, etc. (Kosanic et al. 2018).

The tree species have been divided into three groups by different studies using the APTI: tolerant, intermediate, and sensitive (Uka et al. 2019, Padmavathi et al. 2013). Trees with an APTI value of <12 are deemed sensitive, trees with a value between 12 and 17 are classified as intermediate, and trees with an APTI value of >17 are viewed as tolerant (Uka et al. 2019, Bharti et al. 2018). In the present study the *Shorea robusta, Bombax ceiba, Mangifera indica, Zyzyphus mauritiana, Ailanthus excelsa, Buchanaia lanzan, Terminalia bellirica, Ficus benghalensis, Azadirachta indica, Anthocephalus cadamba, Ficus religiosa, Tectona grandis, Peltophorum pterocarpum, Madhuca indica, Albizia procera,*
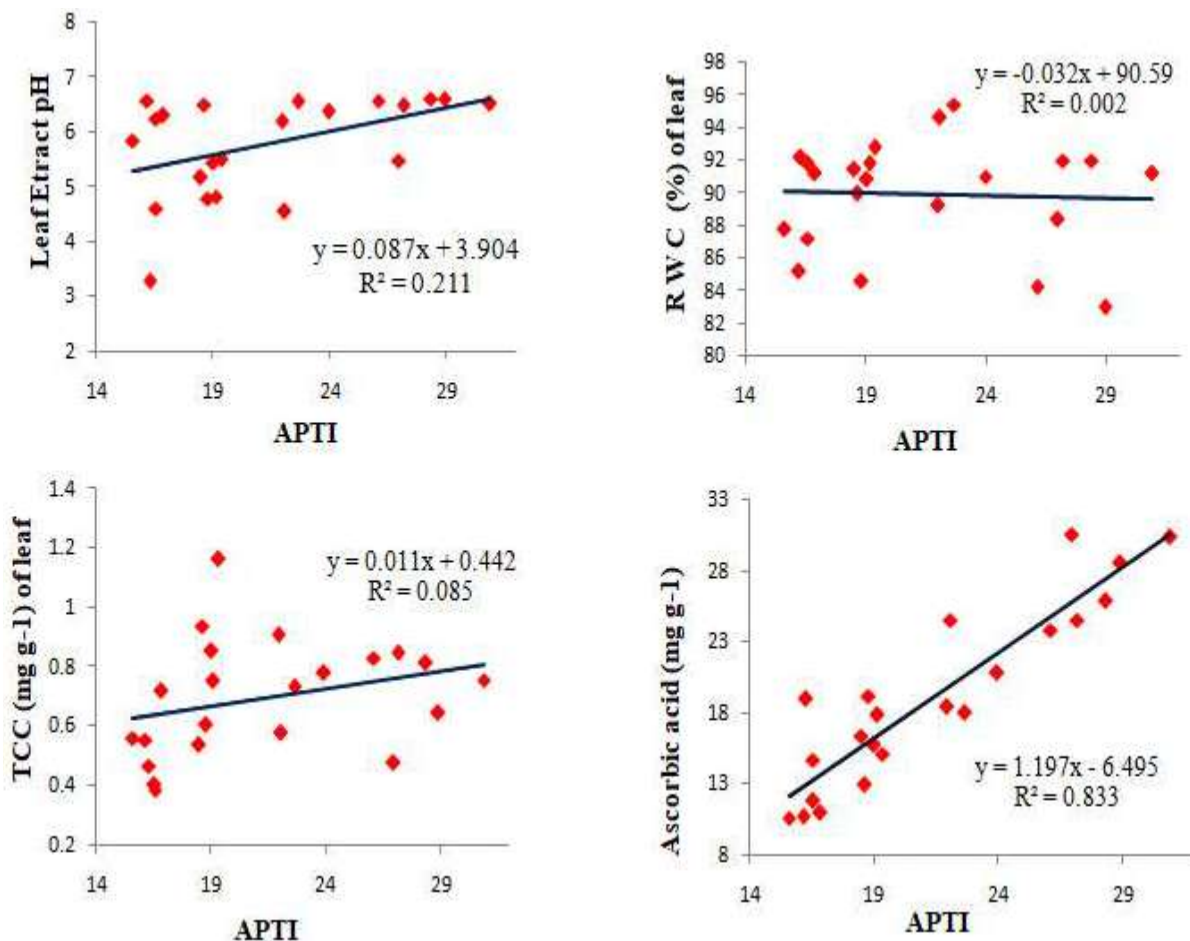
Fig. 2: Linear regressions between APTI and leaf biochemical parameters.

and *Terminalia tomentosa* showed tolerance response against coal dust air pollution and may be adopted for plant barriers to traffic pollution as well as for the establishment of urban green belts (Shrestha et al. 2021). Whereas, *Alstonia scholaris, Millettia pinnata, Schlecharia oleosa, Cassia seamia, Butea monosperma*, and *Sysygium cuminii* showed intermediate tolerance response against coal dust air pollution used a kind of bio-indicator as well as tolerant tree for air pollution.

The correlation between leaf extract pH, relative water content, total chlorophyll content of leaves, ascorbic acid content, and air pollution tolerance index (APTI) was displayed using linear regression analysis as shown in (Fig. 2). There was a marginally weak correlation between the chlorophyll content (R2 = 0.085), the leaf extract pH (R2 = 0.211), and the relative water content (R2 = 0.002). While a strong positive correlation was observed between ATPI and leaf ascorbic acid (R2 = 0.833). As a means to alleviate the stressed condition in the environment, the ascorbic acid level

in tree leaves increases. Under stressful conditions, ascorbic acid, an effective antioxidant, protects plant cell division and cell membrane stability by absorbing harmful free radicals and reactive oxygen released when protoxidized of SO_2 to SO_3 (Uka et al. 2019, Rai & Panda 2014, Kamesh et al. 2023, Wang & Chen 2021). Similar correlations between APTI and biochemical parameters were found in several other studies (Nayak et al. 2015, Noor et al. 2015, Bharti et al. 2018).

Dust Capturing Capacity of Leaf

The dust-capturing capacity of the leaf significantly differs (P<0.05) for all species. Fig. 3 showed the highest dust-capturing capacity of the leaf surface 3.18±0.09 mg cm^{-2} for *Shorea robusta* and 0.032 mg/cm^{-2} for *Terminalia bellirica*. The size of the leaf and the properties of the leaf surface of a tree species are linked to its ability to trap and hold dust (Krishnaveni & Lavanya 2014). Moreover, leaf surface attributes like toughness, hairiness, and cuticle attributes significantly affect the ability of any species to capture dust.
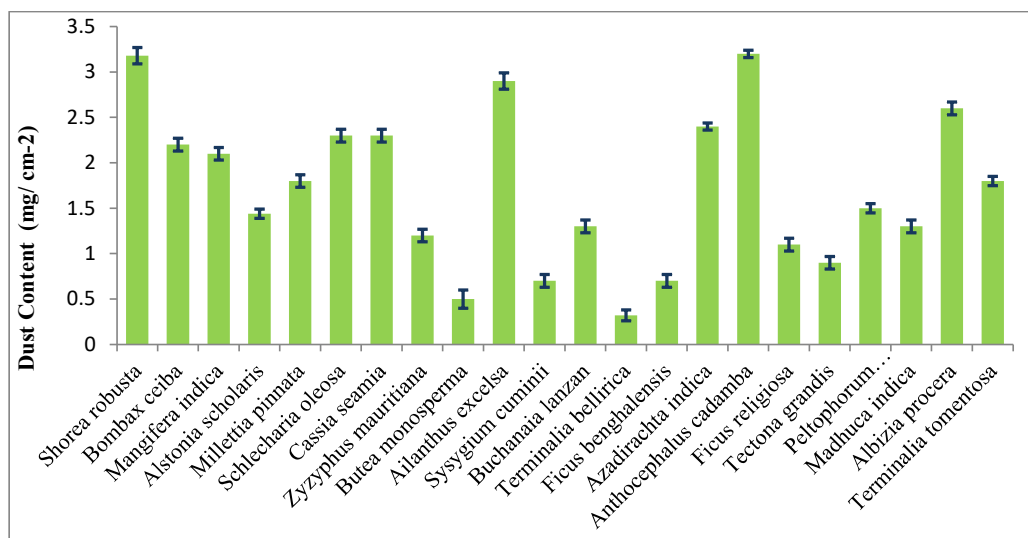
Fig. 3: Representation of dust content on the surface of the leaf for selected tree species.

Table 5: Evaluation of trees based on their APTI values and some biological and socioeconomic characteristics.

Tree species	APTI	Morphological			Laminar Structure			EI	Grade allotted		API value	Assessment
		TH	CS	TT	TX	SZ	HD		Total +	Score %		
Shorea robusta	++++	++	++	+	+	++	+	++	15	93.75	7	Best
Bombax ceiba	++++	++	+	-	+	++	+	+	12	75	5	Very Good
Mangifera indica	++++	+	++	+	+	++	+	++	14	87.5	6	Excellent
Alstonia scholaris	++++	+	-	+	+	++	+	+	11	68.75	4	Good
Millettia pinnata	++++	+	+	+	+	++	+	+	12	75	5	Very Good
Schleichera oleosa	++++	++	++	+	+	++	+	+	14	87.5	6	Excellent
Cassia siamea	++++	+	+	+	+	+	+	+	11	68.75	4	Good
Ziziphus mauritiana	++++	+	+	+	+	+	+	++	12	75	5	Very Good
Butea monosperma	++++	+	-	-	+	++	+	+	10	62.5	4	Good
Ailanthus excelsa	++++	++	-	-	+	+	+	+	10	62.5	4	Good
Syzygium cumini	++++	+	+	+	+	++	+	+	12	75	5	Very Good
Buchanaia lanzan	++++	+	-	-	+	++	+	+	10	62.5	4	Good
Terminalia bellirica	++++	+	+	+	+	++	+	++	13	81.25	6	Excellent
Ficus benghalensis	+++++	++	++	+	+	++	+	++	16	100	7	Best
Azadirachta indica	+++++	+	+	+	-	+	+	++	12	75	5	Very Good
Anthocephalus cadamba	+++++	++	+	+	+	++	+	+	14	87.50	6	Excellent
Ficus religiosa	+++++	++	++	+	-	++	+	++	15	93.75	7	Best
Tectoana grandis	+++++	++	-	-	-	++	+	+	11	68.75	4	Good
Peltophorum pterocarpum	+++++	+	++	+	+	+	+	+	14	87.50	6	Excellent
Madhuca indica	+++++	+	+	-	+	++	+	++	13	81.25	6	Excellent
Albizia procera	+++++	++	+	+	+	+	+	-	12	75	5	Very Good
Terminalia tomentosa	+++++	++	+	-	+	++	+	++	14	87.50	6	Excellent

TH tree height, CS canopy structure, TT type of tree, TX texture, SZ leaf size, HD hardness, EI economic importance

Because long petioles cause the leaves to swing rapidly in gusts of wind, they are less effective at catching dust (Rai & Panda 2014, Noor et al. 2015, Wang & Chen 2021). The dust content on the leaf also depends on the number of vehicles running in the area and the presence of dust on the ground. Those tree species with greater capacity to trap dust contribute to the reduction of fine particles in the environment surrounding highways. They perform as natural air filtering. Foliage with small height trees captured more particulate matter than the tall trees (Shrestha et al. 2021).

Anticipated Performance Index

API plays a significant role in providing reliable data through the combining of APTI value and physiological as well as socioeconomic traits, in which multiple grades were assigned for a particular tree species. The API values fell into different categories, such as not recommended (<30), very poor (31–40), poor (41–50), moderate (51–60), good (61–70), very good (71–80), excellent (81–90), and best (91–100) (Kaur & Nagpal 2017, Sharma et al. 2019, Rai & Panda 2014, Nayak et al. 2015). Those species have the best performance score in the API score; they are suitable for green belt development in polluted sites as well as urban greenery. In the present study (Table 5), the highest API score was recorded best performance for *Shorea robusta* and *Ficus religiosa* (93.75%), which were suitable to be planted along the roadside of air-polluted areas; while the lowest was recorded for *Butea monosperma*, *Ailanthus excelsa*, and *Buchanaia lanzan* (62.75%). Overall, selected tree species have been recommended for plantation at polluted sites. Similar results were reported by many researchers such as for the anticipated performance index (Sharma et al. 2019, Sahu et al. 2020, Yadav & Pandey 2020, Pandey et al. 2015).

CONCLUSIONS

This research indicates that various trees exhibit their responses against air pollution. Tree species need to be appropriately evaluated using both APTI and API values to determine tolerate capacity in pollution loads areas. The study showed the APTI value significantly differs ($p<0.05$) for tree species in coal dust air pollution. The highest API values received for *Shorea robusta, Mangifera indica, Schleichera oleosa, Terminalia ballerica, Ficus benghalensis, Anthocephalus cadamba, Ficus religiosa, Peltophorum pterocarpum, Madhuca indica,* and *Terminalia tomentosa*. Trees with low API values can function as bio-indicators of air pollution, whereas trees that have high API values can be adopted as bio-accumulators. The assessment of tolerance and performance level is the best method for identifying suitable trees for the establishment of green

zones on the roadsides of polluted areas and commercial and industrially polluted regions. This study provides suitable tree species for plantations along the roadside which is affected by coal dust air pollution areas.

ACKNOWLEDGMENT

REFERENCES

Amulya, L., Kumar, N. K. H. and Jagannath, S., 2015. Air pollution impact on micro morphological and biochemical response of *Tabernaemontana divaricata* L. (Gentianales: Apocynaceae) and *Hamelia patens* Jacq. (Gentianales: Rubiaceae). *Brazilian Journal of Biological Sciences*, 2(4), pp.287–294. Available at: http://revista.rebibio.net/v2n4/v02n04a11.pdf.

Bharti, S. K., Trivedi, A. and Kumar, N., 2018. Air pollution tolerance index of plants growing near an industrial site. *Urban Climate*, 24, pp.820-829. Available at: https://doi.org/10.1016/j.uclim.2017.10.007.

Bhattacharya, T., Kriplani, L. and Chakraborty, S., 2013. Seasonal variation in air pollution tolerance index of various plant species of Baroda city. *Universal Journal of Environmental Research & Technology*, 3(2), pp.199-208. Available at: http://www.environmentaljournal.org/3-2/ujert-3-2-8.pdf.

Bora, M. and Joshi, N., 2014. A study on variation in biochemical aspects of different tree species with tolerance and performance index. *The Bioscan*, 9(1), pp.59–63.

Chauhan, A., Iqbal, S., Maheshwari, R. S. and Bafna, A., 2012. Study of air pollution tolerance index of plants growing in Pithampur industrial area sector 1, 2 and 3. *Research Journal of Recent Sciences*, 1, pp.172–177. Available at: http://www.isca.me/rjrs/archive/v1/iISC-2011/27.ISCA-ISC-2011-8EnvS-26.pdf.

Council on Energy, Environment and Water (CEEW), 2024. Vehicular emissions in India. [online] Available at: https://www.ceew.in/cef/quick-reads/explains/vehicular-emissions-in-india [Accessed 25 June 2024].

Das, S., Mallick, S. N., Padhi, S. K., Dehury, S. S., Acharya, B. C. and Prasad, P., 2010. Air pollution tolerance indices (APTI) of various plant species growing in industrial areas of Rourkela. *Indian Journal of Environmental Protection*, 30, pp.563-567.

Govindaraju, M., Ganeshkumar, R. S., Muthukumaran, V. R. and Visvanathan, P., 2012. Identification and evaluation of air-pollution-tolerant plants around lignite-based thermal power station for greenbelt development. *Environmental Science and Pollution Research*, 19, pp.1210-1223. Available at: https://doi.org/10.1007/s11356-011-0637-7.

Kamesh, Singh, B. P., Misra, S., Verma, K. K., Singh, C. K. and Kumar, R., 2023. An emerging adsorption technology and its applicability on trees as an adsorbent for the remediation of water pollution: A review. *Eco. Env. & Cons.*, 29(2), pp.627-640. Available at: http://doi.org/10.53550/EEC.2023.v29i02.014.

Kaur, M. and Nagpal, A. K., 2017. Evaluation of air pollution tolerance index and anticipated performance index of plants and their application in development of green space along the urban areas. *Environmental Science and Pollution Research*, 24, pp.18881–18895.

Kosanic, A., Anderson, K., Harrison, S., Turkington, T. and Bennie, J., 2018. Changes in the geographical distribution of plant species and climatic variables on the West Cornwall peninsula (South West UK). *PLoS One*, 13(2), pp. e0191021.

Krishnaveni, M. and Lavanya, K., 2014. Air pollution tolerance index of plants: A comparative study. *International Journal of Pharmacy and Pharmaceutical Sciences*, 6(5), pp.320–324.

Kumar, M., Alezona, and Nandini, N., 2018. Comparative assessment of air pollution tolerance index of selected tree species of Bengaluru, India. *International Journal of Scientific Research in Multidisciplinary Studies*, 4(11), pp.25-29. Available at: https://www.researchgate.net/publication/329983751_Comparative_Assessment_of_Air_Pollution_Tolerance_Index_of_selected_Tree_Species_of_Bengaluru_India

Kumari, J. and Deswal, S., 2017. Assessment of air pollution tolerance index of selected plants unveils to traffic roads of Noida, Uttar Pradesh. *International Journal on Emerging Technologies*, 8(1), pp.179–184.

Maawali, R.A. and Sulaiman, H., 2017. Trees for air pollution tolerance to develop green belts as an ecological mitigation. *World Academy of Science, Engineering and Technology International Journal of Environmental, Chemical, Ecological, Geological and Geophysical Engineering*, 11(2), pp.106–109.

Nayak, D., Patel, D.P., Thakare, H.S., Satashiya, K. and Shrivastava, P.K., 2015. Evaluation of air pollution tolerance index of trees. *Research in Environment and Life Sciences*, 8(1), pp.7-10.

Noor, M., Sultana, S., Fatima, S., Ahmad, M., Zafar, M., Sarfraz, M. and Ashraf, M., 2015. Retraction: Estimation of anticipated performance index and air pollution tolerance index of vegetation around the marble industrial areas of Potwar region: Bioindicators of plant pollution response. *Environmental Geochemistry and Health*, 37(3), pp.441-455. DOI: 10.1007/s10653-014-9657-9.

Ogunkunle, C.O., Suleiman, L.B., Oyedeji, S., Awotoye, O.O. and Fatoba, P.O., 2015. Assessing the air pollution tolerance index and anticipated performance index of some tree species for biomonitoring environmental health. *Agroforestry Systems*, 89, pp.447–454.

Ogunrotimi, D., Adebola, S., Akinpelu, B. and Awotoye, O., 2017. Evaluation of biochemical and physiological parameters of the leaves of tree species exposed to vehicular emissions. *Journal of Applied Life Sciences International*, 10(4), pp.1-9. Available at: https://doi.org/10.9734/JALSI/2017/31854

Padmavathi, P., Cherukuri, J. and Reddy, M.A., 2013. Impact of air pollution on crops in the vicinity of a power plant: A case study. *International Journal of Engineering Research and Technology*, 2(12), pp.3641-3651.

Pandey, A.K., Pandey, M. and Tripathi, B.D., 2015. Air pollution tolerance index of climber plant species to develop vertical greenery systems in a polluted tropical city. *Landscape and Urban Planning*, 144, pp.119-127. Available at: https://doi.org/10.1016/j.landurbplan.2015.08.014

Rai, P.K. and Panda, L.L., 2014. Dust capturing potential and air pollution tolerance index (APTI) of some roadside tree vegetation in Aizawl, Mizoram, India: An Indo-Burma hot spot region. *Air Quality, Atmosphere and Health*, 7, pp.93–101. Available at: https://doi.org/10.1007/s11869-013-0217-8

Rai, P.K., Panda, L.L., Chutia, B.M. and Singh, M.M., 2013. Comparative assessment of air pollution tolerance index (APTI) in the industrial (Rourkela) and non-industrial area (Aizawl) of India: An eco-management approach. *African Journal of Environmental Science and Technology*, 7(10), pp.944-948. Available at: https://www.ajol.info/index.php/ajest/article/view/94959

Roy, A., Bhattacharya, T. and Kumari, M., 2020. Air pollution tolerance, metal accumulation and dust capturing capacity of common tropical trees in commercial and industrial sites. *Science of the Total Environment*, 722:137622. Available at: https://doi.org/10.1016/j.scitotenv.2020.137622

Sahu, C. and Sahu, S.K., 2015. Air pollution tolerance index (APTI), anticipated performance index (API), carbon sequestration and dust collection potential of Indian tree species – A review. *International Journal of Emerging Research in Management and Technology*, 4(11), pp.37–40.

Sahu, C., Basti, S. and Sahu, S.K., 2020. Air pollution tolerance index (APTI) and expected performance index (EPI) of trees in Sambalpur town of India. *SN Applied Sciences*, 2, pp.1-14. Available at: https://doi.org/10.1007/s42452-020-3120-6

Shah, K., An, N., Ma, W., Ara, G., Ali, K., Kamanova, S., Zuo, X., Han, M., Ren, X. and Xing, L., 2020. Chronic cement dust load induces novel damages in foliage and buds of *Malus domestica*. *Scientific Reports*, 10(1):12186. DOI: 10.1038/s41598-020-68902-6.

Sharma, B., Bhardwaj, S.K., Sharma, S., Nautiyal, R., Kaur, L. and Alam, N.M., 2019. Pollution tolerance assessment of temperate woody vegetation growing along the national highway-5 in Himachal Pradesh, India. *Environmental Monitoring and Assessment*, 191: 1-14.

Sharma, B., Sharma, S. and Bhardwaj, S.K., 2017. Plant-pollutant interactions with a special mention of dust accumulation by plants - A review. *Nature, Environment and Pollution Technology*, 16(2), pp.375–384.

Shrestha, S., Baral, B., Dhital, N.B. and Yang, H.H., 2021. Assessing air pollution tolerance of plant species in vegetation traffic barriers in Kathmandu Valley, Nepal. *Sustainable Environment Research*, 31, pp.1-9. Available at: https://doi.org/10.1186/s42834-020-00076-2

Singare, P.U. and More, S.N., 2020. Identification of the most tolerant plant species along the Chembur industrial area of Mumbai: A key step to mitigate global air pollution. *SN Applied Sciences*, 2(10):1663. Available at: https://doi.org/10.1007/s42452-020-03431-5

Singh, S., Tiwari, S., Singh, R. and Chate, D., 2018. Air pollutants concern in field crops under changing environment scenarios. *Journal of Agrometeorology*, 20(Special Issue), pp.302–306.

Swami, A. and Chauhan, D., 2015. Impact of air pollution induced by automobile exhaust pollution on air pollution tolerance index (APTI) on few species of plants. *Science*, 4(3), pp.342-343.

Tak, A.A. and Kakde, U.B., 2017. Assessment of air pollution tolerance index of plants: A comparative study. *International Journal of Pharmacy and Pharmaceutical Sciences*, 9(7), pp.83-89.

Uka, U.N., Belford, E.J. and Hogarh, J.N., 2019. Roadside air pollution in a tropical city: physiological and biochemical response from trees. *Bulletin of the National Research Centre*, 43, pp.1-12. Available at: https://doi.org/10.1186/s42269-019-0117-7

Verma, J., Singh, P. and Sharma, R., 2023. Evaluation of air pollution tolerance index and anticipated performance index of selected roadside tree species in Ludhiana, India. *Environmental Monitoring and Assessment*, 195(1), pp.240.

Wang, Y.C. and Chen, B., 2021. Dust capturing capacity of woody plants in clean air zones throughout Taiwan. *Atmosphere*, 12(6), pp.696. Available at: https://doi.org/10.3390/atmos12060696

Yadav, R.K., Prasad, S. and Raje, A., 2020. Air pollution tolerance index and anticipated performance index of roadside plants: A study from Roorkee, Uttarakhand, India. *Indian a Journal of Ecology*, 47(2), pp.413-417.

ORCID DETAILS OF THE AUTHORS

Kamesh- https://orcid.org/0000-0001-7518-691X
Brijendra Pratap Singh: https://orcid.org/0000-0002-8392-4801
Shailly Misra- https://orcid.org/0000-0003-3302-1169
Ramesh- https://orcid.org/0000-0002-5573-1455

A Comprehensive Review on the Role of Bioremediation in Heavy Metal Contamination

Princy Rajput†, Shashank Benjwal and Rohit Pandey

Department of Biotechnology, Hemvati Nandan Bahuguna Garhwal University, Srinagar, Garhwal, India

†Corresponding author: Princy Rajput; rajputprincy99@gmail.com

ABSTRACT

Heavy metal contamination, along with other pollutants, presents significant environmental hazards. These substances not only endanger human health but also disrupt natural ecosystem. Bioremediation emerges as a sustainable and economically viable approach to tackling pollution. It harnesses the capabilities of microorganisms, plants, and their enzymes to degrade or neutralize pollutants. This paper categorizes bioremediation into two primary types: ex-situ and in-situ. Ex-situ bioremediation treats contaminated material away from its original location, while in-situ bioremediation addresses contamination directly at the site. This paper also explores how microbes tolerate heavy metals through various mechanisms. These mechanisms encompass extracellular barriers, efflux pumps, enzymatic reduction, and intracellular sequestration. Extracellular barriers function to block the entry of metals into the cell, whereas efflux pumps work actively to expel metals from the cell. Enzymatic reduction facilitates the conversion of metals into less harmful forms, while intracellular sequestration involves storing metals within the cell. Moreover, the paper examines diverse applications of bioremediation in environmental restoration. These applications encompass natural attenuation, enhanced reductive dechlorination, sewage treatment, bioleaching, biosorption, constructed wetlands, biostimulation, and bioaugmentation. This paper emphasizes the need for further research to optimize bioremediation technologies for broader real-world environmental management applications.

INTRODUCTION

The substantial increase in human population is negatively impacting the environment. The rate of industrialization and other human activities is rising daily, leading to contamination. The presence of contaminants in the environment may cause harm or upset the natural balance of ecosystem referred to as pollutants. These pollutants can be solid, liquid, or gaseous particles and can come from various human operations, industrial operations, or environmental factors Organic solvents, herbicides, pesticides, textile dyes, PAHs (polycyclic aromatic hydrocarbons), nitrates and nitrites, personal care products, and heavy metals are the sources of pollution (Martinez et al. 2019, Shah et al. 2021). The primary sources of PAHs are human activities, including incomplete fossil fuel combustion, burning of biomass, oil spills, and some industrial processes (Li et al. 2010, Bezza & Chirwa 2016). Soils from a variety of locations, including coal storage regions, coke oven plants, produced gas plants, and coal tar spill sites, have high levels of PAH pollution (Li et al. 2010, Bezza & Chiwra 2016). Herbicides and pesticides are crucial for farming but can heavily pollute the

environment. They might seep into drinking water sources, affecting people's health by potentially messing with the nervous, hormonal, and immune systems (Rahman 2018, International Federation of Organic Agriculture Movements 2009). Textile dyes pollute waterways, harming aquatic ecosystems (Dutta et al. 2024). Chemicals like nitrates and nitrites from farm runoff can get into our drinking water and make it unsafe (Prickett et al. 2023). Personal care products (PCPs) are the main types of new pollutants coming from cities. They're getting into the soil and water systems through untreated or treated wastewater, polluting the environment (Bester 2004). Chlorinated aliphatic chemicals, particularly chlorinated solvents, are typically found in soil and groundwater near hazardous waste sites (Barbee et al. 1994)

Improper waste management procedures, industrial waste, and agricultural runoff into the environment are the sources of organic pollutants. The permanent existence of these substances in nature poses a major threat to the health and safety of both humans and animals (Pavlostathis et al. 2001). One of the hardest materials for life in the environment is heavy metal (Siddiquee et al. 2015, Maddela

& García 2021). Heavy metals are classified as elements with a specific density greater than 5 g/cm^3 (Jarup et al. 2003). Heavy metals are not polymers or biodegradable and have detrimental effects (Malik et al. 2022). Toxic heavy metals including mercury, chromium, cadmium, arsenic, lead, and others in high quantities can cause a variety of health problems as well as harm the ecosystem. Metal-containing contaminants are either indirectly or directly introduced into the environment, threatening the health of people, soil, and sediment (Siddique et al. 2011). Additionally, the maximum amount of dangerous heavy metals in irrigation water was permitted by the Food and Agricultural Organisation.

Heavy metals pose a grave threat to human health through various exposure routes such as inhalation, ingestion, and skin contact, leading to a myriad of health issues including neurological impairment, kidney dysfunction, cardiovascular complications, and increased cancer risks (Mahurpawar 2015). Certain heavy metals, such as lead, arsenic, mercury, cadmium, copper, nickel, and tin, have different harmful effects on the body. Consumption of arsenic can cause serious gastrointestinal issues, and long-term exposure can cause diseases like hypertension and black foot disease (Mahurpawar 2015, Bharti & Sharma 2022). Exposure to lead destroys various organs, but cadmium mostly harms the kidneys and bones. There is a danger of neurotoxicity from mercury, particularly from methylmercury in shellfish. Overconsumption of copper can damage the kidneys and liver, while exposure to nickel is associated with several malignancies and respiratory problems (Martin & Griswold 2009).

The effects of metal pollution on marine ecosystems are significant, even though it may not be as readily apparent as other types of marine pollution. The level of metals present in fish can vary depending on factors such as species, age, developmental stage, and physiological conditions (Singh & Kalamdhad 2011). Fish tend to accumulate significant amounts of mercury in their tissues, making them a primary dietary source of this element for humans (Singh & Kalamdhad 2011). Fish serve as the primary sources of mercury and arsenic exposure for humans. Mercury, a well-known human toxin, is primarily introduced into human systems through fish consumption (Singh & Kalamdhad 2011).

Heavy metal toxicity in plants occurs when metal concentrations within the plant surpass acceptable limits and indirectly and directly impact the plant (Tyagi et al. 2022). Excessive amounts of metal can block cellular enzymes and cause oxidative stress-induced cellular structural damage (Van Assche & Clijsters 1990, Uchenna et al. 2020).

Heavy metals' deleterious impact on the growth and function of soil microorganisms has an indirect impact on the development of plants. Excessive metals may reduce the amount of helpful soil microorganisms, resulting in a decrease in organic matter breakdown and poorer soil fertility (Hossain et al. 2022) Enzyme activities are critical for plant metabolism; yet, they are hampered by heavy metal interactions with soil microbial activity. These negative impacts (both direct and indirect) reduce plant development, which finally leads to plant death (Hossain et al. 2022).

Even though these materials are often resistant, under the right circumstances, microbially mediated processes can transform and eliminate them (Ferguson & Pietari 2000). Various approaches and techniques have been researched and implemented to eliminate these pollutants. Some of the most used methods include phytoremediation, chemical precipitation, electrochemical treatment, ion exchange, adsorption, membrane filtration, soil washing, stabilization, solidification, and bioremediation. Bioremediation is often considered a more environmentally safe remediation method based on self-generated biological processing rather than adding chemicals. The use of dangerous chemicals can be reduced or even eliminated with the help of bioremediation. Bioremediation employs biomass, both alive and dead, and mineralizes organic contaminants to form carbon dioxide, nitrogen gas, water, and other compounds.

BIOREMEDIATION

Bioremediation is one way to reduce or replace harmful chemicals (Manorma et al. 2023). Bioremediation utilizes alive or dead biomass to break down organic contaminants into carbon dioxide, nitrogen gas, water, and other chemicals. Additionally, it can be utilized to get rid of dangerous pollutants including heavy metals and poisonous elements from contaminated surroundings (Arya et al. 2023, Manorma et al. 2023, Kapahi & Sachdeva 2019, Alori et al. 2022).

Bioremediation is the procedure of restoring polluted sites into less hazardous or innocuous forms by using biological organisms, mainly microorganisms, green plants, and their enzymes, to remove, break down, mineralize, change, and detoxify pollutants from the environment and hazardous waste elements (Vishwakarma et al. 2023, Jain et al. 2023, Azubuike et al. 2016, Tyagi & Kumar 2021). Bioremediation is frequently less expensive than other cleanup procedures. Its implementation takes fewer resources, equipment, and energy. Bioremediation proves advantageous across various pollutants and environments, effectively eliminating substances such as pesticides, heavy metals, petroleum hydrocarbons, and chlorinated solvents from soil, water, and subterranean aquifers. Bioremediation technologies are frequently non-intrusive and can be done without interfering with the natural ecosystem.

FUNDAMENTALS OF ENVIRONMENT RESTORATION THROUGH BIOREMEDIATION

The fundamental concept of bioremediation is to use living things, such as plants, fungi, algae, and bacteria (Saxena et al. 2020) to decrease and detoxify toxic chemicals in the environment and transform them into less toxic substances, like CO_2, H_2O, microbial biomass, and metabolites (Tyagi & Kumar 2021) (Fig. 1). Hot springs, glaciers, salt lakes, deserts, and oceans are just a few of the various environments where microorganisms can be found. Degradable microbes are capable of breaking down a variety of toxins when isolated from polluted habitats, including heavy metal-polluted areas, waste landfills, pesticide-contaminated sites, and wastewater treatment plants.

Microorganisms from the genera *Bacillus*, *Enterobacter*, *Flavobacterium*, *Alteromonas*, *Arthrobacter*, *Achromobacter*, and *Pseudomonas* are the main ones used in bioremediation procedures (Ojuederie & Babalola 2017, Xu et al. 2018). *Alcanivorax*, *Marinobacter*, *Thallassolituus*, *Cycloclasticus*, and *Oleispira* are examples of hydrocarbonoclastic bacteria (OHCB), renowned for their distinctive capacity to degrade hydrocarbons (Yakimov et al. 2007).

Certain enzymes, such as laccases, peroxidases, and catalases (Varjani et al. 2018), have been reported to be produced by fungi and can either break down organic contaminants or immobilize inorganic ones. Moreover, microbes are also capable of producing these enzymes (Morel et al. 2013, Durairaj et al. 2015, Shah et al. 2021).

Several fungal taxa are capable of degrading aromatic hydrocarbons, including *Aspergillus*, *Fusarium*, *Curvularia*, *Lasiodiplodia*, *Drechslera*, *Mucor*, *Penicillium*, *Rhizopus*, and *Trichoderma* (Lladó et al. 2013, Balaji et al. 2014, Chang et al. 2016).

It has been shown that microalgae, primarily green algae from the genera *Scenedemus*, *Selenastrum*, or *Chlorella*, may immobilize metals and break down certain polycyclic aromatic hydrocarbons like phenanthrene, pyrene, and naphthalene (Lei et al. 2007, Takáčová et al. 2014, García et al. 2016, Ghosal et al. 2016).

CATEGORIES OF BIOREMEDIATION

Ex-situ bioremediation and in situ, bioremediation are two widely recognized classifications for the bioremediation process as shown in Fig. 2 (Gkorezis et al. 2016).
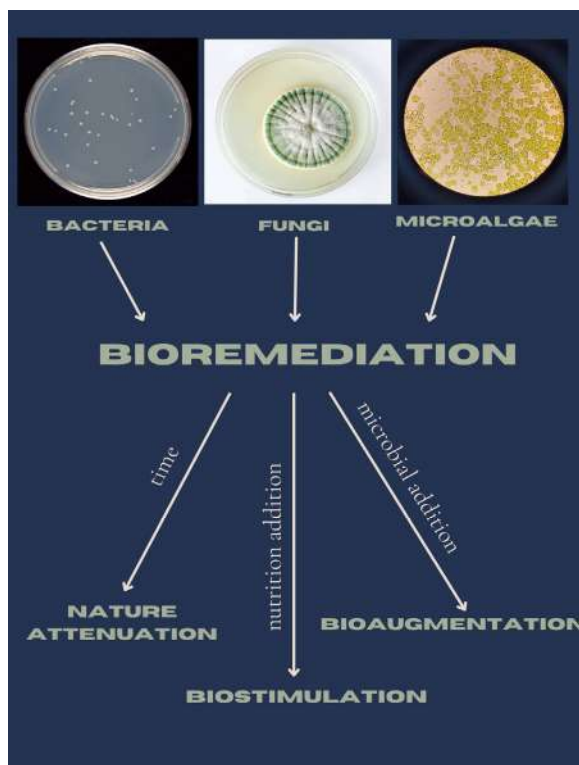

Fig. 1: General framework for bioremediation techniques using various microbial species.
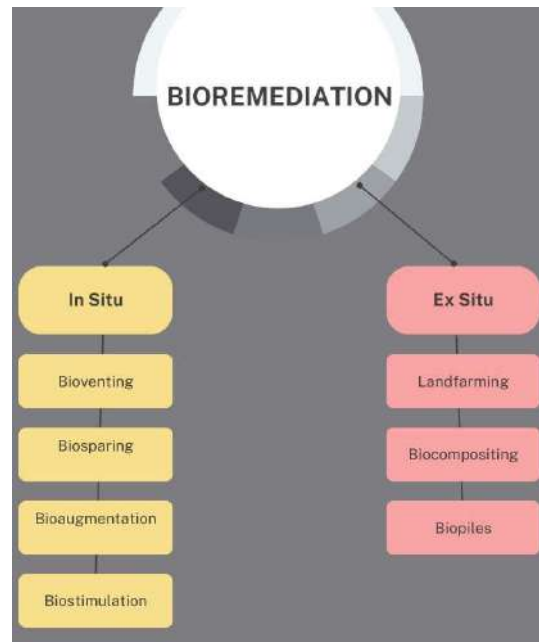
Fig. 2: Techniques of bioremediation.

MECHANISM OF HEAVY METAL TOLERANCE

Now, four basic mechanisms of heavy metal tolerance were determined, as depicted in Fig. 3, and they can even be present in the same microbe (Cánovas et al. 2003, Cazorla et al. 2002, Cervantes et al. 2001, Cervantes & Gutierrez-Corona 1994, Cha & Cooksey 1991, Antonucci et al. 2017, Lin et al. 2006, Kumar & Thakur 2022).

1. **A selectively permeable system, the extracellular barrier:** The heavy metals subsequently bind to different chemical structures on the cell wall. The metal-binding capability of Gram-positive bacteria and Gram-negative bacteria is determined by a peptidoglycan layer containing various groups. Carboxyl groups bind metal cations avidly because they are numerous and negatively charged (Doyle et al. 1980). However, some metal ions penetrate the cell by crucial element ingestion pathways; As an example, the sulfate transport system is responsible for bringing Cr(II) into the cell (Gilotra & Srivastava 1997). The magnesium transport mechanism facilitates the entry of Cd(II), Zn(II), Co(II), Ni(II), and Mn(II) into cells (Nies & Silver 1989). Furthermore, As(V) is transported via phosphate transport systems, whereas As(III) is transported by glucose permeases (Yang & Rosen 2016). Recent studies indicate that capsular polysaccharides in both Gram-positive and Gram-negative bacteria can contribute to the extracellular heavy metal barrier, in addition to the well-established involvement of peptidoglycan in Gram-positive bacteria. Divalent and trivalent cations can be bound by these intricate sugar molecules (Grass et al. 2010). In addition to the physical barriers, efflux pumps are another crucial component of the extracellular barrier. Heavy metals are actively transported out of the cell by these specific membrane proteins, which decreases the accumulation of heavy metals inside cells. Two such examples are the ArsB arsenic efflux pump in *S. cerevisiae* and the CadA cadmium efflux pump in *E. coli* (Nies et al. 2003, Wysocki et al. 2006).

2. **Transport of Metal Ions:** Efflux Systems: Efflux systems in thermophiles are a series of molecular mechanisms that allow these organisms to remove poisonous or undesired chemicals from their cells. It is essential for thermophile survival in severe environments by maintaining cellular homeostasis and protecting them from external stresses. The function of specialized membrane proteins known as efflux pumps, which actively transport chemicals across the cell membrane, is often involved in these systems. Genetic determinants of the efflux system are present in chromosomes and plasmids. Bacteria have three main efflux systems: CDF (cation diffusion facilitator) proteins, RND (resistance, nodulation, and cell division), and P-type ATPases (Nies et al. 2003). The passage of particular substrates across the cell membrane and into the periplasm of Gram-negative bacteria is facilitated by P-type ATPases and CDF proteins. The three domains of life are home

to metal transporters found in these bacteria, which go by the name of CDF proteins. Divalent metal ions like Zn(II), Co(II), Ni(II), Cd(II), and Fe(II) are handled by these CDF proteins. It is possible to export metals by using a chemiosmotic gradient produced by H+ or K+ (Paulsen & Saier 1997, Kolaj-Robin et al. 2015, Joshi et al. 2023). P-type ATPases can transfer both monovalent and bivalent metal ions, in contrast to CDF proteins. By hydrolyzing ATP, these ATPases may move ions like Cu(I)/Ag(I) and Zn(II)/Cd(II)/Pb(II) across cellular membranes. They also show a great affinity for sulfhydryl groups (Nies et al. 2003). These three domains make up these efflux systems: i) a soluble ATP binding domain with a transiently phosphorylated aspartate residue; ii) a soluble actuator domain (AD). The transmembrane helix bundle facilitates substrate translocation. P1B-type ATPases can eliminate hazardous metals like Ag(I), Cd(II), and Pb(II) as well as necessary transition metal ions like Zn(II), Cu(I), and Co(II). This helps maintain cellular homeostasis. Members of the RND family are efflux pumps classified into subfamilies according to the substrates they transport. These pumps are primarily found in Gram-negative bacteria. They actively eliminate hydrophobic substances, heavy metals, and nodulation factors (Tseng et al. 1999). Another common family of efflux pumps that is present in both Gram-positive and Gram-negative bacteria is the MacA/B family. These pumps are very good at moving substances that are amphiphilic, such as some heavy metals (Paulsen et al. 1997). Moreover, newer studies indicate that RND efflux pumps may have

a bigger function in heavy metal efflux than previously thought. Research has indicated that the CzcCBA RND pump in Escherichia coli is capable of effluxing a wide variety of heavy metals, such as lead, zinc, cobalt, and cadmium. (Valencia et al. 2013).

3. **Metal ion reduction by enzymatic means:** Specialised enzymes, such as reductases or metal reductases, catalyze the reduction of metal ions once within the bacterial cell (Martinez et al. 2019). To promote the reduction reaction, these enzymes use electron donors, which are frequently produced from cellular metabolic activities (Ranawat & Rawat 2018). Metal ions are often reduced from a higher oxidation state to a lower oxidation state, transforming them into a less hazardous form. To develop heavy metal resistance, many thermophilic bacteria use internal enzymatic transformations in conjunction with efflux mechanisms. A wide range of additional heavy metal ions, including Cr(V), Mo(VI), and V(V) (Smirnova 2005), which act as terminal acceptors of electrons during their anaerobic respiration (Poli et al. 2009), can also be reduced by the thermophilic bacteria isolated from diverse ecological settings. Safer versions of metal ions can be produced by enzymatic reduction; for instance, Cr(V) can be changed into Cr(III) and Hg(II) to Hg(0). (Ranawat & Rawat 2018). The flavoprotein MerA from Sulfolobus solfataricus catalyzes the transformation of poisonous mercury ions into comparatively benign elemental mercury by reducing Hg(II) to volatile Hg(0) (Schelert et al. 2004).
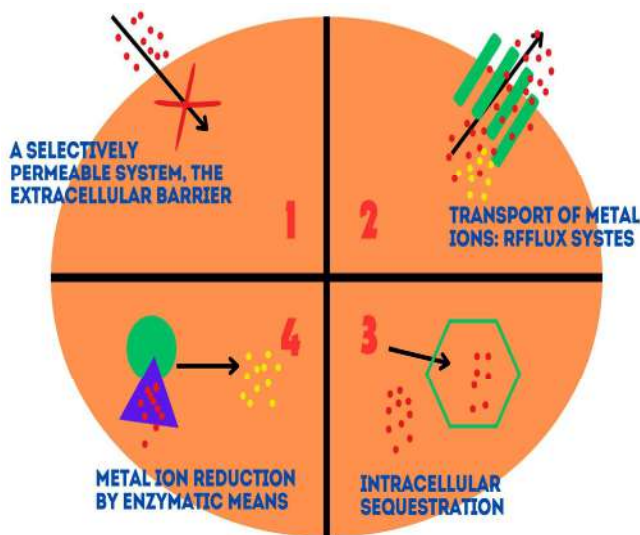

Fig. 3: A generalised interpretation of the genetic pathway underlying microorganism resistance to toxic metals: 1) A selectively permeable system, the extracellular barrier. 2)Transport of metal ions: Efflux systems; 3) Metal ion reduction by enzymatic means:4) Intracellular sequestration.

4. **Intracellular sequestration:** The process by which thermophilic bacteria store or sequester various chemicals within their cells is referred to as intracellular sequestration. This technique enables thermophilic bacteria to protect themselves from potentially hazardous molecules or to amass beneficial substances for diverse purposes. Peptides containing cysteine residues that bind metal ions through sulfhydryl groups are called Phytochelatins and Metallothioneins (Kumar et al. 2022, Ranawat & Rawat 2018). A superfamily of short cytosolic proteins with an average length of 25–82 amino acids is known as the metallothioneins. They have seven to twenty-one conserved cysteine residues, which contributes to their high cysteine concentration. Even in the lack of aromatic amino acids and histidine residues, metallothioneins can bind metal ions, specifically $Cd(II)$, $Zn(II)$, and $Cu(I)$, by forming metal-thiolate clusters (Coyle et al. 2002). The creation of the adaptable proteins known as metallothioneins is triggered by a variety of ecological stresses and environmental contaminants such as heavy metals. Based on the findings of this study, scientists developed a whole-cell biosensor that can detect heavy metals by using the *Tetrahymena* thermophiles metallothionein activator (Amaro et al. 2011, Mehta et al. 2016). In addition to these protein-based methods, thermophiles employ inorganic polyphosphates for intracellular sequestration. These linear polymers of inorganic phosphate residues can bind heavy metals, among other cations (Rao et al. 2009). Interestingly, there is a close relationship between polyphosphate metabolism and heavy metal tolerance, as polyphosphate levels are elevated in cultivated bacteria and fungi in the presence of heavy metal cations. Polyphosphate functions in bacteria by binding heavy metals, and some metal cations even enhance the activity of exopolyphosphatase, which liberates phosphate from polyphosphates and subsequently transports $MeHPO_4$-ions out of cells for excretion and storage (Kulakovskaya 2018). Polyphosphate builds up in cytoplasmic inclusions, vacuoles, and cell walls in fungi to produce cation/polyphosphate complexes that help them overcome heavy metal stress (Gajewska et al. 2022, Kulakovskaya 2018). Inclusion bodies are structured intracellular formations consisting of aggregated proteins. These bodies serve as repositories for either vital or potentially harmful metals such as cadmium (Cd) (Magalhães et al. 2007).

APPLICATIONS OF NATURAL CLEANUP

Bioremediation is not a recent concept, but recent advancements in process engineering and molecular biology have given rise to innovative techniques (Bonaventura & Johnson 1997). Among the contemporary bioremediation methods employed for site cleanup, natural attenuation, and enhanced reductive dichlorination stand out as cutting-edge approaches. The natural removal of pollutants from a site occurs through organic, inorganic, and biological processes without human intervention (Rysz et al. 2010). Electron donors such as lactic acid, molasses, volatile fatty acids, or commercial goods must be added in situ to enhance reductive dechlorination. This promotes biological hydrogen production and facilitates the dechlorination of organic molecules like trichloroethene (TCE) (Evans et al. 2002).

Processing biological nitrogen waste from people and the animals they eat, such as feces and urine, is one well-known, well-established, and getting the harder and harder field of bioremediation. The development of the human population, industrial output, and chemical use have all contributed to the expansion of animal populations (Bonaventura & Johnson 1997). Twenty-five thousand tonnes of nitrogen, thirteen thousand tonnes of phosphorus, and thirteen thousand tonnes of potassium were produced by feed animals in North Carolina alone in 1993, totaling almost 27,000,000 tonnes of fresh manure (Barker & Zublena 1995).

Sewage Treatment Plants (STPs) are the largest and most important bioremediation firms in the world because of the requirement for clean water for human health (Bonaventura & Johnson 1997). Thirty billion cubic meters of raw wastewater is processed annually by the sixteen thousand municipal STPs that make up the United States. Raw wastewater mostly consists of suspended particles, nitrogen, organic debris, phosphorus, pathogenic bacteria, and chemicals (such as pesticides and toxic metals). Certain components are reduced even in the most basic STPs (Bonaventura & Johnson 1997).

The atomic structure of metals is intrinsically harmful, unlike organic contaminants, and they cannot be further transformed or mineralized into an entirely safe state. Despite variances in the solubility, oxidizing state, and relationships with other substances, both organic and inorganic, bacteria and larger organisms can improve bioremediation by concentrating metals to minimize their accessibility and potential hazard (Bonaventura & Johnson 1997). Microbial bioleaching can be applied to different metals and mineral wastes, including contaminated soil, for recycling, metal recovery, and bioremediation (Purchase et al. 2016, White et al.1998, Xu & Sparks 2013). Sulfide generated by sulfate reduction has been used in leachates and waters for metal bioremediation (White & Gadd 1998, White & Gadd 2000, White et al. 2003 Tabak et al. 2005). Recovery of precious metals like gold is another application for the bioremediation technique called biosorption (Gadd et al. 2009, Volesky

et al. 1990, Wang & Chen 2009). Biosorption is also one of the bioremediation mechanisms used to treat metal contamination. Many bacteria and algae have cell walls or envelopes that can passively absorb relatively high amounts of metallic substances, usually by charge-mediated attraction (Mohamed et al. 2001, Macaskie & Dean 1990).

Interest in mercury pollution has grown significantly since the 1950s, when eating seafood tainted with methylmercury resulted in hundreds of serious illnesses and deaths in Japan. Several states in the US now regularly check the mercury levels in freshwater fish, including North Carolina. The World Health Organisation and the US Food and Drug Administration have set warning standards for mercury levels, which are exceeded in a large number of freshwater and saltwater species (Bonaventura & Johnson 1997). The edible (fillet) part of fish in North Carolina recorded mercury levels higher than 1 part per million (ppm), within a range of 1 to 6.9 ppm (Bonaventura & Johnson 1997). Constructed wetlands are artificial habitats primarily composed of vascular vegetation and algal colonies (Bonaventura & Johnson 1997). These habitats offer structural and nutritional support to a diverse range of microorganisms inside the area. One extremely promising application for artificial wetlands is in situ bioremediation of heavy metal pollution (Bonaventura & Johnson 1997).

Biostimulation and bioaugmentation are two commonly employed processes that promote the bioremediation of soils contaminated with hydrocarbons. Biostimulation is the process of adding nutrients (Betancur-Galvis et al. 2006) humic compounds (Nam & Kim 2002), or other substances that could affect the bacterial state to increase the activity of various bacterial strains that are present in the contaminated soil (Kalantary et al. 2014).

According to certain research, soil bioaugmentation is effective in eliminating pesticides that include triazine (Cycoń et al. 2017). Researchers investigated the impact of biostimulation using *Pseudomonas sp.* ADP (at concentrations of 107–108 viable cells/g of soil) and citrate (up to 4.8 mg/g of soil) on the biodegradation of atrazine in soil contaminated with Atrazerba FL, at levels 20 and 200 times higher than the recommended doses (RD) (Lima et al. 2009, Cycoń et al. 2017). Oil biodegradation in the United States was accelerated after the 1989 oil disaster by the utilization of fertilizers and bioaugmentation, which involved the application of naturally occurring bacteria that break down oil. In a matter of years, the joint strategy dramatically decreased oil contamination (Betancur-Galvis et al. 2006).

Although biostimulation is one of the most well-established techniques for bioremediation of hydrocarbons, recent developments in stable isotope analysis, molecular microbiology, and geophysics promise to significantly expand the breadth, depth, and throughput of biostimulation approaches (Upton et al. 2002). In Washington's Creosote-Contaminated Soil Creosote-contaminated soil at a former wood processing facility was successfully remedied through biostimulation with nitrogen and phosphorus and the addition of native fungi (Betancur-Galvis et al. 2006).

Naturally occurring biodegradation, albeit a slow one, is frequently the means of bioremediation. Some argue that the best course of action for cleaning up certain types of pollution, especially marine oil spills, is to "do nothing" if time-scale concerns are disregarded (National Academy Press 1989).

CONCLUSIONS

In conclusion, bioremediation emerges as a potent and sustainable approach for addressing environmental contamination, particularly in the realm of heavy metals. By harnessing the natural capabilities of microorganisms, this method offers a plethora of advantages, including environmental friendliness, cost-effectiveness, and adaptability to various pollutants and site conditions. Metal-ion transport proteins and specialized microbial mechanisms play crucial roles in enhancing the efficiency of bioremediation processes. Additionally, the integration of microbial processes with engineering techniques has paved the way for innovative strategies that promise to refine soil and water remediation. While challenges such as the lengthy treatment times and the necessity for monitoring persist, the continuous advancement in understanding microbial resistance mechanisms and the development of biostimulation and bioaugmentation techniques hold promise to overcome these hurdles. Future research focused on optimizing these bioremediation technologies will be essential in transitioning from theoretical applications to practical, real-world solutions for environmental management.

ACKNOWLEDGMENT

REFERENCES

Alori, E.T., Dimowo, F.O., Olaniyan, F.T., Adekiya, A.O., Ayorinde, B.B., Daramola, F.Y. and Babalola, O.O., 2022. The effects of plant growth-promoting bacteria on lead uptake by *Chromolaena odorata* (Siam Weed). Preprint from Research Square. https://doi.org/10.21203/rs.3.rs-1525259/v1

Amaro, F., Turkewitz, A.P., Martín□González, A. and Gutiérrez, J.C., 2011. Whole□cell biosensors for detection of heavy metal ions in

environmental samples based on metallothionein promoters from Tetrahymena thermophila. *Microbial Biotechnology*, 4(4), pp.513-522.

Antonucci, I., Gallo, G., Limauro, D., Contursi, P., Ribeiro, A.L., Blesa, A. and Fiorentino, G., 2017. An ArsR/SmtB family member regulates arsenic resistance genes unusually arranged in Thermus thermophilus HB27. *Microbial Biotechnology*, 10(6), pp.1690-1701. Available at: http://dx.doi.org/10.1111/1751-7915.12761 [Accessed 22 November 2023].

Arya, M., Patil, A., Singh, S. and Sharma, B., 2023. Heavy metal pollution in natural water resources and impact of metal toxicity on human health. *Water: Management & Governance*, 10, pp.194-207.

Azubuike, C.C., Chikere, C.B. and Okpokwasili, G.C., 2016. Bioremediation techniques–classification based on site of application: principles, advantages, limitations, and prospects. *World Journal of Microbiology and Biotechnology*, 32, pp.1-18.

Balaji, V., Arulazhagan, P. and Ebenezer, P., 2014. Enzymatic bioremediation of polyaromatic hydrocarbons by fungal consortia enriched from petroleum-contaminated soil and oil seeds. *Journal of Environmental Biology*, 35(3), pp.521-529.

Barbee, G., 1994. Fate of Chlorinated Aliphatic Hydrocarbons in the Vadose Zone and Ground Water. *Ground Water Monitoring and Remediation*, 14, pp.129-140. Available at: https://doi.org/10.1111/J.1745-6592.1994. TB00098.X [Accessed 22 November 2023].

Barker, J.C. and Zublena, J.P., 1995. Livestock manure nutrient assessment in North Carolina. Final Report. Raleigh, NC: North Carolina Agricultural Extension Service, North Carolina State University.

Bester, K., 2004. Retention characteristics and balance assessment for two polycyclic musk fragrances (HHCB and AHTN) in a typical German sewage treatment plant. *Chemosphere*, 57(8), pp.863-870.

Betancur-Galvis, L.A., Alvarez-Bernal, D., Ramos-Valdivia, A.C. and Dendooven, L., 2006. Bioremediation of polycyclic aromatic hydrocarbon-contaminated saline-alkaline soils of the former Lake Texcoco. *Chemosphere*, 62(11), pp.1749-1760.

Bezza, F.A. and Chirwa, E.M.N., 2016. Biosurfactant-enhanced bioremediation of aged polycyclic aromatic hydrocarbons (PAHs) in creosote contaminated soil. *Chemosphere*, 144, pp.635-644.

Bharti, R. and Sharma, R., 2022. Effect of heavy metals: An overview. *Materials Today: Proceedings*, 51, pp.880-885.

Bonaventura, C. and Johnson, F., 1997. Healthy environments for healthy people: bioremediation today and tomorrow. *Environmental Health Perspectives*, 105, pp.5-20. Available at: https://doi.org/10.1289/EHP.97105S15 [Accessed 22 November 2023].

Cánovas, D., Cases, I. and De Lorenzo, V., 2003. Heavy metal tolerance and metal homeostasis in Pseudomonas putida as revealed by complete genome analysis. *Environmental Microbiology*, 5(12), pp.1242-1256. Available at: http://dx.doi.org/10.1111/j.1462-2920.2003.00463.x [Accessed 22 November 2023].

Cazorla, F.M., Arrebola, E., Sesma, A., Pérez-García, A., Codina, J.C., Murillo, J. and de Vicente, A., 2002. Copper resistance in *Pseudomonas syringae* strains isolated from mango is encoded mainly by plasmids. *Phytopathology*, 92(8), pp.909-916. Available at: http://dx.doi.org/10.1094/PHYTO.2002.92.8.909 [Accessed 22 November 2023].

Cervantes, C. and Gutierrez-Corona, F., 1994. Copper resistance mechanisms in bacteria and fungi. *FEMS Microbiology Reviews*, 14(2), pp.121-137. Available at: http://dx.doi.org/10.1111/j.1574-6976.1994.tb00083.x [Accessed 22 November 2023].

Cervantes, C., Campos-García, J., Devars, S., Gutiérrez-Corona, F., Loza-Tavera, H., Torres-Guzmán, J.C. and Moreno-Sánchez, R., 2001. Interactions of chromium with microorganisms and plants. *FEMS Microbiology Reviews*, 25(3), pp.335-347. Available at: http://dx.doi.org/10.1111/j.1574-6976.2001.tb00581.x [Accessed 22 November 2023].

Cha, J.S. and Cooksey, D.A., 1991. Copper resistance in *Pseudomonas syringae* mediated by periplasmic and outer membrane proteins. *Proceedings of the National Academy of Sciences*, 88(20), pp.8915-8919. Available at: http://dx.doi.org/10.1073/pnas.88.20.8915 [Accessed 22 November 2023].

Chang, Y.T., Lee, J.F., Liu, K.H., Liao, Y.F. and Yang, V., 2016. Immobilization of fungal laccase onto a nonionic surfactant-modified clay material: application to PAH degradation. *Environmental Science and Pollution Research*, 23, pp.4024-4035.

Coyle, P., Philcox, J.C., Carey, L.C. and Rofe, A.M., 2002. Metallothionein: the multipurpose protein. *Cellular and Molecular Life Sciences CMLS*, 59, pp.627-647.

Cycoń, M., Mrozik, A. and Piotrowska-Seget, Z., 2017. Bioaugmentation as a strategy for the remediation of pesticide-polluted soil: A review. *Chemosphere*, 172, pp.52-71. Available at: https://doi.org/10.1016/j.chemosphere.2016.12.129 [Accessed 22 November 2023].

Doyle, R.J., Matthews, T.H. and Streips, U., 1980. Chemical basis for selectivity of metal ions by the Bacillus subtilis cell wall. *Journal of Bacteriology*, 143(1), pp.471-480.

Durairaj, P., Malla, S., Nadarajan, S.P., Lee, P.G., Jung, E., Park, H.H. and Yun, H., 2015. Fungal cytochrome P450 monooxygenases of Fusarium oxysporum for the synthesis of ω-hydroxy fatty acids in engineered Saccharomyces cerevisiae. *Microbial Cell Factories*, 14(1), pp.1-16.

Dutta, S., Adhikary, S., Bhattacharya, S., Roy, D., Chatterjee, S., Chakraborty, A. and Rajak, P., 2024. Contamination of textile dyes in aquatic environment: Adverse impacts on aquatic ecosystem and human health, and its management using bioremediation. *Journal of Environmental Management*, 353, p.120103.

Evans, P., 2002. A dissolved hydrogen analyzer and a bioavailable ferric iron assay for bioremediation analysis. pp.139-144. Available at: https://doi.org/10.1007/978-94-010-0564-7_22 [Accessed 22 November 2023].

Ferguson, J.F. and Pietari, J.M.H., 2000. Anaerobic transformations and bioremediation of chlorinated solvents. *Environmental Pollution*, 107(2), pp.209-215.

Gadd, G.M., 2009. Biosorption: Critical review of scientific rationale, environmental importance and significance for pollution treatment. *Journal of Chemical Technology and Biotechnology*, 84, pp.13-28.

Gajewska, J., Floryszak-Wieczorek, J., Sobieszczuk-Nowicka, E., Mattoo, A. and Arasimowicz-Jelonek, M., 2022. Fungal and oomycete pathogens and heavy metals: an inglorious couple in the environment. *IMA Fungus*, 13(1), p.6.

Gandahi, A.W. and Hanafi, M.M., 2014. Bio-composting oil palm waste for improvement of soil fertility. *Composting for Sustainable Agriculture*, pp.209-243.

García de Llasera, M.P., Olmos-Espejel, J.D.J., Díaz-Flores, G. and Montaño-Montiel, A., 2016. Biodegradation of benzo(a)pyrene by two freshwater microalgae *Selenastrum capricornutum* and *Scenedesmus acutus*: a comparative study useful for bioremediation. *Environmental Science and Pollution Research*, 23, pp.3365-3375.

Ghosal, D., Ghosh, S., Dutta, T.K. and Ahn, Y., 2016. Current state of knowledge in microbial degradation of polycyclic aromatic hydrocarbons (PAHs): a review. *Frontiers in Microbiology*, 7, p.1369.

Gilotra, U. and Srivastava, S., 1997. Plasmid-encoded sequestration of copper by *Pseudomonas pickettii* strain US321. *Current Microbiology*, 34, pp.378-381. Available at: http://dx.doi.org/10.1007/s002849900199 [Accessed 22 November 2023].

Gkorezis, P., Daghio, M., Franzetti, A., Van Hamme, J.D., Sillen, W. and Vangronsveld, J., 2016. The interaction between plants and bacteria in the remediation of petroleum hydrocarbons: an environmental perspective. *Frontiers in Microbiology*, 7, p.214884.

Grass, G., Rensing, C. and Solioz, M., 2010. Metallic bonding in metallophores: Bioinorganic perspectives. *Chemical Society Reviews*, 39(7), pp.2560-2595. Available at: https://edu.rsc.org/download?ac=527128 [Accessed 22 November 2023].

Harekrushna, S. and Kumar, D.C., 2012. A review on bioremediation. *International Journal of Research in Chemistry and Environment*, 2(1), pp.13-21.

Hossain, J., Azam, M.G., Gaber, A., Aftab, T. and Hossain, A., 2022. Cytotoxicity of metal/metalloids' pollution in plants. In: *Metals Metalloids Soil Plant Water Systems*. Academic Press, pp.371-394.

Jain, A., Katiyar, K., Kumar, V., Sahu, A. and Mishra, V., 2023. Potential of microbes for the bioremediation of heavy metal–contaminated soil. In: *Integrative Strategies for Bioremediation of Environmental Contaminants, Volume Two*. pp.317-346.

Järup, L., 2003. Hazards of heavy metal contamination. *British Medical Bulletin*, 68(1), pp.167-182.

Joshi, S., Gangola, S., Bhandari, G., Bhandari, N.S., Nainwal, D., Rani, A. and Slama, P., 2023. Rhizospheric Bacteria: The Key to Sustainable Heavy Metal Detoxification Strategies. *Frontiers in Microbiology*, 14, p.1229828.

Kalantary, R., Mohseni-Bandpi, A., Esrafili, A., Nasseri, S., Ashmagh, F., Jorfi, S. and Ja'fari, M., 2014. Effectiveness of biostimulation through nutrient content on the bioremediation of phenanthrene contaminated soil. *Journal of Environmental Health Science and Engineering*, 12. Available at: https://doi.org/10.1186/s40201-014-0143-1 [Accessed 22 November 2023].

Kapahi, M. and Sachdeva, S., 2019. Bioremediation options for heavy metal pollution. *Journal of Health and Pollution*, 9(24).

Kolaj-Robin, O., Russell, D., Hayes, K.A., Pembroke, J.T. and Soulimane, T., 2015. Cation diffusion facilitator family: structure and function. *FEBS Letters*, 589(12), pp.1283-1295. Available at: http://dx.doi.org/10.1016/j.febslet.2015.04.007 [Accessed 22 November 2023].

Kremer, R.J., 2020. Impacts of genetically engineered crops on the soil microbiome, biological processes, and ecosystem services. In: *GMOs: Implications for Biodiversity Conservation and Ecological Processes*. pp.129-147.

Kulakovskaya, T., 2018. Inorganic polyphosphates and heavy metal resistance in microorganisms. *World Journal of Microbiology and Biotechnology*, 34, pp.1-8.

Kumar, V. and Thakur, I.S., eds., 2022. *Omics Insights in Environmental Bioremediation*. Springer Nature.

Kumar, V., Kumari, A., Pandey, M. and Sharma, M., 2022. Molecular mechanism of radio-resistance and heavy metal tolerance adaptation in microbes. In: *Microbial Extremozymes*. Academic Press, pp.275-293.

Leeson, A., Hinchee, R., Alleman, B.A., Downey, D.C., Headington, G., Kittel, J.A. and Tyndall, A.F.B., 1996. *Principles and Practices of Bioventing, Volume II: Bioventing Design*. Battelle Memorial Institute, Columbus.

Lei, A.P., Hu, Z.L., Wong, Y.S. and Tam, N.F.Y., 2007. Removal of fluoranthene and pyrene by different microalgal species. *Bioresource Technology*, 98(2), pp.273-280.

Li, H., Chen, J., Wu, W. and Piao, X., 2010. Distribution of polycyclic aromatic hydrocarbons in different size fractions of soil from a coke oven plant and its relationship to organic carbon content. *Journal of Hazardous Materials*, 176(1-3), pp.729-734.

Lima, D., Viana, P., André, S., Chelinho, S., Costa, C., Ribeiro, R. and Viegas, C.A., 2009. Evaluating a bioremediation tool for atrazine contaminated soils in open soil microcosms: the effectiveness of bioaugmentation and biostimulation approaches. *Chemosphere*, 74(2), pp.187-192.

Lin, Y.F., Walmsley, A.R. and Rosen, B.P., 2006. An arsenic metallochaperone for an arsenic detoxification pump. *Proceedings of the National Academy of Sciences*, 103(42), pp.15617-15622.

Available at: http://dx.doi.org/10.1073/pnas.0603974103 [Accessed 22 November 2023].

Lladó, S., Covino, S., Solanas, A.M., Viñas, M., Petruccioli, M. and D'annibale, A., 2013. Comparative assessment of bioremediation approaches to highly recalcitrant PAH degradation in a real industrial polluted soil. *Journal of Hazardous Materials*, 248, pp.407-414.

Macaskie, L.E. and Dean, A.C., 1990. Metal-sequestering biochemicals. In: *Biosorption of Heavy Metals*. pp.199-248.

Maddela, N.R. and García, L.C., eds., 2021. *Innovations in Biotechnology for a Sustainable Future*. Springer International Publishing.

Magalhães, R.J.S., Lopes, C.A., Miranda, M.T.Q., Coelho, M.A.Z. and Moreno, A.M., 2007. Metal uptake and detoxification in yeast as affected by thermotolerance. *Journal of Bioscience and Bioengineering*, 104(2), pp.119-125. Available at: https://link.springer.com/article/10.1007/s11274-023-03596-2 [Accessed 22 November 2023].

Mahurpawar, M., 2015. Effects of heavy metals on human health. *International Journal of Research in Granthaalayah*, 530(516), pp.1-7.

Maila, M.P. and Cloete, T.E., 2004. Bioremediation of petroleum hydrocarbons through landfarming: are simplicity and cost-effectiveness the only advantages? *Reviews in Environmental Science and Bio/Technology*, 3, pp.349-360.

Malik, J.A., 2022. *Advances in Bioremediation and Phytoremediation for Sustainable Soil Management*. Springer International Publishing.

Manorma, K., Sharma, S., Sharma, A. and Chauhan, P.K., 2023. Potential of microbes for the remediation of heavy metal–contaminated soil. In: *Integrative Strategies for Bioremediation of Environmental Contaminants, Volume Two*. pp.113-138. Academic Press.

Martin, S. and Griswold, W., 2009. Human health effects of heavy metals. *Environmental Science and Technology Briefs for Citizens*, 15(5).

Martinez, L.M.T., Kharissova, O.V. and Kharisov, B.I., 2019. *Handbook of Ecomaterials*. (No Title).

Mehta, J., Bhardwaj, S.K., Bhardwaj, N., Paul, A.K., Kumar, P., Kim, K.H. and Deep, A., 2016. Progress in the biosensing techniques for trace-level heavy metals. *Biotechnology Advances*, 34(1), pp.47-60.

Mohamed, Z.A., 2001. Removal of cadmium and manganese by a non-toxic strain of the freshwater cyanobacterium Gloeothece magna. *Water Research*, 35(18), pp.4405-4409.

Morel, M., Meux, E., Mathieu, Y., Thuillier, A., Chibani, K., Harvengt, L. and Gelhaye, E., 2013. Xenomic networks variability and adaptation traits in wood decaying fungi. *Microbial Biotechnology*, 6(3), pp.248-263.

Nam, K. and Kim, J.Y., 2002. Role of loosely bound humic substances and humin in the bioavailability of phenanthrene aged in soil. *Environmental Pollution*, 118(3), pp.427-433.

National Research Council, 1989. *Using Oil Spill Dispersants on the Sea*. Washington: National Academy Press.

Nies, D.H., 2003. Efflux-mediated heavy metal resistance in prokaryotes. *FEMS Microbiology Reviews*, 27(2-3), pp.313-339. Available at: http://dx.doi.org/10.1016/S0168-6445(03)00048-2 [Accessed 22 November 2023].

Nies, D.H. and Silver, S., 1989. Metal ion uptake by a plasmid-free metal-sensitive *Alcaligenes eutrophus* strain. *Journal of Bacteriology*, 171(7), pp.4073-4075. Available at: http://dx.doi.org/10.1128/jb.171.7.4073-4075.1989 [Accessed 22 November 2023].

Ojuederie, O.B. and Babalola, O.O., 2017. Microbial and plant-assisted bioremediation of heavy metal polluted environments: a review. *International Journal of Environmental Research and Public Health*, 14(12), p.1504.

Paulsen, I.T. and Saier, Jr., M.H., 1997. A novel family of ubiquitous heavy metal ion transport proteins. *The Journal of Membrane Biology*, 156, pp.99-103. Available at: http://dx.doi.org/10.1007/s002329900192 [Accessed 22 November 2023].

Paulsen, I.T., Park, J.H., Choi, P.S. and Saier, Jr., M.H., 1997. A family

of Gram-negative bacterial outer membrane factors that function in the export of proteins, carbohydrates, drugs and heavy metals from Gram-negative bacteria. *FEMS Microbiology Letters*, 156(1), pp.1-8.

Pavlostathis, S.G., Prytula, M.T. and Yeh, D.H., 2003. Potential and limitations of microbial reductive dechlorination for bioremediation applications. *Water, Air and Soil Pollution: Focus*, 3, pp.117-129.

Poli, A., Salerno, A., Laezza, G., Di Donato, P., Dumontet, S. and Nicolaus, B., 2009. Heavy metal resistance of some thermophiles: Potential use of α-amylase from *Anoxybacillus amylolyticus* as a microbial enzymatic bioassay. *Research in Microbiology*, 160(2), pp.99-106.

Prickett, M., Chambers, T. and Hales, S., 2023. When the first barrier fails: public health and policy implications of nitrate contamination of a municipal drinking water source in Aotearoa New Zealand. *Australasian Journal of Water Resources*, pp.1-10.

Purchase, D., ed., 2016. *Fungal Applications in Sustainable Environmental Biotechnology*. Cham, Switzerland: Springer, pp.354-357.

Rahman, M.M., 2018. Impact of leaching of pesticides on ground water quality. *ResearchGate*. Available at: https://www.researchgate.net/publication/379896484_Groundwater_Leaching_Potential_of_Pesticides_A_Historic_Review_and_Critical_Analysis [Accessed 22 November 2023].

Ranawat, P. and Rawat, S., 2018. Metal-tolerant thermophiles: metals as electron donors and acceptors, toxicity, tolerance and industrial applications. *Environmental Science and Pollution Research*, 25, pp.4105-4133.

Rao, N.N., Gómez-García, M.R. and Kornberg, A., 2009. Inorganic polyphosphate: a molecule of many functions. Available at: https://www.annualreviews.org/content/journals/10.1146/annurev.biochem.68.1.89 [Accessed 22 November 2023].

Rysz, M., Connor, M.K., Kamath, R. and Newell, C.J., 2010. Origin and propagation of an incorrect chemical degradation pathway in the literature: cis-1, 2-Dichloroethylene as a daughter product of 1, 1, 1-Trichloroethane. *Environmental Forensics*, 11(1-2), pp.50-59.

Saxena, G., Kishor, R. and Bharagava, R.N., 2020. *Bioremediation of Industrial Waste for Environmental Safety*. Singapore: Springer Singapore, pp.207-221.

Schelert, J., Dixit, V., Hoang, V., Simbahan, J., Drozda, M. and Blum, P., 2004. Occurrence and characterization of mercury resistance in the hyperthermophilic archaeon *Sulfolobus solfataricus* by use of gene disruption. *Journal of Bacteriology*, 186(2), pp.427-437.

Shah, M.P., ed., 2021. *Removal of Emerging Contaminants through Microbial Processes*. Singapore: Springer.

Siddiquee, S., Rovina, K., Azad, S.A., Naher, L., Suryani, S. and Chaikaew, P.J.J.M.B.T., 2015. Heavy metal contaminants removal from wastewater using the potential filamentous fungi biomass: a review. *Journal of Microbial Biochemical Technology*, 7(6), pp.384-395.

Siddiquee, S., Yusof, N.A., Salleh, A.B., Tan, G.S., Bakar, F.A., Yap, C.K., Yusuf, U.K., Ismail, A., Tan, S.G., Naher, L., Ho, C.L. and Yusuf, U.K., 2011. Assessment of surface water quality in the Malaysian coastal waters by using multivariate analyses. *Sains Malaysiana*, 40(10), pp.1053-1064.

Singh, J. and Kalamdhad, A.S., 2011. Effects of heavy metals on soil, plants, human health and aquatic life. *International Journal of Research in Chemistry and Environment*, 1(2), pp.15-21.

Smirnova, G.F., 2005. Distribution of bacteria resistant to oxygen-containing anions-xenobiotics. *Mikrobiolohichnyi Zhurnal (Kiev, Ukraine: 1993)*, 67(5), pp.11-18.

Tabak, H.H., Lens, P., Van Hullebusch, E.D. and Dejonghe, W., 2005. Developments in bioremediation of soils and sediments polluted with metals and radionuclides–1. Microbial processes and mechanisms affecting bioremediation of metal contamination and influencing metal toxicity and transport. *Reviews in Environmental Science and Bio/Technology*, 4, pp.115-156.

Takáčová, A., Smolinská, M., Ryba, J., Mackuľak, T., Jokrllová, J., Hronec, P. and Čík, G., 2014. Biodegradation of Benzo[a]Pyrene through the use of algae. *Central European Journal of Chemistry*, 12, pp.1133-1143.

Tseng, T.T., Gratwick, K.S., Kollman, J., Park, D., Nies, D.H., Goffeau, A. and Saier, Jr., M.H., 1999. The RND permease superfamily: an ancient, ubiquitous and diverse family that includes human disease and development proteins. *Journal of Molecular Microbiology and Biotechnology*, 1(1), pp.107-125.

Tyagi, B. and Kumar, N., 2021. Bioremediation: Principles and applications in environmental management. In: *Bioremediation for Environmental Sustainability*. Elsevier, pp.3-28.

Tyagi, P., Singh, A. and Ranjan, R., 2022. Hazardous elements in plants: sources, effect and management. In: *Hazardous and Trace Materials in Soil and Plants*. Academic Press, pp.113-128.

Uchenna, G., 2020. Abandoned gold mine tailings: mineralogy, environmental hazards, valorization, and remediation strategies–a multidisciplinary approach. University of Johannesburg (South Africa).

Upton, A., 2002. Biostimulation. *Lasers in Surgery and Medicine*, 30. Available at: https://doi.org/10.1002/lsm.1141 [Accessed 22 November 2023].

Valencia, E.Y., Braz, V.S., Guzzo, C. and Marques, M.V., 2013. Two RND proteins involved in heavy metal efflux in *Caulobacter crescentus* belong to separate clusters within proteobacteria. *BMC Microbiology*, 13, pp.1-12.

Van Assche, F. and Clijsters, H., 1990. Effects of metals on enzyme activity in plants. *Plant, Cell & Environment*, 13(3), pp.195-206.

Varjani, S.J., Agarwal, A.K., Gnansounou, E. and Gurunathan, B., eds., 2018. *Bioremediation: Applications for Environmental Protection and Management*. New York, NY: Springer.

Vishwakarma, S.K., Patil, A., Pandey, A. and Arya, M., 2023. Biosorption of Heavy Metal (Mn2+) by Thermophilic Bacterial Strains Isolated from Surya Kund Hot Spring, Yamunotri, Uttarakhand. *Applied Biochemistry and Biotechnology*, pp.1-16.

Volesky, B., 1990. *Biosorption of Heavy Metals*. CRC Press, Boca Raton.

von Fahnestock, F.M. and Wickramanayake, G.B., 1998. *Biopile Design, Operation, and Maintenance Handbook for Treating Hydrocarbon-Contaminated Soils*. Tabak, H.H., Lens, P., Van Hullebusch, E.D. and Dejonghe, W., 2005. Developments in bioremediation of soils and sediments polluted with metals and radionuclides–1. Microbial processes and mechanisms affecting bioremediation of metal contamination and influencing metal toxicity and transport. *Reviews in Environmental Science and Bio/Technology*, 4, pp.115-156.

Takáčová, A., Smolinská, M., Ryba, J., Mackuľak, T., Jokrllová, J., Hronec, P. and Čík, G., 2014. Biodegradation of Benzo[a]Pyrene through the use of algae. *Central European Journal of Chemistry*, 12, pp.1133-1143.

Tseng, T.T., Gratwick, K.S., Kollman, J., Park, D., Nies, D.H., Goffeau, A. and Saier, Jr., M.H., 1999. The RND permease superfamily: an ancient, ubiquitous and diverse family that includes human disease and development proteins. *Journal of Molecular Microbiology and Biotechnology*, 1(1), pp.107-125.

Tyagi, B. and Kumar, N., 2021. Bioremediation: Principles and applications in environmental management. In: *Bioremediation for Environmental Sustainability*. Elsevier, pp.3-28.

Tyagi, P., Singh, A. and Ranjan, R., 2022. Hazardous elements in plants: sources, effect and management. In: *Hazardous and Trace Materials in Soil and Plants*. Academic Press, pp.113-128.

Uchenna, G., 2020. Abandoned gold mine tailings: mineralogy, environmental hazards, valorization, and remediation strategies–a multidisciplinary approach. University of Johannesburg (South Africa).

Upton, A., 2002. Biostimulation. *Lasers in Surgery and Medicine*, 30. Available at: https://doi.org/10.1002/lsm.1141 [Accessed 22 November 2023].

Valencia, E.Y., Braz, V.S., Guzzo, C. and Marques, M.V., 2013. Two RND proteins involved in heavy metal efflux in *Caulobacter crescentus*

belong to separate clusters within proteobacteria. *BMC Microbiology*, 13, pp.1-12.

Van Assche, F. and Clijsters, H., 1990. Effects of metals on enzyme activity in plants. *Plant, Cell & Environment*, 13(3), pp.195-206.

Varjani, S.J., Agarwal, A.K., Gnansounou, E. and Gurunathan, B., eds., 2018. *Bioremediation: Applications for Environmental Protection and Management*. New York, NY: Springer.

Vishwakarma, S.K., Patil, A., Pandey, A. and Arya, M., 2023. Biosorption of Heavy Metal (Mn2+) by Thermophilic Bacterial Strains Isolated from Surya Kund Hot Spring, Yamunotri, Uttarakhand. *Applied Biochemistry and Biotechnology*, pp.1-16.

Volesky, B., 1990. *Biosorption of Heavy Metals*. CRC Press, Boca Raton.

von Fahnestock, F.M. and Wickramanayake, G.B., 1998. *Biopile Design, Operation, and Maintenance Handbook for Treating Hydrocarbon-Contaminated Soils*.

Wang, J. and Chen, C., 2009. Biosorbents for heavy metals removal and their future. *Biotechnology Advances*, 27, pp.195-226.

White, C. and Gadd, G.M., 1998. Accumulation and effects of cadmium on sulphate-reducing bacterial biofilms. *Microbiology*, 144, pp.1407-1415.

White, C. and Gadd, G.M., 2000. Copper accumulation by sulphate-reducing bacterial biofilms and effects on growth. *FEMS Microbiology Letters*, 183, pp.313-318.

White, C., Dennis, J.S. and Gadd, G.M., 2003. A mathematical process model for cadmium precipitation by sulphate-reducing bacterial biofilms. *Biodegradation*, 14, pp.139-151.

White, C., Sharman, A.K. and Gadd, G.M., 1998. An integrated microbial process for the bioremediation of soil contaminated with toxic metals. *Nature Biotechnology*, 16, pp.572-575.

Wysocki, R., Wysocka, A. and Michalik, J., 2006. The ArsB protein from Saccharomyces cerevisiae. *FEMS Yeast Research*, 6(2), pp.220-228.

Xu, J. and Sparks, D.L., 2013. *Molecular Environmental Soil Science*. Netherlands: Springer, pp.193-228.

Xu, X., Liu, W., Tian, S., Wang, W., Qi, Q., Jiang, P. and Yu, H., 2018. Petroleum hydrocarbon-degrading bacteria for the remediation of oil pollution under aerobic conditions: a perspective analysis. *Frontiers in Microbiology*, 9, p.2885.

Yakimov, M.M., Timmis, K.N. and Golyshin, P.N., 2007. Obligate oil-degrading marine bacteria. *Current Opinion in Biotechnology*, 18(3), pp.257-266.

Yang, H.C. and Rosen, B.P., 2016. New mechanisms of bacterial arsenic resistance. *Biomedical Journal*, 39(1), pp.5-13. Available at: http://dx.doi.org/10.1016/j.bj.2015.08.003 [Accessed 22 November 2023].

Zgurska, K., Nies, D.H. and Brandt, U., 2015. Coordinated regulation of efflux pumps in Escherichia coli. *Current Topics in Microbiology and Immunology*, 392, pp.253-287. Available at: https://www.ncbi.nlm.nih.gov/pmc/articles/PMC4732084/ [Accessed 22 November 2023].

Seasonal Variations in Microplastic Abundance and Removal Efficiency in Wastewater Treatment Plants in Bangkok, Thailand

M. Eknai[1], S. Leungprasert[1] and K. Tungsudjawong[2]† (ORCID)

[1]Department of Environmental Engineering, Faculty of Engineering, Kasetsart University, Bangkok 10900, Thailand
[2]Division of Environmental Science and Technology, Faculty of Science and Technology,
Rajamangala University of Technology Phra Nakhon, Bangkok 10800, Thailand
†Corresponding author: K. Tungsudjawong; kitiyot.t@rmutp.ac.th

ABSTRACT

Wastewater treatment plants (WWTP) are significant contributors to the release of microplastics into aquatic environments. Due to the limited information available in Thailand, examining microplastics from WWTPs could assist the Thai government in establishing guidelines for future microplastic control. This study identified microplastics in various WWTPs across Bangkok, Thailand, during two seasons: the dry period (February to May 2022) and the wet period (June to October 2022). The findings revealed a higher abundance of microplastics during the wet season compared to the dry season. In both influent and effluent, fibers were the predominant shape, making up approximately 86.65% during the dry period and 94.37% during the wet period. Fragments, films, granules, and foam were also detected in all samples. Polyethylene terephthalate (PET), polyethylene (PE), and polypropylene (PP) were the most common polymers present in the microplastic samples. The study also highlighted that the removal efficiency of microplastics from WWTPs ranged from 16.7% to 85.4% during the dry period and from 27.6% to 81.0% during the wet period. These results underscore the importance of long-term monitoring and quantification of microplastics in different WWTP systems in Bangkok. This data can be utilized to estimate microplastic loading in WWTPs and develop effective strategies for microplastic removal from wastewater.

INTRODUCTION

Plastics are materials invented and developed for use in daily life (Mao et al. 2020, Plastics Europe and European Association of Plastics Recycling 2017). The demand for plastic products has increased significantly over the past few decades, leading to enormous amounts of plastic waste contaminating the environment. Monomers that are not easily biodegradable, such as polypropylene (PP), are widely used to produce common plastic materials (Geyer & Jambeck 2017) because of their high stability and durability. Generally, microplastics are plastic particles smaller than 5 mm in diameter(Talvitie et al. 2017). Most originate from personal care products such as scrubs, cosmetics, and toothpaste (Suaria et al. 2020) and may occur from the breakdown of large plastic waste through mechanical, biological, chemical, and photo-oxidized degradation (Galafassi et al. 2019, Gatidou et al. 2019).

Microplastics are severe environmental pollutants. Improper disposal of plastic waste worldwide has led to the accumulation of microplastics in a variety of environmental compartments, including soil, air, rivers, lakes, oceans, biota, and food (Eo et al. 2019, Grbic et al. 2020, Karbalaei et al. 2018, Hamid et al. 2018, WHO 2019, Yu et al. 2020, Zhang et al. 2019). Microplastics threaten the environment, animals, and humans because of their toxic components, that is, chemical additives such as Bisphenol A or other toxic compounds such as polychlorinated biphenyls, all of which can be absorbed (Eerkes-Medrano et al. 2015, Gallo et al. 2018, Yong et al. 2020). Marine species are adversely affected by these substances owing to their mechanisms of action, including absorption, ingestion, or unintentional capture and uptake.

Wastewater treatment plants (WWTP) are generally referred to as point sources of microplastics discharged into aquatic environments. Globally, microplastics have been detected in WWTP effluents in Asia, Europe, the USA, Australia, China, and Russia (Prata 2018). Although the relationship between microplastics in aquatic environments and WWTP has not been reported (Carr et al. 2016), several studies have shown that WWTP can effectively remove approximately 50–99% of microplastics (Iyare et al. 2020,

Table 1: Details of selected wastewater treatment plants from Bangkok, Thailand.

Locations	Population	Area (km^2)	Treatment Capacity (m^3/day)	Treatment System	1st Treatment	2nd Treatment
WWTP-A	432,000	33.4	150,000	Cyclically activated sludge	Screening Grit chamber	Sequence-batch activated sludge
WWTP-B	1,080,000	37	350,000	Biologically activated sludge with nutrient sludge	Screening Grit chamber	Conventional activated sludge Sedimentation tank
WWTP-C	120,000	20	120,000	Four-step feed Activated sludge Biological nutrient removal	Screening Grit chamber	Step-feed Anoxic/Oxic Sedimentation tank
WWTP-D	120,000	2.7	30,000	Contact stabilization activated sludge	Screening Grit chamber	Contact stabilization activated sludge Sedimentation tank
WWTP-E	70,000	4.1	40,000	Two-Stage activated sludge	Screening Grit chamber	Two-stage activated sludge Sedimentation tank

Liu et al. 2019). However, owing to the limitations of the different units used in WWTP (Jiang et al. 2020, Lv et al. 2019, Tagg et al. 2020), different amounts of microplastics may be released into the aquatic environment. As a result, this study aimed to investigate the types and amounts of microplastics in the influent and effluent of different WWTP during the wet and dry seasons.

MATERIALS AND METHODS

Five existing domestic WWTPs located in Bangkok, Thailand, namely WWTP-A, WWTP-B, WWTP-C, WWTP-D, and WWTP-E, were selected to identify microplastics in the influents and effluents. Each treatment plant operated under different activated sludge processes, including the use of cyclically activated sludge, biologically activated sludge with nutrient sludge, four-step feed activated sludge biological nutrient removal, contact stabilization activated sludge, and two-stage activated sludge. The treatment capacities of each plant are listed in Table 1. Water samples were collected from February to May 2022 (dry period) and from June to October 2022 (wet period).

A flow diagram of the selected wastewater plants is shown in Fig. 1. All five WWTPs had different treatment systems, which may have affected the microplastic removal efficiency. Therefore, water sample collection in different seasons may help determine the removal efficiency of microplastics from different wastewater treatment processes.

A 50-L water sample from the influent and a 100-L water sample from the effluent were collected using a rotary pump (12V/DC 8A). The pump head was placed on the surface of the water at a depth of approximately 30 cm, and the water samples were passed through a sieve size of 0.3 mm (No. 50) made of stainless-steel mesh sieves. All the particles remaining on the mesh sieves were then rinsed using distilled

water before being passed through a glass bottle. The water samples in the bottles were kept in a refrigerator at 4°C.

Microplastic Analysis

Microplastics were analyzed following modifications to the National Oceanic and Atmospheric Administration method (Masura et al. 2015). Each sample was poured through 0.3-mm (No. 50) stainless-steel mesh sieves and flushed using distilled water to transfer the particles to the beaker. The sample was dried at 90°C in a hot-air oven for 24 hours or more. To digest organic particles, the Fenton reagent was used by mixing 20 mL of 30% hydrogen peroxide with 20 mL of 0.05 M Ferrous sulfate (Gundogdu et al. 2018). Thereafter, the mixtures were heated to 75°C for 30 min. In addition, 5-M sodium chloride (NaCl) was prepared by mixing 6 g of NaCl per 20 mL of sample to increase the density of the aqueous solution. The digested samples were rinsed into a glass funnel and allowed to settle overnight. The floating microplastics were filtered through 0.3-mm (No. 50) stainless-steel mesh sieves. The remaining samples were transferred into a Petri dish and dried at 90°C by using a hot-air oven for 24 h before being taken to identify the amounts and types of microplastics.

Microplastic Identification

The physical characteristics of the MP particles from the remaining samples, including shape, size, and abundance, were determined using a stereomicroscope (Olympus, SZ61TR) at 40X magnification (Crawford 2017, Hidayaturrahman & Lee 2019). In addition, the chemical characteristics of the microplastics were identified using a Fourier-transform infrared spectrophotometry (FT-IR, Bruker Alpha II) attenuated total reflectance technique in the 4000–650 cm-1 wave range with 64 scans at a resolution of 8 cm-1 (Ribeiro-Claro et al. 2017). Different types of microplastic particles were identified by comparing the
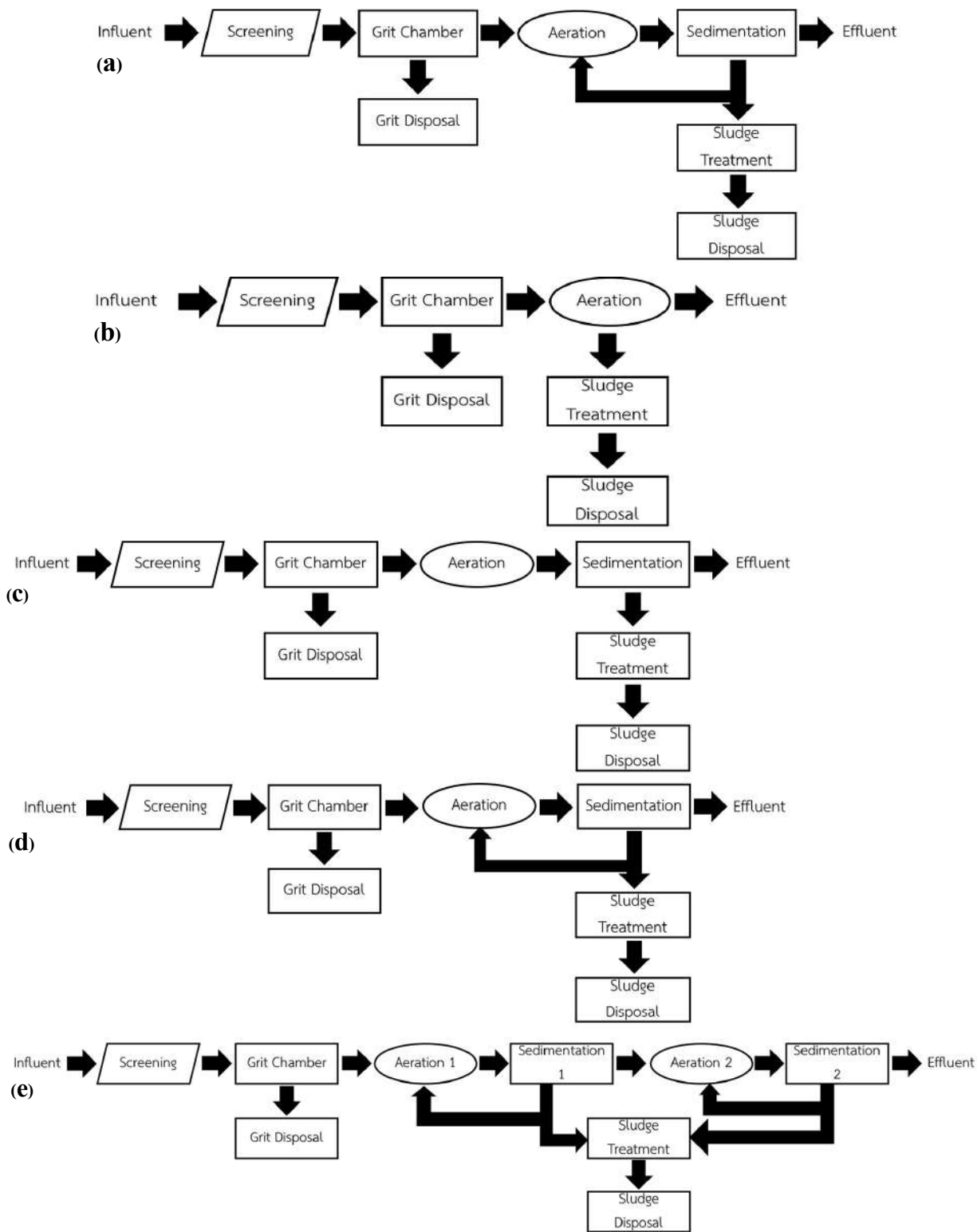
Fig. 1: Flow diagram of existing wastewater treatment systems in Bangkok; (a) WWTP-A, (b) WWTP-B, (c) WWTP-C, (d) WWTP-D and (e) WWTP-E.

standards of polymer spectra in a database (Qiu 2016, Jung et al. 2018).

RESULTS AND DISCUSSION

Variation of Microplastics from the Influent and Effluent of the Existing Wastewater Treatment Plants in Bangkok

In this study, seasonal variations in microplastic concentrations were evaluated to determine the removal efficiency of microplastics from the five existing WWTPs located in Bangkok. The abundances of microplastics from the five existing WWTP (WWTP-A, WWTP-B, WWTP-C, WWTP-D, and WWTP-E) are shown in Table 2. The amount of microplastics in the influent was higher than that in the effluent during both seasons (dry and wet seasons). The concentration of microplastics from the influents of WWTP-D was the highest (approximately 2.04 items/L) while that from the influents of WWTP-C, WWTP-E, WWTP-B, and WWTP-A were approximately 1.85, 1.22, 0.56, and 0.42 items/L, respectively, for the dry period. During the wet period, the highest amount of microplastics in the influent was from WWTP-C (2.69 items/L), followed by WWTP-A, WWTP-D, WWTP-B, and WWTP-E (2.45, 1.70, 1.24, and 0.76 items/L, respectively). Seasonal microplastic abundance was observed in the influent samples. The difference in microplastic concentration depends on a variety of factors, such as population, surrounding land use, combined sewer systems, and domestic water demand (Long et al. 2019, Mason et al. 2016, Tang et al. 2020).

During the COVID pandemic in Thailand since March 2020 (Rajatanavin et al. 2021), the majority of the population was locked down to prevent the spread of COVID-19, leading to a high-density population in a limited area. Consequently, wastewater from human activities, such as the use of personal care products, is the main source of microplastics released into the environment daily (Waller et al. 2017). Therefore, the number of microplastics in the influent of WWTP-D increased. In addition, microplastics from WWTP-A and WWTP-B were found at low concentrations due to an increase in the wastewater receiving area and its

properties, such as the size, shape, density, and buoyancy of microplastics (Kowalski et al. 2016). In addition, most low-density microplastics float on the water surface (Kay et al. 2018). More than half of all microplastics produced can float and disperse on water surfaces (Kukulka et al. 2012).

In Bangkok, the air is easily dried during the dry period, which leads to microplastic accumulation along drainage lines and reduces the amount of microplastics entering WWTP. In contrast, during the wet period, microplastic concentrations increased at WWTP-A, WWTP-B, and WWTP-C.

The increase in the amount of microplastics entering the WWTP may have been due to the use of combined sewer systems in Bangkok (Kuster & Kuster 2017). During the rainy season, water flow velocity and other hydraulic parameters may also affect the amount of microplastics (Roscher et al. 2022). In addition, stormwater runoff causes a resuspension flux, which increases the amount of low-density microplastics (He et al. 2021, Jarlskog et al. 2020, Ziajahromi et al. 2020). As a result, more microplastics entered the WWTP. These results agree well with a previous study (Wilyalodia et al. 2023) reporting that the microplastics concentration of Ciliwung River, Jakarta Indonesia, was higher in the rainy season compared with the dry season and this behavior as consistent with this studies.

The receiving area between wastewater and runoff water is a major pathway for the release of microplastics into the environment (Wang et al. 2022). This leads to low concentrations of microplastics (Le et al. 2023).

This is due to the dilution of runoff water from the WWTP. The type of residential area might be another important factor affecting an increase in microplastic abundance. Therefore, it will be necessary to determine the relationship between residential areas and microplastics in future studies.

The concentrations of microplastics in the effluent of WWTP-D were found to be at the highest level, approximately 0.80 items/L. In addition, the concentrations

Table 2: Abundance of microplastics from WWTPs.

Locations	Microplastics found in wastewater treatment plants (items/L)			
	Dry period		Wet period	
	Influent	Effluent	Influent	Effluent
WWTP-A	0.42±0.21	0.35±0.25	2.45±1.18	0.77±0.38
WWTP-B	0.56±0.14	0.46±0.27	1.24±0.80	0.40±0.25
WWTP-C	1.85±0.45	0.27±0.07	2.69±1.16	0.51±0.10
WWTP-D	2.04±0.39	0.80±0.26	1.70±0.39	0.42±0.15
WWTP-E	1.22±0.47	0.37±0.16	0.76±0.35	0.55±0.27

of microplastics in WWTP-B, WWTP-E, WWTP-A, and WWTP-C were approximately 0.46, 0.37, 0.35, and 0.27 items/L, respectively, during the dry period. During the wet period, the highest concentration of microplastics was found in WWTP-A (0.77 items/L). The concentrations of microplastics in WWTP-E, WWTP-C, WWTP-D, and WWTP-B were approximately 0.55, 0.51, 0.42, and 0.40 items/L, respectively. Yang et al. (2020) reported that 0.59 items/L of microplastics were determined in the final effluent. This was similar to the results of the final effluent from a WWTP in Australia, which contained 0.28 items/L (Ziajahromi et al. 2017). However, the microplastic concentrations in the final effluent from different WWTP worldwide vary from 0.005 to 447 items/L (Lares et al. 2018, Sun et al. 2019). This variation may be due to several factors, including the composition of raw wastewater, units used in the treatment plants (Mahon et al. 2017), sampling, sample processing, and characterization methods (Lares et al. 2018).

Although microplastics in the effluent were detected at relatively low concentrations, the total discharge of microplastics released from the WWTP was of high concern because of the large amount of wastewater discharged into rivers daily. The results showed that the effluent from the WWTP was a potential major source of microplastic pollution in the aquatic environment. As a result, the discharge of the effluent from the WWTP may drastically increase the number of microplastics in the downstream of the river.

Determination of Removal Efficiency of Microplastics from Wastewater Treatment Plants

Fig. 1 shows a flow diagram of the wastewater treatment system of each study area. The same steps were used for the wastewater treatment processes when passing the influent through screening using a grit chamber. In addition, the important steps to eliminate microplastics were grit trapping, grease removal, and primary settlement (Murphy et al. 2016). Secondary treatment processes, such as the use of activated sludge, have been reported to be highly effective in removing microplastics (Lares et al. 2018, Talvitie et al. 2017). This may be because the sludge flocs in the aeration tank accumulated the remaining plastic debris (Jeong et al. 2016, Scherer et al. 2017). In addition, chemicals used (such as flocculating agents) may affect microplastic removal, leading to the formation of suspended particulates as flocs (Murphy et al. 2016). Some microplastics may become trapped in these unstable flocs and may not settle. This leads to their dispersion into aquatic environments (Carr et al. 2016). Generally, microplastics return from the sludge to aeration tanks. The rest is sent to a sludge filter press for further disposal or conversion into fertilizer (Hongprasith

et al. 2020). Consequently, microplastics are released into soil and accumulate in the food chain, which may ultimately affect the environment (Murphy et al. 2016).

Wastewater treatment systems generally remove up to 99% of microplastics (Carr et al. 2016, Hidayaturrahman & Lee 2019, Talvitie et al. 2017).

The efficiency of microplastic removal at the WWTP was calculated by comparing the amount of microplastics in the influent with that in the effluent from the WWTP. Eq. 1 was used to calculate the number of microplastics per liter (items/L).

$$\text{Efficiency of microplastic removal (\%)} = \frac{\text{influent samples} - \text{effluent samples}}{\text{influent samples}} \times 100\% \qquad \dots(1)$$

The results showed that the highest removal efficiency for the dry period was approximately 85.41% at WWTP-C and approximately 69.67%, 60.78%, 17.86%, and 16.67% for WWTP-E, WWTP-D, WWTP-B, and WWTP-A, respectively. During the wet period, the highest removal efficiency at WWTP-C was approximately 81.04%. The removal efficiencies of WWTP-D, WWTP-A, WWTP-B, and WWTP-E were approximately 75.29%, 68.57%, 67.71%, and 27.63%, respectively. In this study, the removal efficiency of microplastics in the wastewater treatment systems was relatively low compared to that in other studies (Carr et al. 2016, Hidayaturrahman & Lee 2019, Talvitie et al. 2017).

Determination of Microplastic Shapes from Wastewater Treatment Plants

All the particles were examined under a stereomicroscope (Olympus SZ61TR). Microplastics are classified into six shapes: fibers, fragments, films, sheets, granules, and foams (Wu et al. 2018). Fig. 2 shows the shapes of the microplastics obtained from the WWTP. The proportions of microplastic particle types are shown in Fig. 3. Fibers were the major shape of microplastics found in both the influent and effluent. The fibers found in the influent and effluent of the five WWTP for the dry and wet periods ranged from 81.65 to 88.34%, 83.85 to 90.65%, and from 91.29 to 96.91% and 88.21 to 95.25%, respectively. These findings are similar to those of Ziajahromi et al. (2017) for the fiber-dominant shape of microplastics from a WWTP. In addition, fibers are the largest source of primary microplastics (Kooi & Koelmans 2019, Obbard 2018). Kittipongvises et al. (2022) found that microplastics were composed of approximately 39–82%. As the shapes of microplastics may originate from shredded products, their origins can be inferred (Cheung et al. 2016, Helm 2017). Physical or chemical processes can break down large plastic packing products into small plastic

particles until they become fragmented microplastics (Liu et al. 2019). Fibers originate from synthetic fiber products used in daily life and are released from shredded clothes and textile washing, thus passing through domestic wastewater (Allen et al. 2019, Hernandez et al. 2017). Browne et al. (2011) reported that the washing of a polyester textile can release more than 100 microplastic fibers per liter. As a result, fibers are most likely to remain in effluents (Liu et al. 2019, Talvitie et al. 2017).

Fragment films, sheet granules, and foam were observed at all time points. Researchers have found that fibers and fragments are the dominant microplastic type (Fu & Wang 2019).

However, in this study, no plastic microbeads, personal cosmetic products, or other industrial products were found in the WWTP. This was probably due to the ban on microbeads in Thailand since January 1, 2020. This regulation was used for Thailand's roadmap of a plastic waste management plan for 2018 to 2030 issued by the Pollution Control Department (Ministry of Natural Resources and Environment 2018).

In summary, seasonal changes are a key factor that differentiates microplastic contamination such as fibers, which is consistent with previous studies to show that the microplastics in the rainy season are higher than in the dry season (Kim et al. 2022).

Polymer Types of Microplastics from Wastewater Treatment Plants

FT-IR was used to identify the polymer types of microplastics in the wastewater. The results of the microplastic polymer types will enhance the quality and performance of the plastic materials produced in WWTP. As a result, the polymer types of microplastics are very important for demonstrating the persistence of plastics in the environment (Sun et al. 2019). As shown in Fig. 4, the transmission spectra of the microplastic particles were mainly found in three types of plastic polymers: polyethylene terephthalate (PET), polyethylene (PE), and polypropylene (PP). There were also different types of microplastic polymers found in the WWTP, including Nylon, Polystyrene, Polyvinyl chloride (PC), and PP. However, the three main types of microplastic polymers found in the influent and effluent of the WWTP during all periods were PET, PE, and PP (Andrady 2011, Ben-David et al. 2021, Ziajahromi et al. 2017).

The types of microplastics were found to be similar in the five WWTPs during both periods (Table 3). For WWTP-A, the major polymer type of microplastic was PET in the influent and PP, PE, PET, and Ethylene-vinyl acetate (EVA) in the effluent. The major polymer types of microplastics in WWTP-B were EVA in the influent and PET in the effluent. The major polymer types of microplastics in WWTP-C were PE and PET in both the influent and effluent. In addition, the
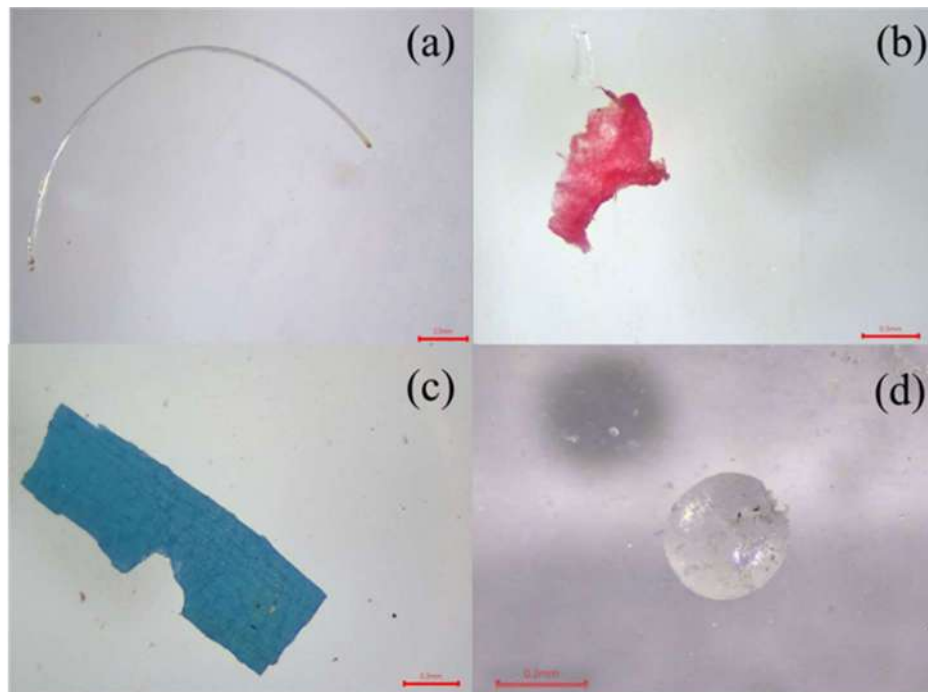
Fig. 2: Examples of microplastic shapes found in wastewater treatment plants: (a) fiber, (b) fragment, (c) sheet, and (d) granule.
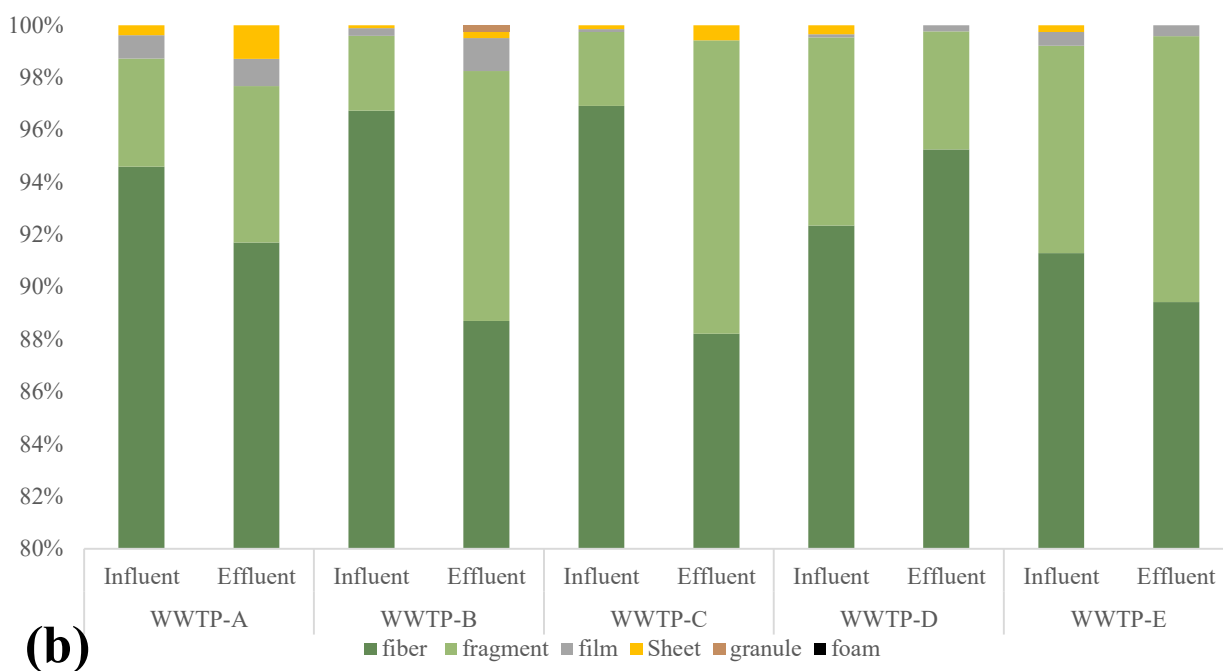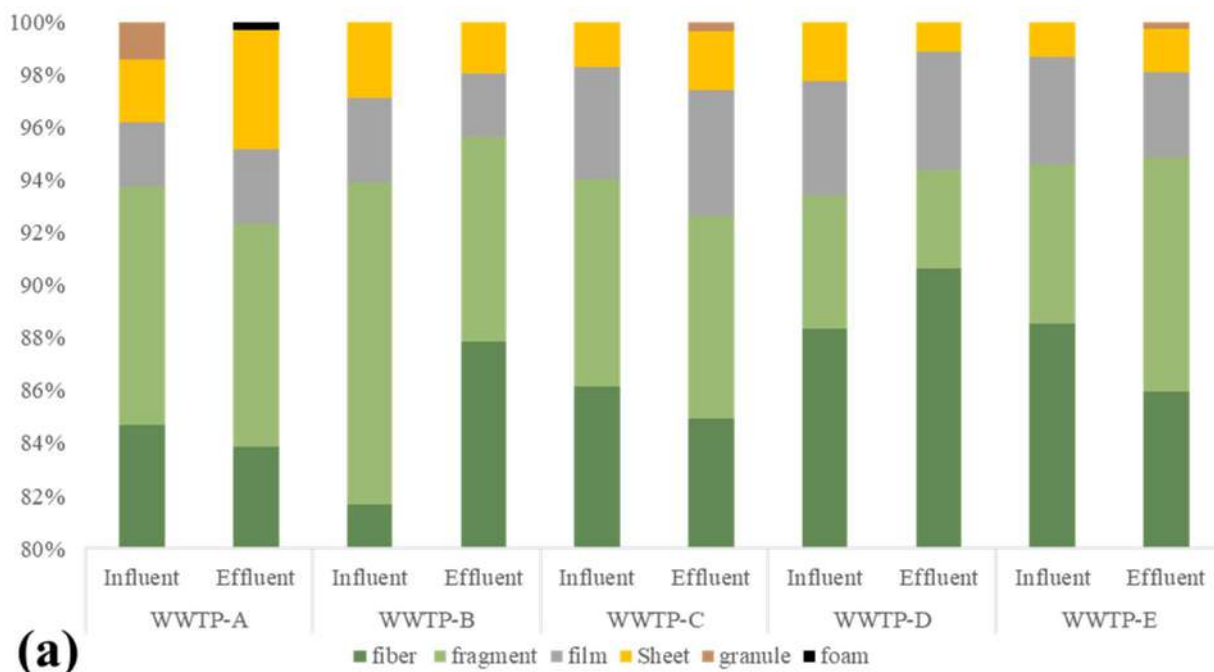
Fig. 3: Proportion of microplastic particle types. (a) dry period and (b) wet period.

major polymer types of microplastics in WWTP-D were PP and PET in the influent and PET in the effluent. The major polymer types of microplastics in WWTP-E were PET and EVA in the influent and PP and PET in the effluent. The types of polymers will enhance the prediction of the origin of microplastic development(Desforges et al. 2014). From

this study, it was found that microplastic generation may originate from food packaging, water bottles, and plastic bags (PE and PP). They may also be generated from packaging fibers and fabrics (PET) (Edgar Hernandez 2017, Zhao et al. 2015). These findings may help in the control of the sources of microplastic production to prevent water pollution from
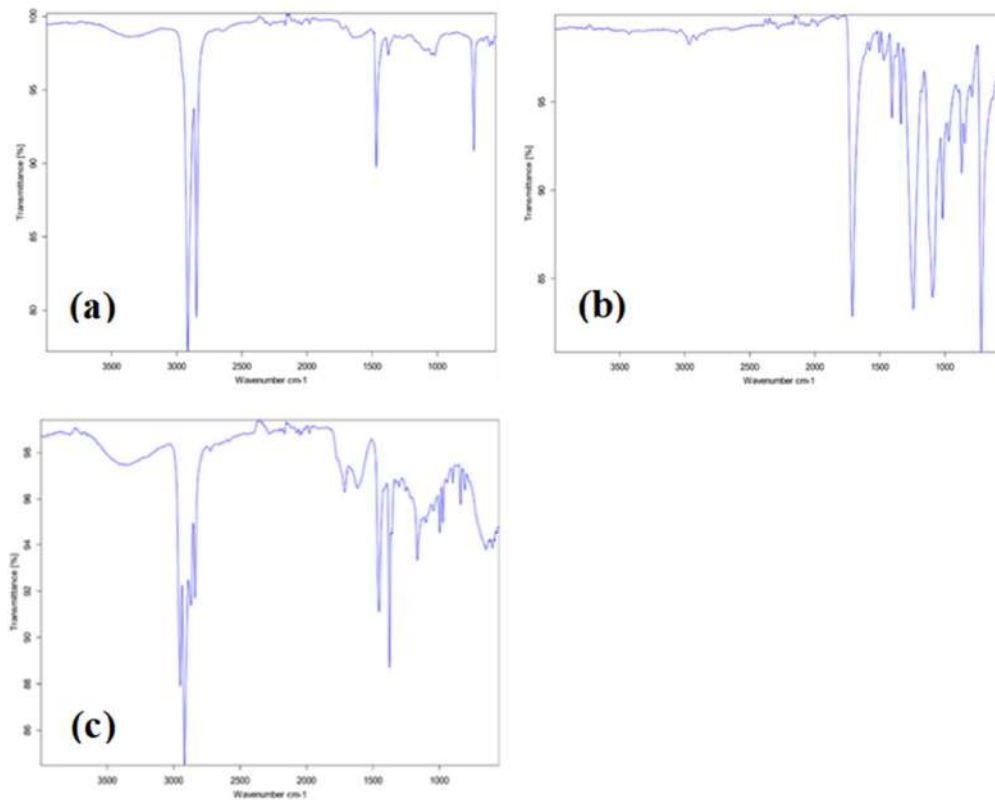
Fig. 4: IR spectrum (from FTIR spectroscope) of microplastic samples found in wastewater treatment plants. (a) Polyethylene, (b) polyethylene tere-phthalate, and (c) polypropylene.

Table 3: Microplastic polymer types from influent and effluent of wastewater treatment plants.

Period	System	Location	Polymer types								
			PP	PE	PET	Nylon	ABS	PTFE	PS	PVC	PC
Dry	WWTP-A	Influent	√		√		√	√			
		Effluent	√	√	√				√		
	WWTP-B	Influent	√		√	√				√	√
		Effluent	√	√	√	√			√	√	
	WWTP-C	Influent	√	√	√		√		√	√	
		Effluent	√	√	√						√
	WWTP-D	Influent	√	√	√	√			√	√	
		Effluent	√	√	√				√	√	√
	WWTP-E	Influent	√	√	√		√				
		Effluent	√	√	√			√		√	
Wet	WWTP-A	Influent		√	√			√		√	√
		Effluent	√	√	√			√		√	
	WWTP-B	Influent	√	√	√	√					√
		Effluent	√	√	√	√			√		
	WWTP-C	Influent		√	√		√			√	
		Effluent	√	√	√						√
	WWTP-D	Influent	√	√	√				√		
		Effluent	√	√	√	√			√	√	
	WWTP-E	Influent	√	√	√		√				
		Effluent	√	√	√	√				√	

WWTP. They can also be used for the improper management of plastic waste in landfills to reduce MP release into the environment.

CONCLUSIONS

Microplastics were quantified in the influent and effluent of existing wastewater treatment plants (WWTP) during both dry and wet periods. The results indicated that microplastic concentrations varied across different WWTPs. Predominantly, fibers were the most common shape of microplastics detected, followed by fragments, films, granules, and foam. Using FT-IR analysis, the primary types of polymers identified were PET, PE, and PP, suggesting that microplastics likely originate from packaging and textile materials. Consequently, microplastics contaminate domestic wastewater and enter WWTPs. The quantity of microplastics also fluctuated between dry and wet seasons. Specifically, the rainy season exhibited higher microplastic influx and discharge at WWTPs due to turbulent flows facilitating their transport. Additional factors, such as laundry activities, may influence the release of microplastics into domestic wastewater. Further research is needed to pinpoint specific sources of microplastics entering WWTPs and to explore additional technologies for their removal.

ACKNOWLEDGEMENTS

REFERENCES

Allen, S., Allen, D., Phoenix, V.R., Le Roux, G., Durántez Jiménez, P., Simonneau, A., Binet, S. and Galop, D., 2019. Atmospheric transport and deposition of microplastics in a remote mountain catchment. *Nature Geoscience*, 12(5), pp.339-344. https://doi.org/10.1038/s41561-019-0335-5.

Andrady, A.L., 2011. Microplastics in the marine environment. *Marine Pollution Bulletin*, 62(8), pp.1596-1605. https://doi.org/10.1016/j.marpolbul.2011.05.030.

Ben-David, E.A., Habibi, M., Haddad, E., Hasanin, M., Angel, D.L., Booth, A.M. and Sabbah, I., 2021. Microplastic distributions in a domestic wastewater treatment plant: Removal efficiency, seasonal variation and influence of sampling technique. *Science of the Total Environment*, 752, p.141880. https://doi.org/10.1016/j.scitotenv.2020.141880.

Carr, S.A., Liu, J. and Tesoro, A.G., 2016. Transport and fate of microplastic particles in wastewater treatment plants. *Water Research*, 91, pp.174-182. https://doi.org/10.1016/j.watres.2016.01.002.

Cheung, P.K., Cheung, L.T.O. and Fok, L., 2016. Seasonal variation in the abundance of marine plastic debris in the estuary of a subtropical macro-scale drainage basin in South China. *Science of the Total Environment*, 562, pp.658-665. https://doi.org/10.1016/j.scitotenv.2016.04.048.

Crawford, C.B. and Quinn, B., 2017. Microplastic identification techniques. In: *Microplastic Pollutants*, pp.219-267.

Desforges, J.P., Galbraith, M., Dangerfield, N. and Ross, P.S., 2014. Widespread distribution of microplastics in subsurface seawater in the NE Pacific Ocean. *Marine Pollution Bulletin*, 79(1-2), pp.94-99. https://doi.org/10.1016/j.marpolbul.2013.12.035.

Edgar Hernandez, B.N. and Mitrano, D.M., 2017. Synthetic Textiles as a Source of Microplastics from Households: A Mechanistic Study to Understand Microfiber Release During Washing. *ACS Publications*.

Eerkes-Medrano, D., Thompson, R.C. and Aldridge, D.C., 2015. Microplastics in freshwater systems: a review of the emerging threats, identification of knowledge gaps and prioritisation of research needs. *Water Research*, 75, pp.63-82. https://doi.org/10.1016/j.watres.2015.02.012.

Eo, S., Hong, S.H., Song, Y.K., Han, G.M. and Shim, W.J., 2019. Spatiotemporal distribution and annual load of microplastics in the Nakdong River, South Korea. *Water Research*, 160, pp.228-237. https://doi.org/10.1016/j.watres.2019.05.053.

Fu, Z. and Wang, J., 2019. Current practices and future perspectives of microplastic pollution in freshwater ecosystems in China. *Science of the Total Environment*, 691, pp.697-712. https://doi.org/10.1016/j.scitotenv.2019.07.167.

Galafassi, S., Nizzetto, L. and Volta, P., 2019. Plastic sources: A survey across scientific and grey literature for their inventory and relative contribution to microplastics pollution in natural environments, with an emphasis on surface water. *Science of the Total Environment*, 693, p.133499. https://doi.org/10.1016/j.scitotenv.2019.07.305.

Gallo, F., Fossi, C., Weber, R., Santillo, D., Sousa, J., Ingram, I., Nadal, A. and Romano, D., 2018. Marine litter plastics and microplastics and their toxic chemicals components: the need for urgent preventive measures. *Environmental Science Europe*, 30(1), p.13. https://doi.org/10.1186/s12302-018-0139-z.

Gatidou, G., Arvaniti, O.S. and Stasinakis, A.S., 2019. Review on the occurrence and fate of microplastics in Sewage Treatment Plants. *Journal of Hazardous Materials*, 367, pp.504-512. https://doi.org/10.1016/j.jhazmat.2018.12.081.

Geyer, R. and Jambeck, J.R., 2017. Production, use, and fate of all plastics ever made. *Science Advances*, 3.

Grbic, J., Helm, P., Athey, S. and Rochman, C.M., 2020. Microplastics entering northwestern Lake Ontario are diverse and linked to urban sources. *Water Research*, 174, p.115623. https://doi.org/10.1016/j.watres.2020.115623.

Gundogdu, S., Cevik, C., Guzel, E. and Kilercioglu, S., 2018. Microplastics in municipal wastewater treatment plants in Turkey: a comparison of the influent and secondary effluent concentrations. *Environmental Monitoring and Assessment*, 190(11), p.626. https://doi.org/10.1007/s10661-018-7010-y.

Hamid, S., Bhatti, M.S., Anuar, N., Anuar, N., Mohan, P. and Periathamby, A., 2018. Worldwide distribution and abundance of microplastic: How dire is the situation? *Waste Management and Research*, 36(10), pp.873-897. https://doi.org/10.1177/0734242X18785730.

He, B., Smith, M., Egodawatta, P., Ayoko, G.A., Rintoul, L. and Goonetilleke, A., 2021. Dispersal and transport of microplastics in river sediments. *Environmental Pollution*, 279, p.116884. https://doi.org/10.1016/j.envpol.2021.116884.

Helm, P.A., 2017. Improving microplastics source apportionment: a role for microplastic morphology and taxonomy? *Analytical Methods*, 9(9), pp.1328-1331. https://doi.org/10.1039/c7ay90016c.

Hernandez, E., Nowack, B. and Mitrano, D.M., 2017. Polyester textiles as a source of microplastics from households: a mechanistic study to understand microfiber release during washing. *Environmental Science and Technology*, 51(12), pp.7036-7046.

Hidayaturrahman, H. and Lee, T.G., 2019. A study on characteristics of microplastic in wastewater of South Korea: Identification, quantification, and fate of microplastics during treatment process. *Marine Pollution Bulletin*, 146, pp.696-702. https://doi.org/10.1016/j.marpolbul.2019.06.071.

Hongprasith, N., Kittimethawong, C., Lertluksanaporn, R., Eamchotchawalit, T., Kittipongvises, S. and Lohwacharin, J., 2020. IR microspectroscopic identification of microplastics in municipal wastewater treatment plants. *Environmental Science and Pollution Research International*, 27(15), pp.18557-18564. https://doi.org/10.1007/s11356-020-08265-7.

Iyare, P.U., Ouki, S.K. and Bond, T., 2020. Microplastics removal in wastewater treatment plants: a critical review. *Environmental Science: Water Research and Technology*, 6(10), pp.2664-2675. https://doi.org/10.1039/d0ew00397b.

Jarlskog, I., Stromvall, A.M., Magnusson, K., Gustafsson, M., Polukarova, M., Galfi, H., Aronsson, M. and Andersson-Skold, Y., 2020. Occurrence of tire and bitumen wear microplastics on urban streets and in sweepsand and washwater. *Science of the Total Environment*, 729, p.138950. https://doi.org/10.1016/j.scitotenv.2020.138950.

Jeong, C. B., Won, E. J., Kang, H. M., Lee, M. C., Hwang, D. S., Hwang, U. K., Zhou, B., Souissi, S., Lee, S. J. and Lee, J. S., 2016. Microplastic size-dependent toxicity, oxidative stress induction, and p-JNK and p-p38 activation in the monogonont rotifer (Brachionus koreanus). *Environmental Science and Technology*, 50(16), pp.8849-8857.

Jiang, J., Wang, X., Ren, H., Cao, G., Xie, G., Xing, D. and Liu, B., 2020. Investigation and fate of microplastics in wastewater and sludge filter cake from a wastewater treatment plant in China. *Science of the Total Environment*, 746, p.141378. https://doi.org/10.1016/j.scitotenv.2020.141378.

Jung, M.R., Horgen, F.D., Orski, S.V., Rodriguez, C.V., Beers, K.L., Balazs, G.H., Jones, T.T., Work, T.M., Brignac, K.C., Royer, S.J., Hyrenbach, K.D., Jensen, B.A. and Lynch, J.M., 2018. Validation of ATR FT-IR to identify polymers of plastic marine debris, including those ingested by marine organisms. *Marine Pollution Bulletin*, 127, pp.704-716. https://doi.org/10.1016/j.marpolbul.2017.12.061.

Karbalaei, S., Hanachi, P., Walker, T.R. and Cole, M., 2018. Occurrence, sources, human health impacts and mitigation of microplastic pollution. *Environmental Science and Pollution Research International*, 25(36), pp.36046-36063. https://doi.org/10.1007/s11356-018-3508-7.

Kay, P., Hiscoe, R., Moberley, I., Bajic, L. and McKenna, N., 2018. Wastewater treatment plants as a source of microplastics in river catchments. *Environmental Science and Pollution Research International*, 25(20), pp.20264-20267. https://doi.org/10.1007/s11356-018-2070-7.

Kim, M.J., Na, S.H., Batoon, R., Byun, I.S. and Kim, E.J., 2022. Seasonal variation and spatial distribution of microplastics in tertiary wastewater treatment plant in South Korea. *Journal of Hazardous Materials*, 438, p.129474. https://doi.org/10.1016/j.jhazmat.2022.129474.

Kittipongvises, S., Phetrak, A., Hongprasith, N. and Lohwacharin, J., 2022. Unravelling capability of municipal wastewater treatment plant in Thailand for microplastics: Effects of seasonality on detection, fate and transport. *Journal of Environmental Management*, 302, p.113990.

Kooi, M. and Koelmans, A.A., 2019. Simplifying Microplastic via Continuous Probability Distributions for Size, Shape, and Density. *Environmental Science and Technology Letters*, 6(9), pp.551-557. https://doi.org/10.1021/acs.estlett.9b00379.

Kowalski, N., Reichardt, A.M. and Waniek, J.J., 2016. Sinking rates of microplastics and potential implications of their alteration by physical, biological, and chemical factors. *Marine Pollution Bulletin*, 109(1), pp.310-319. https://doi.org/10.1016/j.marpolbul.2016.05.064.

Kukulka, T., Proskurowski, G., Morét-Ferguson, S., Meyer, D.W. and Law, K.L., 2012. The effect of wind mixing on the vertical distribution of buoyant plastic debris. *Geophysical Research Letters*, 39(7). https://doi.org/10.1029/2012gl051116.

Kuster, A.T. and Kuster, A.A.C., 2017. Characterization of water quality among direct and delayed wet-weather flows in an urban combined sewer catchment of Thailand. *Songklanakarin Journal of Science and Technology*, 39(4), pp.497-507.

Lares, M., Ncibi, M.C., Sillanpaa, M. and Sillanpaa, M., 2018. Occurrence, identification and removal of microplastic particles and fibers in conventional activated sludge process and advanced MBR technology. *Water Research*, 133, pp.236-246. https://doi.org/10.1016/j.watres.2018.01.049.

Le, T. M. T., Truong, T. N. S., Nguyen, P. D., Le, Q. D. T., Tran, Q. V., Le, T. T., Nguyen, Q. H., Kieu-Le, T. C. and Strady, E., 2023. Evaluation of microplastic removal efficiency of wastewater-treatment plants in a developing country, Vietnam. *Environmental Technology and Innovation*, 29. https://doi.org/10.1016/j.eti.2022.102994.

Liu, K., Wang, X., Fang, T., Xu, P., Zhu, L. and Li, D., 2019. Source and potential risk assessment of suspended atmospheric microplastics in Shanghai. *Science of the Total Environment*, 675, pp.462-471. https://doi.org/10.1016/j.scitotenv.2019.04.110.

Liu, X., Yuan, W., Di, M., Li, Z. and Wang, J., 2019. Transfer and fate of microplastics during the conventional activated sludge process in one wastewater treatment plant of China. *Chemical Engineering Journal*, 362, pp.176-182. https://doi.org/10.1016/j.cej.2019.01.033.

Long, Z., Pan, Z., Wang, W., Ren, J., Yu, X., Lin, L., Lin, H., Chen, H. and Jin, X., 2019. Microplastic abundance, characteristics, and removal in wastewater treatment plants in a coastal city of China. *Water Research*, 155, pp.255-265. https://doi.org/10.1016/j.watres.2019.02.028.

Lv, X., Dong, Q., Zuo, Z., Liu, Y., Huang, X. and Wu, W. M., 2019. Microplastics in a municipal wastewater treatment plant: Fate, dynamic distribution, removal efficiencies, and control strategies. *Journal of Cleaner Production*, 225, pp.579-586. https://doi.org/10.1016/j.jclepro.2019.03.321.

Mahon, A.M., O'Connell, B., Healy, M.G., O'Connor, I., Officer, R., Nash, R. and Morrison, L., 2017. Microplastics in sewage sludge: effects of treatment. *Environmental Science and Technology*, 51(2), pp.810-818.

Mao, Y., Li, H., Gu, W., Yang, G., Liu, Y. and He, Q., 2020. Distribution and characteristics of microplastics in the Yulin River, China: Role of environmental and spatial factors. *Environmental Pollution*, 265(Pt A), p.115033. https://doi.org/10.1016/j.envpol.2020.115033.

Mason, S.A., Garneau, D., Sutton, R., Chu, Y., Ehmann, K., Barnes, J., Fink, P., Papazissimos, D. and Rogers, D.L., 2016. Microplastic pollution is widely detected in US municipal wastewater treatment plant effluent. *Environmental Pollution*, 218, pp.1045-1054. https://doi.org/10.1016/j.envpol.2016.08.056.

Masura, J., Baker, J., Foster, G. and Arthur, C., 2015. Laboratory methods for the analysis of microplastics in the marine environment: Recommendations for quantifying synthetic particles in waters and sediments. NOAA Technical Memorandum NOS-OR&R-48

Murphy, F., Ewins, C., Carbonnier, F. and Quinn, B., 2016. Wastewater Treatment Works (WwTW) as a Source of Microplastics in the Aquatic Environment. *Environmental Science and Technology*, 50(11), pp.5800-5808. https://doi.org/10.1021/acs.est.5b05416.

Obbard, R.W., 2018. Microplastics in Polar Regions: The role of long range transport. *Current Opinion in Environmental Science and Health*, 1, pp.24-29. https://doi.org/10.1016/j.coesh.2017.10.004.

Plastics Europe and European Association of Plastics Recycling (EPRO), 2017. Plastics – the facts 2017. Available at: https://www.plasticseurope.org/en/resources/publications/274-plastics-facts-2017.

Prata, J.C., 2018. Microplastics in wastewater: State of the knowledge on sources, fate and solutions. *Marine Pollution Bulletin*, 129(1), pp.262-265. https://doi.org/10.1016/j.marpolbul.2018.02.046.

Qiu, Q., Tan, Z., Wang, J., Peng, J., Li, M. and Zhan, Z., 2016. Extraction, enumeration and identification methods for monitoring microplastics in the environment. *Estuarine, Coastal and Shelf Science*, 176, pp.102-109.

Rajatanavin, N., Tuangratananon, T., Suphanchaimat, R. and Tangcharoensathien, V., 2021. Responding to the COVID-19 second wave in Thailand by diversifying and adapting lessons from the first wave. *BMJ Global Health*, 6(7). https://doi.org/10.1136/bmjgh-2021-006178.

Ribeiro-Claro, P., Nolasco, M.M. and Araújo, C., 2017. Characterization of microplastics by Raman spectroscopy. *Comprehensive Analytical Chemistry*, 75, pp.119-151. https://doi.org/10.1016/bs.coac.2016.10.001.

Roscher, L., Halbach, M., Nguyen, M.T., Hebeler, M., Luschtinetz, F., Scholz-Bottcher, B.M., Primpke, S. and Gerdts, G., 2022. Microplastics in two German wastewater treatment plants: year-long effluent analysis with FTIR and Py-GC/MS. *Science of the Total Environment*, 817, p.152619.

Scherer, C., Brennholt, N., Reifferscheid, G. and Wagner, M., 2017. Feeding type and development drive the ingestion of microplastics by freshwater invertebrates. *Scientific Reports*, 7(1), p.17006.

Suaria, G., et al., 2020. Microfibers in oceanic surface waters: A global.

Sun, J., Dai, X., Wang, Q., van Loosdrecht, M.C.M. and Ni, B.J., 2019. Microplastics in Wastewater Treatment Plants: Detection, occurrence and removal. *Water Research*, 152, pp.21-37. https://doi.org/10.1016/j.watres.2018.12.050.

Tagg, A.S., Sapp, M., Harrison, J.P., Sinclair, C.J., Bradley, E., Ju-Nam, Y. and Ojeda, J.J., 2020. Microplastic Monitoring at Different Stages in a Wastewater Treatment Plant Using Reflectance Micro-FTIR Imaging. *Frontiers in Environmental Science*, 8. https://doi.org/10.3389/fenvs.2020.00145.

Talvitie, J., Mikola, A., Koistinen, A. and Setala, O., 2017. Solutions to microplastic pollution - Removal of microplastics from wastewater effluent with advanced wastewater treatment technologies. *Water Research*, 123, pp.401-407. https://doi.org/10.1016/j.watres.2017.07.005.

Tang, N., Liu, X. and Xing, W., 2020. Microplastics in Wastewater Treatment Plants of Wuhan, Central China: Abundance, removal, and potential source in household wastewater. *Science of the Total Environment*, 745, p.141026. https://doi.org/10.1016/j.scitotenv.2020.141026.

Waller, C.L., Griffiths, H.J., Waluda, C.M., Thorpe, S.E., Loaiza, I., Moreno, B., Pacherres, C.O. and Hughes, K.A., 2017. Microplastics in the Antarctic marine system: An emerging area of research. *Science of the Total Environment*, 598, pp.220-227. https://doi.org/10.1016/j.scitotenv.2017.03.283.

Wang, C., O'Connor, D., Wang, L., Wu, W. M. and Luo, J., 2022. Microplastics in urban runoff: Global occurrence and fate. *Water Research*, p.119129.

Wilyalodia, H.C., Tybeyuliana, E.V., Mahendra, A.P., Pratama, M.A., Rahmawati, S., Iresha, F.M. and Moersidik, S.S., 2023. Seasonal Variability on Microplastic Pollutions In Water and Sediment of Ciliwung River. *CSID Journal of Infrastructure Development*, 6(2). https://doi.org/10.7454/jid.v6.i2.1118.

World Health Organization (WHO), 2019. Microplastics in drinking water.

Wu, C., Zhang, K. and Xiong, X., 2018. Microplastic Pollution in Inland Waters Focusing on Asia. In *Freshwater Microplastics*, pp.85-99. https://doi.org/10.1007/978-3-319-61615-5_5.

Yong, C.Q.Y., Valiyaveettil, S. and Tang, B.L., 2020. Toxicity of Microplastics and Nanoplastics in Mammalian Systems. *International Journal of Environmental Research and Public Health*, 17(5). https://doi.org/10.3390/ijerph17051509.

Yu, Q., Hu, X., Yang, B., Zhang, G., Wang, J. and Ling, W., 2020. Distribution, abundance and risks of microplastics in the environment. *Chemosphere*, 249, p.126059. https://doi.org/10.1016/j.chemosphere.2020.126059.

Zhang, C., Zhou, H., Cui, Y., Wang, C., Li, Y. and Zhang, D., 2019. Microplastics in offshore sediment in the Yellow Sea and East China Sea, China. *Environmental Pollution*, 244, pp.827-833. https://doi.org/10.1016/j.envpol.2018.10.102.

Zhao, S., Zhu, L. and Li, D., 2015. Microplastic in three urban estuaries, China. *Environmental Pollution*, 206, pp.597-604. https://doi.org/10.1016/j.envpol.2015.08.027.

Ziajahromi, S., Drapper, D., Hornbuckle, A., Rintoul, L. and Leusch, F.D.L., 2020. Microplastic pollution in a stormwater floating treatment wetland: Detection of tyre particles in sediment. *Science of the Total Environment*, 713, p.136356. https://doi.org/10.1016/j.scitotenv.2019.136356.

Ziajahromi, S., Neale, P.A., Rintoul, L. and Leusch, F.D., 2017. Wastewater treatment plants as a pathway for microplastics: Development of a new approach to sample wastewater-based microplastics. *Water Research*, 112, pp.93-99. https://doi.org/10.1016/j.watres.2017.01.042.

ORCID DETAILS OF THE AUTHORS

K. Tungsudjawong: https://orcid.org/0000-0001-6647-3802

Assessing Phytoremediation Potential of *Aloe barbadensis*, *Chrysopogon zizanioides* and *Ocimum tenuiflorum* for Sustainable Removal of Heavy Metals from Contaminated Soil

S. P. Sangeetha[ID]**, S. Sona†**[ID]**, Nabam Tapung, Abhishek Kumar and Suraj Kumar**

Department of Civil Engineering, Aarupadai Veedu Institute of Technology, Vinayaka Missions Research Foundations (DU), Chennai, T.N., India

†Corresponding author: S. Sona; sonasaravananssva@gmail.com

ABSTRACT

India's fast industrialization and population expansion have resulted in heavy metal accumulation from many operations, which has caused massive waste generation and poisoning of soils. Therefore, it is necessary to design reclamation to improve th T.Ne soil. Phytoremediation presents itself as a viable, economical, and environmentally sustainable solution to this problem. This study was carried out by using plants namely, aloe-vera (Aloe-Barbadensis), tulsi (Ocimum Tenuiflorium), and vetiver (Chrysopogon Zizanoides) plants which were planted in a simulated soil of Cd, Zn and Pb, for 4 weeks. The sample of plant and soil were taken in 9 different pots, (15 cm diameter and 25 cm height) among 9 potted soils one will be tested as a controlled sample. An aqueous solution of lead, cadmium and zinc were added separately to the dry soil samples. The moisture level of the soil was maintained to near field water capacity (35.6%) and equilibrated for two weeks. The saplings of vetiver grass, aloe vera and tulsi were selected and pruned (the shoots were originally 20 cm high and the roots 8 cm long), and then transplanted into the pots. The AAS test was conducted after 4 weeks of growing in simulated soil. Tulsi demonstrated the highest efficacy in reducing Zn concentrations from 300 mg/kg to 188.3 mg/kg, followed by vetiver (179.3 mg/kg) and Aloe vera (158.3 mg/kg). Similarly, for Pb, tulsi exhibited the most substantial reduction (from 600 mg/kg to 188.3 mg/kg), followed by vetiver (164.3 mg/kg) and Aloe vera (179.6 mg/kg). Regarding Cd, tulsi reduced concentrations from 80 mg/kg to 18.62 mg/kg, while vetiver achieved a 17.62 mg/kg reduction. The result highlights Tulsi's superior remediation potential, attributed to its efficient heavy metal uptake and translocation mechanisms. Thus, using these plants in the phytoremediation process, the heavy metals are extracted more economically than other plants. This technique highlights the innate ability of hyper-accumulator plant species, which flourish in situations high in heavy metals, to extract contaminants from contaminated soil.

INTRODUCTION

Heavy metal pollution of soil has become a global environmental concern due to increased industrialization and intensification of agricultural practices. Industrialization has emerged as a prominent catalyst for heavy metal pollution, primarily due to its involvement in the extraction, processing, and utilization of metals for manufacturing and energy generation purposes (Mohammed et al. 2011, Kumari et al. 2021). Similarly, contemporary agricultural methodologies that rely extensively on the application of chemical fertilizers, pesticides, and herbicides have inadvertently contributed to the accumulation of heavy metals in soil (Rashid et al. 2023). Although these chemical fertilizers have enhanced agricultural productivity, increased

crop yields, and mitigated hunger, have also unintentionally played a role in the deterioration of soil quality and the accumulation of heavy metals (Bakshi et al. 2018). For instance, using phosphate fertilizers is associated with elevated levels of cadmium, resulting in the accumulation of cadmium in soil, thereby leading to contamination (Lin et al. 2022). Thus, the presence of pollutants resulting from industrial activities, agricultural practices, and urbanization has gradually infiltrated the fundamental structure of our terrestrial environment, posing significant obstacles to ecological integrity, agricultural sustainability, and human health (Zhang & Wang 2020).

There are a variety of repercussions that can arise because of heavy metal contamination in soil. Firstly, contaminated

soil poses a significant threat to agricultural productivity, hampering soil fertility, nutrient cycling, and microbial diversity, ultimately leading to reduced crop yields and compromised quality (Ali et al. 2019). The uptake of heavy metals by plants can also lead to their introduction into the food chain, which eventually puts human health at risk through consuming contaminated crops (Wuana et al. 2011). As a result of prolonged exposure of humans to heavy metals, a wide variety of health problems have been identified, including damage to organs, neurological disorders, and effects that are carcinogenic diseases. Furthermore, heavy metal contamination in soil is a significant environmental threat that has the potential to disrupt ecosystems and biodiversity (Priya et al. 2023, Saxena et al. 2023). Soil-dwelling organisms, essential for the cycling of nutrients and the health of the soil, are especially susceptible to the toxic effects of heavy metals, which can result in population declines and ecological imbalances (Rashid et al. 2023). Furthermore, heavy metals have the potential to leach into groundwater, which can contaminate sources of drinking water and perpetuate a cycle of environmental degradation. Therefore, removing heavy metals from soil is necessary to mitigate these adverse effects and safeguard environmental and human well-being. The removal of heavy metals from soil can be accomplished through various approaches, each of which has its own benefits and drawbacks. One of the most common methods is physical remediation, which entails removing contaminated soil through excavation, dredging, or washing (Azhar et al. 2022). The physical remediation process, despite its efficacy, can be expensive and disruptive to the surrounding environment (Kumar et al. 2021). Heavy metals are dissolved and extracted from soil particles using chemical remediation techniques. Some examples of these techniques include washing soil with chelating agents or acids (Kirpichtchikova et al. 2006). On the other hand, these methods frequently produce hazardous waste and may pose unintended environmental consequences (Khalid et al. 2017).

Thus, among all the available technologies for removing heavy metals from polluted sites, phytoremediation is regarded as the most efficient, cost-effective, environmentally favorable, and preferred method for cleaning up contaminated areas (Singh et al. 2023). It is a more sustainable and environmentally friendly alternative, utilizing biological processes to degrade, sequester, or transform heavy metals in soil (Pang et al. 2023). Phytoremediation, in particular, harnesses the natural abilities of certain plant species to uptake, accumulate, and detoxify heavy metals from the soil. Phytoremediation plants refer to the utilization of living plants to reduce, degrade, or eliminate toxic toxins from soil. Using green plants to decontaminate soil is a progressive and sustainable method that minimizes the need for hefty machinery or additional contaminants by a significant margin (Li et al. 2022). Lucerne, sunflower, corn, date palms, certain mustards, and even willow and poplar trees can be used to remediate contaminated soil in an inexpensive, environmentally friendly, and sustainable manner (Rungwa et al. 2013, Haller et al. 2023). While a wide array of plant species has been employed in phytoremediation projects, recent attention has turned to the unique potential of aromatic plants.

Aromatic plants are cultivated to produce essential oils in addition to their use in culinary applications. Aromatic plant essential oils are utilized in producing soaps, detergents, insect repellents, cosmetics, scents, and even in food preparation. In contrast to grains, legumes, and vegetables, these plants cannot be digested by people or animals and are, therefore, not directly consumed by them. The essential oil derived from aromatic plants does not provide any risks associated with the buildup of heavy metals in plant biomass (Zheljazkov et al. 2006). As a direct outcome of aromatic plant phytoremediation, heavy metals are prevented from entering the food chain (Gupta et al. 2013). Wild animals tend to avoid damaging or eating aromatic crops because of the distinctive odor they give off. There is an abundance of aromatic plant resources that are capable of being utilized on a massive basis. It is a novel approach to the phytoremediation of heavy metal-contaminated sites to utilize these plants in the remediation process (van der Ent & Rylott 2024, Lancheros et al. 2024, Araujo et al. 2024). Aromatic plants that are both ecologically sustainable and practically useful include vetiver (*Vetiveria zizanioides*), lemon grass (*Cymbopogon f lexuosus*), citronella (*Cymbopogon winterianus*), geranium mint (Mentha sp.), and tulsi (*Ocimum basilicum*) (Pandey et al. 2015). Perennial and resistant to the effects of stress are two characteristics shared by several aromatic grasses, including lemon grass, palmarosa, citronella, and vetiver. The plant can be picked for the hydrodistillation of its essential oil in successive years after it has been grown. These goods have a high value but require minimal effort from the buyer.

Thus, heavy metal pollution of soil, driven by industrialization and intensive agricultural practices involving chemical fertilizers and pesticides, has become a global environmental concern due to its detrimental impacts on soil fertility, agricultural productivity, ecological balance, and human health. Traditional remediation methods, while effective, often have significant drawbacks, making phytoremediation a more sustainable and environmentally friendly alternative. When it comes to phytoremediation strategies, the use of aromatic plants presents a new alternative. This is because aromatic plants can absorb heavy metals without it entering the food chain.

Phytoremediation is a green technology that uses the remarkable abilities of plants to clean up contaminated soil. These "nature's vacuum cleaners" absorb pollutants through their roots, transport them to leaves, and either store or transform them into less harmful substances. The process begins with the roots of these plants absorbing pollutants such as heavy metals, pesticides, and hydrocarbons from the soil. Once absorbed, these contaminants are transported through the plant's vascular system to the shoots and leaves and sometimes stored in the roots. Inside the plant, several processes can occur: pollutants can be sequestered in the vacuoles of cells, reducing their bioavailability; they can be transformed into less toxic compounds through metabolic processes such as phytodegradation or phytotransformation; or volatilized through phytovolatilization, where contaminants are converted to gaseous forms and released into the atmosphere at low concentrations (Barroso et al. 2023). Additionally, some plants excrete root exudates that can enhance the microbial degradation of pollutants in the rhizosphere, the zone of soil influenced by root secretions and associated soil microorganisms (Rathore & Kaur 2023). This multifaceted approach not only removes contaminants from the soil but also improves soil structure and fertility, promoting a healthier ecosystem.

A safe, economically viable, and environmentally friendly method for phytoremediation using aromatic plants like tulsi, vetiver, and aloe vera, which are abundantly available, is discussed. The aforementioned plants were assessed for their efficiency in the contaminated soil with cadmium, lead, and zinc. The contamination of the soil was done in relation to the permissible concentration of heavy metals in the soil. The remediation of these elements is considered very important due to their relatively wider spread when compared to other heavy metals and their negative impacts on the ecosystem and human health. Finally, the plants were evaluated for the effects of phytoremediation on the quality of the soil, which included changes in the concentrations of heavy metals and pH levels as shown in Fig.1.

MATERIALS AND METHODS

Red soil: The red soil sample was meticulously collected from the campus of Aarupadai Veedu Institute of Technology, situated in Vinayaka Nagar, Old Mahabalipuram Road, Paiyanoor, Kancheepuram District, Chennai, Tamil Nadu, India. The geographical coordinates of this esteemed institution are approximately 13.0847° N latitude and 80.1924° E longitude. The collected soil was tested and confirmed that it was free from other minerals and heavy metals. The red soil was characterized by its distinctive red hue due to its iron oxide content. They can offer several

benefits for plant health. With its excellent drainage properties, red soil prevents waterlogging and facilitates healthy root growth by ensuring adequate aeration (Gray et al. 2006). Rich in nutrients like iron provides essential elements for plant growth and development (de Souza Costa et al. 2021). Furthermore, its ability to absorb and retain heat promotes root establishment and encourages robust growth, particularly in cooler climates. After characterization, the collected soil was contaminated with zinc, lead, and cadmium. Aqueous solutions containing each metal were individually added to the dry soil samples for experimental studies. Subsequently, phytoremediation studies are conducted on the contaminated soil.

Grow pots and conditions: Nine flower pots were used for this investigation. These pots were categorized into three groups, each representing soil contaminated with zinc (Zn), cadmium (Cd), and lead (Pb), respectively. Within each contamination group, three different plant species were planted separately: Vetiver (*Chrysopogon zizanioides*), Aloe Vera (*Aloe barbadensis* Miller), and Tulsi (*Ocimum tenuiflorum*). The contaminated soil was then carefully placed into the flower pot. The soil moisture level was carefully maintained at near-field water capacity (35.6%) and allowed to equilibrate for two weeks. Saplings of the selected plant species, each pruned to a uniform height of 20 cm with roots measuring 8 cm in length, were transplanted into the pots. These plant species were chosen based on their resilience and ability to thrive under varying soil conditions. The pots were watered daily to 60% of the field water capacity throughout the experiment to ensure optimal growth conditions.

Metal powder: Heavy metals, including zinc, lead, and cadmium, were procured from Labogens Fine Chem, Maharashtra, to serve as crucial elements for the deliberate soil contamination in our experimental setup. These specific metals were selected due to their known environmental significance and prevalence in soil pollution scenarios (Kumari & Mishra 2021). By introducing zinc, lead, and cadmium into our experimental setup, we aimed to replicate real-world conditions of soil contamination, facilitating comprehensive investigations into phytoremediation strategies and their effectiveness in mitigating heavy metal pollution.

Zinc (Zn): The deteriorating environmental conditions attributed to the presence of zinc in the soil prompted our investigation into mitigating its effects through phytoremediation studies. Zinc contamination in soil arises from various sources, including industrial activities such as mining and manufacturing, mining operations alongside other metals like lead, agricultural practices utilizing zinc-
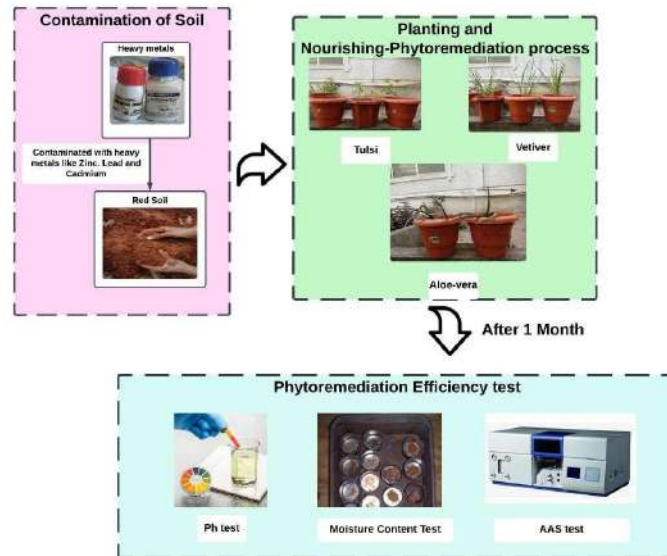
Fig.1: Materials and experimental procedure utilized.

based fertilizers and pesticides, and urban runoff from vehicular traffic and industrial areas (Zhao et al. 2012). The effects of zinc contamination on soil quality encompass soil acidification, reduced fertility, and alterations in soil structure, which impact nutrient availability and hinder plant growth (Korzeniowska et al. 2023). Environmental repercussions of zinc contamination include plant toxicity, water pollution through leaching into groundwater and surface water bodies, bioaccumulation in the food chain, and disruption of soil microbial communities and ecosystem health (Ferrarini et al. 2021). Human health risks associated with zinc exposure include acute symptoms such as nausea and diarrhea, as well as chronic effects like neurological disorders and reproductive toxicity, necessitating mitigation strategies like soil remediation and regulatory measures to safeguard both the environment and public health (Hussain et al. 2022). Recognizing the adverse impact of zinc contamination on soil health and ecosystem integrity, our research endeavors aimed to explore effective plant-based remediation strategies to alleviate its detrimental effects and restore environmental balance.

Lead (Pb): The degradation of ecological conditions due to lead in the soil necessitated its inclusion in our phytoremediation studies. Our research focused on developing effective phytoremediation strategies to mitigate the adverse impact of lead contamination on soil quality, ecosystem health, and human well-being. Lead contamination poses significant risks, including soil degradation, water pollution, and toxicity to plants and animals (Raj et al. 2023). Lead contamination in soil presents multifaceted challenges with far-reaching environmental

and human health implications. This pervasive issue stems from various sources, including historical and current industrial activities, urbanization, agricultural practices, and improper waste disposal (Oorts et al. 2021). The environmental effects of lead contamination are extensive, encompassing soil quality degradation, plant toxicity, water contamination, bioaccumulation, and ecological disruption (Collin et al. 2022). Moreover, lead exposure poses significant health risks to humans, particularly vulnerable populations such as children and pregnant women, leading to neurological, developmental, cardiovascular, renal, and reproductive disorders (Srivastava et al. 2022). Addressing lead contamination demands holistic management strategies focused on prevention, remediation, and regulatory measures to safeguard environmental integrity and public health. By investigating the efficacy of phytoremediation techniques, we aimed to restore environmental balance and protect ecosystems and human health from the harmful effects of lead contamination.

Cadmium (Cd): The adverse change in ecological conditions, exacerbated by heavy metal cadmium contamination in the soil, highlights the critical need to address its adverse impacts. Cadmium contamination threatens soil biodiversity, ecosystem integrity, and overall ecological health (Raza et al. 2020). Its presence can disrupt soil microbial communities, inhibit plant growth, and impair nutrient cycling, leading to cascading effects throughout the ecosystem (Soubasakou et al. 2022). Industrial activities, agricultural practices, urbanization, and improper waste disposal contribute to cadmium contamination in soil, highlighting the need for comprehensive management strategies (Li et al. 2023). The

environmental effects of cadmium contamination include soil degradation, plant toxicity, water contamination, bioaccumulation, and ecological disruption, with adverse impacts on soil health, aquatic ecosystems, and biodiversity (Mahajan et al. 2018). Furthermore, cadmium exposure poses serious health risks to humans, including respiratory problems, kidney damage, bone disorders, and cancer. To address these challenges, preventive measures, remediation efforts, and regulatory interventions are crucial for mitigating the environmental and human health impacts of cadmium contamination and safeguarding ecosystems and public health. In response to these challenges, our research focused on employing phytoremediation as a viable solution. By utilizing cadmium in our phytoremediation studies, we aimed to mitigate the detrimental effects of cadmium contamination and restore ecological balance. Through comprehensive investigations and experiments, we sought to develop effective strategies for remediating cadmium-contaminated environments and safeguarding the health and resilience of affected ecosystems.

Plant Species For The Process Of Phytoremediation

In this research, aromatic plants such as Tulsi (Ocimum tenuiflorum), Aloe Vera (Aloe barbadensis Miller), and Vetiver (*Chrysopogon zizanioides*) were utilized for the phytoremediation process. These plant species were chosen for their resilience to environmental stresses and their potential to thrive in contaminated soil conditions (Pang et al. 2023, Rungwa et al. 2013, Haller et al. 2023). To initiate the phytoremediation process, saplings of the selected plant species were obtained and pruned to ensure uniformity, with a height of 20 cm and roots measuring 8 cm in length. This standardization ensured consistency in the experimental setup and facilitated accurate monitoring of plant growth and metal uptake over time. The collected saplings were then planted in pots filled with soil contaminated with specific levels of heavy metals. Using aromatic plants for phytoremediation presents a promising solution to heavy metal contamination in soil. Unlike traditional crops, aromatic plants are primarily cultivated for their essential oils and industrial applications, not for direct consumption by humans or animals (Gupta et al. 2013). This significantly reduces the risk of heavy metal accumulation in the food chain, providing a sense of security for our ecosystems and human health.

Experimental Investigations

pH Test: The pH level of the soil is essential to ensure optimal plant growth. pH test results will guide the decision whether and how much the soil needs supplements, like fertilizers and soil pH adjusters (Zhang et al. 2022). To measure soil pH accurately, a clean trowel was used to collect soil samples from multiple locations within the testing area to ensure a representative sample. Clumps, debris, or organic matter were removed from the samples. Approximately 15-30 grams of soil was placed into a clean container, and distilled water was added to create a slurry. The mixture was then stirred thoroughly with a clean stirring rod to ensure an even distribution of soil particles in the water. The mixture is then allowed to settle for 30 minutes, letting the soil particles settle at the bottom. A clean pH test paper is dipped into the suspension for a few seconds, then removed, and the color is allowed to develop. The resulting color is compared to the provided pH color chart, and the pH value is recorded once it stabilizes. Control measures include using clean equipment and distilled water to prevent contamination, ensuring consistent sample collection methods, and performing tests under similar environmental conditions to maintain accuracy. These steps ensure reliable pH measurements, providing insights into soil conditions and the effectiveness of phytoremediation.

Moisture content test: The moisture content of a soil sample is determined by measuring the amount of water present in the sample as a percentage of its dry mass. A representative soil sample was collected from the desired depth to determine soil moisture content accurately, ensuring it is free from contaminants, large organic materials, and rocks. Clumps were crushed to ensure uniform drying. An empty drying dish was weighed, the soil sample was added to the dish, and the combined mass was recorded. The dish with the soil sample was then placed in an oven set at a constant temperature of around 105°C for 24 hours to evaporate all moisture. After drying, the dish was transferred to a desiccator to cool, preventing moisture absorption from the air. Once cooled, the dish with the dried soil was weighed, and the mass was recorded. The moisture content was calculated based on the weight difference before and after drying. Control measures include ensuring the oven maintains a constant temperature, using a desiccator to prevent rehydration, and conducting multiple trials to verify consistency. These steps ensure accurate measurement of soil moisture content, which is crucial for assessing soil health and the effectiveness of phytoremediation processes.

AAS Test: The identification of heavy metal absorption by plant species was conducted using Atomic Absorption Spectroscopy (AAS), a widely employed analytical technique for quantifying metal elements. An AA500 instrument was utilized for the AAS test. For the AAS test, soil samples were collected from the desired location using appropriate sampling techniques to ensure representativeness and capture the variability in soil composition. The collected

samples were then air-dried to remove moisture and any volatile organic compounds, with the option to grind the dried samples into a fine powder for homogeneity. Then, the soil samples underwent a digestion process, where a measured amount was transferred into a digestion vessel, and an appropriate digestion method, such as acid digestion, was chosen to extract the metals from the solid matrix into a solution for analysis. Calibration standards were prepared by diluting known concentrations of metal standard solutions, covering the expected concentration range of the metals in the soil samples. The AAS instrument was calibrated using these standards, establishing a linear relationship between the absorbance of metal ions and their concentrations. Specific absorption wavelengths for the metals of interest were selected, and instrument parameters were optimized for sensitivity and resolution. The absorbance of calibration standards and digested soil sample solutions was measured using the AAS instrument, and concentrations of metals in the soil samples were calculated based on the calibration curve obtained from the standards. The analysis was repeated for each metal of interest, and quality control checks, including blank measurements and replicate analyses, were performed to ensure the accuracy and precision of the results. By following these rigorous procedures, accurate data on the levels of heavy metals in soil samples was collected using Atomic Absorption Spectroscopy (AAS), therefore determining the specific metals absorbed by the plant.

RESULTS AND DISCUSSION

pH Test

Phytoremediation, using plants to remove, degrade, or stabilize contaminants in the environment, often involves various mechanisms that can influence soil pH. The pH measurements conducted after the phytoremediation process provide valuable insights into the effectiveness of these plant species in remediation efforts and their potential impact on soil conditions. Table 1 shows, that the consistent pH values observed for tulsi and Aloe vera before and after the

phytoremediation process (both at 7.1) suggest that these plant species maintain their near-neutral pH preferences even after exposure to contaminated soil. This resilience in pH levels indicates the stability of their physiological processes and their capacity to thrive in environments with potentially elevated levels of contaminants. The pH of vetiver remaining at 7.2 post-phytoremediation indicates that this plant species was able to maintain the alkaline pH of the soil. Vetiver is well-known for its ability to tolerate and even thrive in alkaline soil conditions. Its root system, which can penetrate deeply into the soil, facilitates the uptake and sequestration of contaminants while also contributing to soil stabilization and pH regulation. The consistent pH level of 7.2 suggests that vetiver effectively mitigated any potential soil acidification resulting from the phytoremediation process. The stable pH levels observed across all three plant species post-phytoremediation reflect the effectiveness of these plants in facilitating the remediation of contaminated soil without causing significant alterations to soil pH. This is crucial for maintaining the overall health and fertility of the soil ecosystem, as fluctuations in pH can impact nutrient availability, microbial activity, and plant growth. Furthermore, the ability of these plants to maintain their pH preferences underscores their suitability for phytoremediation applications in various environmental settings. By selecting plant species compatible with the existing soil conditions and can thrive throughout the remediation process, phytoremediation efforts can achieve sustainable and long-lasting results while minimizing adverse effects on soil quality. Hence, it is inferred that the stable pH values seen in vetiver, tulsi, and aloe vera throughout the phytoremediation process demonstrate their potential as excellent phytoremediators for polluted soil while maintaining soil health and integrity.

Moisture Content Test

Moisture content is a crucial parameter in assessing soil health and plant performance, particularly in phytoremediation, where plants are utilized to mitigate soil contaminants.

Table 1: pH test results on soil.

S. No.	Plant name	Metal name	Before Contamination	After Contamination	After Phytoremediation (4 weeks later)
1.	Vetiver	Zn	7	8	7.2
2.	Tulsi	Zn	7	8.2	7.1
3.	Aloe Vera	Zn	7	8.2	7.1
4.	Vetiver	Pb	7	8.1	7.1
5.	Tulsi	Pb	7	8	7.1
6.	Aloe Vera	Pb	7	8.2	7.3
7.	Vetiver	Cd	7	8	7.2
8.	Tulsi	Cd	7	8.3	7.2

Table 2: Moisture Content after one month of plantation.

S. no.	Metal	Plant name	Empty wt. of tier (g)	Wt. of tier with wet soil (g)	Wt. of tier with dry soil (g)	Moisture content (%)
1.	Zn	Vetiver	7	12	11	25
2.	Zn	Tulsi	6	13	12	16.67
3.	Zn	Aloe vera	7	19	17	20
4.	Pb	Vetiver	6	14	12	33.3
5.	Pb	Tulsi	11	18	17	16.67
6.	Pb	Aloe vera	12	24	22	20
7.	Cd	Vetiver	7	13	12	20
8.	Cd	Tulsi	7	14	13	16.67

The moisture content measurements obtained after the phytoremediation process offer insights into the soil's water retention capacities and the physiological responses of the plant species involved.

Vetiver: Vetiver, with a moisture content ranging from 20% to 25% as shown in Table 2, demonstrates a moderate level of water retention capacity following the phytoremediation process. This moisture range indicates adequately hydrated soil, essential for sustaining plant growth and facilitating the biochemical processes involved in remediation. Vetiver's fibrous root system, known for its ability to absorb water and nutrients efficiently, likely contributed to maintaining optimal moisture levels in the soil while aiding in contaminant uptake and stabilization.

Tulsi: Tulsi, with a moisture content of 15-17% as shown in Table 2, exhibits a slightly lower moisture range compared to vetiver. However, this moisture level is still acceptable for supporting plant growth and remediation activities. Tulsi is recognized for its drought tolerance and adaptive capacity, enabling it to thrive in diverse soil conditions. Despite the lower moisture content, tulsi's resilience may have contributed to its effective participation in the phytoremediation process, albeit with slightly reduced water availability.

Aloe Vera: Aloe vera, displaying the highest moisture content ranging from 25% to 35%, indicates a significant water retention capacity in the soil post-phytoremediation. Aloe vera is renowned for its succulent leaves and water-storing capabilities, making it well-suited for arid environments and water-stressed conditions. The elevated moisture content observed in the soil associated with Aloe vera suggests efficient water uptake and retention by the plant, which may have facilitated its remediation performance while ensuring its own hydration needs.

The variation in moisture content among the three plant species reflects their distinct physiological characteristics and adaptive strategies in response to environmental conditions. Thus, the moisture content measurements obtained after the phytoremediation process reflect the role of vetiver, tulsi, and aloe vera in maintaining soil moisture balance while actively participating in the remediation of contaminated soil. By effectively managing water availability and uptake, these plant species contribute to sustainable soil restoration efforts and ecosystem resilience in contaminated environments**.**

AAS Test

Soil-metal remediation: The Atomic Absorption Spectroscopy (AAS) content test results for zinc (Zn), lead (Pb), and cadmium (Cd) concentrations in the contaminated soil before and after the phytoremediation process, using tulsi

Table 3: Soil Contamination with various metals.

S.No.	Metals	Plant	Contaminated soil Mg/kg	After phytoremediation process Mg /kg
1.	Zn	Tulsi	300	188.3
2.	Zn	Vetiver	300	179.3
3.	Zn	Aloe vera	300	158.3
4.	Pb	Tulsi	600	188.3
5.	Pb	Vetiver	600	164.3
6.	Pb	Aloe vera	600	179.6
7.	Cd	Tulsi	80	18.62
8.	Cd	vetiver	80	17.62

(Ocimum sanctum), vetiver (*Chrysopogon zizanioides*), and aloe vera, are summarized in Table 3.

Zinc remediation in soil: All three plant species, vetiver, and aloe demonstrated considerable efficacy in reducing Zn concentrations in the soil post-phytoremediation. Tulsi exhibited the highest reduction, with Zn levels decreasing from 300 mg/kg to 188.3 mg/kg as shown in Fig. 2. This reduction indicates the effectiveness of tulsi in remediation, as it absorbed and accumulated zinc within its tissues. Tulsi possesses efficient mechanisms for heavy metal uptake and translocation, making it effective in reducing the bioavailability of zinc in the soil. The decrease in zinc concentration post-phytoremediation suggests that Tulsi successfully remediated the contaminated soil, thereby mitigating the potential adverse effects of zinc pollution on the environment. Vetiver and aloe vera also significantly reduced Zn concentrations to 179.3 mg/kg and 158.3 mg/kg, respectively. Vetiver's extensive root system, characterized by deep penetration and high surface area, enables effective uptake and accumulation of heavy metals like zinc.

While the reduction in zinc concentration is substantial, it indicates that vetiver contributed significantly to the remediation process, albeit to a slightly lesser extent compared to tulsi. Aloe vera also demonstrated remediation potential, although its efficiency in reducing zinc concentration appeared to be lower compared to tulsi and vetiver. Aloe vera's succulent leaves and efficient water uptake mechanisms contribute to its ability to absorb and accumulate heavy metals. While the reduction in zinc concentration is notable, it suggests that Aloe vera may have a lower uptake capacity or affinity for zinc compared to tulsi and vetiver. However, Aloe vera's contribution to remediation should not be discounted, as even marginal reductions in heavy metal concentrations can significantly improve soil quality and environmental health. These results show the potential of these plant species to uptake and accumulate Zn, thereby mitigating its adverse effects on soil and environmental health. Each plant species exhibited varying remediation efficiency, with tulsi demonstrating the highest efficacy followed by vetiver and aloe vera.

Lead remediation in soil: Similar to Zn, all three plant species exhibited notable remediation capabilities for Pb contamination. Tulsi, vetiver, and aloe vera reduced Pb concentrations from 600 mg/kg to 188.3 mg/kg, 164.3 mg/kg, and 179.6 mg/kg, as shown in Fig. 3 respectively. Following the intervention of tulsi, the Pb concentration significantly decreased to 188.3 mg/kg. This remarkable reduction indicates the high remediation efficiency of tulsi in mitigating Pb contamination. Tulsi possesses mechanisms for Pb uptake, translocation, and accumulation within its tissues, thereby effectively removing Pb from the soil matrix. The substantial decrease in Pb concentration post-phytoremediation highlights the effectiveness of tulsi as a potential candidate for Pb remediation in contaminated sites. Vetiver also exhibited notable remediation capabilities for Pb contamination. The Pb concentration in the soil decreased from 600 mg/kg to 164.3 mg/kg after the phytoremediation process involving vetiver. Vetiver's extensive root system, characterized by deep penetration and high surface area, facilitates the uptake and sequestration of Pb from the soil. The significant reduction in Pb concentration reflects the effectiveness of vetiver in immobilizing Pb and reducing its bioavailability in the soil, thereby minimizing potential risks to human health and the environment. Aloe vera demonstrated efficacy in reducing Pb concentrations in the contaminated soil, albeit slightly less than tulsi and vetiver. The Pb concentration decreased from 600 mg/kg to 179.6 mg/kg following the phytoremediation process involving Aloe vera. Aloe vera's succulent leaves and efficient water uptake mechanisms contribute to its ability to absorb and accumulate
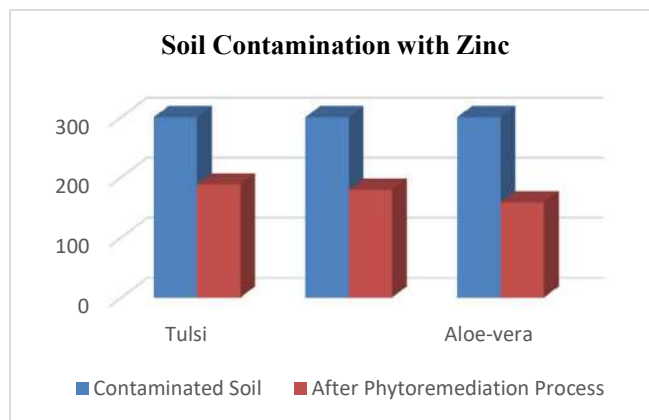

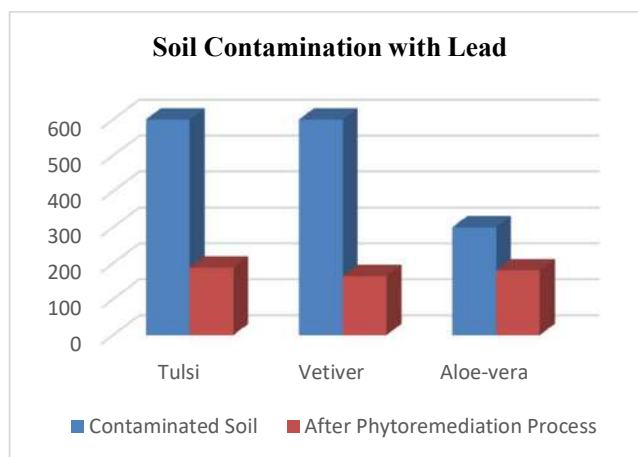Fig. 2: AAS test results of soil contaminated with zinc.

Fig. 3: AAS test results of soil contaminated with Lead.

Pb, thereby aiding in its remediation potential. While the reduction in Pb concentration is significant, it suggests that Aloe vera may have a lower uptake capacity or affinity for Pb compared to tulsi and vetiver. The efficacy of tulsi in Pb remediation is particularly noteworthy, indicating its strong affinity for Pb uptake and sequestration. Vetiver and aloe vera also demonstrated substantial reductions in Pb levels, further highlighting their potential for phytoremediation of Pb-contaminated soils.

Cadmium remediation in soil: Before the phytoremediation process, the Cd concentration in the soil was recorded as 80 mg/kg. Following the intervention of Tulsi, the Cd concentration significantly decreased to 18.62 mg/kg as shown in Fig. 4. This substantial reduction indicates the high remediation efficiency of Tulsi in mitigating Cd contamination. Tulsi possesses mechanisms for Cd uptake, translocation, and accumulation within its tissues, thereby effectively removing Cd from the soil matrix. The significant decrease in Cd concentration post-phytoremediation highlights the effectiveness of Tulsi as a potential candidate for Cd remediation in contaminated sites. Similarly, vetiver demonstrated notable remediation capabilities for Cd contamination. The Cd concentration in the soil decreased from 80 mg/kg to 17.62 mg/kg after the phytoremediation process involving vetiver. Vetiver's extensive root system, characterized by deep penetration and high surface area, facilitates the uptake and sequestration of Cd from the soil. The significant reduction in Cd concentration reflects the effectiveness of vetiver in immobilizing Cd and reducing its bioavailability in the soil, thereby minimizing potential risks to human health and the environment. These findings suggest that both tulsi and vetiver are capable of effectively sequestering Cd, thereby mitigating its environmental impact. The significant reduction in Cd levels underscores the importance of utilizing these plant species in Cd-contaminated soil remediation efforts.
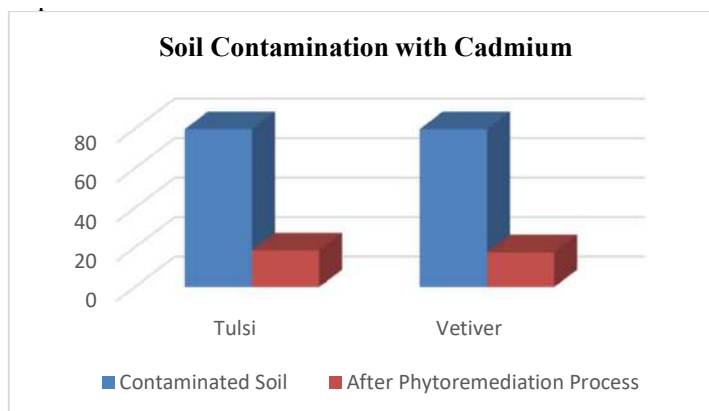

Fig. 4: AAS test results of soil contaminated with cadmium.

Plant-Metal Accumulation

a) **Tulsi:**

- Zinc (Zn): Table 4 suggests tulsi accumulated a moderate amount of zinc, with a concentration of 44.92 mg/kg. This suggests that tulsi can uptake and store zinc from the soil, contributing to its potential role in phytoremediation efforts targeting zinc pollution.

- Cadmium (Cd): The concentration of cadmium in tulsi was below the quantification limit (BQL), indicating that it either did not absorb significant amounts of cadmium from the soil or accumulated it below detectable levels. This could suggest that tulsi may not be as effective in accumulating cadmium compared to other metals.

- Lead (Pb): Tulsi accumulated a relatively high concentration of lead, with a value of 66.32 mg/kg. This indicates tulsi's ability to uptake and sequester lead from the soil, making it potentially useful for phytoremediation of lead-contaminated environments.

b) **Vetiver:**

- Zinc (Zn): Vetiver accumulated a relatively lower concentration of zinc compared to tulsi, with a value of 19.62 mg/kg. While lower, this still indicates the vetiver's capacity to uptake and store zinc, albeit to a lesser extent.

- Cadmium (Cd): Similar to tulsi, vetiver's cadmium concentration was below the quantification limit (BQL), suggesting limited accumulation or accumulation below detectable levels.

- Lead (Pb): Vetiver accumulated a moderate concentration of lead, with a value of 46.9 mg/kg. This indicates its potential for phytoremediation of lead-contaminated soils, although it may be less effective than tulsi in this regard.

c) *Aloe vera*:

- Zinc (Zn): Aloe vera accumulated a significantly higher concentration of zinc compared to both tulsi and vetiver, with a value of 176.3 mg/kg. This suggests that Aloe vera has a strong affinity for zinc uptake and may be highly effective in phytoremediation of zinc-contaminated environments.

- Cadmium (Cd): Similar to tulsi and vetiver, Aloe vera's cadmium concentration was below the quantification limit (BQL), indicating limited accumulation or accumulation below detectable levels.

Table 4: Phytoremediation of plant species.

S.No.	Plant	Metals	Amount of metal absorbed
1.	Tulsi	Zn	44.92
2.	Tulsi	Cd	BQL(LOQ:0.1)
3.	Tulsi	Pb	66.32
4.	vetiver	Zn	19.62
5.	Vetiver	Cd	BQL(LOQ:0.1)
6.	vetiver	Pb	46.9
7.	Aloe vera	Zn	176.3
8.	Aloe vera	Cd	BQL(LOQ:0.1)
9.	Aloe vera	Pb	11.3

- Lead (Pb): Aloe vera accumulated a relatively low concentration of lead, with a value of 11.3 mg/kg. While lower than tulsi and vetiver, this still suggests Aloe vera's potential for phytoremediation of lead-contaminated soils, particularly in conjunction with its other beneficial properties.

Overall, the AAS test results highlight the varying metal accumulation capacities of tulsi, vetiver, and Aloe vera, indicating their potential roles in phytoremediation efforts targeting specific heavy metal pollutants.

CONCLUSIONS

Revegetating heavy metal-polluted land using phytoremediation offers a promising and sustainable solution to mitigate environmental contamination while promoting ecosystem restoration. Through the utilization of metal-accumulating plants, known as hyperaccumulators, and the natural processes of phytoextraction, rhizofiltration, and phytostabilization, phytoremediation effectively removes, stabilizes, or transforms heavy metals in contaminated soils, reducing their bioavailability and potential ecological and human health risks. The phytoremediation project utilizing tulsi (*Ocimum sanctum*), vetiver (*Chrysopogon zizanioides*), and Aloe vera (*Aloe barbadensis*) have yielded promising results in addressing soil contamination. Through this innovative approach, these plant species have demonstrated their effectiveness in mitigating heavy metal pollution while contributing to overall soil health and ecosystem restoration. Hence, it was concluded that:

- **pH Stability:** The consistent pH values observed for tulsi, Aloe vera, and vetiver before and after the phytoremediation process indicate their resilience in maintaining near-neutral or alkaline soil pH levels. This stability is crucial for preserving soil health and supporting plant growth in contaminated environments.

- **Moisture Regulation:** Vetiver, tulsi, and Aloe vera

exhibited varying moisture content levels post-phytoremediation, reflecting their adaptive strategies to environmental conditions. Vetiver's moderate moisture retention, tulsi's drought tolerance, and Aloe vera's water-storing capabilities contribute to soil moisture balance and plant health during remediation processes.

- **Metal Remediation:** The phytoremediation process effectively reduced zinc, lead, and cadmium concentrations in contaminated soil. Tulsi demonstrated the highest efficacy in reducing metal concentrations, followed by vetiver and Aloe vera. These findings highlight the potential of these plant species in mitigating heavy metal pollution and restoring soil quality.

- **Metal Accumulation:** Tulsi, vetiver, and Aloe vera exhibited varying capacities for metal accumulation, with Tulsi accumulating the highest concentrations of zinc and lead. These differences in metal accumulation profiles underscore the importance of selecting appropriate plant species based on specific remediation requirements and metal pollutants present in the soil.

- **Soil Health and Ecosystem Restoration:** The findings suggest that phytoremediation not only mitigates heavy metal pollution but also contributes to soil health and ecosystem restoration. By stabilizing soil pH, regulating moisture content, and reducing heavy metal concentrations, tulsi, vetiver, and Aloe vera play a pivotal role in improving soil fertility, promoting plant growth, and enhancing biodiversity in polluted environments.

- **Long-Term Viability:** The long-term viability of phytoremediation as a sustainable remediation strategy is underscored by the resilience of the selected plant species and their ability to thrive in contaminated soil conditions. However, ongoing research is needed to assess the persistence of remediation effects over time and to address any potential limitations or challenges associated with the prolonged use of phytoremediation in diverse environmental settings.

Thus, the stable pH levels, effective moisture regulation, and significant metal remediation capabilities exhibited by tulsi, vetiver, and Aloe vera demonstrate their potential as efficient phytoremediators for polluted soil environments, while also emphasizing the need for tailored plant selection in remediation efforts. Future research directions in this field are crucial for advancing our understanding and optimizing the efficacy of phytoremediation. Critical areas for further investigation can include:

- **Enhancing Remediation Efficiency:** Research efforts should focus on identifying and optimizing the factors influencing the remediation efficiency of phytoremediation, such as plant selection, soil conditions, and pollutant concentrations. Developing tailored approaches and employing genetic engineering techniques to enhance the metal uptake and tolerance of plants can improve remediation outcomes.

- **Understanding Plant-Metal Interactions:** Further studies are needed to elucidate the mechanisms underlying plant-metal interactions, including metal uptake, translocation, and sequestration within plant tissues. Investigating the physiological and biochemical processes involved in metal accumulation and detoxification can inform the selection of hyperaccumulator species and the development of strategies to enhance metal remediation.

- **Long-Term Monitoring and Evaluation:** Longitudinal studies are essential to assess the long-term effectiveness and sustainability of phytoremediation over extended periods. Monitoring changes in soil quality, plant health, and ecosystem dynamics over time can provide insights into the persistence of remediation effects and potential ecological impacts, guiding management decisions and remediation strategies.

- **Integration with Sustainable Land Management Practices:** Future research should explore the integration of phytoremediation with other sustainable land management practices, such as agroforestry, biochar application, and soil amendment techniques. Evaluating the synergistic effects of combining phytoremediation with these practices can enhance remediation outcomes, improve soil fertility, and promote ecosystem resilience.

In conclusion, the practical significance of phytoremediation lies in its potential to address heavy metal pollution in soil effectively while promoting environmental sustainability as presented in this research work. By advancing our understanding of plant-soil interactions, optimizing remediation strategies, and integrating phytoremediation with sustainable land management practices, future research can contribute to harnessing the full potential of this eco-friendly remediation technique for environmental restoration and protection.

STATEMENT OF PERMISSION

This research project involves the collection and study of plant species including aloe vera (*Aloe barbadensis*), vetiver (*Chrysopogon zizanioides*), and tulsi (*Ocimum sanctum*). The collection of these plant specimens has been conducted in accordance with all applicable regulations and permissions.

ACKNOWLEDGEMENTS

REFERENCES

Ali, H., Khan, E. and Ilahi, I., 2019. Environmental chemistry and ecotoxicology of hazardous heavy metals: environmental persistence, toxicity, and bioaccumulation. *Journal of Chemistry*, 2019(1), p.6730305. https://doi.org/10.1155/2019/6730305.

Araujo, G.R., de Paiva Ferreira, G.A., Vaz, V., da Costa Lima, A., Spolidorio, E.S. and Mendes, K.F., 2024. Canavalia ensiformis enhances the phytoremediation of remineralized and sulfentrazone-contaminated tropical soils. *Chemosphere*, 348, p.140725. https://doi.org/10.1016/j.chemosphere.2023.140725.

Azhar, U., Ahmad, H., Shafqat, H., Babar, M., Munir, H.M.S., Sagir, M., Arif, M., Hassan, A., Rachmadona, N., Rajendran, S. and Mubashir, M., 2022. Remediation techniques for elimination of heavy metal pollutants from soil: A review. *Environmental Research*, 214, p.113918. https://doi.org/10.1016/j.envres.2022.113918.

Bakshi, S., Banik, C. and He ZhenLi, H.Z., 2018. The impact of heavy metal contamination on soil health. In: *Managing soil health for sustainable agriculture. Volume 2: Monitoring and management*, pp. 63-95. https://doi.org/10.19103/AS.2017.0033.20.

Barroso, G.M., Dos Santos, E.A., Pires, F.R., Galon, L., Cabral, C.M. and Dos Santos, J.B., 2023. Phytoremediation: a green and low-cost technology to remediate herbicides in the environment. *Chemosphere*, 334, p.138943. https://doi.org/10.1016/j.chemosphere.2023.138943.

Collin, S., Baskar, A., Geevarghese, D.M., Ali, M.N.V.S., Bahubali, P., Choudhary, R., Lvov, V., Tovar, G.I., Senatov, F., Koppala, S. and Swamiappan, S., 2022. Bioaccumulation of lead (Pb) and its effects in plants: A review. *Journal of Hazardous Materials Letters*, 3, p.100064. https://doi.org/10.1016/j.hazl.2022.100064.

Ferrarini, A., Fracasso, A., Spini, G., Fornasier, F., Taskin, E., Fontanella, M.C., Beone, G.M., Amaducci, S. and Puglisi, E., 2021. Bioaugmented phytoremediation of metal-contaminated soils and sediments by hemp and giant reed. *Frontiers in Microbiology*, 12(4). https://doi.org/10.3389/fmicb.2021.645893.

Gray, C.W., Dunham, S.J., Dennis, P.G., Zhao, F.J. and McGrath, S.P., 2006. Field evaluation of in situ remediation of a heavy metal contaminated soil using lime and red-mud. *Environmental Pollution*, 142(3), pp.530-539. https://doi.org/10.1016/j.envpol.2005.10.017.

Gupta, A.K., Verma, S.K., Khan, K. and Verma, R.K., 2013. Phytoremediation using aromatic plants: A sustainable approach for remediation of heavy metals polluted sites. *Environmental Science and Technology*. https://doi.org/10.1021/es403469c.

Haller, H., Pronoza, L., Dyer, M., Ahlgren, M., Bergqvist, L., Flores-Carmenate, G. and Jonsson, A., 2023. Phytoremediation of heavy-metal-contaminated soils: Capacity of amaranth plants to extract cadmium from nutrient-poor, acidic substrates. *Challenges*, 14(2), p.28. https://doi.org/10.3390/challe14020028.

Hussain, S., Khan, M., Sheikh, T.M.M., Mumtaz, M.Z., Chohan, T.A., Shamim, S. and Liu, Y., 2022. Zinc essentiality, toxicity, and its bacterial bioremediation: A comprehensive insight. *Frontiers in Microbiology*, 13(5). https://doi.org/10.3389/fmicb.2022.900740

Khalid, S., Shahid, M., Niazi, N.K., Murtaza, B., Bibi, I. and Dumat, C., 2017. A comparison of technologies for remediation of heavy metal contaminated soils. *Journal of Geochemical Exploration*, 182(11), pp.247-268. https://doi.org/10.1016/j.gexplo.2016.11.021.

Kirpichtchikova, T.A., Manceau, A., Spadini, L., Panfili, F., Marcus, M.A. and Jacquet, T., 2006. Speciation and solubility of heavy metals in contaminated soil using X-ray microfluorescence, EXAFS spectroscopy, chemical extraction, and thermodynamic modeling. *Geochimica et Cosmochimica Acta*, 70(9), pp.2163-2190. https://doi.org/10.1016/j.gca.2006.02.006.

Korzeniowska, J. and Stanislawska-Glubiak, E., 2023. The phytoremediation potential of local wild grass versus cultivated grass species for zinc-contaminated soil. *Agronomy*, 13(1), p.160. https://doi.org/10.3390/agronomy13010160.

Kumar, M., Seth, A., Singh, A.K., Rajput, M.S. and Sikandar, M., 2021. Remediation strategies for heavy metals contaminated ecosystem: A review. *Environmental and Sustainability Indicators*, 12(12), p.100155. https://doi.org/10.1016/j.indic.2021.100155.

Kumari, S. and Mishra, A., 2021. Heavy metal contamination. In: *Soil Contamination - Threats and Sustainable Solutions*. IntechOpen. https://doi.org/10.5772/intechopen.93412.

Lancheros, A., Cajamarca, F., Guedes, C., Brito, O. and Guimarães, M.F., 2024. Exploring the potential of Canavalia ensiformis for phytoremediation of B10 biodiesel-contaminated soil: Insights on aromatic compound degradation and soil fertility. *International Journal of Phytoremediation*, pp.1-9. https://doi.org/10.1080/15226514.2024.2357646.

Li, C., Yang, G., Liu, Z. and Cai, J., 2022. Overview of phytoremediation technology for heavy metal contaminated soil. In: *E3S Web of Conferences*. Vol. 350. EDP Sciences. https://doi.org/10.1051/e3sconf/202235001006.

Li, G., Yan, L., Chen, X., Lam, S.S., Rinklebe, J., Yu, Q., Yang, Y., Peng, W. and Sonne, C., 2023. Phytoremediation of cadmium from soil, air and water. *Chemosphere*, 320(4), p.138058. https://doi.org/10.1016/j.chemosphere.2023.138058.

Lin, T., Zheng-Qi, X., You-guo, L., Zhong-min, J., Tao-yuan, X., Bin-chen, Z. and Xingbing, L., 2022. Eco-environmental, human health risk assessment of soils and crops heavy metals in the typical black-rock series area in the northern Daba Mountains, China. *Doklady Earth Sciences*, 506(2), pp.839-848. https://doi.org/10.1134/S1028334X2260044X.

Mahajan, P. and Kaushal, J., 2018. Role of phytoremediation in reducing cadmium toxicity in soil and water. *Journal of Toxicology*, 2018(1), pp.1-16. https://doi.org/10.1155/2018/4864365.

Mohammed, A.S., Kapri, A. and Goel, R., 2011. Heavy metal pollution: source, impact, and remedies. *Biomanagement of metal-contaminated soils*, pp.1-28. https://doi.org/10.1007/978-94-007-1914-9_1.

Oorts, K., Smolders, E., Lanno, R. and Chowdhury, M.J., 2021. Bioavailability and ecotoxicity of lead in soil: Implications for setting ecological soil quality standards. *Environmental Toxicology and Chemistry*, 40(7), pp.1948-1961. https://doi.org/10.1002/etc.5051.

Pandey, V.C., Pandey, D.N. and Singh, N., 2015. Sustainable phytoremediation based on naturally colonizing and economically valuable plants. *Journal of Cleaner Production*, 86(1), pp.37-39. https://doi.org/10.1016/j.jclepro.2014.08.030.

Pang, Y.L., Quek, Y.Y., Lim, S. and Shuit, S.H., 2023. Review on phytoremediation potential of floating aquatic plants for heavy metals: A promising approach. *Sustainability*, 15(2). https://doi.org/10.3390/su15021290.

Priya, A.K., Muruganandam, M., Ali, S.S. and Kornaros, M., 2023. Clean-up of heavy metals from contaminated soil by phytoremediation: A multidisciplinary and eco-friendly approach. *Toxics*. MDPI. https://doi.org/10.3390/toxics11050422.

Raj, K. and Das, A.P., 2023. Lead pollution: Impact on environment and human health and approach for a sustainable solution. *Environmental Chemistry and Ecotoxicology*, 5, pp.79-85. https://doi.org/10.1016/j.enceco.2023.02.001.

Rashid, A., Schutte, B.J., Ulery, A., Deyholos, M.K., Sanogo, S., Lehnhoff, E.A. and Beck, L., 2023. Heavy metal contamination in agricultural

soil: Environmental pollutants affecting crop health. *Agronomy*. MDPI. https://doi.org/10.3390/agronomy13061521.

Rathore, D. and Kaur, L., 2023. Assessment of heavy metal remediation potential of selected local plants in industrial soils: A case study of Bikaner city, India. *Journal of Phytological Research,* 36(2).

Raza, A., Habib, M., Kakavand, S.N., Zahid, Z., Zahra, N., Sharif, R. and Hasanuzzaman, M., 2020. Phytoremediation of cadmium: Physiological, biochemical, and molecular mechanisms. *Biology*, 9(7), p.177. https://doi.org/10.3390/biology9070177.

Rungwa, S., Arpa, G., Sakulas, H., Harakuwe, A. and Timi, D., 2013. Phytoremediation – an eco-friendly and sustainable method of heavy metal removal from closed mine environments in Papua New Guinea. *Procedia Earth and Planetary Science*, 6, pp.269-277. https://doi.org/10.1016/j.proeps.2013.01.036.

Saxena, G., Purchase, D., Mulla, S.I., Saratale, G.D. and Bharagava, R.N., 2020. Phytoremediation of heavy metal-contaminated sites: eco-environmental concerns, field studies, sustainability issues, and future prospects. *Reviews of Environmental Contamination and Toxicology*, 249, pp.71-131.

Singh, S.R., Bhadra, A., Kademane, A., Shrivastava, R. and Patil, S.J., 2023. Phytoremediation-a promising approach for pollution management. *Phytoremediation* [online]

Soubasakou, G., Cavoura, O. and Damikouka, I., 2022. Phytoremediation of cadmium-contaminated soils: A review of new cadmium hyperaccumulators and factors affecting their efficiency. *Bulletin of Environmental Contamination and Toxicology*, 109(5), pp.783-787. https://doi.org/10.1007/s00128-022-03604-5.

Souza Costa, E.T., Lopes, G., Santos Carvalho, G., Penha, H.G.V., Curi, N. and Guimarães Guilherme, L.R., 2021. Phytoremediation of arsenic-contaminated soils amended with red mud combined with phosphogypsum. *Water, Air, & Soil Pollution*, 232(10), p.417. https://doi.org/10.1007/s11270-021-05360-4.

Srivastava, P., Bolan, N., Casagrande, V., Benjamin, J., Adejumo, S.A.,

Sabir, M., Farooqi, Z.U.R., Saifullah, and Sarkar, A., 2022. Lead in soils: sources, bioavailability, plant uptake, and remediation. In: *Appraisal of Metal (Loids) in the Ecosystem*, pp.331-360. Elsevier. https://doi.org/10.1016/B978-0-323-85621-8.00005-4.

van der Ent, A. and Rylott, E.L., 2024. Inventing hyperaccumulator plants: improving practice in phytoextraction research and terminology. *International Journal of Phytoremediation*, pp.1-4. https://doi.org/10.1080/15226514.2024.2322631.

Wuana, R.A. and Okieimen, F.E., 2011. Heavy metals in contaminated soils: a review of sources, chemistry, risks and best available strategies for remediation. *International Scholarly Research Notices*, 2011(1), p.402647. https://doi.org/10.5402/2011/402647.

Zhang, Q. and Wang, C., 2020. Natural and human factors affect the distribution of soil heavy metal pollution: a review. *Water, Air, & Soil Pollution*, 231(7), p.350. https://doi.org/10.1007/s11270-020-04728-2.

Zhang, Q., Han, Y., Chen, W., Guo, Y., Wu, M., Wang, Y. and Li, H., 2022. Soil type and pH mediated arable soil bacterial compositional variation across geographic distance in North China Plain. *Applied Soil Ecology*, 169, p.104220. https://doi.org/10.1016/j.apsoil.2021.104220.

Zhao, L., Yuan, L., Wang, Z., Lei, T. and Yin, X., 2012. Phytoremediation of zinc-contaminated soil and zinc-biofortification for human nutrition. *Phytoremediation and Biofortification: Two Sides of One Coin,* pp.33–57. https://doi.org/10.1007/978-94-007-1439-7_3.

Zheljazkov, V.D., Craker, L.E. and Xing, B., 2006. Effects of Cd, Pb, and Cu on growth and essential oil contents in dill, peppermint, and basil. *Environmental and Experimental Botany*, 58(1–3), pp.9-16. https://doi.org/10.1016/j.envexpbot.2005.06.008.

ORCID DETAILS OF THE AUTHORS

S. Sona: https://orcid.org/0009-0008-3483-0666

S. P. Sangeetha: https://orcid.org/0000-0001-5143-961X

Enhancing Food Security Through Sustainable Agriculture: Investigating the Allelopathic Effects of Sorghum on Weed Management in Field Pea (*Pisum sativum* var. *arvense*)

Prantick Patra[1] , **Anita Jaswal[1†]** and **Iza Fatima[2]**

[1]Department of Agronomy, School of Agriculture, Lovely Professional University, Phagwara-144 411, Punjab, India
[2]Department of Entomology and Plant Pathology, Oklahoma State University, Stillwater, Oklahoma, USA
†Corresponding author: Anita Jaswal; anita.27139@lpu.co.in

ABSTRACT

Allelopathy can be a viable approach to address the issues of environmental degradation by reducing the use of herbicides and herbicide-resistant weeds. Allelopathic crop residues have a lot of potential for improving soil quality and suppressing weed growth. A field experiment at an agronomic research farm, Lovely Professional University in Phagwara, Punjab, examined the effects of water extracts and crop residues from sorghum on the population of weeds, indices of weed management, and the productivity of field peas. The experiment during the year 2022-2023 comprised in randomized block design with 2 levels of Sorghum water extract (1:10, 1:20 w/v), 3 levels of Sorghum stalk soil incorporation @ 2, 4, 6 Mg.ha^{-1}, Sorghum surface mulching at 10tonnes ha^{-1}, Field pea and rabi sorghum intercropping at 2:1, Weedy check and hand weeding. The findings showed that the sorghum surface mulching, addition of sorghum water extract, and sorghum stalk incorporation significantly altered the dynamics of weeds which was comparable with hand weeding. In the case of weed density (9.17 no.m^{-2}), weed fresh (7.66g), and dry weight (3.0g) hand weeding gave the best result which was followed by sorghum surface mulching with 10.77 weeds no.m^{-2}, 10.11 g weed fresh weight and 4.26gm weed dry weight. The highest weed control efficiency (80.9%) was recorded in hand weeding which was followed by sorghum water extract (1:10) and sorghum stalk incorporation (4 Mg.ha^{-1}). The weed management index, weed persistence index, and agronomic management index showed an inverse relationship with weed control efficiency. Hand weeding (20, 40, 60 DAS) gave the highest grain yield (2897 kg.ha^{-1}) of field pea followed by Sorghum surface mulching. Yield attributes were calculated which prescribed that all the treatments significantly reduced the weed infestation and increased the yield attributes over a weedy check. Hand weeding gave the best result, but it is not economical due to the intensive labor requirement. Initiating sustainable weed control and significantly improving the nutrient content of field peas can be achieved through sorghum surface mulching, sorghum stalk incorporation at 4 Mg.ha^{-1}, and sorghum water extract (1:10). These practices can contribute to environmentally friendly and sustainable agriculture.

INTRODUCTION

In addition to food security, "nutritional security" is currently a major concern for the scientific community on a global scale. A frequent term for pulse crops is "poor man's meat." It can be strongly considered a potential alternative in the battle against nutritional insecurity due to its high protein content. Grown mostly in milder temperate zones, field peas (*Pisum sativum* L.) are an important grain legume crop for the winter season. Garden and field peas are the two types of grown peas. When garden peas are collected fresh, they are either preserved or cooked fresh for later use (Reddy et al. 2023). Typically, field peas are cultivated for their dry seeds, which

are used to make dal and a variety of snack dishes. It is very nutrient-dense and rich in readily digested carbohydrates, protein, minerals, and vitamins. The following components are included in 100g of dried edible portion: 11g of moisture, 22.5g of protein, 1.8g of fat, 62.1g of carbohydrates, 64g of calcium, 4.8g of iron, riboflavin (0.15g), thiamine (0.72g), and 2.4g of niacin. According to (Jaswal et al. 2022), field peas make up about 3% of India's total pulse area and approximately 5% of its overall pulse production.

Field peas are produced worldwide on an area of 7.04 million hectares, yielding an estimated 12.40 million tonnes of yield annually in 2021. Field peas are produced on

7.45 lakh hectares of land in India, and between 2020 and 2021, they will produce roughly 9.10 lakh tonnes annually. This crop's average productivity has grown significantly over time, reaching 1.4 tonne ha^{-1} currently. Orissa, Bihar, Assam, U.P., and MP are the principal growing regions for field peas. About 43,860 hectares of pea are grown in Punjab, producing 4, 0,450 tonnes of pea (Singh et al. 2022). India, a developing nation, has a severe problem with nutritional imbalance. Most of the nation's population lives in poverty and has little access to animal protein in their regular diet. The WHO recommends that people consume 80 g of pulse crops per day, yet our country's yearly report on pulse availability shows that people only consume 36 gm of pulses per day. Rather than nutritional security, the pursuit of food security may be what led to this concerning situation. Field pea yield can only be increased through a variety of biotic and abiotic variables, as there is limited opportunity to expand its area inside the nation (1, 3). Field pea productivity is limited by several factors, including inadequate irrigation and drainage techniques, stagnant water, flower drop issues caused by temperature fluctuations, an increased area entirely devoted to wheat and rice crops, a lack of high-yielding disease-resistant cultivars, small land holdings, cultivation on marginal land, and pest and weed infestation (Singh et al. 2023).

Weeds are a major component among the many biotic and abiotic variables limiting field pea productivity and production. Weed infestations hinder yield by posing competition for nutrients, space, light and moisture, and make pea picking more challenging. According to (Raje et al. 2022), weed competition causes pea yield losses ranging from 40 to 70% and an average 63% increase in weed control. The lack of labor availability causes this issue. Peas are related to a variety of weeds. Any crop's level of weeds changes depending on the agroecological conditions and the various management techniques used. The major weeds found in pea crop are *Chenopodium album* (bathua), *Fumaria parviflora* (gajri), *Lathyrus* sp. (chatri-matri), *Melilotus alba* (senji), *Vicia sativa* (ankari), *Lepidium sativum* (wild hallon), *Cyprus rotandus* (Purple nut sedge), *Phlaris minor* (canary grass), *Poa annua* (annual blue grass), *Spergulla arvensis* (corn spurrey), *Trigonella polycerata* (Jungli fenugreek) (Lake et al. 2021).

The manual weeding method used in earlier times performs best when labor is affordable and readily accessible. However, because of increasing wages and a labor shortage, field pea weeding has become a challenging operation. As a result, they are forced to choose a simpler, less expensive, and alternative way of chemical weed management (Kovács et al. 2023). Herbicides and chemical weed control both significantly increase crop productivity by suppressing weed growth. Chemical weed control is a particularly effective means of doing this. However, overuse and carelessness in the application of herbicides can result in agricultural damage, health issues for humans and animals, contamination of soil and water, and herbicide resistance (Raje et al. 2022). The demand for alternative weed control methods has emerged because of environmental degradation and the danger that inappropriate or excessive usage of plant-protection agents poses to human and animal health (Hetta et al. 2023). Sustainable management principles are respected as decisions are made to optimize plant production. The use of less hazardous plant protection techniques, like biological techniques, that pose less of a threat to the environment is becoming more and more common. This pattern is indicative of the development of greener technologies across many domains of human endeavor. One of the possible strategies for reducing the usage of herbicide may be the use of natural substances and allelopathy manipulation of the environmental population (Abbas et al. 2021). The allelopathic manipulation can be utilized by crop rotation, using sorghum extract (sorgaab), sorghum stalks soil incorporation, and hand weeding. By using sorghum water extracts (sorgaab), the biomass of weeds was decreased by 33–35%. It works in combination to lessen the need for herbicides. As new methods are discovered and old ones are improved, organic farmers are getting access to a greater variety of weed management choices (Blaise et al. 2020). Considering these factors, the current study examined the effectiveness of allelopathic water extract and sorghum soil inclusion for weed management in field peas (*Pisum sativum* var. *arvense*). Additionally, various weed indices of treatments were computed since weed indices offer logistical support for impact assessments, interpretations, and deriving relevant findings in research on weed control.

MATERIALS AND METHODOLOGY

During the Rabi season of 2022, a field experiment was carried out at Lovely Professional University's agriculture research farm in Phagwara, Punjab. The research aimed to examine the management of weeds in field pea (*Pisum sativum* var. *arvense*) through the application of allelopathic water extract and sorghum soil incorporation. The testing location was 228 meters (748 feet) above sea level at 31.25° North, 75° East. The location, which is underneath Punjab's middle plain, has a subtropical monsoon climate with 600 mm of rainfall on average. Punjab-89 was the variety that was used for this experiment, which was sowed on November 15th, 2022, with a 30 cm × 10 cm spacing. The current study's experiment material, which included three replications and nine treatments, was designed using a randomized block design as represented in Fig. 1. Treatments details are

T_0-Weedy check (control), T_1- Sorghum surface mulch, T_2- Field pea and rabi sorghum intercropping (2:1), T_3-Sorghum stalk soil incorporation (2 Mg.ha^{-1}), T_4-Sorghum stalk soil incorporation (4 Mg.ha^{-1}), T_5- Sorghum stalk soil incorporation (6 Mg.ha^{-1}), T_6-Sorghum water extract (1:10), T_7- Sorghum water extract (1:20), T_8- Hand weeding (20, 40, 60 DAS). The hand-weeding plots were maintained in such a way that as and when the weed emerged weeding was done. Generally, hand-weeding was done at an interval of 20, 40, and 60 DAS. The sorghum water extract was applied at 20 DAS 1:10 and 1:20 (volume) ratio means 1 mL of extract in 10 mL of water and 1 mL of extract in 20 mL of water. Sorghum stalks soaked in clean water for 24 hours. Then filtered and filtrate was collected. At last, the filtrate boiled and reduced volume to 10%. Sorghum stalk cut into small pieces with a chaff cutter 16 inches in length and 5.25 inches in width and incorporated into soil before sowing. Dried leaves of sorghum are used for mulching and spread after the germination.

Yield Parameters: Each net plot's pods were threshed and cleaned, and their seed weight was noted. The yield per hectare was calculated and given in kgha^{-1}. A random sample of 100 seeds was selected from each treatment's product, and these samples were counted and weighed, and the seed index was expressed in grams (g). The number of pods on each plant and the number of Seeds pod^{-1} counted were calculated by averaging the number of pods on each plant.

Weed parameters- Different weed management indices were calculated to advocate the results as per the following formulas:

Weed Density (No.m^{-2}): Using the quadrant method, the number of weeds was counted from a randomly selected 0.16 m^2 (quadrant size) area and converted on a m^2 basis.

Weed Control efficiency: Formula was used to calculate the weed control efficiency on a dry weight basis.

WCE=

$$\frac{\text{Dry matter of weeds in weedy check} - \text{Dry matter of weeds in treated plot}}{\text{Dry matter of weeds in weedy check}}$$

$\times\ 100$

Weed dry weight (g): After being removed, the weeds in the quadrant area were placed in brown bags. The weeds were allowed to air dry before being dried at 65–70°C in a hot air oven until a consistent weight was reached.

Weed fresh weight (g): The weeds present in the quadrant area were uprooted and then transferred to a brown bag. After cutting the weed fresh weight of the weed samples was taken with the help of weighing balance.

Weed persistence index: This index, which was calculated using the provided formula as recommended by (Mishra & Mishra 1997), shows the resistance in weeds against the tested treatments and confirms the efficacy of the specified treatments:

$$WPI = \frac{Weed\ dry\ weight\ in\ treated\ plot}{weed\ dry\ weight\ in\ control\ plot}$$

$$\times \frac{\text{Weed population in control}}{Weed\ population\ in\ treated\ plot}$$

Weed management index: WMI was calculated using the following method, representing the ratio of yield acquired over control due to weed management and the percentage of weeds controlled by the associated treatment.

$$WMI = \frac{\text{Yield of treated plot.} - \text{Yield of control plot.}}{\text{Yield of control plot}} / $$

$$\frac{\text{Weed dry weight in control (unweeded) plot} - \text{Weed dry weight in treated plot.}}{\text{Weed dry weight in control (unweeded) plot.}}$$
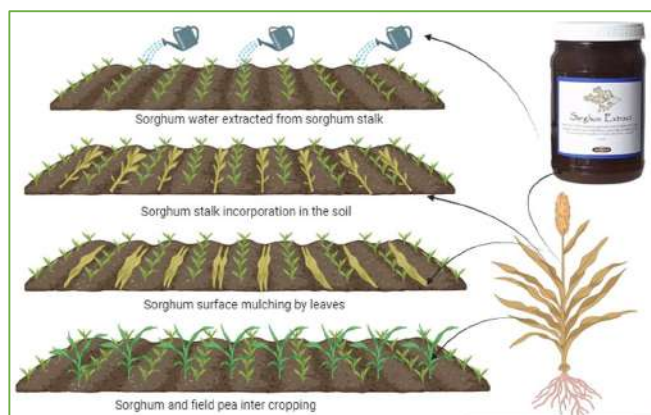
Fig. 1: Representing how different parts of sorghum used as allelopathy for weed control in field pea field viz. Sorghum water extract extracted from the stalk of sorghum is used as a foliar spray, sorghum stalk is chopped into small pieces and incorporated in the soil, sorghum dried leaves is used as mulching between the rows of field pea, sorghum is used as an intercrop between the rows of field pea.

Agronomic management index:

$$\overline{\frac{\text{Yield of treated plot} - \text{Yield of control plot}}{\text{Yield of control plot.}}}$$

$$-\overline{\frac{\text{Weed dry weight in control (unweeded)plot} - \text{Weed dry weight in treated plot}}{\text{Weed dry weight in control (unweeded) plot}}}$$

$$\overline{\frac{\text{Weed dry weight in control (unweeded)plot} - \text{Weed dry weight in treated plot}}{\text{Weed dry weight in control (unweeded) plot}}}$$

Nutrient uptake by weeds and plants: Nitrogen in plant material can be determined by using KELPLUS digestion and distillation processes. Estimation of Phosphorus by Colorimetric Method. By comparing the intensity of the color of unknown samples with the standard curve, the concentration of phosphate in the unknown sample can be estimated. Total potassium in plant and weed samples is determined by flame photometer reading for the standard solutions (0, 2, 4, 6, 8 and 10 ppm K) and construct a standard curve with the readings.

Statistical analysis: Analysis of variance (ANOVA) was used to analyze the experiment's data, which was presented via a randomized block design. SPSS (Statistical Package of Social Services Version 2022) software was used to analyze the data. To examine the variation between the treatments, the Duncan Multiple Range Test (DMRT) is employed. Pearson's correlation was used to determine the relationship between the growth parameters at the 5% significance level (to assess the significance and non-significant parameters).

RESULTS

The most dominant weed species found in the experimental site were *Fumaria parviflora*, *Cornopus didymus*, *Spergula arvensis*, *Cannabis sativa*, *Chenopodium album*, *Rumex* sp., *Melilotus* sp., *Cynodon dactylon*, *Phalaris minor*, *Solanum nigrum*, *Cyperus* sp.

Yield attributes: The various weed management practice treatments had a substantial impact on the yield-attributing parameters seeds pod^{-1}, harvest index, pod length (cm), and seed index (100-grain weight). When compared to the weedy check, all weed control methods had a substantial impact on the yield attributes.

Pods plant^{-1}, Seeds pod^{-1}, Pod length (cm): Table 1 revealed that among the treatments highest no. of pods plant^{-1} (18.79) was reported in hand weeding followed by sorghum surface mulching@10 tonnes ha^{-1} at harvest. However lowest number of pods plant^{-1} (7.25) was reported in the weedy check at harvest. The highest number of seed pods^{-1} (8.33) was reported in hand weeding followed by sorghum surface mulching@10 tonnes ha^{-1} and sorghum stalk soil incorporation @ 4 Mg ha^{-1} at harvest. Significantly lowest no. of seeds pod^{-1} (4.67) was reported in the weedy check. The highest Pod length (9.21cm) was reported in hand weeding followed by sorghum surface mulching@10 tonnes ha^{-1}. The lowest Pod length (7.81cm) was reported in the weedy check.

Table 1-Effect of Different Weed Control Treatment on Yield Attributes

Treatments	No. of pods plant^{-1}	Pod length (cm)	Seeds pod^{-1}	Seed index (g)	Pod yield (kg ha^{-1})	Haulm yield (kg ha^{-1})	Harvest index (%)
Weedy check	7.25^h± 0.41	7.81^c± 0.59	4.67^{e}82. 0±	13.41^d± 2.11	980.23^f± 16.37	1387.29^e± 78.42	41.44^d± 1.25
Sorghum surface mulch	15.08^b± 0.35	9.2^a± 0.27	7.66^b± 0.72	18.02^a± 0.25	2060.43^b± 67.09	2566.16^b± 84.49	44.54^c± 1.62
Field pea and rabi sorghum intercropping (2:1)	10.33^f± 0.31	8.66^b± 0.07	5.78^d± 0.54	16.75^{bc}± 0.96	1677.23^e± 40.38	2085.40^d± 43.84	44.57^c± 0.43
Sorghum stalk soil incorporation (2 Mg.ha^{-1})	10.5^{fg}± 0.42	8.79^b± 0.51	7.00^{bc}± 0.72	16.67^{bc}± 0.52	1813.60^d± 41.04	2116.05^d± 19.55	46.15^{ab}± 0.78
Sorghum stalk soil incorporation (4 Mg.ha^{-1})	11.00^d± 0.54	8.90^b± 0.85	7.55^b± 0.42	15.09^c± 1.99	1907.20^{cd}± 65.21	2355.62^c± 7.84	44.73^c± 0.80
Sorghum stalk soil incorporation (6 Mg.ha^{-1})	10.75^{ef}± 0.24	8.30^b± 0.46	6.00^c± 0.27	16.94^b± 0.76	1980.61^{bc}± 64.63	2367.18^c± 16.88	45.54^b± 0.78
Sorghum water extract (1:10)	12.05^c± 0.67	8.09^b± 0.46	6.78^c± 0.32	16.95^b± 1.18	2010.53^{bc}± 64.98	2418.57^c± 49.84	45.39^b± 0.66
Sorghum water extract (1:20)	10.17^{de}± 0.31	8.40^b± 0.50	6.44^c± 0.42	17.34^{ab}± 0.30	1804.07^d± 53.29	2077.32^d± 87.37	46.49^{ab}± 1.31
Hand weeding (20, 40, 60 DAS)	18.79^a± 0.59	9.21^a± 0.66	8.33^a± 0.42	18.57^a± 0.84	2897.43^a± 62.34	3172.84^a± 81.99	47.74^a± 1.11

*Original Data given in parenthesis were subjected to square root $\sqrt{(x+1)}$ transformation before analysis

Table 2- Weed density, weed fresh weight, weed dry weight as affected by different weed control treatment of Field pea

Treatments	Weed density at (30 DAS) (No.m⁻²)	Weed density at (60 DAS) (No.m⁻²)	Weed density at (90 DAS) (No.m⁻²)	Weed fresh weight (gm⁻²) at 30 DAS	Weed fresh weight(gm⁻²) at 60 DAS	Weed fresh weight(gm⁻²) 90 DAS	Weed dry weight (gm⁻²) at (30 DAS)	Weed dry weight (gm⁻²) at (60 DAS)	Weed dry weight (gm⁻²) at (90 DAS)
Weedy check	$12.22(137.25^a)\pm$ 0.74	$15.24(217.33^a)\pm$ 1.12	$14.8(205.25^a)\pm$ 0.82	$2.86 (5.58^a)\pm$ 0.11	$9.24 (76.45^a)\pm$ 1.03	$13.63(172.36^a)\pm$ 0.61	$1.94(2.08^a)\pm$ 0.39	$4.34(14.78^a)\pm$ 0.66	$7.23(45.28^a)\pm$ 0.61
Sorghum surface mulch	$10.10(92.08^f)\pm$ 1.43	$12.51(144.33^f)\pm$ 0.66	$10.77(105.50^h)\pm$ 0.74	$1.84 (1.81^e)\pm$ 0.49	$6.21 (32.59^g)\pm$ 0.95	$10.11(92.29^g)\pm$ 0.76	$1.04(0.29^e)\pm$ 0.11	$2.3 (3.23^g)\pm$ 0.24	$4.26(14.13^d)\pm$ 0.82
Field pea and rabi sorghum intercropping (2:1)	$10.51(100.23^d)\pm$ 0.75	$12.97(155.42^e)\pm$ 0.72	$13.69(174.08^b)\pm$ 0.72	$2.38(3.54^{bc})\pm$ 0.33	$7.96 (55.66^b)\pm$ 1.07	$11.73(126.17^c)\pm$ 0.76	$1.19(0.47^{de})\pm$ 0.09	$4.05(12.59^b)\pm$ 0.32	$5.55(25.48^b)\pm$ 0.84
Sorghum stalk soil incorporation (2 Mg.ha⁻¹)	$10.82(106.42^c)\pm$ 1.03	$13.7(174.25^c)\pm$ 0.74	$12.76(150.33^c)\pm$ 0.85	$2.41(3.65^b)\pm$ 0.38	$7.60 (50.35^c)\pm$ 0.67	$11.01(110.44^d)\pm$ 0.89	$1.67(1.38^b)\pm$ 0.19	$3.42(8.51^e)\pm$ 0.78	$5.07(20.93^c)\pm$ 0.60
Sorghum stalk soil incorporation (4 Mg.ha⁻¹)	$10.26(95.33^e)\pm$ 1.12	$13.73(175.15^c)\pm$ 0.64	$11.39(118.50^f)\pm$ 0.54	$2.21(2.94^{cd})\pm$ 0.30	$7.41(47.72^d)\pm$ 0.70	$10.87(107.44^e)\pm$ 1.13	$1.44(0.89^{bcd})\pm$ 0.05	$3.28(7.72^e)\pm$ 0.35	$5.15(21.58^c)\pm$ 0.63
Sorghum stalk soil incorporation (6 Mg.ha⁻¹)	$10.76(105.23^c)\pm$ 0.75	$13.88(179.08^b)\pm$ 0.72	$11.95(131.17^d)\pm$ 0.72	$2.08 (2.49^d)\pm$ 0.26	$7.24(45.48^e)\pm$ 1.09	$10.86(107.24^e)\pm$ 0.95	$1.23(0.54^{cde})\pm$ 0.02	$3.89(11.46^c)\pm$ 0.40	$5.16(21.71^c)\pm$ 0.54
Sorghum water extract (1:10)	$10.10(92.17^f)\pm$ 1.33	$12.95(155.08^e)\pm$ 0.92	$11.09(112.25^g)\pm$ 0.74	$2.04(2.37^{de})\pm$ 0.29	$6.99(42.15^f)\pm$ 0.61	$10.26(95.35^f)\pm$ 0.96	$1.09(0.35^e)\pm$ 0.07	$2.90(5.74^e)\pm$ 0.53	$5.11(21.26^c)\pm$ 0.91
Sorghum water extract (1:20)	$10.96(109.33^b)\pm$ 0.51	$13.21(161.50^d)\pm$ 0.82	$11.69(125.15^e)\pm$ 0.64	$2.08 (2.51^d)\pm$ 0.15	$7.31(46.32^{de})\pm$ 0.68	$12.63(147.12^b)\pm$ 1.37	$1.51(1.01^{bc})\pm$ 0.52	$3.68(10.11^d)\pm$ 0.54	$5.22(22.30^c)\pm$ 1.30
Hand weeding at (20, 40, 60 DAS)	$8.34(61.50^g)\pm$ 0.94	$8.78(68.50^g)\pm$ 0.94	$9.17(75.25^i)\pm$ 0.54	$1.78 (1.65^f)\pm$ 0.16	3.84 $(11.18^h0.35\pm)$	7.66 $(51.26^h0.75\pm)$	0.91 $(0.17^e0.03\pm)$	$2.25(3.06^g)\pm$ 0.73	$3.0(6.27^e)\pm$ 0.69

*Original Data given in parenthesis were subjected to square root $\sqrt{(x+1)}$ transformation before analysis

Table 3- Effect of Different Weed Control Treatment on Weed Control Index (WCI), Weed Persistence Index (WPI), Weed Management Index (WMI), Agronomic Management Index (AMI)

Treatments	Weed control efficiency (%) at 30 DAS	Weed control efficiency (%) at 60 DAS	Weed control efficiency (%) at 90 DAS	Weed persistence index at 30 DAS	Weed persistence index at 60 DAS	Weed persistence index at 90 DAS	Weed management index	Agronomic management index
Weedy check	-	-	-	-	-	-	-	-
Sorghum surface mulch	46.7^{de}± 0.67	47.1^b± 0.25	41.1^b± 0.75	0.65^d± 0.41	0.70^d± 0.66	0.81^b± 0.41	1.26^{ab}± 0.61	0.23^b± 0.08
Field pea and rabi sorghum intercropping (2:1)	72.8^a± 0.59	12.9^g± 0.56	39.5^c± 0.58	0.71^c± 0.33	1.10^a± 0.31	0.83^b± 0.33	1.32^a± 0.42	0.33^a± 0.05
Sorghum stalk soil incorporation (2Mg.ha^{-1})	22.6^g± 0.69	22.9^e± 0.44	38.8^d± 0.27	0.97^a± 0.59	0.88^c± 0.27	0.82^b± 0.59	1.27^{ab}± 0.77	0.28^{ab}± 0.07
Sorghum stalk soil incorporation (4 Mg.ha^{-1})	29.8^f± 0.53	31.1^d± 0.52	41.1^b± 0.41	0.88^b± 0.16	0.84^c± 0.51	0.93^a± 0.16	1.24^b± 0.47	0.25^{ab}± 0.06
Sorghum stalk soil incorporation (6 Mg.ha^{-1})	49.1^d± 0.65	14.1^f± 0.62	40.2^{bc}± 0.52	0.72^c± 0.66	0.98^b± 0.85	0.89^{ab}± 0.66	1.30^a± 0.66	0.30^a± 0.06
Sorghum water extract (1:10)	69.2^b± 0.28	37.3^c± 0.44	41.1^b± 0.12	0.68^{cd}± 0.80	0.78^d± 0.46	0.94^a± 0.8	1.26^{ab}± 0.35	0.27^{ab}± 0.09
Sorghum water extract (1:20)	39.9^e± 1.25	22.9^e± 0.58	39.2^c± 0.42	0.87^b± 0.44	0.98^b± 0.50	0.92^a± 0.4	1.31^a± 0.61	0.31^a± 0.12
Hand weeding (20, 40, 60 DAS)	68.3^{bc}± 0.73	56.9^a± 0.46	80.9^a± 0.49	0.69^{cd}± 0.17	0.64^e± 0.59	0.67^c± 0.8	1.0^{4b}± 0.54	0.04^c± 0.13

Seed Index, pod yield (kg.ha^{-1}), haulm yield (kg.ha^{-1}) and harvest Index (%): Significantly highest seed index (18.57 g) was reported in hand weeding which was statistically at par with sorghum surface mulching @ 10 tonnes.ha^{-1}. Lowest seed index (13.41g) was reported in the weedy check (Table 1). Significantly highest Pod yield (2897.43 kgha^{-1}) and Haulm yield (3172.84 kg.ha^{-1}) were reported in hand weeding where three hand weeding at 20, 40, 60 DAS was done which was followed by sorghum surface mulching @ 10-tonnes.ha^{-1}. Significantly lowest Pod yield (980.23 kg.ha^{-1}) and Hulm yield (1387.29 kg.ha^{-1}) were reported in the weedy check. Significantly maximum Harvest index (47.74%) was observed in hand weeding which was statistically at par with sorghum water extract (1:20) and sorghum stalk soil incorporation. The lowest harvest index (41.44%) was observed in the weedy check as indicated in Table 1.

Weed density (no. m^{-2}): Table 2 revealed that there was significant variation recorded in weed density with different weed management practices. Significantly highest weed density (12.22 m^{-2}, 15.24 m^{-2}, 14.8 no.m^{-2}) was recorded under weedy check at 30, 60, and 90 DAS. However, significantly Lowest weed density (8.34 no.m^{-2}, 8.78 no. m^{-2}, 9.17 no.m^{-2}) was recorded in Hand weeding (20, 40, 60 DAS) followed by Sorghum surface mulching@ 10 tonnes ha^{-1} at 30, 60, 90 DAS.

Weed Fresh weight and Dry weight (gm): Table 2 revealed that significantly the highest weed fresh weight (2.86 g, 9.24 g) and dry weight (1.94g, 4.34g) was reported in

the weedy check at 30,60 DAS. However lowest weed fresh weight (1.78g, 3.84g) and dry weight (0.91g, 2.25 g) was reported in Hand weeding (20, 40 and 60 DAS) was followed by Sorghum surface mulching @ 10 tonnes.ha^{-1} at 30, 60 DAS. At 90 DAS, the significantly highest weed fresh weight (13.63g) and dry weight (7.23g) were reported in the weedy check. However, the lowest weed fresh weight

Table 4: Pearson's correlation of Weed indices

Correlations		WCE	WPI	AMI	WMI
WCE	Pearson Correlation	1	-.770*	-.949**	-.961**
	Sig. (2-tailed)		.026	.000	.000
	N	8	8	8	8
WPI	Pearson Correlation	-.770*	1	.715*	.694
	Sig. (2-tailed)	.026		.046	.056
	N	8	8	8	8
AMI	Pearson Correlation	-.949**	.715*	1	.989**
	Sig. (2-tailed)	.000	.046		.000
	N	8	8	8	8
WMI	Pearson Correlation	-.961**	.694	.989**	1
	Sig. (2-tailed)	.000	.056	.000	
	N	8	8	8	8

*. Correlation is significant at the 0.05 level (2-tailed).
**. Correlation is significant at the 0.01 level (2-tailed).

Table 5: Nutrient content % (N, P, K) in plants and weed samples

Treatments	Nitrogen content in plant (%)	Nitrogen content in weed (%)	Phosphorous content in plant (%)	Phosphorous content in weeds (%)	Potassium content in plant (%)	Potassium content in weed (%)
Weedy check	1.69[e]± 0.45	3.19[a]± 0.32	0.41[b]± 0.34	0.68[a]± 0.15	0.43[b]± 0.42	1.02[a]± 0.13
Sorghum surface mulch	3.08[b]± 0.62	2.95[ab]± 0.25	0.65[a]± 0.75	0.55[ab]± 0.41	0.60[a]± 0.66	0.64[c]± 0.41
Field pea and rabi sorghum intercropping (2:1)	2.94[bc]± 0.54	2.6[b]± 0.51	0.60[a]± 0.58	0.41[b]± 0.33	0.53[ab]± 0.31	0.98[a]± 0.33
Sorghum stalk soil incorporation (2 Mg.ha^{-1})	2.69[c]± 0.61	2.35[c]± 0.42	0.60[a]± 0.27	0.25[c]± 0.59	0.53[ab]± 0.27	0.80[c]± 0.59
Sorghum stalk soil incorporation (4 Mg.ha^{-1})	2.33[d]± 0.53	2.49[bc]± 0.47	0.63[a]± 0.41	0.43[b]± 0.16	0.56[ab]± 0.51	0.62[c]± 0.16
Sorghum stalk soil incorporation (6 Mg.ha^{-1})	3.00[b]± 0.60	2.88[ab]± 0.59	0.55[ab]± 0.52	0.44[b]± 0.66	0.60[a]± 0.85	0.56[c]± 0.66
Sorghum water extract (1:10)	3.67[a]± 0.28	2.77[b]± 0.43	0.54[ab]± 0.12	0.46[b]± 0.80	0.63[a]± 0.46	0.65[c]± 0.8
Sorghum water extract (1:20)	3.22[ab]± 0.34	2.94[ab]± 0.54	0.65[a]± 0.42	0.34[bc]± 0.44	0.48[b]± 0.50	0.83[b]± 0.4
Hand weeding (20, 40, 60 DAS)	3.55[a]± 0.73	2.5[bc]± 0.42	0.60[a]± 0.49	0.58[ab]± 0.17	0.56[ab]± 0.59	0.88[b]± 0.8

(7.66 g) and dry weight (3.0 g) was reported in Hand weeding (20, 40 and 60 DAS) followed by Sorghum surface mulching @ 10 tonnes ha^{-1}.

Weed Control efficiency (%) and Weed persistence index: Table 3 revealed that at 30 DAS significantly highest WCE (72.8%) and lowest WPI (0.65) was observed in Field pea and Rabi sorghum intercropping (2:1) which was statistically at par with Sorghum water extract (1:10) in terms of WPI (0.68). At 60, 90 DAS significantly highest WCE (80.9%, 56.9%) and lowest WPI (0.64, 0.67) was reported in hand weeding where three hand weeding at 20, 40 and 60 DAS was done which was followed by sorghum surface mulch with WCE 47.1,41.1% and WPI (0.70,0.81).

Weed management index (WMI) and Agronomic management index (AMI): There was a significant effect of treatments observed in WMI and AMI. The highest WMI and AMI (1.32 and 0.33) were observed under field pea and sorghum intercropping whereas no significant effect was observed between Sorghum water extract (1:20) and sorghum stalk incorporation (6 Mg ha^{-1}). The lowest WMI (1.04) and AMI (0.04) were observed under hand weeding plots which was followed by sorghum surface mulching. WCE and yield increase are inversely correlated with WMI and AMI. Higher WMI or AMI indicates lower WCE or/and relatively lower addition of yield due to treatment effect, whereas lowest values of WMI and AMI show greater WCE or/and comparatively higher addition of yield occurs due to treatment effect.

Correlation between WCE, WPI, WMI and AMI: From Table 4 of correlation, it is found that Weed control efficiency was negatively correlated with the weed persistence index, weed management index and agronomic management index. This indicated that higher WCE lowers the WMI, AMI and WPI.

Nutrient Content uptake by weeds and crop: Table 5 summarizes and presents the data on N, P, and K uptake by weeds and crops as influenced by various weed management techniques. A review of the data showed that the weedy check plot had the greatest value of nitrogen uptake by weeds, whereas the treatments produced the lowest value. The different weed control methods caused a considerable variation in the nitrogen uptake by weeds. Under the weedy check, a much higher value of N depletion by weeds was reported (3.19%), which was comparable to that of sorghum water extract (1:20) and surface mulch (2.95% and 2.94%). Incorporation of sorghum stalks (2 Mg.ha^{-1}) recorded the lowest (2.35%) of N. The weedy check had the highest P depletion by weeds (0.68%), whereas the Sorghum stalk incorporation (2 Mg.ha^{-1}) had the lowest (0.25%). The P uptake by weeds over weedy check was significantly reduced upon adoption of the weed control option. The K (0.56%) depletion rate by weeds under Sorghum stalk integration (6 Mg.ha^{-1}) was the lowest. The findings showed that different weed management treatments considerably reduced the quantity of potassium lost as compared to the weedy check (1.02%), which was comparable to the intercropping of field pea and rabi sorghum (2:1) with (0.98%). When weed management was implemented, weeds' uptake of potassium was significantly reduced compared to weedy check as represented in Figs. 2, 3. In the case of field peas significant variation was recorded in nutrient content among different weed management practices. The highest nitrogen content in the plant (3.67%) was recorded in Sorghum water extract (1:10) which was at par with hand weeding with 3.55% and the minimum nitrogen content in the plant (1.69%) was recorded in weedy check plots. Maximum P content in plants (0.65% and 0.63%) was recorded in Sorghum surface mulch, Sorghum water extract (1:20) and Sorghum stalk soil incorporation (4 Mg.ha^{-1}) whereas minimum content of phosphorous (0.41%). Maximum K uptake (0.63%) was recorded in Sorghum water extract (1:20)
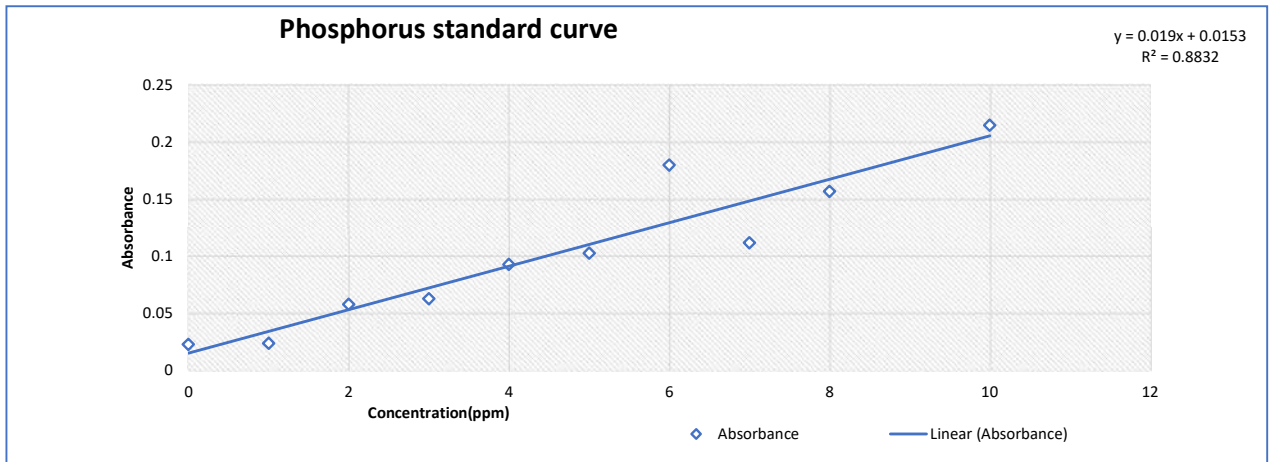
Phosphorus standard curve

$y = 0.019x + 0.0153$
$R^2 = 0.8832$

Fig. 2: Phosphorus standard curve for estimation of nutrient content from plant samples.

Potassium standard curve
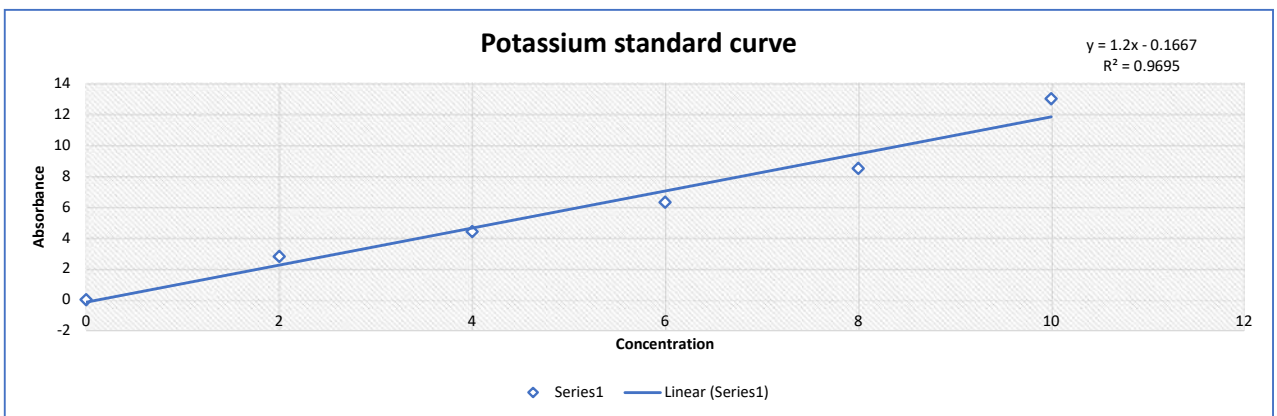
$y = 1.2x - 0.1667$
$R^2 = 0.9695$

Fig. 3: Potassium standard curve for estimation of nutrient content from plant samples.

which was at par with Sorghum surface mulch and Sorghum stalk soil incorporation whereas the least K content (0.43%) was recorded in weedy check.

DISCUSSION

Effect of sorghum allelopathy on weed management: An environmentally friendly way to control weeds in field crops is to incorporate allelopathic crop residues. With a multitude of allelochemicals that inhibit weed growth, sorghum (*Sorghum bicolor* L.) is one of the possible allelopathic crops. Plant stems, leaves, and roots all contain allelochemicals. Additionally, different plant sections may have different allelopathic potentials (Khan et al. 2021, Farooq et al. 2020). Kristó et al. (2022) revealed that in sorghum plants, numerous vital secondary metabolites have been found, including polyphenols, alkaloids, flavonoids, and terpenoids. The phenolic acids found in sorghum include gallic acid, ferulic acid, syringic acid, coumaric acid, benzoic acid, and caffeic

acid. According to our findings, adding sorghum stalk and water extract significantly increased the potential for weed suppression (Kumar et al. 2016). The field pea weed species' fresh weight, dry weight, and weed density were all reduced to a maximum by this method. Motmainna et al. (2021) revealed that Phenolic substances, such as phenolic acids (Dhurrin, p-hydroxybenzaldehyde, sorgleone, vanillic acid, p-hydroxybenzoic acid, p-hydroxybenzaldehyde, p-coumaric acid, and ferulic acid), which have a variety of biological functions, including allelopathy, were released when this reduction occurred. Sahu et al. 2022 found that sorghum allelochemicals have an inhibitory effect on weeds with grassy and broad leaves. Using water extract from mature sorghum crop plants reduced weed density and biomass by 35–49% when compared to the control group. In comparison to sorghum water extract treatments, sorghum residue treatments demonstrated the greatest weed suppression. By adding 2-4 Mg.ha^{-1} of sorghum to the soil, weed biomass was reduced by 40–50%. Shiv et al. 2023 revealed that the

addition of crop wastes has the potential to inhibit weeds and alter their frequency and distribution. The physical resistance of the sorghum residues integration or the chemicals released from them may have contributed to the growth inhibition of the dominant weed biota in this experiment. Allelo chemicals generated by various plant components are influenced by a multitude of parameters, including the crop family used, the amount and size of mulch applied, the rate of decomposition, the moisture level, the soil's texture, and the soil microbiota (Won et al. 2023). The amount of allelopathic products taken has a direct impact on the level of weed control. The overall amount of allelochemicals released and present in the mulch increases with the amount of plant material used, which results in a higher concentration of allelochemicals in the soil (Tibugari et al. 2021). In general, it was found that weed suppression increased with the amount of crop waste added. Ullah et al. (2022, 2020) found that in comparison to the weedy control, the integration of sorghum residue greatly decreased the density of weeds and increased the production of broad beans. Sorghum water extract applied topically decreased the weight and density of dry weeds relative to the control. Selectivity and extract concentration are key factors in sorghum's allelopathic activity. When allelochemical concentrations are low, they have stimulatory effects on weed growth and germination, but when they are higher, they demonstrate inhibitory effects Won et al. (2013), Meleta et al. (2024). The fact that allelochemicals function as herbicides in high concentrations and as hormones in low concentrations may account for the greater suppression of weeds with concentrated extract. The findings of Ullah et al. (2023) and Khamare et al. (2022), who observed that the inhibitory effect on germination indices increased as water extract content grew from 25 to 100%, are consistent with our observations. Our findings are consistent with those of Murimwa et al. (2022), Bailey-Elkin et al. (2021) who described a noteworthy reduction in the density of weeds using an allelopathic crop water extract. Allelochemicals were found to be present and efficacious in both materials based on the suppression of weed density observed with leaf and stem water extracts. According to Murimwa et al. (2022) and Georgieva 2021, foliar application of sorghum leaf and stem water extract significantly reduced the density of weeds. These results are consistent with their findings. Similarly, due to allelopathy (Georgieva 2021, Scavo & Mauromicale 2021, Sharmili & Yasodha 2021) found that plant extract had a major impact on other plants' growth. When sorghum was interplanted with maize, the weight of black pigweed, field bindweed, and *Cyperus rotundus* was minimal. The hydrophilic chemicals (phenolic acids and their aldehyde derivatives) and hydrophobic compounds (sorgleone and its analogs) present in the mixture dictate its potential to control weed growth. To assess allelopathic effects on weed and crop growth, sorghum residues are used as a mulch or integrated into the soil in place of sorgaab in another kind of study. Sorghum wastes in container studies can be pulverized or chopped and mixed into the soil (Alsaadawi et al. 2019, Scavo et al. 2019, Głąb et al. 2017). Using a disc plow, sorghum residues are integrated into the soil twice during field experiments. Additionally, several researchers have investigated how intercropping sorghum with a primary crop can reduce weeds due to its allelopathic properties (Georgieva et al. 2016, Singh et al. 2016).

Effect of sorghum allelopathy on yield attributes: Effective allelopathic weed management strategies increased field pea yield in our study by more than 34%. Jabran et al. (2015) stated that improved soil characteristics and less weed competition during the crucial stages of crop growth may be the reasons for this increase in the production of crops. Reducing weeds effectively also makes resources like light, moisture, nutrients, and yield more accessible. Increased soil moisture conservation, particularly throughout the experimental crop's crucial growth stage (Ashraf & Akhlaq 2007). Along with contributing nutrients to crop plants, fully decomposed residues in the soil also supply allelochemicals. Therefore, a plant with enough nutrients produces more pods overall, more seeds within each pod, and pods that fully develop (Cheema et al. 2007). Cheema (2000a) found that applying sorghum residues as biological weed management may have contributed to the increase in pod count per plant, number of seeds per pod, pod length, and seed yield observed with sorghum stalk incorporation, mulching, and intercropping. This process aids in nitrogen mineralization and improves nitrogen availability in the rhizosphere. But later in crop growth, mineralization improved the obtainability of nitrogen, thus this constant supply of nitrogen provided test crops and subsequent crops with a constant source of nutrition (Farooq et al. 2020). Because of the phenolic compounds present in the residues, the incorporation of sorghum residues improved the moisture retention, physical qualities, microbial activity, and physical hindrance of the residue (Won et al. 2013, Meleta et al. 2024, Georgieva 2021). Additionally, the presence of allelochemicals released from the residues reduced light penetration and suppressed weed growth. Ultimately, the incorporation of sorghum residues improved field pea profitability and seed yield (Farooq et al. 2020). In addition to improving nodulation and nitrogen fixation processes, as well as the physical, chemical, and nutritional statuses of field soils, the addition of sorghum residues had a positive impact on weed population and biomass reduction (Hetta et al. 2022, Abbas et al. 2021, Murimwa et al. 2022). Significant increases in grain output with hand

weeding and SWE spraying may be the result of reducing the density of weeds in these plots, which lessened resource competition and allowed more nutrients to get to the seed and photosynthesis to move to reproductive regions. These findings are consistent with studies by Scavo et al. (2019) and Alsaadawi et al. (2019) who observed increased grain yields following foliar application of allelopathic crop water extract.

Effect of allelopathy on nutrient content: The main source of organic matter supplied to the soil is crop residues, which are also excellent suppliers of nutrients. They improve the soil's ability to hold water and release nutrients. The primary advantage of residue incorporation is moisture retention (Meleta et al. 2024, Ullah et al. 2023, Georgieva 2021). It results from less water evaporating from the land and less runoff. One possible explanation for the increased nutrient buildup (particularly P and K) could be improved soil moisture retention. Increased soil moisture availability as a result of residue assimilation also suggested that the soil's ability to store water had increased and that soil moisture was accessible to promote plant growth for longer periods. Field peas compete less with weeds for nutrients, such as nitrogen, phosphate, and potash, as well as other resources like space, light, and water, which are necessary in sufficient amounts for healthy growth and development. This could lead to a higher yield (Głąb et al. 2017).

CONCLUSIONS

Weed infestation can cause a 40–70% reduction in field pea yield. The allelopathy of the sorghum crop had a major effect on field pea yield and weeds. We found that different treatments of applying water extract and sorghum residue had variable levels of weed suppression. Allelopathic water extract, sorghum surface mulching, and sorghum soil inclusion are excellent methods for managing weeds in field pea. Additionally, by applying the experimental treatment dose, weed indices in field pea can be effectively improved. Nonetheless, the results indicate that when compared to other treatments, hand weeding and sorghum surface mulching had superior outcomes in terms of field pea output and weed management indices. Field pea yields increased, and profitability increased as a result of improved soil conditions and weed suppression. As a result, applying sorghum surface mulch at a rate of 10 tonnes per hectare proved to be a profitable and efficient substitute for the current field pea weed control advice, which calls for three-hand weeding at 20, 40, and 60 DAS.

REFERENCES

Abbas, T., Ahmad, A., Kamal, A., Nawaz, M.Y., Jamil, M.A., Saeed, T. and Ateeq, M., 2021. Ways to use allelopathic potential for weed management: a review. International Journal of Food Science and Agriculture, 5, pp.492-498. Available at: http://www.hillpublisher.com/journals/jsfa/ [Accessed 28 Sep. 2024].

Alsaadawi, I.S., Hadwan, H.A. and Malih, H.M., 2019. Weed management in cowpea through combined application of allelopathic sorghum residues and less herbicide. Journal of Advanced Agricultural Technologies, 6(3).

Ashraf, M. and Akhlaq, M., 2007. Effects of sorghum leaves, roots and stems water extract, hand weeding and herbicide on weeds suppression and yield of wheat. Sahrad Journal of Agriculture, 23(2), pp.321-327.

Bailey- Elkin, W., Carkner, M. and Entz, M.H., 2021. Intercropping organic field peas with barley, oats, and mustard improves weed control but has variable effects on grain yield and net returns. Canadian Journal of Plant Science, 102(3), pp.515-528. Available at: https://cdnsciencepub.com/doi/full/10.1139/cjps-2021-0182 [Accessed 28 Sep. 2024].

Blaise, D., Manikandan, A., Verma, P., Nalayini, P., Chakraborty, M. and Kranthi, K.R., 2020. Allelopathic intercrops and its mulch as an integrated weed management strategy for rainfed Bt-transgenic cotton hybrids. Crop Protection, 135, p.105214. Available at: https://doi.org/10.1016/j.cropro.2020.105214 [Accessed 28 Sep. 2024].

Cheema, Z.A., Khaliq, A., Abbas, M. and Farooq, M., 2007. Allelopathic potential of sorghum (Sorghum bicolor L. Moench) cultivars for weed management. Allelopathy Journal, 20(1), p.167.

Cheema, Z.A., Rakha, A. and Khaliq, A., 2000a. Use of sorgaab and sorghum mulch for weed management in mungbean. Pakistan Journal of Agricultural Sciences, 101(3-4), pp.141-143.

Choudhary, C.S., Behera, B., Raza, M.B., Mrunalini, K., Bhoi, T.K., Lal, M.K. and Das, T.K., 2023. Mechanisms of allelopathic interactions for sustainable weed management. Rhizosphere, p.100667. Available at: https://doi.org/10.1016/j.rhisph.2023.100667 [Accessed 28 Sep. 2024].

Coulibaly, S.S., Touré, M., Kouamé, A.E., Kambou, I.C., Soro, S.Y., Yéo, K.I. and Koné, S., 2020. Incorporation of crop residues into soil: a practice to improve soil chemical properties. Available at: https://doi.org/10.4236/as.2020.1112078 [Accessed 28 Sep. 2024].

Farooq, M., Khan, I., Nawaz, A., Cheema, M.A. and Siddique, K.H., 2020. Using sorghum to suppress weeds in autumn planted maize. Crop Protection, 133, p.105162. Available at: https://doi.org/10.1016/j.cropro.2020.105162 [Accessed 28 Sep. 2024].Farooq, N., Abbas, T., Tanveer, A. and Jabran, K., 2020. Allelopathy for weed management. Co-evolution of secondary metabolites, pp.505-519. Available at: https://link.springer.com/referenceworkentry/10.1007/978-3-319-96397-6_16 [Accessed 28 Sep. 2024].

Georgieva, N. and Nikolova, I., 2016. Allelopathic tolerance of pea cultivars to Sorghum halpense L. (Pers.) extracts. Pesticides and Phytomedicine, 31(1-2).

Georgieva, N., 2021. Allelopathic tolerance in broad bean (Vicia faba L.) accessions to Sorghum halepense extracts. Bulgarian Journal of Agricultural Science, 27(3), pp.524-530. Available at: https://journal.agrojournal.org/page/en/details.php?article_id=3440 [Accessed 28 Sep. 2024].

Georgieva, N., Kosev, V. and Kalapchieva, S., 2021. A study on the allelopathic tolerance of garden pea varieties to Sorghum halepense (L.) Pers. extracts. Pesticidi i fitomedicina, 36(2), pp.91-99. Available at: https://doi.org/10.2298/PIF2102091G [Accessed 28 Sep. 2024].

Głąb, L., Sowiński, J., Bough, R. and Dayan, F.E., 2017. Allelopathic potential of sorghum (Sorghum bicolor (L.) Moench) in weed control: a comprehensive review. Advances in Agronomy, 145, pp.43-95. Available at: https://doi.org/10.1016/bs.agron.2017.05.001 [Accessed 28 Sep. 2024].

Hetta, G., Rana, S.S., Kumar, S. and Mujahed, B.A., 2022. Promising cultural weed management practices to limit crop-weed competition in Peas (Pisum sativum L.) in the North-western Himalayan Region. Available at: http://www.thepharmajournal.com/ [Accessed 28 Sep. 2024].

Jabran, K., Mahajan, G., Sardana, V. and Chauhan, B.S., 2015. Allelopathy for weed control in agricultural systems. Crop Protection, 72, pp.57-65. Available at: https://doi.org/10.1016/j.cropro.2015.03.004 [Accessed 28 Sep. 2024].

Jaswal, A., Singh, A., Sarkar, S. and Singh, M., 2022. Influence of weed management practices on weed density, growth and yield of green gram (Vigna radiata).

Khamare, Y., Chen, J. and Marble, S.C., 2022. Allelopathy and its application as a weed management tool: A review. Frontiers in Plant Science, 13, p.1034649. Available at: https://doi.org/10.3389/fpls.2022.1034649 [Accessed 28 Sep. 2024].

Khan, S.U., Wang, X., Mehmood, T., Latif, S., Khan, S.U., Fiaz, S. and Qayyum, A., 2021. Comparison of organic and inorganic mulching for weed suppression in wheat under rain-fed conditions of Haripur, Pakistan. Agronomy, 11(6), p.1131. Available at: https://doi.org/10.3390/agronomy11061131 [Accessed 28 Sep. 2024].

Kovács, E.B., Dorner, Z., Csík, D. and Zalai, M., 2023. Effect of Environmental, Soil and Management Factors on Weed Flora of Field Pea in South-East Hungary. Agronomy, 13(7), p.1864. Available at: https://doi.org/10.3390/agronomy13071864 [Accessed 28 Sep. 2024].

Kristó, I., Vályi Nagy, M., Rácz, A., Tar, M., Irmes, K., Szentpéteri, L. and Ujj, A., 2022. Effects of weed control treatments on weed composition and yield components of winter wheat (Triticum aestivum L.) and winter pea (Pisum sativum L.) intercrops. Agronomy, 12(10), p.2590. Available at: https://doi.org/10.3390/agronomy12102590 [Accessed 28 Sep. 2024].

Kumar, N., Nath, C.P., Hazra, K.K. and Sharma, A.R., 2016. Efficient weed management in pulses for higher productivity and profitability. Indian Journal of Agronomy, 61(4), pp.5199-5213.

Lake, L., Guilioni, L., French, B. and Sadras, V.O., 2021. Field pea. In: Crop Physiology Case Histories for Major Crops. Academic Press, pp.320-341. Available at: https://doi.org/10.1016/B978-0-12-819194-1.00009-8 [Accessed 28 Sep. 2024].

Mahmood, A.R.I.F. and Cheema, Z.A., 2004. Influence of sorghum mulch on purple nutsedge (Cyperus rotundus L.). International Journal of Agriculture and Biology, 6(1), pp.86-88. Available at: http://www.ijab.org [Accessed 28 Sep. 2024].

Meleta, T., Dargei, R., Kora, D. and Dajane, B., 2024. Effect of Chemical and Hand weeding Control Methods on Growth Yield Components and Yield of Field Pea in Bale Highlands, Southeastern Ethiopia. In Regional Review Workshops on Completed Research Activities, p.171. Available at: https://doi.org/10.36349/easjals.2024.v07i02.001 [Accessed 28 Sep. 2024].

Mishra, M.M., Dash, R. and Mishra, M., 2016. Weed persistence, crop resistance and phytotonic effects of herbicides in direct-seeded rice. 13-16.

Motmainna, M., Juraimi, A.S., Uddin, M.K., Asib, N.B., Islam, A.K.M.M. and Hasan, M., 2021. Assessment of allelopathic compounds to develop new natural herbicides: A review. Allelopathy Journal, 52, pp.21-40. Available at: https://www.allelopathyjournal.com/10.26651/2021-52-1-1305 [Accessed 28 Sep. 2024].

Murimwa, J.C., Rugare, J.T., Mabasa, S. and Mandumbu, R., 2022. Effect of sorghum mulches on emergence and seedling growth of beggarticks, goose grass, and sesame. International Journal of Agronomy, 2022. Available at: https://doi.org/10.1155/2022/2751106 [Accessed 28 Sep. 2024].

Reddy, R.H.V., Singh, A., Jaswal, A., Sarkar, S. and Fatima, I., 2023. Effect of nutrient management on physio morphological and yield attributes of field pea (Pisum sativum L.). Journal of Experimental Biology and Agricultural Sciences, 11(4), pp.736-745. Available at: https://doi.org/10.18006/2023.11(4).736.745 [Accessed 28 Sep. 2024].

Sahu, M.P., Kewat, M.L., Jha, A.K., Sondhia, S., Choudhary, V.K., Jain, N.

and Verma, B., 2022. Weed prevalence, root nodulation and chickpea productivity influenced by weed management and crop residue mulch. AMA, Agricultural Mechanization in Asia, Africa and Latin America, 53(6), pp.8511-8521.

Scavo, A. and Mauromicale, G., 2021. Crop allelopathy for sustainable weed management in agroecosystems: Knowing the present with a view to the future. Agronomy, 11(11), p.2104. Available at: https://doi.org/10.3390/agronomy11112104 [Accessed 28 Sep. 2024].

Scavo, A., Abbate, C. and Mauromicale, G., 2019. Plant allelochemicals: Agronomic, nutritional and ecological relevance in the soil system. Plant and Soil, 442, pp.23-48. Available at: https://link.springer.com/article/10.1007/s11104-019-04190-y [Accessed 28 Sep. 2024].

Sharmili, K. and Yasodha, M., 2021. Agronomic Research on Intercropping Millets and Pulses-A Review. Mysore Journal of Agricultural Sciences, 55(4). Available at: https://www.cabidigitallibrary.org/doi/full/10.5555/20220081085 [Accessed 28 Sep. 2024].

Shiv, S., Agrawal, S.B., Verma, B., Yadav, P.S., Singh, R., Porwal, M. and Patel, R., 2023. Weed dynamics and productivity of chickpea as affected by weed management practices. Pollution Research, 42(2), pp.21-24. Available at: http://doi.org/10.53550/PR.2023.v42i02.004 [Accessed 28 Sep. 2024].

Singh, A., Sarkar, S., Bishnoi, U., Kundu, T., Nanda, R., Robertson, A. and Mor, M., 2023. Effect of integrated weed management practices on weed dynamics and performance of maize crop. Indian Journal of Agricultural Research, 57(2), pp.184-188.

Singh, A., Sarkar, S., Jaswal, A. and Singh, M., 2022. Herbicides performance in management of weeds in transplanted basmati rice (Oryza sativa).

Singh, M., Kumar, R., Kumar, S. and Kumar, V., 2016. Critical period for weed control in field pea. Legume Research-An International Journal, 39(1), pp.86-90. Available at: http://10.0.73.117/lr.v0iOF.6787 [Accessed 28 Sep. 2024].

Tibugari, H., Manyeruke, N., Mafere, G., Chakavarika, M., Nyamuzuwe, L., Marumahoko, P. and Mandumbu, R., 2019. Allelopathic effect of stressing sorghum on weed growth. Cogent Biology, 5(1), p.1684865. Available at: https://doi.org/10.1080/23312025.2019.1684865 [Accessed 28 Sep. 2024].

Ullah, H., Khan, N. and Khan, I.A., 2023. Complementing cultural weed control with plant allelopathy: Implications for improved weed management in wheat crop. Acta Ecologica Sinica, 43(1), pp.27-33. Available at: https://doi.org/10.1016/j.chnaes.2021.06.006 [Accessed 28 Sep. 2024].

Ullah, R., Aslam, Z., Attia, H., Sultan, K., Alamer, K.H., Mansha, M.Z. and Zaman, Q.U., 2022. Sorghum Allelopathy: Alternative Weed Management Strategy and Its Impact on Mung Bean Productivity and Soil Rhizosphere Properties. Life, 12(9), p.1359. Available at: https://doi.org/10.3390/life12091359 [Accessed 28 Sep. 2024].

Ullah, R., Aslam, Z., Maitah, M., Zaman, Q.U., Bashir, S., Hassan, W. and Chen, Z., 2020. Sustainable weed control and enhancing nutrient use efficiency in crops through Brassica (Brassica compestris L.) allelopathy. Sustainability, 12(14), p.5763. Available at: https://doi.org/10.3390/su12145763 [Accessed 28 Sep. 2024].

Won, O.J., Uddin, M.R., Park, K.W., Pyon, J.Y. and Park, S.U., 2013. Phenolic compounds in sorghum leaf extracts and their effects on weed control. Allelopathy Journal, 31(1), p.147.

ORCID DETAILS OF THE AUTHORS

Prantick Patra: https://orcid.org/0009-0005-3613-1090
Anita Jaswal: https://orcid.org/0000-0002-7214-8747
Iza Fatima: https://orcid.org/0000-0003-0898-190X

Bioactivity of Rhizospheric *Acinetobacter baumannii* Siderophore Combined with Antibiotics Against Lower Respiratory Tract Pathogenic Bacteria

Rafal Moayad Abdul-Latif† and Amel Hussaein Mussa

Department of Biology, College of Science, Al-Mustansiriyah University, Baghdad, Iraq
†Corresponding author: Rafal Moayad Abdul-Latif; rafal.m98@uomustansiriyah.edu.iq

ABSTRACT

The study focused on extracting and purifying siderophore produced by *Acinetobacter baumannii* isolated from rhizospheric soil in Baghdad city and evaluating its bioactivity both independently and in combination with selected antibiotics. Bacterial identification was performed using CHROM agar, biochemical, and physiological tests, with confirmation via PCR amplification of the 16S rDNA housekeeping gene. The siderophore was extracted using ethyl acetate after culturing the bacteria in succinate broth and was purified through HPLC, detected at a wavelength of 403 nm. A total of 38 bacterial isolates were obtained from lower respiratory tract infections, including *Escherichia coli*, *Klebsiella pneumoniae*, *Pseudomonas aeruginosa*, *Acinetobacter baumannii*, *Staphylococcus aureus*, and *Serratia marcescens*. Antibiotic susceptibility testing with 13 antibiotics showed the highest resistance rates to ampicillin (65.7%) and ceftriaxone (63.1%), while the lowest resistance was observed with amikacin (15.7%). The synergistic activity of the siderophore combined with sub-MIC concentrations of ceftriaxone, ceftazidime, and gentamycin was tested against multidrug-resistant (MDR) isolates. The most significant antibacterial activity was observed with the combination of siderophore and gentamycin against *S. aureus*, whereas a minimal effect was noted on *A. baumannii*. In conclusion, 38 bacterial isolates were successfully identified from lower respiratory tract infections. The combination of siderophore with gentamycin exhibited notable antibacterial activity against *S. aureus* but was ineffective against *A. baumannii*.

INTRODUCTION

Acinetobacter spp. are saprophytic organisms found in soil, water, wastewater, vegetables, and animal and human skin. They resist many antibiotics due to chromosome-mediated genetic elements and can persist on surfaces and medical devices in hospitals for long periods(Asif et al. 2018). Microorganisms and plants produce low molecular weight (500–1000 Daltons) iron chelators called siderophores to enhance iron acquisition from the soil, especially under iron-limited conditions. These siderophores selectively bind iron (III) with high affinity(Lis et al. 2015). Siderophores are high-affinity iron chelator proteins that compete with host cells for iron (Chan & Burrows 2023). Iron acquisition mechanisms are crucial virulence factors for bacterial pathogens, including *A. baumannii*, enabling their survival in hosts. Iron is an essential nutrient for nearly every life on earth(Ilbert &Bonnefoy 2013, Artuso et al. 2023).

Siderophores can be employed as a "Trojan Horse Strategy" in the medical profession, forming a complex with antibiotics and delivering them to the appropriate places, notably in antibiotic-resistant bacteria (Prabhakar 2020, Cheng et al. 2024).

Biofilms are one of the primaries that cause lower respiratory tract infections that may particularly complicate the treatment and are one of the foremost causes of death in developing countries worldwide. Patients with chronic respiratory diseases are at a higher risk of such infections and are one of the main causes of morbidity and mortality rate in this group, besides, respiratory infections can also impact economies because they can lead to increasing in treatment costs (Smith et al. 2019, Perry & Tan 2023).

This study aims to extract and purify siderophores produced from *Acinetobacter baumannii* and investigate the activity of synergism against some antibiotics and its action as an antibacterial agent on pathogenic bacteria.

MATERIALS AND METHODS

Isolation and Identification of *A. baumannii*

The soil samples were taken from the wetland rhizosphere region from the plant to isolate *A. baumannii* isolates. Soil sample culturing on (CHROM agar) in a selective media for *A .baumannii* and then were subjected to numerous cultural, and biochemical tests and vitek2 using PCR. All earlier

Table 1: Primer sequences used in molecular detection of *A. baumannii* isolated from soil.

Gene name	Primer name	Sequence 5'→3'	size	Annealing Temperature	Reference
16s rRNA	F	TTTAAGCGAGGAGGAGG	242bp,	56°C,	(Sepahvand*et al.* 2017)
	R	ATTCTACCATCCTCTCCC			

F = Forward   R= Reverse

diagnosed isolates underwent DNA extraction using the ABIO pure TM kit (Alliance Bio, USA). The concentration and purity of the extracted DNA were measured with a Nanodrop. The samples were further confirmed by diagnosing with the housekeeping gene 16S rDNA(Tawfeeqet al.2023) (Table 1). The bacterial isolates were cultured overnight in a nutrient broth medium, then subjected to DNA extraction,

Screening for Siderophore Produced from *A. baumannii* Isolates

Chrome Azurol S (CAS) agar assay was used to detect the siderophore producer from *A. baumannii* isolates. According to the modified method of Srimathi & Suji (2018), the isolates were streaked on CAS agar and incubated at 30ºC for 48 hours. The isolate is considered a siderophore producer when bacterial growth can grow and change the medium blue color to green or yellow, indicating a positive result.

Antibiotic Susceptibility Test (AST)

Antibiotic sensitivity of all lower respiratory tract infection isolates was tested using the agar disc diffusion method (Kirby-Bauer method) against 13 different antibiotics(Ampicillin, Ceftriaxone, Ceftazidime, AmoxillinCalvunic acid, Gentamicin, Ciprofloxacin, Cefotaxime, Nitrofurantion, Norfloxacin, Cefepime, Levolfloxacn, Cefazolin, Amikacin). The results obtained were justified according to (Weinstein & Lewis2020).

Extraction of Siderophore

The Siderophore produced by an isolate of *Acinetobacter baumannii* was precultured at 28ºC for 12 hours in succinate liquid broth and incubated in a rotary shaker for 4 days at 110rpm, then siderophore was extracted by centrifuging at 12000rpm for 10min. The supernatant was acidified with pH 2 and was mixed with ethyl acetate. Using a reparatory funnel, the upper layer was collected which represents the crude siderophore, then dried in a desiccated vacuum at 40°C and then dissolved in 1mL of methanol as explained by (Taher 2016).

Purification of Siderophore

The extracted siderophore was analyzed by HPLC using a C18 reverse-phase column with methanol:water (8:2 v/v) mobile phase. The sample was injected at a flow rate of 1 mL/min at 25°C and detected at 403nm. Preparatory separation used the same mobile phase, and retention times (RT) of peaks with similar heights were analyzed.

Synergistic Effect Between Purified Siderophore with Some Antibiotics

The Minimum Inhibition Concentration (MIC) of three antibiotics—ceftriaxone, ceftazidime, and gentamycin—was determined. Overnight cultures of *Staphylococcus aureus*, *Escherichia coli*, *Acinetobacter baumannii*, *Serratia marcescens*, and *Klebsiella pneumoniae* were inoculated into nutrient broth (N.B) in 96-well microtitration plates. Serial dilutions of the antibiotic solutions were added to each well, with each isolate at approximately $1.5 \times 10⌷$ CFU/mL. The plates were then incubated at 37°C for 24 hours.

The antibacterial activity of purified siderophore in combination with sub-MIC of antibiotics was also carried out by mixing 50μL of sub-MIC of antibiotics with 50μL of purified siderophore. The agar well diffusion method was applied by spreading each isolate on the surface of Muller Hinton Agar and using a cork borer to make 3 wells and loaded with 100μLof (50μL sub-MIC of antibiotic + 50μL purified siderophore) and second loaded with 100μL of sub-MIC of antibiotic alone and the last was control filled with D.W.

RESULTS

Conventional PCR was employed to detect the housekeeping 16S rRNA gene to identify A. baumannii species. The PCR-amplified fragments were 242 bp, Fig. 1.

The method used CAS agar for detecting the production of siderophore was also carried out as shown in Fig. 2.

Extraction and purification of siderophore from *A. baumannii* were also carried out using HPLC Chromatogram for siderophore purification C-18 column (250mm×4.6mm, 5; flow rate:1 mL/min at μm) 25°C; detection wavelength: 403nm; methanol: water (8:2 v/v).

Figs. 4, 5 and 6 show the Antibiotic Susceptibility Test (AST) indicating the resistance percentage of bacteria against different antibiotics.

Combination Effectiveness of Siderophore with some Antibiotics

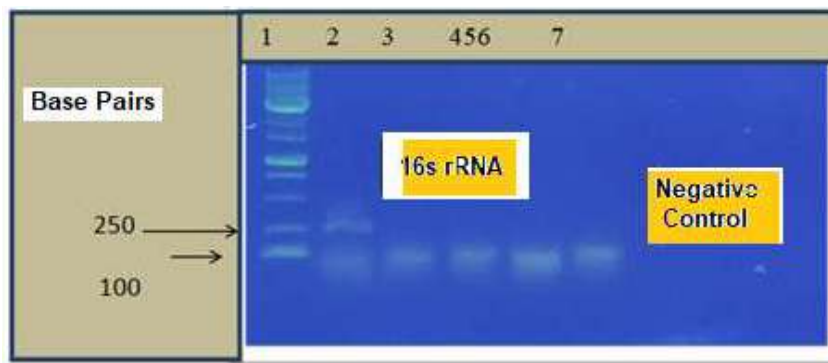The combination of antibiotics with siderophore was

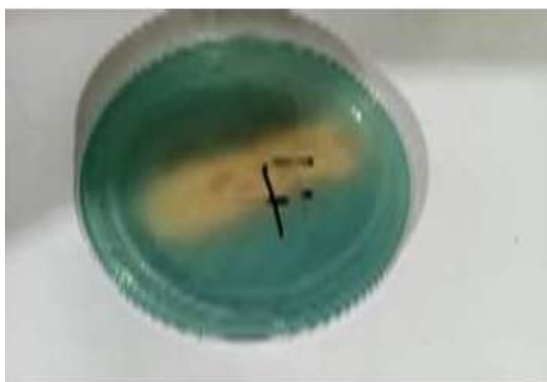Fig. 1: PCR for 16s rRNA gene (amplified sizes were 242bp).

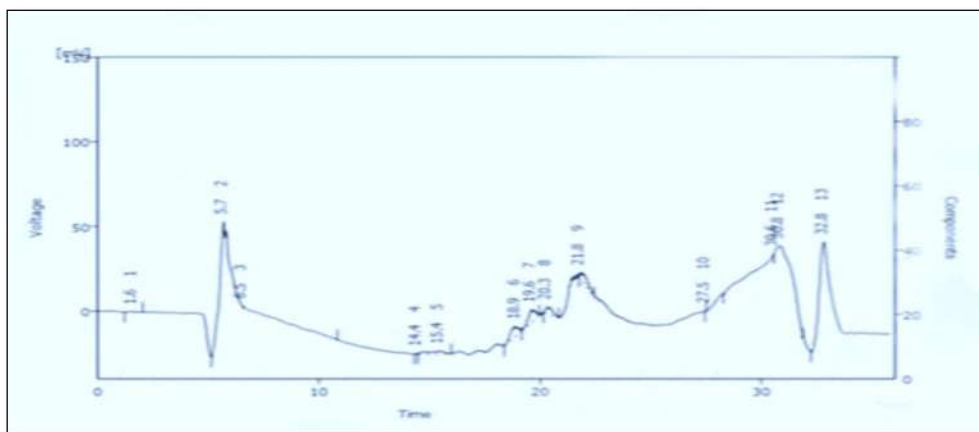Fig. 2: CAS agar assay for siderophore detection.

Fig. 3: HPLC Chromatogram flowchart for siderophore purification.

determined against some test bacteria causing lower respiratory tract infections. MIC was determined to 3 antibiotics (Gentamicin, Ceftazidime and Ceftriaxone) and the results were explainable according to clinical laboratory standard institutes (CLSI, 2022) (Tables 2 & 3).

DISCUSSION

Isolation and Identification of *A.baumannii*Isolates

Soil sample culturing on (CHROM agar) selective media for *A. baumannii* isolates were able to grow on CHROM agar and were suspected to be belonging to the genus *Acinetobacter*,
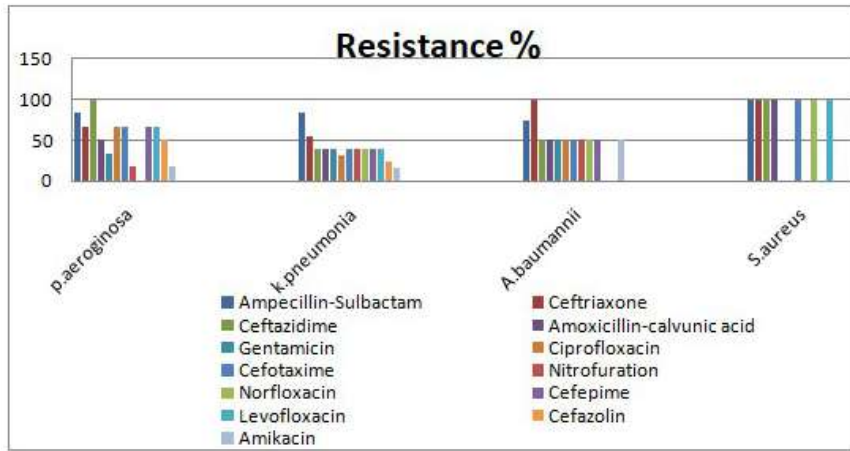
Fig. 4: The resistance percentage of *P. aeruginosa*, *K. pneumonia*, *A. baumannii* and *S. aureus* against different antibiotics.
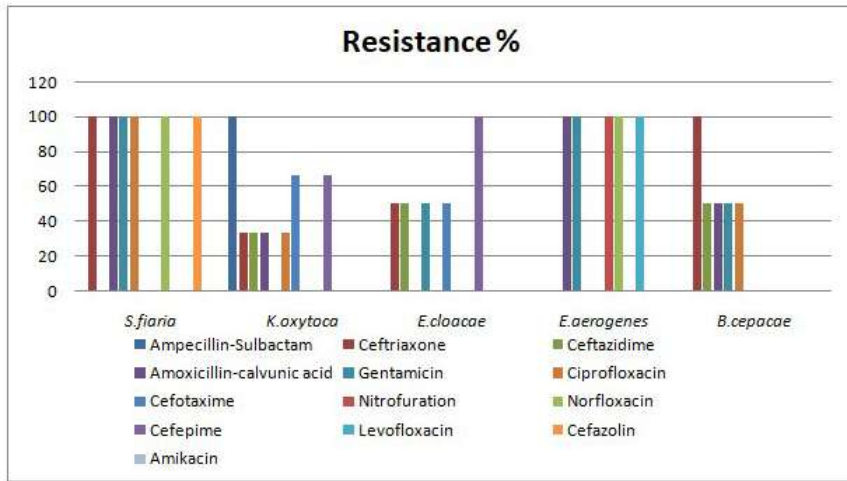

Fig. 5: The resistance percentage of *S. pyogenes*, *E. faecalis*, *E. coli* and *S. marscenes* against different antibiotics.
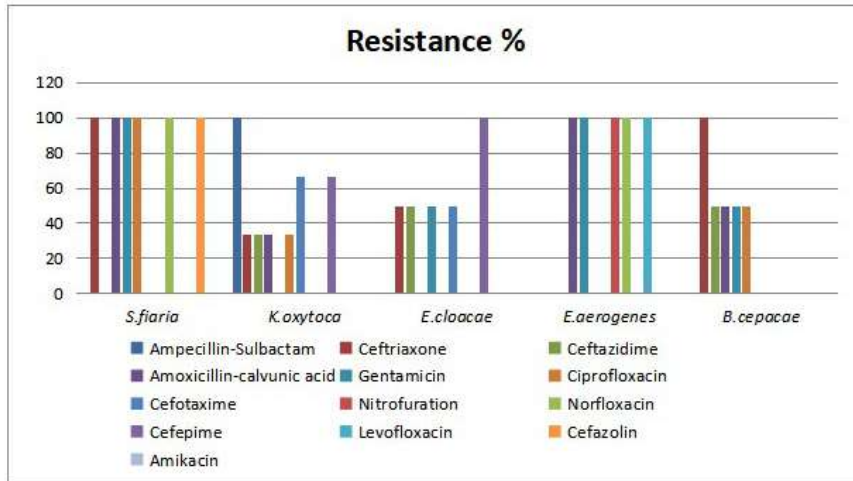

Fig. 6: The resistance percentage of *S. fiaria*, *K.oxytoca*, *E. cloacae*, *E. aerogenes* and *B. cepacian* against different antibiotics.

Table 2: The Value of MIC (µg/mL) for antibiotics against pathogenic bacteria isolates.

Bacterial isolates	MIC value (µg/mL)		
	GN	CAZ	CTX
S. aureus	16	16	64
K. pneumonia	16	32	128
A. baumannii	16	16	128

Table 3: Inhibition zone (mm) of the synergistic effect of antibiotic with siderophore antibacterial against tested bacteria.

Synergistic antibiotic with siderophore	Inhibition zone (mm)		
	S. aureus	*K. pneumoniae*	*A. baumannii*
Gentamicin	25	20	20
Ceftriaxone	28	15	15
Ceftazidime	24	24	18

then subjected to numerous cultural, biochemical tests and vitek2 finely using PCR for confirming the identification. The PCR is a more reliable method for diagnosing A. baumannii in laboratories than Chromogenic media and other methods used, the result appeared only one isolate was diagnosed as *A. baumannii*, which is used in the production of siderophore. The genotypic detection of *A. baumannii* on agarose gel electrophoresis of 16srRNA shows positive results with 242bp bands for 16s rRNA, line 3-6: negative result, line 7: negative control. UV light was used to visualize the DNA bands (Fig. 1).

Detection of Siderophores CAS Agar Medium

By changing the color of colonies into orange or yellow after the incubation period due to the removal of iron Fe from the dye which indicated the + ability of *A. baumannii* isolates for siderophore production. It is a colorimetric method by changing the color of colonies into orange or yellow after the incubation period due to the removal of iron Fe from the dye which indicates the + ability of isolates .*A. baumannii* for siderophore production.

Extraction and Purification of Siderophore from *A. baumannii*

The peaks obtained in retention times RT between 14 to 20 minutes belong to siderophore (Fig. 3). These results agree with Tank et al. (2012). When using the same condition and solvent obtained peaks at RT 14.9, 16.9, and 18.4 min at wavelength 403 using Data. RT allowed dissemination between siderophore and different peptide chains produced by bacterial species.

Antibiotic Susceptibility Test (AST)

The clinical isolates of *P. aeruginosa* were highly

confrontation to beta-lactams (Ampicillin, Amoxicillin, Ceftazidime, Ceftriaxone, and Cefepime), this could be related to the hyperproduction of beta-lactamase through the genes of resistance and mutational processes, while the resistance against non-beta lactam antibiotics (Figs. 4, 5 and 6). The results recorded that 33.3% and 16.6% of isolates were resistant to aminoglycoside (gentamycin and amikacin, respectively) this may be due to the inactivation of aminoglycosides by resistant *P. aeruginosa* isolates involving their modification by enzymes that phosphorylate, acetylate, or adenylate these antimicrobials and enzymes are frequent determinants of aminoglycoside resistance in *P. aeruginosa*. Resistance of *Pseudomonas aeruginosa* isolates to cephalosporins was 66.6% (Cefotaxime) this is often associated with stable synthesis of the chromosomal beta-lactamase that robustly hydrolyzes cephalosporins (Barnes et al. 2018).

According to beta-lactam resistance by *A. baumannii* (each of Ampicillin 75% Amoxicillin and Ceftazidime were 50%, ceftriaxone 100%, and Cefepime was 50%), *Acinetobacter* spp. display multidrug confrontation via the creation of β-lactamases, changes in external membrane proteins and penicillin-binding proteins, and increased activity of efflux pumps (Cerqueira et al. 2011).In *K. pneumoniae*, the results show higher resistance for each of Ampicillin 84.6% and Ceftriaxone 53.8%, The production of β-lactamases, particularly extended-spectrum β-lactamases and AmpC β-lactamases, is a major drug resistance mechanism in *K. pneumoniae*, making these isolates resistant to broad-spectrum cephalosporins and β-lactam/β-lactamase inhibitors(Ali 2008).In *A. baumannii*, resistance to aminoglycosides is often due to aminoglycoside-modifying enzymes, with genes for these enzymes commonly located on mobile elements like plasmids and transposes, facilitating their transfer among the *A. baumannii* inhabitants (Lin et al. 2013).

The resistant to Beta-lactam (Amoxicillin, Ampicillin, Ceftazidime, Ceftriaxone, and Cefepime) *Staphylococci* are resistant to beta-lactam antibiotics through two different mechanisms. One is the creation of beta-lactamases, which are hydrolytic enzymes that eliminate beta-lactams. The other is the expression of the beta-lactam antibiotic-resistant penicillin-binding protein 2a. Resistance of *S. aureus* strains to cephalosporins was 100% (Cefotaxime) this is often associated with the widely used of Cephalosporins for the treatment of *staphylococcal* infections. The resistance mechanisms to quinolones in *Staphylococcus aureus* (Levofloxacin, Ciprofloxacin, and Norfloxacin), may be due to mutations in the genes encoding target enzymes, the expression of the efflux pump, fluoroquinolones inhibit

altered enzymes, and cefotaxime has a broader spectrum compared to ampicillin. Cefotaxime is often used alone, offering the benefits of fewer line entries and potentially lower toxicity.

Combination Effectiveness of Siderophore with some Antibiotics

The bacteria are regarded to be sensitive when the MIC value is less than the cut-off value as depicted by Kowalska et al. (2017). The results shown in Table 2 indicate that test isolates were highly resistant as they could grow in concentrations higher than the premium value for certain antibiotics. To determine the synergism effects of siderophore produced from the isolate of *A. baumannii* with sub-MIC of the antibiotics, the results in Table 3 declared the combination effects of siderophore with sub-MIC of gentamycin on *S. aureus* the inhibition zone was 25mm, *K. pneumoniae* and *A. baumannii* the inhibition zone was 20mm, then the combination of Ceftazidime with siderophore on *S. aureus* and *K. pneumoniae* inhibition zone was 24, *A. baumannii* the inhibition zone was 18mm, while the Ceftriaxone with siderophore gave 15 on *K. pneumonia* and *A. baumannii* 25mm. Whereas the inhibition zone gave 28 on *S. aureus*. The capacity of bacteria to acquire antibiotic resistance complicates the treatment of a wide range of bacterial infections. The 'Trojan horse' technique is one method for combating permeability-mediated drug resistance. The Trojan horse concept is the use of a bacterial iron absorption system to enter and kill bacteria after building complexes with antibiotics, as well as facilitating the selective delivery of drugs to antibiotic-resistant bacteria cells (Fan& Fang 2021).

Specific siderophore receptors identify the siderophore-antibiotic combination, which is then actively related across the external membrane. The goal of such an approach is to make it easier for present use or future antibiotics to enter bacterial cells, by increasing their activity or making them active against a wider variety of infections. It has been noticed that siderophore-drug conjugates allow for the development of medicines with enhanced cell transport and lower resistance rates Nguyen et al. (2020) concluded in their research that the combination of siderophore and cephalosporin antibiotics exhibited potent action against various MDR strains of *E. coli*, *K. pneumoniae*, and *Acinetobacter spp*. When coupled with antibiotics, Braun et al. (2009)found that Danomycins and salmycins, natural siderophore–antibiotic conjugates produced by Streptomycin, might decrease protein synthesis in Gram-positive bacteria, particularly staphylococci, and streptococci. Furthermore, various researchers and pharmaceutical companies have produced siderophore-antibiotic hybrids known as

cefiderocol, which has advanced to clinical trials in terms of antibacterial activity against Gram-negative species).

CONCLUSIONS

Acinetobacter baumannii, derived from the rhizospheric soil was prepared successfully. The Isolation and purification were carried out via HPLC. Thirty-eight bacterial isolates were obtained successfully from injuries in the lower respiratory tract. The mixed siderophore with gentamycin shows a significant effect on *S. aureus*, while it does not affect *A. baumannii*.

List of Abbreviations

Abbreviation	Scientific Name
rDNA	Ribosomal Deoxyribonucleic acid
HPLC	High performance liquid chromatography
RT	Retention time
MIC	Minimum inhibitory concentration
MDR	Multi-drug resistance
PCR	Polymerase chain reaction
CAS agar	Chrome azurolsulfonate (CAS) Blue Dye solution
AST	Antibiotic Susceptibility Test
CLSI	Clinical and Laboratory Standards Institute
N.B	Nutrient broth
D.W	Distilled water
GN	Gentamicin
CAZ	Ceftazidime
CTX	Ceftriaxone

REFERENCES

Ali, M.R., 2008. Study of prodigiosin and virulence factor produced by multi-drug-resistant *Serratia marcescens* isolated from some of Baghdad hospitals' environments. *AL-Mustansiriyah Journal of Science*, 19(5). https://www.iasj.net/iasj/download/6aba69f1da39f440

Artuso, I., Poddar, H., Evans, B.A. and Visca, P., 2023. Genomics of *Acinetobacter baumannii* iron uptake. *Microbial Genomics*, 9(8), mgen001080. https://doi.org/10.1099/mgen.0.001080

Asif, M., Alvi, I.A. and Rehman, S.U., 2018. Insight into *Acinetobacter*

baumannii: Pathogenesis, global resistance, mechanisms of resistance, treatment options, and alternative modalities. *Infection and Drug Resistance*, 11, pp.1249-1260. https://doi.org/10.2147/IDR.S167391

Barnes, M.D., Taracila, M.A., Rutter, J.D., Bethel, C.R., Galdadas, I., Hujer, A.M., Caselli, E., Prati, F., Dekker, J.P., Papp-Wallace, K.M. and Haider, S., 2018. Deciphering the evolution of cephalosporin resistance to ceftolozane-tazobactam in Pseudomonas aeruginosa. *MBio*, 9(6), pp.10-1128. e02085-18. https://doi.org/10.1128/mBio.02085-18.

Braun, V., Pramanik, A., Gwinner, T., Köberle, M. and Bohn, E., 2009. Sideromycins: Tools and antibiotics. *Biometals*, 22(1), pp.3-13. https://doi.org/10.1007/s10534-008-9187-7

Cerqueira, G.M. and Peleg, A.Y., 2011. Insights into *Acinetobacter baumannii* pathogenicity. *IUBMB Life*, 63(12), pp.1055-1060. https://doi.org/10.1002/iub.531

Chan, D.C.K. and Burrows, L.L., 2023. *Pseudomonas aeruginosa* FpvB Is a High-Affinity Transporter for Xenosiderophores Ferrichrome and Ferrioxamine B. *mBio*, 14(1), e0314922. https://doi.org/10.1128/mbio.03149-22

Cheng, J., Pan, W., Zheng, Y., Zhang, J., Chen, L., Huang, H., Chen, Y. and Wu, R., 2024. Piezocatalytic Schottky Junction Treats Atherosclerosis by a Biomimetic Trojan Horse Strategy. *Advanced Materials*, 36(19), e2312102. https://doi.org/10.1002/adma.202312102

Fan, D. and Fang, Q., 2021. Siderophores for medical applications: Imaging, sensors, and therapeutics. *International Journal of Pharmaceutics*, 597, 120306. https://doi.org/10.1016/j.ijpharm.2021.120306

Ilbert, M. and Bonnefoy, V., 2013. Insight into the evolution of the iron oxidation pathways. *Biochimica et Biophysica Acta (BBA) - Bioenergetics*, 1827(2), pp.161-175. https://doi.org/10.1016/j.bbabio.2012.10.011

Kowalska-Krochmal, B. and Dudek-Wicher, R., 2021. The minimum inhibitory concentration of antibiotics: Methods, interpretation, clinical relevance. *Pathogens*, 10(2), 165. https://doi.org/10.3390/pathogens10020165

Lin, M.F., Liou, M.L., Tu, C.C., Yeh, H.W. and Lan, C.Y., 2013. Molecular epidemiology of integron-associated antimicrobial gene cassettes in the clinical isolates of *Acinetobacter baumannii* from northern Taiwan. *Annals of Laboratory Medicine*, 33(4), pp.242-247. https://doi.org/10.3343/alm.2013.33.4.242

Lis, H., Shaked, Y., Kranzler, C., Keren, N. and Morel, F.M., 2015. Iron bioavailability to phytoplankton: An empirical approach. *The ISME Journal*, 9(4), pp.1003-1013. https://doi.org/10.1038/ismej.2014.198

Nguyen, L.P., Pinto, N.A., Vu, T.N., Lee, H., Cho, Y.L., Byun, J.-H.,

D'Souza, R. and Yong, D., 2020. In vitro activity of a novel siderophore cephalosporin, GT-1 and serine-type β-lactamase inhibitor, GT-055, against *Escherichia coli*, *Klebsiella pneumoniae*, and *Acinetobacter* spp. panel strains. *Antibiotics*, 9(5), 267. https://doi.org/10.3390/antibiotics9050267

Perry, E.K. and Tan, M.W., 2023. Bacterial biofilms in the human body: prevalence and impacts on health and disease. *Frontiers in Cellular and Infection Microbiology*, 13, 1237164. https://doi.org/10.3389/fcimb.2023.1237164

Prabhakar, P.K., 2020. Bacterial siderophores and their potential applications: A review. *Current Molecular Pharmacology*, 13(4), pp.295-305. https://doi.org/10.2174/1874467213666200429153715

Sepahvand, S., Davarpanah, M.A., Roudgari, A., Bahador, A., Karbasizade, V. and Kargar Jahromi, Z., 2017. Molecular evaluation of colistin-resistant gene expression changes in *Acinetobacter baumannii* with real-time polymerase chain reaction. *Infection and Drug Resistance*, 10, pp.455-462. https://doi.org/10.2147/IDR.S142417

Smith, K.M., Machalaba, C.C., Seifman, R., Feferholtz, Y. and Karesh, W.B., 2019. Infectious disease and economics: The case for considering multi-sectoral impacts. *One Health*, 7, 100080. https://doi.org/10.1016/j.onehlt.2018.100080

Srimathi, K. and Suji, H.A., 2018. Siderophores detection by using blue agar CAS assay methods. *Int. J. Sci. Res. in Biological Sciences Vol*, 5, p.6.

Taher, N.A., 2016. Antimicrobial effect of bacteriocin produced by *Pediococcus pentosaceus* on some clinical isolates. *AL-Mustansiriyah Journal of Science*, 27(5), pp.26-30. https://mjs.uomustansiriyah.edu.iq/index.php/MJS/article/view/163

Tank, N., Rajendran, N., Patel, B. and Saraf, M., 2012. Evaluation and biochemical characterization of a distinctive pyoverdin from a *Pseudomonas* isolated from chickpea rhizosphere. *Brazilian Journal of Microbiology*, 43(2), pp.639-648. https://doi.org/10.1590/S1517-83822012000200033

Tawfeeq, H.R., Al-Jubori, S.S. and Mussa, A.H., 2023. Purification and characterization of catechol 1,2-dioxygenase (EC 1.13.11.1; catechol-oxygen 1,2-oxidoreductase; C12O) using the local isolate of phenol-degrading *Pseudomonas putida*. *Folia Microbiologica*. Advance online publication. https://doi.org/10.1007/s12223-023-01063-9

Weinstein, M.P. and Lewis, J.S., 2020. The Clinical and Laboratory Standards Institute Subcommittee on Antimicrobial Susceptibility Testing: Background, organization, functions, and processes. *Journal of Clinical Microbiology*, 58(3), e01864-19. https://doi.org/10.1128/JCM.01864-19

Unveiling Optimal Conditions for Phenol Degradation: Response Surface Methodology and ANOVA Analysis of ZnO and Ag-Doped ZnO Photocatalysts

G. Mohan[1], S. Meenachi[2]†[iD], K. Kiruthika[1][iD] and D. Kirthiga[2][iD]

[1]Department of Mathematics, K.S. Rangasamy College of Technology, Namakkal-637215, Tamil Nadu, India
[2]Department of Chemistry, K.S. Rangasamy College of Technology, Namakkal-637215, Tamil Nadu, India
†Corresponding author: S. Meenachi; smeena26@gmail.com

ABSTRACT

This research explores the effectiveness of ZnO and Ag-doped ZnO photocatalysts in degrading organic pollutants, specifically focusing on phenol removal in wastewater treatment. The catalysts were synthesized using sol-gel and precipitation methods and characterized through XRD, SEM, and EDX analyses. The study assessed the degradation efficiency of phenol under various conditions, including different catalyst dosages, irradiation times, and initial phenol concentrations. UV-vis spectroscopy was used to measure degradation efficiency, revealing significant differences between the two catalysts. Ag-doped ZnO showed superior performance, achieving degradation efficiencies of over 90%, compared to ZnO's 60-70%. Statistical analyses, including ANOVA and Response Surface Methodology (RSM), identified key factors influencing degradation efficiency. The enhanced performance of Ag-doped ZnO was attributed to its narrower band gap energy and improved irradiation responsiveness. These findings indicate that Ag-doped ZnO is a promising candidate for efficient and sustainable wastewater treatment, offering a robust solution for removing organic impurities and supporting environmental preservation. This research provides valuable insights into advanced photocatalytic processes and sets the stage for future wastewater treatment innovations.

INTRODUCTION

Wastewater treatment has emerged as a critical concern in the face of escalating environmental challenges, particularly within industries such as textiles, cement, and dye manufacturing. The release of wastewater from these sectors contributes significantly to the contamination of natural water bodies, posing serious threats to ecosystems and public health. In response, there has been a growing emphasis on harnessing advanced materials for effective wastewater treatment. In light of these advancements, this study seeks to explore the potential of ZnO and silver-doped zinc oxide as photo-catalytic agents for wastewater treatment using a continuous method. In the study, the authors describe the utilization of ZnO and silver-doped ZnO as photocatalysts for wastewater treatment through a continuous method. This implies that the application of these catalysts is not limited to treating specific volumes of wastewater in batches but is designed to handle a continuous inflow of wastewater, making the treatment process more consistent and potentially more suitable for industrial applications with continuous wastewater discharge. Continuous methods are often favored for their efficiency and the ability to handle large-scale and

ongoing wastewater treatment needs. By evaluating their respective photocatalytic efficiencies, this research aims to contribute to the development of efficient and sustainable solutions for mitigating wastewater pollution in critical industries.

Zinc oxide (ZnO) nanoparticles have demonstrated remarkable photo-catalytic activity in wastewater treatment. Under UV irradiation, ZnO nanoparticles generate electron-hole pairs, which initiate redox reactions that degrade various organic pollutants present in wastewater (Dove et al. 2023). The large surface area and high reactivity of ZnO nanoparticles contribute to their effective pollutant removal capabilities (Goodarzi et al. 2023). Zinc oxide potential in wastewater treatment has spurred research into optimizing its synthesis methods and enhancing its photo-catalytic efficiency.

Zinc oxide (ZnO) and its derivatives have garnered considerable attention due to their exceptional photo-catalytic properties. These properties arise from ZnO's wide band gap, enabling it to efficiently harness solar energy for the catalytic degradation of organic pollutants in wastewater (Smith et al. 2018). The zinc oxide band gap width, recorded at 3.10

eV, positions it as a promising candidate for photocatalysis (Mohamed et al. 2023). Furthermore, researchers have sought to enhance its photo-catalytic activity by doping ZnO with various elements. Among these elements, silver (Ag) doping has demonstrated considerable potential in enhancing the photo-catalytic efficiency of ZnO. Silver-doped zinc oxide shows a narrower band gap width of 2.40 eV (Janani et al. 2023). This reduced band gap width enables Ag-doped ZnO to effectively harness a broader range of wavelengths, thereby enhancing its ability to degrade organic contaminants in wastewater. The shift in the wavelength absorption spectrum, with Ag-doping causing an increase in the absorption wavelength to 326 nm (Williams et al. 2020), holds significant promise for improving the overall efficiency of wastewater treatment processes.

The incorporation of silver (Ag) into ZnO nanoparticles introduces additional functionalities, particularly antibacterial activity. Ag ions released from Ag-doped ZnO nanoparticles exhibit strong bactericidal effects, inhibiting the growth of pathogenic microorganisms in wastewater (Dove et al. 2023). This dual functionality of Ag-doped ZnO nanoparticles, combining photocatalytic degradation and antibacterial action, presents a comprehensive solution for wastewater treatment (Wang et al. 2017). Recent studies have investigated the synthesis and application of zinc oxide and silver-doped zinc oxide nanoparticles in wastewater treatment. Zinc oxide nanoparticles were prepared by the sol-gel method (Raj et al. 2022) and reported the efficient deprivation of organic pollutants using UV light. Ag-doped ZnO nanoparticles demonstrated enhanced antibacterial activity against Escherichia coli, showcasing their potential for microbial disinfection (Li et al. 2020). Tannery and dye wastewater contain a mixture of chemicals used in different processes. When these chemicals interact and undergo various treatment processes, lead to the formation of phenol and other phenolic compounds as waste products (Meenachi & Kandasamy 2019). The objective of this study is to assess the suitability of ZnO and silver-doped ZnO as photocatalysts for continuous wastewater treatment, specifically in industries such as textiles, tannery, and dyeing. The investigation includes characterizations through XRD, SEM, and EDX, offering insights into the morphological changes induced by silver doping. Additionally, the study explores the application of these photocatalysts in a continuous process for wastewater treatment, contributing to the existing body of knowledge in the field.

MATERIALS AND METHODS

Photocatalysis with mild conditions, a simple and continuous process can degrade the organic pollutants in wastewater into water and other small molecules or reduce them to harmless substances.

Preparation of Photo Catalyst

Preparation of ZnO photocatalyst: The synthesis of the zinc oxide nanostructure was conducted through the sol-gel method. This involved weighing and dissolving zinc acetate di-hydrate and sodium hydroxide (in a 1:4 ratio) with continuous rousing for approximately five minutes for each component (Figs. 1a & 2). Subsequently, the sodium hydroxide solution was gradually introduced into the zinc acetate solution under constant stirring, resulting in the formation of a white precipitate when combined with 100 mL of ethanol (Fig. 1b).

Synthesis of silver-doped zinc oxide photocatalyst: The synthesis of silver-doped zinc oxide photocatalysts was accomplished using the precipitation method, employing varying doping concentrations of 0.25%, 0.50%, 0.75%, and 1%. The initial step involved preparing a 0.3M solution of

Fig. 1: a) Stirred solution of Ag-doped ZnO. b) Silver-doped zinc oxide photocatalyst powder.

zinc acetate by dissolving 11 g of zinc acetate in 200 mL of distilled water. Subsequently, a solution containing 0.025 g of silver nitrate (AgNO$_3$) was introduced into the mixture while continuously stirring for 30 minutes (Fig. 1a).

To this amalgamation, a solution composed of 6 g of sodium hydroxide dissolved in 200 mL of distilled water was meticulously added drop by drop, all the while maintaining an intense stirring process lasting for about 4 hours. After this phase, the resultant precipitate was isolated using centrifugation, subjected to thorough washing with distilled water, and then suspended in ethanol for 2 hours. After yet another round of centrifugation, the resultant products underwent oven-drying at a temperature of 75°C, followed by an annealing process carried out at 500°C (refer to Fig. 1b)

Photocatalytic Reactor Setup

The photocatalytic reactor setup plays a pivotal role in advancing wastewater treatment processes through the utilization of photocatalytic nanomaterials (Fig. 2). This innovative technology harnesses the power of light-activated catalysts to degrade organic pollutants and disinfect water sources effectively. The reactor system typically comprises a reaction chamber, light source, and catalyst support, creating an environment conducive to photocatalytic reactions.

To ensure efficient pollutant removal, optimal reactor design, light intensity, and catalyst loading are essential considerations (Li et al. 2020). Additionally, advanced reactor configurations, such as immobilized catalysts on various substrates and the use of light filters, enhance reaction efficiency (Zhang et al. 2015). The integration of monitoring and control systems ensures real-time assessment of reaction progress, promoting the development of sustainable and

Fig. 2: Photocatalytic reactor setup.

energy-efficient wastewater treatment solutions (Kim et al. 2017).

The samples that underwent the photocatalytic reaction were subjected to absorbance testing using a UV-visible spectrometer (Smith et al. 2019). This analytical technique enables the measurement of absorbance changes in the samples, providing insights into the degradation of phenol in wastewater. By comparing the absorbance readings before and after the photocatalytic treatment, the degradation efficiency of phenol can be accurately calculated. This method offers a quantitative assessment of the extent to which the photo-catalytic process effectively breaks down the phenolic compounds present in the wastewater, shedding light on the efficacy of the treatment strategy.

The photocatalytic degradation of phenol typically involves the generation of highly reactive oxygen species (ROS), such as hydroxyl radicals (*OH) and superoxide radicals (*O^{2-}), in the presence of a photo-catalyst like ZnO or Ag-doped ZnO. These ROS then react with phenol molecules, breaking them down into simpler and less harmful byproducts. Here's a simplified representation of the possible reactions Eq. (1-4):

Hydroxyl Radical Attack:

$$*OH + Phenol \rightarrow Hydroxylated\ Phenol\ Products \qquad …(1)$$

Superoxide Radical Attack:

$$*O^{2-} + Phenol \rightarrow Radical\ Products \qquad …(2)$$

Reaction with Photogenerated Holes (h$^+$):

$$h^+ + Phenol \rightarrow Phenol\ Cation\ Radical \qquad …(3)$$

Further Reactions:

$$Phenol\ Cation\ Radical \rightarrow Breakdown\ Products \qquad …(4)$$

These reactions were highly complex and may result in a variety of intermediate products and pathways. The exact degradation products will depend on the specific conditions and catalyst used. It's important to note that the primary goal of photo-catalytic degradation is to convert the toxic phenolic compounds into less harmful substances or completely mineralize them into CO$_2$ and H$_2$O.

Photocatalyst Characterization

The Ag-doped ZnO photocatalysts, synthesized for this study, were subjected to a thorough analysis using techniques such as X-ray Diffraction (XRD), Scanning Electron Microscopy (SEM), and Energy-Dispersive X-ray Spectroscopy (EDX).

Field emission scanning electron microscopy: Silver-doped zinc oxide nanoparticle surface morphology was analyzed by FESEM analysis, as shown in the accompanying
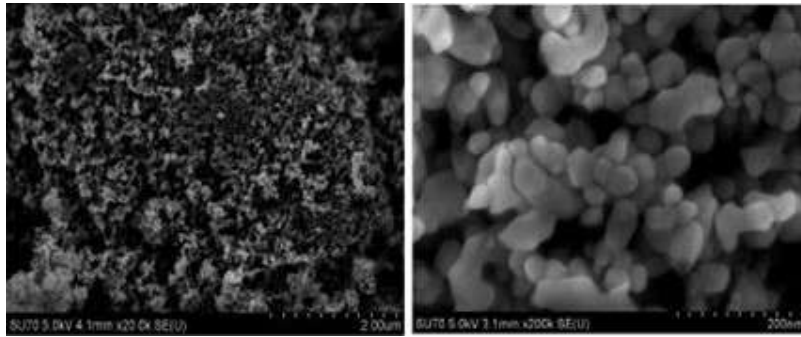
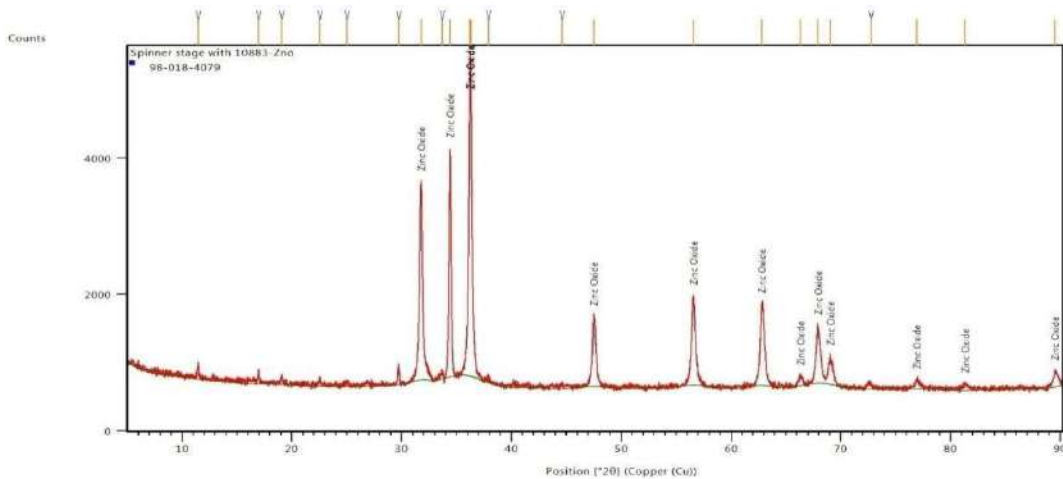Fig. 3: FESEM image of silver-doped zinc oxide photocatalyst.

Fig. 4: Spinner stage of Ag-doped ZnO nano particles.

image. The obtained FESEM images distinctly illustrate the formation of Ag-doped ZnO nanoparticles that exhibit uniform distribution and homogeneity. Notably, the increase in silver doping leads to a reduction in the average grain size, indicative of minimal particle aggregation during the preparation process. The introduction of Ag alters the morphology from nanorods to spherical nanoparticles, a transformation potentially attributed to the effects of Ag-doping on the morphological characteristics (Smith et al. 2020). The findings from the SEM analysis depict zinc oxide nanoparticles with a spherical morphology, exhibiting a particle size distribution spanning from 15 to 35 nm (refer to Fig. 3).

XRD analysis: The crystallographic structure was determined using XRD analysis to identify the phases present in the nanopowder. The obtained XRD results depict distinctive patterns of Ag-doped ZnO nanoparticles across various profiles of peak intensity and diffraction angles (2θ), reflecting the diffraction behavior of Ag-doped ZnO nanoparticles.

The XRD analysis encompassed a fraction angle range of 20° to 80°. The depicted figure showcases well-defined

sharp peaks, affirming the hexagonal crystalline nature of Ag-doped ZnO nanoparticles (Smith et al. 2019). The synthesized Ag-doped ZnO nanoparticles exhibited a singular phase with discernible diffraction peaks that corresponded to established data. Notably, the most prominent peak occurred at an angle of 37.15°, confirming the compound's identity as Ag-doped ZnO nanoparticles (Fig. 4).

EDX analysis of Ag-ZnO catalyst: Energy Dispersive X-ray (EDX) microanalysis serves as a valuable tool for determining the elemental composition of specimens. EDX emerges as a prominent method for characterizing nanoparticles through SEM measurements. In this approach, nanoparticles are activated and analyzed using an EDS X-ray spectrophotometer, commonly integrated into contemporary SEM setups (Johnson et al. 2020). Through this technique, the elemental composition of the analyzed specimen is effectively revealed. The process of activation for nanoparticles in this context typically involves exposure to an external stimulus or energy source. In photocatalysis, such as the case of ZnO and Ag-doped ZnO nanoparticles,

activation commonly occurs through exposure to light, specifically ultraviolet (UV) light.

The activation process involves the absorption of photons by the nanoparticles, which excites electrons from the valence band to the conduction band, creating electron-hole pairs. These highly reactive electron-hole pairs then participate in redox reactions with adsorbed species on the nanoparticle surface, leading to the degradation of organic pollutants in the surrounding environment. In our investigation, we applied this technique to confirm the silver doping of ZnO.

The EDX results for silver-doped zinc oxide nanoparticles reveal the elemental composition of the synthesized nanoparticles, providing insights into the successful incorporation of silver into the zinc oxide matrix. The EDX analysis confirms the presence of both zinc (72.01%) and oxygen (27.95%) as well as the additional presence of silver (0.04%) within the nanoparticles, confirming the effective doping process. The EDX spectrum, as depicted in Fig. 6, indicates the presence of silver, zinc, and oxygen within the sample. The distinct peaks observed in the spectrum unequivocally indicate the purity of the silver, zinc, and oxygen metals. ZnO boasts a band gap wide of 3.10 eV (Meenachi & Kandasamy 2023), while silver-doped zinc oxide exhibits a narrower band gap of 2.40 eV. This distinct difference in band gap widths holds significance for effective wastewater treatment. A reduced band gap width leads to an extended wavelength range for the photocatalyst, thereby enhancing the degradation rate in wastewater treatment. Specifically, ZnO possesses a wavelength of 310 nm, whereas Ag-doped ZnO exhibits a wavelength of 326 nm (Fig. 5).

Decolorization Efficiency

The efficiency of decolorization can be quantified using a mathematical formula that utilizes absorbance values obtained from UV-visible spectrometry.

$$DE = \frac{(Initial\ absorbance - Final\ absorbance) \times 100}{Initial\ absorbance}$$

RESULTS AND DISCUSSION

The absorbance of the photo-catalyzed solution was indomitable by UV-Visible spectrometer and the degradation efficiency of phenol was calculated using the formula mentioned above. To analyze the final absorbance, employed Response Surface Methodology (RSM), which generated various graphical representations, including predicted versus actual, 2D contour, and 3D plots.

The results presented in the dataset (Table 1) highlight the process efficiency of photocatalytic degradation based on various experimental parameters, including dosage, irradiation time, and initial concentration. The degradation efficiency was evaluated in terms of the final absorbance and percentage degradation. Upon analyzing the dataset, several observations can be made regarding the influence of different parameters on the degradation efficiency. A higher dosage (1g) resulted in a degradation efficiency of 73.72%, while a dosage of 0.6g showed an improvement in degradation efficiency to 76.4%. This suggests that a moderate dosage can lead to better degradation outcomes. For instance, with a dosage of 1 g, a longer irradiation time (2 hours) led to a slightly decreased degradation efficiency (75.5%) compared to the shorter irradiation time (1.5 hours) (73.72%). This
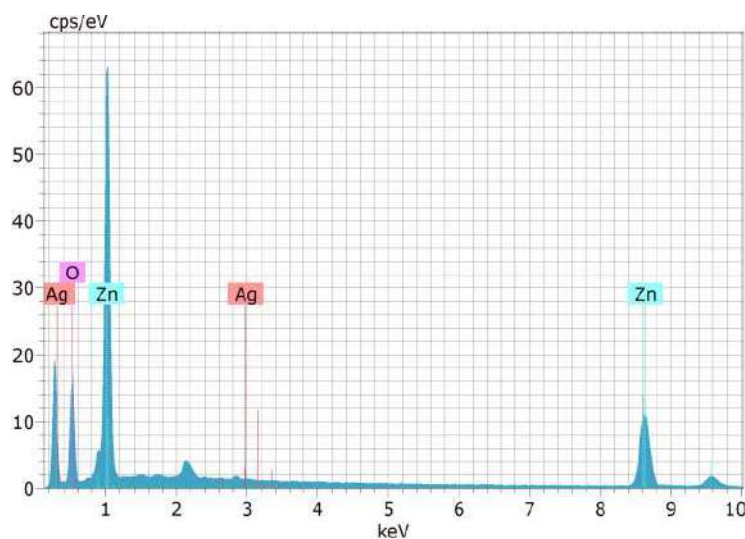

Fig. 5: EDX analysis of Ag-doped ZnO photocatalyst.

Table 1: Response surface methodology for treated wastewater using ZnO photocatalyst.

S.No.	Dosage	Irradiation	Concentration	Final Absorbance	Degradation
1.	1	1.5	50	0.657	73.72
2.	0.6	2	50	0.589	76.4
3.	1	1.5	10	0.532	78.7
4.	0.2	1.5	10	0.511	79.5
5.	1	2	30	0.612	75.5
6.	0.6	2	10	0.495	80.2
7.	0.6	1.5	30	0.724	71.04
8.	1	1	30	0.676	72.96
9.	0.6	1.5	30	0.724	71
10.	0.6	1	50	0.765	69.4
11.	0.6	1.5	30	0.724	71
12.	0.2	1	30	0.456	81.76
13.	0.6	1.5	30	0.724	71.04
14.	0.6	1	10	0.622	75.1
15.	0.6	1.5	30	0.732	70.72
16.	0.2	2	30	0.781	68.6
17.	0.2	1.5	50	0.812	67.9

could indicate that there might be an optimal irradiation duration beyond which the degradation efficiency plateaus. With a constant dosage and irradiation time, a lower initial concentration (10 ppm) led to higher degradation efficiencies (78.7% and 79.5%, respectively) compared to a higher initial concentration (50 ppm) resulting in lower degradation efficiency (67.9%). However, slight variations in the process conditions still result in different degradation efficiencies (71.04%, 71%, and 70.72%, respectively). This underscores the significance of subtle changes in experimental conditions. The dosage of 0.2 g, irradiation time of 1 hour, and initial concentration of 30 ppm yielded the highest degradation efficiency of 81.76%. This combination of parameters indicates a potential optimal setup for maximizing the degradation process.

The "Model" represents the overall relationship between the factors (A-Dosage, B-Irradiation time, C-concentration) and the response variable (Table 2). The low p-value (<0.0001) indicates that the model is statistically significant, meaning that at least one of the factors has a significant impact on the response variable for the degradation efficiency of phenolic groups. Factors A, B and C, which represent the dosage of a certain variable, are statistically significant in influencing the response variable for degradation efficiency. The low p-value (<0.0001) indicates that the concentration factor has a significant impact on the degradation efficiency. The "Residual" represents the variation in the response variable that is not explained by the factors in the model. In summary, the ANOVA results indicate that the quadratic model is significant, and factors A (Dosage) and C (Concentration) have a significant impact on the degradation efficiency of phenolic groups. Factor B (Irradiation Time) does not show a significant impact in this specific analysis. The relatively large F-values and low p-values for the significant factors

Table 2: ANOVA results of treated wastewater using ZnO photocatalyst.

Source	Sum of Squares	df	Mean Square	F-Value	P-Value Prob >F
Model	0.85	9	0.094	915.44	<0.0001
A-Dosage	0.049	1	0.049	470.8	<0.0001
B-Irradiation time	2.10	1	2.10	2.04	0.1967
C-concentration	0.15	1	0.15	1465.5	<0.0001
Residual	7.23	7	1.03		
Cor Total	0.85	16			

suggest that they contribute significantly to the variation in the response variable.

The parity plot visually presents a comparison between the experimental and actual values of the percentage of phenol degradation. This graphical representation showcases the efficiency of removal, as determined by Response Surface Methodology (RSM). When observing the plot, points that align closely along a diagonal line crossing through the predicted and actual axes indicate a strong correlation between the predicted and actual values (Fig. 6). The highest correlation is evident when these points perfectly align along the diagonal line, suggesting accurate prediction of degradation efficiency through RSM. In essence, the closer the points are to this diagonal line, the better the agreement between the predicted and actual values, highlighting the reliability of the Response Surface Methodology in estimating the efficiency of phenol degradation.

Utilize a three-dimensional surface plot to visualize the correlation between a response variable and two predictor variables, namely A and B. This form of graph, known as a 3D surface plot, proves valuable in understanding the interplay between desired response outcomes and operational parameters (Fig. 7). In this context, the variables A and B represent irradiation time and catalyst dosage. The peaks and troughs observed in the plot signify specific combinations of these variables (x and y) that lead to local maximum or minimum values. The creation of the surface area between data points is facilitated by interpolation techniques employed by tools such as Minitab.

The dosage of Ag-doped ZnO nanoparticles is a critical factor affecting the photocatalytic degradation process. A lower dosage of 0.2 g, generally leads to higher degradation efficiencies, with displaying the highest efficiency of 97%. In contrast, a higher dosage of 1 g often results in lower degradation efficiencies. This suggests that lower dosages might provide a more favorable surface-to-volume ratio for enhanced catalytic activity. The effect of varying irradiation times while keeping dosages and initial concentrations constant. Longer irradiation times (2 hours) generally lead to higher degradation efficiencies compared to shorter times (1.5 hours). This implies that prolonged exposure to
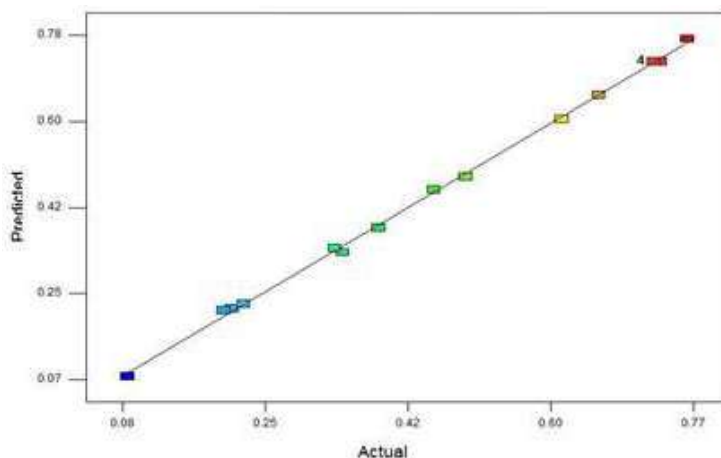

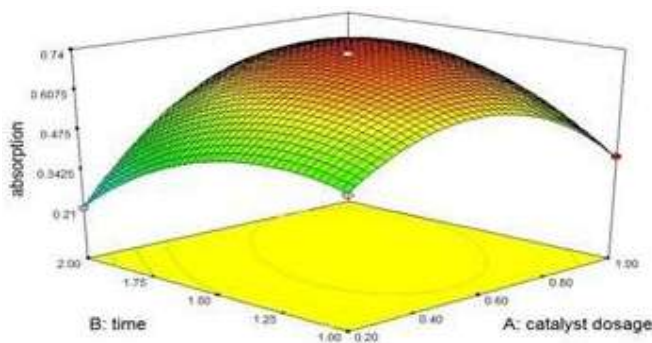Fig. 6: Predicted and actual value of photocatalytic process using ZnO nanoparticles.

Fig. 7: Effect of irradiation time and dosage with ZnO nanoparticles.

Table 3: Response surface methodology for treated wastewater using Ag-doped ZnO photocatalyst.

S.No.	Dosage	Irradiation	Concentration	Final Absorbance	Degradation
1.	1	1.5	50	0.659	73.64
2.	0.6	2	50	0.252	89.92
3.	1	1.5	10	0.25	90
4.	0.2	1.5	10	0.211	91.5
5.	1	2	30	0.17	93.2
6.	0.6	2	10	0.72	71.2
7.	0.6	1.5	30	0.252	89.9
8.	1	1	30	0.43	82.8
9.	0.6	1.5	30	0.359	85.64
10.	0.6	1	50	0.391	84.36
11.	0.6	1.5	30	0.289	88.44
12.	0.2	1	30	0.251	89.96
13.	0.6	1.5	30	0.252	89
14.	0.6	1	10	0.198	92.08
15.	0.6	1.5	30	0.252	89.92
16.	0.2	2	30	0.075	97
17.	0.2	1.5	50	0.139	94.44

Table 4: ANOVA results of treated wastewater using Ag-doped ZnO photocatalyst.

Source	Sum of Squares	df	Mean Square	F- Value	P-Value Prob >F
Model	0.46	9	0.051	445.47	<0.0001
A-Dosage	0.031	1	0.031	271.99	<0.0001
B-Irradiation time	4.05	1	4.05	35.39	0.0006
C-concentration	6.90	1	6.90	60.32	0.0001
Residual	8.00	7	1.14		
Cor Total	0.46	16			

irradiation allows for more comprehensive photo-catalytic reactions, resulting in greater pollutant removal. The initial concentration of the target substance in the solution also plays a significant role in the photo-catalytic process. A lower initial concentration (10 ppm) consistently leads to higher degradation efficiencies compared to higher initial concentrations (30 ppm). This can be attributed to the fact that a lower initial concentration provides a higher availability of reactive sites for the catalyst to act upon. The differing dosages, irradiation times, and initial concentrations. Notably, with a dosage of 0.6 g, an irradiation time of 1.5 hours, and an initial concentration of 30 ppm exhibits a degradation efficiency of 89.92%. In contrast, with the same dosage and irradiation time, but a lower initial concentration of 10 ppm, shows a significantly lower degradation efficiency of 71.2%. This demonstrates the combined effect of dosage, irradiation time, and initial concentration on the overall efficiency of the photo-catalytic process (Table 3).

The ANOVA outcomes (Table 4) indicate the statistical significance of the reduced quadratic model in phenol degradation, as reflected by the probability value of <0.0001. The accompanying graph illustrates the predicted versus actual plot for Ag-doped ZnO. Notably, numerous data points converge along a diagonal line, forming a distinct cross-strait pattern (Fig. 8). This pattern aligns with the intersection of the predicted and actual axes, signifying the predictive accuracy of the model in representing the experimental outcomes.

The RSM investigations outlined above highlight a notable difference in phenol degradation efficiency between Ag-doped ZnO and ZnO photocatalysts. This variation can be attributed to the respective band gap energies of the materials. ZnO's band gap width measures 3.10 eV, while Ag-doped ZnO boasts a lower band gap energy of 2.40 eV. This disparity contributes to the enhanced effectiveness of Ag-doped ZnO in wastewater treatment. A reduced band gap energy facilitates the absorption of longer wavelengths
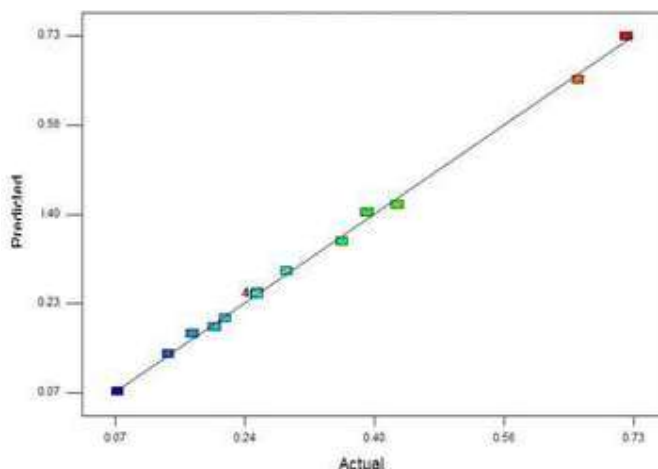
Fig. 8: Predicted and actual value of photocatalytic process using Ag-ZnO nanoparticles.
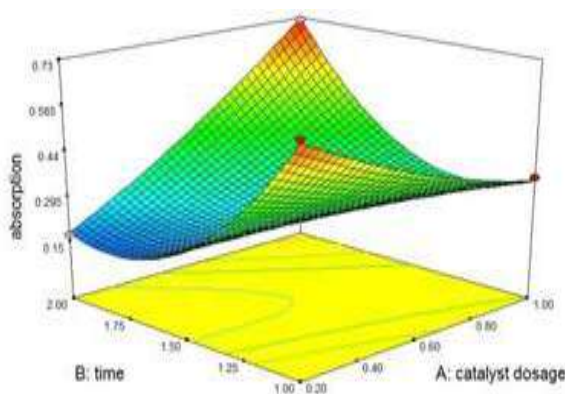

Fig. 9: Effect of Irradiation time and dosage Ag-ZnO nanoparticles.

by the photocatalyst, thus leading to an elevated degradation rate (Fig. 9).

Photocatalytic Efficiency of Zinc Oxide and Silver-Doped Zinc Oxide catalyst

The comparison of the results obtained from the degradation of organic impurities, specifically phenol, using ZnO and Ag-doped ZnO photocatalysts reveals valuable insights into the efficiency and effectiveness of these two photo-catalytic materials. ZnO has demonstrated significant potential as a photocatalyst for organic pollutant degradation due to its unique properties, such as its wide band gap and high surface area. It has been reported that ZnO nanoparticles, when exposed to UV irradiation, generate electron-hole pairs that initiate redox reactions, leading to the degradation of various organic pollutants, including phenol. The inherent photo-catalytic activity of ZnO in phenol removal is well-documented (Goodarzi et al. 2023, Li et al. 2020). However, its performance can sometimes be limited by factors like

the recombination of electron-hole pairs. The disparity in efficiency can be attributed to the distinct band gap energies of the two materials. ZnO, with a band gap width of 3.10 eV, pales in comparison to the enhanced capabilities of Ag-Doped ZnO, boasting a band gap energy of 2.40 eV. This energy differential is pivotal, as it influences the wavelengths absorbed by the photocatalysts. The reduced band gap energy of Ag-Doped ZnO enables it to harness longer wavelengths, amplifying its degradation efficiency and thereby rendering it a more effective solution for wastewater treatment.

The Ag-doped ZnO nanoparticles generally exhibit a wider range of degradation efficiencies (68.6% to 97%) compared to the ZnO nanoparticles (67.9% to 81.76%). This suggests that Ag-doped ZnO may have higher photocatalytic activity in degrading the target substances. Both ZnO and Ag-doped ZnO datasets show that lower dosages tend to result in higher degradation efficiencies. This indicates a similar trend in the sensitivity of the two materials to dosage. Longer irradiation times consistently lead to higher

degradation efficiencies for both ZnO and Ag-doped ZnO. This similarity suggests that the photocatalytic process benefits from extended exposure to irradiation regardless of the material used. Both materials exhibit the trend of higher degradation efficiencies at lower initial concentrations, indicating that a lower concentration of the target substance in the solution is favorable for the photo-catalytic process. The highest achieved degradation efficiency is higher in the Ag-doped ZnO dataset (97%) compared to the ZnO dataset (81.76%), indicating that Ag-doped ZnO has the potential for more effective pollutant removal.

On the other hand, the incorporation of silver (Ag) into ZnO nanoparticles (Ag-doped ZnO) has shown enhanced photocatalytic activity, especially in degrading organic pollutants. The reduced band gap width and altered absorption spectrum of Ag-doped ZnO enable it to harness a broader range of wavelengths, enhancing its capability to degrade phenolic compounds effectively (Janani et al. 2023, Williams et al. 2020). Additionally, the antibacterial properties of Ag-doped ZnO nanoparticles provide an added advantage in wastewater treatment by inhibiting the growth of pathogenic microorganisms (Rajabi et al. 2019, Wang et al. 2017).

When comparing the results of phenol removal using ZnO and Ag-doped ZnO photocatalysts, the latter will likely exhibit superior performance due to its enhanced photo-catalytic and antibacterial properties. However, it's important to consider factors like the concentration of doping, reaction conditions, and the nature of the wastewater matrix, which can influence the overall degradation efficiency. In conclusion, the comparison between ZnO and Ag-doped ZnO photocatalysts for the degradation of phenol highlights the potential benefits of Ag-doping in terms of enhanced photocatalytic activity and antibacterial effects. The selection of the appropriate photocatalyst depends on the specific requirements of the wastewater treatment process and the target pollutant.

Comparing the results obtained from Response Surface Methodology (RSM) experiments using ZnO and Ag-doped ZnO photocatalysts for the degradation of organic impurities, particularly phenol, provides insights into the influence of different variables and their interactions on the efficiency of the photocatalytic process. In the RSM analysis, both ZnO and Ag-doped ZnO photocatalysts were assessed for their ability to degrade phenolic compounds. Both ZnO and Ag-doped ZnO photocatalysts exhibited a significant influence of dosage on the degradation efficiency. This suggests that the quantity of photocatalyst plays a crucial role in enhancing phenol removal. While ZnO showed less sensitivity to irradiation time, Ag-doped ZnO demonstrated a

significant impact. This implies that the doping of ZnO with silver enhances its responsiveness to irradiation time, leading to more effective phenol degradation. Both photo catalysts demonstrated that concentration significantly affects the degradation process. This reaffirms the importance of phenol concentration in the wastewater as a determinant of degradation efficiency. The overall performance of Ag-doped ZnO appears superior due to its significant influence on irradiation time. This suggests that the addition of silver enhances the photo-catalytic activity and responsiveness of the material to light exposure. The relatively lower sensitivity of ZnO to irradiation time might indicate its inherent limitations in fully utilizing light energy for phenol degradation.

The ANOVA results indicate that interactions between factors and their quadratic terms were not reported, but their effects on degradation efficiency could be further explored. In summary, the RSM results suggest that Ag-doped ZnO outperforms ZnO in terms of phenol degradation efficiency, primarily due to its sensitivity to irradiation time. The interaction between factors and their quadratic terms might provide additional insights into optimization strategies for maximizing degradation efficiency. Further studies could delve deeper into the mechanisms behind the observed trends, potentially involving advanced characterization techniques to understand the enhanced performance of Ag-doped ZnO in comparison to ZnO photocatalysts.

CONCLUSIONS

In conclusion, this study delved into the impact of organic impurity degradation, specifically phenol removal, utilizing ZnO and Ag-Doped ZnO photocatalysts through experimental investigation. The synthesized nanoparticles underwent rigorous analysis using XRD, SEM, and EDAX techniques. The research presents a comprehensive comparative assessment of the photocatalytic performance of these two materials in terms of decolorization efficiency. The investigation encompassed the systematic evaluation of various parameters, including irradiation time, catalyst dosage, and phenol concentration. Utilizing the absorbance data from UV-vis spectrophotometry, the efficiency of degradation was meticulously calculated. The findings unveiled a remarkable disparity in performance between the two photocatalysts. Notably, Ag-Doped ZnO exhibited a degradation efficiency exceeding 90%, while ZnO demonstrated an efficiency ranging from 60% to 70%. The outcomes of this research underscore the potential of Ag-Doped ZnO as a potent agent for efficient and sustainable wastewater treatment. As environmental concerns escalate, such innovative materials offer promising avenues to combat

organic impurities in wastewater and contribute to a cleaner ecosystem. This study not only enhances our understanding of advanced photocatalytic processes but also provides valuable insights for the design and optimization of future wastewater treatment methodologies.

REFERENCES

Dove, A.S., Dzurny, D.I., Dees, W.R., Qin, N., Nunez Rodriguez, C.C., Alt, L.A. and Czy□, D.M., 2023. Silver nanoparticles enhance the efficacy of aminoglycosides against antibiotic-resistant bacteria. *Frontiers in Microbiology*, 13, p.1064095.

El Faroudi, L., El Jemli, Y., Zari, R., Barakat, A., Ismael, M.K., Abdelouahdi, K. and Solhy, A., 2023. Optimization of photocatalytic parameters using Doehlert experimental design to improve the photodegradation of Orange G. *Journal of Photochemistry and Photobiology A: Chemistry*, 445, p.115012.

Goodarzi, N., Ashrafi-Peyman, Z., Khani, E. and Moshfegh, A.Z., 2023. Recent Progress on Semiconductor Heterogeneous Photocatalysts in Clean Energy Production and Environmental Remediation. *Catalysts*, 13(7), p.1102.

Janani, F.Z., Taoufik, N., Khiar, H., Elhalil, A., Qourzal, S., Sadiq, M. and Barka, 2023. Effect of Ag doping on photocatalytic activity of ZnO-Al2O3 derived from LDH structure: Synthesis, characterization and experimental study. *Applied Surface Science Advances*, 16, p.100430. https://doi.org/10.1016/j.apsadv.2023.100430

Johnson, A.C., Velaga, S.P. and Rajendran, S., 2021. Synthesis and characterization of Ag doped ZnO nanocomposites by green synthesis method and their photocatalytic degradation of dye pollutants. *Journal of Photochemistry and Photobiology A: Chemistry*, 409, p.112819.

Johnson, R.A., Smith, C.D. and Brown, E.F., 2020. Energy dispersive X-ray Microanalysis: A comprehensive overview. *Journal of Analytical Techniques*, 55(8), pp.1015-1032.

Kim, H.G., Kim, Y.M. and Cho, J., 2017. A novel wastewater treatment system using photocatalytic oxidation and ceramic membrane filtration. *Journal of Hazardous Materials*, 321, pp.287-295.

Li, Q., Mahendra, S., Lyon, D.Y., Brunet, L., Liga, M.V., Li, D. and Alvarez, P.J., 2008. Antimicrobial nanomaterials for water disinfection and microbial control: Potential applications and implications. *Water Research*, 42(18), pp.4591-4602.

Li, Y., Bai, Y., Sun, J., Jin, Y., Li, D. and Feng, Q., 2020. Antibacterial activity and mechanism of Ag-doped ZnO nanoparticles. *Environmental Science and Pollution Research*, 27(10), pp.10068-10077.

Meenachi, S. and Kandasamy, S., 2019. Investigation of tannery liming waste water using green synthesised iron oxide nanoparticles. *International Journal of Environmental Analytical Chemistry*, 99(13), pp.1286-1297.

Mohamed, K.M., John Benitto, J., Judith Vijaya, J. and Bououdina, M., 2023. Recent advances in ZnO-based nanostructures for the photocatalytic degradation of hazardous, Non-Biodegradable Medicines. *Crystals*, 13(2), pp.329-335. https://doi.org/10.3390/cryst13020329

Raj, V. and Paulraj, M., 2022. Synthesis, characterization and photocatalytic activity of ZnO nanoparticles. *Materials Today: Proceedings*, 46, pp.2484-2488. https://doi.org/10.1016/j.matpr.2021.11.177

Rajabi, H.R. and Mohammadi, M., 2019. Green synthesis of ZnO/Ag nanocomposite and its application for the photocatalytic degradation of organic dyes under visible light irradiation. *Journal of Materials Science: Materials in Electronics*, 30(12), pp.11329-11339.

Smith, A.B., Johnson, C.D. and Brown, E.F., 2019. Spectroscopic analysis of wastewater treatment by photocatalytic oxidation. *Environmental Science and Pollution Research*, 26(36), pp.36816-36827.

Smith, J.A., Johnson, B.C. and Thompson, L.K., 2020. Surface morphology analysis of Ag-Doped ZnO nanoparticles by FESEM. *Nanomaterials Research Journal*, 45(3), pp.281-289.

Smith, Y.R., Mali, M.G. and Patil, D.P., 2018. Emerging trends in environmental nanotechnology for water treatment: Principles, applications, and future prospects. In *Nanomaterials for Environmental Protection*, pp.65-87. Springer.

Sundaram, M., Sengodan, K. and Arumugam, S., 2023. Mathematical modeling and statistical approach in tannery wastewater treatment. *Water Environment Research*, 95(10), p.10851. https://doi.org/10.1002/wer.10851

Wang, Z., Li, Q., Huang, Y. and Li, X., 2017. Photocatalytic inactivation mechanisms of *Escherichia coli* and *Lactobacillus casei* by Ag/ZnO: The role of reactive oxygen species and biochemical changes. *Environmental Science and Pollution Research*, 24(8), pp.7707-7715.

Williams, G.R., Miao, Y., Williams, J.D., Jin, S., McKenna, K., Long, M. and Yang, J., 2020. Hydrothermal synthesis of Ag-Doped ZnO nanoparticles for improved photocatalytic activity under UV and visible light. *The Journal of Physical Chemistry C*, 124(6), pp.3842-3853.

Zhang, L., Li, J. and Sun, D.D., 2015. Photocatalytic reaction engineering for water treatment using TiO2-based photocatalysts: A review. *Journal of Environmental Management*, 151, pp.445-460. https://doi.org/10.1016/j.jenvman.2014.12.018

ORCID DETAILS OF THE AUTHORS

S. Meenachi: https://orcid.org/0000-0003-0265-2021
G.Mohan: https://orcid.org/0000-0002-9873-1762
K.Kiruthiga: https://orcid.org/0000-0002-1740-3362

Fly Ash in Concrete Production: A Legal and Regulatory Review of Environmental Impacts

M. Z. M. Nomani[1], Omair Shaquib[2†] and **Mansi Sharma[2]**

[1]Faculty of Law, Aligarh Muslim University, Aligarh-202001, India
[2]School of Law, Indira Gandhi National Open University, New Delhi-110068, India
†Corresponding Author: Omair Shaquib; omairshaquib1227@gmail.com

ABSTRACT

From 2016 to 2040, global energy demand is expected to increase by almost 50%. A substantial proportion of this expansion will remain concentrated in emerging economies, predominantly India and China. The energy demand, namely for coal, will increase due to reasons such as population growth, industrialization, and the remarkable expansion of the middle class. In India, the coal employed is categorized as low-grade and exhibits a notable ash content, ranging from 30 to 45 percent. Using lignite or coal in thermal power stations leads to generating a significant quantity of fly ash. The issues of controlling fly ash due to its propensity to cause air and water pollution must be addressed efficiently, especially given the large volume of ash produced and the environmental impact it causes in India. This article thoroughly examines Indian fly ash, encompassing its distinctive attributes, a wide array of uses, environmental ramifications, and regulatory structure. The volume of fly ash produced has experienced a significant rise in the last ten years, primarily because coal-fired thermal power plants are responsible for meeting more than 70% of the nation's electricity demands. Currently, India is responsible for the production of about 180 million metric tonnes of fly ash. Moreover, this article provides a thorough examination of the global landscape about the manufacturing and utilization of fly ash, with a particular focus on India.

INTRODUCTION

Energy has emerged as the primary catalyst for the modern economy, owing to its indispensable function in enabling economic expansion and advancement. Conventional fossil fuels have served as the main source of energy since the 1970s. However, the same can be observed from the graph (Fig. 1), data which has been collected from the year 2013 to 2040. In 1970, oil emerged as the primary energy source, meeting approximately 43 percent of the total energy demand. In contrast, the demand for natural gas and coal accounted for 15 and 27 percent, respectively. Nevertheless, a slight modification became evident in these statistics by the year 2016. In juxtaposition to the decrease in the oil proportion to 32%, there was a notable increase in the natural gas proportion to 22%. Conversely, the percentage of coal remained relatively stable throughout the entire duration (World Oil Outlook 2016).

The overreliance on coal as a primary energy source has caused environmental issues due to air pollution and greenhouse gas emissions from combustion, as well as difficulties in managing coal ash disposal. The move to cleaner alternatives such as natural gas and renewables creates both opportunities and challenges in terms of scientific breakthroughs, economic feasibility, and policy frameworks. This change highlights the fundamental challenge of how to successfully incorporate alternative energy sources into existing infrastructure while maintaining environmental sustainability and economic prosperity.

Coal has become an important energy source because it is stable and easy to get all over the world. This trend is likely to continue for a while. Pulverized coal is typically incinerated to generate energy. The process of combustion is responsible for the release of carbon and volatile substances into the atmosphere, while impurities such as clays, shale, quartz, and feldspar, among others, predominantly undergo fusion and remain suspended within the coal. In conjunction with the fused particles, the flue gas is conveyed. At the low-temperature region, the flue gas undergoes coagulation, leading to the creation of fly ash, primarily composed of spherical particles. When the remaining substances within the boiler undergo solidification and subsequently settle at the bottom of the boiler, they are categorized as "bottom ash". The distribution of ESP ash accounts for 80% of the total, whereas the distribution of bottom ash accounts for 20% (Malhotra 1983).
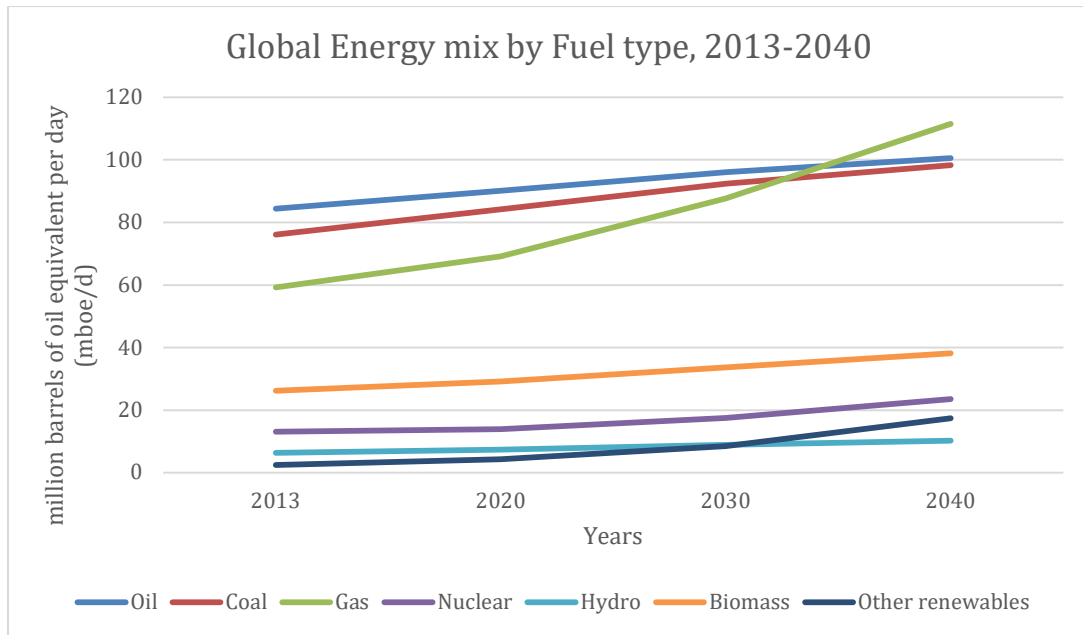
Fig. 1: Global Energy mix by Fuel type, 2013-2040 (World Oil Outlook 2016).

The Roman Colosseum's enduring structural integrity, which has endured for a thousand years, was exemplified by the incorporation of fly ash in its construction. Ancient Roman builders utilized volcanic ash to construct a significant number of buildings. In addition, fly ash and volcanic ash are indistinguishable; the sole distinction resides in the fact that fly ash is generated via the deliberate combustion of coal. The term "fly ash" refers to the finely divided residue that is produced when ground or powdered coal is burned. The ashes are transported from the firebox to the boiler via flue gases. This definition includes the specific terminology commonly used in the cement and concrete industries.

The processes employed for the collection of fly ash include bag fillers, electrostatic precipitators, and mechanical separators. According to the ASTM C-618 standard, Coal combustion produces fly ash which is categorized into two distinct classifications, namely Class C and Class F. The production of Class F fly ash typically involves the incineration process of bituminous or anthracite coal. In contrast, Class C fly ash is commonly produced by burning sub-bituminous or lignite coal. In contrast, Class C fly ash exhibits a higher percentage of CaO (10-40%) compared to Class F fly ash, which contains less than 10% CaO. Fly ashes that are categorized as class C demonstrate involvement in both cementitious and pozzolanic reactions as a result of their increased calcium oxide (CaO) concentration. However, fly ash of class F primarily affects the pozzolanic reactions during the hydration process.

The physical characteristics of fly ash, together with its chemical qualities, have a substantial influence on cement (Nath & Sarker 2011).

Moreover, the addition of fly ash to concrete has been observed to have a beneficial effect on the microstructure and rheology of the material. The fly's ash is non-reactive with water. The generation of free lime is an essential requirement for the purpose at hand, as it occurs during the hydration process of Portland cement. Consequently, this process enables the initiation of its pozzolanic characteristics. The durability of concrete structures is extended as a result. Fly ash has been utilized in the construction of both the Burj Khalifa in Dubai, the tallest structure in the world, and the Ghatghar Dam in India, which is regarded as a prime illustration of such a structure.

MATERIALS AND METHODS

The expansion of the nation's power capacity has been primarily driven by the widespread adoption of thermal energy production using coal and lignite. Indian coal often contains ash ranging from 30 to 45 percent, while imported coal generally has an ash concentration of around 10 to 15 percent. This implies that the imported coal from India exhibits a higher quality compared to the domestic coal produced in India. To accommodate the increasing need for electricity in the industrial and agricultural sectors, several thermal power plants are being built using lignite and coal. Among these, coal-based thermal plants account for seventy percent of the

total electricity generated. It is projected that India's total coal consumption will surge from around 730 million tonnes in 2010-2011 to approximately 2000 million tonnes in 2031-32, to sustain an economic expansion rate of 8-9 percent. It is expected that 75% of this coal will be transported to thermal power plants (Freeda & Tensing 2011).

Consequently, thermal power stations that are operational within the country and depend on coal or lignite combustion generate a significant amount of ash. Moreover, this phenomenon exacerbates the issue of air and water pollution, necessitating the utilization of a substantial amount of valuable land for its disposal. Fig. 2 depicts an annual

fluctuation in the volume of fly ash samples produced from coal in India (Rai et al. 2010).

To address the issue stemming from fly ash production, it is now mandatory for all government schemes and programs to incorporate fly ash-based products. Fig. 3 provides a visual representation of the various locations associated with the fly ash mission project (Lahtinen 2001, Surabhi 2017).

Fly ash consists of significant amounts of lime, alumina, and silica, making it a viable substitute for Portland cement. While replacement rates can be higher, they generally fall within the range of twenty to thirty percent. Fly ash undergoes
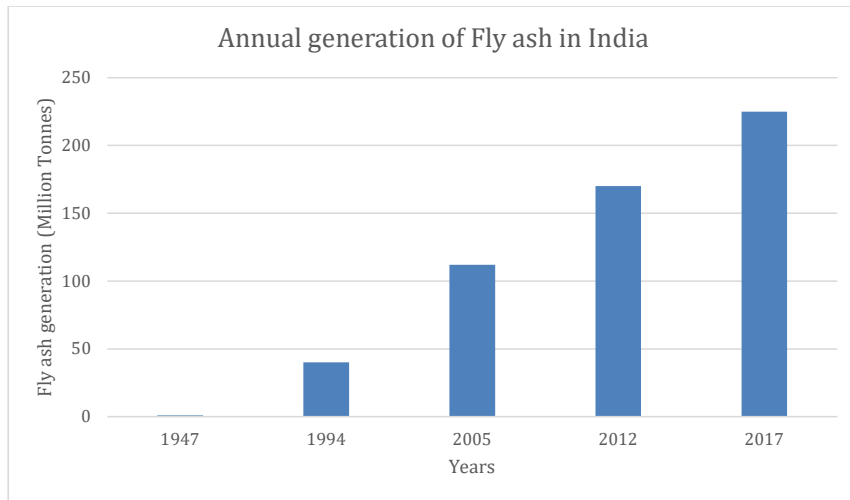

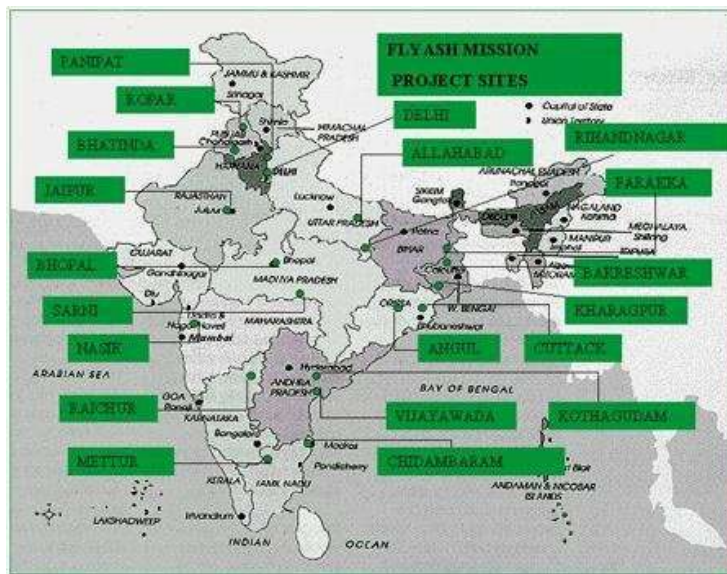Fig. 2: Annual Generation of Fly Ash in India (1947-2017).

Fig. 3: Fly Ash Mission Project Sites (Surabhi 2017).

a reaction with the lime in cement, forming a pozzolan during the lime's hydration process. This leads to the formation of a larger amount of the long-lasting binder. Incorporating fly ash into the concrete composition demonstrates improved durability and strength when compared to traditional concrete that contains Portland cement. Moreover, its decreased vulnerability to chemical attack makes it an ideal choice for the atmospheric conditions found in coastal areas.

The cement manufacturing industry, which accounts for a significant proportion of India's fly ash consumption, holds great importance within the country. Due to the pozzolanic characteristics of fly ash, it is frequently employed as a partial replacement for Portland cement in concrete. The utilization of fly ash as a partial substitute for Portland cement is typically limited to CLASS F fly ash. The categorization is employed for this particular pozzolanic characteristic of fly ash and lime content, which is below twenty percent calcium oxide (Cao). The current fly-ash utilization rate in the cement industry is 48.13 percent, according to the Annual Report 2020-22 of the Central Electricity Authority. The cement industry in India is anticipated to undergo a capacity expansion ranging from thirty to forty million tonnes per annum (MTPA) in the year 2023. Currently, the industry is operating at a utilization rate that falls within the range of 75 to 80 percent, while simultaneously maintaining a current capacity of 324 MTPA (WBCSD 2013) (Table 1).

RESULTS AND DISCUSSION

Over the past decade, a significant amount of fly ash has been produced in India as a result of the prevalence of coal-based thermal power plants for electricity generation. The secure method of eliminating fly ash is a matter of utmost importance in the realm of environmental protection. Fly ash finds its principal application within the construction sector as a cement-based material. The utilization of this technology offers several benefits, such as the alleviation

Table 1: Expected Fly-ash adsorption in the Cement Industry (WBCSD 2013).

S.No.	Year	Expected fly-ash adsorption in Indian Cement Industry (MTPA)
1.	2015	52.65
2.	2020	73.01
3.	2025	94.63
4.	2030	120.50
5.	2035	143.72
6.	2040	158.02
7.	2045	167.74
8.	2050	177.45

of energy requirements, the resolution of a substantial waste management challenge faced by the power generation industry, and the decrease in greenhouse gas emissions. Projections suggest that India's yearly production will experience a significant rise to approximately 600 to 700 million tonnes in 2024-25, indicating a roughly twofold increase compared to its present output.

In recent years, there has been a significant increase in the use of fly ash in the brick industry, which was founded in 2012-2013. The manufacturing of fly ash bricks has been initiated at the Jindal Steel Power Limited facility, which is located in the districts of Angul, Raigarh, and Patratu in India. The facility's daily brick production is estimated to be 1,80,000, which requires the use of 400 tonnes of fly ash (JSPL 2012, Angul Plant). The Raigarh Plant consumes 550 tonnes of fly ash per day to produce 500,000 bricks. Furthermore, the Patratu plant's daily production of 50,000 bricks necessitates the utilization of 100 tonnes of fly ash (Md Emamul 2013).

In the field of environmental protection, fly ash is widely utilized for various purposes, including wastewater treatment and the production of diverse technologies. In contrast, the application of fly ash in India has experienced an expansion in various sectors, such as transitioning from an open, dusty, and dry approach to transporting the fly ash or pumping a water/fly ash mixture to a specialized pumping system with low water content. A pond that was previously characterized by dust and dryness, necessitating additional care to avoid blowing away, or filled with transport water overflowing, transforms into a sticky, semi-dry, and uniform state, as exemplified by the WEIR pumping system. Further investigation into fly ash is imperative in the subsequent domains (Sinha & Agrawal 1999).

- Factors to consider regarding the economic value of fly ash.
- The second objective of this study is to develop and execute the production of high-quality cement-free ash-slag concrete using secondary mineral resources.
- The utilization of fly ash in the polymer sector

Undoubtedly, the increasing utilization of fly ash in various sectors, including agriculture, mine filling, cement production, road and embankment construction, and low-lying area reclamation, would effectively address the growing demand for fly ash in India.

Hazard to Environment and Life

The significant amount of greenhouse gas emissions is mainly caused by the excessive demand for raw materials and energy. Consequently, this request triggers a series of

complications associated with environmental consequences, which are increasingly detrimental to human beings. Concrete is one of the construction materials that releases the highest amount of carbon dioxide into the atmosphere. There is an expectation that the global production of concrete will persistently rise, with a particular emphasis on developing countries, until the year 2050. Ongoing research is focused on developing environmentally sustainable alternatives that can effectively address these issues. One of the most effective solutions currently being considered is the partial replacement of concrete components with FA. Empirical research has confirmed that FA has a synergistic effect on concrete, which helps to reduce the conflicts related to the environmental impact mentioned earlier. Hence, there exists a significant focus on the progress of structural concretes that demonstrate a considerable level of sustainability when compared to conventional concretes (Chang et al. 1977).

In the context of environmental sustainability, the incorporation of alternative cementitious materials, such as fly ash, serves to augment the physical characteristics of the concrete mixture. These materials demonstrate, through experimental protocols, that using this specific composite mix results in concrete that is both environmentally sustainable and has excellent mechanical properties (Ram et al. 2007a).

FA may contain traces of hazardous metals (such as Th, U, Pb, Cr, Cd, and Hg), which could potentially endanger the health of plants and humans. A multitude of inquiries have been conducted to evaluate the potential risks that FA poses to the adjacent ecological system and its plant life. The TPP's release of sulfur dioxide and nitrogen oxides is a significant factor in the occurrence of acid rain. The corrosion of structural surfaces by acid rain has the potential to induce the yellowing of green leaves, thereby exerting an impact on agricultural practices. Thermal pollution caused by disposal in surface water sources is a major disturbance to aquatic life. On the other hand, the introduction of toxic metals into subterranean water sources can be considered a source of contamination. Prolonged and light inhalation has the potential to induce various respiratory conditions, including allergy, pneumonia, lung fibrosis, asthma, bronchitis, silicosis, and cancer.

The existing literature on the potential correlation between the crystalline silica constituent of FA and lung cancer, particularly silicosis, is relatively scarce. Hicks and Yager conducted a study to evaluate the amount of respirable crystalline silica (specifically quartz) in the breathing area of workers who were exposed to coal fly ash (CFA) from six coal-fired facilities that used sub-lignite, lignite,

and bituminous coal. While conducting maintenance on bituminous and sub-bituminous ignited power plants, it was found that 60% of the air samples obtained surpassed the threshold limit value (TLV). During the normal production activities of sub-bituminous plants, 65% of the collected samples exceeded the Total Limit Values (TLVs), while for bituminous plants, 54% of the collected samples exceeded the TLVs. The dust samples collected from bituminous and sub-bituminous plants exhibited an average concentration of crystalline silica at 7.5%. On the other hand, the dust samples collected from lignite plants exhibited a crystalline silica content of 1.7%. Dhadse et al. conducted a study which revealed that construction workers were subjected to levels of dust and silica that exceeded the established safety thresholds for their occupation (Dhadse et al. 2008). The act of a power station employee inhaling pulverized fuel ash has been linked to the onset of asthma. In addition, a case of acute pulmonary disease has been recorded in a 48-year-old male who did not have any previous medical records of pulmonary ailments. Both of these illnesses were caused by extended and intense exposure to fatty acids (Ram et al. 2007b).

The authors conducted a study in which Bird et al. examined the occupational exposures to silica, arsenic (As), noise, heat stress, and coal dust in five coal-fired power plants. The coal samples displayed a variation in the concentration of silica (quartz) ranging from 0.6% to 4.4%. The detection limit for asbestos was determined to be 0.003 f/cc, and it was observed that twelve out of the total sixty-one area samples exhibited a higher concentration of the particular substance. A comprehensive analysis was conducted on a set of fifty-five noise samples, all of which met or surpassed the acceptable threshold of eighty-five decibels. Yager et al. conducted a supplementary study to evaluate the elimination of arsenic metabolites through urine and the level of occupational exposure to inorganic arsenic in a group of forty healthy workers who were performing regular maintenance tasks at a coal-fired power plant in Slovakia. According to the research findings, the average concentration of arsenic (As) in the atmosphere was determined to be 48.3 $\mu g/m^3$, with a range spanning from 0.2 to 375. Additionally, the estimated concentration of As in urine was found to be 13 $\mu g/m^3$, with a baseline concentration of 10 $\mu g/m^3$. The arithmetic means of air for boiler cleaners, boilermakers, and technicians were recorded as 138.9 $\mu g/m^3$, 67.7 $\mu g/m^3$, and 5.7 $\mu g/m^3$, respectively. The study revealed that the presence of CFA in the atmosphere can enhance the absorption of arsenic into the body.

Government of India's Initiatives in Fly Ash Utilization: A Comprehensive Analysis of MoEF Notification (14th September 1999)

The Ministry of Environment and Forests (MoEF) of the Government of India unveiled a notable initiative through a notification issued on September 14, 1999, aimed at promoting the utilization of fly ash (FA) in diverse construction endeavors. This initiative set forth several salient features designed to incentivize the incorporation of fly ash into construction materials and infrastructure projects across the country. One key provision mandated that within a 50-kilometer radius of lignite or coal based Thermal Power Plants (TPPs), manufacturers of bricks, clay, blocks, or tiles for construction must blend at least 25% fly ash, bottom ash, or pond ash with soil on a weight-to-weight basis. This requirement aimed to curtail the environmental impact of fly ash by encouraging its reuse in construction materials, thus reducing the reliance on traditional clay-based products and mitigating soil depletion concerns (Ram et al. 2007c).

One important requirement of the notification was for TPPs to provide fly ash free of charge for a minimum of 10 years, beginning from the date of the notification's release. This provision effectively incentivized the production of fly ash-based products, such as concrete blocks, cement, panels, bricks, and others, by eliminating financial barriers for manufacturers. By ensuring the accessibility of fly ash for construction purposes, the government aimed to spur the establishment of production units specializing in fly ash-based materials, thereby fostering a sustainable ecosystem for utilizing this industrial by-product (Ram et al. 2007d).

Moreover, the notification outlined the responsibilities of various governmental agencies, including State and Central government agencies, National Thermal Power Corporation (NTPC), TPPs, and State Electricity Boards (SEBs), in facilitating the necessary infrastructure for fly ash-based production units. These agencies were directed to provide land, electricity, water, and access to ash-lifting areas to promote the establishment and operation of production units close to TPPs. This strategic approach aimed to streamline the logistics of fly ash utilization, reduce transportation costs, and encourage local manufacturing, thereby optimizing the utilization of this abundant industrial waste material.

Furthermore, the notification emphasized the importance of institutional support and collaboration in promoting the adoption of fly ash in construction practices. It mandated that key construction agencies, including the State Public Works Departments (SPWDs), Central Public Works Department (CPWD), the National Highways Authority of India (NHAI), development authorities and housing boards include regulations for the use of fly ash and items made from fly ash in their specific standards and uses in construction. The agencies were assigned the responsibility of incorporating suitable standards and codes of conduct

regarding the consumption of fly ash within a specified period of four months from the release of the notification.

Overall, the MoEF's notification of September 14, 1999, represented a comprehensive policy framework aimed at promoting the sustainable application of fly ash in construction activities across India. By mandating the blending of fly ash in clay-based construction materials, ensuring the availability of fly ash without financial barriers, facilitating infrastructure support for fly ash-based production units, and institutionalizing the use of fly ash in construction specifications, the government demonstrated its commitment to addressing environmental challenges while fostering innovation and sustainable development in the construction sector.

Fly Ash Utilization Program (FAUP)

The Fly Ash Utilization Program (FAUP) was launched in 1994 by the Technology Information Forecasting and Assessment Council (TIFAC) under the Department of Science & Technology (DST), Government of India. This program aims to effectively utilize fly ash (FA), which is a valuable by-product of thermal power generation. With its inception, FAUP aimed to address multiple objectives, including the transformation of fly ash into a useful resource, the mitigation of environmental pollution resulting from its disposal, the reduction of land requirements for fly ash disposal, and the promotion of cost-effective construction practices. Through the utilization of coal ash in various sectors such as land and mine fill, agriculture, and bulk usage in construction, FAUP sought to unlock the economic and environmental benefits associated with fly ash utilization (Ram et al. 2007e).

One of the primary goals of FAUP was to redefine fly ash from being perceived as a waste material to being recognized as a valuable resource with multifaceted applications. By promoting the application of fly ash in diverse sectors, FAUP aimed to minimize the adverse impact of fly ash disposal on the environment while simultaneously creating avenues for its beneficial reuse. This shift in perspective from waste management to resource utilization aligned with broader sustainability objectives, fostering a paradigm shift in how fly ash was perceived and managed within the context of India's energy and industrial sectors.

Furthermore, FAUP sought to address the pressing issue of environmental pollution arising from the disposal of fly ash generated by thermal power plants. By incentivizing the utilization of fly ash in various applications, FAUP aimed to mitigate the adverse environmental effects associated with traditional disposal methods such as landfills and ash ponds. Through the adoption of environmentally friendly practices

and technologies, FAUP aimed to reduce water, soil and air pollution, thereby contributing to the preservation of ecological integrity and public health.

Moreover, FAUP recognized the imperative to optimize land utilization by minimizing the footprint of fly ash disposal sites. By promoting the utilization of fly ash in construction materials, land reclamation, mine fill operations, and agricultural applications, FAUP aimed to alleviate the strain on land resources while concurrently addressing the challenge of fly ash disposal. This integrated approach to land management underscored FAUP's commitment to sustainable development principles, wherein waste materials were repurposed to fulfill societal needs while minimizing adverse environmental impacts (Kumar & Yudhbir 2003).

Looking ahead, FAUP anticipated a significant increase in fly ash generation, with projections indicating a rise to 170 million metric tons by the end of the Eleventh Five-Year Plan period. In response to this anticipated surge in fly ash production, FAUP underscored the urgency of scaling up fly ash utilization initiatives and implementing innovative strategies to maximize its beneficial reuse across various sectors. By leveraging technological advancements, policy interventions, and stakeholder collaborations, FAUP aimed to realize its vision of transforming fly ash into a valuable resource for sustainable development and environmental stewardship.

The Fly Ash Utilization Program (FAUP), initiated by the Technology Information Forecasting and Assessment Council (TIFAC) under the Department of Science & Technology (DST), Government of India, is a proactive and comprehensive strategy for tackling the issues related to fly ash management. FAUP is an innovative program in India that focuses on using fly ash to promote sustainable development and environmental resilience. It emphasizes the efficient use of resources, protection of the environment, optimal use of land, and economic efficiency.

The comprehensive analysis of the legal and regulatory landscape surrounding the utilization of fly ash in concrete production, with a particular emphasis on the initiatives undertaken by the states, particularly the states of Orissa, Rajasthan, and Maharashtra, will be discussed now. These three states were strategically selected as exemplars due to their distinct yet complementary approaches to promoting the beneficial reuse of fly ash, a byproduct of coal-fired thermal power plants.

Orissa Government

The Government of Orissa has taken proactive measures to incentivize the establishment and operation of fly ash

(FA) based production units within the state, recognizing the potential of fly ash utilization in fostering economic development and environmental sustainability. Through a series of strategic decisions, the Orissa Government has demonstrated its commitment to supporting entrepreneurs and industries engaged in the utilization of fly ash as a valuable resource.

An important measure implemented by the Orissa Government is the distribution of dry or wet fly ash at no charge to businesses for a duration of 20 years starting from the beginning of FA-based production by the power station or unit. This decision not only addresses the financial barriers associated with procuring raw materials but also encourages entrepreneurs to invest in FA-based production by offering long-term stability and cost-effectiveness. By eliminating the cost burden of acquiring fly ash, the Orissa Government aims to facilitate the establishment and growth of FA-based industries, thereby contributing to job creation, industrial growth, and economic prosperity within the state.

Furthermore, the Orissa Government has committed to providing land and water required for setting up FA-based plants free of charge by the concerned power plant. This proactive approach to infrastructure support underscores the government's dedication to creating an enabling environment for FA-based industries to thrive. By streamlining the process of acquiring land and water resources, the Orissa Government aims to reduce administrative hurdles and expedite the establishment of FA-based production units, thereby fostering a conducive ecosystem for industrial development and investment.

Moreover, the Orissa Government has implemented measures to provide additional incentives to FA-based industries, including exemptions from electricity payment duties and the provision of power free of cost for a duration of five years. This incentive scheme aims to further enhance the viability and competitiveness of FA-based production units by reducing operational costs and enhancing financial sustainability during the initial years of operation. By easing the financial burden associated with electricity expenses, the Orissa Government seeks to encourage entrepreneurs to invest in FA-based industries, thereby stimulating economic growth and industrial diversification within the state.

In summary, the Government of Orissa's initiatives to support FA-based industries through the provision of free fly ash, infrastructure support, and electricity incentives reflect its commitment to promoting sustainable industrial development and environmental stewardship. By creating a conducive policy environment and offering tangible incentives to entrepreneurs, the Orissa Government aims to harness the potential of fly ash utilization to create

employment opportunities, mitigate environmental pollution and drive economic growth within the state. Through strategic partnerships and collaborative efforts with stakeholders, the Orissa Government seeks to realize its vision of fostering a vibrant and sustainable industrial sector powered by the utilization of fly ash as a valuable resource.

Rajasthan Government

The Rajasthan Government has introduced a substantial policy measure to encourage the creation of manufacturing plants for bricks, building materials, and other items using fly ash (FA) in the state. This program involves granting extensive tax breaks, including sales tax and octroi, for 10 years starting from the date when the FA-based manufacturing facilities begin commercial production. By offering such extensive tax exemptions, the Rajasthan Government aims to create a favorable business environment for entrepreneurs and industries interested in investing in FA-based manufacturing. The exemption from sales tax and octroi not only reduces the initial financial burden on businesses but also enhances the overall competitiveness and profitability of FA-based production units. This policy measure is particularly significant as it provides long-term stability and predictability to investors, enabling them to make strategic decisions and investments with confidence (Surabhi et al. 2014).

Furthermore, the tax exemptions provided by the Rajasthan Government serve as a powerful incentive for attracting investment in the manufacturing sector, particularly in industries that utilize FA as a primary raw material. The availability of tax incentives encourages entrepreneurs to explore opportunities in FA-based manufacturing, thereby promoting industrial growth, job creation, and economic development within the state. Moreover, by fostering the growth of FA-based industries, the government aims to leverage the abundant availability of fly ash from thermal power plants to address environmental challenges associated with its disposal while simultaneously supporting the development of sustainable construction materials and infrastructure.

The Rajasthan Government's policy grants complete exemption from sales tax and octroi for 10 years, starting from the date of commercial production, to encourage the establishment of manufacturing facilities for bricks, building materials, and other FA-based products. This policy demonstrates the government's dedication to fostering industrial growth and ensuring environmental sustainability. The government intends to attract investment, encourage economic growth, and generate employment opportunities in the FA-based manufacturing sector by offering appealing

tax benefits. This effort not only promotes the use of fly ash as a valuable resource but also enhances the general socio-economic development of the state of Rajasthan.

Maharashtra Government

The Maharashtra Government has implemented aggressive strategies to encourage the utilization of fly ash (FA) in construction activities within a specified distance from lignite or coal-based Thermal Power Plants (TPPs). As per the government mandate, any agency engaged in constructing buildings within a range of 50-100 kilometers from such TPPs is required to incorporate FA bricks, blocks, tiles, or other FA-based construction materials. This regulatory requirement aims to harness the potential of fly ash as a sustainable alternative to traditional building materials, thereby reducing environmental impact and promoting resource efficiency in construction practices.

The inclusion of FA-based construction materials in building projects within the specified radius underscores the Maharashtra Government's commitment to environmental sustainability and pollution mitigation. By mandating the use of FA blocks, tiles, and bricks, the government seeks to address concerns related to fly ash disposal while simultaneously promoting the adoption of eco-friendly construction practices. This regulatory measure not only reduces the dependence on conventional clay-based bricks but also contributes to the conservation of natural resources and the preservation of ecosystem integrity (Mullick 2005).

Furthermore, the Maharashtra Government's initiative extends beyond regulatory mandates to facilitate the application of fly ash in various sectors and applications. During the fiscal year 2005-06, significant quantities of fly ash, amounting to 25.16%, were produced by nine TPPs located within Maharashtra. This fly ash was utilized across diverse industries and activities, including brick kiln manufacturing, cement industry, ash-based product manufacturing, agriculture, landfills, and other sectors. By promoting the multi-sectoral utilization of fly ash, the Maharashtra Government aims to maximize the value derived from this industrial by-product while minimizing its environmental footprint.

The application of fly ash in cement production, brick manufacturing, and other industries underscores its versatility and potential as a valuable resource. By incorporating fly ash into various products and applications, Maharashtra's industrial sector contributes to resource conservation, waste minimization, and sustainable development goals. Moreover, the government's support for fly ash utilization initiatives reflects its proactive approach toward addressing environmental challenges and fostering

a green economy based on circular resource management principles.

In conclusion, the Maharashtra Government's initiatives to promote the application of fly ash in construction activities and across diverse industries exemplify its commitment to sustainable development and environmental stewardship. By mandating the use of FA-based construction materials within designated areas and facilitating multi-sectoral utilization of fly ash, the government strives to create a conducive environment for resource-efficient practices and eco-friendly innovation. These initiatives not only contribute to the conservation of natural resources but also drive economic growth and social well-being in Maharashtra.

CONCLUSIONS

In conclusion, the legal and regulatory landscape surrounding the application of fly ash in concrete production presents a multifaceted framework aimed at balancing environmental considerations, industrial needs, and sustainable development goals. The review of pertinent laws, regulations, and notifications in India reveals a concerted effort by governmental bodies to address the environmental impacts associated with fly ash while fostering its beneficial reuse in the construction sector.

The Gazette of India notifications (1999) from the Ministry of Environment, Forest and Climate Change and later amended notification of the year 2016 further strengthen and exemplify a strategic approach towards fly ash management, emphasizing its incorporation in concrete production to mitigate environmental pollution and promote sustainable construction practices. These regulations not only mandate specific utilization percentages but also underscore the responsibility of thermal power plants in facilitating the availability of fly ash for construction purposes. The integration of Bureau of Indian Standards (BIS) specifications and quality standards further ensures the compatibility and reliability of fly ash in concrete applications.

At the state level, the initiatives taken by governments such as Orissa and Rajasthan showcase a proactive stance in incentivizing fly ash-based industries. Exemptions from taxes, provision of essential resources, and financial incentives demonstrate a commitment to creating a conducive environment for entrepreneurs and industries to invest in fly ash utilization. These state-specific policies not only encourage economic growth but also contribute to the overall reduction of environmental burdens associated with fly ash disposal.

Additionally, the mandatory application of fly ash in construction endeavors within specified radii of thermal power plants, as seen in Maharashtra, reflects a localized approach to enhancing the sustainability of building practices. By imposing regulatory requirements on construction agencies, the government aims to drive the adoption of eco-friendly construction materials, ultimately contributing to a reduction in carbon footprints and the conservation of natural resources.

In the broader context, the legal and regulatory measures underscore the transformative potential of fly ash in the concrete production landscape. The shift from viewing fly ash as a waste material to recognizing it as a valuable resource aligns with the principles of a circular economy, where industrial by-products are repurposed to create sustainable solutions. The legal frameworks in place not only address environmental concerns related to fly ash disposal but also foster innovation, economic development, and the creation of a more resilient and eco-conscious construction industry.

As the demand for concrete continues to rise globally, the legal and regulatory review of fly ash in concrete production is a crucial step towards promoting responsible industrial practices and mitigating environmental impacts. The collaboration between regulatory bodies, industries, and research institutions is essential to further refine and update these regulations, ensuring their effectiveness in addressing emerging challenges and fostering a sustainable future for concrete production.

REFERENCES

Chang, A.C., Lund, L.J., Page, A.L. and Warneke, J.E., 1977. Physical properties of fly ash-amended soils. *Journal of Environmental Quality*, 6(3), pp.267-270. [Online] Available at: https://doi.org/10.2134/jeq1977.00472425000600030007x [Accessed 12 September 2024].

Dhadse, S., Majumdar, P. and Bhagia, L.J., 2008. Fly ash characterization, utilization and Government initiatives in India - A review. *Journal of Scientific & Industrial Research*, 67(11).

Freeda, C.C. and Tensing, D., 2011. Greener building material with fly ash. *Asian Journal of Civil Engineering (Building and Housing)*, 12(1), pp. 87-105.

Kumar, S. and Yudhbir, D., 2003. Chemistry and mineralogy of some Indian fly ashes. *Indian Concrete Journal*, 77(12), pp.1491-1494.

Lahtinen, P., 2001. Fly ash mixtures as flexible structural materials for low-volume roads. Helsinki University of Technology.

Malhotra, V.M., 1983. Fly ash, silica fume, slag & other mineral by-products in concrete (79th ed., Vol. 2). *American Concrete Institute*.

Md Emamul, H., 2013. Indian fly-ash: production and consumption scenario. *International Journal of Waste Resources (IJWR)*, 3(1), pp.22-25.

Mullick, A.K., 2005. Use of fly ash in structural concrete: Part I- Why? *Indian Concrete Journal*, 79(5), pp.13-22.

Nath, P. and Sarker, P., 2011. Effect of fly ash on the durability properties of high strength concrete. *Procedia Engineering*, 14, pp.1149-1156.

Organization of the Petroleum Exporting Countries, 2016. OPEC World Oil Outlook. October 2016. [Online] Available at: http://www.opec.org [Accessed 12 September 2024].

Rai, A.K., Paul, B. and Singh, G., 2010. A study on backfill properties and use of fly ash for highway embankments. *Journal of Advanced Laboratory Research in Biology*, 1(2).

Ram, L.C., Srivastava, N.K., Jha, S.K., Sinha, A.K., Masto, R.E. and Selvi, V.A., 2007. Management of lignite fly ash for improving soil fertility and crop productivity. *Environmental Management*, 40(3), pp.438-452.

Sinha, S.N. and Agrawal, M.K., 2000. Fly ash: a new resource material. In *Fly Ash Disposal and Deposition: Beyond 2000 AD* (pp. 70-75). Narosa Publishing House New Delhi, India.

Surabhi, 2015. Removal of unburnt carbon from fly ash to use it as an adsorbent. *Pollution Research*, 34, pp.68-692.

Surabhi, S., 2017. Fly ash in India: generation vis-à-vis utilization and global perspective. *International Journal of Applied Chemistry*, 13(1), pp.29-52.

Surabhi, U. G. and Suresh, N., 2014. Characterization and beneficiation of carbonaceous material in Indian fly ash. *Journal of the Indian Chemical Society*, 91(1), pp.73-80.

World Business Council for Sustainable Development (WBCSD), 2013. Technology roadmap: Low-carbon technology for the Indian cement industry. *International Energy Agency*. [Online] Available at: https://www.wbcsd.org/Sector-Projects/Cement-Sustainability-Initiative/Resources/Technology-Roadmap-Low-Carbon-Technology-for-the-Indian-Cement-Industry [Accessed 12 September 2024].

ORCID DETAILS OF THE AUTHORS

Omair Shaquib: https://orcid.org/0000-0003-2639-4063

Chlorella vulgaris – A Potential Biodiesel Feedstock's Effect on the Performance, Emission and Combustion Phenomenon of a CI Engine with Hydrogen Inductance

S. Pughazhraj[1], D. Balaji[1], V. Hariram[1†], R. Kumaraswamy[1], J. Godwin John[2], P. Naveen[1] and T. S. Ravikumar[1]
[1]Department of Mechanical Engineering, Hindustan Institute of Technology and Science, Padur, Chennai- 603103, Tamil Nadu, India
[2]Department of Mechanical Engineering, Rajalakshmi Institute of Technology, Chennai-600 124, Tamil Nadu, India
†Corresponding author: V. Hariram; connect2hariram@gmail.com

ABSTRACT

In the modern world, the rise of industrialization and motorization has significantly increased the use of internal combustion engines powered by petroleum products. This has led to the unsustainable exploitation and depletion of petroleum reserves. Consequently, the use of biodiesel-based biofuels, particularly those derived from microorganisms, along with gaseous fuel supplementation in internal combustion engines, has gained prominence. The urgent need to explore alternative fuels for combustion engines has become evident over the past few decades due to the rapid decline in fossil fuel reserves. This study examines the impact of hydrogen induction in the throttle body of a CI engine powered by blends of biodiesel from *Chlorella vulgaris* and mineral diesel in various proportions, without major engine modifications. The research aims to evaluate the performance, combustion, and emission characteristics of the engine when supplemented with hydrogen, biodiesel, and their blend B20. The experiments involve varying fuel compositions and engine operational parameters to assess their influence on efficiency, pollutant emissions, and combustion stability.

INTRODUCTION

The modern era of transportation and other technologies, demands high energy sources that are dependent upon fossil fuels, which are fast depleting and take much time to be produced again, which takes around 150-200 million years. Premiere fossil fuels like coal, products of petroleum, and natural gas are the major sources of energy in transportation, electricity, and much more. These fossil fuels cause harmful pollutants, and atmospheric effects due to carbon emissions (Godwin et al. 2018).

Especially, in internal combustion engines, the emission of harmful pollutants is higher due to the consumption of large amounts of fossil fuels. Researchers have attempted many amicable and efficacious solutions towards reduction in exhaust emission formation and after treatment, thereby replacing the conventional petro-diesel with vegetable/microorganism-based biofuel in the economically feasible aspects. That produces or emits fewer pollutants in the atmosphere (Hariram et al. 2018). Even though the emission of harmful pollutants produced by biofuel is way less than the traditional diesel fuel or petroleum products. It does not produce the same amount of BTE produced in the conventional, but this can be improved with the addition of

hydrogen, which is sent through a manifold with a pilot port into the air inlet. Running Bio-gas biodiesel has resulted in a significant decrement in NOx emissions, Due to alteration in CR and fuel-injection timing CO and HC emissions were reduced. On the addition of nanoparticle CeO_2 and hydrogen to the WCO biodiesel fuel, there is a significant improvement in the BTE and BSFC. Using the response surface method, optimization of hydrogen addition in the various blends of biodiesel according to ASTM D6751, which shows B2O has a significant difference in lower emission and also produces similar efficiency such as BTE, SFC (Subramanian et al. 2020). Using (SME) safflower n Methyl ester, Neem, and Free Methyl can result in the reduction of CO, HC, EGT smoke, vibration, and BTE, when added to the fuel mixture also it increases the BSFC and NOX emission, and also there is a notable increase in consumption of more fuel, but when the combustion chamber is coated with Cr_2O_3, it improves the combustion efficiency. Using CNG with hydrogen has been shown to improve result in heat release rate and reduction in exhaust emission, and brake thermal efficiency such as CO, CO_2, HC (Sarpal et al. 2015)

Oni et al. (2021), did an analysis in which it was seen, that escalated engine loads (i.e., 61%-98%) resulted in higher BTEs with improved engine performance for all fuel blends

in the range of 19–33.9% compared to the Brake Thermal Efficiency (15.1%–19%) of the unblended H-CNG fuel confirming its suitability as an improver to enhance the thermal and combustion efficacy of the compression ignition engine. Additionally, all MB–HCNG fuels exhibited lower exhaust emissions of CO_2, CO, HC, NO_x and O_2 when the unblended H-CNG fuel was used. Suzuki et al. (2015) did an analysis in which it was seen, that we assess how EGR (Exhaust Gas Recirculation) affects performance in light of the rise in NO_x emissions during hydrogen DDF operation. under conditions of 40kW power and 55% H_2 rate. The hydrogen DDF engine's emission level is comparable to that of a heavy-duty diesel engine produced in large quantities when the EGR rate is approximately 20%. Soot emission and pressure variance from cylinder to cylinder are still issues, though.

Raja et al. (2018), did an analysis in which it was seen, that when waste cooking oil (emulsified) was compared to injection timing (advancement), a decrease in smoke emission trend (i.e., 25%) was observed after executing the two alternative control approaches. The merits of lower NO_x emissions from neat Waste Cooking Oil were also attained by the emulsification process. Nevertheless, using emulsified fuels resulted in a slight (i.e., 8%) reduction in BTE, which improved with advancements in injection timing. Therefore, research indicates that the better option is emulsification for running the engine when reducing smoke emissions is the main goal, while advancements in injection timing are recommended for optimal operation when running the engine with pure WCO. Murad et al. (2020), studied the energy contribution of 15 and 38% respectively of hydrogen and ethanol fuel in a dual fuel operation where the brake thermal efficiency increased from 25.2% of neat MO to a maximum of 28.5% and 30% with those fuels, whereas the neat diesel showcased 30.8%. Smoke emission was detailed as 51% under neat diesel operation, whereas the opacity was reduced from 78% (neat MO) to 58% under hydrogen energy sharing of 15% which was better in terms of efficiency. Because of hydrogen induction, it was noted that the NO_x was increased and also it was noted that by adding ethanol and water towards intake the knock limit was extended which increased the BTE. The highest BTE was 30.1% when 5% water was added, and 30.8% when 10% ethanol was injected. Khan et al. (2018), did an analysis in which it was seen, that the results show the lowest HC and CO concentration, greatest BTE, and minimal BSFC, although the NO_x content increased somewhat. It has been discovered that cottonseed biodiesel and its diesel mix closely resembled conventional diesel in terms of combustion properties.

It has shown better combustion efficiency gives higher peak cylinder pressure and does not form any kind of impact danger on the engine structure. However the combustion duration at low engine loads was a bit longer than the conventional fuels with the mixture of rapeseed methyl ester RME, there is a much lower combustion duration at low engine loads. In using waste cooking oil as a biofuel, the effect of different engine parameters and load conditions on the performance and emission of a dual engine has been experimented with. With additional hydrogen gas as gaseous fuel, it improves the increase in BTE and power output but it also increases the emission of pollutants such as CO_2, CO, and NO_X, to reduce the emission, the fuel injection can be turned to reduce emission. Major parameters that can project the characteristics of combustion of WCO are engine speed, H_2 flow rates, and pilot fuel (WCO biodiesel), as the parameter increases a similar increase in BTE and power output can be noticed. During H_2 addition, the oxygen content in the air inlet will be less, which can increase the opacity of the smoke. For every possible parameter experiment, there is an inverse relation shown between BTE and BSFC when there is a rich mixture is combusted, there will be an increase in BTE and a significant decrease in BSFC. Das & Das (2023), worked with waste cooking oil biodiesel and enrichment of hydrogen which improves the thermal efficiency and there is a significant reduction in the emissions when working in CRDI Engine. They introduced iron nanoparticles as a thermal enhancer, limiting their concentration in the biodiesel to 75 ppm. Hydrogen was supplied at a constant rate of 10 LPM through the primary manifold. The addition of iron nanoparticles and hydrogen notably affected nitrogen oxide (NO_x) formation, possibly due to increased oxygen content and nano-additives. Combustion using modified fuel showed decreased levels of smoke, CO, HC, and CO_2 due to more complete combustion. Under maximum engine load, engine efficiency (BTE) increased by approximately 2.6% compared to straight diesel fuel, likely due to enhanced atomization of fuel aided by iron nanoparticles, promoting micro-explosions with hydrogen fuel (Chetia et al. 2024).

Biodiesel derived from microalgae using the transesterification process, which is a process of exchange of organic functional group R'' of an ester with R' of alcohol, a single-cylinder diesel engine run by biodiesel as alternative fuel and hydrogen was also added into the air inlet. The engine was operated at different loads with B20 blend, B20 with hydrogen at 2 LPM, B20 blend with hydrogen at 4 LPM, and conventional diesel fuel. Conventional diesel is to compare the results of the biodiesel outcomes. Performance outcomes such as B.TE, SFC, TFC, and indicated power are observed. Combustion characteristics such as in-cylinder pressure and net heat release rate are observed. Emission parameters such as CO, HC, CO_2, NO_X, and opacity are also monitored tabulated, and shown in graphs and discussed.

MATERIALS AND METHODS

This section details the biodiesel source (algae), how it was cultivated, and collected, the oil extraction, the transesterification process, characterization techniques used, and the experimental setup that was utilized for this study.

< fa[_!>ofmp[ni h

Chlorella vulgaris can grow and thrive in its suitable environment. Temperature, pH, light intensity, and carbon dioxide concentration are parameters that can be calibrated to grow the algae. It was noted from the literature that *Chlorella* species produce more lipids than a mixture of lipids produced in photoautotrophic and heterotrophic cultures. *Chlorella vulgaris* was noted to grow well in temperatures ranging from 20°C to 30°C. pH emerges as the conductor in algal growth and also it was seen that *Chlorella vulgaris* thrives in slightly alkaline waters, with pH levels maintained between 6.5 and 9.0. Providing CO_2 to the Algae utilizes them for chlorophyll, which also indulges in growth rate and biomass yield. In the Bold Basal medium, the algae were grown using the nutrients nitrogen and phosphorous (in the form of ammonium nitrate and potassium phosphate) which acted as the catalyst for cellular proliferation and enhanced the algal growth. It was noted that the biomass yield was ranging from 0.5 to 2 g/L/day. The microscopic view of chlorella vulgaris is shown in Fig. 1A.

Bd g [mb>i ff_]ni h

To collect the algal biomass, the centrifugation method was used since separating the cells developed in the aqueous medium can be leveraged efficiently using centrifugal force. Later this stage the biomass was filtered using porous media to drain the aqueous medium from the collected biomass. This filtration will be the parameter that decides the flexibility and scalability of biomass concentration. The flocculation process was also deemed necessary to aggregate larger biomass and its recovery. The collected biomass was then dried for further process Oil Extraction.

Bio-Oil Extraction

To extract oil from the algal biomass, a Soxhlet extractor was used. The procedure was to put the dried algal biomass inside a filter paper thimble and then put the filter paper into a glass cylinder that had an intake tube and a siphon tube attached to it. A water condenser was fastened to the cylinder's top. The setup was then placed into the neck of a flask with a circular bottom that would hold the solvent after it had been heated. The solvent's vapors rise through the inlet tube and into the cylinder as it is heated, condensing will occur at the condenser. The dried mass interacted with the condensed solvent and was dissolved as a result. The solution ensured a steady supply of solvent vapors inside the cylinder by flowing back into the flask whenever it reached the top of the siphon tube. After the extraction process, the heating was stopped and the extracted oil was separated from the solvent by distilling the flask's solution. The effective extraction of algal oil from intricate mixtures is done through this process which takes 5 hours. The collected oil was then evaporated using a rotary evaporator to obtain the microalgae
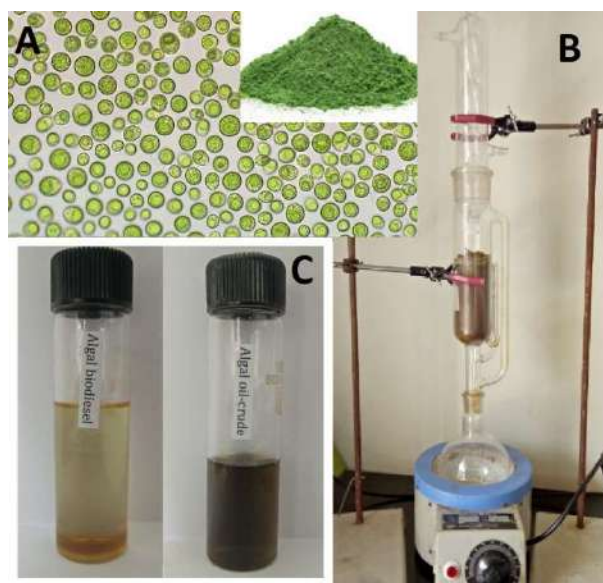

Fig. 1: Biodiesel from *Chlorella vulgaris* Microalgae – Microscopic view (A), Soxhlet Bio-oil Extraction (B) and Extracted Bio-oil and Biodiesel (C).

oil (Godwin et al. 2017) as shown in Fig. 1.

Ol[hmm_lc̀c][mi h

Preparation of biodiesel from *Chlorella vulgaris* Microalgae by single-stage esterification using Potassium hydroxide (KOH) as a catalytic agent and methanol (CH$_3$OH) as base solvent. The chemical reaction disintegrates the crude algal bio-oil into biodiesel and glycerol, the by-product. The procedural steps involved in the transesterification process in forming the potassium methoxide solution and disintegration process are followed below.

The microalgae extract was taken in a container and the transesterification procedure was carried out where the content was 1000 mL. Laboratory use of methanol was taken in the measured beaker. Potassium hydroxide (KOH) and alcohol were mixed properly by stirring until the KOH was dissolved. The extract content of microalgae taken for the study was kept in a container and was mechanically stirred while heating. When the temperature achieved 60°C, the methoxide solution was poured inside the contained and the stirring was continued until proper dissolvent occurred, during this entire procedure the speed of the stirrer was kept minimal. Past this stage, the container is closed airtight and the solution was stirred at higher speeds (say 720 rpm). The temperature should be maintained at 60°C during the entire process since beyond that temperature methanol may evaporate (Hariram et al. 2017). After two hours the solution should be transferred to a separate glass container which will be kept idle for 24 hours, during which the separation of glycerol and biodiesel occurs. In the upper portion of the container is the biodiesel which will be collected after removing glycerol from the container. The cleaning procedure is followed until the glycerol is completely removed from the biodiesel. After this procedure, the biodiesel will be heated to 100°C so that the remaining water present in the biodiesel is evaporated and the result of this procedure will be the microalgae biodiesel that is used for this study.

Fi olc_l!Ol[hm̀i lg !D̀`l[-l_^!N̑p_]rli g_rls

Chlorella vulgaris algae were used as a source to produce the biodiesel for which the transmittance was analyzed through the Fourier transform infrared spectroscopy. For analyzing this study Attenuated Total Reflectance Fourier Transform Infra-Red Spectrometer. The chlorella vulgaris biodiesel sample was used in the instrument to study the transmittance of the sample through internal reflection. A single reflection module was used in this study analysis, where an infrared beam will pass through the biodiesel sample which produces a vibration signal (transmittance). During this process, the angle of incidence will be produced while the internal reflection occurs. The instrument used has a range of 450 to 4000 cm^{-1}, it also has a resolution of 2 cm^{-1}. Based on the

one mL of sample biodiesel that is kept over the crystal upon passing the infrared will share the signals through evanescent waves (Tan et al. 2023).

G[m̑>bli g [mi al[pbs -M[m̑t̑Np_]rli g _n l!(G>MN̑!

To verify the presence of fatty acid methyl esters in the biodiesel produced from chlorella vulgaris oil. The instrument used is a single quadrupole mass spectrometer which is along with a gas chromatography system. An SSL injector and capillary columns with a 7500:1 inlet split ratio were installed in the GC system. The GC system has a 450°C oven temperature limit. In the chemical and electron impact ionization modes, a pre-heated monolithic hyperbolic quadrupole mass filter was utilized. There was a range of 106°C to 200°C for the quadruple temperature and 150°C to 350°C for the ion source temperature.

@xp_lcg _hr[f!O_m̑N_mp!

The specifications of the engine used are detailed in Table 1 which is a single-cylinder diesel engine. The engine test bed that was used to operate and test the fuel efficiency and the instruments used can be seen in Fig. 2. The measuring parameter, accuracy, range, and uncertainty of the measuring devices used such as Smoke meter, smoke analyzer, tachometer, and the dynamometer are also mentioned in Table 2.

Hs ^li a_h!D̀^o]r[h]_̀dh!O_m̀d@hach_

Table 1: Test Engine Specs.

Product	One-cylinder four stroke Diesel engine
Make	Kirloskar, Model TV1x
Stroke	87.5 mm
Bore	110 mm
Rated Power and speed	5.2 kW and 1500 rpm
Compression ratio/ Engine capacity	17.5/661 cc
Cooling arrangement	Water cooling
Piezo sensor	Range 5000 PSI, with low noise cable
Dynamometer	Type eddy current, water cooled
Calorimeter	Type Pipe in pipe
Crank angle sensor	Resolution 1 Deg, Speed 5500 RPM
Propeller shaft	With universal joints
Load indicator	Digital, Range 0-50 kg, Supply 230VAC
Fuel tank	Capacity 15 lit with glass fuel metering column
Load sensor	Load cell, type strain gauge, range 0-50 kg
Air box	M S fabricated with orifice meter and manometer.

Table 2: Emission Analyser Specification.

Instrument	Measuring parameter	Accuracy	Range	Uncertainty (%)
Tachometer	Speed	± 1 rpm	450–6500 rpm	0.22
AVL	NO_x	± 12 ppm	0–6000 ppm	0.24
	CO	± 0.02 %	0–16 % vol	0.14
	HC	± 10 ppm	0–3000 ppm	0.25
	CO_2	± 0.01 %	0–22 % vol	0.22
Smoke meter(AVL)	Smoke opacity	± 1 %	0–100 %	1.2

Comprising the gas cylinder & valve with high pressure, the regulator is stated as the hydrogen supply system which was connected with the engine inlet manifold which is in contact with the flowmeter (utilized to see visually the hydrogen supply from the tank to the engine). The pressure regulator used in the system will reduce the atmospheric pressure value which will be passed through the flame arrester-trap setup through the H_2 flow meter. H_2 flow meter along with a controller is utilized to measure and control the flow rate of hydrogen. The Injection system used here is electronically actuated which will inject microalgae biodiesel at the intake manifold. The injection system comprises a control unit and electronic injector, it can be seen that a microcontroller which is connected to a personal computer controls the amount of microalgae biodiesel injection. Considering the engine speed, the injection strategy for algal biodiesel was calculated while the injection was done at the air intake procedure (Gultekin et al. 2023).

The microalgae biodiesel is sent through the fuel injection system to the engine combustion chamber with hydrogen and air mixture inlet. Initially, the air and hydrogen mixture is allowed to be atomized in the combustion chamber of the diesel engine during 1st stroke of the cycle and allowed to pre-heat in the cylinder during the 2nd stroke of the cycle. Biodiesel is sprayed with the help of a fuel injection system into the cylinder and allowed to combust during the 3rd stroke, and at the final step, exhaust gas is sent out. During the four strokes of the cycle, the air inlet temperature, inlet pressure, hydrogen inlet pressure, flow rate, and the amount of fuel flow are all collected using sensors that are placed and monitored with the help of the computer monitoring the engine setup test rig. The temperature of the fuel flow during

Fig. 2: The engine test rig.

the fuel injection will be observed, and the peak pressure that occurred during the 3rd stroke can be monitored. During the 4th stroke, air exhaust outlet temperature, pressure, pollutant content, and other parameters can be observed to study the combustion behavior of the diesel engine. Using a smoke meter and smoke analyzer the CO, HC, NO_x, CO_2, and opacity of the engine can also be surveyed.

Engine outputs such as brake power, brake thermal efficiency, specific fuel consumption, and total fuel consumption will be derived with the help of the dynamometer and engine soft software to determine the characteristics of the performance behavior of the engine. Single-cylinder Diesel engine setup with Dynamometer and smoke analyzer setup during experiment with Biodiesel B20 blend mixture using Kirloskar, Model TV1, Type 1 cylinder, 4 stroke Diesel, water-cooled, power 5.2 kW at 1500 rpm, stroke 110 mm, bore 87.5 mm. 661 cc, CR 17.5. The performance testing of internal combustion engines, medium and small motors, car transmission components, gas turbines, water turbines, engineering machinery, and oil drilling can all be done with an eddy current dynamometer. This experiment is used to analyze the performance characteristics of the engine by inducing load on the shaft of the engine output and observing the other outputs.

Fo_f!Kli p_lnc m

The fuels used in the diesel engine were checked for their properties to verify with the standard operating values and it detailed closer values as shown in Table 3.

RESULTS AND DISCUSSION

The results determined by the analysis are discussed in this section briefly where the FTIR, GCMS, performance, and emission characteristics.

Fi ol c l!Ol[hmi l g !D`l[-R_^!Np_]rli nhi ps

The stretched bending values range from 500 to 3000 cm^{-1} in the *Chlorella vulgaris* FTIR spectrum as detailed in Fig. 3. The conversion of biodiesel of *Chlorella vulgaris* is confirmed through the highest peak (the vibration stretch) shown in FTIR analysis at 1741 cm^{-1}. The hydrocarbon presence in the sample is confirmed through the stretches from 1460 to 1019 cm^{-1}. A very strong signal was seen at stretch 2923 cm^{-1}, a signal somewhat strong was seen at stretch 2853 cm^{-1} and there is a signal which was weak seen at stretch 3008 cm^{-1}, these signals detail and verify the biodiesel conversion. It can also be noted that there is

Table 3: Properties of biodiesel, hydrogen and diesel.

Properties	Unit	*Chlorella vulgaris* Biodiesel	.	Diesel	ASTM biodiesel standard
Density	Kg/m^3	864	0.0881	838	ASTM D240
Viscosity (at 40° C)	mm^2/s	5.2	-	1.9-4.1	ASTM D445
Calorific value	MJ/kg	41.0	119.3	43.8	ASTM D240
Cloud Point	°C	7	-	-15 to 5	ASTM D2500
Pour point	°C	-6	-	-35 to -15	ASTM D2500
Flash Point	°C	115	-	75	ASTM D93
Solidification Point	°C	-12	-	-50 to 10	-
Acid value	Mg KOH/g	0.374	-	0.5 max	-
H/C ratio	-	1.81	-	1.81	-
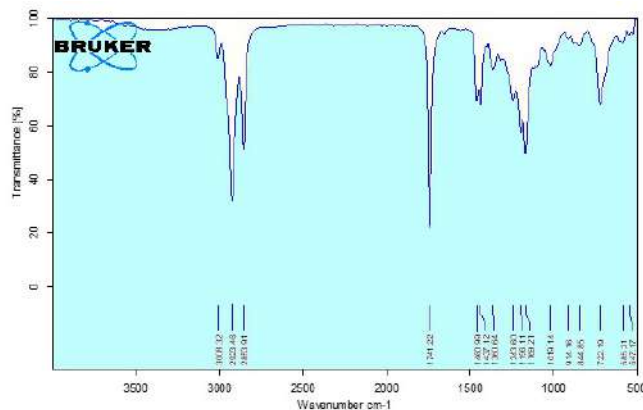
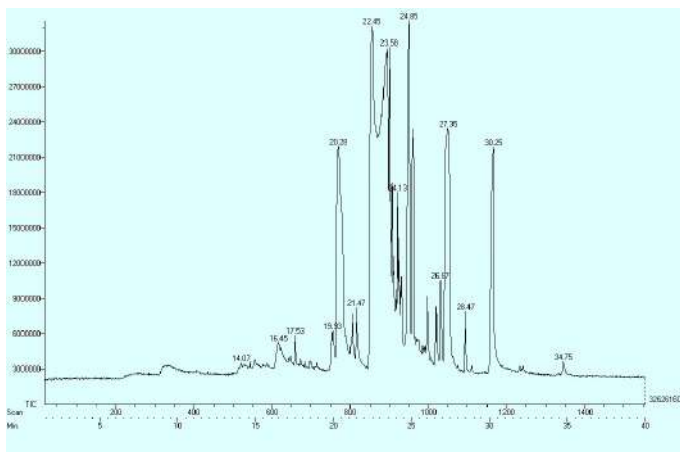Fig. 3: FTIR Transmittance of *Chlorella vulgaris* biodiesel

Fig. 4: GCMS spectrum of Biodiesel from *Chlorella vulgaris*.

no trace of stretches between 1741 and 2853 cm^{-1} which is obtained through the single-stage transesterification. Various weak signals were seen near 844, 914, and 1437 cm^{-1} which informs that the carboxylic group is present.

The presence of these distinctive long-chain fatty acid methyl ester (FAME) molecules indicates that these functional groups form the biodiesel.

G[n⊳bli g [n̄ial[pbs -M[nᴺp_]nli g _rls

An esterified biodiesel sample was subjected to Gas Chromatography-Mass Spectrometer analysis to determine the existence of different FAMEs and to assess the effectiveness of the process (transesterification). As seen in Fig. 4, the biodiesel's mass chromatogram examined the presence of nine distinct FAMEs at retention times (RT) ranging from 14.07 to 34.75 minutes. Many FAME mass fragmentation patterns demonstrate the loss of carbo-methoxy-ions as a result of β cleavage.

A handful of the mass fragmentation patterns also showed multiple profusions, which could be the result of the group

Table 4: Fatty acid methyl ester with respect to retention time.

S.No.	FAME	Retention Time (RT)
1.	9-hexadecenoic acid methyl ester	19.93
2.	hexadecanoic acid methyl ester	20.28
3.	heptadecanoic acid methyl ester	21.47
4.	14, 17-octadecadienoic acid methyl ester	22.45
5.	eicosanoic acid methyl ester	24.85
6.	13-docosenoic acid methyl ester	26.87
7.	docosanoic acid methyl ester	27.35
8.	tricosanoic acid methyl ester	28.47
9.	tetracosanoic acid methyl ester	30.25

(methoxy) being lost and the hydrogen and carbon atoms being rearranged during the process (transesterification). The hydrogen ion in the carbonyl group rearranges and reorganizes at RT 22.45 min, resulting in the existence of fatty acids (unsaturated) such as 14, 17-Octadecadienoic acid methyl ester (Reang et al. 2020). There were various FAMEs found in the sample analyzed as shown in Table 4.

K_l`i l g [h]_!>b[l[]n_l omc]m

This section details the performance of the hydrogen-inducted fuel (microalgae biodiesel) in the diesel engine. The characteristics of performance that are studied here are indicated power, brake thermal efficiency, friction power, indicated thermal efficiency, specific fuel consumption, and total fuel consumption.

Fig. 5 represents Brake power (BP) vs Indicated power (IP) for the study Engine. The IP varies along the BP, it shows that the diesel has the highest point at 4.92 kW (100% load) at higher load which is 7.22 kW brake power, B20 blend at 7.27 kW, H$_2$ at 2 LPM 7.39 kW and 4 LPM at 7.45 kW. Where the hydrogen with b20 blend shows higher indicated power with respect to brake power due to the higher combustible nature of hydrogen, it shows higher indicated power produced when the rate of hydrogen flow is increased, and the IP increases also when the rpm increases (Rajak et al. 2022).

Fig. 6 represents Brake power (BP) vs friction power (FP) for the taken study Engine. The FP varies along the BP, it shows that the diesel has the highest point at 2.29 kW at higher load which is 4.92 kW brake power (50% load), B20 blend at 2.38 kW, H$_2$ at 2 LPM 2.48 kW and 4 LPM at 2.54 kW. Where the b20 blend shows higher friction power with respect to brake power because of higher oxygen availability existing in the fuel B20 blend which enhanced the rate of combustion. Though the O$_2$ percentage in the biodiesel
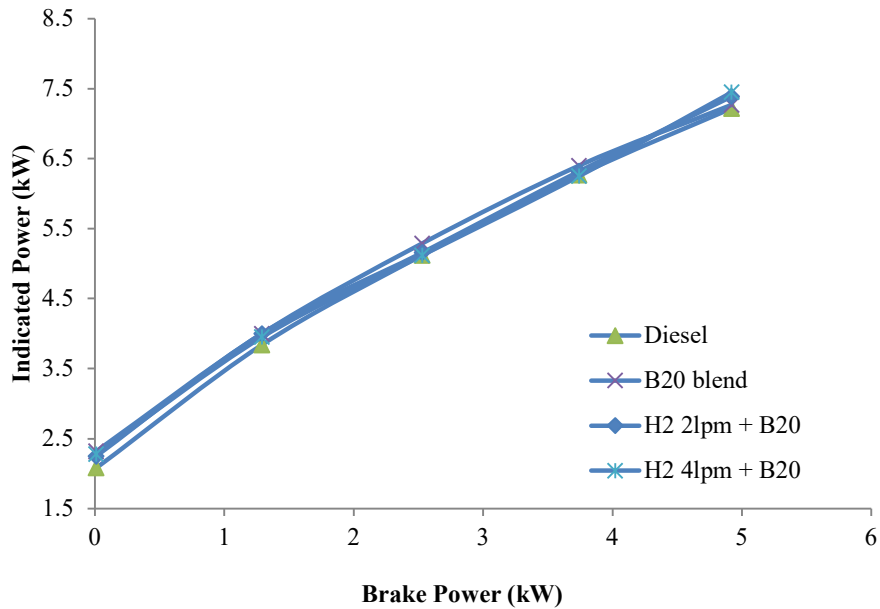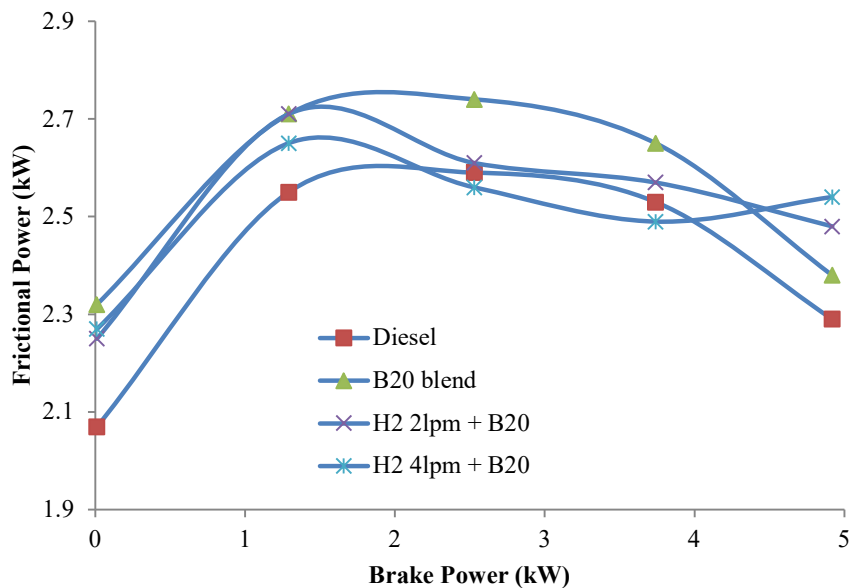
Fig. 5: Variation in Indicated Power.

Fig. 6: Variation in Frictional Power.

is high, due to the higher viscosity of the biofuel it is difficult to inject into the chamber which contradicts the combustion rate (Hazar et al. 2022). This is why the friction power decreases when the flow of biodiesel increases at a higher load.

Fig. 7 represents the Brake power (BP) vs Brake thermal efficiency (BTE) of the Engine taken for the analysis. The BTE varies along the Brake power, it shows that the diesel has the highest point at 33.48% at higher load which is 4.92 kW brake power, B20 blend at 30.94%, H_2 at 2 LPM 32.23%, and 4 LPM at 33.6%. Where the hydrogen 4 LPM with B20 blend shows higher BTE with respect to BP due to a higher percentage availability of oxygen present in the biodiesel B20 blend which enhanced the rate of combustion and also with the higher flow rate of hydrogen. It is also to be noted that increasing the ester presence in the fuel will increase the BTE.

Fig. 8 represents Brake power (BP) vs Indicated thermal efficiency (ITE) of the given single cylinder four stroke
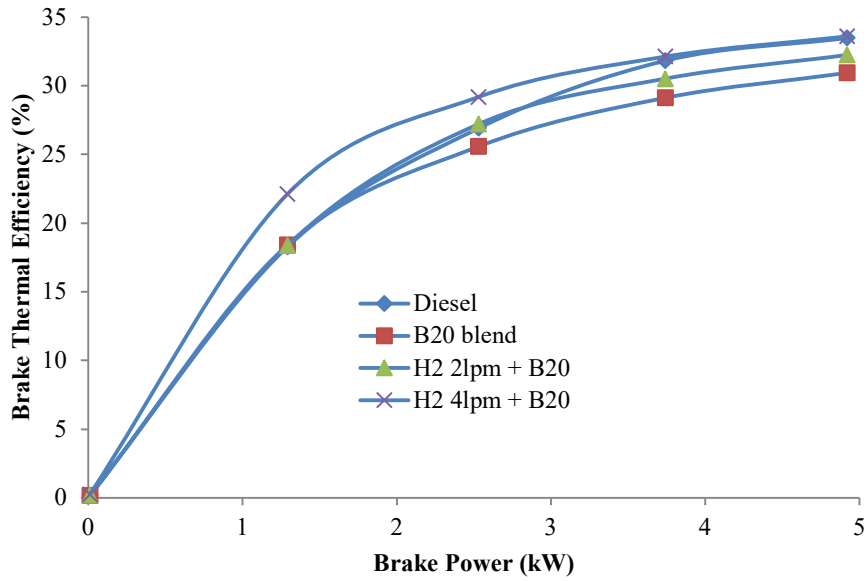
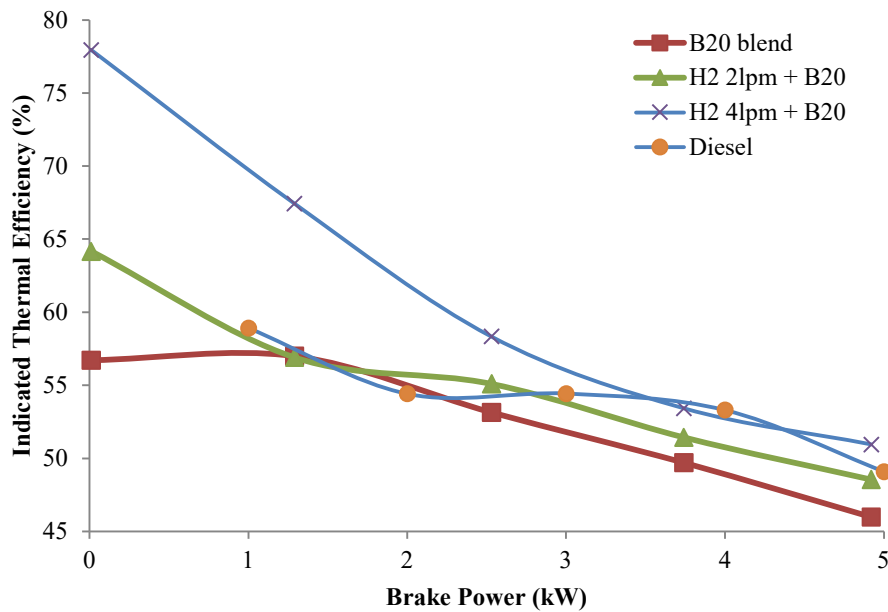Fig. 7: Variation in Brake Thermal Efficiency.

Fig. 8: Variation in Indicated Thermal Efficiency.

diesel Engine. The ITE varies along the B, it shows that the diesel has the highest point at 45.99% at higher load which is 0.01 kW brake power, B20 blend at 48.55 %, H_2 at 2 LPM at 50.95 %, and 4 LPM at 49.09 %. Where the hydrogen 4 LPM with B20 blend shows higher Indicated thermal efficiency with respect to BP due to the higher availability of oxygen present in the biodiesel B20 blend which enhanced the rate of combustion and also with the higher flow rate of hydrogen, and it lowers along the brake power with higher loads and also it is to be noted that heat supplied in the fuel form will influence the indicated thermal efficiency (Zareei et al. 2020).

Fig. 9 represents Brake power vs Specific Fuel Consumption (SFC) of the diesel engine. The SFC varies along the Brake power, it shows that the diesel has the highest point at 0.46 kg/kWh at higher load which is 1.29 kW brake power, B20 blend at 0.47 kg/kWh, H_2 at 2 LPM 0.47 kg/kWh and 4 LPM at 0.39 kg/kWh. Since the

viscosity is higher for the B20 blend, the engine consumes more fuel than the other mixtures, and also due to the lower calorific value of the B20 blend, it needs excess fuel to achieve the expected power output. However, adding H_2 to the fuel mixture decreases the fuel consumption and able the fuel mixture of B20 and H_2 to attain the SFC of diesel fuel. It is to be noted that fuel consumption will increase when the heating value of the fuel decreases, but adding hydrogen in this study has a good influence on SFC.

Fig. 10 represents Brake power vs Total fuel consumption (TFC) of the Diesel Engine. The TFC varies along the BP, it shows that the B20 blend has the highest point at 1.37 kg/hr at Brake power of 4.92 kW, H_2 at 1.32 kg/hr, diesel at 1.25 kg/hr and 4 LPM at 1.26 kg/hr. Where the B20 blend shows higher Total fuel consumption in relation to brake power due to the high viscosity of the B20 blend biofuel which consists of denser molecules that make much volume of fuel and consume a comparatively higher amount of fuel. Because of the viscous nature of the B20 fuel blend, the engine consumes more fuel than the other mixtures, and also due to the lower calorific value of the B20 blend, it is clear that excess fuel is required to produce the expected power output. However, adding H_2 to the fuel mixture decreases the fuel consumption
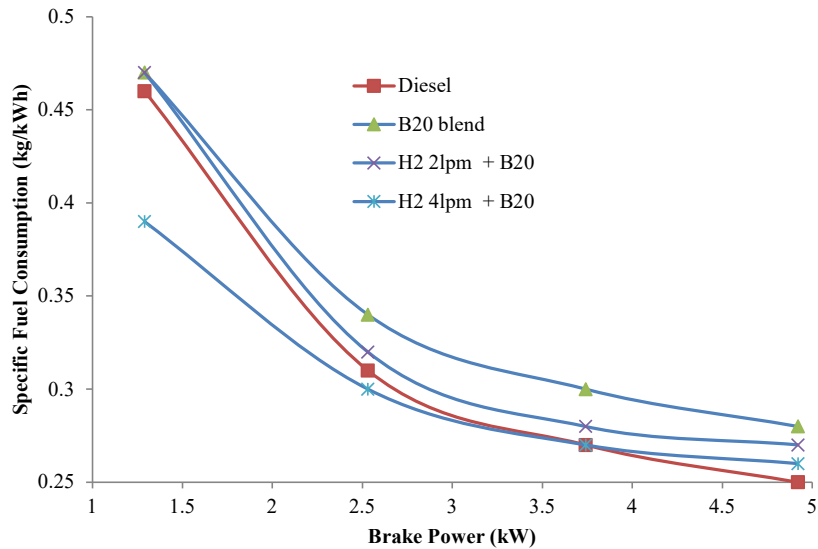

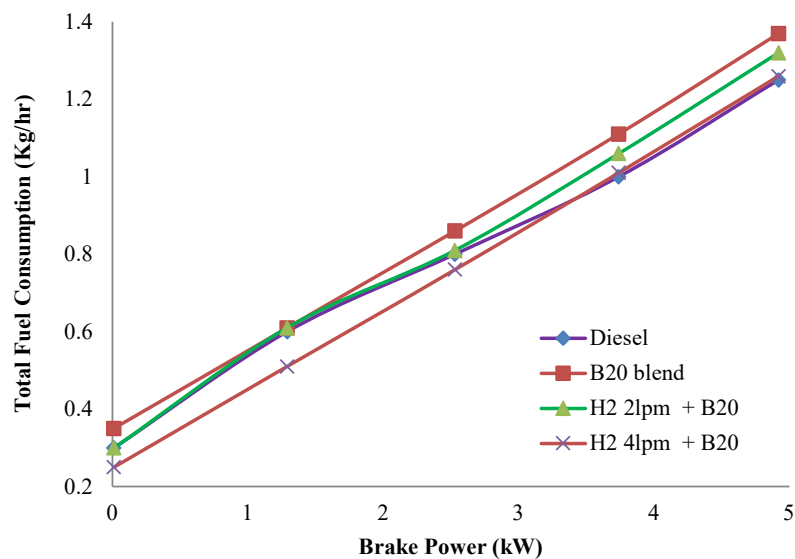Fig. 9: Variation in Specific Fuel Consumption (SFC).

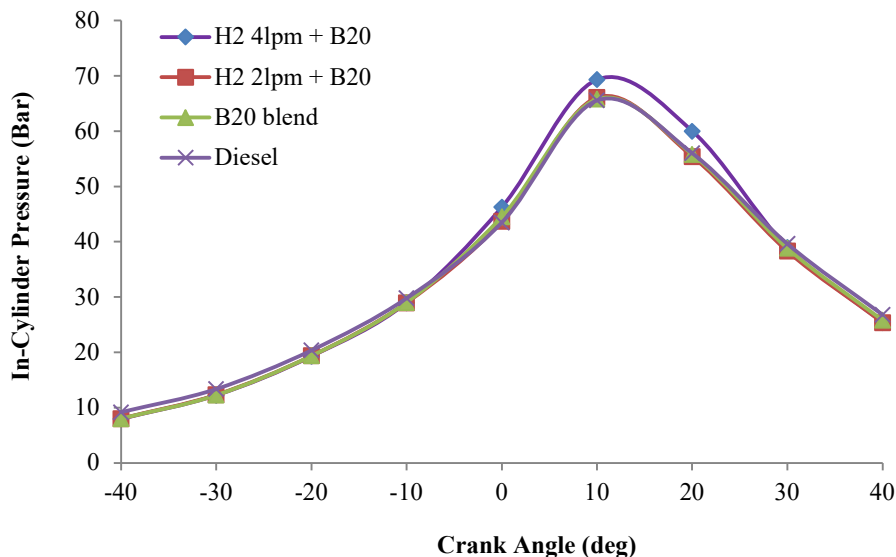Fig. 10: Variation in Total Fuel Consumption.
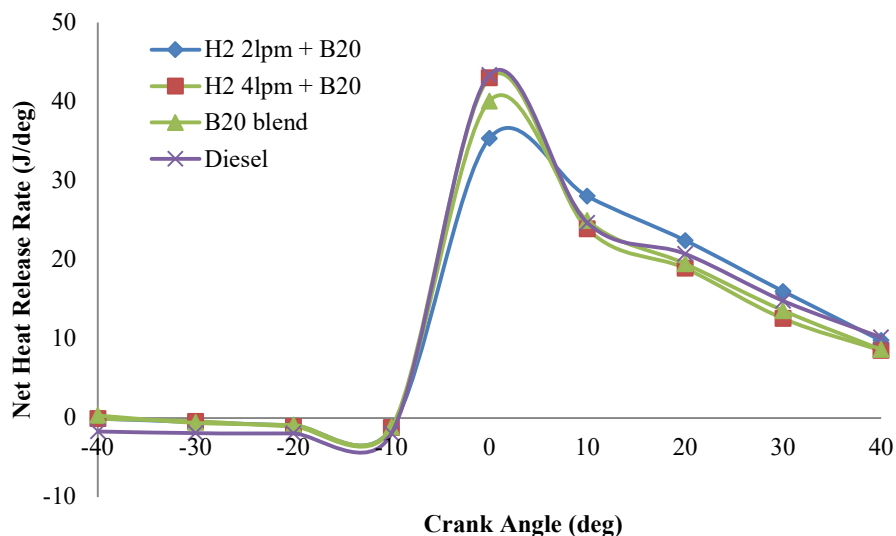
Fig. 11: Variation in in-cylinder pressure.

Fig. 12: Variation in Heat Release Rate.

and enables the fuel mixture of B20 and H_2 to attain the TFC of diesel fuel (Avase et al. 2015).

> i g bomi h!>b[l[]n_lomd]m

This section details about pressure inside the cylinder and rate of heat release representing the combustion characteristics of the *Chlorella vulgaris* biodiesel.

Fig. 11 represents the Crank angle (deg) vs Cylinder pressure of the diesel engine. The cylinder pressure varies along the crank angle. It shows that the H_2 at 4 LPM has the highest point at 69.33 bar at a 10° crank angle, B20 blend at 65.81 bar, diesel at 65.57 bar, and 2 LPM at 66.07 bar. Where

the hydrogen 4 LPM with b20 blend shows higher cylinder pressure in relation to crank angle due to the higher flame speed of hydrogen, the B20 blend mixed with hydrogen at 4 LPM shows much increase in the pressure rise rate, in addition, the pressure increased stays a moment and drops down. It is also to be noted that the increase of heat inside the cylinder will affect the pressure of the cylinder (Das et al. 2023).

Fig. 12 represents the Crank angle (deg) vs the Net Heat Release rate of the given diesel Engine. The Net Heat Release rate varies along the crank angle. It shows that the diesel has the highest point at 43.37 J/deg at 0° Crank angle, B20 blend at 40.06 J/deg, H_2 2 LPM at 35.34 J/deg and 4

LPM at 42.98 J/deg. Where diesel shows a higher Net Heat Release rate in relation to crank angle due to high heating value and possessed by its characteristics and lower viscosity compared to biofuel. Even though diesel has the highest heat release rate, hydrogen at 4LPM with B20 blend also shows a similar heat release rate at 0.39 J/deg difference due to the higher calorific value of hydrogen. It is also to be noted that the calorific value and density of the fuel influences widely the heat release rate.

@g and h!>b[l[]n_l and m

This section details the characteristics of emission released by the study engine when utilizing the prepared fuel.

Fig. 13 represents Brake power (kW) vs CO (%) of the study engine which is single cylinder four stroke. The CO exhaust varies along the brake power. It shows that the diesel has the highest point at 0.242% at zero loads where brake power is 0.01 kW, B20 blend at 0.087%, H_2 2 LPM + B20 at 0.102% and 4 LPM at 0.196%. Where diesel shows higher CO with respect to brake power because of incomplete combustion of fuel and due to insufficient oxygen compared to biofuel. Because of the enriched oxygen in the biodiesel, it can combust evenly with less amount of CO content emitted

Fig. 13: Variation in CO Emission.

Fig. 14: Variation in Unburned Hydrocarbon Emission.

Fig. 15: Variation in CO_2 Emission.

from the B20 blend batch, this case differs when it is added with H_2, this again changes due to less amount of oxygen in the air inlet. This is why the emission of B20 with H_2 is increased compared to the B20 blend (Khan et al. 2018).

Fig. 14 represents Brake power (kW) vs HC (ppm) of the four-stroke diesel engine. The HC exhaust varies along the brake power. It shows that the diesel has the highest point at 94 ppm at zero load where brake power is 0.01 kW, B20 blend at 40 ppm, H_2 2 LPM + B20 at 44 ppm, and 4 LPM at 46 ppm. Due to the high cetane present in the biofuel compared to diesel, it improves the quality of ignition in the fuel and increases the combustion efficiency, and also due to the higher viscosity of the biofuel, there is a delay in ignition of the fuel, this also cause the fuel to burn more even during combustion stroke (Raja et al. 2018). Even though the biodiesel emits less HC, with the addition of H_2, it again increases the Hydrogen content in the exhaust and causes HC to increase.

Fig. 15 represents the Brake power (kW) vs CO_2 (%) of the given diesel Engine. The CO_2 exhaust varies along the BP, it shows that the diesel has the highest point at 10.6% at zero loads where brake power is 0.01 kW, B20 blend at 9.1%, H_2 2 LPM + B20 at 10% and 4 LPM at 9.45%. Where the diesel shows higher CO_2 with respect to brake power because of the combustion of fuel which is incomplete and due to insufficient oxygen compared to biofuel. Because of the enriched oxygen in the biodiesel, it c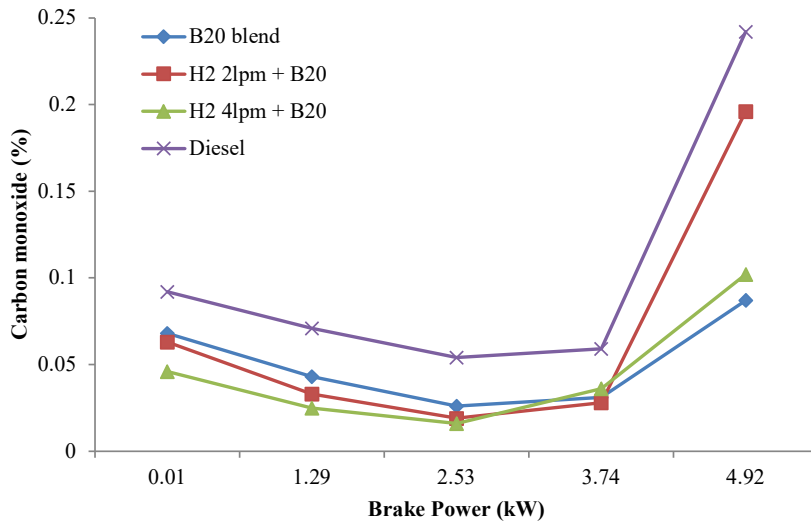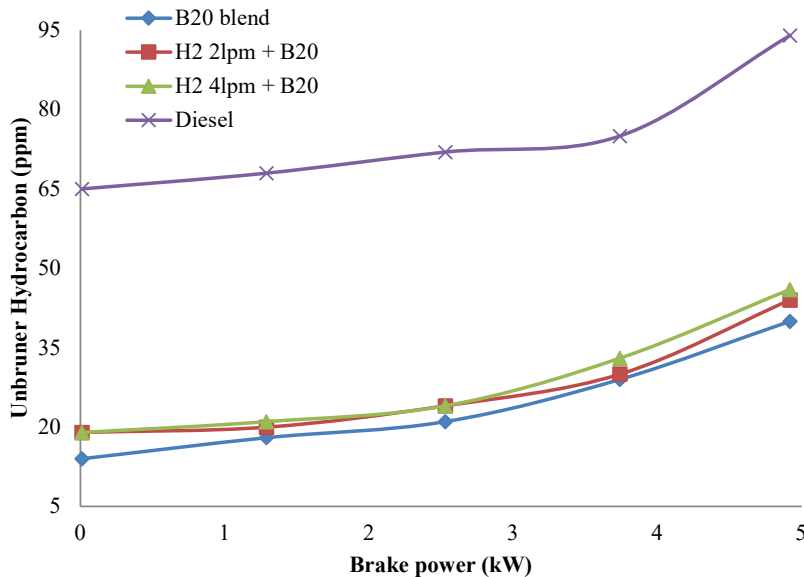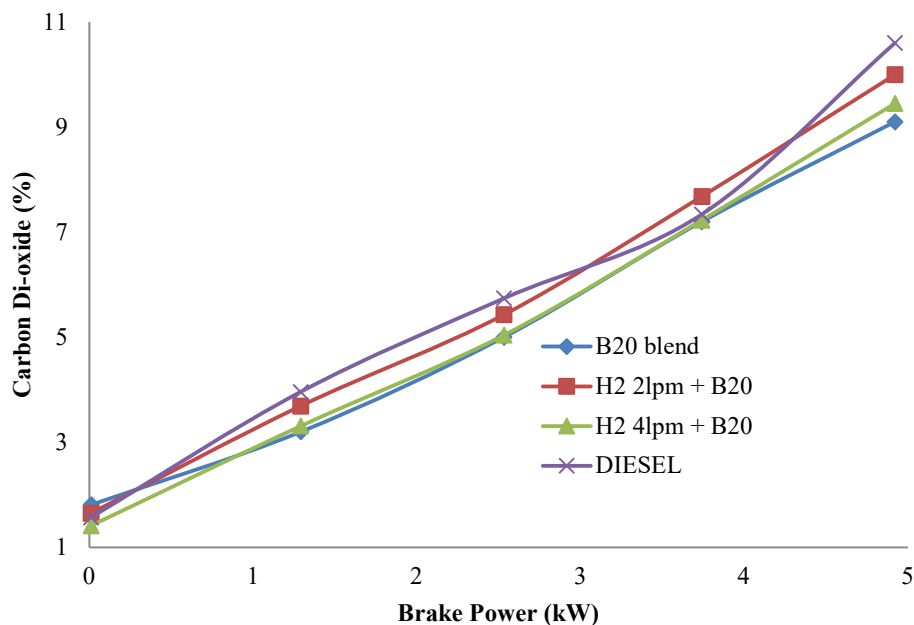an combust evenly with less amount of CO_2 content emitted from the B20 blend batch, this case differs when it is added with H_2, this again

changes due to less amount of oxygen in the air inlet. As a result, the emission of B20 with H_2 was increased compared to the B20 blend (Suzuki et al. 2015).

Fig. 16 represents Brake power (kW) vs NOx ppm of the Engine. The NOx exhaust varies along the brake power. It shows that the B20 + H_2 at 4 LPM has the highest point at 2059 ppm at zero load where brake power is 0.01 kW, B20 blend at 1901 ppm, H_2 2 LPM + B20 at 2002 ppm, and diesel at 1834 ppm. Where diesel shows higher NOx with respect to brake power as a result of incomplete combustion of fuel and because of insufficient oxygen compared to biofuel. Due to the availability of oxygen in the biodiesel, it can combust evenly with less amount of NO_x content emitted from the B20 blend batch, this case differs when it is added with H_2, this again changes due to less amount of oxygen in the air inlet (Oni et al. 2021). Due to this, the emission of B20 with H_2 is increased compared to the B20 blend.

Fig. 17 represents the Brake power (kW) vs O_2 (%) of the Diesel Engine. The O_2 intake varies along the brake power. It shows that the diesel has the highest point at 18.38% at zero load where brake power is 0.01 kW, B20 blend at 18.16%, H_2 2 LPM + B20 at 18.28% and H_2 4 LPM + B20 at 18.3%. Where the diesel shows higher O_2 intake with respect to brake power due to the absence of any kind of supplement air supply and its need to combust the fuel in the combustion chamber.

CONCLUSIONS

An engine that is a single-cylinder four-stroke has been tested at 4 different loads such as 25%, 50%, 75%, and
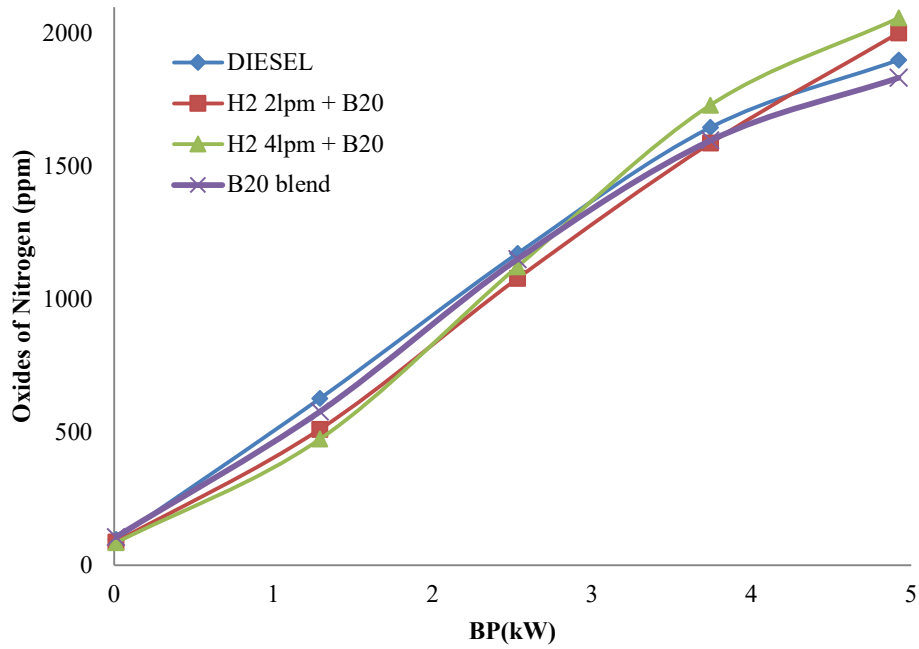
Fig. 16: Variation in NO$_x$ Emission.
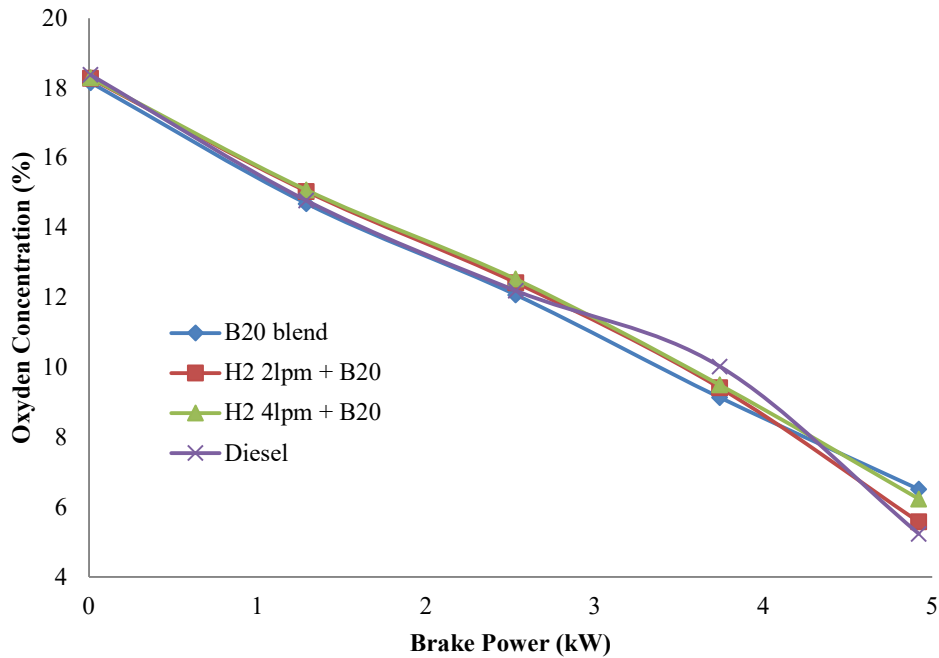
Fig. 17: Variation in O$_2$ Concentration.

100% load under different hydrogen-biodiesel blend mix ratios. Initially, the engine is tested with a microalgae biodiesel B20 blend and the outputs are observed with various aspects of the engine with such devices as a dynamometer, smoke analyzer, and smoke meter to analyze the performance and emission characteristics of the engine.

To observe the combustion traits, there are many flow sensors, temperature, and pressure sensors placed in various inlets and outlets of the combustion chamber. The focal characteristics of the diesel engine such as performance, combustion, and emission are observed and analyzed to conclude.

- B20 blend has higher friction power at 50% load gaining 2.54 kW. Additional O_2 gained from the biodiesel significantly increased the performance of the engine compared to diesel in producing friction power. However, the F.P. reduces at higher loads due to the higher viscosity of the B20 due to which injection of fuel in the combustion chamber becomes difficult which contradicts the combustion property of B20.

- At 100% load, B20 + H_2 at 4 LPM produces higher Brake thermal efficiency, compared to diesel and other fuel mixtures due to an increase in the H_2 flow to the engine. Producing 33.6% BTE at higher loads, comparing Diesel which only produced 33.48% BTE. Though the difference is minimal, the addition of more H_2 to the fuel mixture can produce a significant difference. B20 blend produces only up to 30.94%, so on the whole there is a major difference with increasing H_2.

- Because of the highly viscous nature of the B20 blend, the engine consumes more fuel than the other mixtures, and due to the lower calorific value of the B20 blend, it requires more fuel to produce the expected power output. But adding H_2 to the fuel mixture, decreases the fuel consumption and enables the fuel mixture of B20 and H_2 to attain the SFC of diesel fuel and it also helps in decreasing the total fuel consumption. The specific fuel consumption varies along the Brake power. It shows that the diesel has the highest point at 0.46 kg/kWh at higher load which is 1.29 kW brake power, B20 blend at 0.47 kg/kWh, H_2 at 2 LPM 0.47 kg/kWh, and 4 LPM at 0.39 kg/kWh. BP vs TFC shows that the B20 blend has the highest point at 1.37 kg/hr at brake power of 4.92 kW, H_2 at 1.32 kg/hr, diesel at 1.25 Kg/hr, and 4LPM at 1.26 kg/hr.

- B20 blend + H_2 at 4 LPM mixture has higher indicated power compared to other mixtures, where it is at 7.45 kW due to the high combustible nature of H_2 and due to the availability of a higher amount of oxygen present in the biodiesel, which also helps in increasing the Indicated power of the engine with respect to the brake power produced. With less hydrogen, the I.P. also decreases when compared to diesel which is at 7.22 kW.

- Combustion characteristics show that the cylinder pressure of H_2 at 4 LPM has its highest point at 69.33 bar at a 10° Crank angle, because of the higher flame speed of hydrogen, the B20 blend mixed with hydrogen at 4 LPM shows a significant increase in the rate of pressure rise, in addition, the pressure increased stays a moment and drops down.

- Net Heat Release rate with respect to the Crank angle of H_2 at 4 LPM + B20 produces a higher amount of heat compared to other biofuel mixtures, due to higher calorific value and possessed by its characteristics and lower viscosity compared to biofuel. It shows that the diesel has the highest point at 43.37 J/deg at 0° Crank angle, B20 blend at 40.06 J/deg, H_2 2 LPM at 35.34 J/deg and 4 LPM at 42.98 J/deg. Even though the diesel has the highest Heat release rate, hydrogen at 4 LPM with B20 blend also shows a similar heat release rate at 0.39 J/deg difference due to the higher calorific value of hydrogen.

Comparing other fuel mixtures, the emission of carbon pollutants occurs because of incomplete combustion of fuel in the combustion chamber, but in B20 blend fuel, the fuel combusts more evenly compared to other mixtures. This causes the B20 blend to produce less emission than the mixture with H_2 and conventional fuel.

REFERENCES

Avase, S.A., Srivastava, S., Vishal, K., Ashok, H.V. and Varghese, G., 2015. Effect of pyrogallol as an antioxidant on the performance and emission characteristics of biodiesel derived from waste cooking oil. *Procedia Earth and Planetary Science*, 11, pp.437-444.

Chetia, B., Debbarma, S. and Das, B., 2024. An experimental investigation of hydrogen-enriched and nanoparticle blended waste cooking biodiesel on diesel engine. *International Journal of Hydrogen Energy*, 49, pp.23-37.

Das, S. and Das, B., 2023. The characteristics of waste-cooking palm biodiesel-fueled CRDI diesel engines: effect hydrogen enrichment and nanoparticle addition. *International Journal of Hydrogen Energy*, 48(29), pp.14908-14922.

Godwin John, Hariram, V. and Seralathan, S., 2018. Emission reduction using improved fuel properties of algal oil biodiesel and its blends. *Energy Sources, Part A: Recovery, Utilization, and Environmental Effects*, 40(1), pp.45-53.

Godwin John, Hariram, V., Seralathan, S. and Jaganathan, R., 2017. Effect of Oxygenate on Emission and Performance Parameters of a CI Engine Fuelled with Blends of Diesel-Algal Biodiesel. *International Journal of Renewable Energy Research*, 7(4), pp.2041-2047.

Gultekin, N. and Ciniviz, M., 2023. Experimental investigation of the effect of hydrogen ratio on engine performance and emissions in a compression ignition single cylinder engine with electronically controlled hydrogen-diesel dual fuel system. *International Journal of Hydrogen Energy*, 48(66), pp.25984-25999.

Hariram, V., Godwin John, J. and Seralathan, S., 2017. Spectrometric analysis of algal biodiesel as a fuel derived through base-catalyzed transesterification. *International Journal of Ambient Energy*, 40(2), pp.195-202.

Hariram, V., Prakash, S., Seralathan, S. and Micha Premkumar, T., 2018. Data set on optimized biodiesel production and formulation of emulsified Eucalyptus teriticornisis biodiesel for usage in compression ignition engine. *Data in Brief*, 20, pp.6-13.

Hazar, H., Telceken, T. and Sevinc, H., 2022. An experimental study on emission of a diesel engine fuelled with SME (safflower methyl ester) and diesel fuel. *Energy*, 241, p.122915.

Khan, N., Balunaik, B. and Yousufuddin, S., 2018. Performance and emission characteristics of a diesel engine with varying injection pressure and fueled with hydrogen and cottonseed oil methyl ester blends. *Materials*, 5(2), pp.3369-3377.

Murad, M.E. and Al-Dawody, M.F., 2020. Biodiesel production from spirulina microalgae and its impact on diesel engine characteristics-review. *Al-Qadisiyah Journal for Engineering Sciences*, 13, pp.158-166.

Oni, B.A., Sanni, S.E., Ibegbu, A.J. and Aduojo, A.A., 2021. Experimental optimization of engine performance of a dual-fuel compression-ignition engine operating on hydrogen-compressed natural gas and Moringa biodiesel. *Energy Reports*, 7, pp.607-619.

Raja, S., Mayakrishnan, J., Nandagopal, S., Elumalai, S. and Velmurugan, R., 2018. Comparative study on smoke emission control strategies of a variable compression ratio engine fueled with waste cooking oil. *SAE Technical Paper*, 2018-01-0908.

Rajak, U., Nashine, P., Verma, T.N., Veza, I. and Ağbulut, Ü., 2022. Numerical and experimental investigation of hydrogen enrichment in a dual-fueled CI engine: A detailed combustion, performance, and emission discussion. *International Journal of Hydrogen Energy*, 47(76), pp.32741-32752.

Reang, N.M., Dey, S., Debbarma, B., Deb, M. and Debbarma, J., 2020. Experimental investigation on combustion, performance and emission analysis of 4-stroke single cylinder diesel engine fuelled with neem methyl ester-rice wine alcohol-diesel blend. *Fuel*, 271, p.117602.

Sarpal, A.S., Teixeira, C.M.L.L., Silva, P.R.M., Vieira da Costa Monteiro, T., Itacolomy da Silva, J., Smarcaro da Cunha, V. and Daroda, R.J., 2016. NMR techniques for determination of lipid content in microalgal biomass and their use in monitoring the cultivation with biodiesel potential. *Applied Microbiology and Biotechnology*, 100, pp.2471-2485.

Subramanian, B. and Thangavel, V., 2020. Experimental investigations on performance, emission and combustion characteristics of Diesel-Hydrogen and Diesel-HHO gas in a Dual fuel CI engine. *International Journal of Hydrogen Energy*, 45(46), pp.25479-25492.

Suzuki, Y., Tsujimura, T. and Mita, T., 2015. The performance of multi-cylinder hydrogen/diesel dual fuel engine. *SAE International Journal of Engines*, 8(5), pp.2240-2252.

Tan, D., Wu, Y., Lv, J., Li, J., Ou, X., Meng, Y., Lan, G., Chen, Y. and Zhang, Z., 2023. Performance optimization of a diesel engine fueled with hydrogen/biodiesel with water addition based on the response surface methodology. *Energy*, 263, p.125869.

Zareei, J.A.V.A.D., Haseeb, M., Ghadamkheir, K., Farkhondeh, S.A., Yazdani, A. and Ershov, K., 2020. The effect of hydrogen addition to compressed natural gas on performance and emissions of a DI diesel engine by a numerical study. *International Journal of Hydrogen Energy*, 45(58), pp.34241-34253.

Reviewing the Impact of Earthquakes on Flood Occurrence: Insights from Kota Belud, Sabah, Malaysia

K. Sharir[1] and **R. Roslee[2]†**

[1]Faculty of Engineering (FKJ), Universiti Malaysia Sabah, 88400 Kota Kinabalu, Sabah, Malaysia
[2]Faculty of Science & Natural Resources (FSSA), Universiti Malaysia Sabah, 88400 Kota Kinabalu, Sabah, Malaysia
†Corresponding author: R. Roslee; rodeano@ums.edu.my

ABSTRACT

This study investigates the trends and processes of flooding in Kota Belud, Sabah, Malaysia, following the 2015 Ranau Earthquake. The earthquake caused landslides that altered river systems and significantly impacted flood patterns. Using an interdisciplinary methodology, we examined geological processes, river morphology, sediment dynamics, and erosion mechanisms to understand the correlation between geological forces and flooding. The investigation spanned a decade (2010-2020), revealing an increase in flood incidents post-earthquake. Key findings include the impact of sediment dynamics on river behavior, the role of river morphology, and the importance of erosion and sedimentation in flood timing. This research offers valuable insights into disaster management strategies, emphasizing the need for understanding geological influences on flood susceptibility.

INTRODUCTION

In the complex interplay of Earth's geological forces, the relationship between seismic events and hydrological phenomena can change landscapes, disturb communities, and modify natural processes (Chen et al. 2015). One significant problem related to earthquakes is flooding, especially in regions where seismic activity intersects with complex drainage systems. This connection between tectonic movements and hydrological responses is both fascinating and crucial, necessitating further research to fully understand it.

Our study delves into the relationship between earthquakes and floods, explicitly focusing on Kota Belud, Sabah, Malaysia, in the aftermath of the 2015 Ranau Earthquake. This location, where geological forces intersect with drainage systems, offers an ideal context for investigating how earthquakes can initiate flooding events. The aftermath of the Ranau Earthquake, marked by landslides, erosion, and debris flow, has significantly altered flood patterns in this area (Rosli et al. 2021, Tongkul 2017, Yusoff et al. 2016).

The primary objective of this study is to unravel the complex interactions between seismic activity and hydrological responses, specifically the increased flooding in Kota Belud following the 2015 Ranau Earthquake. This

research aims to answer the following questions: How do geological processes, triggered by seismic events, alter flood patterns? What role do sediment dynamics and river morphology play in post-earthquake flooding?

OBJECTIVES

The main objectives of this study are:

1. To investigate the impact of the 2015 Ranau Earthquake on flood patterns in Kota Belud.
2. To analyze the role of sediment dynamics and river morphology in post-earthquake flooding.
3. To develop insights for disaster management strategies based on the findings.

METHODOLOGY

We employed a combination of field surveys, remote sensing techniques, and GIS analysis to collect data on river morphology, sediment deposition, and flood events. Instruments included LiDAR for topographical mapping, sediment traps for measuring deposition rates, and flow meters for assessing river discharge. Data were collected from various sources, including the Department

of Irrigation and Drainage and the National Disaster Management Agency, ensuring a comprehensive analysis (Fig. 1).

RESULTS

Our results indicate a significant increase in flood events post-earthquake, even with lower rainfall intensities. Sediment deposition in river channels was identified as a major factor influencing flood patterns. Borehole analyses revealed varying sediment thickness downstream, correlating with increased flood frequency. Detailed tables and figures illustrate the spatial distribution of floods and sedimentation patterns, supporting our findings.

Flood Distribution

The objective of flood distribution is to assess the areas impacted by floods and identify locations that consistently experience flood events. This study also plays an important role in identifying places that are frequently prone to flood occurrences. Flood distribution data, commonly referred to as flood inventory, and all the factors that influence flooding are essential when generating flood susceptibility maps. Moreover, the flood inventory map is used to determine factors that contribute to flood recurrence.

To assess the distribution of floods, we employed data collected from on-site inspections conducted between 2018 and 2022. Incorporated into the analysis are data obtained from several government entities such as the Department of Irrigation and Drainage, the National Disaster Management Agency, the Civil Defence Force, and the Kota Belud District Council.

A total of 217 flood events were recorded within the study area over a decade from 2010 to 2020. These events affected 48 different locations (Department of Irrigation and Drainage Sabah 2020). Out of these places, 30 had repeated flood events happening multiple times over this period as specified in Table 1. These specific locations are considered hotspots because they are very prone to flooding.

Fig. 2 depicts the spatial distribution of flood occurrences for the five-year periods before (2010-2015) and after (2015-2020) the 2015 Ranau Earthquake. Surprisingly, the number of areas affected by floods increased from 87 to 130 after the earthquake, even though the timeframe of five years remained consistent before and after the seismic event. The changes in flood patterns pre- and post-earthquakes can be associated with sedimentary deposits caused by landslides triggered by earthquakes which pile in river channels leading to a decrease in river depth. Furthermore, erosion processes occurring in drainage development zones exacerbate this

Data Collection:	Analysis of Geological Factors:	Flood Pattern Analysis:	Borehole Investigations:	Result Synthesis:
• Gathering data from various sources including on-site inspections, government agencies, and historical records.	• Examining river morphology, sediment dynamics, and erosion mechanisms.	• Assessing the frequency and distribution of flood events before and after the earthquake.	• Conducting borehole analysis to understand sediment thickness and its impact on river channels.	• Integrating findings to understand the interplay between geological forces and flooding.

Fig. 1: Methodology flowchart.

Table 1: Flood hot-spot location.

Location	No. of events	Location	No. of events	Location	No. of events
Kg Bobot	13	Kg Tombol	2	Kg Limatok	2
Kg Gunding	12	Kg Pirasan	2	Kg Linau	13
Kg Jawi-Jawi	2	Kg Sangkir	2	Kg Lingkodon	17
Kg Keranjangan	6	Kg Sembirai	18	Kg Menunggui	18
Kg Kesapang	2	Kg Siasai	13	Kg Merabau	2
Kg Kota Bunga	3	Kg S. Punggur	2	Kg Pgkln Abai	6
Kg Labuan	7	Kg Tg Pasir	4	Kg Wakap	5
Kg Lebak Engad	11	Kg Tg Wakap	2	Kota Belud	4
Kg Lebak Moyoh	15	Kg Taun Gusi	3	Padang Pekan	5
Kg Lentigi	2	Kg Tawadakan	2	Pasar Tani	5
Total number of repeating locations					30

Fig. 2: The flood hot-spot location.

issue. Together, these factors contribute to an increase in flood episodes after an earthquake, even if the amount of rainfall is not unusually great.

Analysis of Flood Trends

The research we conducted in Kota Belud, Sabah, examines the complex connection between sedimentation and flooding that occurs after an earthquake. An examination of data collected from government entities, including the Department of Irrigation and Drainage 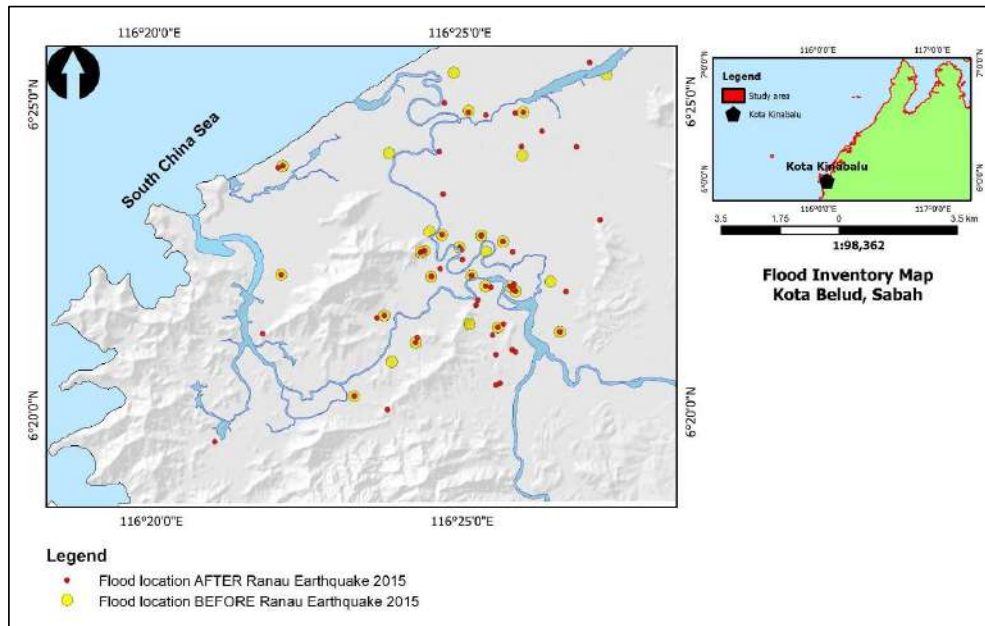Sabah and the Department of Meteorology Malaysia, indicates a significant pattern: a rise in the occurrence of floods after the 2015 Ranau Earthquake. It is noteworthy that this trend encompasses flood occurrences that happen at precipitation intensities lower than the standard heavy rain threshold of 60 mm per hour set by the National Flood Forecasting and Warning Centre.

To obtain a broader understanding, we compare the daily precipitation data from the years before the earthquake (1996, 2008, and 2014) with the years after the earthquake (2015, 2016, 2017, and 2018). This analysis reveals a significant change in flood patterns as floods are now occurring even with lower levels of rainfall. Significantly, an occurrence of flooding in August 2015 characterized by a rainfall intensity of 17 mm (classified as moderate rain) and other incidents in 2016, such as the severe rainfall event in May (55.5 mm), defy traditional assumptions. The observed variation can be ascribed to alterations in the flow patterns of the river caused by the deposition of sediment due to seismic activity, erosion, and the collapse of slopes in the upper areas, specifically in the Kadamaian River and Wariu River basins. Our analysis reveals how seismic events can significantly change river behavior by affecting sediment dynamics, leading to post-earthquake flooding scenarios.

Geological Factors in Flood Occurrence

The flow of water within the drainage systems is a key geological force that causes erosion, transportation, and deposition of material across landscapes. Almost every part of our world shows evidence of erosion or sediment accumulation caused by rivers. Understanding these geological processes is extremely important as they can greatly impact the frequency and severity of floods in a certain area. To thoroughly examine these processes, this part will be divided into several important elements: river morphology, drainage order, erosion and its impact on sediment deposition, and the movement and settling of sediment that is unique to the area being studied.

Unveiling the River Morphology

Learning about river morphology and how it changes over time is important before getting into the more complicated parts of flood research. A comprehensive study of the properties of rivers and drainage systems is crucial due to their close connection with flood events. To structure our research, we categorize the river basin into three main zones:

1. Zone 1: The Erosion Zone functions as a source of sediment in the upstream section, exerting geological pressures that result in erosion.

2. Zone 2: The Sediment Transport Zone, is located in the middle of the river's course. This area is frequently affected by erosion and sedimentation processes.

3. Zone 3: The Sedimentation Zone, is the area downstream where sediment accumulates, playing a crucial role in the river's environment.

The study area encompasses five main rivers: Sungai Wariu, Sungai Tempasuk, Sungai Kadamaian, Sungai Abai, and Sungai Gurong-Gurong. There are three essential river basins: Tempasuk, Kadamaian, and Wariu. The rivers demonstrate various phases of development, with Sungai Kadamaian and Sungai Wariu being mature rivers in lowland and hilly regions, displaying extensive plains and integrated drainage systems. On the other hand, Sungai Kuala Abai and Sungai Tempasuk are categorized as matured rivers located further downstream, characterized by distinctive attributes such as sandbanks and valleys with ridges. This initial investigation establishes the foundation for a comprehensive examination of the interaction between geological characteristics and flood patterns in the area, highlighting the significance of comprehending river development.

Analyzing River Order and its Significance in Flood Studies

Analyzing river order provides valuable insights into flood dynamics. Higher-order rivers indicate increased

Fig. 3: The order of stream network.

flow, which is crucial for flood studies, while lower-order rivers are significant due to their potential to disrupt the drainage system. Our study area, lacking rapid urbanization, experiences predominantly natural disturbances in Orders 1 and 2, aligning with earlier findings of landslide-prone terrain in the upper Kadamaian River basin (Fig. 3). These geological features impact river dynamics, providing critical insights into flood susceptibility.

Erosion and its Impact on Sediment Deposition

For our investigation into the erosion dynamics in the Kota Belud district, we utilize the Revised Universal Soil Loss Equation (RUSLE) to evaluate erosion rates. This approach considers factors such as precipitation, the susceptibility of soil to erosion, the characteristics of the slope, the kind of cultivation, and the effectiveness of erosion control measures. The results of our study depicted in Fig. 4 classify soil erosion into five distinct categories, ranging from very low to very high.

Most of Kota Belud, specifically 63.29% or 87,657 hectares, experiences a very low erosion risk. However, a significant portion, 26.17% or 36,245 hectares, suffers a very high danger of erosion. The medium-risk zones encompass 4.52% of the total land area, equivalent to 6,260 hectares. The low-risk regions cover 3.69% of the land, around 5,111 hectares. Lastly, the high-risk areas account for 2.33% of the land, a total of 3,227 hectares.

In 2021, Roslee and Sharir confirmed that the Kadamaian River Basin in south-eastern Kota Belud is a significant area at risk of land loss. Areas adjacent to main rivers, particularly the specific location we are studying, exhibit elevated rates of erosion. The heightened erosion close to rivers leads to sediment build-up in riverbeds, impeding efficient drainage during periods of intense precipitation. The complex interplay between erosion, sediment deposition, and river dynamics provides a valuable understanding of the susceptibility of the study area to flooding.

Sediment Dynamics: A Key Player in Post-Earthquake Flooding

Sedimentary deposits originating from the physical or chemical breakdown of rocks within the Earth's crust comprise a diverse range of particle sizes, from block-sized to colloidal dimensions (Joe et al. 2019, Quigley & Duffy 2020). When water serves as the vehicle for transporting these sediments, they are referred to as fluvial or river sediments (Rentschler & Salhab 2020). In nature, these sediments are a natural by-product of erosional processes that occur within drainage systems (Liu et al. 2020). However, an excess accumulation of these sediments beneath the drainage
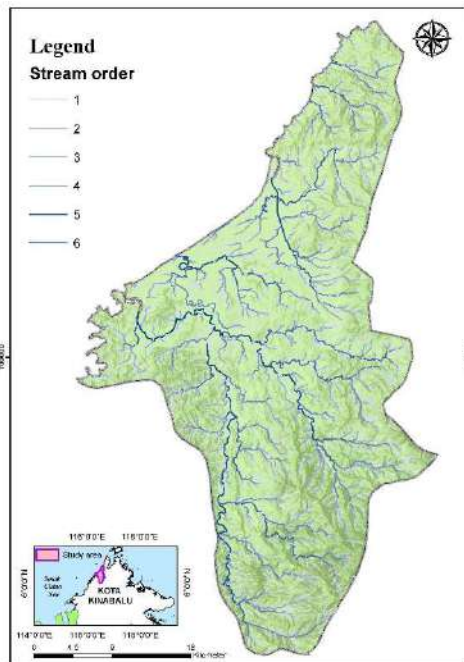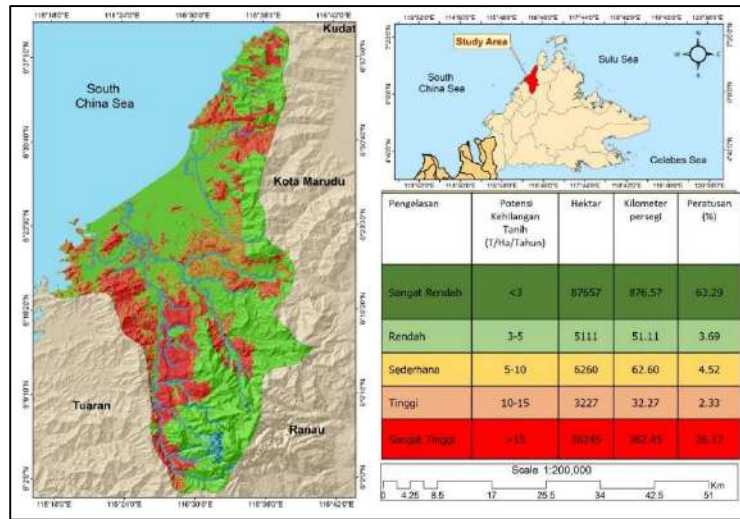
Fig. 4: The potential of soil erosion in Kota Belud.

system can have profound implications. Specifically, it can lead to the shallowing of river channels, thereby impeding their capacity to accommodate water during precipitation events, ultimately culminating in flooding (Sharir et al. 2022).

To gain a better grasp of the situation, we selected the daily rainfall data from the three years before the 2015 Ranau Earthquake for comparison with the years following the earthquake. Specifically, we chose 1996, 2008, and 2014 to represent the pre-earthquake events, while 2015, 2016, 2017, and 2018 represent the post-earthquake events. The selection of these assessment years was based on the availability of the information provided. The daily precipitation data is compared to the occurrence of floods in the study area. The rainfall data is constrained by a threshold value of 60 mm, representing the intensity range used to measure the amount of rain within an hour. This value is provided by the National Flood Forecasting and Warning Centre (Table 2).

Based on the rainfall data depicted in Fig. 5a, it was observed that the flood event before the 2015 Ranau Earthquake surpassed the established threshold for measuring heavy rainfall (>60 mm). In 1996, there were no reports of flooding. However, a flood was documented on February 17,

Table 2: Rainfall intensities classification.

Rainfall intensities	Range (mm/hour)
Light	1-10
Moderate	11-30
Heavy	30-60
Extremely Heavy	>60

Source: National Flood Forecasting & Warning Center (2021).

2008, with a recorded rainfall of 104.7 mm. Compared to 2014, one year before the earthquake, the highest recorded flood occurred on October 8, 2014, with a precipitation level of 86.5 mm.

The flood patterns observed during the monitoring periods of 2015, 2016, 2017, and 2018 showed changes following the impact of the earthquake (Fig. 5b). According to the recorded data, flood episodes happen not just when it rains more than 60 mm, which is considered heavy rain, but also when it rains less than that amount. Based on the information provided, there was a single flood event in 2015 following the August 2015 earthquake with a rainfall of 17 mm, falling into the moderate rain category. In 2016, there were three flood occurrences recorded in May (with heavy rainfall of 55.5 mm) and September (with rainfall of 19.5 mm and 16 mm, falling into the moderate rain category). In 2017, five flood events were detected, all of which were caused by very heavy rain. These events occurred in August, September, and December, with rainfall intensities ranging from 17 mm to 46 mm, classified as moderate to heavy rain. In 2018, there were three flood events recorded in January, June, and July, with rainfall intensities ranging from 15 mm to 45 mm, also classified as moderate to heavy rainfall.

The difference in flood patterns pre- and post-the 2015 Ranau Earthquake can be linked to the deposition of sediments, which reduces the river's depth as a consequence of the mountain's collapse caused by seismic activity, as well as the erosion that takes place in the surrounding drainage basin region. Consistent with previous research, it has been observed that soil erosion has a significant impact in the upper region of the river basin, specifically in the Kadamaian River and Wariu River basins. Erosion and
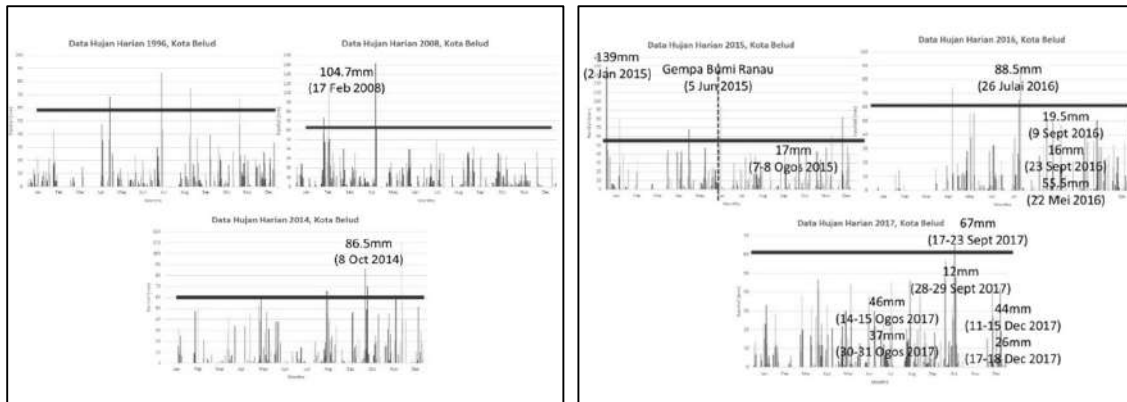
Fig. 5: Daily rainfall and flood records for the year before (a) and after (b) the 2015 Ranau Earthquake.

slope instability in the upper section of the drainage system result in the accumulation of sediment on the river bed in the middle and lower sections. The field survey results indicate that sediments deposited in the downstream section of the Kadamaian River, Tempasuk River, and Abai River have created a substantial and compact layer as a result of the parent rock's high clay content. The river in the area of Kota Belud experienced shallowing as a result of sediment transportation and deposition on its bed after the earthquake.

In our pursuit to unravel the intricate dynamics of sediment accumulation within the river system, we conducted extensive borehole investigations spanning from the upstream to the downstream regions. These boreholes provided critical insights into the various soil types, physical attributes, and engineering properties at each location, shedding light on the intricate nature of sediment deposition. Our study, however, places a special emphasis on Layer 1, known as the Fluvial Deposit Layer, as it is the focal point for assessing deposit thickness-a key factor linked to the upstream river collapse around Mount Kinabalu and erosion processes.

The data collected from these boreholes reveal a compelling trend: sediment thickness increases as one moves further downstream along the river (Table 3). This phenomenon significantly impacts the region's flood dynamics, extending beyond heavy rainfall events. The accumulation of thick sediment deposits at the riverbed contributes to the shallowing of river channels, ultimately constraining their capacity to manage water during

Table 3: Fluvial sediment thickness for each borehole.

Borehole	Location	Thickness of sediment (meter)
BH 1	Kg Melangkap	4.50m
BH 2	Pekan Kota Belud	15.32m
BH 3	Kg Sembirai	10.50m
BH 4	Kg Kulambai	25.5m

precipitation events effectively. It is worth noting that in BH2-Pekan Kota Belud, technical constraints in the field rendered the precise measurement of sediment thickness challenging, with a recorded value of 15.32 meters. Nevertheless, this discrepancy could be attributed to the unique geographical location of BH2, situated at the confluence of two major rivers—the Kadamaian River and the Wariu River-both originating from Mount Kinabalu. The collision of these river systems in the BH2 area leads to the accumulation of sediment transported from upstream, further enhancing our understanding of flood hazard dynamics within the region, a topic we delve into in the subsequent section.

CONCLUSIONS

This comprehensive investigation explores the complex relationship of geological phenomena that impact floods in Kota Belud, Sabah, specifically following the occurrence of the 2015 Ranau Earthquake. The area encountered escalated environmental difficulties, such as increased floods, landslides, soil erosion, and debris flow. The scope of our analysis was centered on the incidence of floods before and after earthquakes, to pinpoint the underlying reason for the increased severity of flooding.

The investigation begins with an examination of the geological elements that influence flooding. The hydrological flow within drainage networks, regulated by geological factors, influences the processes of sediment erosion, transit, and deposition. Rivers' complex shape and dynamic behavior were studied to understand flood dynamics. The study examined fundamental elements such as river order, drainage patterns, and erosion mechanisms to comprehend the complex correlation between geological characteristics and flooding.

The concept of river order, which is crucial in geomorphology, provides valuable insights about the

volume and intensity of river flow. Rivers of higher order signify augmented water flow, whilst rivers of lower order necessitate care due to their capacity to damage drainage systems. The Revised Universal Soil Loss Equation (RUSLE) identified Kota Belud as being prone to soil erosion, with a heightened risk near large rivers, including the Kadamaian River Basin.

The occurrence of post-earthquake floods was impacted by the movement of sediment, resulting in an unforeseen change in flood patterns that occurred at lower levels of rainfall. The accumulation of material caused by seismic activity resulted in changes to the flow of the river, making it difficult to control the water during rainfall. The examination of boreholes determined the thickness of sediment downstream, providing insights into the occurrence of floods and highlighting the accumulation of materials in shallower sections of the river channels.

Our research has clarified the complex relationship between geological variables and floods in Kota Belud. Gaining knowledge of sediment dynamics, river behavior, and erosion mechanisms is essential for understanding the occurrence of floods that happen after an earthquake. This work contributes to the understanding of regional flood risks, facilitating the formulation of efficient measures to mitigate the impact of disasters and supporting at-risk populations in their efforts to prepare for catastrophic events.

ACKNOWLEDGMENT

REFERENCES

Chen, X., Chen, H., You, Y. and Liu, J., 2015. Susceptibility assessment of debris flows using the analytic hierarchy process method - A case study in Subao river valley, China. *Journal of Rock Mechanics and Geotechnical Engineering*, 7(4), pp.404–410. https://doi.org/10.1016/j.jrmge.2015.04.003

Department of Irrigation and Drainage Sabah, Malaysia, 2020. *Sabah Flood Distribution*.

Joe, E., Tongkul, F., Roslee, R. and Sharir, K., 2019. Behaviour of channelised debris flow in the Crocker Range of Sabah, Malaysia: A case study at Ulu Moyog, Penampang. *ASM Science Journal*, 12(Special Issue 3).

Liu, M., Chen, N., Zhang, Y. and Deng, M., 2020. Glacial lake inventory and lake outburst flood/debris flow hazard assessment after the Gorkha earthquake in the Bhote Koshi Basin. *Water (Switzerland)*, 12(2). https://doi.org/10.3390/w12020464

Malaysia Meteorological Department, 2021. *Sabah Earthquake Distribution*.

Quigley, M. and Duffy, B., 2020. Effects of earthquakes on flood hazards: A case study from Christchurch, New Zealand. *Geosciences (Switzerland)*, 10(3). https://doi.org/10.3390/geosciences10030114

Rentschler, J. and Salhab, M., 2020. *People in Harm's Way: Flood Exposure and Poverty in 189 Countries*. (Issue October). http://documents1.worldbank.org/curated/en/669141603288540994/pdf/People-in-Harms-Way-Flood-Exposure-and-Poverty-in-189-Countries.pdf

Roslee, R., Termizi, A.K., Indan, E. and Tongkul, F., 2018. Earthquake vulnerability assessment (EVAs): A study of physical vulnerability assessment in Ranau area, Sabah, Malaysia. *ASM Science Journal*, 11(Special Issue 2), pp.66–74.

Rosli, M.I., Mohd Kamal, N.A. and Razak, K.A., 2021. Assessing earthquake-induced debris flow risk in the first UNESCO World Heritage in Malaysia. *Remote Sensing Applications: Society and Environment*, 23, p.100550. https://doi.org/10.1016/j.rsase.2021.100550

Sharir, K. and Roslee, R., 2022. Flood susceptibility assessment (FSA) using GIS-based frequency ratio (FR) model in Kota Belud, Sabah, Malaysia. *International Journal of Design and Nature and Ecodynamics*, 17(2), pp.203–208. https://doi.org/10.18280/ijdne.170206

Sharir, K., Lai, G.T., Simon, N., Ern, L.K., Abd Talip, M. and Roslee, R., 2022. Assessment of flood susceptibility analysis using analytical hierarchy process (AHP) in Kota Belud area, Sabah, Malaysia. *IOP Conference Series: Earth and Environmental Science*, 1103(012005). https://doi.org/10.1088/1755-1315/1103/1/012005

Tongkul, F., 2017. The 2015 Ranau earthquake: Cause and impact. April. *Sabah Society Journal*, 32, pp. 1-28

Ujang, Z., 2021. *Indikator dan Deskripsi Banjir*. Kementerian Alam Sekitar Dan Air. Available at: https://www.kasa.gov.my/

Wang, Y., Wei, S., Wang, X., Lindsey, E.O., Tongkul, F., Tapponnier, P., Bradley, K., Chan, C.H., Hill, E.M. and Sieh, K., 2017. The 2015 Mw 6.0 Mt. Kinabalu earthquake: An infrequent fault rupture within the Crocker fault system of East Malaysia. *Geoscience Letters*, 4(1), pp.0–12. https://doi.org/10.1186/s40562-017-0072-9

Yusoff, H.H.M., Razak, K.A., Yuen, F., Harun, A., Talib, J., Mohamad, Z., Ramli, Z. and Razab, R.A., 2016. Mapping of post-event earthquake-induced landslides in Sg. Mesilou using LiDAR. *IOP Conference Series: Earth and Environmental Science*, 37(1). https://doi.org/10.1088/1755-1315/37/1/012068

ORCID DETAILS OF THE AUTHORS

K. Sharir: https://orcid.org/0000-0002-0679-2913
G. Mukherjee: https://orcid.org/0000-0002-4501-7477

Efficient Removal of Congo Red Dye Using Activated Carbon Derived from Mixed Fish Scales Waste: Isotherm, Kinetics and Thermodynamics Studies

Vevosa Nakro[1], Ketiyala Ao[1], Tsenbeni N. Lotha[1], Imkongyanger Ao[1], Lemzila Rudithongru[1], Chubaakum Pongener[1], Merangmenla Aier[2], Aola Supong[3] and Latonglila Jamir[1]†

[1]Department of Environmental Science, Nagaland University, Lumami Campus-798627, Nagaland, India
[2]Department of Chemistry, National Institute of Technology, Nagaland, Chumoukedima-797103, Nagaland, India
[3]Department of Chemistry, Sao Chang College, Nagaland, India
†Corresponding author: Latonglila Jamir; latongli.jamir@gmail.com

ABSTRACT

The discharge of large quantities of organic dyes into the environment causes significant harm to humans and the environment. Thus, there is an urgent need to develop cost-effective adsorbents for removing these dyes. In the present study, the synthesis of activated carbon (AC) derived from mixed fish scale waste using KOH activation was investigated for Congo red (CR) dye removal. The finding shows that the obtained biocarbon has a fixed carbon of 42.9% with a crystallinity index of 15.01%. N_2 adsorption-desorption isotherm was found to be type IV, signifying mesoporous structure with a surface area and total pore volume of 150.049 m^2 g^{-1} and 0.119 $cm^3.g^{-1}$. Batch adsorption was carried out by various adsorbent doses, initial concentration, contact time, and pH to comprehend the effect of operating parameters on its removal efficacy. The isotherm studies fitted well for Freundlich with an R^2 of 0.99%. Adsorption kinetics was best fitted by the pseudo-second-order model and thermodynamic studies revealed the adsorption process to be exothermic and spontaneous. The efficiency of AC was also studied by an amount of sorption and desorption cycles which showed its potential for reusability up to the sixth cycle. Thus, the findings suggest that activated carbon derived from mixed fish scale waste is a promising adsorbent for removing Congo red dye from aqueous solutions.

INTRODUCTION

Dyes present in aqueous solutions are highly visible even at low concentrations and pose significant health and environmental risks due to their harmful effects on humans and ecosystems. It can be classed as cationic, anionic, or non-ionic depending on its properties and structure(Agarwal et al. 2023). The sources include industries like food, printing, textiles, leather, pulp/paper mills, plastics, cosmetics, and pharmaceuticals (Jasińska et al. 2019), which can lead to the creation of a hypoxic environment in water. Approximately 10,000 diverse dyes and pigments, totaling 700,000 tons, are used in industries each year out of which 10-15% end up in water bodies (Bhatia et al. 2017). Among them, congo red (CR) is a widely used anionic azo dye in textile and paper dyeing (Fig. 1) (Lade et al. 2015). Known for its six aromatic rings, this anionic diazo dye is highly toxic and mutagenic, also resistant to natural degradation. It can irritate the skin and gastrointestinal tract, and it decomposes into carcinogens, posing significant risks to both human health and environmental safety (Li et al. 2023). Additionally,

it is often illicitly added to meat and meat products as a coloring agent due to its low cost, high stability, and excellent dyeing properties (Wang et al. 2023). According to Jain and co-workers (Jain & Sikarwar 2014), it is stable in the atmosphere and may also be used as an indicator. It can also be used in gamma-ray dosimeters since its color diminishes with radiation strength(Rajhans et al. 2020). Prolonged dye contact with the skin or eyes might cause severe irritability due to the dye's extreme toxicity and when consumed it can cause nausea, vomiting, and diarrhea (Lade et al. 2015). CR dye displays different types of toxic effects including skin-related, environmental, microbial, yeast, bacterial, algal, and protozoan toxicity that exhibits genotoxic and cytotoxic effects with the ability to produce genetic alterations and cancer (Rajhans et al. 2020).

Over the decades, wastewater has been treated using diverse approaches like photocatalysis(Jorfi et al. 2016, Khan et al. 2023b), ultrafiltration (Hoslett et al. 2018, Yin et al. 2019), electrochemical processes (Islam et al. 2023), adsorption (Ukanwa et al. 2019, Burchacka et al. 2021), etc.

due to its effectiveness and cost efficiency, the adsorption technique is commonly employed methods for removing dyes from wastewater. AC branded by its significant surface area, high adsorption capacity, and cost-effectiveness, is a preferred choice for removing pollutants from aqueous solutions (Prajapati & Mondal 2020, Lotha et al. 2024, Sh et al. 2024).

Following this, a range of plant sources have been used to synthesize activated carbon, including rice husk rice (Feuzer-Matos et al. 2021), pistachio shells (Nejadshafiee & Islami 2019) coconut shells (Kosheleva et al. 2019, Muzarpar et al. 2020, Prajapati & Mondal 2020), bamboo (Lou et al. 2022), agricultural residues (Adamu & Adie 2020), bagasse (Van Tran et al. 2017), olive stone (Limousy et al. 2017), Manihot esculenta (Pongener et al. 2018), palm shell (Muzarpar et al. 2020), neem husk (Pathak 2023), apple peels (Jedynak & Charmas 2024), banana peels (Shukla et al. 2020), pine cone (Bhomick et al. 2018), almond shells (Boulika et al. 2023), litchi shell (Zhang et al. 2014) and *Tithonia diversifolia* (Supong et al. 2019a), etc. On the contrary, AC derived from animal biomass has not received significant attention in the existing literature with only a few reports which include cow manure (Park et al. 2022), pig bone (Liu et al. 2020), buffalo bone (Khan et al. 2023a), chicken bones (Khan et al. 2023a), donkey and horse bones (Jerome Sunday 2019), egg shells (Ahmad et al. 2020a), animal hair (Liu et al. 2013a), snail shell (Adiotomre 2015), sheep and goat dung (Kandasamy et al. 2023), etc. as it is known to hold many advantages, especially regarding its efficiency in removing pollutants and cost-effectiveness (Sh et al. 2024).

Fish scales, among other animal biowaste, have been found to have high percentages of carbon content and an insignificant amount of ash content, making them a promising source for AC synthesis (Stevens & Batlokwa 2017, Côrtes et al. 2019, Kodali et al. 2022). The removal of CR has been achieved by AC synthesized from shrimp shells which possess an adsorption capacity of 288.2 mg.g^{-1} (Zhou et al. 2018). Similarly, bael shells-based AC showed high adsorption capacity of 98.03 mg.g^{-1} towards the removal of CR (Ahmad & Kumar 2010). Hence, this study aims to utilize mixed fish scales (mFS) waste for AC production in CR dye removal. Various analytical techniques were used to characterize the synthesized adsorbent. Additionally, the effects of adsorbent dose, CR concentration, contact time, and pH on its adsorption were thoroughly investigated (Manjuladevi & Sri 2017, Mondal & Basu 2019). Furthermore, the isotherm, kinetics, and thermodynamics of the CR adsorption process on AC were examined and the potential reusability of the adsorbent was explored.

The unique aspect of using fish scales is their abundant availability, cost-effectiveness, and high carbon content, making them a sustainable and efficient raw material for activated carbon production. Although fish scales have been used before for this purpose, our study introduces a novel approach by utilizing mixed fish scale waste. This approach has the potential to improve adsorption capabilities, providing a practical solution for both waste management and dye removal. While previous research has investigated the use of AC derived from other biomass sources for CR removal, there is a gap in the literature regarding its application using waste mixed fish scales biomass.

MATERIALS AND METHODS

Materials

Mixed fish scales (mFS) were collected from the local fish market in Mokokchung town, Nagaland, India (26°19'38" N latitude and 94°31' 26" E longitude). Initially, the collected mFS were washed with distilled water, rinsed, and then dried in an oven at 120°C for 48 h. CR dye used in the current work was procured from Thermo Scientific™. KOH, HCl, and NaOH were acquired from HI MEDIA (India) while HNO$_3$, KNO$_3$, and H$_2$SO$_4$ were obtained from Sigma Aldric.
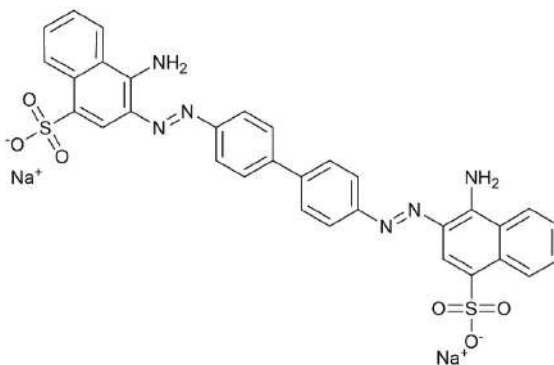

Fig. 1: Chemical structure of Congo Red.

Preparation of mixed fish scales (mFS) activated carbon: The collected biomass i.e. mixed fish scales were pyrolyzed at 500 °C for 1 h in a muffle furnace. After carbonization, the sample was ground and sieved into a fine powder using 212μ mesh and then subjected to KOH activation. Here, KOH was chosen as an activating agent because it creates a highly porous structure with a large surface area, allowing the AC to remove dye more efficiently from aqueous solutions. The resulting powder was labeled as mixed fish scales unactivated carbon (mFSUC). For activation, 200 mL of 10% KOH solution was mixed with 10 g of mFSUC. It was then stirred at 24°C for 3 h before drying in an oven for 30 h at 130°C. Subsequently, the dried sample was pyrolyzed at 700ºC for 3 h. The sample was subsequently rinsed with 0.1 M HCl and deionized water to achieve a neutral pH. The prepared AC is further subjected to oven drying at 105°C, labeled as mixed fish scales activated carbon (mFSAC) for further analysis. The scheme of mFSAC production is depicted in Fig. 2.

Carbon yield % is represented using the equation below.

$$\text{Yield \%} = \frac{W_1}{W_2} \times 100 \qquad \qquad …(1)$$

where W_1 = AC final weight; W_2 = dried raw biomass initial weight (mixed fish scales).

Adsorbate preparation: A concentration of 1000 mg.L^{-1} stock solution of CR dye was prepared with an addition of 0.5 g dye to 500 mL of de-ionized water. This stock solution was then used as the base for creating various concentrations at a range of 10 to 100 mg.L^{-1}. Throughout the study, chemicals were utilized without additional purification, and all experiments were conducted using de-ionized water.

Characterization of mFSAC: Proximate analysis of the prepared AC was conducted following the guidelines provided by the American Society for Testing and Materials (Standard A.S.T.M. 1999, Mukherjee et al. 2011), whereas

ultimate analysis was conducted by CHNS elemental analyzer (Model: EA30000, Eurovector, Italy). The measurement for determining the iodine number followed the procedure specified by ASTM (American Society for Testing and Materials) D4607-94(2006) (ASTM 2006). Brunauer–Emmett–Teller (BET) surface area was also analyzed by (Smart instrument, SS93/02). The dried sample of AC was applied as a thin layer onto carbon conducting tape and subsequently gold coated. The microstructure and morphology of the prepared mFSAC were examined using a Scanning Electron Microscope (SEM) at an accelerating voltage of 3 kV (Model: JSM-6360, JEOL). The prepared AC was then characterized using a Fourier Transform Infrared (FTIR) spectrometer (Model: Spectrum Two, made: PerkinElmer, USA) to analyze the surface functional groups and XRD analysis was performed (Model: ULTIMA IV, Rigaku, Japan) using CuKα radiation, scanning at a rate of °0.2 per minute. X-ray photoelectron spectroscopy (XPS) for the sample was also examined (Model: OHI 5000 VersaProbe 111, USA), whereas the zero-point charge of the AC was determined through a batch equilibrium test (Babić et al. 1999).

Adsorption experiments: The batch method was performed to study the CR dye adsorption from the aqueous solution. Each experiment was conducted in an Erlenmeyer flask with an initial CR concentration shaken at 160 rpm in a rotary shaker for a fixed time. The parameters considered for investigating the CR dye removal were: Adsorbent dose (0.1-0.5 g.L^{-1}), pH (3-10), concentration (10-100 mg.L^{-1}), contact time (10-100 min) and temperature (298-328 K). The filtrate of CR dye was measured at 497 nm using a UV-Vis Spectrophotometer (lambda 35, PerkinElmer). Three separate sets of adsorption tests were conducted. Removal Percentage (%) and adsorption capacity were calculated using the equation below.
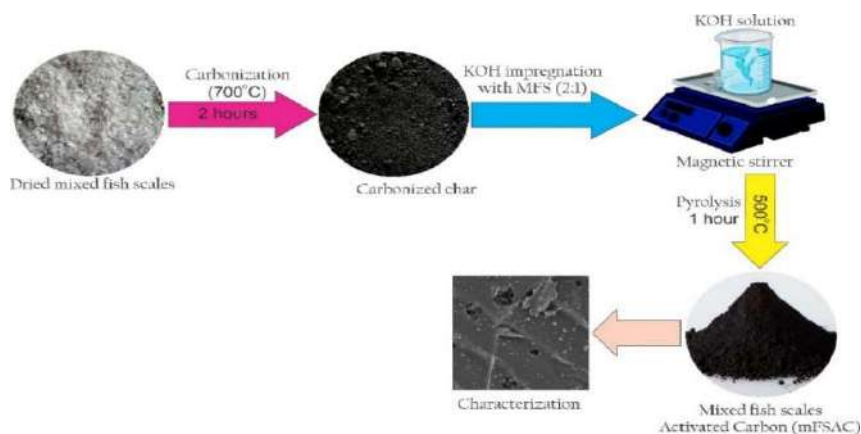

Fig. 2: Graphic illustration of mFSAC preparation.

$$\%\text{Removal of CR dye} = \frac{C_o - C_e}{C_o} \times 100 \qquad \ldots(2)$$

$$q_e = \frac{(C_o - C_e)}{M} \times V \qquad \ldots(3)$$

Adsorption isotherms and kinetic experiments were investigated to comprehend the pollutant-adsorbent interaction (Belaib & Meniai 2016). The total quantity of CR retained by the AC was determined at various time intervals using the equation,

$$q_t = \frac{C_o - C_t}{m} \times V \qquad \ldots(4)$$

Here, C_o and C_e = initial and final concentrations, V = volume of CR solution; M = adsorbent mass, qt = amount of dye adsorbed, t = time taken, Ct = dye concentration at time t.

RESULTS AND DISCUSSION

Characterization of Prepared mFSAC

Physico-chemical properties of mFSAC are given in Table 1. The outcomes of the ultimate analysis are: carbon (C) 22.84%, hydrogen (H) 0.994%, nitrogen (N) 2.25%, and sulfur (S) 0.55%. The N_2 adsorption-desorption isotherm initiates the sample to be of type IV, indicating a mesoporous structure with a surface area of 150.049 $m^2.g^{-1}$ and a pore volume of 0.119 $cm^3.g^{-1}$. The values attained are in line with the synthesized AC's porosity and adsorptive properties. The prepared AC's elemental analysis revealed a much greater carbon content of 57.83% and a significantly lower ash level. The pHzpc, which correlates to the adsorbent's charge on its surface, was found to be 7.64 indicating that the carbon surface will be predominantly negative or positively charged respectively at a pH below or above 7.64 (Liu et al. 2013b, Habeeb et al. 2017).

Table 1: Different physio-chemical properties of mFSAC.

Proximate analysis (wt%)		Ultimate analysis: CHNS (wt%)	
Moisture	12.5%	C	22.84
Volatile	29.8 %	H	0.994
Ash	14.8 %	N	2.25
Fixed carbon	42.9%	S	0.055
Iodine number	210.67 mg.g^{-1}	BET surface area	150.049 m^2.g^{-1}
pH$_{ZPC}$	pH=7.64	Pore size	0.119 cm^3.g^{-1}

Scanning electron microscopy (SEM) analysis offers valuable data on the surface morphology of the synthesized mFSAC. The micrograph of the AC revealed an uneven surface with variable-sized pores and shapes dispersed throughout the surface (Fig. 3a). This could be owing to the interaction of KOH with the mFSAC, which results in the expansion of pores as a consequence of the elimination of volatile chemicals throughout the activation process (Supong et al. 2020, 2022). After the dye adsorption on the AC (Fig. 3b), SEM analysis can offer valuable insights into the alterations in the shape and structure of the material. The surface of the mFSAC post-dye adsorption appears rougher and more defined compared to the surface of AC before adsorption. This roughness is attributed to the attachment of CR dye molecules to the AC surface, leading to the formation of a complex three-dimensional network of dye molecules.

The FT-IR analysis was used to determine the existing functional groups as depicted in Fig.4. For mFSAC, at a wavelength of 3436 cm^{-1}, the adsorption band is attributed to the (O-H) hydroxyl group whereas the band at 2908 cm^{-1} may be ascribed to the stretching vibrations of the C-H bonds in alkanes and alkyl groups (Jiang et al. 2021). The vibrational modes of C=N bonds are also associated with
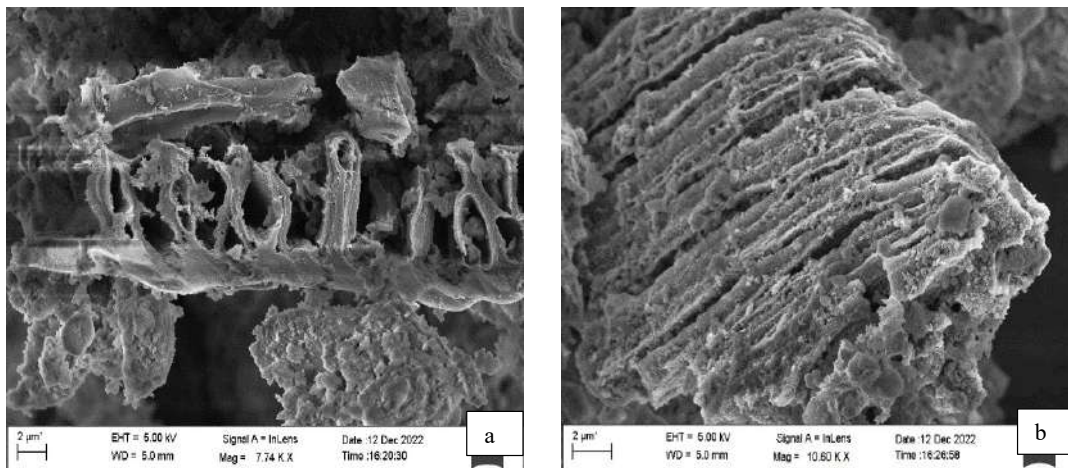

Fig. 3: SEM Micrograph of mFSAC (a) before, and (b) after adsorption.

bands at 1637 cm^{-1} and 2264 cm^{-1} (Bal Altuntaş et al. 2020). Furthermore, the existence of ether and ester functional groups which produce asymmetric stretching can be seen at wavelength 1208.66 cm^{-1} and 1020 cm^{-1} respectively (Alau et al. 2010). The prominent stretching vibrations of C–O, bending vibration of -OH groups, and C–H bonds result in IR peaks between 400 cm^{-1} and 800 cm^{-1} (Bhomick et al. 2018, Supong et al. 2019b). mFSUC at wavelength 3701 cm^{-1} attributes to the stretching vibration of the O-H (hydroxyl) groups. This can be indicative of free O-H groups, which are not hydrogen-bonded whereas the band at 1539 cm^{-1} is typically associated with the stretching vibrations of C=C bonds in aromatic rings or the bending vibrations of N-H bonds in amines. The absorption band at 1025 cm^{-1} is also commonly associated with the stretching vibrations of C-O bonds. After dye adsorption on the mFSAC, the band at 3733 cm^{-1} is typically attributed to the stretching vibration of free O-H groups whereas the absorption band at 1527 cm^{-1} is typically associated with the N-H bending vibration in amines or amides. It could also correspond to the aromatic C=C stretching vibrations.

XRD analysis was conducted on the prepared mFSAC with 2θ scan from 10° to 90°. The main peaks were found at 2θ = 26.24°, 32.15°, 39.8°, 49.0°, 58.86°, 64.33°, 76.0° and 88.10°, conforming to the d spacing of 0.34, 0.278, 0.225, 0.185, 0.145, 0.156, 0.125 and 0.12 nm respectively. The peaks about at 2θ = 26.24° and 32.15° indicate hydroxyapatite(Al-Malack & Basaleh 2016, Muthukumaran et al. 2016) and a peak at 2θ = 49.0° represents CaCO3 (Luo et al. 2020). Several peaks are in agreement with the reported peaks at 25.8°, 31.8°, 39.6°, and 49.3°, which resemble d spacings of 0.345, 0.281, 0.227, and 0.184 nm (Torres et al.

2008). The XRD profile of the mFSAC (Ratio 2:1) is depicted in Fig 5. The crystallite size of mFSAC is 4.2 nm and the degree of crystallinity was observed as 15.01% following the equation below,

$$D = \frac{k\lambda}{\beta \cos \theta} \qquad \ldots(5)$$

$$\text{Crystallinity} = \frac{\text{Area of crystalline peak}}{\text{The overall area of peaks (crystalline+amorphous)}} \times 100$$

$$\ldots(6)$$

The electron dispersive X-ray spectroscopy (EDX) analysis of the element percentage composition of mFSAC (Ratio 2:1) at 700 °C is shown in Fig. 6. The study revealed that the main components in its chemical structure were carbon (C) at 57.83% and oxygen (O) at 23.04% (Habeeb et al. 2017). Additionally, small amounts of Al, P, S, Ca, Br, Sb, and Pt were also detected.

The surface chemical composition of mFSAC using X-ray Photoelectron Spectroscopy (XPS) was analyzed. The wide scan spectra illustrating the chemical composition of mFSAC are presented in [Fig. 7 (a-c)]. The study indicated that carbon and oxygen were the most abundant elements. Specifically, carbon was observed at 284 eV and oxygen at 531 eV as the primary components. Further examination of the XPS spectrum at the Cls spectra with a binding energy of 284 eV revealed the presence of C-H or C-C groups, characteristic of graphitic carbon, and C-O groups, indicative of hydroxyl or ester functionalities. The major peaks in the O1s XPS spectra, with a binding energy of approximately 531 eV, corresponded to C-O carbonyl groups (Liu et al. 2020, An et al. 2022). The research offers valuable insights
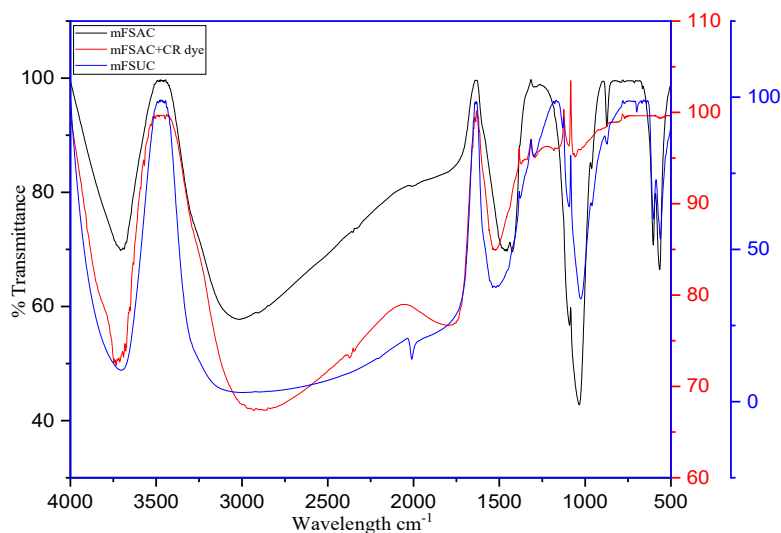
Fig. 4: FT-IR spectrum of mFSAC, mFSAC + CR dye, mFSAC.
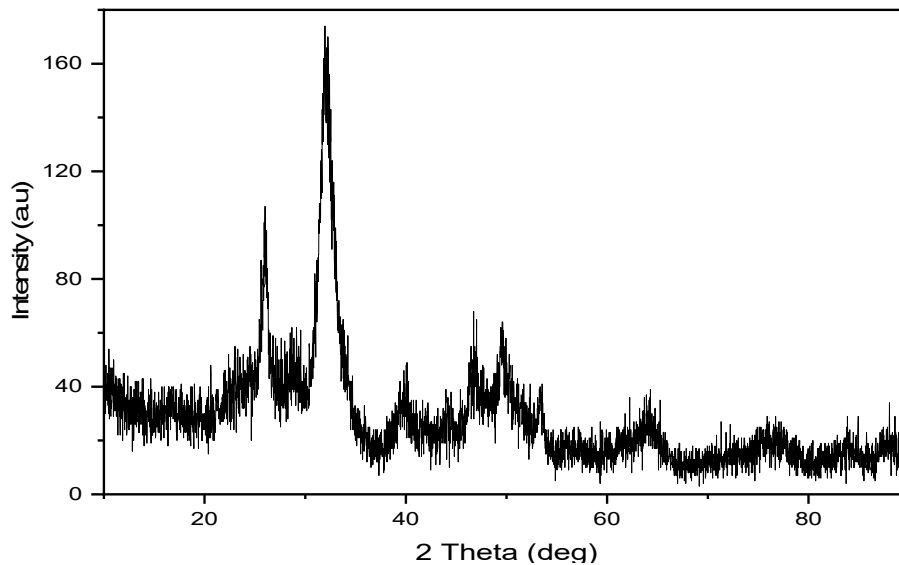
Fig. 5: XRD patterns of mFSAC.

Element	Weight%	Atomic%
C K	57.83	71.46
O K	23.04	21.37
Al K	0.15	0.08
P K	0.18	0.09
S K	7.26	3.36
Ca K	8.78	3.25
Br L	1.14	0.21
Sb L	1.23	0.15
Pt M	0.40	0.03
Totals	100.00	
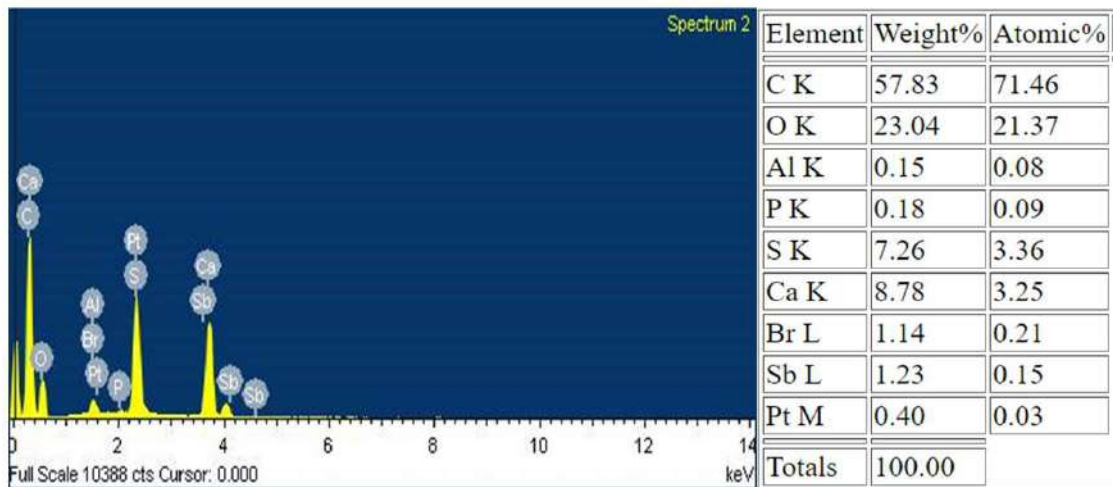
Fig. 6: EDX spectrum of mFSAC.

into the composition of mFSAC, specifically highlighting the presence of oxygen and carbon elements. Examination of the XPS spectrum indicated the existence of carbonyl groups and carbon bonds within the AC structure. These results are instrumental in characterizing AC and advancing our knowledge of its chemical composition, thereby facilitating the exploration of its potential applications.

Batch adsorption studies: Experimental variables like adsorbent dosage, initial concentration, contact time, pH, and temperature in the adsorption process were evaluated. Optimization of the equilibrium conditions was achieved through systematic variation of these parameters. At 25 °C, the CR concentrations were adjusted from 10-100 mg L^{-1}, AC dose: 0.1-0.5 g L^{-1}, and pH: 2-10 which was then shaken at 160 rpm. After the optimized conditions, the initial CR concentration, dosage, temperature, and contact time were 20 mg L^{-1}, 0.25 g L^{-1}, 25 °C, and 60 minutes, respectively. Mostly, significant removal of 99% was achieved at pH 4, making it an ideal pH for CR dye removal. The occurrence of OH^{-} ions in the solution, particularly at higher pH levels resulted in a decrease in adsorption capacities at elevated pH levels. These ions compete for available adsorption sites with the anionic dye (Beshkar et al. 2017, Alkurdi et al. 2019, Rajkumar et al. 2019).

For adsorbent efficiency, it is vital to study the effect of CR concentration and contact time. Various dye concentrations ranging from 10 to 100 mg L^{-1} were evaluated over a contact time of 0 to 100 minutes to understand the influence of
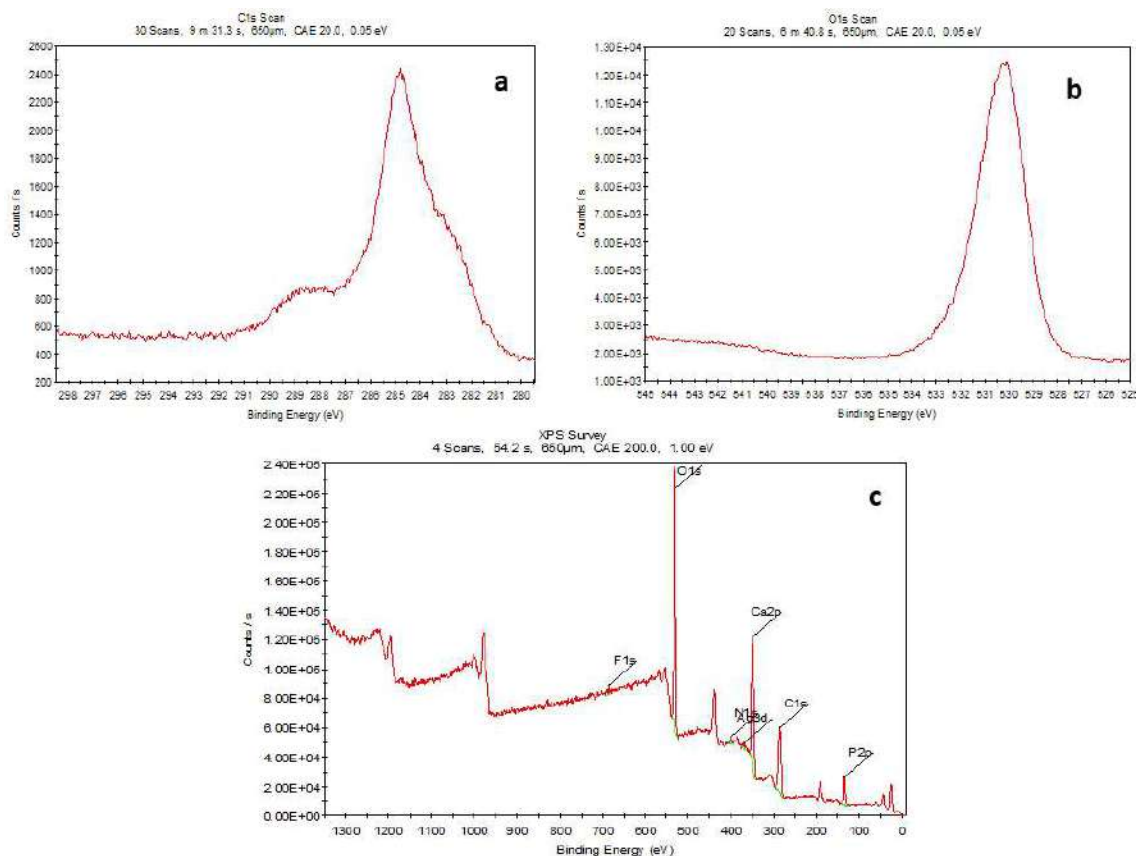
Fig. 7: XPS spectra of mFSAC; a) C1s, b) O1s, c) Overall wide scan.

the adsorption process. The results are shown in Fig 8(a) and (c), indicating that as dye concentration increased, the adsorption uptake also increased, reaching equilibrium at 60 minutes. Following an initial phase of rapid adsorption, the pace at which the adsorbent extracted dye from the solution decreased. This deceleration could be attributed to a decrease in the number of active sites accessible on the adsorbent's surface. Initially, numerous active sites may have been present for dye molecules to adhere to, resulting in rapid adsorption. However, as more dye molecules adhered to the surface, the number of active sites dwindled, leading to a deceleration in the adsorption rate (Ibrahim et al. 2016). Fig. 8(b) depicts the relationship between AC dosage and the removal percentage of CR at various concentrations. The removal efficiency of CR improved as the adsorbent dose increased for all CR concentrations until a dosage of 0.25 g of carbon was reached. This can be attributed to the large surface area of the mFSAC (Zhang et al. 2014, Dai et al. 2020). However, as the dosage exceeded 0.25 g, no significant changes were observed, indicating saturation of adsorbent binding sites with the dye molecules. Similar findings were found in a study on Ponceau 4R adsorption

by Tilapia fish scales activated carbon treated with NaOH (Zhu et al. 2013). Subsequent readings were made keeping the optimal adsorbent dosage at 0.25 g.

pH levels from 2 to 10 were explored for CR dye adsorption utilizing mFSAC (Fig. 8d). The study shows that with an increase in pH from 2 to 10, the removal percentage and adsorption capacity of CR declined. This phenomenon can be ascribed to electrostatic interactions where pH levels lower than pH_{ZPC}, negatively charged CR molecules were attracted to the surface with a net positive charge. However, at pH levels exceeding the ZPC, the surface acquired a net negative charge, which repelled the negatively charged CR molecules, leading to decreased adsorption. Despite this trend, a high removal rate of 99% was observed at pH 4. The activated carbon's pHzpc was found to be close to neutral pH: 7.64, suggesting that both electrostatic and non-electrostatic interactions likely influenced CR dye adsorption. An increase in negatively charged -OH groups may compete with adsorption sites for negatively charged CR molecules at pH values greater than the pHZPC, which would reduce the percentage of dye removed (Bhomick et al. 2019). For instance, previous research has examined the adsorption of

Alizarin Red S using pine cone biocarbon and the adsorption of Ponceau 4R using Tilapia fish scales activated carbon (Zhu et al. 2013, Bhomick et al. 2018).

Adsorption isotherm studies: For equilibrium adsorption studies, the Langmuir, Freundlich, and Temkin adsorption models were analyzed with the experimental data such as the initial CR concentration: 20 mg.L^{-1}, dosage: 0.25 g.L^{-1}, temperature: 25°C and contact time: 60 minutes, respectively. One of many assumptions of the Langmuir isotherm is that adsorption happens on homogenous surfaces possessing equally energetic adsorption sites. Furthermore, equilibrium in the adsorbate-adsorbent system is reached when the adsorption of the adsorbate is confined to a single molecular layer, occurring at or before a relative pressure of unity is achieved (Shen et al. 2018). Our findings indicate that the Langmuir isotherm provides a q$_{max}$ value of 19.58 mg.g^{-1} with an R^2 = 0.96, suggesting a good fit. Additionally, the calculated separation factor, R$_L$ = 0.035, indicates a favorable adsorption process (Giraldo & Moreno-Piraján 2014). The Freundlich isotherm analysis utilizes the heterogeneity factor,

represented as nF, to determine if the adsorption process is linear (nF = 1), chemical (nF < 1), or physical (nF > 1). Our results indicating nF = 0.278 and 1/nF = 3.602, suggest the favorability of physical processes and cooperative adsorption (Idrees et al. 2018). High R^2 = 0.99, obtained when fitting the data to Freundlich isotherm confirms its appropriateness for our study. The preference for the Freundlich model in describing the adsorption process indicates adsorption on a heterogeneous surface with varying energies, allowing for multiple layers of adsorbate molecules. This aligns with AC's complex surface structure and diverse active sites. Additionally, the Freundlich model fits well for adsorbents with high capacities, like AC with its large surface area. Overall, the choice of the Freundlich model suggests it best captured the observed adsorption behavior, likely due to its good fit with the experimental data.

Temkin isotherm is designed to explicitly assess adsorbent-adsorbate interactions, yet its effectiveness in explaining CR dye adsorption onto mFSAC is reduced by R^2 = 0.92, particularly when associated with the Langmuir and
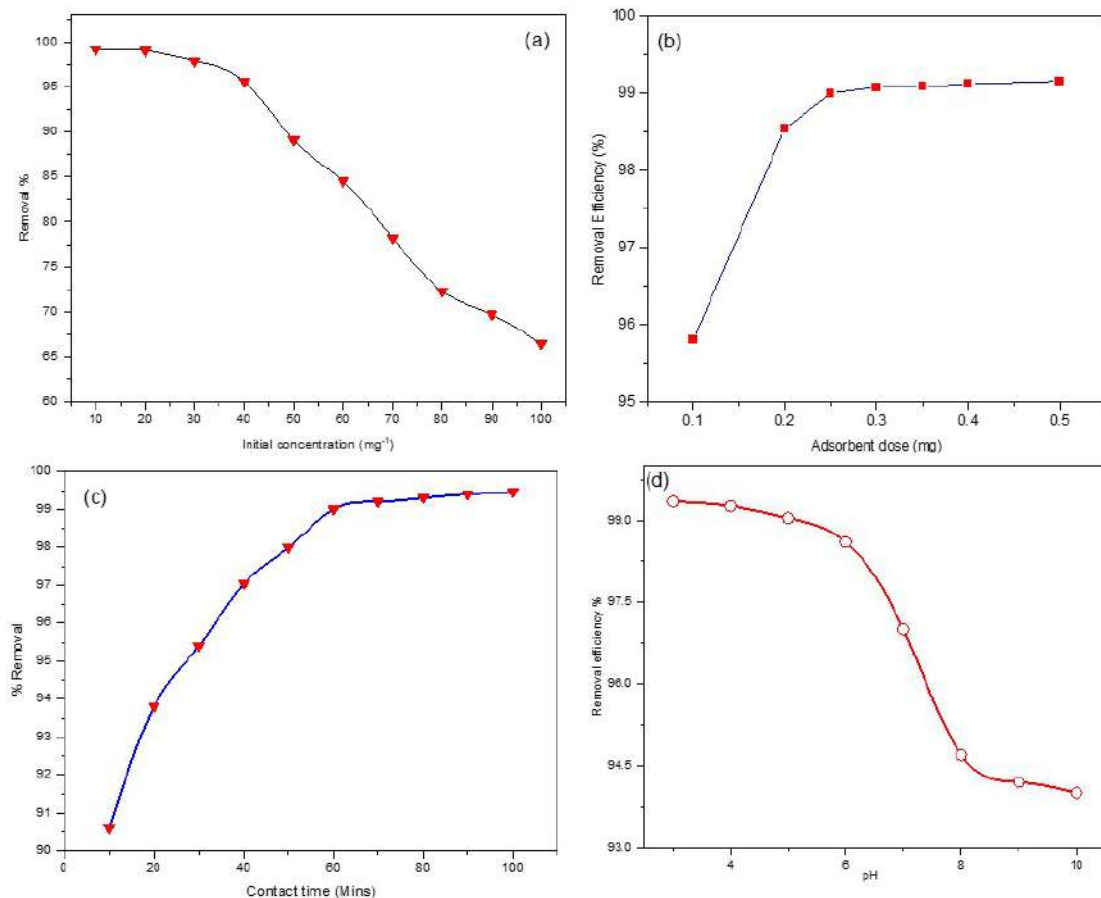

Fig. 8: Effect of mFSAC (a) Initial CR concentration (b) adsorbent dose (c) contact time and (d) pH.

Freundlich isotherms. The trial data indicates an exothermic process, as evidenced by a positive, BT = 8.56 which is associated with the heat of adsorption (Toor & Jin 2012, Ahmad et al. 2020b). Each adsorption isotherm model was confirmed using chi-square analysis. The Freundlich model exhibited the lowest χ^2 values followed by the Langmuir and Temkin models using equation 7. This suggests that the Freundlich model more accurately describes the CR dye adsorption. Table 2 shows the values for each adsorption isotherm parameter.

$$\chi^2 = \sum \frac{(q_{e(exp)} - q_{e(cal)})^2}{q_{e(cal)}} \qquad …(7)$$

Adsorption kinetics studies: Kinetic parameters are essential for developing and modeling the adsorption process, as well as understanding adsorption dynamics in relation to the order of rate constant. To know the experimental data for CR adsorption on mFSAC, models like pseudo-first-order (PFO), pseudo-second-order (PSO), intraparticle diffusion, and the Elovich model were analyzed. The earliest known equation that describes the adsorption capacity-based adsorption rate is the PFO (Bahgat et al. 2013). Whereas, the PSO is a chemisorption-based account of the adsorption process that contains valency forces and is explained by electron exchange between the sorbate and the solvent (Prajapati & Mondal 2020).

The PFO constant K_1 is derived from a linear plot of $\ln(q_e-q_t)$ vs time (Fig 9a). CR sorption on the mFSAC system was found to have a K_1 value of 0.00126/min, $R^2 = 0.85$, and an equilibrium sorption capacity $q_{e} = 1.958$ mg g^{-1}. PFO is less advantageous than pseudo-second order due to its lower correlation coefficient and higher Sum of Squares Error (SSE) value (Table 3). The PSO model's correlation coefficient value of $R^2 = 0.999$ demonstrates the applicability

of mFSAC (Fig 9b). In this context, the R^2 values have been determined to exhibit a stronger correlation, surpassing those of the PFO model by a significant margin. The results of the SSE study as well as $q_{e(cal)}$ and $q_{e(exp)}$ values further show that the PSO can more accurately and satisfactorily define the adsorption kinetics of CR onto mFSAC. Fig 9(c) depicts plots indicating the correlation between qt and $t_{1/2}$ for intraparticle diffusion. According to Demirbas and co-workers (Demirbas et al. 2008), the thickness of the boundary layer relies on the specific value of the intercept such that a thicker boundary layer results in a greater intercept value. The result indicates a different stage in the adsorption process, suggesting that intraparticle diffusion is the factor in the influence adsorption process. High $R^2 = 0.958$ indicates homogeneous pore structures with a strong linear relationship between solute uptake and the square root of time throughout the adsorption process (Adane et al. 2015). The Elovich model signifies that the rate of adsorption decreases over time and considers diffusion as the rate-determining phase (Grassi et al. 2019, Al-Harby et al. 2022). The outcomes are illustrated through a plot of qt against ln(t) resulting in a correlation coefficient $R^2 = 0.926$.

Thermodynamic studies: The assessment of thermodynamic parameters is a crucial and essential aspect of research on sorption processes which offer insights into whether the mechanism is predominantly influenced by chemical or physical interactions. The temperature range covered by the thermodynamic analysis of CR adsorption was 298 K to 328 K. The thermodynamic parameters can be calculated by using the equation below.

$$\ln K_d = \frac{\Delta S°}{R} - \frac{\Delta H°}{RT} \qquad …(8)$$

$$K_d = \frac{q_e}{C_e} \qquad …(9)$$

Table 2: Isotherm parameters for CR dye adsorption.

Isotherm	Equations	Parameters	R^2	
Langmuir	$q_e = \dfrac{K_L C_e}{1 + \alpha_L C_e}; \dfrac{C_e}{q_e} = \dfrac{1}{K_L} - \dfrac{\alpha_L}{K_L} C_e$	$q_{max}\left(\dfrac{\alpha_L}{K_L}\right) = 19.58$	0.96	0.0034
		$\dfrac{1}{nF} = 0.787$		
		$K_L = 0.961$		
		$R_L = 0.035$		
Freundlich	$Log\left(\dfrac{X}{M}\right) = \dfrac{1}{nF}(logC_e) + logK_F$	$\dfrac{1}{nF} = 3.602$	0.99	0.00031
		$K_L = 0.166$		
		$R_L = 0.231$		
		$K_F = 46.697$		
Temkin	$q_e = \dfrac{RT}{B_T} \ln(A_T C_e)$	$B_T = 8.56$	0.92	0.1801
		A= 3.16		

Table 3: Kinetic parameters of CR dye adsorption on mFSAC.

Kinetics	Equations	Parameters	R^2
Pseudo-first order	$\log(q_e - qt_t) = \log q_e - \dfrac{k1}{2.303}t$	$q_{e(exp)} = 1.958$ $k_1 = 0.00126$ SSE= 5.16 MSE= 0.73	0.85
Pseudo-Second order	$\dfrac{t}{q_t} = \dfrac{1}{k_2 q_e^2} + \dfrac{1}{q_e}t$	$q_{e(exp)} = 1.95$ $q_{e(cal)} = 1.97$ $k_2 = 1.08$ SSE=0.042 MSE= 0.007	0.99
Intraparticle diffusion	$q_t = k_b t^{1/2} + A$	$k_b = 0.010$ $q_{e(exp)} = 1.95$ $A(mg\ g^{-1}) = 1.864$	0.95
Elovich	$q_t = \dfrac{1}{\beta}\ln(\alpha\beta t) + \dfrac{1}{\beta}\ln(t)$	$a = 2.765$ $b = 3.278$ SSE = 0.54 MSE = 0.18	0.92
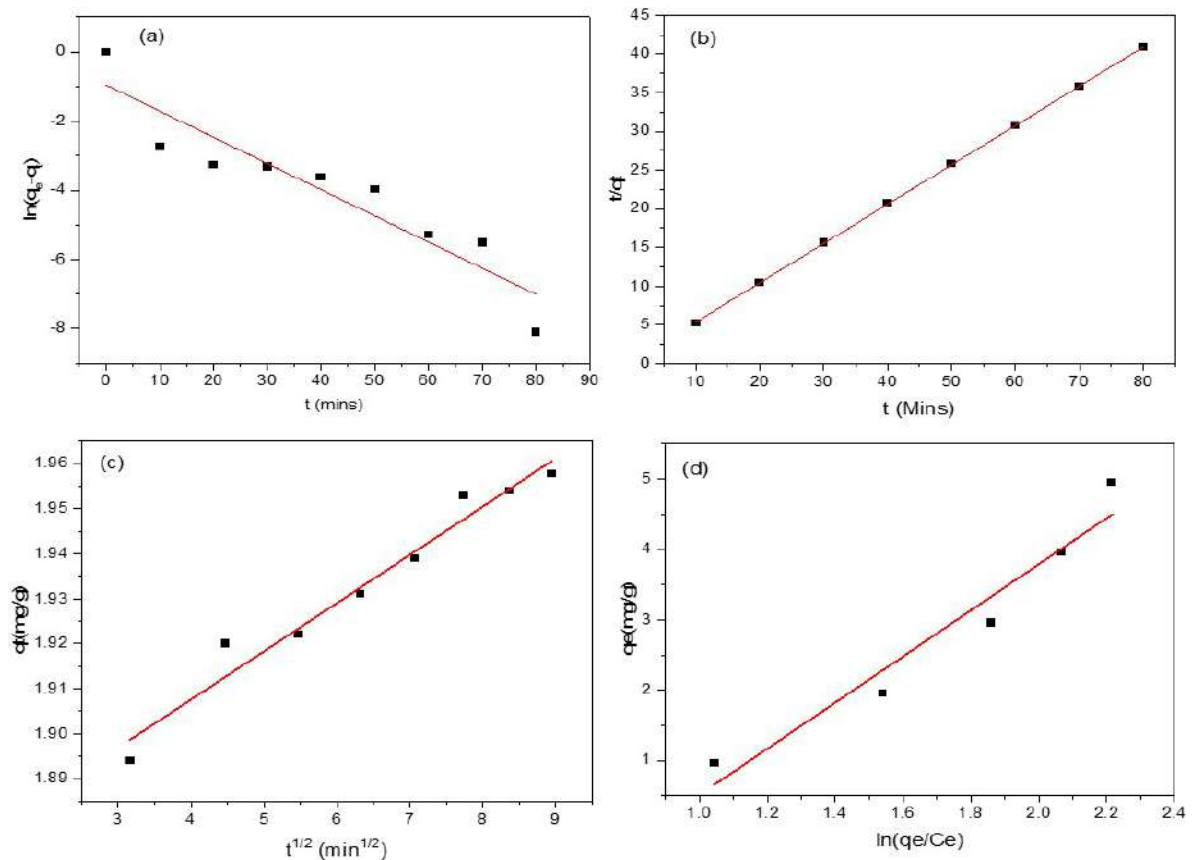
Fig. 9: (a) PFO (b) PSO (c) Intraparticle diffusion and (d) Elovich model.

$$\Delta G° = \Delta H° - T\Delta S° \qquad \ldots(10)$$

Here, Ce =equilibrium concentration (mg.L^{-1}), R = 8.314 J mol/K, T = temperature, and qe = amount of dye adsorbed.

The study revealed ΔH values of -96.62 kJ mol^{-1} for CR adsorption, suggesting an exothermic behavior, and -ΔG values indicating the spontaneity and vitality of the adsorption process. Whereas - ΔS proposed that the sorption is enthalpy-driven throughout the adsorption phase and the rise in ΔG value with temperature up to 318 K highlighted its viability at lower temperatures (Table 4).

Comparative study of mFSAC and other absorbents: To evaluate the effectiveness of the mFSAC, a comparison was made with other adsorbents for the removal of CR. The study analyzed the removal % of mFSAC in comparison to various other adsorbents (Table 5). The results indicate that the AC derived from mixed fish scale wastes demonstrates a comparable adsorptive capacity to that of other adsorbents, highlighting its potential as an effective adsorbent for the removal of CR.

Regeneration studies: A regeneration study of mFSAC was performed by mixing 0.25 g of mFSAC with 20 mL of a 20 mg L^{-1} CR solution and allowing it to stir for 60 minutes. The saturated carbon was then subjected to desorption for 2 hours with the addition of 0.1 M NaOH solution. After desorption, the mFSAC was dehydrated at 110°C in an oven, filtered, and rinsed with distilled water. Fig 10 illustrates the removal % of mFSAC over six cycles. The results indicate a removal efficacy of 99% in the first cycle, decreasing to 72.68% by the sixth cycle. These findings suggest that the mFSAC can be reused multiple times and can be calculated using the following equation.

$$\text{Desorption efficiency (\%)} = \frac{q_{de}}{q_{ad}} \times 100 \qquad \text{...(11)}$$

CONCLUSİONS

This research explores potential applications for waste mixed fish scales (mFS) in generating activated carbon (AC) for adsorption purposes. Various physical properties of mFSAC were examined through approaches such as CHNS, BET, SEM, FTIR, XRD, EDX, and XPS. By employing batch mode operation, parameters like AC dose, initial CR dye concentration, contact time, pH, and temperature were explored. The Freundlich isotherm showed the strongest correlation ($R^2 = 0.99$) for dye adsorption, indicating a favorable adsorption process. The pseudo-second-order model suggests that the adsorption mechanism is chemisorption, implying a strong interaction between CR dye molecules and the AC surface. Thermodynamic analysis revealed that the adsorption process is temperature-dependent and exothermic. In conclusion, the study highlights the potential of using AC derived from discarded fish scales as an effective adsorbent for CR dye. This suggests an opportunity to repurpose waste fish scales into AC, which can address waste management issues and provide a valuable resource for various industries thus offering economic benefits, promoting environmental sustainability, and reducing reliance on non-renewable resources.

Table 4: Thermodynamic parameters for CR dye onto mFSAC.

Adsorbent	ΔH° (kJ mol^{-1})	ΔS° (kJ mol^{-1})	ΔG° (kJ mol^{-1})			
			298K	308K	318K	328K
mFSAC	-96.62	-287.9	-11.40	-8.57	-3.19	-3.76

Table 5: Adsorption capacities of various adsorbents for CR removal.

| Adsorbate	Adsorbent	Optimum parameters				Adsorption capacity (mg.g^{-1})	Removal %	References
		Dosage	Initial concentration (mg.L^{-1})	Contact time	pH			
Congo red	Fishbone	5g	150	60 min	2	666.67	96.3	(Parvin et al. 2021)
	Cuttlefish bone	50mg	50	60 min	2	69.9	94	(Yazid et al. 2021)
	Bael shell	50mg	50	180 min	3	98.03	92	(Ahmad and Kumar 2010)
	Trichoderma	-	50	24 h	6	81.82	88	(Argumedo-Delira et al. 2021)
	Coffee waste	4g	50	180 min	3	90.90	96.8	(Lafi et al. 2019)
	Azolla filiculoides	2g	200	-	6.2	243	95	(Sundararaman et al. 2021)
	Saw dust	1g	-	2.5 h	2	209	96.76	(Srinivas Kini et al. 2017)
	Raphanus sativus peels	2g	-	20 min	3	0.06	94	(Rehman et al. 2012)
	Grewiaasiatica leave	0.5g	-	30 min	7	0.56	95	
	Mixed Fish Scales	0.25g	20	60 min	4	19.58	99	This Study
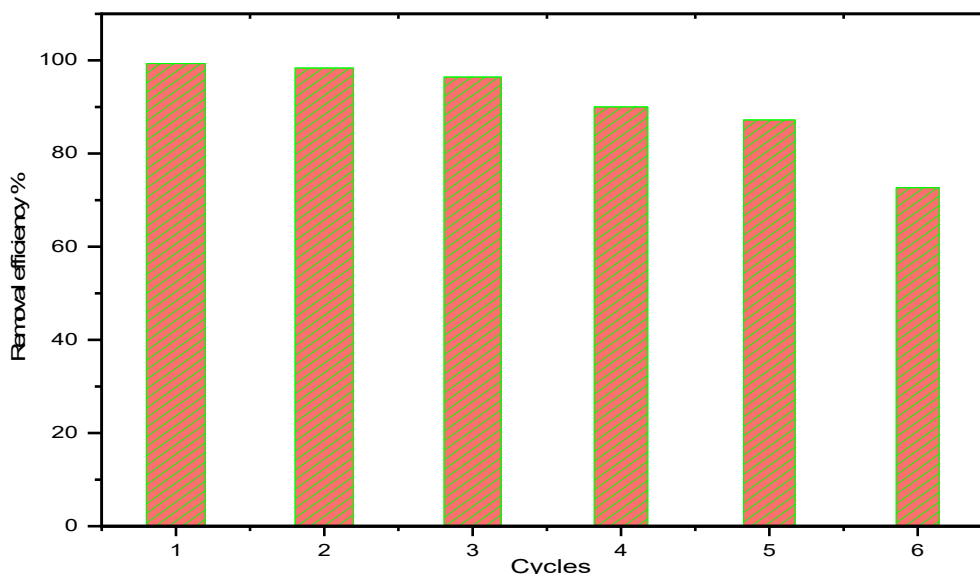
Fig. 10: Regeneration of mFSAC over six cycles.

REFERENCES

Adamu, A.D. and Adie, D.B., 2020. Assessment of lead adsorption onto rice husk activated carbon. *Nigerian Journal of Engineering*, 27(2), pp.2705–3954.

Adane, B., Siraj, K. and Meka, N., 2015. Kinetic, equilibrium and thermodynamic study of 2-chlorophenol adsorption onto Ricinus communis pericarp activated carbon from aqueous solutions. *Green Chemistry Letters and Reviews*, 8(3–4), pp.1–12. https://doi.org/10.1080/17518253.2015.1065348.

Adiotomre, K., 2015. Effectiveness of snail shell as an adsorbent for the treatment of waste water. *International Journal of Innovative Environmental Studies Research*, 3(3), pp.1–12.

Agarwal, S., Singh, A.P. and Mathur, S., 2023. Removal of COD and color from textile industrial wastewater using wheat straw activated carbon: an application of response surface and artificial neural network modeling. *Environmental Science and Pollution Research*, 30(14), pp.41073–41094. https://doi.org/10.1007/s11356-022-25066-2.

Ahmad, A., Jini, D., Aravind, M., Parvathiraja, C., Ali, R., Kiyani, M.Z. and Alothman, A., 2020a. A novel study on synthesis of egg shell based activated carbon for degradation of methylene blue via photocatalysis. *Arabian Journal of Chemistry*, 13(12), pp.8717–8722. https://doi.org/10.1016/j.arabjc.2020.10.002.

Ahmad, R. and Kumar, R., 2010. Adsorptive removal of congo red dye from aqueous solution using bael shell carbon. *Applied Surface Science*, 257(5), pp.1628–1633. https://doi.org/10.1016/j.apsusc.2010.08.111.

Ahmad, S., Kothari, R., Shankarayan, R. and Tyagi, V.V., 2020b. Temperature dependent morphological changes on algal growth and cell surface with dairy industry wastewater: an experimental investigation. *3 Biotech*, 10(1), pp.1–12. https://doi.org/10.1007/s13205-019-2008-x.

Alau, K.K., Gimba, C.E., Kagbu, J.A. and Nale, B.Y., 2010. Preparation of activated carbon from neem (Azadirachta indica) husk by chemical activation with H_3PO_4, KOH and $ZnCl_2$. *Arch. Appl. Sci. Res.*, 2(5), pp.451-455.

Al-Harby, N.F., Albahly, E.F. and Mohamed, N.A., 2022. Synthesis and Characterization of novel uracil-modified chitosan as a promising adsorbent for efficient removal of congo red dye. *Polymers*, 14(2), p.271. https://doi.org/10.3390/polym14020271.

Al-Malack, M.H. and Basaleh, A.A., 2016. Adsorption of heavy metals using activated carbon produced from municipal organic solid waste. *Desalination and Water Treatment*, 57(02), pp.24519–24531. https://doi.org/10.1080/19443994.2016.1144536.

Alkurdi, S.S.A., Herath, I., Bundschuh, J., Al-Juboori, R.A., Vithanage, M. and Mohan, D., 2019. Biochar versus bone char for a sustainable inorganic arsenic mitigation in water: What needs to be done in future research? *Environment International*, 127(3), pp.52–69. https://doi.org/10.1016/j.envint.2019.03.012.

An, J., Nhung, N.T.H., Ding, Y., Chen, H., He, C., Wang, X. and Fujita, T., 2022. Chestnut shell-activated carbon mixed with pyrolytic snail shells for methylene blue adsorption. *Materials*, 15(22), pp.1–25. https://doi.org/10.3390/ma15228227.

Argumedo-Delira, R., Gómez-Martínez, M.J. and Uribe-Kaffure, R., 2021. Trichoderma biomass as an alternative for removal of congo red and malachite green industrial dyes. *Applied Sciences*, 11(1), pp.1–15. https://doi.org/10.3390/app11010448.

ASTM, D., 2006. 4607-94, Standard test method for determination of iodine number of activated carbon. *ASTM International: West Conshohocken, PA, USA*.

Babić, B.M., Milonjić, S.K., Polovina, M.J. and Kaludierović, B.V., 1999. Point of zero charge and intrinsic equilibrium constants of activated carbon cloth. *Carbon*, 37(3), pp.477–481. https://doi.org/10.1016/S0008-6223(98)00216-4.

Bahgat, M., Farghali, A.A., El Rouby, W., Khedr, M. and Mohassab-Ahmed, M.Y., 2013. Adsorption of methyl green dye onto multi-walled carbon nanotubes decorated with Ni nanoferrite. *Applied Nanoscience*, 3(3), pp.251–261. https://doi.org/10.1007/s13204-012-0127-3.

Bal Altuntaş, D., Nevruzoğlu, V., Dokumacı, M. and Cam, Ş., 2020. Synthesis and characterization of activated carbon produced from waste human hair mass using chemical activation. *Carbon Letters*, 30(3), pp.307–313. https://doi.org/10.1007/s42823-019-00099-9.

Belaib, F. and Meniai, A.-H., 2016. The removal of cationic dye (Methyl green) dye by adsorbant based Silica gel/Polymer. *Algerian Journal of Engineering Research*, pp.1–5.

Beshkar, F., Zinatloo-Ajabshir, S., Bagheri, S. and Salavati-Niasari, M., 2017. Novel preparation of highly photocatalytically active copper chromite nanostructured material via a simple hydrothermal route. *PLoS One*, 12(6), pp.17–18. https://doi.org/10.1371/journal.pone.0158549.

Bhatia, D., Sharma, N.R., Singh, J. and Kanwar, R.S., 2017. Biological

methods for textile dye removal from wastewater: A review. *Critical Reviews in Environmental Science and Technology*, 47(19), pp.1836–1876. https://doi.org/10.1080/10643389.2017.1393263.

Bhomick, P.C., Supong, A., Baruah, M., Pongener, C. and Sinha, D., 2018. Pine Cone biomass as an efficient precursor for the synthesis of activated biocarbon for adsorption of anionic dye from aqueous solution: Isotherm, kinetic, thermodynamic and regeneration studies. *Sustainable Chemistry and Pharmacy*, 10(June), pp.41–49. https://doi.org/10.1016/j.scp.2018.09.001.

Bhomick, P.C., Supong, A., Karmaker, R., Baruah, M., Pongener, C. and Sinha, D., 2019. Activated carbon synthesized from biomass material using single-step KOH activation for adsorption of fluoride: Experimental and theoretical investigation. *Korean Journal of Chemical Engineering*, 36(4), pp.551–562. https://doi.org/10.1007/s11814-019-0234-x.

Boulika, H., El Hajam, M., Hajji Nabih, M., Riffi Karim, I., Idrissi Kandri, N. and Zerouale, A., 2023. Definitive screening design applied to cationic & anionic adsorption dyes on Almond shells activated carbon: Isotherm, kinetic and thermodynamic studies. *Materials Today: Proceedings*, 72(8), pp.3336–3346. https://doi.org/10.1016/j.matpr.2022.07.358.

Burchacka, E., Pstrowska, K., Beran, E., Fałtynowicz, H., Chojnacka, K. and Kułazynski, M., 2021. Antibacterial agents adsorbed on active carbon: a new approach for S. aureus and E. coli pathogen elimination. *Pathogens*, 10(8), pp.1–15.

Côrtes, L.N., Druzian, S.P., Streit, A.F.M., Godinho, M., Perondi, D., Collazzo, G.C., Oliveira, M.L.S., Cadaval, T.R.S. and Dotto, G.L., 2019. Biochars from animal wastes as alternative materials to treat colored effluents containing basic red 9. *Journal of Environmental Chemical Engineering*, 7(6), pp.1–39. https://doi.org/10.1016/j.jece.2019.103446.

Dai, Y., Wang, W., Lu, L., Yan, L. and Yu, D., 2020. Utilization of biochar for the removal of nitrogen and phosphorus. *Journal of Cleaner Production*, 257(2), p.120573. https://doi.org/10.1016/j.jclepro.2020.120573.

Demirbas, E., Kobya, M. and Sulak, M.T., 2008. Adsorption kinetics of a basic dye from aqueous solutions onto apricot stone activated carbon. *Bioresource Technology*, 99(13), pp.5368–5373. https://doi.org/10.1016/j.biortech.2007.11.019.

Feuzer-Matos, A.J., Testolin, R.C., Cotelle, S., Sanches-Simões, E., Pimentel-Almeida, W., Niero, G., Walz, G.C., Ariente-Neto, R., Somensi, C.A. and Radetski, C.M., 2021. Degradation of recalcitrant textile azo-dyes by fenton-based process followed by biochar polishing. *Journal of Environmental Science and Health - Part A*, 56(9), pp.1019–1029. https://doi.org/10.1080/10934529.2021.1959774.

Giraldo, L. and Moreno-Piraján, J.C., 2014. Study of adsorption of phenol on activated carbons obtained from eggshells. *Journal of Analytical and Applied Pyrolysis*, 106(12), pp.41–47. https://doi.org/10.1016/j.jaap.2013.12.007.

Grassi, P., Reis, C., Drumm, F.C., Georgin, J., Tonato, D., Escudero, L.B., Kuhn, R., Jahn, S.L. and Dotto, G.L., 2019. Biosorption of crystal violet dye using inactive biomass of the fungus Diaporthe schini. *Water Science and Technology*, 79(4), pp.709–717. https://doi.org/10.2166/wst.2019.091.

Habeeb, O.A., Kanthasamy, R., Ali, G.A.M. and Yunus, R.M., 2017. Isothermal modelling based experimental study of dissolved hydrogen sulfide adsorption from waste water using eggshell based activated carbon. *Malaysian Journal of Analytical Sciences*, 21(2), pp.334–345. https://doi.org/10.17576/mjas-2017-2102-08.

Hoslett, J., Massara, T.M., Malamis, S., Ahmad, D., van den Boogaert, I., Katsou, E., Ahmad, B., Ghazal, H., Simons, S., Wrobel, L. and Jouhara, H., 2018. Surface water filtration using granular media and membranes: A review. *Science of the Total Environment*, 639(05), pp.1268–1282. https://doi.org/10.1016/j.scitotenv.2018.05.247.

Ibrahim, W.M., Hassan, A.F. and Azab, Y.A., 2016. Biosorption of toxic heavy metals from aqueous solution by Ulva lactuca activated activated carbon. *Egyptian Journal of Basic and Applied Sciences*, 3(3), pp.241–249. https://doi.org/10.1016/j.ejbas.2016.07.005.

Idrees, M., Batool, S., Kalsoom, T., Yasmeen, S., Kalsoom, A., Raina, S. and Kong, J., 2018. Animal manure-derived biochars produced via fast pyrolysis for the removal of divalent copper from aqueous media. *Journal of Environmental Management*, 213(2), pp.109–118. https://doi.org/10.1016/j.jenvman.2018.02.003.

Islam, M.M., Mohana, A.A., Rahman, M.A., Rahman, M., Naidu, R. and Rahman, M.M., 2023. A comprehensive review of the current progress of chromium removal methods from aqueous solution. *Toxics*, 11(3), pp.1–43. https://doi.org/10.3390/toxics11030252.

Jain, R. and Sikarwar, S., 2014. Adsorption and desorption studies of Congo red using low-cost adsorbent: activated de-oiled mustard. *Desalination and Water Treatment*, 52(37–39), pp.7400–7411. https://doi.org/10.1080/19443994.2013.837004.

Jasińska, A., Soboń, A., Góralczyk-Bińkowska, A. and Długoński, J., 2019. Analysis of decolorization potential of *Myrothecium roridum* in the light of its secretome and toxicological studies. *Environmental Science and Pollution Research*, 26(25), pp.26313–26323. https://doi.org/10.1007/s11356-019-05324-6.

Jedynak, K. and Charmas, B., 2024. Adsorption properties of biochars obtained by KOH activation. *Adsorption*, 30(2), pp.167–183. https://doi.org/10.1007/s10450-023-00399-7.

Jerome Sunday, N., 2019. Efficiency of animal (cow, donkey, chicken and horse) bones, in removal of hexavalent chromium from aqueous solution as a low cost adsorbent. *American Journal of Applied Chemistry*, 7(1), p.1. https://doi.org/10.11648/j.ajac.20190701.11.

Jiang, H., Guo, G., Chen, W. and Cui, Z., 2021. Reactive dyeing of synthetic fibers employing dyes containing a diazirine moiety. *Dyes and Pigments*, 194(1), p.109555. https://doi.org/10.1016/j.dyepig.2021.109555.

Jorfi, S., Barzegar, G., Ahmadi, M., Darvishi Cheshmeh Soltani, R., Alah Jafarzadeh Haghighifard, N., Takdastan, A., Saeedi, R. and Abtahi, M., 2016. Enhanced coagulation-photocatalytic treatment of Acid red 73 dye and real textile wastewater using UVA/synthesized MgO nanoparticles. *Journal of Environmental Management*, 177(07), pp.111–118. https://doi.org/10.1016/j.jenvman.2016.04.005.

Kandasamy, S., Madhusoodanan, N., Senthilkumar, P., Muneeswaran, V., Manickam, N. and Myneni, V.R., 2023. Adsorption of methylene blue dye by animal dung biomass–derived activated carbon: optimization, isotherms and kinetic studies. *Biomass Conversion and Biorefinery*, (8), pp.1–15. https://doi.org/10.1007/s13399-023-04710-y.

Khan, A.M., Usmani, M.A., Yasmeen, K., Ahmed, M.N., Obaid, M., Afshan Naz, S., Wajid, M., Chan, H. and Khan, A., 2023a. Conversion of waste animal bones to biofertilizer and adsorbent for wastewater treatment: An innovative approach to develop zero-waste technology.

Khan, Z.U.H., Gul, N.S., Sabahat, S., et al., 2023b. Removal of organic pollutants through hydroxyl radical-based advanced oxidation processes. *Ecotoxicology and Environmental Safety*, 267(10), p.115564. https://doi.org/10.1016/j.ecoenv.2023.115564.

Kodali, D., Hembrick-Holloman, V., Gunturu, D.R., Samuel, T., Jeelani, S. and Rangari, V.K., 2022. Influence of Fish Scale-Based Hydroxyapatite on Forcespun Polycaprolactone Fiber Scaffolds. *ACS Omega*, 7(10), pp.8323–8335. https://doi.org/10.1021/acsomega.1c05593.

Kosheleva, R.I., Mitropoulos, A.C. and Kyzas, G.Z., 2019. Synthesis of activated carbon from food waste. *Environmental Chemistry Letters*, 17(1), pp.429–438. https://doi.org/10.1007/s10311-018-0817-5.

Lade, H., Govindwar, S. and Paul, D., 2015. Mineralization and detoxification of the carcinogenic azo dye Congo red and real textile effluent by a polyurethane foam immobilized microbial consortium in an upflow column bioreactor. *International Journal of Environmental Research and Public Health*, 12(6), pp.6894–6918. https://doi.org/10.3390/ijerph120606894.

Lafi, R., Montasser, I. and Hafiane, A., 2019. Adsorption of congo

red dye from aqueous solutions by prepared activated carbon with oxygen-containing functional groups and its regeneration. *Adsorption Science & Technology*, 37(1–2), pp.160–181. https://doi.org/10.1177/0263617418819227.

Li, H., Fei, J., Chen, S., Jones, K.C., Li, S., Chen, W. and Liang, Y., 2023. An easily-synthesized low carbon ionic liquid functionalized metal-organic framework composite material to remove Congo red from water. *Water Cycle*, 4(5), pp.127–134. https://doi.org/10.1016/j.watcyc.2023.05.004.

Limousy, L., Ghouma, I., Ouederni, A. and Jeguirim, M., 2017. Amoxicillin removal from aqueous solution using activated carbon prepared by chemical activation of olive stone. *Environmental Science and Pollution Research*, pp.9993–10004. https://doi.org/10.1007/s11356-016-7404-8.

Liu, H., Ning, W., Cheng, P., Zhang, J., Wang, Y. and Zhang, C., 2013a. Evaluation of animal hairs-based activated carbon for sorption of norfloxacin and acetaminophen by comparing with cattail fiber-based activated carbon. *Journal of Analytical and Applied Pyrolysis*, 5(101), pp.156–165.

Liu, H., Ning, W., Cheng, P., Zhang, J., Wang, Y. and Zhang, C., 2013b. Evaluation of animal hairs-based activated carbon for sorption of norfloxacin and acetaminophen by comparing with cattail fiber-based activated carbon. *Journal of Analytical and Applied Pyrolysis*, 101, pp.156–165. https://doi.org/10.1016/j.jaap.2013.01.016.

Liu, Y., Xu, J., Cao, Z., Fu, R., Zhou, C., Wang, Z. and Xu, X., 2020. Adsorption behavior and mechanism of Pb(II) and complex Cu(II) species by biowaste-derived char with amino functionalization. *Journal of Colloid and Interface Science*, 559(10), pp.215–225. https://doi.org/10.1016/j.jcis.2019.10.035.

Lotha, T.N., Sorhie, V., Bharali, P. and Jamir, L., 2024. Advancement in Sustainable Wastewater Treatment: A Multifaceted Approach to Textile Dye Removal through Physical, Biological and Chemical Techniques. *ChemistrySelect*, 11(9), p.e202304093. https://doi.org/10.1002/slct.202304093.

Lou, Z., Wang, Q., Kara, U.I., Mamtani, R.S., Zhou, X., Bian, H., Yang, Z., Li, Y., Lv, H., Adera, S. and Wang, X., 2022. Biomass-derived carbon heterostructures enable environmentally adaptive wideband electromagnetic wave absorbers. *Nano-Micro Letters*, 14(1), pp.1–16. https://doi.org/10.1007/s40820-021-00750-z.

Luo, X., Song, X., Cao, Y., Song, L. and Bu, X., 2020. Investigation of calcium carbonate synthesized by steamed ammonia liquid waste without use of additives. *RSC Advances*, 10(13), pp.7976–7986. https://doi.org/10.1039/c9ra10460g.

Manjuladevi, M. and Sri, O.M., 2017. Heavy metals removal from industrial wastewater by nano adsorbent prepared from *Cucumis melopeel* activated carbon. *Journal of Nanomedicine Research*, 5(1), pp.1–4. https://doi.org/10.15406/jnmr.2017.05.00102.

Mondal, N.K. and Basu, S., 2019. Potentiality of waste human hair towards removal of chromium(VI) from solution: kinetic and equilibrium studies. *Applied Water Science*, 9(3), pp.1–8. https://doi.org/10.1007/s13201-019-0929-5.

Mukherjee, A., Zimmerman, A.R. and Harris, W., 2011. Surface chemistry variations among a series of laboratory-produced biochars. *Geoderma*, 163(3–4), pp.247–255. https://doi.org/10.1016/j.geoderma.2011.04.021.

Muthukumaran, C., Sivakumar, V.M. and Thirumarimurugan, M., 2016. Adsorption isotherms and kinetic studies of crystal violet dye removal from aqueous solution using surfactant modified magnetic nanoadsorbent. *Journal of the Taiwan Institute of Chemical Engineers*, 63(6), pp.354–362. https://doi.org/10.1016/j.jtice.2016.03.034.

Muzarpar, M.S., Leman, A.M., Rahman, K.A., Shayfull, Z. and Irfan, A.R., 2020. Exploration sustainable base material for activated carbon production using agriculture waste as raw materials: a review. *IOP Conference Series: Materials Science and Engineering*, 864(1). https://doi.org/10.1088/1757-899X/864/1/012022.

Nejadshafiee, V. and Islami, M.R., 2019. Adsorption capacity of heavy metal ions using sultone-modified magnetic activated carbon as a bio-adsorbent. *Materials Science and Engineering: C*, 101(July), pp.42–52. https://doi.org/10.1016/j.msec.2019.03.081.

Park, J.E., Lee, G.B., Kim, H. and Hong, B.U., 2022. High surface area–activated carbon production from cow manure controlled by heat treatment conditions. *Processes*, 10(7), pp.1–13. https://doi.org/10.3390/pr10071282.

Parvin, S., Hussain, M.M., Akter, F. and Biswas, B.K., 2021. Removal of congo red by silver carp (hypophthalmichthys molitrix) fish bone powder: kinetics, equilibrium, and thermodynamic study. *Journal of Chemistry*, 2021. https://doi.org/10.1155/2021/9535644.

Pathak, H., 2023. Impact, adaptation, and mitigation of climate change in Indian agriculture. *Environmental Monitoring and Assessment*, 195(1), pp.1–22. https://doi.org/10.1007/s10661-022-10537-3.

Pongener, C., Bhomick, P.C., Supong, A., Baruah, M., Sinha, U.B. and Sinha, D., 2018. Adsorption of fluoride onto activated carbon synthesized from Manihot esculenta biomass - Equilibrium, kinetic and thermodynamic studies. *Journal of Environmental Chemical Engineering*, 6(2), pp.2382–2389. https://doi.org/10.1016/j.jece.2018.02.045.

Prajapati, A.K. and Mondal, M.K., 2020. Comprehensive kinetic and mass transfer modeling for methylene blue dye adsorption onto CuO nanoparticles loaded on nanoporous activated carbon prepared from waste coconut shell. *Journal of Molecular Liquids*, 307(3), p.112949. https://doi.org/10.1016/j.molliq.2020.112949.

Rajhans, G., Sen, S.K., Barik, A. and Raut, S., 2020. Elucidation of fungal dye-decolourizing peroxidase (DyP) and ligninolytic enzyme activities in decolourization and mineralization of azo dyes. *Journal of Applied Microbiology*, 129(6), pp.1633–1643. https://doi.org/10.1111/jam.14731.

Rajkumar, S., Murugesh, S., Sivasankar, V., Darchen, A., Msagati, T.A.M. and Chaabane, T., 2019. Low-cost fluoride adsorbents prepared from a renewable biowaste: Syntheses, characterization and modeling studies. *Arabian Journal of Chemistry*, 12(8), pp.3004–3017. https://doi.org/10.1016/j.arabjc.2015.06.028.

Rehman, R., Abbas, A., Murtaza, S., Mahmud, T., Waheed-Uz-Zaman, Salman, M. and Shafique, U., 2012. Comparative removal of Congo Red dye from water by adsorption on *Grewia asiatica* leaves, Raphanus sativus peels and activated charcoal. *Journal of the Chemical Society of Pakistan*, 34(1), pp.112–119.

Sh, H., El-taweel, R.M., Alrefaey, K.A., Labena, A., Fahim, I.S., Said, L.A. and Radwan, A.G., 2024. Enhanced removal of crystal violet using raw fava bean peels, its chemically activated carbon compared with commercial activated carbon. *Case Studies in Chemical and Environmental Engineering*, 9(10), p.100534. https://doi.org/10.1016/j.cscee.2023.100534.

Shen, F., Liu, J., Zhang, Z., Dong, Y. and Gu, C., 2018. Density functional study of hydrogen sulfide adsorption mechanism on activated carbon. *Fuel Processing Technology*, 171(9), pp.258–264. https://doi.org/10.1016/j.fuproc.2017.11.026.

Shukla, S.K., Al Mushaiqri, N.R.S., Al Subhi, H.M., Yoo, K. and Al Sadeq, H., 2020. Low-cost activated carbon production from organic waste and its utilization for wastewater treatment. *Applied Water Science*, 10(2), pp.1–9. https://doi.org/10.1007/s13201-020-1145-z.

Srinivas Kini, M., Balakrishna Prabhu, K., Gundecha, A. and Devika, U., 2017. Statistical analysis of Congo red dye removal using sawdust activated carbon. *International Journal of Applied Engineering Research*, 12(19), pp.8788–8804.

Standard, A.S.T.M., 1999. Standard test methods for moisture in activated carbon. *Philadelphia, PA: ASTM Committee on Standards*.

Stevens, M.G.F. and Batlokwa, B.S., 2017. Environmentally friendly and cheap removal of lead (ii) and zinc (ii) from wastewater with fish scales

waste remains. *International Journal of Chemistry*, 9(4), p.22. https://doi.org/10.5539/ijc.v9n4p22.

Sundararaman, S., Kumar, P.S., Deivasigamani, P., Jagadeesan, A.K., Devaerakkam, M., Al-Hashimi, A. and Choi, D., 2021. Assessing the plant phytoremediation efficacy for azolla filiculoides in the treatment of textile effluent and redemption of Congo red dye onto azolla biomass. *Sustainability*, 13(17). https://doi.org/10.3390/su13179588.

Supong, A., Bhomick, P.C., Baruah, M., Pongener, C., Sinha, U.B. and Sinha, D., 2019a. Adsorptive removal of Bisphenol A by biomass activated carbon and insights into the adsorption mechanism through density functional theory calculations. *Sustainable Chemistry and Pharmacy*, 13(April), p.100159. https://doi.org/10.1016/j.scp.2019.100159.

Supong, A., Bhomick, P.C., Karmaker, R., Ezung, S.L., Jamir, L., Sinha, U.B. and Sinha, D., 2020. Experimental and theoretical insight into the adsorption of phenol and 2,4-dinitrophenol onto Tithonia diversifolia activated carbon. *Applied Surface Science*, 529(06), p.147046. https://doi.org/10.1016/j.apsusc.2020.147046.

Supong, A., Bhomick, P.C., Sinha, U.B. and Sinha, D., 2019b. A combined experimental and theoretical investigation of the adsorption of 4-Nitrophenol on activated biocarbon using DFT method. *Korean Journal of Chemical Engineering*, 36(12), pp.2023–2034. https://doi.org/10.1007/s11814-019-0382-z.

Supong, A., Sinha, U.B. and Sinha, D., 2022. Density functional theory calculations of the effect of oxygenated functionals on activated carbon towards cresol adsorption. *Surfaces*, 5(2), pp.280–289. https://doi.org/10.3390/surfaces5020020.

Toor, M. and Jin, B., 2012. Adsorption characteristics, isotherm, kinetics, and diffusion of modified natural bentonite for removing diazo dye. *Chemical Engineering Journal*, 187, pp.79–88. https://doi.org/10.1016/j.cej.2012.01.089.

Torres, F.G., Troncoso, O.P., Nakamatsu, J., Grande, C.J. and Gómez, C.M., 2008. Characterization of the nanocomposite laminate structure occurring in fish scales from Arapaima Gigas. *Materials Science and Engineering: C*, 28(8), pp.1276–1283. https://doi.org/10.1016/j.msec.2007.12.001.

Ukanwa, K.S., Patchigolla, K., Sakrabani, R., Anthony, E. and Mandavgane, S., 2019. A review of chemicals to produce activated carbon from agricultural waste biomass. *Sustainability*, 11(22), pp.1–35. https://doi.org/10.3390/su11226204.

Van Tran, T., Bui, Q.T.P., Nguyen, T.D., Le, N.T.H. and Bach, L.G., 2017. A comparative study on the removal efficiency of metal ions (Cu²⁺, Ni²⁺,

and Pb²⁺) using sugarcane bagasse-derived ZnCl₂-activated carbon by the response surface methodology. *Adsorption Science & Technology*, 35(1–2), pp.72–85. https://doi.org/10.1177/0263617416669152.

Wang, X., Zhang, A., Chen, M., Seliem, M.K., Mobarak, M., Diao, Z. and Li, Z., 2023. Adsorption of azo dyes and Naproxen by few-layer MXene immobilized with dialdehyde starch nanoparticles: Adsorption properties and statistical physics modeling. *Chemical Engineering Journal*, 473(10), p.145385.

Yazid, H., Achour, Y., Kassimi, A.E., Nadir, I., Himri, M.E., Laamari, M.R. and Haddad, M.E., 2021. Removal of congo red from aqueous solution using cuttlefish bone powder. *Physical Chemistry Research*, 9(4), pp.565–577. https://doi.org/10.22036/pcr.2021.278943.1901.

Yin, H., Qiu, P., Qian, Y., Kong, Z., Zheng, X., Tang, X.Z. and Guo, H., 2019. Textile wastewater treatment for water reuse: A case study. *Processes*, 7(1), pp.1–21. https://doi.org/10.3390/pr7010034.

Zhang, S., Zheng, M., Lin, Z., Li, N., Liu, Y., Zhao, B., Pang, H., Cao, J., He, P. and Shi, Y., 2014. Activated carbon with ultrahigh specific surface area synthesized from natural plant material for lithium-sulfur batteries. *Journal of Materials Chemistry A*, 2(38), pp.15889–15896. https://doi.org/10.1039/c4ta03503h.

Zhou, Y., Ge, L., Fan, N. and Xia, M., 2018. Adsorption of Congo red from aqueous solution onto shrimp shell powder. *Adsorption Science & Technology*, 36(5–6), pp.1310–1330. https://doi.org/10.1177/0263617418768945.

Zhu, K., Gong, X., He, D., Li, B., Ji, D., Li, P., Peng, Z. and Luo, Y., 2013. Adsorption of Ponceau 4R from aqueous solutions using alkali boiled Tilapia fish scales. *RSC Advances*, 3(47), pp.25221–25230. https://doi.org/10.1039/c3ra43817a.

ORCID DETAILS OF THE AUTHORS

Vevosa Nakro: https://orcid.org/0000-0002-0487-0148
Ketiyala Ao: https://orcid.org/0009-0001-2330-2963
Tsenbeni N Lotha: https://orcid.org/0000-0002-5337-7851
Imkongyanger Ao: https://orcid.org/0009-0002-7116-6756
Lemzila Rudithongru: https://orcid.org/0000-0003-3983-9279
Chubaakum Pongener: https://orcid.org/0000-0002-7708-7162
Merangmenla Aier: https://orcid.org/0000-0002-3672-3126
Aola Supong: https://orcid.org/0000-0003-4367-6775
Latonglila Jamir: https://orcid.org/0000-0003-4039-9426

Utilization of Plastic Waste and Dry leaves in Brick Manufacturing

P. Muthupriya[1]† and **B. Vignesh Kumar[2]**

[1]Department of Civil Engineering, Sri Krishna College of Engineering and Technology, Coimbatore, Tamil Nadu, India
[2]Department of Civil Engineering, Dr. N.G.P. Institute of Technology, Coimbatore, Tamil Nadu, India
†Corresponding author: P. Muthupriya; drmuthupriya@gmail.com

ABSTRACT

The utilization of plastic waste and dry leaves in bricks is a sustainable approach to reducing environmental pollution and managing waste. This study aims to investigate the feasibility of incorporating plastic wastes and dry leaves into the manufacturing of bricks, as well as the potential benefits of using such bricks. The study involves the collection of plastic wastes and dry leaves, sorting and cleaning them before mixing them with clay, sand, and cement in varying proportions. The mixtures are then compressed and molded into bricks, which are allowed to dry and cure before being tested for their physical and mechanical properties. To create plastic soil blocks, the soil was added to the molten plastic paste along with dry leaves in the following ratios: 1.5:1.5:0.5 (plastic, soil, and dry leaves, respectively). Results of the study showed that the inclusion of plastic wastes and dry leaves in brick production can lead to significant improvements in properties such as compressive strength, water absorption, and durability. Furthermore, the use of such bricks can help to reduce the amount of plastic waste and dry leaves in the environment, and also provide a sustainable alternative to traditional bricks that use finite natural resources. In conclusion, the utilization of plastic wastes and dry leaves in bricks is a promising approach toward sustainable construction. Further research is needed to optimize the proportions of the materials used and to investigate the long-term durability of the bricks under different environmental conditions.

INTRODUCTION

Plastic waste is a growing environmental challenge, with large quantities accumulating in landfills and marine ecosystems. In landfills, this waste contributes to the emission of harmful greenhouse gases like methane and carbon dioxide, which accelerate climate change. In marine environments, plastic pollution endangers aquatic life, increasing the risks of entanglement, ingestion, and suffocation for countless species. More than 1,500 species in terrestrial and marine settings have been found to consume plastics, according to research.

Innovative approaches are needed to address these issues sustainably. One such solution is the incorporation of plastic waste and dry leaves into brick production. This method not only diverts plastic from landfills and oceans but also provides an opportunity to reduce the reliance on traditional, resource-intensive brick-making materials. The global production of plastic and the accumulation of plastic waste have been escalating at an alarming rate, resulting in environmental pollution and ecological damage.

Plastic waste and dry leaves can be used as alternative materials in the production of bricks, which can have environmental and economic benefits. Plastic waste, which is a major contributor to pollution and environmental degradation, can be collected and shredded into small pieces to create a material that can be mixed with traditional brick-making materials such as clay or cement. The resulting bricks can be more durable and weather-resistant than traditional bricks and also have the potential to reduce the amount of plastic waste that ends up in landfills and oceans. Dry leaves, which are a common agricultural waste product, can also be used in the production of bricks. When mixed with clay or other materials, they can improve the insulation properties of the bricks and also reduce the amount of energy needed to fire them. Combining plastic waste and dry leaves in brick production can create a sustainable solution that helps reduce waste and provides an alternative to traditional building materials. However, more research and development are needed to ensure the durability and safety of these alternative bricks and to optimize their production processes.

Recycling waste has the dual benefits of conserving natural resources and ensuring safe, effective disposal of waste. The goal of this research is to create bricks with structural performance that is either the same or better than that of traditional clay-fired bricks by using waste

materials, such as waste plastic and dry leaves. A variety of tests, including compressive, splitting tensile, flexural, density, efflorescence, and water absorption, were used to evaluate the manufactured brick's mechanical and physical characteristics. By converting the building sector from a linear to a circular economy, waste material utilization can make it more sustainable. Additionally, lowering pollution levels would guarantee a safe environment for coming generations.

This research aims to explore sustainable alternatives in brick manufacturing by incorporating waste materials such as plastic and dry leaves. The primary objective is to reduce dependence on soil, a key resource in traditional brick production, thereby conserving natural resources. Another goal is to lower construction costs by developing cost-effective bricks using readily available waste materials. Additionally, the study aims to effectively utilize agricultural residues, specifically guava dry leaves, by analyzing their properties and integrating them into the brick-making process. Furthermore, the research seeks to introduce innovative construction materials that advance sustainable practices in civil engineering.

Swinnerton et al. (2024) highlighted in their study on plastic waste that the use of small-scale recycling plants to manufacture plastic-waste bricks is expanding globally. This approach provides an opportunity not only to remove plastic waste from landfills and the environment but also to foster economic opportunities and development, particularly in underserved communities with mismanaged solid waste facilities. However, the rapid expansion of these facilities, coupled with the lack of control measures or consistency in manufacturing procedures, highlights the urgent need to improve understanding of their occupational health and environmental impacts.

LITERATURE REVIEW

The utilization of dry leaves and plastic waste in the manufacturing of bricks has been gaining significant attention in recent years as a sustainable approach to waste management. Several studies have investigated the feasibility and potential benefits of incorporating plastic waste into bricks, and the following is a literature review of some of these studies.

Ram & Singh (2017) investigated to study the feasibility of using plastic waste in the manufacturing of bricks. The study involved mixing varying amounts of plastic waste with clay and then firing the resulting bricks at different temperatures. The authors evaluated the physical and mechanical properties of the bricks, including compressive strength, water absorption, and density. The study found that the addition of plastic waste had a positive impact on

the properties of the bricks, including increased compressive strength and reduced water absorption. Overall, the article provides valuable insights into the potential of using plastic waste in brick production and highlights the importance of exploring sustainable alternatives to traditional building materials.

Jadhav & Nimbalkar (2018) investigated to explore the feasibility of using plastic waste as a raw material in the manufacturing of bricks. The study found that the addition of plastic waste had a positive impact on the properties of the bricks, including increased compressive strength and reduced water absorption. The authors noted that the use of plastic waste in brick production can be an effective strategy for reducing environmental impact and promoting sustainable development.

El-Mohr et al. (2019) studied the utilization of sawdust and waste plastic in the manufacturing of eco-friendly fired bricks. It is observed that the addition of sawdust and waste plastic in the clay mixture resulted in a reduction in the water absorption capacity and an increase in compressive strength. Also found that the incorporation of sawdust and waste plastic in fired bricks improved their thermal insulation properties. It is suggested that the use of sawdust and waste plastic in the manufacturing of fired bricks could provide a sustainable solution for waste management and reduce the environmental impact of conventional brick manufacturing. The study highlights the potential of fired bricks as a sustainable alternative to conventional clay bricks, and the addition of sawdust and waste plastic further improves their properties and sustainability. Nampoothiri et al. (2019) investigated the effect of adding plastic waste to fly ash bricks, which are a type of sustainable brick made from industrial waste. The researchers found that adding up to 5% plastic waste to fly ash bricks improved their compressive strength and reduced their water absorption capacity.

Agrawal & Bhakar (2020) examined the various methods of recycling plastic waste and discussed the advantages and disadvantages of using plastic waste in brick-making. It discusses the potential environmental and economic benefits of using plastic waste in brick-making, including the reduction of waste in landfills and the creation of low-cost building materials. The review concludes that using plastic waste in brick-making has the potential to be a sustainable solution for both waste management and building construction.

Khatib et al. (2020) investigated the feasibility of using plastic waste in the production of interlocking paving blocks. The researchers found that adding up to 10% plastic waste to the blocks improved their compressive strength and reduced their water absorption capacity.

Kumar et al. (2020) investigated the utilization of agricultural waste and plastic waste in the manufacturing of eco-friendly bricks. It was found that the addition of agricultural waste (rice husk ash and sugarcane bagasse ash) and plastic waste in the clay mixture resulted in a reduction in the water absorption capacity and an increase in compressive strength. They also found that the incorporation of agricultural and plastic waste in bricks improved their thermal insulation properties. The authors suggested that the use of agricultural and plastic waste in the manufacturing of bricks could provide a sustainable solution for waste management and reduce the environmental impact of conventional brick manufacturing.

Yadav & Pandey (2020) conducted a study to investigate the potential of using waste plastic and biomass as raw materials for the production of eco-friendly bricks. The study involved mixing varying amounts of waste plastic and biomass with clay and then firing the resulting bricks at different temperatures. They evaluated the physical and mechanical properties of the bricks, including compressive strength, water absorption, and density. The study found that the addition of waste plastic and biomass had a positive impact on the properties of the bricks, including increased compressive strength and reduced water absorption. The article also discusses the environmental benefits of using waste plastic and biomass in brick production, including reducing waste and emissions associated with traditional brick production.

Dubey et al. (2021) investigated the utilization of plastic waste in the manufacturing of geopolymer bricks. Geopolymer bricks are an eco-friendly alternative to conventional clay bricks and are manufactured using industrial by-products such as fly ash, slag, and metakaolin. It was found that the addition of plastic waste in the geopolymer mix resulted in a reduction in the water absorption capacity and an increase in compressive strength. Also found that the incorporation of plastic waste in geopolymer bricks improved their thermal insulation properties. It is suggested that the use of plastic waste in the manufacturing of geopolymer bricks could provide a sustainable solution for waste management and reduce the environmental impact of conventional brick manufacturing. The study highlights the potential of geopolymer bricks as a sustainable alternative to conventional clay bricks, and the addition of plastic waste further improves their properties and sustainability.

Han et al. (2021) investigated the effect of sawdust on the thermal properties of biomass plastic bricks and found that the addition of sawdust to the plastic mixture resulted in a reduction in the thermal conductivity and an increase in the thermal resistance of the bricks. Also found that the incorporation of sawdust in biomass plastic bricks improved their thermal insulation properties. It is suggested that the use of sawdust in the manufacturing of biomass plastic bricks could provide a sustainable solution for waste management and improve the thermal insulation properties of the bricks. The study highlights the potential of biomass plastic bricks as a sustainable alternative to conventional clay bricks, and the addition of sawdust further improves their thermal properties and sustainability.

Singh et al. (2021) investigated the use of dry leaves and plastic waste as partial or complete substitutes for traditional materials used in brick production. The authors also highlighted some of the challenges associated with using these waste materials, such as the need for proper sorting and processing of the waste, as well as the need for additional testing to ensure that the resulting bricks meet the necessary standards for strength and durability. Overall, the article provides a comprehensive overview of the potential benefits and challenges of using dry leaves and plastic waste in brick production, and it can serve as a valuable resource for researchers and practitioners interested in sustainable building materials.

The literature review explores the utilization of dry leaves and plastic waste in the manufacturing of bricks. Several studies have shown that incorporating dry leaves and plastic waste into brick production can lead to the production of eco-friendly and sustainable building materials. Dry leaves, when added to clay soil, can enhance the thermal insulation and reduce the weight of the bricks. Plastic waste, on the other hand, can improve the durability and strength of the bricks while also reducing the amount of plastic waste in the environment. Research has also shown that the addition of dry leaves and plastic waste can affect the mechanical, thermal, and physical properties of the bricks. However, the optimal mix proportions of the materials and the effects of aging on the properties of the bricks require further investigation. Additionally, the economic viability of producing these bricks on a large scale also needs to be considered. Overall, the literature suggests that the utilization of dry leaves and plastic waste in brick manufacturing can be a promising approach to creating sustainable building materials. However, more research is needed to fully understand the potential of this approach and to optimize the properties of the resulting bricks.

MATERIALS AND METHODS

This study explores the production of eco-friendly bricks using recycled plastic waste, dry leaves, and soil as primary materials. These materials are combined in specific proportions to create lightweight, durable, and sustainable

construction materials that address plastic pollution and resource conservation.

Materials

Plastic waste: Plastic waste is being used in plastic bricks as a way to address the issue of plastic pollution and waste management. Plastics are durable and non-biodegradable materials, which means that they do not easily decompose and can persist in the environment for hundreds of years. By using plastic waste in plastic bricks, we can divert this waste from landfills and oceans, and repurpose it into a useful construction material. This not only helps to reduce the amount of plastic waste in the environment, but it also conserves natural resources by using plastic waste as a substitute for traditional building materials, such as concrete or bricks. Furthermore, plastic bricks can offer several advantages over traditional building materials. They are lightweight, durable, and easy to manufacture. They can also provide good insulation and can be made in a range of sizes and shapes to suit different construction needs. Using plastic waste in plastic bricks is a sustainable solution that addresses both the issue of plastic waste and the need for affordable building materials.

Dry leaves: Dry leaves, often discarded as agricultural waste, were integrated into the brick-making process. Although traditionally used as natural soil conditioners or fertilizers, dry leaves can also serve as a lightweight filler in eco-friendly brick production. The dry leaves were shredded into small particles and mixed with plastic waste and soil. This combination contributes to the sustainability of the bricks by adding organic matter and improving their insulation properties.

Dry leaves are versatile materials that can be used in various construction applications, such as insulation in walls or ceilings and as lightweight fillers in concrete or bricks. The organic matter in dry leaves also introduces nutrients that enhance the soil's fertility when used in combination. However, careful consideration was given to the proportion of dry leaves used in the mixture to ensure proper compression and structural integrity of the bricks. Additionally, it's important to ensure that the plastic waste used is clean and free from contaminants that could affect the quality of the final product. While using dry leaves in combination with soil and plastic waste to create eco-friendly bricks is an innovative approach, it requires careful attention to the materials used and the production process to ensure that the resulting bricks are safe, durable, and sustainable.

Soil: Soil was used as an essential component to provide stability and structural strength to the bricks. It was mixed with water to achieve a clay-like consistency before being

Table 1: Composition of Materials.

Percentage	Composition of Materials
70-80%	Shredded Plastic Waste (such as HDPE, LDPE, PET, or PP)
20-30%	Sand
10%-5%	Dry Leaves

combined with shredded plastic waste and dry leaves. Soil plays a key role in binding the materials together, ensuring that the final product is strong, durable, and suitable for construction.

Mix proportion: The materials were mixed in the proportions given in Table 1 to achieve the desired properties:

Constructional suitability of waste plastic, dry leaves, and dirt combined to make bricks. The waste plastic is correctly batched and heated from below while also containing dry leaves and soil. To create plastic soil bricks, the soil was added to the molten plastic paste in the following ratios: 1.5: 1.5: 0.5 (plastic, soil, and dry leaves, correspondingly). The shredded plastic waste and filler material should be mixed thoroughly and evenly and then melted together in a high-temperature extruder machine. The resulting molten mixture is then extruded through a die to create plastic brick-shaped molds, which are cooled and then cut to the desired size and shape. It's important to note that the specific mix proportion for plastic bricks may vary depending on the desired strength, durability, and other properties of the final product.

Methods

Method of Casting Bricks

The materials used for casting plastic bricks were sourced from various suppliers (Figs. 1, 2 and 3). The plastic waste was collected from AS Plastic Company, located in Peelamedu, Coimbatore, Tamil Nadu. The soil was collected from the ground, where it was carefully graded to meet the required specifications. The dry leaves used in the brick-making process were obtained as guava dry leaves powder from ARS Herbal (an online shopping platform). The procedure for preparing these materials, mixing them, and casting the bricks is detailed below.

Fig. 1: Grinded Plastic.

Fig. 2: Soil.

Fig. 3: Guava Dry Leaves.

Materials Preparation

1. **Plastic waste:** The collected plastic waste was shredded into small pieces to facilitate proper melting and mixing with other materials. This shredded plastic was used as the primary binding agent in the brick-making process, helping to repurpose plastic waste into a sustainable building material.

2. **Soil:** The soil was collected from the ground and subjected to grading to meet specific size requirements. Only soil passing through a 4.75 mm sieve and retaining particles greater than 600 microns was considered. This ensures that any soil particles smaller than 600 microns or larger than 4.75 mm, which could create voids and lumps and weaken the final brick structure, were removed. Proper soil grading ensures that the bricks have adequate structural integrity.

3. **Dry leaves:** The dry leaves used in the brick production were sourced from guava trees. These leaves were shredded into a fine powder and used in combination with plastic and soil to create a composite material that could be formed into bricks.

Manufacturing of Bricks

Mixing Process: The plastic waste, soil, and dry leaves were carefully measured and mixed. These materials were then thoroughly blended to ensure uniform distribution of all components (Figs. 4 & 5) before moving on to the next step of the manufacturing process.

Molding: Once the materials were properly mixed, the mixture was poured into a mold to form the shape of the bricks. The mold used measured 190 mm × 90 mm × 90 mm, a standard size according to IS 1077:1992, which is commonly used for traditional clay bricks (Fig. 6). This size ensures consistency in the final product and facilitates ease of handling during construction. The mixture was poured into the mold as quickly as possible to prevent it from cooling and hardening before the molding process was complete.

After the mixture was poured into the mold, it was compacted using a vibrating table to remove any air pockets and to ensure that the mixture filled the mold. The compaction process is crucial for achieving optimal strength and durability in the final brick. Once compacted, the mold was left to set, allowing the brick to cool and harden over time.

Curing: Curing is an essential step in ensuring that the plastic bricks achieve maximum strength and durability. After about 30 minutes of setting, the brick was mechanically removed

BATCHING → MELTING → MIXING → MOULDING → CURING

Fig. 4: Melting.

Fig. 5 Mixing.

Fig. 6: Moulding.

Fig. 7: Curing.

Fig. 8: Plastic Bricks.

from the mold. The bricks were then left to cool down for 1 to 1.5 hours before being fully hardened (Fig. 7). This cooling process is crucial as it allows the materials to solidify and the structure of the brick to stabilize (Fig. 8).

Testing and Evaluation of Bricks

After manufacturing, a series of tests were performed to evaluate the properties and performance of the plastic bricks. Three bricks were cast for each test to ensure consistent results. The following tests were carried out:

Water absorption test: A brick is taken and it is weighed dry. It is then immersed in water for 24 hours. It is weighed again and the difference in weight indicates the amount of water absorbed by the brick. According to standard guidelines, the water absorption should not exceed 20% of the dry weight of the brick.

The specimen is dried in a ventilated oven at a temperature of 105°C to 115°C till it attains substantially constant mass. The specimen is cooled to room temperature and its weight (W1) specimen too warm to touch shall not be used for this purpose. The dried specimen is immersed in clean water at a temperature of 27+2°C for 24 hours. The specimen is removed and wipe out any traces of water with a damp cloth and weigh the specimen after it has been removed from water (W2). Water absorption, % by mass, after 24-hour immersion in cold water is given by the formula,

$$W = {}^{w1-w2}/_{w1} \times 100$$

Compressive strength test: The compressive strength of the brick was tested by placing it in a compression testing machine. The brick was subjected to pressure until it broke., According to BIS: 1077-1957, the maximum crushing strength of a brick should be 3.50 N/mm². Bricks with a crushing strength of 7–14 N/mm² are graded as 'A,' while those with strength above 14 N/mm² are classified as 'AA'. The ultimate compressive strength was calculated by dividing the ultimate load by the area of the brick's cross-section.

Hardness: The hardness of the brick was tested by attempting to scratch its surface with a fingernail. If no impression was left on the surface, the brick was considered sufficiently hard.

Efflorescence test: The soluble salts if present in bricks will cause efflorescence on the surface of the bricks. To find out the presence of soluble salts in brick, it is immersed in water for 24 hours. It is then taken out and allowed to dry sunshade. The absence of grey or white deposits on its surface indicates the absence of soluble salts. If the white deposit covers about 10% surface, the efflorescence is said to be slight and considered moderate, while the white deposit covers about 50% surface. If grey or white deposits are found on more than 50% of the surface, the efflorescence becomes heavy and it is treated as serious, when such deposits are converted to powdery mass.

Shape and size: The bricks were closely examined to ensure they adhered to standard size and shape. Ten bricks were selected at random and stacked to measure the uniformity of length, width, and height. The bricks were required to be rectangular with sharp edges to meet the required quality standards.

Soundness test: The soundness of the brick was tested by striking two bricks against each other. The brick should not break, and a clear ringing sound should be produced if the brick is of good quality.

RESULTS AND DISCUSSION

After casting the bricks, they are analyzed for use in construction. Various tests are carried out to check the properties of the bricks and the results of that test are analyzed. The following discusses the outcomes of each test conducted.

Water absorption test: The results, as shown in Table 2, indicate that both sample 1 and sample 2 exhibited 0% water absorption.

Table 2: Water Absorption test.

S.No	Composition	Water Absorption
1.	Sample 1	0%
2.	Sample 2	0%

Table 3: Compressive strength test.

Samples	Load Taken By Specimen	Compressive Strength
Specimen 1	130 kN	7.6 N/mm^2
Specimen 2	160 kN	9.5 N/mm^2
Specimen 3	210 kN	12.28 N/mm^2
Average	166.67 kN	9.74 N/mm^2

Fig. 9: Water absorption test.

Fig. 10: Compressive strength test.

Plastic soil bricks do not absorb water hence water absorption of plastic soil bricks is 0% (Fig. 9). Khan et al. (2018) investigated the effect of adding different types of plastic waste, including polyethylene terephthalate (PET) and low-density polyethylene (LDPE), on the properties of fired clay bricks. They found that adding 2-4% PET waste improved the compressive strength of the bricks while adding 2-6% LDPE waste resulted in increased water absorption capacity.

Compressive strength test: The compressive strength test measures the load-carrying capacity of the bricks and is crucial for determining their suitability in load-bearing applications (Fig. 10). The test results are presented in Table 3, showing the maximum load each specimen could withstand before failure, along with the corresponding compressive strength.

The average compressive strength of the plastic soil bricks was found to be 9.74 N/mm². This is comparable to the compressive strength of conventional bricks, which

typically ranges between 5 N/mm² and 15 N/mm². Jadhav & Nimbalkar (2018) evaluated the physical and mechanical properties of the bricks, including compressive strength, water absorption, and density. The study found that the addition of plastic waste had a positive impact on the properties of the bricks, including increased compressive strength and reduced water absorption.

Nampoothiri et al. (2019) found that adding up to 5% plastic waste to fly ash bricks improved their compressive strength and reduced their water absorption capacity. El-Mohr et al. (2019) investigated and reported that the addition of sawdust and waste plastic in the clay mixture resulted in a reduction in the water absorption capacity and an increase in compressive strength.

Efflorescence Test: A sample of the plastic brick is taken and its dimensions are measured accurately. The brick is placed in a glass container and covered with distilled water.
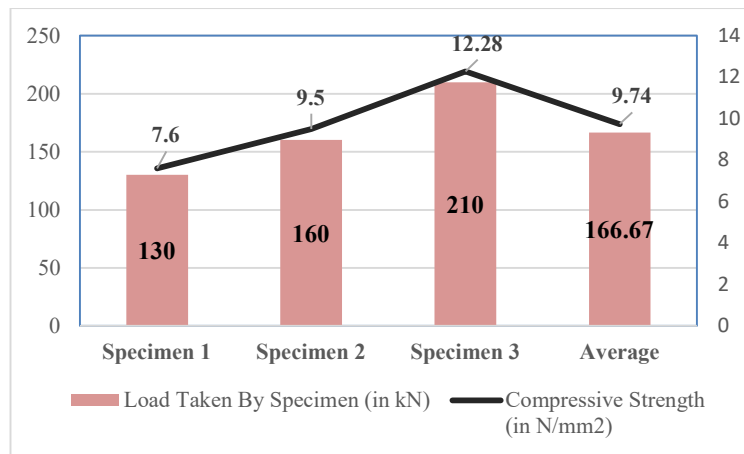

Fig. 11: Comparison of compressive strength.

Fig. 12: Efflorescence Test.

The container is sealed and allowed to stand for 28 days. After 28 days, the container is examined for any signs of efflorescence. If efflorescence is present, the extent of efflorescence is recorded. Since bricks don't contain any soluble salts, they don't develop any white or grey color deposits after being submerged in water for 24 hours and dried in the shadow. No efflorescence: No visible deposits on the surface of the brick (Fig. 12).

Hardness test: The hardness of the plastic soil bricks was assessed by attempting to scratch the surface using a fingernail. No impressions were left on the surface, suggesting that the bricks were sufficiently hard. While this method provides a basic indication of hardness, a more precise measure would require specialized instruments such as a Rockwell or Vickers hardness tester. Nevertheless, the absence of scratches indicates that the bricks are hard enough for construction purposes.

Soundness test: The soundness test evaluates the bricks' ability to withstand sudden impacts without breaking. In this test, two bricks were struck together, and the sound produced was observed. A clear, ringing sound was heard, and neither brick broke. This indicates that the bricks are sound and can withstand the mechanical stresses they may encounter during handling and use in construction.

CONCLUSIONS

The utilization of plastic wastes and dry leaves in brick production is an innovative and sustainable approach that addresses two pressing environmental challenges: waste management and depletion of natural resources. The global production of plastic and the accumulation of plastic waste have been escalating at an alarming rate, resulting in environmental pollution and ecological damage. On the other hand, traditional brick production requires the extraction of finite natural resources, such as clay and sand, which contributes to land degradation and habitat loss. By incorporating plastic waste and dry leaves into brick production, it is possible to reduce the amount of plastic waste and dry leaves in the environment while conserving natural resources. In addition, this approach can enhance the physical and mechanical properties of the bricks, providing

a durable and cost-effective alternative to traditional bricks. This study aimed to investigate the feasibility of using plastic wastes and dry leaves in brick production and to assess the physical and mechanical properties of the resulting bricks. The study explored the optimal proportions of plastic wastes and dry leaves that can be incorporated into the brick mix, as well as the effects of different variables on the properties of the bricks, such as curing time, temperature, and humidity. The results of this study contribute to the development of sustainable and innovative building materials that promote a circular economy and environmental stewardship.

REFERENCES

Agrawal, R. and Bhakar, M., 2020. Recycling of plastic waste in bricks: A review. *Journal of Materials Research and Technology*, 9(1), pp.854-864.

Dubey, R., Singh, S., Suresh, S. and Mukherjee, A., 2021. Sustainable management of plastic waste using geopolymer bricks. *Journal of Building Engineering*, 43, p.102616.

El-Mohr, M.A., Mahmoud, S.A. and Ragab, A.A., 2019. Eco-friendly fired bricks incorporating sawdust and waste plastic. *Construction and Building Materials*, 211, pp.1056-1065.

Han, X., Li, X., Li, S., Yang, S., Liu, S. and Huang, Q., 2021. Effect of sawdust on thermal properties of biomass plastic bricks. *Energy Reports*, 7, pp.3867-3872.

Jadhav, V.V. and Nimbalkar, S.S., 2018. Experimental investigation on utilization of plastic waste in manufacturing of bricks. *International Journal of Engineering Research & Technology (IJERT)*, 7(10), pp.265-270.

Khan, M.I., Rana, M.A. and Usman, M., 2018. Utilization of plastic waste for making hollow blocks and bricks. *Journal of Materials in Civil Engineering*, 30(7), p.04018166.

Khatib, J.M., Sadeek, S.A. and Issa, C.A., 2020. Experimental study on the use of plastic waste as aggregate in concrete. *International Journal of Civil Engineering and Technology*, 11(6), pp.490-498.

Kumar, M., Kumar, A., Kumar, A. and Singh, V., 2020. Utilization of agricultural waste and plastic waste in manufacturing of eco-friendly bricks. *Journal of Materials Research and Technology*, 9(1), pp.611-618.

Nampoothiri, S.V., Arunachalam, K. and Ramachandran, T., 2019. Studies on properties of fly ash bricks containing waste plastic. *Materials Today: Proceedings*, 18, pp.542-548.

Ram, A. and Singh, G., 2017. Use of plastic waste in the manufacturing of bricks. *International Journal of Innovative Research in Science, Engineering and Technology*, 6(2), pp.66-72.

Singh, V., Singh, A., Kumar, A. and Kumar, M., 2021. Experimental investigation on dry leaves and plastic waste incorporated fired bricks. *Journal of Building Engineering*, 44, p.103217.

Swinnerton, S., Kurtz, K., Neba Nforsoh, S., Crave, V. and Tsai, C., 2024. The manufacturing process and consequent occupational health and environmental risks associated with the use of plastic waste in construction bricks in small-scale recycling plants. *Journal of Cleaner Production*, 477, p.143818.

Yadav, M. and Pandey, K., 2020. Utilization of waste plastic and biomass for the production of eco-friendly bricks. *Journal of Materials Research and Technology*, 9(1), pp.474-485.

ORCID DETAILS OF THE AUTHORS

P. Muthupriya: https://orcid.org/0000-0002-3814-7185

Deciphering Sustainable Product Preferences: Insights from Indian Consumer Behavior

Poorani G.† and Banumathi M.

Department of Business Administration, Annamalai University, Chidambaram-608002, Tamilnadu, India

†Corresponding author: Poorani G.; pooraniganapathi@gmail.com

ABSTRACT

Consumer health and wellness are increasingly threatened by the deteriorating state of the environment, both locally and globally. Pollution, deforestation, habitat destruction, and climate change are among the myriad environmental challenges that directly impact human well-being. From air and water pollution to the depletion of natural resources, these environmental issues have profound implications for public health, exacerbating respiratory diseases, waterborne illnesses, and other health problems. In response to these environmental challenges, consumers are becoming more environmentally conscious in their purchasing decisions. They are seeking products and services that minimize harm to the environment, promote sustainability, and contribute positively to ecological conservation efforts. This shift in consumer preferences is driving the demand for sustainable products across various industries, including food and beverages, personal care, fashion, and household goods. Sustainable product marketing plays a critical role in addressing these consumer demands while also mitigating environmental impacts. By promoting products that are ethically sourced, eco-friendly, and produced using environmentally sustainable practices, businesses can align their operations with environmental conservation goals. This involves adopting eco-friendly packaging, reducing carbon emissions throughout the supply chain, and supporting renewable energy initiatives. In the context of the current study aiming to examine consumer purchasing patterns for sustainable products in India, the results offer valuable insights into the interplay between environmental consciousness, demographic factors, and consumer behavior. By delving into these dynamics, the study sheds light on the multifaceted influences that shape consumers' decisions regarding sustainable products.

INTRODUCTION

Globalization and modernity have catalyzed a profound transformation in the patterns of consumption worldwide, triggering a sharp escalation in the demand for goods and services across diverse sectors. However, this surge in consumption has come at a significant cost to the environment, exerting immense pressure on ecosystems and natural resources. From rampant deforestation to rampant pollution and climate change-induced disruptions, the consequences of unsustainable consumption are increasingly evident. To address these pressing environmental challenges and ensure the sustainability of our planet for future generations, there is an urgent need to advocate for and promote sustainable consumption practices on a global scale Schiffman and Kanuk (2007). At the heart of sustainable consumption lies the recognition that overconsumption, driven by the pursuit of endless growth and material accumulation, is inherently unsustainable. Instead, there is a growing consensus that the prevailing culture of excess consumption must be replaced with a more measured and mindful approach to consumption, commonly referred to as "gradual consumption." This shift entails reevaluating our relationship with material possessions and prioritizing products and services that align with principles of environmental sustainability, social equity, and ethical responsibility.

In recent years, there has been a noticeable shift in societal attitudes towards environmental conservation, with increasing numbers of individuals expressing concern about the state of the planet and the impacts of human activities on ecosystems. This heightened environmental awareness has translated into a growing demand for eco-friendly products and services, placing pressure on businesses to adapt their practices and offerings to meet evolving consumer preferences. However, effecting meaningful change in consumer behavior requires more than just the availability of green alternatives; it necessitates a deeper understanding of the psychological, social, and economic factors that influence consumer decision-making processes. One of

the key challenges in promoting sustainable consumption lies in bridging the gap between consumer attitudes and actions. Despite widespread support for environmental conservation, many consumers struggle to translate their pro-environmental attitudes into concrete behaviors and purchasing decisions. Understanding the underlying drivers of this attitude-behavior gap is critical for designing effective interventions and marketing strategies that encourage sustainable consumption practices.

From a marketing perspective, comprehending consumer perceptions about sustainable products and their motivations for choosing eco-friendly options is essential for developing targeted campaigns and communication strategies. By tapping into consumer values, aspirations, and concerns, businesses can tailor their messaging to resonate with target audiences and foster greater adoption of sustainable products and behaviors. The concept of sustainable consumption is intricately linked to broader principles of sustainable development, as articulated by the Brutland Commission's seminal definition in "Our Common Future." Sustainable consumption involves not only meeting present needs but also ensuring that future generations have the resources and opportunities to meet their own needs. This necessitates a fundamental reimagining of our economic systems and consumption patterns, with a focus on maximizing well-being while minimizing environmental degradation and social inequalities.

To assess progress towards sustainable development goals (SDGs), it is imperative to develop robust metrics that go beyond traditional economic indicators to encompass broader social and environmental dimensions. This requires redefining notions of progress and prosperity to prioritize holistic well-being and planetary health over narrow measures of GDP growth and material wealth. Thus, promoting sustainable consumption is not just a matter of environmental stewardship but a fundamental imperative for safeguarding the future of our planet and ensuring the well-being of present and future generations. By embracing principles of sustainability and ethical responsibility, businesses can not only mitigate their environmental footprint but also gain a competitive edge in an increasingly conscious consumer market (Fig.1). Ultimately, fostering sustainable consumption requires a collective effort from businesses, policymakers, civil society, and consumers alike to drive systemic change and create a more equitable and sustainable world. This article contributes to a better understanding of Indian consumers' attitudes towards eco-friendly practices and sustainable products, offering insights for developing strategies and policies. By aligning efforts with current and future policies and comprehending the environmental repercussions, organizations can gain a competitive advantage while contributing to environmental sustainability. Ultimately, fostering sustainable consumption is not just an economic imperative but also a moral obligation to safeguard the planet for future generations.

REVIEW OF LITERATURE

The literature on consumption presents a rich tapestry of perspectives on fostering environmentally sustainable consumption practices, touching upon various concepts and strategies. Two prominent approaches that have garnered attention in recent years are minimalism and decluttering, influenced by Marie Kondo's philosophy. These concepts advocate for reducing material possessions to those that "spark joy" or hold significant value, thereby promoting a more intentional and clutter-free lifestyle. Rani Yaduvanshi
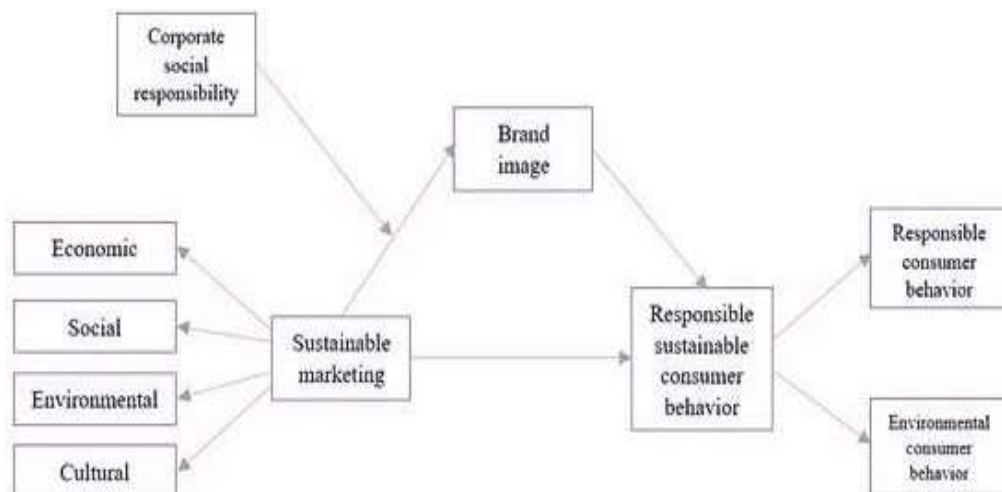

Fig. 1: Classification of Sustainability Marketing.

et al. (2016) While minimalism and decluttering have gained popularity for their potential to simplify one's life and reduce excess consumption, critics argue that they may not fully align to reduce the overall flow of products. This is because decluttered items are often replaced with new purchases at a rapid pace, contributing to a cycle of consumption that perpetuates resource depletion and environmental degradation. Furthermore, McKenzie Mohr (2011) the distinction between anti-materialism and anti-consumerism provides insights into differing philosophies regarding consumption and happiness. Anti-materialism challenges the notion that material possessions bring true happiness and fulfillment, advocating for a simpler, less materialistic lifestyle focused on experiences, relationships, and personal growth. On the other hand, Gupta & Singh (2020) anti-consumerism takes a more radical stance by critiquing the entire culture of consumption itself. It questions the pervasive belief that increased consumption leads to greater happiness and well-being, highlighting the negative social, environmental, and psychological impacts of consumerism. Anti-consumerism advocates for systemic changes in production and consumption patterns to reduce overall resource consumption and promote sustainability.

In the context of anti-consumption as a strategy for environmentally sustainable consumption, Makri et al. (2020) offer a comprehensive classification of various types of consumption resistance. This includes green/sustainable consumption, ethical/moral consumption, and alternative consumption practices. However, some forms of consumer resistance, such as symbolic consumption and brand/product avoidance, were not included in their analysis due to their focus on specific brands or items. Several studies have explored consumer perceptions and behaviors related to sustainable products, particularly in the context of India. Sarkar & Kota (2015) highlight a lack of awareness about sustainable living among Indian consumers, suggesting it as a barrier to adoption. Singh & Verma (2017) delve into the characteristics perceived as key impediments to transitioning to sustainable consumption, including factors such as the local environment and resource availability. Sangvikar et al. (2019) examine marketing prospects for sustainable products in India, noting demographic influences on awareness levels. Prakash (2017) investigates the impact of environmentally friendly packaging on consumer response, while Yaduvanshi et al. (2016) emphasize the importance of waste management in India and common strategies for promoting sustainable practices, such as education and advertising. Bläse et al. (2024) indicate that customer purchase intentions are significantly influenced by both brand reputation and FOMO. This implies that when it comes to fashion purchases, customers consider both the effect of FOMO and a brand's

trustworthiness. Khare & Sadachar (2017) examine the changing patterns of green clothes purchasing behavior among young people in India, with a focus on the interaction of factors such as consumer socialization for environmentally friendly products, previous green behavior, peer influence, and awareness of sustainable clothing. The study of Arora & Manchanda (2021) enhances the existing literature by investigating the correlation between internal environmental locus of control (IELOC) and consumer behavior regarding sustainable clothes. Claudio (2017) highlights the ecological repercussions of the apparel business, including how mass production, consumption, and waste of garments exacerbate numerous environmental issues. Paul et al. (2016) offer significant insights into this issue by employing two prevalent psychological frameworks—the Theory of Planned Behavior (TPB) and the Theory of Reasoned Action (TRA)—to analyze the determinants affecting customers' decisions to acquire green products. Rathod and Bhatt (2013) provide significant insights for shops aiming to augment the attractiveness of their own label clothes collections.

Overall, these studies contribute valuable insights into the complexities of promoting environmentally sustainable consumption, offering nuanced perspectives on consumer behavior, awareness levels, and the role of marketing strategies and policies in driving change. By understanding the challenges and opportunities inherent in promoting sustainable consumption (ref. Fig.2), businesses, policymakers, and practitioners can develop more effective strategies for fostering positive environmental outcomes.

OBJECTIVES OF THE STUDY

A. To understand consumer awareness towards sustainable products

B. To investigate the cost-effectiveness of environmentally friendly products

C. To examine the brand value associated with sustainable practices

Overall, these objectives (ref. Table 1) collectively seek to deepen understanding of consumer behavior and attitudes towards sustainable products, assess the economic viability of environmentally friendly options, and explore the branding implications of sustainable practices. By addressing these objectives, businesses can gain valuable insights to inform their sustainability strategies, drive positive environmental impact, and strengthen their competitive position in the market.

RESEARCH METHODOLOGY

The following research approach has been used to analyze the aforementioned objectives.
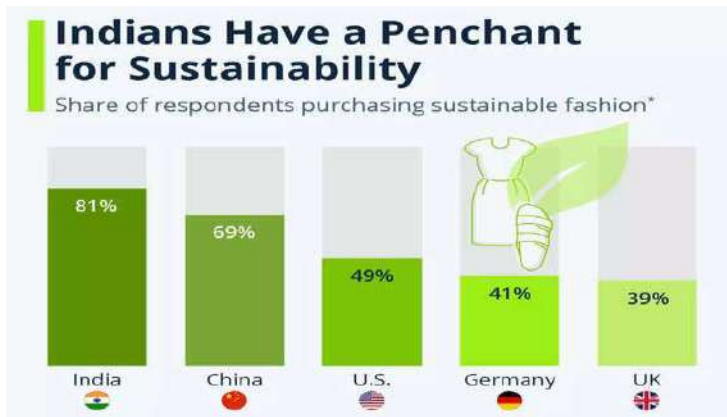
Indians Have a Penchant for Sustainability
Share of respondents purchasing sustainable fashion*

India 81%
China 69%
U.S. 49%
Germany 41%
UK 39%

Fig. 2: Illustration of Sustainability Levels.

Table 1: Research Objectives for Sustainable Products.

Objective	Description	Focus
Understand Consumer Awareness	Gain insights into consumer knowledge, perceptions, attitudes, and behaviors toward sustainable products.	Consumer awareness of eco-friendly labels, understanding of sustainability issues, and recognition of environmental impact.
Investigate Cost-Effectiveness	Evaluate the economic viability of environmentally friendly products compared to traditional alternatives.	Comparative analysis of costs associated with production, purchase, use, and lifecycle impact.
Examine Brand Value Association	Explore how sustainability initiatives and commitments impact consumer perceptions and purchasing decisions.	Consumer trust, loyalty, and willingness to pay a premium for sustainable brands.

A. Data Gathering: Primary data have been gathered for this investigation. The data-gathering process employed a comprehensive and systematic approach to collect primary data relevant to the research objectives (ref. Table 2). By leveraging a well-designed questionnaire, targeting a diverse sample, and carefully structuring the data collection process, the study aims to generate insights that contribute to a deeper understanding of consumer perceptions and behaviors toward sustainability.

B. Statistical Tools: In our study, we utilized Python, another powerful programming language renowned for its versatility in data analysis and visualization. While our statistical analyses were conducted using Python, it's important to note that R, with its extensive suite of statistical and graphical tools, is a widely used software package in the field of data science and statistical analysis.

Python offers a plethora of libraries and packages tailored for data manipulation, statistical analysis, and visualization, making it a popular choice among data scientists and researchers. In our analysis, we leveraged libraries such as pandas for data manipulation and matplotlib for data visualization, both of which are widely used in the Python ecosystem.

Table 2: Data Gathering Process for Sustainable Product Research.

Aspect	Description
Questionnaire Design	A meticulously designed questionnaire was used to collect primary data. The questionnaire addressed all aspects of consumer perceptions, brand association, and product awareness related to sustainability. Wording, order of questions, and structure were carefully considered to minimize bias and ensure clarity.
Sampling Method	A purposive sampling approach may have been used to target individuals knowledgeable about sustainable consumption practices. The sample aimed for diversity across demographics (age, location, socioeconomic background, environmental awareness).
Data Collection Period	Data collection occurred over two months (July-August 2021). This strategic timeframe aimed to capture potential variations in consumer behavior across seasons.
Sample Size	115 participants were included in the study. While modest, the sample size may be sufficient for meaningful conclusions if representative and rigorously collected. Focus on qualitative insights may further enhance data richness.

DATA INTERPRETATION

Supervised Learning Model

The model used in the program is called the Supervised Learning Model. Specifically, it's a Classification model.

This model predicts the class labels based on input features. In this case, it could predict whether an individual is aware of sustainable products based on demographic information such as age, education, working status, etc. The classification task involves assigning a label to each instance from a finite

Table 3: Data Analysis and Visualization

Algorithm 1 Data Analysis and Visualization in Python

Require: Dataset in CSV format.

Ensure: Visualization of awareness of sustainable products by age group an working status

1: Import necessary libraries: pandas, matplotlib
2: Load the dataset into a pandas DataFrame
3: Display the first few rows of the data frame
4: Calculate the percentage of people aware of sustainable products
5: visualize the data using matplotlib
6:

7: **Input**: Dataset file path

8: **Output**: Bar plot showing awareness of sustainable products by age group and working status

9:

10: **Procedure:**

11:　　**Import** pandas as pd
12:　　**Import** matplotlib.pyplot as plt
13:
14:　　**Load** the dataset into a DataFrame: df=pd.read *csv(" Dataset.csv")*
15:　　**Display** the first few rows of the data frame: print(df.head())
17:

18:　　**Calculate the percentage of people aware of sustainable products**:

19:　　total_response =len(df)
20:　　aware_responses =len(df[df['Are you aware of sustainable products?']=='Yes'])
21:　　aware_percentage=(aware_responses/total_responses)*100
22:　　print(f"Percentage of people aware of sustainable products:　　{aware_percentage:.2f}%")
23:

24:　　**Visualize the data using matplotlib:**

25: aware_by_age　=df.goupby('Age')['Are you ware of sustainable products?'.value_counts(normalize=true).unstack().fillna(0)
26: aware_by_age =df.groupby('Age')['Are you ware of sustainable products?'].value_counts(normaize=True).unstack().fillna(0)
27: plt.title('Awareness of sustainable products by Age Group')
28: plt.xlabel('Age Group')
29: plt.ylabel('Percentage')
30: plt.xticks(rotation=45)
31: plt.legend(title+'Awareness')
32:

33: **Add another visualization for working status and location:**

34: working_status=['working', 'Not working']
35: urban=[47,12]
36: rural=[10,18]
37: index=range(len(working_status))
38: bar_width=0.35
39: plt.figure()
40: plt.bar(index,urban,bar_width,label='Urban')
41: plt.bar(i+bar_width for i in index],rural,bar_width, label='Rural')
42: plt.xlabel('Working Status')
43: plt.ylabel('Awareness')
44: plt.title('Awareness of Sustainable Products by Working Status and Location')
45: plt.xticks([i+bar_width/2 for *i* in index],working_status
46: plt.legend()
47: plt.tight_layout()
48: plt.show()=0

---

set of labels (in this case, "Yes" or "No" for awareness of sustainable products).

The study is presented in Algorithm 1 (Table 3). aimed to explore consumer awareness of sustainable products using a dataset comprising responses from individuals across various demographic groups. The dataset was initially loaded into a Panda DataFrame for analysis, and the structure and content of the data were examined through a display of the first few rows. Subsequently, the analysis delved into understanding the extent of consumer awareness regarding sustainable products.

Output Interpretation

Upon analysis of the dataset, it was found that a considerable percentage of respondents exhibited awareness of sustainable products, indicating a growing trend towards environmental consciousness among consumers. This insight is crucial in understanding the evolving preferences and priorities of individuals, particularly in the context of sustainability and eco-friendly practices.

The visualization presented in the form of a stacked bar plot (Fig. 3), offers a comprehensive depiction of awareness levels across different age groups. Each bar in the plot represents a distinct age category, while the height of the bar signifies the percentage of individuals within that age group who reported being aware of sustainable products. By examining the distribution of awareness across various age demographics, notable trends or disparities may emerge, providing valuable insights for stakeholders in the sustainability domain. The visualization may reveal that certain age groups exhibit higher levels of awareness compared to others, indicating potential target demographics for sustainable product campaigns or initiatives. Conversely,

it may also highlight age groups with lower awareness levels, signaling areas for further education or outreach efforts to enhance awareness and promote sustainable consumption habits.

Furthermore, the stacked nature of the plot allows for the identification of variations in awareness levels within each age group. By distinguishing between different response categories (e.g., "Yes" and "No" for awareness), the plot facilitates a nuanced understanding of the distribution of responses within each demographic segment. The additional bar chart illustrates awareness levels based on working status and location. This visualization enables stakeholders to understand how awareness varies across different demographic segments. For example, it may reveal that working-class individuals in urban areas demonstrate higher awareness of sustainable products compared to other groups. Such insights are crucial for tailoring strategies effectively, whether for businesses, policymakers, or advocacy groups, to foster greater engagement and adoption of sustainable practices among diverse consumer populations. Overall, the output interpretation underscores the importance of understanding consumer awareness patterns within specific demographic cohorts. Such insights enable businesses, policymakers, and advocacy groups to tailor their strategies effectively, fostering greater engagement and adoption of sustainable practices among diverse consumer populations.

Analyzing Consumer Attitudes: Sustainability Perception and Brand Engagement

In today's increasingly eco-conscious world, consumer attitudes towards sustainability play a pivotal role in shaping market dynamics and brand engagement strategies. Two
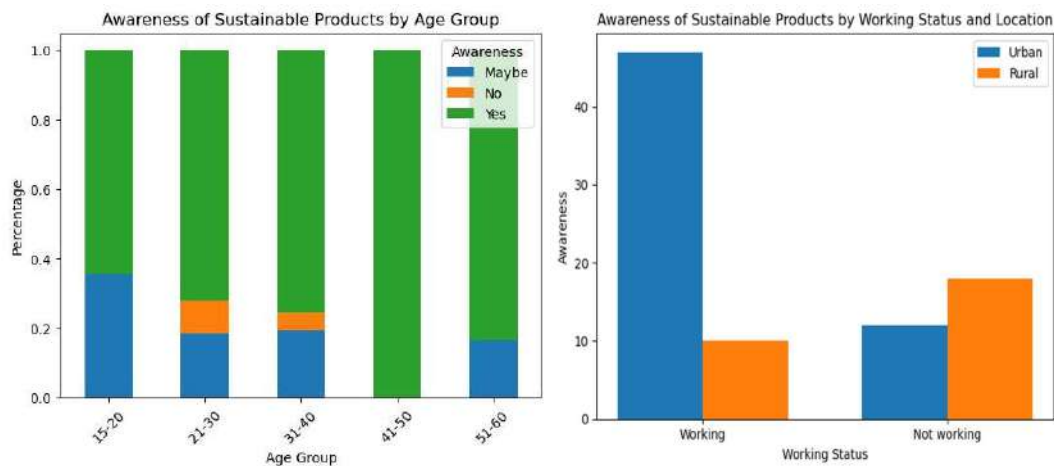

Fig. 3: Depiction of Awareness Levels.

Table 4: Investigating the cost-effectiveness of environmentally friendly products.

Working status/Usage of sustainable products/Affordability of Sustainable products	Working		Not working	
	Yes	No	Yes	No
Yes	30	3	16	6
No	13	1	7	1
Maybe	19	3	10	6

critical dimensions of consumer perception of environmentally friendly products and awareness of sustainable brand practices are key areas of focus for businesses aiming to align their offerings with evolving societal values.

Table 4 suggests that a significant number of individuals, both working and not working, find environmentally friendly products affordable. This indicates a positive attitude towards sustainable options. However, there are still some individuals who find sustainable products not affordable, particularly among those who are not working. This might imply economic barriers to adopting environmentally friendly alternatives for this group. The "Maybe" category suggests there is a portion of the population open to the idea of using sustainable products but may need more information or incentives to make the switch. Overall, the data highlights the importance of addressing affordability concerns and promoting awareness about the environmental benefits of sustainable products to encourage their widespread adoption.

Table 5 suggests varying levels of awareness of sustainable brands across different age groups. This indicates that younger age groups might be more aware or interested in sustainable practices compared to older age groups. It's notable that in some age groups, there are individuals who are not aware of sustainable brands at all. This underscores the importance of increasing awareness and education about sustainability across all age demographics. The presence of individuals in the "Maybe" category indicates a level of uncertainty or ambivalence towards sustainable brands. This highlights an opportunity for companies and organizations to engage with these individuals and provide more information about the environmental benefits of sustainable practices. Overall, the data suggests that there is potential for increasing the brand value associated with sustainable practices, particularly by targeting younger age groups and improving awareness and understanding of sustainability across all demographics.

In essence, these tables serve as invaluable tools for businesses seeking to navigate the complex terrain of consumer attitudes toward sustainability. By deciphering the interplay of factors such as affordability, age, and brand awareness, organizations can craft more nuanced and effective strategies to foster a culture of environmental stewardship among consumers, thereby driving positive ecological impact while enhancing brand equity.

Sustainable Product Perception: Exploratory Data Analysis

Table 5: Examining the brand value associated with sustainable practices.

Age	15-20		21-30		31-40		41-50		51-60	
Brand value/Awareness on sustainable brands	yes	No	Yes	No	Yes	No	Yes	No	Yes	No
Yes	1	10	7	18	5	28	3	7	0	4
No	0	0	2	3	0	1	0	0	1	0
May be	1	2	4	9	1	5	1	1	1	0

Table 6: Exploartory Data Analysis

Algorithm 2 Exploratory Data Analysis(EDA)
1: Import the panda's library as pd and the matplotlib.pyplot library as plt.
2: Read the dataset from the CSV file into a pandas DataFrame (df).
3: Remove rows with missing values from the DataFrame using dropna()method.
4: Group the Dataframe (df) by' Are you aware of sustainable products?' and 'Can Sustainable marketing practices make the product affordable?' columns and count the occurrences
5: Unstack the grouped data to create a pivot table.
6: Create a bar plot with stacked bars for Perception of Affordability vs. Awareness of Sustainable Products.
7: Set title, labels for x and y-axxis, and legend.
8: Display the plot.
9: Group the DataFrame (df) by 'Education' and ' Can Sustainable marketing practices make the product affordable?' columns and count the occurrences.
10: Unstack the grouped data to create a pivot table.
11: Create a bar plot with stacked bars for the Perception of Affordability vs. Education Level.
12: Set title, labels for x and y-ais and legend.
13: Display the plot.=0

The program in Table 6 utilizes data visualization techniques to explore and analyze perceptions regarding the affordability of sustainable products. By visualizing the data, we gain insights into how awareness levels and educational backgrounds influence individuals' perceptions, which can be valuable for marketing strategies and policy-making in the sustainability domain.

Output Interpretation

The output program provides insights into individuals' perceptions of sustainable products, particularly regarding their awareness and the perceived affordability of such products, analyzed against their education level.

The first plot, "Perception of Affordability vs. Awareness of Sustainable Products," (Fig. 4) illustrates how respondents' awareness of sustainable products correlates with their perception of affordability. The x-axis represents the level of awareness of sustainable products, while the y-axis indicates the number of respondents. The stacked bars show the distribution of respondents based on their perception of affordability, with light blue representing those who perceive sustainable products as affordable and light green representing those who don't. Interpreting this plot, we can observe the distribution of respondents across different levels of awareness. For instance, among respondents with high awareness of sustainable products, a significant portion perceive them as affordable, as indicated by the larger light blue section. Conversely, for respondents with low awareness, the perception of affordability appears less pronounced.

The second plot, "Perception of Affordability vs. Education Level," (Fig.4) delves into how education level influences individuals' perceptions of the affordability of sustainable products. Here, the x-axis represents different levels of education, while the y-axis indicates the number of respondents. Similar to the first plot, the stacked bars show the distribution based on the perception of affordability. Analyzing this plot provides insights into how education level impacts the perception of affordability. For instance, among respondents with higher education levels, there seems to be a larger proportion who perceive sustainable products as affordable compared to those with lower education levels. This suggests that education might play a role in shaping perceptions regarding the affordability of sustainable products.
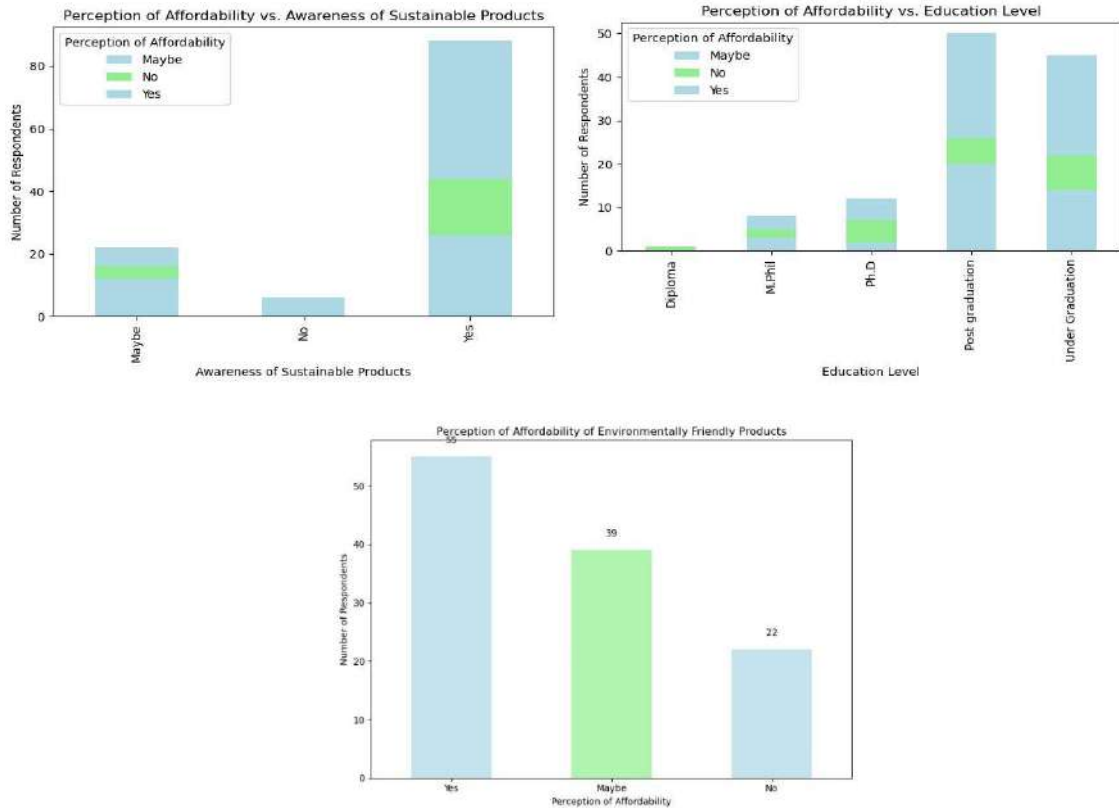

Fig. 4: Perception Analysis.

The third bar plot illustrates the distribution of respondents' perceptions regarding the affordability of sustainable products. The x-axis represents the different perceptions of affordability, while the y-axis indicates the number of respondents who hold each perception. The bars are color-coded, with light blue representing respondents who perceive sustainable products as affordable and light green representing those who do not. Interpreting this plot, we gain valuable insights into the general sentiment regarding the affordability of environmentally friendly products. For instance, if the number of respondents who perceive such products as affordable is significantly higher than those who don't, it suggests a positive inclination toward embracing sustainable consumption practices. Conversely, if the opposite holds true, it indicates potential barriers or challenges in adopting environmentally friendly products due to perceived cost issues. Understanding individuals' perceptions of affordability is crucial for policymakers, businesses, and environmental advocates. It helps tailor strategies to promote sustainable consumption patterns effectively. For instance, if the perception of affordability is low, targeted initiatives such as subsidies, incentives, or marketing campaigns highlighting long-term cost savings could be devised to encourage more widespread adoption of environmentally friendly products. Conversely, if the perception is already positive, efforts might focus on further enhancing accessibility and availability to capitalize on the existing favorable sentiment.

Overall, these visualizations offer valuable insights into the relationship between awareness, education, and the perceived affordability of sustainable products, providing valuable information for policymakers and businesses aiming to promote environmentally friendly consumption patterns.

FINDINGS

1. **Consumer Understanding**: The data indicates a positive trend with 75.86% of consumers demonstrating an understanding of the importance of sustainable products. This suggests a growing awareness and consciousness among consumers regarding sustainable lifestyle choices.

2. **Usage of Environmentally Friendly Products**: A significant majority (82.6%) of consumers have used environmentally friendly products at some point. However, the data also suggests that usage hasn't been committed to any specific product, indicating a need for further exploration into consumer preferences and behavior regarding sustainable products.

3. **Awareness of Sustainable Brands**: Despite the high usage of environmentally friendly products, a substantial portion (76.5%) of consumers is still unfamiliar with sustainable brands. Notably, "Oh Scrap Madras" emerges as the most preferred brand among those familiar with sustainable brands, suggesting potential areas for brand promotion and awareness campaigns.

4. **Perception of Product Pricing**: Nearly half (47.8%) of consumers believe that sustainable methods are inexpensive. However, a significant percentage of consumers are skeptical about product pricing, indicating a perceived barrier to adoption. This finding underscores the importance of pricing strategies and communication of value propositions for sustainable products.

5. **Impact on Brand Value**: The majority (72.2%) of consumers feel that sustainable practices increase brand value. This suggests that integrating sustainability into business practices can positively influence consumer perceptions and brand reputation.

6. **Urban vs. Rural Awareness**: The data highlights a disparity in awareness levels between urban and rural consumers, with urban consumers showing higher awareness of sustainable products compared to their rural counterparts. This finding underscores the importance of tailored marketing and educational initiatives to reach diverse consumer segments effectively.

The findings suggest both opportunities and challenges in the adoption of sustainable products. While there is a growing understanding and usage of environmentally friendly products, there is still a need for increased awareness, brand familiarity, and addressing perceived barriers such as pricing concerns. Additionally, the urban-rural disparity highlights the importance of targeted interventions to ensure inclusivity in sustainability initiatives.

CONCLUSIONS

In conclusion, the findings of this study underscore the growing influence of sustainability on consumer buying patterns, driven by increasing awareness of social responsibility, inclusivity, and environmental concerns. It is evident that consumers are becoming more conscious of their overall consumption habits and are showing a willingness to prioritize sustainability in their purchasing decisions. However, despite the strong intentions to adopt sustainable practices, there exists a notable gap between consumer beliefs and actual knowledge about sustainability. This highlights the need for ongoing education and awareness initiatives to bridge this gap and empower consumers to make informed choices.

One particularly encouraging finding is that consumers are willing to pay a premium for ecologically friendly products. This presents a significant opportunity for businesses to invest in sustainable practices and products, knowing that there is a receptive market willing to support such initiatives. Nevertheless, it is clear from the survey results that there is still a lack of familiarity with sustainable brands among consumers. This underscores the importance of developing effective brand promotion strategies to build trust and credibility in the marketplace. Businesses should consider leveraging marketing campaigns, partnerships, and endorsements to raise awareness of their sustainability initiatives and differentiate themselves from competitors.

FUTURE WORK

In considering future avenues of research, several key areas warrant further exploration to deepen our understanding of consumer behavior and attitudes toward sustainability:

Longitudinal Studies: Conducting longitudinal studies to track changes in consumer behavior and attitudes over time would provide valuable insights into the evolving nature of sustainability trends. By examining how consumer preferences, purchasing habits, and awareness levels shift in response to changing societal, economic, and environmental factors, researchers can identify emerging patterns and anticipate future trends.

Consumer Education and Awareness: Future research could focus on developing and evaluating the effectiveness of various educational interventions aimed at enhancing consumer awareness and understanding of sustainability issues. This could involve conducting experimental studies to assess the impact of different communication strategies, educational programs, and information campaigns on consumer knowledge, attitudes, and behaviors related to sustainability.

Psychological and Behavioral Drivers: Delving deeper into the psychological and behavioral drivers of sustainable consumption would provide valuable insights into the underlying motivations and decision-making processes of consumers. Research could explore factors such as social norms, perceived social responsibility, environmental values, and personal identity in shaping sustainable purchasing decisions. Understanding these psychological mechanisms can inform the development of targeted interventions and marketing strategies to promote sustainable behavior change.

Market Segmentation and Targeting: Examining market segmentation and targeting strategies based on consumer attitudes and preferences towards sustainability could help businesses better tailor their products, services, and marketing messages to different consumer segments. By identifying distinct consumer segments with varying levels of environmental consciousness and willingness to engage in sustainable practices, businesses can develop more effective strategies for reaching and engaging their target audience.

Technological Innovations: Investigating the role of technology and innovation in driving sustainable consumption offers promising avenues for future research. This could involve exploring the adoption and impact of technological solutions such as eco-friendly products, sustainable packaging materials, recycling technologies, and digital platforms for promoting sustainable behavior. Research in this area can help identify opportunities for leveraging technology to facilitate and incentivize sustainable consumption practices.

Cross-Cultural Perspectives: Examining cross-cultural differences in consumer attitudes and behaviors towards sustainability would provide valuable insights into the cultural, social, and economic factors that influence sustainable consumption patterns across different regions and demographics. Comparative studies across diverse cultural contexts can help identify universal principles as well as culturally specific factors that shape consumer responses to sustainability initiatives.

Policy and Regulatory Frameworks: Finally, future research could explore the role of policy and regulatory frameworks in promoting sustainable consumption at both the individual and institutional levels. This could involve evaluating the effectiveness of existing policies, incentives, and regulations in incentivizing sustainable practices, as well as identifying opportunities for policy interventions to address barriers and catalyze positive change.

By addressing these research priorities and advancing our understanding of consumer behavior and attitudes toward sustainability, scholars, and practitioners can contribute to the development of more effective strategies for promoting environmentally sustainable consumption and fostering positive social and environmental outcomes.

REFERENCES

Arora, N. and Manchanda, P., 2021. Investigating the relationship between internal environmental locus of control and behaviour towards sustainable apparel: The mediating role of intention to purchase. *Transnational Marketing Journal*, 9(3). https://doi.org/10.33182/tmj.v9i3.1305.

Bläse, R., Filser, M., Kraus, S., Puumalainen, K. and Moog, P., 2024. Non‐sustainable buying behavior: How the fear of missing out drives purchase intentions in the fast fashion industry. *Business Strategy and the Environment*, 33(2), pp.626-641.

Claudio, L., 2017. Waste couture: Environmental impact of the clothing industry. *Environmental Health Perspectives*, 115(9), pp.448-454. https://doi.org/10.1289/ehp.115-a449.

Gupta, K. and Singh, N., 2020. Consumer attitude towards sustainable living in India. *Social Responsibility Journal*, ahead-of-print(ahead-of-print). https://doi.org/10.1108/srj-03-2018-0081.

Khare, A. and Sadachar, A., 2017. Green apparel buying behaviour: A study on Indian youth. *International Journal of Consumer Studies*, 41(5), pp.558-569. https://doi.org/10.1111/ijcs.12367.

Kumar, A., Prakash, G. and Kumar, G., 2021. Does environmentally responsible purchase intention matter for consumers? A predictive sustainable model developed through an empirical study. *Journal of Retailing and Consumer Services*, 58, p.102270. https://doi.org/10.1016/j.jclepro.2017.08.106.

Makri, K., Schlegelmilch, B.B., Mai, R. and Dinhof, K., 2020. What we know about anticonsumption: An attempt to nail jelly to the wall. *Psychology & Marketing*, *37*(2), pp.177-215. https://doi.org/10.1002/mar.21319

McKenzie-Mohr, D., 2011. *Fostering sustainable behavior: An introduction to community-based social marketing*. New Society Publishers.

Paul, J., Modi, A. and Patel, J., 2016. Predicting green product consumption using theory of planned behavior and reasoned action. *Journal of Retailing and Consumer Services*, 29(29), pp.123-134.

Prakash, G. and Pathak, P., 2017. Intention to buy eco-friendly packaged products among young consumers of India: A study on developing nation. *Journal of Cleaner Production*, 141, pp.385-393. https://doi.org/10.1016/j.jclepro.2016.09.116.

Rani Yaduvanshi, N., Myana, R. and Krishnamurthy, S., 2016. Circular economy for sustainable development in India. *Indian Journal of Science and Technology*, 9(46). https://doi.org/10.17485/ijst/2016/v9i46/107325.

Rathod, C.B. and Bhatt, N.H., 2013. Role of psychological factors in purchase behaviour with reference to private label apparels. *Asia-Pacific Journal of Management Research and Innovation*, 9(2), pp.191-200. https://doi.org/10.1177/2319510x13504333.

Sangvikar, B., Pawar, A., Kolte, A., Mainkar, A. and Sawant, P., 2019. How does green marketing influence consumers? the market trend examination towards environmentally sustainable products in emerging Indian cities. *International Journal of Recent Technology and Engineering*, 8(3S), pp.561-571. https://doi.org/10.35940/ijrte.c1114.1083s19.

Sarkar, P., Kota, S. and Kumar, B., 2015. Understanding Consumers' Perceptions of Sustainable Products in India. In *ICoRD'15–Research into Design Across Boundaries Volume 2: Creativity, Sustainability, DfX, Enabling Technologies, Management and Applications* (pp. -99 112). Springer India. https://doi.org/10.1007/978-81-322-2229-3_9

Schiffman, L.G. and Kanuk, L.L., 2007. *Consumer behavior*. 9th ed. Pearson Prentice Hall.

Singh, A. and Verma, P., 2017. Factors influencing Indian consumers' actual buying behaviour towards organic food products. *Journal of Cleaner Production*, 167, pp.473-483. https://doi.org/10.1016/j.jclepro.2017.08.106.

A Sustainable Approach Toward Food Security: Investigating the Effect of Intercropping on Soil Rhizospheric Activity, Weed Flora and Yield Attributes of Maize (*Zea mays*)

Kritika[1] , **Arshdeep Singh[1]†** , **Shimpy Sarkar[2]** and **Jaspreet Kaur[3]**

[1]Department of Agronomy, School of Agriculture, Lovely Professional University, Phagwara-144411, Punjab, India
[2]Department of Entomology, School of Agriculture, Lovely Professional University, Phagwara-144411, Punjab, India
[3]Faculty of Business and Professional Studies, School of Business, Capilano University, North Vancouver, BC, V7J 3H5, Canada
†Corresponding author: Arshdeep Singh; arshdeep.27269@lpu.co.in

ABSTRACT

Maize is one of the staple food crops after wheat and rice crops. There is a reduction in the yield of maize due to biotic and abiotic factors. Due to more spacing in maize weeds are highly infested in the field which leads to reduced fertility of soil and sustainability. To maintain the fertility of soil and reduce the wastage of resources intercropping is the best option. By growing crops in between the rows of maize crops we can increase production and can achieve zero hunger. A field experiment was conducted at Lovely Professional University (Kharif 2022) to check the effect of black gram and French bean as intercrop in maize on weed flora, rhizospheric bacterial count, and yield parameters of maize. The experiment comprised 9 treatments i.e. Sole maize, Sole French bean and Sole black gram, Maize + French bean (1:1, 1:2, 1:3), Maize + black gram (1:1, 1:2, 1:3). Weed density and biomass recorded by quadrant 1 m^2 method at 30 and 60 DAS (Days after sowing). Results of the study showed that minimum weed count of grasses (3.44, 3.26), sedges (3.13, 2.73), and BLW (Broad leaf weed) (3.26, 4.58) at 30 and 60 DAS recorded in those plots where intercropping of maize and black gram practiced in 1:3 proportion. Rhizospheric bacterial count viz. THB (total heterotrophic bacteria) (232.82), NRB (nitrate-reducing bacteria) (41.89), and NB (nitrifying bacteria) (161.86) were recorded highest in Maize + French bean 1:3 at 30 DAS. Whereas THB, NRB, and PSB (phosphate solubilizing bacteria) highest count recorded in Maize + Black gram 1:3 at 90 DAS. In the case of maize yield attributes maize + Black gram 1:2 gave the best result. Land Equivalent ratio and Maize Equivalent yield (2.23, 11671.03 kg.ha^{-1}) were recorded maximum in those plots where Maize + Black gram 1:2 proportion was practiced. Intercropping can be used as an eco-friendly alternative to herbicides to reduce the weed population and infestation, which leads to maintaining soil fertility and enhancing sustainability.

INTRODUCTION

Since maize (*Zea mays*) has a higher yield potential than other cereals, it is grown in a variety of environments and is used for a wide range of purposes, including food, feed, and fodder. In terms of cereal crop production, maize is ranked second only to wheat, after rice; however, it is the most popular crop in Latin America and Africa and ranks third among growing countries in Asia, after rice and wheat. India ranks seventh out of all the countries that produce maize worldwide; based on total area, it is the fourth largest producer of maize globally, accounting for 2% of the total amount produced globally (Economic Survey 2021-22 Statistical Appendix). The use of fertilizers, the introduction of High Yielding Variety (HYV) seeds, and

the ease of access to irrigation systems all contributed to a sharp increase in India's maize production. According to the Agricultural Market Intelligence Centre (PJTSAU), Bihar has the most area utilized for maize production at 14.73 lakh acres, followed by Maharashtra and Andhra Pradesh at 8.33 and 4.82 lakh acres, respectively. With 5.18 million tonnes, Karnataka, however, leads the output tables, while Madhya Pradesh and Maharashtra generate 3.58 million and 3.44 million tonnes, respectively (Economic Survey 2021-22 Statistical Appendix). In addition to being high in protein (32.1%), maize also includes significant amounts of vitamins E and A, crude fiber (3-0.8%), carbohydrates (66-75.9%), starch (1-3%), fatty acids (palmitic acid, stearic acid, oleic acid, and nicotinic acid), oil (4%), and riboflavin (Das & Singh (2016). Crop weed competition has lowered global

maize production by 37%, which is a significant loss for the growers. Due to rising cultivation costs, small farmers now have an additional strain. However, due to maize's larger row spacing and sluggish development initially, together with friendly weather that encourages luxuriant weed growth that can cut production by 28–100%, the first six weeks following crop planting are the most essential for crop weed competition (Rani et al. 2020). Weeding, whether chemically or non-chemically, is practically necessary during this crucial time. Yield losses can range from 40 to 60% if proper weed control isn't implemented (Choudhary & Dixit 2018). Mechanical and manual weeding methods are costly, and during the monsoon season, persistent rains frequently make timely operations impractical. Microbiological activity in the rhizosphere is significantly higher than in soil that is not near plant roots due to the food supply. The microbes provide the plants, with nourishment in exchange. The rhizosphere is the most active soil environment because of all this activity. Different kinds of chemicals can be produced by free-living, symbiotic, or endophytic root-associated bacteria. By controlling the nutritional and hormonal balance of plants, fostering systemic tolerance to biotic and abiotic stressors, and promoting plant development, rhizosphere bacteria reduce the effects of stress on plants. The extensive monoculture of cereals has raised agricultural yields globally, but it has also ruined the environment, misused resources, and upset the natural equilibrium. Intercropping increases land utilization since different crop species share inputs, light, and space. Intercropping offers several advantages by enabling two or more crops to coexist for a portion of their lifespan. Maize is a widely spread crop that is good for legume growth and enables intercropping (Kritika et al. 2023).

Key objective of the study: To assess the effect of intercropping with legumes on weed dynamics of Maize crops.

MATERIALS AND METHODS

Experimental Site

The research was conducted in the kharif season, 2022 at the agricultural farm of Lovely Professional University, Jalandhar. The farm is situated at 31º22'31.81'' North latitude and 75º23'03.02 East longitude with 252 m average elevation above mean sea level having lower water availability and potential water scarcity (Fig. 1). The climate of the experimental location was subtropical, featuring mild winters, hot summers, and a rainy season with an average annual precipitation of 711 mm. The experiment had a total of 9 treatments with 3 replications i.e., (T_1) Sole Maize (60 cm), (T_2) Sole French bean (20cm), (T_3) Sole Black gram (20cm), (T_4) Maize + French bean (1:1), (T_5) Maize + French bean (1:2), (T_6) Maize + French bean (1:3), (T_7) Maize + Black gram (1:1), (T_8) Maize + Black gram (1:2) and, (T_9) Maize + Black gram (1:3) (Fig. 2). Sole Maize and intercropped maize were provided with the recommended dose of fertilizer of Maize, while in the sole Black gram and French bean plot, recommended doses of the respective legume were provided. The Sandy loam soil contained 0.152% organic carbon (low), available nitrogen (300 kg.ha^{-1}) (medium), available phosphorus (16 kg.ha^{-1}) (high), available potassium
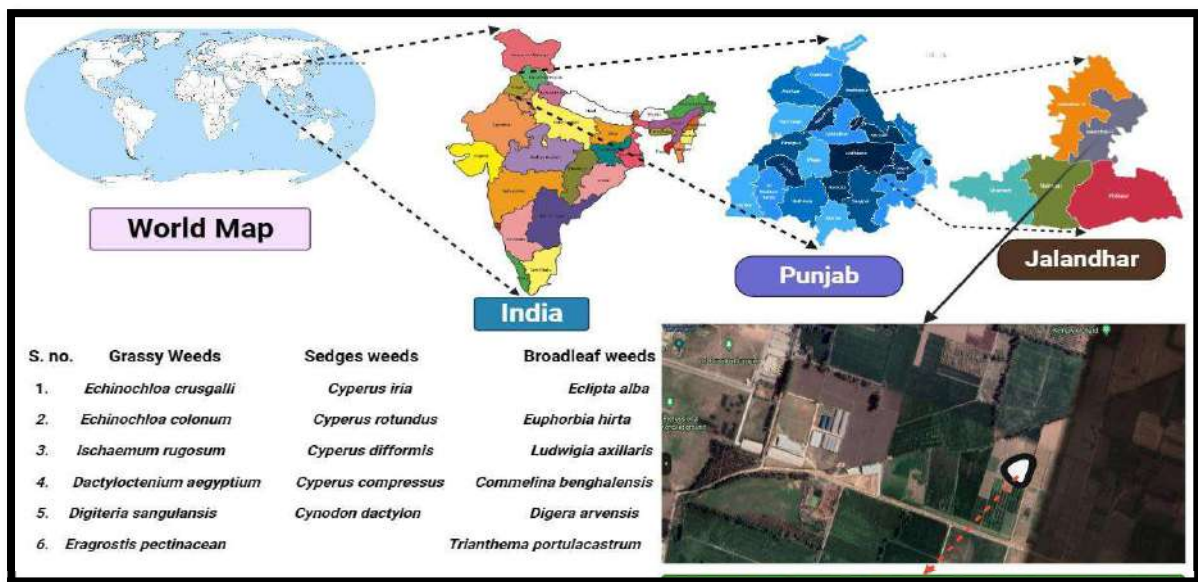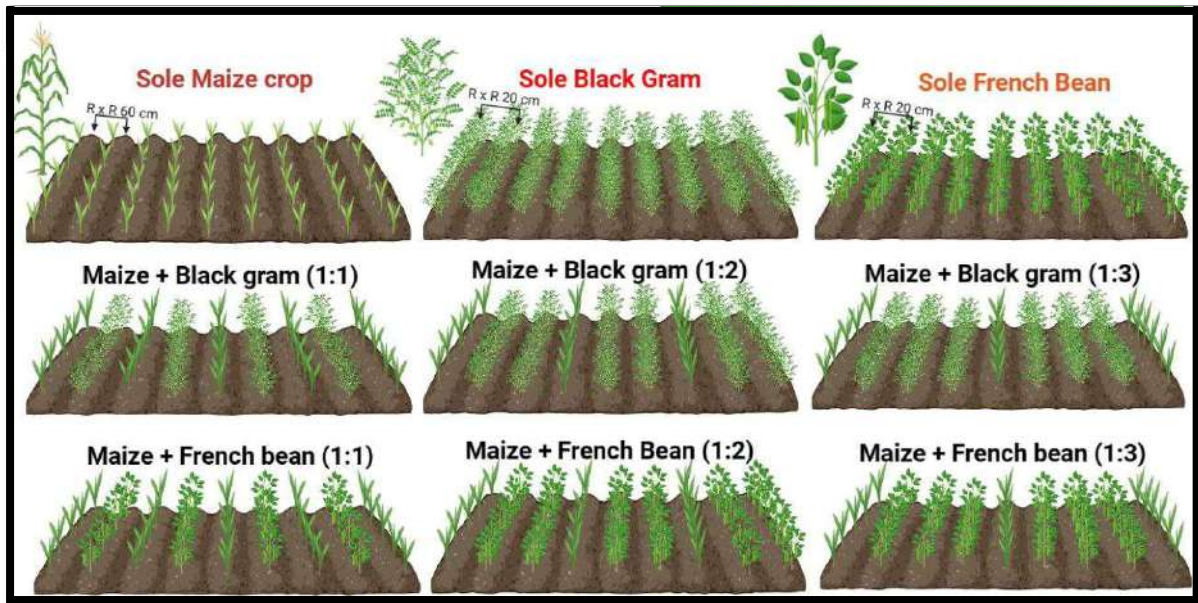

Fig. 1: The research experimental site.

Fig. 2: The treatments' row ratios.

(125 kg.ha^{-1}) (medium), electrical conductivity (0.370 dsm^{-1}) (normal), and pH 7.9 (normal).

Weed Density and Weed Biomass

Weed density was calculated with the help of a quadrant of 1 m^2 from each plot at 30 DAS and 60 DAS. A sickle was used to cut the weeds, and an electric balance was used to weigh them. Weeds were then sun-dried for a week, stored in an oven at 42°C, and repeatedly weighed until, after 24 hours, a stable dry weight was reached.

Yield Attributes of Maize

The number of rows cob^{-1}, number of cobs plant^{-1}, number of grains row^{-1} cob^{-1}, length of cob, number of pods plant^{-1}, and seed pod^{-1} were manually counted when the crop was harvested at its maximum maturity. Cob thickness was recorded with the help of an electric vernier caliper. Following threshing, an electronic weighing scale was used to measure the yield characteristics, including seed index, grain yield, and stover yield. The plant samples were then dried in the sun for three days and then dried in an oven for 72 hours at 60°C to measure the biomass. The seed index was noted with the help of the seed counter. Grain and stover yield were calculated at harvest maturity. The Harvest index was calculated by the formula given by Donald in 1968. Land equivalent ratio and Maize equivalent yield were using the following formula.

$$\text{LER} = \frac{Yield\ of\ intercropped\ maize}{Yield\ of\ sole\ maize} +$$

$$\frac{Yield\ of\ intercropped\ pulse}{Yiel\ of\ sole\ pulse}$$

$$\text{MEY} = Grain\ yield\ of\ maize +$$

$$\frac{Yield\ of\ intercrop \times Price\ of\ intercrop}{Price\ of\ maize}$$

Soil Physico-Chemical and Biological Properties

The soil samples were collected before sowing from each plot (Four from the corner and one from the center) and thoroughly homogenized for subsequent analyses. The pH and EC of soil were measured with pH meter and EC meter respectively (Jackson 1973). Walkley & Black (1934) method was used for Organic Carbon estimation. For estimating total nitrogen (N) content, distillation in the Kjeldahl apparatus was performed that was followed by titration with the concentrated H_2SO_4. Available Phosphorus was estimated using Olsen's method (1954) by spectrophotometer at 660 nm wavelength and Available Potassium was determined with the help of a flame photometer as described by Merwin & Peech (1950).

Soil Rhizosphere Bacterial Analysis

Standard approaches (Ellinghausen & Pelczar 1957, Lacey 1997, Collins et al. 2006, Chatterjee et al. 2014, Azmi & Chatterjee 2016) were followed to count the population of several bacterial groups. Phosphate solubilizing bacteria (PSB), nitrate-reducing bacteria (NRB), nitrifying bacteria (NB), aerobic heterotrophic bacteria, or total heterotrophic

bacteria (THB) were among the 0.1–1% of soil bacteria that were grown. One-gram samples of soil were suspended in 99 ml of distilled water and diluted to a 10^{-3} ratio. These diluted soil samples were combined with various specialized media to count the number of bacteria belonging to various groups.

Statistical Analysis

ANOVA was carried out on the data by applying the function of Post hoc, Tukey, and Duncan using SPSS 22 software. Homogeneity of variance was adapted, and results were expressed as means ± standard deviation. To find out the most efficient treatment Duncan's multiple range test (DMRT) a mean separation technique was applied with probability $p < 0.05$. Fisher's LSD test as a post hoc test was used to test the significance of the variation components.

RESULTS

Weed Infestation

Incidentally, the weed flora recorded at the experimental site mainly consisted of Grasses, sedges, and broad-leaf weeds as mentioned in Table 1.

Grassy weed density (No.m^{-2}) at 30 and 60 DAS: The density of grassy weeds in sole and intercropped treatments was recorded at 30 and 60 DAS (Tables 2 and 3). The data indicated that at 30 DAS the minimum (3.44 m^{-2}) grassy weed density was measured in Maize + Black gram (1:3) and maximum (5.30 m^{-2}) was observed in Sole Maize followed by Sole French bean (4.93 m^{-2}) which was at par with Sole Black gram (4.78 m^{-2}). At 60 DAS, the minimum (3.26 m^{-2}) grassy weed density was measured in Maize + Black gram (1:3), and the maximum (6.6 m^{-2}) was recorded in Sole Maize followed by Sole French bean (5.46 m^{-2}) and Sole Black gram (4.7 m^{-2}).

Weed sedges density (No.m^{-2}) at 30 and 60 DAS: The density of sedges weeds in sole and intercropped treatments was recorded at 30 and 60 DAS, represented, and discussed below in Tables 2 and 3 respectively. Sedges weed density varied greatly over different treatments. Density was remarkably lower in intercrops than in their sole crops. The data indicated that at 30 DAS, the minimum (3.13 m^{-2}) weed sedge density was recorded in Maize + Black gram (1:3), and maximum (5.19 m^{-2}) was observed in Sole Maize followed by Sole French bean (4.46 m^{-2}) and Sole Black gram (4.41 m^{-2}). At 60 DAS, the minimum (2.73 m^{-2}) weed sedges density was observed in Maize + Black gram (1:3), and maximum (5.19 m^{-2}) was recorded in Sole Maize followed by Sole French bean (4.10 m^{-2}) which was at par with Sole Black gram (4.01 m^{-2}).

Broadleaf weeds density (BLWD) (No.m^{-2}) at 30 and 60 DAS: Broad leaf weed density varied greatly over different treatments and is discussed below. The data indicated that at 30 DAS as seen in Table 2, the minimum (3.26 m^{-2}) BLWD was recorded in Maize + Black gram (1:3), and maximum (6.19 m^{-2}) was observed in Sole Maize followed by Sole French bean (4.97 m^{-2}) and Sole Black gram (4.89 m^{-2}). As seen in Table 3 at 60 DAS, the minimum (4.58 m^{-2}) BLWD was measured in Maize + Black gram (1:3), and the maximum (8.96 m^{-2}) was recorded in Sole Maize followed by Sole French bean (6.50 m^{-2}) which is followed by Sole Black gram (6.16 m^{-2}).

Total weed density (TWD) (No.m^{-2}) at 30 and 60 DAS: The Total weed density was remarkably lower in intercrops than in their sole crops. The data in Table 2 indicated that at 30 DAS, the minimum (5.66 m^{-2}) TWD was measured in Maize + Black gram (1:3) maximum weed density (9.23 m^{-2}) was seen in Sole Maize followed by followed by Sole French bean (7.55 m^{-2}) and Sole Black gram (7.55 m^{-2}). At 60 DAS the data indicated in Table 3, the minimum (5.91 m^{-2}) TWD was measured in Maize + Black gram (1:3), and maximum (12.02 m^{-2}) was observed in Sole Maize followed by Sole French bean (8.87 m^{-2}) which is followed by Sole Black gram (8.33 m^{-2}).

Grass biomass density (g.m^{-2}) at 30 and 60 DAS: The density of grasses weed biomass in sole and intercropped treatments was recorded at 30 and 60 DAS, represented, and discussed below in Tables 4 and 5 respectively. The data

Table 1: Weed infestation species-wise mentioned in the table during the field trial.

S.No.	Grassy weeds	Common name	Sedges weeds	Common name	Broadleaf weeds	Common name
1.	*Echinochloa crusgalli*	Swank	*Cyperus iria*	Chatri wala dila	*Eclipta alba*	Jalbhan grass
2.	*Echinochloa colonum*	Barnyard grass	*Cyperus rotundus*	Nut grass	*Euphorbia hirta*	Dhodhak
3.	*Ischaemum rugosum*	Wrinkle grass	*Cyperus difformis*	Dila motha	*Ludwigia axillaris*	Gharilla
4.	*Dactyloctenium aegyptium*	Egyptian crowfoot grass	*Cyperus compressus*	Motha	*Commelina benghalensis*	Benghal dayflower
5.	*Digiteria sangulansis*	Crab grass	*Cynodon dactylon*	Bermuda grass	*Digera arvensis*	False amaranth
6.	*Eragrostis pectinacean*	Tufted lovegrass			*Trianthema portulacastrum*	Pigweed

Table 2: Effect of intercropping of maize with legumes on weed density at 30 DAS.

Weed density at 30 DAS				
Treatments	Grassy weed density (No.m^{-2})	Sedges weed density (No.m^{-2})	Broadleaf weed density (No.m^{-2})	Total weed density (No.m^{-2})
T$_1$- Sole Maize	5.30^a(23.00) ± 0.09	5.19^a(22.00) ± 0.17	6.19^a(32.33) ±0.11	9.23^a(76.33) ± 0.23
T$_2$- Sole French bean	4.93^b(19.67) ± 0.05	4.46^b(15.67) ± 0.06	4.97^b(20.00) ± 0.09	7.55^b(53.67) ± 0.03
T$_3$- Sole black gram	4.78^{bc}(18.33) ± 0.05	4.41^b(15.33) ± 0.12	4.89^b(19.33) ± 0.14	7.55^b(49.67) ± 0.03
T$_4$- Maize + French bean (1:1)	4.66^c(17.33) ± 0.06	4.24^b(14.00) ±0.11	4.78^{bc}(18.33) ±0.14	7.52^b(43.67) ± 0.12
T$_5$-Maize + French bean (1:2)	4.24^e(14.00) ± 0.11	3.86^{bc}(11.33) ± 0.18	4.24^d(14.00) ± 0.11	7.11^c(49.33) ± 0.04
T$_6$-Maize + French bean (1:3)	4.01^f(12.33) ± 0.14	3.38^{cd}(9.33) ±0.21	3.96^e(12.00) ± 0.12	6.30^d(33.67) ± 0.08
T$_7$-Maize + Black gram (1:1)	4.46^d(15.67) ± 0.06	4.15^b(13.33) ± 0.13	4.62^c(17.00) ± 0.10	7.50^b(49.67) ± 0.31
T$_8$-Maize + Black gram (1:2)	3.76^g(10.67) ± 0.14	3.26^d(8.33) ± 0.23	3.61^f(9.67) ± 0.08	5.79^e(33.67) ± 0.15
T$_9$-Maize + Black gram (1:3)	3.44^h(8.67) ± 0.08	3.13^d(7.33) ± 0.64	3.26^e(7.67) ± 0.16	5.66^e(26.67) ± 0.12

*Data is in the form of mean ± SDM at p ≤ 0.05. the mean followed by different letters was significantly different at p ≤ 0.05, according to DMRT for separation of means. Figures in the parenthesis are original values as observation, while without parentheses are transformed (√x+0.5) values.

Table 3: Effect of intercropping of maize with legumes on weed density at 60 DAS.

Weed density at 60 DAS				
Treatments	Grassy weed density (no.m^{-2})	Sedges weed density (No.m^{-2})	Broadleaf weed density (No.m^{-2})	Total weed density (No.m^{-2})
T$_1$- Sole Maize	6.69^a(38.33) ±0.11	5.19^a(22.00) ±0.09	8.96^a(71.67) ± 0.09	12.02^a(132.67)0.11±
T$_2$- Sole French bean	5.46^b(24.67) ± 0.10	4.10^b(13.00) ± 0.11	6.50^b(36.00) ± 0.11	8.87^b(70.00) ± 0.10
T$_3$- Sole black gram	4.70^c(17.67) ± 0.06	4.01^{bc}(12.33) ± 0.18	6.16^c(32.00) ± 0.18	8.33^c(61.33) ± 0.06
T$_4$- Maize + French bean (1:1)	4.58^{cd}(16.67) ± 0.10	3.76^c(10.67) ±0.14	6.10^c(31.33) ± 0.14	7.92^d(55.00) ± 0.10
T$_5$-Maize + French bean (1:2)	4.24^{cd}(14.00) ± 0.07	3.32^d(8.00) ±0.14	5.53^d(25.33) ± 0.14	7.62^e(50.67) ± 0.07
T$_6$-Maize + French bean (1:3)	4.12^d(11.00) ±0.08	2.97^e(6.33) ±0.03	5.12^e(21.33) ± 0.03	6.55^f(36.67) ± 0.08
T$_7$-Maize + Black gram (1:1)	4.45^{cd}(15.67) ± 0.15	3.44^d(8.67) ±0.08	5.70^d(27.00) ± 0.08	7.85^{de}(54.00) ± 0.15
T$_8$-Maize + Black gram (1:2)	3.44^e(8.67) ±0.15	2.88^e(5.67) ±0.10	4.62^f(17.00) ± 0.10	6.21^g(32.67) ± 0.15
T$_9$-Maize + Black gram (1:3)	3.26^e(7.67) ± 0.16	2.73^e(5.00) ±0.18	4.58^f(16.67) ± 0.18	5.91^h(29.33) ± 0.16

*Data is in the form of mean ± SDM at p ≤ 0.05. the mean followed by different letters was significantly different at p ≤ 0.05, according to DMRT for separation of means. Figures in the parenthesis are original values as observation, while without parentheses are transformed (√x+0.5) values.

indicated that at 30 DAS the minimum (2.52 g.m^{-2}) grasses biomass density was recorded in Maize + Black gram (1:3) and maximum (3.69 g.m^{-2}) was observed in Sole Maize followed by followed by Sole French bean (3.44 g.m^{-2}) and it was at par with Sole Black gram (3.33 g.m^{-2}). At 60 DAS, the minimum (2.08 g.m^{-2}) grasses biomass density was recorded in Maize + Black gram (1:3), and maximum (4.16 g.m^{-2}) was observed in Sole Maize followed by Sole French bean (3.65 g.m^{-2}) and Sole Black gram (3.45 g.m^2).

Sedges biomass density (g.m^{-2}) at 30 and 60 DAS: The sedges biomass density was recorded at 30 and 60 DAS (Tables 4 and 5) in sole and intercropped treatments. The data indicated that at 30 DAS, the minimum (2.24 g.m^{-2}) sedges biomass density was recorded in Maize + Black gram (1:3), and maximum (4.05 g.m^{-2}) was observed in Sole Maize followed by which was at par with Sole French bean (3.64

g.m^{-2}) and Sole Black gram (3.55 g.m^{-2}). At 60 DAS, the minimum (1.50 g.m^{-2}) sedges biomass density was recorded in Maize + Black gram (1:3), and the maximum (3.56 g.m^{-2}) was measured in Sole Maize followed by Sole French bean (2.36 g.m^{-2}) and Sole Black gram (2.14 g.m^{-2}).

Broadleaf weeds biomass density (BLWBD) (g.m^{-2}) at 30 and 60 DAS: The broadleaf weeds biomass density was recorded at 30 and 60 DAS (Table 4 and 5) in sole and intercropped treatments. Broadleaf weed biomass varied greatly over different treatments. The data indicated that at 30 DAS, the minimum (2.33 g.m^{-2}) BLWBD was recorded in Maize + Black gram (1:3), and maximum (3.64 g.m^{-2}) was observed in Sole Maize followed by which was at par with Sole French bean (3.19 g.m^{-2}) and Sole Black gram (3.19 g.m^{-2}). At 60 DAS, the minimum (2.67 g.m^{-2}) BLWBD was recorded in Maize + Black gram (1:3), and maximum (5.05 g.m^{-2}) was observed in Sole Maize followed

Table 4: Effect of intercropping of maize with legumes on weed biomass at 30 DAS.

Weed biomass at 30 DAS				
Treatments	Grassy weed biomass (No.m^{-2})	Sedges weed biomass (No.m^{-2})	Broadleaf weed biomass (No.m^{-2})	Total weed biomass (No. m^{-2})
T$_1$- Sole Maize	3.69^a(10.17) ± 0.03	4.05^a(12.60) ± 0.03	3.64^a(12.60) ± 0.05	6.21^a(9.83) ± 0.05
T$_2$- Sole French bean	3.44^b(8.63) ± 0.07	3.64^{ab}(9.83) ± 0.05	3.19^b(9.83) ± 0.02	5.51^b(7.24) ± 0.02
T$_3$- Sole black gram	3.33^{bc}(8.04) ± 0.03	3.55^{ab}(9.32) ± 0.08	3.18^b(9.32) ± 0.05	5.50^b(7.17) ± 0.05
T$_4$- Maize + French bean (1:1)	3.31^c(7.90) ± 0.03	3.54^{ab}(9.28) ± 0.02	3.00^{bc}(9.28) ± 0.16	5.34^{bc}(6.30) ± 0.16
T$_5$-Maize + French bean (1:2)	3.11^d(6.85) ± 0.04	2.79^{cd}(7.72) ± 0.04	2.82^c(7.72) ± 0.07	5.09^d(5.37) ± 0.07
T$_6$-Maize + French bean (1:3)	2.89^e(5.70) ± 0.02	2.79^{cd}(5.26) ± 0.95	2.58^{de}(5.26) ± 0.04	4.41^e(4.33) ± 0.04
T$_7$-Maize + Black gram (1:1)	3.24^c(7.52) ± 0.02	3.28^{bc}(8.87) ± 0.05	2.97^c(8.87) ± 0.03	5.14^{cd}(6.10) ± 0.03
T$_8$-Maize + Black gram (1:2)	2.73^f(5.00) ± 0.11	2.61^{cd}(4.44) ± 0.01	2.47^{de}(4.44) ± 0.11	3.87^f(3.37) ± 0.11
T$_9$-Maize + Black gram (1:3)	2.52^g(4.07) ± 0.01	2.24^d(3.02) ± 0.04	2.33^e(3.02) ± 0.16	3.73^f(3.10) ± 0.16

*Data is in the form of mean ± SDM at p ≤ 0.05. the mean followed by different letters was significantly different at p ≤ 0.05, according to DMRT for separation of means. Figures in the parenthesis are original values as observation, while without parentheses are transformed ($\sqrt{x+0.5}$) values.

Table 5: Effect of intercropping of maize with legumes on weed biomass at 60 DAS

Weed biomass at 60 DAS				
Treatments	Grassy weed biomass (g.m^{-2})	Sedges weed biomass (g.m^{-2})	Broadleaf weed biomass (g.m^{-2})	Total weed biomass (g.m^{-2})
T$_1$- Sole Maize	4.16^a(15.07) ± 0.06	3.56^a(10.31)± 0.36	5.05^a(20.73) ± 0.12	7.29^a(46.11) ± 0.12
T$_2$- Sole French bean	3.65^b(11.73) ± 0.16	2.36^b(4.92) ± 0.24	4.57^b(16.57) ± 0.05	6.06^b(30.95) ± 0.07
T$_3$- Sole black gram	3.45^b(7.15) ± 0.35	2.14^b(3.50) ± 0.30	4.48^b(15.87) ± 0.04	5.59^{bc}(25.91) ± 0.05
T$_4$- Maize + French bean (1:1)	2.95^{bc}(6.70) ± 0.12	1.94^{bc}(2.50) ± 0.16	4.28^c(14.30) ± 0.07	5.43^{bc}(24.28) ± 0.02
T$_5$-Maize + French bean (1:2)	2.71^{cd}(5.44) ± 0.23	1.85^{bc}(1.88) ± 0.46	3.99^d(12.20) ± 0.05	4.57^{cde}(21.01) ± 0.07
T$_6$-Maize + French bean (1:3)	2.47^{de}(4.38) ± 0.15	1.83^{bc}(1.76) ± 0.16	3.97^d(12.07) ± 0.03	4.23^{def}(16.56) ± 1.43
T$_7$-Maize + Black gram (1:1)	2.93^c(6.53) ± 0.13	1.92^{bc}(2.20) ± 0.16	4.11^d(13.07) ± 0.06	5.08^{bcd}(22.27) ± 0.12
T$_8$-Maize + Black gram (1:2)	2.11^{ef}(2.60) ± 0.07	1.56^c(1.20) ± 0.06	2.81^e(5.33) ± 0.07	3.80^{ef}(10.92) ± 0.09
T$_9$-Maize + Black gram (1:3)	2.08^f(2.51) ± 0.10	1.50^c(1.14) ± 0.25	2.67^e(4.73) ± 0.09	3.39^f(8.38) ± 0.08

*Data is in the form of mean ± SDM at p ≤ 0.05. the mean followed by different letters was significantly different at p ≤ 0.05, according to DMRT for separation of means. Figures in the parenthesis are original values as observation, while without parentheses are transformed ($\sqrt{x+0.5}$) values.

by Sole French bean (4.57 g.m^{-2}) and Sole Black gram (4.48 g.m^{-2}).

Total weed biomass density (TWBD) (g.m^{-2}) at 30 and 60 DAS: Total weed biomass density varied greatly over different treatments and is discussed in Tables 4 and 5 respectively. The data indicated that at 30 DAS, the minimum (3.73 g.m^{-2}) TWBD was recorded in Maize + Black gram (1:3), and the maximum (6.21 g.m^{-2}) TWBD was recorded in Sole Maize followed by Sole French bean (5.51 g.m^{-2}) which was at par with Sole Black gram (5.50 g.m^{-2}). At 60 DAS, the minimum (3.39 g.m^{-2}) TWBD was observed in Maize + Black gram (1:3), and maximum (7.29 g.m^{-2}) TWBD was recorded in Sole Maize followed by Sole French bean (6.06 g.m^{-2}) which was at par with Sole Black gram (5.59 g.m^{-2}).

Yield Attributes of Maize

Number of cobs plant^{-1}, Length of cob and Cob diameter: The number of cob plant^{-1} was maximum (2) in Maize + Black gram (1:2) and Maize + Black gram (1:3) intercropping system followed by Maize + French bean (1:2) (1.73). The length of cob was maximum (19.33 cm) in Maize + Black gram (1:2) followed by Maize + Black gram (1:2) (18.45 cm) which was almost like Maize + French bean (1:2) (18.36 cm). Cob diameter had similar results i.e., it was maximum (8.37 mm) in Maize + Black gram (1:2) followed by Maize + Black gram (1:3) (8.10 mm) and Maize + French bean (1:2) (8.03 mm) (Table 6).

Number of grains row^{-1}cob^{-1} and, Number of rows cob^{-1}: The maximum number of grains row^{-1} cob^{-1} (484.33) was noticed in Maize + Black gram (1:2) intercropping system

Table 6: Effect of intercropping of maize with legumes on yield attributes of maize.

Treatments	No. of cobs plant⁻¹	Length of cob (cm)	Cob diameter (mm)	No. of rows cob⁻¹	No. of grain rows⁻¹ cob⁻¹	Grain yield (kg.ha⁻¹)	Stover yield (kg. ha⁻¹)	Harvest index (%)	Seed index (g)
T_1	$1.00^c\pm0.00$	$16.70^d\pm0.12$	$7.37^e\pm0.2$	$14.33^d\pm0.47$	$455.67^e\pm3.7$	$5434.5^e\pm37.16$	$6597.10^f\pm38.62$	$43.78^d\pm0.05$	$20.8^d\pm0.4$
T_4	$1.17^b0.24\pm$	$17.03^{cd}\pm0.17$	$7.67^d\pm0.1$	$15.33^c\pm0.47$	$465.33^d\pm3.4$	$5629.33^d\pm18.01$	$7150.40^e\pm16.51$	$43.93^{cd}\pm0.02$	$22.9^c\pm1.4$
T_5	$1.73^a\pm0.21$	$18.36^b\pm0.24$	$8.03^{bc}\pm0.1$	$16.80^b\pm0.43$	$476.67^{bc}\pm2.5$	$5776.33^b\pm22.40$	$7328.40^c\pm27.53$	$44.15^{bc}\pm0.04$	$26.1^b\pm0.6$
T_6	$1.67^{ab}\pm0.24$	$18.17^b\pm0.12$	$7.93^{bc}\pm0.0$	$16.30^b\pm0.42$	$474.00^{bc}\pm0.8$	$5723.00^c\pm8.29$	$7274.33^{cd}\pm59.00$	$44.03^{bcd}\pm0.02$	$25.7^b\pm0.4$
T_7	$1.33^{bc}\pm0.24$	$17.5^c\pm0.23$	$7.82^{cd}\pm0.1$	$15.67^c\pm0.47$	$471.33^c\pm0.9$	$5696.33^c\pm12.71$	$7223.00^{de}\pm27.86$	$43.99^{cd}\pm0.05$	$23.3^c\pm0.9$
T_8	$2.00^a\pm0.00$	$19.33^a\pm0.39$	$8.37^a\pm0.1$	$18.33^a\pm0.47$	$484.33^a\pm1.7$	$5911.50^a\pm35.72$	$7519.00^a\pm43.23$	$45.17^a\pm0.31$	$28.4^a\pm1.0$
T_9	$2.00^a\pm0.00$	$18.45^b\pm0.19$	$8.10^b\pm0.1$	$17.27^b\pm0.25$	$479.00^b\pm2.2$	$5805.50^b\pm19.93$	$7414.67^b\pm17.00$	$44.30^b\pm0.10$	$27.3^{ab}\pm0.2$

*Data is in the form of mean ± SDM at $p \leq 0.05$. the mean followed by different letters was significantly different at $p \leq 0.05$, according to DMRT for separation of means. Figures in the parenthesis are original values as observation, while without parentheses are transformed ($\sqrt{x+0.5}$) values.

followed by Maize + Black gram (1:3) (479.00) and Maize + French bean (1:2) (476.67). The lowest (455.67) number of grains row⁻¹ cob⁻¹ was recorded in sole Maize. The number of rows cob⁻¹ was found maximum (18.33) in Maize + Black gram (1:2) followed by Maize + Black gram (1:3) (17.27) and Maize + French bean (1:2) (16.80) (Table 6).

Grain Yield and Stover Yield

Table 6 indicated that the maximum grain yield (5911.50 kg.ha⁻¹) was recorded in Maize + Black gram (1:2) followed by Maize + Black gram (1:3) (5805.50 kg.ha⁻¹) and Maize + French bean (1:2) (5776.33). Similarly, stover yield was also noted as maximum (7519.00 kg.ha⁻¹) in Maize + Black gram (1:2) followed by Maize + Black gram (1:3) (7414.67 kg.ha⁻¹) and Maize + French bean (1:2) (7328.40 kg.ha⁻¹).

Seed Index and Harvest Index

Intercropping of Maize and legumes considerably impacts the Maize's harvest index and seed index (Table 6). It is seen that other treatments with legumes had an almost similar reading, but the maximum seed index (28.40 g) was found in Maize + Black gram (1:2) followed by Maize + Black gram (1:3) (27.30 g) and Maize + French bean (1:2) (26.10 g). Similarly, maximum harvest index (45.17 %) was recorded in Maize + Black gram (1:2) followed by Maize + Black gram (1:2) (44.30%) and Maize + French bean (1:2) (44.15%).

Land Equivalent Ratio and Maize Equivalent Yield

Maize equivalent yield and land equivalent ratio were higher with maize + Black gram intercropping followed by maize + French bean and sole maize (Table 7). LER showed positive influences on the growth and yield of maize and legume intercrops (LER > 1) in Maize + Black gram and maize + French bean intercropping (Table 7). Maximum LER (2.23) is obtained from Maize + Black gram (1:2). Maize + French bean (1:2) and Maize + French bean (1:3) had equal LER (2.16). This indicates that the sole maize crop would need 123% (1.23 ha) and 116% (1.16 ha) more land to produce the same amount as an intercropping system. MEY of sole maize was recorded as a minimum (5434.50 kg.ha⁻¹) and found maximum (11671.03 kg.ha⁻¹) in Maize + Black gram (1:2).

Rhizosphere Soil Bacterial Community

The Rhizosphere soil bacterial community varied greatly over different treatments recorded at 30 and 90 DAS (Fig. 3).

Total heterotrophic bacteria (THB)- The data indicated that at 30 DAS, the minimum (5.08) total heterotrophic bacteria (THB) were recorded in sole maize and maximum (232.82) (THB) was recorded in Maize + French bean (1:3). At 90 DAS, the minimum (20.33) (total heterotrophic

Table 7: Effect of intercropping on Land equivalent ratio (LER) and Maize equivalent yield (MEY kg.ha^{-1})

Treatments	LER	MEY kg.ha^{-1}
T1- Sole Maize	$1.00^e \pm 0$	$5434^e.50$
T2- Sole French bean	$1.00^e \pm 0$	-
T3- Sole Black gram	$1.00^e \pm 0$	-
T4-Maize+French bean (1:1)	$2.11^d \pm 0$	$7916.26^d \pm 45.99$
T5-Maize+ French bean (1:2)	$2.16^c \pm 0.01$	$8536.81^c \pm 104.58$
T6-Maize+French bean (1:3)	$2.16^c \pm 0.03$	$8165.19^d \pm 57.53$
T7-Maize+ Black gram (1:1)	$2.11^d \pm 0.03$	$10969.55^b \pm 134.18$
T8-Maize+Black gram (1:2)	$2.23^a \pm 0.01$	$11671.03^a \pm 229.67$
T9-Maize+Black gram (1:3)	$2.19^b \pm 0.01$	$11165.18^b \pm 96.44$

bacteria (THB) was measured in sole maize and maximum (341.6) was recorded in maize + black gram (1:3).

Phosphate solubilizing bacteria (PSB)- The 30 DAS data indicated that the minimum (1.83) PSB was recorded in maize + French bean (1:3) and the maximum (18.7) PSB was recorded in sole French bean. AT 90 DAS the PSB minimum (1.12) sole maize and maximum (113.87) was observed in maize + black gram (1:3).

Nitrate-reducing bacteria (NRB)- The 30 DAS data indicated that the minimum (0.49) NRB was observed in sole maize and maximum (41.89) was recorded in maize + French bean (1:3). At 90 DAS the minimum (1.53) was recorded in sole maize and maximum (73.2) was observed in maize + black gram (1:3).

Nitrifying bacteria (NB)- The 30 DAS data indicated that the minimum (0.16) NB was measured in sole maize

and maximum (161.86) maize + black gram (1:3) and at 90 DAS minimum (29.18) nitrifying bacteria was recorded and maximum (473.77) (NB) was observed in the sole french bean.

DISCUSSION

The results of the study supported the notion that using maize as an intercrop with black or French beans suppresses weeds. Our findings demonstrated that intercropping systems, namely one row of maize planted with three rows of Black gram and French bean (T$_9$ and T$_6$), greatly reduced the density and biomass of weeds. This contrasted with maize monocultures. Because legumes compete with grassy weeds for nutrients, light, and water, they can shade out weed seedlings and grow swiftly, impeding their establishment and growth. Examples of legumes that do this are soybeans, peas, and clover. Certain legumes naturally emit compounds called allelochemicals, which can inhibit the development of neighboring plants, especially grassy weeds (Kanatas et al. 2020). These compounds could possess herbicidal qualities that prevent weeds from germinating and spreading. Studies (Gu et al. 2021) that found intercropping decreased broadleaf weed density by 47% have demonstrated this influence. Yang et al. (2021) report that intercropping dramatically reduces broadleaf weed biomass by 62%. These outcomes show how effective intercropping is in controlling weeds. Legumes and maize interplanted together form a thick canopy that shadows the ground and blocks the light needed for weed germination and growth. The taller maize plants offer shade and compete to reduce weed growth between rows, hence restricting weed establishment and development, while the spreading legume plants fill the interrow areas (Geetha et al. 2019). The
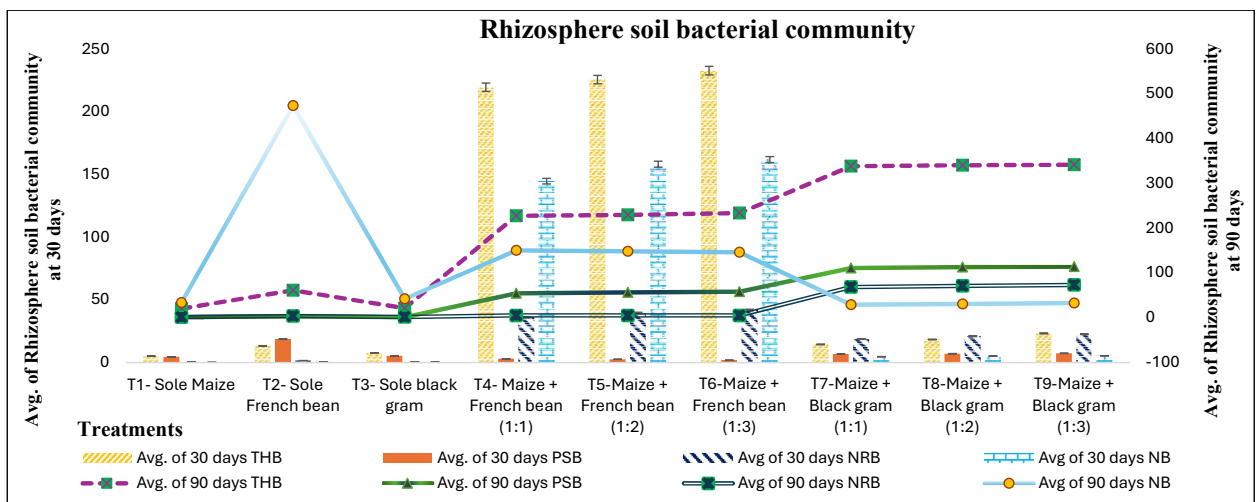

Fig. 3: Rhizosphere soil bacterial community at 30 and 90 DAS.

effective use of resources (such as water, light, and nutrients) is often responsible for intercropping's positive effects on growth and production (Raza et al. 2019). According to the most recent study, intercropping outperforms monocropping in terms of maize's physio-agronomic traits. This is most likely due to nitrogen fixation, which promotes better plant growth and development (Kebede 2021). Prior research has shown that when maize and legumes are interplanted rather than mono-cropped, there is an increase in the cob length, cob weight, number of rows cob^{-1}, 100-grain weight, stover output, and grain yield of the maize crop (Kritika et al. 2023). This is because enough N-fixation promotes increased light absorption, enzyme activity, and chlorophyll in plant leaves. Plots with intercropping produced greater grain and stover yields because intercropping raises yields by increasing total biomass. By adding nitrogen-fixing legumes to the soil, it also increases soil nitrogen, which enhances maize's ability to absorb nutrients. This is explained by legumes' complementing role in intercropping systems as a means of nutritional transmission (Thilakarathna et al. 2016) produced similar results. This might contribute to the explanation of the greater LER and MEY in both intercropping systems. Because of its sensitivity to the spatial arrangement of intercropping component crops, maize has the most significant land equivalent ratio (LER) and maize equivalent yield (MEY). Kintl et al. (2018) observed similar outcomes in their research. Intercropping maize with legumes modifies the chemical and microbiological characteristics of the rhizosphere of maize while also improving its PSB nutrition through the impacts of the rhizosphere. Richard & Ogunjobi (2016) showed that when maize cultivation length increases, so does the THB population. During the 30 DAS planting stage and the 90 DAS harvest, higher THB populations were seen in the intercropping system than in the monocropping system. According to Udom & Benwari (2019), the presence of legumes promotes a high microbial population, which improves soil structure by forming macro-aggregates from micro-aggregates, which are the foundational elements of soil structure. According to Suryanto et al. (2023), a healthy soil structure improves soil moisture and water penetration. Similarly, the PSB population needed time and the right rhizosphere conditions to thrive. Furthermore, the formation of the PSB population in the rhizospheric soil was significantly influenced by the pH and temperature of the soil (Rosalia & Hakim 2021). Early in the intercropping system with French beans, the NRB population was found to be abundant. On the other hand, in the Black gram intercropping system, the NRB population's abundance was noted throughout the mature stage of the maize plant, indicating the legume's synergistic role. The findings showed that legumes had a favorable impact on the

NB population growth .because of NB population is growing faster at 90 DAS than at 30 DAS.

CONCLUSIONS

Weed infestation caused a reduction of 40-47% in maize yield. Intercropping of maize with Black gram and French bean had a major effect on maize yield and weed population. A current study suggested that intercropping helps suppress weeds. The method proved efficient in controlling the weeds belonging to different species and helped to increase the bacterial count in the soil thereby improving the soil health and fertility. Maize yield and profitability increased as a result of better soil conditions and free from weed allelopathy effect. As a result, adopting maize + black gram 1:3 proved to be a profitable and efficient substitute for weed control in maize.

REFERENCES

Azmi, S.A. and Chatterjee, S., 2016. Population dynamics of soil bacteria in some areas of Midnapore coastal belt, West Bengal, India. *3 Biotech*, 6, pp.1-7.

Chatterjee, A.K., Chakraborty, R. and Basu, T., 2014. Mechanism of antibacterial activity of copper nanoparticles. *Nanotechnology*, 25(13), p.135101.

Choudhary, V.K. and Dixit, A., 2018. Herbicide weed management on weed dynamics, crop growth and yield in direct-seeded rice. *Indian Journal of Weed Science*, 50(1), pp. 6-12

Collins, K.M., Onwuegbuzie, A.J. and Jiao, Q.G., 2006. Prevalence of mixed-methods sampling designs in social science research. *Evaluation & Research in Education*, 19(2), pp.83-101.

Das, A.K. and Singh, V., 2016. Antioxidative free and bound phenolic constituents in botanical fractions of Indian specialty maize (*Zea mays* L.) genotypes. *Food Chemistry*, 201, pp.298-306.

Donald, C.T., 1968. The breeding of crop ideotypes. *Euphytica*, 17, pp.385-403.

Ellinghausen Jr, H.C. and Pelczar Jr, M.J., 1957. Effect of diphenylamine on pigment production by *Neisseria*. *Journal of Bacteriology*, 73(1), pp.130-132.

Geetha, A., 2019. Chapter-2 Phytotoxicity due to fungicides and herbicides and its impact in crop physiological factors. In: R.K. Naresh, ed. *Advances in Agriculture Sciences*, p.29.

Gu, C., Bastiaans, L., Anten, N.P.R., Makowski, D. and van der Werf, W., 2021. A meta-analysis on weed suppression in annual intercropping. In *Intercropping for sustainability*, 146, pp.263-264).

Jackson, W.A., Flesher, D. and Hageman, R.H., 1973. Nitrate uptake by dark-grown corn seedlings: Some characteristics of apparent induction. *Plant Physiology*, 51(1), pp.120-127.

Kanatas, P., Travlos, I., Papastylianou, P., Gazoulis, I., Kakabouki, I. and Tsekoura, A., 2020. Yield, quality and weed control in soybean crop as affected by several cultural and weed management practices. *Notulae Botanicae Horti Agrobotanici Cluj-Napoca*, 48(1), pp.329-341.

Kebede, E., 2021. Contribution, utilization, and improvement of legumes-driven biological nitrogen fixation in agricultural systems. *Frontiers in Sustainable Food Systems*, 5, p.767998.

Kintl, A., Elbl, J., Lošák, T., Vaverková, M.D. and Nedělník, J., 2018. Mixed intercropping of wheat and white clover to enhance the sustainability of the conventional cropping system: Effects on biomass production and leaching of mineral nitrogen. *Sustainability*, 10(10), p.3367.

Kritika, A.S., Jaswal, A. and Sarkar, S., 2023. Impact on maize (*Zea mays*)

productivity and yield parameters with intercropping with French bean (*Phaseolus vulgaris* L) and blackgram (*Vigna mungo*).

Lacey, L.A. (Ed.), 1997. *Manual of techniques in insect pathology*. Academic Press.

Merwin, H. and Peech, M., 1950. The release of potassium upon continuous leaching with acetic acid and different salt solutions. *Proceedings of the Soil Science Society of America*, 15, p.125.

Rani, B.S., Chandrika, V., Sagar, G.K. and Reddy, G.P., 2020. Weed management practices in maize (*Zea mays* L.): A review. *Agricultural Reviews*, 41(4), pp.328-337.

Raza, M.A., Feng, L.Y., van der Werf, W., Cai, G.R., Khalid, M.H.B., Iqbal, N. et al., 2019. Narrow-wide-row planting pattern increases the radiation use efficiency and seed yield of intercrop species in relay-intercropping system. *Food and Energy Security*, 8(3), p.e170.

Richard, P.O. and Ogunjobi, A.A., 2016. Effect of organic and inorganic fertilizer applications on phosphate solubilizing bacteria in the rhizosphere of maize (*Zea mays* L.). *African Journal of Microbiology Research*, 10(48), pp.2021-2028.

Rosalia, A.C.T. and Hakim, L., 2021. Spatial analysis of the impact of flood and drought on food security index. *Nature Environment and Pollution Technology*, 20(2), pp.721-727. http://doi.org/10.46488/NEPT.2021.v20i02.031.

Schmehl, W.R., Olsen, S.R. and Gardner, R., 1954. Effect of method of application on the availability of phosphate for sugar beets. *American Society of Sugar Beet Technologists*, 8(2), pp. 363-369.

Suryanto, S., Trinugroho, I., Susilowati, F., Aboyitungiye, J.B. and Hapsari, Y., 2023. The impact of climate change, economic growth, and population growth on food security in Central Java Indonesia. *Nature Environment & Pollution Technology*, 22(2). http://doi.org/10.46488/NEPT.2023.v22i02.048.

Thilakarathna, M.S., McElroy, M.S., Chapagain, T., Papadopoulos, Y.A. and Raizada, M.N., 2016. Belowground nitrogen transfer from legumes to non-legumes under managed herbaceous cropping systems: A review. *Agronomy for Sustainable Development*, 36, pp.1-16.

Udom, B. and Benwari, A., 2019. Soil structure, organic matter and microbial diversity in soil under some tropical cover crops. *Asian Journal of Biological Sciences*, 12(4), pp.742-749.

Walkley, A. and Black, I.A., 1934. An examination of the Degtjareff method for determining soil organic matter, and a proposed modification of the chromic acid titration method. *Soil Science*, 37(1), pp.29-38.

Yang, H., Zhang, W. and Li, L., 2021. Intercropping: Feed more people and build more sustainable agroecosystems. *Frontiers in Agricultural Science and Engineering*, 8, pp.373-386.

ORCID DETAILS OF THE AUTHORS

Kritika: https://orcid.org/0009-0002-5702-7215
Arshdeep Singh: https://orcid.org/0000-0001-8199-3494
Shimpy Sarkar: https://orcid.org/0000-0003-2856-9461
Jaspreet Kaur: https://orcid.org/0009-0002-6884-2223

Utilizing Agricultural Waste Materials for the Development of Sustainable Sound Absorption Materials

Venkatesan B.[1] , **Kannan V.[2]†** , **Raja Priya P.[3]** and **Karthiga Shenbagam N.[4]**

[1]Department of Civil Engineering, Anna University Regional Campus, Tirunelveli-627007, Tamilnadu, India

[2]Department of Civil Engineering, National Engineering College, Kovilpatti, Thoothukudi-628503, India

[3]Department of Civil Engineering, Francis Xavier Engineering College, Tirunelveli-627003, Tamilnadu, India

[4]Department of Civil Engineering, Bannari Amman Institute of Technology, Sathyamangalam, Erode District 638401, Tamilnadu, India

†Corresponding author: Kannan V.; kannanvpandian@gmail.com

ABSTRACT

Environmental pollution is escalating due to inadequate waste management, with the open burning of agricultural waste being a significant contributor. This process releases various harmful gases into the environment. This study introduces an innovative approach to creating sound absorption materials using agricultural by-products, specifically paddy straw and coconut coir, along with newspaper by-products. The research was conducted in two phases: first, the production of sound absorption panels with different densities and adhesive quantities, and second, the evaluation of these panels' sound absorption capabilities through laboratory experiments. The impedance tube test was used to determine the sound absorption coefficient (SAC). The results showed effective sound absorption, especially at lower frequencies ranging from 125 Hz to 6300 Hz. Notably, paddy straw and coconut coir exhibited significant sound absorption values at 1,000 Hz (0.59 and 0.52, respectively). This study highlights the potential of paddy straw and coconut coir as sustainable, cost-effective materials for sound absorption panels. These natural materials demonstrate excellent sound-absorbing properties, making them suitable for various applications such as classrooms, sound recording rooms, auditoriums, and theaters at low to medium frequencies.

INTRODUCTION

An acoustic panel serves as an effective sound-absorbing solution to mitigate background noise, minimize reverberation, and address echoes within a given space. Typically, these panels are sizable, soft-furnished installations strategically positioned to enhance sound quality (Carme et al. 2017, Yu et al. 2014). Constructed from a combination of foam and fabric, acoustic panels can be customized in various shapes and sizes to complement the aesthetic design of the room. Their primary function is to eliminate lingering sounds within a space (Carme et al. 2016, Fan et al. 2013, Gao et al. 2017). When appropriately installed, acoustic panels can absorb or diffuse sound right from its initial point of reflection. These sound-absorbing materials find application on the ceilings and walls of venues like auditoriums, concert halls, and theatres, where unwanted reverberation is highly undesirable. The incorporation of sound-absorbing materials in these spaces ensures that sound reflected from rigid surfaces is absorbed, thereby suppressing reverberation (Chen et al. 2011, Emms & Fox 2001, Rubino et al. 2023).

Typically, acoustic panels are crafted with a timber frame and multiple layers of acoustic foam. Foam is particularly effective as it absorbs frequencies at the surface, generating resonance within the cavity. Vertical panels, in general, play a crucial role in mitigating sound transfer within a space, preventing it from traveling across the room (Emms 2000, Rubino et al. 2023, Tsukamoto et al. 2020). Additionally, vertical panels contribute to reducing background noise to an acceptable level (Fig. 1). While achieving complete removal of background noise may require floor-to-ceiling partitions or distancing oneself from the noise source, vertical panels significantly aid in sound reduction (Redondo et al. 2021, Gao et al. 2017).

In polymeric materials, sound absorption occurs through the conversion of sound waves into heat. This process is crucial for soundproofing, with foamed plastics being the preferred choice due to their characteristic impedance similar to air. Effective soundproofing is essential for controlling unwanted noise. Acoustic treatment plays a key role in addressing three aspects of sound that can present challenges (Gao et al.
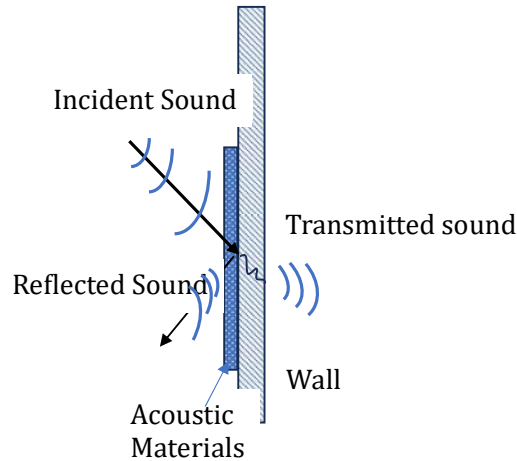
Fig. 1: Sound Transmission.

2017): reflection, reverberation, and resonance. Reflection is a common issue in various spaces where sound waves encounter surfaces, such as walls and furniture. Some surfaces absorb sound waves, while others cause them to bounce off, potentially deflecting away from the intended target, especially in places like school auditoriums, concert venues, and churches. Reflection can lead to reverberation. Reverberation occurs when multiple sound waves bounce off surfaces and converge, creating an echoey effect in certain rooms (Lam & Gan 2016, Lam et al. 2018). This phenomenon is more pronounced in large, empty spaces without sufficient sound-absorbing elements. Reverberation not only affects the clarity of music or speech but also interferes with communication in places like restaurants. Resonance is the amplification of sound when an object or material vibrates at its natural frequency upon encountering a sound wave. This can lead to boomy and distorted sounds, creating acoustic challenges for facilities.

To counter these issues, sound-absorbing acoustical panels and soundproofing materials are employed to eliminate sound reflections. Common materials include open-cell polyurethane foam, cellular melamine, fiberglass, fluffy fabrics, and other porous materials (Pàmies et al. 2018, Wang et al. 2018). These materials come in varying thicknesses and shapes to achieve different absorption ratings based on specific sound requirements. Various sound absorption materials are available, such as acoustical foam panels, paintable acoustical wall panels, fabric-wrapped panels, acoustical wall coverings, ceiling tiles, baffles, banners for ceilings, fiberglass blankets, and rolls, among others. These materials offer diverse options for effectively managing sound in different environments (Fig. 2).

MATERIALS SPECIFICATIONS AND THEIR BEHAVIOUR

Sound absorber samples were fabricated using dried paddy straw, coconut coir, and waste paper. The experimental results indicate that these agricultural by-products exhibit promising characteristics as sound absorbers, establishing them as a viable alternative among various natural fibers. Natural fibers, such as those derived from paddy straw, coconut coir, and waste paper, offer several advantages over synthetic materials like glass fiber and mineral-based substances. Notably, natural fibers are cost-effective, lightweight, and environmentally friendly (Murao &

Fig. 2: Various sound-absorbing panel systems.

Nishimura 2012, Murao et al. 2017). When compared to glass fiber and mineral-based synthetics, they prove to be more sustainable options. Additionally, natural fibers align with principles of environmental sustainability by providing a resource that can be continually produced to meet present needs without compromising the ability of future generations to meet their own requirements (Kwon & Park 2013, Pàmies et al. 2018). This inherent sustainability adds to the appeal of natural fibers as sound absorbers, making them not only effective but also in harmony with eco-friendly practices.

Paddy Straw Properties and Composition

Paddy straw, a readily available natural fiber in Southeast Asia, has been widely utilized in various applications such as roofing, rope production, animal feed, and floor mats over the past decade. However, its potential as a sound absorber panel has not been thoroughly explored until now. This paper aims to investigate the feasibility of utilizing dried paddy straw fiber as a raw material for sound-absorbing materials, a prospect motivated by its abundant availability (Carme et al. 2017, Kwon & Park 2013). Paddy straw was specifically chosen as the raw material due to its extensive availability, with a global annual production of 580 million tons. Being an annually renewable, abundant, and cost-effective source of natural cellulose fibers, rice straw presents an opportunity for creating high-value fibrous applications. This not only enhances the value of rice crops but also contributes to the sustainability of fiber resources and benefits the environment (Nelson & Elliott 1992, Huang et al. 2011, Xiao et al. 2020).

The investigation into paddy straw reveals its suitability for acoustic panels, attributed to its high elasticity and hollow structure. The properties of paddy straw fibers demonstrate superior characteristics compared to other natural cellulose fibers derived from agricultural by-products (see Table 1). The usage of rice straw depends on the extensive study of its characteristics such as the physical properties of the rice straw, thermal properties, and chemical composition. A comprehensive characterization of rice straw is indispensable

for conducting life cycle analyses and efficiency calculations in applications involving this versatile material.

As per the study conducted in previous work, it can be identified that the density of the rice straw varies from one form to other forms. When the rice straw is directly collected from the agriculture field, the density varies from 13 to 18 kg/m^3 in dry conditions. In the case of chopped rice straw, with lengths varying from 5 to 10 mm, the density varies from 55 to 120 kg/m^3. The specific experiments discussed in this context involved paddy straw chopped into lengths of 2.5 to 5.0 cm. In these experiments, the mean bulk density, true density, and porosity of the chopped paddy straw were determined. The results indicated a mean bulk density of 43.5±5 kg/m^3, a true density of 53±2.5 kg/m^3, and a porosity of 80.32±5% (see Table 2). These findings provide valuable insights into the physical characteristics of the chopped paddy straw, offering essential data for further understanding its potential applications, especially in the context of sound absorption materials (Hansen et al. 2012, Hongo & Serizawa 1999, Xu et al. 2018).

The pressure needed to compact the chopped paddy straw varied, correlating with a bulk density range of 74.54 to 475.8 kg/m^3, spanning from 65.4 to 1389.1 kPa. Within this range, the highest compaction ratio reached 6.36, with density and relaxation ratios of 0.78 and 1.43, respectively. This resulted in a significant percentage volume reduction of 465%. These parameters provide insights into the compressibility of the chopped paddy straw, essential for understanding its behavior under different pressure conditions. Moreover, the study delved into the impact of compression levels on the final moisture content of paddy straw. This investigation is crucial for comprehending how the compaction process influences

Table 1: Properties of Paddy Straw.

S. No.	Properties	Value
1	Heating value, MJ/Kg (dry basis)	17.12
2	Proximate analysis (wet basis, wt. %)	
i	Moisture	8.19
ii	Ash	12.14
iii	Volatiles	65.24
iv	Fixed carbon	12.91
3	Thermogram Vimetrical analysis, wt. %	
i	Hemicellulose	33.10

Table 2: Composition of Paddy Straw.

S.No.	Component	Percentage (%)
1	Moisture	21
2	Lignin	14.45
3	Cellulose	33
4	Nitrogen-free extract	4.21
5	Ash	18.5
6	Silica	14.23
7	Calcium	0.16
8	Phosphor	0.11
9	Potassium	0.23
10	Magnesium	0.12
11	Sulphur	0.09
12	Cobalt	0.04 (mg/kg)
13	Copper	0.40 (mg/kg)
14	Manganese	0.50 (mg/kg)

the moisture characteristics of the material, offering valuable information for various applications, including those related to sound absorption materials or other potential uses (Arenas 2007).

Waste Paper Properties and Composition

Basis weight is the weight of paper measured in pounds per ream (500 sheets). Paper and paperboard, available in a multitude of varieties, exhibit a wide range of properties. Among the thousands of paper types, some properties show only minor variations, while others differ significantly. To maintain consistency, all tests are conducted under standard conditions (24°C or 75°F; 50 percent relative humidity) as paper properties are known to change with moisture content. The surface pattern of paper can vary from smooth to slightly rough (Park & Eom 1997).

The surface sheen of paper can range from glossy (with the highest shine) to luster (medium shine) to matte (dull). In glossy papers, dark areas appear darker than in matte papers, and excessive-gloss can lead to distracting reflections. The key optical properties of paper include brightness, color, opacity, and gloss. Brightness, specifically, refers to the degree to which white or near-white papers reflect light in the blue end of the spectrum. This reflectance is measured by an instrument illuminating paper at a 45° angle with a wavelength of 457µ (microns). Brightness, measured in this way, closely correlates with subjective assessments of the paper's relative whiteness. Opacity, brightness, whiteness, color, and gloss are the five main optical properties influencing the visual perception of a printed sheet. Paper fibers, characterized by high porosity, can be easily manufactured with controlled properties, making them suitable for sound absorbers. Additionally, paper is biodegradable, poses no health risks, and can be shaped into various forms with ease. These qualities make the paper an ideal material for sound absorption applications (Tong & Tang 2013).

COCONUT COIR PROPERTIES AND COMPOSITION

Coconut fiber, derived from the husk of coconuts, stands out as a prominent fibrous waste generated by the cultivation of coconuts. Annually, the world produces a substantial 30 million tons of coconuts, particularly abundant in the coastal regions of tropical countries. The composition of the coconut husk comprises 30% fiber and 70% pith, boasting high lignin and phenolic content. The elevated lignin content renders coconut fiber exceptionally elastic, durable, and resistant to rotting (Park & Eom 1997, Hongo & Serizawa 1999, Tong et al. 2015).

Following the extraction of coconut meat and water, what remains is the fibrous coconut husk. When mature and dried, this husk can be further processed to yield another valuable product known as coconut coir. Coconut coir proves to be an excellent addition to gardening practices, enhancing the texture of clay or sandy soil, and promoting sturdy root growth in plants. Moreover, it facilitates access to additional nutrients during the feeding and watering processes. The versatility of coconut coir extends to various applications, including upholstery, agriculture, horticulture, hydroponics, and geo-textile, making it a valuable and sustainable resource in multiple industries.

Coconut coir's versatility extends to various applications beyond gardening. It can be transformed into ropes, twines, brooms, brushes, doormats, rugs, and more. Despite its multifunctionality, coconut coir has gained significant recognition in hydroponics, a gardening method that doesn't rely on soil for plant growth.

Coconut coir possesses properties that make it well-suited for hydroponics. These include:

1. **High Water Absorption:** Coconut coir has a remarkable ability to absorb and retain water, providing consistent moisture to plants in hydroponic systems.

2. **High Nutrient Absorption:** It can absorb and retain nutrients effectively, promoting the healthy growth of plants in the absence of soil.

3. **High Durability:** Coconut coir is durable and can withstand the conditions of hydroponic systems, ensuring a longer lifespan and sustained support for plant growth.

4. **Better Air-to-Water Ratio:** It offers an optimal balance between air and water, creating an environment conducive to root development and nutrient absorption.

These characteristics make coconut coir an excellent choice for hydroponics, contributing to its popularity in modern soilless cultivation systems. Its use in hydroponics has become widespread due to its positive impact on plant health and overall crop yield (see Table 3).

Some advantages of coir fibers include insect insect-proof, resistant to fungi and decay, provide good insulation against temperature and sound. They remain unaffected by external factors like humidity. Compared to other typical natural fibers, coconut fiber has higher lignin and lower cellulose and hemicellulose, together with its high microfibrillar angle, offers various valuable properties, such as resilience, strength, and damping, wear, resistance to weathering, and high elongation at break.

MATERIALS

Raw Material Preparation and Manufacturing of Panel

The construction of an absorber sample involves two distinct

Table 3: Physical and Chemical Properties of Coconut Coir Fiber.

Sl. No.	Physical Parameter		Values
1	Ultimate length		0.6 mm
2	Diameter/width		16 micron
3	Single fiber	Length	5 to 8 inches
		Density	1.42 g/cc
		Tenacity	10 g/tex
4	Breaking Elongation		20 mm
5	Moisture regains at 65% RH		10.2%
6	Swelling in water		5% in diameter
Sl.No.	Chemical Parameter		Values
1	Water soluble		5.15%
2	Pectin & related compounds		3.10%
3	Hemi-Cellulose		0.22%
4	Cellulose		41.44%
5	Lignin		44.84%
6	Ash		2.20%

Table 4: Sample specifications.

Parameter	Values
Diameter (d) of the samples	30 mm & 100 mm
Thickness of the samples	25 mm
Materials	Paddy straw, waste paper, and coconut coir
density	400 kg/m^3

stages: material cutting and sample preparation. In the material cutting stage, the raw material is processed into 2mm to 5mm lengths, as illustrated in the process flow chart. The preparation stage involves blending the raw material with various compositions of binders. The composites are defined by a weight/area of 400g/m^2, a diameter of 30mm, and a dimension of 100mm.

Paddy straw, waste paper, and coconut coir are precisely cut into small pieces ranging from 2mm to 5mm. The total weight of waste paper, coconut, and paddy straw is determined to achieve the desired concentration for a weight/area of 400g/m^2 (see Table 4). The composition of the panel primarily consists of fibers, ensuring that other factors do not affect the performance of the acoustic panel. The adhesive additives are the only additional ingredient

Fig. 5: Paddy Straw, Coconut Coir, and Waste Paper Panel (100 Mm).

Fig. 6: Paddy Straw, Coconut Coir and Waste Paper Panel (30 Mm).

applied during the panel manufacturing process. The panels are ideally bonded using adhesive additives, and the size of the panels is standardized according to impedance tube testing requirements (Figs. 5 & 6). This meticulous approach to material selection, cutting, and preparation aims to create acoustic panels with optimal performance characteristics.

Therefore, this work aims to study the potential use of Paddy Straw, Waste Paper, and coconut coir as a sound absorption material to replace synthetic materials such as glass wool, mineral wool, felts, or polyester fibers in the current market. This study revolved around the sound absorption properties of the Paddy Straw, Waster Paper, and Coconut coir fibers together with its characteristics and the form of the coir fibers.

METHODS

Impedance Tube

The research employs the two-microphone transfer function method as outlined in the International Standard ISO 10534-2 (1998) to collect data through the impedance tube method. This method offers a swift means of obtaining normal incidence factors from small samples, facilitating the assembly and disassembly of materials on the impedance tube equipment (Fig. 7).

The impedance tube method serves as the primary approach for gauging the sound absorption characteristics of fibrous materials. Utilizing the Impedance Tube Kit (Type 4206), which covers the frequency range of 50 Hz to 6.4 kHz, this method is applicable to various materials such as hood liners, headliners, fiberglass, mineral fiber, cellulose boards or blankets, as well as other fibrous materials, foam products, facing materials, fabrics, papers, and screens. The apparatus accommodates samples of up to 100 mm in diameter and 6 inches in thickness.

Testing of Impedance Tube

A sound source, typically a loudspeaker, is positioned at one end of the impedance tube, while the material sample is placed at the opposite end. The loudspeaker emits broadband, stationary random sound waves, which propagate within the tube and interact with the sample, leading to absorption. The schematic diagram illustrates the impedance tube setup employing the two-microphone transfer function method.

The interaction of sound waves within the tube generates a standing-wave interference pattern due to the combination of forward- and backward-traveling waves. By measuring sound pressure at two fixed locations and utilizing a two-channel digital frequency analyzer to calculate the complex transfer function, it becomes feasible to determine sound absorption, reflection coefficients, and the normal acoustic impedance of the material. The frequency range suitable for measurement depends on the tube diameter and microphone spacing.

In both large and small tube setups, the positioning of microphones is crucial for accurate measurements. Flush mounting of microphones prevents leakage, ensuring precise results. The impedance tube method is favored for its compactness and cost-effectiveness. It adheres to ISO and ASTM standards and is ideal for analyzing small objects exposed to normal sound waves.

Test Procedure

The test procedure entails measuring the normal incidence of sound absorption of acoustical products within an impedance tube apparatus. The apparatus comprises a tube with two microphones mounted on the sidewall, a loudspeaker affixed at one end, and a sample holder at the other end. Tube diameter selection is based on the desired frequency range: 100 mm for frequencies between 50 and 1,600 Hz, 57 mm for frequencies between 200 and 3,150 Hz, and 29 mm for frequencies between 500 and 6,300 Hz.
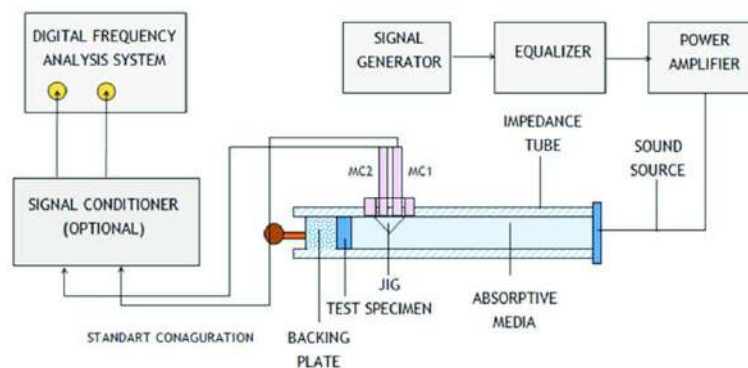

Fig. 7: Impedance Tube Kit Type 4206.

Test specimens, tailored to fit snugly into the sample holder, are subjected to the broadband sound generated within the tube. Sound amplitude and phase are measured by the microphones and a two-channel Fast Fourier Transform (FFT) analyzer. Multiple test specimens from each product are evaluated to ensure accuracy, with results averaged for comprehensive analysis.

RESULTS AND DISCUSSION

The test for sound absorption was conducted using an impedance tube, with the results presented in Fig. 8. The test samples, derived from the original molded panel with dimensions of 30mm x 100mm, included paddy straw, coconut coir, and waste paper. The samples underwent testing at different sound frequencies: 125Hz, 250Hz, 500Hz, 1000Hz, 2000Hz, 2500Hz, 3150Hz, 4000Hz, 5000Hz, and 6000Hz.

The sound absorption coefficient values for paddy straw, coconut coir, and waste paper are provided in Figs. 8, 9 and 10, respectively. These values correspond to varying densities ranging from 250 to 800 kg/m^3. The comprehensive testing across different frequencies and densities offers valuable insights into the acoustic performance of each material, aiding in the assessment of their suitability for sound absorption applications.
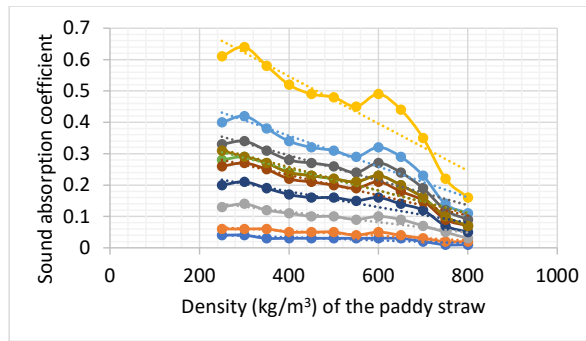

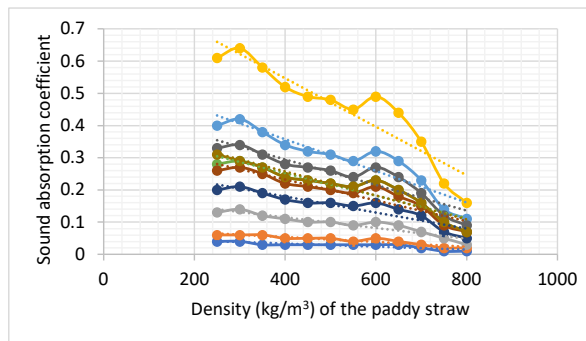Fig. 8: Sound absorption coefficient for Paddy straw.

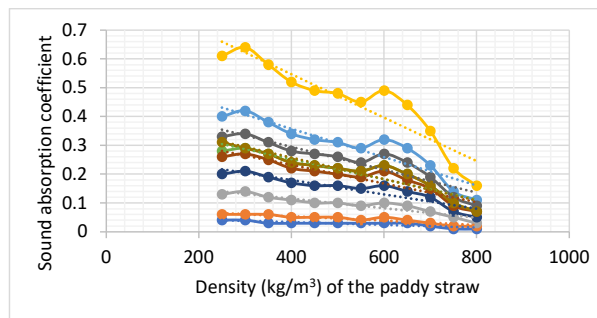Fig. 9: Sound absorption coefficient for Coconut coir.

Fig.10: Sound absorption coefficient for waste paper.

The critical property under consideration is the normal incidence sound absorption coefficient, which is a function of frequency and ranges between zero and one. The sound absorption coefficient represents the percentage of sound energy absorbed by the material sample and is a primary indicator of how an absorber material will perform in a
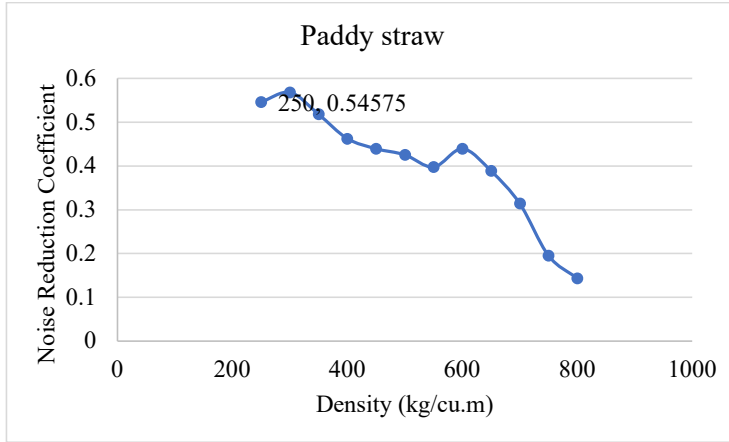

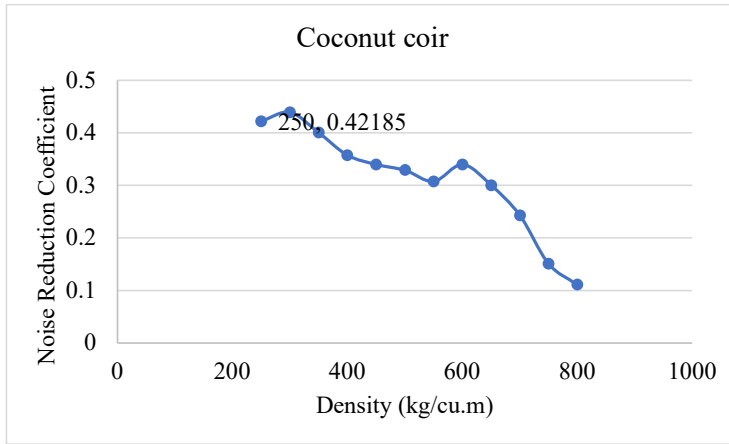Fig.11: NRC value for paddy straw sample.
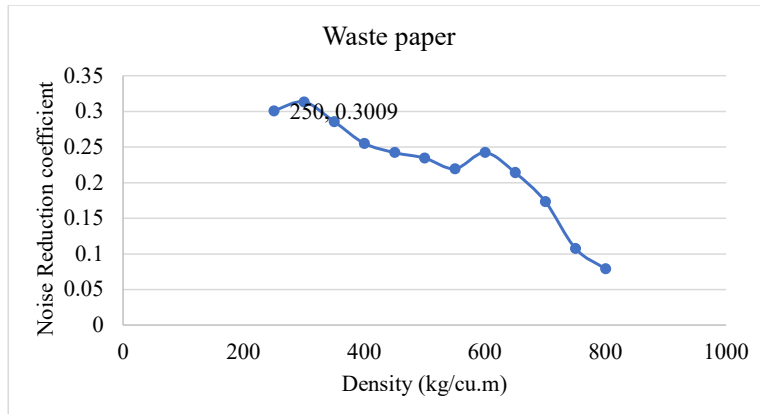

Fig. 12: NRC value for coconut coir sample.

Fig. 13: NRC value for the waste paper sample.

given environment. Sound absorbers made from agricultural byproducts, such as paddy straw, waste paper, and coconut coir, exhibit excellent properties for reducing sound and are commonly used for self-adhesive sound insulation. However, the quality of acoustic panels is crucial for them to realize their full potential as sound absorbers and effectively protect against noise. Besides high-quality materials, the installation of sound absorbers plays a crucial role in the effectiveness of soundproofing or acoustic treatment.

Notably, adhesives like spray glue or conventional assembly adhesive may not always work well when installing sound absorbers. The amount and type of adhesive used can impact the sound absorption quality of the sample, and finding the appropriate dosage to securely attach the absorber to a support surface can be challenging. The type of adhesive used may need to vary for different materials, as observed in the study where the same adhesive worked well for paddy straw and coconut coir but not for waste paper. In the process of producing and processing the samples from paddy straw, waste paper, and coconut coir, the relationship between density and sound absorption coefficients was examined. Increasing density resulted in fluctuating or slightly increased sound absorption coefficients at low frequencies, primarily due to the creation of small pores in the interior sample, making it hard for low-frequency acoustic waves to enter. However, improper compression in the manufacturing process may block the acoustic advantages of porous materials, resulting in poor sound absorption properties at both low and high frequencies. The study concludes that increasing density only insignificantly improves sound absorption properties.

Despite conventional materials having a higher sound absorption coefficient compared to agricultural byproducts, panels made from paddy straw, waste paper, and coconut coir exhibited significant performance in terms of sound absorption properties. Lower-density samples of these agricultural byproducts demonstrated higher sound absorption coefficients and noise reduction coefficients (NRC) compared to higher-density samples. The NRC values for different densities of paddy straw, coconut coir, and waste paper samples are presented in Fig. 11, 12, and 13, respectively. This observation suggests that sound absorption efficiency increases with a decrease in density and vice versa.

In the experimental results, the absorption coefficient of Paddy Straw and Coconut Coir panels was notably high, reaching values close to 0.88 and 0.82 at a density of 250 kg/m3, respectively. The performance aligns with expectations. Conversely, the waste paper sample exhibited a slightly lower sound absorption coefficient value of 0.31 at the same density. Similarly, the noise reduction coefficient values for

the samples followed a similar trend as the sound absorption coefficient values.

The sound absorption panel made by paddy straw demonstrated and showed superior performance in sound absorption properties compared to the other samples. The high absorption coefficient values, especially for Paddy Straw and Coconut Coir panels, suggest that these materials can be considered effective sound-absorbing materials. A crucial aspect highlighted in the conclusion is the positive relationship between frequency and sound absorption coefficients for Paddy Straw, Waste Paper, and Coconut Coir materials. The results steadily fell within the 0.70 or higher range, indicating a very high positive correlation between these variables. This correlation underscores the effectiveness of the materials across different frequencies, contributing to their overall suitability as sound absorbers.

CONCLUSION

The experiment demonstrates that natural fibers, particularly Paddy Straw, can serve as a viable alternative sound absorber among various other natural fibers. The choice of the methylcellulose binder was found to influence the absorption coefficient. However, it's noted that the performance, especially at lower frequencies, could be further enhanced by increasing sample thickness or coupling with a perforated panel facing. These aspects will be explored in future work by adjusting thickness and utilizing suitable adhesives, as well as incorporating an optimal number of perforations.

Key findings from the experiment include:

1. Paddy Straw shows better sound absorption performance at higher frequencies than at lower frequencies. Whereas waste Paper shows better sound absorption performance in the range of (125-1000 Hz) than at higher frequencies.

2. Coconut Coir demonstrates better sound absorption performance in the range of (1000-6300 Hz) than at higher frequencies. Increasing density has also an insignificant impact on improving the sound absorption properties of samples.

3. Increasing the number of holes effectively enhances the low-frequency sound absorption coefficients of samples. Also, increasing the adhesive quality and the amount of adhesive required can effectively enhance the low-frequency sound absorption coefficients of samples. These observations provide valuable insights into the factors influencing the sound absorption properties of the materials and suggest potential avenues for optimizing their performance in future applications.

REFERENCES

Carme, C., Schevin, O. and Clavard, J., 2017. Active noise control at the opening of a compact acoustic enclosure. *INTER-NOISE NOISE-CON Congress and Conference Proceedings*, Hong Kong SAR, China, pp.1707-1713.

Carme, C., Schevin, O., Romerowski, C. and Clavard, J., 2016. Active opening windows. *Proceedings of the 23rd International Congress on Sound and Vibration (ICSV23)*, Athens, Greece.

Chen, W., Rao, W., Min, H. and Qiu, X., 2011. An active noise barrier with unidirectional secondary sources. *Applied Acoustics*, 72, pp.969-974. http://dx.doi.org/10.1016/j.apacoust.2011.06.006.

Emms, G.W. and Fox, C., 2001. Control of sound transmission through an aperture using active sound absorption techniques: A theoretical investigation. *Applied Acoustics*, 62, pp.735-747. http://dx.doi.org/10.1016/S0003-682X(00)00063-3.

Emms, G.W., 2000. Active sound power absorbers: Their effect on sound transmission through wall openings. PhD Thesis, The University of Auckland.

Fan, R., Su, Z. and Cheng, L., 2013. Modeling, analysis, and validation of an active T-shaped noise barrier. *Journal of the Acoustical Society of America*, 134, pp.1990-2003. http://dx.doi.org/10.1121/1.4817887.

Gao, K., van Dommelen, J.A.W. and Geers, M.G.D., Investigation of the effects of the microstructure on the sound absorption performance of polymer foams using a computational homogenization approach. *European Journal of Mechanics*. https://doi.org/10.1016/j.euromechsol.2016.10.011.

Hansen, C., Snyder, S., Qiu, X., Brooks, L. and Moreau, D., 2012. Active control of free-field sound radiation. In: *Active Control of Noise and Vibration*, 2nd ed. CRC Press, pp.823-982. http://dx.doi.org/10.1201/b15923-9.

Hongo, K. and Serizawa, H., 1999. Diffraction of an acoustic plane wave by a rectangular hole in an infinitely large rigid screen. *Journal of the Acoustical Society of America*, 106, pp.29-35. http://dx.doi.org/10.1121/1.427033.

Huang, H., Qiu, X. and Kang, J., 2011. Active noise attenuation in ventilation windows. *Journal of the Acoustical Society of America*, 130, pp.176-188. http://dx.doi.org/10.1121/1.3596457.

Kwon, B. and Park, Y., 2013. Interior noise control with an active window system. *Applied Acoustics*, 74, pp.647-652. http://dx.doi.org/10.1016/j.apacoust.2012.11.005.

Lam, B. and Gan, W.S., 2016. Active acoustic windows: Towards a quieter home. *IEEE Potentials*, 35, pp.11-18. http://dx.doi.org/10.1109/MPOT.2014.2310776.

Lam, B., Elliott, S., Cheer, J. and Gan, W.S., 2018. Physical limits on the performance of active noise control through open windows. *Applied Acoustics*, 137, pp.9-17. https://doi.org/10.1016/j.apacoust.2018.02.024.

Murao, T. and Nishimura, M., 2012. Basic study on active acoustic shielding. *Journal of Environmental Engineering*, 7, pp.76-91.

Murao, T., Shi, C., Gan, W.S. and Nishimura, M., 2017. Mixed-error approach for multi-channel active noise control of open windows. *Applied Acoustics*, 127, pp.305-315. https://doi.org/10.1016/j.apacoust.2017.06.024.

Nelson, P.A. and Elliott, S.J., 1992. Point source and the active suppression of free field radiation. In: *Active Control of Sound*. Academic Press, pp.231-271.

Pàmies, T., Romeu, J., Genescà, M. and Arcos, R., 2018. Active control of aircraft fly-over sound transmission through an open window. *Applied Acoustics*, 84, pp.116-121. http://dx.doi.org/10.1016/j.apacoust.2014.02.018.

Park, H.H. and Eom, H.J., 1997. Acoustic scattering from a rectangular aperture in a thick hard screen. *Journal of the Acoustical Society of America*, 101, pp.595-598. http://dx.doi.org/10.1121/1.417971.

Redondo, J., Peiró-Torres, M.P., Llinares, C., Bravo, J.M., Pereira, A. and Amado-Mendes, P., 2021. Correlation between objective and subjective assessment of noise barriers. *Applied Acoustics*, 172, p.107640. https://doi.org/10.1016/j.apacoust.2020.107640.

Rubino, C., Liuzzi, S., Stefanizzi, P. and Martellotta, F., 2023. Characterization of sustainable building materials obtained from textile waste: From laboratory prototypes to real-world manufacturing processes. *Journal of Cleaner Production*, 390, p.136098. https://doi.org/10.1016/j.jclepro.2023.136098.

Tong, Y.G. and Tang, S.K., 2013. Plenum window insertion loss in the presence of a line source—a scale model study. *Journal of the Acoustical Society of America*, 133, pp.1458-1467. http://dx.doi.org/10.1121/1.4788996.

Tong, Y.G., Tang, S.K., Kang, J., Fung, A. and Yeung, M.K.L., 2015. Full scale field study of sound transmission across plenum windows. *Applied Acoustics*, 89, pp.244-253. http://dx.doi.org/10.1016/j.apacoust.2014.10.003.

Tsukamoto, Y., Tomikawa, Y., Sakagami, K., Okuzono, T., Maikawa, H. and Komoto, Y., 2020. Experimental assessment of sound insulation performance of a double window with porous absorbent materials its cavity perimeter. *Applied Acoustics*, 165, p.107317. https://doi.org/10.1016/j.apacoust.2020.107317.

Wang, Y., Jiao, Y. and Chen, Z., 2018. Research on the well at the top edge of noise barrier. *Applied Acoustics*, 133, pp.118-122. https://doi.org/10.1016/j.apacoust.2017.12.018.

Xiao, Y., Lai, H., Li, Q., Wang, X. and Wang, X., 2020. Improved interference-type sound barriers: Use of hyperbolic phase modulation. *Applied Acoustics*, 161, p.107186. https://doi.org/10.1016/j.apacoust.2019.107186.

Xu, X., Wang, H., Sun, Y., Han, J. and Huang, R., 2018. Sound absorbing properties of perforated composite panels of recycled rubber, fiberboard sawdust, and high-density polyethylene. *Journal of Cleaner Production*, 187, pp.215-221. https://doi.org/10.1016/j.jclepro.2018.03.174.

Yu, X., Lv, L., Wei, C., Cui, Y., Wang, X. and Li, T., 2014. Research on sound absorption properties of multilayer structural material based on discarded polyester fiber. *Journal of the Textile Institute*, 105(10), pp.1009-1013.

ORCID DETAILS OF THE AUTHORS

Venkatesan B.: https://orcid.org/0000-0001-5159-4265
Kannan V.: https://orcid.org/0000-0002-4104-1269
Raja Priya P.: https://orcid.org/0000-0003-0325-1852
Karthiga Shenbagam N.: https://orcid.org/0000-0002-4921-8487

Original Research Paper | https://doi.org/10.46488/NEPT.2025.v24iS1.031 | Open Access Journal

Enhancing Sustainability in the Indo-Gangetic Plains Through Biochar: A Solution to Stubble Burning

Meenu Yadav[1], Deepak Kumar Yadav[2] and Anuradha Jayaraman[1†]

[1]Institute of Allied Medical Science and Technology, NIMS Institute of Engineering and Technology, Jaipur-303121, Rajasthan, India

[2]Department of Environmental Science and Engineering, Guru Jambheshwar University of Science and Technology, Hisar-125001, Haryana, India

†Corresponding author: Anuradha Jayaraman; j.anuradha@nimsuniversity.org

ABSTRACT

In the Indo-Gangetic Plains (IGP) of northern India, the prevalent rice-wheat cropping system (RWS) is marked by a continuous cycle of planting wheat from October to April and rice from June to September. However, the transition between these crops necessitates the burning of stubble due to the short time frame available for land preparation before planting wheat. This practice contributes significantly to environmental pollution and poses health risks to both humans and ecosystems. To address this issue, alternative management strategies for crop residue are imperative. Utilizing stubble as fuel, feedstock for biofuels, or raw material for the pulp and paper industry offers promising solutions. Among these, biochar emerges as a particularly effective option. Biochar, derived from the pyrolysis of agricultural waste, not only mitigates environmental pollution but also enhances soil health, crop productivity, and overall agricultural sustainability. Our proposal emphasizes the potential of biochar as a soil conditioner, promoting soil carbon sequestration, improving soil quality, and ultimately enhancing food security.

INTRODUCTION

The Rice-Wheat Cropping System (RWS) is a highly productive and efficient cropping system that has helped meet the food demands of the growing population in India. Therefore, an enormous quantity of crop residue is expected to be produced as a result of monoculture and intensive farming (Manna et al. 2020). Northwest India produces about 40 metric tons of paddy straw, with Punjab and Haryana contributing the majority of it (Dhanda et al. 2022). Crop residue burning in Haryana, as well as in other parts of India, has been a significant contributor to air pollution and greenhouse gas emissions (Saxena et al. 2021). Burning crop residue releases a variety of hazardous pollutants into the atmosphere, including carbon monoxide (CO), nitrogen oxides (NO_X), and particulate matter (PM) (Mor et al. 2022). This practice is frequently used to clean up fields quickly following a harvest. Because so much rice and wheat are farmed there, crop residue burning is particularly common in Haryana and Punjab (Kumar & Singh 2021). According to data from the Indian Council of Agricultural Research, Haryana was responsible for around 14% of India's total crop residue burning in 2018 (Govindaraj et al. 2019).

Wheat straw has been used as feed for cattle, and leftover residue is burned every year. According to Chhabra & Mehta (2019), one kilogram of paddy produces one to one and a half kg of straw. Disposing of such a massive amount of crop residue is very difficult. The height of crop stubbles, the low nutritional value of paddy straw, the expense of collecting and transportation, the absence of markets for crop stubbles, and the lack of an effective in situ stubble management system present farmers with several challenges (Kaur et al. 2022). Due to these reasons, open stubble burning is perceived by farmers who are not aware of public health issues as the easiest and most economical way to manage stubble (Abdurrahman et al. 2019). The pollutants released during burning can have significant negative impacts, including respiratory problems and heart disease (Chanana et al. 2023). After being released into the air, these pollutants scatter in the environment, may go through physical and chemical changes, and ultimately have a negative impact on both human health and the environment are shown in Fig. 1. Furthermore, the practice contributes to global warming by releasing significant amounts of greenhouse gases into the atmosphere, including carbon dioxide and methane (Chawala & Sandhu 2020). However, it also poses significant

challenges such as soil degradation, and nutrient depletion (Nunes et al. 2020). To overcome these challenges, there is an urgency to implement sustainable and diversified agricultural practices, such as sustainable agriculture, integrated pest management, and crop diversification (Prasad et al. 2020). Biochar made from wheat paddy straw might be a useful tool for managing wheat paddy stubble (Manna et al. 2020). When biomass feedstocks, such as crop leftovers, are pyrolyzed under low oxygen conditions, biochar, a persistent and recalcitrant carbon-rich compound, is produced (Kumar & Bhattacharya 2021). Due to variations in the biomass and pyrolysis temperature, it demonstrates various properties. Biochar has the potential to significantly contribute to the agro-economy's efforts to enhance soil health and improve crop yields (Zhang et al. 2020). When biochar is added to soil, it can enhance the soil's ability to retain water and nutrients, which can lead to improved plant growth and crop yields (Farid et al. 2022). Additionally, biochar can also help the soil's ability to store carbon, which can lessen greenhouse gas emissions and help in the fight against climate change. By employing organic waste as a feedstock, biochar may help lower the quantity of trash produced by agricultural activities (Guo et al. 2020). Overall, using biochar in the agro-economy has the potential to bring about a number of advantages, such as higher crop yields, better soil health, lower greenhouse gas emissions, and less waste (Sessions et al. 2019). However, the effectiveness of biochar will depend on various factors, including the quality of the biochar, the soil type, and the specific crop being grown. Today, biochar is considered a reliable method for mitigating climate change and is predicted to retain carbon and reduce greenhouse gas emissions from crop residue burning (Brassard et al. 2019). Biochar is a useful soil additive for combating climate change because the pyrogenic carbon, also known as carbon black, which is produced when the biochar is partially burned transforms into a long-term carbon sink with a relatively gradual chemical transformation (Luo et

al. 2022). Consequently, converting wheat and rice straw into biochar and using it in agriculture could be a current example of a climate-smart approach.

Rice and Wheat as Feedstocks and Their Physico-chemical Properties

Paddy and wheat straws are agricultural residues that can be used as a potential source of biomass for various applications such as bioenergy, pulp and paper industries, and animal feed (Cao et al. 2018). The physicochemical properties of paddy-wheat straw can provide important insights into its potential applications (Kalkhajeh et al. 2021). Here are some of the physicochemical properties of paddy-wheat straw: The moisture content of paddy-wheat straw can vary from 10% to 20%. High moisture content can affect its handling and storage properties (Iftikhar et al. 2019). According to Manna et al. (2020), the nitrogen content of paddy-wheat straw ranges from 0.5% to 1.5%. The nitrogen content affects the quality of the straw as animal feed. The lignin content of paddy-wheat straw can vary from 15% to 25%. The lignin content affects the quality of the straw as a pulp and paper raw material (Ríos-Badrán et al. 2020). The cellulose content of paddy-wheat straw ranges from 35% to 45%. The cellulose content affects the quality of the straw as a raw material for bioenergy production (Du et al. 2019). The hemicellulose content of paddy-wheat straw ranges from 25% to 35%. The hemicellulose content affects the quality of the straw as a raw material for bioenergy production (Satlewal et al. 2018). In Table 1 the physiochemical properties of rice and wheat straw are described. Parameters include crop management, soil type, agricultural variety, season, and other factors that influence the nutrients in agricultural wastes. Under ongoing fertilization procedures, the continuous removal and burning of crop residues can result in net nitrogen losses, increasing nutrient costs input in the short term and degrading productivity and soil quality (Zhang et al. 2020).
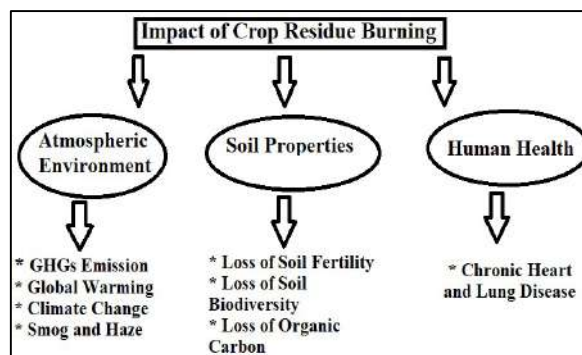

Fig. 1: Impacts of crop residue burning on environment, human health, and soil environment.

Table 1: Physiochemical properties of rice and wheat straw.

Chemical component	Chemical composition of rice straw (% on dry matter basis)	Chemical composition of wheat straw (% on dry matter basis)
Total ash	15.6	7.9
Water content	5.4	4.6
Organic matter	44	48
Cellulose	37	43.42
Hemicellulose	24.5	29.48
Lignin	9	15
Silica (Si)	8	5.5

Crop Residue Burning in Haryana and Punjab

Since the beginning of the Green Revolution in the nation, Punjab and the Haryana state have been actively involved in the RWS cropping method (Sarkar et al. 2018). These two small states account for around 69% of the government of India's entire food procurement, including about 54% of the rice and 84% of the wheat, although possessing less than 3% of the country's total land area (Bhuvaneshwari et al. 2019). Experts estimate that 90% of the rice crop is harvested by combine harvesters and leftover residues are burned in the Indian states of Punjab and Haryana, where emissions can substantially affect regional air quality periodically. In 2017, According to Sarkar et al. 2018 India produced 488 Mt of total crop residue, of which 24% was burned in agricultural areas. This led to emissions of 239 Gg of organic carbon (OC), 58 Gg of elemental carbon (EC), and 824 Gg of particulate matter ($PM_{2.5}$). In addition, 211 Tg of greenhouse gases (CO_2, CH_4, and N_2O) comparable to CO_2 were released into the atmosphere. Crop residue may also have the potential to generate 120 TWh of electricity when used in biomass power plants, which accounts for 10% of India's total energy output. The inability to store straw, the lack of market demand for its future use, the high cost of labor, and the farmers' need to have their agricultural products transported to grain markets and sold as soon as possible make disposal particularly challenging. Because of this, the agricultural residue is allowed to stay in the open field and is subsequently burned (Kulkarni et al. 2020). This crop-based biomass burning causes a massive cloud of smoke to cover the whole of Haryana and Punjab states (Fig. 2), endangering the quality of the soil, water, air, and environment as well as human health, between October and November.

Stubble Burning Causes

Rice-wheat cropping system (RWS): One of the primary causes of stubble burning in north India is the short period between rice harvesting and wheat sowing. In this region crops are cultivated, wheat is usually sown in November, and rice is often harvested in October (Jat et al. 2019). Farmers now have a limited time to clear their fields from rice straw and get it ready for wheat cultivation. Manual labor or the use of bullock carts are two traditional ways to remove the straw, both of which can be costly and time-consuming (Kumar et al. 2019). Due to this, many farmers use stubble burning as a quick and affordable means of clearing the fields and getting the soil ready for the following crop (Biswakarma et al. 2021).

Scarcity of labor: In Punjab and Haryana, where farm sizes are enormous and automated harvesters are frequently used, labor expenses are extremely high (Khedwal et al. 2023). Additionally, both in the states of Punjab and Haryana, there has been a steady and significant rise in the area under paddy cultivation. Therefore, the use of mechanical and electrical power has increased as a result of the fact that human and animal power cannot keep up with the rising demand for labor. Additionally, the issue of stubble burning was exacerbated by rising costs and a shortage of agricultural labor (Shirsath et al. 2020). In the past, the majority of laborers moved to the Haryana Punjab region from the states of Bihar and UP. However, labor migration has decreased over the past few years as a result of the MNREGA program's enormous success. As a result, they are leading to increased dependency on combined harvesters (Dhaliwal et al. 2021).

Extensive use of heavy machinery: Due to its low labor and time requirements, the use of combining harvesters has significantly increased over the last few decades. Before now, the waste straw bundles could be collected and removed from the fields more easily thanks to the physical cutting of the standing crop (Yadav et al. 2021). On the other hand, manual paddy harvesting costs approximately three times as much and needs 15–20 persons per acre. The combined harvesters, on the other hand, work quickly and are significantly less expensive, but they have a tendency to scatter the leftover straw around the field (Dhaliwal et al. 2021). This makes collecting it more time-consuming and expensive, which encourages the farmer to burn it instead of collecting it.

Nutrient content of rice straw: The poor quality of rice straw is another factor in the burning of crop residue. Due to its poor palatability and low protein content (4%), high lignin, cellulose, and silica content, paddy straw is not as favored as wheat straw which also lowers milk production in dairy animals (Yadav et al. 2022). Additionally, paddy straw has a low dry matter digestibility, ranging from 42 to 48% in various cattle (Yan et al. 2019, Sharma et al. 2020). Additionally, it was noted in a study by Chivenge et al. (2020) that both rice and wheat crops use in-situ burning as a method of soil preparation. In contrast to wheat residues, rice residues are burned on a considerably bigger scale.
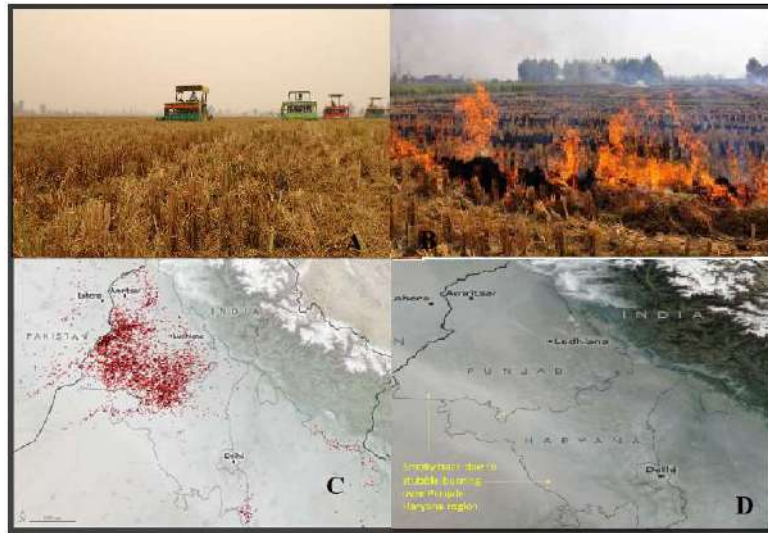
Fig. 2: (A) Use of heavy machinery in fields by the farmers (B) Crop residues burning in open fields (C). Region of Punjab and Haryana burning openly as captured by VIIRS during crop residue burning (D). Burning stubble in the Haryana-Punjab region has caused hazy smoke.

The Negative Environmental Impacts of Crop Residue Burning

Depletion of air quality: The burning of crop residues releases a range of pollutants into the atmosphere, including particulate matter, carbon monoxide, nitrogen oxides, sulfur dioxide, and volatile organic compounds. These pollutants can have serious health impacts, particularly for people with respiratory or cardiovascular conditions, and can contribute to the formation of smog and other types of air pollution (Mor et al. 2022). In paddy straw, over 70% of the carbon is emitted as CO_2, while 7 % and 0.66% in CO and CH_4, respectively. In addition, when straw is burned, 2.09% of the nitrogen is released as N_2O (Satlewal et al. 2018). These gases and aerosols contain carbonaceous material, which could cause acid deposition, an increase in tropospheric ozone, and the thinning of the stratospheric ozone layer in a particular area (Bhuvaneshwari et al. 2019). After carbon dioxide emissions, black carbon emissions are the main cause of the current global warming. Stubble-burning produced particulate matter (PM2.5), which is exceedingly light, may stay in the air for a very long time, cause smog, and move hundreds of miles with the wind (Kulkarni et al. 2020).

Stubble burning contributes to emissions of harmful air pollutants, which can cause severe impacts on human health. For example, shortness of breath, coughing, eye irritation. Old age people, kids, and pregnant women are the main groups affected by irritation, asthma, bronchitis, and other lung problems (Jain et al. 2014). Numerous investigations have also revealed greater dangers for aplastic anemia, blood cancer, bone marrow disorder, pancytopenia, vertigo, nausea, drowsiness, and headache (Von et al. 2020).

The release of carbon dioxide, methane, and other greenhouse gases from burning crop residues contributes to climate change, while the deposition of pollutants onto land and water can damage ecosystems and harm wildlife.

Deterioration of soil health and fertility: Crop residue burning can also have a significant negative impact on soil health and fertility. When crop residues are burned, valuable organic matter is lost, which can reduce soil fertility and degrade the overall health of the soil (Dadhich et al. 2021). Organic matter is an essential component of soil health, as it provides nutrients, improves soil structure, and helps to retain moisture. When crop residues are burned, this organic matter is lost, reducing the availability of nutrients for plants and

Table 2: Emission of pollutants from rice and wheat residue burning in India (Gg/year).

Air Pollutants	Rice	Wheat
$PM_{2.5}$	418	264.57
PM_{10}	458.29	175.35
Sulfur dioxide	9.07	12.31
Carbon dioxide	59275.54	54974.27
Carbon monoxide	4683.64	861.38
Nitrous oxide (N_2O)	24.17	22.76
Nitrous oxides (NOx)	114.82	52.30
Ammonia (NH_3)	206.48	39.99
Organic carbon (OC)	150.58	8.92
Volatile organic compounds (VOC)	352.53	215.34
Elemental carbon (EC)	25.68	4.92
Polycyclic aromatic hydrocarbons (PAH)	0.026	0.04

making it more difficult for soil to retain moisture (Bisen et al. 2017). Stubble burning raises the soil temperature (33.8-42.2 °C) up to 1cm, influencing the soil ecology (Rathod et al. 2019). Because of the increased soil temperature, 23–73% of the soil's nitrogen is eliminated in various forms, and the population of helpful microorganisms decreases to a depth of 2.5 cm. Total N and C are decreased in the 0-150 mm soil layer by continuous burning. Burning the residue destroys soil-beneficial micro-flora and fauna and removes a large amount of the organic material, and decreasing the organic matter in the fields (Turmel et al. 2015).

Loss of nutrients: When these residues are burned, these nutrients are lost from the soil, reducing soil fertility and the potential yield of future crops. Nitrogen is one of the most important nutrients that can be lost due to stubble burning. When crop residues are burned, nitrogen is released into the atmosphere in the form of nitrogen oxides. This can lead to a significant reduction in the amount of nitrogen available for plant growth in the soil, which can result in reduced crop yields and poorer soil health (Lin & Begho 2022). When rice and wheat straw are burned, the carbon, nitrogen, and sulfur it contains are completely burned off and lost to the atmosphere. One ton of paddy residue contains 6.1 kg N, 0.8 kg P, and 11.4 kg K. Burning of paddy straw causes intact loss of about 79.38 kg ha^{-1} N, 183.71 kg ha^{-1} P and 108.86 kg ha^{-1} K (Dotaniya et al. 2013). The soil would have been greatly improved if the stubble residues had been left in the ground, mostly with organic carbon and nitrogen. These nutrients must subsequently be replaced through expensive organic or inorganic fertilizers.

Wheat-Paddy Biochar as an Ecological and Economical Solution

Farmers use biochar, a carbon-rich, reliable, and long-lasting substance, to enhance the health and quality of their soil. Crop leftovers are thermally treated to produce biochar. The thermal processes used to produce biochar include pyrolysis, gasification, torrefaction, carbonization, and combustion (Naeem et al. 2017). The most popular method for producing biochar is pyrolysis because it is a quick and efficient process. In a furnace, where oxygen-deficient conditions may be produced, pyrolysis can be accomplished (Manna et al. 2020). The use of biochar has shown promise (Fig. 3) for enhancing soil carbon sequestration, boosting agricultural production, cleaning up contaminated soil and water, reducing greenhouse gas emissions, and minimizing nutrient leaching (Singh et al. 2024).

A solution to waste management: The generation of biochar provides us with a fantastic solution to the threat posed by agriculture waste production. The large amounts

of rice-wheat stubble produced in the northwest region of India could potentially be pyrolyzed to generate biochar as an effective alternative to burning stubble. This would not only be economical but simultaneously beneficial by making waste profitable. Additionally, biochar has enormous potential for reducing greenhouse gas emissions and mitigating climate change through carbon sequestration, reduced waste biomass burning, clean bioenergy production, and decreased methane and nitrous oxide emissions, enabling the achievement of sustainable development goals.

Biochar as a soil amendment: Biochar is a great soil conditioner because it has several advantageous characteristics. The combination of a large surface area, high carbon content, and the capacity to improve soil aeration support and encourage the rhizospheric microbial community to enhance soil fertility and health. The soil ability to retain water is also improved by its application. The use of biochar has also been linked to a decrease in nutrient leaching, according to published research (Yadav et al. 2024). This is a result of the increased soil cation exchange capacity, which has a significant impact on slowing down the leaching of nutrients. Additionally, biochar has an alkaline pH that aids in neutralizing acidic soils and so helps to increase plant yield.

Micronutrients (Cu, Zn, Fe, and Mn) and macronutrients (P, K, N, Ca, and Mg) that are essential for productive agriculture are also added by biochar. It may have a major impact on nutrient retention and be essential for a variety of biogeochemical processes in the soil, particularly nutrient cycling. As a result, it can serve as a soil conditioner to

Table 3: Physiochemical properties of wheat and rice straw biochar.

Parameters	Wheat straw biochar	Rice straw biochar
Chemical properties		
pH	8.1	8.7
Electrical Conductivity (dS m^{-1})	2.56	3.23
Cations Exchange Capacity (cmol kg^{-1})	63	56
Nutrient composition		
Organic Carbon (%)	66	63
Nitrogen (g kg^{-1})	16.2	16.6
Phosphorus (g kg^{-1})	42	30
Potassium (g kg^{-1})	12.6	9.2
Iron (mg kg^{-1})	418	348
Calcium (mg kg^{-1})	11.24	8.42
Manganese (mg kg^{-1})	186.66	152.42
Zinc (mg kg^{-1})	92.48	69.5
Magnesium (mg kg^{-1})	10.8	6.84

promote plant growth more significantly, storing nutrients as well as by performing other tasks like strengthening the physical and biological characteristics of the soil (Brassard et al. 2019) (Kamali et al. 2022). Due to its slow rate of breakdown, it is also a great soil additive for storing carbon and raising soil organic carbon (SOC) concentration.

Bioenergy from biochar: Depending on the temperature at which the biomass is pyrolyzed, a varying amount of biochar, bio-oil, and syngas are produced. Biomass that is pyrolyzed quickly yields more bio-oil and less charcoal (Li et al. 2022). The emissions (air pollutants) that are emitted during the pyrolysis of biomass have the potential to be trapped and condensed into bio-oil, a source of bioenergy. The use of bio-oil as a substitute for fossil fuels would result in decreased carbon emissions. It's interesting to note that some aspects of biochar may be improved to aid in catalysis. Sulfonated biochar is an appropriate catalyst for the production of biodiesel, according to a different study (Lee et al. 2017). Gasification of biomass results in the production of syngas. In such a procedure, tar reduction can improve syngas output. As a result, biochar can be a fantastic tar reduction catalyst. Several studies have employed biochar to support the sulfonated solid acid catalyst in the manufacture of biodiesel. Therefore, the synthesis of biochar could encourage the development of both biofuel and bioenergy (Yadav et al. 2023).

Biochar as bioremediation technology: Heavy metal removal with biochar has been recognized as a promising application. Among the aforementioned heavy metal cleanup strategies, it has emerged as an incredibly affordable, enormously potent, and enormously reliable solution (Yi et al. 2020). Applying biochar is a great way to reduce the bioavailability of contaminants in the soil. Even in arid and semi-arid environments, biochar is a highly effective sorbent and an innovative carbonaceous substance for eliminating organic and inorganic pollutants, including heavy metals, from the soil and water. Using maize as a test crop, a study was done to examine the effects of biochar made from wheat straw on the bioavailability of Pb, Cd, and Cr (Xie et al. 2015) (Sizmur et al. 2016). The results showed that when data were averaged over the contamination levels, soil Pb, Cd, and Cr decreased from 15.5, 5.38, and 5.85 mg kg^{-1} in control to 1.34, 0.69, and 0.75 mg kg^{-1}, respectively.

In addition, compared to the control, the Pb, Cd, and Cr accumulation in the maize crop also decreased. In general, it was determined that biochar made from wheat straw has a high capacity to immobilize heavy metals in soil and lessen their uptake by crop plants. Similar to that, biochar works well for biologically cleaning up organic pollutants. In one experiment, the effects of applying biochar to paddy straw

on the coupled adsorption-biodegradation of the organic pollutant nonylphenol were examined. Biochar derived from rice straw was applied to the soil as the adsorbent. The results showed that when 0.005 g biochar was introduced to 50 mg L^{-1} of nonylphenol, roughly 47.6% of the nonylphenol was biodegraded in two days, which was 125% more than the relative amount biodegraded without biochar. The nonylphenol components resistant to desorption, however, reached 87.1% (Wang et al. 2020, Yang et al. 2021).

Role of Biochar in Carbon Stabilization

To effectively sequester carbon, biomass must resist chemical oxidation into CO_2 or reduction into methane, which results in a decrease in the atmospheric emission of CO_2 or methane (Gupta et al. 2017). The partially burned products, pyrogenic carbon/carbon black, have a very gradual chemical change that makes them perfect for soil amendment (Thompson et al. 2016). These partially burned products, also known as pyrogenic carbon or black carbon, may serve as a crucial long-term carbon sink because of how slowly they decompose through microbial action and chemical modification. The process of making carbon molecules resistant to microbial decay, respiration, soil erosion, and leaching is known as carbon stabilization. Biochar made from wheat and paddy straw has high ash content, and an alkaline pH, and nutrients including nitrogen, phosphorus, manganese, iron, and zinc can be found in it (Chagas et al. 2022). Be effectively employed to increase soil C sequestration. Another study (Lee et al. 2017) looked into the effects of rice straw and its biochar on labile soil C and soil organic carbon (SOC). They found that adding straw to soils increased the fraction of labile carbon, whereas adding biochar to soils increased the quantity of stabilized carbon (Aryl C, carboxyl C), indicating the importance of biochar's recalcitrance as a management tool for enhancing soil carbon sink. Biochar have ability to sequester carbon is limited by its recalcitrance, it was revealed in another study (Colomba et al. 2022) that adding biochar encourages the physical stabilization of organic matter of soil through aggregate formation. Biochar production from agricultural waste, such as wheat paddy straw, can be a low-cost alternative to conventional burning for enhancing soil fertility, stabilizing carbon, and eventually reducing GHG emissions (Majumder et al. 2019).

CONCLUSION AND FUTURE ASPECTS

Despite numerous efforts, the problem of wheat-paddy stubble burning has only somewhat decreased and has not yet decreased to tolerable levels. Due to inadequate farmer education regarding the effects of this practice on soil,
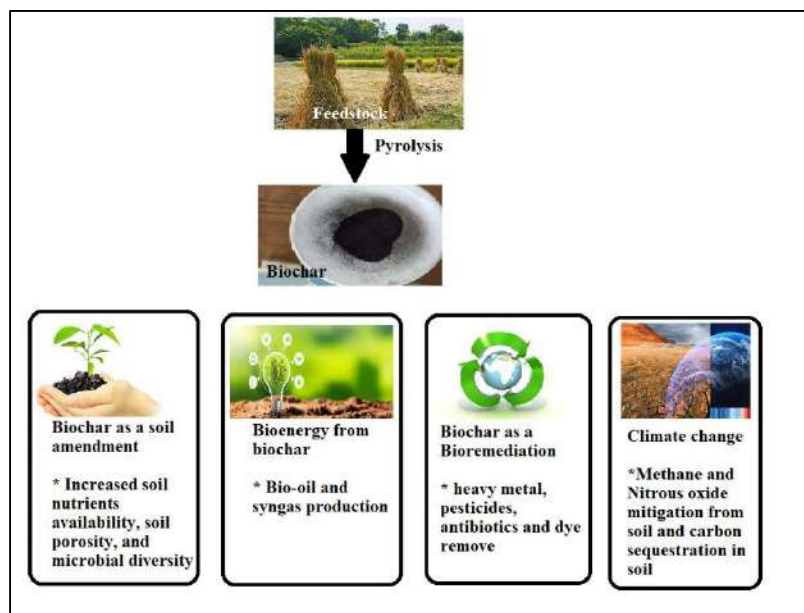
Fig. 3: Environmental and agronomical advantages of biochar.

human, and animal health, it is illegal to burn crop leftovers. Although farmers are aware of the negative effects of burning paddy straw on a farm, they are limited by a lack of equipment that is economically viable, appropriate, and can be used to dispose of rice wastes. Although the government has developed many strategies for the mechanical management of wheat and paddy stubble, the farmers have not effectively adopted them. Therefore, to manage wheat-paddy straw and prevent losses, an appropriate management strategy must be developed. On the other side, it might also be advantageous to the environment. A particularly effective and beneficial method of getting rid of the stubble and using biochar as a soil amendment is the use of biochar as a strategy for the management of crop residues. By educating farmers on how to apply this strategy properly, the government should go in this direction.

Farmers will be encouraged to adopt common farming practices that result in pollution and the waste of potential resources if organic recycling procedures and incentives are promoted. Furthermore, rather than using tough legal enforcement to restrict residue burning, the government should promote and offer need-based support for alternative measures. This is how, via cooperative efforts between farmers and the government, a proper self-sustaining environment may be attained.

REFERENCES

Abdurrahman, M.I., Chaki, S. and Saini, G., 2020. Stubble burning: Effects on health and environment, regulations and management practices. *Environmental Advances*, 2, p.100011.

Bhuvaneshwari, S., Hettiarachchi, H. and Meegoda, J.N., 2019. Crop residue burning in India: policy challenges and potential solutions. *International Journal of Environmental Research and Public Health*, 16(5), p.832.

Bisen, N. and Rahangdale, C.P., 2017. Crop residues management option for sustainable soil health in the rice-wheat system: A review. *International Journal of Chemical Studies*, 5(4), p.1038-1042.

Biswakarma, N., Pooniya, V., Zhiipao, R.R., Kumar, D., Verma, A.K., Shivay, Y.S., Lama, A., Choudhary, A.K., Meena, M.C., Bana, R.S. and Pal, M., 2021. Five years integrated crop management in direct seeded rice–zero till wheat rotation of north-western India: Effects on soil carbon dynamics, crop yields, water productivity and economic profitability. *Agriculture, Ecosystems & Environment*, 318, p.107492.

Brassard, P., Godbout, S., Lévesque, V., Palacios, J.H., Raghavan, V., Ahmed, A., Hogue, R., Jeanne, T. and Verma, M., 2019. Biochar for soil amendment. In: *Char and Carbon Materials Derived from Biomass*. 1st ed. Elsevier, p.109-146.

Cao, Y., Sun, H., Zhang, J., Chen, G., Zhu, H., Zhou, S. and Xiao, H., 2018. Effects of wheat straw addition on dynamics and the fate of nitrogen applied to paddy soils. *Soil and Tillage Research*, 178, p.92-98.

Chagas, J.K., de Figueiredo, C.C. and Ramos, M.L., 2022. Biochar increases soil carbon pools: Evidence from a global meta-analysis. *Journal of Environmental Management*, 305, p.114403.

Chanana, I., Sharma, A., Kumar, P., Kumar, L., Kulshreshtha, S., Kumar, S. and Patel, S.K., 2023. Combustion and stubble burning: A major concern for the environment and human health. *Fire*, 6(2), p.79.

Chawala, P. and Sandhu, H.A., 2020. Stubble burn area estimation and its impact on ambient air quality of Patiala and Ludhiana district, Punjab, India. *Heliyon*, 6(1), p.1.

Chhabra, V. and Mehta, C.M., 2019. Rice straw management for sustainable agriculture—a review. *Plant Archives*, 19(2), p.47-49.

Chivenge, P., Rubianes, F., Van Chin, D., Van Thach, T., Khang, V.T., Romasanta, R.R., Van Hung, N. and Van Trinh, M., 2020. Rice straw incorporation influences nutrient cycling and soil organic matter. *Sustainable Rice Straw Management*, p.131-144.

Colomba, A., Berruti, F. and Briens, C., 2022. Model for the physical activation of biochar to activated carbon. *Journal of Analytical and Applied Pyrolysis*, 168, p.105769.

Dadhich, S.K., Yadav, G.K., Yadav, K., Kumawat, C. and Munalia, M.K., 2021. Recycling of crop residues for sustainable soil health management: A review. *International Journal of Plant and Soil Science*, p.66-75.

Dhaliwal, S.S., Sharma, S., Shukla, A.K., Sharma, V., Bhullar, M.S., Dhaliwal, T.K., Alorabi, M., Alotaibi, S.S., Gaber, A. and Hossain, A., 2021. Removal of biomass and nutrients by weeds and direct-seeded rice under conservation agriculture in light-textured soils of north-western India. *Plants*, 10(11), p.2431.

Dhanda, S., Yadav, A., Yadav, D.B. and Chauhan, B.S., 2022. Emerging issues and potential opportunities in the rice–wheat cropping system of North-Western India. *Frontiers in Plant Science*, 13, p.832683.

Dotaniya, M.L., Sharma, M.M., Kumar, K. and Singh, P.P., 2013. Impact of crop residue management on nutrient balance in rice-wheat cropping system in an Aquic hapludoll. *Journal of Rural Agricultural Research*, 13(1), p.122-123.

Du, J., Qian, Y., Xi, Y. and Lü, X., 2019. Hydrothermal and alkaline thermal pretreatment at mild temperature in solid state for physicochemical properties and biogas production from anaerobic digestion of rice straw. *Renewable Energy*, 139, p.261-267.

Farid, I.M., Siam, H.S., Abbas, M.H., Mohamed, I., Mahmoud, S.A., Tolba, M., Abbas, H.H., Yang, X., Antoniadis, V., Rinklebe, J. and Shaheen, S.M., 2022. Co-composted biochar derived from rice straw and sugarcane bagasse improved soil properties, carbon balance, and zucchini growth in a sandy soil: A trial for enhancing the health of low fertile arid soils. *Chemosphere*, 292, p.133389.

Govindaraj, G., Hiremath, J., Reddy, G.B., Siju, S.J., Yogishardhaya, R. and Prajapati, A., 2019. *ICAR NIVEDI Annual Report 2018-19*.

Guo, X.X., Liu, H.T. and Zhang, J., 2020. The role of biochar in organic waste composting and soil improvement: A review. *Waste Management*, 102, p.884-899.

Gupta, S. and Kua, H.W., 2017. Factors determining the potential of biochar as a carbon capturing and sequestering construction material: Critical review. *Journal of Materials in Civil Engineering*, 29(9), p.04017086.

Iftikhar, M., Asghar, A., Ramzan, N., Sajjadi, B. and Chen, W.Y., 2019. Biomass densification: Effect of cow dung on the physicochemical properties of wheat straw and rice husk based biomass pellets. *Biomass and Bioenergy*, 122, p.1-6.

Jain, N., Bhatia, A. and Pathak, H., 2014. Emission of air pollutants from crop residue burning in India. *Aerosol and Air Quality Research*, 14(1), p.422-430.

Jat, H.S., Kumar, P., Sutaliya, J.M., Kumar, S., Choudhary, M., Singh, Y. and Jat, M.L., 2019. Conservation agriculture based sustainable intensification of basmati rice-wheat system in North-West India. *Archives of Agronomy and Soil Science*, 65(10), p.1370-1386.

Kalkhajeh, Y.K., He, Z., Yang, X., Lu, Y., Zhou, J., Gao, H. and Ma, C., 2021. Co-application of nitrogen and straw-decomposing microbial inoculant enhanced wheat straw decomposition and rice yield in a paddy soil. *Journal of Agriculture and Food Research*, 4, p.100134.

Kamali, M., Sweygers, N., Al-Salem, S., Appels, L., Aminabhavi, T.M. and Dewil, R., 2022. Biochar for soil applications: Sustainability aspects, challenges and future prospects. *Chemical Engineering Journal*, 428, p.131189.

Kaur, A., Kaur, P. and Kumar, P., 2022. Problems with paddy straw management technologies in South-Western Punjab. *Journal of Community Mobilization and Sustainable Development*, 2, p.335-339.

Khedwal, R.S., Chaudhary, A., Sindhu, V.K., Yadav, D.B., Kumar, N., Chhokar, R.S., Poonia, T.M., Kumar, Y. and Dahiya, S., 2023. Challenges and technological interventions in rice–wheat system for resilient food–water–energy-environment nexus in North-western Indo-Gangetic Plains: A review. *Cereal Research Communications*, 51(1), p.1-23.

Kulkarni, S.H., Ghude, S.D., Jena, C., Karumuri, R.K., Sinha, B., Sinha, V., Kumar, R., Soni, V.K. and Khare, M., 2020. How much does large-scale crop residue burning affect the air quality in Delhi? *Environmental Science & Technology*, 54(8), p.4790-4799.

Kumar, A. and Bhattacharya, T., 2021. Biochar: A sustainable solution. *Environment, Development and Sustainability*, 23, p.6642-6680.

Kumar, P. and Singh, R.K., 2021. Selection of sustainable solutions for crop residue burning: An environmental issue in northwestern states of India. *Environment, Development and Sustainability*, 23, p.3696-3730.

Kumar, S., Sharma, D.K., Singh, D.R., Biswas, H., Praveen, K.V. and Sharma, V., 2019. Estimating loss of ecosystem services due to paddy straw burning in North-west India. *International Journal of Agricultural Sustainability*, 17(2), p.146-157.

Lee, J., Yang, X., Cho, S.H., Kim, J.K., Lee, S.S., Tsang, D.C., Ok, Y.S. and Kwon, E.E., 2017. Pyrolysis process of agricultural waste using CO2 for waste management, energy recovery, and biochar fabrication. *Applied Energy*, 185, p.214-222.

Li, J., Li, L., Suvarna, M., Pan, L., Tabatabaei, M., Ok, Y.S. and Wang, X., 2022. Wet wastes to bioenergy and biochar: A critical review with future perspectives. *Science of the Total Environment*, 817, p.152921.

Lin, M. and Begho, T., 2022. Crop residue burning in South Asia: A review of the scale, effect, and solutions with a focus on reducing reactive nitrogen losses. *Journal of Environmental Management*, 314, p.115104.

Luo, Y., Li, Z., Xu, H., Xu, X., Qiu, H., Cao, X. and Zhao, L., 2022. Development of phosphorus composite biochar for simultaneous enhanced carbon sink and heavy metal immobilization in soil. *Science of the Total Environment*, 831, p.154845.

Majumder, S., Neogi, S., Dutta, T., Powel, M.A. and Banik, P., 2019. The impact of biochar on soil carbon sequestration: Meta-analytical approach to evaluating environmental and economic advantages. *Journal of Environmental Management*, 250, p.109466.

Manna, S., Singh, N., Purakayastha, T.J. and Berns, A.E., 2020. Effect of deashing on physico-chemical properties of wheat and rice straw biochars and potential sorption of pyrazosulfuron-ethyl. *Arabian Journal of Chemistry*, 13(1), p.1247-1258.

Mor, S., Singh, T., Bishnoi, N.R., Bhukal, S. and Ravindra, K., 2022. Understanding seasonal variation in ambient air quality and its relationship with crop residue burning activities in an agrarian state of India. *Environmental Science and Pollution Research*, 29, p.4145-4158.

Naeem, M.A., Khalid, M., Aon, M., Abbas, G., Tahir, M., Amjad, M., Murtaza, B., Yang, A. and Akhtar, S.S., 2017. Effect of wheat and rice straw biochar produced at different temperatures on maize growth and nutrient dynamics of a calcareous soil. *Archives of Agronomy and Soil Science*, 63(14), pp.2048-2061.

Nunes, M.R., Karlen, D.L., Veum, K.S., Moorman, T.B. and Cambardella, C.A., 2020. Biological soil health indicators respond to tillage intensity: A US meta-analysis. *Geoderma*, 369, p.114335.

Prasad, S., Singh, A., Korres, N.E., Rathore, D., Sevda, S. and Pant, D., 2020. Sustainable utilization of crop residues for energy generation: A life cycle assessment (LCA) perspective. *Bioresource Technology*, 303, p.122964.

Rathod, P.H., Bhoyar, S.M., Katkar, R.N., Kadu, P.R., Jadhao, S.D., Konde, N.M., Deshmukh, P.W. and Patle, P.N., 2019. Recycling and management of crop residues for sustainable soil health in climate change scenario with farmer's profit as frontline moto. *Journal of Pharmacognosy and Phytochemistry*, 8(2S), pp.51-55.

Ríos-Badrán, I.M., Luzardo-Ocampo, I., García-Trejo, J.F., Santos-Cruz, J. and Gutiérrez-Antonio, C., 2020. Production and characterization of fuel pellets from rice husk and wheat straw. *Renewable Energy*, 145, pp.500-507.

Sarkar, S., Singh, R.P. and Chauhan, A., 2018. Crop residue burning in northern India: Increasing threat to Greater India. *Journal of Geophysical Research: Atmospheres*, 123(13), pp.6920-6934.

Satlewal, A., Agrawal, R., Bhagia, S., Das, P. and Ragauskas, A.J., 2018. Rice straw as a feedstock for biofuels: Availability, recalcitrance, and chemical properties. *Biofuels, Bioproducts and Biorefining*, 12(1), pp.83-107.

Saxena, P., Sonwani, S., Srivastava, A., Jain, M., Srivastava, A., Bharti, A., Rangra, D., Mongia, N., Tejan, S. and Bhardwaj, S., 2021. Impact of crop residue burning in Haryana on the air quality of Delhi, India. *Heliyon*, 7(5).

Sessions, J., Smith, D., Trippe, K.M., Fried, J.S., Bailey, J.D., Petitmermet, J.H., Hollamon, W., Phillips, C.L. and Campbell, J.D., 2019. Can biochar link forest restoration with commercial agriculture? *Biomass and Bioenergy*, 123, pp.175-185.

Sharma, A., Singh, G. and Arya, S.K., 2020. Biofuel from rice straw. *Journal of Cleaner Production*, 277, p.124101.

Shirsath, P.B., Jat, M.L., McDonald, A.J., Srivastava, A.K., Craufurd, P., Rana, D.S., Singh, A.K., Chaudhari, S.K., Sharma, P.C., Singh, R. and Jat, H.S., 2020. Agricultural labor, COVID-19, and potential implications for food security and air quality in the breadbasket of India. *Agricultural Systems*, 185, p.102954.

Singh, G., Mavi, M.S., Choudhary, O.P., Gupta, N. and Singh, Y., 2021. Rice straw biochar application to soil irrigated with saline water in a cotton-wheat system improves crop performance and soil functionality in north-west India. *Journal of Environmental Management*, 295, p.113277.

Sizmur, T., Quilliam, R., Puga, A.P., Moreno-Jiménez, E., Beesley, L. and Gomez-Eyles, J.L., 2016. Application of biochar for soil remediation. *Agricultural and Environmental Applications of Biochar: Advances and Barriers*, 63, pp.295-324.

Thompson, K.A., Shimabuku, K.K., Kearns, J.P., Knappe, D.R., Summers, R.S. and Cook, S.M., 2016. Environmental comparison of biochar and activated carbon for tertiary wastewater treatment. *Environmental Science & Technology*, 50(20), pp.11253-11262.

Turmel, M.S., Speratti, A., Baudron, F., Verhulst, N. and Govaerts, B., 2015. Crop residue management and soil health: A systems analysis. *Agricultural Systems*, 134, pp.6-16.

Von Schneidemesser, E., Driscoll, C., Rieder, H.E. and Schiferl, L.D., 2020. How will air quality effects on human health, crops and ecosystems change in the future? *Philosophical Transactions of the Royal Society A*, 378(2183), p.20190330.

Wang, Y., Liu, Y., Zhan, W., Zheng, K., Wang, J., Zhang, C. and Chen, R., 2020. Stabilization of heavy metal-contaminated soils by biochar: Challenges and recommendations. *Science of the Total Environment*, 729, p.139060.

Xie, T., Reddy, K.R., Wang, C., Yargicoglu, E. and Spokas, K., 2015. Characteristics and applications of biochar for environmental remediation: a review. *Critical Reviews in Environmental Science and Technology*, 45(9), pp.939-969.

Yadav, D.B., Yadav, A., Vats, A.K., Gill, G. and Malik, R.K., 2021. Direct seeded rice in sequence with zero-tillage wheat in north-western India: addressing system-based sustainability issues. *SN Applied Sciences*, 3, pp.1-7.

Yadav, D.K., Bishnoi, N.R., Bajar, S. and Singh, A., 2022. An in-depth evaluation of feedstock, production process, catalyst for biodiesel production. *Zero Waste Biorefinery*, pp.515-533.

Yadav, D.K., Yadav, M., Mittal, R., Rani, P., Yadav, A., Bishnoi, N.R. and Singh, A., 2023. Impact of silica oxide and functionalized silica oxide nanoparticles on growth of *Chlorella vulgaris* and its physicochemical properties. *Sustainable Chemistry for the Environment*, 3, p.100029.

Yadav, M., Yadav, D. K., and Anuradha, J. 2024. Biochar produced through the pyrolysis of wheat and rice straw: Examining its physiochemical properties. *African Journal of Biomedical Research,* 27, pp.01-07. 10.53555/AJBR.v27i1S.1222.

Yan, C., Yan, S.S., Jia, T.Y., Dong, S.K., Ma, C.M. and Gong, Z.P., 2019. Decomposition characteristics of rice straw returned to the soil in northeast China. *Nutrient Cycling in Agroecosystems*, 114, pp.211-224.

Yang, Y., Ye, S., Zhang, C., Zeng, G., Tan, X., Song, B., Zhang, P., Yang, H., Li, M. and Chen, Q., 2021. Application of biochar for the remediation of polluted sediments. *Journal of Hazardous Materials*, 404, p.124052.

Yi, Y., Huang, Z., Lu, B., Xian, J., Tsang, E.P., Cheng, W., Fang, J. and Fang, Z., 2020. Magnetic biochar for environmental remediation: A review. *Bioresource Technology*, 298, p.122468.

Zhang, X., Zhang, P., Yuan, X., Li, Y. and Han, L., 2020. Effect of pyrolysis temperature and correlation analysis on the yield and physicochemical properties of crop residue biochar. *Bioresource Technology*, 296, p.122318.

Application of Graphene and Chitosan in Water Splitting/Catalysis

Nimra Iqbal[1], Shaukat Ali[1,2], Asif Hanif Chaudhry[3], Nosheen Sial[4], Syed Asim Abbas Zaidi[1], Waqar Ahmad Murtaza[1†] and Shumaila Shabbir[1]

[1]Department of Chemistry, Superior University, Lahore, Pakistan
[2]Building Research Station, Communication and Works Department, Lahore, Pakistan
[3]Geologiacl Survey of Pakistan, Lahore, Pakistan
[4]Government Graduate College for Women, Gulberg, Lahore, Pakistan
†Corresponding author: Waqar Ahmad Murtaza; mallikwaqarmurtaza@gmail.com

ABSTRACT

This study aims to explore the applications of graphene and chitosan in water splitting and catalysis, focusing on their unique properties and synergistic effects. A comprehensive review of the literature was conducted to examine their roles in photocatalytic activity and environmental remediation. Graphene, known for its high surface area and conductivity, was analyzed for its ability to enhance charge separation and light harvesting through doping and hybridization with metal nanoparticles. Similarly, chitosan's biopolymeric nature and strong affinity for transition metals were evaluated for their utility in enzymatic and catalytic applications. Results indicate that graphene's photocatalytic performance can be significantly improved through doping and functionalization, while chitosan proves effective in wastewater treatment and as a polymeric support for catalysts. The study concludes that the combined use of graphene and chitosan offers promising potential for advancing sustainable energy solutions and environmental technologies.

INTRODUCTION

For the production of solar fuel cells, photocatalysis is one of the most important techniques used. Due to its remarkable properties and production potential, graphene materials are considered attractive for water splitting. To improve charge separation and visible light harvesting, graphene-based materials are commonly used as additive agents to enhance the photocatalytic activity of graphene. For further improvement of graphene's photocatalytic activity, small amounts of metal and metal oxide nanoparticles are introduced onto the surface of graphene. Additionally, two special features, crystal alignment, and solid grafting, are recognized in graphene-based materials to enhance water splitting. Because of its large surface area and high sorption capacity, graphene is projected as an excellent catalyst for catalysis applications. The most significant applications of graphene in catalysis include the use of graphene-based materials as electrocatalysts and doped graphene as catalysts. Chitosan is an optically active polymer recognized for its strong affinity for transition metals. Polymers can be utilized as heterogeneous catalysts in forms such as gels, beads, and colloids. Chitosan is particularly suitable for enzymatic catalysis in various catalytic applications.

CHITOSAN

Historica!Background

In 1179, Hatchet decalcified the shells of crabs, lobsters, prawns, and crayfish using mineral acid and observed that they produced moderately energetic, soft, and plastic material of a yellowish color, resembling cartilage but retaining their original shape. This was the first mention of calcified chitin in invertebrates.

The discovery of chitin's characteristics began in 1811 when Braconnot identified chitin in fungi. Later, in 1823, another scientist, Odier, extracted a horn-like material from cockchafer elytra using potassium hydroxide. Braconnot initially named the material "chitin," a term later adopted and popularized by Odier. In 1824, the nitrogenous nature of chitin was revealed by the researchers referred to as "the children." By 1894, Hoppe-Seyler introduced the term "chitosan," with Lederhose identifying its first derivative, Glykosamin, in 1876 (Crini 2019).

Properties of Chitosan

Typically, naturally occurring polysaccharides such as

pectin, dextrin, agar, agarose, and cellulose are acidic, but chitosan is an extremely basic polysaccharide (Jayakumar et al. 2010). Chitosan exhibits superior properties such as viscosity, solubility, metal chelation, optical activity, polyelectronic behavior, the ability to form films, and structural characteristics. It is considered an important candidate for tissue engineering, particularly for regenerating connective tissue (Shukla et al. 2013). In bone formation, chitosan plays a significant role in the creation of osteoblasts. It also displays antifungal, hemostatic, antitumor, and anti-cholesteremic properties (Franco & Peter 2010; Dutta et al. 2004).

The heteropolymer of chitosan contains glucosamine and acetyl-glucosamine units. Properties such as acid-base behavior and solubility can be controlled by the relative portion of chitosan, which regulates the degree of acylation (Deutsche Chemische Gesellschaft 1888; Sorlier et al. 2001). The carbohydrate backbone of chitosan is similar to cellulose. In chitosan, the $-OH$ group on the second carbon atom is replaced by an $-NH_2$ group or an acetyl group. The copolymer consists of two repeating units: N-acetyl-2-D-glucopyranose and 2-amino-2-deoxy-D-glucopyranose. These repeating units are linked by (1–4) glycosidic bonds, which give chitosan a rigid crystalline structure due to intermolecular and intramolecular bonding (Roberts & Robert 1992, Dash et al. 2011).

Chitosan contains one $-NH_2$ group and two $-OH$ groups on each glycosidic unit, which indicates that it is a polycationic polymer (Agrawal et al. 2010). Due to these two reactive groups, chitosan exhibits unique chemical and biological properties. Chitosan is an ideal candidate for biofabrication because its active amino group is reactive and provides a platform for side group attachment under various reaction conditions (Yi et al. 2005). By altering its biological and physical properties, chitosan can provide elasticity and enhance functionality. The pKa value of chitosan depends on the ionic strength, diacylation, and charge neutralization of the $-NH_2$ group. The pKa value typically lies between 6.3 and 6.7 when the degree of acylation is no more than 50% (Suh et al. 2000).

Applications of Chitosan

Most industries discharge large amounts of wastewater containing inorganic and organic contaminants such as dyes, toxicants, suspended solids, and pesticides. This wastewater creates serious environmental issues and poses a threat to water quality, even when discharged into rivers and lakes. The treatment of wastewater can be made possible with the help of the nontoxic and biodegradable biopolymer chitosan, as it carries a partial positive charge, making it an effective polycationic coagulating agent in water treatment. Chitosan is helpful because it attracts heavy metal ions for separation from wastewater and also binds to all groups of transition metal ions at very low concentrations. Due to the presence of the amino group on chitosan, it serves as a chelation agent for transition metal ions.

Advantages and Disadvantages of Chitosan

Advantages of chitosan: Chitosan, which is derived from chitin, has wide biomedical and pharmaceutical advantages due to its widespread availability, biocompatibility, biodegradability, non-toxicity, and high drug-loading capacity. Chitosan is very important for drug delivery applications in the treatment of various diseases. It is also useful for improving patient compliance in infectious disease drug therapy (Rajitha et al. 2016).
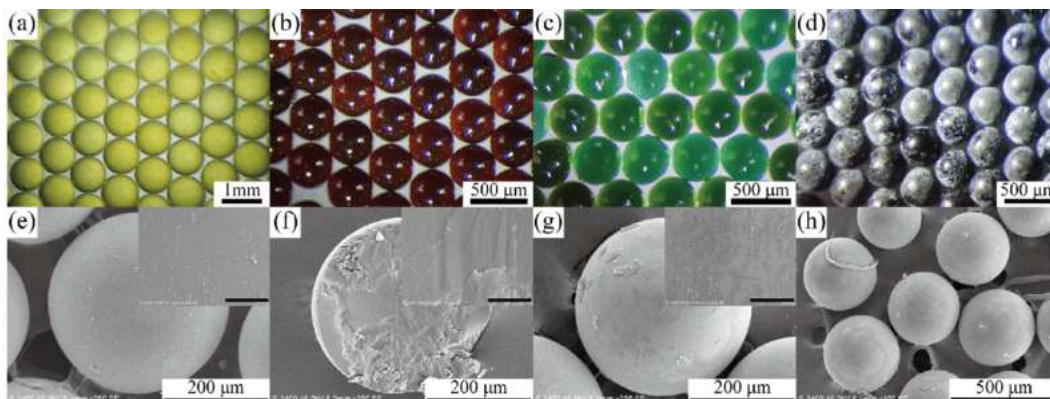

Fig. 1: Optical micrographs of (a) chitosan emulsion templates with crosslinking time 30 min and (b) PEI-CS biosorbents; Optical micrographs of (c) CS biosorbents and (d) PEI-CS bio sorbents after adsorption equilibrium; The SEM micrographs of (e) the surface and (f) inner structures of a CS biosorbent, (g) the surface of a PEI-CS biosorbent and (h) a certain amount of PEI-CS biosorbents. The scale bar of insert images in (e)-(g) is 20 lm (Rodrigues et al. 2012).

Techniques like emulsion cross-linking, which involves the emulsification of an aqueous solution of chitosan in oil, in the presence of an appropriate emulsifier, followed by its stabilization using crosslinkers to form nanoparticles enhance its application in forming nanoparticles for targeted drug delivery (Venkatesan et al. 2013, Rodrigues et al. 2012). Optical and SEM micrographs, shown in Fig. 1, highlight the structure and efficiency of chitosan emulsion templates and biosorbents, highlighting their potential in biomedical and environmental applications.

Another technique i.e. spray drying in which nanoparticle powder is obtained through a single-step process. The drug, dissolved in an aqueous solution of chitosan in acetic acid, is atomized with a crosslinker (Wang et al. 2011). This is also beneficial for the application in targeted drug delivery

Furthermore, chitosan demonstrates adhesive properties, with its amino and carboxyl groups forming hydrogen bonds with glycoproteins in mucus. This interaction improves drug bioavailability and ensures sustained drug release (Jin & Hu 2008).

Additionally, chitosan exhibits antitumor effects by interfering with cell metabolism and act on tumor cells to inhibit cell growth or induce apoptosis. It plays a vital role in enhancing the body's immune function as an antitumor agent (Cao & Zhou 2005, Maeda & Kimura 2004). Studies have shown that low molecular weight chitosan and chito-oligosaccharides can obstruct tumor growth in S180-bearing mice. Torzsas et al. (1996) demonstrated that a diet containing chitosan could reduce the formation of precancerous lesions in colon cancer.

Disadvantages of chitosan: Despite its advantages, chitosan faces limitations such as poor solubility in neutral and alkaline solutions, scalability challenges, and variability in its properties depending on its source and preparation method. Additionally, its performance can be affected by environmental conditions, requiring further research to optimize its stability and functionality in diverse applications.

GRAPHENE

Graphene has captured the interest of the scientific community due to its distinctive properties, which are not found in traditional materials. It is a two-dimensional material capable of maintaining a tensile elastic strain exceeding 20%, providing an exciting opportunity to tune its strain properties. This has opened a new field known as straintronics.

Known for its exceptional mechanical strength, high electrical and thermal conductivity, and large surface area, graphene stands as a revolutionary material in various fields. Its zero-band-gap nature and ability to undergo functionalization further enhance its applicability across a wide range of disciplines, from electronics to energy systems. One of the most significant advancements in graphene research is its application in photocatalysis and water splitting. To address the limitations posed by its zero-band-gap property, graphene is often doped with heteroatoms or combined with metal and metal oxide nanoparticles, effectively enhancing its catalytic activity. This tailored approach allows graphene to serve as an effective catalyst for processes requiring high electron mobility and stability.

Recent advancements in characterizing and assembling graphene have made some approaches scalable, while others remain at the laboratory scale (Ghany et al. 2017).
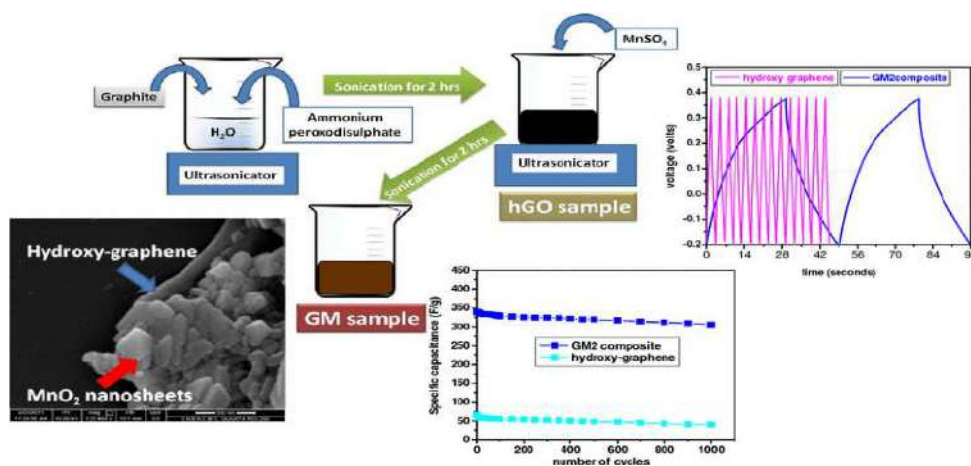

Fig. 2: Synthesis of functionalization hydroxy graphene (Brodie 1859).

Properties!of!Graphene

Graphene exhibits a wide range of unique properties that make it highly versatile for scientific and industrial applications. Its derivatives further enhance its functionality by introducing specific chemical and structural modifications. Below are the key properties of graphene:

Hydroxy graphene: Hydroxy graphene is synthesized through the hydroboration of graphene oxide, an addition reaction on carbon-carbon double bonds that results in an organoboron moiety. The preparation of graphol involves reacting fluorinated graphite or iodographene with sodium hydroxide under solvothermal conditions. This one-step process is simple and high-yielding, where hydrophilic hydroxyl substituents allow water molecules to penetrate the layers, leading to complex exfoliation.

Hydroxyl groups in graphene are critical for enhancing tribological properties by introducing hydrogen bonding within the layer lattice structure, improving inter-sheet shear resistance. Fig. 2 illustrates the synthesis of functionalized hydroxy graphene.

Carboxy graphene: For several applications, such as electrochemical sensing and transparent conductive films assembled with inorganics, the carboxylic acid functional group on the graphene structure is crucial. The carboxylic (COOH) functional groups are highly hydrophilic, significantly enhancing the stability of colloidal solutions and improving the dispersibility of graphene in water.

Carbon atoms located at the edges and defect sites of graphene are more reactive due to their higher volatility. These reactive sites are utilized to form covalent bonds with larger molecules, enabling control over graphene oxide (GO) separation and transport properties. This also enhances its sorption capacity for heavy metals, making it valuable for environmental remediation applications.

Additionally, the presence of COOH groups on GO improves its mechanical properties. These groups contain electronegative oxygen atoms, which strongly influence the electronic structure of the material (Jeon et al. 2012).

Functionalization of graphene oxide (GO): Like other chemical systems, stoichiometric derivatives exhibit a high degree of functionalization. In 2D material research, there is significant interest in structures with mixed compositions. Graphene oxide (GO) contains a non-stoichiometric number of oxygenated groups and graphene derivatives, where the presence of carboxyl and hydroxyl groups is particularly important.

For transformation and device implementation, graphene can covalently interact with other elements, such as hydrogen (graphane), fluorine (fluorographene), and sulfur (thiographene) (Pumera & Sofer 2017).

Electrical double-layer: Using the theory of the electrical double layer, the surface charge of graphene oxide (GO) can be described as a flat slab with two faces. At high electrolyte concentrations, the pH conditions and the presence of electrolytes determine the surface charge density, interactions between GO sheets, and the potential.

GO can orient and migrate in the presence of a magnetic field. The interaction between GO and the magnetic field will vary depending on the size of the GO sheets. These factors are crucial in influencing the separation of GO during electromagnetic separation (Fig. 3).

Interaction: Graphene oxide (GO) can be described as a single-layer graphite sheet with various hydrophilic oxygenated functional groups. The ionizable groups are
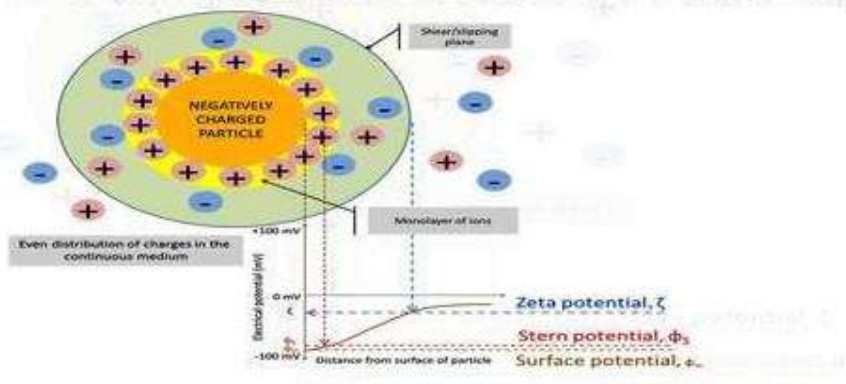

Fig. 3: Study of electrical double layer (Zhao et al. 2011).

located at the edges of the GO sheet, while the hydroxyl and epoxide groups are present on the basal planes.

The ionized carboxyl and phenol groups generate electrostatic repulsion between the GO sheets, preventing aggregation in an aqueous medium. By reducing the cross-dimensional size of the GO sheet, the surface area-to-volume ratio increases. Due to the higher density of ionized groups, GO sheets exhibit enhanced solubility (Li & Muller 2008).

Stacking and structural variability: In graphene oxide (GO), the hydrogen, oxygen, and carbon atoms are organized into a monolayer with a thickness of approximately 1 nm, depending on the degree of hydration and the method used for its preparation, quantity, and thickness. The shape of GO particles can vary, appearing as flakes, quantum dots, sheets, ribbons, or plates, with dimensions ranging from nanometers (e.g., 4 nm) to millimeters (e.g., 3 mm).

GO membranes can be fabricated through the self-assembly of hydrosol by evaporation or by spin coating to create ultra-thin GO foils, a few nanometers thick, suitable for radio frequency resonators (Thebo et al. 2018).

Applications of Graphene

Graphene is a conductive material that can replace traditional electrode materials, such as indium tin oxide, in optical and electrical devices. It also possesses several advantageous properties, including high optical transparency, low sheet resistance, and excellent mechanical properties. The following applications of graphene include electrode materials in transistors, light-emitting diodes, solar cells, and flexible devices. Through synthesis, modification, and doping strategies, the performance of graphene can be further enhanced.

Optoelectronic properties: Graphene is a conductive material that can replace traditional electrode materials such as indium tin oxide in optical and electrical devices. Its high optical transparency, low sheet resistance, and excellent mechanical properties make it ideal for use in transistors, light-emitting diodes, solar cells, and flexible devices. By altering the thickness of graphene films, sheet resistance, and visible light transmission can be independently adjusted to desired values, enhancing performance in transparent electrodes.

Engineering of graphene: Graphene has become an attractive material for transparent conductive electrodes due to its low optical absorption and high conductivity. Graphene films with high conductivity and low optical loss can be engineered by applying various methods to achieve:

1. Development of graphene technology
2. Surface modification of graphene films
3. Doping of graphene films

Work function tuning: Recent investigational studies have revealed that work function engineering can be achieved by shifting the Fermi level of the graphene band structure through electric fields (Yu et al. 2009), dipole formation, and metal contacts (Giovannetti et al. 2018), in addition to doping. Controlling the graphene work function is essential for reducing the contact barrier in graphene electrode devices such as transistors, solar cells, and light-emitting diodes (Jo et al. 2010; Lee et al. 2011).

Chemical doping: Graphene, a two-dimensional material, consists of a single atomic layer of sp² carbon atoms. By shifting the Fermi level of the graphene band structure away from the Dirac point, the carrier concentration of the carbon
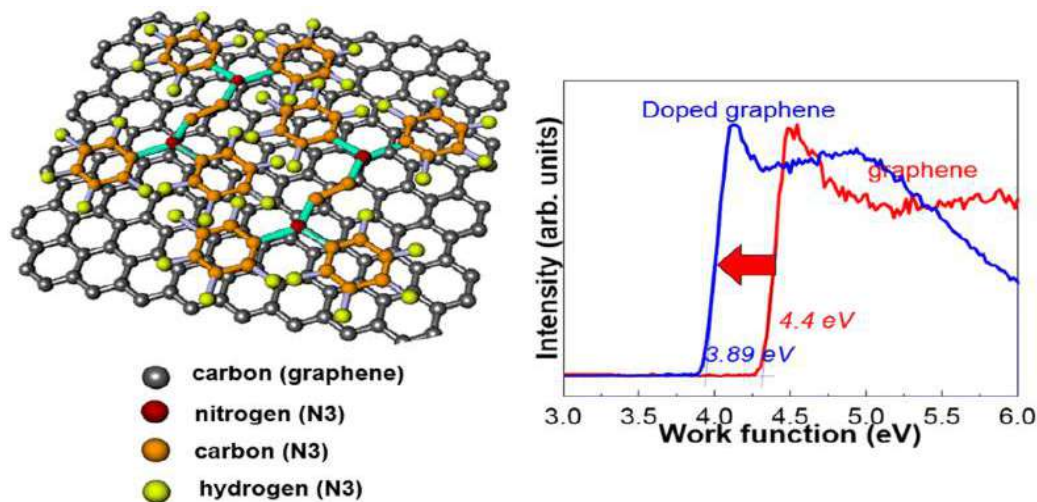

Fig. 4: Doping process in graphene (Wu et al. 2011).

layer is adjusted, which helps to improve the conductivity of the graphene films where the density is zero (Nistor et al. 2011). To modulate the conductive properties of graphene, the desired rigid band shift can be induced through chemical doping (Bae et al. 2010; Huh et al. 2011), electrostatic gating, metal contact, or dipole formation (Li et al. 2010; Huang et al. 2011). For example, the achievement of elements such as B or N (Wang et al. 2009) can be accomplished through hole (p) or electron (n) doping, which directly substitutes into the carbon lattice during layer growth to donate or remove electrons from the delocalized pz-band. Fig. 4 illustrates the doping process.

Advantages and Disadvantages of Graphene

Advantages: Graphene nanoplatelets (GNPs) are added to epoxy resins, improving properties such as mechanical, thermo-mechanical, thermal diffusivity, electrical conductivity, hydrophobic behavior, and barrier properties. The accumulation of GNPs leads to a significant stiffening of thermosetting resins, with notable increases in thermal diffusivity and electrical conductivity. These properties are proportional to each other—when thermal diffusivity increases, electrical conductivity also rises. By measuring the contact angle of a water drop, it is observed that GNP addition enhances the hydrophobic behavior, which is an advantage of graphene. However, excessive accumulation of GNPs reduces the diffusion coefficient and increases water absorption. The addition of carbon nanotubes improves thermal and mechanical properties while also increasing electrical conductivity. Low thermal interference resistance and two-dimensional properties make these types of graphene effective fillers for manufacturing composite materials, enhancing thermal conductivity (Chatterjee et al. 2012, Prolongo et al. 2013).

Graphene also plays a crucial role in photocatalytic applications. It is used as an additive to semiconductor materials, improving photocatalytic activity by enhancing charge separation and light harvesting. These features make graphene highly effective in water splitting and solar fuel cell production (Albero et al. 2019).

Mateo et al. (2016) focused on the development of renewable fuels from solar light, which is a major challenge in energy science today. Over the past decade, hydrogen and oxygen have been produced from solar light and water using various photocatalysts. However, photon-to-hydrogen mole conversion remains a real application of solar fuel cells. Facet-oriented gold nanoplates or multilayer graphene films, placed on quartz, serve as highly active photocatalysts for water splitting, converting sunlight into oxygen and hydrogen in the absence of a sacrificial electron donor, achieving hydrogen production. Durable gold-graphene interaction occurs in the composite system, and photocatalytic activity arises from the preferential orientation. Additionally, it has been suggested that constructing three-dimensional permeable carbon foam, pretreated by glutaraldehyde cross-linking and decorated with discrete molybdenum carbide (CF-Glu-MO) or co-doped FeNi carbonate hydroxide (CF-Glu-CoFeNi), which is structurally derived from chitosan hydrogel, could further improve photocatalytic performance (Ding et al. 2021).

Disadvantages: Despite its advantages, excessive accumulation of graphene nanoplatelets can lead to reduced diffusion coefficients and increased water absorption, limiting their effectiveness in certain applications. The high production cost of graphene materials remains a significant challenge, restricting their scalability for industrial use. Furthermore, maintaining consistent photocatalytic performance over extended periods requires addressing issues such as material degradation and efficiency losses.

GRAPHENE AND CHITOSAN AS SURFACE ENHANCERS

Sulfonated Graphene Oxide and Nanohybrid Membranes

Sulfonated graphene oxide (SGO), sulfonic acid, and nanosheets are synthesized using a facile distillation, polymerization, and precipitation method. These components are then incorporated into a chitosan matrix to prepare nanohybrid membranes. The physiological and microstructural properties of these membranes are extensively studied.

Due to the strong electrostatic attraction between the SO_3H groups of SGO and the $-NH_2$ groups of chitosan, both GO-filled membranes and chitosan/SGO-filled membranes exhibit enhanced thermal and mechanical properties, which reduce the mobility of chitosan chains. This reduction in mobility decreases the swelling area of the SGO-filled membranes, thereby increasing their structural stability. Conductivity can be optimized by adjusting the content of chitosan and sulfonic acid groups. For example, incorporating 2% S4GO results in a 122% increase in hydrated conductivity and a 90% increase in anhydrous conductivity, compared to the control chitosan membrane. Other conduction properties show significant improvement in H_2 and O_2 cells, demonstrating that the nanohybrid membrane holds promise as a proton exchange membrane. Fig. 5 shows a polymer brush functionalized Janus graphene oxide/chitosan hybrid membranes.
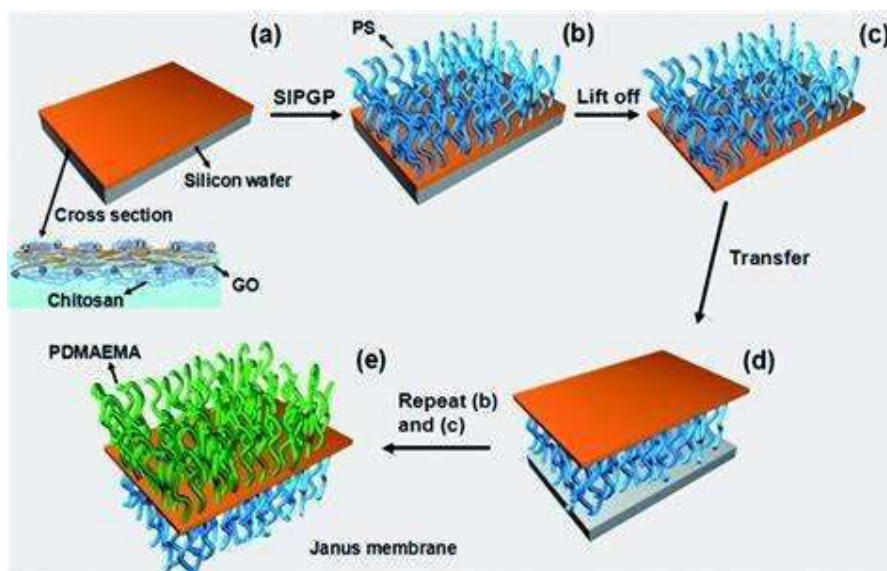
Fig. 5: Polymer brush functionalized Janus graphene oxide/chitosan hybrid membranes.

Application of Graphene in Water Splitting

Graphene-based materials as photocatalysts: Due to electronic band overlap, graphene is a zero-band-gap semiconductor. When electrons and holes recombine suddenly, the conductive properties of graphene block its application in photocatalysis. To address this, the band gap can be opened by doping with heteroatoms. In comparison to ideal graphene, graphene oxide (GO) and reduced graphene oxide (r-GO) both contain oxygen functionalities and act as semiconductor materials. Minor alterations to the oxygenated functional groups change the properties of graphene, converting the sp² carbon atoms into sp³. Due to low electron mobility, graphene oxide behaves as a p-type semiconductor. The band gap of graphene oxide ranges from 2.4 to 3.4 eV, depending on the oxidation level (Liu et al. 2014). The band gap increases with higher oxygen content. The valence band maximum (VBM) gradually shifts from the G π orbital to the oxygen 2p orbital, while the conduction band minimum (CBM) remains unchanged in the G π orbital (Ito et al. 2008).

Graphene for electrocatalytic water splitting: Graphene, with a single layer of carbon atoms arranged in a honeycomb structure, has various applications in water splitting. Ideal graphene has a zero-band-gap property with poor catalytic activity. However, graphene offers many benefits for electrocatalytic water splitting. When doped, graphene can act as an effective catalyst for water splitting. When graphene is hybridized with an electroactive component, the following benefits occur:

- The conductivity of the graphene hybrid increases, accelerating charge transfer kinetics.
- It improves the dispersion of the loaded catalyst, providing more catalytic sites.
- It prevents catalyst degradation, aggregation, and sintering under severe reaction conditions, thereby increasing the lifetime of the electrocatalyst.
- It regulates the electronic structure of the active center due to the combined interaction between graphene and transition metal catalysts (TM-Cs), improving their catalytic process.

Graphene hybrids for water splitting: Recent studies have shown that chemically doped graphene and graphene hybrids have superior catalytic activity and stability, making them well-suited for hydrogen evolution reactions (HER) and oxygen evolution reactions (OER). HER typically occurs in acidic electrolytes, while OER occurs in basic media. Both HER and OER are especially attractive for bifunctional catalysts (Sayama & Arakawa 1997).

From alkaline to neutral pH: Transition metal clusters (TMCs) have been primarily studied as active catalysts in several pH environments. They show excellent OER activity in alkaline media, which is useful for practical applications in alkaline water electrolyzers based on TMC bifunctional catalysts. In the OER catalyst family, Co-Pi/Co-Bi are the only potential catalysts that perform well in neutral media, but they are inert for HER. However, the development of a systematic bifunctional catalyst for overall water splitting in neutral media remains a significant challenge.

From monofunctional her/oer electrocatalysts to bifunctional catalysts for overall water splitting: Transition metal clusters (TMCs) possess bifunctional activity for both HER and OER. To improve the performance of TMC catalysts, graphene is considered a star material and is coupled with TMCs to create graphene hybrids. These hybrids act as bifunctional catalysts, providing superior performance for overall water splitting.

Application of Chitosan in Water Splitting

Enzymatic production of water-soluble chitosan: A chitinolytic enzyme complex produced by the gram-positive bacteria Streptomyces kurssanovii was immobilized on macroporous cross-linked chitin via physical adsorption. This biocatalyst was used to synthesize acid-free water-soluble chitosan with a molecular weight of 2-9 kDa through two-step hydrolysis. The first hydrolysis, at pH 4.6, produced chitosan with a solubility of 22-24 kDa in water, while the second hydrolysis at pH 6.2 resulted in acid-free, water-soluble chitosan (Gamzazade et al. 1985).

Immobilization of chitinolytic enzymes: The chitinolytic enzyme complex is produced by the Gram-positive bacterium *Streptomyces kurssanovii*, which is used for the enzymatic production of low-molecular-weight (LMW) chitosan (Ilyina et al. 1999). Unfortunately, the use of this chitosan for biomedical and food applications is restricted due to the pyrogenicity of the chitosan, which results from the presence of approximately 0.1% (w/w) of the protein enzyme complex.

Protein desorption: The interaction between the enzyme and the polymer matrix complex (PMC) under optimum conditions involves weak hydrogen bonds in the chitosan solution, which is exposed to the immobilized enzyme for hydrolysis. In the first 3 hours, a significant decrease in intrinsic viscosity occurs. After the next 24 hours, only small changes are observed, but these do not result in LMW chitosan. The final product, 24 kDa, has low solubility in acid-free water (Tikhonov et al. 1998).

Biocatalytic stability and PMC chitin regeneration: A two-step chitin hydrolysis method (3 hours at pH 4.6 and 0.5 hours at pH 6.2) was repeated 80 times, with complete recovery of the PMC chitin matrix, allowing further immobilization of chitinolytic enzymes (Miller 1959). After a 50% loss of its initial catalytic activity, the second-step biocatalyst was used. The *S. kurssano6ii* enzyme complex is utilized in a large-scale process suitable for the production of acid-free, water-soluble LMW chitosan, which is physically adsorbed onto a stable, macroporous, cross-linked chitin matrix. This method allows the production of LMW chitosan oligosaccharides with minimal protein contamination.

Application!of!Graphene!in!Catalysis

Doped graphene in catalysis: In several reactions, graphene materials are doped with various heteroatoms, which are being explored as effective metal-free catalysts (Kong et al. 2014). Among these, nitrogen (N)-doped graphene has been widely studied. N-doping is frequently achieved by reacting graphene oxide (GO) with ammonia (Li et al. 2009), lithium nitride (Deng et al. 2014), aniline, or by CVD (Wei et al. 2009) and arc discharge methods (Li et al. 2010). Nitrogen-doped graphene has most of its applications in oxidation-reduction reactions related to fuel cells (Lee et al. 2010, Lin et al. 2013). N-graphene behaves as an excellent metal-free catalyst for oxidation-reduction reactions in alkaline fuel cells. Other catalytic applications of N-graphene include the reduction of nitro compounds (Kong et al. 2013, Chen et al. 2012), peroxides (Long et al. 2012), and the oxidation of glucose (Wang et al. 2010) and benzyl alcohol (Shao et al. 2010). Like N-graphene, sulfur-doped graphene is also used as a metal-free catalyst with high stability and selectivity in oxidation-reduction reactions. For hydrolysis reactions, sulfur-doped graphene exhibits good water tolerance and high reactivity. The catalytic applications of sulfated graphene include the dehydration of xylose and the esterification of acetic acid (Lam et al. 2012, Liu et al. 2012), among others.

Graphene in photocatalysis: In photocatalysis, graphene-based materials have significant applications, including reactions such as pollutant degradation, selective organic transformations, and water splitting for hydrogen energy production, with graphene being used as a photocatalyst (Zhang et al. 2012). The hybridization of graphene with various metal catalysts helps improve photocatalytic performance due to the extended light absorption range, high specific surface area, and excellent electron conductivity of graphene. By hybridizing graphene oxide with organic dyes or photocatalysts, photosensitization can be promoted through charge transfer across the graphene interface, producing a synergistic effect that enhances catalytic transformation.

Application of Chitosan in Catalysis

Chitosan-based!Schiff!Bases!(CSBs): In heterogeneous catalysis, the role of CSBs as supports is crucial because they can attach catalytically active metal ions or metal nanoparticles, which provide effective reusability. These supports can be either organic polymers or inorganic materials. Polymers that are functionalized or have functional groups are preferred over other types of polymers, as their chemical interactions help prevent metal ion leaching from the support. Inorganic materials, such as silica, require very

strong reaction conditions to become functionalized, whereas chitosan contains inherent NH2 groups that can easily form CSBs. In heterogeneous catalysis, chitosan proves to be an effective polymeric support due to its biodegradability. CSB catalysts are used in C-C coupling (Peng et al. 1998), oxidation reactions (Shen et al. 2017), reduction reactions (Gong et al. 2012), arylation, and cyclopropanation.

Enzymatic!catalysis:!The model for any chemical reaction aimed at achieving measurable yields under mild, energy-efficient, low-cost, and safe conditions, with minimal separation steps and without the production of toxic or harmful substances, is catalyzed by enzymes. Chitosan dissolved in dilute organic acid solutions readily precipitates, forming inclusion complexes. Enzymes can be chemically attached to chitosan through reactive groups (-OH and –NH2). Chitosan is non-toxic, has high protein affinity, and is also inexpensive (Zhao et al. 2015).

Limitations

- Graphene and chitosan in water splitting, particularly in hydrogen production, face stability challenges such as scalability, cost-effectiveness, and durability.

- Graphene has a high production cost, and its catalytic activity decreases over time.

- Chitosan is renewable and biodegradable, but it suffers from stability issues under water-splitting conditions.

- Chitosan has partial durability and large-scale cost execution challenges.

FUTURE PERSPECTIVES

Graphene and chitosan show promise for future research and development across various fields, including advanced biomedicine, sustainable technology, energy revolution, smart materials, high-performance composites, nanotechnology, digital transformation, and environmental remediation. Overall, graphene and chitosan hold significant potential for addressing global challenges and driving innovation across numerous sectors in the years to come.

CONCLUSIONS

The review highlights that the photocatalytic activity of graphene can be enhanced for water splitting when graphene is doped with various metals such as H, N, P, B, and S, which opens the band gap of graphene-based materials. The photocatalytic activity of graphene can further be improved by adding small amounts of metal nanoparticles to graphene-based materials. Graphene, with its good chemical stability, can reduce catalyst bleaching, aggregation, and sintering under reaction conditions. Graphene-based materials and hybrids are beneficial for overall water splitting. From the above discussion, it is clear that chitosan and its composite materials can be functionalized with considerable control. Chitosan is also useful for enzyme immobilization and enzymatic catalysis due to its low cost and non-toxic nature. Additionally, chitosan is employed as a biocatalyst for PMC chitin regeneration.

REFERENCES

Agrawal, P., Strijkers, G.J. and Nicolay, K., 2010. Chitosan-based systems for molecular imaging. *Advanced Drug Delivery Reviews*, 62(1), pp.42-58.

Albero, J., Mateo, D. and García, H., 2019. Graphene-based materials as efficient photocatalysts for water splitting. *Molecules*, 24(5), p.906.

Bae, S., Kim, H., Lee, Y., Xu, X., Park, J.S., Zheng, Y., Balakrishnan, J., Lei, T., Ri Kim, H., Song, Y.I. and Kim, Y.J., 2010. Roll-to-roll production of 30-inch graphene films for transparent electrodes. *Nature Nanotechnology*, 5(8), pp.574-578.

Brodie, B.C., 1859. XIII. On the atomic weight of graphite. *Philosophical Transactions of the Royal Society of London*, 149, pp.249-259.

Cao, J. and Zhou, N.J., 2005. Progress in antitumor studies of chitosan. *Chinese Journal of Biochemical Pharmaceutics*, 26(2), p.127.

Chatterjee, S., Wang, J.W., Kuo, W.S., Tai, N.H., Salzmann, C., Li, W.L., Hollertz, R., Nüesch, F.A. and Chu, B.T., 2012. Mechanical reinforcement and thermal conductivity in expanded graphene nanoplatelets reinforced epoxy composites. *Chemical Physics Letters*, 531, pp.6-10.

Chen, T.W., Xu, J.Y., Sheng, Z.H., Wang, K., Wang, F.B., Liang, T.M. and Xia, X.H., 2012. Enhanced electrocatalytic activity of nitrogen-doped graphene for the reduction of nitro explosives. *Electrochemistry Communications*, 16(1), pp.30-33.

Crini, G., 2019. Historical review on chitin and chitosan biopolymers. *Environmental Chemistry Letters*, 17(4), pp.1623-1643.

Dash, M., Chiellini, F., Ottenbrite, R.M. and Chiellini, E., 2011. Chitosan—A versatile semi-synthetic polymer in biomedical applications. *Progress in Polymer Science*, 36(8), pp.981-1014.

Deng, D., Pan, X., Yu, L., Cui, Y., Jiang, Y., Qi, J., Li, W.X., Fu, Q., Ma, X., Xue, Q. and Sun, G., 2011. Toward N-doped graphene via solvothermal synthesis. *Chemistry of Materials*, 23(5), pp.1188-1193.

Deutsche Chemische Gesellschaft, 1888. *Berichte der Deutschen Chemischen Gesellschaft*. Berlin: Verlag Chemie.

Ding, J., Zhong, L., Huang, Q., Guo, Y., Miao, T., Hu, Y., Qian, J. and Huang, S., 2021. Chitosan hydrogel derived carbon foam with typical transition-metal catalysts for efficient water splitting. *Carbon*, 177, pp.160-170.

Dutta, P.K., Dutta, J. and Tripathi, V.S., 2004. Chitin and chitosan: Chemistry, properties and applications.

Liu, F., Sun, J., Zhu, L., Meng, X., Qi, C. and Xiao, F.S., 2012. *Journal of Materials Chemistry*, 22, pp.5495-5502.

Franco, T.T. and Peter, M.G., 2010. Advances in chitin science. *Santiago*, 6.

Gamzazade, A.I., Šlimak, V.M., Skljar, A.M., Štykova, E.V., Pavlova, S.S. and Rogožin, S.V., 1985. Investigation of the hydrodynamic properties of chitosan solutions. *Acta Polymerica*, 36(8), pp.420-424.

Ghany, N.A., Elsherif, S.A. and Handal, H.T., 2017. Revolution of Graphene for different applications: State-of-the-art. *Surfaces and Interfaces*, 9, pp.93-106.

Giovannetti, G.A., Khomyakov, P.A., Brocks, G., Karpan, V.V., van den Brink, J. and Kelly, P.J., 2008. Doping graphene with metal contacts. *Physical Review Letters*, 101(2), p.026803.

Gong, S.W., He, H.F., Zhao, C.Q., Liu, L.J. and Cui, Q.X., 2012. Convenient deoxygenation of aromatic ketones by silica-supported chitosan Schiff base palladium catalyst. *Synthetic Communications*, 42(4), pp.574-581.

Huang, J.H., Fang, J.H., Liu, C.C. and Chu, C.W., 2011. Effective work function modulation of graphene/carbon nanotube composite films as transparent cathodes for organic optoelectronics. *ACS Nano*, 5(8), pp.6262-6271.

Huh, S., Park, J., Kim, K.S., Hong, B.H. and Kim, S.B., 2011. Selective n-type doping of graphene by photo-patterned gold nanoparticles. *ACS Nano*, 5(5), pp.3639-3644.

Ilyina, A.V., Tatarinova, N.Y. and Varlamov, V.P., 1999. The preparation of low-molecular-weight chitosan using chitinolytic complex from *Streptomyces kurssanovii*. *Process Biochemistry*, 34(9), pp.875-878.

Ito, J., Nakamura, J. and Natori, A., 2008. Semiconducting nature of the oxygen-adsorbed graphene sheet. *Journal of Applied Physics*, 103(11).

Jayakumar, R., Menon, D., Manzoor, K., Nair, S.V. and Tamura, H., 2010. Biomedical applications of chitin and chitosan based nanomaterials - A short review. *Carbohydrate Polymers*, 82(2), pp.227-232.

Jeon, I.Y., Shin, Y.R., Sohn, G.J., Choi, H.J., Bae, S.Y., Mahmood, J., Jung, S.M., Seo, J.M., Kim, M.J., Wook Chang, D. and Dai, L., 2012. Edge-carboxylated graphene nanosheets via ball milling. *Proceedings of the National Academy of Sciences*, 109(15), pp.5588-5593.

Jin, H.Q. and Hu, Q.H., 2008. Characterization and application in bioadhesive drug delivery system of chitosan. *Centre South Pharm*, pp.324-327.

Jo, G., Na, S.I., Oh, S.H., Lee, S., Kim, T.S., Wang, G., Choe, M., Park, W., Yoon, J., Kim, D.Y. and Kahng, Y.H., 2010. Tuning of a graphene-electrode work function to enhance the efficiency of organic bulk heterojunction photovoltaic cells with an inverted structure. *Applied Physics Letters*, 97(21).

Kong, X.K., Chen, C.L. and Chen, Q.W., 2014. Doped graphene for metal-free catalysis. *Chemical Society Reviews*, 43(8), pp.2841-2857.

Kong, X.K., Sun, Z.Y., Chen, M. and Chen, Q.W., 2013. Metal-free catalytic reduction of 4-nitrophenol to 4-aminophenol by N-doped graphene. *Energy & Environmental Science*, 6(11), pp.3260-3266.

Lam, E., Chong, J.H., Majid, E., Liu, Y., Hrapovic, S., Leung, A.C. and Luong, J.H., 2012. Carbocatalytic dehydration of xylose to furfural in water. *Carbon*, 50(3), pp.1033-1043.

Lee, K.R., Lee, K.U., Lee, J.W., Ahn, B.T. and Woo, S.I., 2010. Electrochemical oxygen reduction on nitrogen doped graphene sheets in acid media. *Electrochemistry Communications*, 12(8), pp.1052-1055.

Lee, S., Jo, G., Kang, S.J., Wang, G., Choe, M., Park, W., Kim, D.Y., Kahng, Y.H. and Lee, T., 2011. Enhanced charge injection in pentacene field-effect transistors with graphene electrodes. *Advanced Materials*, 23(1), pp.100-105.

Li, D., Muller, M.B., Gilje, S., Kaner, R.B. and Wallace, G.G., 2008. *Nature Nanotechnology*, pp.3-101.

Li, N., Wang, Z., Zhao, K., Shi, Z., Gu, Z. and Xu, S., 2010. Large scale synthesis of N-doped multi-layered graphene sheets by simple arc-discharge method. *Carbon*, 48(1), pp.255-259.

Li, X., Magnuson, C.W., Venugopal, A., An, J., Suk, J.W., Han, B., Borysiak, M., Cai, W., Velamakanni, A., Zhu, Y. and Fu, L., 2010. Graphene films with large domain size by a two-step chemical vapor deposition process. *Nano Letters*, 10(11), pp.4328-4334.

Li, X., Wang, H., Robinson, J.T., Sanchez, H., Diankov, G. and Dai, H., 2009. Simultaneous nitrogen doping and reduction of graphene oxide. *Journal of the American Chemical Society*, 131(43), pp.15939-15944.

Lin, Z., Waller, G.H., Liu, Y., Liu, M. and Wong, C.P., 2013. 3D Nitrogen-doped graphene prepared by pyrolysis of graphene oxide with polypyrrole for electrocatalysis of oxygen reduction reaction. *Nano Energy*, 2(2), pp.241-248.

Liu, Y., Wang, J., Zhang, H., Ma, C., Liu, J., Cao, S. and Zhang, X., 2014. Enhancement of proton conductivity of chitosan membrane enabled by sulfonated graphene oxide under both hydrated and anhydrous conditions. *Journal of Power Sources*, 269, pp.898-911.

Long, J., Xie, X., Xu, J., Gu, Q., Chen, L. and Wang, X., 2012. Nitrogen-doped graphene nanosheets as metal-free catalysts for aerobic selective oxidation of benzylic alcohols. *ACS Catalysis*, 2(4), pp.622-631.

Maeda, Y. and Kimura, Y., 2004. Antitumor effects of various low-molecular-weight chitosans are due to increased natural killer activity of intestinal intraepithelial lymphocytes in sarcoma 180-bearing mice. *The Journal of Nutrition*, 134(4), pp.945-950.

Mateo, D., Esteve-Adell, I., Albero, J., Royo, J.F.S., Primo, A. and Garcia, H., 2016. 111 oriented gold nanoplatelets on multilayer graphene as visible light photocatalyst for overall water splitting. *Nature communications*, 7(1), p.11819.

Miller, G.L., 1959. Use of dinitrosalicylic acid reagent for determination of reducing sugar. *Analytical Chemistry*, 31(3), pp.426-428.

Nistor, R.A., Newns, D.M. and Martyna, G.J., 2011. The role of chemistry in graphene doping for carbon-based electronics. *ACS Nano*, 5(4), pp.3096-3103.

Peng, C., Wang, Y., Tan, S. and Cheng, G., 1998. Preparation of chitosan derivatives. Synthesis of N-Schiff base type and N-secondary amino type chitosan-crown ethers. *Polymer Journal*, 30(10), pp.843-845.

Prolongo, S.G., Jimenez-Suarez, A., Moriche, R. and Ureña, A., 2013. In situ processing of epoxy composites reinforced with graphene nanoplatelets. *Composites Science and Technology*, 86, pp.185-191.

Pumera, M. and Sofer, Z., 2017. Towards stoichiometric analogues of graphene: graphane, fluorographene, graphol, graphene acid and others. *Chemical Society Reviews*, 46(15), pp.4450-4463.

Rajitha, P., Gopinath, D., Biswas, R., Sabitha, M. and Jayakumar, R., 2016. Chitosan nanoparticles in drug therapy of infectious and inflammatory diseases. *Expert Opinion on Drug Delivery*, 13(8), pp.1177-1194.

Roberts, G.A.F. and Robert, G.A.F. (Ed.), 1992. *Chitin Chemistry*. MacMillan, Houndmills, pp.1-53.

Rodrigues, S., Dionísio, M., Remunan Lopez, C. and Grenha, A., 2012. Biocompatibility of chitosan carriers with application in drug delivery. *Journal of Functional Biomaterials*, 3(3), pp.615-641.

Sayama, K. and Arakawa, H., 1997. Effect of carbonate salt addition on the photocatalytic decomposition of liquid water over Pt–TiO₂ catalyst. *Journal of the Chemical Society, Faraday Transactions*, 93(8), pp.1647-1654.

Shao, Y., Zhang, S., Engelhard, M.H., Li, G., Shao, G., Wang, Y., Liu, J., Aksay, I.A. and Lin, Y., 2010. Nitrogen-doped graphene and its electrochemical applications. *Journal of Materials Chemistry*, 20(35), pp.7491-7496.

Shen, C., Qiao, J., Zhao, L., Zheng, K., Jin, J. and Zhang, P., 2017. An efficient silica supported Chitosan@ vanadium catalyst for asymmetric sulfoxidation and its application in the synthesis of esomeprazole. *Catalysis Communications*, 92, pp.114-118.

Shukla, S.K., Mishra, A.K., Arotiba, O.A. and Mamba, B.B., 2013. Chitosan-based nanomaterials: A state-of-the-art review. *International Journal of Biological Macromolecules*, 59, pp.46-58.

Sorlier, P., Denuzière, A., Viton, C. and Domard, A., 2001. Relation between the degree of acetylation and the electrostatic properties of chitin and chitosan. *Biomacromolecules*, 2(3), pp.765-772.

Suh, J.K. and Matthew, H.W., 2000. Application of chitosan-based polysaccharide biomaterials in cartilage tissue engineering: a review. *Biomaterials*, 21(24), pp.2589-2598.

Thebo, K.H., Qian, X., Wei, Q., Zhang, Q., Cheng, H.M. and Ren, W., 2018. Reduced graphene oxide/metal oxide nanoparticles composite membranes for highly efficient molecular separation. *Journal of Materials Science & Technology*, 34(9), pp.1481-1486.

Tikhonov, V.E., Radigina, L.A., Yamskov, I.A., Gulyaeva, N.D., Ilyina, A.V., Anisimova, M.V. and Varlamov, V.P., 1998. Affinity purification of major chitinases produced by *Streptomyces kurssanovii*. *Enzyme and Microbial Technology*, 22(2), pp.82-85.

Torzsas, T.L., Kendall, C.W.C., Sugano, M., Iwamoto, Y. and Rao, A.V., 1996. The influence of high and low molecular weight chitosan on colonic cell proliferation and aberrant crypt foci development in CF1 mice. *Food and chemical toxicology*, 34(1), pp.73-77.

Venkatesan, C., Vimal, S. and Hameed, A.S., 2013. Synthesis and characterization of chitosan tripolyphosphate nanoparticles and its encapsulation efficiency containing Russell's viper snake venom. *Journal of Biochemical and Molecular Toxicology*, 27(8), pp.406-411.

Wang, J.J., Zeng, Z.W., Xiao, R.Z., Xie, T., Zhou, G.L., Zhan, X.R. and Wang, S.L., 2011. Recent advances of chitosan nanoparticles as drug carriers. *International Journal of Nanomedicine*, pp.765-774.

Wang, X., Li, X., Zhang, L., Yoon, Y., Weber, P.K., Wang, H., Guo, J. and Dai, H., 2009. N-doping of graphene through electrothermal reactions with ammonia. *Science*, 324(5928), pp.768-771.

Wang, Y., Shao, Y., Matson, D.W., Li, J. and Lin, Y., 2010. Nitrogen-doped graphene and its application in electrochemical biosensing. *ACS Nano*, 4(4), pp.1790-1798.

Wei, D., Liu, Y., Wang, Y., Zhang, H., Huang, L. and Yu, G., 2009. Synthesis of N-doped graphene by chemical vapor deposition and its electrical properties. *Nano Letters*, 9(5), pp.1752-1758.

Wu, Z.S., Ren, W., Xu, L., Li, F. and Cheng, H.M., 2011. Doped graphene sheets as anode materials with superhigh rate and large capacity for lithium ion batteries. *ACS Nano*, 5(7), pp.5463-5471.

Yi, H., Wu, L.Q., Bentley, W.E., Ghodssi, R., Rubloff, G.W., Culver, J.N. and Payne, G.F., 2005. Biofabrication with chitosan. *Biomacromolecules*, 6(6), pp.2881-2894.

Yu, Y.J., Zhao, Y., Ryu, S., Brus, L.E., Kim, K.S. and Kim, P., 2009. Tuning the graphene work function by electric field effect. *Nano Letters*, 9(10), pp.3430-3434.

Zhang, N., Zhang, Y. and Xu, Y.J., 2012. Recent progress on graphene-based photocatalysts: current status and future perspectives. *Nanoscale*, 4(19), pp.5792-5813.

Zhao, J., Chen, G., Zhang, W., Li, P., Wang, L., Yue, Q., Wang, H., Dong, R., Yan, X. and Liu, J., 2011. High-resolution separation of graphene oxide by capillary electrophoresis. *Analytical Chemistry*, 83(23), pp.9100-9106.

Zhao, J., Xie, Y., Guan, D., Hua, H., Zhong, R., Qin, Y., Fang, J., Liu, H. and Chen, J., 2015. BaFe$_{12}$O$_{19}$-chitosan Schiff-base Ag(I) complexes embedded in carbon nanotube networks for high-performance electromagnetic materials. *Scientific Reports*, 5(1), p.12544.

Geopolymers as Supplementary Cementitious Materials to Reduce Carbon Dioxide Emissions

A. Mushtaq[1], S. Ali[1†], A. H. Chaudhry[2], N. Sial[3], M. Aslam[4] and H. Batool[1]

[1]Department of Superior University, Lahore, Pakistan
[2]Geological Survey of Pakistan, Lahore, Pakistan
[3]Government Graduate College for Women, Gulberg, Lahore, Pakistan
[4]Department of Chemistry, University of Education, Lahore, Pakistan
†Corresponding author: S. Ali; shaukat_ali_48@yahoo.com

ABSTRACT

Geopolymers are an alternative and sustainable substitute for ordinary Portland cement (OPC) Geopolymers are being investigated as supplementary cementitious materials to lower carbon dioxide emissions in the building sector. To lower emissions, geopolymer concrete also improves the environment by substituting OPC with supplementary cementitious materials. In addition to keeping waste out of landfills, it produces lightweight, environmentally friendly building materials that fit the circular economy model. Geopolymer concrete reduces global warming as compared to traditional OPC concrete, offering sustainable solutions for construction applications and mitigating carbon dioxide emissions, thereby promoting sustainable development in the construction sector. In the building sector, geopolymer materials provide environmentally friendly substitutes for OPC materials by enhancing water absorption, lowering carbon dioxide emissions, and fostering environmental sustainability. In terms of mechanical qualities, robustness, and environmental sustainability, geopolymers have demonstrated encouraging outcomes.

INTRODUCTION

In the construction industry, the use of cement as a binding building material has enormous and serious impacts on the environment. Its preparation in the kiln takes place when the raw materials are heated for clinker production. However, firstly, these raw materials, because of their extraction from the environment, become reduced, and secondly, during the process of cement manufacturing, the large amount of energy usage produces a large amount of carbon dioxide, which causes an increase in temperature around the world, leading to global warming and influencing drastic effects on the environment, climate change, rising sea levels, pollution, severe health issues, and other global issues. The cement industry emits 8 percent of greenhouse gases; however, to keep global warming to 1.5°C and safeguard public health and welfare, immediate action is required. To ensure a sustainable future, carbon dioxide emissions must be reduced. So, to prevent these issues, there is a need to use industrial waste, such as fly ash or slag, because of their harmful nature. It is better to reuse them, so they react with alkaline solutions and generate the binding gel. However, supplementary cementitious materials, which are

solid wastes that include aluminosilicate, can effectively substitute cement. They improve the properties of hardened concrete such as geopolymer (alkali activated) materials (de Oliveira et al. 2022), i.e., they are healthier, and more durable in both acidic and alkaline solutions, and because of their ability to absorb water, they can resist changes in temperature as well as freeze-thaw cycles (Alahmari et al. 2023) high mechanical strength, sustainable for the environment, lesser carbon dioxide emissions from these gases, and lower energy use (Chen et al. 2010, Mohamad et al. 2022, Sbahieh et al. 2023) with lower permeability, improving strength, and making concrete mixtures more cost-effective. It had been suggested that artificial binders, rather than natural stones, were used in the construction of the pyramids. Rather than being organized in layers like calcium remains, the blocks were arranged like an artificial binder (Davidovits & Cordi 1979). Geopolymers are long-range, covalently bonded, non-crystalline networks made of inorganic ceramic and aluminosilicate; certain blends of geopolymers contain octahedral fragments. Their network structure is three-dimensional, and they are inorganic polymers consisting of Al-O and Si-O in tetrahedral form linked with an oxygen bridge (Wan et al. 2017). To generate geopolymers based on

the chemical nature of these polymers, Davidovits proposed the term poly (sialate) as shown in Table 1. Sialate, which stands for silicon-oxo-aluminate, is made up of tetrahedra of SiO_4 and AIO_4 joined by oxygen atoms.

RAW MATERIALS FOR GEOPOLYMERS PRODUCTION

Clay minerals and other raw materials with high silica and alumina contents are used in the production of geopolymers. Because of its cohesive and pliable earthy structure, clay, an aluminosilicate salt with small particles, is an appropriate precursor for the synthesis of geopolymers.

Metakaolin, as shown in Table 2, a mineral, is a popular starting material for geopolymerization due to its predictable properties and chemical makeup. The natural minerals in which silica and alumina are present are more than 65% in the earth's crust. MK is essentially a pozzolanic substance made from kaolin clay employing high-temperature calcination. When compared to OPC, metakaolin geopolymers improve mechanical properties, workability, and resistance to heat,

corrosion, and water. When compared to alternative binding materials, they offered improved compressive and flexural strength. Even though metakaolin is a key product, its production is unable to keep up with the world's demand for pozzolanic ingredients used in the manufacturing of cement and concrete. The geopolymerization of Al-Si minerals and clays, such as metakaolin and kaolinite, takes place (Xu & Van Deventer 2000). Metakaolin is the starting material for geopolymerization, but it is too soft and has too many water requirements. The thermal and mechanical processing of kaolin can increase its reactivity and surface energy while decreasing its crystallinity. This method can decrease gases and pollution i.e. released in heat treatment.

Despite their benefits, metakaolin-based geopolymers have restrictions in the areas in which they can be used due to their low mechanical strength and high water requirements. Much work has been done in the last few decades on the geopolymerization of Al-Si minerals and clays, especially metakaolin and kaolinite. However, these raw materials are naturally occurring and are primary sources. So, the usage of secondary raw materials such as fly ash, GGBS, etc.

Table 1: Classification of geopolymers based on sialate composition and Si:Al ratios.

Polymer Type	Chemical Composition	Si:Al Ratio
Poly (sialate)	Silicon-oxo-aluminate	1
Poly (sialate-siloxo)	Silicon-oxo-aluminate with siloxo	2
Poly (sialate-disiloxo)	Silicon-oxo-aluminate with disiloxo	3

Table 2: Primary raw materials.

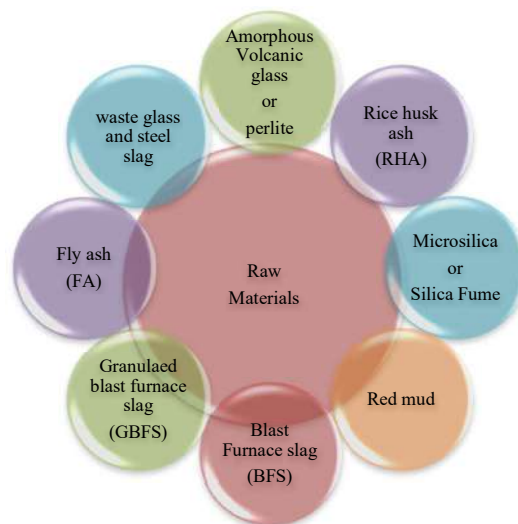|	Aluminosilicate source material	Uses
Metakaolin ($2SiO_2 \cdot Al_2O_3$)	The thermal treatment of kaolinite at 600–800°C leads to the collapse of the original clay structure and the formation of metakaolin.	In ceramics production, but is used as cement in concrete replacement.

Fig. 1: Raw materials for Geopolymer production.

Their nature is harmful, so it is better if we use and recycle them. And use them as a replacement for cement for construction purposes in buildings. However, these raw materials from aluminosilicate sources were created artificially, and although any silicate or hydroxide can be used, sodium hydroxide and sodium silicate are the main alkaline activators. Fly ash and blast furnace slag are examples of industrial wastes and products that can be used as raw materials to produce geopolymers in a more for geopolymer ecologically responsible way. On the other hand, the final product's strength, setting times, slump, and shrinkage can all change if contaminants are included.

Fly ash, as shown in Fig. 1, an anthropogenic element obtained by industrial waste from coal-fired power plants, is a valuable material for geopolymer synthesis due to its low water demand, high workability, and easy availability. The primary constituents of fly ash (FA) are SiO_2 and Al_2O_3 as shown in Table 3. It poses environmental issues. It is separated into two classes: Class F fly ash and Class C fly ash. Class F fly ash is a low-calcium fly ash derived from bituminous coal or anthracite, which is pozzolanic. Class C fly ash is a high-calcium fly ash derived from lignite or sub-bituminous coal. It possesses self-cementing and pozzolanic qualities. FA's special qualities, like its mix of silicate and alumina, can be utilized in the synthesis of geopolymers (Guo et al. 2017), and its uses in construction, road replacement, brick production, and soil stabilization. So, to protect the environment, it is better to reuse it. Despite its availability worldwide, its utilization is limited. Geopolymerization can be an effective method to use fly ash, considering its heterogeneous nature and low reactivity. Mechanical activation and metakaolin addition can make fly ash an appropriate base material for geopolymers with high mechanical strength and enhanced durability (Duxson et al. 2007, Rangan 2008).

Granulated blast furnace slag (GBFS) as shown in Fig. 1, is an iron-making byproduct that is glassy and granular and contains SiO_2, CaO, Al_2O_3, and MgO as shown in Table 3. For more than 75 years, it has been utilized as a substitute material for the manufacturing of cement and geopolymeric systems (Duxson et al. 2007). At 0°C, it can still attain ideal reaction rates. Mix reactivity, strength, resistance to sulfate, and mineral structure are all enhanced by GBFS. (Katarzyna et al. 2020) Clinker requirements were decreased by using blast furnace slag in place of cement. Because of its high alumina and silica concentrations, it may also be used to produce geopolymers, providing a greener method of building.

Blast-furnace slag (BFS) as shown in Fig. 1, is produced by blast furnaces using iron ore, coke, and limestone to produce iron. Slag is removed, iron is transformed, and cooling occurs. The clinker requirements decreased with it.

Red mud (RD) as shown in Fig. 1, is a by-product of the Bayer process, which uses sodium hydroxide to dissolve bauxite into alumina. It is composed of both metallic and solid oxides, with iron oxides making up more than 60% of its mass (Singh 2018). It is also an industrial waste generated during alumina extraction. Red mud leaching can be reduced by using geopolymers. It is appropriate for the manufacturing of geopolymers because of its high alkalinity and alumina content. Red mud geopolymers can also be utilized to make high-quality paving blocks when employed as cementitious materials in the construction of roads. Red mud (RM) is produced over 1 to 2.5 tons for every tonne of alumina extracted from bauxite. Its iron oxide content, which ranges from 20% to 60%, gives it its red color. Researchers investigated the use of RM in alkali-activated binder formulations and OPC production. It has been demonstrated that adding a tiny amount of RM to cement could improve its mechanical qualities.

Microsilica, or silica fume, as shown in Fig. 1, is a valuable by-product of ferrosilicon and silicon alloy production. Its compact size reduces permeability and increases strength, durability, and density by filling voids in the microstructure. Both natural and artificial sources could yield SF, a highly reactive pozzolan with chemical, mineralogical, and physical characteristics. It is a useful additional material for geopolymers in concrete applications due to its nano-porous formation. The addition of silica fume improved the properties of geopolymers and offered sustainable substitutes.

A filler known as rice husk ash (RHA), as shown in Fig. 1, is a byproduct of processing and growing rice that has special pozzolanic qualities and a high silica concentration. It is made by calcining rice husks, which poses a risk to the environment. When RHA is burned in a boiler, 100 kg of husks give 25 kg. The chemical composition is sensitive to the conditions of combustion; unburned carbon results in a grayish-black color and small, fine particles ranging in size from 3 to 75 µm (Singh 2018). In concrete, it could be applied to increase workability, decrease permeability, and lengthen the setting time. The potential of geopolymers to improve mechanical properties, durability, sustainability, and lower production costs when compared to regular polyethylene (OPC) intrigued RHA.

Amorphous volcanic glass, or perlite, as shown in Fig. 1, is a raw material used in the manufacturing of geopolymers. In agriculture, perlite, which is high in SiO_2 and Al_2O_3 as shown in Table 3, is utilized as a water absorbent. But it's waste because of its porosity or tiny particle size. Waste

geopolymerized perlite can be utilized alone as a thermal insulator or in combination with fly ash to create building materials and immobilize hazardous waste (Vance et al. 2009).

Waste glass, silica fume, and steel slag as shown in Fig. 1, are the materials that include amorphous structures and a large amount of silicate and aluminum components. Metakaolin and other waste materials can be added to geopolymer-based constructions to make them better. Particle fineness, oxide concentration, and composition of the amorphous phase all affect the microstructure of geopolymer materials (Helmy 2016). To generate a three-dimensional network of silico-aluminate, the geopolymer binding process involves dissolving aluminosilicate precursors to form reactive particles, restructuring and altering structures, releasing water, and polymerization/polycondensation. Aluminosilicate powder and an alkali solution are combined to create a geopolymer, which is a gel-like material with remarkable qualities like low density, high strength, thermal stability, fire resistance, and chemical resistance. These non-polluting materials can have their excellent adhesive qualities enhanced by adding carbon fiber reinforcement.

In the geopolymerization reaction, as shown in Fig. 2, the waste products containing aluminosilicate mix with alkaline activators like sodium hydroxide or KOH and sodium silicate or potassium silicate. However, when Si-O-Si bonds break aluminum atoms penetrate them to form aluminosilicate gel. With more alkali, these gels harden into a geopolymer cement. This cement is mixed with aggregate and water to form geopolymer concrete. In geopolymerization, activator solutions play a critical role in promoting reactions and establishing the structure of the material. Strongly alkaline activators promote stable hydrates with limited solubility by accelerating the dissolution of aluminosilicate. Their chemical and physical characteristics have a big impact on the way the activated material performs. Alkali activators play a crucial role in the activation process of geopolymer materials, influencing their alkalinity, durability, resistance to

Table 3: Raw materials and their composition.

| Raw Material	Composition	The cement replacement percentage of these raw materials
Fly ash	SiO_2, Al_2O_3, Fe_2O_3 and CaO	15-30%
GBFS	CaO, SiO, Al_2O_3, MgO	Normal conditions 40-50% and for marine conditions 50-60%
BFS	CaO, SiO_2, Al_2O_3, small quantity of Fe, Ti, Mg and Mn (Li *et al*., 2022)	50-85% Gruyaert et al. 2013)
Red mud	Fe_2O_3, Al_2O_3, TiO_2	20% (Viyasun et al. 2021)
Microsilica	SiO_2 main impurities C, SiC, and oxides of alkaline (earth) metals	5% and 15% (Tak et al. 2023)
Rice husk ash (RHA)	90% Si, 5% C, 2% K_2O	5% partial replacement of cement with RHA for structural concrete 15% for non-structural construction (Singh 2013)
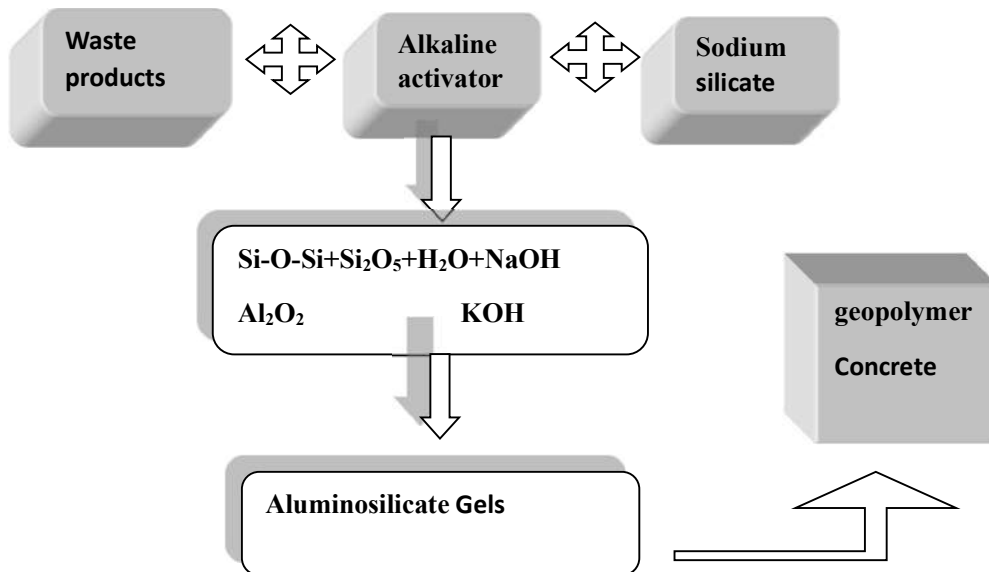
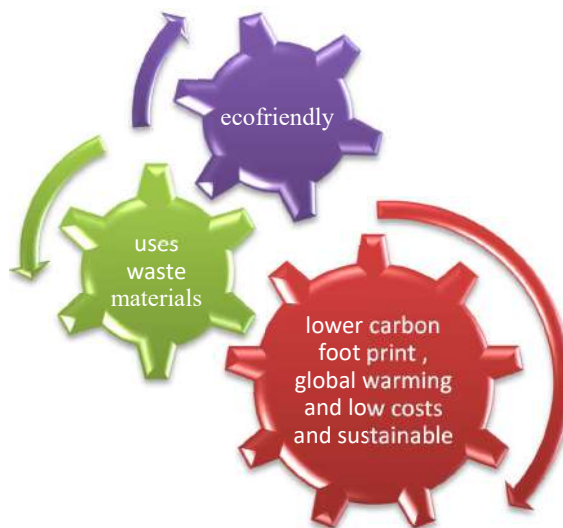Fig. 2: Mechanism of Geopolymer Concrete.

Fig. 3: Geopolymer cement.

chemical attacks, and strength growth. Aluminosilicates are polymerized by it, resulting in GPC. The Si and Al atoms dissolved in alkaline solutions and were then reassembled into the geopolymeric network. The microstructure, mechanical characteristics, and activation efficiency of the material were all influenced by the type of activator used; sodium-based activators exhibit higher levels of efficiency. Research indicated that potassium compounds, as opposed to NaOH, can raise alkalinity in geopolymer systems. While acidic activators are sometimes used to activate geopolymers, alkali activators are typically used to do so. It was preferable to use acid-based activators rather than alkaline ones, which are formed from phosphate or humic acids. Phosphoric acid and aluminum phosphate-based activators were two common phosphate-based activators. Silicate solutions, carbonates, and activators based on sodium or potassium are frequently utilized because they are readily available and reasonably priced. Sodium waterglass, ash from solid waste, and organic material can also be employed as activators; however, sodium-based activators exhibit higher activation efficiency in the formation of FA. In geopolymers, alkali activators are frequently utilized, while acidic activators are also used in some compositions. The MK-based geopolymer exhibits better mechanical properties, increased temperature resistance, and compressive strength of up to 93.8 MPa. Geopolymers with phosphoric acid as a base could act as heat- or fire-retardants (Tchakouté & Rüscher 2017).

PROPERTIES OF GEOPOLYMERS

An eco-friendly as shown in Fig. 3, cementless binder geopolymer with superior strength, strong mechanical characteristics, and resistance to chemical attacks Waste products such as silica fume, fly ash, and blast furnace slag can be used to make them. Recent investigations concentrate on improving qualities and broadening usage, providing a useful and sustainable substitute for conventional concrete (Xu et al. 2022). Geopolymers are being investigated as sustainable substitutes for conventional concrete because of their superior mechanical qualities and tolerance to high temperatures. They use waste materials as binders and lower carbon dioxide emissions. Geopolymer composites have promising qualities, are long-lasting, and have many beneficial applications. They are cost-effective, satisfy specification standards, and show resistance to acid, carbonation, and high temperatures (Noviks 2023). In this study, the research approach to geopolymers-alumino-silicon gels manufactured from natural and artificial mineral components from Latvia-such as sand, clay, wood ash, and brick waste examined. Using sodium silicate and sodium alkali solutions, the study sought to ascertain that the content of the interacting components affected the geopolymer formation process at constant exposure factors. They concluded that geopolymers are inexpensive, green materials with superior mechanical, thermal, and chemical characteristics. Because composite geopolymer materials perform better, researchers are now concentrating on them. Because of their high specific surface area, porous structure, ion exchange capabilities, and compressive strength, geopolymers perform exceptionally well in adsorption. They are perfect for industrial uses in wastewater treatment, waste gas treatment, purification, separation, and pigment removal because of their high porosity, which enables pollutant interception and increased surface area.

Geopolymers can have their surface charge and pore size changed to accommodate different purposes. Nevertheless, this characteristic necessitates high levels of alkali activator usage, high environmental conditions, and great experimental precision. This results in higher expenses and emissions, which makes the practical use of geopolymers difficult. New materials are being developed to address these challenges. The components of geopolymers have a considerable impact on material qualities, necessitating continued research and development. To create a thorough theoretical system, variables such as the ratio of raw materials and coupling agents should be investigated. Similar in structure to zeolite, geopolymers can be made from pure chemicals or naturally occurring minerals. Flat membranes, tubular membranes, multi-channel membranes, and single or multiple geopolymer membranes are only a few of the industrial uses for them. To apply geopolymer innovation to real-world uses, more study is required in the areas of performance, cost, emissions, and practical application (Noviks 2023). Recent studies have demonstrated the potential uses of metakaolin-based geopolymers as environmentally friendly building materials because of their quick coagulation, superior resilience, and compact structure which can be further increased by the appropriate use of cement. Applications include materials for pavement repair, heavy metal curing, silt solidification, and soil stability (Dai et al. 2023). With room temperature curing, the metakaolin-based geopolymer was created as a quick repair material. Improvements in bulk density, flowability, mechanical qualities, and consistency were achieved by adding Portland cement. The geopolymer's strength was shown to be enhanced by a 40% cement component. Cement exhibited its promise in on-site geopolymer construction as the modified geopolymer created a compact skeleton structure (Wei et al. 2023).

COMPRESSIVE STRENGTH OF GEOPOLYMERS

Geopolymers the composite materials known for their exceptional mechanical strength, endurance, stability in acidic and alkaline conditions, and heat resistance. A few examples of the variables that affect their compressive strength are the water content, contaminants, alkaline activator concentration, activator weight ratio, and curing temperature. Higher curing temperatures and periods are preferred for high-strength geopolymers with Si/Al ratios. On the other hand, contaminants and greater water content may weaken its compressive strength (Castillo et al. 2021, Teo et al. 2023). The advancement of geopolymers with high compressive strength will help the building, geotechnical, and architectural industries. The weight ratios of the activator to the binder and the sodium silicate to the NaOH determine the compressive strength of geopolymers. The goal of this work is to predict the qumax by utilizing the chemical compositions of binders that combine SiO_2, Al_2O_3, and CaO (Teo et al. 2023). The compressive strength of zeolite-based geopolymer which is made with different alkali to zeolite ratios and curing temperatures investigated in this work. The findings indicate that A/Z and curing temperature have a major impact on strength values, with 60°C being the optimal temperature for strength (Djamaluddin et al. 2022). An alternative to concrete manufacturing that produces less pollution is geopolymers, which are made by combining aluminosilicates with an alkaline solution. Tailings from copper flotation can be utilized as a starting material to make geopolymers, which have both financial and environmental advantages. The alkaline activator impact determined on the compressive strength of geopolymers based on copper flotation tailings was investigated at the Sustainable Mining Research Center (CIMS) of Engineering Consulting Company JRI. The highest compressive strength was found in 100% sodium silicate (SS) geopolymers, which reached 36.46 MPa after 7 days of curing at 90°C. The two geopolymers were impermeable and non-toxic. (Castillo et al. 2022). The impact of sodium silicate (Na_2SiO_3) on fly ash type F (low calcium) geopolymerization is examined in this work. Three sources of fly ash from power plants were characterized using varying quantities of Na2SiO3. The 32% Na_2SiO_3 produced the best geopolymer, with a compressive strength of 21.62 MPa and a setting time of 30 hours (Hidayati et al. 2021). In comparison to Portland cement concrete, geopolymer concrete has many benefits, such as increased fracture energy, corrosion resistance, superior bond strength, and stability at high temperatures, because of its polymer formwork. Based on compressive strength, research utilizing the finite element method and the 3D ATENA program determines ductility values. The highest ductility value was found in specimens at 25 MPa, with a value of 5.33, and in specimens at 45 MPa, with a value of 3.39 (Aziz et al. 2022). Geopolymer concrete, which employs industrial or agricultural by-product ashes as binder materials instead of Portland cement, is one way that the concrete industry is trying to become more environmentally friendly. The compressive strength of geopolymer concrete is affected by many factors, including an alkaline solution to binder ratio, binder type, chemical composition, aggregate, alkaline solutions, curing regime, and specimen age. A systematic assessment was carried out to determine the effect of these parameters on fly ash-based geopolymer concrete (FA-GPC), and multi-scale models, such as artificial neural networks, were developed to predict the compressive strength of FA-GPC composites (Ahmed et al. 2023). A prediction model for the compressive

strength of geopolymer concrete is provided in this study, emphasizing the significance of different components and curing times. Variables including hydroxide concentration, the ratio of alkaline liquid to geopolymer solids, the ratio of sodium hydroxide to sodium silicate, temperature, curing time, water/geopolymer solids ratio, age, binder fineness, rest duration, admixtures, and aggregates are identified in the study (Faluyi et al. 2022). The composition and strength of the geopolymer paste and mortar specimens are the primary fields of investigation in this work. According to the investigation, the maximum compressive strength of 12.59 MPa and 21.75 MPa at 28 days was obtained at 12M NaOH molarity and an alkaline ratio of 2.5. The study also discovered that longer setting times are caused by higher alkaline ratios and NaOH molarity. Green materials geopolymers have the potential to take the place of conventional cementitious materials (Chairunnisa & Nurwidayati 2023). For concrete, a building material, to perform as intended, a mixed design is needed. An alkaline solution is needed for the polymerization process in geopolymer concrete, an environmentally acceptable substitute for Portland cement that uses fly ash instead. Although there are no regulations governing mix design for geopolymer concrete, modeling can be done using the data already available. Concrete compressive strength is negatively impacted by water and NaOH, according to a regression model with a standard error of 9,60179 that was created using SPSS multiple linear regression (Karongkong et al. 2022). Because of its lower carbon dioxide emissions than Portland cement, geopolymer has gained popularity as a substitute. Because of its low cost and potential, fly ash (FA) is the most widely utilized binder material for geopolymer concrete. Using 247 experimental datasets, this study created multiscale models to forecast the compressive strength (CS) of fly-ash-based geopolymer mortar. The models were assessed using R2, RMSE, SI, OBJ, and other statistical measures. The alkaline liquid-to-binder ratio and the SiO_2% of FA were the most useful characteristics in the NLR model, which outperformed the LR and MLR models (Ahmed et al. 2022).

ADVANTAGES OF GEOPOLYMERS OVER TRADITIONAL CEMENT

Because of their improved mechanical and physical qualities, geopolymers are a sustainable substitute for conventional cement. They offer good mechanical and thermal qualities, are safe for the environment, and can be used as building materials (Kočí & Černý 2022). Waste binders used in geopolymer composites provide excellent mechanical strength and resistance to corrosion. In addition, they are inexpensive and emit less CO_2. To reinforce and fill gaps and cracks, grouting technology entails pumping a slurry made of cement into these areas. Although cement-based materials have many

applications, high strength, and low cost, they also have high water separation rates, poor stability, and lengthy setting times. Made from industrial waste leftovers and volcanic ash, geopolymer materials have drawn interest due to their environmentally friendly qualities. Geopolymer materials are environmentally friendly, use little energy, and are efficient in recovering and reusing industrial waste residue. The characteristics of geopolymer grouting cementitious materials are significantly influenced by temperature. The impact of these variables on the characteristics of geopolymer grouting cementitious materials is thoroughly investigated (Yang 2022). Threats to current and future construction come from rising sea levels and erratic weather. Due to its lightweight, corrosion resistance, and magnetic neutrality, geopolymer concrete has drawn interest from researchers. Owing to the lower pH of alkali-activated materials compared to regular Portland cement, future projects requiring environmental proofing may find it feasible to use a dual system of suitable concrete and reinforcing bars (Pradhan et al. 2022). Compared to regular concrete, geopolymer concrete has greater strength, flexibility, and durability. In this work, ground granulated blast furnace slag and sugar cane bagasse ash are combined with alkaline liquids for reactivity to substitute ordinary Portland cement. Using the Taguchi method, the binder content, molarity, and alkaline activator-to-inder content ratios were the main areas of attention for geopolymer concrete optimization (Hadi et al. 2017). A dependable and long-lasting building material, concrete accounts for 5-7% of global CO_2 emissions. A recent innovation is geopolymer concrete (GPC), which is made from fly ash, powdered granulated blast furnace slag, and silica fume. When compared to traditional concrete, GPC is less expensive and provides superior resistance to chemical attacks as well as strong early strength. The environment, human health, and land scarcity can all benefit from the reuse of industrial waste materials in GPC manufacture (Kakasor et al. 2022). When used as a binder, geopolymer concrete (GPC), which uses marginal materials like fly ash and ground-granulated blast furnace slag (GGBS), is a sustainable alternative to conventional concrete. According to the study, GGBS enhanced strength rapidly, peaking at 81.43 MPa after 28 days. GPC was a high-resistance substitute for traditional concrete since it was resistant to water and chemicals and had a higher molarity. This environmentally friendly substitute for cement composites is essential for cutting carbon emissions (Bhikshma et al. 2012).

COMPARISON OF GEOPOLYMERS AND ORDINARY PORTLAND CEMENT IN TERMS OF CARBON DIOXIDE EMISSIONS

Concrete, a widely used construction material, has become less environmentally friendly due to its high CO_2 content in

the Portland cement manufacturing process. To replace OPC, fly ash is being used as a substitute. Geopolymer concrete, with 0% cement content, can reduce carbon emissions by up to 56.02% compared to normal concrete, which contains 552.22 kg. This innovative approach is based on the $A1$-A_3 carbon factor value (Setiawan et al. 2023). Although Portland cement (PC) is a commonly used material in civil infrastructure engineering, 8% of global emissions are attributed to its manufacture. The utilization of agro-industrial waste (AIW) in cement-based products is examined. Geopolymers (GPs) have the potential to replace PC in the building industry entirely or in part, while also lowering carbon dioxide emissions. AIW and an alumina-silicate phase are combined in GP technology to create GP-cement, which has exceptional mechanical and durability properties. The mechanical qualities, longevity, and environmental sustainability of AIW-based geopolymer composites are encouraging, indicating that they have great potential as building materials in the future (Alawi et al. 2023). To evaluate sustainability and identify environmental practices, this study examines the last seven years of research on geopolymer concrete. For SO_x and NO_x, the study indicated that emissions ranged from 1,865 g-SO_x/m^3 to 1,161 g-NO_x/m^3, respectively. Nominal CO_2-e equivalent emissions were observed to vary from 56 to 661 kg-CO_2/m^3. For upcoming geopolymer research, the report suggests a straightforward way of determining the nominal carbon dioxide emissions value (Talaat et al. 2023). Climate change is seriously threatened by the carbon-intensive process used in the production of Portland cement (OPC), which produces large amounts of CO_2 emissions. Carbon footprints may be decreased by using geopolymer, a binding material derived from industrial by-products like fly ash and GGBS. However, because of the risks associated with handling and mixing, it has not been extensively used. One-part geopolymer concrete emits about 65% less CO_2 and 23% less than OPC concrete, according to research comparing it with OPC and other forms of concrete (Neupane 2022). The emission of carbon dioxide from Portland cement, the world's most popular product, leads to pollution and climate change. A greener substitute is geopolymer cement, which is made from industrial waste that is high in silicon and aluminum. This study examines the mechanical characteristics, performance, and features of geopolymer concrete and concludes that it is on par with or superior to Portland cement in certain areas. Geopolymer exhibits great potential as a material of choice in the future (Ahmed et al. 2022). The carbon dioxide emissions from Portland cement, a common building ingredient, contribute to global warming. Alternative binders are required for the manufacturing of concrete to prevent this. A study employed an alkaline solution and a thermal power plant to make a

low-calcium fly ash-based geopolymer. An alkaline solution to fly ash ratio enhanced the strength of the geopolymer concrete, indicating the possibility of using different binders while making concrete (Ryu et al. 2013). Ten percent of global warming is caused by the extremely energy-intensive building ingredient known as Portland cement (PC). Researchers are researching environmentally friendly and sustainable concrete substitutes, such as geopolymer concrete (GPC), which is stronger and more durable than regular concrete. Because of its workability and comparable strength, GPC is a green building material that lowers CO_2 emissions and has shown effectiveness in structural applications. The mechanical qualities of GPC concrete are on par with or even superior to those of PC concrete, although many variables can impact its microstructure (Saeed et al. 2022). For fifty years now, concrete material that is widely used because of its affordability, adaptability, and water resistance has been crucial to the development of the world. Nonetheless, the process of making cement, which mostly entails burning fossil fuels and decarbonizing limestone, increases carbon dioxide emissions. Reduced use of Portland cement is made in preference to geopolymer concrete and fly ash, two lower-temperature alternatives, to protect the environment. This creative invention provides a low-cost, greener substitute for traditional concrete. According to the study, geopolymer concrete has the potential to be a sustainable substitute for regular Portland cement concrete because it may be utilized in similar circumstances (Farooq et al. 2021). In comparison to traditional OPC concrete, sustainable geopolymer concrete combinations have lower thermal energy and CO_2 emissions, according to a life cycle analysis. The mixtures with fly ash binder and sodium silicate had the lowest CO_2 emissions and thermal energy consumption. Alternatives to sodium hydroxide, a major source of energy and CO_2 emissions, are being investigated by researchers (Saidjon & Bakhrom 2021). Because of its significant CO_2 emissions, Portland cement is one of the main greenhouse gas emissions and is being reduced. A well-liked substitute, geopolymer, gained attention for its qualities of fire resistance, low permeability, chemical resistance, and compressive strength. It investigates the microstructure and strength of fly ash and metakaolin-based geopolymers (Barbhuiya & Pang 2022). The fire resistance of geopolymer concrete, an environmentally friendly building material, has been investigated because of its special three-dimensional mesh structure. This study examines the inorganic geopolymer concrete's static characteristics at high temperatures, emphasizing the necessity for more investigation into the material and structural design requirements before the material's use in engineering construction (Zhu & Zha 2023). The study investigates the application of geopolymer concrete, a fly

ash-based substitute for traditional concrete, to strengthen it and address environmental issues. Comparing geopolymer concrete to ordinary concrete, the study discovered that it had a slightly lower Poisson's ratio but a greater modulus of elasticity, splitting tensile strength, and compressive strength. This creative method provides a sustainable substitute for conventional concrete (Indriyantho et al. 2023). Because of its better mechanical qualities, geopolymer concrete low-carbon and environmentally friendly substitute for cementitious composites drew attention. The potential of fibers to increase compressive strength, splitting tensile strength, flexural strength, and fracture toughness lies in the analysis of the types and characteristics of fibers employed to increase the toughness of geopolymer concrete. The kind of fiber determines the ideal fiber volume rate, and aspect ratio and hybrid fiber combinations have a big influence on the geopolymer concrete's characteristics (Wang et al. 2023). This study investigates the use of fly ash, silica fume, manufactured sand, and ground granulated blast furnace slag as fine aggregate and binder in high-strength geopolymer concrete (HSGPC). The mix design methodology produced a maximum compressive strength of 104 MPa at 28 days, and all concrete grades showed promising mechanical properties. Microstructural analysis revealed a dense microstructure of various gel formations, and the environmental impact assessment of HSGPC revealed a 90% lower carbon emission than conventional concrete (Jagad et al. 2023). Fly ash, aggregates, and an alkaline activator are the three components of geopolymers, which were developed in response to environmental concerns. Fiber reinforcements made of carbon, basalt, glass, cotton, and PVA fibers are examples of recent innovations that concentrate on mechanical qualities and appropriate substitutes (Jat et al. 2022). A green substance, geopolymer recycled aggregate concrete (GPRAC), uses recycled aggregates in place of Portland cement. By altering the curing temperature, utilizing various precursor materials, including fibers and nanoparticles, and establishing ideal mix ratios, it is possible to enhance the material's mechanical qualities, durability, and microscopic features. GPRAC can help modern society move toward low-carbon and green development by lowering carbon emissions, energy loss, and environmental degradation. In order to offer recommendations for the implementation of GPRAC in geopolymer concrete, the research examines variables including curing temperature and the amount of recycled aggregate included (Zhang et al. 2023).

New substitute materials, such as Alccofine-1203(A), Metakaolin (MK), and Ground Granulated Blast-furnace Slag (GGBS), have been developed as a result of recent research in concrete technology. To create a geopolymer concrete mix, this study examined the interactions between the microstructure and the chemistry of the materials. Finer particles decrease voids and boost concrete strength, according to the study. SEM and EDAX were used to examine the microstructure of the mix, and the results showed good interlocking qualities that have a direct effect on the mechanical properties of the concrete (Karthikadevi & Saraswathi 2023). The mechanical characteristics of geopolymer concrete with a somewhat low alkali activator are examined in this study, with particular attention paid to the following: bond strength, shear strength, flexural strength, elastic modulus, compressive strength, and split tensile strength. The fly ash and alkaline activator ratios were changed during the experiment. The outcomes demonstrated that higher than 19 MPa could still be produced using geopolymer concrete with a 4% alkaline activator (Romadhon 2022). This study investigates the use of fly ash geopolymer concrete (GPC) instead of ordinary Portland cement (OPC) in the building sector, emphasizing the material's durability and mechanical qualities as well as its capacity to lower CO_2 emissions (Shebli et al. 2023).

As a result of aggregate quarrying and Portland cement production's energy inefficiency, the building industry is moving toward environmentally friendly materials. Geopolymer concretes can be made using construction and demolition waste (CDW), which eliminates the requirement for PC and natural aggregates. Using recycled aggregates and precursors such as bricks, tile, concrete, and glass, this study examined the durability of geopolymer concretes based on CDW. As compared to PC-based concrete, the results indicated no discernible loss of weight or compressive strength, and there was similar chloride penetration (Ozcelikci et al. 2023). Because ordinary Portland cement (OPC) emits hazardous amounts of carbon dioxide, it is not a good choice for concrete used in green infrastructure development. Despite being a superior material with sustainable qualities, geopolymer concrete (GPC) is not yet widely adopted because there is little knowledge regarding its long-term qualities. Twelve traits and twenty elements were found in a study on the durability of GPC over the previous thirty years, which also identified major and secondary affecting factors. The study also emphasized the gaps in the field's understanding of global acceptance and the need for more GPC research (Pradhan et al. 2022). A sustainable substitute for ordinary Portland cement (OPC), geopolymer concrete is made using the geopolymerization process. With this environmentally friendly method, aluminosilicate materials such as fly ash and metakaolin may be converted into a geopolymer binder with just an alkaline activator. Promising findings have been found in studies on the durability of geopolymer concrete, particularly with regard

to its resistance to heat and chemical attack. It is a possible substitute due to its high compressive strength, resistance to acid attack, and low to medium chloride ion penetrability (Wong 2022).

The longevity of metakaolin-based geopolymer concrete (MGPC) in harsh settings is examined in this work. The study examined four experimental factors: the duration of exposure to the hostile environment, the type of aggressive environment, the weight ratio of sand to metakaolin, and the curing temperature. The outcomes demonstrated that the performance of the MGPC was greatly impacted by each of the four parameters. It was discovered that the most effective weight ratios for harsh conditions were those that validated the tolerable durability of MGPC. The study emphasizes how crucial it is to take these things into account when designing geopolymer concrete (Forouzandeh Jounaghani et al. 2023). This study assesses the durability of fly ash (FA) and ground-granulated blast furnace slag (GGBS) geopolymer concrete (GPC) that has been activated with sodium silicate and hydroxide. The mixes were put to the test for depth of water penetration, resistance to sulfate and acid attacks, and strength. In tests of water penetration, all GPC mixtures showed moderate permeability and good performance in both acidic and alkaline environments. The findings imply that GPC mixes can successfully take the place of concrete made with ordinary Portland cement (OPC) in the building sector (Srividya & Kannan Rajkumar 2022). Concrete and geopolymeric cement are being used more frequently in the construction industry as substitutes for conventional OPC. Four variables that impact the characteristics of metakaolin-geopolymeric cement specimens are identified in this investigation. The findings demonstrate that the activator and metakaolin contents greatly increase the specimen's durability. The optimal durability is obtained when the ratio of metakaolin to cement is 1.5 and the ratio of activator to cementitious material is 0.3, according to microscopic tests such as SEM and FT-IR (Feng & Liu 2022). A dependable and long-lasting building material, concrete accounts for 5-7% of global CO_2 emissions. A recent innovation is geopolymer concrete (GPC), which is made from fly ash, powdered granulated blast furnace slag, and silica fume. When compared to traditional concrete, GPC is less expensive and provides superior resistance to chemical attacks as well as strong early strength. The environment, human health, and land scarcity can all benefit from the reuse of industrial waste materials in GPC manufacture (Kakasor et al. 2022). Waste materials like GGBS, fly ash, and slag are increasingly being utilized to make geopolymer concrete, which is made by reacting silicate and aluminate minerals with a caustic activator. New materials, such as Alcofine, have been added recently by research, increasing

its endurance even at room temperature. The higher strength, durability, and environmental sustainability of geopolymer concrete are attributed to its enhanced polymerization processes and improved resistance to chemical assault. (Niveditha & Koniki 2020)

CARBON DIOXIDE EMISSION REDUCTION POTENTIAL

The development of strategies to lower carbon dioxide emissions is essential in light of the seriousness of climate change. Waste material streams appropriate for the disposal of carbon-negative concrete were mapped by a study. 1.9 Mt/a of total carbon dioxide uptake potential was revealed in the study, which is sufficient for the production of cement and concrete in Finland from secondary raw materials. Finland's carbon dioxide emissions might be decreased from 1.9% to a negative 1.3% if carbon-negative concrete were utilized (Mäkikouri et al. 2021). With its significant role in the world's CO_2 emissions, the cement industry needs a sustainable future. This study investigates the decrease of CO_2 emissions in the Macedonian cement sector, which is a prospective member of the EU. The steps include removing CO_2 from flue emissions, using additives to lower the ratio of clinker to cement, increasing energy efficiency, and switching from fossil fuels to alternative fuels. By 2020, these actions can enhance local environmental effects, cut emissions by 65-70%, and help Macedonia produce cement more sustainably (Mikulčić et al. 2012). The study investigates how CDM initiatives might improve energy efficiency in South Africa, Brazil, Indonesia, China, and India's heavy industrial sectors. Promising project types are suggested, such as cement blending, ammonia manufacturing process integration, and near net shape casting. On the other hand, estimating the whole potential is challenging (Hayashi & Krey 2005). The population, urbanization, GDP per capita, energy intensity, and industrial structure of East and South Coastal China are among the elements analyzed in this research that have an impact on carbon emissions between 2000 and 2015. The findings indicate that while energy intensity lowers emissions, GDP raises them. Slightly over the national objective, carbon intensity was lowered by 48.5% in 2020 and 59.7% in 2030. It was higher in the advanced scenario, though. Mitigation strategies for carbon intensity include restructuring the industrial organization, optimizing energy structure, and increasing energy efficiency (Wang et al. 2018). India lags in technical management even though modern aircraft and engine technology may attain fuel efficiency of 3.5 liters per 100 passenger kilometers. The sixth busiest air route in the world, from Delhi to Mumbai, produces 5.62 million tonnes of CO_2, 3.03 million tonnes of NO_x, 0.57 million tonnes of N_2O, and 0.15 million tonnes

of CH_4 emissions every liter of fuel used. Three strategies-installing dryers, installing air units, and installing blended winglets-are how the lower CO_2 emissions. The report focuses on the significant cost of flight delays between Delhi and Mumbai, as well as India's technology management lag (Komalirani & Rutool 2012). The environment and society may suffer from excessive CO_2 emissions. Though its steady linear structure presents obstacles, reducing CO_2 is one possible way to mitigate its effects. With distributed atomic catalysts exhibiting great efficiency, Cu/TiO_2 has demonstrated potential for CO_2 photocatalytic reduction. In supported single atom catalysts for CO_2 reduction, surface oxygen vacancies and photoexcited electrons are important. Even at ambient temperature, the bending, anionic CO_2 production that is facilitated by Cu atoms with O_v allows for a rapid reduction of CO_2 (Chen et al. 2018). The necessity of cutting-edge technologies to lower CO_2 emissions in the connection between automobile transportation and climate change. It examines possible fuel-efficiency-boosting technologies as well as the effects of LPG, CNG, and battery-electric cars as well as their compatibility and maturity (Krail & Schade 2011). The study calculates potential reductions by examining China's energy and CO_2 emissions intensity from 2000 to 2013. The findings point to decreasing emissions, a less pronounced north-south distribution, and a slower trend in energy demand that will peak before 2030. China has enormous potential to reduce its carbon emissions; the most promising regions are Shanxi, Inner Mongolia, and Hebei (Chen et al. 2019).

CONCLUSIONS

In conclusion, when used in place of regular Portland cement in concrete, geopolymer cement has demonstrated the ability to cut carbon dioxide emissions by up to 80%, hence lowering the environmental effect of construction materials. Utilizing fly ash and other supplementary cementitious materials, geopolymer types of cement address environmental issues associated with standard cement production techniques and provide a sustainable way to lower carbon dioxide emissions in the construction industry. Through the reduction of CO_2 emissions and improvement of sustainability in construction operations, geopolymer technology presents an environmentally benign substitute for traditional cement manufacture. This shift is in line with international initiatives to mitigate climate change and lower carbon emissions. In addition to being a more affordable option to traditional cement concrete, geopolymer concrete has several advantages over cement concrete in terms of the environment, strength, durability, and greenhouse gas emissions. This highlights the need of sustainable construction methods. In order to combat climate change and encourage greener building techniques, geopol-

ymer cements provide a viable way to lower carbon dioxide emissions throughout the cement-making process. They improve sustainability in the building sector by providing a viable substitute for conventional cement production.

REFERENCES

Ahmed, H.U., Abdalla, A.A., Mohammed, A.S., Mohammed, A.A. and Mosavi, A., 2022. Statistical methods for modeling the compressive strength of geopolymer mortar. *Materials*, 15(5), p.1868.

Ahmed, H.U., Mohammed, A.S., Qaidi, S.M., Faraj, R.H., Hamah Sor, N. and Mohammed, A.A., 2023. Compressive strength of geopolymer concrete composites: a systematic comprehensive review, analysis and modeling. *European Journal of Environmental and Civil Engineering*, 27(3), pp.1383-1428.

Ahmed, L.A.Q., Frayyeh, Q. and Abd Al Ameer, O., 2022. Geopolymer as a Green Concrete Alternative to Portland Cement Concrete: Article review. *Journal of Al-Farabi for Engineering Sciences*, 1(2).

Alahmari, T.S., Abdalla, T.A. and Rihan, M.A.M., 2023. Review of recent developments regarding the durability performance of eco-friendly geopolymer concrete. *Buildings*, 13(12), p.3033.

Alawi, A., Milad, A., Barbieri, D., Alosta, M., Alaneme, G.U. and Imran Latif, Q.B., 2023. Eco-Friendly Geopolymer Composites Prepared from Agro-Industrial Wastes: A State-of-the-Art Review. *CivilEng*, 4(2), pp.433-453.

Aziz, M.W., Suprobo, P. and Tajunnisa, Y., 2022. Numerical analysis study of the effect geopolymer concrete compressive strength on ductility of reinforced concrete beams. *Journal of Civil Engineering*, 37(1), pp.33-38.

Barbhuiya, S. and Pang, E., 2022. Strength and microstructure of geopolymer based on fly ash and metakaolin. *Materials*, 15(10), p.3732.

Bhikshma, V., Koti, R.M. and Srinivas, R.T., 2012. An experimental investigation on properties of geopolymer concrete (no cement concrete).

Castillo, H., Collado, H., Droguett, T., Sánchez, S., Vesely, M., Garrido, P. and Palma, S., 2021. Factors affecting the compressive strength of geopolymers: A review. *Minerals*, 11(12), p.1317.

Castillo, H., Droguett, T., Vesely, M., Garrido, P. and Palma, S., 2022. Simple Compressive Strength Results of Sodium-Hydroxide-and Sodium-Silicate-Activated Copper Flotation Tailing Geopolymers. *Applied Sciences*, 12(12), p.5876.

Chairunnisa, N. and Nurwidayati, R., 2023. The Effect of Natrium Hydroxide Molarity Variation and Alkali Ratio on the Compressive Strength of Geopolymer Paste and Mortar. *IOP Conference Series: Earth and Environmental Science*.

Chen, C., Habert, G., Bouzidi, Y. and Jullien, A., 2010. Environmental impact of cement production: detail of the different processes and cement plant variability evaluation. *Journal of Cleaner Production*, 18(5), pp.478-485.

Chen, J., Iyemperumal, S.K., Fenton, T., Carl, A., Grimm, R., Li, G. and Deskins, N.A., 2018. Synergy between defects, photoexcited electrons, and supported single atom catalysts for CO2 reduction. *ACS Catalysis*, 8(11), pp.10464-10478.

Chen, L., Li, X., Xue, S., Qu, L. and Wang, M., 2019. Carbon intensity and emission reduction potential in China: spatial measuring method. *Journal of Economic Structures*, 8, pp.1-12.

Dai, S., Wang, H., Wu, H. and Zhang, M., 2023. Exploration of the mechanical properties, durability and application of geopolymers: a review. *European Journal of Environmental and Civil Engineering*, 27(10), pp.3202-3235.

Davidovits, J. and Cordi, S., 1979. Synthesis of new high temperature geo-polymers for reinforced plastics/composites. *SPE PACTEC*, 79, pp.151-154.

de Oliveira, L.B., de Azevedo, A.R., Marvila, M.T., Pereira, E.C., Fediuk, R. and Vieira, C.M.F., 2022. Durability of geopolymers with industrial waste. *Case Studies in Construction Materials*, 16, p.e00839.

Djamaluddin, A.R., Harianto, T., Muhiddin, A.B., Arsyad, A., Nur, S.H. and Ariningsih, A., 2022. Compressive strength of zeolite-based geopolymer paste. *AIP Conference Proceedings*.

Duxson, P., Fernández-Jiménez, A., Provis, J.L., Lukey, G.C., Palomo, A. and van Deventer, J.S., 2007. Geopolymer technology: the current state of the art. *Journal of Materials Science*, 42, pp.2917-2933.

Faluyi, F., Arum, C., Ikumapayi, C.M. and Alabi, S.A., 2022. A Review of the Compressive Strength Predictor Variables of Geopolymer Concrete. *FUOYE Journal of Engineering and Technology*, 7, pp.404-414.

Farooq, F., Jin, X., Javed, M.F., Akbar, A., Shah, M.I., Aslam, F. and Alyousef, R., 2021. Geopolymer concrete as sustainable material: A state of the art review. *Construction and Building Materials*, 306, p.124762.

Feng, B. and Liu, J., 2022. Durability of Repair Metakaolin Geopolymeric Cement under Different Factors. *Processes*, 10(9), p.1818.

Forouzandeh Jounaghani, M., Jahangiri, A. and Jamekhorshid, A., 2023. Experimental investigation on the durability of metakaolin-based geopolymer concrete in aggressive environments. *Asian Journal of Civil Engineering*, pp.1-15.

Gruyaert, E., Maes, M. and De Belie, N., 2013. Performance of BFS concrete: k-value concept versus equivalent performance concept. *Construction and Building Materials*, 47, pp.441-455.

Guo, Y., Zhao, Z., Zhao, Q. and Cheng, F., 2017. Novel process of alumina extraction from coal fly ash by pre-desilicating—Na_2CO_3 activation—Acid leaching technique. *Hydrometallurgy*, 169, pp.418-425.

Hadi, M.N., Farhan, N.A. and Sheikh, M.N., 2017. Design of geopolymer concrete with GGBFS at ambient curing condition using Taguchi method. *Construction and Building Materials*, 140, pp.424-431.

Hayashi, D. and Krey, M., 2005. CO_2 emission reduction potential of large-scale energy efficiency measures in heavy industry in China, India, Brazil, Indonesia and South Africa. (No. 4-6). HWWI Research Paper.

Helmy, A.I.I., 2016. Intermittent curing of fly ash geopolymer mortar. *Construction and Building Materials*, 110, pp.54-64.

Hidayati, R.E., Faradilla, F.S., Dadang, D., Harmelia, L., Nurlina, N., Prasetyoko, D. and Fansuri, H., 2021. Setting time and compressive strength of geopolymers made of three Indonesian low calcium fly ash with variation of sodium silicate addition. *Archives of Metallurgy and Materials*, pp.1115-1121.

Indriyantho, B.R., Purwanto, P. and Riko, R., 2023. Mechanical performance analysis of geopolymer concrete using fly ash Tanjung Jati B for sustainable construction materials. *TEKNIK*, 44(1), pp.39-45.

Jagad, G., Modhera, C., Patel, D. and Patel, V., 2023. Mechanical and microstructural characteristics of manufactured sand-based high-strength geopolymer concrete and its environmental impact. *Practice Periodical on Structural Design and Construction*, 28(4), pp.04023036.

Jat, D., Motiani, R., Dalal, S. and Thakar, I., 2022. Mechanical properties of geopolymer concrete reinforced with various fibers: A review. *Proceedings of the 2nd International Symposium on Disaster Resilience and Sustainable Development*, Volume 2-Disaster Risk Science and Technology.

Kakasor, J.D., Ismael, A.P. and Qarani, A.S., 2022. Geopolymer concrete: Properties, durability and applications. *Recycling and Sustainable Development*, 15(1), pp.61-73.

Karongkong, L.L., Setiawan, A.A. and Hardjasaputra, H., 2022. Predicting of geopolymer concrete compressive strength using multiple linear regression method. *International Journal of Applied Science and Engineering*, 19(2), pp.1-7.

Karthikadevi, S. and Saraswathi, R., 2023. Enhancement of the mechanical properties of a geopolymer concrete due to chemical and microstructural interaction of the binder material. *Silicon*, 15(7), pp.3071-3082.

Katarzyna, B., Le, C.H., Louda, P., Michał, S., Bakalova, T., Tadeusz, P. and Prałat, K., 2020. The fabrication of geopolymer foam composites incorporating coke dust waste. *Processes*, 8(9), pp.1052.

Kočí, V. and Černý, R., 2022. Directly foamed geopolymers: A review of recent studies. *Cement and Concrete Composites*, 130, pp.104530.

Komalirani, Y. and Rutool, S., 2012. CO_2 emission reduction potential through improvements in technology from civil aviation sector in India: A case of Delhi-Mumbai air route. *Research Journal of Recent Sciences*, 2277, pp.2502.

Krail, M. and Schade, W., 2011. Technological potential for CO_2 emission reductions of passenger cars. In *Transport Moving to Climate Intelligence: New Chances for Controlling Climate Impacts of Transport after the Economic Crisis* (pp. 271-287). Springer.

Li, C., Li, X., Yu, Y., Zhang, Q., Li, L., Zhong, H. and Wang, S., 2022. A novel conversion for blast furnace slag (BFS) to the synthesis of hydroxyapatite-zeolite material and its evaluation of adsorption properties. *Journal of Industrial and Engineering Chemistry*, 105, pp.63-73.

Mäkikouri, S., Vares, S., Korpijärvi, K. and Papakonstantinou, N., 2021. The carbon dioxide emissions reduction potential of carbon-dioxide-cured alternative binder concrete. *Recent Progress in Materials*, 3(2), pp.1-28.

Mikulčić, H., Markovska, N., Vujanović, M., Filkoski, R.V., Ban, M. and Duić, N., 2012. Potential for CO2 emission reduction in the cement industry. *Digital Proceedings of the 7th Conference on Sustainable Development of Energy, Water and Environment Systems* – SDEWES Conference, Ohrid, Makedonija.

Mohamad, N., Muthusamy, K., Embong, R., Kusbiantoro, A. and Hashim, M.H., 2022. Environmental impact of cement production and solutions: A review. *Materials Today: Proceedings*, 48, pp.741-746.

Neupane, K., 2022. Evaluation of environmental sustainability of one-part geopolymer binder concrete. *Cleaner Materials*, 6, pp.100138.

Niveditha, M. and Koniki, S., 2020. Effect of durability properties on geopolymer concrete: A review. *E3S Web of Conferences*.

Noviks, G., 2023. Physical properties of geopolymers made from mineral waste. *Environment. Technologies. Resources. Proceedings of the International Scientific and Practical Conference*.

Ozcelikci, E., Yildirim, G., Alhawat, M., Ashour, A. and Sahmaran, M., 2023. An investigation into durability aspects of geopolymer concretes based fully on construction and demolition waste. *International Symposium of the International Federation for Structural Concrete*.

Pradhan, P., Dwibedy, S., Pradhan, M., Panda, S. and Panigrahi, S.K., 2022. Durability characteristics of geopolymer concrete: Progress and perspectives. *Journal of Building Engineering*, 105100.

Rangan, B.V., 2008. Fly ash-based geopolymer concrete.

Romadhon, E.S., 2022. Mechanical properties of geopolymer concrete containing low-alkaline activator. *Annales de Chimie Science des Matériaux*.

Ryu, G.S., Lee, Y.B., Koh, K.T. and Chung, Y.S., 2013. The mechanical properties of fly ash-based geopolymer concrete with alkaline activators. *Construction and Building Materials*, 47, pp.409-418.

Saeed, A., Najm, H.M., Hassan, A., Sabri, M.M.S., Qaidi, S., Mashaan, N.S. and Ansari, K., 2022. Properties and applications of geopolymer composites: A review study of mechanical and microstructural properties. *Materials*, 15(22), pp.8250.

Saidjon, K. and Bakhrom, U., 2021. Energy-saving materials in residential architecture. *The American Journal of Engineering and Technology*, 3(01), pp.44-47.

Sbahieh, S., McKay, G. and Al-Ghamdi, S.G., 2023. Comprehensive analysis of geopolymer materials: Properties, environmental impacts, and applications. *Materials*, 16(23), pp.7363.

Setiawan, A.A., Hardjasaputra, H. and Soegiarso, R., 2023. Embodied carbon dioxide of fly ash-based geopolymer concrete. *IOP Conference Series: Earth and Environmental Science*.

Shebli, A., Khatib, J. and Elkordi, A., 2023. Mechanical and durability properties of fly ash geopolymer concrete: A review. *BAU Journal-Science and Technology*, 4(2), pp.5.

Singh, B., 2018. Rice husk ash. *Waste and supplementary cementitious materials in concrete*, pp. 417-460. Elsevier.

Singh, S., 2013. Compressive strength of concrete with rice husk ash as partial replacement of ordinary Portland cement.

Srividya, T. and Kannan Rajkumar, P., 2022. Durability properties of geopolymer concrete from fly ash and GGBS. *Recent Advances in Materials, Mechanics and Structures: Select Proceedings of ICMMS 2022*, pp. 601-608. Springer.

Tak, S., Gupta, P., Kumar, A., Sofi, A. and Yun, C.M., 2023. Effect of using silica fume as a partial replacement of cement in concrete. *Materials Today: Proceedings*.

Talaat, A., Emad, A. and Kohail, M., 2023. Environmental impact assessment for performance-oriented geopolymer concrete research. *Journal of Materials in Civil Engineering*, 35(1), 04022370.

Tchakouté, H.K. and Rüscher, C.H., 2017. Mechanical and microstructural properties of metakaolin-based geopolymer cements from sodium waterglass and phosphoric acid solution as hardeners: A comparative study. *Applied Clay Science*, 140, pp.81-87.

Teo, W., Shirai, K. and Lim, J.H., 2023. Characterisation of "one-part" ambient cured engineered geopolymer composites. *Journal of Advanced Concrete Technology*, 21(4), pp.204-217.

Vance, E., Perera, D., Imperia, P., Cassidy, D., Davis, J. and Gourley, J., 2009. Perlite waste as a precursor for geopolymer formation.

Viyasun, K., Anuradha, R., Thangapandi, K., Kumar, D.S., Sivakrishna, A. and Gobinath, R., 2021. Investigation on performance of red mud based concrete. *Materials Today: Proceedings*, 39, pp.796-799.

Wan, Q., Rao, F., Song, S., García, R.E., Estrella, R.M., Patino, C.L. and Zhang, Y., 2017. Geopolymerization reaction, microstructure and simulation of metakaolin-based geopolymers at extended Si/Al ratios. *Cement and Concrete Composites*, 79, pp.45-52.

Wang, T., Fan, X., Gao, C., Qu, C., Liu, J. and Yu, G., 2023. The influence of fiber on the mechanical properties of geopolymer concrete: A review. *Polymers*, 15(4), 827.

Wang, W., Wang, J. and Guo, F., 2018. Carbon dioxide (CO2) emission reduction potential in east and south coastal China: Scenario analysis based on STIRPAT. *Sustainability*, 10(6), 1836.

Wei, J., Liu, J., Feng, B., Chen, Y., Zhang, Y., Zhang, T., Fu, W., Tan, X. and Zhu, G., 2023. Research preparation and properties of geopolymer-based rapid repair materials. *Journal of Testing and Evaluation*, 51(2), pp.1204-1218.

Wong, L.S., 2022. Durability performance of geopolymer concrete: A review. *Polymers*, 14(5), 868.

Xu, H. and Van Deventer, J., 2000. The geopolymerisation of alumino-silicate minerals. *International Journal of Mineral Processing*, 59(3), pp.247-266.

Xu, J., Li, M., Zhao, D., Zhong, G., Sun, Y., Hu, X., Sun, J., Li, X., Zhu, W. and Li, M., 2022. Research and application progress of geopolymers in adsorption: A review. *Nanomaterials*, 12(17), 3002.

Yang, J., 2022. Research progress on the influence of geopolymer grouting material properties. *Frontiers in Computing and Intelligent Systems*, 1(1), pp.30-33.

Zhang, P., Sun, X., Wang, F. and Wang, J., 2023. Mechanical properties and durability of geopolymer recycled aggregate concrete: A review. *Polymers*, 15(3), 615.

Zhu, L. and Zha, X., 2023. Latest progress of mechanical properties of geopolymer concrete at elevated temperature. *Journal of Physics: Conference Series*.

Prediction and Comparison of Nonlinear Mathematical Models for the Biodegradation of Two Herbicides Under the Effect of Manure in Soils

Cheloufi R[1,2†], Alayat H.[2] and Messaadia H.[3]

[1]Université de Blida, faculté de SNV, Département Biotechnologie et Agroécologie, Route de Saumaa 9000, Algérie
[2]Agricultural laboratory and Functioning of Ecosystems, University of El-Tarf 36000, Algeria
[3]Université Hadj Lakhdar, Département d'Agronomie, Batna 5000, Algérie
†Corresponding author: Cheloufi R.; hindcheloufi0909@gmail.com

ABSTRACT

The study was for the comparison and to know the choice of Models of appreciation of the mineralization of the two herbicides under the effect of two manures (cattle and sheep) in two agricultural soils of different textures. During this work, we used two types of manure, cattle F1 and sheep F2 with two doses. The application of respirometry for monitoring biological activity has been conducted in the laboratory. The treatments were measured for carbon-labeled herbicides released ($^{14}CO_2$) after 1, 3, 7, 14, 28, 42, 60, 90, 120 and 150 days of incubation. Non-linear mathematical models have been developed for the study of the kinetics of the mineralization of herbicides under the effect of manures. The selection criteria for these fit models are R^2 and RMCE. The comparison of six models stated to choose the single-compartmental model to a first-order ascending exponential that best fits the experimental data. These models show a strong positive correlation between labeled carbon and the biodegradation time of herbicides, especially in clay-textured soil.

INTRODUCTION

The repeated actions of the use of phytosanitary products intended to protect crops, over time lead to the sterilization of soils and consequently, the pollution of groundwater (Pimentel 1995, Auterives & Baran 2015). To do this, manure is added to degrade the herbicides into non-toxic substances to stimulate the native microflora (Entry & Emmingham 1995, Topp et al 1996, Savadogo et al 2008, Mansooreh 2013, Olu-arotiowa & Agarry 2019).

Our objective is to make mathematical modeling to predict the effect of manure spreading on the biodegradation of two herbicides in soils. Simulation of the results based on laboratory measurements of the labeled C of the herbicide.

To study the kinetics of carbon mineralization ($^{14}C_{Herbicide}$) of the herbicide glyphosate and 2,4-D, non-linear regression models were used. These are the zero-order models, then the first-order mono-compartmental exponential models, the two-compartmental double-exponential and two-compartmental exponential and linear models, and finally, the Hyperbolic model. The latter is compared for monitoring and selecting the adapted model of the kinetics of the mineralization of the herbicides. The parameters of choice are R^2 and RMCE.

MATERIALS AND METHODS

Sampling

Sampling consisted of taking two samples of agricultural soil of different textures from a depth of 30 cm. These samples were subjected to granulometry and physico-chemical analysis (Table 1).

The study of the soil analysis results recorded in the Tables (Table 1), reveals that soil 1 has a clay-sandy texture (G.E.P.P.A texture triangle) (Baize 1995), a slightly alkaline pH (7.54), a very high Electrical Conductivity (EC). A very low scale rate and the retention capacity is 32.54 % (a little high). The cation exchange capacity is 72 meq/100 g of soil. Organic Carbon is 2.13% and this gives the high organic matter rate of 3.66%, soil rich in humus. But the N content is average and reaches 0.18% (Table 1) which gives a C/N ratio is 11.83 and this indicates a fairly good biological activity.

The soil analysis results reported in Table 1 show that soil 2 has a sandy texture (Baize 1995), a low alkaline pH (7.65), and an electrical conductivity (EC) of 50 µS/cm. The rate of limestone is very low (traces), the retention capacity

is 25.25% and the cationic exchange capacity is 16.65 meq/100g soil. Carbon C is 0.8% giving the low organic matter level of 1.38% (Table 2), but the N content is (0.08%) very low (Table 1). The C/N ratio is 10 and this indicates healthy soil and a good activity of the telluric microflora, that is the well decomposed organic matter, which means the stable soil humus.

It is inferred that the soil C content varies from 0.8% to 3.66%. The N content varies from 0.08 % to 0.18 %. The soils with the highest C and N content are clayey, and the C and N content of the soils is correlated with the clay content. The soil is low in clay (sandy), and has low C and N content.

Choice of Herbicides and Their Doses

The two herbicides most commonly used in the study area are Glyphosate ($C_3H_8NO_5P$) and 2,4-D ($C_8H_6Cl_2O_3$). The agronomic dose (single) (D1) of 2.5 µg for glyphosate and 2.1 µg for 2,4-D was used.

Manure Supply

We used two types of organic amendments. These are cattle manure (F1) and sheep manure (F2) of one year of age. The physico-chemical characteristics of the two manures are given in Table 2. The rate of the amendment is based on the organic matter content of the soil, which will be 5% for clay

Table 1: Texture and physico-chemical characteristics of the soils studied.

Physico-chemical characteristics	Unit of measure	Soil (S1)		Soil (S2)
Granulometry	%	sand	35	78
		Clay	15	10
		silt	40	12
Texture classes	Textured triangle (G.E.P.P.A)	Sandy-clays		Sandy
pH	-	7.54		7.65
Electrical conductivity CE	µS/cm	99.00		68
Water retention capacity CR	%	32.54		25.25
total limestone	%	0		0
K^+	ppm	173.10		57
Na^+	meq/100g	0.35		0.1
Mg^{+2}	meq/100g	1.84		0.32
Ca^{+2}	meq/100g	17.82		5.87
CEC	meq/100g	72		16.55
P (Olsen)	ppm	8.30		1.23
PT	ppm	175		28.22
NT	ppm	1800		800
C	%	2.13		0.8
OM	%	3.66		1.376
C/N	-	11.83		10

Table 2: Physico-chemical characteristics of the two manures.

Characteristics	Units	Cattle manure F1	Sheep manure F2
		F1D1	F2D1
Dry matter	%	28.4	29.3
C_{org}		13.43	14.65
N	g/kg	6.2	8.6
P_2O_5		1.41	1.8
K_2O		5.93	11.03
pH	-	7.9	8.3
C/N		21.66	17.03

soil and 15% for sandy soil. Analytical results for cattle and sheep manure are presented in Table 2.

The pH values balance between slightly basic to basic levels with pH 7.9 to 8.3 respectively for cattle manure (F1) and sheep manure (F2), a dry matter rate of 28.4% and 29.3% respectively for Cattle manure F1 and Sheep manure F2, which tells us about the pasty nature of these two types of manure. These two manures are moderately rich in total nitrogen with a content of 6.3 g/kg for F1 and 8.6 g/kg for F2. Levels 1.41 g/kg for F1 and 1.8 g/kg for F2 are considered as low P_2O_5. The organic fertilization guide GFOR in Chabalier et al. (2006) indicates that cattle manure is average (5.93 g/kg) and sheep manure is rich (11.03 g/kg) for K_2O.

The C/N ratio, which indicates the rate of decomposition of organic matter, is thus deduced. Indeed, F1 to C/N slightly high (21.66) will cause slow mineralization or immobilization of nitrogen by terrestrial microorganisms because of its low nitrogen content. However, the other has a C/N of 17.03. According to Chabalier et al. (2006) manure F2, once brought to the ground, will quickly mineralize by supplying a lot of mineral nitrogen.

Preparation of the Samples of the Experimental Device and the Determination of the 14C of the Herbicides

The treatments for experimenting with the 14C mineralization of the two herbicides are:

S1+H1, S1+H1+F1, S1+H1+F2

S1+H2, S1+H2+F1, S1+H2+F2

S2+H1, S2+H1+F1, S2+H1+F2

S2+H2, S2+H2+F1, S2+H2+F2

The radiorespirometric device used consists of a one-liter jar, in which is placed a 250 mL glass jar (cup) containing 10 g of dry weight equivalent soil, a 20 mL liquid scintillation vial containing 5 mL of sodium hydroxide (NaOH 0.2 N) which traps the $^{14}CO_2$ released during incubation at 28°C in the dark in flasks hermetically sealed with a rubber seal, is replaced regularly (after 1, 3, 7, 14, 21, 28, and 42, 60, 90, 120 and 150 days of incubation) and a 20 ml liquid scintillation vial containing 10 mL of distilled water to saturate the atmosphere of the jar. Finally, the determination of radioactivity is carried out using a liquid scintillation meter (Soulas 1993).

For each soil type, three radiorespirometric devices containing the soil treated with a glyphosate solution (2.5 µg Glyphosate and 2000 Bq Glyphosate ^{14}C per sample), and three radiorespirometric devices containing the soil treated with a 2,4-D solution (2.1 µg of 2,4-D and 2000 Bq of ^{14}C-2,4-D per sample) were prepared. ^{14}C-glyphosate and ^{14}C-2,4-D were determined by the regional nuclear center of Algiers.

Statistical Treatment of Results

Nonlinear regression (NLR) is a method for determining a nonlinear model of the relationship between the dependent variable and a group of independent variables. This approach was used to model and simulate the carbon mineralization kinetics of the two herbicides, according to XLSTAT software. Six models were applied to estimate the mineralization potential of the two herbicides (Table 3). These are time-based mathematical models that use experimental results of herbicide biodegradation kinetics under the effect of both manures over a long incubation period (90 days).

Where,

Cm: represents the amount of carbon mineralized at time t;

Co: the quantity of potentially mineralizable carbon;

k: as mineralization rate constant;

t: represents the time.

In this study, we will deal with the comparative aspect of nonlinear adjustment models.

RESULTS AND DISCUSSION

Comparisons and Selection of Models for Assessing Herbicide Mineralization by Non-Linear Regression

The results obtained in standardized laboratory conditions (temperature 28°C, soil humidity 2/3 CR) reveal, a favorable

Table 3: The mathematical models used.

Model	Equation	Reference
M1: The single-compartment model (first-order exponential)	$Cm = Co*(1-exp^{(-k*t)})$	Murwira et al. (1988)
M2: The single compartmental model (zero order)	$Cm = Yt$	Riffaldi et al. (1996);
M3 : The bi-compatimental model (exponential + linear)	$Cm = Co*(1-exp(-k*t)) +h*t,$	Nicolardot (1988) Houot et al. (1989)
M4 : The bi-compatimental Linear model	$Cm = CoH*t/ (b.C_oH+t)$	Blet-Chraudeau et al. (1990)
M5 : The bi-compatimental model double exponential	$Cm = C1 (1 - e^{-kt}) + C2 (1 - e^{-ht})$	Delphin (1988)
M 6: Hyperbolic model	$Cm = CoH. t/(b + t)$	Juma et al. (1984)

effect of the two manures (F1 and F2) on the mineralization ($^{14}CO2$) of glyphosate and 2.4-D in the different systems compared to controls without organic matter "S1H1, S1H2, S2H1 and S2H2" over an incubation period of 150 days (Table 4, 5, 6 and 7).

In order to model and simulate the results recorded in the previous Tables (Tables 4, 5, 6 and 7) of mineralization kinetics of the two herbicides according to the XLstat software, we used nonlinear regression methods that to say the statistical analysis consisted of standout nonlinear correlations. For the parameter prediction equations of the six herbicide mineralization kinetics models under the effect of the two manures, non-linear adjustment was used:

1. M 1: The single-compartment model (first-order exponential)

2. M 2: The single compartmental model (zero order)

3. M 3: The bi-compartmental model (exponential + linear)

4. M 4: The bi-compartmental model (double Linear)

5. M 5: The bi-compartmental model (double exponential)

6. M 6: Hyperbolic model

The classification and selection criteria of the Models are the mean values of the indicators of the coefficient of determination R² and the square root of the mean squares of the RMCE deviations extracted from the equations of six nonlinear regression models cited above. This model adequately describes the experimental data. The results obtained are recorded in the tables (Tables 8, 9, 10 and 11). Indeed, the chosen model has the highest mean value of R² and contains the smallest mean value of RMCE.

Effect of F1 and F2 on the Choice of Models (RNL) for Assessing the Biodegradation of Glyphosate and 2.4-D in the S1H1 System

For model 2 (M2) (zero order): No mathematical prediction,

Table 4: Effects of two manures (F1 and F2) on the mineralization kinetics of ^{14}C-glyphosate in the soil of Beni Ammar (S1) during 150 days of incubation.

Time (days)	S1+H1	S1+H1+F1	S1+H1+F2
0	0.100	2.000	2.500
3	3.000	9.530	16.750
7	8.750	19.220	40.890
10	13.150	34.750	64.090
14	26.120	48.170	78.080
21	28.270	59.120	82.100
28	29.190	64.920	86.790
42	30.190	72.210	89.190
60	32.130	77.120	90.230
90	70.930	79.550	91.130
120	42.37	82.21	92.21

Table 5: Effects of two manures (F1 and F2) on the mineralization kinetics of ^{14}C-2,4-D in the soil of Beni Ammar (S1) during 150 days of incubation.

Time (days)	S1+H2	S1+H2+F1	S1H2F2
0	1.930	0.780	1.050
3	8.250	8.150	4.490
7	9.370	13.750	30.980
10	14.850	30.230	55.110
14	20.210	42.120	63.890
21	22.350	50.950	69.220
28	24.210	64.920	72.320
42	25.380	66.780	75.230
60	25.920	68.970	76.390
90	27.130	71.120	77.230
120	29.25	73.12	77.82

Table 6: Effects of two manures (F1 and F2) on the mineralization kinetics of ^{14}C-glyphosate in the soil of Maiz el Bachir (S2) during 150 days of incubation.

Time (days)	S2+H1	S2+H1+F1	S2+H1+F2
0	0.10	1.75	2.75
3	3.00	7.33	6.00
7	8.75	21.00	16.95
10	13.15	37.15	32.67
14	23.21	48.79	50.35
21	26.12	60.23	60.24
28	28.27	67.33	67.23
42	29.19	70.09	71.19
60	30.19	73.19	75.13
90	32.13	76.16	75.92
120	70.93	76.82	85.23

Table 7: Effects of two manures (F1 and F2) on the mineralization kinetics of ^{14}C-2.4-D in the soil of Maiz el Bachir (S2) during 150 days of incubation.

Time (days)	S2+H2	S2+H2+F1	S2+H2+F2
0	0.03	1.25	1.35
3	1.75	4.35	6.25
7	6.38	7.39	11.79
10	11.59	16.07	27.67
14	18.76	29.93	38.21
21	20.23	44.28	51.33
28	20.82	54.33	60.23
42	22.20	60.09	64.10
60	23.55	62.12	67.92
90	25.13	63.82	70.10
120	66.28	76.01	78.13

Table 8: Effects of two manure on model simulation evaluation parameters in S1H1 system.

Treatments	Classification parameter	Selected models					
		M1	M2	M3	M4	M5	M6
S1H1	R^2	0.93	/	0.92	0.44	0.93	0.90
	RMCE	199.16	/	193.98	9584.33	205.45	260.95
S1H1F1D1	R^2	0.989	/	0.989	0.59	0.97	0.95
	RMCE	80.65	/	89.73	2080.67	89.013	203.20
S1H1F2D1	R^2	0.95	/	0.96	0.31	0.95	0.93
	RMCE	195.61	/	444.46	2759.49	228.39	782.25

Table 9: Effects of two manure on model simulation evaluation parameters in S1H2 system.

Treatments	Classification parameter	Selected models					
		M1	M2	M3	M4	M5	M6
S1H2	R^2	0.985	/	0.96	0.56	0.97	0.96
	RMCE	14.62	/	14.15	936.16	0.973	32.29
S1H2F1D1	R^2	0.98	/	0.98	0.64	0.98	0.55
	RMCE	14.31	/	108.57	2141.68	116.89	123
S1H2F2D1	R^2	0.973	/	0.95	0.43	0.948	0.924
	RMCE	242.195	/	493.30	5600.024	522.161	721.52

which translates into slashes in the Table (/), logical result because it is a linear function in the straight form (Cm = Yt). Note that the M1 model has the highest average R2 values of 0.930 in the S1H1 system. However, under the influence of manure 1 (F1) and manure 2 (F2), these coefficients of determination become 0.989 and 0.95 respectively. However, the smallest mean root value of the mean square deviations noted in model M1 is 199.16, 80.65, and 195.61 for S1H1, S1H1F1D1, and S1H1F2D1 (Table 8).

About the four rest models, the choice according to the mean values of the adjustment parameters R2 (0.93 0.92, 0.90, 0.64) and RMCE ranked as follows M5, M3, M6 and M4 in S1H1. While for the two systems S1H1F1 and S1H1F2, the choice is classified in descending order M 3, M5, M6 and M4 according to R2 and RMCE

Finally, we conclude that the average values of R2 are the highest and RMCE the lowest, the mono-compartmental

M1 model would be the model that adequately describes the experimental data.

Effect of F1 and F2 on the Choice of Models (RNL) for Assessing the Biodegradation of Glyphosate and 2.4-D in the S1H2 System

It was noted that M1 offers a relatively higher coefficient of determination (R^2 = 0.93 in S1H2, 0.98 and 0.96 in S1H2F1eand S1H2F2 respectively) and relatively low RMCE values which leads to the conclusion that the M1 mono-compartmental (first-order exponential) is prioritized in the S1H2, S1H2F1 and S1H2F2 systems and best adjusts to our data (Table 8). By comparing the different mean values of R^2 and RMCE for the other models, we will conclude that these models are ranked in descending order M3, M5, M6 and M4.

However, the M2 model remains unable to simulate the mineralization kinetics of 2.4-D (H2).

Table 10: Effects of two manure on model simulation evaluation parameters in S2H1 system.

Treatments	Classification parameter	Selected models					
		M1	M2	M3	M4	M5	M6
S2H1	R^2	0.93	/	0.69	0.392	0.91	0.821
	RMCE	840.306	/	44.95	3346.51	769.052	627.027
S2H1F1D1	R^2	0.966	/	0.973	0.183	0.955	0.949
	RMCE	253.423	/	201.55	6372.96	229.637	361.688
S2H1F2D1	R^2	0.76	/	0.66	0.23	0.55	0.54
	RMCE	1090	/	198	434	564	546

Finally, the effect of F1 and F2 on the average values of the potentially mineralizable carbon of H2 generated by the nonlinear regression of the mono-compartmental model characterized by the largest R^2 (0.98 and 0.97) while the lowest RMCE (4.31 and 242.195).

Effect of F1 and F2 on the Choice of Models (RNL) for Assessing the Biodegradation of Glyphosate and 2.4-D in the S2H1 System

The various indicators of the quality of the adjustments testify to the good-made optimizations (Table 10). The different mean of regression coefficients obtained on the dataset of M1, M5, and M6 are strong, that's to say they are the best, and the highest in M1. However, R^2 for the M4 model is very low, this poor fit (M4) when it is a linear bi-compartmental, which may be due to positions related to the majority of the points being gold of the two lines.

The RMCE values decrease less in M1 than those of M5, M6, and M3, which means that the simulation by the mono-compartmental model at an ascending exponential is better than those of the others. By against, the M2 remains incapable of affecting the results, because the latter resembles a straight line (linear regression).

Effect of F1 and F2 on the Choice of Models (RNL) for Assessing the Biodegradation of Glyphosate and 2.4-D in the S2H2 System

For soil (S2) system +2.4-D, the models have generated relatively high average R^2, either R^2 is equal to 0.91, 0.90, 0.88 and 0.82 respectively for M1, M5, M6 and M3, while the M4 model is generated from very low R^2 (Table 11).

Under the effect of the bovine amendment, the average values of R2 are high. Indeed, R2 is equal to 0.96, 0.95, 0.85 and 0.90 respectively for M1, M5, M6 and M3. In parallel, under the effect of ovine, these coefficients (R^2) are also higher, being 0.977, 0.94, 0.96 and 0.94 respectively for M1, M5, M6 and M3.

However, for the linear bi-behavioral M4 model, R^2 is low under the effect of the two manures and what concerns the M2 model is still unable to simulate the effect of manure on the mineralization kinetics of the 2.4-D herbicide.

For the second parameter, we distinguish the average value of RMCE as the smallest in M1, either 185.81 (Table 11). Finally, the M1 model has a higher value of R^2 and a lower value of RMCE.

For this reason, we deduce that a priori it is the M1 model which offers a better adjustment of the experimental data and which simulates well the effect of cattle manure and sheep manure on the kinetics of mineralization of glyphosate and 2.4-D. In light of the results (Tables 8, 9, 10 and 11), the mono-compartmental model with an ascending exponential is best suited to describe this biodegradation. This model is expressed by the equation:

$$^{14}C_m = C_0 \, [1\text{-exp}\,(-K*t)]$$

Or,

Cm: Quantity of mineralized carbon in a given time t;

C0: Quantity of easily mineralizable carbon;

k: Mineralization rate constant.

CONCLUSIONS

To simulate our experimental data, mathematical nonlinear regression methods were adjusted. We tried to test six models; indeed, we carried out with the statistical software XLSTAT 2009. These models used to predict the degradation and disappearance of herbicides mixed with manures in the agrosystem are frequently used. The two parameters of choice are the highest coefficients of determination R^2 and the lowest roots of the mean of the squared deviations (RMCE) to the point of making it possible to retain the best model of the biodegradation of the two herbicides under the effect of manures in the agricultural soils of the Bounamoussa irrigable perimeter.

Table 11: Effects of two manure on model simulation evaluation parameters in S2H2 system.

Treatments	Classification parameter	Selected models					
		M1	M2	M3	M4	M5	M6
S2H2	R^2	0.91	/	0.82	0.30	0.90	0.88
	RMCE	185.81	/	554.05	2373.10	635.03	702.65
S2H2F1D1	R^2	0.96	/	0.90	0.10	0.95	0.85
	RMCE	228.13	/	224.94	6485.65	237.65	315.91
S2H2F2D1	R^2	0.977	/	0.94	0.203	0.94	0.96
	RMCE	183.28	/	182.56	5935.52	162 .2	272.93

For the prediction equations of the parameters of the nonlinear adjustment, six models of the mineralization kinetics of the herbicides under the effect of these manures were used, which are the first-order exponential model (M1), the zero-order model (M2), The exponential + linear model (M3), the bi-compartmental Linear model (M4), the double exponential model (M5) and Hyperbolic model (M6).

The mathematical prediction model that best met these two conditions is the mono-compartmental model with a first-order ascending exponential. Although this model faithfully expresses the kinetics of the disappearance (mineralization) of glyphosate and 2.4-D in soils, the active ingredient of the herbicide needs a single degradation rate. It appears that this model is designed to reproduce reality because it gives the description, explanation, and prediction of this process.

REFERENCES

Auterives, C. and Baran, N., 2015. Pressions et impacts des produits phytosanitaires sur les eaux souterraines : état de l'art sur les approches méthodologiques. *Rapport final*. BRGM/RP-64623-FR, 69 p.

Baize, D., 2000. *Guide des analyses en pédologie : choix, expression, présentation, interprétation*. 2nd ed. Paris: INRA, p. 257.

Blet-Charaudeau, C., Muller, J. and Laudelout, H., 1990. Kinetics of carbon dioxide evolution in relation to microbial biomass and temperature. *Soil Science Society of America Journal*, 55, pp.1324–1328.

Chabalier, P.F., Van de Kerchove, V. and Saint Macary, H., 2006. *Guide de la fertilisation organique à la Réunion*. CIRAD, p. 166.

Delphin, J.E., 1988. Utilisation des cinétiques de premier ordre en vue de caractériser la minéralisation de quelques sols agricoles. *Agronomie*, 8, pp.289–294.

Entry, J. and Emmingham, W.H., 1995. Influence of forest age on nutrient availability and storage in coniferous soils of the Oregon Coast Range. *Canadian Journal of Forest Research*, 25(1), pp.67–83.

Juma, N.G., Paul, E.A. and Mary, B., 1984. Kinetic analysis of net nitrogen mineralization in soil. *Soil Science Society of America Journal*, 48, pp.753–757.

Kazemilari, M., Mardani, A. and Aghaeiboorkheili, M., 2013. Day of the week effect, annual returns and volatility of five stock markets in Southeast Asia. *Asian Journal of Finance & Accounting*, 5(1), p.446.

Murwira, H.K., Krichmann, H. and Swift, M.J., 1990. The effect of moisture on the decomposition rate of cattle manure. *Plant and Soil*, 122, pp.197–199.

Nicolardot, B., 1988. Évolution du niveau de la biomasse microbienne des sols au cours d'une incubation de longue durée : relation avec la minéralisation du carbone et de l'azote organique. *Revue d'Écologie et Biologie du Sol*, 25(3), pp.287–304.

Olu-Arotiowa, O.A., Ajani, A.O., Aremu, M.O. and Agarry, S.E., 2019. Adsorption of methylene blue from aqueous solution using microwave-assisted BaCl modified activated carbon produced from mango seed shell. *Journal of Applied Sciences and Environmental Management*, 23(1), pp.99–109.

Pimentel, D., 1995. Amounts of pesticides reaching target pests: Environmental impacts and ethics. *Journal of Agricultural and Environmental Ethics*, 8, pp.17–29.

Riffaldi, R., Saviozzi, A. and Levi-Minzi, R., 1996. Carbon mineralization kinetics as influenced by soil properties. *Biology and Fertility of Soils*, 22, pp.293–298.

Savadogo, A., Ouattara, C.A.T., Basssole, I.H.N. and Traore, S.A., 2006. Bacteriocins and lactic acid bacteria: A minireview. *African Journal of Biotechnology*, 5, pp.678–683.

Soulas, G., 1993. Evidence for the existence of different physiological groups in the microbial community responsible for 2,4-D mineralization in soil. *Soil Biology and Biochemistry*, 25(4), pp.443–449.

Topp, P., 1996. Dairy manure incorporation stimulates rapid atrazine mineralization in an agricultural soil. *Canadian Journal of Soil Science*, 76(3), pp.263–273.

Impact of Acid Gases on Total Precipitation Over Iraqi Stations

Nadia M. Abd, Zainab M. Abbood, Nagham Abbas Mohammed, Osama T. Al-Taai† and Wedyan G. Nassif
Department of Atmospheric Sciences, College of Science, Mustansiriyah University, Baghdad, Iraq
†Corresponding author: Osama T. Al-Taai; osamaaltaai77@uomustansiriyah.edu.iq

ABSTRACT

Acid gas is a type of natural gas or any other gas mixture that contains significant quantities of hydrogen sulfide, carbon dioxide, sulfur oxides, nitrogen oxides, hydrogen halides, or similar acidic gases. Acid gases form acidic solutions when dissolved in water. A major cause of acid rain is emissions of sulfur dioxide and nitrogen oxide, which react with water molecules in the atmosphere to produce acids. Acid rain refers to a mixture of wet and dry precipitation from the atmosphere that contains more than normal amounts of nitric and sulfuric acids. In this study, the data of the European Center for Medium-Range Weather Forecasts (ECMWF) as total precipitation (Tp), as well as the Vertical Column amount of SO_2 from the Giovanni Center were adopted. The purpose of the research was to find the relationship between rain and sulfur dioxide in Baghdad, Mosul, and Basra cities for the period (2003-2016). The study was carried out for monthly and annual (or yearly) data variations. To find the correlation strengths of the relationship between Total precipitation (Tp) and sulfur dioxide, the correlation coefficients of Spearman's rho test (rs) were used. It was found that the relationship between (Tp Vs. CO_2) and (Tp Vs. SO_2) for Mosul station was inverse and positive, with a value of 0.7 that's due to sulfur water eyes. Also, CO_2 was found throughout all months but with different ratios, where the highest concentration was in 2016 in all the stations.

INTRODUCTION

The definition of acid gases Carbon dioxide (CO_2) and hydrogen sulfide (H_2S) are the two most prevalent types of acid gas, but there are others as well, such as hydrogen chloride (HCl), hydrogen fluoride (HF), sulfur oxides (SO_2 and SO_3), and nitrogen oxides (NOx). Which means it has a low PH and high concentrations of hydrogen ions. Negative effects could befall water plants, wildlife, and infrastructure. Sulfur dioxide and nitrogen oxide emissions cause acid rain because they mix with water molecules in the atmosphere to produce acids (Chestnut & Mills 2005). Some governments have successfully worked since the 1970s to reduce the quantity of sulfur dioxide and nitrogen oxide discharged into the environment. Nitrogen oxides can also naturally be produced by lightning, while volcanic eruptions can naturally produce sulfur dioxide (Hajer 2002). It has been shown that acid rain has bad effects on freshwater, soil, and life. It also affects human health and causes paint to peel, corrodes steel structures like bridges, and weathers stone buildings and statues (Grennfelt et al. 2020).

Sources of Acid Gases

Carbon dioxide and sulfur dioxide are the two principal causes of acid gases (Hajer 2005, Yehia et al. 2022). These gases are by-products of high-temperature combustion operations (such as factory and auto exhaust, forest fires, and fertilizer manufacturing) as well as chemical industries (Larssen & Carmichael 2000).

Sulfur Dioxide (SO_2): Sulfur-containing fossil fuels that are burned release sulfur dioxide, an invisible gas. Several industrial processes, including the production of iron and steel, factories, and crude oil manufacturing operations, produce this gas (Livingston 2016).

Natural catastrophes can cause sulfur dioxide emissions into the atmosphere, which make up about 10% of the total sulfur dioxide emissions from volcanoes, seawater spray, plankton (organisms suspended in water), and decaying plants (Abbood & Al-Taai 2018). Sulfur dioxide is typically created by industrial combustion at a rate of 69.4%. In terms of transportation, it is accountable for 3.7% of sulfur dioxide emissions (Ahmed et al. 2021, Al-Jaf & Al-Taai 2019).

Carbon Dioxide (CO_2): The biosphere, aquifer, rocky atmosphere, and atmosphere of the Earth's atmosphere all contain carbon dioxide. The carbon element that is important for the existence of life on the Earth's surface is in the case of an exchange between the Earth's casing in the so-called carbon cycle (Al-Taai et al. 2021). There is an estimated 800 gigatons of carbon dioxide in the atmosphere, and the

water envelope is 38,000 gigatons, in the form of physically dissolved gas in the form of bicarbonate and carbonate, while the carbon dioxide in the lithosphere is chemically linked to rocks Carbonates such as calcite and dolomite, which contain an estimated 60,000 tons of carbon dioxide (Hashim et al. 2023, Nassif et al. 2021).

Acid rain is created when sulfur-containing gases react. When sulfur dioxide and oxygen mix with UV radiation from the sun, the most significant of these processes produce sulfur trioxide, which reacts with atmospheric water vapor to make sulfuric acid (Al-Taai & Abbood 2020). Which remains suspended in the air as a fine mist that the wind carries from one area to another, and which may combine with some airborne gases, such as ammonia, to create a new chemical called ammonia sulfate (Abbood et al. 2023). Acid rain is created when sulfur and ammonia sulfate particles dissolve in rainwater and fall to the earth's surface and nitrogen oxides and sulfur oxides both contribute to the formation of acid rain (Mahdi et al. 2021).

These particles remain suspended in still air and appear as a light mist, especially when conditions are favorable for rain (Abbasi et al. 2013). When oxygen and ultraviolet light are present, nitrogen oxides are converted into nitrogenous acid (Abbood & Al-Taai 2020).

MATERIALS AND METHODS

The reason for choosing sulfur oxides and carbon in this study is because the main factor in the formation of acid rain and the main reason for choosing the three governorates of Baghdad, Basra, and Mosul, were different due to population density, human activities, and land use, Mosul was similar to the behavior of the Anbar governorate, which includes many sulfurs Springs.

Forms of Acid Rain or Acid Precipitation

Wet Sedimentation: is acid rain where the sulfuric and nitric acids that form in the atmosphere fall to the ground mixed with precipitation such as rain, swell, hail, or fog(Al-Taai & Abbood 2020, Hames et al. 2002).

Dry Sedimentation: When there is no moisture in the atmosphere, labor particles and gases remain suspended in the atmosphere (Chan et al. 2018). The particles and acid gases may be deposited on the surfaces of water bodies, plants, and buildings quickly, or they might interact while being transported by air to create larger particles that could be dangerous to people's health (Chen et al. 2013). The accumulating acids are removed by rain. This water is corrosive and rushes over and across the ground, harming vegetation and wildlife. The amount of rain that the area receives determines how much acidity in the atmosphere is deposited by dry precipitation (Zhang et al. 2012). For example, in desert areas, the percentage of dry precipitation is higher than that of wet precipitation because of the low rate of rain during the year (Nagase & Silva 2007). Numerous studies detail the function of sulfur dioxide on rain acid for certain stations as well as the biological effects that were discovered. Structures and items built by humans are also harmed by acid rain (Singh & Agrawal 2007, Nassif et al. 2023).

RESULTS AND DISCUSSION

The Behavior of the Monthly and Yearly Rate of Tp for Iraqi Stations (Baghdad, Basra, and Mosul)

Figs. 1, 2, and 3, show the highest monthly amount of Tp recorded in November, December, January, February, March, and April months for Baghdad, Basra, and Mosul stations over 2003-2016. In 2013, the highest TP concentration was recorded in Baghdad and Basra stations, while in Mosul station, the highest concentration was in 2006. The weather is erratic and can generate heavy to moderate rain in areas with a wide range of cloud types. During this period, Iraq was distinguished by its different types of clouds, including low, medium, and high clouds. Low and medium clouds had heavy rain during the months of winter and spring. This is brought on by climatic changes, surface characteristics, and atmospheric and astronomical causes. Fig. 4, shows the high annual Tp concentration of the three selected stations during the tested period.

The Manner of the Monthly and Yearly rate of Carbon Dioxide in Iraqi Stations for 2003-2016

Figs. 5 and 6 show the CO_2 concentration during all months of the study period. The concentration of carbon dioxide showed different ratios during the tested years, with the highest concentration appearing in 2016 in all stations.

The majority of fossil fuels that are high in carbon and hydrocarbons, such as coal, peat, oil, and natural gas, as well as the exhalations of humans and other aerobic animals, volcanoes, organic matter decomposition, during the fermentation of sugars, as a byproduct for burning wood and sugars, and organic matter decomposition are to blame for this (Singh & Agrawal 2007). In addition to car smoke, fires, factories, and many other sources of pollution.

The Behavior of the Monthly and Yearly Mean of Sulfur Dioxide for Iraqi Stations

Figs. 7 and 8 show the concentration rates of sulfur dioxide gas during all months of the study period, which show
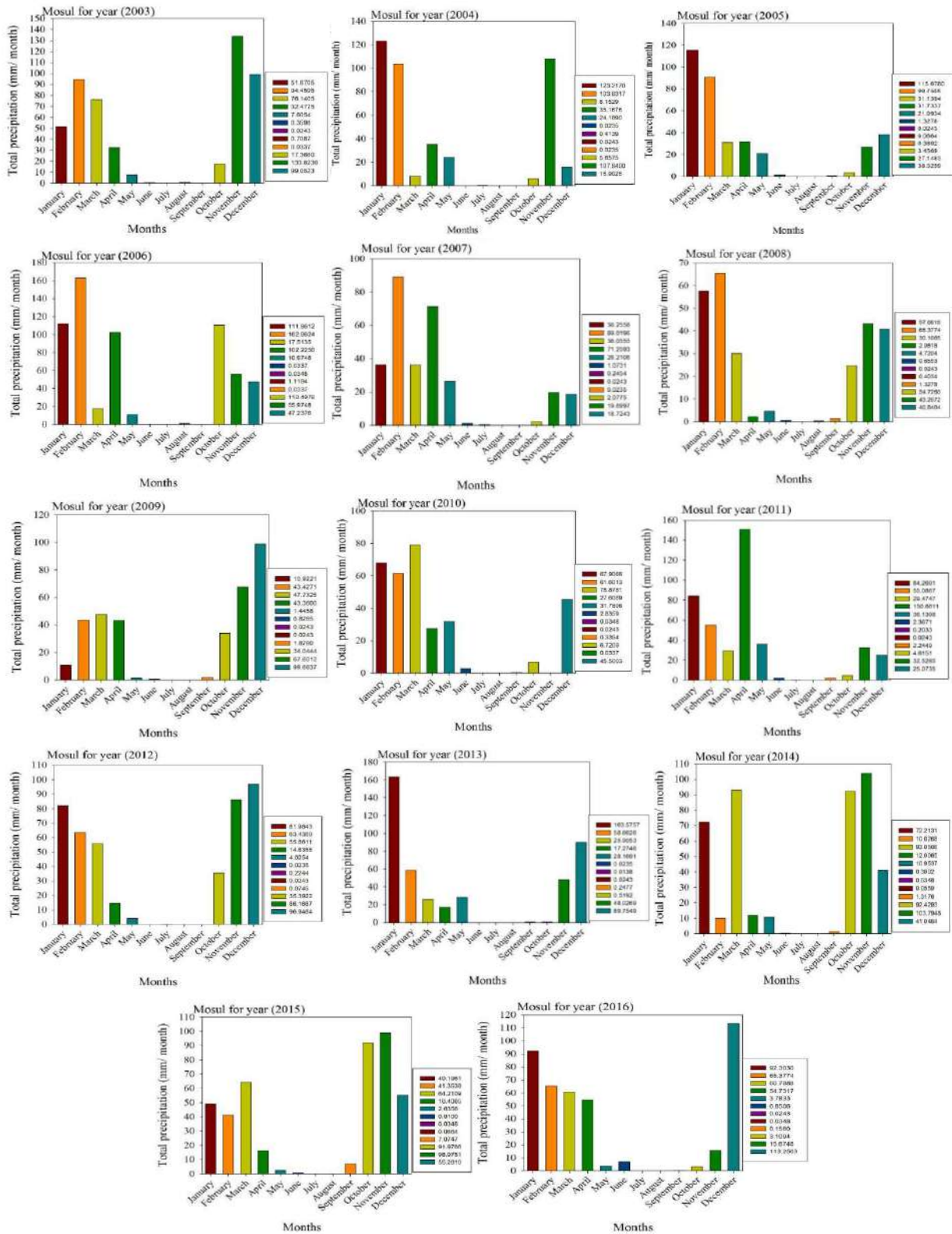
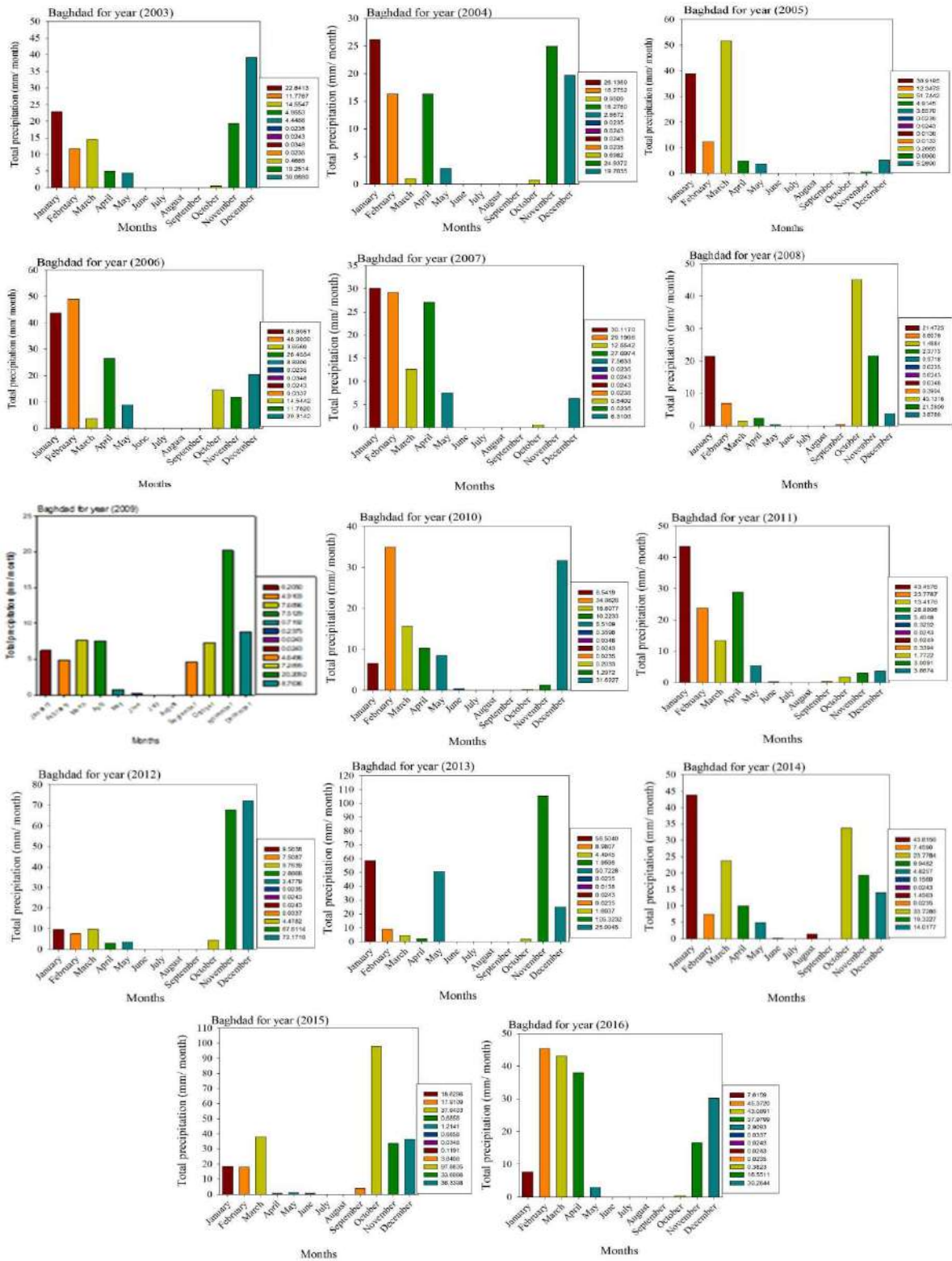Fig. 1: The high monthly average of Tp of Mosul station.

Fig. 2: The high monthly average of Tp of Baghdad station.
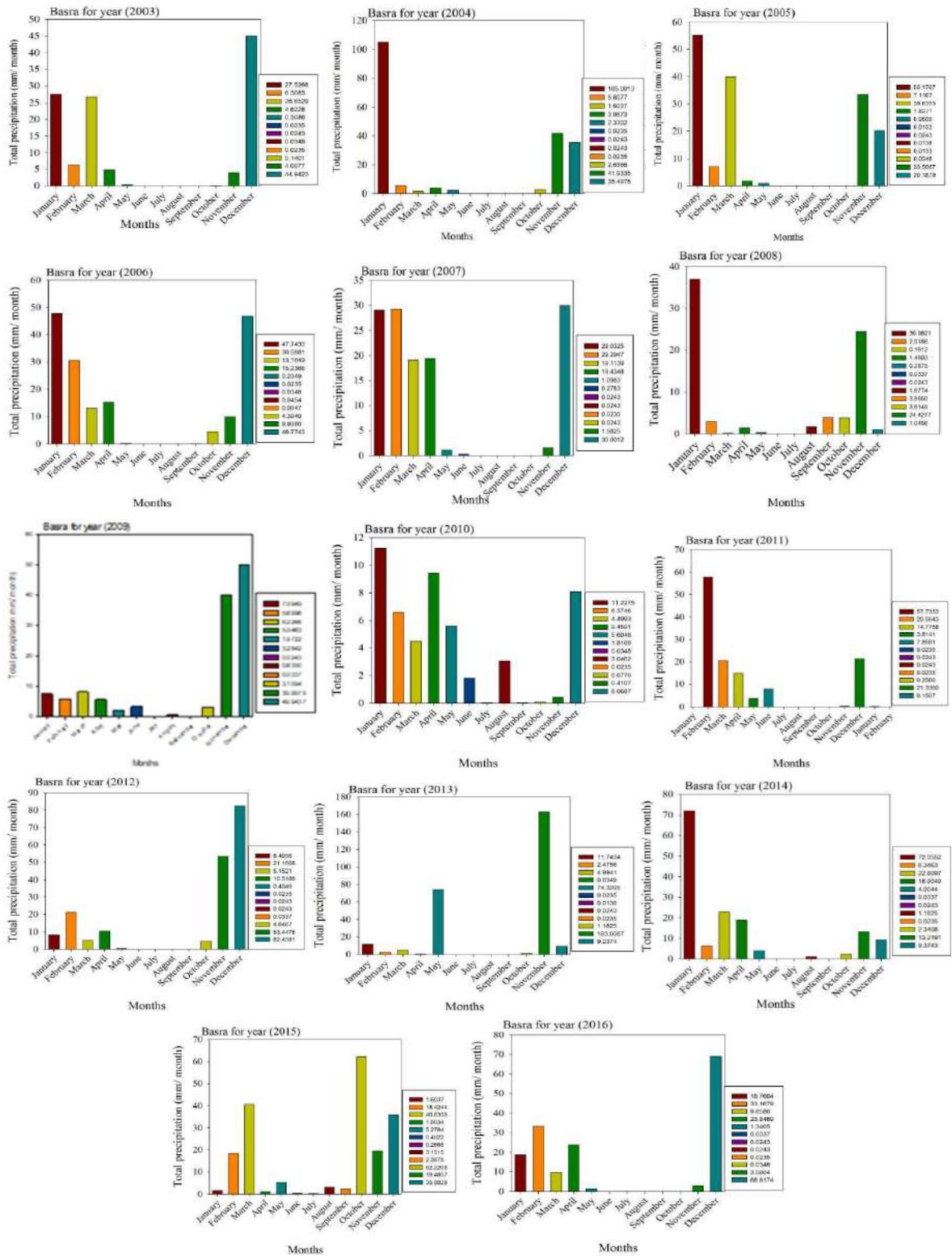
Fig. 3: The high monthly average of Tp of Basra station.
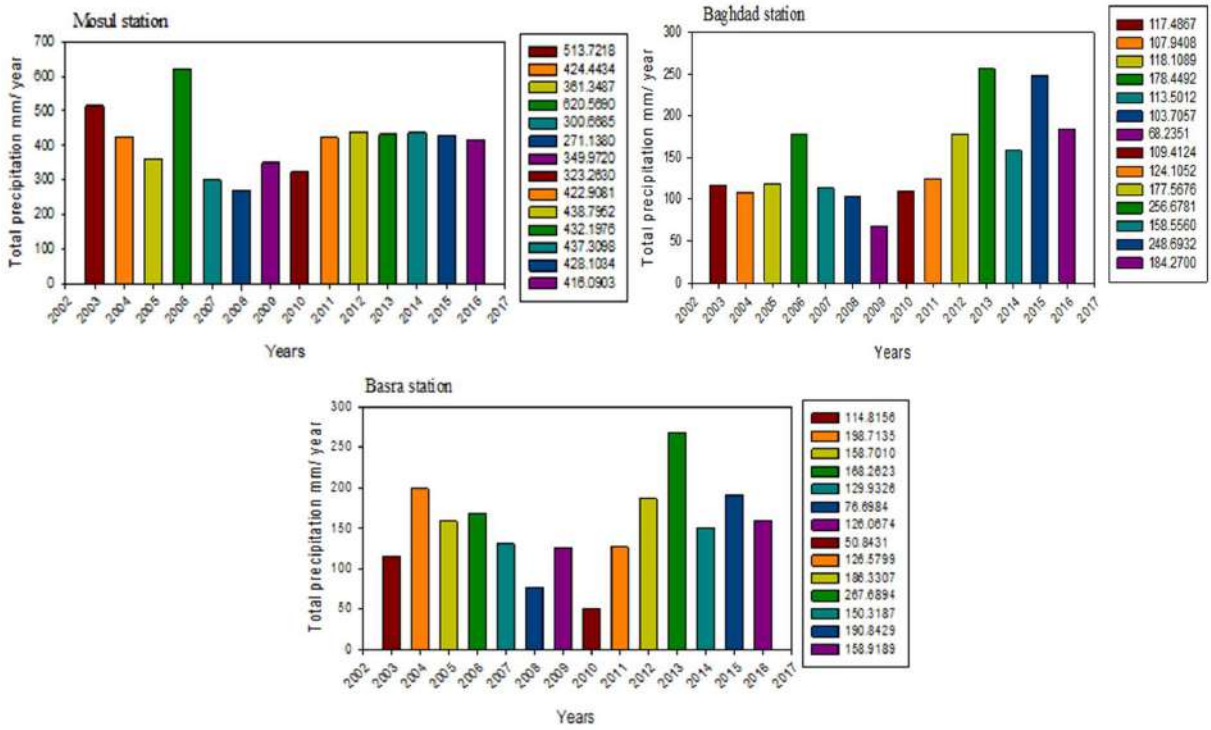
Fig. 4: The high yearly average of Tp for Iraqi stations (Mosul, Baghdad, and Basra) for the period (2003-2016).
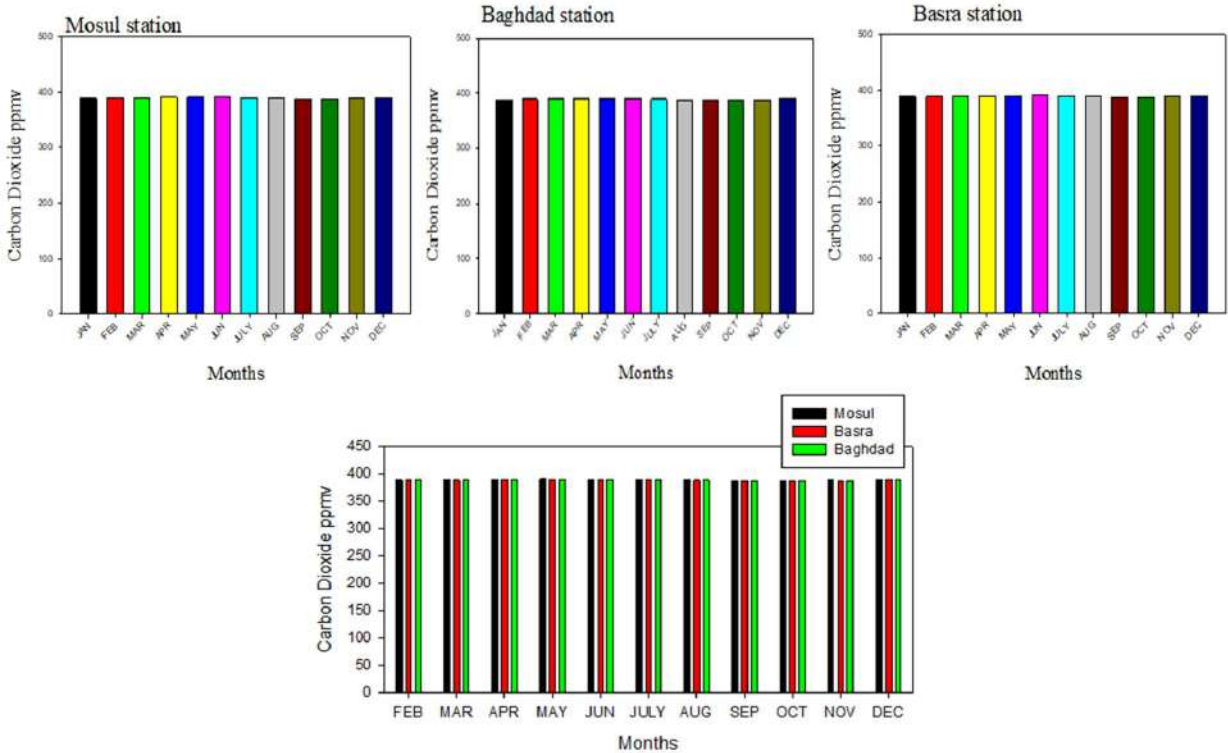

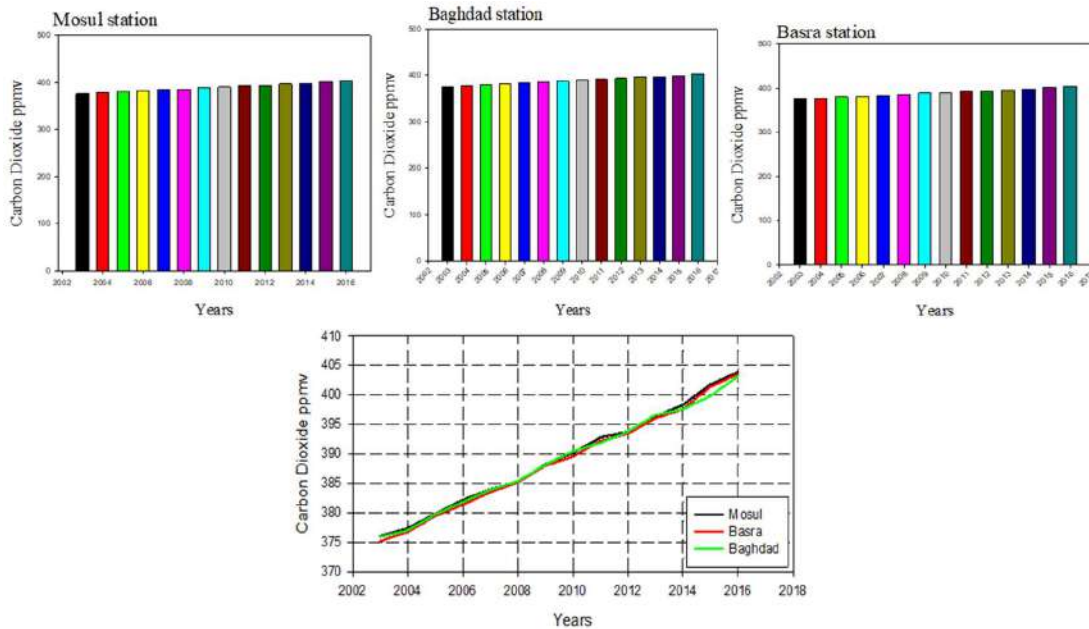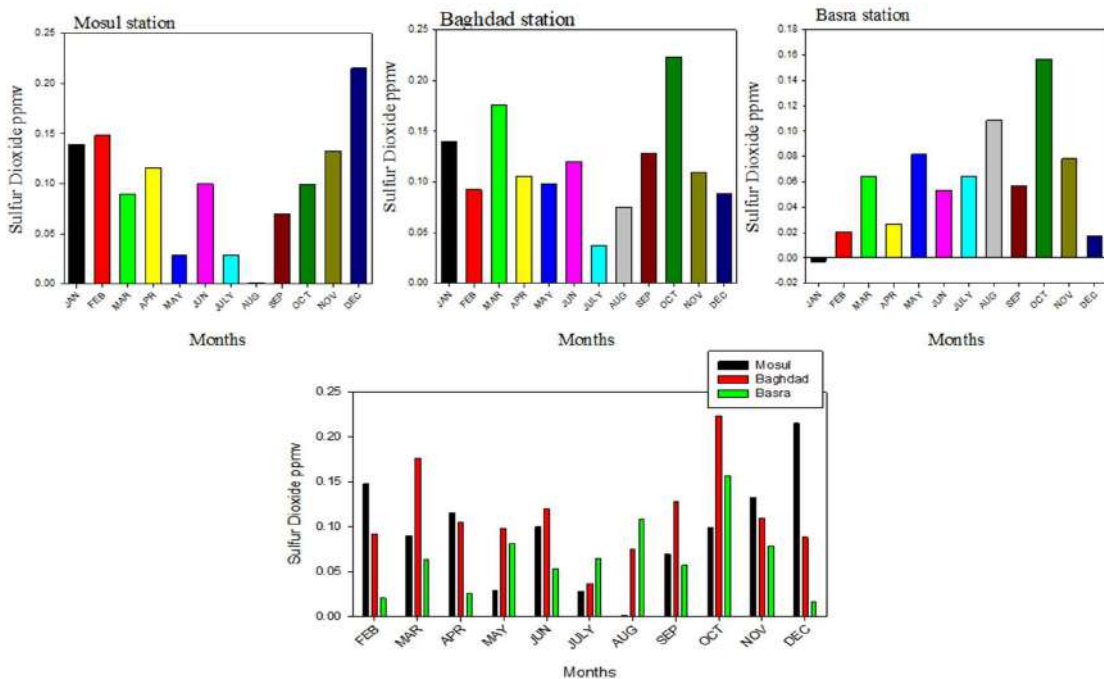Fig. 5: The monthly average of Carbon Dioxide for Iraqi stations (Mosul, Baghdad, and Basra).

Fig. 6: The year average of Carbon Dioxide for Iraqi stations (Mosul, Baghdad, and Basra) for the period (2003-2016).

different rates of concentrations of sulfur dioxide gas, indicating that the highest concentration rate was in October 2016, which is found in the atmosphere and is often found in large quantities in industrial and urban environments. The burning of fossil fuels is the primary source of sulfur dioxide, as its pollution reaches hazardous levels in and around industrialized areas, close to coal-fired power stations, and oil refineries. Exposure to sulfur dioxide increases the risk

Fig. 7: The monthly mean of sulfur dioxide for the Iraqi stations (Mosul, Baghdad, and Basra).
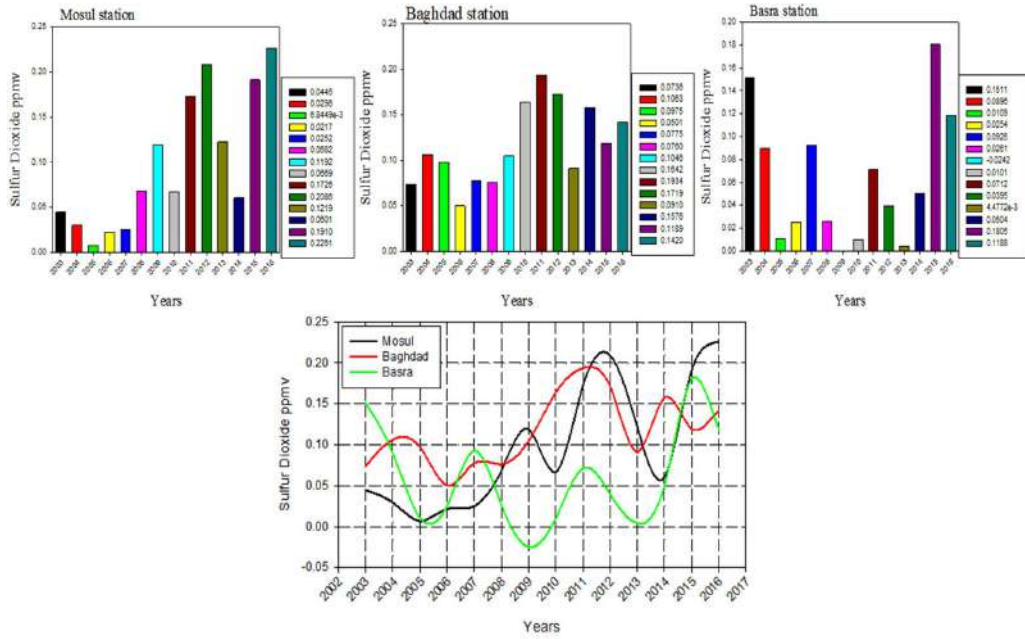
Fig. 8: The year means of sulfur dioxide for Iraqi stations (Mosul, Baghdad, and Basra) for the period (2003-2016).
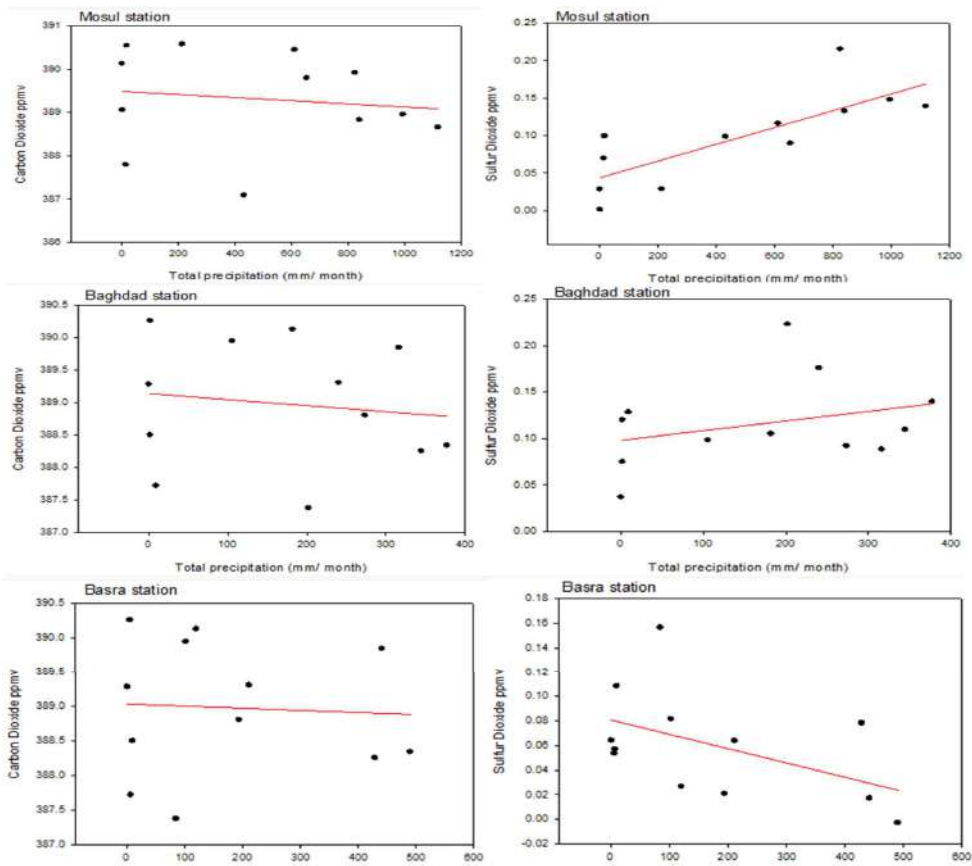

Fig. 9: The relation between the monthly average of CO_2, SO_2, and Tp for Iraqi stations (Mosul, Baghdad, and Basra).

Table 1: The relationship between CO_2, SO_2, and Tp for the 14 years over Iraq.

Station	Relation.	Spearman-rho		Linear Regression Simple	
		R	Correlation	P-value	Interpretation
Mosul	CO_2 vs Tp	-0.10	Very Low	0.0001	Linear
	SO_2 vs Tp	+0.70	High	0.0006	Linear
Baghdad	CO_2 vs Tp	-0.10	Very Low	0.0001	Linear
	SO_2 vs Tp	+0.40	Low	0.0013	Linear
Basra	CO_2 vs Tp	-0.10	Very Low	0.0001	Linear
	SO_2 vs Tp	-0.50	Medium	0.0034	Linear

of early mortality and illnesses like lung cancer, asthma, heart disease, and stroke. Additionally, it causes breathing problems, particularly for people with chronic illnesses (Singh & Agrawal 2007).

The Relationship Between the Monthly Rate of CO_2, SO_2, and Total Precipitation for Iraqi Stations for 2003-2016

Fig. 9, and Table 1 present the nature and degree of the correlation between Tp, CO_2, and SO_2 at the stations in Baghdad, Basra, and Mosul for the period from 2003 to 2016. The findings showed that the relationship between Tp with CO_2 and Tp with SO_2 for Baghdad station is inverse and positive.

The relationship between Tp with CO_2 and Tp with SO_2 for Basra station is inverse and the relationship between Tp with CO_2 and Tp with SO_2 for Mosul station is inverse and positive. That indicates a strong relation due to when solar radiation incident on sulfur water eyes will acts on water evaporate then cloud this led to form acid rain. Also, meteorological factors, and the nature of the region. The large presence of gases led to acid rain, which is caused by many pollutants.

CONCLUSIONS

Acid rain is created when sulfur-containing gases react. When sulfur dioxide and oxygen mix with UV radiation from the sun, the most significant of these processes produce sulfur trioxide, which reacts with atmospheric water vapor to make sulfuric acid. The relationship between Tp with CO_2 and Tp and SO_2 for Mosul station is inverse and positive was 0.7 due to sulfur water eyes. CO_2 was found throughout all months but with different ratios and the highest concentration in the 2016 year for all the stations. The largest amount of Tp occurred in November, December, January, February, March, and April months for Mosul, Baghdad, and Basra stations for the period (2003-2016). While was the highest amount of Tp occurred in 2013 in Baghdad and Basra. And 2006 in Mosul SO_2 was found throughout all

months but with different ratios and the highest concentration in October Month and 2016 year. The large presence of gases led to acid rain, which is caused by many pollutants.

ACKNOWLEDGMENTS

REFERENCES

Abbasi, T., Poornima, P., Kannadasan, T. and Abbasi, S., 2013. Acid rain: past, present, and future. *International Journal of Environmental Engineering*, 5, pp.229-272.

Abbood, Z.M., Al-Jiboori, M.H. and Al-Taai, O.T., 2023. Temporal and Spatial Analysis of Particulate Matter Concentrations in Iraq. *IOP Conference Series: Earth and Environmental Science*, 1215(1), 012018.

Abbood, Z.M. and Al-Taai, O.T., 2018. Calculation of absorption and emission of thermal radiation by clouds cover. *ARPN Journal of Engineering and Applied Sciences*, 13(24), pp.9446-9456.

Abbood, Z.M. and Al-Taai, O.T., 2022. Data analysis for cloud cover and rainfall over Baghdad city, Iraq. *Plant Archives*, 20(1), pp.822-826.

Al-Jaf, S.J. and Al-Taai, O.T., 2019. Impact of carbon dioxide concentrations on atmospheric temperature changes over Iraq and some neighboring countries. *Plant Archives*, 19, pp.1450–1456.

Al-Taai, O.T. and Abbood, Z.M., 2020. Analysis of convective available potential energy by convective and total precipitation over Iraq. *Indian Journal of Ecology*, 47(10), pp.263-269.

Al-Taai, O.T. and Abbood, Z.M., 2020. Analysis of the convective available potential energy by precipitation over Iraq using ECMWF data for the period of 1989–2018. *Scientific Review Engineering and Environmental Sciences*, 29(2), pp.196-211.

Al-Taai, O.T., Abbood, Z.M. and Kadhum, J.H., 2021. Determination Stability Potential Energy of Thunderstorms for Some Severe Weather Forecasting Cases in Baghdad City. *Journal of Green Engineering (JGE)*, 11(1), pp.779-794.

Chan, H.R., Chupp, B.A., Cropper, M.L. and Muller, N.Z., 2018. The impact of trading on the costs and benefits of the Acid Rain Program. *Journal of Environmental Economics and Management*, 88, pp.180-209.

Chen, M.C., Wang, K. and Xie, L., 2013. Deterioration mechanism of cementitious materials under acid rain attack. *Engineering Failure Analysis*, 27, pp.272-285.

Chestnut, L.G. and Mills, D.M., 2005. A fresh look at the benefits and costs of the US acid rain program. *Journal of Environmental Management*, 77, pp.252-266.

Grennfelt, P., Engleryd, A.M., Forsius, Hov, O., Rodhe, H. and Cowling, E., 2020. Acid rain and air pollution: 50 years of progress in environmental science and policy. *Ambio*, 49, pp.849-864.

Hajer, M.A., 2002. Discourse coalitions and the institutionalization of practice: the case of acid rain in Great Britain. *Argument turn policy anal plan*, pp.51-84.

Hames, R.S., Rosenberg, K.V., Lowe, J.D., Barker, S.E. and Dhondt, A.A., 2002. Adverse effects of acid rain on the distribution of the Wood Thrush *Hylocichla mustelina* in North America. *Proceedings of the National Academy of Sciences*, 99, pp.11235-11240.

Hashim, S.A., Kadhum, J.H., Abbood, Z.M., Al-Taai, O.T. and Nassif, W.G., 2023. Determination of the Dynamics of Thunderstorms Through the Dry Adiabatic Lapse Rate and Environmental Lapse Rate. *Nature Environment and Pollution Technology*, 22(3), pp. 1447–1455.

Larssen, T. and Carmichael, G., 2000. Acid rain and acidification in China: the importance of base cation deposition. *Environmental Pollution*, 110, pp.89-102.

Livingston, R.A., 2016. Acid rain attack on outdoor sculpture in perspective. *Atmospheric Environment*, 146, pp.332-345.

Mahdi, Z.S., Abbood, Z.M. and Al-Taai, O.T., 2021. Thunderstorm Dynamic Analysis based on Total Precipitation over Iraq. *Journal of Engineering Science and Technology*, 16, pp.62–70.

Nagase, Y. and Silva, E.C., 2007. Acid rain in China and Japan: A game-theoretic analysis. *Regional Science and Urban Economics*, 37, pp.100-120.

Nassif, W.G., Jasim, F.H. and Al-Taai, O.T., 2021. Analysis of air temperature, relative humidity and evaporation over Iraq using ECMWF reanalysis. *Indian Journal of Ecology*, 48(2), pp.446–452.

Nassif, W.G., Lagenean, F.H.S. and Al-Taai, O.T., 2023. Impact of vegetation cover on climate change in different regions of Iraq. *Caspian Journal of Environmental Sciences*, 21(2), pp.333-342.

Singh, A. and Agrawal, M., 2007. Acid rain and its ecological consequences. *Journal of Environmental Biology*, 29, pp.15.

Yehia, M.A., Al-Taai, O.T. and Ibrahim, M.K., 2022. The Chemical Behavior of Greenhouse Gases and its Impact on Climate Change in Iraq. *Egyptian Journal of Chemistry*, 65, pp.1373-1382.

Zhang, X., Jiang, H., Jin, J., Xu, X. and Zhang, Q., 2012. Analysis of acid rain patterns in northeastern China using a decision tree method. *Atmospheric Environment*, 46, pp.590-596.

... Continued from inner front cover

- The text of the manuscript should run into Abstract, Introduction, Materials & Methods, Results, Discussion, Acknowledgement (if any) and References or other suitable headings in case of reviews and theoretically oriented papers. However, short communication can be submitted in running with Abstract and References. The references should be in full with the title of the paper and mentioning names of all the authors.

- The figures should preferably be made on a computer with high resolution and should be capable of withstanding a reasonable reduction with the legends provided separately outside the figures. Photographs may be black and white or colour.

- Tables should be typed separately bearing a short title, preferably in vertical form. They should be of a size, which could easily be accommodated in the page of the Journal.

- References in the text should be cited by the authors' surname and year. In case of more than one reference of the same author in the same year, add suffix a,b,c,.... to the year. For example: (Thomas 1969, Mass 1973a, 1973b, Madony et al. 1990, Abasi & Soni 1991).

List of References

The references cited in the text should be arranged alphabetically by authors' surname in the following manner: (Note: The titles of the papers should be in running 'sentence case', while the titles of the books, reports, theses, journals, etc. should be in 'title case' with all words starting with CAPITAL letter). The references should be given in the **"Harvard Pattern"** as exemplified below.

- Dutta, A. and Chaudhury, M., 1991. Removal of arsenic from groundwater by lime softening with powdered coal additive. *Journal of Water Supply: Research and Technology—Aqua*, 40(1), pp.25-29. **(For Papers Published in Journals)**

- Goel, P.K., 2006. *Water pollution: Causes, Effects and Control*. New age international, New Delhi. **(For Authored Books)**

- Environmental Protection Agency (EPA), 2023. Air Quality and Pollution Data. Retrieved June 25, 2024, from https://www.epa.gov/air-quality-and-pollution-data **(For Data Retrieved from a Website)**

- Hammer, D.A. (ed.), 1989. *Constructed Wetlands for Wastewater Treatment-Municipal, Industrial and Agricultural*. Lewis Publishers Inc., pp.831. **(For Edited Book)**

- Haynes, R.J., 1986. Surface mining and wetland reclamation. In: J. Harper and B. Plass (eds.) *New Horizons for Mined Land Reclamation*. Proceedings of a National Meeting of the American Society for Surface Reclamation, Princeton, W.V. **(For Papers published in Edited Books)**

Submission of Papers

- The paper has to be submitted online in a single WORD file through the online submission portal of journal's website: **www.neptjournal.com**

Attention

1. Any change in the authors' affiliation may please be notified at the earliest.
2. Please make all the correspondence by e-mail, and authors should always quote the manuscript number.

Note: In order to speed up the publication, authors are requested to correct the galley proof immediately after receipt. The galley proof must be checked with utmost care, as publishers owe no responsibility for mistakes. The papers will be put on priority for publication only after receiving the processing and publication charges.

For further details of the Journal, please visit the website. All the papers published on a particular subject/topic or by any particular author in the journal can be searched and accessed by typing a keyword or name of the author in the 'Search' option on the Home page of the website. All the papers containing that keyword or author will be shown on the home page from where they can be directly downloaded.

www.neptjournal.com